Transactions of the ASME®

Transactions of the ASME, Journal of Heat Transfer (ISSN 0022-1481) is published quarterly (Feb., May, Aug., Nov.) for $165.00 per year by The American Society of Mechanical Engineers, 345 East 47th Street, New York, NY 10017. Second class postage paid at New York, NY and additional mailing offices. POSTMASTER: Send address changes to Transactions of the ASME, Journal of Heat Transfer, c/o THE AMERICAN SOCIETY OF MECHANICAL ENGINEERS, 22 Law Drive, Box 2300, Fairfield, NJ 07007-2300.
CHANGES OF ADDRESS must be received at Society headquarters seven weeks before they are to be effective. Please send old label and new address.
PRICES: To members, $40.00, annually: to nonmembers, $165.00. Add $24.00 for postage to countries outside the United States and Canada.
STATEMENT from By-Laws. The Society shall not be responsible for statements or opinions advanced in papers or . . . printed in its publications (B7.1, para. 3).
 INDEXED by Applied Mechanics Reviews and Engineering Information, Inc.
Canadian Goods & Services Tax Registration #126148048.

Journal of Heat Transfer

Published Quarterly by The American Society of Mechanical Engineers

VOLUME 115 • NUMBER 3 • AUGUST 1993

ANNOUNCEMENTS

548 Errata on a previously published paper by A. Kar, C. L. Chan, and J. Mazumder

706 Change of address form for subscribers

762 Announcement: 7th International Symposium on Transport Phenomena in Manufacturing Processes

Inside back cover Information for authors

TECHNICAL PAPERS

Thermal Conduction

526 Thermal Waves Emanating From a Fast-Moving Heat Source With a Finite Dimension
D. Y. Tzou and J. Li

533 Thermal Gap Conductance of Conforming Surfaces in Contact
S. Song, M. M. Yovanovich, and F. O. Goodman

541 Kinetic Theory Analysis of Flow-Induced Particle Diffusion and Thermal Conduction in Granular Material Flows
S. S. Hsiau and M. L. Hunt

Forced Convection and Heat Exchangers

549 Eddy Diffusivity Based Comparisons of Turbulent Prandtl Number for Boundary Layer and Free Jet Flows With Reference to Fluids of Very Low Prandtl Number
K. Bremhorst and L. Krebs

553 Analytic Prediction of the Friction and Heat Transfer for Turbulent Flow in Axial Internal Fin Tubes
Nae-Hyun Kim and R. L. Webb

560 Local Heat Transfer Distribution in a Rotating Serpentine Rib-Roughened Flow Passage
N. Zhang, J. Chiou, S. Fann, and W.-J. Yang

568 An Experimental Study on Heat/Mass Transfer and Pressure Drop Characteristics for Arrays of Nonuniform Plate Length Positioned Obliquely to the Flow Direction
Huai-Zhang Huang and Wen-Quan Tao

576 Enhanced Heat Transfer, Missing Pin, and Optimization for Cylindrical Pin Fin Arrays
B. A. Jubran, M. A. Hamdan, and R. M. Abdualh

584 Crystallization Fouling in Plate Heat Exchangers
B. Bansal and H. Müller-Steinhagen

Natural Convection

592 Experimental and Numerical Studies of Natural Convection With Flow Separation in Upward-Facing Inclined Open Cavities
R. A. Showole and J. D. Tarasuk

606 Combined Heat and Mass Transfer by Natural Convection With Opposing Buoyancies
R. L. Mahajan and D. Angirasa

613 Internal Standing Waves in a Cylindrical Vessel and Their Near-Wall Features
S. Ushijima, S. Moriya, and N. Tanaka

621 Analysis of a Transient Asymmetrically Heated/Cooled Open Thermosyphon
G. F. Jones and J. Cai

631 Three-Dimensional Natural Convection in a Confined Fluid Overlying a Porous Layer
A. K. Singh, E. Leonardi, and G. R. Thorpe

639 Three-Dimensional Free Convection in a Long Rotating Porous Box: Analytical Solution
P. Vadasz

Radiative Transfer

645 Nongray Gas Analyses for Reflecting Walls Utilizing a Flux Technique
J. A. Menart and HaeOk Skarda Lee

653 A Study of In Situ Specific Absorption Coefficients of Soot Particles in Laminar Flat Flames
Y. R. Sivathanu, J. P. Gore, J. M. Janssen, and D. W. Senser

Boiling, Condensation, and Evaporation

659 Effect of Surface Wettability on Active Nucleation Site Density During Pool Boiling of Water on a Vertical Surface
C. H. Wang and V. K. Dhir

670 On the Gas Entrapment and Nucleation Site Density During Pool Boiling of Saturated Water
C. H. Wang and V. K. Dhir

(Contents continued)

680 Forced Convection Boiling of Nonazeotropic Refrigerant Mixtures Inside Tubes
K. Murata and K. Hashizume

690 Direct-Contact Condensation of Low-Density Steam on Seawater at High Inlet Noncondensable Concentrations
F. Zangrando and D. Bharathan

699 Droplet Vaporization in a High-Pressure Gas
J. P. Hartfield and P. V. Farrell

707 Evaporation of Multicomponent Drop Arrays
K. Annamalai, W. Ryan, and S. Chandra

717 Heat Transfer From a Molten Phase to an Immersed Coal Particle During Devolatilization
R. H. Hurt, T. H. Fletcher, and R. S. Sampaio

Transport in Porous Media

724 Effects of Moisture on Temperature During Drying of Consolidated Porous Materials
F. Kallel, N. Galanis, B. Perrin, and R. Javelas

734 Steam Injection Into a Slow Water Flow Through Porous Media
M. Chung and I. Catton

744 A Numerical Investigation of Premixed Combustion Within Porous Inert Media
P.-F. Hsu, J. R. Howell, and R. D. Matthews

Applications

751 Experimental Investigation of Micro Heat Pipes Fabricated in Silicon Wafers
G. P. Peterson, A. B. Duncan, and M. H. Weichold

757 Heat Transfer and Thermoelectric Voltage at Metallic Point Contacts
P. E. Phelan, O. Nakabeppu, K. Ito, K. Hijikata, T. Ohmori, and K. Torikoshi

TECHNICAL NOTES

763 Thermal Contact Resistance Between Two Flat Surfaces That Squeeze a Film of Lubricant
A. Bejan and Al. M. Morega

767 Theory of Multilayers Heated by Laser Absorption
K. D. Cole and W. A. McGahan

771 Melting of Snow With Double Effect of Temperature and Concentration
M. Sugawara and S. Sasaki

775 Unification of Source-and-Sink Method and Boundary Element Method for the Solution of Potential Problems
C. K. Hsieh

777 Freezing of the NaCl-H_2O Binary Compound From Above in a Partially Open Cylindrical Geometry
K. Medjani and R. G. Watts

782 The Effects of Moderately Strong Acceleration on Heat Transfer in the Turbulent Rough-Wall Boundary Layer
W. Chakroun and R. P. Taylor

785 Heat and Mass Transfer With Dehumidification in Laminar Boundary Layer Flow Along a Cooled Flat Plate
M. A. Yaghoubi, H. Kazeminejad, and A. Farshidiyanfar

788 Heat Transfer Characteristics in a Wavy-Walled Channel
N. Saniei and S. Dini

792 Effects of a Slit in a Rib on the Heat Transfer From a Rib-Mounted Wall
M. K. Chyu and V. Natarajan

796 The Effect of Torsion on Convective Heat Transfer in a Helicoidal Pipe
G. Yang, Z. F. Dong, and M. A. Ebadian

800 A Numerical Study of Two-Dimensional High Rayleigh Number Natural Convection Between Two Reservoirs Connected by a Horizontal Duct
G.-F. Yao and J. A. Khan

803 Three-Dimensional Mixed Convection in a Horizontal Chemical Vapor Deposition Reactor
K. C. Karki, P. S. Sathyamurthy, and S. V. Patankar

807 Natural Convection Within Spherical Annuli by Symbolic Algebra
K. G. TeBeest, S. A. Trogdon, and R. W. Douglass

810 Convective Instability in a Porous Enclosure With a Horizontal Conducting Baffle
Falin Chen and C. Y. Wang

813 On the Hot-Spot-Controlled Critical Heat Flux Mechanism in Saturated Pool Boiling: Part II—The Influence of Contact Angle and Nucleation Site Density
C. Unal, P. Sadasivan, and R. A. Nelson

816 Boundary Conditions for an Evaporating Thin Film for Isothermal Interfacial Conditions
H. C. Chebaro and K. P. Hallinan

819 Conjugate Modeling of High-Temperature Nosecap and Wing Leading Edge Heat Pipes
Y. Cao and A. Faghri

Thermal Waves Emanating From a Fast-Moving Heat Source With a Finite Dimension

D. Y. Tzou
Associate Professor.
Mem. ASME

J. Li
Postdoctoral Fellow.

Department of Mechanical Engineering,
University of New Mexico,
Albuquerque, NM 87131

Characteristics of thermal waves emanating from a fast-moving heat source are studied in this paper. The heat source is assumed to occupy a finite region to model real situations in local heating. Analytical solutions are obtained respectively for a heat source moving in the subsonic, transonic, and supersonic regimes. The Green's functions obtained previously from a point source are used to generate temperature distributions for all cases. The temperature jump across the shock surface is found to be weaker than the case with a point heat source, while the swinging phenomenon for the temperature variations with the thermal Mach number still exists.

Introduction

Local heating is an important phenomenon in the interdisciplinary areas of engineering science. Especially for the heat source with a high intensity impinging upon a small area, the heat flux is large and the temperature rise in the local area may be significant. The elevated temperature may alter the thermomechanical properties of the medium due to their sensitivity to temperature. A detailed understanding of the temperature distribution in the vicinity of the heat source, therefore, is necessary for quantifying the thermomechanical performance of a structural component. Typical examples for this type of problem include short-pulse laser heating on metals, high-speed grinding, high-speed friction in penetration, and plastic heating induced by dynamic crack propagation. These examples are referred to here for emphasizing the *rate* effect in local heating. The most obvious environment involving high-rate heating may be the relative motion between the heating agent and the object. The heat source in this case quickly propagates on the surface of a solid and the thermal energy dissipates into the surrounding media before the heat source escapes. The rate of heating in this situation, obviously, increases with the speed of the moving heat source. Although this problem is traditional in heat conduction theory employing Fourier's law, Tzou (1989a, b; 1990a; 1991) analyzed the wave effect in response to high-rate heating. The swinging phenomenon for temperatures in transition of the thermal Mach number from subsonic to supersonic ranges and the physical mechanisms of thermal shock formation are rate effects, which cannot be depicted by diffusion. Extended later to the problem of local heating induced by dynamic crack propagation, the transonic solution obtained by Tzou (1990b, c) yields perfect agreement with the experimental results obtained by Zehnder and Rosakis (1991). Because the transonic wave solution does capture several unusual behaviors for the temperature distribution in the near-tip region; moreover, the speed of heat propagation in 4340 steel at 450°C is estimated as 900 m/s. This value confirms the analytical expression obtained by Tzou and Özişik (1992) and Özişik and Tzou (1992) when compared to the microscopic two-step model. The rate effect of temperature waves may become pronounced even for a stationary heat source. For short-pulse (on the order of picoseconds) laser heating on metals, Qiu and Tien (1992) demonstrated the effect of nonequilibrium temperature on the reflectivity of the surfaces subjected to laser irradiation. Again, the classical diffusion theory cannot capture the essential features in high-rate heating.

Wave behavior in heat conduction is one of the most important features in high-rate heating. Motivated by Maxwell (1867) in his work of the dynamic theory of gases, Vernotte (1958, 1961) is one of the pioneers in the development of the field of heat conduction. Since then, wave theory has been examined from various physical points of view. These works have been categorized in detail according to their nature and individual emphases in a recent work by Özişik and Tzou (1992). In addition, the review articles by Joseph and Preziosi (1989, 1991) and Tzou (1992a) provide sufficient and thorough surveys on the past research. They will not be repeated here. Also, the most important issue in the wave theory of heat conduction, namely the physical meaning and engineering interpretation of the relaxation time, is explored by Tzou (1992b). It is extended from the irreversible thermodynamics by Jou et al. (1988). These works provide a firm foundation for the engineering applications of the thermal wave theory.

The present paper studies the temperature waves emanating from a fast-moving, heat-generation zone. It is concerned with the evolution of temperature distributions as the speed of the heating zone transits from the subsonic, transonic, to the supersonic regions. The speed of heat-generation zone will be characterized with respect to the speed of heat propagation. The thermal Mach number is defined for this purpose. The point-source solution obtained previously by Tzou (1989a, b) in the respective region will be used as the Green's function to generate the temperature distributions. Special applications of the results are illustrated through the heat-generation zone with a circular geometry and possessing a constant intensity of heating. Projecting at future extensions to the high-speed penetration and rapid crack propagation, we emphasize the wave phenomenon in 4340 steel.

The Green's Function

The thermal wave equation governing the temperature distribution around a moving point heat source is (Tzou, 1989a, b)

$$(1-\mathrm{M}^2)T_{,11}+T_{,22}+2cT_{,1} = -\frac{Q}{\rho\,\alpha\,C_p}\left[\delta(x_1)\delta(x_2)-\left(\frac{\mathrm{M}^2}{2c}\right)\delta_{,1}(x_1)\delta(x_2)\right] \quad (1)$$

where (x_1, x_2) are the material coordinates convecting with the heat generating zone as shown in Fig. 1, c a parameter defined as $c=v/2\alpha$, and M the thermal Mach number, defined as $\mathrm{M}=v/C$, with C being the thermal wave speed. The subscripts in this work denote differentiations. $T_{,11}$, for example, is $\partial^2 T/\partial x_1^2$. The two terms involving M^2 in Eq. (1) result from

Contributed by the Heat Transfer Division for publication in the JOURNAL OF HEAT TRANSFER. Manuscript received by the Heat Transfer Division August 1992; revision received February 1993. Keywords: Conduction. Associate Technical Editor: Y. Bayazitoglu.

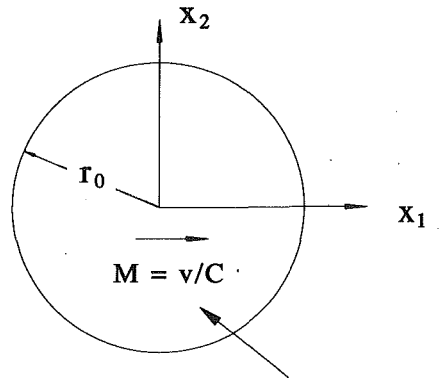

Fig. 1 A moving circular region with speed v that generates heat with a constant intensity

the wave effect in heat propagation. The apparent heat source, derivative of $\delta(x_1)$ with respect to x_1, provides additional heating besides the real heat source applied to the solid (Frankel et al., 1985). The mathematical type of Eq. (1) depends on the thermal Mach number M. For the classical diffusion model assuming an infinite wave speed ($C \to \infty$), the thermal Mach number is zero and Eq. (1) reduces to the diffusion equation. In the subsonic region with $M<1$, the equation is elliptic. In transition to the transonic ($M=1$) and the supersonic ($M>1$) regions, respectively, the equation transits to a parabolic and a hyperbolic type. An intrinsic difference in the temperature distributions, therefore, is expected in the three regions of the thermal Mach number.

The temperature distributions depicted by Eq. (1) has been obtained by Tzou (1989a, b). In summary, they are

$$\frac{T(x_1, x_2)}{Q/(\rho\sigma C_p)} = \exp[-cx_1/(1-M^2)] \cdot \left\{\frac{2-M^2}{2(1-M^2)} K_0\left[\frac{cr}{\sqrt{1-M^2}}\right] - \frac{M^2}{2(1-M^2)} K_1\left[\frac{cr}{\sqrt{1-M^2}}\right]\right\}$$

in the subsonic region with $M<1$; (2)

$$\frac{T(x_1, x_2)}{Q/(\rho\alpha C_p)} = \frac{1}{\sqrt{8\pi c}} \exp[cx_2^2/(2x_1)] \cdot \left\{\frac{1}{\sqrt{-x_1}} + \frac{cx_2^2 + x_1}{4c\sqrt{(-x_1)^5}}\right\}$$

at the transonic stage with $M=1$; (3)

$$\frac{T(x_1, x_2)}{Q/(\rho\alpha C_p)} = -\exp[cx_1/(M^2-1)] \cdot \left\{\frac{2-M^2}{2(M^2-1)} K_0\left[\frac{cr}{\sqrt{M^2-1}}\right] - \frac{M^2}{2(M^2-1)} K_1\left[\frac{cr}{\sqrt{M^2-1}}\right]\right\}$$

in the supersonic region with $M>1$. (4)

The quantity r in Eqs. (2) and (4) is the distance in the stretched hypospace. It is defined as, respectively,

$$r = \sqrt{\frac{x_1^2}{1-M^2} + x_2^2} \quad \text{for} \quad M<1$$

$$\text{and} \quad r = \sqrt{\frac{x_1^2}{M^2-1} - x_2^2} \quad \text{for} \quad M>1. \quad (5)$$

While r is well defined everywhere in the subsonic region, the condition

$$\frac{x_1^2}{M^2-1} > x_2^2 \quad \text{or} \quad \theta < \sin^{-1}\left(\frac{1}{M}\right) = \theta_M \quad (6)$$

must be satisfied for r to be well defined in the supersonic region. The polar angle θ in Eq. (6) is measured from the *trailing* edge of the point heat source in a clockwise sense. Equation (6) defines the physical domain of the *heat-affected zone* in which Eq. (4) applies. The rest of the physical domain is defined as the *thermally undistributed zone* where temperature remains at the reference level due to the finite speed of heat propagation. When the value of M approaches one, i.e., at the transonic stage, the θ value in Eq. (6) approaches 90 deg and the heat-affected zone is confined to the domain of $x_1<0$. Equation (5) applies in this case. Note also that a strong singularity in temperature exists at the thermal *shock* surface at $\theta = \sin^{-1}(1/M)$ for $M \geq 1$. It results from the mathematical idealization of a point heat source without a physical dimension. Nonetheless, the angle θ does reveal the *preferential* direction for the accumulation of thermal energy when the transient time is short (Tzou, 1990b).

Nomenclature

A = area, m^2
c = parameter = $v/2\alpha$, 1/m
C = thermal wave speed, m/s
C_p = heat capacity, kJ/kg-°C
F, G = combined functions
k = thermal conductivity, W/m-°C
K_i = modified Bessel function of the second kind of order i, $i=0, 1$
M = thermal Mach number
q = volumetric heat rate, W/m^3
Q = heat source density per unit length, W/m
r = distance in the hypospace, m
R = distance between the differential heat source and the observation point in the hypospace, m
R^* = dimensionless R
r_0 = radius of the circular heating zone, m
s = dimensionless radial distance centered at the origin of the heat source
t = physical time, s
T = temperature, °C
v = speed of the moving heat source, m/s
x_i = physical coordinates centered at the origin of the heat source, m; $x=1, 2$
α = thermal diffusivity, m^2/s
δ = dimensionless distance
η = radial distance measured from the center of the heat source, m
γ = polar angle centered at the observation point, rad
θ = polar angle measured from the trailing edge of the heat source, rad
θ_M = thermal shock angle = $\sin^{-1}(1/M)$, rad
ϕ = polar angle centered at the origin of the heat source, rad
ρ = mass density, kg/m^3
ξ_i = dimensionless coordinates centered at the origin of the heat source; $i=1, 2$
ζ = dimensionless radial distance centered at the observation point

Subscripts and Superscripts

$(\ ),_i$ = differentiations with respect to x_i; $x=1, 2$

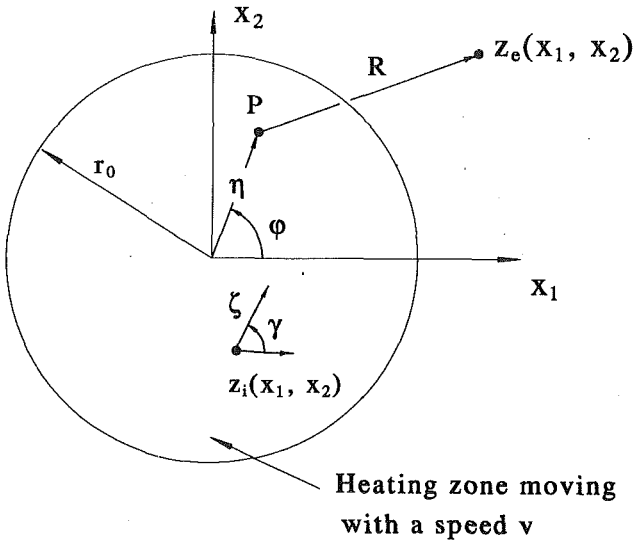

Fig. 2 Polar coordinates (η, ϕ) for the exterior observation points z_e and (ζ, γ) for the interior observation points z_i

Superposition

The point-source solutions represented by Eqs. (2)-(4) can be used as the Green's function to integrate the temperature distributions in a heating zone with a finite dimension. Without loss in generality, we exemplify this procedure by considering a circular-shaped source with a radius r_0 moving at a constant speed v. The heat generation is assumed to be constant within the circular area as shown in Fig. 1. Because the temperature possesses different expressions in the three regions of the thermal Mach number, the temperature distributions must be integrated individually in the subsonic, transonic, and supersonic regions.

(a) The Subsonic Case With $M<1$. Consider a differential heat source $Q=q\,dA$ located at P as shown in Fig. 2. In terms of the polar coordinates (η, ϕ) centered at the origin of the circular region, the differential surface area dA is $\eta\,d\eta\,d\phi$. The resulting temperature rise at an observation point (either z_e or z_i) located at (x_1, x_2) is then the integral contribution from all the differential heat sources within the circular region:

$$T(x_1, x_2)=\frac{q}{\rho\alpha C_p}\int_0^{2\pi}\int_0^{r_0}\exp[-c(x_1-\eta\cos\phi)/(1-M^2)]\cdot\left\{\frac{2-M^2}{2(1-M^2)}K_0\left[\frac{cR}{\sqrt{1-M^2}}\right]-\frac{M^2}{2(1-M^2)}K_1\left[\frac{cR}{\sqrt{1-M^2}}\right]\right\}\eta\,d\eta\,d\phi \quad \text{for } M<1 \tag{7}$$

where

$$R=\sqrt{\frac{(x_1-\eta\cos\phi)^2}{1-M^2}+(x_2-\eta\sin\phi)^2}. \tag{8}$$

The radius r_0 of the heating zone may be very small in practice. The characteristic dimension of the plastic zone around a moving crack tip from which heat is generated due to intensified plasticity, for example, is on the order of nanometers (Weichert and Schönert, 1974, 1978). In order to develop the present formulation to handle this situation, we normalize all the length parameters with respect to the radius r_0:

$$s=\frac{\eta}{r_0},\quad \xi_1=\frac{x_1}{r_0},\quad \xi_2=\frac{x_2}{r_0}. \tag{9}$$

Equation (7) then becomes

$$T(\xi_1, \xi_2)=\frac{q r_0^2}{\rho\alpha C_p}\int_0^{2\pi}\int_0^{1}\exp[-cr_0(\xi_1-s\cos\phi)/(1-M^2)]\cdot\left\{\frac{2-M^2}{2(1-M^2)}K_0\left[\frac{cr_0R^*}{\sqrt{1-M^2}}\right]-\frac{M^2}{2(1-M^2)}K_1\left[\frac{cr_0R^*}{\sqrt{1-M^2}}\right]\right\}s\,ds\,d\phi \quad \text{for } M<1 \tag{10}$$

with

$$R^*=\sqrt{\frac{(\xi_1-s\cos\phi)^2}{1-M^2}+(\xi^2-s\sin\phi)^2}. \tag{11}$$

Numerical integrations are necessary due to complexity of the integrand in Eq. (10). For the observation points (z_e in Fig. 2) in the exterior of the heating zone, a direct numerical integration can be applied by the regular Gaussian quadrature formula. For the observation points inside the heating zone, on the other hand, a special treatment is needed since Eq. (10) contains a singularity at $R^*=0$. It implies that the observation point coincides with the differential heat source in this case, or mathematically, $\xi_1=s\cos\phi$ and $\xi_2=s\sin\phi$. The origin of the coordinate system is first shifted to the observation point z_i. The new polar coordinates (ζ, γ) relate the the old (s, ϕ) coordinates by

$$s=\sqrt{(\zeta\cos\gamma+\xi_1)^2+(\zeta\sin\gamma+\xi_2)^2},\quad \tan\phi=\frac{\zeta\sin\gamma+\xi_2}{\zeta\cos\gamma+\xi_1}, \tag{12}$$

and the integrand in Eq. (10) can be expressed in terms on ζ and γ. Accordingly, the domains of integrations are changed to

$$0\le\gamma\le 2\pi$$

and

$$0\le\zeta\le\sqrt{1+\xi_1\xi_2\sin 2\gamma-(\xi_1\sin\gamma)^2-(\xi_2\cos\gamma)^2}-(\xi_1\cos\gamma+\xi_2\sin\gamma). \tag{13}$$

The integration with respect to γ is well behaved and the regular Gaussian quadrature formula can be applied. The singular part of the integration with respect to ζ is now reduced to the type of

$$\int_0^1\ln\left(\frac{1}{\zeta}\right)f(\zeta)\,d\zeta \tag{14}$$

where $f(\zeta)$ is *bounded* at $\zeta=0$. The logarithmic Gaussian quadrature formula is then readily applicable for this type of numerical integration (Stroud and Secrest, 1966, for example).

(b) The Supersonic Case with $M>1$. The procedure of integrations for temperature in the supersonic region is similar to those in the subsonic region. The temperature expression in Eq. (10), of course, is replaced by Eq. (4) with $M>1$. Due to the formation of the thermally undisturbed zone for $\theta\in[0,\sin^{-1}(1/M)]$ (refer to Eq. (6)), however, the domains of integrations need to be carefully examined. Any point in region A, represented by

$$\xi_1\le-\frac{1}{\sin\theta_M},\quad 0\le\xi_2\le-\cos\theta_M-(\xi_1+\sin\theta_M)\tan\theta_M, \tag{15}$$

as shown in Fig. 3(a) for a typical situation, is located in the heat-affected zone emanating from any differential heat source inside the circular region. The domains of integration, therefore, are $s\in[0, 1]$ and $\phi\in[0, 2\pi]$, which covers the entire heating zone. Similar considerations are given to the observation points in regions B, C, and D, which are shown by Figs. 3(b) to (d).

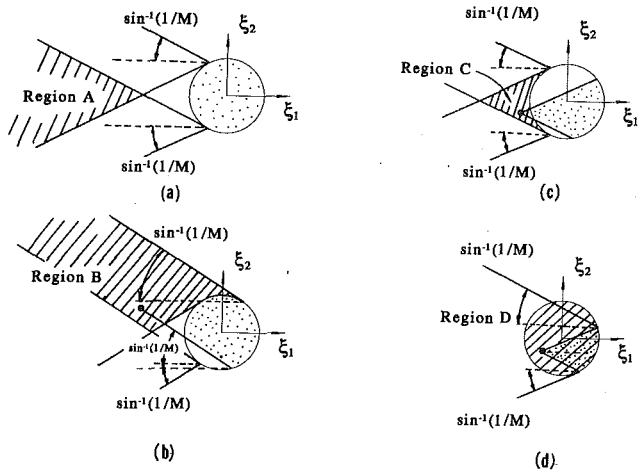

Fig. 3 Physical domains of Regions *A*, *B*, *C*, and *D* (shaded areas) and the corresponding domains of integrations inside the heating zone (dotted areas): supersonic case with M > 1

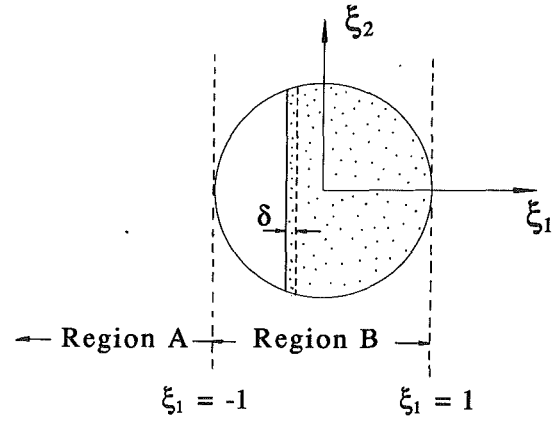

Fig. 4 Regions *A* and *B* and the corresponding domains of integration at the transonic stage with M = 1

These regions are all in contact with the heating zone, which renders a singularity in the numerical integrations. Transformation of the polar coordinates to the local observation point is thus necessary. In summary, the integration domains for region *B*, *C*, and *D* are, respectively,

Region B

$$-\theta_M \le \gamma \le \cos^{-1}\frac{\xi_2 - \xi_1\sqrt{\xi_1^2+\xi_2^2-1}}{\xi_1^2+\xi_2^2},\quad F \le \zeta \le G \qquad (16)$$

with

$$F = -(\xi_1\cos\gamma + \xi_2\sin\gamma) - \sqrt{1+\xi_1\xi_2\sin 2\gamma - \xi_1^2\sin^2\gamma - \xi_2^2\cos^2\gamma}$$

$$G = -(\xi_1\cos\gamma + \xi_2\sin\gamma) + \sqrt{1+\xi_1\xi_2\sin 2\gamma - \xi_1^2\sin^2\gamma - \xi_2^2\cos^2\gamma}. \qquad (17)$$

Region C

$$-\theta_M \le \gamma \le \theta_M,\quad F \le \zeta \le G. \qquad (18)$$

Region D

$$-\theta_M \le \gamma \le \theta_M,\quad 0 \le \zeta \le G. \qquad (19)$$

For the temperature distributions in a certain region, the integration domains are first selected from Eqs. (16)–(19) accordingly. Numerical integrations employing the regular and logarithmic Gaussian quadrature formula are then performed in the same fashion as that in the subsonic cases.

(c) The Transonic Stage with M = 1. Two types of integration domain are involved at the transonic stage. Referring to Fig. 4, the observation points in region *A* ($\xi_1 < -1$) are affected by the differential heat source in the heating zone. The domain for numerical integrations is therefore $s \in [0, 1]$ and $\phi \in [0, 2\pi]$, the same as that of region *A* in the supersonic region. For an observation point in region *B* with $-1 < \xi_1 < 1$, only the differential heat sources in the shaded area contribute to its temperature rise. The domain of integration is thus from ξ_1 to 1.

Unlike the previous cases with a $\ln(r)$-type of singularity, the singularity in Eq.(4) is unremovable. A similar expression to Eq. (14), and hence a special type of Gaussian quadrature formula, does not exit at the transonic stage with M = 1. When approaching the boundary of region *B* at a certain value of ξ_1, instead, we integrate the physical domain from $\xi_1 + \delta$ to 1 and study the convergence of the temperature solution as the value of δ approaches zero.

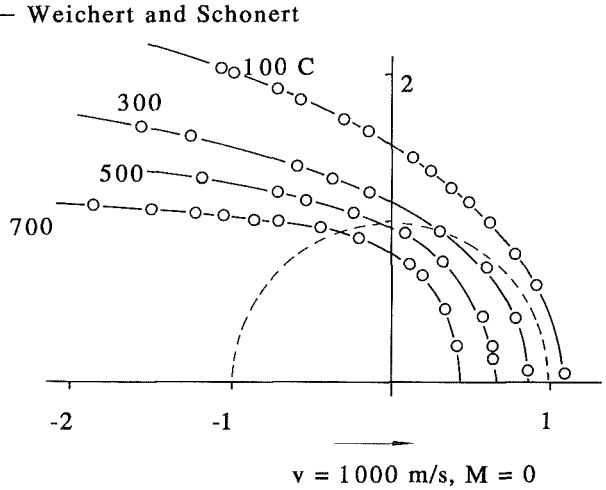

Fig. 5 Comparisons of the numerical integrations with the results obtained by Weichert and Schönert (1974); diffusion model with $v = 1000$ m/s and M = 0

Numerical Examples

The crack-tip heating problems considered by Weichert and Schönert (1974, 1978) assume diffusion, which corresponds to the special case of M = 0 in Eq. (10). As a benchmark for the numerical algorithms involved in the present analysis, therefore, we first substitute M by zero in Eq. (10) and compare the results to those obtained by Weichert and Schönert. For $v = 1000$ m/s and *C* approaching infinity (M → 0), the case with slower convergence, Fig. 5 compares the temperature contours obtained by the numerical integrations of Eq. (10) (empty circles) and those of Weichert and Schönert (1974) (solid lines). The following parameters for the glass and the heating zone:

$$r_0 = 3\times10^{-9}\ \text{m},\quad k = 1\ \text{W/m-K},\quad \alpha = 5\times10^{-7}\ \text{m}^2/\text{s} \qquad (20)$$

are used in the analysis. The dashed circle represents the physical domain of the heating zone, which, according to Eq. (9), has been normalized to $\xi_1 \in [-1, 1]$ and $\xi_2 \in [-1, 1]$. The numerical integration employing the ten-point Gaussian quadrature provides excellent agreement with the results obtained by Weichert and Schönert. The thermal wave speed *C* plays a dominant role in the wave theory of heat conduction. An analytical expression

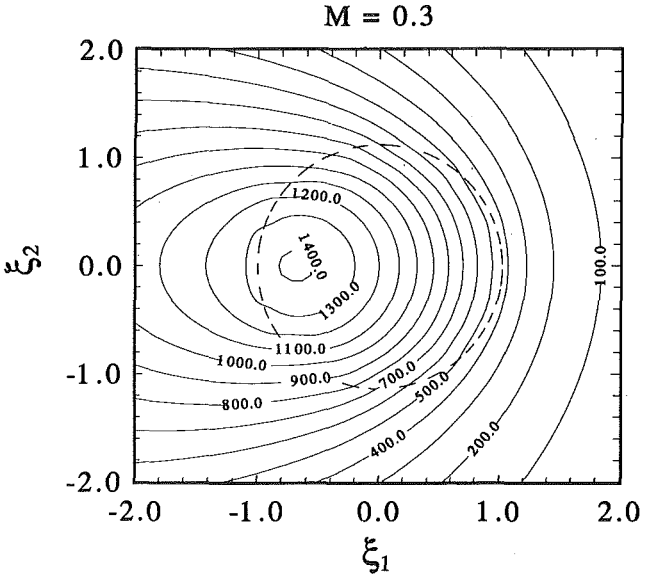

Fig. 6 Temperature contour pattern in the neighborhood of the heating zone with a circular shape: subsonic case with M = 0.3 and $C = 900$ m/s

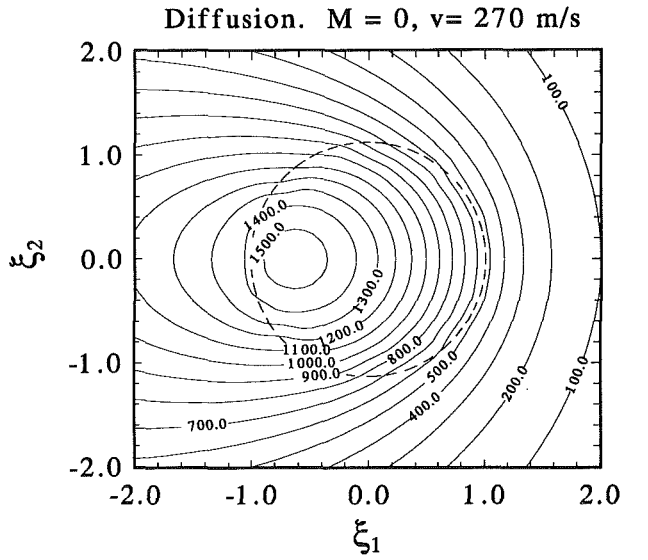

Fig. 7 Diffusion results for case shown in Fig. 6: $v = 270$ m/s and M = 0

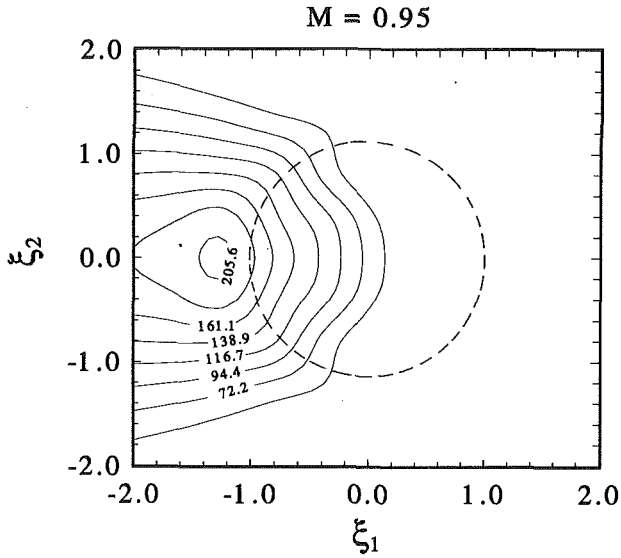

Fig. 8 Temperature contour pattern in the neighborhood of the heating zone with a circular shape: subsonic case with M = 0.95

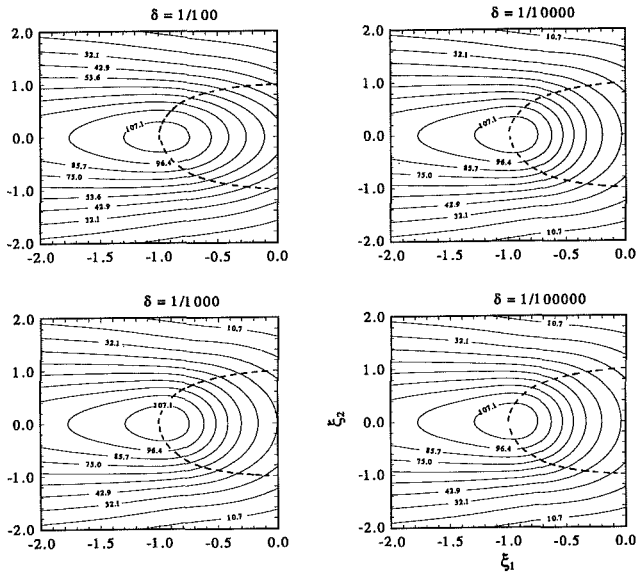

Fig. 9 Transonic stage with M = 1: convergence of temperature distributions with the deviation δ away from the heat source; identical patterns result for $\delta = 10^{-4}$ and 10^{-5}

has been derived in terms of the Planck and Boltzmann constants, Debye temperature, the thermal conductivity, and the number densities of atoms and free electrons in metal lattice (Tzou and Özişik, 1992). Due to uncertainties of the number density of free electrons (Qiu and Tien, 1992), however, its value can only be estimated as an order of magnitude. For glass, the value of C should be around 10^2 m/s. Moreover, Tzou (1992c-e) recently compared the transonic solution with the experimental result of temperature contours obtained by Zehnder and Rosakis (1991) for dynamic crack propagation in 4340 steel. The perfect coincidences between the theory and the experiment reveal a threshold value of $C = 900$ m/s. With a more confident value established, we switch the material to 4340 steel in the numerical example. It has the following properties:

$$r_0 = 5 \times 10^{-8} \text{ m}, \quad k = 34 \text{ W/m-K}, \quad \alpha = 1.0 \times 10^{-5} \text{ m}^2/\text{s},$$
$$q = 5 \times 10^{18} \text{ W/m}^3, \quad C = 900 \text{ m/s}. \quad (21)$$

When the thermal Mach number increases slightly to 0.3, Fig. 6 shows the contour patterns of temperature. The high-temperature region shifts to the rear end (left) of the circular region while the heat source is moving to the front (right). For a detailed comparison, Fig. 7 displays the contour pattern obtained by diffusion. The value of v is taken as 270 m/s (corresponding to the case in Fig. 6 (M = 0.3 and C = 900 m/s) employing the wave theory) while the thermal Mach number (M) is forced to zero. Though not very clear for this stage at the lower end of the subsonic region, the wave theory (Fig. 6) predicts a more localized result than diffusion (Fig. 7). Note also that the temperature level predicted by the wave theory is lower than that by diffusion. Figure 8 displays the contour pattern when the thermal Mach number further increases to 0.95, a stage very close to the transonic case. While the temperature levels decrease continuously due to increase of the heat-source velocity, referring to Figs. 6 and 8, the high-temperature region gradually shifts to the exterior of the heating zone. At M = 0.95, the thermally undisturbed zone is gradually formed as shown by the low-temperature region ($T < 50$ C) in the front half of the heating zone.

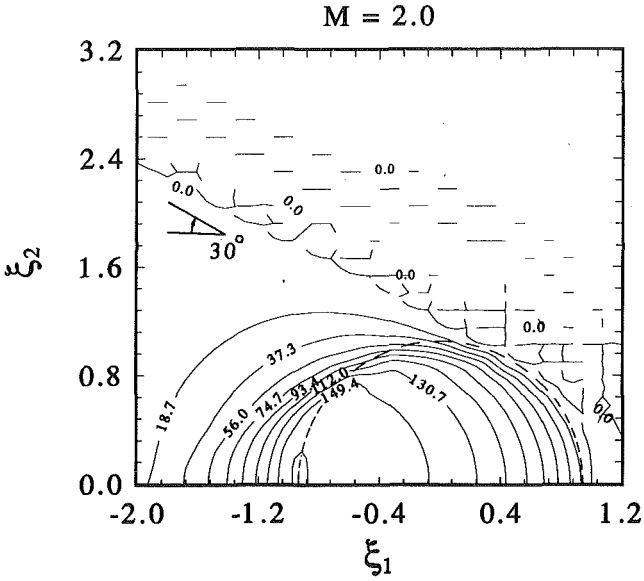

Fig. 10 Temperature contour pattern in the neighborhood of the circular heating zone and formation of the thermally undistributed zone beyond 30 deg ($\sin^{-1}$ (1/2)): supersonic case with M = 2.0

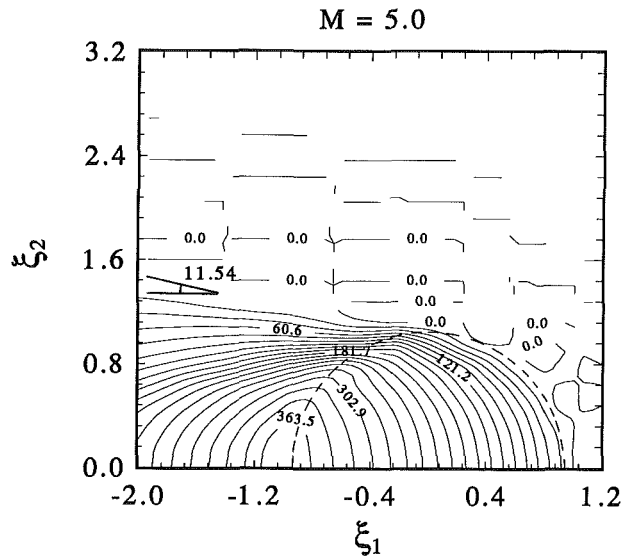

Fig. 11 Temperature contour pattern in the neighborhood of the circular heating zone and formation of the thermally undistributed zone beyond 11.54 deg ($\sin^{-1}$ (1/5)): supersonic case with M = 5.0

Unlike the subsonic and supersonic regions where the singularities in temperature are removable, the transonic stage (M = 1) possesses a strong singularity that can only be approached asymptotically in numerical integrations. Denoting the distance away from the singularity by δ, Fig. 9 demonstrates the convergence of the temperature contour patterns when the value of δ decreases from 10^{-2} (1/100) to 10^{-5} (1/100000). The contour patterns for $\delta = 10^{-4}$ and 10^{-5} are essentially identical. The circular shape of the heating zone is distored to an ellipse due to the different aspect ratios used in the ξ_1 and ξ_2 axes. In comparison with Fig. 8, M = 0.95 in the subsonic region, the temperature levels in the heat affected zone decrease continuously when the thermal Mach number increases to one.

Figure 10 shows the contour patterns of M = 2.0 in the supersonic region. The physical domain beyond 30 deg ($\sin^{-1}$ (1/2)) is thermally undisturbed and the temperature thereby remains at the reference level. The magnitude of temperature, however, starts to *increase* from those at M = 1 (Fig. 9). Note also that

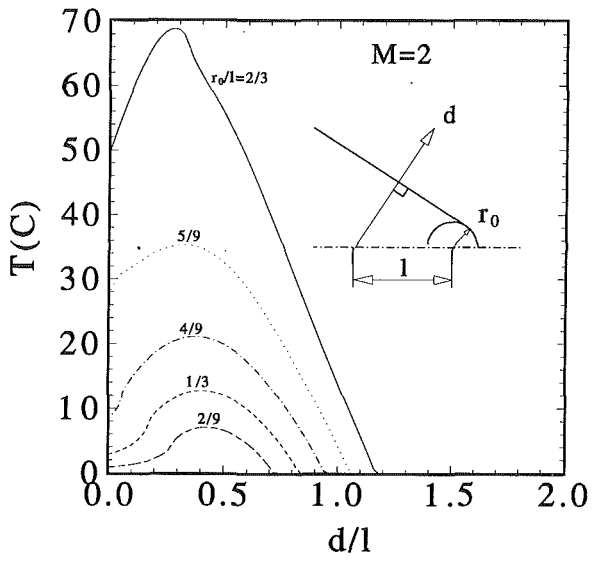

Fig. 12 Temperature distributions in the direction perpendicular to the thermal shock surface *(d/l)* at $r_0/l = 2/3$, 5/9, 4/9, 1/3, and 2/9.

the temperature contours in the rear end bend toward the trailing edge of the moving heat source. This is the "tip-down" behavior preserved in the supersonic temperature waves (Tzou, 1992c–e) and observed experimentally (Zehnder and Rosakis, 1991). The temperature levels increase continuously when the thermal Mach number increases to 5, as shown in Fig. 11. The physical domain of the heat-affected zone further shrinks to 11.54 deg ($\sin^{-1}$ (1/5)). The temperature contours in the heating zone become more perpendicular to the direction of the moving heat source. The swinging phenomenon of temperature in transition of the thermal Mach number is clear. Referring to Figs. 6 and 8, the temperature levels in the subsonic region decrease with the source speed due to insufficient time of responses. In transition to the supersonic region with M > 1, referring to Figs. 9–11, the temperature levels increase with the source speed due to shrinkage of the heat-affected zone. This is a physical phenomenon pertinent to the wave theory of heat conduction and cannot be depicted by diffusion. In comparison with the case of a point heat source (Tzou, 1989a, b), lastly, a distinct shock surface can still be observed in Figs. 10 and 11. The temperature jump across the shock surface, however, becomes much weaker. For M = 2, Fig. 12 shows the effect of r_0 on transition of temperature across the thermal shock surfaces. The radius r_0 is normalized with respect to 1, the distance measured from the center of the heating zone. While 9×10^{-8} m is taken for the value of l, the results for r_0/l decreasing from 2/3 to 2/9 are shown in the figure. At a distance d measured from the location l behind the heat source, the temperature level decreases with the radius (r_0) because less energy is dissipated from a heating zone with a smaller dimension. When approaching the thermal shock surface, the temperature first increases with the distance (d/l). At various threshold values of d/l ranging from 0.28 ($r_0/l = 2/3$) to 0.42 ($r_0/l = 2/9$), the temperature decreases toward the thermal shock surface where the temperature remains at the reference level ($T = 0°C$). This is due to shift of the high-temperature zone (refer to Fig. 10) behind the circular region at high Mach numbers.

In passing, we note that a rigorous examination on the thermal wave speed is still needed. The value of 900 m/s assumed for the 4340 steel is based on the qualitative coincidences between the theory and the experiment in dynamic crack propagation. It is still indirect in nature. At this point of development, therefore, Figs. 10 and 11 for the temperature contours in the supersonic region are provided for the sake of completeness. They serve the purpose of revealing special fea-

tures such as the swinging phenomenon and the "tip-down" behavior of temperature contours in high-speed situations. When extending the present results to a dynamically propagating crack tip, in other words, whether a crack tip could propagate at a supersonic speed, still needs further exploration.

Conclusion

The Green's function solutions obtained from a point moving heat source have been used to investigate the temperature waves emanating from a heating zone with a finite dimension. A general formulation has been provided while a special application is made to a heating zone with a circular shape, which generates heat with a constant magnitude. In the subsonic region with $M < 1$, the high-temperature area shifts out of the heating zone when the speed of the moving source increases. At the transonic and in the supersonic regions with $M \geq 1$, the swinging phenomenon for temperature and the thermal shock formation still exist. The temperature jump across the shock surfaces, however, remains bounded and is much weaker than that induced by a point heat source (Tzou, 1989a, b).

Since a heat source must occupy a finite region in space, the results obtained in this work can be readily applied to practical problems. Although a special application to a circular heating zone with a constant intensity was considered in the numerical example, Eq. (10) can be easily generalized to the case with a variable intensity of heat. The volumetric heating rate q in this case must be retained inside the integral and integrated along with the exponential and the Bessel functions. Since Eq. (10) is integrated numerically due to complications induced by the Bessel functions, extension toward this direction does not constitute any additional difficulty. The results obtained so far can be used to study the heating zone with an arbitrary shape. Equations (16)-(19) for the appropriate domains of integrations, however, must be modified accordingly for determining the temperature distributions in different regions.

For engineering problems involving high-rate heating, the intensity of the heat generation as well as the physical dimension of the heating zone may not be known as a priori. The heat crack-tip heating in metals, for example, depends strongly on the crack speed (Freund, 1990). A faster crack speed induces a higher strain rate in the near-tip region, which reduces the size of the plastic zone. As indicated by Freund and Hutchinson (1985), however, the amount of heat thus generated may be dramatically increased should the strain-rate limit for the phonon-drag process be exceeded. The present formulation has to be made more general to handle this situation and research is currently being developed in this direction.

Acknowledgments

This work results from the research support from the National Science Foundation under Grant No. MSS-9200993 with the University of New Mexico. Valuable discussions and encouragement from Dr. Sackman are gratefully acknowledged.

References

Frankel, J. I., Vick, B., and Özişik, M. N., 1985, "Flux Formulation of Hyperbolic Heat Conduction," *Journal of Applied Physics*, Vol. 58, pp. 3340-3345.

Freund, L. B., and Hutchinson, J. W., 1985, "High Strain-Rate Crack Growth in Rate-Dependent Plastic Solids," *Journal of the Mechanics and Physics of Solids*, Vol. 33, pp. 169-191.

Freund, L. B., 1990, *Dynamic Fracture Mechanics*, Cambridge University Press, New York, Chap. 8.

Joseph, D. D., and Preziosi, L., 1989, "Heat Waves," *Reviews of Modern Physics*, Vol. 61, pp. 41-73.

Joseph, D. D., and Preziosi, L., 1991, "Addendum to the Paper on Heat Waves," *Reviews of Modern Physics*, Vol. 62, pp. 375-392.

Jou, D., Casas-Váquez, J., and Lebon, G., 1988, "Extended Irreversible Thermodynamics," *Report on the Progress of Physics*, Vol. 51, pp. 1105-1179.

Maxwell, J. C., 1867, "On the Dynamic Theory of Gases," *Philosophical Transactions, London*, Vol. 157, pp. 49-88.

Özişik, M. N., and Tzou, D. Y., 1992, "On the Wave Theory in Heat Conduction," presented at the Session on Significant Questions: Fundamental Issues in Microscale Heat Transfer, 1992 ASME Winter Annual Meeting, Anaheim, CA.

Qiu, T. Q., and Tien, C. L., 1992, "Short-Pulse Laser Heating on Metals," *International Journal of Heat and Mass Transfer*, Vol. 35, pp. 719-726.

Stroud, A. H., and Secrest, P., 1966, *Gaussian Quadrature Formula*, Prentice-Hall, Englewood Cliffs, NJ.

Tzou, D. Y., 1989a, "On the Thermal Shock Wave Induced by a Moving Heat Source," ASME JOURNAL OF HEAT TRANSFER, Vol. 111, pp. 232-238.

Tzou, D. Y., 1989b, "Shock Wave Formation Around a Moving Heat Source in a Solid With Finite Speed of Heat Propagation," *International Journal of Heat Mass Transfer*, Vol. 32, pp. 1979-1987.

Tzou, D. Y., 1989c, "The Effects of Thermal Shock Waves on the Crack Initiation Around a Moving Heat Source," *Journal of Engineering Fracture Mechanics*, Vol. 34, pp. 1909-1118.

Tzou, D. Y., 1990a, "Three-Dimensional Structures of the Thermal Shock Waves Around a Rapidly Moving Heat Source," *International Journal of Engineering Science*, Vol. 28, pp. 1003-1017.

Tzou, D. Y., 1990b, "Thermal Shock Waves Induced by a Moving Crack—A Heat Flux Formulation," *International Journal of Heat Mass Transfer*, Vol. 33, pp. 877-885.

Tzou, D. Y., 1990c, "Thermal Shock Waves Induced by a Moving Crack," ASME JOURNAL OF HEAT TRANSFER, Vol. 112, pp. 21-27.

Tzou, D. Y., 1991, "Thermal Shock Formation in a Three Dimensional Solid Due to a Rapidly Moving Heat Source," ASME JOURNAL OF HEAT TRANSFER, Vol. 113, pp. 242-244.

Tzou, D. Y., 1992a, "Thermal Shock Phenomena Under High-Rate Response in Solids," in: *Annual Review of Heat Transfer*, Chang-Lin Tien, ed., Hemisphere Publishing Inc., Washington, DC, Chap. 3, pp. 111-185.

Tzou, D. Y., 1992b, "An Engineering Assessment to the Relaxation Time in Thermal Waves," *International Journal of Heat and Mass Transfer*, in press.

Tzou, D. Y., 1992c, "The Transonic Temperature Wave Around a Rapidly Propagating Crack Tip: An Experimental Evidence," *International Journal of Engineering Science*, Vol. 30, pp. 757-769.

Tzou, D. Y., 1992d, "An Experimental Evidence for the Temperature Waves Around a Rapidly Propagating Crack Tip," ASME JOURNAL OF HEAT TRANSFER, Vol. 114, pp. 1042-1045.

Tzou, D. Y., 1992e, "The Thermal Shock Phenomena Induced by a Rapidly Propagating Crack Tip: An Experimental Evidence," *International Journal of Heat and Mass Transfer*, Vol. 35, pp. 2347-2356.

Tzou, D. Y., and Ozi☆ik, M. N., 1992, "Interrelations Between the Microscopic Two-Step Model and the Macroscopic Thermal Wave Model," ASME JOURNAL OF HEAT TRANSFER, submitted for publication.

Vernotte, P., 1958, "Les Paradoxes de la Théorie Continue de l'Équation de la Chaleur," *Compte Rendus*, Vol. 246, pp. 3154-3155.

Vernotte, P., 1961, "Some Possible Complications in the Phenomena of Thermal Conduction," *Compte Rendus*, Vol. 252, pp. 2190-2191.

Weichert, R., and Schönert, K., 1974, "On the Temperature Rise at the Tip of a Fast Running Crack," *Journal of the Mechanics and Physics of Solids*, Vol. 2, pp. 127-133.

Weichert, R., and Schönert, K., 1978, "Heat Generation at the Tip of a Moving Crack," *Journal of the Mechanics and Physics of Solids*, Vol. 26, pp. 151-161.

Zehnder, A. T., and Rosakis, A. J., 1991, "On the Temperature Distribution at the Vicinity of Dynamically Propagating Cracks in 4340 Steel," *Journal of the Mechanics and Physics of Solids*, Vol. 39, pp. 385-415.

S. Song
International Business Machine Corporation,
Poughkeepsie, NY 12602

M. M. Yovanovich
Microelectronics Heat Transfer Laboratory,
Department of Mechanical Engineering.

F. O. Goodman
Department of Applied Mathematics
and Department of Physics,
University of Waterloo,
Waterloo, Ontario, Canada

Thermal Gap Conductance of Conforming Surfaces in Contact

Heat transfer through gas layers of contact interfaces formed by two microscopically rough surfaces is studied. Rarefied gas conduction between smooth parallel plates is examined with data obtained from the literature. Two important dimensionless parameters are introduced; one representing the ratio of the rarefied gas resistance to the continuum gas resistance, and the other representing gas rarefaction effects. Effects of gas rarefaction and surface roughness are studied in relation to the parallel plates case. It is proposed that the effective gap thickness at light loads may be estimate by a roughness parameter, the maximum peak height R_p. Experiments were performed to measure gap conductance for a number of Stainless Steel 304 pairs and Nickel 200 pairs over a range of roughnesses and gas pressures. Three different types of gases, helium, argon, and nitrogen, were employed as the interstitial gas. The comparison between the theory and the measured values of gap conductance shows excellent agreement.

1 Introduction

Heat transfer through interfaces formed by the mechanical contact of two solids has many important applications, such as in heat exchangers, microelectronic-chip cooling, and nuclear fuel-temperature control. One of the fundamental (and perhaps most important) studies in contact heat transfer involves the contact of two surfaces that are flat but microscopically rough.

Typically heat transfer through contact interfaces is associated with the presence of interstitial gases/fluids. Under such conditions, the rate of heat transfer across the interfaces depends upon a number of parameters: thermal properties of solids and gases/fluids, surface roughness characteristics, applied mechanical load, microhardness characteristics of solids, etc. Because of the large number of parameters involved, numerous attempts by various researchers to model the thermal gap conductance have not been completely successful. While analytical models tend to neglect some of the important parameters, experimental correlations are valid only for limited ranges of these parameters (Shlykov, 1965; Veziroglu, 1967; Rapier et al., 1963). Often, the disagreement between the measured and predicted values of the conductance is found to be in the order of magnitude of the experimental values.

In the present paper various effects on the gap heat transfer are examined, using a rarefied gas kinetic theory and an accurate gap conductance model (Yovanovich et al., 1982). Also presented here are accurate gap conductance measurements obtained for interfaces formed by the contact of a bead-blasted surface and a smooth lapped surface. Helium, argon, and nitrogen were used as the interstitial gases with Stainless Steel 304 pairs and Nickel 200 pairs. Contact pressure was maintained at a very low level (0.4–0.6 MPa), so that the contribution of the contact conductance to the total (joint) conductance is small. Gas pressure was varied over 10 to 700 torr to study the effect of gas rarefaction on gap conductance. The model of Yovanovich et al. (1982) is verified using the experimental measurements. The comparison between the predicted and the measured conductance values shows excellent agreement.

2 Review of Contact Interface Heat Transfer

2.1 Conductance Definitions. Heat transfer through interfaces formed by the contact of two nominally flat surfaces, when radiation effects are neglected, takes the following form:

$$Q_j = Q_c + Q_g \tag{1}$$

where Q_c, Q_g, Q_j are the rates of heat transfer through the solid contact spots, through the interstitial gas layer, and the total rate of heat transfer, respectively. The conductance is introduced in the same manner as the film coefficient in convective heat transfer:

$$h = \frac{Q/A_a}{\Delta T}$$

where h is the conductance, ΔT is the effective temperature difference across the interface, and A_a is the apparent contact area.

2.2 Gap Conductance. The earliest and simplest form of gap conductance models (Cetinkale and Fishenden, 1951; Fenech and Rohsenow, 1959; Laming, 1961; Shlykov and Ganin, 1964) assumes that the contact interface gap may be represented by two parallel plates separated by an effective gap thickness δ. The gap conductance h_g is modeled as

$$h_g = \frac{k_g}{\delta} \tag{2}$$

where the effective gap thickness, δ, depends upon the roughness characteristics of the two surfaces, the contact pressure and the microhardness. These models, however, ignore the effect of the contact pressure upon the gap thickness. The effective gap thickness δ is estimated by correlating the gap conductance measurements in terms of the surface roughness, typically the sum of the centerline averages (CLA) of the two surfaces.

The magnitude of the effective gap thickness of contact interfaces is typically of the range $0.1 < \delta < 100\ \mu$m. When the physical size of the gas layer, through which the gas conduction takes place, is comparable to the level of the gas molecular movement, the continuum assumption of the gas medium is no longer valid. This effect is commonly referred to as "rarefied gas" heat conduction.

This effect results in retardation of the heat transfer, and is often modeled in the form of a distance serially added to the physical heat flow path (Henry, 1964; Veziroglu, 1967; Yovanovich, 1982):

$$h_g = \frac{k_g}{\delta + M} \tag{3}$$

Contributed by the Heat Transfer Division for publication in the JOURNAL OF HEAT TRANSFER. Manuscript received by the Heat Transfer Division April 1992; revision received February 1993. Keywords: Conduction, Electronic Equipment, Thermal Packaging. Associate Technical Editor: L. S. Fletcher.

The gas parameter, M, depends upon the gas type, gas pressure and temperature, and the thermal accommodation coefficient (a measure of the energy exchange between the gas molecules and the solid surfaces). This parameter, which will be discussed in detail in Section 3, can vary in the order of the magnitude of the effective gap thickness, δ.

The manner in which the gas rarefaction effect is modeled has not been agreed upon, as there appear to be a number of different approaches (Rapier et al., 1963; Lloyd et al., 1973; Garnier and Begej, 1979; Mentes et al., 1981; Loyalka, 1982). Furthermore, it is difficult to obtain an accurate estimate of the thermal accommodation coefficient (TAC), which is a parameter of critical importance in rarefield gas heat transfer. Most of the authors involved with contact interface gap heat transfer research have relied upon TAC measurements obtained in environments much different from the contact situations, and these estimates within themselves showed a great deal of uncertainties. There appears to be no previous serious effort taken to estimate TAC directly within the environment of the contact interface heat transfer.

Instead of making parallel-plate assumptions (Eqs. (2) and (3)), several authors (Shvets and Dyban, 1964; Shlykov, 1965; Popov and Krasnoborod'ko, 1975) took the approach of representing the geometry of the interface gap by correlating the surface height distributions obtained from several machined and ground surfaces. Dutkiewicz (1966) took a statistical approach by assuming that the roughness heights of the contact surfaces are distributed according to the Gaussian model, and presented tabulated results for the gap conductance predictions (with some restriction in the range of the surface height distributions).

Yovanovich et al. (1982), also assuming Gaussian distribution of the surface height, developed a gap conductance model in an integral form. In this model the effect on the deformation of the gap due to the contact pressure is taken into consideration. The development of the model is presented (briefly) here since this model is later modified and used extensively in the present work.

The integral model for the gap conductance, which is denoted in the present work as the YIGC (Yovanovich Integral Gap Conductance) model, takes into consideration the variation in the local gap thickness due to the surface roughness. The model assumes that the temperatures of the two surfaces in contact are uniform at T_1 and T_2, and the entire interface gap consists of many elemental flux tubes of different thermal resistance. The resistances of these elemental flux tubes are then connected in parallel to result in the overall gap conductance in an integral form:

$$h_g = \frac{k_g}{\sqrt{2\pi}\,\sigma} \int_0^\infty \frac{\exp[-(Y/\sigma - t/\sigma)^2/2]}{(t+M)/\sigma}\, d(t/\sigma) \tag{4}$$

where t = length of the elemental flux tube or the local gap thickness; M = gas parameter to be discussed in Section 3; k_g = thermal conductivity of the gas; Y = mean plane separation distance or effective gap thickness. The term $t + M$ may be regarded as the effective heat flow distance of the local elemental flux tube.

3 Rarefied Gas Heat Transfer Between Parallel Plates

Gas conduction in the contact interface is a complex phenomenon mainly due to the statistical nature of the gap geometry. In addition, the uncertainty associated with the present understanding of rarefied gas heat transfer, which arises from the small size (comparable to the gas molecular movement level) of the gap thickness, makes it difficult to model the gap gas heat transfer accurately. Here, the case of the rarefied gas conduction between two smooth parallel plates is considered and the accuracy of a single parallel-plate, heat transfer model, which numerous researchers have incorporated into their contact interface gap conductance models, is verified with experimental data. The contact interface gas conductance may then be examined in relation with the parallel-plate case. During this analysis, a pair of important dimensionless parameters will be introduced.

3.1 Heat-Flow Regimes. Conduction heat transfer through a gas layer between two noncontacting parallel plates is commonly classified into four heat-flow regimes; continuum, temperature-jump, transition, and free-molecular (Springer, 1971). A convenient parameter that characterizes the regimes is the Knudsen number, defined as:

$$\mathrm{Kn} = \frac{\Lambda}{d} \tag{5}$$

where Λ is the molecular mean free path and d is the distance separating the two plates.

In the continuum regime ($\mathrm{Kn} \ll 1$), the heat transfer between the plates takes place mainly through the collisions of the gas molecules. The rate of heat transfer in this regime is independent of the gas pressure, but varies with the gas temperature. Fourier's law of conduction can be used in this regime.

Nomenclature

A_a = apparent area of contact
CLA = centerline average surface roughness
d = gap thickness
f = dimensionless term in Eq. (13)
G = dimensionless gap resistance $= \frac{k_g}{h_g d}$
h = conductance $= \frac{Q/A_a}{\Delta T}$
Kn = Knudsen number $= \Lambda/d$
k_g = thermal conductivity of gas
L = sample trace length
M = gas parameter $= \frac{2-\mathrm{TAC}_1}{\mathrm{TAC}_1} + \frac{2-\mathrm{TAC}_2}{\mathrm{TAC}_2}\beta\Lambda$
M^+ = gas rarefaction parameter $= M/d$
P = apparent contact pressure
P_g = gas pressure
Pr = Prandtl number $= c_p\mu/k$
Q = heat transfer rate
q = heat flux $= Q/A_a$
R_p = maximum peak height
T = temperature
TAC = thermal accommodation coefficient
ΔT = effective temperature difference across interface $= T_1 - T_2$
t = local gap thickness
Y = mean plane separation, effective gap thickness
γ = ratio of specific heats $= C_p/Cv$
δ = effective gap thickness
ϵ = emissivity
Λ = molecular mean free path
Λ_0 = at reference temperature and pressure
σ = rms surface roughness

Subscripts

1, 2 = surfaces 1 and 2
c = contact
FM = free molecular
g = gas
j = joint

As the gas pressure is reduced, the intermolecular collisions become less frequent, and the exchange of energy between gas molecules and the plates starts to affect the heat transfer rate between the plates. Typically characterized by the Knudsen number range of $0.01 < \text{Kn} < 0.1$, the heat flow under this conditions exhibits a "temperature-jump" behavior (Kennard, 1938). In this regime, the heat exchange of energy between the gas molecules and the plate wall is incomplete, and, as a result, a "discontinuity" of temperature develops at the wall-gas interface.

At the extreme end of very low gas pressure (or high gas temperature), intermolecular collisions are rare, and the essential mechanism of heat transfer in this regime is the exchange of energy between gas molecules and the plates. This heat-flow regime, typically with $\text{Kn} > 10$, is called the "free-molecular regime."

Between the temperature-jump and the free-molecular regimes is the "transition regime," in which intermolecular collisions and the energy exchange between the gas molecules and the plate walls are both important. The Knudsen number range for this regime is typically $0.1 < \text{Kn} < 10$.

3.2 Simple Kinetic Theory Models. For the temperature-jump and the free molecular heat-flow regimes, there exist simple models for heat transfer through gases between two parallel isothermal plates. These models assume that the gas molecules are in thermal equilibrium and obey Maxwell's velocity distribution law. The heat transfer rate is modeled in terms of the gas molecular mean free path, and thus these models are sometimes referred to as "mean free path models."

When Maxwell's theory for temperature-jump distance is employed, the conduction between two parallel plates for the temperature-jump regime may be modeled as (Kennard, 1938):

$$q = \frac{k_g}{d + M}(T_1 - T_2) \tag{6}$$

where T_1 and T_2 are the uniform temperatures of the two plates, and q is the heat flux. The gas parameter, M is defined as:

$$M = \left(\frac{2 - \text{TAC}_1}{\text{TAC}_1} + \frac{2 - \text{TAC}_2}{\text{TAC}_2}\right)\left(\frac{2\gamma}{\gamma + 1}\right)\left(\frac{1}{\text{Pr}}\right)\Lambda \tag{7}$$

where

TAC_1, TAC_2 = thermal accommodation coefficients corresponding to the gas-solid combination of plates 1 and 2, respectively; γ = ratio of specific heats; Pr = Prandtl number; Λ = molecular mean free path. The thermal accommodation coefficient (TAC) depends upon the type of gas-solid combination, and is, in general, very sensitive to the condition of the solid surface. It represents the degree to which the kinetic energy of a gas molecular is exchanged while in collision with the solid wall.

The gas parameter, M, which has the unit of length, represents in Eq. (6) the temperature-jump distances for the two plates. It is of the order of the gas mean free path, which in turn varies proportionally with the gas temperature and inversely with the gas pressure (Λ is inversely proportional to P_g).

The heat flux in the free-molecular regime was modeled by Knudsen (Kennard, 1938):

$$q_{FM} = \frac{k_g}{M}(T_1 - T_2) \tag{8}$$

It is observed from this model that the heat flow in the free-molecular regime is independent of the distance separating the two plates. Furthermore, the heat flux q_{FM} is inversely proportional to M and thus is directly proportional to the gas pressure.

The heat transfer mechanism of the transition regime is very complex, and there is no simple theory for this regime.

3.3 Interpolated Simple Kinetic Theory Model. Yovanovich (1982), in developing his approximate expression for h_g (Eq. (3)), assumed that Eq. (6) effectively represents the heat transfer for all four flow regimes. This assumption seems reasonable since for the continuum regime the gas parameter, M is negligibly small compared to d, and as the Knudsen number increases M begins to affect the term $k_g/d + M$. In the free-molecular regime, Eq. (6) effectively reduces to the free-molecular model, Eq. (8).

Various other researchers, in developing models for the gap conductance, have assumed this interpolated form for the rarefied-gas heat transfer. In the present work, Eq. (6) is referred to as the interpolated simple kinetic theory (ISKT) model. It will be seen in the following sections that this model provides an accurate representation of heat transfer for all conduction regimes of the parallel-plate configuration. Also, there exist some approximate solutions of the Boltzmann transport equation (Liu and Lees, 1961; Bassanini et al., 1967), and the ISKT model is in very good agreement with these solutions.

3.4 Comparison of ISKT Model With Experimental Data. The ISKT Model (Eq. (6)) may be written in terms of two dimensionless parameters as:

$$G = M^+ + 1 \tag{9}$$

where

$$G = \frac{k_g}{h_g d}$$

and

$$M^+ = \frac{M}{d}$$

The dimensionless gap resistance, G, may be interpreted as the ratio of the rarefied gas resistance to the continuum resistance. The dimensionless parameter, M^+, represents the degree of gas rarefaction, and accordingly it is here referred to as the rarefaction parameter. It is important to note that all experimental data discussed in this section essentially form one curve when normalized to these parameters.

Teagan and Springer (1968) made measurements of heat transfer between parallel plates using argon ($0.06 \le \text{Kn} \le 5$) and nitrogen ($0.03 \le \text{Kn} \le 0.5$). Two aluminum plates of 25.4 cm diameter were used with a gap distance of 0.13 cm separating them. Braun and Frohn (1976, 1977) used stainless steel plates of 27.5 cm diameter and 1 cm gap spacing to measure the heat transfer through helium and argon. The Knudsen number range covered for the helium measurements was $10^{-4} \le \text{Kn} \le 2$ and for the argon, 10^{-4} Kn ≤ 1.

Figure 1 shows the measured values of G in comparison with the predicted values of the ISKT model (Teagan and Springer reported their measurements in the form of Q/Q_{FM} against 1/Kn, and Braun and Frohn, $Q/Q_{\text{continuum}}$ against 1/Kn). It is seen from the figure that, for the wide range (nearly five orders of magnitude) of M^+ covered by these authors, the agreement between the predicted values of G and the measurements is excellent. It is important to observe that the ISKT model is also valid for the transition regime.

Two major conclusions concerning the rarefied-gas heat transfer between parallel plates may be drawn as a result of the preceding study:

- The ISKT model accurately predicts the heat flow rate for all conduction regimes.
- The heat flow rate, when normalized to G (dimensionless gap resistance), depends upon one parameter, M^+ (rarefaction parameter).

4 Contact Interface Gap Heat Transfer

4.1 Effect of Surface Roughness on Gap Conductance. Rarefied gas conduction between parallel plates may

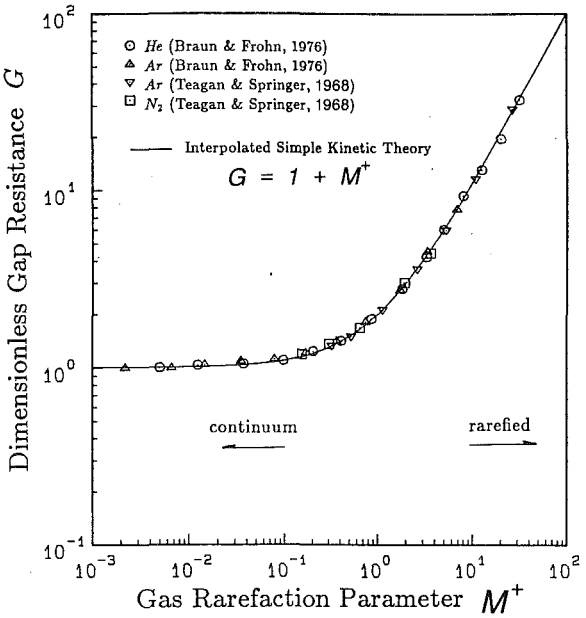

Fig. 1 Comparison of ISKT model with experimental data

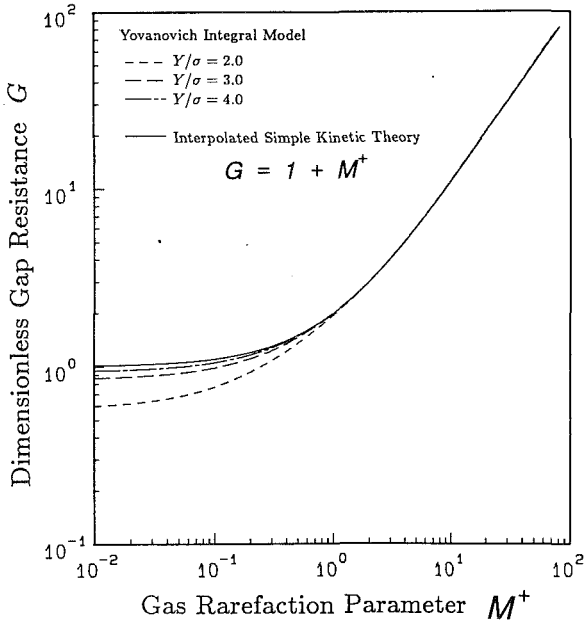

Fig. 2 YIGC model in terms of G and M^+

be considered as the limiting case of the contact interface gas conduction as the surface roughness diminishes. The degree of the roughness effect upon the gap conductance has not been clearly understood. The integral gap conductance model (YIGC) provides an excellent description of the effect due to the surface roughness.

The YIGC model may be written for the dimensionless resistance, G, in terms of the gas rarefaction parameter, M^+, as:

$$G=\frac{k_g}{h_g Y}=\frac{\sqrt{2\pi}}{\int_0^\infty \frac{\exp\{-(Y/\sigma-t/\sigma)^2/2\}}{(t/\sigma)/(Y/\sigma)+M^+}\,d(t/\sigma)} \tag{10}$$

where G and M^+ are defined in Eq. (9) with d replaced by the effective gap thickness Y.

The dimensionless resistance G, according to the YIGC model, depends on two parameters, M^+ and Y/σ:

$$G=G(M^+,\ Y/\sigma) \tag{11}$$

As discussed in the previous section, the parameter M^+ accounts for the gas rarefaction effect, and it is independent of surface roughness. According to the YIGC model, the surface roughness effect appears in the form of the ratio of the effective gap thickness to the rms roughness.

Figure 2 shows, in terms of the parameters G and M^+, the YIGC model (Eq. (10)) along with the ISKT model (Eq. (9)) of the parallel-plate gas conduction. The YIGC and ISKT models are essentially equivalent for the region of large M^+ ($M^+>1$), and also for smooth surfaces (large Y/σ). The parallel plates may be considered to be associated with negligible surface roughness, and thus the corresponding Y/σ value would be very large. Therefore, lower G values of YIGC model (compared to those of ISKT) may be interpreted to be due to the surface roughness effect. The surface roughness effect is significant only in the region of small M^+ ($M^+<1$). Near the continuum regime (lower end of M^+) the surface roughness effect, for the normal range of Y/σ ($2.0\le Y/\sigma\le 4.0$) is seen to produce about 40 percent enhancement in the gap conductance (compared to the perfectly smooth surface with the same effective gap thickness Y).

The gas rarefaction effect, which depends upon the rarefaction parameter M^+ is shown as an increase in the dimensionless resistance G. For the range $M^+>1$, the gap heat transfer does not appear to depend upon the surface roughness, and thus the gap conductance in this regime (and only in this regime) may be effectively estimated as:

$$h_g=\frac{k_g}{M+Y} \tag{12}$$

The analysis presented in this section based on the YIGC model reveals several important aspects of the gap conductance:

- The dimensionless gap resistance G represents the relative magnitude of the gap resistance in reference to the resistance associated with the gas layer (in the continuum conduction regime) between the parallel plates.
- The gap conductance, when normalized to G, is influenced by two effects: the gas rarefaction and the surface roughness. These effects are characterized by the dimensionless parameters M^+ for the gas rarefaction and Y/σ for the surface roughness.
- In the region $M^+>1$, the influence on the gap conductance of the surface roughness effect is negligible.

4.2 Simplified Expression for YIGC Model. Equation (10) is in an integral form, and its evaluation requires numerical integration. The integral was correlated by the first author to yield the following simple expression:

$$G(M^+,\ Y/\sigma)=f+M^+ \tag{13}$$

where

$$f=1+\frac{0.304}{(Y/\sigma)(1+M^+)}-\frac{2.29}{\{(Y/\sigma)(1+M^+)\}^2}$$

For the range $2.5\le Y/\sigma$ and $0.01\le M^+$, the maximum difference in G values computed by the simple expression and the integral model (Eq. (10)) is about 2 percent. When M^+ is very small (continuum regime), Eq. (13) becomes independent of M^+ and reduces to:

$$G\simeq f_{\text{continuum}} \tag{14}$$

where

$$f_{\text{continuum}}=1+\frac{0.304}{Y/\sigma}-\frac{2.29}{(Y/\sigma)^2}$$

This expression should be useful for applications where the interstitial fluid is liquid or grease.

5 Effective Gap Thickness

A critical part of the gap conductance model is to predict the effective gap thickness of the gas/fluid layer in the contact interface accurately. This is a difficult task mainly because there are many parameters that influence the gap thickness, e.g., surface roughness characteristics, mechanical load, and microhardness characteristics. Here the effective gap thickness is defined as the separation distance of the mean planes between two surfaces, and is given the symbol Y. The effective gap thickness Y increase with the surface roughness, and it decreases with increase in the mechanical load.

Yovanovich et al. (1982) developed an effective gap thickness model, which takes into consideration the effects of surface roughness and the mechanical load. The model assumes that the distribution of the surface roughness height is Gaussian, and inherent in this assumption is that the range of the surface height is unbounded. This implies that, hypothetically, under an extremely light load condition the effective gap thickness Y would take on a very large value. In reality this is not valid, especially for the contact of a rough and a smooth surface, because under the zero-load (or near the zero-load) condition the effective gap thickness for the contact of the real surface would correspond to the largest value of the surface height (from the mean plane of the rough surface), which would be the height of the highest peak. The increase of mechanical load from the zero-load condition results in the reduction of the effective gap thickness, and thus the increase in the gap conductance (Song et al., 1989).

In the present work, the contact of a rough and a smooth surface under very light mechanical load is considered, and the effective gap thickness is estimated as the maximum peak height of the rougher surface. The maximum peak height, R_p, is defined (Dagnall, 1980) as the height of the highest point of the profile above the mean line within the trace length L. The maximum peak height is an extreme value characteristic of the surface roughness, and thus, unlike other roughness parameters, such as the rms height (σ) or the centerline average height (CLA), it depends upon the trace length (R_p increases with L). Therefore for an estimate of the effective gap thickness at light loads, R_p should be measured based on sufficiently long trace lengths.

The normalized value of the maximum peak height, R_p/σ, is of great interest in the present work, since it provides an estimate for the relative effective gap thickness (Y/σ) at light mechanical pressure. There appears to be a trend that R_p/σ of real surfaces in general decreases with increase in surface roughness (Rupert, 1959; Tsukada and Anno, 1975).

6 Experimental Program

6.1 Test Apparatus. A pyrex bell jar and a base plate enclose the test column (Fig. 3) consisting of the heater block, the heat meter, the upper and lower test specimens, the heat sink, and the load cell. The gas pressure inside the chamber was controlled by the vacuum system, which consisted of a mechanical pump connected in series with an oil diffusion pump. This system provided a vacuum level lower than 10^{-5} torr. The brass heater block with two pencil-type heaters provided the maximum combined power of 200 W. Cooling was accomplished with an aluminum cold plate, which, in turn, was chilled by a closed-loop thermobath. Axial load was applied to the test column via a level system, which was activated by a diaphragm-type air cylinder. The mechanical load was measured by a calibrated load cell. A metal diaphragm type of gage was used to measure gas pressure inside the test chamber. The uncertainty associated with the gas pressure measurement was within 0.5 torr. Temperature measurements were made with 30 gage type "T" copper-constantan thermocouples. Data acquisition and reduction were performed under the control of a PC. The mechanical loads and the heater levels were adjusted through the computer.

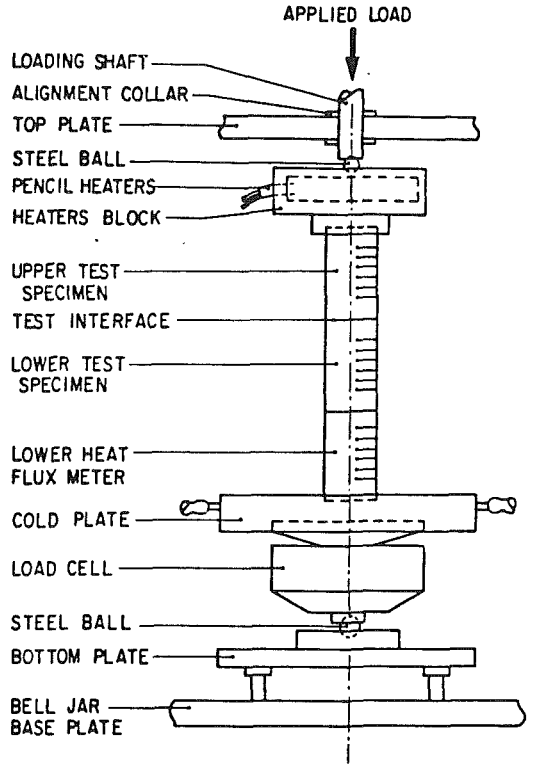

Fig. 3 Experimental setup

6.2 Test Specimens and Gases. Test specimens of Stainless Steel 304 and Nickel 200 (Table 1) were prepared from commercial bars. The specimens were machined to cylindrical shape of 25 mm diameter and 45 mm long. For each specimen, six holes of 0.64 mm diameter and 2.5 mm deep were drilled for the thermocouples. These holes were located 5 mm apart with the first one 10 mm from the contact surface.

The contact surfaces were prepared by bead-blasting. A Talysurf profilometer was used to measure various surface roughness parameters. The roughness parameters estimated from the profilometer were as follows: σ = rms surface roughness; CLA = centerline average surface roughness; R_p = maximum peak height roughness. Typically, three to six traces were randomly selected, and the roughness parameters were measured over 1 cm trace lengths.

Three different types of gas, helium, argon, and nitrogen, were used in the experiments. Thermal conductivity correlations used for the gases were as follows:

Helium

$$k_g\ (\mathrm{W/m\cdot K}) = 0.145 + 3.24\times 10^{-4}\mathrm{T} \text{ for } 27 \le T \le 400^\circ\mathrm{C} \tag{15}$$

Argon

$$k_g\ (\mathrm{W/m\cdot K}) = 0.0171 + 4.05\times 10^{-5}\mathrm{T} \text{ for } 20 \le T \le 400^\circ\mathrm{C} \tag{16}$$

Nitrogen

$$k_g\ (\mathrm{W/m\cdot K}) = 0.0250 + 5.84\times 10^{-5}\mathrm{T} \text{ for } 27 \le T \le 400^\circ\mathrm{C} \tag{17}$$

The thermal conductivity expressions for helium and nitrogen are the correlations of Hegazy (1985) and for argon the tabulated values of Gandhi and Saxena (1968) were correlated by the first author. The values of TAC for He, Ar, and N_2 were

Table 1 Ranges of parameters for experiments

Parameters	Exp. No. 1	Exp. No. 2	Exp. No. 3	Exp. No. 4
Specimens	SS 304	SS 304	Ni 200	Ni 200
σ (μm)	1.53	4.83	2.32	11.8
R_p (μm)	5.55	14.7	8.61	30.6
R_p/σ	3.63	3.04	3.71	2.59
h_c (W/m$^2\cdot$°C)	452 ± 25	241 ± 3	1130 ± 30	725 ± 30
h_g (W/m$^2\cdot$°C)	711–9660	460–5150	625–17900	417–7830
h_g/h_c	1.57–21.4	1.91–21.4	0.553–15.8	0.575–10.8
P_g (torr)	9.4–710.9	9.5–665.0	9.6–697.7	9.4–699.7
Kn	0.019–4.2	0.0078–1.6	0.013–2.6	0.0034–0.76
P (MPa)	0.60 ± 0.02	0.47 ± 0.02	0.52 ± 0.02	0.38 ± 0.01
T_c (°C)	172 ± 4	168 ± 4	170 ± 3	172 ± 4
ΔT (°C)	5.8–85.5	6.7–105.9	5.5–39.9	12.2–63.8
q (kW/m^2)	27.7–58.7	34.4–55.5	52.7–104.9	55.9–104.1

$\sigma = \sqrt{\sigma_1^2 + \sigma_2^2}$.

Table 2 Properties of gases

Gas	γ	Pr	Λ_0 (μm)
Helium	1.67	0.67	0.186
Argon	1.67	0.67	0.0666
Nitrogen	1.41	0.69	0.0628

Note: Λ_0 values (Kennard, 1938) are at 288 K and 760 torr.

estimated according to a method proposed by Song and Yovanovich (1989).

The estimated values of TAC are 0.55, 0.90, and 0.78 for He, Ar, and N_2, respectively. The values of other relevant properties of the gases (ratio of specific heats, Prandtl number, and molecular mean free path) are shown in Table 2.

6.3 Experimental Procedures

Specimen Placement. For the stainless steel tests, two specimens, one with smooth and the other with bead-blasted surfaces, were employed for each test. The specimen with the bead-blasted surface was always placed on top of the smooth-surface specimen.

For the nickel tests, an Armco iron heat meter was placed underneath the smooth-surfaced specimen in order to raise the mean interface contact temperature to the level compatible to that of the stainless steel tests. The placement of the Armco iron also provided a means to confirm correct measurement of heat flow rates through the upper and lower specimens. The test column was shielded with aluminum foil, and insulated with about a 2-cm-thick layer of quartz wool, which was then covered again with aluminum foil.

Test Order. All tests under a gas environment (helium, argon, and nitrogen) were preceded by at least one measurement under vacuum.

In general, the tests were performed in the following order:

(*a*) at least one vaccum test
(*b*) series of helium tests at various gas pressure
(*c*) vacuum test
(*d*) series of nitrogen tests
(*e*) vacuum test
(*f*) series of argon tests

Occasionally, different permutations of the above test orders were tried, so that any possible effect on gap conductance of the test order for the different gases may be observed.

Joint Conductance Measurements. The joint conductance h_j was obtained from the temperature measurements of the specimens according to its usual definition:

$$h_j = \frac{Q/A_a}{\Delta T} \tag{18}$$

The heat transfer rate Q was taken as the average value of the heat flow rates of the upper and lower specimens. The interface temperature difference ΔT was obtained from the difference in the extrapolated values of the temperature of the interface from least-square fitted temperature distributions within the two specimens.

The time duration between the establishment of the control parameters (gas pressure, load level, and heater level) and the measurement was typically 30–120 minutes. In the case of "cold" starts, at least three hours of elapse time were allowed before the first measurement.

Before each measurement was made, the change with time of joint conductance and the temperature readings from the thermocouples were closely monitored.

Gap Conductance Measurements. Gap conductance measurements reported in the present work are based on the difference of the values of joint conductances obtained for the gas-environment and vacuum tests. In terms of the conductance coefficients, measured values of h_g correspond to the following:

$$(h_g)_{\text{measured}} = (h_j)_{\text{gas}} - (h_j)_{\text{vacuum}} \tag{19}$$

where

$(h_j)_{\text{gas}} = h_j$ measured in a gas environment

$(h_j)_{\text{vacuum}} = h_j$ measured in a vacuum

This is the most common means by which experimental values of h_g are estimated. The values of h_g obtained according to Eq. (19) most accurately reflect the actual values of h_g when the contribution of the heat transfer through the contacting solid spots is small compared to that through the gas layer. Throughout this work, measured values of h_g will refer to the values obtained according to Eq. (19). The effective gap thickness Y was estimated by the maximum peak height R_p of the rougher surface of each specimen pair, as discussed in Section 5.

6.4 Experimental Uncertainty. The error associated with the joint conductance measurement (Eq. (18)) is attributed mainly to the uncertainty in the estimate of the heat transfer rate Q across the contact interface. The heat loss, as estimated by the difference between the heat transfer rates through the upper and lower specimens, was as great as 21 percent of the mean value for the tests with helium as the interstitial gas. The heat loss for the tests with nitrogen was much less (maximum 11 percent), and was the least with argon (maximum 8 percent). The mean value of the heat transfer rates between the upper and the lower specimen was used as the estimate for Q in the present work, and this implies that the maximum uncertainty associated with the h_j measurement is estimated to be less than 10 percent for the tests with helium, 6 percent with nitrogen, and 4 percent with argon. For vacuum tests $(h_j)_{\text{vacuum}}$ is estimated to be less than about 3 percent.

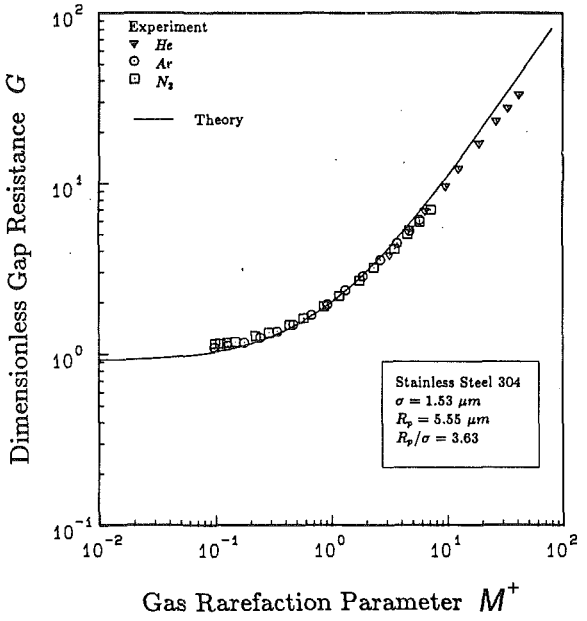

Fig. 4 Dimensionless gap resistance results of Exp. No. 1

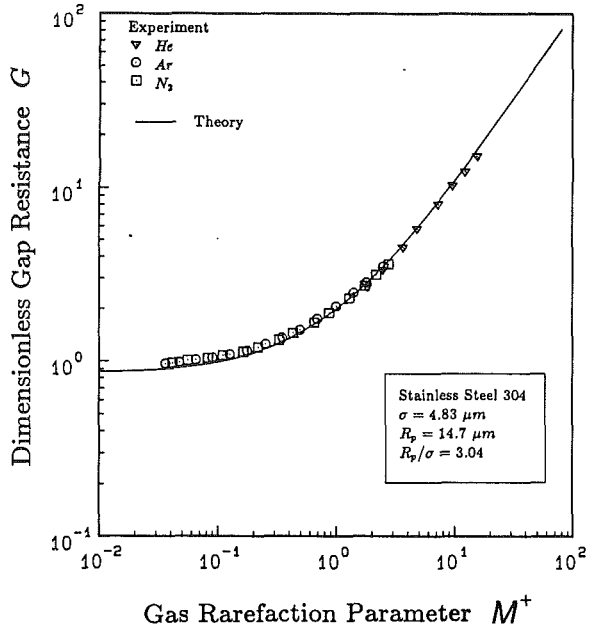

Fig. 5 Dimensionless gap resistance results for Exp. No. 2

The radiation heat exchange across the contact interface is estimated to be less than 1 percent of the total heat transfer rate. The radiative component of the joint conductance, estimated by assuming two isothermal parallel plates (T_1) and (T_2), diffusive grey surfaces with emissivities $\epsilon_1 = \epsilon_2 = 0.2$, is about 0.9 percent for the case of the lowest h_j measurement under a vacuum.

7 Experimental Results

Stainless Steel 304 Pair Experiments. The roughness of the bead-blasted surface for Exp. No. 1($\sigma = 1.53\ \mu$m) is the lowest of all bead-blasted surfaces. Due to the low combined roughness of the surface pair, an effective gap thickness Y as low as 5.6 μm was obtained. Thus, it was possible to achieve a high degree of gas rarefaction (Knudsen number as high as 4.2 for the helium test at $P_g = 9.4$ torr). When the results of all helium, argon, and nitrogen tests are combined, the gap conductance tests for this sample pair span a wide Knudsen number range, $0.019 < \text{Kn} < 4.2$, which nearly covers the continuum, temperature-jump, and transition heat conduction regimes. Figure 4 shows the comparison between the measured and the predicted values of the gap conductances in the form of the dimensionless resistance G over a range of the rarefaction parameter M^+. It is observed from the figures that in terms of the two dimensionless parameters M^+ and G, the test results for the three gases essentially form a single curve and there is no longer the need to distinguish between different gases. The test results of this specimen pair combined with the three different gases cover three orders of magnitude range of the rarefaction parameter M^+, and for this range, the measured values of the gap conductances (or G) agree well with the predicted values (Eq. (13)).

The Knudsen number range covered by Exp. No. 2 ($\sigma = 4.83\ \mu$m) is $0.0078 < \text{Kn} < 1.6$, whose lower end would be considered to be well within the continuum regime. The dimensionless gap resistance results are shown in Fig. 5.

Nickel 200 Pair Experiments. The thermal conductivity of nickel is about 3.5 (at 170°C) times that of stainless steel. Thus the contribution to the joint conductance of the contact conductance is significantly greater than that of the stainless steel contact of similar conditions. The ratio of measured values of the joint and contact conductances varies from 0.65 for argon at 11 torr to 16.2 for helium at 640 torr. For both argon and nitrogen measurements, the contact conductance contributed at least 30 percent of the joint conductance. The gap conductance results are in excellent agreement, as shown in Fig. 6. Even for the argon measurements at $P_g = 11$ torr ($M^+ = 4.0$), where the gap conductance is approximately half of the contact conductance, the agreement is very good.

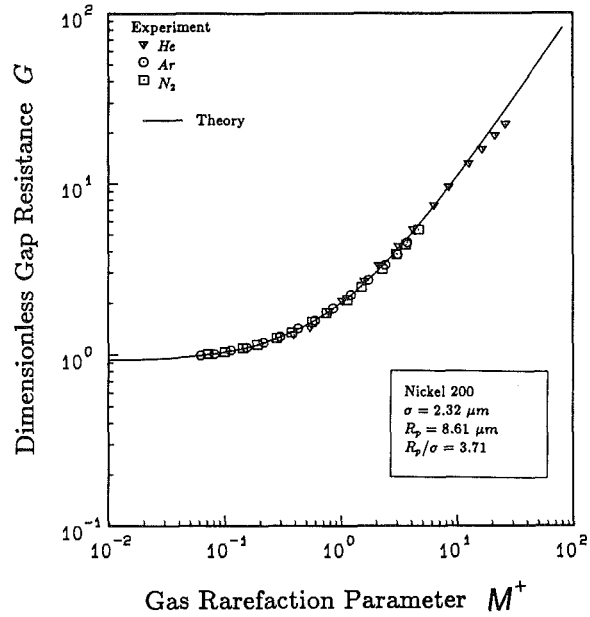

Fig. 6 Dimensionless gap resistance results for Exp. No. 3

The surface roughness for Exp. No. 4 ($\sigma = 11.8\ \mu$m) is the highest of all bead-blasted surfaces. Because of the high value of σ (thus large Y), the lower end of the Knudsen number range of the test is situated well within the continuum regime. The value of R_p/σ (and thus Y/σ estimate) for the sample pair is 2.59 (compared to 3.63, 3.04, and 3.71 for the samples in Exp. Nos. 1-3, respectively). At this low level of Y/σ the effect on the gap conductance due to the nonuniformity of the local heat flow length becomes significant, and this experiment provides a test to verify the modeling of the surface roughness effect. The gap conductance results (Fig. 7) are in excellent agreement with the theory. The Knudsen number of the argon

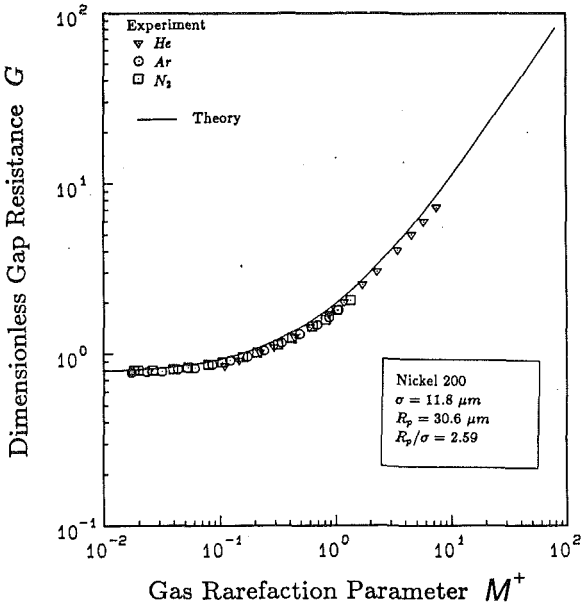

Fig. 7 Dimensionless gap resistance results for Exp. No. 4

test at $P_g = 670$ torr ($M^+ = 0.018$ in the figure) is 0.0034 and the corresponding heat-flow regime may be considered continuum. At this point the predicted and the measured values of G are in excellent agreement at 0.80. This seems to suggest that the enhancement in the gap conductance due to the nonuniformity of the local heat flow length (arising from the surface roughness) for the particular test surface pair is about 20 percent. Thus the surface roughness effect, as modeled by the present gap conductance theory, may be significant and should not be ignored.

8 Summary

The accuracy of the simple model (ISKT) for predicting the rarefied gas heat transfer between two smooth parallel plates was verified through available experimental data. Two important dimensionless parameters, G and M^+, were introduced. Using the existing gap conductance model (YIGC), two predominant effects on gap conductance, gas rarefaction and surface roughness, were discussed. For light-load conditions it was proposed that the maximum peak height R_p may be used to estimate gap thickness.

Gap conductance measurements for light contacts of Stainless Steel 304 pairs and Nickel 200 pairs with helium, argon, and nitrogen as interstitial gases are presented. The measurements were obtained over wide ranges of surface roughness and gas pressure. The measured values of gap conductance are in excellent agreement with the predictions that use the roughness parameter R_p as the estimate for the light-load effective gap thickness. It was also demonstrated that for a given contact interface geometry (i.e., specified roughness and mechanical load) the gap conductance measurements of various gases, when normalized to G, depend upon only one parameter M^+.

Acknowledgments

The authors gratefully acknowledge the assistance of Ms. B. G. Herles for preparation of the manuscript.

References

Bassanini, P., Cercignani, C., and Pagani, C. D., 1967, "Comparison of Kinetic Theory Analysis of Linearized Heat Transfer Between Parallel Plates," *Int. J. Heat Mass Transfer*, Vol. 10, pp. 447–460.

Braun, D., and Frohn, A, 1976, "Heat Transfer in Simple Monatomic Gases and in Binary Mixtures of Monatomic Gases," *Int. J. Heat Mass Transfer*, Vol. 19, pp. 1329–1335.

Braun, D., and Frohn, A., 1977, "Heat Transfer in Binary Mixtures of Monatomic Gases for High-Temperature Differences and for a Large Knudsen Number Range," *Rarefied Gas Dynamics*, J. L. Potter, ed., pp. 149–159.

Cetinkale, T. N., and Fishenden, M., 1951, "Thermal Conductance of Metal Surface in Contact," *Proc. of General Discussion on Heat Transfer*, IMechE, London, pp. 271–275.

Dagnall, H., 1980, *Exploring Surface Texture*, Rank Taylor Hobson, United Kingdom.

Dutkiewicz, R. K., 1966, "Interfacial Gas Gap for Heat Transfer Between Two Randomly Rough Surfaces," *Proc. of the 3rd Int. Heat Transfer Conf.*, Vol. 4, pp. 118–126.

Fenech, H., and Rohsenow, W. M., 1959, "Thermal Conductance of Metallic Surfaces in Contact," Report, Heat Transfer Lab., M.I.T., Cambridge, MA.

Gandhi, J. M., and Saxena, S. C., 1968, "Correlated Thermal Conductivity Data of Rare Gases and Their Binary Mixtures at Ordinary Pressures," *J. of Chemical and Engineering Data*, Vol. 13, No. 3, pp. 357–367.

Garnier, J. E., and Begej, S., 1979, "Ex-reactor Determination of Thermal Gap and Contact Conductance Between Uranium Dioxide: Zircaloy-4 Interfaces," U.S. Nuclear Regulartory Commission Report.

Hegazy, A. A., 1985, "Thermal Contact Conductance of Rough Surfaces: Effect of Surface Micro-hardness Variation," Ph.D. Thesis, Department of Mechanical Engineering, University of Waterloo, Ontario, Canada.

Henry, J. J., 1964, "Thermal Contact Resistance," Ph.D. Thesis, M.I.T., Cambridge, MA.

Kennard, E. H., 1938, *Kinetic Theory of Gases*, McGraw-Hill, New York–London.

Laming, L. C., 1961, "Thermal Conductance of Mechanical Contacts," *ASME Int. Heat Transfer Conf.*, Part 1, No. 8, pp. 65–76.

Liu, C. Y., and Lees, L., 1961, "Kinetic Theory Description of Plane Compressible Couette Flow," *Rarefied Gas Dynamics*, L. Talbot, ed., Academic Press, New York, pp. 391–428.

Lloyd, W. R., Wilkins, D. R., and Hill, P. R., 1973, "Heat Transfer in Multicomponent Monatomic Gases in the Low, Intermediate and High Pressure Regime," presented at the Nuclear Thermonics Conference.

Loyalka, S. K., 1982, "A Model for Gap Conductance in Nuclear Fuel Rods," *Nuclear Technology*, Vol. 57, pp. 220–227.

Mentes, A., Veziroglu, T. N., Samudrala, R., Sheffield, J. W., and Williams, A., 1981, "Effects of Interface Gases on Contact Conductance," presented at the AIAA 19th Aerospace Sciences Meeting, St. Louis, MO, Jan. 12–15.

Popov, V. M., and Krasnoborod'ko, A. I., 1975, "Thermal Contact Resistance in a Gaseous Medium," *Inzhenero-Fizicheskii Zhurnal*, Vol. 28, No. 5, pp. 875–883.

Rapier, A. C., Jones, T. M., and McIntosh, J. E., 1963, "The Thermal Conductance of Uranium Dioxide/Stainless Steel Interfaces," *Int. J. Heat Mass Transfer*, Vol. 6, pp. 397–416.

Rupert, M. P., 1959, "Confusion in Measuring Surface Roughness," *Engineering*, Oct., pp. 393–395.

Shlykov, Yu. P., and Ganin, Ye. A., 1964, "Thermal Resistance of Metallic Contacts," *Int. J. Heat Mass Transfer*, Vol. 7, p. 921–929.

Shlykov, Yu. P., 1965, "Calculating Thermal Contact Resistance of Machined Metal Surfaces," *Teploenergetika*, Vol. 12, No. 10, pp. 79–83.

Shvets, I. T., and Dyban, E. P., 1964, "Contact Heat Transfer Between Plane Metal Surfaces," *Int. Chemical Engineering*, Vol. 4, No. 4, pp. 621–624.

Song, S., and Yovanovich, M. M., 1989, "Contact Interface Gas Heat Transfer: A Method of Measuring Thermal Accommodation Coefficient," *Proceedings of 9th Annual International Electronics Packaging Conference*, San Diego, Ca., Sept. 10–14.

Song, Y., Yovanovich, M. M., and Nho, K., 1989, "Thermal Gap Conductance: Effect of Gas Pressure and Mechanical Load," AIAA Paper No. 89-0429.

Springer, G. S., 1971, "Heat Transfer in Rarefied Gases," *Advances in Heat Transfer*, T. F. Irvine and J. P. Hartnett, eds., Academic Press, Vol. 7, pp. 163–218.

Teagan, W. P., and Springer, G. S., 1968, "Heat-Transfer and Density-Distribution Measurements Between Parallel Plates in the Transition Regime," *Physics of Fluids*, Vol. 11, No. 3, pp. 497–506.

Tsukada, T., and Anno, Y., 1975, "An Evaluation of Machined Surface Topography (2nd Report)," *Bull. Japan Soc. of Prec. Eng.*, Vol. 9, No. 1.

Veziroglu, T. N., 1967, "Correlation of Thermal Contact Conductance Experimental Results," presented at the AIAA Thermophysics Specialist Conference, New Orleans, LA, Apr. 17–20.

Yovanovich, M. M., 1982, "Thermal Contact Correlations," *Spacecraft Radiative Transfer and Temperature Control*, T. E. Horton, ed., Vol. 83 of Progress in Astronautics and Aeronautics, New York, pp. 83–95.

Yovanovich, M. M., DeVaal, J. W., and Hegazy, A. A., 1982, "A Statistical Model to Predict Thermal Gap Conductance Between Conforming Rough Surfaces," AIAA Paper No. 82-0888.

Kinetic Theory Analysis of Flow-Induced Particle Diffusion and Thermal Conduction in Granular Material Flows

S. S. Hsiau

M. L. Hunt

Division of Engineering and
Applied Science,
California Institute of Technology,
Pasadena, CA 91125

The present study on granular material flows develops analytical relations for the flow-induced particle diffusivity and thermal conductivity based on the kinetic theory of dense gases. The kinetic theory model assumes that the particles are smooth, identical, and nearly elastic spheres, and that the binary collisions between the particles are isotropically distributed throughout the flow. The particle diffusivity and effective thermal conductivity are found to increase with the square root of the granular temperature, a term that quantifies the kinetic energy of the flow. The theoretical particle diffusivity is used to predict diffusion in a granular-flow mixing layer, and to compare qualitatively with recent experimental measurements. The analytical expression for the effective thermal conductivity is used to define an apparent Prandtl number for a simple-shear flow; this result is also qualitatively compared with experimental measurements. The differences between the predictions and the measurements suggest limitations in applying kinetic theory concepts to actual granular material flows, and the need for more detailed experimental measurements.

Introduction

The phrase granular-material flows has been used to describe dense gas-solid flows in which the particle-to-particle collisions govern the bulk behavior (see reviews by Savage, 1984; Campbell, 1990; Jaeger and Nagel, 1992). Examples of such flows include grain or coal traveling down an inclined chute, the mixing of dry food products in industrial rotary blenders, and the discharging of particulate material from hoppers and bins. In these dry noncohesive solid flows, the gaseous phase plays a negligible role in the flow mechanics, and hence the flows differ considerably from suspensions of fluidized beds. Instead the mechanics of the flow depends on collisional interactions between the particles, and between the particles and any solid surfaces. As a result the rheology of the flow is complex and not well understood. In addition, the appropriate boundary flow conditions are unclear, since the particle may slip or roll along a solid surface and is not subject to the traditional no-slip boundary condition. Because of these complications, the review by Ahn and Brennen (1991) on granular material flows down inclined chutes suggests that predictions for the velocity or the density profiles within these flows cannot be calculated readily, thus illustrating the lack of fundamental understanding for even the simplest of granular material flows.

In recent years, one method of analysis for the momentum transport relations for granular material flows has evolved from concepts from dense-gas kinetic theories (Jenkins and Savage, 1983; Lun et al., 1984). In applying kinetic theory concepts to granular material flows, the term granular temperature has been used to quantify the particle kinetic energy per unit mass (Savage, 1984; Campbell, 1990); the term evokes the similarity drawn between the motion of particles in a granular flow to the motion of molecules in a gas (Chapman and Cowling, 1970). Unlike the motions of molecules, the particle motion is not self-sustaining since the particle collisions are inelastic. Instead the granular temperature is generated by shearing or vibration of the flow, and this kinetic energy is then conducted into the bulk of the material. The difficulty with applying the kinetic theory analysis to granular flows is that the theory depends on many underlying assumptions that are appropriate for gas molecules. Among these assumptions is that there are only binary particle interactions, the particles are smooth with negligible frictional effects, and that the granular temperature is isotropically distributed between its velocity components (Campbell, 1990). Although these assumptions may not always be appropriate for granular flows, the kinetic theory ideas have significantly advanced the development of the governing transport relations for granular material flows (Ahn and Brennen, 1991).

In conjunction with many of the transport processes, many industries also dry, heat, or cool the granular material while the material is flowing (Kunii, 1980; Richard and Raghavan, 1984; Ferron and Singh, 1991). An important aspect in many of these applications is the degree of mixing that occurs in the handling of the materials (Clump, 1967). Most modeling efforts rely on empirical information that is difficult to apply to a range of material flow rates and different types of material (Stephens and Bridgwater, 1978; Bridgwater et al., 1985). In heat transfer problems, several studies have measured the heat transfer coefficient for flows in inclined chutes (Patton et al., 1986), in vertical channels (Sullivan and Sabersky, 1975), and from heat exchanger tubes (Colakyan and Levenspiel, 1984). These studies, however, have not investigated the effects of the particle mixing on the overall transport rates (Hunt, 1990).

The focus of the present work is in examining the mixing that occurs during a flow of granular material, and the effect that the mixing has on any associated heat transfer processes. The approach of this work follows earlier granular flow work that is based on dense-gas kinetic theories. However, this work develops relations for the effective diffusivity and the effective thermal conductivity, which results from the local motions of the particles. These effects have not been previously investigated from a kinetic theory standpoint except for the recent

Contributed by the Heat Transfer Division and presented at the National Heat Transfer Conference, San Diego, California, August 9–12, 1992. Manuscript received by the Heat Transfer Division March 1992; revision received September 1992. Keywords: Multiphase Flows, Packed and Fluidized Beds. Associate Technical Editor: L. S. Fletcher.

work by Hunt and Hsiau (1990), and Savage (1992). Unlike the diffusivity and thermal conductivity for single-phase fluids, these granular-flow quantities depend both on the properties of the gas and solid phases, and on the flow itself through the distribution of the granular temperature. In this sense, the diffusion coefficient and thermal conductivity are similar to dispersion coefficients in flow through a porous medium (Hunt, 1990), and to turbulent diffusivities used in Reynolds mixing-length models.

The relations developed from the kinetic theory analysis are used to estimate experimental results from two recent studies. The experiments by Hsiau and Hunt (1992) involved a granular-flow mixing layer using differently colored glass spheres. The experiment was designed to investigate particle diffusion by measuring the growth of a mixing layer with downstrean distance. The work by Wang and Campbell (1992) is a heat transfer experiment using an annular shear cell. A temperature gradient was applied across the cell, and the effective thermal conductivity was determined from the applied heat flux and the temperature difference between the walls. The comparisons between the experiments and theory are qualitative, since the granular temperature was not measured directly in either of the studies and had to be inferred from other information.

Development of the Kinetic Theory Analysis

As described in the introduction, much of the recent modeling of granular material flows has been derived from kinetic theory analysis of nonequilibrium flows such as found in the texts by Chapman and Cowling (1970), Kennard (1938), and Present (1958). This section is a brief outline of the kinetic theory analysis as developed for granular material flows, which is used to develop expressions for the particle diffusivity and the effective thermal conductivity.

Similar to the molecular motion of gases, individual particles within a granular material flow may have velocities and associated properties that vary from the mean value. As a result, the ensemble averages of local flow properties are determined by averaging the single-particle properties over the velocity space. Using Φ to represent a single-particle property such as mass, momentum, or energy at some position within the flow, the ensemble average is defined as

$$\langle \Phi \rangle = \frac{1}{n} \int \Phi f^{(1)}(\mathbf{C}) d\mathbf{C} \tag{1}$$

where n is the number density, $f^{(1)}(\mathbf{C})$ is the single-particle velocity distribution function, and $\mathbf{C}$ is the particle fluctuating velocity. The product $f^{(1)}(\mathbf{C})d\mathbf{C}$ represents the probable number of particles per unit volume with a fluctuating velocity within the velocity element $d\mathbf{C}$ centered at $\mathbf{C}$, where $d\mathbf{C} = dC_x dC_y dC_z$. The particle fluctuating velocity is found from the difference between the local velocity $\mathbf{c}$ and the ensemble average velocity $\langle \mathbf{c} \rangle$, $\mathbf{C} \equiv \mathbf{c} - \langle \mathbf{c} \rangle$. Note that the ensemble average of the fluctuating velocity is zero, $\langle \mathbf{C} \rangle = 0$.

The velocity distribution function is decomposed into a local Maxwellian velocity distribution function, $f^{(0)}(\mathbf{C})$ and a correction term, $f^{(c)}(\mathbf{C})$ (Savage and Jeffrey, 1981; Jenkins and Savage, 1983; Campbell, 1990):

$$f^{(1)}(\mathbf{C}) = f^{(0)}(\mathbf{C}) + f^{(c)}(\mathbf{C}) \tag{2}$$

where the Maxwellian term is

$$f^{(0)}(\mathbf{C}) = \frac{n}{(2\pi\Upsilon)^{3/2}} \exp\left(-\frac{C^2}{2\Upsilon}\right) \tag{3}$$

Nomenclature

A = particle surface area
A_1, A_2 = coefficients for $f_1^{(c)}$ and $f_2^{(c)}$
Bi = Biot number = hl_p/k_p
$\mathbf{C}$ = particle fluctuating velocity vector
$\mathbf{C}_{12}$ = relative velocity vector = $\mathbf{C}_1 - \mathbf{C}_2$
$\mathbf{C}'$ = velocity vector after collision
$\overline{C}$ = mean absolute velocity
$\mathbf{c}$ = particle local velocity vector
c_p = particle specific heat
D = diffusion coefficient
d = particle diameter
e_p = restitution coefficient between particles
$f^{(0)}(\mathbf{C})$ = Maxwellian velocity distribution function
$f^{(1)}(\mathbf{C})$ = single-particle velocity distribution function
$f^{(2)}(\mathbf{C}_1, \mathbf{C}_2)$ = pair-distribution function
$f^{(c)}(\mathbf{C})$ = correction term for the single-particle velocity distribution function
Fo = Fourier number = $k_p t A/l_p m c_p$
$g_0(\nu)$ = radial-distribution function
$g_2(\nu, e_p)$ = coefficient used in kinetic theory analysis
h = heat transfer coefficient between the particle and the fluid
$\mathbf{k}$ = vector from the center of particle 1 to particle 2
k_{eff} = effective thermal conductivity
k_p = particle thermal conductivity
l = length scale
l_p = characteristic length
m = particle mass
$\dot{m}$ = mass flux
$\mathbf{M}_{12}$ = average momentum transfer vector
n = number density
$\mathbf{P}$ = stress tensor
Pe_m = Peclet number = $u_m d/D_{11,m}$
Pr = apparent Prandtl number = $\mu c_p/k_{\text{eff}}$
q_y = heat flux in y direction
T = temperature
T_0, T_f = fluid temperatures
t = time scale
t_c = collision interval
u = ensemble-averaged velocity in the flow direction $\equiv \langle c_x \rangle$
u'^2 = ensemble average of the square of fluctuating velocities in the flow direction $\equiv \langle C_x^2 \rangle$
v = diffusion velocity
α^{-1} = relaxation time
$\mathbf{\Gamma}$ = fluctuating energy flux vector
Δe = extra energy carried by a particle
δ = mixing layer thickness
η = $(1+e_p)/2$
θ = collisional turning angle
λ = mean free path
μ = apparent viscosity coefficient
ν = solid fraction
ν^* = maximum shearable solid fraction
ξ = angle between $\mathbf{C}$ and y axis
ρ = bulk density = $\rho_p \nu$ = mn
ρ_p = particle density
σ = mc_p/hA
τ = time variable
Υ = granular temperature
Φ = single-particle property
χ = color concentration
ψ = collision frequency

Subscripts

1, 2 = particle group 1, 2
c = collisional contribution
k = kinetic contribution
m = average property across the mixing layer

In Eq. (3), Υ is the granular temperature, which is defined as the ensemble average of the square of the fluctuating velocities, $\Gamma = \langle C^2 \rangle / 3$. The Maxwellian distribution function assumes an isotropic distribution of the fluctuating velocity components. The correction term is zero if the flow is in equilibrium; however, if a gradient in velocity or granular temperature exists, the flow is not in equilibrium and the correction term should be included. The magnitude of the correction term is small compared with the Maxwellian term, $f^{(c)}(\mathbf{C}) \ll f^{(0)}(\mathbf{C})$. For granular flows of slightly inelastic particles, Lun et al. (1984) derived a general correction term that applies to homogeneous flows with gradients in velocity, granular temperature, or density.

In granular flows there are two important transport mechanisms: the streaming or kinetic mode, and the collisional mode (Campbell, 1990). The streaming or kinetic mode accounts for the transfer of particle properties as the particles move freely between collisions. The collisional mode accounts for the transfer of the properties during collisions. The streaming mode is dominant for dilute flows, which have larger mean-free paths. The collisional mode is more important for high-solid-fraction flows because of the higher collisional frequency.

As developed by Chapman and Cowling (1970), the streaming transport properties are determined by considering the flux of a single-particle property across an imaginary surface within the flow. The flux of a single-particle property is evaluated as $\langle \mathbf{C}\Phi(\mathbf{C}) \rangle$. The kinetic stress tensor, $\mathbf{P}_k$, is found from the flux of momentum; using $\Phi(\mathbf{C}) = \rho \mathbf{C}$ yields

$$\mathbf{P}_k = \rho \langle \mathbf{CC} \rangle \tag{4}$$

Similarly, the flux of the kinetic energy, $\mathbf{\Gamma}_k$, is determined using $\Phi(\mathbf{C}) = 1/2\,\rho C^2$, which yields

$$\mathbf{\Gamma}_k = \frac{1}{2} \rho \langle C^2 \mathbf{C} \rangle \tag{5}$$

Here ρ is the bulk flow density, and is determined from the product of particle mass, m, and the number density, $\rho = mn$, or from the product of the particle density, ρ_p, and the solid fraction, ν, $\rho = \rho_p \nu$.

The collisional contributions are determined by considering the rate of transfer of momentum or energy during a binary collision, as outlined in dense-gas kinetic theories (Chapman and Cowling, 1970). To analyze a binary collision, the pair-distribution function $f^{(2)}(\mathbf{C}_1, \mathbf{C}_2)$ is used instead of the single-particle velocity distribution function. The pair-distribution function accounts for the number of pairs of particles 1 and 2 that are in contact and that have impact velocities within the range $\mathbf{C}_1$ to $\mathbf{C}_1 + d\mathbf{C}_1$ and $\mathbf{C}_2$ to $\mathbf{C}_2 + d\mathbf{C}_2$. Using the Enskog assumption for dense gases, Lun et al. (1984) defined the pair-distribution function from the product of the single-particle velocity distribution function for particles 1 and 2, and a correction factor $g_0(\nu)$,

$$f^{(2)}(\mathbf{C}_1, \mathbf{C}_2) = g_0(\nu) f^{(1)}(\mathbf{C}_1) f^{(1)}(\mathbf{C}_2) \tag{6}$$

The correction factor $g_0(\nu)$ in Eq. (6) is referred to as the radial-distribution function evaluated when the particles are in contact. The radial distribution function equals unity for low-density flows and approaches infinity as the flow approaches a packed, rigid state. An empirical form of this radial distribution function is given by Carnahan and Starling (1969) as follows:

$$g_0(\nu) = (2 - \nu)/2(1 - \nu)^3 \tag{7}$$

However, for sheared granular flows, the work by Lun and Savage (1986) suggests the following form:

$$g_0(\nu) = (1 - \nu/\nu^*)^{-2.5\nu^*} \tag{8}$$

where ν^* is the maximum shearable solid fraction for spherical particles. The radial distribution functions as given by Eqs. (7) or (8) assume an isotropic distribution of collision angles between the two colliding spheres.

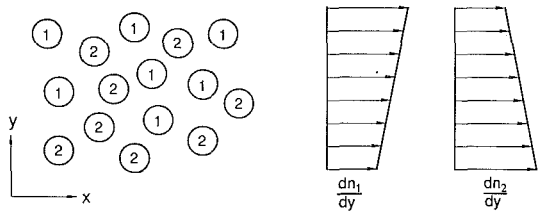

Fig. 1 . Configuration for the concentration gradient

For dense systems, the transfer of momentum and energy during a collision cannot be neglected. The stress tensor, $\mathbf{P}$, and fluctuating energy flux, $\mathbf{\Gamma}$, are found from the sum of streaming and collisional contributions,

$$\mathbf{P} = \mathbf{P}_k + \mathbf{P}_c \tag{9}$$

$$\mathbf{\Gamma} = \mathbf{\Gamma}_k + \mathbf{\Gamma}_c \tag{10}$$

where $\mathbf{P}_c$ and $\mathbf{\Gamma}_c$ represent the collisional contribution to the stress tensor and the fluctuating energy flux vector (Lun et al., 1984).

Particle Diffusion

Let the subscripts 1 and 2 denote two groups of spherical particles with the same diameter, d, and mass, $m_1 = m_2 = m$. To determine the diffusive flux of particles 1 into particles 2, assume that transport by diffusion only occurs in the y direction as shown in Fig. 1. Then the determination of the mass flux is similar to the method used to determine the streaming contributions to the stress tensor and the kinetic-energy flux vector. The mass fluxes of the two groups of particles are

$$\frac{\dot{m}_1}{m} = \Sigma C_{1y} = \int C_{1y} f_1^{(1)}(\mathbf{C}_1) d\mathbf{C}_1 = -D_{12} \frac{dn_1}{dy} \tag{11}$$

$$\frac{\dot{m}_2}{m} = \Sigma C_{2y} = \int C_{2y} f_2^{(1)}(\mathbf{C}_2) d\mathbf{C}_2 = -D_{21} \frac{dn_2}{dy} \tag{12}$$

where ΣC_y symbolizes the y-direction fluctuating velocity integrated over the whole velocity space. Fick's law is used in Eqs. (11) and (12) to define the diffusion coefficients, D_{12} and D_{21}. If the velocity distribution function is Maxwellian ($f^{(c)} = 0$), then the diffusive fluxes $\dot{m}_1$ and $\dot{m}_2$ are zero. Because of the concentration gradient, however, the flow is not in equilibrium and the correction term should be included. For nonequilibrium transport in gases, Kennard (1938) added a correction term to the Maxwellian distribution function and found a nonzero diffusive flux. A similar technique is applied here to derive the self-diffusion coefficient for granular material flows.

In kinetic gas theories, the Boltzmann equation is used to describe the rate of change in the velocity-distribution function that results from particle collisions (Chapman and Cowling, 1970). Similarly, for granular-material flows, the Boltzmann equation is used to determine the distribution functions $f_1^{(1)}$ and $f_2^{(1)}$. Assuming there are no external forces applied to the particles, the Boltzmann equation for particles of type 1 is

$$\frac{\partial f_1^{(1)}}{\partial t} + \mathbf{C}_1 \cdot \nabla f_1^{(1)} = \left[\frac{\partial f_1^{(1)}}{\partial t} \right]_{\text{coll}} \tag{13}$$

where the right-hand side represents the change of velocity distribution function due to the collisions. For steady-state conditions and assuming only variation in the y direction, Eq. (13) becomes

$$C_{1y} \frac{\partial f_1^{(1)}}{\partial y} = \left[\frac{\partial f_1^{(1)}}{\partial t} \right]_{\text{coll}} \tag{14}$$

The general form for the distribution function, Eq. (2), is substituted into Eq. (14), and the derivative of the correction

term is neglected since $f^{(c)} \ll f^{(0)}$. By noting that the collisions do not alter the Maxwellian distribution function, and assuming that Υ_1 is independent of y within the local region of interest, Eq. (14) becomes

$$C_{1y}\frac{\partial f_1^{(0)}}{\partial y}=\frac{C_{1y}}{(2\pi\Upsilon_1)^{3/2}}\exp\left(-\frac{C_1^2}{2\Upsilon_1}\right)\frac{dn_1}{dy}=\left[\frac{\partial f_1^{(c)}}{\partial t}\right]_{\text{coll}} \tag{15}$$

As described by Kennard (1938), one method of solving Eq. (15) is to substitute for the right-hand side an integral expression for the rate of change of the distribution function. The distribution function is then found by solving the integro-differential equation. A simpler method, referred to as the Maxwell–Chapman method as outlined by Kennard (1938), involves substituting an assumed form for $f_1^{(c)}$. Following the arguments by Kennard, the form of Eq. (15) suggests representations for the correction terms:

$$f_1^{(c)}=A_1 C_{1y}\exp\left(-\frac{C_1^2}{2\Upsilon_1}\right) \tag{16}$$

$$f_2^{(c)}=A_2 C_{2y}\exp\left(-\frac{C_2^2}{2\Upsilon_2}\right) \tag{17}$$

where A_1 and A_2 are coefficients that need to be determined. Since the particles are identical, the granular temperatures are equal, $\Upsilon_1=\Upsilon_2=\Upsilon$. Using Eq. (16) to re-evaluate Eq. (11) yields:

$$\frac{\dot{m}_1}{m}=\Sigma C_{1y}=A_1\Upsilon^{5/2}(2\pi)^{3/2}=-D_{12}\frac{dn_1}{dy} \tag{18}$$

A similar expression is obtained for $\dot{m}_2$. For a flow without a net mass flux, $\dot{m}_2$ is equal to $-\dot{m}_1$, and as a result A_2 must be equal to $-A_1$.

To find A_1 it is necessary to examine the rate of change of ΣC_{1y} by collisions. This quantity is determined by multiplying the Boltzmann equation by C_{1y} and integrating over the velocity space. From Eq. (15) and using $D\Sigma C_{1y}$ to represent the rate of change of ΣC_{1y},

$$D\Sigma C_{1y}=\int C_{1y}\left[\frac{\partial f_1^{(c)}}{\partial t}\right]_{\text{coll}} d\mathbf{C}_1=\Upsilon\frac{dn_1}{dy} \tag{19}$$

The first step to determine $D\Sigma C_{1y}$ is to examine the effect of each collision on the velocity C_{1y}. To proceed, consider a collision between an incoming particle 1 and a scattering particle 2; the particles are of equal mass, smooth, and slightly inelastic. By the conservation of linear momentum, the change in y velocity of particle 1 is

$$C'_{1y}-C_{1y}=-C_{12,y}(1+e_p)(1-\cos\theta)/4 \tag{20}$$

where $'$ indicates the velocity after collision, $\mathbf{C_{12}}$ is the relative velocity vector $\mathbf{C_{12}}=\mathbf{C_1}-\mathbf{C_2}$, e_p is the coefficient of restitution between the inelastic particles, and θ is the angle through which $\mathbf{C_{12}}$ is turned during the collision. The next step is to consider all possible collisions between the scattering particle 2 and incoming particles 1. Using the scattering coefficient of $d^2/4$, the fraction of incoming particles 1 per unit area scattered into the angle from θ to $\theta+d\theta$ is $2\pi(d^2/4)\sin\theta\, d\theta$. The number of encounters between the pairs of particles 1 and 2 that result in the movement of particle 1 into an angle $d\theta$ centered at θ is found from the product of the scattering coefficient, $2\pi(d^2/4)\sin\theta\, d\theta$, the relative velocity, C_{12}, and the pair-distribution function, $f^{(2)}(\mathbf{C_1}, \mathbf{C_2})d\mathbf{C_1}d\mathbf{C_2}$. Therefore, the total change in ΣC_{1y} is found by integrating over all possible angles $d\theta$ and over the velocity spaces $d\mathbf{C_1}$ and $d\mathbf{C_2}$,

$$D\Sigma C_{1y}=\int_{-\infty}^{\infty}\int_{-\infty}^{\infty}\int_0^{\pi}\left(2\pi\frac{d^2}{4}\sin\theta\right)C_{12}(C'_{1y}-C_{1y})\times f^{(2)}(\mathbf{C_1}, \mathbf{C_2})d\theta\, d\mathbf{C_1}d\mathbf{C_2} \tag{21}$$

Equation (21) is evaluated by substituting in Eqs. (2), (3), (6), (16), (17), and (20) and neglecting the second-order term, $f_1^{(c)} f_2^{(c)}$. The integral becomes

$$D\Sigma C_{1y}=-(A_1 n_2-A_2 n_1)\frac{8\sqrt{2}}{3}\pi^2 d^2 g_0(\nu)(1+e_p)\Upsilon^3 \tag{22}$$

By combining Eqs. (18), (19), and (22) with $A_2=-A_1$ and $n=n_1+n_2$, the self-diffusion coefficient is

$$D_{11}=\frac{d\sqrt{\pi\Upsilon}}{8(1+e_p)\nu g_0(\nu)} \tag{23}$$

The same result is also derived using a momentum transfer method as outlined by Present (1958). The following is a brief outline of this method. Present used a modified Maxwellian velocity distribution function:

$$f^{(1)}(\mathbf{C})=\frac{n}{(2\pi\Upsilon)^{3/2}}\exp\left[-\frac{C_x^2+(C_y-v_y)^2+C_z^2}{2\Upsilon}\right] \tag{24}$$

where v_y is the diffusion velocity and $v_y \ll C_y$. Equation (24) is linearized, which yields

$$f^{(1)}(\mathbf{C})=\frac{n}{(2\pi\Upsilon)^{3/2}}\exp\left(-\frac{C^2}{2\Upsilon}\right)\left(1+\frac{v_y}{\Upsilon}C_y\right) \tag{25}$$

This correction term has a similar form to the distribution function in Eqs. (16) and (17).

Let $\mathbf{M_{12}}$ denote the average momentum transfer resulting from collisions between group 1 and group 2 per unit volume per unit time. For slightly inelastic particles of uniform mass, the conservation of linear momentum $\mathbf{M_{12}}$ in the y direction is

$$M_{12,y}=\frac{4}{3}(1+e_p)d^2\sqrt{\pi\Upsilon}mg_0(\nu)n_1 n_2(v_{1y}-v_{2y}) \tag{26}$$

From Eq. (4), the kinetic normal stress in the y direction is

$$P_{1k,yy}=\rho_1\langle C_{1y}C_{1y}\rangle=mn_1\Upsilon \tag{27}$$

If the granular temperature is constant in a small local region dy, then the net force acting on group 1 particles is $dP_{1k,yy}=m\Upsilon dn_1$, which is equivalent to $-dP_{2k,yy}$. By the conservation of momentum,

$$dP_{1k,yy}=-M_{12,y}dy \tag{28}$$

Using the fact that the total mass flux is zero, $n_1 v_{1y}=-n_2 v_{2y}$ and $n_1+n_2=n$, the self-diffusion coefficient is derived, which results in the same relation as given by Eq. (23).

Savage (1992) applied the Einstein relation (McQuarrie, 1976), which relates the self-diffusion coefficient to the velocity autocorrelation function:

$$D_{11}=\frac{1}{3}\int_0^{\infty}\langle\mathbf{C}(0)\cdot\mathbf{C}(\tau)\rangle d\tau \tag{29}$$

where τ is a time variable. He followed kinetic-theory arguments and assumed that

$$\langle\mathbf{C}(0)\cdot\mathbf{C}(\tau)\rangle=\langle C^2\rangle\exp(-\alpha t) \tag{30}$$

where α^{-1}, a relaxation time, is influenced by the average momentum change due to collisions (McQuarrie, 1976). When Eq. (29) is evaluated, the resulting expression for the diffusion coefficient is the same as Eq. (23).

Equation (23) indicates that the diffusion coefficient increases with the square root of the granular temperature. To apply the expression to actual flows, the distribution of the granular temperature is needed; however, the granular temperature is difficult to measure experimentally. The experimental study by Hsiau and Hunt (1992) does include measurements of the local fluctuating velocities in the flow direction. These measurements are used to estimate the magnitude of the granular temperature for their experimental conditions.

The experimental work by Hsiau and Hunt (1992) examined

particle diffusion in granular flows by measuring the growth in thickness of a mixing layer. Differently colored but otherwise identical 3-mm-dia glass beads were fed into an upper hopper leading to a vertical glass-walled channel. The flow rate in the channel was controlled by the opening of the bottom hopper. The average solid fraction ranged from 0.59 to 0.64 for all of the experiments. The results indicate that the diffusion process increased with the flow shear rate. The shear rate was varied by changing the spacing and the roughness of the side walls and by varying the flow rates. The ensemble averages of the local velocities and of the square of the fluctuating velocities in the flow direction across the channel were also measured.

To determine the mixing layer thickness, Hsiau and Hunt used a video camera and a frame grabber board operated by a personal computer to digitize the images of the flows. The contrast between the two colors of particles was then enhanced so that one color appeared black and the other appeared white. The distribution of color concentration was calculated after averaging a sequence of images. The mixing layer thickness, δ, was defined by the distance that the color concentration varied from 0.01 to 0.99. Using glass side walls, the thickness remained about one particle diameter, indicating almost no diffusion. The corresponding velocity measurements showed that with the glass walls, the velocity profile was flat, indicating negligible shearing of the flow. The one-particle diameter thickness, rather than a zero mixing-layer thickness, resulted from measurement limitations when the contrast of images was enhanced during image processing, and from the finite thickness of the splitter plate. With the side walls roughened with a layer of particles, the mixing layer thickness increased with downstream distance, and was larger in the narrower channel and for the higher flow rates. For these conditions, the corresponding velocity profiles also indicated that the shear rate is higher than that in the wider channel or for the lower flow rate. Although the transverse velocities were not measured, the authors concluded that the transverse particle movement increased with the shear rate, which yielded the wider mixing layers. The measured mixing-layer thicknesses are plotted as δ/d versus x/d in Fig. 2.

Assuming that the flow is steady with no average transverse velocity, the diffusion equation for the mixing layer is

$$u\frac{\partial \chi}{\partial x}=\frac{\partial}{\partial y}\left(D_{11}\frac{\partial \chi}{\partial y}\right) \tag{31}$$

where χ is color concentration and u is the ensemble-averaged velocity in the flow direction, $u\equiv\langle c_x\rangle$. This equation is simplified by assuming that the local velocity and the diffusivity do not vary across the mixing layer. These assumptions are consistent with the experimental measurements, which indicate that within the mixing layer the velocity distribution is relatively flat. Using the subscript m to denote the average properties across the maximum mixing layer thickness in the experiments, Eq. (31) can be rewritten as

$$u_m\frac{\partial \chi}{\partial x}=D_{11,m}\frac{\partial^2 \chi}{\partial y^2} \tag{32}$$

The boundary conditions for the flow are $\chi\to 1$ when $y\to\infty$ and $\chi\to 0$ when $y\to-\infty$; the initial conditions are at $x=0$ and $y>0$, $\chi=1$, and at $x=0$ and $y<0$, $\chi=0$. Using these conditions, the concentration distribution is evaluated by integrating Eq. (32). This yields

$$\chi(x,y)=\frac{1}{2}\pm\frac{1}{2}\,\mathrm{erf}\left(\frac{\pm y}{2\sqrt{xd}}\mathrm{Pe}_m^{1/2}\right) \tag{33}$$

where the + is for $y>0$ and the − is for $y<0$; Pe_m is the Peclet number, $\mathrm{Pe}_m=u_m d/D_{11,m}$, and erf is the error function. From this expression, the mixing layer thickness is determined as

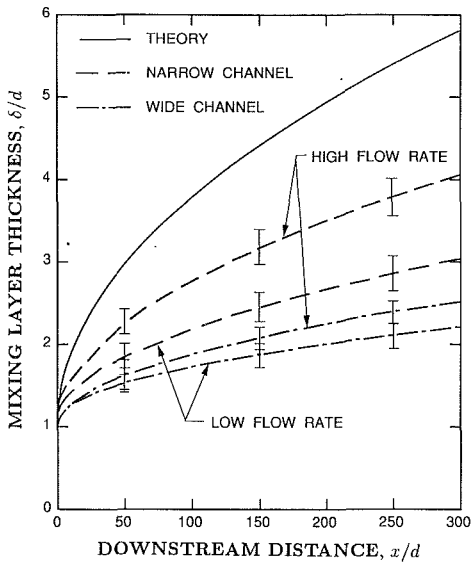

Fig. 2 The growth of mixing layer thickness, δ/d, as a function of downstream distance, x/d, in the wide and narrow channels for 3-mm glass beads. The dashed lines are from the measurements by Hsiau and Hunt (1992), and the error bars are for ±one standard deviation.

$$\frac{\delta}{d}=6.60\left(\frac{x}{d}\frac{1}{\mathrm{Pe}_m}\right)^{1/2} \tag{34}$$

The granular temperature can be estimated by assuming an isotropic distribution in fluctuating velocities. Then the granular temperature is equal to the ensemble average of the square of fluctuating velocities in the flow direction, $\Upsilon=u'^2$, where $u'^2\equiv\langle C_x^2\rangle$. From Eq. (23), Pe_m is

$$\mathrm{Pe}_m=\frac{u_m d}{D_{11,m}}=\frac{8(1+e_p)}{\sqrt{\pi}}\left(\frac{u_m}{u_m'}\right)\nu g_0(\nu) \tag{35}$$

From the experimental results, u_m'/u_m is close to 0.15 for all the experiments in the rough-walled channel. Equation (7) is used to evaluate $g_0(\nu)$ since the shear rate in the central channel is small. Using $\nu=0.64$ and $e_p=0.95$ in Eq. (35), the Peclet number is estimated as 550. By substituting this value into Eq. (34), a mixing layer thickness profile is determined. Since the ratios of u_m'/u_m are close to 0.15 for the four experimental conditions, only one predictive line is shown in Fig. 2. Due to the uncertainty in the initial mixing layer thickness, the theoretical profiles are started at $\delta/d=1$ to compare with the experimental results as shown in Fig. 2.

The comparison between the experimental measurements and the estimates for the mixing layer thickness based on the kinetic-theory diffusivity indicates that the calculations overestimate the experimental results by 60 to 300 percent. Some of the discrepancy may result from the assumptions regarding the magnitude of the granular temperature and from the variations of the granular temperature within the flow. As previously noted, these quantities were not measured in the experiments.

In addition, Savage and Jeffrey (1981) stated that the radial distribution function expressed by Carnahan and Starling (1969, Eq. (7)) agrees well with the numerical molecular dynamics calculations for solid fractions lower than 0.5, but the value is too low for solid fractions greater than 0.5. An underestimate of $g_0(\nu)$ would result in an overprediction of the diffusivity. Equation (8) is proposed as the form of $g_0(\nu)$ by Lun and Savage (1986) for sheared flows of high solid fraction. If Eq. (8) is used for the above calculations, then the kinetic theory estimates would underpredict the experimental mixing layer thickness by 50 to 90 percent. This comparison illustrates the sensitivity of the calculations to the radial distribution function

especially for dense flows. An appropriate distribution function for dense flows has not been examined in the literature. When the solid fraction is close to that of a packed bed, the binary collision assumption used in the kinetic theory model may not be appropriate. Instead the particles slide or roll past each other, and the rotation of particles may increase the diffusive process. In addition, the granular temperature may not be isotropic as assumed in the kinetic theory.

The recent study by Savage (1992) compared the kinetic-theory diffusivity with the results from a computer simulation based on molecular dynamics. Equation (29) was used to calculate the self-diffusion coefficients. He used Eq. (7) as the form of the radial distribution function in the calculations of the kinetic theory. Savage found the self-diffusion coefficients determined from the simulation results were from 50 to 200 percent higher than those predicted by the theory. The deviation was especially large for high solid fractions. He noted that the deviation may result from the use of the isotropic radial distribution function.

Effective Thermal Conductivity

Hunt and Hsiau (1990) used mean-free-path arguments to develop analytical expressions for the effective thermal conductivity for low-density granular flows. They assumed constant properties and determined expressions for the effective thermal conductivity by integrating over the entire flow field. Instead of considering the entire flow with constant properties, a small local region is considered here and properties are assumed constant in this small region. The effective thermal conductivity due to the motion of the particles is developed from dense-gas kinetic theory. Since the heat capacity of the fluid is much smaller than that of the particles, the heat transfer due to the movement of the fluid is neglected. Sun and Chen (1988) verified that conduction between particles during collisions is negligible because of the short duration of the collision time and the small contact area. Therefore, only the heat transfer due to the streaming mode is considered for the heat transfer study. Thermal radiation is also neglected in the present analysis.

Consider a particle of thermal conductivity, k_p, specific heat, c_p, total surface area, A, characteristic length, l_p, and a heat transfer coefficient between the particle and the fluid, h. The temperature gradient only exists in the y direction, as shown in Fig. 3. For Biot number, $\mathrm{Bi}=hl_p/k_p$, less than 0.1, the lumped system analysis is applied and the energy equation becomes

$$mc_p\frac{dT}{dt}=hA\,(T_f-T) \tag{36}$$

where T is particle temperature and T_f is the local temperature of the surrounding fluid. As shown in Fig. 3, consider a particle initially at the fluid temperature T_f that moves a short distance l to a new position with fluid temperature $T_0=T_f+l_y(dT/dy)$, where l_y is the y component of l. Assuming that C_y is constant in this small local region and using t as a characteristic time equal to l_y/C_y, the particle temperature becomes

$$T=T_0-C_y\sigma\frac{dT}{dy}[1-\exp(-l_y/\sigma C_y)] \tag{37}$$

where $\sigma=mc_p/hA$. The group $l_y/\sigma C_y=thA/mc_p$ is the product of the Biot number and the Fourier number, where the Fourier number is $\mathrm{Fo}=k_ptA/l_pmc_p$. When the particle Biot–Fourier number is small, $\mathrm{BiFo}\ll 1$, Eq. (37) reduces to

$$T-T_0=-l_y\frac{dT}{dy} \tag{38}$$

The excess energy carried by the particle to this position relative to the surrounding fluid is $\Delta e=-mc_pl_y(dT/dy)$. The length

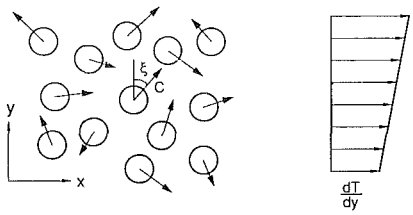

Fig. 3 Configuration for the thermal energy flux

l_y is found from the mean-free path, λ, and the angle ξ between $\mathbf{C}$ and the y axis, $l_y=\lambda\cos\xi$. Therefore,

$$\Delta e=-mc_p\lambda\cos\xi\frac{dT}{dy} \tag{39}$$

Similar to the streaming transport relations, the heat flux in the y direction is found by integrating the product of C_y and the excess energy carried by particles over the entire velocity space:

$$q_y=n\langle\Delta eC_y\rangle=\int\Delta eC_yf^{(1)}(\mathbf{C})d\mathbf{C} \tag{40}$$

By substituting Eqs. (2) and (39) into Eq. (40) and noting that the product of ΔeC_y and the correction term of velocity distribution function is an odd function, Eq. (40) becomes

$$q_y=-\frac{2\sqrt{2}}{3\sqrt{\pi}}mnc_p\lambda\Upsilon^{1/2}\frac{dT}{dy} \tag{41}$$

The next step is to find the mean free path by using techniques from dense-gas theory. Let $\mathbf{k}$ represent the vector from the center of particle 1 to particle 2. Then $d^2(\mathbf{C}_{12}\cdot\mathbf{k})d\mathbf{k}$ is the oblique volume in which particle 2 will collide with particle 1 per unit time for particles 1 and 2 with the relative position vector between $\mathbf{k}$ and $\mathbf{k}+d\mathbf{k}$ (Chapman and Cowling, 1970). The collision frequency is

$$\psi=d^2\int_{\mathbf{C}_{12}\cdot k>0}(\mathbf{C}_{12}\cdot\mathbf{k})f^{(2)}(\mathbf{C}_1,\,\mathbf{C}_2)d\mathbf{k}d\mathbf{C}_1d\mathbf{C}_2$$

$$=4n^2d^2g_0(\nu)\sqrt{\pi\Upsilon} \tag{42}$$

The collision interval, which is the mean time between two successive collisions, t_c, is

$$t_c=\frac{n}{\psi}=\frac{1}{4nd^2g_0(\nu)\sqrt{\pi\Upsilon}} \tag{43}$$

The mean-free path is the product of the mean absolute velocity $\overline{C}$ and the collision interval, t_c, so

$$\lambda=\overline{C}t_c=\frac{\overline{C}}{4nd^2g_0(\nu)\sqrt{\pi\Upsilon}} \tag{44}$$

where $\overline{C}$ in Eq. (44) is defined as

$$\overline{C}=\int Cf^{(1)}d\mathbf{C}=\sqrt{\frac{8\Upsilon}{\pi}} \tag{45}$$

By introducing Eq. (45) into Eq. (44) and using $\nu=\pi nd^3/6$, the mean free path is

$$\lambda=\frac{d}{6\sqrt{2}\nu g_0(\nu)} \tag{46}$$

Finally, the local heat flux is determined,

$$q_y=-\frac{\rho c_p}{9\sqrt{\pi}}\frac{d}{\nu g_0(\nu)}\Upsilon^{1/2}\frac{dT}{dy} \tag{47}$$

and the effective conductivity k_{eff} is

$$k_{\mathrm{eff}}=\frac{\rho c_p}{9\sqrt{\pi}}\frac{d}{\nu g_0(\nu)}\Upsilon^{1/2} \tag{48}$$

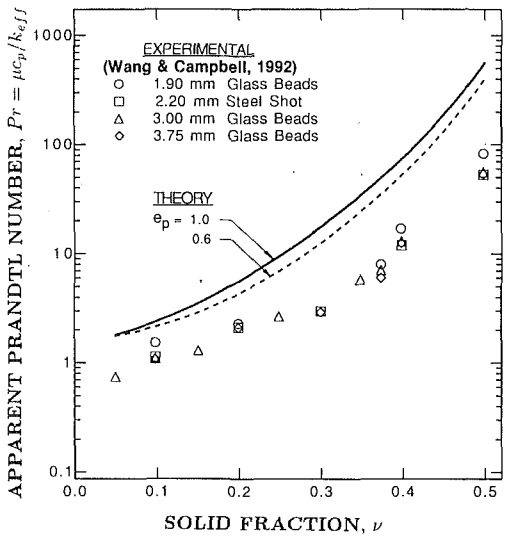

Fig. 4 Comparison of the theoretical predictions for the apparent Prandtl number with the experimental shear-flow measurements of Wang and Campbell (1992)

The expression for the effective conductivity is similar to that for the diffusion coefficient since each increases with d and $\Theta^{1/2}$ and decreases with $g_0(\nu)$.

The recent experiments by Wang and Campbell (1992) measured the effective thermal conductivity of a granular flow. Their experiment involved an annular Couette shear cell in which the rotating surface was heated, and the stationary surface was cooled. Wang and Campbell operated their experiment for solid fractions ranging from 0.1 to 0.5, and for four different types of particle: steel shot ($d = 2.2$ mm) and three sizes of glass bead ($d = 1.9$, 3.0, and 3.75 mm). The temperatures of the plates and the input heat flux were measured. The effective thermal conductivity of the flow was determined by balancing the heat conducted by the flows and the heat dissipated due to the shearing process with the appropriate heat input boundary condition. In addition, force transducers were used to determine the shear force on the materials. The apparent viscosity coefficient, μ, was calculated from the shear stress and shear rate, and then used to define the apparent Prandtl number. As shown in Fig. 4, the apparent Prandtl number increases with solid fraction, and appears to be independent of particle type and size.

To compare with the experimental results of Wang and Campbell, the granular temperature must be known, but neither the velocities nor the granular temperature were measured in the experiment. However, the Prandtl number does not depend on granular temperature and can be more easily compared by defining an apparent viscosity based on kinetic theory results. In the work by Lun et al. (1984), the shear stress depends on both the kinetic and the collisional contributions and is expressed as

$$P_{xy} = -d\rho_p g_2(\nu, e_p)\Theta^{1/2}\frac{du}{dy} \tag{49}$$

where $g_2(\nu, e_p)$ is a function of solid fraction and the coefficient of restitution between particles and is determined from

$$g_2(\nu, e_p) = \frac{5\sqrt{\pi}}{96}\left[\frac{1}{\eta(2-\eta)}\frac{1}{g_0(\nu)} + \frac{8}{5}\frac{3\eta-1}{2-\eta}\nu + \frac{64}{25}\eta\left(\frac{3\eta-2}{2-\eta}+\frac{12}{\pi}\right)\nu^2 g_0(\nu)\right] \tag{50}$$

where $\eta = (1+e_p)/2$. Using $-\mu$ to denote the term preceding du/dy in Eq. (49), the apparent Prandtl number is defined by

$$\mathrm{Pr} = \frac{\mu c_p}{k_{\mathrm{eff}}} = 9\sqrt{\pi}g_0(\nu)g_2(\nu, e_p) \tag{51}$$

For the flows in Wang and Campbell's experiment, Eq. (8) is used as the form of $g_0(\nu)$ since the flows are sheared. The curves in Fig. 4 are plotted from Eq. (51) using $e_p = 1$ and 0.6. The theoretical curves overpredict the results and the discrepancy increases with the solid fraction. This comparison suggests that the theoretical thermal conductivity is lower than that of the experiments for the same apparent viscosity.

The differences between the experimental results and the kinetic theory estimates may be attributed to some of the same reasons stated in the diffusion analysis. In addition, it should be noted that the height of the annulus in the experiment by Wang and Campbell was at most 5.4 cm, which was from 14 to 28 particle diameters. For this finite-sized annulus, the shearing of the flow and the heat transfer near the wall may vary significantly from that in the bulk region. Near-wall variations may alter the determination of the apparent viscosity and the effective thermal conductivity. The analysis also assumes that the Biot–Fourier number for the particles is small. An estimate can be made using a heat transfer coefficient between a stationary particle and a flowing fluid. Using the collisional interval for the time (Eq. (43)), and assuming that the square root of the granular temperature is 15 percent of the bulk average velocity, the Biot–Fourier number is of the order of 0.001. Hence the small Biot–Fourier number assumption seems to be justified for the Wang and Campbell's experiments.

Conclusions

The focus of this work is in developing constitutive relations for the particle diffusion coefficient and the effective thermal conductivity in granular flows. Using concepts from dense-gas kinetic-theory analysis, these transport coefficients are shown to depend on the square-root of the granular temperature, the particle size and the radial distribution function. The coefficients are used to estimate transport rates in two different experimental studies. The comparisons demonstrate that the kinetic theory analysis is valuable for developing functional dependences for the various flow properties; however, there are discrepancies between the kinetic theory estimates and the experimental measurements. Several reasons are suggested for the discrepancy: the binary collision model, the uniform distribution of particle collisions, and the isotropic distribution of granular temperature as assumed in the kinetic theory model. These effects are generally not included in the kinetic-theory analysis for granular material flows. In addition, there exist difficulties in comparing the theory to the experiments because fundamental granular flow quantities such as the local density or solid fraction are not easily measured. Future work should focus on experimental techniques to measure these quantities. These measurements would provide a better indication of the applicability of kinetic theory analysis for granular flows.

References

Ahn, H., and Brennen, C. E., 1991, "Channel Flows of Granular Material and Their Rheological Implications," *Particulate Two-Phase Flow*, M. C. Roco, ed., Butterworth Publishing, Chap. 7.

Bridgwater, J., Foo, W. S., and Stephens, D. J., 1985, "Particle Mixing and Segregation in Failure Zones—Theory and Experiment," *Powder Technology*, Vol. 41, pp. 147–158.

Campbell, C. S., 1990, "Rapid Granular Flows," *Ann. Rev. Fluid Mech.*, Vol. 22, pp. 57–92.

Carnahan, N. F., and Starling, K. E., 1969, "Equations of State for Nonattracting Rigid Spheres," *J. Chem. Phys.*, Vol. 51, pp. 635–636.

Chapman, S., and Cowling, T. G., 1970, *The Mathematical Theory of Nonuniform Gases*, 3rd ed., Cambridge University Press, Cambridge, UK.

Clump, C. W., 1967, "Mixing of Solids," *Mixing, 2*, Academic Press, New York–London, Chap. 10, pp. 263–286.

Colakyan, M., and Levenspiel, O., 1984, "Heat Transfer Between Moving Bed of Solid and Immersed Cylinders," *AIChE Symp. Ser. 241*, Vol. 80, pp. 156–168.

Ferron, J. R., and Singh, D. K., 1991, "Rotary Kiln Transport Processes," *AIChE J.*, Vol. 37, pp. 747–758.

Hsiau, S. S., and Hunt, M. L., 1992, "Shear-Induced Particle Diffusion and Longitudinal Velocity Fluctuations in a Granular-Flow Mixing Layer," *J. Fluid Mech.*, in press.

Hunt, M. L., 1990, "Comparison of Convective Heat Transfer in Packed Beds and Granular Flows," *Ann. Rev. Heat Transfer, 3*, Chap. 6, pp. 163–193.

Hunt, M. L., and Hsiau, S. S., 1990, "Thermal Conductivity of Granular Flows," *Heat Transfer, 5*, G. Hetsroni, ed., Hemisphere Publishing Co., Washington, DC, pp. 177–182.

Jaeger, H. M., and Nagel, S. R., 1992, "Physics of the Granular State," *Science*, Vol. 255, pp. 1523–1530.

Jenkins, J. T., and Savage, S. B., 1983, "A Theory for the Rapid Flow of Identical, Smooth, Nearly Elastic Spherical Particles," *J. Fluid Mech.*, Vol. 130, pp. 187–202.

Kennard, E. H., 1938, *Kinetic Theory of Gases*, McGraw-Hill, New York.

Kunii, D., 1980, "Chemical Reaction Engineering and Research and Development of Gas Solid System," *Chemical Engineering Science*, Vol. 35, pp. 1887–1911.

Lun, C. K. K., Savage, S. B., Jeffrey, D. J., and Chepurniy, N., 1984, "Kinetic Theories for Granular Flow: Inelastic Particles in Couette Flow and Slightly Inelastic Particles in a General Flowfield," *J. Fluid Mech.*, Vol. 140, pp. 223–256.

Lun, C. K. K., and Savage, S. B., 1986, "The Effects of Impact Velocity Dependent Coefficient of Restitution on Stresses Developed by Sheared Granular Materials," *Acta Mechanica*, Vol. 63, pp. 15–44.

McQuarrie, D. A., 1976, *Statistical Mechanics*, Harper and Row, New York.

Patton, J. S., Sabersky, R. H., and Brennen, C. E., 1986, "Convective Heat Transfer to Rapidly Flowing, Granular Materials," *Int. J. Heat Mass Transfer*, Vol. 29, pp. 1263–1269.

Present, R. D., 1958, *Kinetic Theory of Gases*, McGraw-Hill, New York.

Richard, P., and Raghavan, G. S. V., 1984, "Drying and Processing by Immersion in a Heated Particulate Medium," in: *Advances in Drying*, Vol. 3, A. S. Mujumdar, ed., Hemisphere Publishing, pp. 39–70.

Savage, S. B., 1984, "Mechanics of Rapid Granular Flows," *Adv. Appl. Mech.*, Vol. 24, pp. 298–366.

Savage S. B., and Jeffrey, D. J., 1981, "The Stress Tensor in a Granular Flow at High Shear Rates," *J. Fluid Mech.*, Vol. 110, pp. 255–272.

Savage, S. B., 1992, "Disorder, Diffusion and Structure Formation in Granular Flows," in: *Disorder and Granular Media*, D. Bideau, ed., Elsevier Science Publishers, Amsterdam.

Stephens, D. J., and Bridgwater, J., 1978, "The Mixing and Segregation of Cohesionless Particulate Materials. Part I. Failure Zone Formation," *Powder Technology*, Vol. 21, pp. 17–28.

Sullivan, W. N., and Sabersky, R. H., 1975, "Heat Transfer to Flowing Granular Media," *Int. J. Heat Mass Transfer*, Vol. 18, pp. 97–107.

Sun, J., and Chen, M. M., 1988, "A Theoretical Analysis of Heat Transfer Due to Particle Impact," *Int. J. Heat Mass Transfer*, Vol. 31, pp. 969–975.

Wang, D. G., and Campbell, C. S., 1992, "Reynolds' Analogy for Particle Flows: The Relationship Between the Apparent Thermal Conductivity and Viscosity for a Sheared Granular Material," *J. Fluid Mech.*, in press.

ERRATA

To the paper "Comparative Studies on Nonlinear Hyperbolic and Parabolic Heat Conduction for Various Boundary Conditions: Analytic and Numerical Solutions," by A. Kar, C. L. Chan, and J. Mazumder, published in the ASME JOURNAL OF HEAT TRANSFER, Vol. 114, No. 1, February 1992, pp. 14–20.

1 The title of Table 2 on p. 18:

Original: Table 2 Temperature field for Case 3 at $t = 0.05$ for $T_o = 9$, $q_a = -7$, $\delta = 0.2$, and $\epsilon = 0.2$

Change to: Table 2 Temperature field for Case 3 at $t = 0.05$ for $T_o = 9$, $q_a = -7$, $\delta = 0.2$, and $\epsilon = 20.0$

2 On p. 19 we discuss the results for Case 2:

Original: We will now present the results for Case 2 (specified heat flux on both ends). In all cases presented below, the flux is specified to be 0.3 on the left-hand boundary and -0.2 on the right.

Change to: We will now present the results for Case 2 (specified heat flux on both ends). In all cases presented below, the flux is specified to be 0.5 on the left-hand boundary and -0.2 on the right.

3 On p. 19 we discuss the results for Case 3:

Original: For Case 3, the temperature is kept at $T^*/T_r^* = 3.0$ at $x = 0$ and the flux is kept at -1.0 at $x = 1$ in this study.

Change to: For Case 3, the temperature is kept at $T^*/T_r^* = 3.0$ at $x = 0$ and the flux is kept at -2.0 at $x = 1$ in this study.

Eddy Diffusivity Based Comparisons of Turbulent Prandtl Number for Boundary Layer and Free Jet Flows With Reference to Fluids of Very Low Prandtl Number

K. Bremhorst
Professor,
Department of Mechanical Engineering,
The University of Queensland,
Queensland 4072 Australia

L. Krebs
Research Scientist,
Kernforschungszentrum Karlsruhe GmbH,
Institut für Angewandte Thermo- und Fluiddynamik
7500 Karlsruhe 1,
Federal Republic of Germany

It is shown that turbulent Prandtl numbers for turbulent boundary layer and jet flows correlate well if compared on the basis of eddy diffusivity. Experimental data for liquid sodium (Pr = 0.0058) lead to a universal expression relating turbulent Prandtl number to eddy diffusivity of heat with the same expression applying to boundary layer and jet flows. This suggests that the length and velocity scale dependence of the turbulent Prandtl number is associated predominantly with the eddy diffusivity of momentum. Since turbulent flow codes generally include eddy diffusivity of momentum calculations, simple and accurate estimates of eddy diffusivity of heat are possible without reliance on a variety of turbulent Prandtl number functional relationships for prediction of the temperature field. Available results also indicate that turbulent Prandtl number can be set at 0.9–1.0 irrespective of molecular Prandtl number, provided that $\epsilon_M/\nu > 3Pr^{-1}$ and the structures of the mean temperature gradient and mean shear are similar.

Introduction

Prediction of heat transfer rates in turbulent flows generally centers around the solution of the Reynolds form of the energy equation which in its simplest form for incompressible, subsonic flows with no internal heat generation is given by

$$\overline{U}_i \frac{\partial T}{\partial x_i} = \frac{\partial}{\partial x_i}\left[\alpha + \epsilon_H\right] \frac{\partial T}{\partial x_i} \tag{1}$$

Difficulties arise because of the need to model ϵ_H. A frequently used technique is to assume that ϵ_H is related to ϵ_M through the turbulent Prandtl number and that the latter equals 0.9–1.0 for the more commonly used fluids, such as air and water.

Considerable interest does, however, exist in applications using liquid metals, such as mercury, sodium-potassium eutectic, or sodium. These have much higher thermal conductivities and also much lower Prandtl numbers than air or water. Developmental work in sodium cooled nuclear reactors, for example, is carried out in models with water as the working fluid. Transfer of results from such experiments then requires a knowledge of turbulent Prandtl numbers for heat transfer predictions.

Several reviews of the turbulent Prandtl number problem are available and include those by Reynolds (1975), Launder (1976), Jenkins (1951) and Jischa and Rieke (1979). For very low Prandtl number fluids, the latter derived a particularly simple relationship by application of the transport equations for turbulent heat flux and turbulent kinetic energy. These authors showed that

$$\mathrm{Pr}_t = C + \frac{B}{\mathrm{Pr}} \tag{2}$$

where B is Reynolds number dependent and C is a constant. A direct consequence of this result is that Pr_t becomes very large for liquid metals.

A more phenomenological derivation based on the renewal-penetration model was used with some success by Thomas (1970). Cebeci (1973) commenced with the simplified one-dimensional, unsteady momentum and enthalpy equations with unsteady boundary conditions to develop mixing length models for eddy diffusivities of momentum and heat. These give the turbulent Prandtl number and its dependence on Pr, flow velocity and length scale.

The mixing length used by Cebeci (1973) is the distance from the wall, thus making it a wall-based model. The full model for a constant total shear stress layer is available in Cebeci and Bradshaw (1984) in dimensionless form as

$$\epsilon_M/\nu = \kappa^2 y^{+2}[1-\exp(-y^+/A^+)]^2 \frac{\partial u^+}{\partial y^+} \tag{3a}$$

$$\epsilon_H/\nu = \kappa\kappa_H y^{+2}[1-\exp(-y^+/A^+)][1-\exp(-y^+/B^+)] \frac{\partial u^+}{\partial y^+} \tag{3b}$$

$$B^+ = \frac{1}{\sqrt{\mathrm{Pr}}} \sum_{i=1}^{5} C_i (\log_{10}\mathrm{Pr})^{i-1} \tag{3c}$$

$$\mathrm{Pr}_t = \frac{\kappa}{\kappa_H} \frac{1-\exp(-y^+/A^+)}{1-\exp(-y^+/B^+)} \tag{3d}$$

$$\frac{\partial u^+}{\partial y^+} = (2a)^{-1}(-1+\sqrt{1+4a}) \tag{3e}$$

where $A^+ = 26$, $\kappa = 0.4$, $\kappa_H = 0.44$, $C_1 = 34.96$, $C_2 = 28.79$, $C_3 = 33.95$, $C_4 = 6.3$, $C_5 = -1.186$, and $a = (\kappa y^+)^2[1-\exp(-y^+/A^+)]^2$.

Selecting typical fluids of interest, namely, liquid sodium (Pr = 0.0058), mercury (Pr = 0.02), air (Pr = 0.72), water (Pr = 5.7) and water-salt solution (Pr = 14.3), gives the Pr_t results of Fig. 1. It is seen that Pr has little effect for air and

Contributed by the Heat Transfer Division for publication in the JOURNAL OF HEAT TRANSFER. Manuscript received by the Heat Transfer Division April 1991; revision received December 1992. Keywords: Forced Convection, Modeling and Scaling, Turbulence. Associate Technical Editor: R. J. Simoneau.

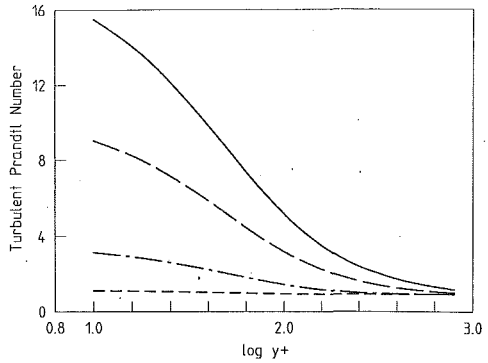

Fig. 1 Turbulent Prandtl number as a function of distance from the wall, Eqs. 3(*a*)-(*e*). Pr: —— = 0.0058, — — — = 0.02, — · — = 0.1, ---- = 0.72, 5.7, and 14.3

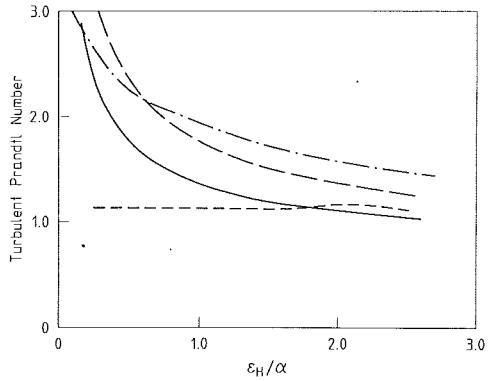

Fig. 2 Turbulent Prandtl number as a function of eddy diffusivity; symbols as for Fig. 1

the high Prandtl number fluids, although for fluids with Pr = 0.1 or less, a significant y^+ effect is evident. The effect for mercury and liquid sodium is rather dramatic, but is consistent with experiment. Na and Habib (1973) used a modified form of the Cebeci (1973) model for turbulent pipe flow and found good agreement with experimental data for the Pr range 0.02–14.3.

Application of the renormalization group procedure to turbulent heat transfer in an incompressible fluid has led Yakhot et al. (1987) to the universal relationship, Eq. (4), between eddy diffusivity of heat and momentum with Prandtl number as a parameter. This result contains no wall distance or Reynolds number dependence other than that already included in the determination of the eddy diffusivity of momentum.

$$\left(\frac{\mathrm{Pr}_{\mathrm{tot}}^{-1}-1.1793}{\mathrm{Pr}^{-1}-1.1793}\right)^{0.65}\left(\frac{\mathrm{Pr}_{\mathrm{tot}}^{-1}+2.1793}{\mathrm{Pr}^{-1}+2.1793}\right)^{0.35}=\frac{\nu}{\nu+\epsilon_M} \tag{4}$$

Neither model has been tested for Prandtl numbers below 0.02 although experimental results using liquid sodium with Pr = 0.0058 are now available. These are close to the lower Prandtl number limit of practical interest.

Liquid Sodium Data

Fuchs (1973) measured temperature profiles in fully developed pipe flow with constant wall heat flux at a nominal temperature of 220°C (Pr = 0.0071). These gave ϵ_H in the core region and ϵ_M was obtained by use of published velocity field data. Sheriff and O'Kane (1981) reported ϵ_H and Pr_t data for point source injection placed on the centerline of fully developed pipe flow at Pr = 0.0071–0.0072. This flow is essentially like a free jet in a coflowing stream of the same velocity, thus making direct comparison with the boundary layer model of Cebeci (1973) difficult. Bremhorst et al. (1989) performed measurements in water and liquid sodium with a point source using a multibore jet block. As no cross-stream velocity gradients existed, direct calculation of a turbulent Prandtl number is not readily possible, although eddy diffusivities of heat are determinable. Bremhorst and Krebs (1992) extended the latter results by significantly reducing the ambient flow surrounding the point source flow. The resultant flow is similar to a free jet for which Pr_t can be calculated from measured velocity and temperature profiles but comparison with boundary layer measurements is difficult.

Attempts at scaling these Pr_t results with various Reynolds numbers proved fruitless. Bremhorst and Krebs (1992) found, however, that for liquid sodium ($0.0058 < \mathrm{Pr} < 0.0072$) their own data and those of Fuchs (1973), and Sheriff and O'Kane (1981) collapsed on to the curve given by Eq. (5) for the range of $0.053 < \epsilon_H/\alpha < 3.0$. This contains no additional length or velocity scale other than that associated with ϵ_M. Such a result is attractive, as modern computer codes already calculate ϵ_M. Equation (5) will then give ϵ_H, without in fact having to know Pr_t first.

$$\mathrm{Pr}_t=\frac{\epsilon_M}{\epsilon_H}=1.8\,\exp(-1.5\epsilon_H/\alpha)+0.9 \tag{5}$$

Rescaling of Fig. 1 to highlight the eddy diffusivity dependence leads to the result of Fig. 2. It should be noted that the y^+ dependence of Cebeci's wall model is no longer evident, as the turbulent diffusivities are now the prime variables. Only the molecular Prandtl number enters as a parameter. Consequently, jet flow data and wall bounded flow data can now be compared easily. Furthermore, direct comparison with the Yakhot et al. model of Eq. (4) is also possible. For Pr = 0.0058, which is being used as representative of liquid sodium data, excellent agreement exists between these two quite different model results, Fig. 3.

Furthermore, excellent agreement is also noted between these theoretical models and the experimental data represented by

Nomenclature

A^+ = 26
B = constant or function of Reynolds number
B^+ = function of Prandtl number, Eq. (3*c*)
C = constant
C_i = constants for i = 1 to 5
C_μ = constant in k-ϵ model of turbulence
k = turbulent kinetic energy
Pr = molecular Prandtl number
Pr_t = turbulent Prandtl number
$\mathrm{Pr}_{\mathrm{tot}}$ = total Prandtl number
$\overline{T}$ = mean temperature
u^+ = mean velocity nondimensionalized with friction velocity
x_i = ith coordinate direction
y^+ = distance from wall nondimensionalized with friction velocity and kinematic viscosity
α = molecular diffusivity of heat
ϵ = dissipation rate of turbulent kinetic energy
ϵ_M = eddy diffusivity of momentum
$\epsilon_{M,\chi}$ = eddy diffusivity of momentum evaluated at χ
ϵ_H = eddy diffusivity of heat
κ = 0.4
κ_H = 0.44
ν = kinematic viscosity
χ^+ = dimensionless distance = y^+A^+/B^+

Subscripts

water = working fluid is water
sodium = working fluid is sodium

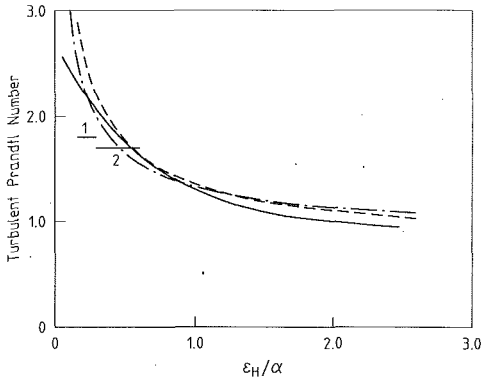

Fig. 3 Turbulent Prandtl number comparisons for liquid sodium:
—— **Eq. (5)**
— — — — **Cebeci model for Pr = 0.0058**
—·— **Yakhot et al., Eq. (4), for Pr = 0.0058**
1 2 **jet block data of Bremhorst et al. (1989)**

Eq. (5), Fig. 3. This would suggest that there is no essential difference between wall flows and fully turbulent free flows as far as Prandtl number dependence is concerned. The wall distance in the Cebeci model is, therefore, better considered as a turbulent length scale such as is contained in the Prandtl formulation of diffusivity as a product of turbulence velocity and a length. The small difference between Cebeci's curve and Eq. (5) as ϵ_H/α increases vanishes at large ϵ_H/α, where both results tend toward $\mathrm{Pr}_t = 0.9$. Whether or not this difference is of physical significance would require availability of further suitable data.

The scaling chosen for Fig. 2 highlights another unexpected feature, namely that mercury for which the molecular Prandtl number is significantly larger than for sodium, yields turbulent Prandtl numbers above those for sodium. Thus, a consistently increasing trend for Pr_t with decreasing Pr at given ϵ_H/α does not exist even though a monotonic increase in Pr_t with decreasing Pr at a given y^+ is noted in Fig. 1. Measurements by Brown et al. (1957) for mercury (Pr = 0.02) in fully developed pipe flow and by Awad (1965) with sodium-potassium (Pr = 0.02–0.025) in fully developed pipe flow show turbulent Prandtl numbers which are consistent with the above observation. It is interesting to note that for a given ϵ_H, Pr_t is a maximum in the range Pr = 0.07–0.08 which is near that of liquid aluminum.

The results of Bremhorst et al. (1989) for a point source in an essentially shear free flow can be compared with the above results in two ways. Firstly, it is readily possible to compare values of thermal diffusivities for identical measurements in water and liquid sodium which yield the ratio of the respective turbulent Prandtl numbers for the two fluids as $\epsilon_{H,\mathrm{water}}/\epsilon_{H,\mathrm{sodium}} = \mathrm{Pr}_{t,\mathrm{sodium}}/\mathrm{Pr}_{t,\mathrm{water}}$ since ϵ_M, whatever its value, can be made the same for both flows if Reynolds number similarity is applied. The second possibility is to calculate a nominal turbulent diffusivity based on the k-ϵ model of turbulence, Eq. (6).

$$\epsilon_M = C_\mu \frac{k^2}{\epsilon} \tag{6}$$

The first approach gives a turbulent Prandtl number ratio of 1.57 and 1.48 for a jet Reynolds number of 17070 and 34140, respectively. In the downstream flow, corresponding values of ϵ_H/α are 0.17–0.32 and 0.33–0.64 for the two Reynolds numbers. Application of Eq. (6) gives 0.72–1.1 and 1.06–1.64 for the turbulent Prandtl number ratio at these Reynolds numbers. Clearly, the latter approach is somewhat dubious as extrapolation of Eq. (6) to the zero mean shear case is not based on the equations of motion. Nevertheless, quite plausible values result. Taking the first approach as more meaningful, and accepting Pr_t for water (Pr = 5.7) as given by Eqs. 3(a)–(e), leads to an effective turbulent Prandtl number for the liquid sodium case of 1.8 and 1.7 at the two Reynolds numbers. These two values are shown in Fig. 3 and are seen to be in close agreement with Eq. (5) and the Cebeci model. The limited results of Fig. 3 clearly indicate a simple and unique relationship between ϵ_H and ϵ_M irrespective of the type of flow, at least for $\epsilon_H/\alpha \geq 0.2$. Such a finding is consistent with that of Yakhot et al. (1987).

Reconciliation with the Cebeci Wall-Layer Model

It may appear that the Cebeci model expressed by Eqs. 3(a–e) is at variance with the above finding that ϵ_H is a direct function of ϵ_M. If Eq. 3(a) is rewritten in the general length variable $\chi^+ = y^+A^+/B^+$, then a modified eddy diffusivity of momentum given by the Eq. (7) results.

$$(\epsilon_{M,\chi}/\nu)^{0.5} = \kappa\chi^+[1-\exp(-\chi^+/A^+)]\sqrt{\frac{\partial u^+}{\partial \chi^+}} \tag{7}$$

Substitution of Eqs. 3(a) and (7) in Eq. 3(b) yields

$$\epsilon_H/\nu = (\epsilon_M\epsilon_{M,\chi})^{0.5}\left(\frac{\kappa_H}{\kappa}\right)\frac{(B^+)^{0.5}}{(A^+)^{0.5}\nu} \tag{8}$$

The Prandtl number dependence is contained in B^+. ϵ_M and $\epsilon_{M,\chi}$ are the same function but ϵ_M is evaluated at y^+ whereas $\epsilon_{M,\chi}$ is taken at the modified distance χ^+. Equation (8) makes the y^+ dependence more transparent and shows that ϵ_H is proportional to the geometric mean of the two eddy diffusivities, ϵ_M and $\epsilon_{M,\chi}$, which is consistent with the more general result by Yakhot et al. (1987), and that for liquid sodium by Bremhorst and Krebs (1992).

Concluding Remarks

For fully turbulent flows, new and existing data, especially for very low Prandtl number fluids, show the local eddy diffusivity to be the main scaling parameter for turbulent Prandtl number. Turbulent Prandtl number increases significantly only when $\epsilon_H/\alpha < 0.3$–0.4 and then only for low Prandtl number fluids, such as liquid sodium and mercury or sodium-potassium.

From data presented, it can be seen that $\mathrm{Pr}_t \leq 1.0$ for $\epsilon_H/\alpha \geq 3.0$ irrespective of Prandtl number. Thus, points in the flow where $\epsilon_M/\nu \geq 3\ \mathrm{Pr}^{-1}$ require no correction to, or model for the generally accepted value of $\mathrm{Pr}_t \simeq 0.9$–1.0. For lower values of ϵ_M/ν, the Cebeci model, or that by Yakhot et al. (1987), or Eq. (5) in the case of liquid sodium, gives a good representation of turbulent Prandtl number. Although the Cebeci model is a wall-based one, it has been shown to be consistent with the proposition that ϵ_H is a direct function only of ϵ_M and Pr. This leads to the conclusion that the flow length and velocity scale information is contained mainly in the eddy diffusivity of momentum. If ϵ_M is known, the complex functional dependencies of turbulent Prandtl number on flow length and velocity scales become superfluous for determination of ϵ_H.

For practical purposes, three flow regimes exist. The first is for $\epsilon_H/\alpha \geq 3\mathrm{Pr}^{-1}$, where $\mathrm{Pr}_t = 0.9$–1.0. The second covers $0.2 \leq \epsilon_H/\alpha < 3\mathrm{Pr}^{-1}$, for which the Cebeci model, or that by Yakhot et al. (1987) or Eq. (5) for liquid sodium, gives a good prediction for ϵ_H from ϵ_M. When $\epsilon_H/\alpha < 0.2$, molecular conduction dominates so that uncertainties arising from lack of accurate knowledge of turbulent Prandtl number are of little consequence. Since commonly used computer codes calculate eddy diffusivity of momentum, the above findings relating ϵ_H to ϵ_M can be implemented quite easily and with a large degree of certainty.

Although the present approach gives good correlation of available data for liquid sodium, it should be noted that this may be due to the similarity of the structures of mean temperature gradients and mean shear as shown by Rogers et al.

(1989) from direct simulation data. The latter showed that when such a similarity does not exist, turbulent Prandtl numbers can become much less than 1.0. This is a regime not contained in the Cebeci model which can yield only turbulent Prandtl numbers near unity and above. In view of the exactness of direct numerical simulation data, some caution is required in the application of Eq. (5) until more experimental data become available for flow situations with low Prandtl number fluids where similarity between momentum and thermal fields is less pronounced.

References

Awad, A. S., 1965, "Heat Transfer and Eddy Diffusivity in NaK in a Pipe at Uniform Wall Temperature," Dis., University of Washington (Univ. microfilms, Ann Arbor 66-5809).

Bremhorst, K., and Krebs, L., 1992, "Experimentally Determined Turbulent Prandtl Numbers in Liquid Sodium at Low Reynolds Numbers," *Int. J. Heat Mass Transfer*, Vol. 35, No. 2, pp. 351–359.

Bremhorst, K., Krebs, L., Müller, U., and Listijono, J. H. B., 1989, "Application of Gradient Diffusion and Dissipation Time Scale Ratio Model for Prediction of Mean and Fluctuating Temperature Fields in Liquid Sodium Downstream of a Multi-Bore Jet Block," *Int. J. Heat Mass Transfer*, Vol. 32, No. 11, pp. 2037–2046.

Brown, H. E., Amstead, B. H., and Short, B. E., 1957, "Temperature and Velocity Distribution and Transfer of Heat in a Liquid Metal," *Trans. ASME*, Vol. 79, pp. 279–285.

Cebeci, T., 1973, "A Model for Eddy Conductivity and Turbulent Prandtl Number," *J. Heat Transfer, Trans. ASME*, Vol. 95, pp. 227–234.

Cebeci, T., and Bradshaw, P., 1984, "Physical and Computational Aspects of Convective Heat Transfer," Springer Verlag, New York.

Fuchs, H., 1973, "Heat Transfer to Flowing Sodium," Thesis, Institut für Reaktorforschung, Würenlingen, Switzerland, EIR, Bericht, No. 241.

Jenkins, R., 1951, "Variation of the Eddy Conductivity With Prandtl Modulus and its use in Prediction of Turbulent Heat Transfer Coefficient," *Proc. Heat Transfer Fluid Mech. Int.*, Stanford Univ., Vol. 147.

Jischa, M., and Rieke, H. B., 1979, "About the Prediction of Turbulent Prandtl and Schmidt Numbers From Modeled Transport Equations," *Int. J. Heat Mass Transfer*, Vol. 27, pp. 1547–1555.

Launder, B. E., 1976, "Heat and Mass Transport," in: *Turbulence*, P. Bradshaw, ed., p. 232, Springer, Berlin.

Na, T. Y, and Habib, I. S., 1973, "Heat Transfer in Turbulent Pipe Flow Based on a New Mixing Length Model," *Appl. Sci. Res.*, Vol. 28, pp. 415, 302.

Reynolds, A. J., 1975, "The Prediction of Turbulent Prandtl and Schmidt Numbers," *Int. J. Heat Mass Transfer*, Vol. 18, p. 1055.

Rogers, M. M., and Mansour, N. N., and Reynolds, W. C., 1989, "An Algebraic Model for the Turbulent Flux of a Passive Scalar," *J. Fluid Mech.*, Vol. 203, pp. 77–101.

Sheriff, N., and O'Kane, D. T., 1981, "Sodium Eddy Diffusivity of Heat Measurements in a Circular Duct," *Int. J. Heat Mass Transfer*, Vol. 24, pp. 205–211.

Thomas, L. C., 1970, "Temperature Profiles for Liquid Metals and Moderate Prandtl Number Fluids," ASME JOURNAL OF HEAT TRANSFER, Vol. 92, pp. 565–567.

Yakhot, V., Orszag, S. A., and Yakhot, A., 1987, "Heat Transfer in Turbulent Fluids—I. Pipe Flow," *Int. J. Heat Mass Transfer*, Vol. 30, pp. 15–22.

Analytic Prediction of the Friction and Heat Transfer for Turbulent Flow in Axial Internal Fin Tubes

Nae-Hyun Kim
Assistant Professor,
Kum-Oh National Institute of Technology,
Kumi City, Korea

R. L. Webb
Professor,
The Pennsylvania State University,
University Park, PA 16802

An analytic model is developed to predict the friction factors and Nusselt numbers for turbulent flow in axial internal fin tubes. The present model uses the Law of the Wall and applies the logarithmic universal velocity and temperature profile to the interfin and core regions of the flow. The fin shape is assumed trapezoidal, and the fin parameters such as fin height, fin root thickness and fin tip thickness are determined from the tube dimensional data. Theoretically based friction and heat transfer equations are developed for internally finned tubes in an algebraic form. The analytic model predicts Carnavos friction data for 11 axial internal fin tubes within ±10 percent, and heat transfer data of air, water, and water-glycol within ±15 percent when proper velocity and temperature profiles are used.

1 Introduction

The need for high performance heat exchangers has led to the development of many types of surfaces that enhance the tube-side heat transfer performance of circular tubes. One method of augmenting the heat transfer performance is the use of internal fins.

Carnavos (1979, 1980) provides heat transfer and friction data for turbulent flow in axial and helical finned tubes. His data spanned $0.7 \le \mathrm{Pr} \le 25$. He initially attempted to correlate the data using the hydraulic diameter concept in the Dittus-Boelter heat transfer and Blasius friction factor equations. Figure 1 shows Carnavos's axial fin data compared with the hydraulic diameter correlations. If the helical fin data were included, the scatter would be approximately the same as for Fig. 1. Figure 1 shows that the correlations poorly predict the data. To correlate the data, Carnavos developed empirical correction factors to the hydraulic diameter-based correlation. The correction factors given by Eqs. (1) and (2) are multiplied by the hydraulic diameter-based correlations:

$$F_f = f/f_h = (A_{fa}/A_n)^{0.5}\cos^{0.5}\theta \quad (1)$$

$$F_h = \mathrm{Nu}/\mathrm{Nu}_h = (A_{fa}/A_{fc})^{0.1}(A_n/A_a)^{0.5}\sec^3\theta \quad (2)$$

Equations (1) and (2) do not explicitly account for such geometric parameters as the dimensionless fin height (e/D) and the interfin region aspect ratio $(p-t)/e$, on which the heat transfer and friction characteristics should depend.

Patankar et al. (1979) used a numerical model to predict the heat transfer and friction characteristics of axial internal fin tubes. This model employs one empirical constant to fit the results with Carnavos's (1979) data. Watkinson et al. tested internally finned tubes with turbulent air (1973) and water (1975). Their correlation uses the hydraulic diameter with a correction factor from Ornatskii et al. (1970). The correlations do not agree with those of Carnavos. The literature survey shows that the empirical correlation by Carnavos (1979) is the best available correlation, based on reliable data for air, water and water-glycol mixtures.

In this study, an analytic model is developed assuming the validity of the Law of the Wall across the flow area. The Law of the Wall was successfully applied to predict the friction in internal fin tubes by Scott and Webb (1981). In this study, their model is critically evaluated, and the idea is extended to predict the heat transfer in internal fin tubes. In the following section, the model will be developed and applied to a smooth tube, and then to axial internal fin tubes.

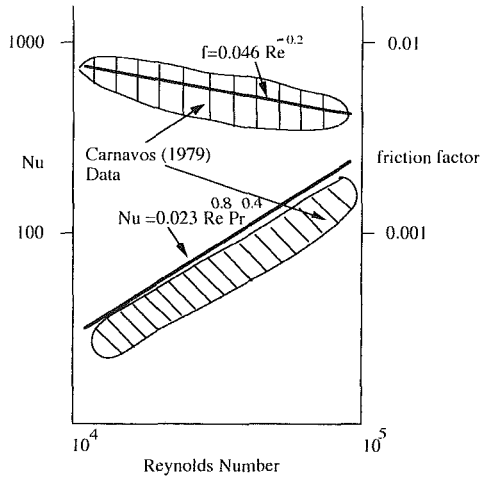

Fig. 1 Carnavos's (1979) experimental data

2 Theoretical Development

2.1 Smooth Tube. Developed turbulent velocity profile measurements in pipe flow in a region outside the viscous sublayer ($y^+ > 26$) are well described by the universal velocity profile, that is,

$$u^+ = 2.5 \ln y^+ + 5.5 \quad (3)$$

The velocity profile has been shown to be independent of the channel shape or pipe diameter, and thus is often called Law of the Wall (Hinze, 1975). The Law represents the velocity profile over more than 90 percent of the pipe radius and deviates only near the pipe center.

By analogy, the fully developed temperature profile in the turbulence-dominating region may be expressed in a similar form.

$$T^+ = A_s \ln y^+ + B_s \quad (4)$$

Equation (4) describes the temperature profile outside the molecular transport sublayer, and is known as the universal temperature profile. The dimensionless thickness of the molecular

Contributed by the Heat Transfer Division for publication in the JOURNAL OF HEAT TRANSFER. Manuscript received by the Heat Transfer Division March 1992; revision received October 1992. Keywords: Augmentation and Enhancement, Finned Surfaces, Forced Convection. Associate Technical Editor: W. A. Fiveland.

transport sublayer depends on the Prandtl number of the fluid. At moderate Prandtl numbers ($\mathrm{Pr} \approx 1$), it is approximately the same as the viscous sublayer thickness ($y^+ \approx 26$). At larger Prandtl numbers, the dimensionless thickness gets smaller, and at smaller Prandtl numbers, it gets larger. The literature shows two temperature profile correlations which are applicable over a range of Prandtl numbers—one by Gowen and Smith (1967) and the other by Kader (1981). Gowen and Smith measured the temperature profile for a range of Prandtl numbers ($0.7 \le \mathrm{Pr} \le 14$), and obtained correlations for A_s and B_s. The values of A_s given by Gowen and Smith (1967) are approximately constant over the Pr range ($A_s \cong 2.5$). However, B_s is strongly dependent on the Prandtl number, and is given by,

$$B_s = 5 \ln\left(\frac{5\mathrm{Pr}+1}{30}\right) + 8.55 + 5\mathrm{Pr} \tag{5}$$

Kader (1981) provides a temperature profile of a similar form. The applicable range of Kader's correlation, however, is much wider ($6 \times 10^{-3} \le \mathrm{Pr} \le 4 \times 10^4$) than Gowen and Smith's. Kader developed the correlation from general similarity arguments and fitting with a wide range of experimental data. The A_s value of the Kader's correlation is 2.12 and B_s is given by

$$B_s = (3.85\mathrm{Pr}^{1/3} - 1.3)^2 + 2.12 \ln \mathrm{Pr} \tag{6}$$

The expressions for A_s and B_s are summarized in Table 1. The Nusselt number (or Stanton number) in circular tubes may be obtained by integrating the velocity and temperature profiles over the pipe cross section

$$\frac{1}{\mathrm{St}} = \frac{\mathrm{RePr}}{\mathrm{Nu}} = \frac{1}{A}\int_A u^+ T^+ dA \tag{7}$$

where

$$\mathrm{St} = \frac{h}{\rho \bar{u} c_p}$$

$$u^+ = u/u^*$$

$$T^+ = \frac{(T_w - T)\rho c_p u^*}{q''}$$

$$h = \frac{q''}{(T_w - \bar{T})}$$

The present authors predicted the Nusselt number for flow in a smooth tube, and the results are listed in Table 2. The friction factor is needed for the calculation of Eq. (7), for which Blasius friction correlation was used. The Reynolds and Prandtl numbers are chosen to encompass Carnavos's (1980) internal fin tube test range—Prandtl number 0.7 for air, 6.5 for water and 25 for water-glycol mixture. Also shown are the Nusselt numbers computed from the well-accepted Petukhov (1970) and Kader and Yaglom (1972) equations, which are

$$\mathrm{St} = \frac{\mathrm{Nu}}{\mathrm{RePr}} = \frac{f/2}{1.07 + 12.7\sqrt{f/2}(\mathrm{Pr}^{2/3} - 1)} \quad \text{(Petukhov)} \tag{8}$$

$$\mathrm{St} = \frac{\sqrt{f/2}}{2.12 \ln (\mathrm{Re}\sqrt{f}) + 12.5\mathrm{Pr}^{2/3} + 2.12 \ln (\mathrm{Pr}) - 10.1} \quad \text{(Kader and Yaglom)} \tag{9}$$

Gowen and Smith (1967) originally proposed $A_s \cong 2.2$ at $\mathrm{Pr} = 0.7$ and $A_s = 2.5$ at other Prandtl numbers. However, usage of $A_s = 2.5$ yields a better agreement with other correlations at $\mathrm{Pr} = 0.7$. Thus, A_s was set to 2.5 throughout the Prandtl number range. Table 2 shows that, at moderate Prandtl numbers (up to $\mathrm{Pr} = 6.5$), the Gowen and Smith based predictions agree with the reference correlations better than Kader-based predictions. At higher Prandtl numbers, however, the Kader-based predictions agree much better than the Gowen and Smith based predictions. This is expected because Gowen and Smith

Table 1 Comparisons between temperature profile correlations

	Gowen and Smith (1967)	Kader (1981)
A_s	$\cong 2.5$	2.12
B_s	$5 \ln\left(\frac{5\,\mathrm{Pr}+1}{30}\right) + 8.55 + 5\,\mathrm{Pr}$	$(3.85\,\mathrm{Pr}^{1/3} - 1.3)^2 + 2.12 \ln \mathrm{Pr}$

Table 2 Comparison between predicted Nusselt numbers for a smooth tube

		Nu			
Re	Pr	Gowen & Smith	Kader	Petukhov	Kader & Yaglom
10000	0.7	31.9	33.1	29.9	32.5
100000	0.7	177.	191.	166.	187.
10000	6.5	76.6	84.2	82.8	78.0
100000	6.5	533.	589.	567.	548.
10000	13.	91.	108.	108.	102.
100000	13.	657.	777.	766.	739.
10000	25.	102.	135.	137.	132.
100000	25.	753.	990.	996.	966.

Nomenclature

A = flow area, m^2
A_a = actual heat transfer area, m^2
A_{fa} = actual flow area, m^2
A_{fc} = core flow area based on fin tip diameter, m^2
A_n = nominal flow area based on fin root diameter, m^2
A_s = constant used in Eq. (4)
b = half the fin spacing, m
B_s = constant used in Eq. (4)
c_p = specific heat, J/kg K
D = tube inside diameter, m
D_i = tube diameter at the fin tip, m
D_h = hydraulic diameter, m
e = fin height, m
f = friction factor
h = heat transfer coefficient $= q''/(T_w - \bar{T})$, W/m^2K
k = thermal conductivity, W/m K
n = number of fins in a tube
Nu = Nusselt number $= hD_h/k$
p = fin pitch based on fin root diameter, m
p_i = fin pitch based on fin tip diameter, m
Pr = Prandtl number $= \mu c_p/k$
q'' = heat flux, W/m^2
R = tube radius, m
Re = Reynolds number $= \rho \bar{u} D_h/\mu$
St = Stanton number $= h/\rho \bar{u} c_p$
t = fin thickness, m
T^+ = dimensionless temperature $= (T_w - \bar{T})\rho c_p u^*/q''$
u = velocity, m/s
u^+ = dimensionless velocity $= u/u^*$, m/s
u^* = friction velocity $= \sqrt{\tau_w/\rho}$, m/s
Δu = shift of the velocity profile, m/s
y = coordinate normal to the flow direction, m
y^+ = dimensionless y coordinate $= yu^*/\nu$
θ = spiral fin tube helix angle
μ = viscosity, Ns/m^2
η = fin efficiency
ρ = density, kg/m^3
τ_w = wall shear stress, N/m^2

Superscripts and Subscripts

h = based on hydraulic diameter characteristic dimension
f = fin region
c = core region
m = measured
p = predicted
r = fin root
t = fin tip
w = at the wall
$\bar{}$ = averaged value

Table 3 Carnavos's tube dimensions

Tube No.	D (mm)	D_i (mm)	n	A_{fa}, (mm^2)	A_n, (mm^2)	D_h (mm)	D_h (S&W) (mm)	t_t (mm)	t_r (mm)
5	9.93	9.40	41	75.4	77.5	7.24	5.70	0.0	0.40
6	10.6	8.08	10	79.4	89.0	5.56	5.43	0.63	0.77
10	8.00	5.46	16	40.6	50.3	2.71	2.47	0.28	0.67
11	7.87	4.79	16	36.1	46.7	2.29	1.95	0.12	0.90
12	7.87	5.72	16	40.6	48.7	3.02	2.75	0.29	0.65
13	7.04	4.75	10	29.9	38.7	3.39	2.66	0.12	1.46
14	13.9	10.9	10	137.	151.	8.15	7.44	0.63	1.34
16	7.64	3.18	6	33.4	45.9	2.63	2.63	0.93	0.93
19	11.0	5.97	6	78.9	95.9	5.24	4.88	0.66	1.48
27	14.6	8.38	6	147.	168.	7.54	7.07	0.63	1.56
28	10.7	8.18	16	80.8	89.3	4.81	4.37	0.22	0.68
29	10.9	5.61	5	80.7	94.1	5.64	5.32	0.58	1.33

correlation was obtained from the experimental data of $0.7 \le \mathrm{Pr} \le 14$, and the Kader correlation was based on the data for a much wider Prandtl number range ($6 \times 10^{-3} \le \mathrm{Pr} \le 4 \times 10^4$). Thus, the Gowen and Smith correlation may be more accurate within the specified Prandtl number range of interest here. In this study, both correlations will be considered to predict the Nusselt numbers in internal fin tubes.

2.2 Axial Internal Fin Tube. As mentioned previously, Carnavos (1979, 1980) tested internal fin tubes. The tube dimensions are listed in Table 3 for 11 axial internal fin tubes. The 11 tubes tested by Carnavos have $3.3 \le p/e \le 5.6$, $0.02 \le e/D \le 0.29$ and $5 \le n \le 41$. Carnavos obtained the tube dimensions from the enlarged tube cross-sectional photos. The hydraulic diameters were calculated from the actual flow areas and wetted perimeters.

The Law of the Wall was successfully applied to Carnavos's axial internal fin tube data by Scott and Webb (1981) for friction factor prediction. They predicted the Carnavos friction data within ±10 percent. Figure 2 defines the basis of the model used by Scott and Webb. They assumed a rectangular fin shape. The fin shape is an important parameter because it affects the hydraulic diameter, and eventually the friction and heat transfer characteristics. The fin parameters—fin height "e" and fin thickness "t"—were determined from Carnavos's tube geometry data assuming the fins are of rectangular cross section.

$$e = \frac{D - D_i}{2} \tag{10}$$

$$t = \frac{A_n - A_{fa}}{ne} \tag{11}$$

where D is the nominal inside diameter (tube inside diameter to the fin root), D_i is the fin tip diameter, A_n is the nominal flow area and A_{fa} is the actual flow area. The resulting hydraulic diameters are shown in Table 3 along the those from Carnavos's paper. Carnavos calculated the hydraulic diameters from the actual flow areas and wetted perimeters as determined by enlarged photographs of the tube cross sections. Table 3 shows that the calculated Scott and Webb's hydraulic diameters are smaller than the actual values by as much as 22 percent (for tubes 5 and 13). The smaller hydraulic diameters yield higher friction factors at the same flow velocity, because the friction factor is proportional to a negative power of Reynolds number. Scott and Webb tried to explain the increased friction by introducing the velocity shift concept in the core region.

In this study, the fin shape is taken as trapezoidal, as shown in Fig. 3. The actual cross-sectional photos (Fig. 1 of Carnavos's 1979 paper) show that the fin shape is trapezoidal, rather than rectangular. In this model, the number of fin parameters are three—fin height "e", fin tip thickness "t_t", and fin root thickness "t_r"—whereas two parameters (fin height and fin thickness) determine the fin shape in Scott and Webb's model. The additional fin parameter may be determined using

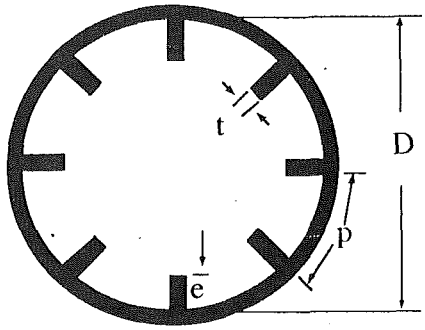

Fig. 2 Geometric model by Scott and Webb (1981)

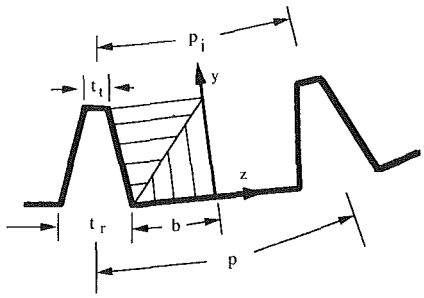

Fig. 3 Geometric model in the fin region

the actual hydraulic diameter, as reported by Carnavos. In this way, the mismatch between the calculated and actual hydraulic diameters which existed in Scott and Webb's model does not occur. The trapezoidal fin shape parameters are determined from the actual tube dimensions (D, D_i, A_n, A_{fa}, p, D_h, n) as follows:

$$e = \frac{D - D_i}{2} \tag{12}$$

$$t_t = \frac{e^2 - \beta^2 + \delta^2/4}{\delta - 2\beta} \tag{13}$$

$$t_r = \delta - t_t \tag{14}$$

where

$$\beta = \frac{2A_{fa}}{nD_h} - \frac{p - \delta}{2} \tag{15}$$

$$\delta = \frac{2(A_n - A_{fa})}{ne} \tag{16}$$

The values of t_t and t_r are listed in Table 3. The calculated fin geometry may be checked with Carnavos's actual fin geometry through the enlarged cross-sectional photos. This was not done in this study, because the enlarged photos were not available to the authors. However, when compared with the actual size photos shown in Fig. 1 of Carnavos's (1979) paper, the calculated fin geometry appears to be reasonable. As shown in Eqs. (12) to (16), all Carnavos's actual fin geometry data are used in determining the fin parameters, except the interfin area. The interfin area is an important parameter, because the universal velocity and temperature profiles are integrated over the area yielding friction and heat transfer coefficients for the region. The calculated interfin areas were compared with those reported by Carnavos, and they agreed within ±1 percent. In the following section, an analysis is performed to obtain an algebraic expression for friction and heat transfer coefficients in internally finned tubes.

The cross sectional flow area (A) of a circular finned channel may be divided into two regions: (1) the interfin region (A_f) for $0 < y < e$, and (2) the core region (A_c) for $y \ge e$. Thus,

$$A = A_c + A_f \tag{17}$$

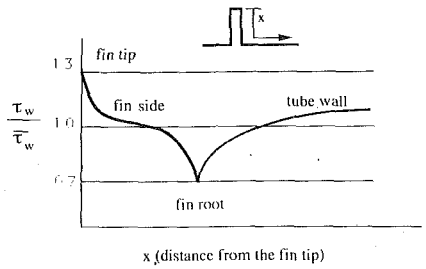

Fig. 4 Local wall shear stress distribution in finned tube (Trupp et al., 1983)

Writing the continuity equation for the two regions yields

$$\bar{u}A = \bar{u}_f A_f + \bar{u}_c A_c \tag{18}$$

In the derivation of Eq. (18), density is assumed constant across the flow area. Dividing Eq. (18) by u^* and using $\bar{u}/u^* = \sqrt{2/f}$ allows Eq. (18) to be written as

$$\sqrt{2/f} = \frac{\bar{u}_f}{u^*}\frac{A_f}{A} + \frac{\bar{u}_c}{u^*}\frac{A_c}{A} \tag{19}$$

where

$$\frac{\bar{u}_f}{u^*} = \frac{1}{A_f}\int_{A_f} u^+ dA \tag{20}$$

$$\frac{\bar{u}_c}{u^*} = \frac{1}{A_c}\int_{A_c} u^+ dA \tag{21}$$

The friction velocity u^* is defined as $\sqrt{\bar{\tau}_w/\rho}$. For a smooth tube, the local wall shear stress τ_w is uniform peripherally, and is the same as the average wall shear stress $\bar{\tau}_w$. For an internally finned tube, however, τ_w should vary along the periphery. The literature does not show local wall shear stress measurements in a trapezoidal fin tube. The available wall shear stress information is for a rectangular fin tube. The wall shear stress variation in a rectangular fin tube may be considered as an extreme case of the wall shear stress in a trapezoidal fin tube. Trupp et al. (1983) measured the shear stress distribution in a rectangular finned tube. The finned tube had very high fins ($e/D = 0.33$). The measured wall shear stress distribution is reproduced in Fig. 4. In the figure, local wall shear stress τ_w is normalized by the average wall shear stress $\bar{\tau}_w$. Figure 4 shows that τ_w is maximum at the fin tip ($\tau_w/\bar{\tau} \cong 1.3$), decreases along the fin surface, and is minimum at the fin root ($\tau_w/\bar{\tau}_w \cong 0.7$). The shear stress distribution along the tube wall is approximately uniform ($\tau_w/\bar{\tau}_w \cong 1.0$) at the center region and gradually decreases to $\tau_w/\bar{\tau}_w \cong 0.7$ at the fin root corner. The shear stress distribution needs to be modeled for the friction factor calculation. In this study, the local wall shear stress τ_w is assumed to be equal to the average wall shear stress $\bar{\tau}_w$. This may cause some error in the friction and heat transfer prediction. However, the error may not be significant considering that the integration and addition process involved in evaluating the tube friction and heat transfer coefficients acts to smooth the local effects. The uniform shear stress assumption may be evaluated from the following example.

Consider the finned tube of Trupp et al. (1983). The shear stress distribution along the fin surface may be modeled to vary linearly from $\tau_w/\bar{\tau}_w = 1.3$ at the fin tip to $\tau_w/\bar{\tau}_w = 0.7$ at the fin root. Figure 5 illustrates the shear stress distribution. Trupp et al.'s finned tube have very high fins ($e/D = 0.33$) compared with commercial finned tubes, and the shear stress variation along the fin surface would be much larger for the Trupp et al.'s tube than for commercial finned tubes. Then, Trupp et al.'s tube may be considered as an extreme case.

Writing the continuity equation for the fin region A_f assuming "n" element divisions in the region,

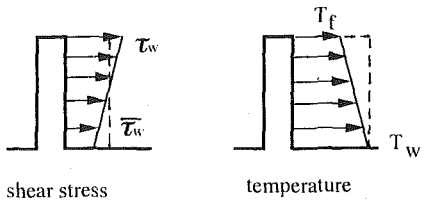

Fig. 5 Wall shear stress and temperature model along fin surface

$$\bar{u}_f A_f = \int \bar{u}_{f,i} dA_i \cong \sum_{i=1}^{n} \bar{u}_{f,i} dA_i \tag{22}$$

Dividing by the fin average friction velocity u_f^* yields

$$\left(\frac{\bar{u}_f}{u_f^*}\right)_{\text{linear}} = \sum_{i=1}^{n} \frac{\bar{u}_{f,i}}{u_{f,i}^*}\frac{u_{f,i}^*}{u_f^*}\frac{dA_i}{A_f} \tag{23}$$

where

$$\frac{\bar{u}_{f,i}}{u_{f,i}^*} = \frac{1}{dA_i}\int_i u^+ dA_i \tag{24}$$

In Eq. (23), $u_{f,i}^*$ is the local friction velocity. Next, assume a uniform shear stress distribution along the fin surface. In this case, the local friction velocity $u_{f,i}^*$ equals the fin average fiction velocity u_f^*. Then, Eq. (23) becomes

$$\left(\frac{\bar{u}_f}{u_f^*}\right)_{\text{uniform}} = \sum_{i=1}^{n} \frac{\bar{u}_{f,i}}{u_{f,i}^*}\frac{dA_i}{A_f} \tag{25}$$

The adequacy of the uniform wall shear stress assumption may be checked by comparing Eqs. (23) and (25). For simplicity, assume that elemental flow areas (dA_i) are equal along the fin surface. Then,

$$\left(\frac{\bar{u}_f}{u_f^*}\right)_{\text{linear}} = \left(\frac{\bar{u}_f}{u_f^*}\right)_{\text{uniform}} \sum_{i=1}^{n} \frac{1}{n}\frac{u_{f,i}^*}{u_f^*} = \left(\frac{\bar{u}_f}{u_f^*}\right)_{\text{uniform}} \sum_{i=1}^{n} \frac{1}{n}\sqrt{\frac{\tau_w}{\bar{\tau}_w}} \tag{26}$$

When $n = 5$ and $\tau_w/\bar{\tau}_w$ varies from 1.3 to 0.7,

$$\left(\frac{\bar{u}_f}{u_f^*}\right)_{\text{linear}} = 0.996\left(\frac{\bar{u}_f}{u_f^*}\right)_{\text{uniform}} \tag{27}$$

Equation (27) shows that the calculated $\bar{u}_f/u_f^*$ are almost the same both when the wall shear stress distribution is linear and when it is uniform. The preceding example suggests that the wall shear stress distribution along the fin surface (and eventually in an internal fin tube) may be assumed uniform. Finally, the friction factor is obtained by substituting appropriate expressions of velocity profile in each region into Eq. (19).

The heat transfer coefficients may be similarly predicted. Using the definition of the mixing cup temperature $\bar{T}$ assuming constant density across the flow area,

$$\bar{u}(T_w - \bar{T})A = \bar{u}_f(T_w - \bar{T}_f)A_f + \bar{u}_c(T_w - \bar{T}_c)A_c \tag{28}$$

Multiplying by c_p/Aq'' yields

$$\frac{\bar{u}(T_w - \bar{T})c_p}{q''} = \frac{\bar{u}_f(T_w - \bar{T}_f)c_p}{q''}\frac{A_f}{A} + \frac{\bar{u}_c(T_w - \bar{T}_c)c_p}{q''}\frac{A_c}{A} \tag{29}$$

Using the definition of Stanton number and heat transfer coefficient h,

$$\text{St} = \frac{h}{\rho\bar{u}c_p} = \frac{q''}{\rho\bar{u}c_p(T_w - \bar{T})} \tag{30}$$

$$\mathrm{St}_f = \frac{h_f}{\rho \bar{u}_f c_p} = \frac{q''}{\rho \bar{u}_f c_p (T_w - \bar{T}_f)} \tag{31}$$

$$\mathrm{St}_c = \frac{h_c}{\rho \bar{u}_c c_p} = \frac{q''}{\rho \bar{u}_c c_p (T_w - \bar{T}_c)} \tag{32}$$

Then, Eq. (21) becomes

$$\frac{1}{\mathrm{St}} = \frac{1}{\mathrm{St}_f}\frac{A_f}{A} + \frac{1}{\mathrm{St}_c}\frac{A_c}{A} \tag{33}$$

where

$$\frac{1}{\mathrm{St}_f} = \frac{1}{A_f}\int_{A_f} u^+ T^+ dA \tag{34}$$

$$\frac{1}{\mathrm{St}_c} = \frac{1}{A_c}\int_{A_c} u^+ T^+ dA \tag{35}$$

In the preceding analysis, the fin surface temperature is assumed to be the same as the tube wall temperature. In reality, the fin surface temperature is lower than the tube wall temperature because the heat is conducted through the fin cross section while it is lost to the surrounding fluid. The uniform fin surface assumption may also be evaluated following a similar procedure as was done to evaluate the uniform wall shear stress assumption. Consider a rectangular fin with thickness 1 mm and height 2 mm. The fin material is copper ($k = 386$ W/m°C) and the convection coefficient is 10,000 W/m²°C. These are the typical fin shape and the typical operating conditions of an internal fin tube. The fin shape is shown in Fig. 5. The fin efficiency and the fin tip temperature are easily calculated. The resultant fin efficiency is 0.95, and the fin tip temperature difference (between the fin tip and the bulk fluid) is approximately 90 percent of the tube wall temperature difference (between the fin tip and the bulk fluid). For a lower thermal conductivity material such as aluminum ($k = 204$ W/m°C), the fin efficiency becomes slightly lower ($\eta_f = 0.92$). The wall temperature distribution along the fin surface is shown in Fig. 5. The fin surface temperature is assumed to vary linearly from the fin tip to the fin base.

From the definition of the mixing cup temperature for the fin region, assuming "n" divisions of the fin surface temperature,

$$\bar{u}_f (T_w - \bar{T}_f) A_f \cong \sum_{i=1}^{n} \bar{u}_{f,i} (T_{w,i} - \bar{T}_{f,i}) dA_i \tag{36}$$

Multiplying by $\rho c_p / q''$

$$\left[\frac{\bar{u}_f}{u_f^*}\frac{(T_w - \bar{T}_f)\rho c_p u_f^*}{q''}\right]_{\text{linear}} = \sum_{i=1}^{n} \frac{\bar{u}_{f,i}}{u_{f,i}^*}\frac{u_{f,i}^*}{u_f^*}\frac{(T_{w,i} - \bar{T}_{f,i})}{(T_w - \bar{T}_{f,i})}\frac{(T_w - \bar{T}_f)}{(T_w - \bar{T}_f)}\frac{(T_w - \bar{T}_f)\rho c_p u_f^*}{q''}\frac{dA_i}{A_f} \tag{37}$$

In Eq. (37), $u_{f,i}^*$ is the local friction velocity, $T_{w,i}$ is the local surface temperature and $\bar{T}_{f,i}$ is the bulk fluid temperature at region "i". Now, assume that fin surface shear stress is uniform and equal to the average wall shear stress ($u_{f,i}^* = u_f^*$), and the fin surface temperature is uniform and equal to the tube wall temperature ($T_{w,i} = T_w$). Then,

$$\left[\frac{\bar{u}_f}{u_f^*}\frac{(T_w - \bar{T}_f)\rho c_p u_f^*}{q''}\right]_{\text{linear}} = \left[\frac{\bar{u}_f}{u_f^*}\frac{(T_w - \bar{T}_f)\rho c_p u_f^*}{q''}\right]_{\text{uniform}} \sum_{i=1}^{n} \frac{1}{n}\frac{u_{f,i}^*}{u_f^*}\frac{(T_{w,i} - \bar{T}_{f,i})}{(T_w - \bar{T}_{f,i})}$$

$$\cong \left[\frac{\bar{u}_f}{u_f^*}\frac{(T_w - \bar{T}_f)\rho c_p u_f^*}{q''}\right]_{\text{uniform}} \sum_{i=1}^{n} \frac{1}{n}\sqrt{\frac{\tau_w}{\bar{\tau}_w}}\frac{(T_{w,i} - \bar{T}_f)}{(T_w - \bar{T}_f)} \tag{38}$$

Here, for simplicity, we assume that the ratio of the fin tip temperature difference to the tube wall temperature difference at region "i", $(T_{w,i} - \bar{T}_{f,i})/(T_w - \bar{T}_{f,i})$, is equal to the ratio $(T_{w,i} - \bar{T}_f)/(T_w - \bar{T}_f)$ at the fin region. When $n = 5$, $\tau_w/\bar{\tau}_w$ varies from 1.3 to 0.7, and $(T_{w,i} - \bar{T}_f)$ at the fin tip is 90 percent of the tube wall temperature difference $(T_w - \bar{T}_f)$,

$$\left[\frac{\bar{u}_f}{u_f^*}\frac{(T_w - \bar{T}_f)\rho c_p u_f^*}{q''}\right]_{\text{linear}} \cong 0.94\left[\frac{\bar{u}_f}{u_f^*}\frac{(T_w - \bar{T}_f)\rho c_p u_f^*}{q''}\right]_{\text{uniform}} \tag{39}$$

Equation (39) shows that uniform fin surface temperature assumption may slightly underpredict the data. However, the assumption greatly simplifies the analysis, and thus, it is adopted in this study. To solve Eqs. (34) and (35), functional equations for u^+ and T^+ for the interfin and the core regions are needed.

2.2.1 Interfin Region. In this region, the velocity and temperature profiles are assumed to be the same as those of the smooth tube (Eqs. (3) and (4)). The Law of the Wall was shown to be valid for complex geometries such as rectangular channels (Hartnett et al., 1962) and rod bundles (Kim et al., 1991). Equations (19) and (33) were integrated over a pair of triangles as shown in Fig. 3, using the smooth tube u^+ and T^+ and the results are

$$\frac{\bar{u}_f}{u^*} = \frac{2n}{(b+\gamma)}\left[b(A' + 2.5\ln(e) - 3.75) + \gamma(A' + 2.5\ln(\gamma) - 3.75)\right] \tag{40}$$

$$\frac{1}{\mathrm{St}_f} = \frac{2n}{(b+\gamma)}\left[b(A'C' + (2.5A' + A_sC')(\ln(e) - 1.5) + 2.5A_s(\ln(e)(\ln(e) - 3) + 3.5)) + \gamma(A'C' + (2.5A' + A_sC')\cdot(\ln(\gamma) - 1.5) + 2.5A_s(\ln(\gamma)(\ln(\gamma) - 3) + 3.5))\right] \tag{41}$$

where

$$A' = 2.5\ln(\mathrm{Re}\sqrt{f/2}/D_h) + 5.5$$

$$C' = A_s \ln(\mathrm{Re}\sqrt{f/2}/D_h) + B_s$$

$$\gamma = \frac{p_i - t_t}{2}$$

In Eqs. (40) and (41), D_h is the hydraulic diameter of the whole tube, Re is the Reynolds number with D_h as a characteristic length, p_i is the fin pitch at the fin tip, and b is defined in Fig. 3.

2.2.2 Core Region. Core region velocity and temperature profiles are also needed to predict the friction and heat transfer in internally finned tubes. To explain the increased friction resulted from the rectangular fin model, Scott and Webb (1981) postulated that the velocity profile in the core region is shifted some amount from that of a smooth tube due to the increased surface shear of the interfin region. For a rough surface, it is well known that the velocity profile is shifted some amount (Hinze, 1975), and the friction consists of profile drag by the roughness element and wall shear stress between the elements. For internally finned tubes, however, only wall shear stress contributes the friction, and profile drag does not exist. Then, it is questionable whether velocity shift may occur in internally finned tubes as Scott and Webb assumed.

In this study, the velocity and temperature profiles of the smooth tube are assumed to be valid in the core region. Then, the average core region velocity is found by integrating Eq. (21) over $e \le y \le R$.

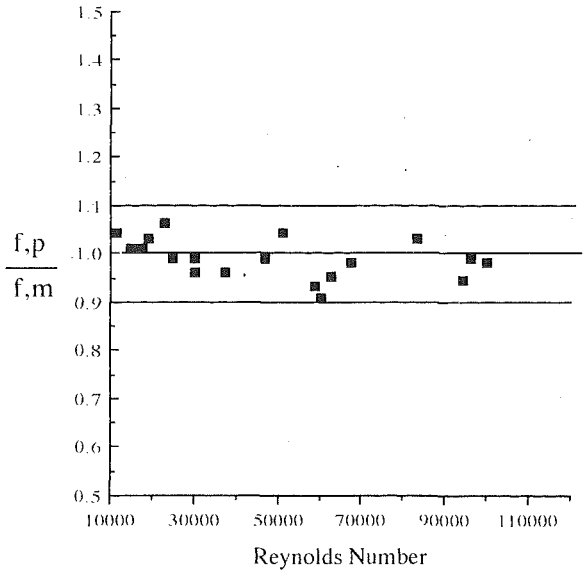

Fig. 6 Prediction of Carnavos's friction data

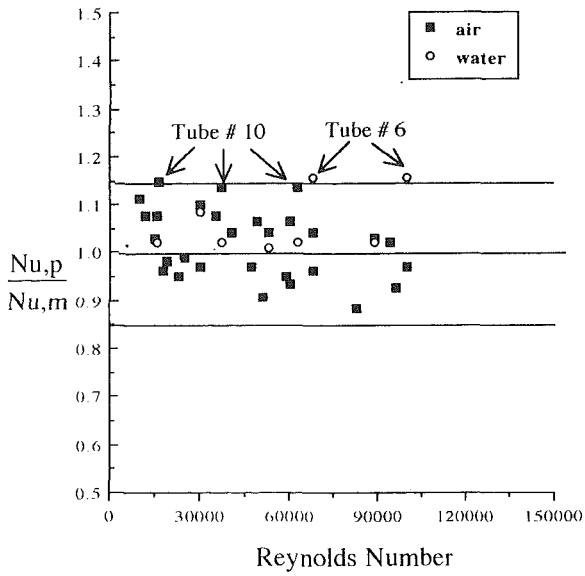

Fig. 7 Prediction of Carnavos's heat transfer data using Gowen and Smith's correlation

$$\bar{u}_c^+ = \frac{1}{A_c}\int_e^R 2\pi(R-y)(2.5\ln y^+ + 5.5)dy \quad (42)$$

The result of the integration is

$$\bar{u}_c^+ = \frac{1}{(1-\alpha)^2}\,2.5\ln\left(\frac{D}{D_h}\mathrm{Re}\sqrt{f/2}\right) - \frac{(2\alpha-\alpha^2)}{(1-\alpha^2)}\,2.5\ln\left(\frac{e}{D_h}\mathrm{Re}\sqrt{f/2}\right) - 2.5\,\frac{(1.5-2\alpha+0.5\alpha^2)}{(1-\alpha)^2} + 5.5 \quad (43)$$

where $\alpha = 2e/D$.

Similarly, the core region Stanton number is obtained by integrating Eq. (35) over $e \le y \le R$.

$$\frac{1}{\mathrm{St}_c} = \frac{1}{A_c}\int_e^R 2\pi(R-y)(2.5\ln y^+ + 5.5)(A_s \ln y^+ + B_s)dy \quad (44)$$

The result of the integration is

$$\frac{1}{\mathrm{St}_c} = A'C'(1-\alpha) + 2.5(A'+C')(\ln R - \alpha\ln e - 1 + \alpha) + 6.25(\ln^2 R - \alpha\ln^2 e - 2\ln R + 2\alpha\ln e + 2 - 2\alpha) - 0.5A'C' \cdot (1-\alpha^2) - 1.25(A'+C')(\ln R - \alpha^2\ln e - 0.5 - 0.5\alpha^2) - 1.563[2(\ln^2 R - \ln R) - 2e^2(\ln^2 e - \ln e) + 1 - \alpha^2] \quad (45)$$

where

$$A' = 2.5\ln(\mathrm{Re}\sqrt{f/2}/D_h) + 5.5$$

$$C' = A_s \ln(\mathrm{Re}\sqrt{f/2}/D_h) + B_s$$

$$\alpha = 2e/D$$

Then, the friction factors are obtained by substituting Eqs. (40) and (43) into Eq. (19), and Stanton numbers are obtained by substituting Eqs. (41) and (45) into Eq. (33).

3 Results and Discussion

3.1 Friction Factor Prediction. Figure 6 shows predicted friction factors compared with Carnavos's data (1979). Carnavos's data are for 11 different axial internal finned tubes. The 11 tubes tested by Carnavos have $3.3 \le p/e \le 5.6$, $0.02 \le e/D \le 0.29$ and $5 \le n \le 41$. The tube dimensions are listed in Table 3. Figure 6 shows that the data are predicted within ±10 percent. The results are as good as those by Carnavos correlation (Eq. (1)) and by Scott and Webb's model. Both Carnavos and Scott and Webb predicted the data within ±10 percent. This implies that the current method is probably the best one considering the rational basis of the model. Carnavos's correlation is just a curve-fit of data, and Scott and Webb did not properly considered the fin shape.

The current model assumes the validity of the universal velocity profile across the flow area. The local wall shear stress is assumed to be the same as the average wall shear stress, and the local velocity was normalized by the average wall shear stress for the dimensionless velocity profile. This implies that, in the current model, the local velocity is determined by the distance from the wall (either fin or tube). Then, the isovelocity lines should follow the contour of the finned tube. Trupp et al. (1983) provides velocity profile measurements of an internal fin tube. The data (Fig. 7 in their paper) show that the isovelocity line generally follows the contour of the fin and the tube wall, and the magnitudes are approximately proportional to the distance from the wall. Trupp et al. also showed that two counterrotating cells of secondary flow exist with the primary cell. The magnitude of the secondary flow was about 4 percent of the bulk average velocity. However, it is questionable whether the secondary flow cells may exist for low fin tubes considered in this study. Trupp et al.'s tube had high fins ($e/D = 0.33$). The current friction model considers axial velocity only.

The theoretical Nusselt number (or Stanton number St = Nu/RePr) is obtained by substituting Eqs. (41) and (45) in Eqs. (33). For the temperature profile, both Gowen and Smith's and Kader's correlations (shown in Table 1) are considered.

3.2 Heat Transfer Prediction Using Gowen and Smith Correlation. The Nusselt numbers are obtained using Gowen and Smith's correlation, and the results are compared with Carnavos's data (1979, 1980) in Fig. 7. Figure 7 shows that the agreement is within ±15 percent for the air and water data. The air data of tube #10 and the water data of tube #6 (tube geometries shown in Table 3 are poorly predicted). Tube #10 has densely packed high fins ($n = 16$, $e/D = 0.16$), and tube #6 has 10 fins with $e/D = 0.12$. Generally, the accuracy of the predictions decreases for high, closely spaced fins.

The water-glycol data are not shown in the figure, because the exact Prandtl numbers of the data were not available.

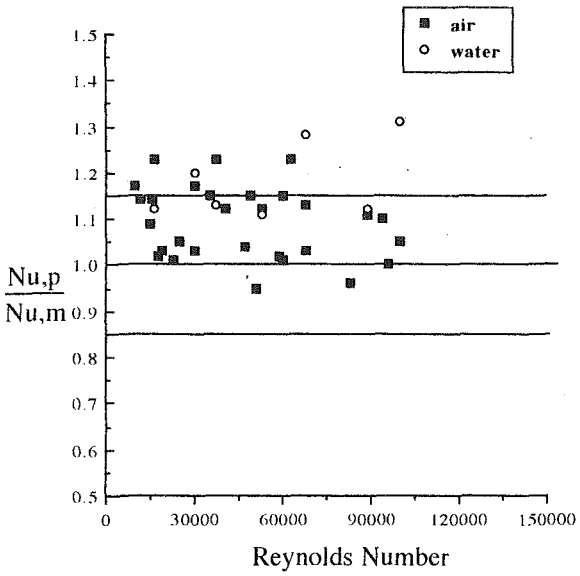

Fig. 8 Prediction of Carnavos's heat transfer data using Kader's correlation

Carnavos (1980) provides three water-glycol data points for an axial internal fin tube (tube #14). He states that the Prandtl number varied 23–30 for water-glycol data, but no specific number is given for each data point. Here, the water-glycol data are predicted at extreme Prandtl numbers (23 and 30). When $Pr = 23$ is used, the data are about 17 percent underpredicted. When Pr was assumed 30, the data are about 20 percent underpredicted. This is anticipated because the Prandtl numbers of Carnavos's water-glycol data exceed the Prandtl number range where Gowen and Smith's correlation is valid. A similar trend was observed for the smooth tube case shown in Table 2.

In the current model, the fin shape is assumed trapezoidal. As was pointed out in the preceding section, the trapezoidal fin shape is a reasonable approximation of the actual fin geometry. The inappropriateness of the rectangular fin assumption may also be confirmed by calculating the Nusselt number, assuming that the fin shape is rectangular. The calculations were performed, and most of the Nusselt numbers overpredicted the Carnavos data more than 20 percent.

Carnavos's heat transfer correlation (Eq. (2)) predicts the data of air, water, and water-glycol within ±10 percent. The current model predicts the data of air and water within ±15 percent. Note that the Carnavos correlation is strictly empirical, as compared to the rational basis of the present model. Hence, it may be safer to extrapolate the present model beyond the range of the Carnavos data. The present model is easier for general use than is the numerical method of Patankar.

3.3 Prediction Using Kader's Correlation. Kader's temperature profile is used to predict Carnavos's internal fin data. Figure 8 shows the results. As shown in the figure, most of the Carnavos's air and water data are overpredicted (some data about 23 percent overprediction). The data were predicted within ±15 percent when Gowen and Smith's correlation was used. The water-glycol data are also predicted using Kader's correlation. The data are about 9 percent overpredicted when $Pr = 23$ is assumed and about 7 percent overpredicted when $Pr = 30$ is used, which is a sure improvement compared with the predictions using Gowen and Smith's correlation. The smooth tube results in Table 2 show a similar trend. Summing up, the current model predicts Carnavos's air and water data within ±15 percent using Gowen and Smith's correlation, and predicts the water-glycol data within ±10 percent using Kader's correlation.

The current model assumes the validity of Law of the Wall across the flow area, and thus is limited to internal fin tubes with zero helix angle. In helical internal fin tubes, flow is likely to swirl at least in the fin region, and considerable tangential velocity may exist near the wall. Then, a predictive model should consider the effect of tangential velocity in addition to that by the axial velocity. The present model considers axial velocity only, and should be limited to axial internal fin tubes.

4 Conclusions

An analytic model was developed to predict the friction factor and Nusselt number for turbulent flow in axial internal fin tubes. The fin shape is trapezoidal, and the fin parameters—fin height, fin root thickness and fin tip thickness—are determined from the actual tube measurement data by Carnavos (1979). The trapezoidal shape appears to simulate the actual fin cross section excellently. The current model applies the Law of the Wall—based universal velocity profile and temperature profile to the interfin and core regions of the flow. The analytic model predicts the Carnavos friction data within ±10 percent, and heat transfer data of air, water, and water-glycol within ±15 percent with the usage of proper temperature profile correlation. Successful application of the Law of the Wall to axial internal fins further extends the range of applicability of the important, fundamental concept.

References

Carnavos, T. C., 1979, "Cooling Air in Turbulent Flow With Internally Finned Tubes," *Heat Transfer Engineering*, Vol. 1, No. 2, pp. 41–46.

Carnavos, T. C., 1980, "Heat Transfer Performance of Internally Finned Tubes in Turbulent Flow," *Advances in Enhanced Heat Transfer*, Vol. 1, No. 4, pp. 32–37.

Gowen, R. A., and Smith, J. W., 1967, "The Effect of the Prandtl Number on Temperature Profiles for Heat Transfer in Turbulent Pipe Flow," *Chem. Eng. Sci.*, Vol. 22, pp. 1701–1711.

Hartnett, J. P., Koh, J. Y. C., and McComas, S. T., 1962, "A Comparison of Predicted and Measured Friction Factors for Turbulent Flow Through Rectangular Ducts," ASME JOURNAL OF HEAT TRANSFER, Vol. 84, pp. 82–88.

Hinze, O. J., 1975, *Turbulence*, 2nd ed., McGraw-Hill, New York, pp. 614–619.

Kader, B. A., 1981, "Temperature and Concentration Profiles in Fully Turbulent Boundary Layers," *Int. J. Heat Mass Trans.*, Vol. 24, pp. 1541–1544.

Kader, B. A., and Yaglom, A. M., 1972, "Heat and Mass Transfer Laws for Fully Turbulent Wall Flows," *Int. J. Heat Mass Trans.*, Vol. 15, pp. 2329–2351.

Kim, N.-H., Chun, T.-H., Lee, S.-K., and Kim, S.-H., 1991, "Application of the Law of the Wall to Predict the Turbulent Friction Factor in Rod Bundles," *1st JSME/ASME Joint International Conference on Nuclear Engineering*, Tokyo, Japan, Nov. 4–7, Vol. 1, pp. 231–235.

Ornatski, A. P., Shcherbakov, V. K., and Semens, M. G., 1970, "Investigation of the Velocity Distribution in Tubes With Internal Longitudinal Fins," *Thermal Engineering*, pp. 108–111.

Patankar, S. V., Ivanovic, M., and Sparrow, E. M., 1979, "Analysis of Turbulent Flow and Heat Transfer in Internally Finned Tubes and Annuli," ASME JOURNAL OF HEAT TRANSFER, Vol. 101, pp. 29–37.

Petukhov, B. S., 1970, "Heat Transfer and Friction in Turbulent Flow With Variable Physical Properties," *Advances in Heat Transfer*, J. P. Hartnett and T. F. Irvine, Jr., eds., Vol. 6, Academic Press, New York, pp. 503–564.

Scott, M. J., and Webb, R. L., 1981, "Analytic Prediction of the Friction Factor for Turbulent Flow in Internally Finned Channels," ASME JOURNAL OF HEAT TRANSFER, Vol. 103, pp. 423–428.

Trupp, A. C., Lau, A. C. Y., Said, M. N. A., and Soliman, H. M., 1983, "Turbulent Flow Characteristics in an Internally Finned Tube," *Joint ASME/JSME Conference*, pp. 11–19.

Watkinson, A. P., Miletti, D. L., and Tarasoff, P., 1973, "Turbulent Heat Transfer and Pressure Drop of Internally Finned Tubes," *AIChE Symposium Series*, Vol. 69, No. 131, pp. 94–103.

Watkinson, A. P., Miletti, D. L., and Kubanek, G. R., 1975, "Heat Transfer and Pressure Drop of Internally Finned Tubes in Turbulent Air Flow," *ASHRAE Trans.*, Vol. 81, No. 1, pp. 330–349.

Local Heat Transfer Distribution in a Rotating Serpentine Rib-Roughened Flow Passage

N. Zhang

J. Chiou

S. Fann

W.-J. Yang

Department of Mechanical Engineering and Applied Mechanics, University of Michigan, Ann Arbor, MI 48109

Experiments are performed to determine the local heat transfer performance in a rotating serpentine passage with rib-roughened surfaces. The ribs are placed on the trailing and leading walls in a corresponding posited arrangement with an angle of attack of 90 deg. The rib height-to-hydraulic diameter ratio, e/D_h, is 0.0787 and the rib pitch-to-height ratio, s/e, is 11. The throughflow Reynolds number is varied, typically at 23,000, 47,000, and 70,000 in the passage both at rest and in rotation. In the rotation cases, the rotation number is varied from 0.023 to 0.0594. Results for the rib-roughened serpentine passages are compared with those of smooth ones in the literature. Comparison is also made on results for the rib-roughened passages between the stationary and rotating cases. It is disclosed that a significant enhancement is achieved in the heat transfer in both the stationary and rotating cases resulting from an installation of the ribs. Both the rotation and Rayleigh numbers play important roles in the heat transfer performance on both the trailing and leading walls. Although the Reynolds number strongly influences the Nusselt numbers in the rib-roughened passage of both the stationary and rotating cases, Nu_o and Nu, respectively, it has little effect on their ratio Nu/Nu_o.

Introduction

It is well known that high heat load and high thermal efficiency are crucial in advanced aeroengine design and, therefore, an effective blade cooling becomes critical. Internal cooling technologies have been widely used in blades and vanes of modern gas turbine engines. When the cooling passages are roughened with turbolators, such as ribs or pins, heat transfer to the cooling air within a blade is significantly enhanced. It is a common practice to install rib turbulators at the midchord region in an internally cooled turbine airfoil, while pin fins are installed at the trailing edge, as shown in Fig. 1. In the present study, attention is focused on heat transfer enhancement in the cooling passage of a turbine blade by means of rib turbulators. It is inherent in the blade structure that heat is transferred mainly from two chord surfaces of the blade to the cooling air. Then, an effective measure to augment heat transfer is to roughen the opposite leading and trailing surfaces of the cooling passage by means of rib turbulators. The present study models the cooling passage as a serpentine square channel with two opposite rib-roughened walls. It is useful as a reference to estimate the effects of ribs on cooling passages, although this experiment may not exactly meet real blade conditions.

A number of experimental investigations treated heat transfer performance in rib-roughened channels for the stationary case. For example, Burggraff (1970) studied the effect of entrance geometry on the regionally averaged heat transfer coefficient in a square duct with two opposite transverse-rib-roughened walls. The effects of the turbulator geometry (rib height, spacing, and angle of attack), flow passage aspect ratio, and Reynolds number on the distributions of local heat transfer and pressure drop were studied by Han and Park (1988). Taslim and Spring (1987, 1988) dealt with the effects of passage aspect ratios on the heat transfer coefficient and friction factor in turbulator-roughened cooling passages. All the abovementioned studies were performed in straight, rectangular, rib-roughened channels. Metzger and Sahm (1986) and Fan and Metzger (1987) investigated the effects of channel geometry on the averaged heat transfer coefficient in a rectangular passage with sharp 180 deg turns. Han et al. (1988) and Chandra et al. (1988) utilized the naphthalene sublimation technique to determine the effect of the sharp 180 deg turn on the distributions of the local heat/mass transfer coefficients around the turn region in two-pass square channels roughened separately by the transverse ribs and by the angled ribs. The study was extended by Han and Zhang (1991) to evaluate the effects of rib-angle orientation on the local heat/mass transfer distributions in a three-pass rib-roughened channel.

When blades are rotating at high speeds, the Coriolis, buoyancy, and centripetal forces can substantially modify the flow patterns of the cooling air, and consequently the heat transfer performance. It becomes difficult and costly to conduct heat transfer tests, especially rotating passages with rib-roughened walls. Only a few experimental results are available in the literature. Wagner et al. (1991a, b, c) and Taslim et al., (1991) reviewed the existing literature on rotating passages with smooth walls and experimentally studied the effects of rotation on the heat transfer performance in rotating square passages with smooth walls and with opposite rib-roughened walls, respectively. Wagner et al. (1991c) and Yang et al. (1992) revealed significant changes in the heat transfer performance at the turning sections and considerable differences between the inward and outward flows in the straight sections of the flow passage with smooth walls. Clifford (1985) conducted a heat transfer study on a rotating multipass model with trip normal to the flow using transient measurement techniques. He observed increases in heat transfer of 36 percent on the pressure side and decreases of 24 percent on the suction side of the first passage. Taslim et al. (1991) obtained heat transfer coefficients in a rotating square passage with trips normal to the flow, for several trip heights. It was limited to a radially (straight) outward flow whose results are not applicable to the actual cooling passages of serpentine type in the air-cooled turbine blades and vanes, as shown in Fig. 1. Using a large-scale, multipass, rotating square passage with trip strips (normal to the flow direction) on the leading and trailing surfaces of the radial coolant passages, Wagner et al. (1991b) obtained an extensive set of convective heat transfer data. Their analysis of the pre-

Contributed by the Heat Transfer Division for publication in the JOURNAL OF HEAT TRANSFER. Manuscript received by the Heat Transfer Division November 1991; revision received January 1993. Keywords: Augmentation and Enhancement, Rotating Flows, Turbines. Associate Technical Editor: R. J. Simoneau.

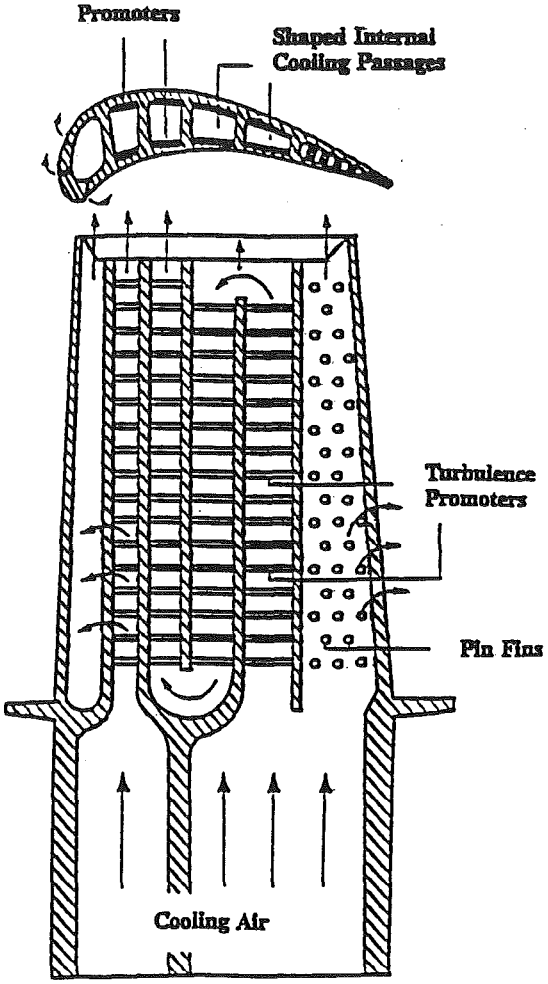

Fig. 1 Conceptual cutaway view of an advanced gas turbine blade

vious results revealed an inconsistent trend, which was attributed to differences in the measurement techniques, models, and test conditions.

This investigation is a continuation of Yang et al. (1992) to determine the effects of transverse ribs on the local heat transfer coefficients in a rotation four-pass serpentine flow passage. The physical limitations of the test device result in rotations at low rotation numbers and the absence of a leading arm.

Experimental Apparatus and Procedure

The experimental apparatus consisted of a test section, a

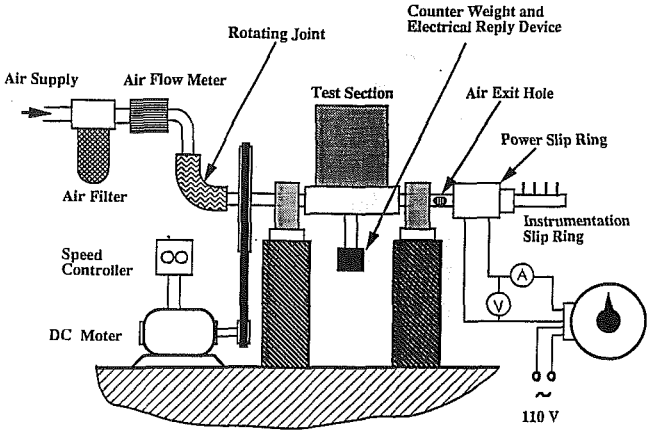

Fig. 2 Experimental apparatus

DC motor with controller, a heat source, an air supply system, including an air filter, a flowmeter, and a high-speed rotating joint, and two slip rings used for power supply and data acquisition, respectively, as shown in Fig. 2.

The test section was comprised of a four-pass serpentine flow channel with a 2.54 × 2.54 cm square cross section. Only the leading and trailing walls of the channel were heated with a thin-film, 0.025 mm stainless steel sheet. For the rib-roughened tests, 20 brass ribs with 0.2 × 0.2 cm square cross section were glued onto the film with angle of attack of 90 deg, and electrically insulated. The rib height-to-hydraulic diameter ratio, e/D_h, is 0.0787. Starting from the third rib, the wall temperature distributions were measured after every other rib by means of four well-distributed thermocouples between two ribs, as shown in Fig. 3. The wall temperature changes in the turns were also measured. All thermocouples were placed along the centerline of the passage. The experimental results from Han et al. (1988) indicated that the local heat transfer coefficients on the ribbed walls were fairly uniform in the lateral direction of the case of angle of attack of 90 deg. Therefore, it is sufficient to measure only the local wall temperatures along the centerline of the channel, as in the present study. The details of each individual thermocouple are available from Yang et al. (1992) and thus is omitted here.

The ribs were located on both the trailing and leading walls, correspondingly positioned. The first rib was placed at 4.24 cm from the inlet of the test section and other ribs were placed consistently at a distance of $s/e = 11$ until the middle of the third straight passage. No heater foil was placed on the side walls with the whole piece of the test section being carefully insulated to minimize heat losses. The cooling air from an air

Nomenclature

D_h = hydraulic diameter, m
e = rib height, m
h = local heat transfer coefficient, $W/m^2\ °C$
k = conductivity of fluid, W/m K
Nu = local Nusselt number, = $h\ D_h/k$
Nu_o = local Nusselt number for stationary case
Nu_∞ = Nusselt number for fully developed flow of stationary case
Pr = Prandtl number = ν/α
q = wall heat flux, W/m^2
R = mean radius of rotation, m
Ra = rotational Rayleigh number = $\beta\Delta T\ R\ Re_r^2 Pr/D_h$
Re = Reynolds number = $U_o D_h/\nu$
Re_r = rotational Reynolds number = $\Omega D_h^2/\nu = Re\ Ro$
Ro = rotation number = $\Omega D_h/U_o$
s = rib pitch, m
T = temperature, °C
T_w = wall temperature, °C
T_a = flow temperature, °C
ΔT = temperature difference between mean wall temperature and mean fluid temperature = $\overline{T_w} - \overline{T_a}$
U_o = mean flow velocity, m/s
x, X = streamwise distance from inlet of the test section, m
X_L = streamwise distance from inlet of the test section to the midpoint of the third straight section, m
α = fluid thermal diffusivity, m^2/s
β = thermal expansion coefficient, 1/K
ν = kinematic viscosity, m^2/s
ρ = density of fluid, kg/m
Ω = rotating speed, 1/s

Subscripts

a = value of cooling air
o = value for the stationary case
w = value at walls
∞ = value of fully developed turbulent flow

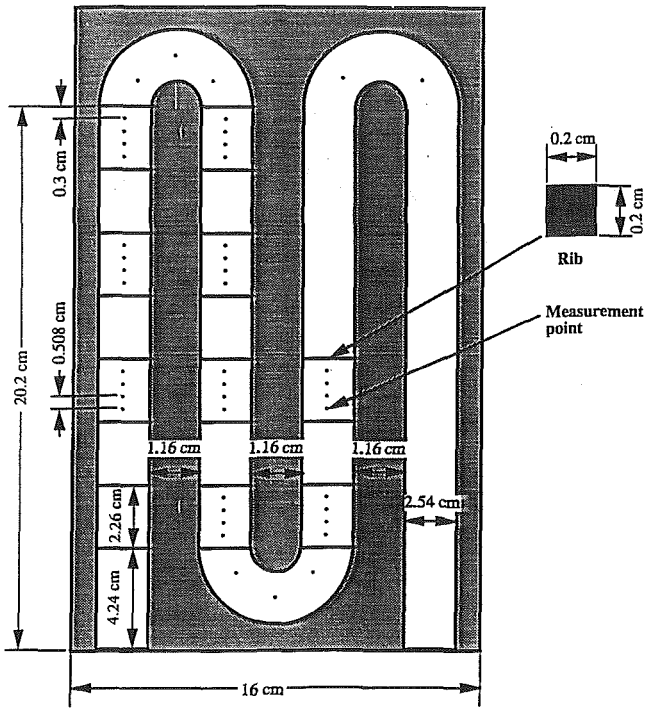

Fig. 3 Position of ribs and thermocouples

supply passed through an air filter, a flowmeter, and a high rotating joint. It then entered one end of the hollow shaft, turned into the serpentine passage, and finally exited through the other end of the shaft. Electrical power was supplied to the film heaters by a variable current power source via a slip ring. A current meter and a voltmeter were used to measure the power. The whole rig of the rotating system was enclosed by a protective metal cover for safety.

Both constant wall temperature and constant wall heat flux experiments have been performed on rotating channels before: Wagner et al. (1991a, b, c) conducted constant wall temperature experiments and Taslim et al. (1991) conducted constant wall heat flux experiments. Each has its own merits while actual turbine blades operate between the two cases. The constant wall heat flux experiment was selected for the present study because of its simplicity in construction and ease in operation. This is especially true to the investigation of the effect of ribs on the local heat transfer coefficients.

First, tests were performed on the stationary channel at three different Reynolds numbers: 23,000, 47,000, and 70,000. It was followed by experiments on the rotating test rig. For each Reynolds number, the test section was rotated at five different speeds: 25, 105, 177, 262 and 327 rpm. For each combination of Reynolds number and rotating speed, two heat fluxes were imposed to investigate the effect of the Rayleigh number on heat transfer performance. All 36 cases were repeated four times to validate the repeatability of the experiments. In each test, data acquisition was initiated 45 minutes after the test rig was started in order to assure that the system had reached steady state.

Data Reduction

Two methods were employed in calculating the energy supplied to the cooling air (Yang et al., 1992): (1) (total energy supplied) – (heat losses) and (2) measuring air inlet/outlet temperatures. Heat losses were measured under steady-state rotational conditions without throughflow. The temperatures at a strategic position (the trailing wall at the first turn, i.e., $X/D_h = 8.86$) was maintained at the same temperature as in the corresponding throughflow case. The following equations are used in the data reduction:

$$h(x) = q/(T_w(x) - T_a(x)) \quad (1)$$

$$\mathrm{Nu}(x) = h(x)D_h/k \quad (2)$$

Here, $h(x)$ is the local heat transfer coefficient; q, wall heat flux; $T_w(x)$ and $T_a(x)$, local wall and air temperature, respectively; Nu(x), local Nusselt number; x, streamwise distance from the inlet along the centerline; D_h, hydraulic diameter; and k, thermal conductivity of air. Two methods were used to normalize experimental data to compare the present results with the existing ones and to evaluate the rotational effects on the heat transfer performance in the roughened channel. One is to normalize the static operating condition while the other one is to normalize a smooth duct condition of fully developed turbulent flow. An equation for turbulent heat transfer inside smooth passages (Kays and Perkins, 1985) reads:

$$\mathrm{Nu} = 0.022\mathrm{Pr}^{0.5}\mathrm{Re}^{0.8} \quad \text{for } \mathrm{Re} < 10^5 \quad (3)$$

For Pr = 0.71 (air) in the present study, Eq. (3) is reduced to

$$\mathrm{Nu} = 0.0185\mathrm{Re}^{0.8} \quad (4)$$

An uncertainty analysis of the data reduction was conducted using the method from Kline and McClintock (1953). The uncertainty in temperature measurements is estimated to be ±1°C. The value of $T_w(x) - T_a(x)$ varies from 10 to 28°C, while the difference between inlet and outlet air temperatures of the test section changes from 10 to 15°C. The relative uncertainty interval for the Nusselt number is in the range of 11 to 22.3 percent. The maximum uncertainty of the Nusselt number occurs at the lowest heat transfer coefficient on the leading wall in the rotating case. The four repeated experiments for all cases yield results varying by an average of 2 percent, with the maximum variation of 4.6 percent, which occurs in the lowest flow rate and heat flux case. All results shown in this paper are based on the averaged values of four repeated experiments for each case.

Results and Discussion

It is well known that the local convective heat transfer performance inside a stationary smooth passage is governed by the Reynolds number, Re, and the nondimensional streamwise distance form the inlet x/D_h. When the passage is set in rotation, the effects of the Coriolis, buoyancy, and centripetal forces exert strong influences on the heat transfer, especially in a rotating serpentine flow channel. The local heat transfer coefficient is a function of not only Re and x/D_h, but also the rotation number, Ro, and the rotational Rayleigh number, Ra. That is

$$\mathrm{Nu}(x) = f(\mathrm{Re}, \mathrm{Ro}, \mathrm{Ra}, x/D_h) \quad (5)$$

where $\mathrm{Ro} = \Omega D_h/U_o$; $\mathrm{Ra} = \beta\Delta T\, R\, (\mathrm{Re\,Ro})^2\, \mathrm{Pr}/D_h$ in which Ω is the rotational speed; β, thermal expansion coefficient; ΔT, the difference between mean wall temperature and mean fluid temperature; and R, mean radius of rotation. Both the stationary and rotating cases were investigated. The results for the stationary cases are compared with those of the corresponding smooth serpentine passage to determine the effects of the ribs on heat transfer performance. The results also serve as the reference to determine the effects of rotation on heat transfer in the rib-roughened serpentine passage.

1 Stationary Cases. Due to the symmetry between the leading and trailing walls in stationary state and the small data variations for each case (within 5 percent), the averaged values of the local heat transfer coefficients between the two walls are adopted.

Figure 4 depicts the effects of the Reynolds number on the streamwise distribution of Nusselt number, Nu_o, for stationary cases. It reveals that Nu_o increases with an increase in Re,

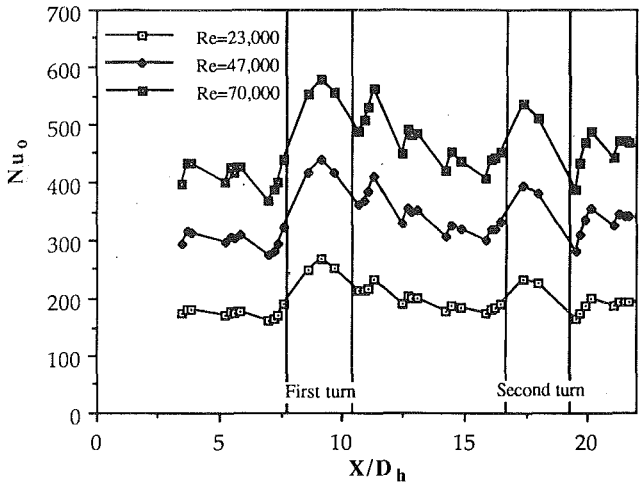

Fig. 4 Effect of Re on Nu_o distribution inside stationary serpentine passage

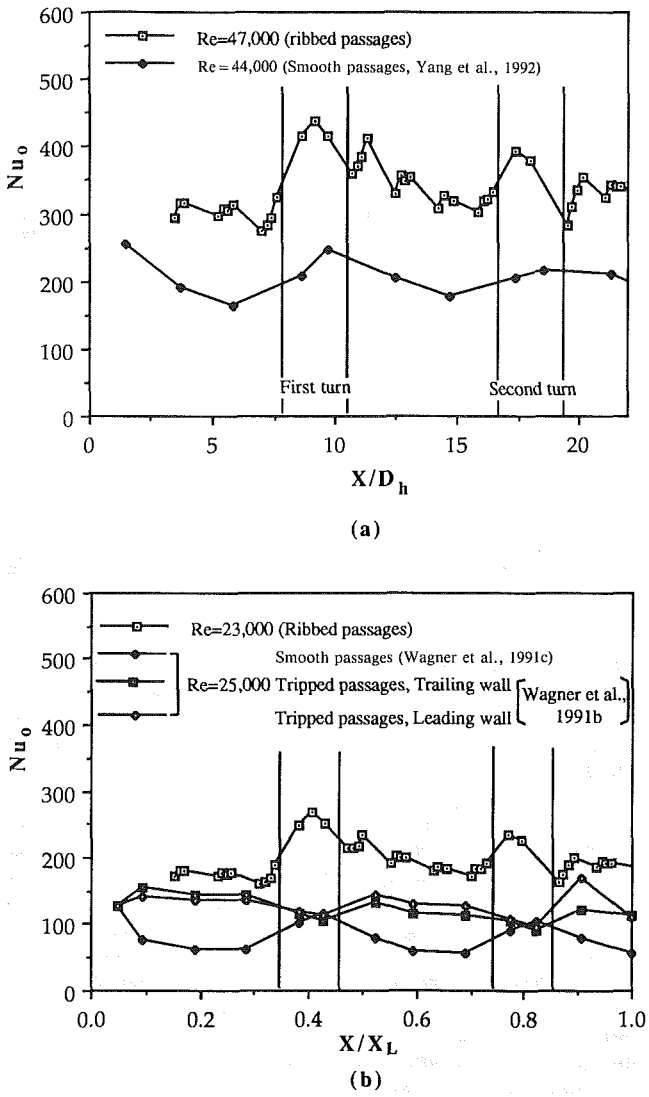

Fig. 5 Heat transfer performance in stationary rib-roughened and smooth serpentine passages

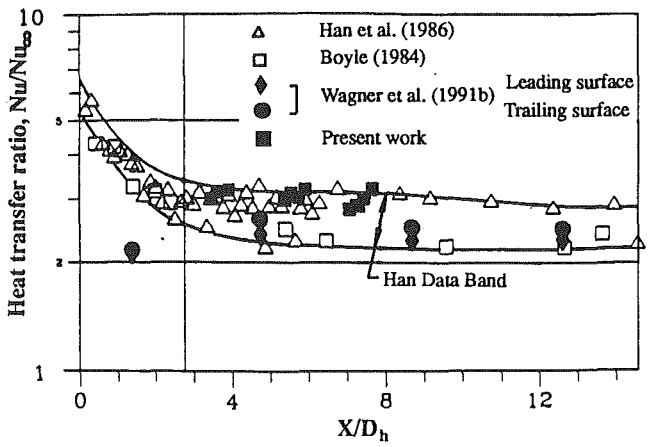

Fig. 6 Comparison of stationary heat transfer results with Wagner et al. (1991b), Boyle (1984), and Han et al. (1986)

preserving the shape of the Nu_o versus X/D_h curve. The value of Nu_o increases abruptly at every rib. This effect has suppressed a retardation of heat transfer performance in the straight sections of the serpentine passage. The heat transfer performance decreases by about 20 percent (Yang et al., 1992) to 25 percent (Wagner et al., 1991c) from the beginning to the end of the second straight section in the smooth serpentine passage. In contrast, the decrease in the local heat transfer coefficients is only 8 to 9.5 percent in the rib-roughened serpentine passage. The Nu_o distribution in the second straight section is generally higher than in the first straight section. Farther downstream from the turns, the Nu_o peak values between two ribs diminish gradually. The Nu_o distribution in the rib-roughened region of the third straight section shows the same trend as that in the first straight section.

It is also disclosed that in the cases of Re = 47,000 and 70,000 the values of Nu_o increase by 35 and 32 percent, respectively, in the first turn and by 19 and 17 percent, respectively, in the second turn. In the smooth passage, however, the enhancements were 37 percent in the first turn and 22 percent in the second turn for Re = 44,000, and 33 percent in the first turn and 18 percent in the second turn for Re = 110,000 (Yang et al., 1992). Such weakened effects of the secondary flow on heat transfer performance at the turns of the rib-roughened passage are due to the fact that the ribs have raised the whole level of heat transfer coefficients in all straight sections. It should be noted that the results of Wagner et al. (1991c) showed, in the smooth passage, increases in the heat transfer performance at Re = 25,000 by 92 and 82 percent in the first and second turns, respectively. However, Wagner et al. (1991b) found that heat transfer in the turn regions was generally lower in the trip-roughened wall case than in the smooth wall case, a decrease of about 20 and 25 percent in the first and second turns, respectively. In contrast, the present study yields heat transfer augmentations at Re = 23,000 of 40 and 23 percent in the first and second turns, respectively. In addition to the reason mentioned above, different turn geometry and different thermal boundary conditions in the two test sections have contributed to such a significant discrepancy between the two experimental results.

Figure 5 depicts typical overall effects of the ribs on heat transfer enhancement. It is observed in Fig. 5(*a*) that the Nu_o distribution in the rib-roughened passage at Re = 47,000 is generally higher than that in the smooth passage at Re = 44,000 (Yang et al., 1992) by 50 percent or more. In Fig. 5(*b*), the Nu_o distribution in the rib-roughened passage at Re = 23,000 is higher than that in the smooth passage at Re = 25,000 (Wagner et al., 1991c) by 150 percent or more. It is also higher than that in the rib-roughened passage at Re 25,000 (Wagner et al., 1991b) by 20 and 30 percent in the first and second straight sections, respectively, and by 57 percent in the first two turns. In order to compare the present results with those of Wagner et al. (1991c), the normalized distance X/X_L is used

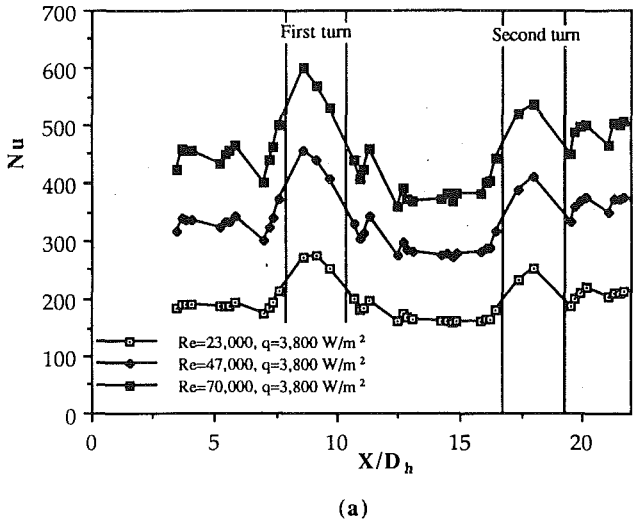

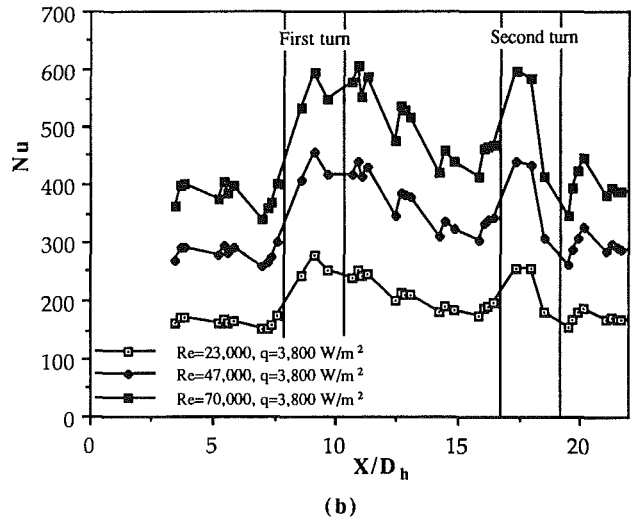

Fig. 7 Variation of local Nusselt number distributions with Reynolds number at Ro = 0.0195: (*a*) trailing walls and (*b*) leading walls

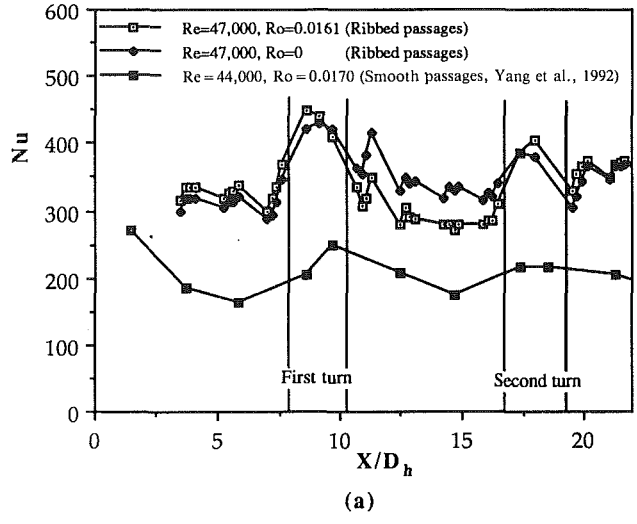

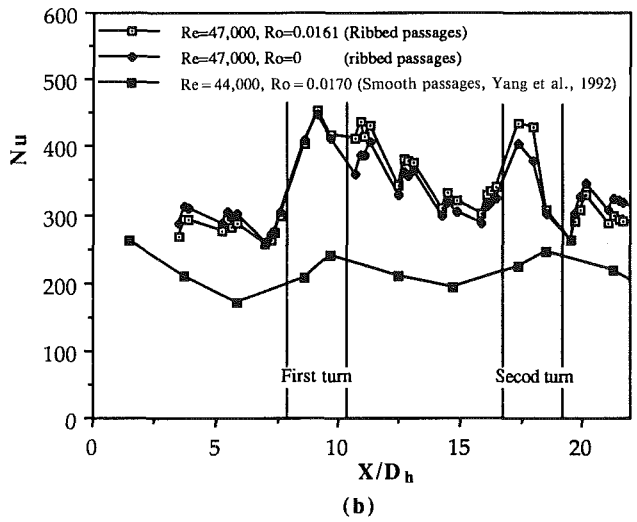

Fig. 8 A comparison of local Nusselt number distributions in rib-roughened and smooth serpentine passages: (*a*) trailing walls and (*b*) leading walls

in which X_L measures the distance from inlet to the midpoint of the third straight section. Although some discrepancy in results exists between Wagner et al. and the present work, the heat transfer ratios for ribbed surfaces both studies fall within the data band of Han et al. (1986), as shown in Fig. 6.

2 Rotating Cases. Figure 7 depicts some representative results of the local heat transfer performance for rotating cases. As in the stationary cases, the Nusselt numbers at both the trailing and leading walls increase with Re, while preserving the shape of the Nu versus X/D_h curve. A comparison between Figs. 7(*a*) and 7(*b*) reveals that the local Nusselt numbers on the trailing wall are generally higher than the leading wall in both the first and third straight sections but lower in both the second straight section and the turn than the respective values on the leading wall. It is also revealed by Taslim et al. (1991) that the Nusselt numbers on both the trailing and leading walls in both the stationary and rotating cases increased with an increase in the Reynolds number. The results are consistent with those in the present study. Figure 8 compares the local heat transfer performance between the rotating case (Ro = 0.0161) and the stationary case, at Re = 47,000. An increase in rotation number increases heat transfer on the trailing wall in the first and third straight sections but decreases it in the second straight section. The heat transfer performance on the leading wall has an opposite behavior, namely a decrease in the first and third straight sections but an increase in the second straight section. It should also be noted that the heat transfer performance on both the trailing and leading walls is enhanced in the first two turns. The local Nu distribution on the smooth wall under almost the same operating condition (Ro = 0.0170 and Re = 44,000) is superimposed in Fig. 8 for reference. It is found that heat transfer enhancement due to the ribs in both the first and third straight sections is stronger on the trailing wall than on the leading wall. However, the heat transfer augmentation by the ribs in the second straight section is stronger on the leading wall than on the trailing wall.

The effect of rotation number on the heat transfer performance is shown in Fig. 9. Stronger effects of rotation on the trailing wall than on the leading wall are observed in the first two straight sections. Conversely, the rotational effect is stronger on the leading wall than on the trailing wall in the third straight section. Rotation causes a heat transfer enhancement on the trailing wall in the first straight section but a retardation in the second straight section. The rotational effect on the trailing wall disappears in the third section. The leading wall exhibits an opposite trend because the high and low-pressure surfaces are swapped. It is important to note that the results for the first two straight sections are consistent with those of Wagner et al. (1991b), who provide no information

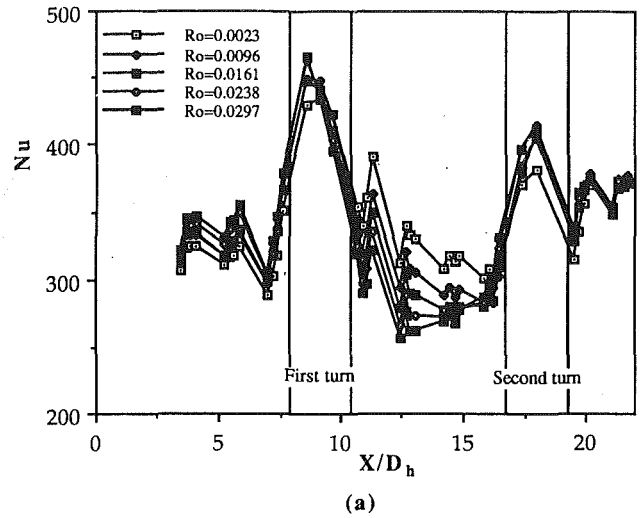

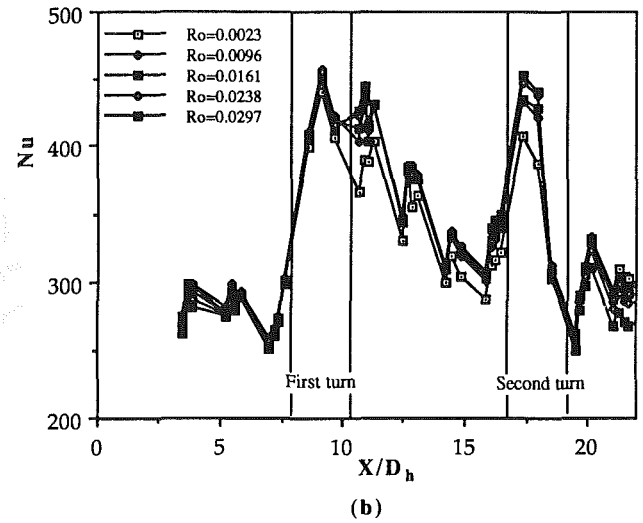

Fig. 9 Variation of local Nusselt number distributions with rotation number at Re = 47,000 and q = 7,200 W/m^2: (*a*) trailing walls and (*b*) leading walls

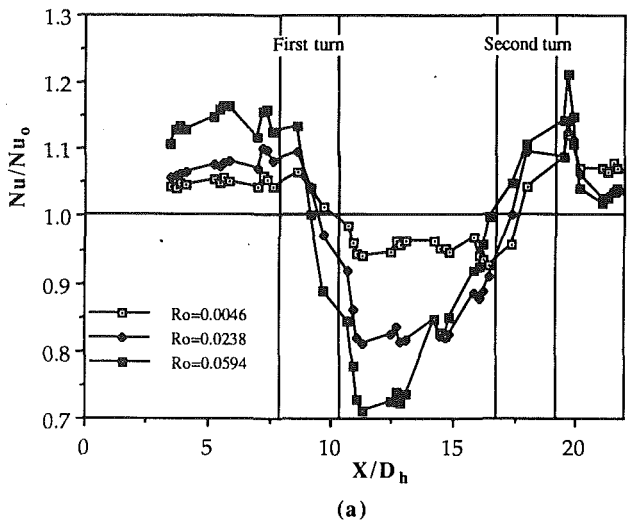

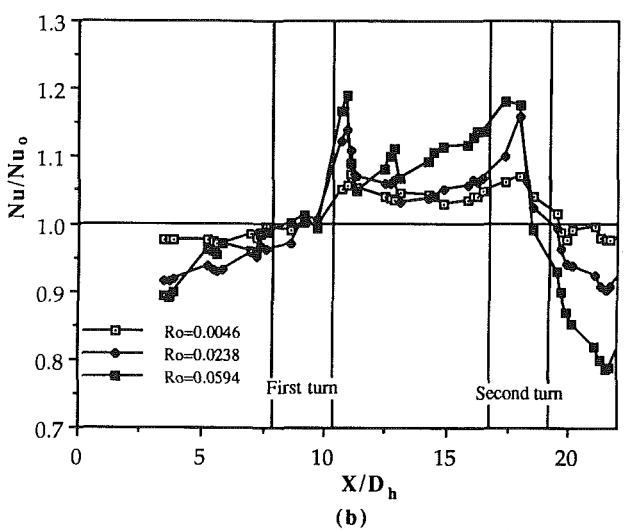

Fig. 10 Variation of Nusselt number ratios, Nu/Nu$_o$, with rotation number at Re = 23,000 and q = 3,800 W/m^2: (*a*) trailing wall and (*b*) leading walls

on the third straight section. The local heat transfer coefficients of both the trailing and leading walls in all turns increase with the rotation number.

The difference in heat transfer performance inside a smooth serpentine passage between the rotating and stationary flow cases is attributed to a combination of the secondary flows induced by the Coriolis force, the buoyancy, and the stability in the near-wall flow. In the case of rib-roughened passages, the ribs periodically disrupt the boundary layer, creating a series of near-wall turbulences. It is the near-wall turbulences that cause a significant enhancement in the heat transfer performance on both the trailing and leading walls in all the straight sections. Furthermore, an increase in the rotation rate causes a substantial enhancement in heat transfer on the trailing wall in the first straight section due to the combined effect of the Coriolis force-induced secondary flow and buoyancy force. On the contrary, the buoyancy-driven near-wall flow cannot induce an additional near-wall turbulence due to the relatively weaker near-wall shear layer in the second straight passage, resulting in less heat transfer enhancement on the leading wall. The heat transfer performance on both the leading wall in the first passage and the trailing wall in the second passage diminishes because of stabilization in near-wall flows caused by Coriolis-generated cross-stream flows (Wagner et al., 1991c). The ribs act to stabilize the near-wall flows, thus promoting a decrease in heat transfer on low-pressure surfaces.

Figure 10 illustrates the distributions of the local Nusselt number ratio, Nu/Nu$_o$, at various rotation numbers for the Reynolds number of 23,000. The deviation of this ratio from unity indicates the change in the local heat transfer coefficient due to rotation. A ratio greater than unity signifies an enhancement, while that less than unity, a retardation. It is revealed in Fig. 10(*a*) that in the first straight section the heat transfer performance on the trailing wall is increased by approximately 5 percent at Ro = 0.0046, 8 percent at Ro = 0.0238, and 15 percent at Ro = 0.0594. In constrast, the performance is diminished in the second straight section by about 5 percent at Ro = 0.0046, 18 percent at Ro = 0.0238, and 28 percent at Ro = 0.0594. It is enhanced again in the third straight section by about 7 percent at Ro = 0.0046 and 3 percent at Ro of 0.0238 and 0.0594. In Fig. 10(*b*) heat transfer on the leading wall shows a weaker rotational effect in the first two straight sections but a stronger effect in the third straight section. The decrease in the first section ranges from 2 percent at Ro = 0.0046 to 10 percent at Ro = 0.0594. Meanwhile, the enhancement in the second section ranges from 3 percent at Ro = 0.0046 to 12 percent at Ro = 0.0594. A larger change appears in the third section with a decrease of

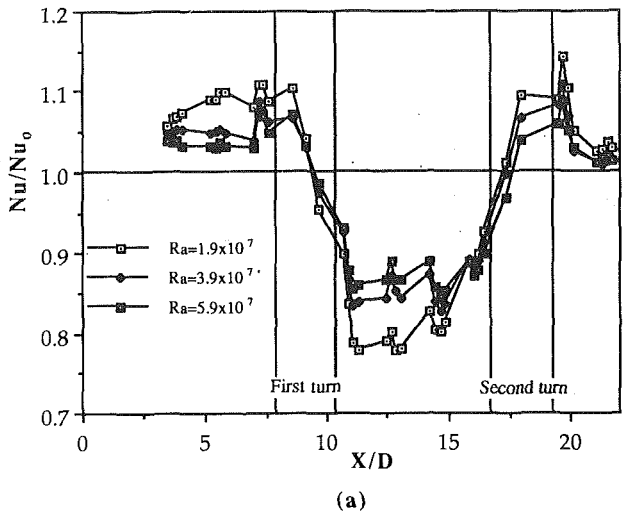

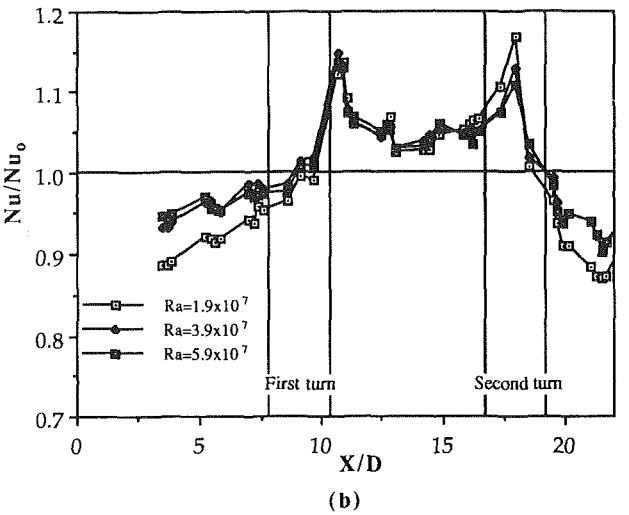

Fig. 11 Variation of Nusselt number ratios, Nu/Nu_o, with Reyleigh number at Re_r = 750: (*a*) trailing walls and (*b*) leading walls

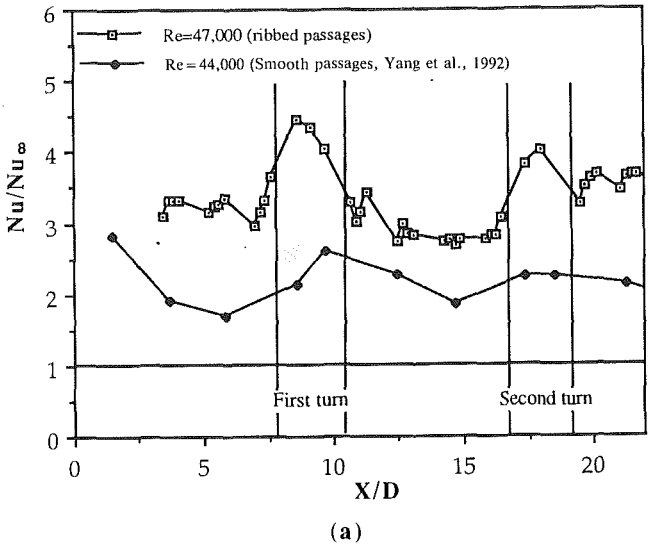

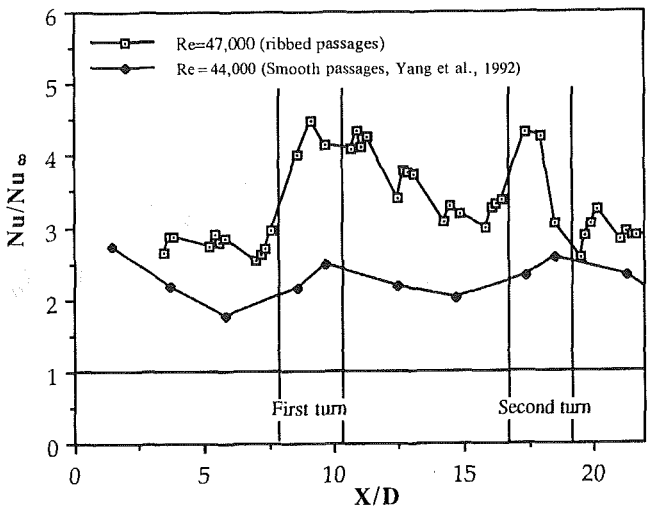

Fig. 12 A comparison of local Nusselt number distributions in rib-roughened and smooth (Yang et al., 1992) serpentine passages at Ro = 0.017: (*a*) trailing walls and (*b*) leading walls

about 2 percent at Ro = 0.0046 to 20 percent at Ro = 0.0594. Similar behavior is found for the Reynolds numbers of 47,000 and 70,000 (not shown).

The effect of Reynolds number on the local Nusselt number ratio, Nu/Nu_o, at the same rotational speed is generally small in the rotating rib-roughened serpentine passage. For example, the deviations of Nu/Nu_o for various Reynolds numbers at Ro = 0.0195 are less than 5 percent (not shown). The disclosure is in contrast with the behavior in a rotating smooth serpentine passage in which the Reynolds number plays an important role on heat transfer on the trailing wall (Yang et al., 1992).

Figure 11 depicts the effect of Rayleigh number on heat transfer at Re_r = 750. Here, Re_r, the product of the Reynolds number and the rotation number, is called the rotational Reynolds number. It reveals that an increase of the Rayleigh number leads to a retardation in the heat transfer performance on the trailing wall of the first straight section in rotation: a decrease from 10 percent at Ra = 1.9×10^7 to 3 percent at Ra = 5.9×10^7. The reduction on the trailing wall of the second straight section ranges from about 20 percent at Ra = 1.9×10^7 to 12 percent at Ra = 5.9×10^7. In contrast, the heat transfer reduction on the leading wall of both the first and third sections is nonlinear, from about 10 percent at Ra = 1.9×10^7 to 5 percent at Ra of 3.9×10^7 and 5.9×10^7. The influence of Rayleigh number on the heat transfer on both the trailing wall of the third section and the leading wall of the second section is not obvious. An increase in the rotational Reynolds number, Re_r, leads to an enhancement in heat transfer on the trailing wall of the first straight section but a reduction on that of the second section. For example, at Ra = 3.9×10^7, Nu/Nu_o on the trailing wall in the first straight section increases from 5 percent at Re_r = 750 to 12 percent at Re_r = 1390. Meanwhile, a reduction in Nu/Nu_o on the trailing wall of the second straight section is enhanced from about 15 percent at Re_r = 750 to 30 percent at Re_r = 1390, not shown. The leading wall experiences a heat transfer reduction in the first and third straight sections. The effect of the rotational Reynolds number on heat transfer is minor on both the trailing wall of the third straight section and the leading wall of the second straight section.

Figures 12 and 13 compare the heat transfer performances in the rib-roughened and smooth serpentine passages in rotation. A baseline of fully developed turbulent flow at rest used by Wagner et al. (1991c) was employed here. The ribs have contributed to a heat transfer enhancement from 130 to 200 percent at Ro = 0.017 and Re of approximately 45,000, and from 150 to 300 percent at Ro = 0.0238 and Re of about

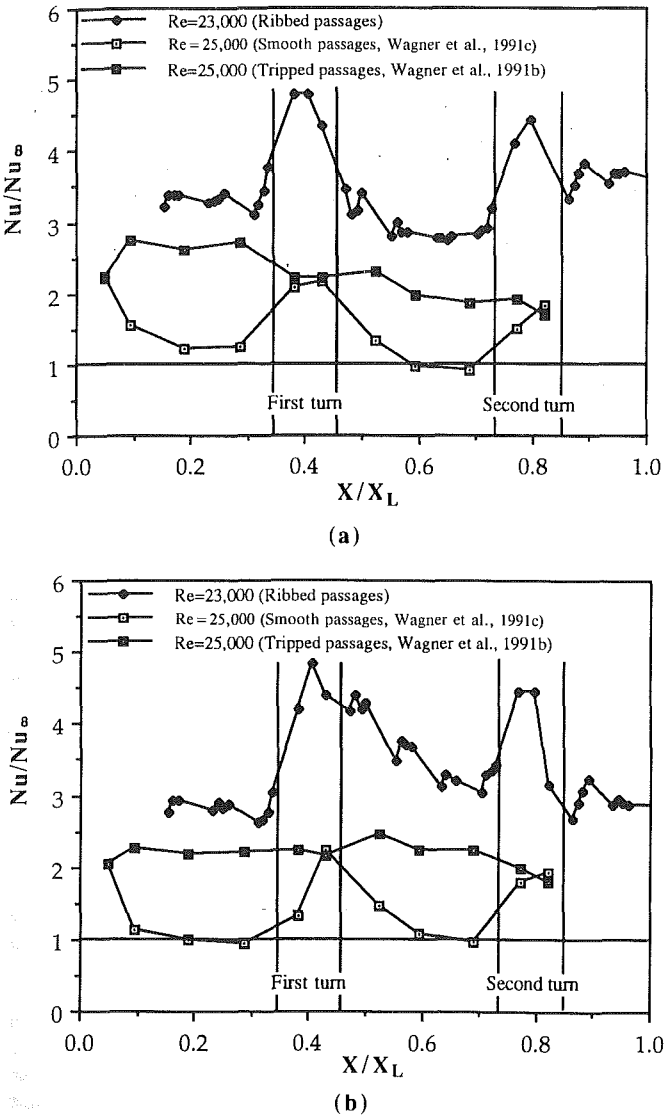

Fig. 13 A comparison of local Nusselt number distributions in rib-roughened and smooth (Wagner et al., 1991c) and tripped (Wagner et al., 1991b) serpentine passages at Ro = 0.0238: (*a*) trailing walls and (*b*) leading walls

24,000. A comparison results in a difference of up to 100 percent between Wagner et al. (1991b) and the present study due to differences in their models, size and rib geometry, measurement methods, and test conditions. Here, the linear interpolated values of Nu/Nu_∞ between Ro = 0.0 and 0.118 for Ro = 0.0238 of Wagner et al. (1991c) are superimposed in Fig. 13 for comparison. Taslim et al. (1991) found that heat transfer coefficients on the leading surface decreased with an increase in the rotation rate. The result is consistent with those of Wagner et al. and the present study. However, the heat transfer performance on the trailing surface contradicted those of Wagner et al. (1991b) and the present study. Additional work is desirable in order to clarify the cause of the inconsistency.

Conclusion

A rather difficult experimental investigation has been conducted to determine the local heat transfer performance in a rotating rib-roughened serpentine passage. It is concluded from the present study that:

1 A significant enhancement in the heat transfer performance is achieved by means of rib turbulator in a serpentine passage at rest as well as in rotation.

2 The rotational effect on heat transfer from rib-roughened surfaces is most significant on both the trailing wall of the first two straight sections and the leading wall of the third straight section.

3 Although the Reynolds number plays an important role on heat transfer from rib-roughened surfaces both at rest and in rotation, its effect on the Nusselt number ratio, Nu/Nu_o, is minor.

4 Both the Rayleigh and rotational Reynolds numbers have considerable effects on heat transfer on both the trailing wall of the first two straight sections and the leading wall of the first and third straight sections.

Acknowledgments

This study was supported by the Electric Power Research Institute under EPRI Agreement RP 8006-11.

References

Boyle, R. J., 1984, "Heat Transfer in Serpentine Passages With Turbulence Promoters," ASME Paper No. 84-HT-24.

Burggraff, F., 1970, "Experimental Heat Transfer and Pressure Drop With Two-Dimensional Turbulence Promoter Applied to Two Opposite Walls of a Square Tube," in: *Augmentation of Convective Heat and Mass Transfer*, A. E. Bergles and R. L. Webb, eds., ASME, New York, pp. 70–79.

Chandra, P. R., Han, J. C., and Lau, S. C., 1988, "Effect of Rib Angle on Local Heat/Mass Distribution in a Two-Pass Rib Roughened Channel," ASME *Journal of Turbomachinery*, Vol. 110, pp. 233–241.

Clifford, R. J., 1985, "Rotating Heat Transfer Investigations on a Multipass Cooling Geometry," AGARD Conference Proceedings No. 390: *Heat Transfer and Cooling in Gas Turbines*, May 6–10.

Fan, C. S., and Metzger, D. E., 1987, "Effects of Channel Aspect Ratio on Heat Transfer in Rectangular Passage Sharp 180° Turns," ASME Paper No. 87-GT-113.

Guidez, J., 1989, "Study of the Convective Heat Transfer in a Rotating Coolant Channel," ASME *Journal of Turbomachinery*, Vol. 111, pp. 43–50.

Han, J. C., Park, J. S., and Ibrahim, M. T., 1986, "Measurement of Heat Transfer and Pressure Drop in Rectangular Channels With Turbulence Promoters," NASA Contractor Report 4015.

Han, J. C., and Park, J. S., 1988, "Developing Heat Transfer in Rectangular Channels With Rib Turbulators," *International Journal of Heat and Mass Transfer*, Vol. 31, pp. 183–195.

Han, J. C., Chandra, P. R., and Lau, S. C., 1988, "Local Heat/Mass Transfer Distributions Around Sharp 180° Turns in Two-Pass Smooth and Rib-Roughened Channels," ASME JOURNAL OF HEAT TRANSFER, Vol. 110, No. 1, pp. 91–98.

Han, J. C., and Zhang, P., 1991, "Effect of Rib-Angle Orientation on Local Mass Transfer Distribution in a Three-Pass Rib-Roughened Channel," ASME *Journal of Turbomachinery*, Vol. 113, pp. 123–130.

Kays, W. M., and Perkins, H. C., 1985, "Forced Convective Internal Flow in Ducts," in: *Handbook of Heat Transfer Fundamentals*, W. M. Rohsenow, J. P. Hartnett, and E. N. Ganic, eds., McGraw-Hill, New York, pp. 7–28.

Kline, S. J., and McClintock, F. A., 1953, "Describing Uncertainties in Single Sample Experiments," *Mechanical Engineering*, Vol. 75, Jan., pp. 3–8.

Metzger, D. E., and Sahm, M. K., 1986, "Heat Transfer Around Sharp 180° Turns in Smooth Rectangular Channels," ASME JOURNAL OF HEAT TRANSFER, Vol. 108, pp. 500–506.

Taslim, M. E., and Spring, S. D., 1987, "Friction Factors and Heat Transfer Coefficients in Turbulated Cooling Passages of Different Aspect Ratios, Part I: Experimental Results," presented at the 23rd AIAA/ASME/SAE/ASEE Joint Propulsion Conference, San Diego, California, Paper No. AIAA-87-2009.

Taslim, M. E., and Spring, S. D., 1988, "An Experimental Investigation of Heat Transfer Coefficients and Friction Factors in Passages of Different Aspect Ratio Roughened With 45° Turbulators," presented at the ASME 25th National Heat Transfer Conference, Houston, TX.

Taslim, M. E., Rahman, A., and Spring, S. D., 1991, "An Experimental Investigation of Heat Transfer Coefficients in a Spanwise Rotating Channel With Two Opposite Rib-Roughened Walls," ASME *Journal of Turbomachinery*, Vol. 113, pp. 75–82.

Wagner, J. H., Johnson, B. V., and Hajek, T. J., 1991a, "Heat Transfer in Rotating Passages With Smooth Walls and Radial Outward Flow," ASME *Journal of Turbomachinery*, Vol. 113, pp. 42–51.

Wagner, J. H., Johnson, B. V., Graziani, R. A., and Yeh, F. C., 1991b, "Heat Transfer in Rotating Serpentine Passages With Trips Normal to the Flow," ASME Paper No. 91-GT-265; ASME *Journal of Turbomachinery*, Vol. 114, 1992, pp. 847–857.

Wagner, J. H., Johnson, B. V., and Kopper, F. C., 1991c, "Heat Transfer in Rotating Serpentine Passages With Smooth Walls," ASME *Journal of Turbomachinery*, Vol. 113, pp. 321–330.

Yang, W. J., Zhang, N., and Chiou, J., 1992, "Local Heat Transfer in a Rotating Four-Pass Serpentine Flow Passage With Throughflow," ASME JOURNAL OF HEAT TRANSFER, Vol. 114, pp. 354–361.

An Experimental Study on Heat/Mass Transfer and Pressure Drop Characteristics for Arrays of Nonuniform Plate Length Positioned Obliquely to the Flow Direction

Huai-Zhang Huang

Wen-Quan Tao

Department of Power Machinery Engineering,
Xi'an Jiaotong University,
Xi'an, Shaanxi 710049,
The People's Republic of China

In this paper, heat/mass transfer and pressure drop characteristics for arrays of nonuniform plate length, aligned at an angle of 25 deg to the flow direction, are investigated experimentally via a naphthalene sublimation technique. The measurements of cyclic average Sherwood numbers and friction factors in the fully developed regime are conducted for nine geometric configurations. The following parameter ranges are studied: length ratio of successive plates 1.5–2.5; ratio of the transverse pitch to the longitudinal pitch 0.381–0.8, and Reynolds number based on short plate length 1.98×10^2 to 1.66×10^3. Comparisons with the results for arrays with uniform plate length are conducted. Two constraints are used, identical pumping power and identical pressure drop. It is found that for most cases studied, the thermal performance of the array with a nonuniform plate length is better than that of the array with a uniform plate length.

Introduction

Flow interruption in a flow passage, at periodic intervals, is a well-known technique for enhancing heat transfer. The slit fins used in compact heat exchangers and automobile radiators are examples of this technique. Due to the repeated interruption of the thermal boundary layer, the slit fin has higher local heat transfer coefficients than that without slits. In the case of louvered fins, the fin segments are positioned obliquely to the flow direction; additional heat transfer enhancement can be obtained because of the impinging effect and the vorticity and turbulence created in the flow. The heat transfer and the pressure drop characteristics are controlled mainly by the geometric factors. These include the positioning of the fin segments (i.e., plates), the transverse pitch between two adjacent plates, the angle of the plates, and the plate thickness. A number of investigations, both experimental and numerical, have been conducted on heat transfer and pressure drop characteristics of this type of fin surface. Lee (1986) and Zhang and Lang (1989) experimentally investigated the heat transfer and pressure drop performances of an array of plates aligned at angles to the flow, which serves as a two-dimensional model of louvered fins. For this type of positioning, Lee (1989) further investigated the effect of segmented-to-total plate width on the heat transfer and pressure drop characteristics. Asako and Faghri (1988) and Pang et al. (1990) performed numerical investigations on an array of interrupted plates positioned convergently-divergently along the flow direction. In the experimental work mentioned above, the transverse pitch was kept constant. However, according to the flow visualization results obtained by Hiramatsu and Kajino (1986), the transverse pitch has a significant effect on the heat transfer performance of louvered fins. In all the research related to the heat transfer performance of louvered fins, the lengths of two successive segments are uniform. Thus, in the periodic fully developed regime, one unit only includes one segment. For arrays of staggered plates aligned with air flow, Yan et al. (1988) conducted an experimental study to reveal the effect of length ratio of successive plates on the heat transfer and pressure drop. They found that when the length ratio of the two successive plates is two, the value of j/f is 8–13 percent higher than that of uniform arrays. This fact stimulated the present authors to perform a similar study for the louvered fin case.

In this work, experimental studies are conducted for a two-dimensional model of louvered fins with a fixed oblique angle. Consistent with the experimental results of Lee (1989) and Zang and Lang (1989), an oblique angle of 25 degrees is adopted. Attention is focused on the effects of the length ratio of successive plates and the ratio of the transverse pitch to one unit length on the heat transfer and pressure drop characteristics of louvered fins. The heat transfer data are obtained via the naphthalene sublimation technique. The mass transfer model adopted here is analogous to a heat transfer problem in which all plates are identically isothermal. The experimental results are compared with those for an array of uniform length under conditions of identical pumping power and identical pressure drop. It is found that the heat transfer performance of the nonuniform plate length array is generally better than that of the uniform length array.

Experimental Apparatus and Procedures

The experimental apparatus is presented in Fig. 1, where various components of the apparatus—the inlet section, preduct, test section, after-duct, rotameter, control valve and blower—are shown schematically. The test section is 553 mm long with a spanwise dimension of 120 mm and a changeable height, ranging from 80 mm to 120 mm.

The test section is illustrated in Fig. 2. It consists of five

Contributed by the Heat Transfer Division for publication in the JOURNAL OF HEAT TRANSFER. Manuscript received by the Heat Transfer Division February 1992; revision received December 1992. Keywords: Analog Techniques, Augmentation and Enhancement, Forced Convection. Associate Technical Editor: T. W. Simon.

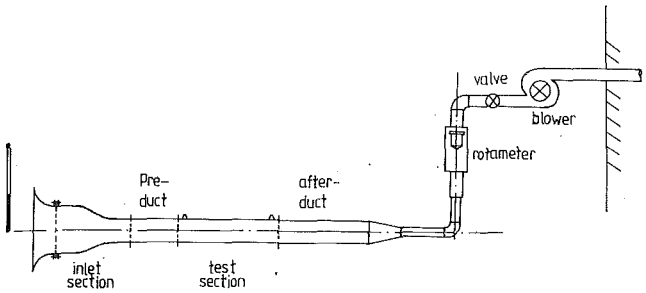

Fig. 1 Experimental apparatus

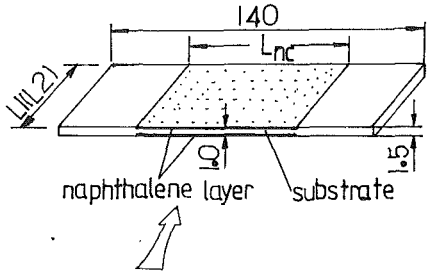

Fig. 3 Test plate

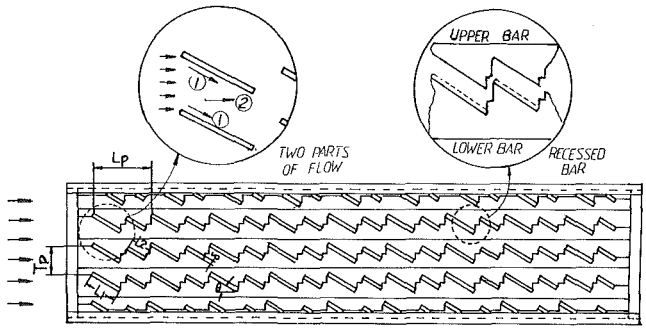

Fig. 2 Side view of test section

columns of plates and duct walls. In each column there are nine units or cycles, each including one long plate and one short plate. The successive plate lengths of the three inner columns are L_1 (long plate) and L_2 (short plate). The plate lengths of the two columns adjacent to the upper and lower wall of the test section are $L_1/2$ and $L_2/2$. Such an elaborately designed test section ensures that the flow and heat transfer on the plates in the middle column can simulate those situations where the flow is not bounded by the upper and lower walls. The two successive plates are so located that the longitudinal pitch (i.e., the streamwise length of one unit), L_P, is always equal to the total length of a long and a short plate ($L_P = L_1 + L_2$). In every run, only the plates in the middle column are naphthalene coated. Other plates that did not participate in the mass transfer process are made of mild steel and are there simply to simulate the fluid dynamic boundary conditions. This practice may be called local simulation, the rationality of which has been demonstrated by Lee's experiments (1986). All the plate edges are right angled as in real fin surfaces. The plates are held in position by recessed bars attached to the two side walls of the test section. The upper wall is removable, so that the test plates can be put in and taken out easily. To prevent leakage from the test section, an O-ring is used.

A pictorial view of a test plate is shown in Fig. 3. It consists of a 1-mm-thick mild steel core sandwiched between two thin (0.25 mm) layers of naphthalene. In order to position the test plate into the recessed bars and to minimize the end effect, at each end of the substrate there is a 30-mm-long section that is not covered by naphthalene. The test plates were made by a casting-machining process. The details may be found from Sparrow and Hajiloo (1980). It should be noted that the leading edge of the test plate is not fully naphthalene coated because of the difficulty in preparation of the test plate. In the calculation of the naphthalene surface area, the inactive part is not included. In the uncertainty analysis, the error of unaccounted-for mass transfer at the inactive part of the leading edge is approximately considered via the term of naphthalene surface area.

The parameters of the test arrays are as follows: the plate thickness $\delta = 1.5$ mm, the oblique angle $\theta = 25$ deg, the short plate length $L_2 = 15$ mm, the ratio of $L_1/L_2 = 1.5$, 2.0, and 2.5 (the corresponding longitudinal pitches L_P are 37.5, 45, and 52.5 mm), and the transverse pitch $T_P = 20$, 25, and 30 mm. It should be noted that in an actual automobile radiator, the thickness of slit fins is about 0.1 mm. It is too small to be simulated by naphthalene sublimation technique. The plate shown in Fig. 3 is an enlarged model, about 15 times as large as a slit fin. In the test, the range of Reynolds number encompasses the actual values of Reynolds number encountered in engineering practice.

It is evident that nine configurations can be obtained from the combination of different L_1/L_2 and T_P/L_P. The characteristics of these configurations, expressed in both dimensional and dimensionless terms, are presented in Table 1. For simplicity of later writing, a case number is assigned to each configuration.

Nomenclature

A_c = cross-sectional area of the wind tunnel
D = diffusion coefficient
f = friction factor
F = transfer area of naphthalene sublimation
j = Colburn j-factor $= \mathrm{Nu}/\mathrm{RePr}^{0.4}$
k = thermal conductivity
K = per-unit average mass transfer coefficient
L = length of plate in array of uniform plate length
L_1 = length of long plate
L_2 = length of short plate
L_{nc} = spanwise length of naphthalene-coated section of each test plate
L_P = longitudinal pitch (length of a unit)
ΔM = corrected mass loss
N = number of plate cycles (units) in the fully developed region
Nu = Nusselt number
Pr = Prandtl number
ΔP_e = entrance/exit loss
ΔP_i = inertia loss through the array
ΔP_f = pressure drop due to friction
ΔP_t = pressure drop of array
Q = volumetric flow rate of air
Re = Reynolds number
Sc = Schmidt number
Sh = Sherwood number
T_P = transverse pitch
V = average air velocity
$\Delta\rho_m$ = log mean concentration difference
δ = thickness of plate
θ = oblique angle of louvered fin
ν = kinematic viscosity of air
ρ = density
ρ_{ne} = concentration at the exit of the test unit
ρ_{ni} = concentration at the inlet of the test unit
ρ_{nw} = concentration of naphthalene vapor at the plate surface
τ = time duration of data run

Table 1 Characteristics of the configurations investigated (L_2 = 15 mm, θ = 25 deg)

case	L_1, mm	T_P, mm	L_P, mm	L_1/L_2	T_P/L_P
1	37.5	30.0	52.5	2.5	0.571
2	30.0	30.0	45.0	2.0	0.667
3	22.5	30.0	37.5	1.5	0.800
4	37.5	25.0	52.5	2.5	0.476
5	30.0	25.0	45.0	2.0	0.556
6	22.5	25.0	37.5	1.5	0.667
7	37.5	20.0	52.5	2.5	0.381
8	30.0	20.0	45.0	2.0	0.444
9	22.5	20.0	37.5	1.5	0.533

In the preduct and test section regions, along the spanwise centerline of the upper wall, a series of small holes (0.5 mm) are made, which are normal to the inner surface of the upper wall and serve as pressure taps to provide pressure signals during the data runs. These small holes are so located that the distance between two successive holes equals the length of one cycle, which is composed of one long plate and one short plate.

The airflow rate going through the wind tunnel is measured by a calibrated rotameter. A calibrated laboratory thermometer positioned in front of the duct inlet is used to determine the temperature of the inlet air. The sublimated mass of the naphthalene is measured with an analytical balance having a resolution of 0.1 mg and a capacity of 200 mg. The pressure signals are sensed by a capacitance-type pressure transmitter and measured with a digital voltmeter. The pressure signal can be read to 10^{-3} mm H_2O. The amount of naphthalene sublimated during a data run is determined by weighing the test plates immediately before and after the data run. In order to ensure that there is no appreciable change in the geometry of the test plates, the run time is adjusted so that the average change in the thickness of the naphthalene coating during a data run is less than 0.025 mm. The room temperature variation during a run is generally less than 0.2°C.

Auxiliary experiments are performed to assess the possible extraneous loss of mass that might have occurred during the installation and removal operations. The extraneous loss is typically about 1–2 mg. The typical sublimated mass of the long plate is about 30 mg and that of the short plate 15 mg.

The experimental runs to determine pressure drops are made separately from those for mass transfer measurements. In this case only metal plates are employed. The details of the experimental procedures of the naphthalene sublimation technique are well documented in the literature and may be found from Xiao and Tao (1990) and Huang (1990), and will not be elaborated here.

Data Reduction

Mass Transfer. The average mass transfer coefficient K of a unit is evaluated from the sublimated mass ΔM and the duration time τ of the test run by the definition

$$K = \Delta M/(F\tau\Delta\rho_m) \tag{1}$$

In the equation, F is the transfer area of the naphthalene surface, ΔM is the corrected mass of naphthalene, from which the extraneous loss of naphthalene during the auxiliary processes has been excluded, and $\Delta\rho_m$ is the log mean wall-to-bulk naphthalene vapor concentration difference:

$$\Delta\rho_m = \frac{\rho_{ne}-\rho_{ni}}{\ln\left((\rho_{nw}-\rho_{ni})/(\rho_{nw}-\rho_{ne})\right)} \tag{2}$$

The quantity ρ_{nw} is the concentration of naphthalene vapor at the plate surface and was determined from the Sogin vapor pressure–temperature relationship provided by Sogin (1957) in conjunction with the perfect gas law. The inlet air temperature is used as the naphthalene surface temperature. The uncertainty caused by this practice is fully tolerable (Sparrow et al., 1983). The ρ_{ne} is calculated by:

$$\rho_{ne} = \rho_{ni} + \Delta M/(\tau Q) \tag{3}$$

The per-unit average Sherwood number and Reynolds number are defined as

$$\mathrm{Sh} = KL_2/D \qquad \mathrm{Re} = QL_2/(\nu A_c) \tag{4}$$

where the diffusion coefficient is calculated by $D = \nu/\mathrm{Sc}$, Sc = 2.5.

In order to generalize the results from naphthalene sublimation to other Schmidt (or Prandtl) numbers, an adequate value of the exponent n in Sc^n or Pr^n must be selected. According to the suggestion of Sparrow and Hajiloo (1980), a 0.4 power relation of Sc (and Pr) is adopted. Then, according to the theory of mass/heat transfer analogy, we have

$$\mathrm{Sh}/\mathrm{Nu} = (\mathrm{Sc}/\mathrm{Pr})^{0.4} \tag{5}$$

Pressure Drop. The total pressure drop ΔP_t through the periodic fully developed region of the test section consists of three components, which are the pressure drop due to friction (ΔP_f), that due to inertia losses (ΔP_i), and the entrance/exit losses (ΔP_e).

In this paper, an average friction coefficient f is used to express the characteristics of the plate array in the periodic fully developed region:

$$f = \Delta P_t/(\rho V^2 N/2) \tag{6}$$

where N is the number of plate cycles (units) in the periodic fully developed region along the flow direction, and ΔP_t is the pressure drop over the N plate units. In this experiment, N = 3–5. The average air velocity is calculated by $V = Q/A_c$.

Results and Discussions

Preliminary Experiments. Two sets of preliminary experiments were conducted. First, to ensure that the results of the present investigation represent the case of a two-dimensional plate array, the effect of the spanwise length of the naphthalene-coated surface, L_{nc}, on the average mass transfer rate was investigated for the array of uniform plate length. Two spanwise lengths of the naphthalene-coated surface were used, L_{nc} = 40 mm and L_{nc} = 80 mm. The results are shown in Fig. 4. It can be seen that the results of the two values of L_{nc} are almost identical with an average deviation of 1.49 percent. This indicates that for the case of L_{nc} = 80 mm the end effect on the mass transfer is negligible. In subsequent experiments, the spanwise length of naphthalene-coated surface is taken as 80 mm.

The second preliminary experiment was conducted to determine the number of units after which the flow and mass transfer may be regarded as periodically fully developed. This experiment was performed for a nonuniform plate array ($L_1 \neq L_2$). Two geometric cases were tested. These are case No. 2 and case No. 7. It was found that in the range of Re = 2.40×10^2–1.65×10^3, from the fifth unit on, the fluid flow and mass transfer can be considered periodically fully developed. The indication is that from the fifth unit on, the per-unit average Sherwood number remains constant with a maximum

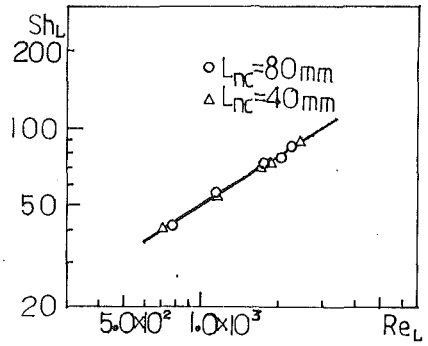

Fig. 4 Comparison of mass transfer results for two spanwise lengths of the naphthalene-coated plate

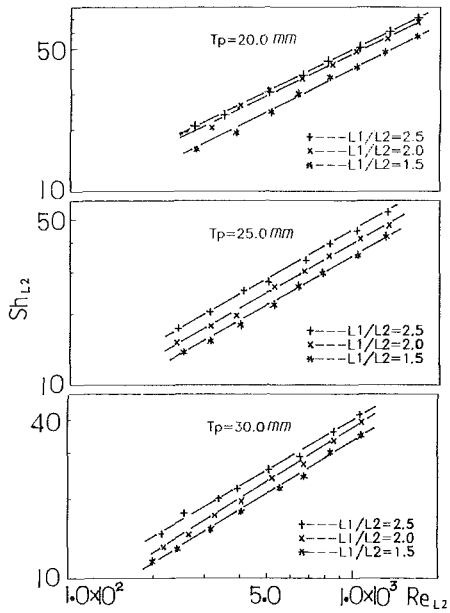

Fig. 5 Effect of the ratio of successive plate length on mass transfer

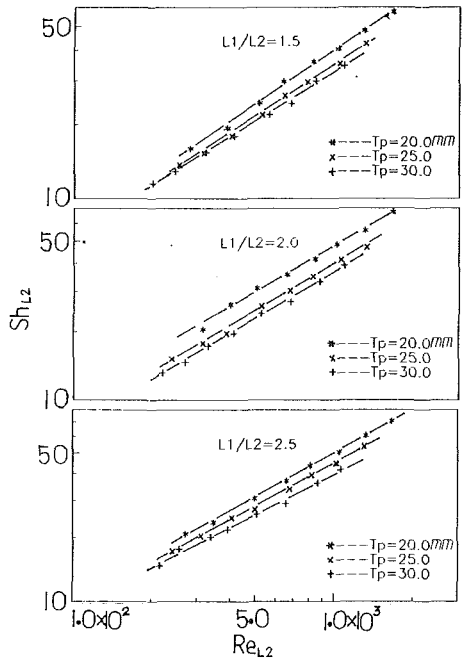

Fig. 6 Effect of the transverse pitch on mass transfer

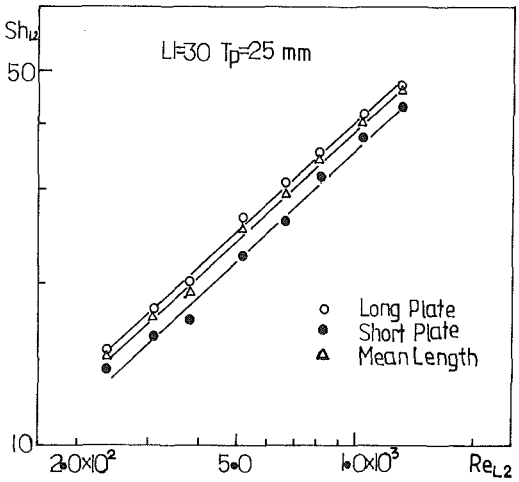

Fig. 7 Per-plate and per-unit average Sherwood number versus Re (L_1 = 30 mm, T_P = 25 mm)

deviation of about 4 percent from unit to unit. In the subsequent experiments, the data of the seventh unit were taken as representative for the fully developed region.

In view of the rapid attainment of the periodic fully developed fluid flow and mass transfer, the following discussion will focus on the fully developed characteristics.

The presentation of the experimental results will begin with the effect of the length ratio of successive plates on mass transfer, followed by the effect of transverse pitch on the Sherwood number, and then a general mass transfer correlation will be presented. The results of pressure drop and friction factor will be provided at the end of this section.

Effect of L_1/L_2 and T_P/L_P on Mass Transfer. The per-unit average Sherwood number in the periodic fully developed region for three ratios of successive plate lengths are shown in Fig. 5. It can be seen that at the same transverse pitch, with the increase in L_1/L_2, the per-unit average mass transfer coefficients increase. The effect of the transverse pitch on mass transfer is shown in Fig. 6. It clearly shows that, at the same L_1/L_2, with decrease in T_P, per-unit average Sherwood number increases.

This variation of the Sherwood number with L_1/L_2 and T_P/L_P may be accounted from the following considerations. According to the flow visualization performed by Hiramatsu and Kajino (1986), the fluid flow between the plates may, in general, be considered as the sum of the following two parts. The first part is the flow along the plate surface, the second part is the flow between the two parallel plate columns. These two parts of flow are schematically shown in Fig. 2 by two arrows labeled with ① and ②, respectively. It is mainly the first part of the flow that takes part in the heat and mass transfer process. The second part is, in some sense, the bypass flow, which does not make a great contribution to the mass/heat transfer. For the same value of T_P, the increase in L_1 leads to an increase in the distance between two successive plates (note, $L_P = L_1 + L_2$, L_2 is fixed). This change in geometry causes an increase in the first part flow (with the same total flow rate, i.e., the same Reynolds number). Thus, the transfer process is enhanced. This discussion also applies to the dependence of Sh on T_P/L_P. The increase in plate length L_1 may cause another effect. Since the two ends of the long plate protrude to the space between the two parallel plate columns, where the second part of the flow goes through, the ends of the long plate may be washed out directly by the second part of flow, and here the mass transfer is enhanced. This consideration may be supported from the data of per-plate average Sherwood number. In Fig. 7, the per-plate Sherwood number versus Re are shown

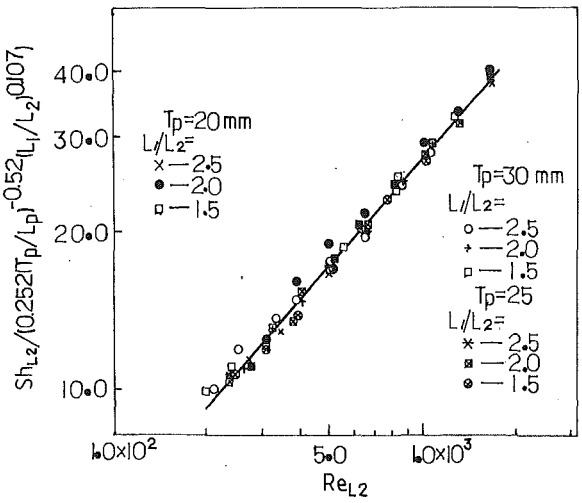

Fig. 8 Experimental data and correlation

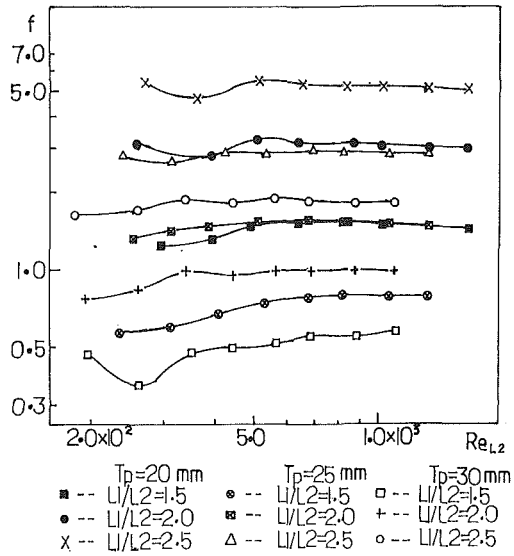

Fig. 9 Per-unit friction factors of nine cases tested

for the case of $L_1 = 30$ mm, $T_P = 25$ mm. The Sherwood number of the plate is higher than that of the short plate (with the same characteristic length L_2). This result is quite different from that of a plate placed along the flow direction, for which the shorter the plate, the higher the heat transfer coefficient.

The mass transfer results were correlated by the least square curve fitting method. The following equation is obtained:

$$\mathrm{Sh} = 0.252 \left(\frac{T_P}{L_P}\right)^{-0.52} \left(\frac{L_1}{L_2}\right)^{0.107} \mathrm{Re}^{0.681} \tag{7}$$

$$L_1/L_2 = 1.5\text{–}2.5, \quad T_P/L_P = 0.38\text{–}0.80$$

$$\delta/T_P = 1/20\text{–}3/40, \quad \theta = 25 \text{ deg}, \quad \mathrm{Re} = 1.98\times10^2\text{–}1.66\times10^3$$

This equation agrees with the experimental data to within ±2.7 percent (average) for 72 test data, with maximum deviation of 9.9 percent (Fig. 8).

According to the mass/heat transfer analogy theory, we have

$$\mathrm{Nu} = \mathrm{Sh}(\mathrm{Pr}/\mathrm{Sc})^{0.4} = 0.175 \left(\frac{T_P}{L_P}\right)^{-0.52} \left(\frac{L_1}{L_2}\right)^{0.107} \mathrm{Re}^{0.681}\mathrm{Pr}^{0.4} \tag{8}$$

where the Sc number (2.5) has been incorporated in the constant term.

Pressure Drop and Friction Factors. In the periodic fully developed regime, the pressure exhibits periodicity characteristics similar to those that occurred to the mass transfer. This implies that the pressures at successive points separated by unit length L_P lie along a straight line. In the experimental apparatus, the successive pressure taps are separated by a distance L_P, and the measured pressures in the fully developed region do, indeed, fall on a straight line, except for the pressure measured from the last two taps, which may be affected by the recirculating flow in the suddenly enlarged part of the afterduct.

The variations of the per-unit friction factors with the Reynolds number are shown in Fig. 9. The major feature of Fig. 9 is that for any case studied, from a certain Reynolds number on, the per-unit friction factor f does not vary with Reynolds number and is almost constant. This means that from a certain Reynolds number on, the inertia loss becomes dominant in the total pressure drop. Figure 9 also shows that the per-unit friction factor increases with the increase in L_1/L_2 and with the decrease in T_P/L_P.

Attention is now turned to the uncertainty analysis. A comprehensive uncertainty analysis for naphthalene sublimation experiments has been made by Xiao et al. In this study the test procedure and instruments are the same as those of Xiao et al., and, therefore, the analysis process will not be elaborated here. The ratio of the exit naphthalene density to the saturated naphthalene vapor density is less than 0.1 in this investigation. Using the method of Kline and McClintock (1953), this leads to a maximum Sherwood number uncertainty of 5.45 percent, and the Reynolds number uncertainty is 3 percent. The per-unit friction factor has an uncertainty of 4.12 percent, for a case of moderate Reynolds number.

Performance Evaluation

In this section, the comparison of the heat/mass transfer and pressure drop characteristics of the array of nonuniform plate length with those of the array of uniform plate length will be made first. Then the heat/mass transfer performance evaluations will be conducted under the identical pumping power and identical pressure drop constraints.

Comparisons of Sh and Pressure Drop for the Two Types of Plate Array. The mass/heat transfer and pressure drop characteristics comparisons between the two types of array are performed for the case of $T_P = 30$ mm. The schematic views of the two arrays are shown in Fig. 10. The variations of the per-unit average Sherwood number with Reynolds number are shown in Fig. 11, where the Sherwood correlation for the array of uniform plate length is adopted from Zhang and Lang (1989). It should be noted that for comparison purposes, the characteristic length for the nonuniform length array is now taken as L_1, the length of the long plate, which equals the plate length of the uniform case. Examination of Fig. 11 shows that for any geometric case compared, there is a somewhat critical Reynolds number, beyond which the Sherwood number of the uniform case is larger than that of the nonuniform case. For the three cases compared, this critical Reynolds number is about $1.1\text{–}1.3\times10^3$.

The following considerations may account for the aforementioned character. As noted earlier, the reason interrupted plates positioned along the flow direction can enhance heat transfer is the entrance effect of the thermal boundary layer. When the plates are positioned obliquely to the flow direction, the impinging effect makes a further contribution to the augmentation of heat and mass transfer process. When Re is less than the critical value, the entrance effect is the major factor contributing to the enhancement. The per-unit average plate length of the nonuniform case (i.e., $(L_1 + L_2)/2$) is less than that of the uniform case (Fig. 10(a)). Thus, the per-unit average

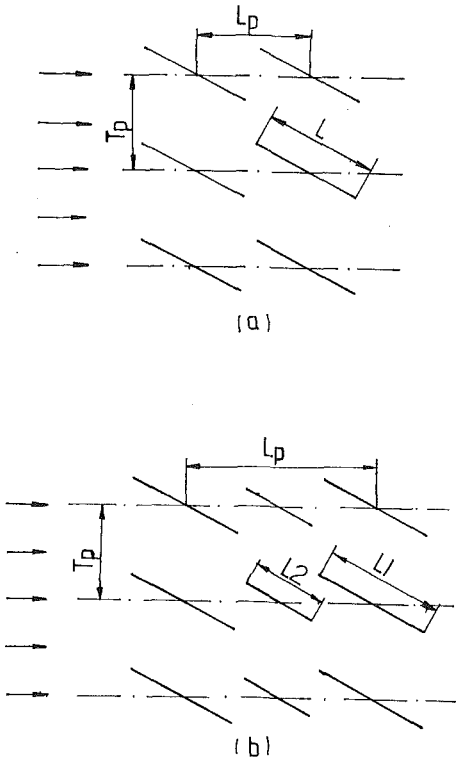

Fig. 10 Schematic view of the two arrays compared

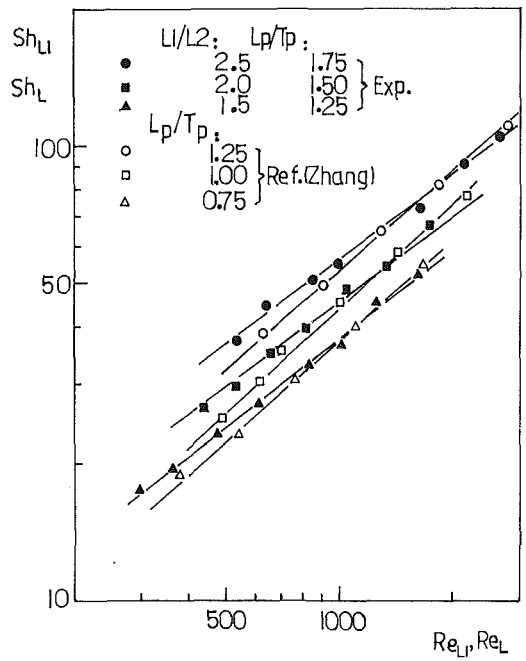

Fig. 11 Per-unit average Sherwood number of the two arrays compared (T_P = 30 mm)

Sherwood number of the nonuniform case is larger than that of uniform case. However, with the increase in the velocity of oncoming flow, the contribution of the impinging effect becomes larger. When Re is larger than the critical value, the impinging effect becomes dominant. Under the same transverse pitch, a stronger impinging effect will occur at the longer plates. This leads to a higher transfer coefficient for the uniform array, the plate length of which is larger than the per-unit average plate length of the nonuniform case.

A comparison of the pressure drops is presented in Fig. 12.

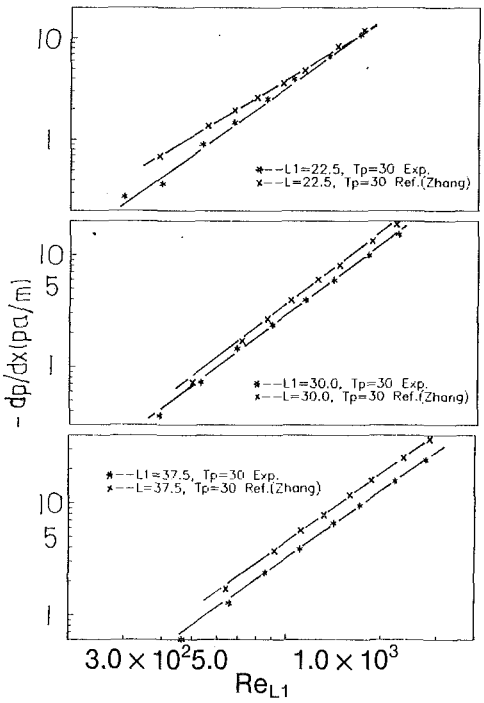

Fig. 12 Pressure drop of the two arrays compared

It can be seen that in the range of this study, the pressure drop of the nonuniform case is less than that of uniform case. This is an outcome of the complex flow phenomena. A detailed flow field analysis will be helpful to understand the results. An numerical investigation is now under way.

Heat/Mass Transfer Performance Evaluation. Attention is now turned to the relative performance of the nonuniform and the uniform arrays. This issue must be dealt with in a manner similar to that used for the performance ranking of enhanced and nonenhanced heat transfer surfaces. For such rankings to be meaningful, it is necessary to specify the constraints under which the comparison is being made (e.g., equal flow rate, equal pumping power, equal pressure drop). In this paper basic heat/mass transfer and pressure drop data have been provided for the array of nonuniform plate length, and those of uniform array can be adopted from Zhang and Lang (1989). Therefore, performance evaluation can be made for any constraints. For simplicity, only two constraints are used, i.e., identical pumping power and identical pressure drop. Since the experiments of Zhang and Lang (1989) were conducted at fixed transverse pitch (T_P = 30 mm), comparisons are made only for the configurations of cases No. 1, 2, and 3. Apart from the comparison between the two types of array, performance evaluations are also performed for different case numbers of the nonuniform array with the data of case No. 1 as a reference.

Identical Pumping Power. From the definition of f (Eq. (6)) and Reynolds number (Eq. (4)), it can be shown that the condition of identical pumping power is satisfied when:

$$(\mathrm{Re}_{L_1})_{\mathrm{uni}} = \frac{L_1}{L_2}\,(\mathrm{Re}_{L_2})_{\mathrm{non}} \sqrt[3]{\frac{L_1}{L_1+L_2}\,\frac{(fA_c)_{\mathrm{non}}}{(fA_c)_{\mathrm{uni}}}} \tag{9}$$

where the subscripts "uni" and "non" refer to the cases of uniform array and nonuniform array, respectively. With Re_{L2} as the abscissa, the ratio $(\mathrm{Sh})_{\mathrm{non}}/(\mathrm{Sh})_{\mathrm{uni}}$ is shown in Fig. 13. For all the situations studied, the heat/mass transfer performance of a nonuniform array is superior to that of a uniform array. In the Reynolds number range compared, the config-

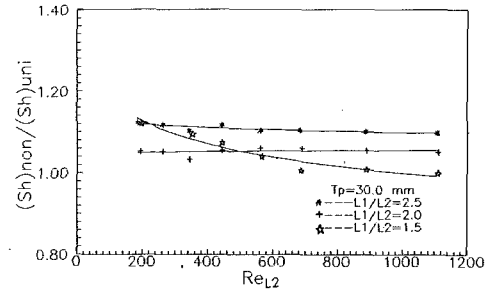

Fig. 13 Ratios of Sherwood numbers of the two arrays compared

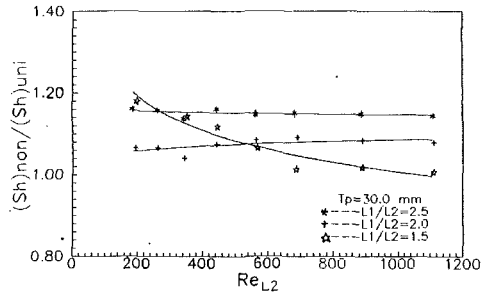

Fig. 15 Ratios of Sherwood number for the two arrays compared at identical pressure drop

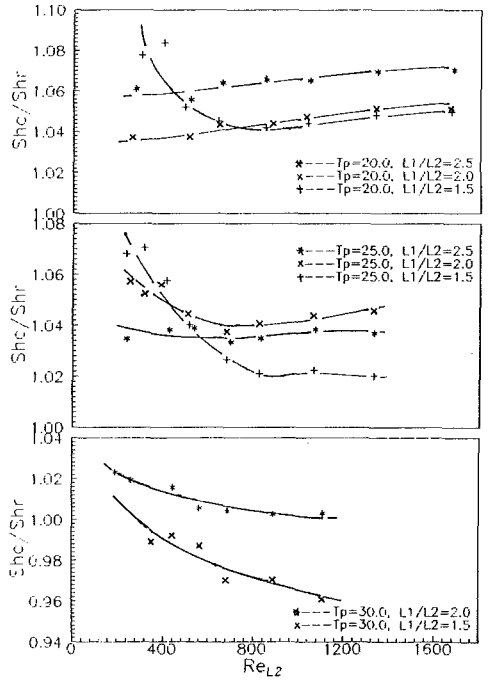

Fig. 14 Results of performance comparison of nonuniform plate length array at identical pumping power (case No. 1 as a reference)

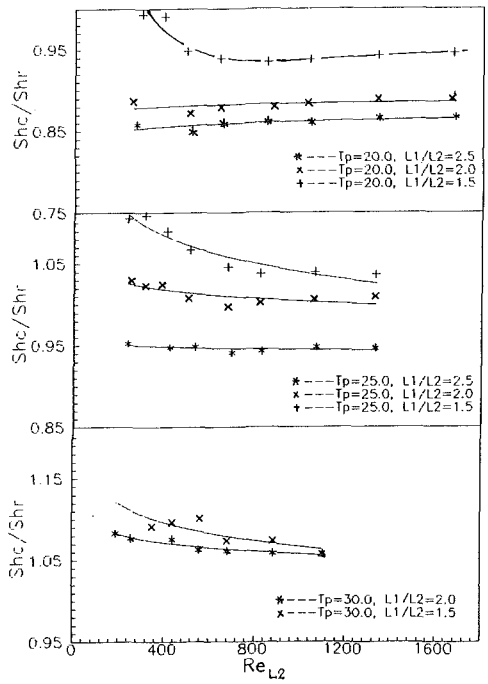

Fig. 16 Results of performance comparison of nonuniform plate length array at identical pressure drop (case No. 1 as a reference)

uration of case No. 1 seems to have the best behavior. It may provide about 10 to 12 percent heat transfer enhancement.

It should be noted that the array with L_1/L_2 has rather different behavior in the low Reynolds number region. By carefully examining the calculation process, we have found that this anomalous behavior resulted from the f-Re characteristics shown in Fig. 9. As seen there, for the case of $L_1/L_2 = 1.5$ (i.e., $L_1 = 22.5$ mm), in the Reynolds number range of 2.5×10^2–7.0×10^2, the value of the friction factor increases with Reynolds number appreciably. This anomalous behavior had been recognized during the course of the experiment, and the data had been checked by repeated tests. In the series of research projects of our group, the same behavior for the plate length of 22.5 mm had been found for other plate positioning. In order to clarify this problem, more research needs to be performed. The same discussion applies for the anomalous behavior of $L_1/L_2 = 1.5$ case in Fig. 14.

The results of performance comparison between different case numbers of the nonuniform array are shown in Fig. 14, where the ordinate represents the Sherwood ratio of the compared case to the reference case. It can be seen that under the condition of identical pumping power, the decrease in the transverse pitch and increase in the length ratio is, in general, in favor of heat transfer enhancement. In the whole range of Reynolds numbers compared, the performance of case No. 9 seems to be the best. It can enhance heat transfer about 6 percent.

Identical Pressure Drop. For the condition of identical pressure drop, the relation between the Reynolds numbers of the two types of array is:

$$(\mathrm{Re}_L)_{\mathrm{uni}} = \frac{L_1}{L_2} (\mathrm{Re}_{L_2})_{\mathrm{non}} \sqrt[2]{\frac{L_1}{L_1 + L_2} \frac{f_{\mathrm{non}}}{f_{\mathrm{uni}}}} \tag{10}$$

The Sherwood number ratios are shown in Fig. 15. Again, the heat transfer performances of the three cases of the nonuniform array are all superior to those of the uniform array, with the maximum heat transfer enhancement as large as 16 percent.

In Fig. 16, the comparison results for different case numbers are presented. Here the performance behavior of the eight cases is quite different from that shown in Fig. 14. At a fixed pressure drop, the decrease in transverse pitch and the increase in length ratio may deteriorate the heat transfer process. The performance of case No. 9 is the worst, for which the heat transfer rate may be 13–15 percent lower than that of the case No. 1. Case No. 3 seems to have the best performance, with an enhancement in heat transfer of about 5–10 percent.

Concluding Remarks

The work reported here is, apparently, the first systematic experimental study of the effects of successive plate length

ratio and transverse pitch on forced convective heat transfer and pressure drop of the plate array positioned obliquely to the flow direction. The naphthalene sublimation technique was successfully used to determine the two-dimensional plate array. Here, one unit consisted of two plates, one long and one short. The mass transfer experiments were carried out over the Reynolds number range from 1.98×10^2 to 1.66×10^3 for nine configurations.

Unit-average fully developed Sherwood numbers and friction factors were evaluated from test data. At a fixed Reynolds number, the increase in L_1/L_2 or the decrease in T_P/L_P brought about an increase in Sherwood number. The anticipated outcome was that the per-unit friction factor increased with the increase in L_1/L_2 or the decrease in T_P/L_P. A general correlation for Sherwood number was obtained via a least square curve-fitting method (Eq. (7)). This equation fitted the 72 experimental data with an average deviation of ± 2.7 percent.

A comprehensive performance evaluation was made to compare the heat/mass transfer and pressure drop characteristics of uniform array and nonuniform array. The plate length of the uniform array was equal to that of the long plate of the nonuniform array. The other geometric conditions were the same. It was found that for mass transfer there was a critical Reynolds number below which the mass transfer of the nonuniform array was higher than that of the uniform array. As far as the friction factor was concerned, at a fixed Reynolds number (based on the same characteristic length), the pressure drops of the nonuniform array were always less than those of the uniform array. For the two constraints adopted, the thermal performance of the nonuniform array studied was always superior to that of the uniform array, with the maximum increase in Sherwood number about 12 percent (for fixed pumping power) and 16 percent (for fixed pressure drop). In this comparison, configuration case No. 1 always has the best performance.

The comparisons between different case numbers of the nonuniform array showed that at fixed pumping power the decrease in transverse pitch and the increase in length ratio were in favor of heat transfer enhancement, while for fixed pressure drop, these two practices might deteriorate heat transfer process. For identical pumping power, case No. 9 behaved the best, while for identical pressure drop, case No. 3 had the best performance.

Acknowledgments

This work was supported by the Doctorate Foundation of Chinese Institutes and Universities.

References

Asako, Y., and Faghri, M., 1988, "Heat Transfer and Fluid Flow Analysis for an Array of Interrupted Plates, Positioned Obliquely to the Flow Direction," *Proceedings of the Eighth International Heat Transfer Conference*, San Francisco, CA, Vol. 2, pp. 421-427.

Hiramatsu, M., and Kajino, M., 1986, "Research and Improvement of Automotive Radiators," *Internal Combustion Engine* [in Japanese], No. 2, pp. 21-28.

Huang, H. Z., 1990, "Experimental and Numerical Studies on Heat Transfer and Pressure Drop for Arrays With Obliquely-Positioned Plates of Non-uniform Length," Thesis, Power Machinery Engineering Department, Xi'an Jiaotong University, Xi'an, People's Republic of China.

Kline, S. J., and McClintock, F. A., 1953, "Describing Uncertainties in Single-Sample Experiments," *Mechanical Engineering*, Vol. 75, Jan., pp. 3-8.

Lee, Y. N., 1986, "Heat Transfer and Pressure Drop Characteristics of an Array of Plates Aligned at Angles to the Flow in a Rectangular Duct," *Int. J. Heat Mass Transfer*, Vol. 29, pp. 1553-1563.

Lee, Y. N., 1989, "Heat Transfer and Pressure Drop Characteristics of an Assembly of Partially Segmented Plates," ASME JOURNAL OF HEAT TRANSFER, Vol. 111, pp. 44-50.

Pang, K., Tao, W. Q., and Zhang, H. H., 1990, "Numerical Analysis of Fully Developed Fluid Flow and Heat Transfer for Arrays of Interrupted Plates Positioned Convergently-Divergently Along the Flow Direction," *Numerical Heat Transfer*, Part A, Vol. 18, pp. 309-324.

Sogin, H. H., 1957, "Sublimation From Disks to Air Streams Flowing Normal to Their Surfaces," *Trans. ASME*, Vol. 89, pp. 61-69.

Sparrow, E. M., and Hajiloo, A., 1980, "Measurements of Heat Transfer and Pressure Drop for an Array of Staggered Plates Aligned Parallel to an Air Flow," ASME JOURNAL OF HEAT TRANSFER, Vol. 102, pp. 426-432.

Sparrow, E. M., Tao, W. Q., and Radidy, D., 1983, "Heat Transfer at an Array of Co-planar Slot-Like Surfaces Oriented Normal to a Forced Convection Flow," *Int. J. Heat Mass Transfer*, Vol. 26, pp. 30-40.

Xiao, Q., and Tao, W. Q., 1990, "Effect of Fin Spacing on Heat Transfer and Pressure Drop of Two-Row Corrugated Fin-and-Tube Heat Exchanger," *Int. Comm. Heat Mass Transfer*, Vol. 17, pp. 577-586.

Xiao, Q., Chen, B., and Tao, W. Q., 1992, "Experimental Study on Effect of Inter-wall Tube Cylinder on Heat/Mass Transfer Characteristics of Corrugated Plate Fin-and-Tube Exchanger Configuration," ASME JOURNAL OF HEAT TRANSFER, Vol. 114, pp. 755-759.

Yan, X. J., Zhang, H. H., and Tao, W. Q., 1988, "An Experimental Investigation of Heat Transfer and Pressure Drop Performance for Arrays of Staggered Plates Aligned With Air Flows," *Proceedings of Eighth International Heat Transfer Conference*, San Francisco, CA, Vol. 4, pp. 2887-2896.

Zhang, H. H., and Lang, X. S., 1989, "The Experimental Investigation of Oblique Angles and Interrupted Plate Lengths for Louvered Fins in Compact Heat Exchangers," *Experimental Thermal and Fluid Science*, Vol. 2, pp. 100-106.

B. A. Jubran

M. A. Hamdan

R. M. Abdualh

Department of Mechanical Engineering,
University of Jordan,
Amman, Jordan

Enhanced Heat Transfer, Missing Pin, and Optimization for Cylindrical Pin Fin Arrays

This paper reports an experimental investigation on the effects of interfin spacing, shroud clearance, and missing pin on the heat transfer from cylindrical pin fins arranged in staggered and in-line arrays. The interfin spacing in the spanwise direction was so small that the pins were almost touching each other. It was found that the optimum interfin spacing in both spanwise and streamwise directions is 2.5 D regardless of both type of array and shroud clearance used. The effect of missing pin for various interfin spacing arrays was found to be negligible for the in-line array but more significant for the staggered arrays.

1 Introduction

Augmentation of heat transfer from engineering components has attracted the attention of researchers for many years. The development of very powerful gas turbine engines for military aeroplanes required the development of a very efficient technique to cool the turbine blades. One way of doing this is through the application of forced convention to a pin fin array configuration inside the blade. Another area where heat transfer augmentation is required is the area of microminiaturization of electronic component for digital computers and the instrumentation of modern aircrafts.

An extensive review of numerous experimental investigations on heat transfer from plate fins is reported by Webb (1980). Brown et al. (1980) conducted heat transfer measurements for array configurations with pins of different length-to-diameter ratios. Bennon and Incropera (1981) carried out heat transfer measurements for a single horizontal cylinder, one row of cylinders, and two rows of cylinders in a crossflow of water. They developed a set of correlations for the combined convection regime. It was found that the type of convection regime dominating the heat transfer from the cylinder is very much dependent on the range of Reynolds number. Metzger et al. (1984) reported measurements of heat transfer associated with staggered arrays of short circular pin fins (length-to-diameter ratio of 1). The staggered array arrangements considered were those encountered in cooled gas turbine engine airfoils. The measurements were conducted over a Reynolds numbers range of 10^3 to 10^5. They found that, in general, the Nusselt number increases for the first three rows and then it declines for the remaining ones.

Sparrow et al. (1983a) investigated the effects of fluid flow and geometric parameters on the heat transfer coefficients of an array of coplanar slatlike surfaces, which face upstream into the oncoming flow. In another paper by Sparrow group, Sparrow et al. (1983b) reported heat transfer, pressure drop, and fluid flow characteristics of blocklike modules affixed to a parallel plate channel, which was cooled by forced convection airflow. They found that it was possible to increase heat transfer enhancement by as much as a factor of two. It was also found that the pressure drop for a multibarrier system is less than that obtained for a single-barrier system. Simoneau and Van Fossen (1984) used staggered and in-line arrays to investigate the effect of location of the array on heat transfer to a short cylinder in crossflow. The experimental heat transfer data were compared based on a single row and heated cylinder. It was found that for in-line arrangements the addition of a single row of cylinders upstream of the flow, which include the heated cylinder, resulted in an increase in the heat transfer by an average of 50 percent.

Metzger et al. (1984) investigated the effects of pin shape and array orientation on heat transfer and pressure loss in pin fin arrays with particular application to cooled turbine airfoil with pin fins. They found that, for a circular cross-sectional pin array, the array orientation with respect to the mean flow significantly affects both heat transfer and pressure drop. However, an increase by as much as 20 percent in the heat transfer resulted when the circular cross section is replaced by an oblong one. This increase in heat transfer was accompanied by an increase in pressure drop. Sparrow et al. (1984) investigated the effect of inlet, exit, and fin geometry on pin fins situated in a turning flow. They measured per-fin heat transfer coefficient and overall pressure drops. They concluded that partial shrouding of the inlet results in uniform per-fin heat transfer coefficients throughout the array. On the other hand the modification of exit geometry affects only the less tightly packed arrays.

Sparrow and Samie (1985) experimentally investigated heat transfer and pressure drop from one and two arrays of tubes in a Reynolds number range from 7500 to 32,000. They found that when one row of tubes was used, both Nusselt number and pressure drop were very sensitive to the pitch distance in the spanwise direction (pitch distance between tubes). Similar trends were obtained for a staggered two-row array of fin tubes. It was also found that the staggered array tends to give higher heat transfer than that given by an in-line one. However, the pressure drop across the in-line array was less than that across the staggered one. A numerical and experimental investigation was conducted by Kadle and Sparrow (1986) to study heat transfer and pressure drop from longitudinal fins. The average convective heat transfer coefficients obtained from both experimental and numerical results were found to agree well with the standard correlation available in literature.

Baughn et al. (1986) developed an experimental technique to provide a uniform wall heat flux that is used to study the local heat transfer coefficients for a single cylinder, cylinders in tandem, and cylinders located in the entrance of a tube bank. It was found that for both in-line and staggered tube arrangements the heat transfer coefficient distribution is very much dependent on the row location and found to be established by the third row. Goshayeshi et al. (1986) used horizontal tubes immersed in a hot fluidized bed to study the average heat transfer coefficients. They found that tubes in the bottom,

Contributed by the Heat Transfer Division for publication in the JOURNAL OF HEAT TRANSFER. Manuscript received by the Heat Transfer Division October 1991; revision received January 1993. Keywords: Finned Surfaces, Forced Convection, Heat Exchangers. Associate Technical Editor: W. A. Fiveland.

top, and interior rows tend to exhibit different heat transfer rates.

Heat transfer and friction factors from an array of shrouded vertical rectangular fins aligned parallel to an undisturbed air stream in a Reynolds number range from 4×10^4 to 2.0×10^5 were investigated by Naik et al. (1987). They concluded that, in the streamwise direction, high values of pressure drop and heat transfer rates were associated with compact arrays at zero gap clearance above the fins. It was also found that increasing the gap clearance above the fins resulted in a decrease in the heat transfer rates. Heat transfer from smooth and rough staggered tubes in crossflow at high Reynolds number was investigated by Achenbach (1989). He used the local heat transfer data to locate the point of boundary layer separation and transition.

Tahat (1988) conducted an experimental investigation on the optimization of pin-fin arrays subjected to forced convective heat transfer. Heat transfer rates as well as pressure drops were measured for in-line and staggered arrays with zero gap clearance ratio. It was found that the optimal spacing for the in-line arrangements is 2.5 cm.

To the best of the authors' knowledge, it appears that the only experimental work on the optimization of pin fin arrays subjected to forced convection is that of Tahat (1988). The present investigation differs from the abovementioned investigation in that heat transfer rates are measured for very close spacings, which have not been investigated before. This means that a more general correlation may be obtained. The present work also aims to optimize the pin fin array configuration at various gap clearance ratios.

2 Experimental Rig and Experimentation

The experimental setup used in this investigation is basically a modified version of that used by Naik et al. (1987) and Tahat (1988). The setup consists mainly of a suction-type wind tunnel. The main body of the test section is a channel-like box 2 m in length and 0.24 m in width and it is constructed using wood board of 16 mm thick. The top cover (shroud) is adjustable to give different shroud clearance spaces over the fin tips. The front side wall of the test section accommodates at its middle section a double glazing window to ease observation of the fin pin array during tests. The middle bottom base of the test section has a rectangular slot (300 mm × 175 mm) to accommodate the light metal alloy base of the pin fin array. A container box is attached to the slot to enclose the duralumin base. This box was filled with insulating material to minimize heat dissipation to the atmosphere, Fig. 1.

A flow straightener is placed at the air intake side of the wind tunnel. At the trailing edge of the test cross section, two honeycombs, at a certain distance apart, were placed perpendicular to the flow to act as turbulizers so that good mixing of the air leaving the pin fin array is ensured. The whole test section was insulated to minimize heat losses.

The pin fin array is composed of a 300 mm × 175 mm horizontal rectangular base with a thickness of 30 mm. Cylindrical pin fins of 60 mm in height, 6.35 mm in diameter are mounted on and protruding vertically upward from the rectangular base. Both the base and the fins are made of light metal alloy (duralumin) which has high thermal conductivity. The number of pin fins can be adjusted to suit the required spacing between the pins in the streamwise (x axis) or spanwise (z axis) direction. The interfin spacing in the spanwise direction (distance between the center of the two adjacent pins) was varied from 7.95 mm to 71.55 mm, and in the streamwise direction from 15.5 mm to 124 mm. For minimum spacing in both z and x directions the number of pin fins was 340, while for maximum spacing in both directions the number of pins was 9. A horizontal heater plate made of six strip heating elements was firmly attached to the bottom of the rectangular base by a set of screws. Each element heater is rated 400 W at 240 V. Radio spares heat sink compound (55-401-1) was used to ensure good thermal contact between the plate heater and base. This was also used between the roots of the pin fins and the base. A guard heater of 500 W at 240 V was placed between the main plate heater and the outside insulation, to reduce the heat losses to the outside surroundings. The electrical power input to the main plate heater was controlled by an auto-transformer (variac), and was measured by an in-line wattmeter. The pin fin array was kept at constant uniform temperature of 50 ± 0.5°C. Figure 2 shows a typical description of shrouded pin fin array geometry and air stream flow.

The steady-state temperature of the rectangular base of the fin array was measured by ten copper-constantan thermocou-

Nomenclature

A_B = fin array total heat transfer area, m^2
A_{ff} = free-flow area = $(C+H)(W-N_{fx}DH)$, m^2
B = uniform side clearance from side rows of pin fins in streamwise direction to the vertical wall of the wind tunnel, m
C = clearance gap between the fin tip and the horizontal shroud, m
C_{pair} = specific heat air at atmospheric pressure, $Jkg^{-1}K^{-1}$
D = pin fin diameter, m
f = friction factor
G_{max} = maximum mass flow rate per unit area, kg/m^2 s
g = acceleration of gravity, ms^{-1}
h = heat transfer coefficient, $Wm^{-2}K^{-1}$
h_{avg} = average coefficient of heat transfer from the finned assembly to the surroundings, $Wm^{-2}K^{-1}$
H = fin height, m
L = length of the fin assembly, m
$\dot{m}$ = forced flow rate of air, kg/s
N_f = number of fins in the assembly
N_{fz} = number of pins per row in the spanwise direction
N_{fx} = number of pins per row in the streamwise direction
P = static pressure, Nm^{-2}
$\dot{Q}_{conv}$ = total steady-state rate of convective heat loss through air, W
$\dot{Q}_{input}$ = total steady rate of heat input to the fin array assembly, W
$\dot{Q}_{loss}$ = total steady-state rate of heat losses from the fin array assembly, W
$\dot{Q}_{rad}$ = total steady-state rate of radiative heat loss from the fin assembly, W
Re = Reynolds number of air flow based on pin fin diameter = $G_{max}D/\nu$
S_x = pin uniform spacing in the streamwise direction, m
S_z = pin uniform spacing in the spanwise direction, m
T_a = ambient air temperature, K
T_b = steady-state temperature of the base of pin fin array, K
T_{in} = inlet temperature of forced air stream to the pin fin array, K
T_{out} = outlet temperature from pin fin array, K
t = thickness of base of pin fin array, m
W = width of wind tunnel duct, m
w = width of base pin fin array, m
x = streamwise direction of flow
y = vertical direction
z = spanwise direction

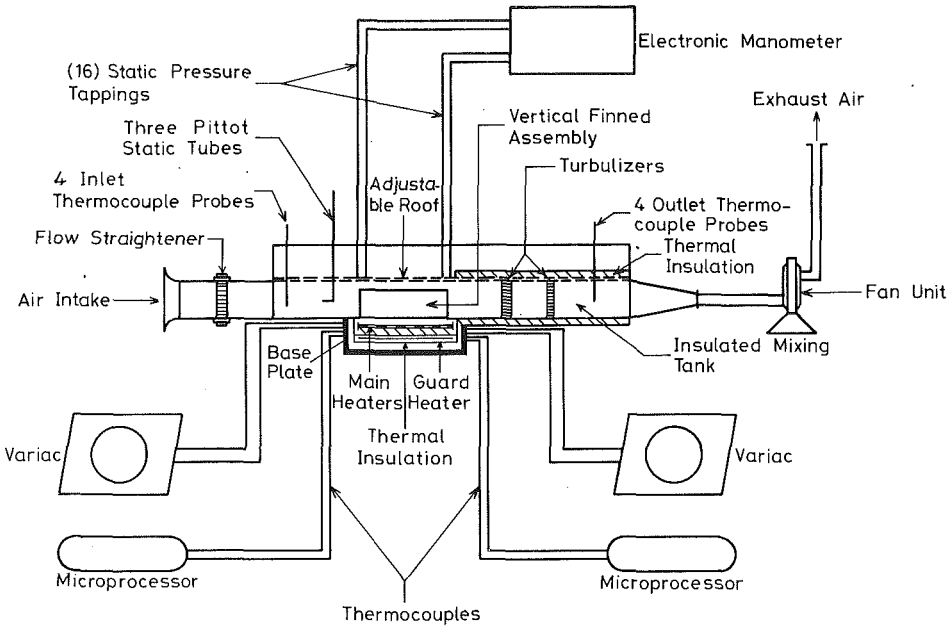

Fig. 1 Schematic diagram of the test rig

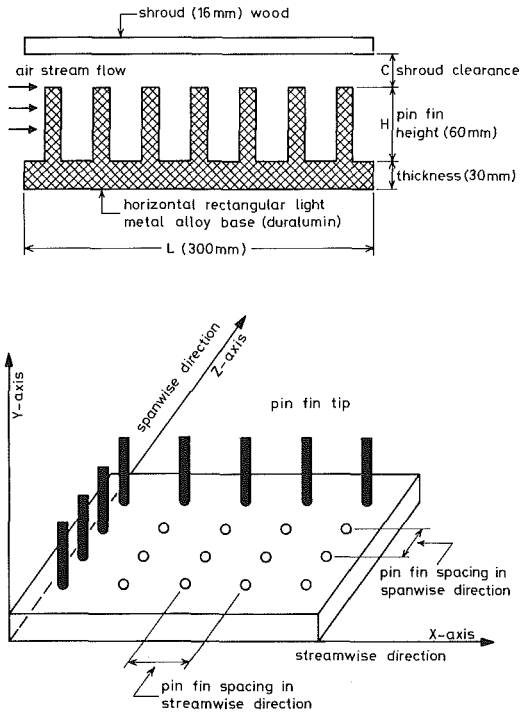

Fig. 2 Description of shrouded pin fin array geometry and air stream flow

ples distributed uniformly over the base and embedded at 10 mm deep from the bottom side. The reading of these thermocouples were recorded using a microprocessor and the average of these readings was taken as the steady-state temperature of the base plate. The inlet temperature of the air stream was taken as the average reading of four copper-constantan thermocouples located uniformly after the flow straightener. Similarly the outlet temperature of the air stream was taken as the average reading of four copper-constantan thermocouples located uniformly in the insulated mixing box. The pressure drop across the pin fin array was measured using a total of 16 static pressure tappings mounted on the roof of the test section just over the pin fin array. These were connected to an electronic manometer.

3 Data Reduction

The theoretical analysis adopted in the present work for the reduction of the data is that used by Naik et al. (1987) and Tahat (1988) for the analysis of basically similar experimental work.

The steady-state energy balance equation for the array may be written as

$$\dot{Q}_{\text{input}} = \dot{Q}_{\text{conv}} + \dot{Q}_{\text{rad}} + \dot{Q}_{\text{loss}} \tag{1}$$

where

$$\dot{Q}_{\text{conv}} = \dot{m} C_{\text{pair}} (T_{\text{out}} - T_{\text{in}}) \tag{2}$$

One could also determine the rate of heat transfer using the following formula:

$$\dot{Q} = h_{\text{avg}} A_B \left(T_b - \frac{T_{\text{in}} + T_{\text{out}}}{2} \right) \tag{3}$$

where A_B is the total heat transfer area given by

$$A_B = wL + (\pi D H N_{fz} N_{fx})$$

Using Eqs. (2) and (3), one could obtain the following expression for h_{avg}:

$$h_{\text{avg}} = \frac{\dot{m} C_{\text{pair}} (T_{\text{out}} - T_{\text{in}})}{A_B \left[T_B - \dfrac{T_{\text{in}} - T_{\text{out}}}{2} \right]} \tag{4}$$

Naik et al. (1987) conducted similar experimental tests using plate fin arrays, and reported that the total radiative heat transfer losses from a duralumin plate fin assembly with almost similar setup was about 0.5 percent of the total heat input. Tahat (1988) conducted similar experimental tests using similar pin fin arrays, and reported that the total heat transfer losses from the pin fin array, with the radiative heat transfer losses being included, were only 2.5 percent of the total heat input. Using these findings together with the fact that the test section was well insulated, one could assume with some confidence that the last two terms of Eq. (1) may be ignored. Then this equation reduces to:

Table 1 Experimental conditions

Parameter	Minimum value	Maximum value
Pin fin spacing in spanwise direction	7.95 mm	71.55 mm
Pin fin spacing in streamwise direction	15.5 mm	124 mm
Air mass flow rate	0.038 kg/s	0.17 kg/s
Air stream velocity at $C/H=0.0$	2.2 m/s	10 m/s
Air stream velocity at $C/H=0.5$	1.5 m/s	6.7 m/s
Air stream velocity at $C/H=1.0$	1.1 m/s	5 m/s

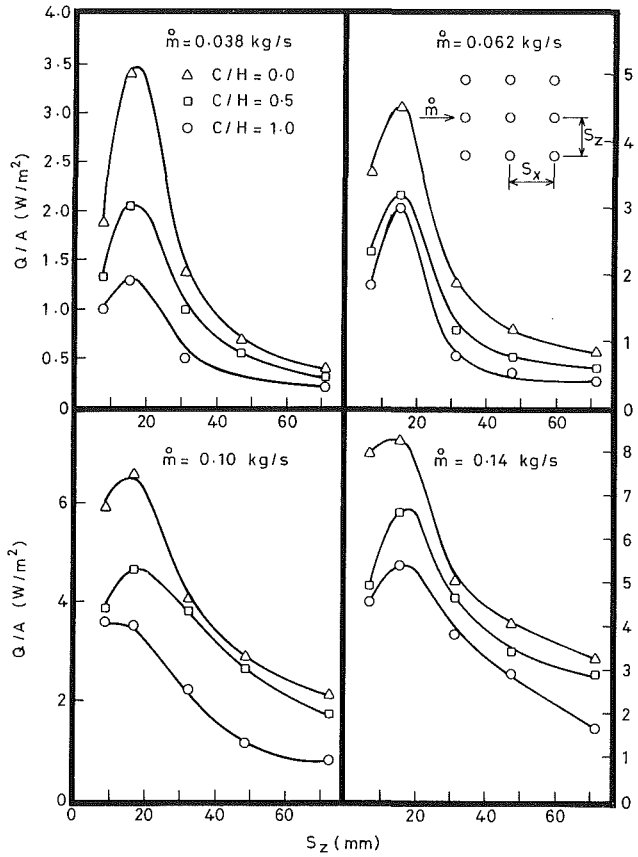

Fig. 3 Variation of steady-state rate of heat transfer from in-line shrouded pin fin array when $S_x = 15.9$ mm

$$\dot{Q}_{\text{input}} = \dot{Q}_{\text{conv}} \tag{5}$$

Reynolds number (Re) and Nusselt number (Nu) may be written as:

$$\text{Re} = \frac{G_{\max} D}{\mu_{\text{air}}} \tag{6}$$

$$\text{Nu} = \frac{h_{\text{avg}} D}{k_{\text{air}}} \tag{7}$$

where

$$G_{\max} = \frac{\dot{m}}{A_{ff}}$$

4 Results and Discussion

Throughout the measurements made to establish the data presented in this paper, care was taken to note possible sources of error, and an error analysis based on the method of Kline and McClintock (1953) was carried out. The error analysis

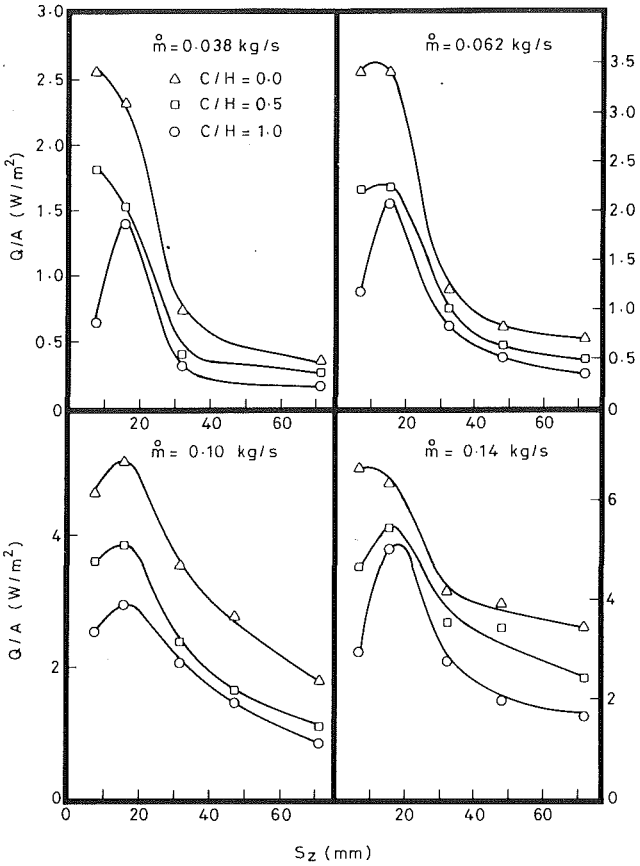

Fig. 4 Variation of steady-state rate of heat transfer from in-line shrouded pin fin array when $S_x = 31$ mm

indicated a ±5 percent uncertainty in the heat transfer rate and a ±3 percent in the velocity. Tests were repeated a few times to ensure the repeatability of the results.

Heat transfer measurements were carried out for three values of C/H, namely 0.0, 0.5, and 1.0. For each one of these values, measurements were carried out for five values of air mass flow rate, namely 0.038, 0.062, 0.1, 0.14, and 0.17 kg/s. The Reynolds number range used in this experiment was from 5×10^3 to 5.4×10^4. Table 1 shows minimum and maximum values of various experimental conditions used in the present investigation.

Under these specified values of C/H and air mass flow rates, and for the in-line arrangement, the heat transfer per unit area variation with the interfin spacing in the spanwise direction is shown in Figs. 3 and 4, with $S_x = 15.9$ and 31 mm, respectively. It can be seen from these figures that in general, the optimum interfin fin spacing in the spanwise direction, which corresponds to maximum heat transfer, occurs at $S_z = 15.9$ mm ($S_z/D = 2.5$), except for $\dot{m} = 0.038$ kg/s and $C/H \leq 0.5$ where the optimum thickness is found to occur at the minimum spacing possible, that is at $S_z/D = 1.25$, where the pins were almost touching each other. It should be noted that for such low mass flow rates and $C/H \leq 0.5$, it was not possible to obtain the part of the curves where the heat transfer drops with the decrease in S_z, because at the point of maximum heat transfer the pins were touching each other, and it was not possible to put them much closer because this would have resulted in the flow being almost fully obstructed by the pins. Similar curves were obtained for fixed values of S_z, as shown in Figs. 5 and 6, with $S_z = 15.9$ and 31 mm, respectively. As shown in the figures, the point of optimum spacing is not in general well defined as before. This is due to the fact that as the spacing between pins is reduced beyond the maximum heat transfer

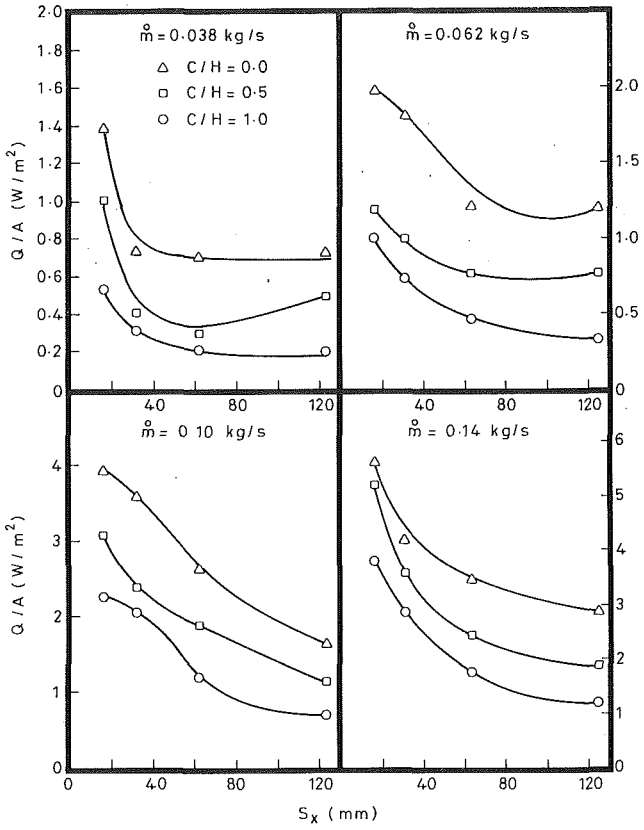

Fig. 5 Variation of steady-state rate of heat transfer from in-line shrouded pin fin array when $S_z = 15.9$ mm

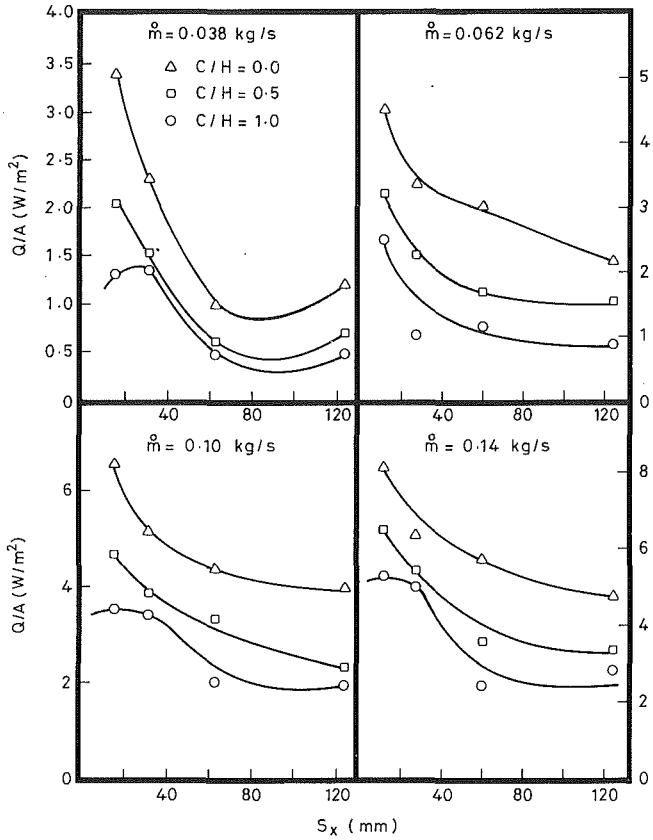

Fig. 6 Variation of steady-state rate of heat transfer from in-line shrouded pin fin array when $S_z = 31$ mm

point shown in these figures, the pressure drop across the pin array was so large that the flow was obstructed by the pins and it was not possible to reduce the distance between the pins further; hence, such a point was taken as the optimum spacing for the array in question. Using this approach, one could see from Figs. 5 and 6 that at the maximum heat transfer the optimum spacing in the streamwise direction is given by $S_x = 15.9$ mm ($S_x/D = 2.5$) for all shroud clearances and flow rates. Other combinations of interfin spacing were used for in-line arrangements, from which it was found that the optimum spacing in both the spanwise and streamwise directions is 2.5 D. It was also found that as the shroud clearance ratio was reduced from unity to zero, and when the optimum spacing was used, a 40 percent increase in the rate of heat transfer dissipation was experienced.

For the staggered arrangement and for the same values of C/H and mass flow rate, using the same experimental procedure used for the in-line arrangement, the optimum interfin spacing may be obtained from Fig. 7, which indicates again that the optimum spacing corresponds to $S_x/D = 2.5$.

The performance of the in-line arrangements compared with that of the staggered one under the same experimental conditions is shown in Fig. 8. This figure indicates clearly that the heat transfer when the staggered arrangements are used is higher, by as much as 16 percent.

The effect of shroud-to-height ratio (C/H) on the average heat transfer coefficient (h_{avg}) is shown in Fig. 9, from which it may be noted that h_{avg} increases with decreasing C/H. A similar observation was reported by Naik et al. (1987) for flat plate fins at various values of C/H. One may explain the effect of C/H on heat transfer rates by the same argument of Naik et al. (1987) that as the clearance above the fins is increased, the flow resistance of the alternative path diminishes relative to that of the entire pin fin spacing, so that the highest velocities occur in the clearance gap. Under these conditions a significant

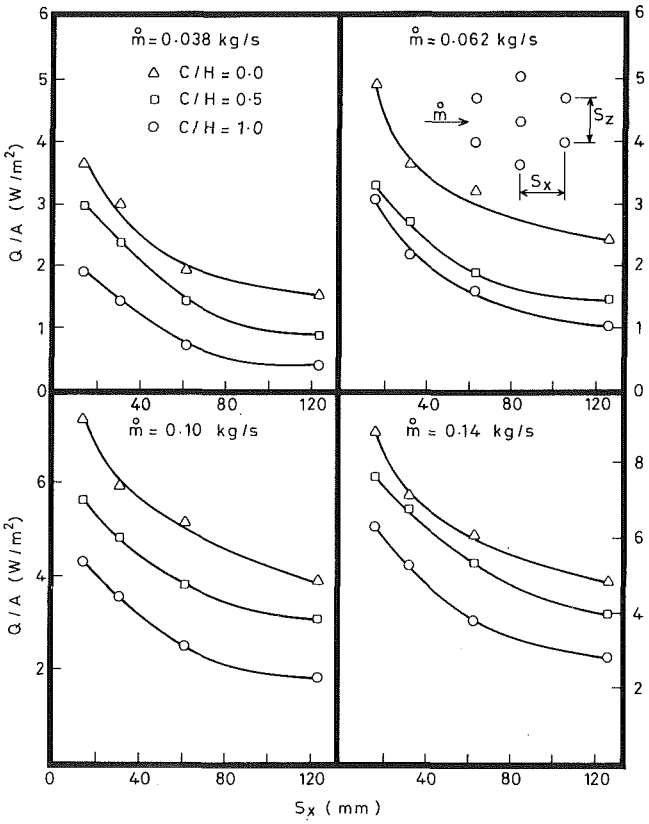

Fig. 7 Variation of steady-state rate of heat transfer from staggered shrouded pin fin array when $S_z = 15.9$ mm

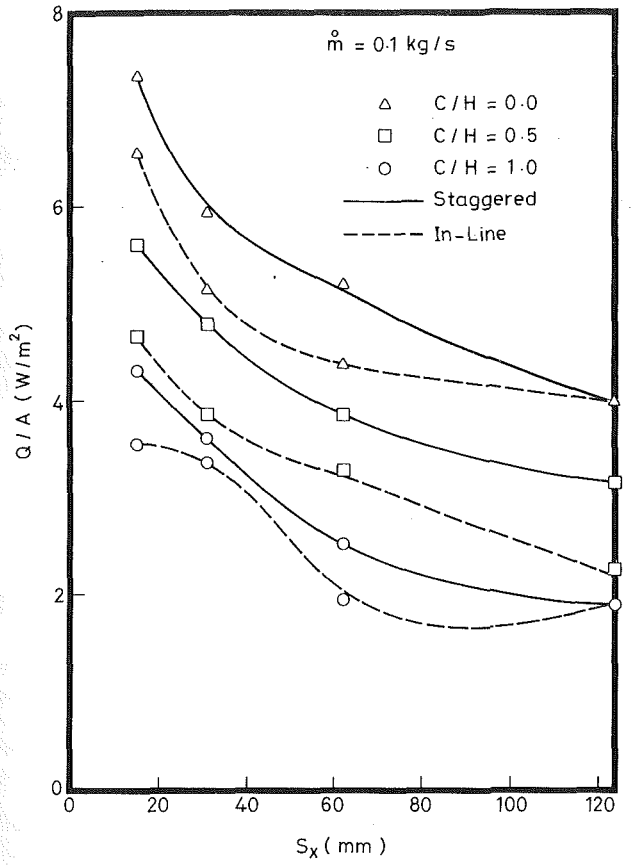

Fig. 8 Comparison of the variations of heat transfer rates between in-line and staggered shrouded pin fin arrays when $S_z = 15.9$ mm

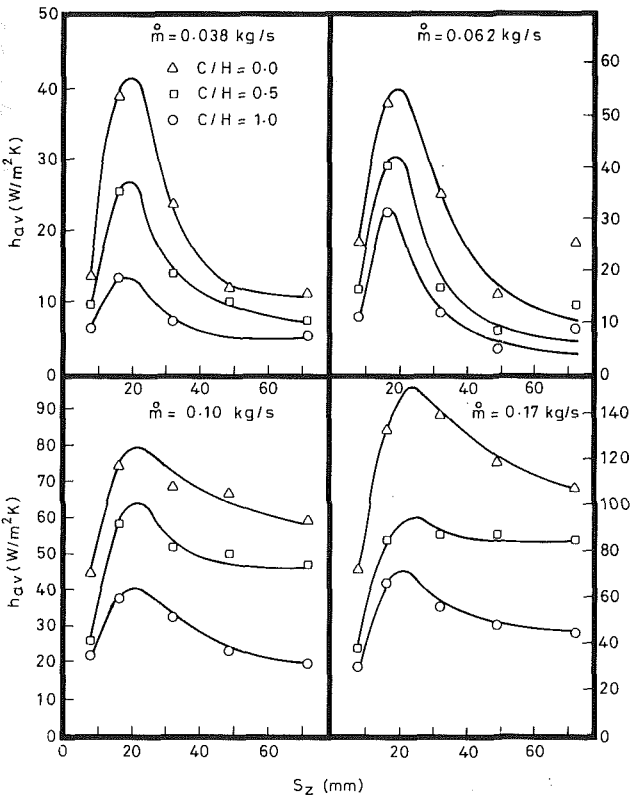

Fig. 9 Variations of average heat transfer coefficient for various spanwise spacing of in-line shrouded pin-fin arrays when $S_x = 15.5$ mm

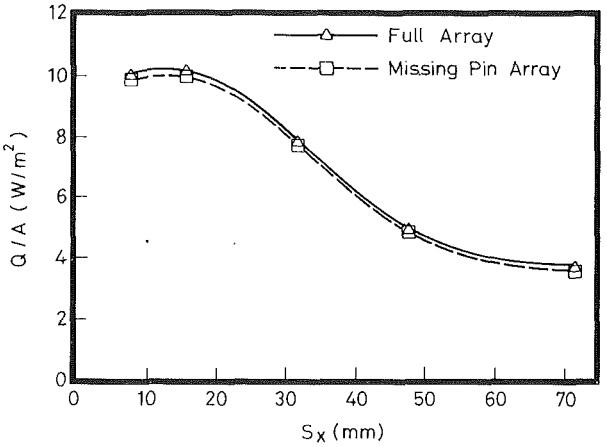

Fig. 10 Effect of missing pin on the heat transfer of pin fin shrouded in-line arrays when $S_z = 15.9$ mm

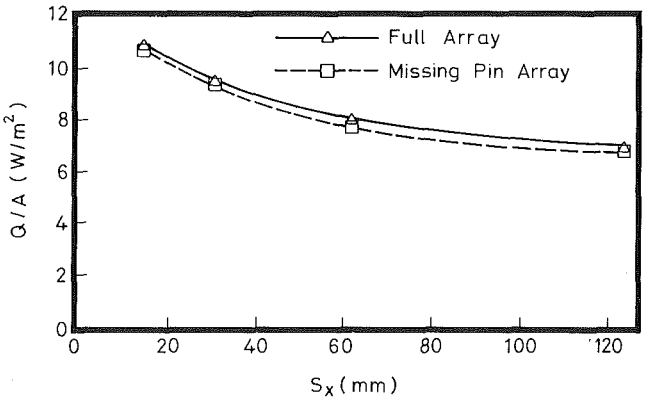

Fig. 11 Effect of missing pin on the heat transfer of pin fin shrouded staggered arrays when $S_z = 15.9$ mm

portion of the pin fin array may be washed by the low-velocity fluid, with the part near the tip being washed by relatively higher velocities, and this explains why the highest heat loss occurs at the fin tip (Sparrow et al., 1987).

Sparrow and Molki (1982) investigated the effect of mixing pins, from both staggered and in-line arrays, on the heat transfer rate from cylinders around the missing pin. It was found that the staggered array is more sensitive to the missing pin than the in-line array. In the present investigation the effects of missing pins from the center of the fin array on heat transfer of various interfin spacing arrays for in-line and staggered arrays were investigated and shown respectively in Figs. 10 and 11. The effect is negligible for both configurations of arrays, but one may still observe that the staggered arrangements of the various interfin spacing arrays are more responsive than the in-line arrays, which agrees with the findings of Sparrow and Molki (1982).

Nusselt number and Reynolds numbers were evaluated for the thermally developed region and were correlated using the following form:

$$\mathrm{Nu} = a(\mathrm{Re})^b \cdot (S_z/w)^c \cdot (S_x/L)^d \tag{8}$$

where a, b, c, and d are arbitrary constants. One other possible way of correlating the data is to use the fin height, H, as the reference length for both S_x and S_z instead of L and w. For a zero value of C/H, a least-squares fit to the data yields the following correlations for in-line and staggered arrangements, respectively (Fig. 12):

$$\mathrm{Nu} = 0.45(\mathrm{Re})^{0.71}\left(\frac{S_z}{w}\right)^{0.40}\left(\frac{S_x}{L}\right)^{0.51} \tag{9}$$

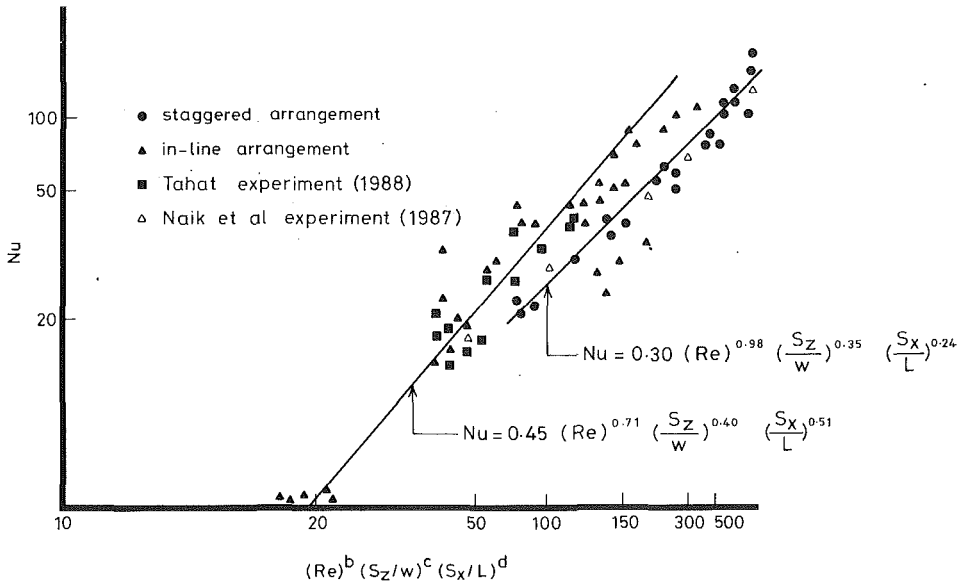

Fig. 12 A generalized heat transfer correlation for cylindrical pin fin arrays at $C/H = 0$

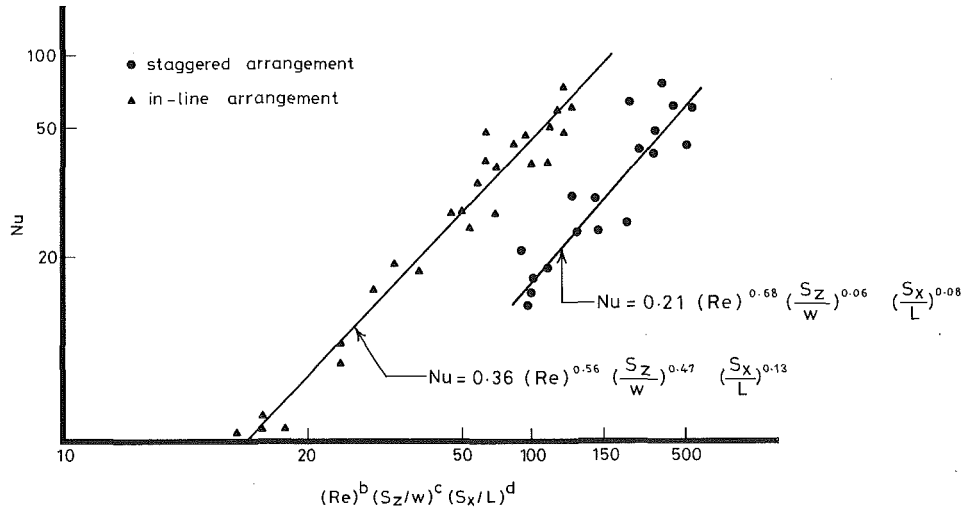

Fig. 13 A generalized heat transfer correlation for cylindrical pin fin arrays at $C/H = 0.5$

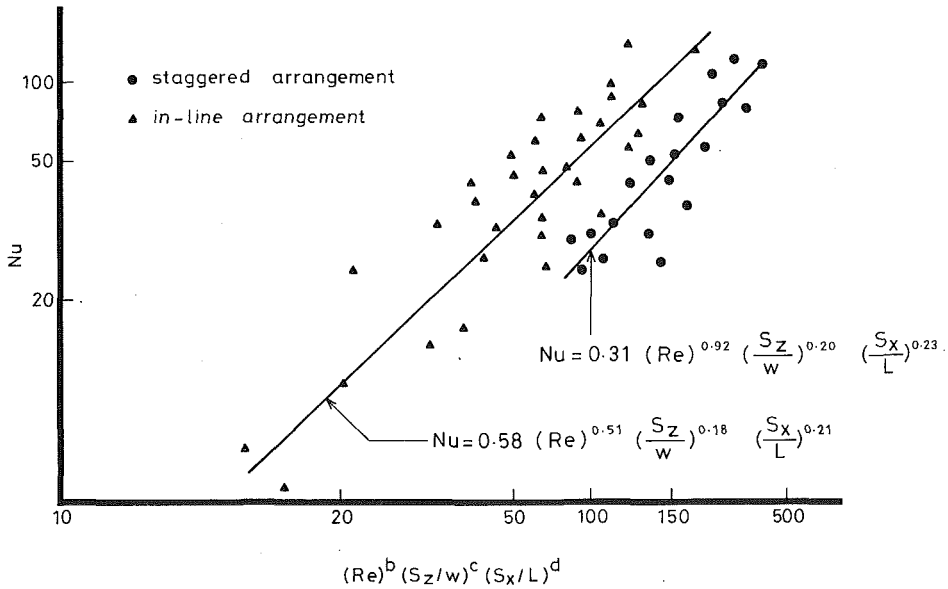

Fig. 14 A generalized heat transfer correlation for cylindrical pin fin arrays at $C/H = 1.0$

$$\mathrm{Nu} = 0.30(\mathrm{Re})^{0.98}\left(\frac{S_z}{w}\right)^{0.35}\left(\frac{S_x}{L}\right)^{0.24} \quad (10)$$

Similarly, the following two correlations were obtained for a C/H value equal to 0.5, for in-line and staggered arrangements (Fig. 13):

$$\mathrm{Nu} = 0.36(\mathrm{Re})^{0.56}\left(\frac{S_z}{w}\right)^{0.47}\left(\frac{S_x}{L}\right)^{0.13} \quad (11)$$

$$\mathrm{Nu} = 0.21(\mathrm{Re})^{0.68}\left(\frac{S_z}{w}\right)^{0.06}\left(\frac{S_x}{L}\right)^{0.08} \quad (12)$$

Finally, for $C/H = 1.0$, the following two correlations were obtained for in-line and staggered arrangements, respectively (Fig. 14):

$$\mathrm{Nu} = 0.58(\mathrm{Re})^{0.51}\left(\frac{S_z}{w}\right)^{0.18}\left(\frac{S_x}{L}\right)^{0.21} \quad (13)$$

$$\mathrm{Nu} = 0.31(\mathrm{Re})^{0.92}\left(\frac{S_z}{w}\right)^{0.20}\left(\frac{S_x}{L}\right)^{0.23} \quad (14)$$

5 Conclusions

An experimental investigation was conducted to explore the effect of interfin spacing of the array, and missing pin for various configurations of arrays on the heat transfer rates as well as obtaining the optimum array configuration. The outcomes of the experimental results suggest the following conclusions:

1 Staggered arrangement of the array tends to give higher heat transfer rate than that of the in-line ones regardless of the value of the shroud clearance-to-height ratio. This agrees with the findings of Naik et al. (1987) for flat plate fin arrays.

2 The optimal values of the interfin spacing in streamwise and spanwise directions are $S_x/D = 2.5$ and $S_z/D = 2.5$, respectively, which means that square or equilateral triangular arrangements of pin fin arrays are the most efficient ones.

3 The effect of missing pin on in-line and staggered arrays with various interfin spacing is negligible but staggered arrays are more sensitive to the missing pin with a 7 percent reduction in the heat transfer, which agrees with the findings of Sparrow and Molki (1982).

References

Achenbach, E., 1989, "Heat Transfer From a Staggered Tube Bundle in Cross-flow at High Reynolds Numbers," *Int. J. Heat Mass Transfer*, Vol. 32, pp. 271–280.

Baughn, J. W., Elderkin, M. J., and Mckillop, A. A., 1986, "Heat Transfer From a Single Cylinder in Tandem and Cylinders in the Entrance Region of a Tube Bank With a Uniform Heat Flux," ASME JOURNAL OF HEAT TRANSFER, Vol. 108, pp. 386–391.

Bennon, W. D., and Incropera, F. P., 1981, "Mixed Convection Heat Transfer From Horizontal Cylinders in Cross-flow of a Finite Water Layer," ASME JOURNAL OF HEAT TRANSFER, Vol. 103, pp. 540–545.

Brown, A., Mandjikas, B., and Mudyiwa, J. M., 1980, "Blade Trailing Edge Heat Transfer," ASME Paper No. 80-GT-45.

Carajilescov, P., and Todreas, N. E., 1976, "Experimental and Analytical Study of Axial Turbulent Flows in an Interior Subchannel of a Bare Rod Bundle," ASME JOURNAL OF HEAT TRANSFER, Vol. 98, pp. 262–268.

Goshayeshi, A., Welty, J. R., Adams, R. L., and Alavizadeh, N., 1986, "Local Heat Transfer Coefficients for Horizontal Tube Arrays in High Temperature Large Particle Fluidized Beds: an Experimental Study," ASME JOURNAL OF HEAT TRANSFER, Vol. 108, pp. 907–912.

Kadle, D. S., and Sparrow, E. M., 1986, "Numerical and Experimental Study of Turbulent Heat Transfer and Fluid Flow in Longitudinal Fin Arrays," ASME JOURNAL OF HEAT TRANSFER, Vol. 108, pp. 16–23.

Kline, S. J., and McClintock, F. A., 1953, "Describing Uncertainties in Single Sample Experiments," *Mechanical Engineering*, Jan., pp. 3–8.

Metzger, D. E., Fan, C. S., and Haley, S. W., 1984, "Effects of Pin Shape and Array Orientation on Heat Transfer and Pressure Loss in Pin Fin Arrays," ASME *Journal of Engineering for Gas Turbines and Power*, Vol. 106, pp. 252–257.

Metzger, D. E., Berry, R. A., and Bronson, J. P., 1989, "Developing Heat Transfer in Rectangular Ducts With Staggered Arrays of Short Pin Fins," ASME JOURNAL OF HEAT TRANSFER, Vol. 104, pp. 700–706.

Naik, S., Probert, S. D., and Shilston, M. J., 1987, "Forced Convective Steady State Heat Transfer From Shrouded Vertical Fin Arrays, Aligned Parallel to an Undisturbed Air Stream," *Applied Energy*, Vol. 26, pp. 137–158.

Simoneau, R. J., and Van-Fossen, G. J., Jr., 1984, "Effect of Location in an Array on Heat Transfer to a Short Cylinder in Cross-flow," ASME JOURNAL OF HEAT TRANSFER, Vol. 106, pp. 42–48.

Sparrow, E. M., and Molki, M., 1982, "Effect of a Missing Cylinder on Heat Transfer and Fluid Flow in an Array of Cylinders in Cross Flow," *Int. J. Heat and Mass Transfer*, Vol. 25, No. 4, pp. 449–456.

Sparrow, E. M., Tao, W. Q., and Radtke, D. D., 1983a, "Heat Transfer at an Array of Co-planar Slat-like Surfaces Oriented Normal to a Forced Convection Flow," *Int. J. Heat Mass Transfer*, Vol. 26, pp. 33–40.

Sparrow, E. M., Vemuri, S. B., and Kadle, D. S., 1983b, "Enhanced and Local Heat Transfer, Pressure Drop, and Flow Visualization for Arrays of Block-like Electronic Components," *Int. J. Heat Mass Transfer*, Vol. 26, pp. 686–699.

Sparrow, E. M., Suopys, A. P., and Ansari, M. A., 1984, "Effect of Inlet, Exit, and Fin Geometry on Pin Fins Situated in a Turning Flow," *Int. J. Heat Mass Transfer*, Vol. 27, pp. 1039–1054.

Sparrow, E. M., and Samie, F., 1985, "Heat Transfer and Pressure Drop Results for One and Two Row Arrays of Finned Tubes," *Int. J. Heat Mass Transfer*, Vol. 28, No. 12, pp. 2247–2259.

Tabat, M. A., 1988, "Thermal Optimization of Pin Fin Arrays Experiencing Forced Convective Heat Transfer," MSc. Thesis, Cranfield Institute of Technology.

Webb, R. L., 1980, "Air Side Heat Transfer in Finned Tube Heat Exchanger," *Heat Transfer Engineering*, Vol. 1, pp. 33–49.

B. Bansal

H. Müller-Steinhagen

Department of Chemical and Materials Engineering, University of Auckland, Auckland, New Zealand

Crystallization Fouling in Plate Heat Exchangers

Crystallization fouling of calcium sulfate was investigated in a plate and frame heat exchanger. The effects of flow velocity, wall temperature, and $CaSO_4$ concentration on the fouling rates have been investigated and the distribution of scale along the heat transfer surface has been observed. The measured fouling curves are compared with predictions from a surface reaction controlled model.

Introduction

The application of plate and frame heat exchangers in the chemical process industry is increasing rapidly, replacing tubular heat exchangers in several traditional applications. Plate and frame heat exchangers are attractive because of higher heat transfer efficiency, less space requirements, easy accessibility to all areas and, if expensive materials are required, lower costs (Marriott, 1971; Walker, 1982). However, as soon as severe fouling is anticipated, several of these advantages may not be valid any longer. While there is plenty of information about the governing equations for clean operation (Buonopane et al., 1963; Cooper and Usher, 1983; Jackson and Troupe, 1964; Marriott, 1971; Raju and Bansal, 1980, 1986; Usher, 1970), information for fouling conditions is scarce. If the TEMA fouling resistances are applied for plate and frame heat exchangers, the required excess heat transfer surface becomes excessive, because of the high clean heat transfer coefficients of these heat exchangers.

For a constant heat duty, Eq. (1) can be derived:

$$\frac{A_f}{A_c} = 1 + U_c R_f \tag{1}$$

Therefore, it is often recommended that the additional surface should not exceed 25 percent of the heat transfer surface requirement for clean operation (Cooper and Usher, 1983).

Continuous change in direction and cross-sectional area results in a complex flow distribution within the plate and frame heat exchanger. The local velocities range from zero up to twice the nominal velocity, or even more depending on the inclination angle of the corrugations. Since the flow conditions affect the wall temperatures and the shear stresses, fouling varies across the heat exchanger plate.

Prior to the early 1960s, the most common application of plate heat exchangers was in the dairy industry. Therefore, research has concentrated mainly on milk fouling (Lalande et al., 1984; Singh and Aneja, 1981a). Cooling water fouling was investigated by Cooper et al. (1980) with deposition being caused by a combination of biological, particulate, and crystallization fouling. To obtain more detailed information, particulate fouling in plate heat exchangers was investigated by Müller-Steinhagen and Middis (1989) and biological fouling by Novak (1982). While crystallization fouling is probably the most serious single fouling mechanism in plate heat exchangers, it has never been studied in detail.

Fouling in heat exchangers is generally modeled using the Kern and Seaton (1959) approach

$$\frac{dR_f}{dt}(\rho\lambda)_d = \frac{dm}{dt} = \dot{m}_d - \dot{m}_r \tag{2}$$

where the deposition rate for diffusion controlled fouling is

$$\dot{m}_d = \beta(c_b - c_w^*) \tag{3}$$

and for reaction-controlled fouling

$$\dot{m}_d = k_r(c_b - c_w^*)^n \tag{4}$$

For $CaSO_4$ deposition, n was found to be equal to 2 (Amjad, 1988). The temperature dependence of the reaction rate constant follows an Arrhenius term

$$k_r = C_1 e^{-E/RT} \tag{5}$$

The removal rate $\dot{m}_r$ in Eq. (2) depends on deposit strength and fluid shear forces.

Hasson et al. (1970) investigated crystallization fouling of gypsum in a double pipe heat exchanger. Since the deposition was pure gypsum, it was assumed that the deposit was strong and adherent and that there was no removal of deposit due to the fluid shear forces. However, this condition is not valid in plate heat exchangers, where the channel between two plates is only a few mm wide. Deposition will reduce the cross-sectional area considerably, causing a significant increase of the local flow velocities and shear forces. High shear forces can break thin crystals resulting in deposit re-entrainment. It is, therefore, not possible to extrapolate results obtained for tubular heat exchangers to plate heat exchangers.

Experimental Setup

The experimental approach used in the present investigation is shown in Fig. 1. The solution was pumped from a 50 liter storage tank to the plate heat exchanger, which was heated by hot water. The hot water was prepared in a second plate heat exchanger using steam as a heating medium. The hot solution was returned to the water-cooled tank. All piping was made from stainless steel to avoid corrosion.

An α-Laval plate heat exchanger P-01 was used in the present

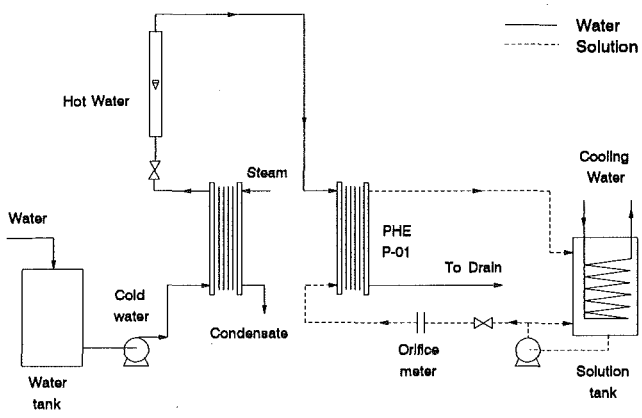

Fig. 1 Flow loop

Contributed by the Heat Transfer Division for publication in the JOURNAL OF HEAT TRANSFER. Manuscript received by the Heat Transfer Division July 1992; revision received January 1993. Keywords: Forced Convection, Fouling, Heat Exchangers. Associate Technical Editor: W. A. Fiveland.

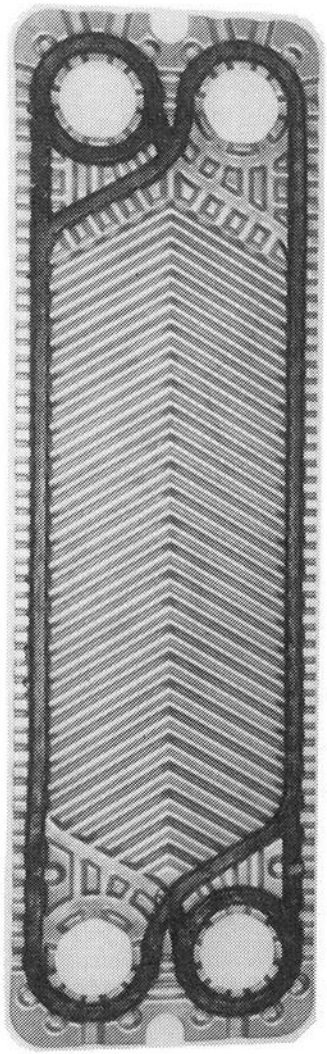

Fig. 2 Chevron plate used in plate heat exchanger P-01

investigation. The stainless steel plates were of chevron type, as shown in Fig. 2. The major dimensions of the plates are given in Table 1.

The flow in the plate heat exchanger was countercurrent as illustrated in Fig. 3. Only three channels were used, in order to keep the setup as simple as possible. The solution is in the central channel surrounded by the channels for the hot water.

Table 1 Plate dimensions

Inclination angle	60°
Plate length	0.430 m
Plate width	0.123 m
Plate spacing	0.0024 m
Plate thickness	0.0006 m
Heat transfer area per plate	0.032 m^2

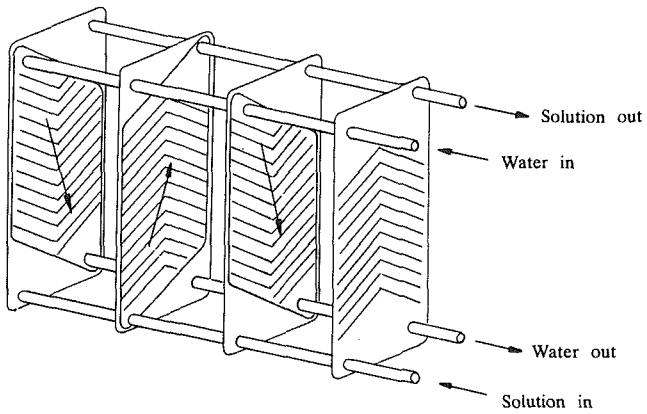

Fig. 3 Flow pattern in plate heat exchanger

In all channels, the flow is diagonal. The solution flowing in the central channel enters on the bottom left side and leaves on the top right side of the plate. Since the inclination of flow channels is 60 deg, the solution will flow predominantly through the furrows (Focke and Knibbe, 1986). Hence, in each flow channel there are two fluid streams flowing in opposite directions (left/right) along the furrows: one on the bottom plate and the other on the top plate. As the channel gap changes throughout the heat exchanger, the local velocities vary as well. Therefore, a nominal channel gap is used to specify the flow rates. In this particular plate heat exchanger, the nominal channel gap is 2.4 mm, with minimum and maximum gap widths of 0 mm and 4.8 mm, respectively. The complete heat exchanger was insulated to reduce heat transfer losses to the ambient air. A computer-controlled data acquisition system was used to record continuously the inlet and outlet temper-

Nomenclature

A = heat transfer area, m^2
C_1 = Arrhenius constant, $m^4/kg\ s$
c_b = bulk concentration, ppm
c_{bo} = bulk concentration at the start of experiment, ppm
c_w^* = concentration at wall, ppm
c_p = specific heat, J/kg K
E = activation energy, J/mol
k_r = reaction rate constant, $m^4/kg\ s$
m = mass of deposit per unit area, kg/m^2
$\dot{m}_d$ = deposition rate, $kg/m^2\ s$
$\dot{m}_r$ = removal rate, $kg/m^2\ s$
$\dot{M}$ = mass flow rate of solution, kg/s
n = order of reaction
$\dot{Q}$ = heat flow rate, W
R = ideal gas constant, J/mol K
R_f = fouling resistance, m^2 K/W
T = temperature of the solution, K
u = velocity based on nominal channel gap, cm/s
U = overall heat transfer coefficient, W/m^2 K
$U_{t=0}$ = initial (clean) overall heat transfer coefficient, W/m^2 K
x_w = thickness of wall, m
α_s = heat transfer coefficient on the solution side, W/m^2 K
α_h = initial heat transfer coefficient on the water side, W/m^2 K
β = mass transfer coefficient, m/s
ΔT = temperature difference, K
λ = thermal conductivity, W/m K
ρ = density of deposit, kg/m^3

Subscripts

b = bulk
c = clean
d = deposit
f = fouled
i = inlet
log = log mean temperature difference
o = outlet
s = solution
w = wall

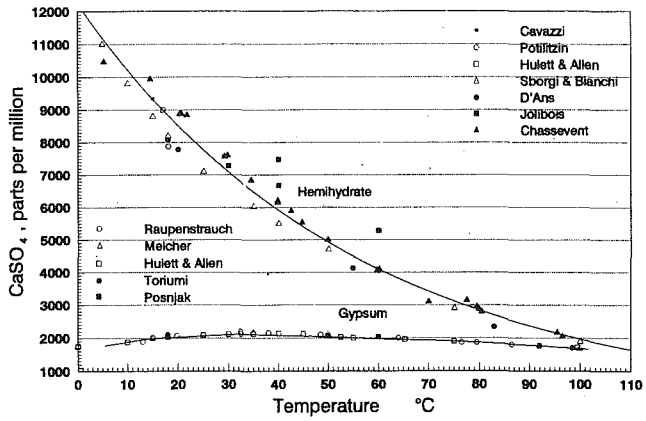

Fig. 4 Solubility curves of calcium sulfate

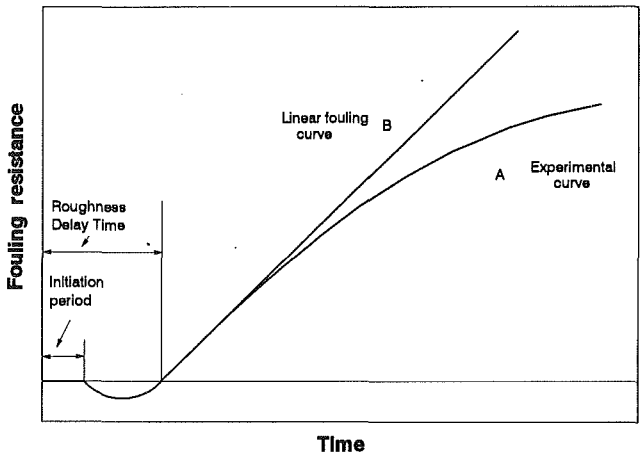

Fig. 5 Typical fouling curves

atures of both streams, which were measured with calibrated thermocouples.

Test Solution

Calcium sulfate was used as hardness salt because of its inverse solubility in water. Calcium sulfate crystallizes from an aqueous solution in three forms, namely gypsum, calcium sulfate hemihydrate, and calcium sulfate anhydride. The solubility of all three forms decreases with increasing temperature (Landolt and Börnstein, 1980; Linke, 1958; Partridge and White, 1929), as shown in Fig. 4. In our test heat exchanger, the wall temperature is always higher than the bulk temperature, resulting in a positive driving force for Eqs. (3) or (4). Therefore, calcium sulfate is deposited on the heat transfer surface.

The calcium sulfate solution was prepared in either distilled water or de-ionized water. Since calcium sulfate crystals do not dissolve easily in water, another method was used to produce the desired solution. Calcium nitrate ($Ca(NO_3)_2 \cdot 4H_2O$) and sodium sulfate ($NaSO_4$) were dissolved in water, resulting in calcium sulfate crystallizing on the heat transfer surface. This method was preferred because of the higher solubilities of calcium nitrate and sodium sulfate in water. Concentrated solutions with supersaturation up to 1200 ppm with respect to gypsum were prepared without any difficulty using this method. Each run was started with 50 liters of solution with the same inlet hot water temperature, unless otherwise stated. The concentrations were measured by EDTA titration.

Experimental Procedure and Data Reduction

During the experiment, inlet temperatures and flow rates of solution and hot water were kept constant. The experiments were carried out for temperatures and concentrations for which the solution was supersaturated with respect to gypsum only. This was preferred over the condition where the solution is supersaturated with respect to hemihydrate and gypsum, since hemihydrate and gypsum will deposit at different rates, which would make it very difficult to evaluate the underlying mechanisms.

Since fouling occurred only on the solution side, the overall heat transfer coefficient is defined as

$$\frac{1}{U}=\frac{1}{\alpha_s}+\frac{1}{\alpha_h}+\frac{x_w}{\lambda_w}+R_f \tag{6}$$

The fouling resistance is defined as

$$R_f=\frac{1}{U}-\frac{1}{U_{t=0}} \tag{7}$$

where the overall heat transfer coefficient is determined from

$$U=\frac{\dot{Q}}{A\Delta T_{\log}} \tag{8}$$

The heat flow rate Q is the heat gained by the solution:

$$\dot{Q}=\dot{M}c_p(T_o-T_i) \tag{9}$$

Thus, by measuring the inlet and outlet temperatures of solution and hot water, the heat transfer coefficient can be calculated. Before the start of each experiment, a certain time period was required to heat the solution from room temperature to the desired inlet temperature by pumping it for 15–20 minutes through the heat exchanger and the tank. This was necessary to obtain steady-state conditions before the measurements as fouling can be determined only for pseudo-steady state. The possibility that the surface fouling process may have started during this period of time was checked in initial experiments. It was found that the time period allowed to attain steady-state conditions did not significantly affect the measured fouling curves. The maximum error in the measured fouling resistances is less than ±5 percent.

Results

Fouling Curve. Two typical fouling curves, which are indicative of the mechanisms of deposition, are shown in Fig. 5. Curve A represents the fouling behavior observed in the present investigation, showing a decreasing fouling rate, whereas curve B shows a linear increase in fouling resistance with time, as was found by Hasson et al. (1970) for crystallization of pure gypsum in a double pipe heat exchanger. There are several reasons for the obvious discrepancy between the two curves:

(*i*) *Removal Mechanisms.* Curve B is closely linked to the assumption that there is no removal rate; see Eq. (2). However, this situation is most unlikely in a plate heat exchanger. Initially, when only few deposits are present, there will be hardly any removal rate because the crystals are still small and do not noticeably reduce the cross-sectional area. Both conditions will change with increasing time of operation, resulting in long, fragile crystals and a considerable increase in the local shear forces. Under these conditions, fracture and removal of crystals occurs. This is illustrated in Figs. 6 and 7. Figure 6 shows the initial deposit formed on the plate surface. The crystals are small with no particulate matter attached to the crystals or trapped in the crystal matrix. Contrariwise, Fig. 7 clearly illustrates that the crystals are much longer and that there are small particles attached to these crystals. The magnification is almost the same for both figures. The presence of particles strongly indicates that there are removal mechanisms in the plate heat exchanger.

Fig. 6 Crystals formed on the plate surface at a flow velocity of 21.9 cm/s

Fig. 7 Crystals formed on the deposit-solution interface at a flow velocity of 21.9 cm/s

While most of the crystal fragments are trapped in the crystal matrix, some particles will also be present in the solution. Hence, there is a possibility that particulate fouling may take place in addition to crystallization. The solution was filtered through a 0.22 μm millipore filter and the total particle concentration determined as only 0.5–0.7 g/50 liters. Most of the particles were comparably large. Since particulate fouling rates decrease strongly with both decreasing concentration and increasing particle size (Blöchl and Steinhagen, 1990), it was concluded that there was no significant contribution of particulate fouling and that the deposits were formed by crystallization only.

(*ii*) *Decreasing Wall Temperature.* Since the solution is not heated with a constant heat flux, increasing deposit thickness causes the temperature at the interface between deposit and solution to decrease, reducing the driving concentration difference. This process is called auto-retardation, i.e., the formation of deposits decreases the rate of fouling. Therefore, the slope of the fouling curve does not remain constant, but decreases with time.

(*iii*) *Increasing Flow Velocity.* As the nominal channel gap is only 2.4 mm, the local velocities increase considerably with deposition. The higher heat transfer coefficient on the solution side reduces the interface temperature by at least 2–3°C, further reducing the fouling rate with time.

(*iv*) *Decreasing $CaSO_4$ Concentration.* As the mass of $CaSO_4$ deposit increases, the concentration of the solution decreases resulting in a decrease in the driving force for diffusion and/or reaction. Hence, the slope of the fouling curve decreases until it levels off. This condition does not represent the situation encountered in industrial processes where the concentration is usually constant with time. To simulate this condition, the $CaSO_4$ concentration was artificially increased to almost the initial level during some of the experiments. However, Fig. 8 shows that the addition of chemicals, while increasing the concentration from 2622 ppm to 2945 ppm, does not seem to have a significant effect on the slope of the fouling curve. The explanation for this surprising behavior, which was observed in several experiments, is most likely that the deposition during the process is controlled by the mechanisms outlined under (*i*)-(*iii*).

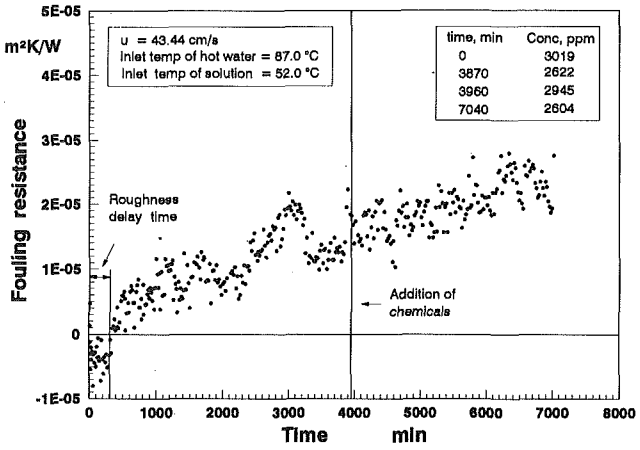

Fig. 8 Fouling resistance as a function of time

Initiation Period. It is sometimes observed that there is no deposition for some time after a new or cleaned heat exchanger has been taken into operation. This time period, called the initiation period (see Fig. 5), may be required to establish conditions that promote fouling. For our experiments, there was no or only a very small delay time. Figure 8 shows that the initial growth of deposit causes the fouling resistance to decrease rather than increase. This can be explained by the changing flow characteristics near the heat transfer surface, as the deposit penetrates the viscous sublayer. The resulting turbulence increases the film heat transfer coefficient at the solid/liquid interface, thus reducing the thermal fouling resistance defined in Eq. (7). This process continues until the additional heat transfer resistance overcomes the advantage of the increased turbulence. In what follows in this paper, the time period from the beginning of the experiment until the moment when the fouling resistance is zero, again, is called roughness delay time (Fig. 5).

Scale Formation Pattern

Figure 9 illustrates the variation of deposit formation over the heat transfer plate. In general, the deposit was not very adherent and could be removed easily. Some crystalline material was removed accidentally when the plate was removed from the frame. The flow in the channel is diagonal, entering on the bottom left-hand side and leaving on the top right-hand side of the plate. For the following reasons, the deposition is more severe in the upper part of the plate than in the bottom part:

(*i*) The driving concentration difference increases because fluid and wall temperature increase from inlet to outlet. This decreases the solubility and, therefore, increases the supersaturation if the bulk concentration is assumed to be constant.

(*ii*) The crystallization rate constant increases with increasing temperature according to Eq. (5).

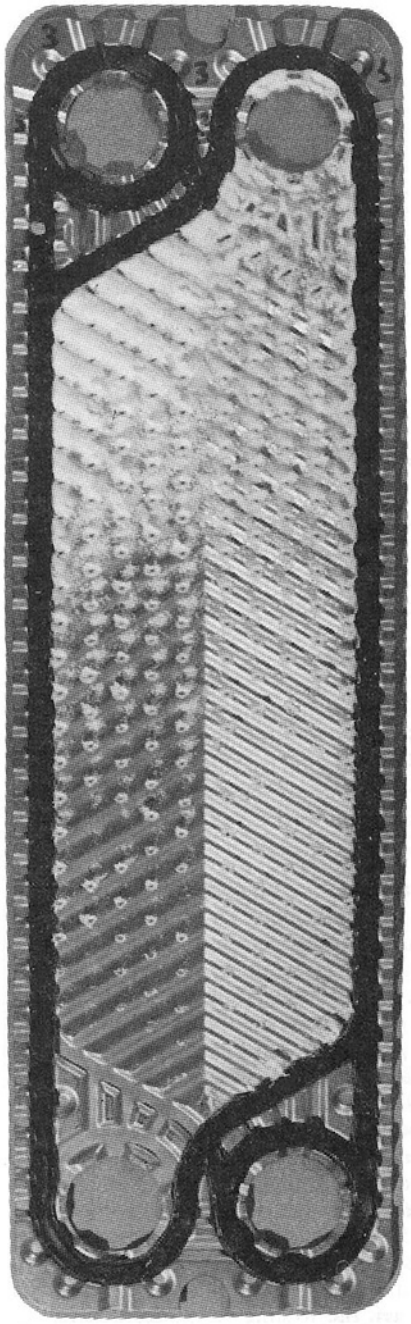

Fig. 9 Deposition pattern at a flow velocity of 21.9 cm/s

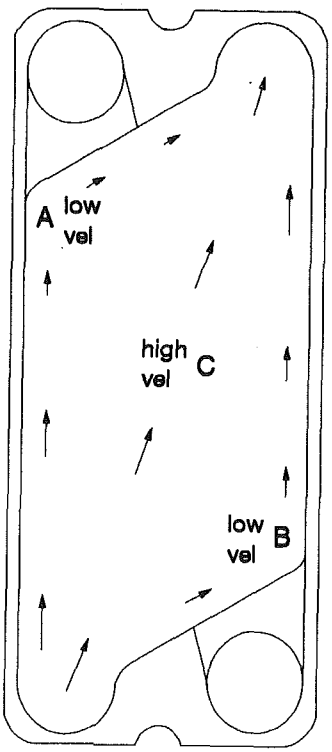

Fig. 10 Velocity distribution in flow channel

The diagonal flow results in low-velocity zones, indicated in Fig. 10 as A and B. In these areas shear forces are at a minimum and the wall temperature is close to the temperature of the heating medium. Therefore, most deposition occurs in the top left-hand corner because of the low flow velocity and high fluid/surface temperature in this area. Comparison of the deposition pattern shown in Figs. 9 and 11 indicates that the extent of the stagnant zones and, therefore, of the deposition, decreases with increasing flow velocity. Obviously, the deposition pattern also gives interesting insight into the flow distribution along the plate, which affects the performance of the heat exchanger.

A closer look at the crystal formation in a certain area of the heat transfer plate (Fig. 11) reveals that the crystals are varying in size and amount. Around the contact points between the plates, the flow velocity is low, resulting in higher wall temperatures and lower removal rates. Due to the particular

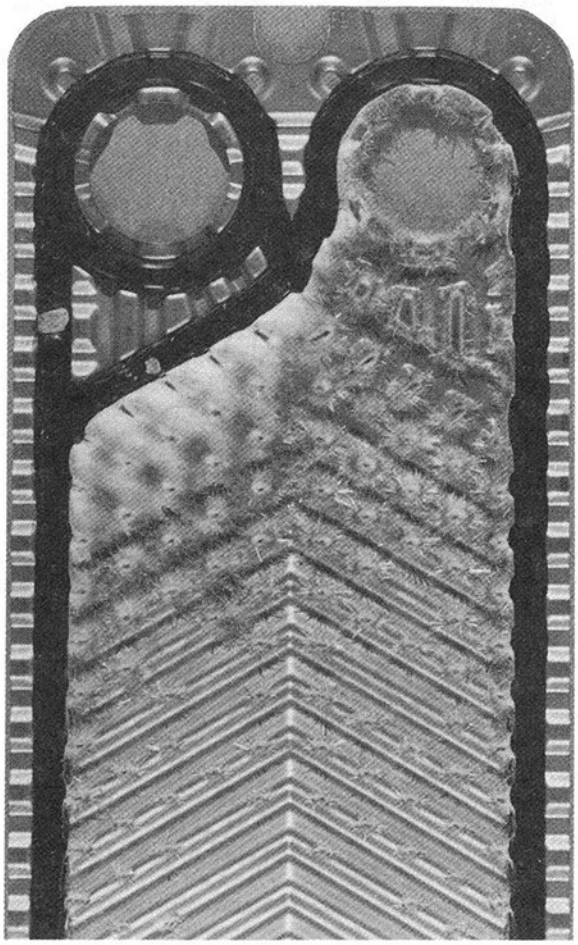

Fig. 11 Deposition pattern for a higher flow velocity of 43.4 cm/s

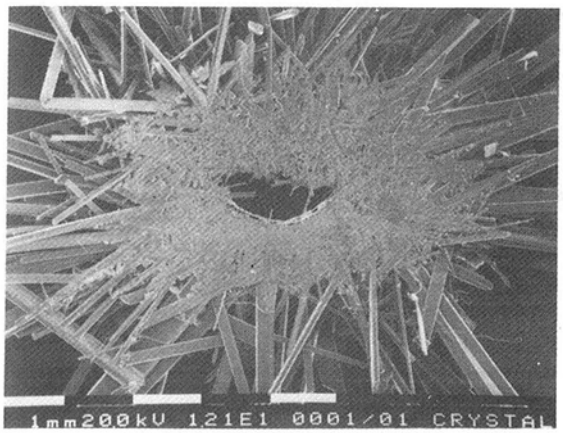

Fig. 12 Crystal growth near contact point

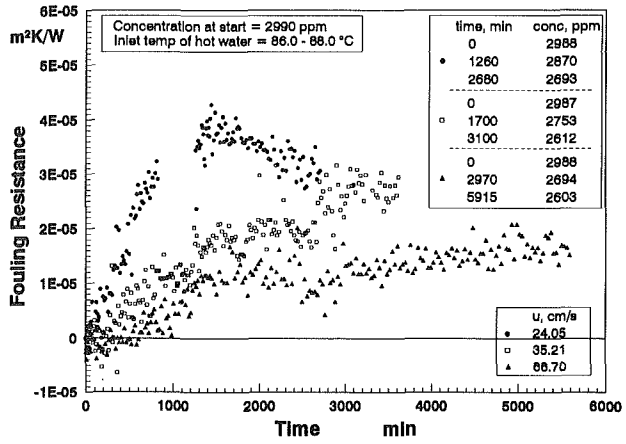

Fig. 13 Effect of flow velocity on fouling

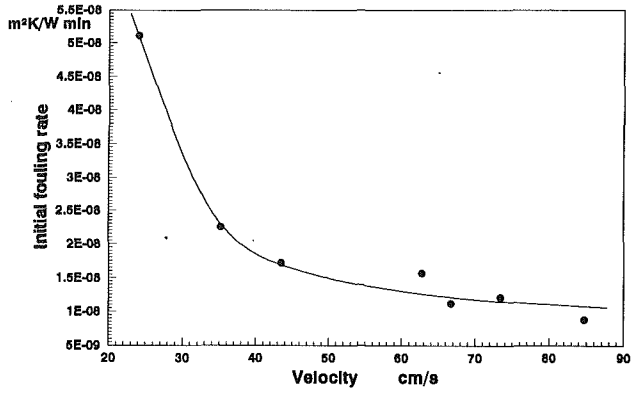

Fig. 14 Effect of velocity on initial fouling rate

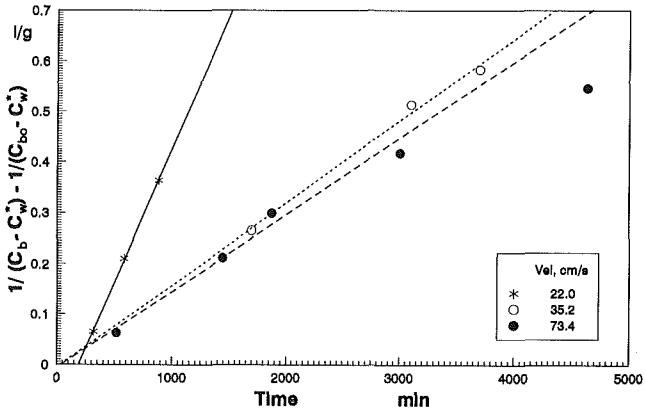

Fig. 15 Kinetic plots of Eq. (12) for the growth of gypsum

geometry at these locations, the temperature profile in the vicinity of the contact points is different from that in the flow channel, since a volume of liquid is heated from several directions. As a result of these effects, most crystal formation is initiated near the contact points. Obviously, this does not apply for the stagnant flow zones in the heat exchanger. Further examination of the crystal formation near a contact point (Fig. 12) shows that the crystals can be divided into two different size categories. An almost homogeneous deposit of small crystals is observed directly on the plate surface, while long single crystals are formed on top of this initial layer.

Effect of Flow Velocity

The effect of the flow velocity (based on the average channel gap) is illustrated by the fouling curves shown in Fig. 13. Obviously, the initial fouling rate as well as the absolute value of the fouling resistance decrease with increasing flow velocity. The reduction in the absolute value of the fouling resistance is readily explained by the increasing removal rate due to the higher shear forces as well as the decreasing solution/interface temperatures due to higher solution-side heat transfer coefficients. However, according to almost all published fouling models, the removal rate at the beginning of the fouling process is zero. Therefore, the reduced initial fouling rate must be the result of a lower deposition rate for the higher flow velocity.

Deposition at the heat transfer surface can be controlled by either diffusion or chemical reaction. To find the controlling mechanism for the present investigations, the initial fouling rates (which in the absence of removal are proportional to the initial deposition rates) after the roughness delay time were determined for all experiments. The effect of flow velocity on the initial fouling rate is illustrated in Fig. 14. The initial fouling rate decreases with increasing flow velocity, demonstrating that the formation of deposits cannot be controlled by diffusion of material from the fluid bulk to the heat transfer surface. Therefore, the deposition process is reaction controlled and can be expressed by Eqs. (4) and (5). Since $n = 2$ for gypsum formation, Eq. (4) reduces to

$$\dot{m}_d = k_r (c_b - c_w^*)^2 \tag{10}$$

Also, the rate of deposition is equal to the rate of change in concentration. Therefore,

$$\frac{dc_b}{dt} = k_r (c_b - c_w^*)^2 \tag{11}$$

Integrating Eq. (11), we get

$$\frac{1}{c_b - c_w^*} - \frac{1}{c_{bo} - c_w^*} = k_r t \tag{12}$$

The left-hand side of Eq. (12) can be plotted against time t as shown in Fig. 15. Since it is a straight line, the fouling process is reaction controlled. The reaction rate constant k_r can be calculated from the slope of the straight line. As the velocity increases, the wall temperature decreases, resulting in a decrease in the reaction rate constant k_r. This is also illustrated in Fig. 15. The decrease in slope for an increase in velocity from 0.22 m/s to 0.35 m/s is considerably more than for an increase from 0.35 m/s to 0.73 m/s. The reason for this is that the initial fouling rate decreases exponentially up to velocities around 0.4 m/s (Fig. 14) and almost levels off for velocities higher than 0.5 m/s. Since the main resistance to heat transfer for solution flow velocities >0.5 m/s was on the hot water side, further increase in the solution flow velocity did not increase the heat duty and caused a proportional reduction in solution outlet temperature.

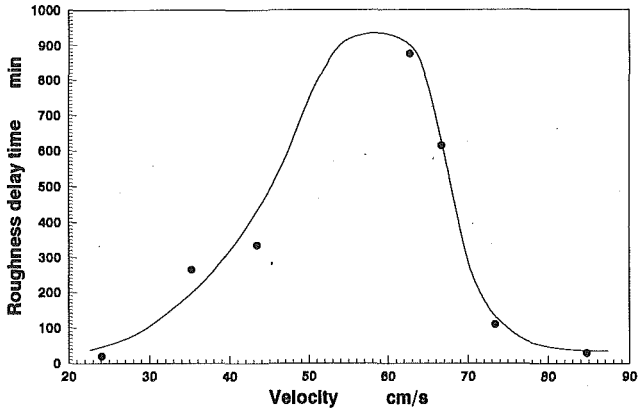

Fig. 16 Roughness delay time as a function of flow velocity

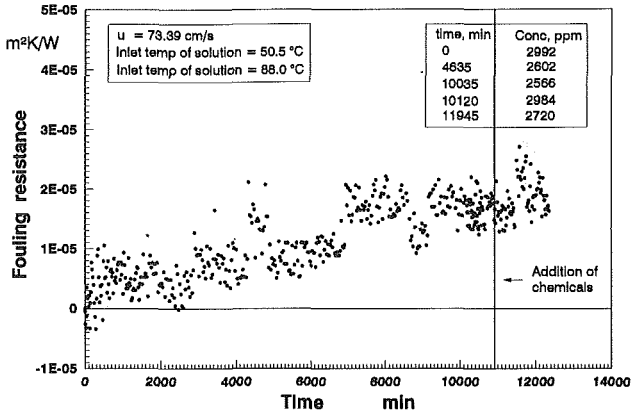

Fig. 18 Effect of change in concentration during the experiment

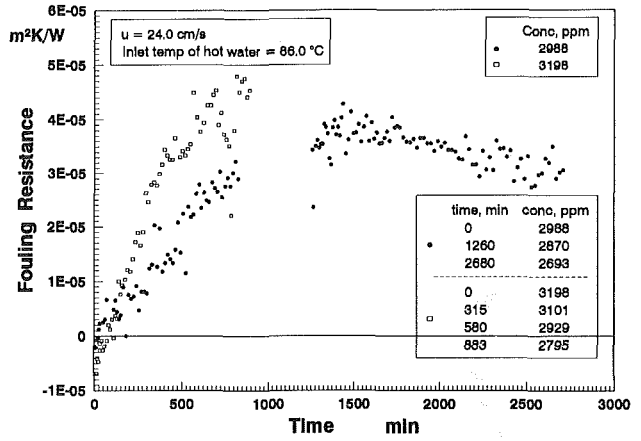

Fig. 17 Effect of concentration on fouling

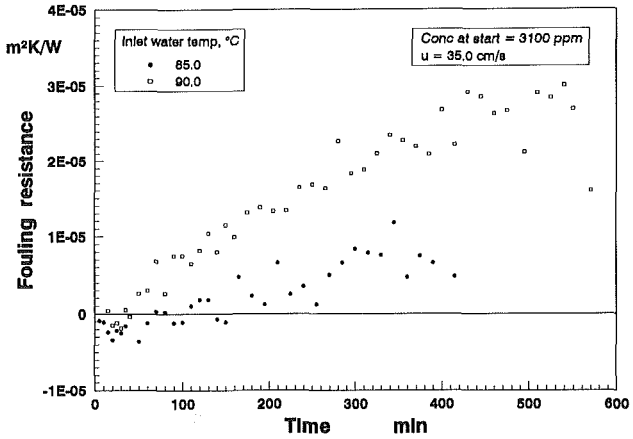

Fig. 19 Effect of temperature on fouling

The effect of flow velocity on the roughness delay time is illustrated in Fig. 16. The roughness delay time has a maximum value for a flow velocity around 0.55 m/s. Surface roughness has a beneficial aspect on heat transfer if the roughness elements penetrate the laminar sublayer (Schlichting, 1968).

- For low flow velocities, the wall temperature is relatively high and the growth of deposit is rapid due to the temperature effect on the reaction rate constant; see Eq. (5). The deposit penetrates the viscous sublayer quickly irrespective of the thickness of the viscous sublayer, increasing the heat transfer coefficient. Soon, however, the deposit thickness reaches a limit where the advantage of the high film heat transfer coefficient due to increased turbulence is compensated by the additional heat transfer resistance of the deposit, and the fouling resistance becomes positive again.
- With increasing flow velocity, the thickness of the viscous sublayer as well as the wall temperature decreases. Since the reaction rate decreases exponentially with the wall temperature, the slow-growing deposits need a considerably longer time to form a layer thick enough to compensate the effect of additional turbulence. Therefore, the roughness delay time is higher than for low flow velocities.
- The thickness of the sublayer decreases continuously with increasing flow velocity (Schlichting, 1968). Thus, the effect of additional roughness becomes less pronounced at higher velocities. Contrariwise, Fig. 14 indicates that the deposition rate (initial fouling rate) remains almost constant for higher velocities. Hence, the advantage of roughness is quickly overcome by the fouling resistance, resulting in a shorter roughness delay time at high flow velocities.

Effect of Concentration

With increasing $CaSO_4$ concentration, the driving force for the surface reaction increases, resulting in a higher deposition rate. This is illustrated in Fig. 17, which shows fouling curves for two $CaSO_4$ concentrations. The effect of concentration is more pronounced at the beginning of an experiment, whereas a change in concentration does not have a significant effect once a relatively constant fouling resistance is reached. For example, Fig. 17 shows that a concentration difference of 210 ppm at the beginning causes rapid fouling. However, if the concentration was changed by 325 ppm or even 415 ppm during the experiment, no major change in fouling pattern occurred, as shown in Figs. 8 and 18, respectively. This may be explained by the increased shear stress (i.e., removal) and lower interface temperature (i.e., reaction rate).

Effect of Temperature

The local flow velocity and correspondingly the wall temperature vary over the whole flow channel. Since the measurement of local wall temperatures and heat fluxes in a plate heat exchanger is complicated, the effect of wall temperature was investigated via the change in average wall temperature at the heat transfer plate. This was achieved by changing the temperature of the heating water at the inlet. Higher average wall temperatures resulted in higher deposition rates, as illustrated in Fig. 19.

The effect of wall temperature can also be investigated by visually observing the crystal formation along the plate; see Fig. 9. As discussed above, more deposits are formed at the hot end of the heat exchanger plate.

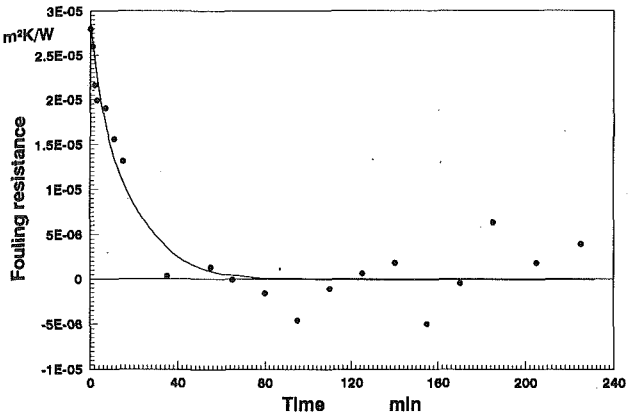

Fig. 20 Cleaning process

The roughness delay time is closely associated with the wall temperature. With increasing wall temperature, deposits grow quicker and the roughness delay time decreases. This is illustrated in Fig. 19.

Cleaning

Chemical cleaning of the fouled heat exchanger was done by circulating a 3–4 percent acetic acid solution. Most deposits were removed within 20–25 minutes with only few spots left. Figure 20 shows that the corresponding fouling resistance falls to zero within this short period of time. An additional two hours were required to remove the remaining spots. The cleaning process was always carried out for 3–4 hours to ensure identical surface conditions at the start of each experiment.

Conclusions

The formation of crystalline deposits in plate and frame heat exchangers is widely different from the fouling in conventional tubular heat exchangers. Because of the narrow flow channels, the formation of deposits significantly increases the local flow velocity, causing deposit removal and lower local interface temperatures.

Crystallization of gypsum is reaction controlled. The rate of deposition increases with increasing wall temperature and bulk concentration and decreasing velocity. With increasing flow velocity, both the initial fouling rate as well as the absolute value of the fouling resistance decreases. The initial fouling rate decreases due to lower wall temperature at higher flow velocities, whereas the absolute value of the fouling resistance decreases due to a higher removal rate in conjunction with a lower interface temperature. Concentration is an important factor only in the initial stages of the fouling process. The channel gap is reduced considerably by the deposit, causing other factors such as higher shear stresses and lower interface temperature to become more important.

There is a major effect of the flow distribution throughout the heat exchanger. If the design of the corrugations can be modified to reduce/eliminate stagnant flow zones, the efficiency of the heat exchanger will increase and its tendency to foul will decrease.

Cleaning of gypsum deposits was done using 3–4 percent acetic acid. It took about 2 hours to clean the heat exchanger completely.

Acknowledgments

The authors are indebted to α-Laval and to APV-Baker for continuing support of their investigations.

References

Amjad, Z., 1988, "Calcium Sulfate Dihydrate (Gypsum) Scale Formation on Heat Exchanger Surfaces: The Influence of Scale Inhibitors," *Journal of Colloid and Interface Science*, Vol. 123, No. 2, pp. 523–536.

Blöchl, R., and Steinhagen, H. M., 1990, "Influence of Particle Size and Particle/Fluid Combination on Particulate Fouling in Heat Exchangers," *Can. J. Chem. Engg.*, Vol. 68, pp. 585–591.

Buonopane, R. A., Troupe, R. A., and Morgan, X. X., 1963, "Heat Transfer Design Method of Plate Heat Exchangers," *Chem. Engg. Prog.*, Vol. 59, No. 7, pp. 57–61.

Cooper, A., Suitor, J. W., and Usher, J. D., 1980, "Cooling Water Fouling in Plate Heat Exchangers," *Heat Trans. Engg.*, Vol. 1, No. 3, pp. 50–55.

Cooper, A., and Usher, J. D., 1983, *Heat Transfer Correlations; Plate Heat Exchangers*, Hemisphere Publishing Corporation, section 3.7, pp. 3.7.5–1.

Focke, W. W., and Knibbe, P. G., 1986, "Flow Visualization in Parallel Plate Ducts With Corrugated Walls," *Journal of Fluid Mechanics*, Vol. 165, pp. 73–77.

Hasson, D., and Jahavi, J., 1970, "Mechanism of Calcium Sulfate Scale Deposition on Heat Transfer Surfaces," *I&EC Fundamentals*, Vol. 9, No. 1, pp. 1–10.

Jackson, B. W., and Troupe, R. A., 1964, "Laminar Flow in Plate Heat Exchangers," *Chem. Engg. Prog.*, Vol. 60, No. 7, p. 64.

Kern, D. Q., and Seaton, R. A., 1959, "A Theoretical Analysis of Thermal Surface Fouling," *Brit. Chem. Eng.*, Vol. 4, No. 5, pp. 258–262.

Lalande, M., Tissier, J., and Corrieu, G., 1984, "Fouling of Plate Heat Exchangers Used in Ultra High Temperature Sterilization of Milk," *Journal of Dairy Research*, Vol. 51, pp. 557–568.

Landolt, X. X., and Börnstein, Y. Y., 1980, *Zahlenwerte und Functionen, 222631 Anorganische Stoffe in Wasser; Binäre Systeme*, Vol. 6, pp. 3–71.

Linke, W. F., 1958, "Solubilities," *Inorganic and Metal Organic Compounds*, Vol. 1, 4th ed., p. 661.

Marriott, J., 1971, "Where and How to Use Plate Heat Exchangers," *Chem. Engg.*, Vol. 78, No. 8, pp. 127–134.

Müller-Steinhagen, H. M., and Middis, J., 1989, "Particulate Fouling in Plate Heat Exchangers," *Heat Trans. Engg.*, Vol. 10, No. 4, pp. 30–36.

Novak, L., 1982, "Comparison of the Rhine River and the Oeresund Sea Water Fouling and Its Removal by Chlorination," ASME JOURNAL OF HEAT TRANSFER, Vol. 104, pp. 663–670.

Partridge, E. P., and White, A. H., 1929, "The Solubility of Calcium Sulfate From 0 to 200°," *J. Chem. Soc.*, Vol. 51, pp. 360–370.

Raju, K. S. N., and Bansal, J. C., 1980, "Consider the Plate Heat Exchanger," *Chem. Engg.*, pp. 133–144.

Raju, K. S. N., and Bansal, J. C., 1986, "Design of Plate Heat Exchangers," *Heat Exchanger Sourcebook*, Hemisphere Publishing Corp., pp. 563–582.

Schlichting, H., 1968, *Boundary Layer Theory*, McGraw-Hill, 6th ed., pp. 596–625.

Singh, J., and Aneja, V. P., 1981a, "Scaling and Heat Transfer Characteristics in Plate Heat Exchangers," *Journal of Institution of Engineers*, India, Vol. 62, pp. 6–8.

Singh, J., and Aneja, V. P., 1981b, "Effect of Acidity and Heating Time on Fouling in Plate Heat Exchangers," *Journal of Institution of Engineers*, India, Vol. 62, pp. 12–14.

Usher, J. D., 1970, "Evaluation of Plate Heat Exchangers," *Chem. Engg.*, Vol. 77, No. 4, pp. 90–94.

Walker, G., 1982, "Plate Heat Exchangers," *Industrial Heat Exchangers*, Hemisphere Publishing Corp., pp. 87–113.

Experimental and Numerical Studies of Natural Convection With Flow Separation in Upward-Facing Inclined Open Cavities

R. A. Showole

J. D. Tarasuk

Department of Mechanical Engineering,
University of Western Ontario,
London, Ontario, N6A 5B9 Canada

Steady two-dimensional laminar natural convection heat transfer from isothermal horizontal and inclined open cavities of rectangular cross section has been investigated experimentally using a Mach-Zehnder interferometer and numerically by a finite difference technique. Experimental results are presented for Prandtl number, Pr = 0.7, Rayleigh numbers from 10^4 to 5×10^5, cavity aspect ratios, A (or h/w) = 0.25, 0.5, and 1.0, and inclination angles (or angles of rotation about the longitudinal axis), θ = 0, 30, 45, and 60 deg to the horizontal. The numerical model uses a relaxation technique to solve the governing elliptic, partial differential equations. Numerical results are presented for the range of Rayleigh number, $10^3 \leq Ra_w \leq 5 \times 10^5$, θ = 0 and 45 deg, and A = 1. Flow and temperature patterns, velocity and temperature profiles, and local and average heat transfer rates are presented. Flow recirculation with two counterrotating convective rolls developed in the cavity at $Ra \geq 10^5$. The inclination of the cavity induced flow entrainment, causing flow separation at the lower corner and flow reattachment at the upper corner of the aperture opening except in shallow cavities, A < 0.5, where the flow reattachment occurred on the base of the inclined cavity. For all Ra numbers, the first inclination of the cavity from the horizontal caused a significant increase in the average heat transfer rate, but a further increase in the inclination angle caused very small increase in heat transfer rate. However, for every angle of inclination considered, the average heat transfer rate increased significantly as Ra was increased. The equation of the form $Nu = mRa^n$, where $0.018 \leq m \leq 0.088$ and $0.325 \leq n \leq 0.484$, correlates the experimental and numerical results satisfactorily for the range of Ra, $10^4 \leq Ra \leq 5 \times 10^5$ and of θ, $0 \leq \theta \leq 60$ deg. The present experimental and numerical results are in good agreement with the results reported in the literature.

Introduction

Separated forced convection flows over open cavities have been the focus of several investigations following the pioneering work of Chapman (1956) on this subject. A comprehensive review of the studies on separated forced convection has been presented by Chilcott (1967). By constrast, separated natural convection flows in open cavities have received very little attention. This class of separated flows, which may occur either by design or natural circumstances, is related to air entrainment into heated open cavities, particularly when the cavities are inclined. Several examples may be found in the environment and in many engineering systems such as natural convection flows over valleys, solar receiver tracking systems, and from electronic systems where cavities are formed in spaces between discrete circuit devices.

Therefore, the objective of this paper is to improve the understanding of natural convection heat transfer with separating and recirculating flows. As a test case, the authors considered an upward-facing open rectangular cavity with variable inclination as shown in Fig. 1. In the figure, all the walls of the cavity are considered to be isothermal and the solid walls in the proximity of the aperture plane are adiabatic. The present study also includes the natural convection from horizontal open cavities for direct comparison and for validation of the present techniques.

There are two distinct cavity orientations that are of interest in problems involving natural convection heat transfer from open cavities, one being cavities with downward-facing inclined orientation and the other with upward-facing inclination. The former has been the focus of recent investigations. Chan and Tien (1985) have numerically investigated natural convection heat transfer in open square cavity with vertical aperture opening for the range $10^3 \leq Ra \leq 10^9$, and observed flow separation

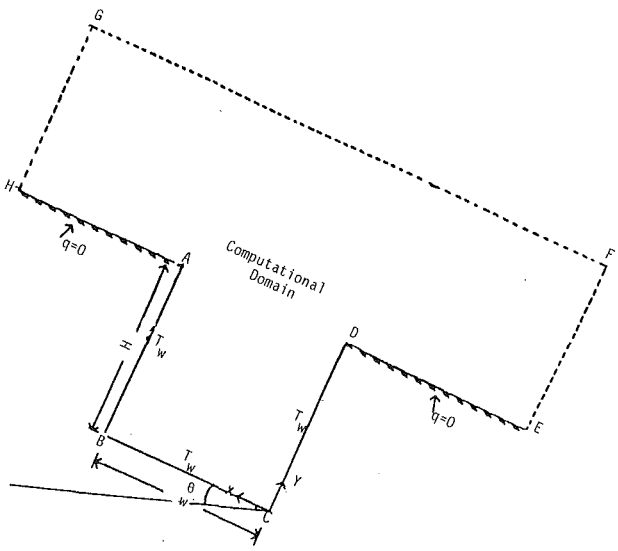

Fig. 1 Schematic of the upward-facing inclined cavity

Contributed by the Heat Transfer Division for publication in the JOURNAL OF HEAT TRANSFER. Manuscript received by the Heat Transfer Division September 1990; revision received August 1992. Keywords: Flow Separation, Natural Convection, Numerical Methods. Associate Technical Editor: J. R. Lloyd.

Table 1 Correlations for average Nusselt number

REFERENCE	GEOMETRY	CORRELATION	COMMENTS
Le Quere et al. (1981)(Numerical)	Sideward-facing Open rectangular cavities, A = 1	$Nu = .091\ Ra^{0.324}$ $0.73 \times 10^4 \leq Ra \leq 2.19 \times 10^7$	Correlations obtained from data published by the authors
Mirenayat (1981) (Experimental)	Sideward-facing open cubical cavity, A = 1	$Nu = cGr^d$ $0.03 \leq c \leq 0.12$ $0.30 \leq d \leq 0.37$	Pr = 0.7 Parameters c and d vary as the angle of inclination
Kraabel (1983) (Experimental)	Side-facing cubical cavity, A = 1	$Nu = 0.088Gr^{0.33}(T_w/T_\infty)^{0.18}$	The terms $(T_w/T_\infty)^{0.18}$ accounts for the physical property variation of air at elevated wall temperature
Siebers et al. (1983) (Experimental)	Vertical flat surface	$Nu_y = 0.098Gr_y^{0.33}(T_w/T_\infty)^{1.04}$	y is the distance measured along the plate from the leading edge; elevated wall temperature term included
Hess and Henz (1984) (Experimental)	Upward facing open cubical cavity, A = 1	$Nu_L \simeq Ra_L^{0.25}$ for y/L = 0.1 $Nu_L \simeq Ra_L^{0.3}$ for y/L = 0.5 $Nu_L \simeq Ra_L^{1.1}$ for y/L = 0.9 $2 \times 10^8 \leq Ra_L \leq 2 \times 10^{11}$	Elevated wall temperature boundary condition Correlations obtained for local heat transfer only.
Present study (Experimental)	Upward facing open rectangular cavity, A = 1	For θ = 0 deg. $\overline{Nu} = 0.088\ Ra^{0.323}$ For θ = 30 deg. $\overline{Nu} = 0.018\ Ra^{0.484}$ For θ = 45 deg. $\overline{Nu} = 0.028\ Ra^{0.442}$ For θ = 60 deg. $\overline{Nu} = 0.029\ Ra^{0.439}$	Correlations were obtained for experimental data at θ = 0 deg. to 60 deg.
Numerical		For θ = 0 deg. $\overline{Nu} = 0.027\ Ra^{0.414}$ $3.16 \times 10^4 \leq Ra \leq 5 \times 10^5$	Numerical correlation for 0 deg. only

at the lower aperture corner for all Ra considered, but a single cell recirculation was apparent only at a very high Rayleigh number, $Ra = 10^9$, near the transition to turbulence. The numerical work by Penot (1982) describes the influence of cavity inclination on natural convection from downward-facing open cavities. For the angles of inclination considered in the study, natural convection is stronger than in the vertical orientation, and the flow fields are characterized by the existence of a hot fluid stagnation in the upper corner region of the cavity.

Le Quere et al. (1981) have predicted numerically the natural convection from downward-facing inclined open cavities with elevated wall temperature using a non-Boussinesq approximation. A similar experimental study has been reported by Chen et al. (1985). In both studies heat transfer results are obtained in the range $10^4 \leq Gr \leq 4 \times 10^7$ at $\theta = 0$ to 45 deg to the vertical. The experimental shadowgraph and the numerical velocity and isotherm distributions obtained in these studies also reveal the flow separation, recirculation, and instabilities reported by Penot (1982).

Laboratory experiments were reported by Mirenayat (1983) for natural convection from downward-facing cubical cavities with variable angle of inclination. The results were summarized by a correlation equation. Kraabel (1983) reported a correlation that accounts for the physical property variations present in a strongly heated cavity with elevated wall temperature. Siebers et al. (1983) also obtained a correlation equation, but for a large vertical flat plate with elevated wall temperature. Hess and Henze (1984) carried out a study on natural convection from an open cubical cavity. The fluid medium employed in the study is water, which makes the range of Ra covered to be much wider. A summary of the correlation equations obtained in the aforementioned studies are presented in Table 1.

As mentioned earlier, the above studies are mostly concerned with the natural convection from open cavities having vertical or downward-facing aperture planes. To the best of the authors' knowledge, the present experimental study, which is concerned with the second class of natural convection in inclined open cavities where the aperture planes are upward-facing, has not been reported in literature. In the upward-facing inclination, the internal flow exhibits a completely different behavior, and the local temperature and the heat transfer distributions are apparently not the same as those reported in the literature for the downward-faced cavities. The reason for this is that in a downward-facing inclined cavity, as in the case of a downward-faced inclined plate, the inclination from the vertical may limit the growth of a thermal boundary layer along a downward-faced wall, suppress the buoyancy forces, and hence impede natural convection. In contrast, in an upward-facing inclined plate or cavity, inclination enhances or aids natural convection processes.

Experimental Apparatus and Procedures

Figure 2 illustrates the key features of the experimental ap-

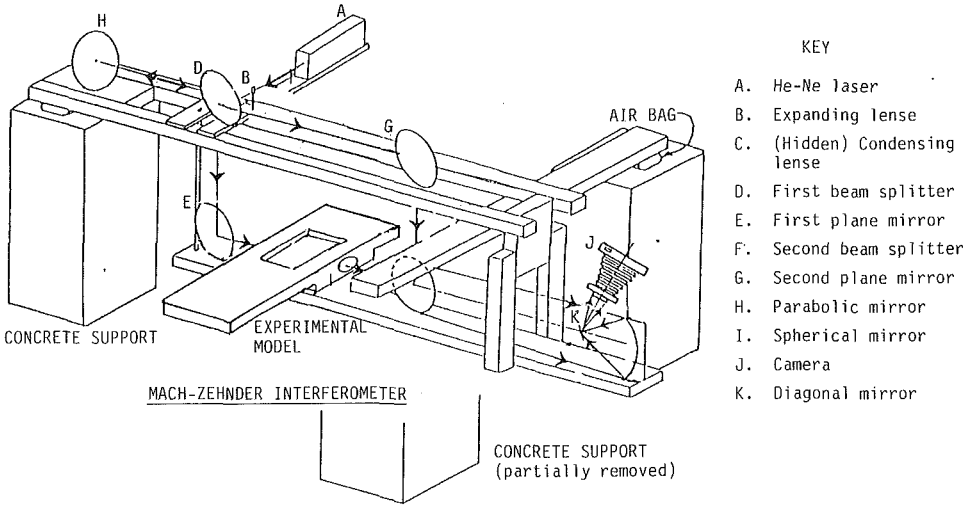

Fig. 2 Schematic of experimental apparatus

paratus. It consisted of a Mach-Zehnder interferometer and an open rectangular cavity test model. The cavity has two sides and the base. The aperture was unconstrained, and opened to the laboratory room air. All the three walls of the cavity were made of copper plates, each with a dimension 6.35 cm wide, 47.0 cm long, and 1.27 cm thick. Behind each copper plate was fastened an aluminum plate on which a strip heater rated at 750 W was flush-mounted. Finally a teflon plate with a thickness a 2 cm was mounted firmly behind each aluminum/copper plate assembly to minimize heat losses. On the front of each hot copper plate were flush-mounted 15 copper-constantan thermocouple wires for monitoring the surface temperature. The thermocouple outputs indicated an isothermal condition at the hot plates where temperature variation over the surfaces was less than 1°C. A steady-state condition in the cavity was always achieved in about twenty minutes with the aid of three temperature controllers installed to monitor and control the temperature of the hot plates. The three hot plate assemblies were arranged to form a rectangular cavity. The cavity was mounted on a pivoting cradle to permit its inclination from 0 to 60 deg to the horizontal. The base of the cavity can be adjusted to vary its height-to-width aspect ratio from 0.25 to 1.0. At a fixed temperature difference (ΔT = 32°C) between the cavity and the ambient, the Ra numbers (defined as Gr × Pr, where Gr = $g\beta(T_w - T_\infty)w^3/\nu^2$ and Pr = ν/α) were computed using different values of cavity width, w, while the aspect ratio is fixed at $A = 1$ (i.e., square cavities with different cross-sectional dimensions). The choice of w as the characteristic dimension is dictated by the fact that cavities of square cross sections ($A = 1$) were used in the supplementary numerical calculations employed to validate the experimental results. A similar choice of characteristic dimensions has been used by several authors, for example, Jacobs et al. (1974). The above method of varying the experimental Ra with w is consistent with the numerical approach and permitted the study of a wider range of Ra.

The interferometer provided the isotherms of the natural convection in the cavity and in the aperture region. This was accomplished when one half of a beam from a 5 mW He-Ne laser traversed the heated cavity and recombined with the other half beam (a reference beam), which has passed through the laboratory room undisturbed. The interference patterns or fringe shifts produced by the test and reference beams resulted from the variation of air density in the heated cavity. The fringe shifts were measured and the raw data obtained were used to compute the temperature gradients using the Lorentz-Lorenz and Gladstone-Dale relations (Eckert and Soehngen, 1948). The temperature gradients were computed at ten locations along each side of the cavity, and then used to calculate the local and average Nusselt numbers defined by:

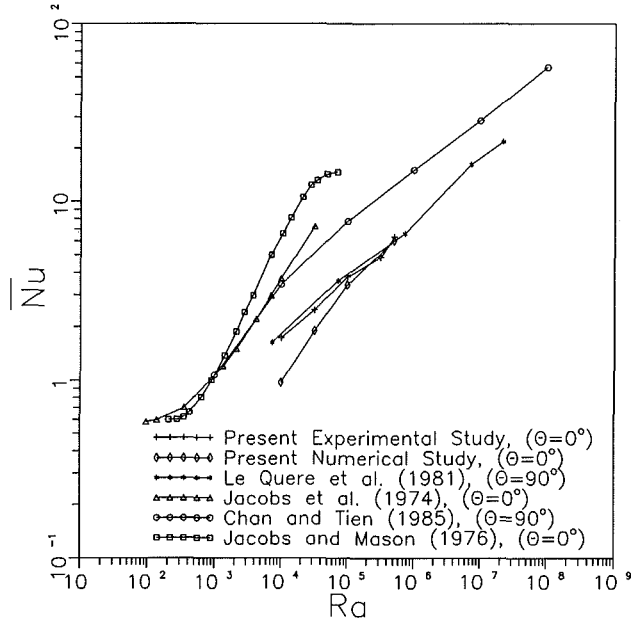

Fig. 3 Comparison of the present results with the results of previous investigators for horizontal and vertical square cavities (cases of θ = 0 deg and 90 deg

$$\mathrm{Nu}_l = h_l w/k_w = dT^*/dx|_{\mathrm{wall}} \quad (1)$$

$$\overline{\mathrm{Nu}} = 1/L \int_0^L dT^*/dx|_{\mathrm{wall}} dy \quad (2)$$

where k_w is the thermal conductivity of air evaluated at the cavity wall, dT^*/dx is the nondimensional temperature gradient, and L the length of the cavity sides. The overall heat transfer rate from the cavity was computed by averaging the $\overline{\mathrm{Nu}}$ values obtained for the three sides of the cavity.

Because the interferometer is very vulnerable to local vibration and minor disturbances, particularly in the case of an open cavity, a number of preliminary testes were carried out to validate and check the reproducibility and accuracy of the experimental data. Fringe shifts were theoretically calculated using the relation introduced by Eckert and Soehngen (1948) and experimentally measured by employing the present inter-

Table 2 Comparison of average Nusselt number on each cavity wall for upward facing and downward facing cavities, $A = 1$, $Ra = 5 \times 10^5$

REFERENCE	θ^* = 0 deg.	θ = 45 deg.
Le Quere et al. (1981) (Sideward/downward-facing cavities)	5.09 (top wall)	1.75 (top wall)
	6.29 (back wall)	2.12 (back wall)
	8.39 (bottom wall)	10.97 (bottom wall)
Present study (Upward facing cavity)	5.25 (vertical wall)	5.84 (top wall)
	5.70 (vertical wall)	9.38 (back wall)
	9.98 (base wall)	9.99 (bottom wall)

*θ is measured from the vertical axis for sideward/downward facing cavity and from the horizontal axis for upward facing cavity.

ferometer apparatus. These were done for selected values of temperature difference, ΔT, between the cavity and the ambient temperatures. The measured and predicted values agreed to within 1.5 percent. Also, at the critical Rayleigh number, $Ra = 10^3$, the $\overline{Nu} = 0.396$ obtained in this study shows a good agreement with $\overline{Nu} = 0.38$ obtained in a numerical study by Schmidt (1984) for an isothermal open cavity. The heat transfer results from two separate experiments conducted at five-day intervals indicate that $\overline{Nu}$ is reproducible to within 2.5 percent. Other errors accounted for are the equipment error, the error due to the evaluation of air physical properties and the interferometric error. The errors associated with the equipment are available from the manufacturer's specifications. The air properties were evaluated from the polynomial equations presented by Touloukian (1975). The errors of these correlations range between 1.0 and 1.7 percent. The interferometric errors are due to the misalignment of the test section with test beam, the imperfections of the interferometer optics, the location of fringe centers and the end effects. The errors arising from the end effects is caused by the finite thickness of the thermal boundary layer, δ_t, which could make the assumption of two-dimensional field invalid at the entrance and exit of the test section. This error, which ranges between 1.5 and 2.0 percent, was evaluated by the method introduced by Goldstein (1976). The experimental uncertainty, in the evaluation by the method introduced by Goldstein (1976). The experimental uncertainly, in the evaluation of $\overline{Nu}$, considering all of the above sources of errors, is estimated to be 4.5 percent.

Experimental Results and Discussion

Figure 3 compares the results of previous investigators where the main focus has been on horizontal and vertical open rectangular cavities with either isothermal base and walls or isothermal base and adiabatic walls boundary conditions. For the case of isothermal base and adiabatic walls, the average Nusselt numbers obtained by Jacobs and Mason (1976) for horizontal cavities are higher than those predicted by Chan and Tien (1985) for a vertical cavity. The reason for this is that in the vertical open cavity, as in vertical flat plates, the boundary layer thickness that develops on the heated vertical wall reduces the overall heat transfer from the cavity. The velocity and temperature profiles in the vertical cavity are also not in agreement with those in horizontal cavity for the same reason given above.

For cavities with isothermal base and walls, Fig. 3 shows that the present results for horizontal cavity are in good agreement with those of Le Quere et al. (1981) for a vertical cavity. However, the velocity and temperature profiles in the two differently oriented cavities are not in agreement. The good agreement in $\overline{Nu}$ can be explained by considering that the decrease in the average heat transfer from the base of an isothermal cavity when inclined from horizontal to vertical is compensated by the increase in the average heat transfer from its side walls. Therefore, as shown in Fig. 3, the overall average heat transfer from horizontal isothermal cavity does not vary significantly from the heat transfer from vertical isothermal cavity. However, as will be seen later, the inclination of the cavity at an angle between the horizontal and vertical results in a higher average heat transfer. At the first inclination of the cavity above the horizontal (for example, 0 to 30 deg), the increase in heat transfer at a given Ra is quite significant. A further increase in the angle of inclination results in no more significant increase in heat transfer. As the vertical (90 deg) is approached the heat transfer rate drops to about the value at horizontal. Figure 3 also shows that the result of Jacobs et al. (1974) on horizontal isothermal open cavity is not in good agreement with the present results and the results of Le Quere et al. The heat transfer prediction by Jacobs et al. is overestimated, as shown in a recent study by Schmidt (1984) in collaboration with Jacobs et al. The result of that study is in good agreement with the present work and the work of Le Quere et al.

A comparison has also been made of the present results for an upward-facing open rectangular cavity inclined at 45 deg from the horizontal with the results presented by Le Quere et al. for a downward-facing open rectangular cavity inclined at 45 deg from the vertical. As shown in Table 2, the $\overline{Nu}$ obtained for the upward-facing inclined cavity is higher than that for the downward-facing inclined cavity. The reason for this is that the inclination of the upward-facing cavity from the horizontal to 45 deg increases the buoyancy force and enhances the heat transfer from the cavity while in the case of the downward-facing inclined cavity, the buoyancy force is suppressed and therefore the heat transfer process is inhibited.

The Rayleigh numbers considered in the present experimental study are 1.0×10^4, 3.16×10^4, 1.0×10^5, and 5.0×10^5. These Ra numbers are calculated based on the width of the cavity, $w = 0.017$ m, 0.025 m, 0.36 m and 0.06 m, respectively at a fixed ΔT. For each Rayleigh number, the angles of inclination considered are 0, 30, 45, and 60 deg. The effect of aspect ratio ($A = 0.25$, 0.5, and 1.0) on heat transfer was investigated at $Ra = 5 \times 10^5$.

The following discussion of the flow and temperature characteristics and the rate of heat transfer from the cavities is based on the infinite fringe interferograms, which have been obtained from the experiments. References are also made to the numerical isotherms and stream-function distributions (or flow patterns) presented in section 5.

Temperature and Flow Characteristics Inside the Cavities

As indicated previously, air is the test medium in this study. Because the Prandtl number ($Pr = 0.71$) of air is close to unity, the thermal and hydrodynamic boundary layer thicknesses on the cavity walls will also be close. Therefore, the air-

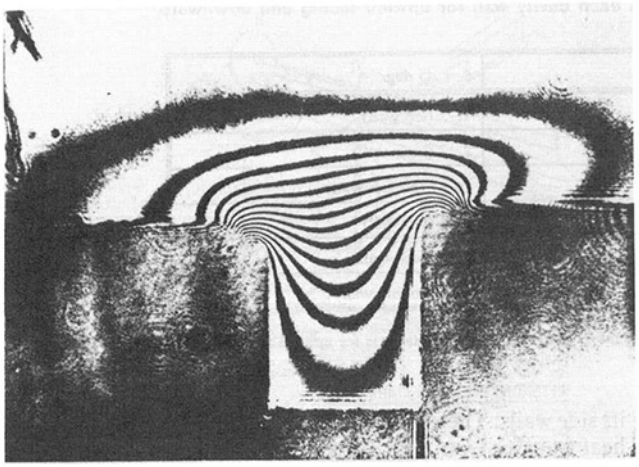

Fig. 4 Experimental isotherms showing the conduction/free convection transition at Ra = 10^3, θ = 0 deg

flow characteristics in the cavity can be inferred from the infinite interferograms that normally represent the isotherms.

Figure 4 shows the isotherms obtained at Ra = 10^3 for a cavity having isothermal base and walls. As shown in the figure, the infinite interferogram, which was uniformly bright before heating, begins to develop fringe shifts that are closely spaced in the aperture region but widely spaced inside the cavity. This is an indication of an onset of convection in the aperture region while heat transfer inside the cavity is by molecular conduction. The isotherms inside the cavity are symmetric. But in the aperture region and in the area outside the cavity the isotherms are not quite symmetric because of the vulnerability of the infinite interferograms to minor disturbances and vibrations. Because the natural convection has been fully established at Ra = 10^4, the isotherms obtained at Ra = 10^3 are considered to represent the transition from conduction to convection. This assumption has been validated by the present numerical prediction (see Fig. 7) where $\overline{Nu}$ = 0.396. The transition to convection at Ra = 10^3 has also been observed by Jacobs et al. (1974) and Schmidt (1984) for a cavity heated from both the base and the walls. For an open cavity heated from only the

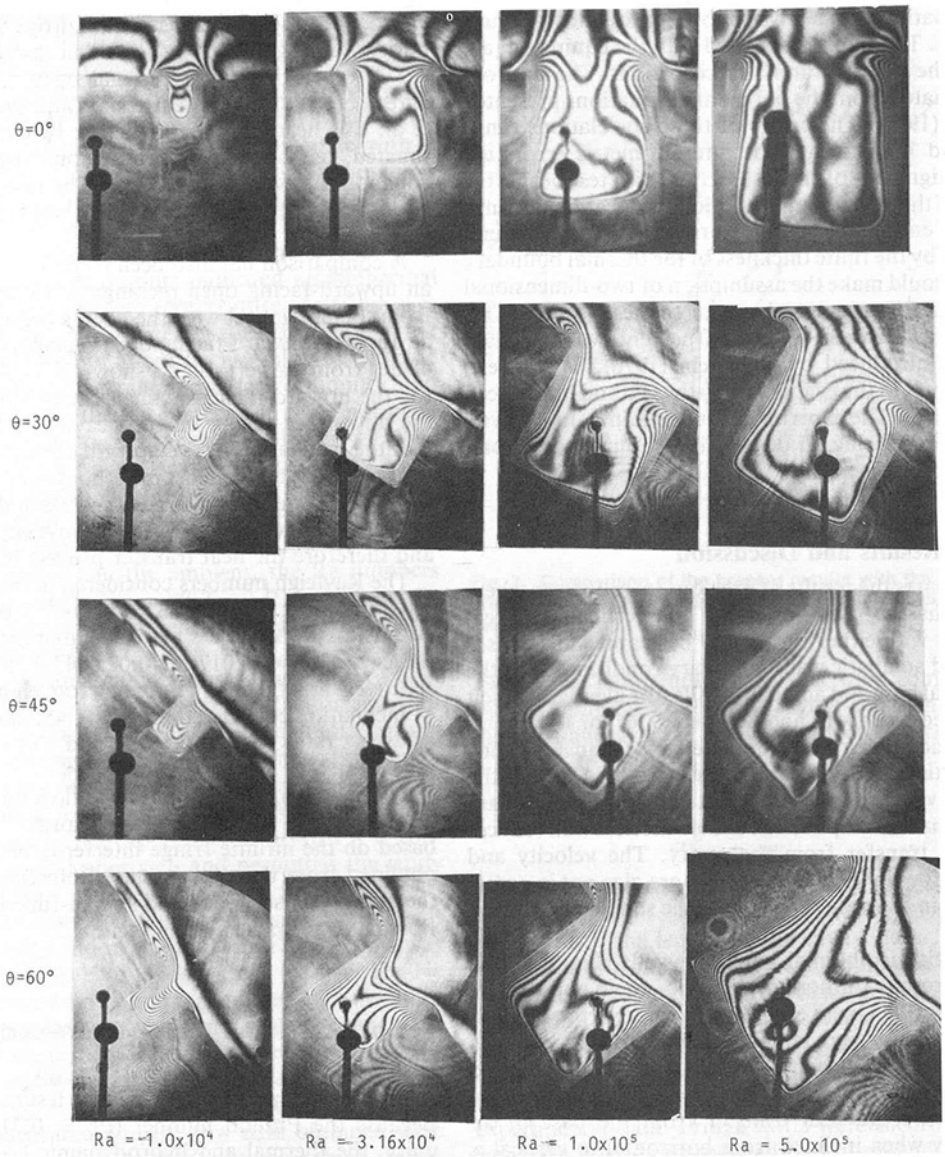

Fig. 5 Experimental isotherms for various Rayleigh numbers and inclination angles at A = 1.0

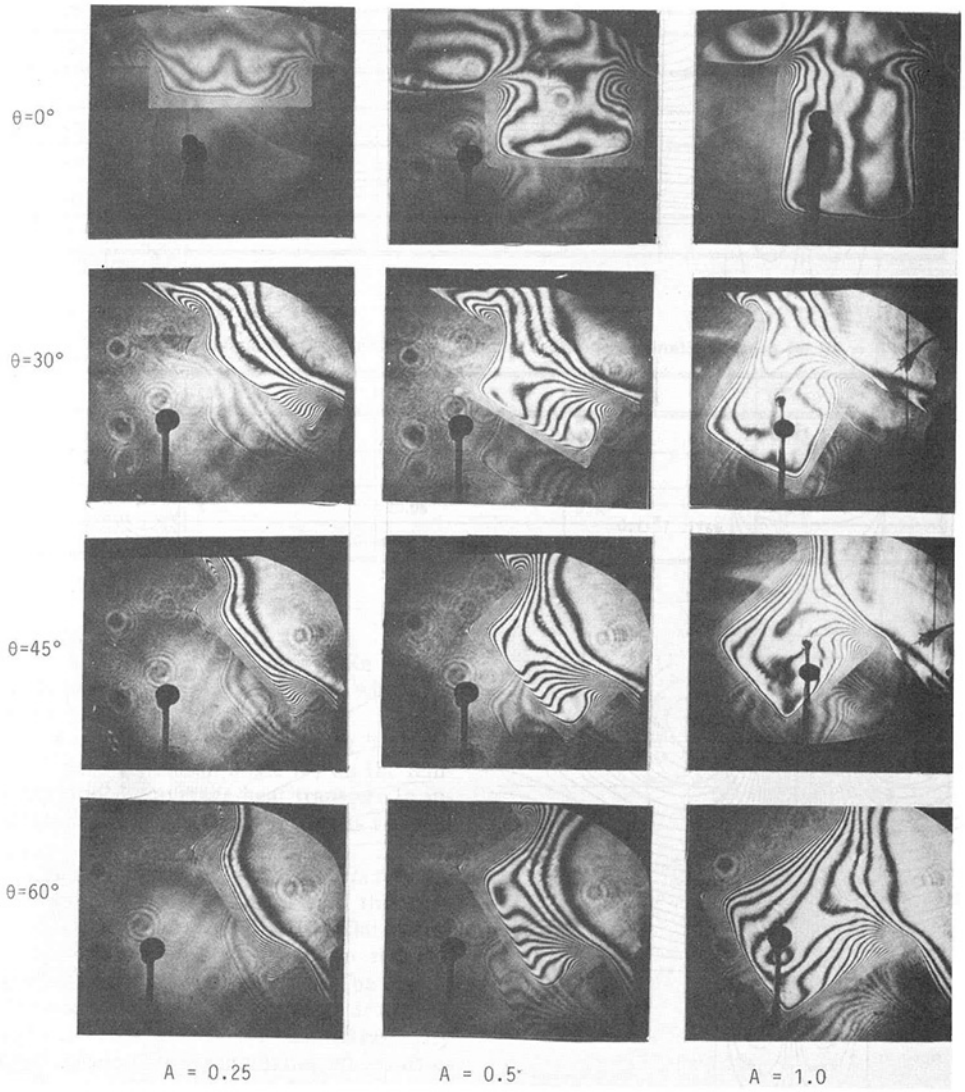

Fig. 6 Experimental isotherms for various cavity aspect ratios and inclination angles at Ra = 5.0 × 10^5

base, Jacobs and Mason (1976) have observed a delayed transition to convection, which occurred at Ra > 10^3.

As a basis for a further discussion of the temperature characteristics inside the cavity, a set of 16 interferograms that depict the isotherms in the cavity is shown in Fig. 5 for $10^4 \leq$ Ra 5 × 10^5 and 0 deg ≤ θ ≤ 60 deg at A = 1.0 Another set of 12 interferograms is shown in Fig. 6 for 0.25 ≤ A ≤ 1.0 and for the above range of θ at Ra = 5 × 10^5.

At θ = 0 deg and Ra = 10^4, the closely spaced isotherms in Fig. 5 indicate the convection has been established in the cavity, and unlike at Ra = 10^3, the convection extended to a deeper region of the cavity where a weak convection roll developed. At Ra = 3 × 10^4, the convection roll becomes larger and perhaps stronger, and at Ra = 10^5 the convection roll breaks into a pair of counterrotating primary rolls, which develop into multicellular secondary rolls at Ra ≥ 5 × 10^5. The convection flow characteristic described above is more clearly illustrated by the numerical isotherms and the streamfunction distributions in Fig. 7.

Figures 5 and 6 show that the higher the value of Ra, the larger the thermal gradient, and the thicker the developing thermal boundary layer along the vertical side-walls of the cavity. Goldstein and Eckert (1960) have also reported steady and unsteady state thermal boundary layer developments along a heated vertical flat plate. In that study the thermal boundary layer thickness increases with time to a steady state. But in the present study the thermal boundary layer thickness increases with Ra, and the interaction of the convective heat transfer from all three walls of the open rectangular cavity results in a more complex temperature distribution than observed by Goldstein and Eckert. As shown in Fig. 5, the heat transfer is characterized by flow instability, which leads to the formation of the two counterrotating cells at Ra = 5 × 10^5.

The effect of inclination of the cavity on the temperature and flow characteristics is shown by the twelve isotherms in Fig. 5. As shown in the figure, an increase in the value of θ from 0 deg to 30 deg at a given value of Ra causes a sudden flow instability and a rapid change in the flow and temperature patterns (see also Fig. 8). The symmetric flow and temperature distributions at θ = 0 deg have changed to nonsymmetric patterns at θ = 30 deg, and the development of thermal boundary layer on the base of the cavity could be noticed. An increase in θ beyond 30 deg appears to cause small change in the temperature distributions in the core region of the cavity, but may have significant effect on the developing thermal boundary layer and the thermal gradient on the walls. However, at a

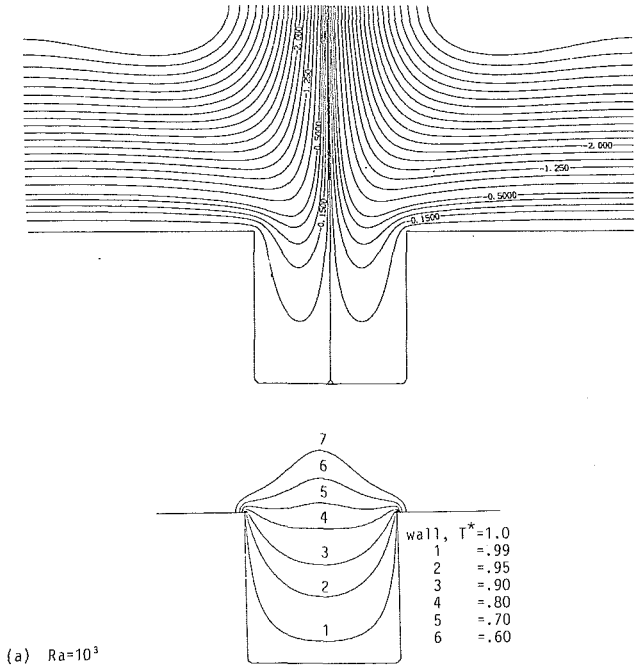

(a) Ra=10^3

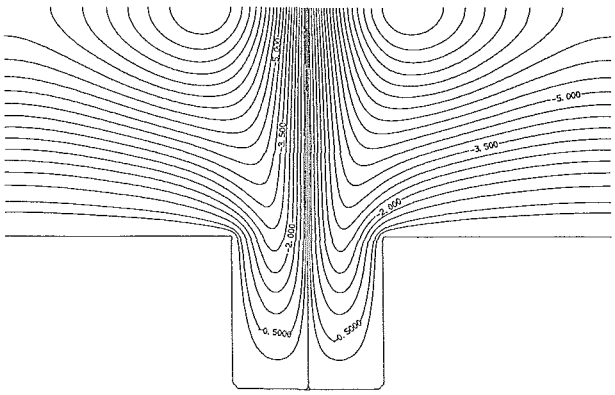

(b) Ra=10^4

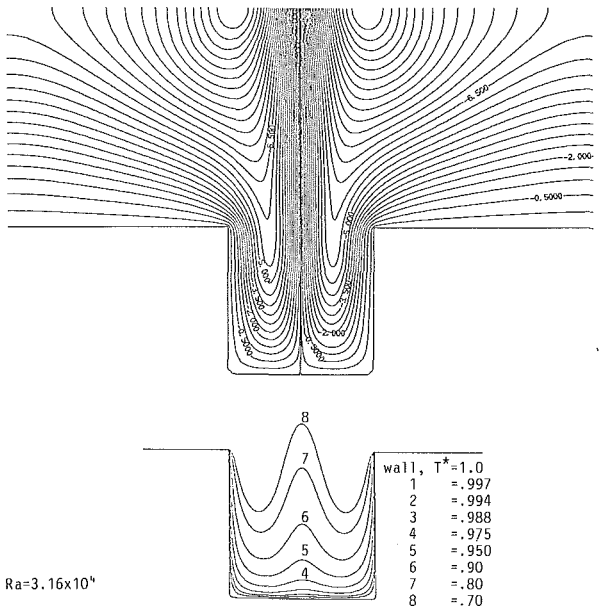

(c) Ra=3.16x10^4

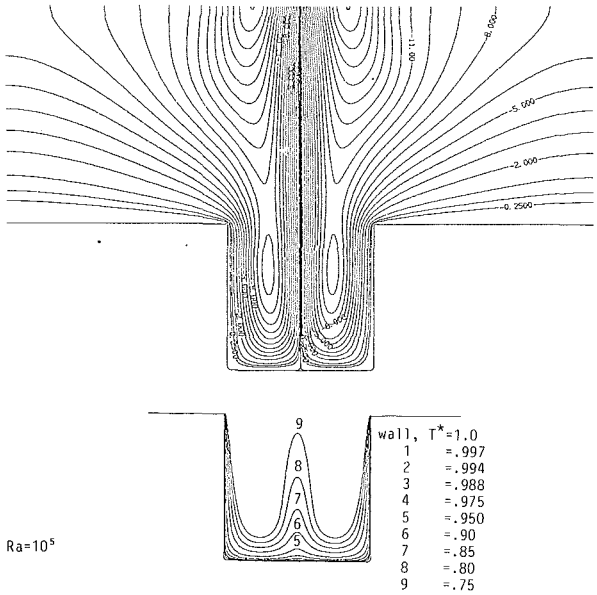

(d) Ra=10^5

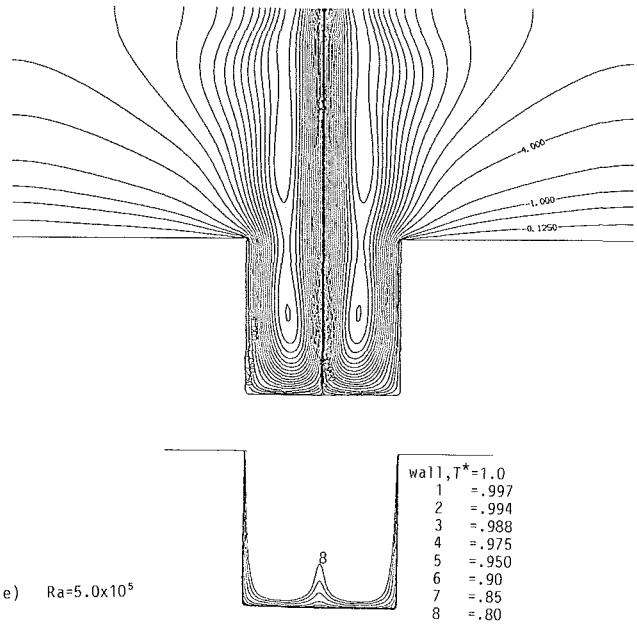

(e) Ra=5.0x10^5

Fig. 7 Numerically computed streamlines (left) and isotherms (right) for Ra = 10^3 to 5.0 × 10^5 at A = 1.0 and θ = 0 deg

fixed value of θ, Fig. 5 shows that temperature distributions change significantly as Ra increases. Table 3 shows that the average Nusselt number, $\overline{Nu}$, also varies with Ra and θ.

In all the cases of inclined cavities, the two upward-face walls, that is, a side-wall and the base, exhibit temperature and flow characteristics like those reported in literature for an upward-facing inclined flat plate. As in the case of inclined flat plate, these two walls enhance natural convection heat transfer from the cavity. The third wall, which is downward-faced, also acts like a downward-facing inclined flat plate, causing flow instability and inhibiting the convection heat transfer process. Lloyd and Sparrow (1970) have also observed flow instability along a downward-faced inclined flat plate. In the present situation, the flow instability propagates through the entire cavity, leading to a strong flow recirculation and thermal instability observed in Figs. 5, 6, and 8. A close look at the isotherms in Figs. 5, 6, and 8(b) and the local heat transfer profiles in Fig. 13 reveals that at the point of flow separation the temperature gradient and the local heat transfer

Table 3 Variation of average Nusselt number with Rayleigh number and inclination angles

Ra	θ = 0 deg.	θ = 30 deg.	θ = 45 deg.	θ = 60 deg.
1.0×10^4	1.73	1.50	1.75	1.55
3.16×10^4	2.41	2.83	2.49	2.90
1.0×10^5	3.78	4.51	4.84	4.95
3.16×10^5	4.85	8.58	7.62	6.91
5×10^5	6.31	9.90	9.38	9.26

Table 4 Variation of average Nusselt number with aspect ratio and inclination angles for Ra = 5×10^5

A	θ = 0 deg.	θ = 30 deg.	θ = 45 deg.	θ = 60 deg.
0 (Flat Plate)	9.01	10.76	12.30	14.36
0.25	10.73	8.44	8.33	8.25
0.5	8.82	10.08	9.06	9.26
1.0	6.31	9.90	9.38	9.26

are lower (for example, about 50 percent lower at Ra = 5×10^5 and θ = 45 deg) than at the reattachment point where the highest values are recorded.

Figure 6 and Table 4 show the effect of varying both the cavity aspect ratio (A) and inclination angle (θ) on the temperature characteristics and the average heat transfer. In investigating these parameters the Rayleigh number is fixed at Ra = 5×10^5.

At $A = 0$ and $\theta = 0$, the temperature and flow characteristics obtained in this study are in good agreement with those reported by Rotem and Claassen (1969) for horizontal flat plates. In a shallow cavity, $A = 0.25$, there is no formation of counterrotating convective rolls observed at $A = 1.0$. The reason is that in the shallow cavity, the flow that separates at the top corners of the vertical walls reattaches on the base of the cavity and therefore does not develop into recirculating eddies as in the case of a deep cavity. As A increases to 0.5, the separated flow no longer reattaches on the base and a single multicellular roll develops in the cavity. As previously indicated, the roll breaks into two symmetric rolls at $A = 1.0$. If A is increased further, that is $A \gg 1.0$, a series of multicellular rolls would form in the very deep cavity.

As θ increases from zero, various temperature and flow characteristics develop for various values of A (see Fig. 6). For example, at θ = 30 deg and $A = 0.25$, the flow that separates at the top corners reattaches on the base of the cavity with pockets of entrapped air in the region between the lower side-wall and the base of the inclined shallow cavity. These pockets of air becomes enlarged as A increases, and at A = 1.0, the pockets of air merged to form the two large recirculating eddies mentioned earlier. Figure 6 shows that the base of the inclined shallow cavity behaves like an inclinded flat plate with the thermal boundary layer developing along its length, becoming thicker as the value of θ increases. Increasing the values of A and θ is found to induce hydrodynamic flow instabilities as shown in Fig. 8. In the figure, a strong vortex appeared at the reattachment corner and a weaker one of opposite sign at the separation corner of the inclined cavity as observed by Charwat et al. (1961) in a study of separated forced convection flows over open cavities and by Showole (1988) in a study of mixed convection flows over an inclined open rectangular cavity.

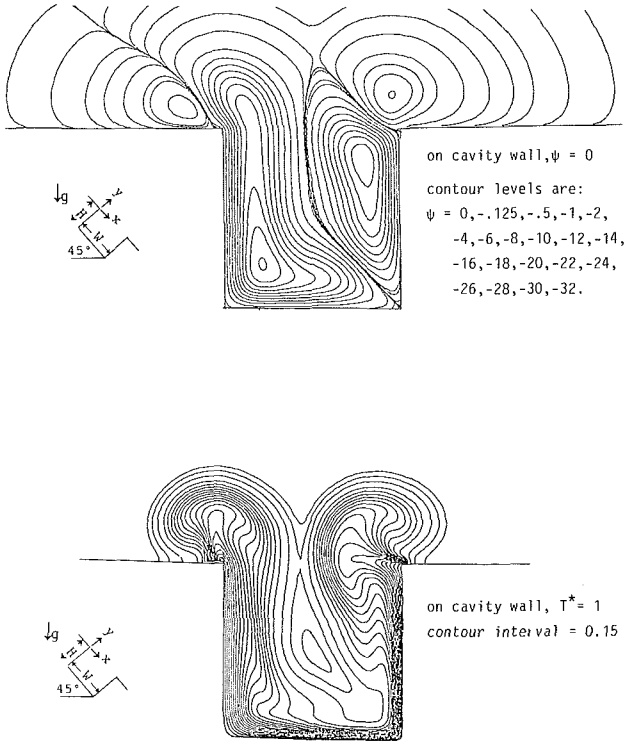

Fig. 8 Numerically computed (*a*) streamlines and (*b*) isotherms for inclined cavity, Ra = 5.0×10^5, A = 1.0, and θ = 45 deg

Heat Transfer

Heat transfer rates are determined from the infinite fringe interferograms shown in Figs. 5 and 6. The infinite fringe shifts of the interferograms are analyzed and the data obtained are used to evaluate the temperature gradients at nine points on each of the three cavity walls. Fringe analysis has been widely covered in the literature (see for example, Eckert and Soehngen, 1948). The local and average Nusselt numbers on each of the three cavity walls are then calculated using the temperature gradients at the nine points according to Eqs. (1) and (2). The overall heat transfer rate for the cavity is obtained from the summation of the average Nusselt numbers on all the three walls as follows:

$$\overline{\mathrm{Nu}}_{\mathrm{cavity}} = \frac{\overline{\mathrm{Nu}}_1 L_1 + \overline{\mathrm{Nu}}_2 L_2 + \overline{\mathrm{Nu}}_3 L_3}{L_1 + L_2 + L_3} \quad (3)$$

where L is the length of a cavity wall.

The uncertainly in $\overline{\mathrm{Nu}}$ due to the test section and the interferometer misalignment, the interferometer optical imperfection, error in locating the fringe center, the end effect, and other equipment errors was estimated to be 4.5 percent.

The experimental heat transfer results are summarized in Tables 3 and 4. The plot of $\overline{\mathrm{Nu}}$ against Ra for the horizontal cavity is shown in Fig. 3. Table 3 shows that at all angles of inclination considered in this study Nu increases as Ra increases. However, for all Ra numbers, the first increase in θ from 0 to 30 deg causes a sharp increase in $\overline{\mathrm{Nu}}$, but a further increase beyond 30 deg results in small increase in $\overline{\mathrm{Nu}}$. The local distributions on each of the cavity wall vary considerably with θ.

The variation of $\overline{\mathrm{Nu}}$ with θ and A is complex. As shown in Table 4, $\overline{\mathrm{Nu}}$ increases as A decreases when $\theta = 0$ deg. But for $\theta > 0$ deg, there is no significant change in $\overline{\mathrm{Nu}}$ as A decreases except at $A = 0$, which corresponds to a flat plate situation. Ostrach (1953) and Siebers et al. (1983) have investigated natural convection flows over vertical flat plates using analytical and experimental techniques, respectively. The data obtained in the present study for horizontal and inclined flat plates are included for comparison with data for open cavities. For the upward-facing flat plates, the thermal boundary layer grows thicker as θ increases than in the case of an open cavity. This results in higher thermal gradients and heat transfer rates in the flat plate than in the cavity for all values of θ except at $A = 0.25$ and $\theta = 0$ deg. As A increases from 0 to 0.25, that is, from a flat plate to a shallow cavity, the lower corners that exist between the base and the side-walls of the cavity alter the growing boundary layer pattern observed on a flat plate and cause the heat transfer rate to drop. A further increase in A at a fixed θ (except $\theta = 0$) or an increase in θ at a fixed value of A (except at $A = 0$.) does not change the value of $\overline{\mathrm{Nu}}$ significantly. But as shown in Figs. 5 and 6, the temperature characteristics vary considerably as a result of flow separation and reattachment processes in the cavity.

The complex variation of $\overline{\mathrm{Nu}}$ with Ra, θ, and A discussed in the foregoing sections makes it rather difficult to express $\overline{\mathrm{Nu}}$ in terms of all these parameters in one equation. The effect of aspect ratio has even been shown above to be insignificant except on the temperature distributions. But as shown in Table 3, for a fixed value of θ, $\overline{\mathrm{Nu}}$ varies significantly with Ra. Therefore, for every value of θ considered in this study, a correlation equation is obtained for $\overline{\mathrm{Nu}}$ as a function of Ra. Previous investigators have adopted similar correlations for $\overline{\mathrm{Nu}}$ in terms of Ra (see Table 1) for the same reason given here.

The correlations for the overall average heat transfer rate ($\overline{\mathrm{Nu}}$) obtained in the present experimental study for upward-facing horizontal and inclined cavities are given as:

For $\theta = 0$ deg:

$$\overline{\mathrm{Nu}} = 0.088\ \mathrm{Ra}^{0.323} \quad (4)$$

The standard deviation of this correlation is 10 percent.

For $\theta = 30$ deg:

$$\overline{\mathrm{Nu}} = 0.018\ \mathrm{Ra}^{0.484} \quad (5)$$

The standard deviation of this correlation is 9 percent.

For $\theta = 45$ deg:

$$\overline{\mathrm{Nu}} = 0.028\ \mathrm{Ra}^{0.442} \quad (6)$$

The standard deviation of this correlation is 12 percent.

For $\theta = 60$ deg:

$$\overline{\mathrm{Nu}} = 0.029\ \mathrm{Ra}^{0.439} \quad (7)$$

The standard deviation of this correlation is 15 percent.

The above correlation equations are obtained in the range of Rayleigh number, $10^4 \le \mathrm{Ra} \le 5.0 \times 10^5$.

Governing Equation for the Numerical Simulation

The objective of the numerical analysis was to validate and provide further insight into the heat transfer results obtained from the experimental study. The flow under consideration here is steady, two dimensional, and incompressible, with negligible viscous heat dissipation. Assuming the Boussinesq approximation, the governing equations that applied to the physical problem in Fig. 1 are the conservation of mass, momentum and energy. In dimensionless forms, they are written in stream-function and vorticity formulation as follows:

$$\partial\psi/dy \quad \partial\omega/\partial x - \partial\psi/\partial x\ \partial\omega/\partial y = \mathrm{Ra\ Pr}\ (\sin\theta \partial T^*/\partial x + \cos\theta \partial T^*/\partial y) + \mathrm{Pr}(\partial^2\omega/\partial x^2 + \partial^2\omega/\partial y^2) \quad (8)$$

$$\partial\psi/\partial y\ \partial T^*/\partial x - \partial\psi/\partial x\ \partial T^*/\partial y = \partial^2 T^*/\partial x^2 + \partial^2 T^*/\partial y^2 \quad (9)$$

$$\partial^2 x/\partial x^2 + \partial^2\psi/\partial y^2 = -\omega \quad (10)$$

The x and y components of velocity may be calculated by:

$$u = \partial\psi/\partial y \text{ and } v = -\partial\psi/\partial x \quad (11)$$

The nondimensional quantities are defined as $x = X/w$, $y = Y/w$ or Y/H, $u = Uw/\alpha$, $v = Vw/\alpha$, and $T^* = (T - T_\infty)/(T_w - T_\infty)$, where α is the thermal diffusivity.

The boundary conditions that applied to the present problem (Fig. 1) are $T^* = 1$ on all the cavity walls, AB, BC, CD, and $T^* = 0$ on the free surface FG above the cavity. The walls AH and DE at the proximity of the aperture plane were taken to be adiabatic, i.e., $\partial T^*/\partial x = 0$. At the nonsolid boundaries GH and EF, the derivative boundary condition $\partial T^*/\partial X = 0$ was used.

At the solid boundaries, no slip and no penetration applied; therefore, $u = v = 0$ while ψ was constant and taken to be zero. Boundary vorticity was therefore, evaluated by the formula:

$$\omega = -\partial^2\psi/\partial x^2 = -\partial^2\psi/\partial y^2 \text{ on } AB, BC, \text{ and } CD \quad (12)$$

$$\omega = -(\partial^2\psi/\partial x^2 + \partial^2\psi/\partial y^2) \text{ on } EF, FG, \text{ and } GH \quad (13)$$

Also

$$\partial\psi/\partial x = 0 \text{ on } EF \text{ and } GH \quad (14)$$

and

$$\partial\psi/\partial y = 0 \text{ on } FG \quad (15)$$

Equations (8)–(15) were approximated by a finite difference method following a procedure outlined by Dennis and Hudson (1978). Matrices of the coefficients of the difference equations derived using this procedure are always diagonally dominant in the range of Rayleigh numbers, which includes those covered in this study, and the results obtained were accurate to the order of h^2, where h is the finite difference grid. The algebraic equations derived from the difference equations were solved using uniform grids at the internal points in the solution domain (see Fig. 1). A uniform rather than a scattered grid was used because accuracy is essential in the entire solution domain in order to compare positively the numerical and the experimental isotherms. In solving the algebraic equations, a successive overrelaxation scheme (see, for example, Burgraf, 1966) was used. A careful choice of relaxation factor, κ, for the Poisson, vorticity, and energy equations ensures the stability and rapid convergence of the steady-state solutions. Because the iterative procedure for the vorticity and energy equations can be sensitive to the relaxation factor, α range of this factor, $0 < \kappa < 1$, was considered in every run of the numerical computation.

Numerical Results and Discussion

The parameters considered in the numerical study are Pr =

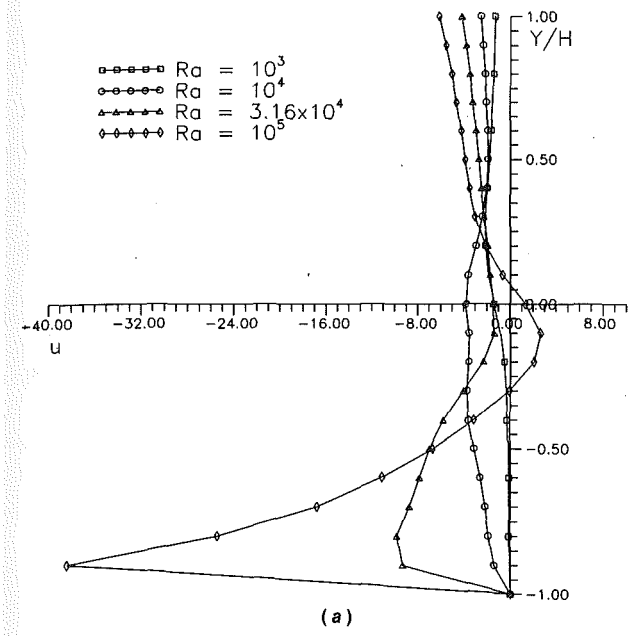

(a)

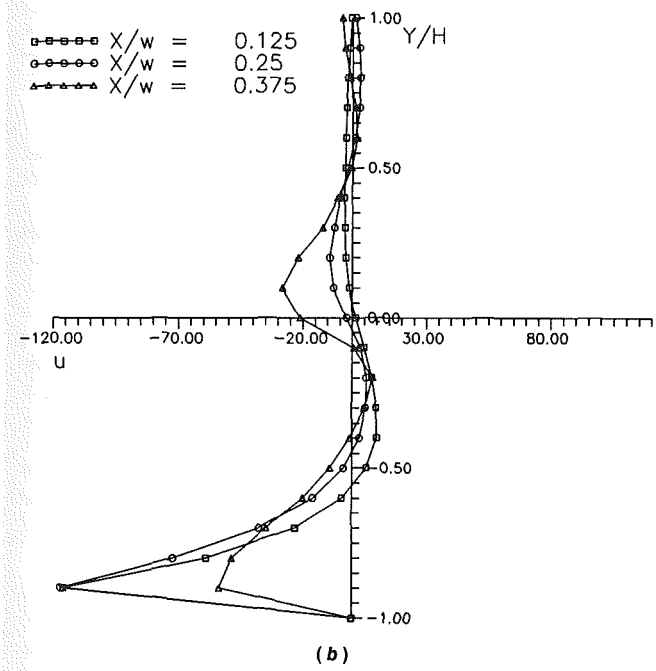

(b)

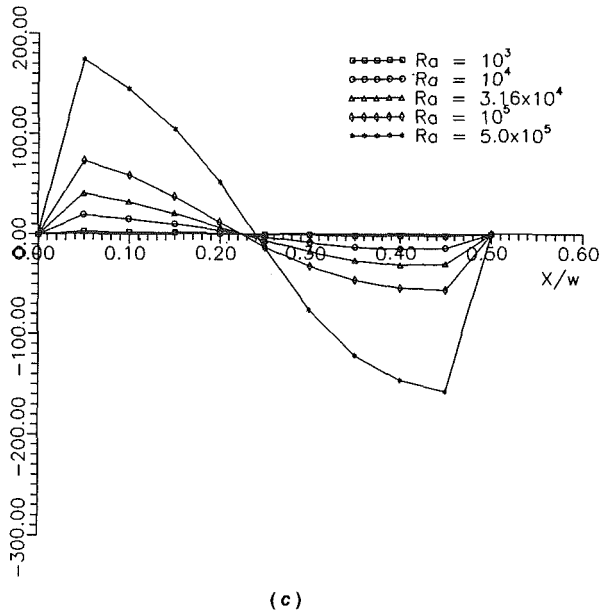

(c)

Fig. 9 (*a*) Profiles of u component of velocity for Ra = $10^3$to 10^5 at $x = \pm0.25$, $A = 1.0$, $\theta = 0$ deg; (*b*) profiles of u component of velocity for Ra = 5×10^5 at $x = \pm0.125$, ±0.25, and ±0.375, $A = 1.0$, $\theta = 0$ deg; (*c*) profiles of v component of velocity for Ra = 10^3 to 5×10^5 at $y = 0$, $A = 1.0$, $\theta = 0$ deg

0.71 and $A = 1.0$. Results are presented for horizontal cavity in the range of Rayleigh number, $10^3 \leq \text{Ra} \leq 5 \times 10^5$, at $\theta = 0$ deg. The effect of inclination on heat transfer from the cavity is investigated at Ra = 5×10^5 and $\theta = 45$ deg. A transformation analysis technique introduced by Shanks (1955) was used to determine the optimum grid size of 0.0125 (or 80 × 80 grids) used in the numerical computation. The general procedure was to use the results obtained at a larger grid size or a lower Ra number as the initial values or conditions for the numerical computation at a smaller grid or a higher Ra in order to speed up the convergence of the solution and reduce the cost of computation. The numerical solution is converged when $|\psi^{n+1} - \psi^n| \leq 10^{-6}$ where n is the number of the iteration.

The numerically computed streamlines and isotherms in horizontal cavities are shown in Fig. 7 for Ra = 10^3 to 5×10^5. A study of the streamlines and the isotherms indicates that at Ra = 10^3, heat transfer in the cavity is by conduction. This validates the experimental result presented earlier in Fig. 4. As Ra is increased beyond the transition Rayleigh number (i.e., Ra = 10^3), the rate of convection heat transfer from the cavity increases. At Ra = 10^5, the streamlines develop into counterrotating rolls, which at Ra = 5×10^5 become multicellular. The strong flow recirculation occurring at this Rayleigh number is due to a high rate of inflow of cold air and outflow of hot air from the cavity, which causes a high rate of heat transfer as shown by the high thermal gradient along the cavity walls.

At 45 deg inclination, the streamlines in Fig. 8(*a*) give an indication of flow separation at the lower corner and flow reattachments at the upper corner of the aperture. The rate of inflow and outflow of air into and out of the cavity appear to be more rapid that at $\theta = 0$ deg. The flow consists of two counterrotating eddies as observed at $\theta = 0$ deg, but at $\theta = 45$ deg, the relative positions of the eddies appear to have shifted due to the inclination of the cavity. As seen in Fig. 8(*a*), the flow pattern is more complex than in the horizontal case. And as mentioned earlier, Fig. 8(*a*) reveals the presence of a strong vortex at the reattachment corner and a weaker vortex of opposite sign at the separation corner of the inclined cavity. A study of the isotherms in Fig. 8(*b*) also reveals that the temperature distribution is more complex in the inclined than in the horizontal cavity. This indicates that a higher rate of heat tansfer occurs in inclined than in the horizontal cavity. In the inclined cavity, the thermal gradient at the flow reattachment point is about twice the value at the flow separation point. Chapman (1956) has observed a similar relationship between heat transfer coefficients at separation and reattachment points in forced convection separated flows over cavities. In that study the heat transfer coefficient at reattachment is about three times the value at the separation point.

Velocity and Temperature Profiles. The velocity profiles in the horizontal cavity are shown in Fig. 9(*a*), 9(*b*), and 9(*c*). The horizontal axis in these figures represents the aperture plane of the cavity, while the areas below and above the axis represent the cavity and the free stream, respectively. Figure 9(*a*) shows the profiles of u component of the velocity at the location $x = \pm0.25$ (from the base to the region outside the

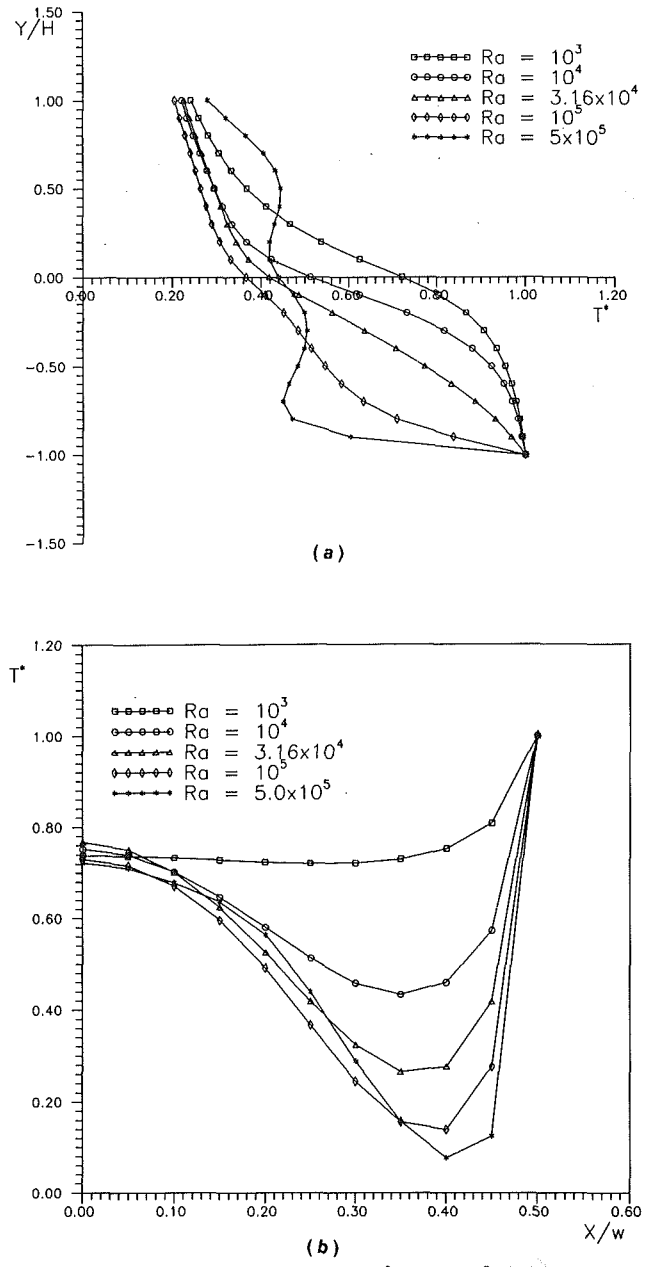

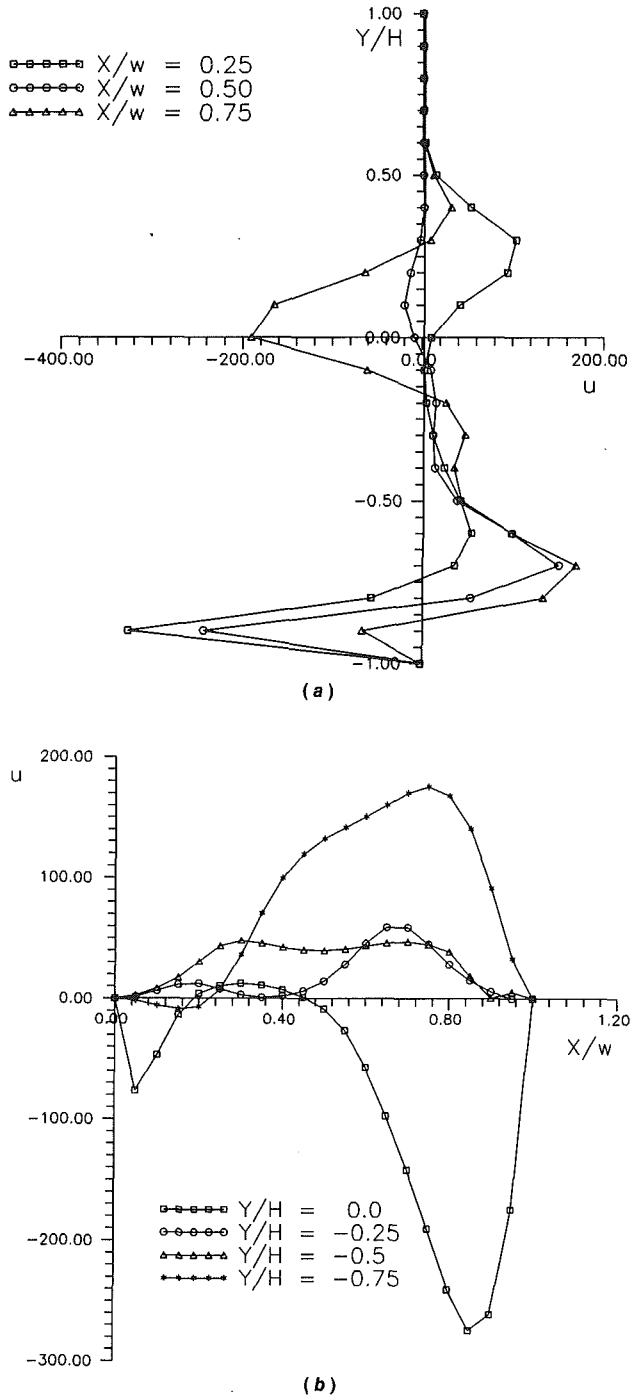

Fig. 10 Temperature profiles for Ra = 10^3 to 5 × 10^5 at (*a*) $x = \pm 0.25$ and (*b*) $y = 0$; $A = 1.0$ and θ = deg

cavity) for Ra = 10^3, 10^4, 3.16×10^4, and 10^5. For Ra = 5×10^5, the profiles of u are obtained at $x = \pm 0.125$, ± 0.25, and ± 0.375 as shown in Fig. 9(*b*). The profiles of the v component are obtained along the aperture plane ($y^* = 0$) of the open cavity as shown in Fig. 9(*c*). A close look at Fig. 9(*a*) reveals that at Ra = 10^3, the air velocity inside the cavity is close to zero, except at aperture region where values much greater than zero are recorded. This indicates that the air inside the cavity as observed in the streamlines is stagnant, and validates the experimental isotherm (Fig. 4), which also indicates that the heat transfer inside the cavity at Ra = 10^3 is by conduction. Figure 9 shows that as Ra increases so also does the air velocity inside the cavity. The recirculating eddies observed in the streamlines at Ra = 10^5 and 5×10^5 (see Fig. 7) can also be inferred from the velocity profiles shown in Figs. 9(*a*) and (*b*). At all Ra numbers considered, Fig. 9(*c*) shows that the v component of the velocity has a sinusoidal profile. This is an indication of an oscillating flow at the aperture region. As shown in Fig. 9(*c*), the amplitude of the oscillating flow increases as the flow becomes more unstable at higher values of Ra.

Figures 10(*a*) and 10(*b*) show the temperature profiles in the horizontal cavity. At $x = \pm 0.25$, temperature profiles are obtained for various values of Ra as shown in Fig. 10(*a*). The temperature profiles along the aperture region are shown in Fig. 10(*b*). The temperature profile grows gradually from a small profile in conduction mode (Ra = 10^3) to a large profile in convection mode (Ra = 5×10^5). The profiles also show that the temperature drops steadily outside the cavity, approaching the free-stream value attained at a distance twice the depth of the cavity from the aperture.

For the inclined cavity, the u profiles are obtained at selected values of x across the width of the cavity and at selected values of y along the height of the cavity as shown in Figs. 11(*a*) and

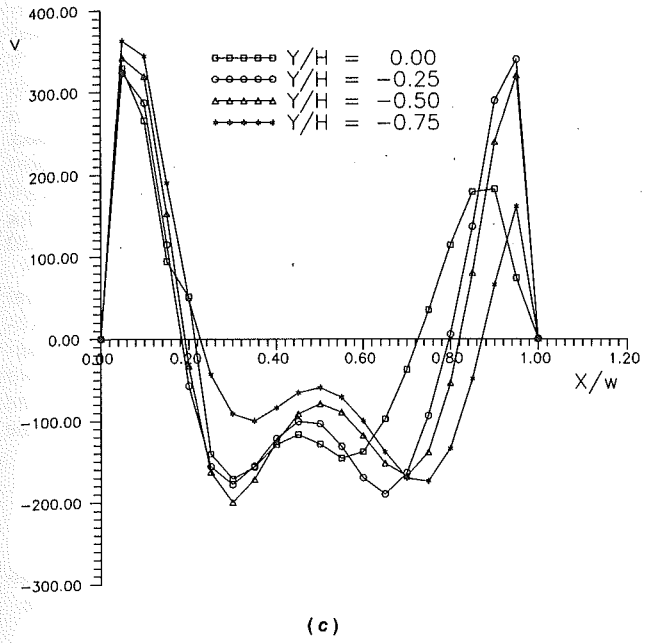

(c)

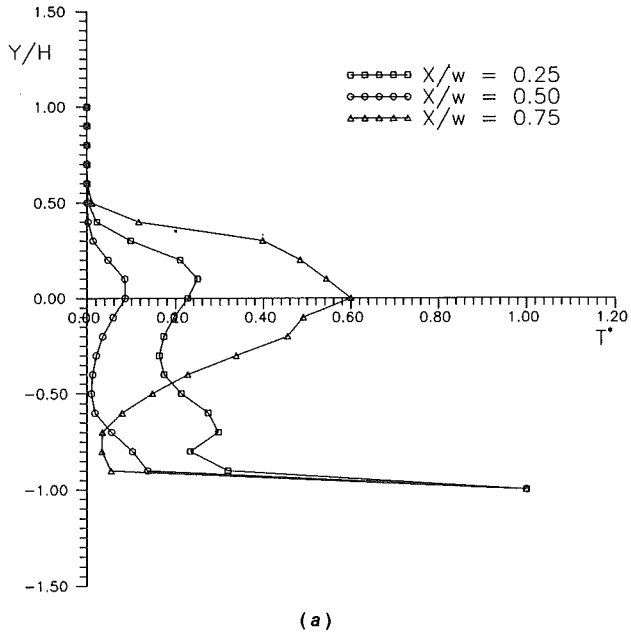

(a)

Fig. 11 (*a*) Profiles of u component of velocity for Ra = 5 × 10^5 at x = 0.25, 0.5, 0.75, A = 1, and θ = 45 deg; (*b*) and (*c*) profiles of u and v components of velocity for Ra = 5 × 10^5 at y = 0, −0.25, −0.5, and −0.75, A = 1.0, θ = 45 deg

11(*b*), respectively. The v profiles are also obtained at selected values of y along the height of the cavity (see Fig. 11*c*). Unlike in the horizontal case, these profiles are irregular, indicating the flow in the inclined cavity is very unstable. The flow instability results in a very strong flow recirculation, which makes the rate of free convection heat transfer higher in the inclined cavity than in horizontal cavity (see Table 3). The temperature profiles are shown in Figs. 12(*a*) and 12(*b*). These profiles show the erratic pattern of the temperature distributions in inclined cavity as previously observed in the isotherms (Fig. 8*b*). In the region outside the cavity, the profiles show the drop in temperature to the free-stream value. A careful study of Fig. 12(*b*) reveals that at x = 0, that is, at the flow reattachment point, the temperature gradient is higher than at the flow separation point (x = 1).

Local Heat Transfer Distribution. Figures 13(*a*) and 13(*b*) show the distribution of local Nusselt number at Ra = 5 × 10^5 and at θ = 0 and 45 deg, respectively. As shown in Fig. 13(*a*), the heat transfer in the horizontal cavity is symmetric, with the highest value of Nu_1 recorded at the aperture corners of the cavity. For the inclined cavity, Fig. 13(*b*) shows that the heat transfer from the base and the upward-facing sidewall (see also Fig. 8*b*) are about the same. The reason is that the two walls are upward-faced and are inclined at an equal angle from the horizontal. As shown in Fig. 8, the third wall with lower heat transfer rate than the other two sides is downward-faced. This again shows that a downward-facing inclined wall inhibits heat transfer while an upward-facing inclined wall enhances the that transfer process. Figure 13(*b*) also shows that the heat transfer rate at the flow reattachment point is higher than at the flow separation point. The higher average heat transfer rate from the cavity at θ = 45 deg than at θ = 0 deg shows that inclination enhances the rate of heat transfer.

A least-square fit for the numerical heat transfer data at θ = 0 deg yields a correlation equation of the form:

$$\overline{Nu} = 0.027\ Ra^{0.414} \tag{16}$$

for the range 3.16 × 10^4 ≤ Ra ≤ 5.0 × 10^5. The standard deviation of the correlation equation is 7 percent. The plot of the Nu against Ra at θ = 0 deg is shown in Fig. 3.

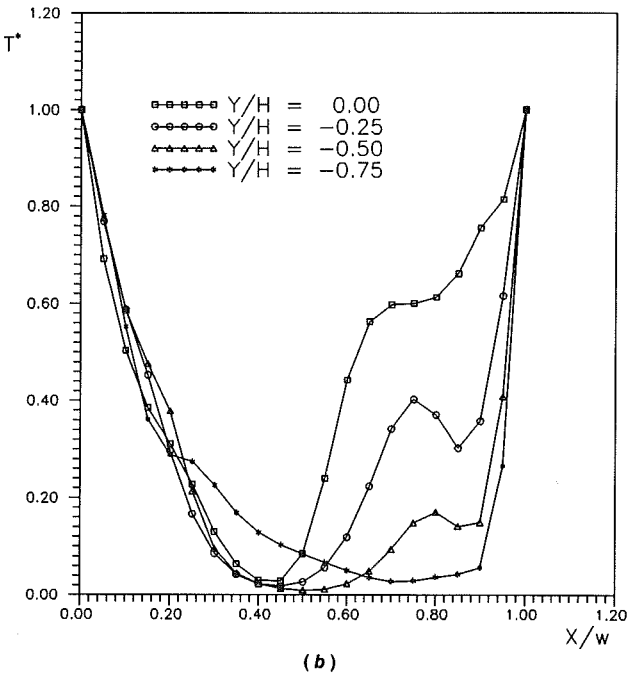

(b)

Fig. 12 Temperature profiles for Ra = 5 × 10^5 at (*a*) x = 0.25, 0.5, 0.75, and (*b*) y = 0, −0.25, −0.5, −0.75; A = 1.0 and θ = 45 deg

Summary and Conclusions

Natural convection with flow separation in upward-facing inclined rectangular cavities has been investigated numerically and experimentally. The local temperature distribution and the local and average heat transfer are computed and measured. Also computed are the numerical temperature and velocity profiles. For Ra ≤ 10^3, heat is transferred inside the cavity primarily by molecular conduction. However, there is an onset of convection in the aperture region of the cavity at this Rayleigh number.

As Ra is increased further, the contribution to heat transfer by convection increases and thermal boundary layers begin to develop along the vertical walls. The observation of the experimental interferograms and the numerical steamlines and isotherms for Ra ≥ 10^5 reveals that there are two counter-

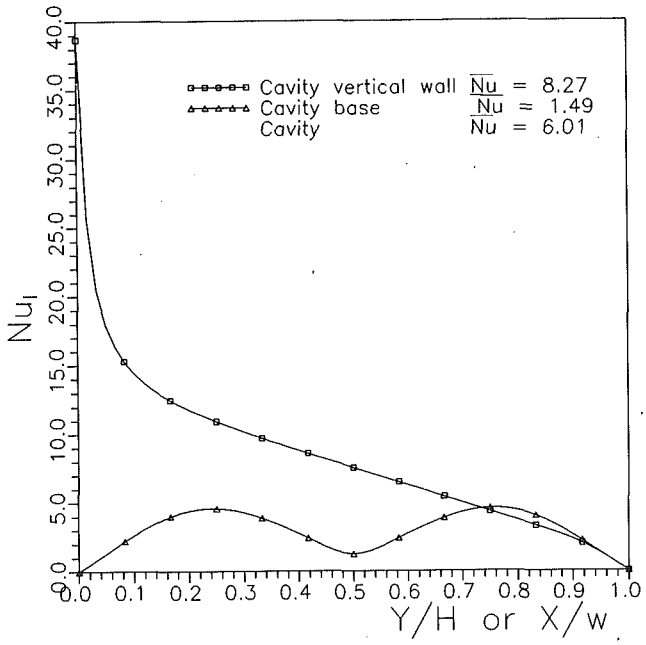

(a)

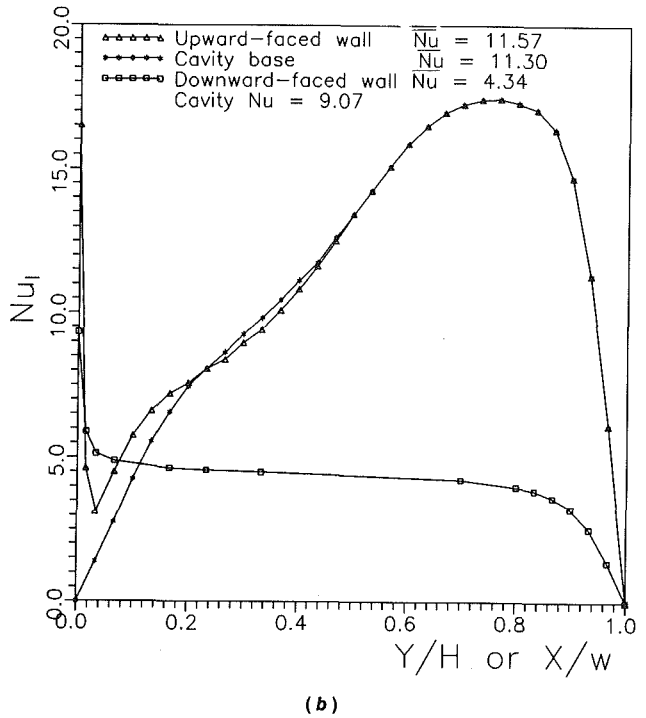

(b)

Fig. 13 Local Nusselt number distributions and the average Nusselt number in (*a*) horizontal and (*b*) inclined (θ = 45 deg) cavities for Ra = 5.0 × 10^5, A = 1.0

rotating convection rolls within the cavity, while at Ra < 10^5, there is only one primary convective roll. The natural convection and the prevailing counterrotating eddies are symmetric at θ = 0 deg, while at θ > 0 deg, the symmetric flow and temperature patterns no longer exist. For inclined cases, the convective rolls shifts in proportion to the degree of inclination. The effect of inclination was to alter the temperature distribution and the local heat transfer rate and to enhance the average heat transfer from the cavity. For all Ra numbers, the initial inclination of the cavity from 0 deg causes a significant increase in average heat transfer rate, but a further increase in the inclination angle appears to cause small increase in average heat transfer rate. However, for every angle of inclination considered, $\overline{Nu}$ increases significantly as Ra increases. Therefore, correlation equations for $\overline{Nu}$ are presented as a function of Ra for every angle of inclination considered in this study.

At θ = 0 deg, average heat transfer rate increases as aspect ratio is decreased. For inclined cases there is no significant increase in average heat transfer rate as aspect ratio is decreased except at A = 0, the case of a flat plate. The effect of decreasing aspect ratio is strong on the flow, temperature, and the local heat transfer distributions.

The heat transfer rate from the upward-facing horizontal cavity is about the same as in an open cavity with a sideward-facing vertical aperture, although the flow patterns, the temperature, and the local heat transfer distributions in the two cavities are different. When the two cavities are inclined, the one that is upward-faced enhances heat transfer while the downward-faced cavitiy tends to suppress it.

Acknowledgments

The authors wish to acknowledge the support from the Natural Sciences and Engineering Research Council of Canada.

References

Burgraf, O. R., 1966, "Analytical and Numerical Studies of the Structure of Steady Separated Flows," *Journal of Fluid Mechanics*, Vol. 24, part 1, pp. 113–151.

Chan, Y. L., and Tien, C. L., 1985, "A Numerical Study of Two-Dimensional Natural Convection in Square Open Cavities," *Numerical Heat Transfer*, Vol. 8, pp. 65–80.

Chapman, D. R., 1956, "A Theoretical Analysis of Heat Transfer in Regions of Separated Flow," NACA Technical Report No. 3792.

Charwat, A. F., Dewey, C. F., Jr., Roos, J. N., and Hitz, J. A., 1961, "An Investigation of Separated Flows—Part II: Flow in the Cavity and Heat Transfer," *Journal of Aerospace Sciences*, Vol. 28, No. 7, pp. 513–527.

Chen, K. S., Humphrey, J. A. C., and Sherman, F. S., 1985, "Free and Mixed Convective Flow of Air in a Heated Cavity of Variable Rectangular Cross-Section and Orientation," *Phil. Trans. R. Soc. London*, Vol. A316, pp. 57–84.

Chilcott, R. E., 1967, "A Review of Separated and Reattaching Flows With Heat Transfer," *International Journal of Heat and Mass Transfer*, Vol. 10, pp. 783–797.

Dennis, S. C. R., and Hudson, J. D., 1978, "A Difference Method for Solving the Navier–Stokes Equations," *Proceedings of the 1st International Conference on Numerical Methods in Laminar and Turbulent Flows*, University College Swansea, Swansea, United Kingdom, pp. 69–80.

Eckert, E. R. G., and Soehngen, E. E., 1948, "Studies on Heat Transfer in Laminar Free Convection With the Zehnder–Mach Interferometer," United States Air Force Technical Report No. 5747.

Goldstein, R. J., 1976, "Optical Techniques for Temperature Measurement," *Measurements in Heat Transfer*, E. R. G. Eckert and R. J. Goldstein, eds., McGraw-Hill, New York.

Goldstein, R. J., and Eckert, E. R. G., 1960, "The Steady and Transient Free Convection Boundary Layer on a Uniformly Heated Vertical Plate," *Int. J. Heat Mass Transfer*, Vol. 1, pp. 208–218.

Hess, C. F., and Henze, R. H., 1984, "Experimental Investigation of Natural Convection Losses From Open Cavities," ASME JOURNAL OF HEAT TRANSFER, Vol. 106, pp. 333–338.

Jacobs, H. R., and Mason, W. E., Jr., 1976, "Natural Convection in Open Rectangular Cavities With Adiabatic Side Walls," *Proceedings of the 1976 Heat Transfer and Fluid Mechanics Institute*, Stanford University Press, Stanford, Ca, pp. 33–46.

Jacobs, H. R., Mason, W. E., Jr., and Hikida, E. T., 1974, "Natural Convection in Open Rectangular Cavities," *Proceedings of the 5th International Heat Transfer Conference*, Tokyo, Vol. 3, pp. 90–94.

Kraabel, J. S., 1983, "An Experimental Investigation of the Natural Convection From a Side-Facing Cubical Cavity," *Proceedings of the ASME–JSME Thermal Engineering Joint Conference*, Honolulu, HI, Vol. 1, pp. 299–306.

Le Quere, P., Humphrey, J. A. C., and Sherman, F. S., 1981, "Numerical Calculation of Thermally Driven Two-Dimensional Unsteady Laminar Flow in Cavities of Rectangular Cross-Section, *Numerical Heat Transfer*, Vol. 4, pp. 249–283.

Lloyd, J. R., and Sparrow, E. M., 1970, "On the Instability of Natural Convection Flow on Inclined Plates," *Journal of Fluid Mechanics*, Vol. 42, part 3, pp. 465–470.

Mirenayat, H., 1983, "Etude Experimentale de Transport de Chaleur par Convection Naturale dans un Cavite Isotherme Ouverte," Ph.D. Thesis, University of Poitiers, France.

Ostrach, S., 1953, "An Analysis of Laminar Free Convection Flow and Heat Transfer About a Flat Plate Parallel to the Direction of the Generating Body Force," NACA Technical Report No. 1111, pp. 1–17.

Penot, F., 1982, "Numerical Calculation of Two-Dimensional Natural Convection in Isothermal Open Cavities," *Numerical Heat Transfer*, Vol. 5, pp. 421–437.

Rotem, Z., and Claassen, L., 1969, "Natural Convection Above Unconfined Horizontal Surfaces," *Journal of Fluid Mechanics*, Vol. 38, part, 1, pp. 173–192.

Schmidt, R. C., 1984, "A Numerical Study of Natural Convection in Upward-Facing Open Cavity," M.Sc. Thesis, The University of Utah, Salt Lake City, UT.

Shanks, D., 1955, "Non-linear Transformation of Divergent and Slowly Convergent Sequences," *Journal of Mathematics and Physics*, Vol. XXXIV, pp. 1–42.

Showole, R. A., 1988, "An Interferometric and Numerical Study of Free and Mixed Convective Heat Transfer From Open Rectangular, Semi-cylindrical, and V-shaped Isothermal Cavities," Ph.D. Thesis, The University of Western Ontario, London, Ontario, Canada.

Siebers, D. L., Moffat, R. J., and Schwing, R. G., 1983, "Experimental Variable Properties Natural Convection From a Large, Vertical, Flat Surface," Paper No. ASME-H-44, presented at the ASME-JSME Thermal Engineering Joint Conference, Honolulu, HI.

Touloukian, Y. S., Powell, R. W., Ho, C. Y., and Kiemens, P. G., 1970, *Thermophysical Properties of Matter—The TPRC Data Series*, IFI/Plenum Data Corporation, New York.

Combined Heat and Mass Transfer by Natural Convection With Opposing Buoyancies

R. L. Mahajan

D. Angirasa

Department of Mechanical Engineering,
University of Colorado,
Boulder, CO 80309-0427

A numerical study is presented for combined heat and mass transfer by natural convection from a vertical surface with opposing buoyancy effects. A comparison with similarity solutions shows that boundary layer analysis is suitable only when the two buoyant forces aid each other. For opposing flows the boundary layer analysis does not predict the transport rates accurately. A detailed comparison with experimental data with opposing buoyancies shows good agreement between the data and the numerical solutions. The heat and mass transfer rates follow complex trends depending on the buoyancy ratio and the Prandtl and Schmidt numbers. Comprehensive Nusselt and Sherwood number data are presented for a wide range of thermal Grashof number, buoyancy ratio, and Prandtl and Schmidt numbers.

1 Introduction

Natural convection flows arising from the combined buoyancies due to thermal and chemical species diffusion have received considerable attention in recent years because of their importance in wide-ranging applications related to manufacturing and process industries. For a review of the fundamental work in this area, see Ostrach (1980) and Gebhart et al. (1988).

Some of the earliest studies on natural convection flows arising from combined buoyancies are due to Professor Boelter's group at Berkeley (Sharpley and Boelter, 1938; Boelter et al., 1946). They conducted a series of experiments on water evaporation under free convection from a horizontal quiet water surface to ambient air. The water temperature was varied to cover a range of temperatures above and below that of the ambient air, and the humidity of the air was controlled. Measured transport rates were presented.

The theoretical work reported so far has been confined to boundary layer type solutions, utilizing either integral techniques (Somers, 1956; Wilcox, 1961), or similarity formulation (Lowell and Adams, 1967; Adams and Lowell, 1968; Bottemanne, 1971). The most comprehensive similarity solutions were given by Gebhart and Pera (1971) who made a general formulation of the vertical two-dimensional boundary layer flows. Their work also dealt with laminar instability. Bottemanne (1971) presented an analysis similar to that of Gebhart and Pera (1971), and Bottemanne's (1972) experimental results for Pr = 0.71 and Sc = 0.63 agreed well with his analysis. Pera and Gebhart (1972) extended the results of Gebhart and Pera (1971) to flows above horizontal surfaces.

Schenk et al. (1976) and Chen and Yuh (1979) studied combined heat and mass transfer in natural convection on inclined surfaces. Chen and Yuh (1980) presented local nonsimilar solutions for natural convection along a vertical cylinder. Mixed convection with combined buoyant mechanisms along vertical and inclined plates was studied by Chen et al. (1980), and over a horizontal plate by Chen and Strobel (1980). In these studies the local nonsimilarity method of analysis of boundary layer flows was employed. A similarity analysis of heat and mass transfer in laminar boundary layer around horizontal cylinders was presented by Hasan and Majumdar (1987). Finite-difference solutions of boundary layer equations for flows adjacent to a vertical plate in constant density, and stable thermally stratified media were given by Srinivasan and Angirasa (1988) and Angirasa and Srinivasan (1989).

The parameter that determines the relative strength of the two buoyant forces is the buoyancy ratio B, defined as the ratio of the two Grashof numbers

$$B = \frac{\mathrm{Gr}_c}{\mathrm{Gr}_t} = \frac{\beta^* \Delta c}{\beta \Delta t} \tag{1}$$

where $\Delta c = c_w - c_\infty$, and $\Delta t = t_w - t_\infty$. For opposing buoyancies, i.e., for negative values of B, the boundary layer solutions reported in several of the studies cited above may not be valid when both components of velocity (u and v) are of the same order. For example, in the detailed similarity solutions presented by Gebhart and Pera (1971) for Pr = 0.7 and 7.0 for various values of Sc and B, the results for $B = -1.6$, Pr = 0.7, and Sc = 5.0 indicated a departure from the boundary layer analysis. The maximum vertical velocity shifted sharply away from the surface, and the velocity did not reach zero at the edge of the boundary layer. Remarkably, however, the solution did predict the flow reversal that is expected near the wall.

The past experimental data, summarized below, point to similar discrepancies between the predictions of the boundary layer solutions and the data. For aiding flows, the experimental measurements of Bottemanne (1972) for water vapor from a large-diameter vertical cylinder in air (Pr = 0.71 and Sc = 0.63) and of Den Bouter et al. (1968) for a vertical copper plate maintained at constant temperature in a sulfate–sulfuric acid solution (Pr ≈ 10 and Sc ≈ 2000) indicated good agreement with the boundary layer analytical solutions. However, the boundary layer analyses appear to fail when the body forces oppose each other, and are of the same order. Adams and McFadden (1966) utilized a Mach-Zehnder interferometer to measure the heat and mass transfer rates from a vertical heated subliming surface of *p*-dichlorobenzene in air (Pr = 0.7 and Sc = 2.23). The body force resulting from the heavy organic vapor opposed the upward thermal buoyancy force. The experimental heat and mass transfer rates were found to be 10–15 percent less than those predicted by the boundary layer integral analyses. The measurements of Den Bouter et al. (1968) for opposing flows show disagreement with the boundary layer solutions up to 30 percent in magnitude.

In this paper we present numerical solutions using the complete set of continuity, Navier–Stokes, energy, and species

Contributed by the Heat Transfer Division and based on a paper presented at the ASME National Heat Transfer Conference, Minneapolis, Minnesota, July 28–31, 1991. Manuscript received by the Heat Transfer Division July 1992; revision received December 1992. Keywords: Double Diffusion Systems, Natural Convection. Associate Technical Editor: J. R. Lloyd.

equations for both aiding and opposing buoyancies, and show that the above-mentioned discrepancy is due to the departure of the flow from that assumed in the boundary layer formulation. We then compare our computed values of Nu and Sh with the experimental data of Adams and McFadden (1966). The underlying physical processes are discussed, and Nusselt and Sherwood number data are presented.

2 Analysis

Consider a heated surface of height L. The temperature of the surface is t_w, and the concentration of the diffusing species on the wall is c_w. In the ambient, the temperature and the concentration are t_∞ and c_∞ respectively. The normal velocity at the surface due to the mass diffusion is assumed to be zero. The x and y axes are aligned with the vertical and the horizontal, respectively. The laminar, two-dimensional, incompressible conservative equations that describe the flow and transport adjacent to the vertical surface can be written as

$$\frac{\partial u}{\partial x}+\frac{\partial v}{\partial y}=0 \tag{2}$$

$$\frac{\partial u}{\partial \tau}+u\frac{\partial u}{\partial x}+v\frac{\partial u}{\partial y}=-\frac{1}{\rho}\frac{\partial p}{\partial x}+\nu\left(\frac{\partial^2 u}{\partial x^2}+\frac{\partial^2 u}{\partial y^2}\right)+g\beta(t-t_\infty)+g\beta^*(c-c_\infty) \tag{3}$$

$$\frac{\partial v}{\partial \tau}+u\frac{\partial v}{\partial x}+v\frac{\partial v}{\partial y}=-\frac{1}{\rho}\frac{\partial p}{\partial y}+\nu\left(\frac{\partial^2 v}{\partial x^2}+\frac{\partial^2 v}{\partial y^2}\right) \tag{4}$$

$$\frac{\partial t}{\partial \tau}+u\frac{\partial t}{\partial x}+v\frac{\partial t}{\partial y}=\alpha\left(\frac{\partial^2 t}{\partial x^2}+\frac{\partial^2 t}{\partial y^2}\right) \tag{5}$$

$$\frac{\partial c}{\partial \tau}+u\frac{\partial c}{\partial x}+v\frac{\partial c}{\partial y}=D\left(\frac{\partial^2 c}{\partial x^2}+\frac{\partial^2 c}{\partial y^2}\right) \tag{6}$$

where

$$\beta=-\frac{1}{\rho}\left(\frac{\partial \rho}{\partial t}\right)_{p,c}$$

$$\beta^*=-\frac{1}{\rho}\left(\frac{\partial \rho}{\partial c}\right)_{p,t} \tag{7}$$

The usual Boussinesq approximations are made, which means that density variations are important only for the buoyancy terms. For most of the fluids at ordinary temperatures and pressures β is positive, but β^* can be positive or negative depending on the contribution of the diffusing species to the density of the surrounding medium.

The following nondimensional parameters are defined:

$$X=x/L;\quad Y=y/L$$

$$U=u/(g\beta\Delta tL)^{1/2};\quad V=v/(g\beta\Delta tL)^{1/2}$$

$$\tau^*=\tau(g\beta\Delta tL)^{1/2}/L$$

$$T=(t-t_\infty)/(t_w-t_\infty);\ \text{and}\ C=(c-c_\infty)/(c_w-c_\infty) \tag{8}$$

With the nondimensional variables (8), Eqs. (2)–(6) become

$$\frac{\partial U}{\partial X}+\frac{\partial V}{\partial Y}=0 \tag{9}$$

$$\frac{\partial U}{\partial \tau^*}+U\frac{\partial U}{\partial X}+V\frac{\partial U}{\partial Y}=-\frac{\partial P}{\partial X}+\frac{1}{\sqrt{\mathrm{Gr}_t}}\left(\frac{\partial^2 U}{\partial X^2}+\frac{\partial^2 U}{\partial Y^2}\right)+T+BC \tag{10}$$

$$\frac{\partial V}{\partial \tau^*}+U\frac{\partial V}{\partial X}+V\frac{\partial V}{\partial Y}=-\frac{\partial P}{\partial Y}+\frac{1}{\sqrt{\mathrm{Gr}_t}}\left(\frac{\partial^2 V}{\partial X^2}+\frac{\partial^2 V}{\partial Y^2}\right) \tag{11}$$

$$\frac{\partial T}{\partial \tau^*}+U\frac{\partial T}{\partial X}+V\frac{\partial T}{\partial Y}=\frac{1}{\sqrt{\mathrm{Gr}_t}\mathrm{Pr}}\left(\frac{\partial^2 T}{\partial X^2}+\frac{\partial^2 T}{\partial Y^2}\right) \tag{12}$$

$$\frac{\partial C}{\partial \tau^*}+U\frac{\partial C}{\partial X}+V\frac{\partial C}{\partial Y}=\frac{1}{\sqrt{\mathrm{Gr}_t}\mathrm{Sc}}\left(\frac{\partial^2 C}{\partial X^2}+\frac{\partial^2 C}{\partial Y^2}\right) \tag{13}$$

In the above equations, $P=p/(\rho g\beta\Delta tL)$, $\mathrm{Gr}_t=(g\beta\Delta tL^3/\nu^2)$, $\mathrm{Pr}=\nu/\alpha$, and $\mathrm{Sc}=\nu/D$. If B is positive the two buoyant forces aid, and if negative, they oppose each other. We define a nondimensional vorticity as

$$\omega=\frac{\partial U}{\partial Y}-\frac{\partial V}{\partial X} \tag{14}$$

and reduce Eqs. (9)–(11) to a single vorticity-transport equation

$$\frac{\partial \omega}{\partial \tau^*}+U\frac{\partial \omega}{\partial X}+V\frac{\partial \omega}{\partial Y}=\frac{1}{\sqrt{\mathrm{Gr}_t}}\left(\frac{\partial^2 \omega}{\partial X^2}+\frac{\partial^2 \omega}{\partial Y^2}\right)+\frac{\partial T}{\partial Y}+B\frac{\partial C}{\partial Y} \tag{15}$$

A streamfunction ψ is defined such that

$$U=\frac{\partial \psi}{\partial Y},\ \text{and}\ V=-\frac{\partial \psi}{\partial X} \tag{16}$$

From Eqs. (14) and (16) we obtain

$$\omega=\nabla^2\psi \tag{17}$$

Nomenclature

B = buoyancy ratio (Eq. (1))
c = concentration of the diffusing species
C = nondimensional concentration (Eq. (8))
D = diffusion coefficient of the species
g = gravitational acceleration
Gr_t = thermal Grashof number = $g\beta\Delta tL^3/\nu^2$
Gr_c = species Grashof number = $g\beta^*\Delta cL^3/\nu^2$
$\bar{h}$ = average heat transfer coefficient (Eq. (18))
$\bar{h}_m$ = average mass transfer coefficient (Eq. (20))
k = thermal conductivity of the ambient fluid
L = height of the surface
Nu = Nusselt number (Eq. (18) and (19))
p = dynamic pressure
Pr = Prandtl number = ν/α
Sc = Schmidt number = ν/D
Sh = Sherwood number (Eq. (20))
t = temperature
T = nondimensional temperature (Eq. (8))
u, v = velocity components
U, V = nondimensional velocity components (Eq. (8))
x, y = space coordinates
X, Y = nondimensional space coordinates (Eq. (8))
α = thermal diffusivity
β = coefficient of thermal expansion (Eq. (7))
β^* = volumetric coefficient due to concentration (Eq. (7))
ν = kinematic viscosity
ρ = density
τ = time
τ^* = nondimensional time (Eq. (8))
ψ = stream function (Eq. (16))
ω = vorticity (Eq. (14))

Subscripts

min = minimum
w = wall
∞ = reference

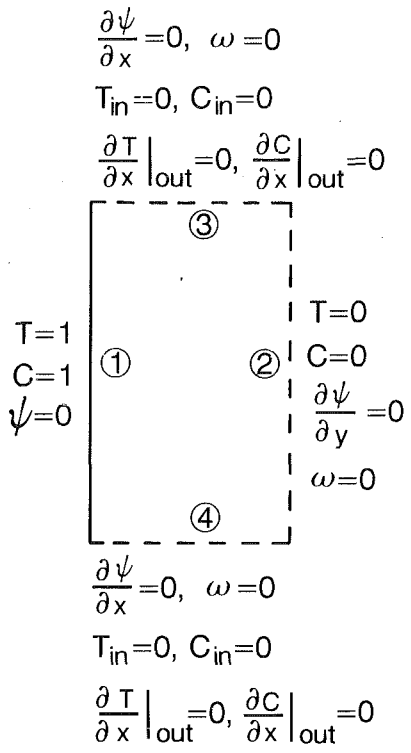

Fig. 1 Numerical boundary conditions

The average Nusselt number Nu is defined as

$$\mathrm{Nu}=\bar{h}L/k, \text{ in which } \bar{h}=\frac{1}{L}\int_0^L\left(-\frac{k}{\Delta t}\frac{\partial t}{\partial y}\right)_{y=0}dx \qquad (18)$$

from which it follows that

$$\mathrm{Nu}=\int_0^1\left(-\frac{\partial T}{\partial Y}\right)_{Y=0}dX \qquad (19)$$

Similarly the average Sherwood number can be evaluated as

$$\mathrm{Sh}=\frac{\bar{h}_m L}{D}=\int_0^1\left(-\frac{\partial C}{\partial Y}\right)_{Y=0}dX \qquad (20)$$

3 Numerical Procedure

The energy, species, and vorticity-transport equations (Eqs. (12), (13), and (15)) are solved using the well-known Alternating Direction Implicit (ADI) scheme of Peaceman and Rachford (Roache, 1982). The time-dependent equations are marched in time until a steady solution is obtained. The upwind-differencing is used for the convective terms because of the large values of Gr. The diffusive terms are discretized with central-differencing. In our computations constant grid-spacings have been employed.

A Successive Over Relaxation (SOR) method is employed for the solution of the streamfunction Eq. (17). The streamfunction equation is iterated for convergence within each time step of the solution of Eqs. (12), (13), and (15). The details of the numerical procedures can be found in Roache (1982).

Numerical boundary conditions are given in Fig. 1. The width of the computations (in the Y direction) is chosen to be 0.4 after checking that higher values did not alter the solution. This value was estimated from the similarity solutions. Wall vorticities are evaluated from the values of the stream function at the adjacent grid points (Roache, 1982).

The following convergence criteria are employed:

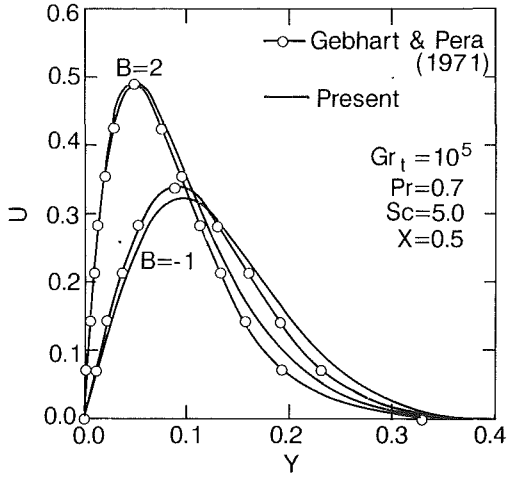

Fig. 2 Comparison with similarity solution

$$\left|\frac{\xi_{ij}^{n+1}-\xi_{ij}^{n}}{\xi_{ij}^{n}}\right|\le\epsilon \text{ and } \left|\xi_{ij}^{n+1}-\xi_{ij}^{n}\right|\le\epsilon \qquad (21)$$

where ξ is T, C, and ω. The superscript n refers to time, and the subscripts i and j refer to space. The value of ϵ is chosen to be 10^{-4}. Convergence is very slow, especially for those values of B at which convection is minimum. For a typical time step of 0.001, it required about 20,000 time steps to reach steady state.

The average Nusselt and Sherwood number are obtained by numerical integration of Eqs. (19) and (20), using Simpson's rule. To account for the gradients at the end points of the wall, an open-ended formula has been employed (Press et al., 1986). In the results that follow we have used a 51 × 51 grid for $\mathrm{Gr}_t = 10^5$, 61 × 61 for $\mathrm{Gr}_t = 10^6$, and 71 × 71 for $\mathrm{Gr}_t = 10^7$. The numerical errors due to the grid size are assessed as 0.5 percent for temperature and concentration, 1 percent for flow field variables, and 2 percent Nu and Sh.

4 Results and Discussion

We first compare our numerical results with the boundary layer solutions of Gebhart and Pera (1971). The detailed numerical results of velocity, temperature, and concentration fields are presented and the inadequacies of the boundary layer analysis are pointed out. In section 4.2, we compare our computational results with the experimental data of Adams and McFadden (1966). Finally, we present comprehensive results of Nusselt and Sherwood numbers for a wide range of Gr_t, B, and Pr and Sc.

4.1 Comparison With Boundary Layer Analysis. The computed velocity profiles for Pr = 0.7 and Sc = 5.0 for B = 2.0 and −1.0 are presented in Fig. 2, while those for B = −1.6 to −5.0 are presented in Fig. 3. The similarity solutions of Gebhart and Pera (1971) are also shown for comparison. For B = 2, the agreement between the two results is very good, indicating boundary layer flow for positive values of B (aiding buoyant forces). For B = −1, there is a difference between the two solutions. Our simulation gives a slightly smaller value of peak vertical velocity, and a flatter velocity profile. This suggests that for this value of B, although the boundary layer analysis predicts a reasonably accurate solution, it does start to depart from the boundary layer type flow. At B = −1.6 (Fig. 3), the similarity solution is not accurate at all. It underpredicts the flow reversal near the surface and exaggerates the magnitude of the upward velocities. The flow reversal, with the upward and downward velocities of the same order, cannot be accounted for by the boundary layer equations. With

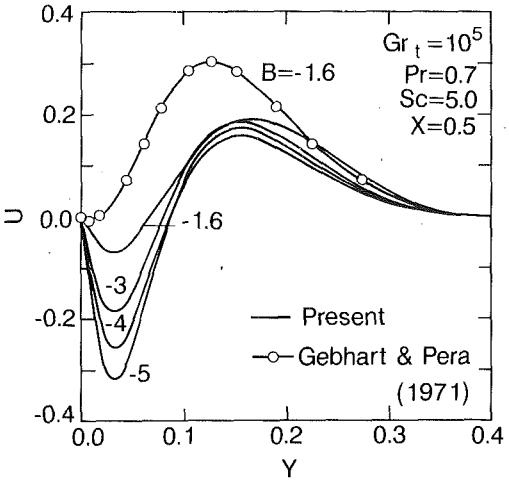

Fig. 3 Comparison with similarity solution for opposing buoyancies

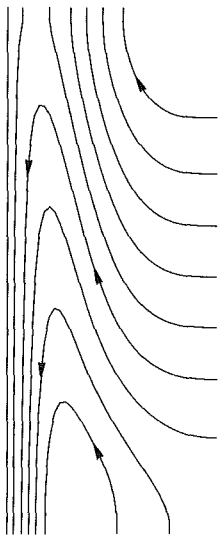

Fig. 4 Contours of streamfunction, $\psi_w = 0$, for $Gr_t = 10^5$, Pr = 0.7, Sc = 5.0, and $B = -5$

increasing negative values of B, the magnitude of the downward velocities increases, and that of the upward velocities away from the surface decreases. For Pr $\geq$ Sc, and $|B| \gg 1$ ($B < 0$), no flow reversal (upward) appears, and $v \ll u$. Then the boundary layer analysis is expected to be valid.

At $B = -1.6$ and $Gr_t = 10^7$, for Pr = 0.7, and Sc = 5.0, Gebhart and Pera (1971) obtained Nu = 19.12 and Sh = 35.42. These values are calculated from Fig. 9 of the above reference. For the same parameters, Wilcox's (1961) integral analysis yields Nu = 20.31 and Sh = 54.28. Our numerical calculations give Nu = 17.46 and Sh = 30.32. The clear indication is that for opposing flows the boundary layer similarity and integral analyses overpredict Nusselt number by 10–20 percent, and Sherwood number by as high as 80 percent. This result is supported by the experimental finding of Adams and McFadden (1966), who found that the measured heat and mass transfer rates with opposing body forces were lower than the prediction of the boundary layer analyses. This discrepancy, most likely, arises because the analyses do not properly account for the flow reversal near the surface, and predict a larger upward force. The departure is consistent with the deviations of velocity field as discussed above. Comparison of numerical results at other values of Prandtl and Schmidt number for opposing buoyancies indicates similar behavior.

In Fig. 4, contours of streamfunction are shown for the case

Table 1 Comparison of Nu and Sh with the experiments of Adams and McFadden (1966)

		Present		Adams and McFadden (1966)	
Gr_t	B	Nu	Sh	Nu	Sh
1.15×10^7	−0.43	23.03	41.44	24.38	42.10
1.85×10^6	−0.414	15.39	27.41	14.27	26.2

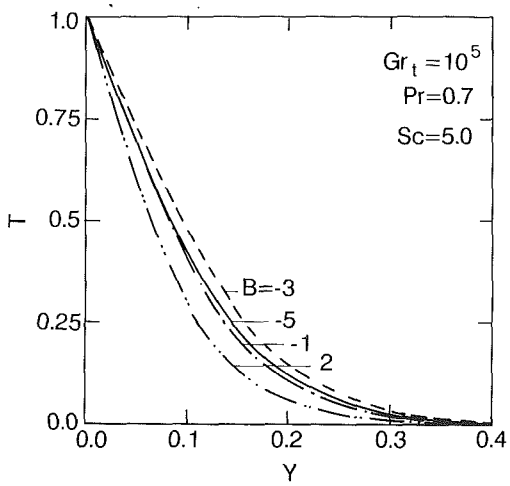

Fig. 5 Temperature profiles at $X = 0.5$ for different values of B

of $B = -5.0$. Because of the larger downward force near the surface due to mass diffusion, the flow near the surface is downward, consequently the U velocity is negative in this region (Fig. 3). The U velocity reverses direction at the end of the concentration layer due to the upward thermal buoyancy. In this latter region the only buoyant force is thermal buoyancy. Vertical velocities reach zero again with the end of the thermal layer. The streamfunction contours clearly show that the nature of the flow is not boundary layer.

In these results, Sc (= 5.0) is far larger than Pr (= 0.7) and hence the concentration layer is much thinner than the thermal layer. This confines the downward flow to a thin region near the surface (Fig. 3). For lower Sc, the thickness of the concentration layer increases and the region of flow reversal will extend farther away from the wall. These characteristics are discussed further in section 4.3.

4.2 Comparison With Experimental Data for Opposing Flows. The experimental data (Pr = 0.7 and Sc = 2.23) are taken from Adams and McFadden (1966), in which *p*-dichlorobenzene sublimes from a heated vertical surface into air. The molecular weight of *p*-dichlorobenzene is approximately five times that of air.

Table 1 presents the detailed comparison of Nu and Sh from our calculations with the experimental values of Adams and McFadden (1966). The two data points correspond to those given in Table 1 of Adams and McFadden (1966). For these points, Gr_t and Gr_c (or B) were calculated from the detailed temperature and concentration (or pressure) profiles given in Figs. 3 and 4 of their paper. The measured average values of Nu and Sh in Table 1 are calculated from the local values given by Adams and McFadden. Since constant wall fluxes were obtained in the experiments, the experimental values were divided by a factor of 1.14. In our numerical calculations, constant wall temperature and concentration were prescribed. We observe from the table that the agreement between our numerical results and the experimental data is very good.

4.3 Detailed Numerical Results. In this section, the calculated flow, temperature, and concentration fields, and the transport rates are discussed for aiding and opposing buoy-

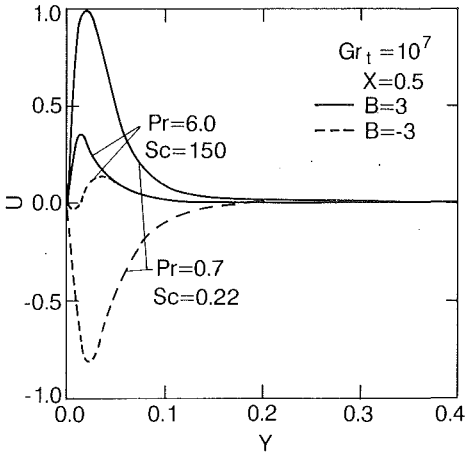

Fig. 6 Vertical velocity profiles at $X = 0.5$ for Pr > Sc and Sc ≫ Pr

ancies. Results are presented for Pr ≠ Sc. For Pr = Sc, the thermal and concentration fields are identical, and the physical processes can be inferred from the results of Pr ≠ Sc.

Flow, Thermal and Concentration Fields. We first present results for Pr = 0.7 and Sc = 5.0, the case considered earlier in section 4.1. Figure 5 shows the temperature profile at $X = 0.5$ for B varying between 2 and −5. A steeper temperature profile is anticipated for flows with aiding buoyant forces ($B = 2$). The profiles turn flatter with increasing negative values of B, i.e., increasing opposing buoyancies. Interestingly the profiles do not monotonously become flatter with increasing negative buoyancies. At $B = -5$, the temperature profile is steeper than that at $B = -3$. This interesting trend can be explained by realizing that it is not the direction of the vertical velocities, but their magnitudes that determine the heat transfer rates at the wall. When the two buoyant forces oppose each other, the upward vertical velocity is reduced, resulting in the flattening of the temperature profile, see $B = 2$ and -1. After reaching a minimum at some value of negative B, a further decrease in B causes the downward velocity to increase, which in turn results in enhanced heat transfer rate at the wall. Since the downward vertical velocities increase with increasing negative B, the slope of the temperature profile increases again ($B = -5$). Note that in Figs. 2 and 3 the *magnitudes* of the vertical velocities are nearly the same for $B = -1$ and -5, although the direction of the flows are opposite to each other. The heat transfer rates and the temperature profiles are, therefore, nearly identical for these two cases.

The above arguments also hold for the concentration profiles (not shown). The trends in these profiles are similar to those for temperature profiles. Nusselt and Sherwood number plots (Figs. 12 and 13) reflect these changes in the slopes of temperature and concentration. Both Nu and Sh first decrease with B, and then increase with further decrease in B, i.e., in negative B.

We now present results for Pr ≪ Sc (Pr = 6.0 and Sc = 150), and Pr > Sc (Pr = 0.7 and Sc = 0.22), both for aiding and opposing buoyancies. For these flows, typical U velocity profiles are presented in Fig. 6 while contour plots for opposing flows are shown in Fig. 7. The results for aiding flows are self-explanatory. For opposing flows with Pr = 0.7 and Sc = 0.22 (Sc < Pr), the flow is entirely downward. This is to be expected, for Sc < Pr, the thickness of the concentration layer is larger than that of the thermal layer, and the wider concentration layer drives the flow entirely downward. For Pr ≪ Sc, a very thin concentration layer forms near the wall (see the mass lines in Fig. 7 for this case). The flow in this thin layer is downward and the velocities are weak. Since the thermal layer thickness is much larger, in the region just away from the wall the flow is upward. The thin downward flow near the wall could not

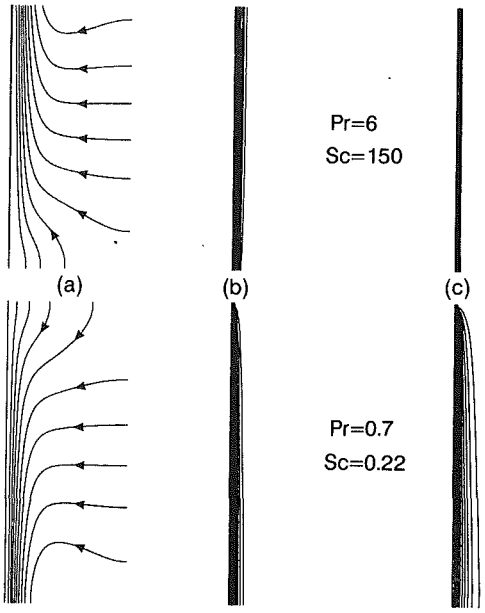

Fig. 7 (*a*) Streamfunction contours, $\psi_{wall} = 0$; (*b*) isotherms, $T_w = 1.0$, $\Delta T = 0.1$; (*c*) iso-concentration lines, $C_w = 1.0$, $\Delta C = 0.1$, for $Gr_t = 10^7$ and $B = -3$ for Pr ≪ Sc and Sc < Pr

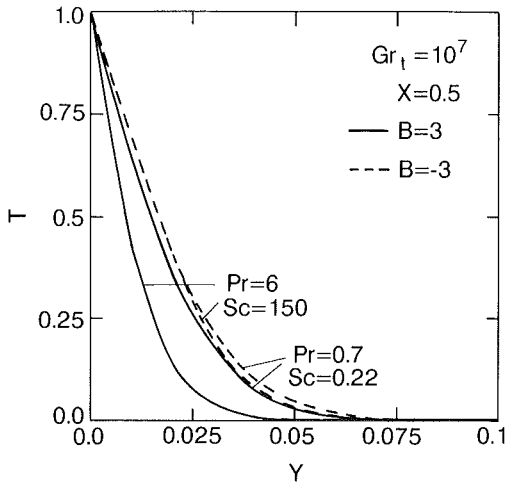

Fig. 8 Temperature profiles at $X = 0.5$ for $Gr_t = 10^7$ for aiding and opposing buoyancies for Pr ≪ Sc and Sc < Pr

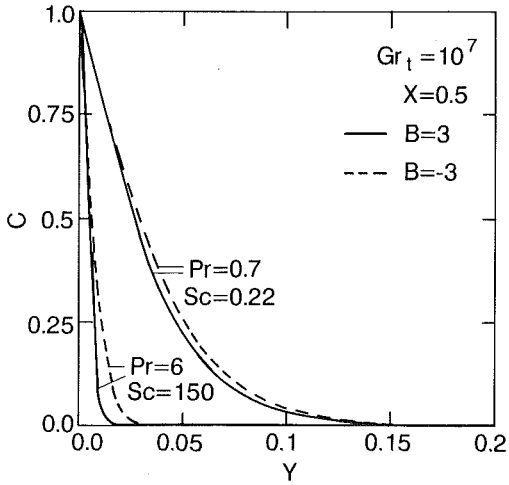

Fig. 9 Concentration profiles at $X = 0.5$ $Gr_t = 10^7$ for aiding and opposing buoyancies for Pr ≪ Sc and Sc < Pr

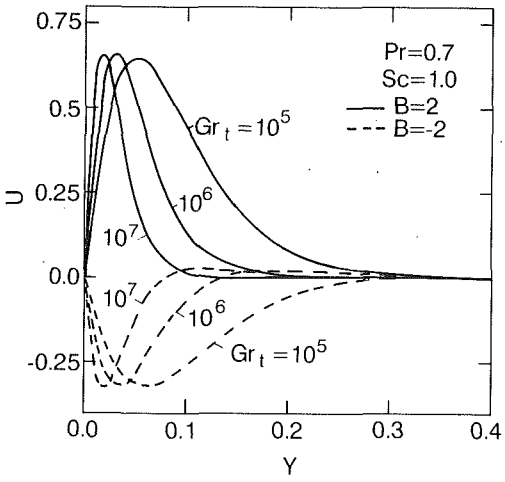

Fig. 10 Vertical velocity profiles at $X = 0.5$ for different values of Gr_t for aiding and opposing flows

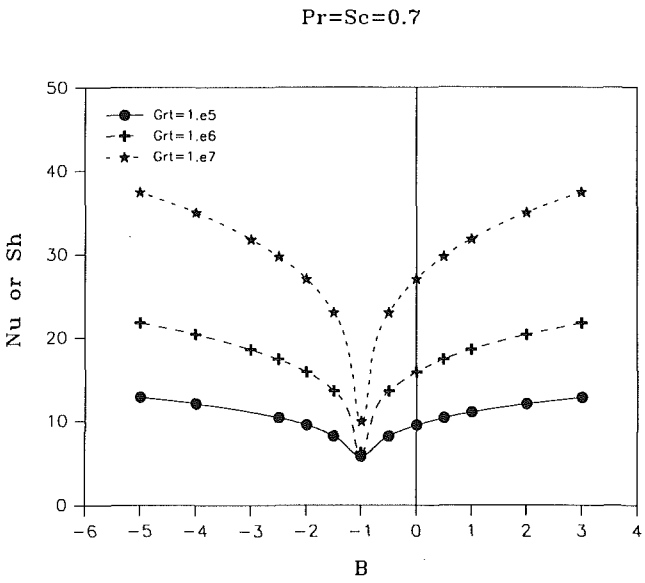

Fig. 11 Nusselt (Sherwood) number for Pr = Sc = 0.7

be captured in the streamfunction contour plotting, but it is clearly shown in the U velocity profile (Fig. 6).

Temperature and concentration profiles, respectively, for aiding and opposing buoyancies with unequal Pr and Sc are presented in Figs. 8 and 9. Temperature profiles are flatter for opposing flows, and concentration profiles are steeper for Sc $\gg$ Pr.

The effect of the thermal Grashof number Gr_t on aiding and opposing flows will now be discussed. Figure 10 shows vertical velocity profiles at $X = 0.5$ for aiding and opposing flows for different values of Gr_t. The effect of decreasing Gr_t is to shift the peak velocity away from the wall both for aiding and opposing flows. The magnitude of the peak velocity, however, remains the same for either type of flow. Since the buoyancy ratio is the same, a change in Gr_t will alter the magnitude of the species Grashof number (Gr_c) too. Hence the velocity profiles spread or shrink with Gr_t, but the peak velocity is unaltered.

For both aiding and opposing flows, the temperature and concentration profiles (not shown) become steeper with increasing Gr_t, thus enhancing heat and mass transfer rates. This is physically anticipated.

Nusselt and Sherwood Number Data. Extensive calculations have been performed to obtain accurate data for Nusselt

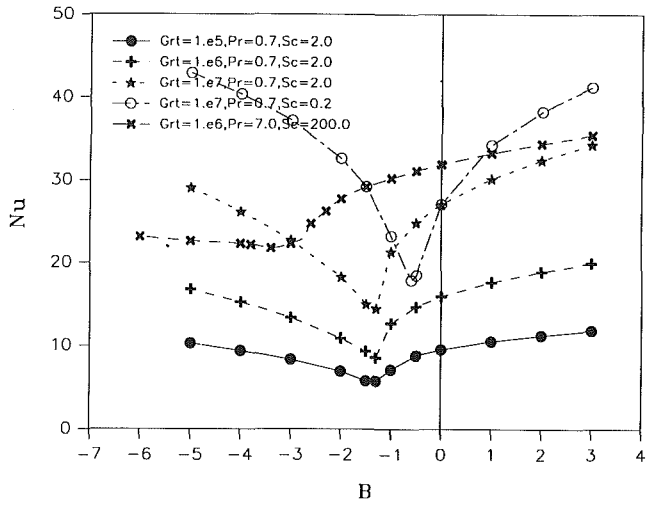

Fig. 12 Nusselt number for Pr ≠ Sc

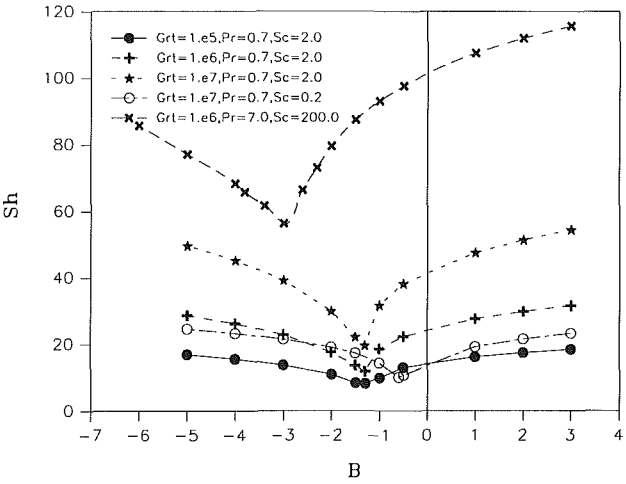

Fig. 13 Sherwood number for Pr ≠ Sc

number, and Sherwood number for a wide range of Gr_t, B, Pr, and Sc. The first set of data are for Pr = Sc = 0.7 at $Gr_t = 10^5$, 10^6, and 10^7. Since the thermal and species diffusion coefficients are equal, Nu and Sh are also equal. The data are shown in Fig. 11.

At $B = -1$, the two buoyancies are equal to and oppose each other. Hence, for Pr = Sc, we obtain the minimum value of Nu (or Sh) at $B = -1$. Defining B_{min} as the value of B at which the minimum value of Nu, Nu_{min}, is attained, we note that $B_{min} = -1$ for Pr = Sc for all values of Gr_t. The B–Nu curve is symmetric about B_{min}. For instance, the magnitudes of the net buoyancy and $B = 1$ and at $B = -3$ are equal, although the directions are reversed.

We note from Fig. 11 that Nu_{min} drops down sharply from its value at $|B| > B_{min}$. At $B = B_{min}$, the transport takes place by diffusion. Even a slightly different value of B from B_{min} induces convection, however small, and the transport rates are substantially increased. This clearly demonstrates the effect of convection in enhancing the heat and mass transfer rates.

For Pr ≠ Sc,the Nu–B and Sh–B curves are not symmetric (see Figs. 12 and 13). Then $B_{min} > -1$ for Pr > Sc, and $B_{min} < -1$ for Sc > Pr. This is explained from the unequal thicknesses of the thermal and concentration layers. For Pr > Sc, the thermal layer is thinner than the concentration layer. Hence, a smaller value of Gr_c (compared to Pr = Sc) is sufficient to attain B_{min}. This gives $B_{min} > -1$. Similar argument leads to $B_{min} < -1$ for Pr < Sc. The Nu and Sh data for various values of Pr and Sc, and Gr_t are shown in Figs. 12 and 13. The value of B_{min} in each case is determined by extrapolation.

An important conclusion from Figs. 12 and 13 is that B_{min} is a function of only Pr and Sc, and is independent of Gr_t; see data for Pr = 0.7, Sc = 2.0, and for various values of Gr_t.

5 Summary

We have presented a numerical study of combined heat and mass transfer by natural convection from a vertical surface with aiding and opposing buoyancies. The main conclusions of this study are:

1 Boundary layer solutions do not yield accurate solutions for natural convection flows with opposing buoyancies, when the two components of the velocity are of the same order. They underpredict the flow reversals and overpredict the magnitude of the upward flow velocities.

2 Finite-difference solutions of the full equations give accurate solutions. Our calculations agree very well with the Nusselt and Sherwood number experimental data of Adams and McFadden (1966) for opposing buoyancies.

3 The heat and mass transfer rates undergo complex changes with B varying from high positive values (aiding buoyancies) to high negative values (opposing buoyancies). With decreasing B, both Nu and Sh decrease. After reaching a minimum at a particular value of negative B, both Nu and Sh increase again with further decrease in B. This is because of the increase of downward vertical velocities with decreasing B. It is the magnitude of the vertical velocity, not its direction, which determines the transport rates.

4 The value of B, at which the minimum Nusselt and Sherwood numbers are attained, is a function of Prandtl and Schmidt numbers, but is independent of thermal Grashof number (Gr_t).

References

Adams, J. A., and McFadden, P. W., 1966, "Simultaneous Heat and Mass Transfer in Free Convection With Opposing Body Forces," *AIChE J.*, Vol. 12, pp. 642–647.

Adams, J. A., and Lowell, R. L., 1968, "Free Convection Organic Sublimation on a Vertical Semi-infinite Plate," *Int. J. Heat Mass Transfer*, Vol. 11, pp. 1215–1224.

Angirasa, D., and Srinivasan, J., 1989, "Natural Convection Flows Due to the Combined Buoyancy of Heat and Mass Diffusion in a Thermally Stratified Medium," ASME JOURNAL OF HEAT TRANSFER, Vol. 111, pp. 657–663.

Boelter, L. M. K., Gordon, H. S., and Griffin, J. R., 1946, "Free Evaporation Into Air of Water From a Free Horizontal Quiet Surface," *Ind. Eng. Chem.*, Vol. 38, pp. 596–600.

Bottemanne, F. A., 1971, "Theoretical Solution of Simultaneous Heat and Mass Transfer by Free Convection About a Vertical Flat Plate," *Appl. Sci. Res.*, Vol. 25, pp. 137–149.

Bottemanne, F. A., 1972, "Experimental Results of Pure and Simultaneous Heat and Mass Transfer by Free Convection About a Vertical Cylinder for Pr = 0.71 and Sc = 0.63," *Appl. Sci. Res.*, Vol. 25, pp. 372–382.

Chen, T. S., and Yuh, C. F., 1979, "Combined Heat and Mass Transfer in Natural Convection on Inclined Surfaces," *Num. Heat Transfer*, Vol. 2, pp. 233–250.

Chen, T. S., and Strobel, F. A., 1980, "Combined Heat and Mass Transfer in Mixed Convection Over a Horizontal Flat Plate," ASME JOURNAL OF HEAT TRANSFER, Vol. 102, pp. 538–543,

Chen, T. S., and Yuh, C. F., 1980, "Combined Heat and Mass Transfer in Natural Convection Along a Vertical Cylinder," *Int. J. Heat Mass Transfer*, Vol. 23, pp. 451–461.

Chen, T. S., Yuh, C. F., and Moutsoglou, A., 1980, "Combined Heat and Mass Transfer in Mixed Convection Along Vertical and Inclined Plates," *Int. J. Heat Mass Transfer*, Vol. 23, pp. 527–537.

Den Bouter, J. A., DeMunnik, B., and Heertjes, P. M., 1968, "Simultaneous Heat and Mass Transfer in Laminar Free Convection From a Vertical Plate," *Chem. Eng. Sci.*, Vol. 23, pp. 1185–1190.

Gebhart, B., and Pera, L., 1971, "The Nature of Vertical Natural Convection Flows Resulting From the Combined Buoyancy Effects of Thermal and Mass Diffusion," *Int. J. Heat Mass Transfer*, Vol. 14, pp. 2025–2050.

Gebhart, B., Jaluria, Y., Mahajan, R. L., and Sammakia, B., 1988, *Buoyancy-Induced Flows and Transport*, Chap. 6, Hemisphere, Washington, DC.

Hasan, M., and Majumdar, A. S., 1987, "Laminar Boundary Layer Analysis of Simultaneous Mass and Heat Transfer in Natural Convection Around a Horizontal Cylinder," *Int. J. Energy Res.*, Vol. 11, pp. 359–371.

Lowell, R. L., and Adams, J. A., 1967, "Similarity Analysis for Multicomponent Free Convection," *AIAA J.*, Vol. 5, pp. 1360–1361.

Ostrach, S., 1980, "Natural Convection With Combined Driving Forces," *PhysicoChemical Hydrodynamics*, Vol. 1, pp. 233–247.

Pera, L., and Gebhart, B., 1972, "Natural Convection Flows Adjacent to Horizontal Surfaces Resulting From the Combined Buoyancy Effects of Thermal and Mass Diffusion," *Int. J. Heat Mass Transfer*, Vol. 15, pp. 269–278.

Press, W. H., Flannery, B. P., Teukolsky, S. A., and Vetterling, W. T., 1986, *Numerical Recipes: The Art of Scientific Computing*, Cambridge University Press, New York.

Roache, P. J., 1982, *Computational Fluid Dynamics*, Hermosa, Albuquerque, NM.

Schenk, J., Altman, R., and Dewit, J. P. A., 1976, "Interaction Between Heat and Mass Transfer in Simultaneous Natural Convection About an Isothermal Inclined Flat Plate," *Appl. Sci. Res.*, Vol. 32, pp. 599–606.

Sharpley, B. F., and Boelter, L. M. K., 1938, "Evaporation of Water Into Quiet Air," *Ind. Eng. Chem.*, Vol. 30, pp. 1125–1131.

Somers, E. V., 1956, "Theoretical Considerations of Combined Heat and Mass Transfer From a Vertical Flat Plate," ASME *Journal of Applied Mechanics*, Vol. 23, pp. 295–301.

Srinivasan, J., and Angirasa, D., 1988, "Numerical Study of Double-Diffusive Free Convection From a Vertical Surface," *Int. J. Heat Mass Transfer*, Vol. 31, pp. 2033–2038.

Wilcox, W. R., 1961, "Simultaneous Heat and Mass Transfer in Free Convection," *Chem. Eng. Sci.*, Vol. 13, pp. 113–119.

Internal Standing Waves in a Cylindrical Vessel and Their Near-Wall Features

S. Ushijima

S. Moriya

N. Tanaka

Central Research Institute of Electric Power Industry (CRIEPI), 1646 Abiko, Abiko-shi, Chiba-ken, 270-11, Japan

This paper describes numerical and experimental investigations on internal standing waves occurring in a cylindrical vessel and their near-wall behavior in the vicinity of an adiabatic cylinder located at the center of the vessel. A numerical prediction method was developed with a low-Reynolds-number turbulence model to stimulate the occurrence of the internal standing waves and their near-wall features. These features are characterized by the attenuation and phase shifts in temperature fluctuations as observed in the present experiments. The measured results were well predicted by the numerical simulation in terms of certain statistical values as well as qualitative internal wave motions and flow patterns.

1 Introduction

Thermal stratification phenomena have been widely investigated, since temperature gradients and fluctuations arising in some stratified flows may bring about thermal fatigue damage to structure surfaces (e.g., Kim et al., 1991). In such problems it is of great importance to estimate near-wall behaviors of thermal interfaces accurately. It is known that temperature fluctuations are suppressed near the surface where neither heat generation nor absorption takes place owing to the presence of boundary layers. This phenomenon may be referred to as the boundary layer attenuation (BLA) effect. The BLA effects alleviate to some extent the thermal influences caused by stratified flows. Therefore, taking the BLA effects into account is necessary to estimate precise thermal-hydraulic features imposed on the structure.

This study was originally conceived as part of an investigation to understand the thermal hydraulics in a liquid metal fast breeder reactor (LMFBR), where thermal stratification of liquid sodium, which has a temperature difference of more than 100 K, occurs under reactor trip conditions. Thus the thermal stratification dealt with in this paper occurs in a cylindrical vessel that represents the basic geometry of the hot pool region in an LMFBR. In earlier experimental investigations using this kind of vessel, Moriya et al. (1987) found that standing wave motions of a thermal interface arise in certain experimental conditions even if no external vibrations are present. Since this type of internal standing waves might cause serious thermal fatigue on structure surfaces in a real situation, it is necessary to develop methods to predict the occurrence of the internal waves and their response to BLA effects. Moriya et al. (1987) attempted to specify the ranges of bulk Reynolds and Richardson numbers over which the internal waves occur. However, it has been recognized that the bulk parameters alone are obviously insufficient to judge whether or not the internal standing waves arise, since their occurrence is governed by the detailed geometry of the vessel, flow patterns, and more complicated conditions.

The present study is focused on a numerical method that enables us to make more precise predictions of the occurrence of internal waves and the BLA effects against their temperature fluctuations. The numerical model used is a low-Reynolds-number turbulence model, which has been extensively refined as reviewed by Patel et al. (1984) following earlier investigations by Jones (1972), Jones and Launder (1973), and Hanjalic and Launder (1976). The near-wall effects are suitably dealt with by the model (Lam and Bremhorst, 1981), which is applicable to viscous sublayers as well as fully turbulent regions. In addition, the model is improved so that it can take into consideration buoyancy effects on eddy diffusivities and the turbulent Prandtl number. The numerical analysis is based on a finite difference method, in which all nonlinear terms are solved with third-order accuracy.

In addition to the numerical study, a detailed experimental investigation is also made in order to understand the mechanism of internal waves and the BLA effects; flow patterns below the internal waves are quantitatively captured with the aid of the image processing technique (Ushijima et al., 1991) and it is made clear that they are closely related to the internal wave motions. Temperature distributions are measured in the vicinity of a thermally insulated cylinder installed at the center of the vessel, which corresponds to the internal structure of an LMFBR, in order to clarify the BLA effects on the large periodic temperature fluctuations caused by the internal standing waves. As a result, it is found that near the surface of the cylinder the amplitudes of the fluctuations are attenuated and phase shifts arise in the internal wave motions. These experimentally obtained features and the occurrence of the internal standing waves are reasonably simulated by the developed numerical method.

2 Experiments on Thermal Stratification

2.1 Experimental Setup. The fundamental thermal-hydraulic features that are likely to appear in reactor trip conditions within the hot pool of an LMFBR can be reproduced in the present experiments. The flow system to create thermal stratification phenomena in the test vessel is illustrated in Fig. 1. The loop, including a hot water tank, is connected to the vessel to form a steady-state condition, in which a high-temperature fluid is supplied to the vessel at a constant flow rate so that uniform temperature and a steady flow pattern can be maintained. After creating a fully established steady flow, a lower temperature fluid is supplied to the vessel by changing the connection of the loops. The transition of the loops is conducted smoothly by regulating four control valves, causing a small quantity of both fluids to mix, in order that the flow rate through the vessel should be maintained constant. Hence the temperature of the incoming flow gradually decreases to that of the fluid in the cold water tank. As a result, thermal stratification occurs in the vessel.

Contributed by the Heat Transfer Division for publication in the JOURNAL OF HEAT TRANSFER. Manuscript received by the Heat Transfer Division April 1992; revision received February 1993. Keywords: Numerical Methods, Stratified Flows, Turbulence. Associate Technical Editor: J. H. Kim.

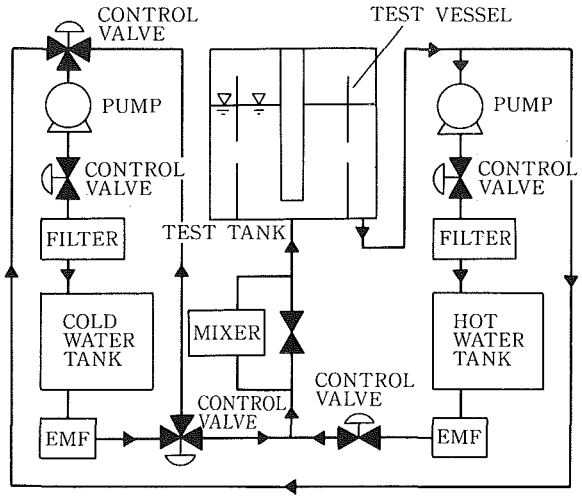

Fig. 1 Flow system

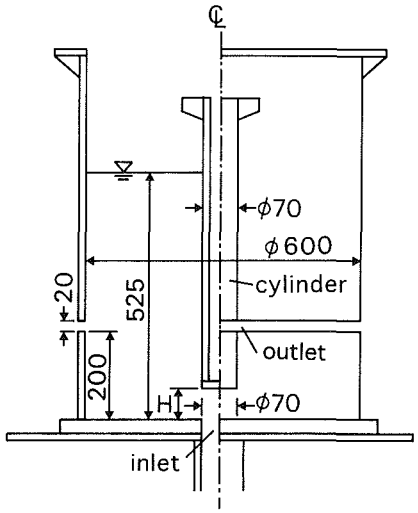

Fig. 2 Test vessel

The details of the test vessel are shown in Fig. 2. An inlet hole, 70 mm in diameter, is located at the center on the bottom surface, from which a lower temperature fluid enters after the loop transition is completed. The outlet has a slit shape, 20 mm in height, surrounding circumferentially along the side wall of the vessel. A cylinder, whose diameter is the same as the inlet hole, is set up just above the inlet hole. The inlet hole and the cylinder represent the simplified forms of a core outlet and an above-core structure, respectively, in an LMFBR. The vertical distance between the lower end of the cylinder and the bottom surface, denoted by H, governs the flow patterns appearing in the vessel in the steady-state condition; the incoming

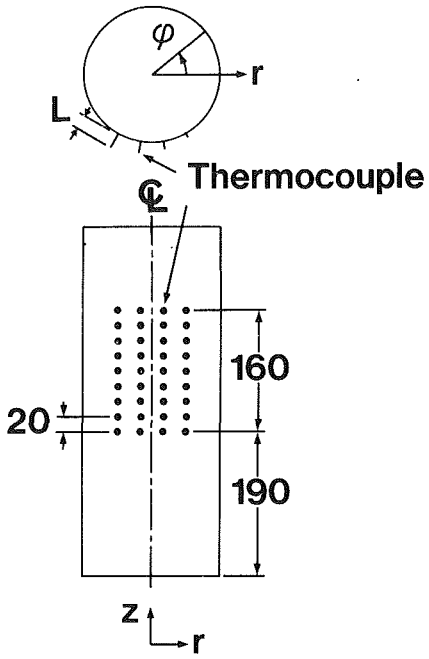

Fig. 3 Thermocouples set up on the cylinder surface

flow clings to the base as a radial wall jet when H is sufficiently small, creating a large circulating flow in the vessel. In contrast, an increase in H causes the jet flow from the inlet to impinge partially on the lower end of the cylinder, producing a diagonal crossflow. As a result, two main circulations occur on both sides of the crossing flow in steady states. In the present condition, H is set at 60 mm, which brings about a crossing jet flow in the vessel resulting in the occurrence of internal standing waves when thermal stratification proceeds.

The surface of the cylinder can be treated as adiabatic, due to the sufficiently low thermal conductivity of its acryl composition. As illustrated in Fig. 3, 36 thermocouples are arranged with distances L from the surface to their tops of 0.5, 1.0, 1.5, and 2.0 mm. The near-wall behaviors of thermal interfaces on the r–z plane are measured by the thermocouples with consideration given to the two dimensionality, or the uniformity in the circumferential direction, of the internal wave motions. In addition to these near-wall sensors, 24 thermocouples are set in the vessel to capture the entire internal wave motions. Their positions are indicated in Fig. 6(a). All the thermocouples used here are 0.25 mm in diameter and their time constant is approximately 10 ms. The electric signals from the thermocouples are amplified and recorded on magnetic tapes as digital signals with a sampling interval of 0.2 s. The accuracy of the measured temperature is estimated at around 0.1 K.

In determining the experimental conditions, listed in Table 1, the occurrence of internal standing waves in the vessel was

Nomenclature

D_v = diameter of the vessel = 600 mm
g = gravity
H = height of cylinder
k = turbulence energy
P = mean pressure
r, z = radial and vertical coordinates
r_1 = $r - R_1$
R_1 = radius of cylinder = 35 mm
t = time
U, V = radial and vertical mean velocities
u, v, w = radial, vertical, and circumferential fluctuating velocities
α = thermal diffusivity
β = thermal expansion coefficient
ϵ = dissipation rate of k
θ = fluctuating temperature
Θ = mean temperature
Θ_S = standard temperature
ν = kinematic viscosity
ρ = fluid density

Table 1 Experimental conditions

T_C (K)	T_H (K)	Q (l/min)	Ri	Re
284.5	314.5	65.3	5.2×10^{-2}	2.0×10^{4}

given priority over the precise replication of actual operational conditions within an LMFBR.

In Table 1, T_C and T_H denote the temperatures of the fluids provided by the cold and the hot water tanks, respectively, while Q stands for the flow rate through the test vessel. The bulk Richardson and Reynolds numbers in the table are based on the diameter of inlet hole D and the mean velocity at inlet U_0 (= 283 mm/s):

$$\mathrm{Ri} = \beta g D(T_H - T_C)/U_0^2 \tag{1}$$

$$\mathrm{Re} = U_0 D/\nu \tag{2}$$

2.2 Image Processing. The flow patterns in the vessel when internal waves arise are of great interest since it is expected that they are closely related to the occurrence and the sustained oscillation of the internal standing waves. However, it is not easy to obtain velocity distributions on a two-dimensional plane at a given instance by means of a usual point-measuring velocimetry system. To solve such problems, extensive efforts have been made to develop image processing techniques, starting with Prandtl and Tietjens (1934). Among the methods employed in analyzing the visualized images, a particle-tracking method (Sommerscales, 1980), which generally utilizes the trajectories of the particles scattered in a fluid, is one of the simplest and most effective techniques. The particle-tracking method has been employed and improved by Imaichi and Ohmi (1983), Kobayashi et al. (1985), Chang et al. (1985), Agui and Jimenez (1987), Nishino et al. (1989), and many other researchers, who also estimated the uncertainties involved in this method. We take up the image processing technique (Ushijima et al., 1991) based on the particle-tracking method to measure the two-dimensional flow patterns of the incoming jet, which crosses diagonally from the inlet below the oscillating thermal interfaces.

The particles used in the flow visualization are made of high polymer (Eslen) with a specific gravity of 1.02, and an average diameter around 0.9 mm. They include fluorescent sodium, which gives clear images in the presence of laser light. A sheet of laser light is illuminated from the top of the vessel. The thickness of the sheet is approximately 5 mm. As a result, a vertical cross section including the centerline of the vessel is visualized. The movements of the particles on the section are recorded on video tapes with a high-speed video camera capable of 200 frames per second. The recorded analogue data are converted to digital values, 512×512 pixels per frame and 256-gray-level resolution for a single pixel, by an image processor, and are then stored on hard disks. The digitized results are transferred to the memories of a high-speed computer so that all analyses can be performed by the computer.

The principle of the vector acquisition is essentially equivalent to that presented by Kobayashi et al. (1985), in which both the initial and the terminal positions of the particle in question are utilized together with its trace image to determine one vector. With a Gaussian window, the velocity vectors obtained are interpolated at regular grid points whose spatial intervals are determined from the number of particles per unit surface. The interpolated vectors are then smoothed on the basis of the bootstrap procedure investigated by Efron (1979, 1983) and Diaconnis and Efron (1983).

Regarding the uncertainties involved in the image processing, it may be necessary to take into account two kinds of errors: a sampling error and a visualization error (Agui and Jimenez, 1987). The latter is associated with the positioning of tracer particles and their traceability to the fluid motion. Present experimental conditions are applied and the total error can be estimated as it was in previous investigations (Ushijima et al., 1991). As a result, the error range is estimated to be 10 percent with respect to the representative velocity determined by the flow rate and the geometries of the test vessel.

3 Numerical Prediction Method

3.1 Numerical Model. While there have been many attempts to apply turbulence models to thermally stratified flows, they have rarely been applied to calculations in predicting unsteady internal waves. Since the averaging procedures used to derive basic equations of turbulence models from Navier–Stokes equations are interpreted as ensemble-averaging as well as time-averaging, turbulence models can be employed in order to simulate time-dependent flows that are detected as ensemble-averaged features.

The dominant motions in low-wavenumber regions associated with the internal waves in the cylindrical vessel can be treated as ensemble-averaged components simulated with turbulence models, since the internal waves have reproducible features that were observed in experiments. Along with the prediction of internal waves, our particular interest lies in the near-wall behavior of thermal interfaces. It is necessary to take into account the near-wall effects, such as the decrease of the local turbulent Reynolds number, in the numerical model. The turbulence model adopted here is the one proposed by Lam and Bremhorst (1981), which has the merit that it needs no additional terms in the transport equation for the dissipation rate of turbulence energy. Since this model becomes a usual two-equation model as the local turbulent Reynolds number increases, it is applicable to both fully turbulent flows and near-wall regions. The governing equations based on this model are described in a cylindrical coordinate system as follows:

$$\frac{1}{r}\frac{\partial}{\partial r}(rU) + \frac{\partial V}{\partial z} = 0 \tag{3}$$

$$\frac{\partial U}{\partial t} + U\frac{\partial U}{\partial r} + V\frac{\partial U}{\partial z} = -\frac{1}{\rho}\frac{\partial P}{\partial r} + \nu\left[\frac{1}{r}\frac{\partial}{\partial r}\left(r\frac{\partial U}{\partial r}\right) + \frac{\partial^2 U}{\partial z^2} - \frac{U}{r^2}\right] - \left[\frac{1}{r}\frac{\partial}{\partial r}(r\overline{uu}) + \frac{\partial}{\partial z}\overline{uv} - \frac{1}{r}\overline{ww}\right] \tag{4a}$$

$$\frac{\partial V}{\partial t} + U\frac{\partial V}{\partial r} + V\frac{\partial V}{\partial z} = -\frac{1}{\rho}\frac{\partial P}{\partial z} - [1-\beta(\Theta-\Theta_S)]g + \nu\left[\frac{1}{r}\frac{\partial}{\partial r}\left(r\frac{\partial V}{\partial r}\right) + \frac{\partial^2 V}{\partial z^2}\right] - \left[\frac{1}{r}\frac{\partial}{\partial r}(r\overline{uv}) + \frac{\partial}{\partial z}\overline{vv}\right] \tag{4b}$$

$$\frac{\partial \Theta}{\partial t} + U\frac{\partial \Theta}{\partial r} + V\frac{\partial \Theta}{\partial z} = \alpha\left[\frac{1}{r}\frac{\partial}{\partial r}\left(r\frac{\partial \Theta}{\partial r}\right) + \frac{\partial^2 \Theta}{\partial z^2}\right] - \left[\frac{1}{r}\frac{\partial}{\partial r}(r\overline{u\theta}) + \frac{\partial}{\partial z}\overline{v\theta}\right] \tag{5}$$

$$\frac{\partial k}{\partial t} + U\frac{\partial k}{\partial r} + V\frac{\partial k}{\partial z} = P_k + \beta\overline{v\theta}g - \epsilon + \frac{1}{\sigma_k}\left(\frac{\partial k}{\partial r}\frac{\partial \epsilon_M}{\partial r} + \frac{\partial k}{\partial z}\frac{\partial \epsilon_M}{\partial z}\right) + \left(\frac{\epsilon_M}{\sigma_k} + \nu\right)\left[\frac{1}{r}\frac{\partial}{\partial r}\left(r\frac{\partial k}{\partial r}\right) + \frac{\partial^2 k}{\partial z^2}\right] \tag{6}$$

$$\frac{\partial \epsilon}{\partial t}+U\frac{\partial \epsilon}{\partial r}+V\frac{\partial \epsilon}{\partial z}=C_1 f_1\frac{\epsilon}{k}P_k-C_2 f_2\frac{\epsilon^2}{k}+\frac{1}{\sigma_\epsilon}\left(\frac{\partial \epsilon}{\partial r}\frac{\partial \epsilon_M}{\partial r}+\frac{\partial \epsilon}{\partial z}\frac{\partial \epsilon_M}{\partial z}\right)+\left(\frac{\epsilon_M}{\sigma_\epsilon}+\nu\right)\left[\frac{1}{r}\frac{\partial}{\partial r}\left(r\frac{\partial \epsilon}{\partial r}\right)+\frac{\partial^2 \epsilon}{\partial z^2}\right] \quad (7)$$

The production term of turbulence energy appearing in Eqs. (6) and (7) is given by

$$P_k=-\left[\overline{uu}\frac{\partial U}{\partial r}+\overline{uv}\left(\frac{\partial U}{\partial z}+\frac{\partial V}{\partial r}\right)+\overline{vv}\frac{\partial V}{\partial z}+\overline{ww}\frac{U}{r}\right] \quad (8)$$

The two-dimensional basic equations used here are derived with the assumption that the gradients of all variables in circumferential direction and the mean velocity in that direction are zero. In the governing equations, Reynolds stresses and turbulent heat fluxes are given by Boussinesq's assumptions in cylindrical coordinates. The eddy viscosity ϵ_M is modeled as

$$\epsilon_M=C_\mu f_\mu f_b\frac{k^2}{\epsilon} \quad (9)$$

Here the function f_μ, representing near-wall effects, is given by Lam and Bremhorst (1981):

$$f_\mu=E^2\left(1+\frac{20.5}{R_t}\right) \quad (10)$$

with

$$E=1-\exp(-A_k R_k) \quad (11a)$$

$$R_t=\frac{k^2}{\nu\epsilon} \quad (11b)$$

$$R_k=\frac{k^{1/2}r_0}{\nu} \quad (11c)$$

where r_0 stands for the distance from the wall surface. Since the early observations made by Stewart (1969), it has been well known that the turbulent diffusivity for temperature tends to be suppressed more than that for momentum as the local Richardson number increases. Thus it is of great importance that the buoyancy effects are taken into consideration in the expressions for turbulence diffusivities. The following relationship has been obtained for the function f_b appearing in Eq. (9) from turbulence measurements in stratified shear flows (Ushijima, 1989):

$$f_b=\frac{1}{1+0.24B} \quad (12)$$

where the parameter B stands for the intensity of stratification, which was proposed by Launder (1975):

$$B=\beta g\left(\frac{k}{\epsilon}\right)^2\frac{\partial \Theta}{\partial z} \quad (13)$$

The eddy conductivity ϵ_H was also evaluated using the following function for turbulent Prandtl number Pr_t based on the results of turbulence measurements in water flows (Ushijima, 1989):

$$\epsilon_H=\frac{\epsilon_M}{\mathrm{Pr}_t}=\frac{1.6}{1+0.24B}\epsilon_M \quad (14)$$

Following Lam and Bremhorst (1981), the functions f_1 and f_2, in which low-Reynolds-number effects are reflected, are given by

$$f_1=1+\left(\frac{A_{C1}}{f_\mu}\right)^3 \quad (15)$$

$$f_2=1-\exp(-R_t^2) \quad (16)$$

Table 2 Model coefficients

σ_k	σ_ϵ	C_1	C_2	C_μ	A_k	A_{C1}
1.0	1.3	1.44	1.92	0.09	0.0165	0.05

The coefficients of the basic equations are listed in Table 2, which are the same values as proposed by Lam and Bremhorst (1981).

3.2 Calculation Method. The numerical analyses are based on the finite difference method. The momentum equation is discretized by the semi-implicit method (Roache, 1976), in which new time-step variables are employed in the pressure-gradient term as well as in the acceleration term. With this difference equation for momentum, a Poisson equation for pressure is derived from the continuity equation, which is also discretized using new time-step velocities. The Poisson equations form a matrix that can be solved by the Biconjugate Gradient (BCG) method, as indicated by Fletcher (1975). The BCG method is superior to the usual iterative solution methods, such as the Successive Overrelaxation (SOR) method as presented by Young (1954) and the Alternating Direction Implicit (ADI) method by Douglas (1957), in terms of its generality and convergence rate. The velocity at the new time instant is obtained by substituting the newly found pressure into the momentum equation. The equations for energy, turbulent kinematic energy, and the dissipation are discretized explicitly. The locations of the variables are defined on a staggered grid system; the scalar variables are defined at the center of each control volume while velocity components are defined on its surfaces.

The nonlinear terms included in the governing equations are solved by a third-order interpolation method, in order to decrease numerical diffusion arising from these terms, which makes the accuracy of calculations inferior (Hirt, 1968). In this method, a convected variable ϕ is interpolated by a polynomial equation on a two-dimensional calculation area. Thus, as schematically shown in Fig. 4, the upstream point $\mathbf{r}_*(r_*, z_*)$, from which a variable at the $n+1$ time-step $\phi_{i,j}^{n+1}$ has been convected, is specified on the r–z plane at the previous time-step using the time-step and mean velocities. The unknown value ϕ_*^n at $\mathbf{r}_*$, which is identical to $\phi_{i,j}^{n+1}$, is evaluated on a two-dimensional curvature of ϕ, generally defined as

$$\phi=f(r, z) \quad (17)$$

Here, the function f is the following polynomial equation including third-order terms of r and z at the highest:

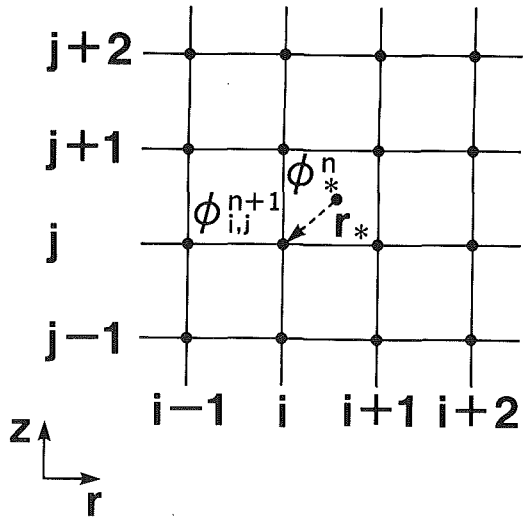

Fig. 4 Calculation scheme on r–z plane

$$f(r, z) = \sum_{m=0}^{3} \sum_{n=0}^{3} c_{m,n} r^m z^n \tag{18}$$

The 16 coefficients $c_{m,n}$ in the above equation are uniquely determined by solving the following matrix equation consisting of the values at the neighboring 16 calculation grids:

$$\begin{bmatrix} r^0_{i-1,j-1} & z^0_{i-1,j-1}, r^0_{i-1,j-1} & z^1_{i-1,j-1}, \cdots, r^3_{i-1,j-1} & z^3_{i-1,j-1} \\ r^0_{i-1,j} & z^0_{i-1,j}, r^0_{i-1,j} & z^1_{i-1,j}, \cdots, r^3_{i-1,j} & z^3_{i-1,j} \\ \cdot & \cdot \quad \cdot & \cdots \quad \cdot & \\ \cdot & \cdot \quad \cdot & \cdots \quad \cdot & \\ \cdot & \cdot \quad \cdot & \cdots \quad \cdot & \\ r^0_{i+2,j+2} & z^0_{i+2,j+2}, r^0_{i+2,j+2} & z^1_{i+2,j+2}, \cdots, r^3_{i+2,j+2} & z^3_{i+2,j+2} \end{bmatrix} \times \begin{bmatrix} c_{0,0} \\ c_{0,1} \\ \cdot \\ \cdot \\ \cdot \\ c_{3,3} \end{bmatrix} = \begin{bmatrix} \phi^n_{i-1,j-1} \\ \phi^n_{i-1,j} \\ \cdot \\ \cdot \\ \cdot \\ \phi^n_{i+2,j+2} \end{bmatrix} \tag{19}$$

Accordingly, the convected value $\phi^{n+1}_{i,j}$ is calculated by applying the coordinates at $\mathbf{r}_*$ to Eq. (18) with the coefficients determined from Eq. (19):

$$\phi^{n+1}_{i,j} = \phi^n_* = \sum_{m=0}^{3} \sum_{n=0}^{3} c_{m,n} r^m_* z^n_* \tag{20}$$

This method, having third-order accuracy, is applied to all the convection terms included in the equations for momentum, energy, turbulent kinematic energy, and its dissipation.

The numerical analyses are carried out on a two-dimensional plane as indicated in Fig. 5. While the BLA effect on the internal waves apparently arises near the cylinder surface and the side wall of the vessel, only the former case is simulated in detail. Thus the calculation area is separated into two regions; the A-region is set up in the vicinity of the cylinder surface to simulate near-wall features and the B-region covers the remaining area of the vessel. The radial width of the A-region was determined in terms of the turbulent Reynolds number defined by Eq. (11b) in the steady-state condition. The mesh sizes are $\Delta r \times \Delta z = 0.5 \times 10$ mm and 5×10 mm in the A and B-regions, respectively. Time-steps in the calculation are 2.5×10^{-4} s and 1.0×10^{-2} s in the A and B-regions, respectively. Thus the 40-step calculation in the A-region proceeds against the one-step calculation in the B-region. At the boundary between the two regions, the calculated variables in one region are linearly interpolated in order to set up the boundary conditions for the other region. When adopting the usual nonuniform mesh divisions, the time-step is restricted by the minimum value in the finer mesh regions, yet the present mesh division makes it possible to decrease such unnecessary CPU time. Along the cylinder surface the following boundary conditions are employed in the A-region:

$$U = V = k = 0 \quad [r = R_1] \tag{21}$$

and

$$\frac{\partial \epsilon}{\partial r} = \frac{\partial \Theta}{\partial r} = 0 \quad [r = R_1] \tag{22}$$

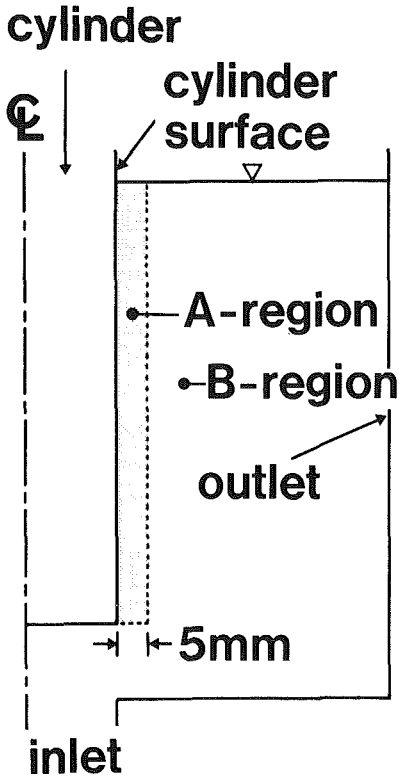

Fig. 5 Calculation area

4 Results

4.1 Experimental Results. The transition of temperature distributions was measured in the test vessel. The thermal interface created begins to take on the form of wave motions at around two minutes after the penetration of cold water. Then the wave motions develop to standing waves, which are quite stable and continue for more than several minutes. The time period (T_0) of the internal standing waves, calculated from ten internal waves, is about 8.6 seconds. Figure 6 shows the isothermal lines obtained in the vessel over one period. The numbers attached to the isothermal lines correspond to normalized temperatures defined by

$$\Theta_* = (\Theta - T_C)/(T_H - T_C) \tag{23}$$

and the time is normalized as

$$t_* = tU_0/D_v \tag{24}$$

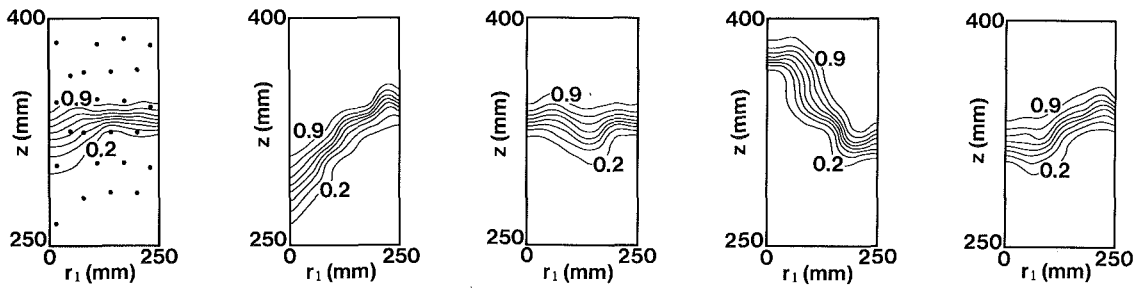

(a) $t_* = 227.2$ (b) $t_* = 227.7$ (c) $t_* = 229.1$ (d) $t_* = 230.0$ (e) $t_* = 231.4$

Fig. 6 Internal wave motions (the black circles in Fig. 6(a) indicate the positions of the thermocouples)

The image processing system enables us to capture the flow patterns arising below the internal standing waves. Two typical distributions of velocity vectors are shown in Fig. 7, which were obtained when the highest level of the internal wave occurred on the side wall of the test vessel and, after a half cycle of the wave motion, when the highest level was observed on the cylinder surface. While the vectors were not obtained for the entire region owing to the limited video-recording area, it is possible to observe that the main flow rising from the inlet hole obviously affects the above internal wave motions. Thus, the main flow moves almost straight from the inlet toward the outlet slit when the thermal interface is highest on the side wall. On the other hand, a half cycle later, regions appear in which descending flows are dominant and the angle of the main flow shifts to a more vertical direction. Accordingly it is seen that the varying angle of the main stream is closely related to the internal waves, which causes the internal standing wave motions lasting for several minutes.

Figure 8 shows the isothermal lines, whose numbers are defined by Eq. (23), over the near-wall area ($r \times z = 2.5$ mm $\times$ 150 mm) measured by the thermocouples installed on the cylinder surface. The results in Figs. 6 and 8 were not obtained simultaneously owing to the limited number of amplifiers. Two notable phenomena caused by the BLA effects are observed in the results; the amplitudes of the internal waves are decreased owing to the suppression of vertical movements and an apparent time lag arises for the motions in the vicinity of the surface, as presented at $t_* = 157.4$ and 159.8 in Fig. 8.

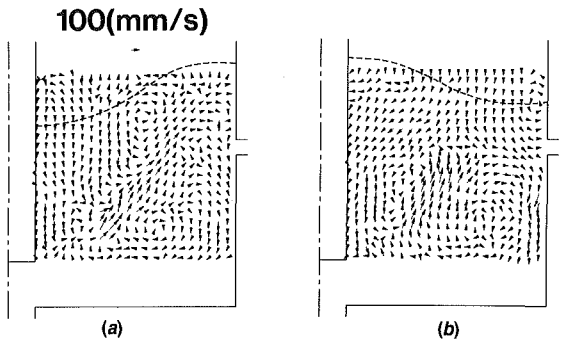

Fig. 7 Velocity vectors obtained by image processing (broken lines indicate approximate shapes of thermal interface)

These facts lead to the decrease of temperature fluctuations caused by the internal waves and the occurrence of their different phase angles, which will be discussed later.

4.2 Results of Numerical Simulations. The unsteady calculation of the thermal stratification proceeded until $t_* = 94.3$, which required 11.4 hours in CPU time on HITAC M680H. The numerically simulated results in both the A and B-regions are shown in Fig. 9. It is noted that the radial scale and the length of the vectors in the A-region are magnified compared with those in the B-region. The internal waves as observed in the experiments are simulated in Fig. 9. The average time period T_0 of five internal waves is around 8.7 seconds in the simulation, which is nearly identical to the experimental value. The direction of the main flow is coupled with the motion of standing waves in a manner similar to the experimental results; the main current runs directly from the inlet to the outlet slit in cases where the internal wave level is high on the outer side of the vessel as shown at $t_* = 83.4$ in Fig. 9, while the flow direction becomes more vertical and a large clockwise circulation is formed on the right corner after a half cycle as presented at $t_* = 85.3$. The simulated BLA effects on the internal waves are also indicated in Fig. 9. The suppression of the internal wave amplitudes and the time lag for their motions shown in Fig. 8 are qualitatively predicted as indicated at $t_* = 83.4$ and 85.3 in Fig. 9.

Figure 10 shows the peak-to-peak values (Θ_P^*) for the temperature fluctuations caused by the internal waves, which are obtained at the points listed in Table 3. The values in Fig. 10 were estimated from five internal waves and normalized by $T_H - T_C$ (= 30 K) both in experiments and calculations. The attenuation of Θ_P^* due to the BLA effect is clearly simulated here, while the calculated results are somewhat smaller than the measured values. From the experimental results, the peak-to-peak value at E_1 is about 50 percent compared with E_4, and the ratio of C_1/C_4 is about 40 percent in the analysis.

The power spectra of the temperatures at the points in Table 3 were derived after subtracting the smoothed time series operated by a moving average with a 30-second window, in other to remove the decreasing trend during the thermal transition. Figure 11 shows the spectra, which were normalized using a temperature fluctuation of E_4 for experiments and that of C_4 for calculated results. The spectra have large values at 0.1–0.2 s^{-1}, corresponding to the frequency of the internal waves.

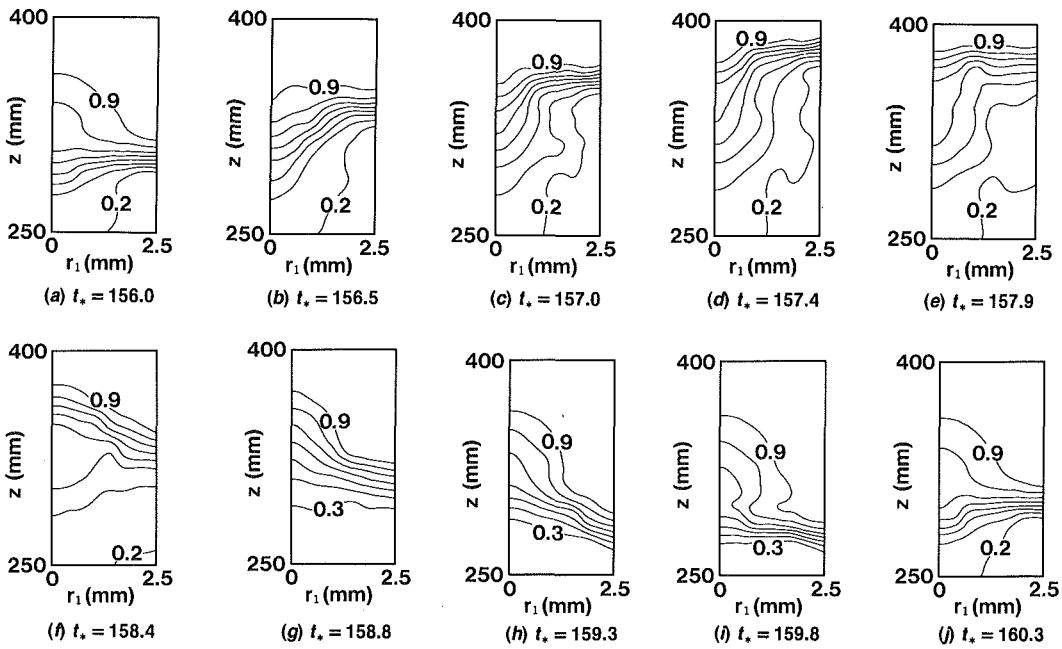

Fig. 8 Measured isothermal lines near the cylinder surface

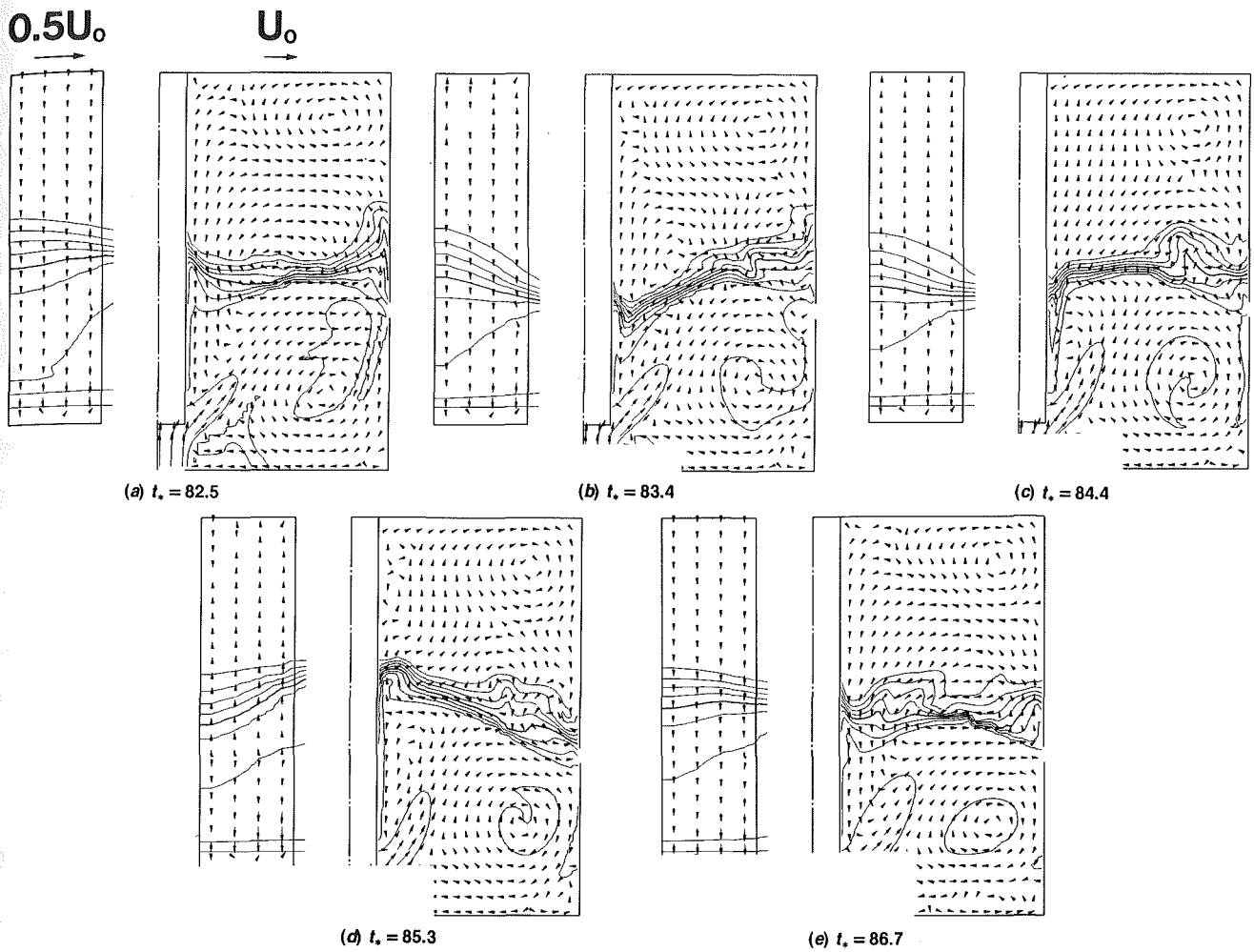

Fig. 9 Numerically simulated internal waves (left: *A*-region, right: *B*-region; thick isothermal lines correspond to $\Theta_* = 0.5$)

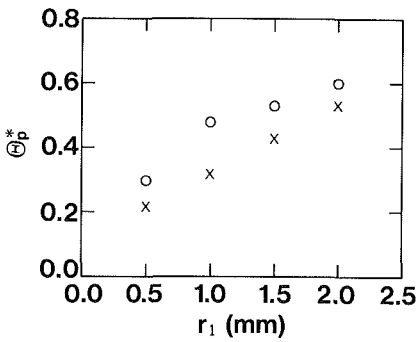

Fig. 10 Peak-to-peak values of temperature fluctuations (O = experiments; X = calculations)

Approaching the cylinder surface, the predicted spectra in the frequency decrease in a manner similar to that observed in the measured results. In the high-frequency ranges, on the other hand, the decreasing trend of the simulated spectra does not coincide with those of the experiments. This seems to result from the fact that the turbulence models employed here predict ensemble-averaged values, in contrast to the instantaneous values measured in the experiments. The differences are not negligible in the high-frequency ranges where random fluctuations are dominant.

The time lag of the temperature fluctuations near the surface can be detected by taking their phase angles. Figure 12 shows the distribution of the phase angles for temperatures at $r_1 = 0.5$ to 1.5 mm with respect to those at $r_1 = 2.0$ mm. Close observation of the meaningful low-frequency ranges reveals that the deviations of phase angles from those at the standard points (E_4 and C_4) grow with decreasing value of r_1. Figure 13 shows the quantitative comparison of the phase angles obtained at 0.1 s^{-1}. The shift of the phase angles is predicted reasonably well, as shown in the figure, and the maximum deviation is about -0.23π in experiments.

Table 3 Locations of measuring and calculation points

Measuring points	Calculation points	r_1 (mm)	z (mm)
E_1	C_1	0.5	290
E_2	C_2	1.0	290
E_3	C_3	1.5	290
E_4	C_4	2.0	290

5 Concluding Remarks

A numerical prediction method has been developed to simulate the occurrence of internal standing waves in a thermally stratified fluid contained in a cylindrical vessel and the near-wall temperature fluctuation behavior near a thermally insulated cylinder located in the vessel. The numerical model adopted here is a low-Reynolds-number k–ϵ model, which is applicable to viscous sublayers as well as fully turbulent regions. The model was improved so that it can take into consideration the buoyancy effects on eddy diffusivities and the turbulent Prandtl number.

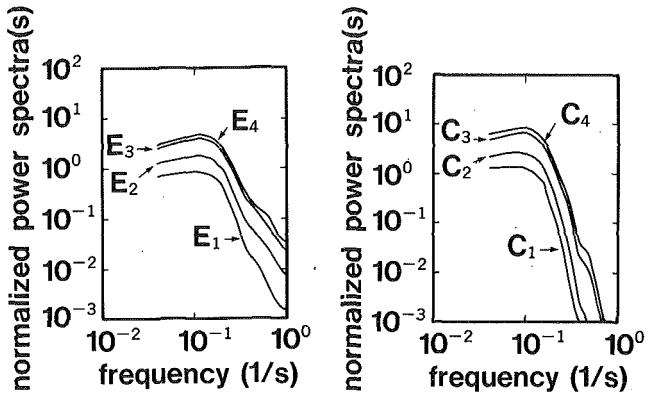

(a) Experiments (b) Calculations

Fig. 11 Power spectra of temperature fluctuations

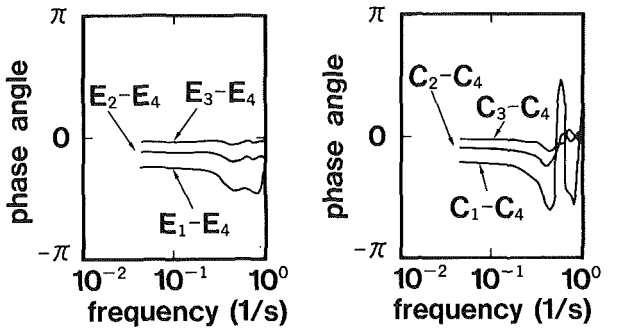

(a) Experiments (b) Calculations

Fig. 12 Phase angles of temperature fluctuations

The prediction method developed simulates the occurrence of the internal standing waves and the interconnection between the internal waves and the varying jet angles, whose state is similar to the experimentally captured features. Furthermore, while the peak-to-peak values of the temperature fluctuations are calculated as somewhat less than the measured values, the tendency of the attenuation in magnitudes for the power spectra and the shifts in phase angles caused by the BLA effect are reasonably predicted near the cylinder surface.

Acknowledgments

The authors are grateful to Mrs. Y. Nakazono, Mrs. F. Taguchi, and Mr. H. Karube for their contribution to this work.

References

Agui, J., and Jimenez, J., 1987, "On the Performance of Particle Tracking," *J. Fluid Mech.*, Vol. 185, pp. 447–468.

Chang, T. P. K., Watson, A. T., and Tatterson, G. B., 1985, "Image Processing of Tracer Particle Motions as Applied to Mixing and Turbulent Flow—II. Results and Discussion," *Chemical Engineering Science*, Vol. 40, No. 2, pp. 277–285.

Diaconnis, P., and Efron, B., 1983, "Computer-Intensive Methods in Statistics," *Scientific American*, Vol. 248, No. 5, pp. 96–108.

Douglas, J., 1957, "A Note on the Alternating Direction Implicit Method for the Numerical Solution of Heat Flow Problem," *Proceedings of the American Mathematical Society*, Vol. 8, pp. 409–412.

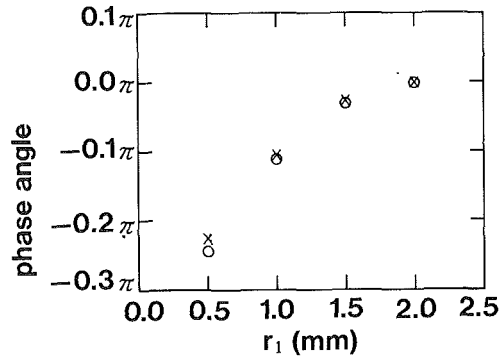

Fig. 13 Comparisons of phase angles at 0.1 s^{-1} (O = experiments, X = calculations)

Efron, B., 1979, "Computers and the Theory of Statistics: Thinking the Unthinkable," *SIAM Review*, Vol. 21, No. 4, pp. 460–480.

Efron, B., 1983, "Estimating the Error Rate of a Prediction Rule: Improvement of Cross-Validation," *J. American Statistical Association*, Theory and Methods Section, Vol. 78, No. 382, pp. 316–331.

Fletcher, R., 1975, *In Lecture Note Mathematics*, Springer, Vol. 506, pp. 73–89.

Hanjalic, K., and Launder, B. E., 1976, "Contribution Towards a Reynolds-Stress Closure for Low-Reynolds-Number Turbulence," *J. Fluid Mech.*, Vol. 74, pp. 593–610.

Hirt, C. W., 1968, "Heuristic Stability Theory for Finite-Difference Equations," *J. Comp. Phys.*, Vol. 2, pp. 339–355.

Imaichi, K., and Ohmi, K., 1983, "Numerical Processing of Flow-Visualization Pictures—Measurement of Two-Dimensional Vortex Flow," *J. Fluid Mech.*, Vol. 129, pp. 283–311.

Jones, W. P., 1972, "The Predictions of Laminarization With a Two-Equation Model of Turbulence," *Int. J. Heat Mass Transfer*, Vol. 15, p. 301.

Jones, W. P., and Launder, B. E., 1973, "The Calculation of Low-Reynolds-Number Phenomena With a Two-Equation Model of Turbulence," *Int. J. Heat Mass Transfer*, Vol. 16, p. 1119.

Kim, J. H., Deardorff, A. F., and Roidt, R. M., 1991, "Thermal Stratification in Nuclear Reactor Piping System," *Proceedings of the 1st JSME/ASME International Conference on Nuclear Engineering*, Vol. 2, pp. 235–241.

Kobayashi, T., Yoshitake, Y., Saga, T., and Segawa, S., 1985, "An Image Processing Technique for Determining Two-Dimensional Flow Fields With Reverse Flow," *Proc. ASME Symp. on Physical and Numerical Flow Visualization*, pp. 39–46.

Lam, C. K. G., and Bremhorst, K., 1981, "Modified Form of the k–ϵ Model for Predicting Wall Turbulence," ASME *Journal of Fluids Engineering*, Vol. 103, pp. 456–460.

Launder, B. E., 1975, "On the Effects of a Gravitational Field on the Turbulent Transport of Heat and Momentum," *J. Fluid Mech.*, Vol. 67, pp. 569–581.

Moriya, S., Tanaka, N., and Katano, N., 1987, "Effects of Reynolds Number and Richardson Number on Thermal Stratification in Hot Plenum," CRIEPI Rep. No. E383006.

Nishino, K., Kasagi, N., and Hirata, M., 1989, "Three-Dimensional Particle Tracking Velocimetry Based on Automated Digital Image Processing," *J. Fluids Eng.*, Vol. 111, pp. 384–391.

Patel, V. C., Rodi, W., and Scheuerer, G., 1984, "Turbulence Models for Near-Wall and Low Reynolds Number Flows: A Review," *AIAA J.*, Vol. 23, No. 9, pp. 1308–1319.

Prandtl, L., and Tietjens, O., 1934, *Applied Hydro and Aerodynamics*, Dover.

Roache, P. J., 1976, *Computational Fluid Dynamics*, Hermosa Publishers Inc.

Sommerscales, E. F. C., 1980, "Fluid Velocity Measurements by Particle Tracking, In Flow, Its Measurement and Control in Science and Industry," Vol. I, R. E. Wendt, ed., Instrum. Soc. Am., pp. 795–808.

Stewart, R. W., 1969, "Turbulence and Waves in a Stratified Atmosphere," *Radio Science*, Vol. 4, No. 12, pp. 1269–1278.

Ushijima, S., 1989, "Study on Turbulence Modeling of Stratified Flow and Its Application," Doctoral Dissertation, Kyoto University [in Japanese].

Ushijima, S., Takeda, H., and Tanaka, N., 1991, "Image Processing System for Velocity Measurements in Natural Convection Flows," *Nuclear Engineering and Design*, Vol. 132, pp. 265–276.

Young, D., 1954, "Iterative Methods for Solving Partial Difference Equations of Elliptic Type," *Trans. Amer. Math. Soc.*, Vol. 76, pp. 92–111.

Analysis of a Transient Asymmetrically Heated/Cooled Open Thermosyphon

G. F. Jones
Mem. ASME

J. Cai

Department of Mechanical Engineering,
Villanova University,
Villanova, PA 19085

We present a numerical study of transient natural convection in a rectangular open thermosyphon having asymmetric thermal boundary conditions. One vertical wall of the thermosyphon is either heated by constant heat flux ("warmup") or cooled by convection to the surroundings ("cooldown"). The top of the thermosyphon is open to a large reservoir of fluid at constant temperature. The vorticity, energy, and stream-function equations are solved by finite differences on graded mesh. The ADI method and iteration with overrelaxation are used. We find that the thermosyphon performs quite differently during cooldown compared with warmup. In cooldown, flows are mainly confined to the thermosyphon with little momentum and heat exchange with the reservoir. For warmup, the circulation resembles that for a symmetrically heated thermosyphon where there is a large exchange with the reservoir. The difference is explained by the temperature distributions. For cooldown, the fluid becomes stratified and the resulting stability reduces motion. In contrast, the transient temperature for warmup does not become stratified but generally exhibits the behavior of a uniformly heated vertical plate. For cooldown and $Ra > 10^4$, time-dependent heat transfer is predicted by a closed-form expression for one-dimensional conduction, which shows that $Nu - Bi^{1/2}/A$ in the steady-state limit. For warmup, transient heat transfer behaves as one-dimensional conduction for early times and at steady state and for $Ra^* \geq 10^5$, can be approximated as that for a uniformly heated vertical plate.

Introduction

A thermal diode is a heat exchanger that transports heat preferentially in one direction only. When used as a solar collector in a building, the diode is very effective because heat that is collected during the day cannot escape from the diode along the same path at night. As shown in Fig. 1, the diode consists of a fluid-filled reservoir connected to a long rectangular slot or "tongue." Typically, the tongue is about 35 cm high and 2 cm wide. Solar radiation striking the outside surface of the tongue initiates convection, transferring heat from the warm tongue to the cooler, higher-placed reservoir. During sunless periods, the tongue and reservoir cool as heat is transferred to the surroundings. Convective motion is weaker for this phase because the tongue is below the reservoir, which introduces some stability to the problem. The combination of large heat transfer during warmup and poor heat transfer during cooldown results in good performance for the diode compared with alternative solar collectors.

Warmup was modeled using integral methods by assuming laminar boundary layer flow in the tongue and complete mixing in the reservoir (Jones, 1986). This approach produced reservoir temperature distributions in good agreement with limited test data. For cooldown, laboratory experiments showed that convective flows from cooling of the tongue enhanced heat transfer when compared with conduction. Empirically determined factors accounting for this enhancement were used in an earlier transient conduction model referenced above. The model was validated for diodes of just one design so the generality of the factors is in question.

The geometry of the tongue is traditionally referred to as an open thermosyphon, the steady-state behavior for which is well established. Lighthill (1953) for constant wall temperature, and Hartnett and Welsh (1957) for constant wall heat flux were among the first to analyze this problem. Both considered symmetric heating. From the latter work, average heat transfer is determined to be independent of the heating condition. The more recent work of Gosman et al. (1971) confirmed Lighthill's results for laminar flow only. Later studies, which included analyses and experiments by Martin (1955), Lockwood and Martin (1964), Martin and Lockwood (1963), and Hasegawa

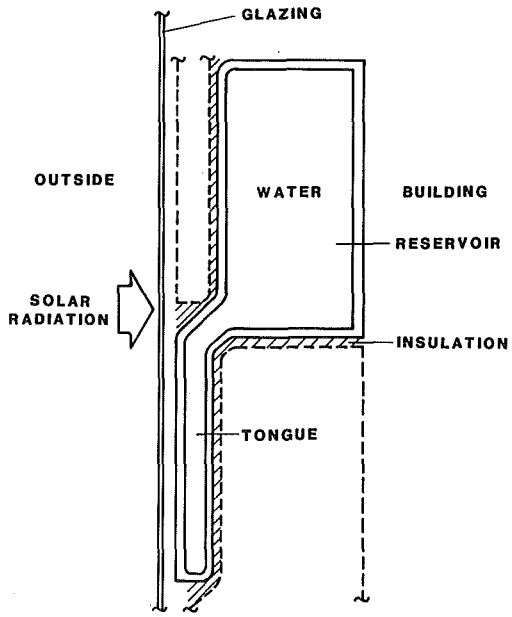

Fig. 1 Schematic diagram of thermal diode

Contributed by the Heat Transfer Division for publication in the JOURNAL OF HEAT TRANSFER. Manuscript received by the Heat Transfer Division July 1992; revision received January 1993. Keywords: Enclosure Flows, Natural Convection, Transient and Unsteady Heat Transfer. Associate Technical Editor: J. R. Lloyd.

et al. (1963), focused on noncircular, symmetrically heated geometries with particular attention paid to entrance effects and the transition to turbulence. Japikse (1973) summarized much of the work on thermosyphons prior to 1973.

We are unaware of any work on asymmetric heating and cooling of the open thermosyphon nor its transient behavior. During warmup, the presence of the adiabatic nonslip wall increases viscous effects and provides no benefit to heat transfer. Thus, one expects the heat transfer to be less than that for symmetric heating.

Insight on the behavior during cooldown can be provided by considering transient natural convection in an enclosed cavity. Hall et al. (1988), Fu et al. (1990), and Nicolette et al. (1985) addressed transient heating or cooling of a square cavity through either one or two vertical walls, the remaining walls being insulated.

Nicolette et al. considered the response of fluid to a suddenly cooled vertical wall. For large Ra they observe the periodic formation of a shear-driven secondary-flow cell as fluid in the descending boundary layer enters the core at the bottom of the enclosure, flows upward, and rejoins the boundary layer without involving the entire cavity. This gives rise to the oscillatory behavior of the Nusselt number with time, an effect also reported by Patterson (1984).

Hall et al. studied the same geometry as Nicolette et al. with a suddenly heated wall but did not report on the formation of a secondary flow. Applying the fundamental work of Patterson and Imberger (1980) and Ivey (1984), Hall et al. addressed two characteristic time scales for transient natural convection in a cavity for $\mathrm{Pr} > 1$. In the "early period," the problem is dominated by conduction (i.e., conduction at the wall balances the rate of energy stored in the fluid) as the momentum and thermal boundary layers are formed. After this, during the "late period," conduction at the wall is balanced by vertical convection in the momentum boundary layer.

An interesting aspect of the thermosyphon cooldown not present in the above works stems from the fact that the top horizontal boundary of the thermosyphon is a constant-temperature reservoir. Heat transfer occurs at a vertical wall of the thermosyphon and at the horizontal thermosyphon-reservoir interface ("orifice"). The former effect is destabilizing, whereas the latter tends to stabilize the flow through temperature stratification. As seen below, both contributions play major roles in determining thermosyphon heat transfer and fluid dynamics.

Analysis

Geometry and Assumptions. The thermosyphon is a rectangular, two-dimensional slot of height H and width W (Fig. 2). The aspect ratio A is H/W. The top horizontal boundary of the thermosyphon is open to an infinitely large reservoir of fluid at temperature T_r. One vertical wall of the thermosyphon is either heated by constant heat flux, q_o, or cooled by convection to the surrounding temperature, T_∞, through a constant heat transfer coefficient, h_∞. The bottom horizontal wall and remaining vertical wall are insulated. We assume two-dimensional, laminar flow of a Boussinesq fluid.

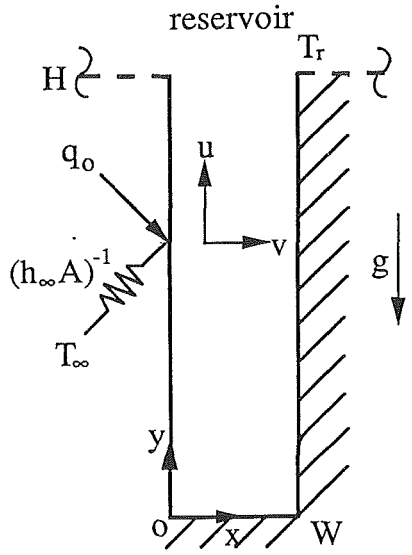

Fig. 2 The thermosyphon

Formulation. The problem is formulated in terms of vorticity, stream function, and temperature. This approach eliminates the unnecessary pressure term, and as shown below, is convenient for treating the inflow boundary conditions at the top of the tongue. The vorticity-transport, energy, and stream-function equations are

$$\frac{\partial \omega}{\partial t} + \frac{\partial (u\omega)}{\partial x} + \frac{\partial (v\omega)}{\partial y} = \nu \left(\frac{\partial^2 \omega}{\partial x^2} + \frac{\partial^2 \omega}{\partial y^2} \right) + g\beta \frac{\partial T}{\partial x}, \tag{1}$$

$$\frac{\partial T}{\partial t} + \frac{\partial (uT)}{\partial x} + \frac{\partial (vT)}{\partial y} = \alpha \left(\frac{\partial^2 T}{\partial x^2} + \frac{\partial^2 T}{\partial y^2} \right), \tag{2}$$

$$\frac{\partial^2 \psi}{\partial x^2} + \frac{\partial^2 \psi}{\partial y^2} = -\omega, \tag{3}$$

Nomenclature

A = aspect ratio = H/W
Bi = Biot number = $h_\infty W/k$
g = acceleration of gravity, m^2/s
h = heat transfer coefficient, W/m^2-K
H = height, m
k = thermal conductivity of fluid, W/m-K
Nu = Nusselt number = hW/k
Pr = Prandtl number = ν/α
q_o = heat flux at wall, W/m^2
Ra = Rayleigh number = $g\beta W^3 (T_r - T_\infty)/\nu\alpha$
Ra* = flux Rayleigh number = $g\beta W^4 q_o/k\nu\alpha$
t = time, s
T = temperature, K
u = x component of velocity, m/s
U = dimensionless x component of velocity [Eq. (8)]
v = y component of velocity, m/s
V = dimensionless y component of velocity [Eq. (8)]
W = width, m
x = horizontal coordinate, m
y = vertical coordinate, m
α = thermal diffusivity, m^2/s
β = coefficient of thermal expansion, K^{-1}
ΔT_{ref} = reference temperature difference [Eq. (9)], K
Δx = grid spacing in x direction, m
Δy = grid spacing in y direction, m
η = dimensionless x coordinate = x/W
θ = dimensionless temperature = $(T - T_\infty)/\Delta T_{\mathrm{ref}}$
ν = kinematic viscosity, m^2/s
ξ = dimensionless y coordinate = y/W
τ = dimensionless time = $\alpha t/W^2$
ψ = stream function, m^2/s
Ψ = dimensionless stream function = ψ/α
ω = vorticity, s^{-1}
Ω = dimensionless vorticity = $\omega/(\alpha/W^2)$

Subscripts

avg = spatial average or mean
eff = effective
r = reservoir
ref = reference
ss = steady state
w = wall
∞ = surroundings

where the vorticity, $\omega = \partial v/\partial x - \partial u/\partial y$. The velocity components are related to the stream function ψ by $u = \partial\psi/\partial y$, $v = -\partial\psi/\partial x$, which identically satisfy the incompressible continuity equation.

The thermal boundary conditions include a mixed condition for the vertical wall at $x = 0$ and adiabatic conditions at the remaining solid walls,

$$-k\left.\frac{\partial T}{\partial x}\right|_{x=0} = q_0 + h_\infty(T_\infty - T|_{x=0}), \tag{4}$$

$$\left.\frac{\partial T}{\partial x}\right|_{x=W} = 0, \quad \left.\frac{\partial T}{\partial y}\right|_{y=0} = 0, \tag{5}$$

where q_0 is a constant heat flux and h_∞ is a constant heat transfer coefficient at the outside of the wall. Equation (4) accommodates both warmup (q_0 nonzero) and cooldown (q_0 of zero). The thermal boundary conditions at $y = H$ are addressed below.

The stream function is arbitrarily taken to be zero at all solid boundaries giving $\psi|_{x=0} = 0$, $\psi|_{x=W} = 0$, and $\psi|_{y=0} = 0$. With no-slip velocity along all solid boundaries we can write

$$\omega|_{x=0} = \left.\frac{\partial v}{\partial x}\right|_{x=0} = -\left.\frac{\partial^2\psi}{\partial x^2}\right|_{x=0}, \tag{6a}$$

$$\omega|_{x=W} = \left.\frac{\partial v}{\partial x}\right|_{x=W} = -\left.\frac{\partial^2\psi}{\partial x^2}\right|_{x=W}, \tag{6b}$$

$$\omega|_{y=0} = -\left.\frac{\partial u}{\partial y}\right|_{y=0} = -\left.\frac{\partial^2\psi}{\partial y^2}\right|_{y=0}. \tag{6c}$$

The orifice at (x, $y = H$) is an inflow boundary. Inflow boundary conditions are a subject of ongoing debate. The exact state of the entering fluid is generally unknown because of possible influence from the outflow. For laminar flow, Lighthill (1953) and Chan and Tien (1985) have both confirmed that because the thermosyphon has a dominant characteristic of its own, heat transfer is not strongly influenced by the state of the incoming reservoir fluid. This prompted Gosman et al. (1971) to assume zero axial gradients of vorticity and stream function for inflow and outflow at the orifice. Likewise, the axial temperature gradient is taken as zero for outflow because of the infinite length scale of the reservoir. For inflow, the temperature at the orifice is appropriately taken as that of the reservoir. We follow this approach and obtain

$$\left.\frac{\partial\omega}{\partial y}\right|_{y=H} = \left.\frac{\partial\psi}{\partial y}\right|_{y=H} = \left.\frac{\partial T}{\partial y}\right|_{y=H} = 0 \quad \text{(outflow)}, \tag{7a}$$

$$\left.\frac{\partial\omega}{\partial y}\right|_{y=H} = \left.\frac{\partial\psi}{\partial y}\right|_{y=H} = 0, \quad T|_{y=H} = T_r \quad \text{(inflow)}. \tag{7b}$$

Scaling. We consider the following scales:

$$\theta = \frac{T - T_\infty}{\Delta T_{\text{ref}}}, \quad \eta = \frac{x}{W}, \quad \xi = \frac{y}{W}, \quad U, V = \frac{u, v}{\alpha/W},$$

$$\Omega = \frac{\omega}{\alpha/W^2}, \quad \Psi = \frac{\psi}{\alpha}, \quad \tau = \frac{\alpha t}{W^2}, \tag{8}$$

where

$$\Delta T_{\text{ref}} = T_r - T_\infty \text{ (cooldown)} \quad \text{or} \quad \frac{q_0 W}{k} \text{ (warmup)}. \tag{9}$$

With these, the governing equations are nondimensionalized and written as

$$\frac{\partial\Omega}{\partial\tau} + \frac{\partial(U\Omega)}{\partial\eta} + \frac{\partial(V\Omega)}{\partial\xi} = \text{Pr}\left(\frac{\partial^2\Omega}{\partial\eta^2} + \frac{\partial^2\Omega}{\partial\xi^2}\right) + \text{RaPr}\frac{\partial\theta}{\partial\eta}, \tag{10}$$

$$\frac{\partial\theta}{\partial\tau} + \frac{\partial(U\theta)}{\partial\eta} + \frac{\partial(V\theta)}{\partial\xi} = \frac{\partial^2\theta}{\partial\eta^2} + \frac{\partial^2\theta}{\partial\xi^2}, \tag{11}$$

$$\frac{\partial^2\Psi}{\partial\eta^2} + \frac{\partial^2\Psi}{\partial\xi^2} = -\Omega, \tag{12}$$

where Ra is the Rayleigh number ($g\beta W^3\Delta T_{\text{ref}}/\nu\alpha$) and Pr is the Prandtl number.

With Eqs. (8) the boundary condition at the heated/cooled wall becomes

$$-\left.\frac{\partial\theta}{\partial\eta}\right|_{\eta=0} = \Gamma - \text{Bi}\,\theta|_{\eta=0}, \tag{13}$$

where $\text{Bi} = h_\infty W/k$ is the Biot number and Γ is 1 for warmup (by definition $\text{Bi}\,\theta|_{\eta=0} < 1$ must be satisfied for warmup to occur) or 0 for cooldown. The remaining boundary conditions are:

$$\left.\frac{\partial\theta}{\partial\eta}\right|_{\eta=1} = 0, \quad \left.\frac{\partial\theta}{\partial\xi}\right|_{\xi=0} = 0, \tag{14}$$

$$\Psi|_{\eta=0} = 0, \quad \Psi|_{\eta=1} = 0, \quad \Psi|_{\xi=0} = 0, \tag{15}$$

$$\Omega|_{\eta=0} = -\left.\frac{\partial^2\Psi}{\partial\eta^2}\right|_{\eta=0}, \quad \Omega|_{\eta=1} = -\left.\frac{\partial^2\Psi}{\partial\eta^2}\right|_{\eta=1},$$

$$\Omega|_{\xi=0} = -\left.\frac{\partial^2\Psi}{\partial\xi^2}\right|_{\xi=0}, \tag{16}$$

$$\left.\frac{\partial\Omega}{\partial\xi}\right|_{\xi=A} = \left.\frac{\partial\Psi}{\partial\xi}\right|_{\xi=A} = \left.\frac{\partial\theta}{\partial\xi}\right|_{\xi=A} = 0 \quad \text{(outflow)}, \tag{17a}$$

$$\left.\frac{\partial\Omega}{\partial\xi}\right|_{\xi=A} = \left.\frac{\partial\Psi}{\partial\xi}\right|_{\xi=A} = 0, \quad \theta|_{\xi=A} = 1 \quad \text{(inflow)}. \tag{17b}$$

We have taken $T_r - T_\infty/(q_0 W/k)$ equal to 1 for warmup.

For simplicity, the initial condition is the same for cooldown and warmup. If the thermosyphon is initially at the reservoir temperature, $\theta(\eta, \xi, \tau = 0)$ is equal to 1.

In dimensionless form, the velocity components and vorticity are written as $U = \partial\Psi/\partial\xi$, $V = -\partial\Psi/\partial\eta$, and $\Omega = \partial V/\partial\eta - \partial U/\partial\xi$.

Method of Solution. Vorticity, temperature, and stream-function distributions are obtained by solving Eqs. (10)–(12) subject to the boundary conditions Eqs. (13)–(17). Finite differences are used with a graded mesh having m, n (odd) number of nodes in the x, y directions. The scheme for grid expansion in the x direction is

$$\Delta\eta_i = e_x\Delta\eta_{i-1}, \quad i = 2, \ (m-1)/2, \tag{18a}$$

where

$$1/\Delta\eta_1 = \sum_{i=0}^{(m-1)/2} e_x^i. \tag{18b}$$

The x-grid expansion factor e_x is set to about 1.1, which produces wall-cell dimensions that are a factor of 5–10 smaller than those in the middle of the domain. Expressions similar to Eqs. (18) are written for the y direction.

The vorticity and energy equations are solved by the Implicit Alternating Direction method (Jaluria and Torrence, 1986) one equation at a time. The tridiagonal system for each line is solved by the Crout method (Hildebrand, 1966). The time step is kept small to avoid numerical instabilities that might arise from this weakly implicit approach. For a given time, no iteration among the equations is needed because of the small time step.

Poisson's equation is solved by iteration with overrelaxation. The relaxation factor varies but is about 1.8. The advective terms in Eqs. (10) and (11) are modeled with conserving upwind

differences (Jaluria and Torrence, 1986), which is superior to usual first-order upwinding. Alternately, the power-law scheme of Patankar (1980) could be used but was not for reasons of convenience. The derivatives in the expressions for vorticity and velocity are written as second-order finite differences.

The expressions for boundary vorticity (Eqs. (16)) are cast in finite-difference form by writing a Taylor series expansion for Ψ about the boundary node (Wilkes and Churchill, 1966; Reddy, 1989). For example, at the heated/cooled wall, we get

$$\Omega_{1,j} = -\frac{2(\Delta\eta_1+\Delta\eta_2)}{\Delta\eta_1^2\Delta\eta_2}\Psi_{2,j} + \frac{2\Delta\eta_1}{(\Delta\eta_1+\Delta\eta_2)^2\Delta\eta_2}\Psi_{3,j}. \quad (19)$$

The terms $\Delta\eta_1$ and $\Delta\eta_2$ are the sizes for the two cells nearest the wall. For a uniform grid, Reddy has shown this approach to produce heat transfer results in good agreement with data for steady natural convection in a square cavity.

The correct inflow or outflow boundary conditions are applied at each node at $\xi = A$ based on the state of the flow at that node from the previous time.

Mean Nusselt Number and Wall Temperature. For cooldown, a mean Nusselt number for the cooled wall is defined as $\mathrm{Nu}(\tau) = h(\tau)W/k$, where $h(\tau)$ is based on $T_r - T_\infty$. We get

$$\mathrm{Nu}(\tau) = -\frac{1}{A}\int_0^A \left.\frac{\partial\theta}{\partial\eta}\right|_{\eta=0} d\xi. \quad (20)$$

The derivative $\partial\theta/\partial\eta|_{\eta=0}$ is evaluated by a second-order finite difference expression.

For warmup with negligible Bi, heat transfer at $\eta = 0$ is known so Eq. (20) is not useful. In this case, we are interested in a mean wall temperature defined as

$$\theta_{w,\mathrm{avg}}(\tau) = \frac{1}{A}\int_0^A \theta(\eta=0,\ \xi,\ \tau)d\xi. \quad (21)$$

The dimensional and dimensionless wall temperatures are related by

$$\theta_{w,\mathrm{avg}} = 1 + \frac{T_{w,\mathrm{avg}} - T_r}{q_0 W/k}. \quad (22)$$

Cases

In this study, we consider aspect ratios of 2, 5, 10, and 20 and Rayleigh numbers of 10^4, 10^5, 10^6, and 10^7. As reported by Jones (1986), aspect ratios for the diodes tested in the past have ranged from about 15 to 20. However, it is of interest to investigate the sensitivity of heat transfer to a larger span of values. The Rayleigh numbers given above correspond to the range of operating conditions for a diode. Ra of 10^4 is close to the lower limit of any appreciable convection, and in the range of Ra from 10^6 to 10^7, transition to turbulence has been reported (Hartnett and Welsh, 1957; Martin and Lockwood, 1963).

A value for Bi of about 4 or less corresponds to natural-convection cooling of the outside wall of the thermosyphon. This is of interest for the diode. We choose two other values to bound this: Bi of 1 and 8. In this study, Pr is equal to 6.1.

The numbers of nodes and grid-expansion factors are chosen to give wall-cell dimensions ($\Delta\xi_1$ and $\Delta\eta_1$) of not more than about 0.025. This is equivalent to 41 nodes in the x direction if grid spacing were uniform. Several cases for large aspect ratio are solved with as many as 131 nodes in the y direction but most have about 51. The number of nodes in the x direction is typically 21.

Dimensionless time steps of about 3×10^{-5} were used to ensure stability of the solution. The time step was automatically accelerated by an ad-hoc method as the solution proceeded toward steady state. With this step size about 50,000 to 100,000 time steps were needed to reach steady state for cooldown with small Ra and Bi. For cooldown cases with high Ra and Bi and for warmup, steady conditions are reached with fewer time steps as described below.

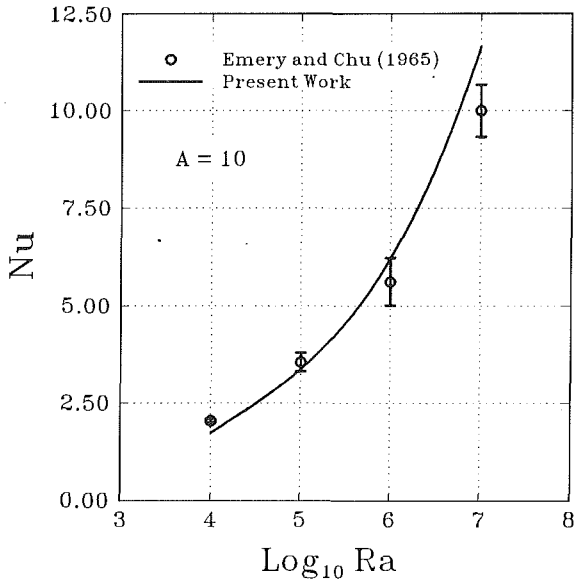

Fig. 3 Comparison of numerical results with data for $A = 10$

For warmup, ΔT_{ref} is such that the Rayleigh number is the flux Rayleigh number, Ra*. To reduce the number of parameters and simplify the presentation of results, the Biot number is set to zero for the warmup cases. To accommodate the effects of nonzero Bi, the mean-wall temperature from the zero-Bi case can be used to calculate a reduced heat flux. This flux is then used to determine a new Ra* and the problem rerun with $\mathrm{Bi} = 0$. The procedure is repeated until the wall temperature distribution no longer changes. This approach produces the exact solution only if the wall temperature is uniform. As we see below the wall temperature varies 5 percent or less over the uppermost 90 percent of the thermosyphon height for the cases considered here.

Results—Comparison with Existing Data

In Fig. 3 we compare Nusselt numbers from the present model with data for steady laminar natural convection in an enclosure of aspect ratio 10 (Emery and Chu, 1965). The Rayleigh-number range, Prandtl number, and cell sizes are given above. From Fig. 3 we see that the deviation between the calculated Nusselt number and data is about 10 percent for Ra of 10^4 and 10^7. For Ra of 10^5 and 10^6, the predicted Nusselt number lies within the error band for the data. The discrepancies are not excessive. de Vahl Davis and Jones (1983) report even greater scatter in heat transfer results for a similar problem when solved by a variety of different methods. Increasing the number of nodes will improve the accuracy of the model, but the large increase in computer time for the transient problem considered makes this option currently impractical.

Results—Cooldown and Warmup

Discussion. Results for cooldown and warmup are discussed in separate sections below. Summarizing the results, we see that the thermosyphon performs quite differently during cooldown compared with warmup. In cooldown, flows are mainly confined to the thermosyphon with little momentum and heat exchange with the reservoir. For warmup, the circulation resembles that for a symmetrically heated thermosyphon where there is a large exchange with the reservoir. The difference is explained by examining the temperature distributions. For cooldown, the fluid is stratified and the resulting

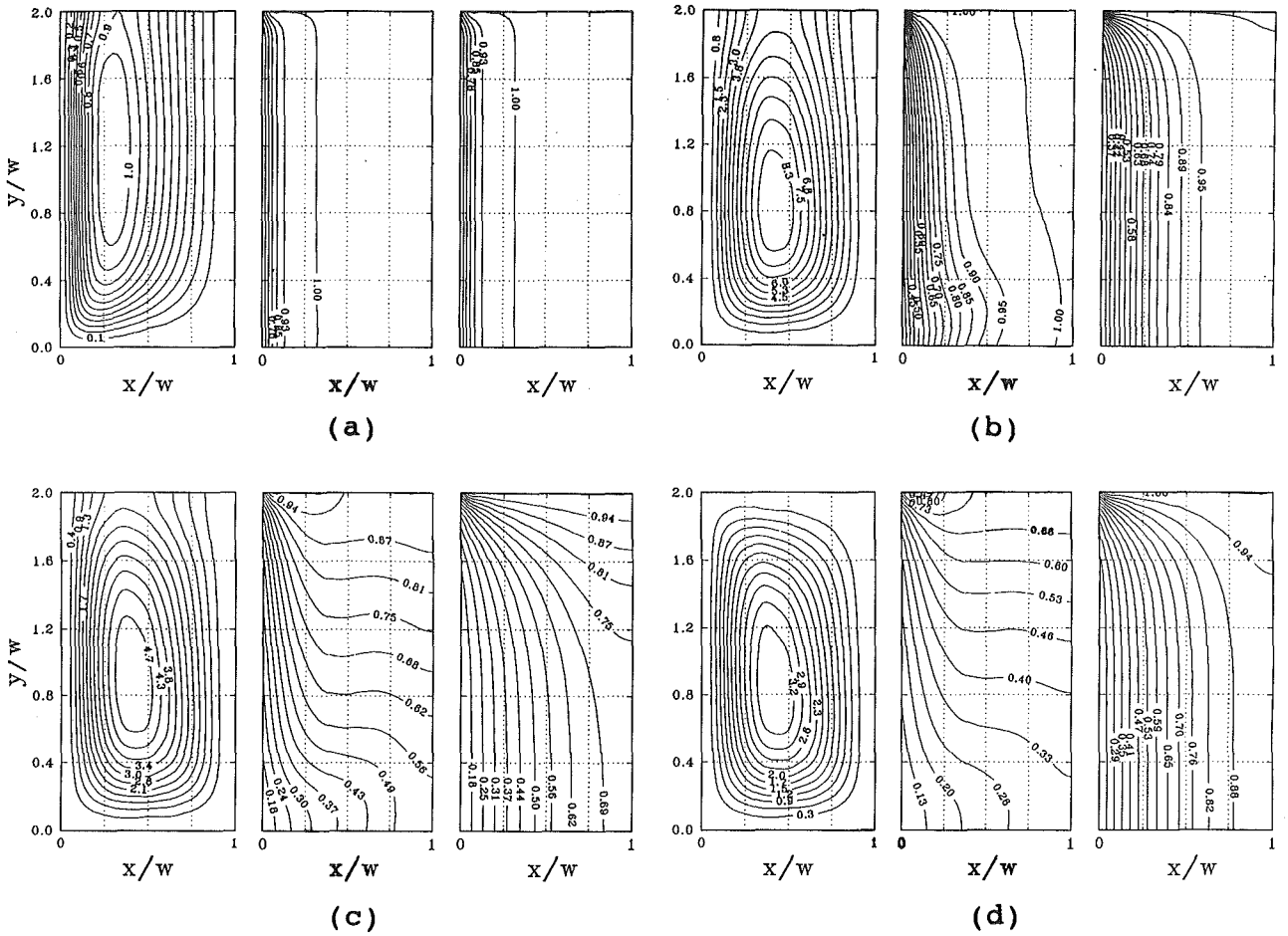

stability reduces motion. In contrast to this, the transient temperature for warmup is not stratified but generally exhibits the behavior of a uniformly heated vertical plate.

Cooldown. We first consider evolution of the flow and temperature fields for two different cases. Stream-function, temperature, and pure-conduction temperature distributions are shown in Fig. 4 for five values of time, A of 2, Ra of 10^4, and Bi of 8. From Fig. 4, we see that the circulation is unicellular: initially increasing with time and, after a brief period, decreasing. The streamline plots indicate relatively weak fluid exchange with the reservoir except for the earliest two times, and virtually no flow across the orifice for τ greater than about 0.3. For τ of 0.0058, the temperature and pure-conduction temperature distributions are identical (Fig. 4*a*) and, except near the reservoir, resemble those for a suddenly cooled semi-infinite medium. For this time, advection is too weak to affect the temperature field.

With increasing time (Figs. 4*b–e*), the isotherms tilt in response to increased intensity of the counterclockwise circulation. The tilting isotherms initiate temperature stratification, which, at steady state, is evident over most of the upper half of the thermosyphon (Fig. 4*e*). Stratification indicates a balance between vertical conduction and vertical advection in the thermosyphon core.

For A of 10, Ra of 10^6, and Bi of 8 (Fig. 5), we see similar behavior as described above. In this case, the streamlines are skewed more toward the cooled wall, and the stratification near the orifice and circulation are more pronounced than in Fig. 4 due to larger Ra. Large stratification is responsible for reducing advection across the orifice but increases orifice conduction. As seen below, the net effect is to decrease the mean heat transfer at the cooled wall. From Fig. 5, we also note the

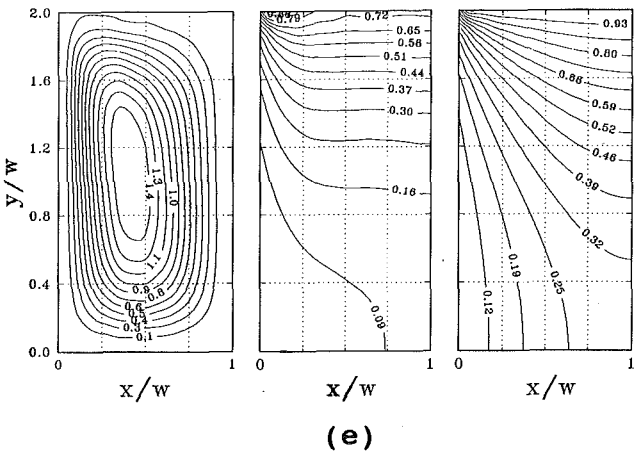

Fig. 4 Cooldown. Evolution of stream-function, temperature, and pure-conduction temperature distributions for $A = 2$, Ra $= 10^4$, and Bi $= 8$. The values of τ are: (*a*) 0.0058, (*b*) 0.029, (*c*) 0.147, (*d*) 0.296, (*e*) 0.851 (steady state).

formation of a second cell of weak circulation (Fig. 5*d*) as a result of the horizontal temperature gradients at the cooled wall that are concentrated near the orifice.

By inspecting the isotherms at the cooled wall in both Figs. 4 and 5, we see that horizontal temperature gradients, and thus heat transfer, decrease with increased time. This result is consistent with the temperature of the thermosyphon approaching zero (the dimensionless temperature of the surroundings) as time progresses, which is most evident in Fig. 5.

From the foregoing discussion of Figs. 4 and 5, we can make

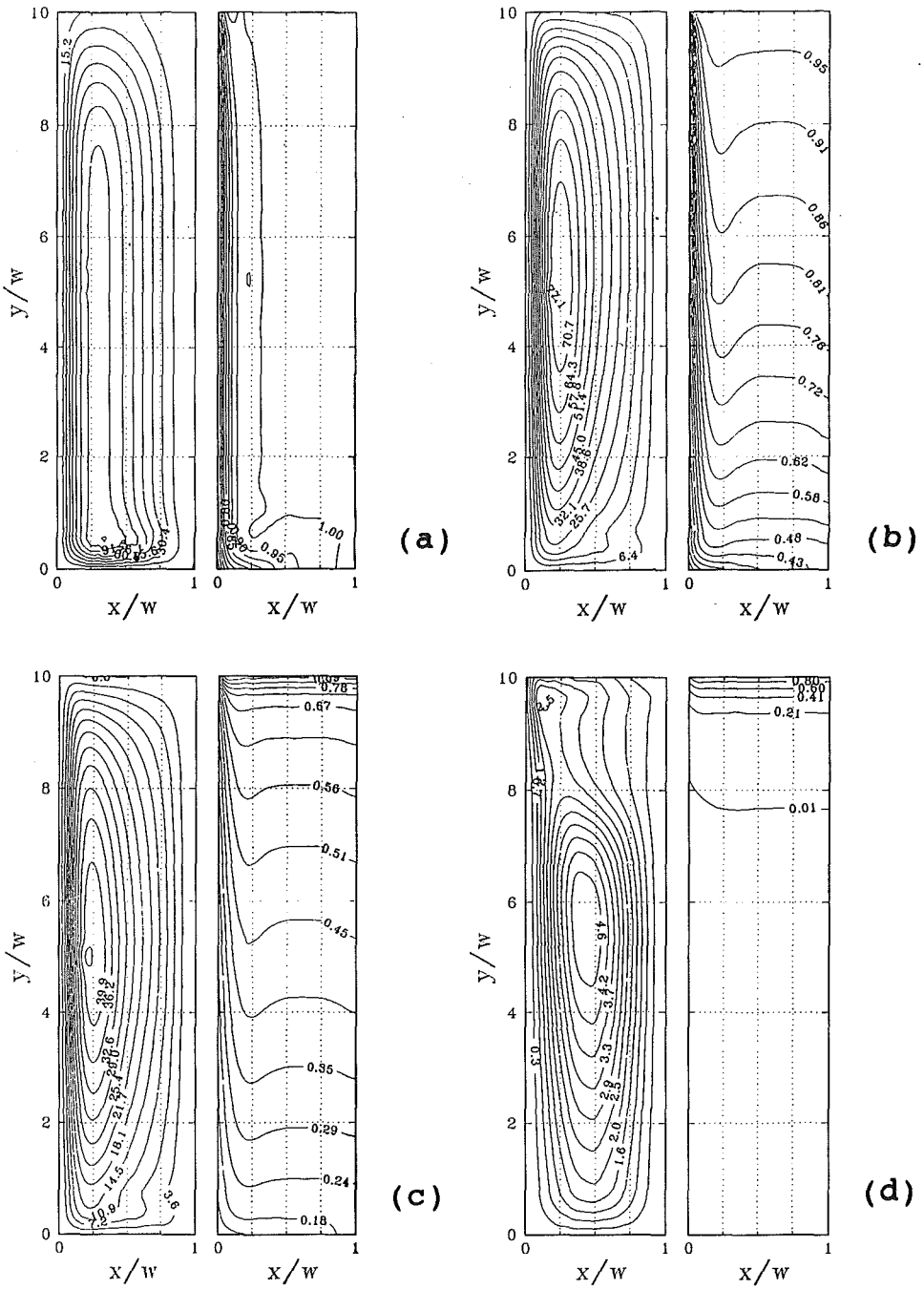

Fig. 5 Cooldown. Evolution of stream function and temperature distributions for $A = 10$, $Ra = 10^6$, and $Bi = 8$. The values of τ are: (*a*) 0.0058, (*b*) 0.059, (*c*) 0.602, (*d*) 1.41 (steady state).

some general observations. For early times ("early period," Hall et al., 1988), conduction dominates as fluid motion in the thermosyphon is weak. Horizontal temperature gradients at the cooled wall initiate fluid motion (see Eq. (1)) which, in turn, stratifies the temperature field as discussed above. The "late period" begins once conduction ceases to dominate. During this period of cooldown, fluid motion is down at the cooled wall and up in the thermosyphon core. As cool fluid flows upward in the core, it loses momentum upon encountering the warmer, stratified fluid and, to satisfy continuity, rejoins the downflow at the wall rather than passing through the orifice. Convective exchange with the reservoir is severely reduced because of stratification. With increased time, horizontal temperature gradients at the cooled wall decrease due to the reduced heat transfer with the reservoir and the approach to steady state. Fluid motion diminishes as a consequence of this, and eventually, motion nearly ceases as the problem again becomes conduction dominated. Evidence of this is seen by noting the similarities in the temperature gradients at the cooled wall for the temperature and the pure-conduction temperature graphs in Fig. 4(*e*).

Transient Nusselt numbers from the present work are in perfect agreement with those of Hall et al. (1988) for the early period (Fig. 6). Slight differences are detected for the late period because Hall et al. included an impermeable, insulated boundary condition instead of the orifice used here.

Transient heat transfer results for $Ra = 10^6$ and 10^7 are presented in Fig. 7 for all Bi. The use of the ordinate scale $Nu * A/$

$Bi^{1/2}$ is motivated by considering heat transfer in the thermosyphon in the limit of large A. In this limit, $Nu * A/Bi^{1/2}$ approaches one as the problem tends to steady state (see the appendix, Eq. (A4)). This scale is used for all heat transfer results since we are principally concerned with large aspect ratios.

In Fig. 7, heat transfer is seen to decrease with increasing time as noted above. With the increase in time, the reduced advection outweighs the increase in conduction at the orifice. For all cases and all time, we see that heat transfer is within 10-20 percent of that predicted by one-dimensional conduction (Eq. (A4)) which is presumably within the range of uncertainty for Bi. There is virtually no difference in heat transfer for the two values of Ra (the small differences seen in Fig. 7*a* are attributed to the expanded scale in this figure) but Bi has a profound effect.

By comparing the results of Fig. 7 with those of Fig. 8 (for Ra of 10^4), we note that increasing Bi and Ra (for $Ra < 10^6$) reduces τ_{ss}. It is apparent that both Bi and Ra play similar roles in their effect on the wall temperature, which is the source of convection for the problem. This suggests that Bi and Ra can be combined in a single expression for the wall temperature referred to as the effective Rayleigh number, Ra_{eff}. An energy balance on the wall gives

$$Ra_{eff}(\tau) \equiv \frac{g\beta W^3 (T_r - T_{w,avg}(\tau))}{\nu\alpha} = Ra\left[1 - \frac{Nu(\tau)}{Bi}\right]. \quad (23)$$

Ra_{eff}, which is based on the difference between T_r and the mean temperature for the cooled wall, can be envisioned as a single controlling parameter for this problem. However, since the wall temperature is not known *a priori* (nor is $Nu(\tau)$), Ra_{eff} is of little practical use. From Eq. (23), we see that as $Bi \to \infty$, the problem becomes one having constant wall temperature.

It is interesting to compare the convection and two-dimensional conduction results appearing in Fig. 8. The latter were obtained by setting $Ra = 0$ in the numerical model. For this case we choose to compare with two-dimensional conduction because the low-Ra cases closely approximate a two-dimensional conduction problem because of the weak fluid motion. Before the onset of fluid motion, the results for convection and conduction are in perfect agreement. After the early period, the convective Nu becomes greater than that for conduction as convection commences. This effect is most obvious in Fig. 8 for $Bi > 1$. After further elasped time, with the bulk of the thermosyphon approaching the temperature of the surroundings, convection nearly ceases and the problem again becomes conduction dominated.

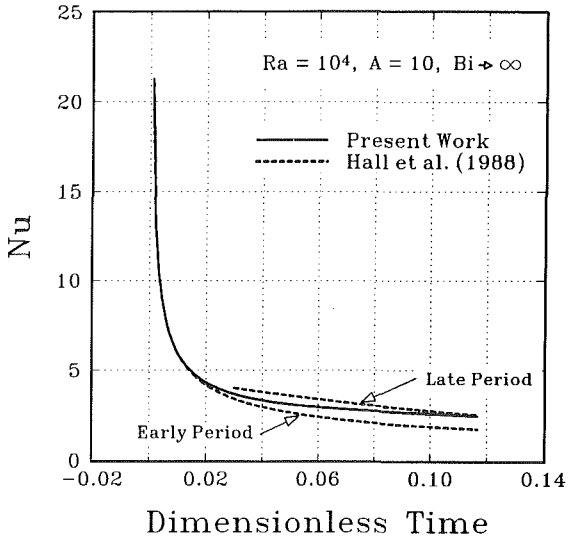

Fig. 6 Cooldown. Comparison of transient Nusselt numbers (Bi infinite) with results of Hall et al. (1988).

Warmup. Attention is first directed at steady stream function, vorticity, and temperature for A of 10 and Ra^* of 10^4 and 10^6 (Fig. 9). For Ra^* of 10^4, the flow is nearly symmetric about the thermosyphon vertical midplane and small Ψ indicates weak circulation. Inspection of the temperature distribution shows that the heated wall is isothermal except at the very bottom verifying the findings of Hartnett and Welsh (1957). The results for Ra^* of 10^6 are in sharp contrast to those above, where the thinner boundary layer at the heated wall skews the distribution of Ψ toward the heated wall (see Fig. 10*b*).

Transient mean-wall temperatures from Eq. (21) are presented in Fig. 10 for A of 2 and 20 along with those for two-

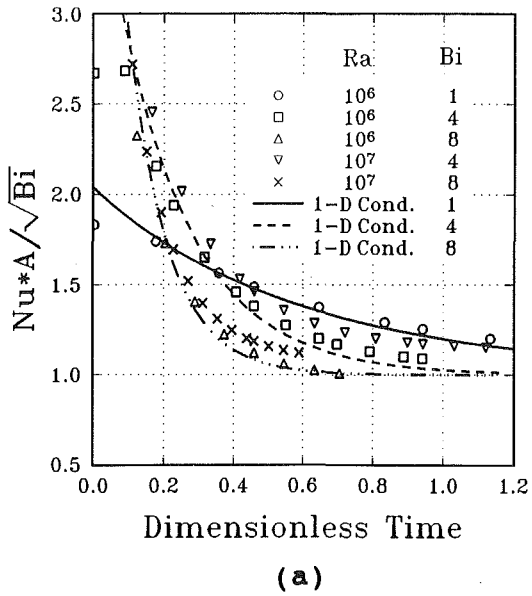

(a)

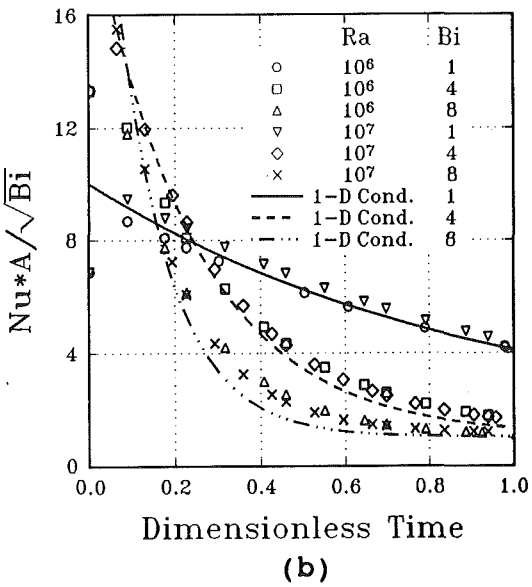

(b)

Fig. 7 Cooldown. Transient Nusselt number for large Ra and $A = 2$ (*a*) and $A = 10$ (*b*). The curves labeled "1-D Cond." are from Eq. (A4).

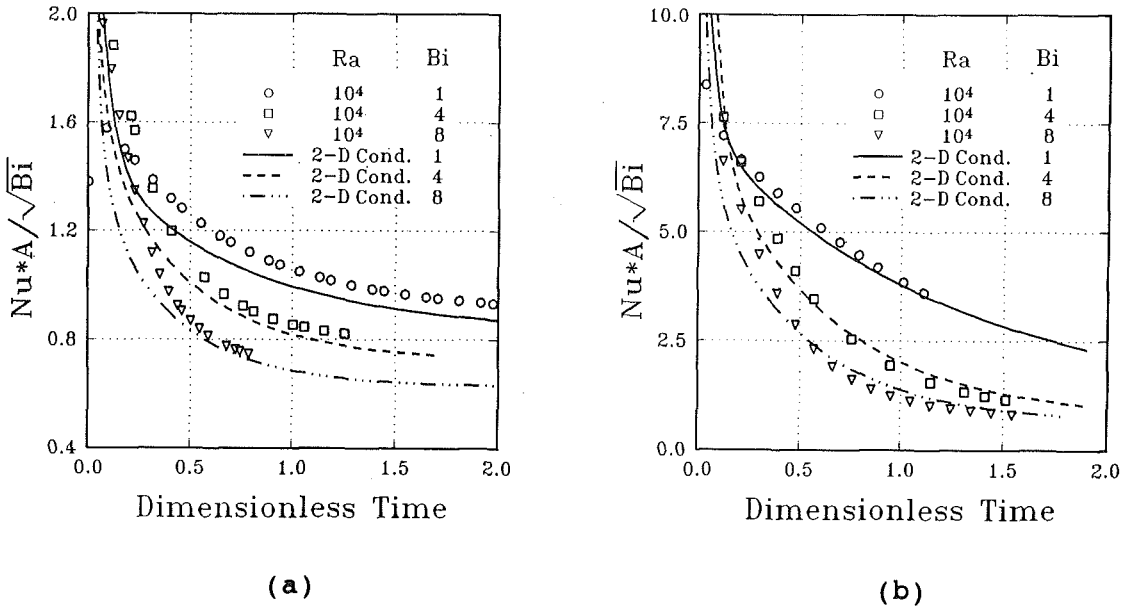

Fig. 8 Cooldown. Transient Nusselt number for moderate Ra and $A = 2$ (*a*) and $A = 10$ (*b*). Curves labeled "2-D cond." correspond to Ra = 0.

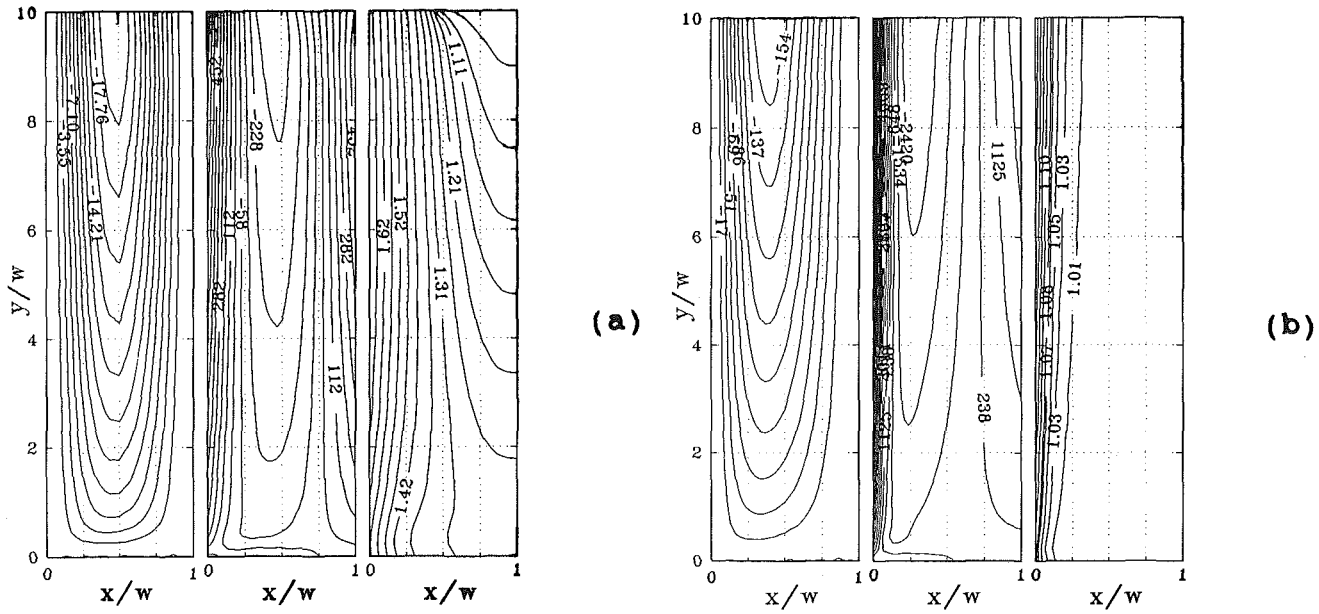

Fig. 9 Warmup. Stream function, vorticity, and temperature distributions for $A = 10$ and, $Ra = 10^4$ (*a*) and $Ra = 10^6$ (*b*).

dimensional conduction ($Ra^* = 0$) and the analytical result of Goldstein and Eckert (1960) for one-dimensional conduction. Also shown are steady temperatures for a uniformly heated vertical plate (Bejan, 1984). All cases follow the conduction curves until convection begins to contribute to heat transfer. For all but Ra^* of 10^4, steady conditions are reached at τ_{ss} of 0.25 or less (for a diode, this is about 12 minutes). We also note that τ_{ss} decreases sharply with A and with increased Ra^*. Clearly, the vigorous convection at large Ra^* and a more open thermosyphon hasten the approach to steady state. For a fixed time and Ra^*, wall temperatures are seen to increase with A, an effect that arises from the increased thermal resistance in the thermosyphon with aspect ratio. From Fig. 10, we see that for $Ra^* \geq 10^5$, transient mean-wall temperatures can be accurately predicted from the one-dimensional conduction model.

It is enlightening to compare wall temperatures for the thermosyphon with those obtained for a uniformly heated vertical plate. From Fig. 10, we note that the two approach each other as Ra^* increases, and to a lesser extent, as A decreases. For $Ra^* \geq 10^5$, they are in good agreement for all A. Note that for large Ra^* and small A, the ratio of the boundary layer thickness to width W is very small. The heated flow leaves the thermosyphon over an area so small that nearly the entire width is open to the relatively slow downflow. From this we can see that the influence of the adiabatic wall on the flow is small for large Ra^* so that heat transfer effectively occurs in a quiescent medium.

The results of Fig. 10 are correlated for steady mean-wall temperature over the range of Ra^* and A shown,

$$\theta_{w,\text{avg}} = 10^{\sum_{i=0}^{3} C_i p^i}, \tag{24}$$

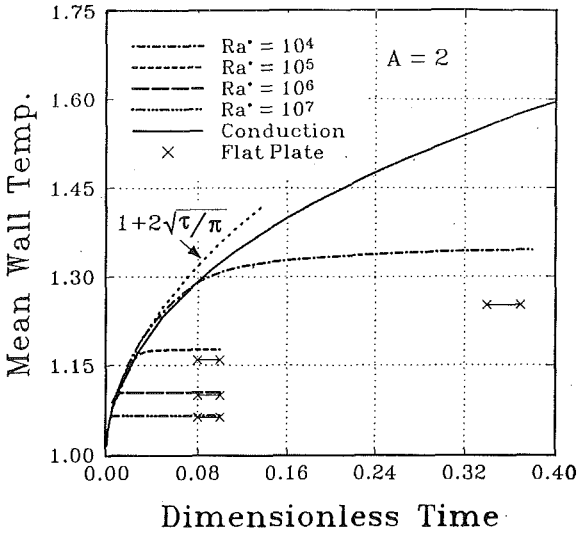

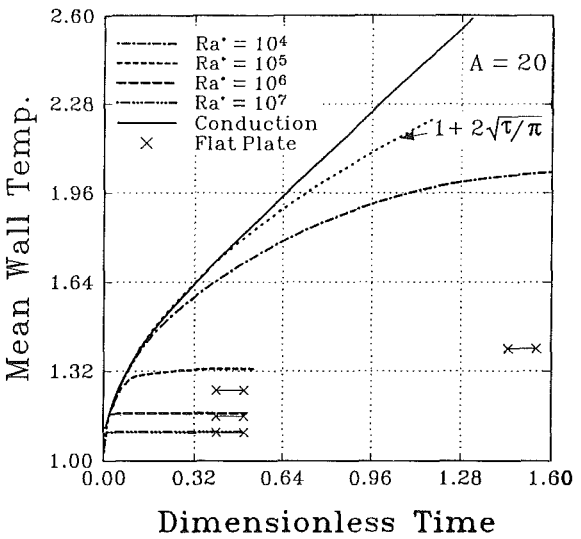

Fig. 10 Warmup. Dimensionless mean-wall temperatures for A of 2 and 20. Also shown are results for two-dimensional conduction ($Ra^* = 0$), and a uniformly heated vertical plate (Bejan, 1984). The results for one-dimensional conduction, $1 + 2(\tau/\pi)^{1/2}$, are from Goldstein and Eckert (1960).

Table 1 Coefficients appearing in Eq. (24)

A	C_0	C_1	C_2	C_3
2	1.04	−0.428	0.0624	−0.00313
5	1.81	−0.793	0.121	−0.00632
10	2.86	−1.30	0.203	−0.0107
20	4.31	−1.98	0.312	−0.0165

where p is the exponent of Ra^*, and C_i are coefficients (Table 1).

Temperatures from Eq. (24) are compared with those of Lighthill (1953), Martin (1955), and Hartnett and Welsh (1957) in Fig. 11, the latter three works having symmetric heating. From the results of Fig. 11, it is clear that asymmetry increases mean-wall temperature for all Ra^*, which is attributable to the fact that the wall adds to the flow resistance but not to heat transfer. As discussed above, however, the difference in wall temperature between the symmetrically and asymmetrically heated cases is quite small for Ra^* greater than about 10^6.

Effect of Grid Size. The effect of grid size is addressed by refining the grid for one warmup and one cooldown case and comparing with the results from the unrefined grid. In both cases the number of nodes was increased by 50 percent in each direction and the grid expansion factors adjusted to halve the wall-cell dimensions (if the grid were uniform, this would correspond to 81 nodes in the x direction). For warmup with A

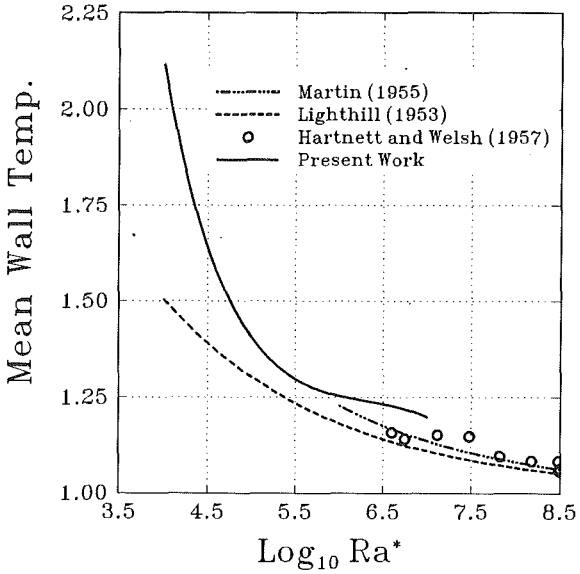

Fig. 11 Warmup. Comparison of steady mean-wall temperature with results of past works.

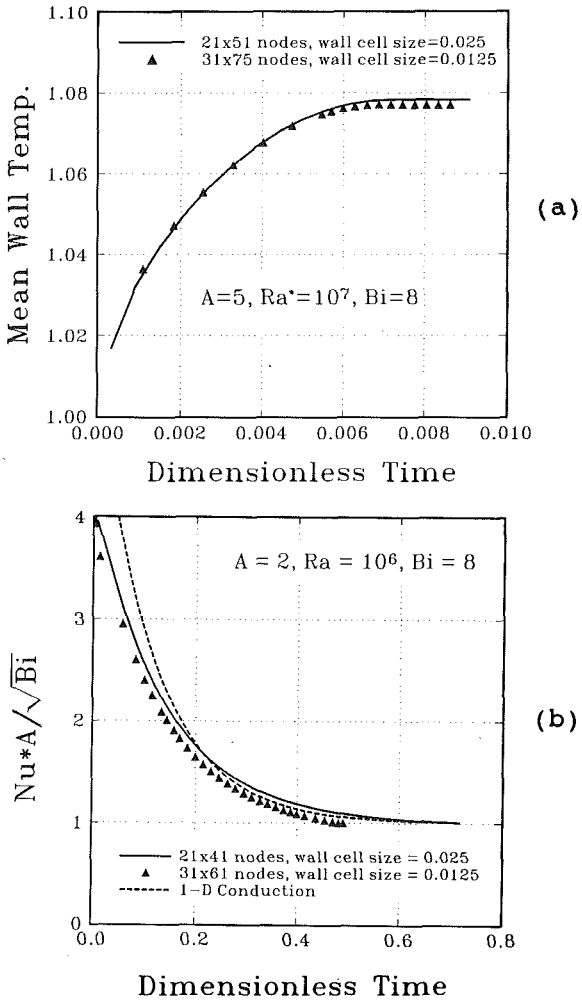

Fig. 12 Effect of grid size for warmup and cooldown

of 5, Ra of 10^7, and Bi of 8, the mean wall temperatures for the unrefined and refined grid cases are nearly indistinguishable (Fig. 12*a*). For cooldown with A of 2, Ra of 10^6, and Bi of 8, heat transfer results for the refined grid are only a percent or two less than those for the unrefined for small and moderate times (Fig. 12*b*). The steady-state Nusselt number is unaffected by grid refinement since, even with the coarser grid, it is in good agreement with the analytical solution.

Conclusions

We have performed a numerical study of transient laminar natural convection in an asymmetrically heated/cooled open thermosyphon. The vorticity, energy, and stream function equations are solved on a graded mesh using ADI and iteration with overrelaxation.

For cooldown, natural circulation increases for small times and then decreases as buoyancy is weakened from reduced horizontal temperature gradients at the cooled wall. The circulation is predominantly contained within the thermosyphon due to the temperature stratification. We demonstrate that stratification is caused initially by the circulation in the thermosyphon, but for later times, it is evidence of a balance between vertical conduction at the orifice and advection in the thermosyphon core. Stratification is the key to good performance of the thermal diode. For $Ra > 10^4$, the time-dependent heat transfer is predicted to within the range of uncertainty for Bi by a closed-form expression for one-dimensional conduction that we developed. This model predicts that $Nu \rightarrow Bi^{1/2}/A$ at steady state. For $Ra < 10^4$ and large τ, Nu is in good agreement with that for two-dimensional conduction. Also from our analysis we find that when convection dominates during cooldown, an aspect ratio of 10 is effectively infinite since there is no difference between heat transfer results for A of 10 and 20.

For warmup, transient heat transfer behaves as one-dimensional conduction, and, for steady state and $Ra^* \geq 10^5$, can be approximated as that for a uniformly heated vertical plate. Mean wall temperatures increase with A and with decreased Ra^*. For $Ra^* > 10^6$, steady state is achieved for a τ_{ss} of about 0.25 or less (corresponding to about 12 minutes for a thermal diode). For Ra^* of 10^4, τ_{ss} approaches 1.6 for A of 20. We produce a correlation for steady, mean-wall temperature that spans the range $10^4 \leq Ra^* \leq 10^7$ and $2 \leq A \leq 20$. Together with the above results for the transient phase of warmup, the correlations can be used for modeling the thermal performance for a passive heating system that includes thermal diodes.

References

Bejan, A., 1984, *Convection Heat Transfer*, Wiley, New York.

Chan, Y. L., and Tien, C. L., 1985, "A Numerical Study of Two-Dimensional Laminar Natural Convection in Shallow Open Cavities," *Int. J. Heat Mass Transfer*, Vol. 28, No. 3, pp. 603–612.

de Vahl Davis, G., and Jones, I. P., 1983, "Natural Convection in a Square Cavity: A Comparison Exercise," *Int. J. Num. Meth. in Fluids*, Vol. 3, pp. 227–248.

Emery, A., and Chu, N. C., 1965, "Heat Transfer Across Vertical Layers," ASME JOURNAL OF HEAT TRANSFER, Vol. 87, pp. 110–116.

Fu, W.-S., Kau, T.-M., and Shieh, W.-J., 1990, "Transient Laminar Convection in an Enclosure From Steady Flow State to Stationary State," *Num. Heat Trans.*, Vol. 18, pp. 189–212.

Goldstein, R. J., and Eckert, E. R. G., 1960, "The Steady and Transient Free Convection Boundary Layer on a Uniformly Heated Vertical Plate," *Int. J. Heat Mass Transfer*, Vol. 1, pp. 208–218.

Gosman, A. D., Lockwood, F. C., and Tatchell, D. G., 1971, "A Numerical Study of the Heat Transfer Performance of the Open Thermosyphon," *Int. J. Heat Mass Transfer*, Vol. 14, pp. 1717–1730.

Hall, J. D., Bejan, A., and Chaddock, J. B., 1988, "Transient Natural Convection in a Rectangular Enclosure With One Heated Side Wall," *Int. J. Heat Fluid Flow*, Vol. 9, pp. 396–404.

Hartnett, J. P., and Welsh, W. E., 1957, "Experimental Studies of Free Convection Heat Transfer in a Vertical Tube With Uniform Wall Heat Flux," *Trans. ASME*, Vol. 79, No. 7, pp. 1551–1557.

Hasegawa, S., Nishikawa, K., and Yamagata, K., 1963, "Heat Transfer in an Open Thermosyphon," *Bull. JSME*, Vol. 6, No. 22, pp. 930–960.

Hildebrand, F. B., 1966, *Methods of Applied Mathematics*, Prentice-Hall, Englewood Cliffs, NJ, pp. 339–346.

Ivey, G. N., 1984, "Experiments on Transient Natural Convection in a Cavity," *J. Fluid Mechanics*, Vol. 144, pp. 389–401.

Jaluria, Y., and Torrance, K. E., 1986, *Computational Heat Transfer*, Hemisphere, pp. 178–183.

Japikse, D., 1973, "Advances in Thermosyphon Technology," *Adv. in Heat Transfer*, Vol. 9, pp. 8–40.

Jones, G. F., 1986, "Heat Transfer in a Liquid Convective Diode," ASME *Journal of Solar Energy Engineering*, Vol. 108, pp. 163–171.

Lighthill, M. J., 1953, "Theoretical Considerations on Free Convection in Tubes," *Quart. J. Mech. Appl. Math.*, Vol. 6, Part 4, pp. 398–439.

Lockwood, F. C., and Martin, B. W., 1964, "Free Convection in Open Thermosyphon Tubes of Non-circular Section," *J. Mech. Eng. Sci.*, Vol. 6, Part 4, pp. 379–393.

Martin, B. W., 1955, "Free Convection in an Open Thermosiphon With Special Reference to Turbulent Flow," *Proc. Roy. Soc.*, Ser. A., Vol. 231, p. 502.

Martin, B. W., and Lockwood, F. C., 1963, "Entry Effects in the Open Thermosyphon," *J. Fluid Mech.*, Vol. 19, Part 2, pp. 246–256.

Nicolette, V. F., Yang, K. T., and Lloyd, J. R., 1985, "Transient Cooling by Natural Convection in a Two-Dimensional Square Enclosure," *Int. J. Heat Mass Transfer*, Vol. 28, pp. 1721–1732.

Patankar, S. V., 1980, *Numerical Heat Transfer and Fluid Flow*, Hemisphere, New York.

Patterson, J. C., and Imberger, J., 1980, "Unsteady Natural Convection in a Rectangular Cavity," *J. Fluid Mechanics*, Vol. 100, pp. 65–86.

Patterson, J. C., 1984, "On the Existence of an Oscillatory Approach to Steady Natural Convection in Cavities," ASME JOURNAL OF HEAT TRANSFER, Vol. 106, pp. 104–108.

Reddy, C. S., 1989, "Method of Boundary Vorticity Formulation and Its Effect on Heat Transfer in Enclosures," *Proc. Ninth Int. Heat Transfer Conf.*, Jerusalem, Israel, Vol. 3, pp. 123–128.

Wilkes, J. O., and Churchill, S. W., 1966, "The Finite-Difference Computation of Natural Convection in a Rectangular Enclosure," *J. AIChE*, Vol. 12, No. 1, pp. 161–166.

APPENDIX

Analytical Solution for Transient Conduction in a Thermosyphon in the Limit of Large Aspect Ratio

In the limit of large aspect ratio, the temperature distribution in the fluid tends toward that for a one-dimensional conducting solid for the late period. The dimensionless heat conduction equation for this is written as

$$\frac{\partial \theta}{\partial \tau} = \frac{\partial^2 \theta}{\partial \zeta^2} - \mathrm{Bi}\,\theta, \tag{A1}$$

where heat transfer in the η direction has been lumped. The coordinate ζ is $A - \xi$. The boundary conditions and initial condition are

$$\theta|_{\zeta=0} = 1, \quad \left.\frac{\partial \theta}{\partial \zeta}\right|_{\zeta=A} = 0, \quad \theta(\zeta, \tau = 0) = 1. \tag{A2}$$

Using classical methods with superposition, Eq. (A1) is solved subject to Eq. (A2) to get the temperature distribution $\theta(\zeta, \tau)$.

An energy balance on the cooled wall gives the following relationship:

$$h_\infty [T(\zeta, \tau) - T_\infty] = h(\zeta, \tau)[T_r - T_\infty]. \tag{A3}$$

The temperature $T(\zeta, \tau)$ in Eq. (A3) is evaluated from the solution $\theta(\zeta, \tau)$. The mean Nusselt number is obtained by integrating $h(\zeta, \tau)$ in Eq. (A3) over ζ. Neglecting terms of order $e^{-\beta}$, where $\beta = A\,\mathrm{Bi}^{1/2}$, we get

$$\frac{\mathrm{Nu}(\tau) A}{\sqrt{\mathrm{Bi}}} = 1 + \frac{8A\,\mathrm{Bi}^{3/2}}{\pi^2} \sum_{n=0}^{\infty} \frac{e^{-\left[\mathrm{Bi} + \left[\frac{(2n+1)\pi}{2A}\right]^2\right]\tau}}{(2n+1)^2 \left[\mathrm{Bi} + \left[\frac{(2n+1)\pi}{2A}\right]^2\right]}. \tag{A4}$$

In the steady-state limit, $\mathrm{Nu} \rightarrow \mathrm{Bi}^{1/2}/A$.

Three-Dimensional Natural Convection in a Confined Fluid Overlying a Porous Layer

A. K. Singh
Research Fellow,
Department of Civil and Agricultural Engineering,
University of Melbourne,
Parkville, Victoria, Australia-3052

E. Leonardi
Associate Professor,
School of Mechanical and Manufacturing Engineering,
University of New South Wales,
Kensington, NSW, Australia-2033

G. R. Thorpe
Associate Professor,
Department of Civil and Building Engineering,
Victoria University of Technology,
Footscray, Victoria, Australia-3011

This paper presents a numerical study of three-dimensional, laminar natural convection in an enclosure containing a fluid layer overlying a porous layer saturated with the same fluid. The Brinkman-extended Darcy formulation is used to model fluid flow in the porous layer as this facilitates the imposition of a no-slip boundary condition at the fluid/porous layer interface. The enclosure is heated from one side wall and cooled from an opposite wall, while the remaining walls are adiabatic. The mathematical analysis is carried out in terms of a vorticity-vector potential formulation that ensures the conservation of mass. The governing equations in nondimensional form are transformed into parabolic equations by means of a false transient method in order to facilitate a solution procedure by an alternating direction implicit method. Accuracy of the numerical solutions with respect to uniformly and nonuniformly spaced grid points has been tested by performing extensive numerical experiments. As expected, it is found that the intensity of free convection is much more profound in the fluid layer. The numerical results indicate that penetration of the fluid into the porous region depends strongly upon the Darcy and Rayleigh numbers. The effect of the ratio of thermal conductivities (porous to fluid regions) is to intensify the convection current in the fluid layer.

1 Introduction

Experimental and theoretical studies of free convection in single-phase fluids and porous media have intensified our recent decades. While mathematical analyses of simply defined systems involving transport phenomena in rectangular enclosures, say, have become well established, there is a need to simulate the behavior of more realistic and complicated systems both that occur naturally and that are engineered. Essentially, this entails solving the equations that govern the transport phenomena subjected to a wider range of boundary conditions. This has enabled free convection phenomena to be studied in systems consisting of composite porous media or composites of fluid and porous layers, heterogeneous porous media, and systems with irregular boundaries. In this work we are concerned principally with buoyancy-driven transport phenomena in a composite system consisting of a fluid layer and a porous medium saturated with the same fluid contained within a three-dimensional enclosure. This system is of interest not only from a mathematical point of view, but results of the work can be applied to the processes of heat, mass, and momentum transfer in bulk stored grains, thermal energy storage, and the analysis of the performance of thermal insulation materials.

Although there is a large number of applications of confined fluid/porous layer systems, they have received little attention in the literature, and the work published to date appears to be confined to systems that are two dimensional. Nield (1977) presents stability criteria in systems consisting of superposed porous and fluid layers. Numerical studies of free convection have been performed by Poulikakos et al. (1986) and Chen and Chen (1988) for the case of a fluid layer on top of a porous layer. Their analysis is based on the assumption that Darcy's empirical law (1856) applies in the porous region, and that the Beavers–Joseph (B–J) (1967) condition is satisfied at the interface of the overlaying fluid and porous layer. As a result of numerical studies Pillatsis et al. (1987) and Taslim and Narusawa (1989) concluded that no significant improvement is gained by making use of the generalized B–J condition proposed by Jones (1973), which relates the slip velocity at the porous layer/fluid interface instead of using the standard B–J condition. An alternative formulation of the boundary conditions at the interface is the Brinkman–extended Darcy model (1947), which preserves continuity of all components of velocity at the interface. Nishimura et al. (1986), Beckermann et al. (1987, 1988) and Sathe et al. (1988) have made use of this boundary condition in their studies of two-dimensional natural convection in rectangular enclosures containing a porous/fluid composite. Beckermann et al. (1988) conducted a series of experiments in rectangular enclosures with aspect ratios sufficiently high for the flow to be assumed two dimensional in which they demonstrated good agreement between measured and numerically predicted temperature and flow fields.

The above studies on natural convective heat and mass transfer phenomena in enclosures containing fluid and porous layers have been limited to two-dimensional geometries. This is because the mathematical descriptions of two-dimensional systems are particularly simple and they give rise to tractable numerical solutions, and for some geometries they yield a reasonable approximation to three-dimensional systems. Lack of readily available computing power has also no doubt been a factor in limiting theoretical studies to two-dimensional systems. However, natural convection in a confined system is inherently three-dimensional and improved access to computers of sufficient capacity now permits us to simulate the heat and mass transfer processes in systems with three-dimensional geometries. Studies on three-dimensional systems consisting of either a single-phase fluid or a saturated porous medium have been performed by Chorin (1967), Aziz and Hellums (1967), Williams (1969), Hirt and Cook (1972), Holst and Aziz (1972), Mallinson and de Vahl Davis (1973, 1977), Ozoe et al. (1976, 1990), Daiguji (1978), Chan and Banerjee (1979a, 1979b), Horne (1979), Raul et al. (1990), and Fusegi et al. (1991).

The present study aims to extend the above work and in-

Contributed by the Heat Transfer Division for publication in the JOURNAL OF HEAT TRANSFER. Manuscript received by the Heat Transfer Division February 1992; revision received September 1992. Keywords: Natural Convection, Numerical Methods, Porous Media. Associate Technical Editor: C. E. Hickox, Jr.

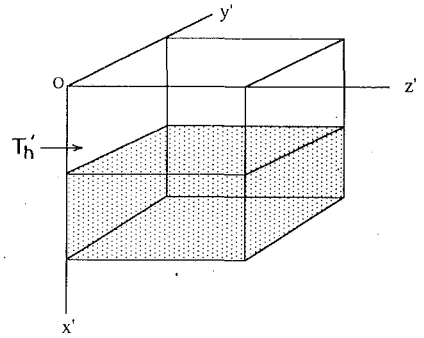

Fig. 1 Physical model and coordinate system

vestigate natural convection in a three-dimensional composite system. The Darcy model, extended by Brinkman (1947), is used to describe transport phenomena in the porous domain that result in no slip at the impermeable walls, and it permits continuity of the velocity to be imposed at the porous medium/fluid interface. There are sound theoretical and empirical arguments for adopting this formulation (cf. Chan et al., 1970; Neale and Nader, 1974). The equations that govern the transport phenomena in the fluid and porous layers are coupled by matching the temperature, heat flux, velocity components, and stresses at the interface. The transport equations are formulated in terms of derived variables such as vorticity and a vector potential first proposed by Aziz and Hellums (1967) as a means of obtaining numerically efficient and stable solutions for three dimensional systems. In this paper, the set of coupled, nonlinear PDEs that governs the behavior of the system is solved by the false transient method proposed by Mallinson and de Vahl Davis (1973). This method is well suited to determining steady-state solutions.

In the numerical procedure, the governing equations in nondimensional form are discretized by replacing the spatial derivative with a three-point difference approximation, which incorporates nonuniform mesh sizes that minimize the amount of computational intensity. The resulting finite difference equations are then solved by the Samarskii–Andreyev (1963) alternating direction implicit method, which was developed for solving parabolic and elliptic equations in two- and three-dimensional geometries. In this paper we investigate the effects of mesh size and the geometric disposition of the nodes on the convergence and accuracy of the solution. In discussing free convective phenomena in composite systems confined in a three-dimensional enclosure, we focus on the effects of two important numbers, namely the Darcy and Rayleigh numbers, and also the ratio of thermal conductivities of the porous and fluid layers.

2 Analysis

2.1 Governing Equations. The composite system considered in this paper consists of a horizontal porous bed situated below a horizontal fluid layer as shown in Fig. 1. The direction of gravity is along the x' axis while the y' and z' axes are taken in the horizontal plane. The porous medium is assumed to be macroscopically homogeneous and isotropic, and the solid and fluid phases are deemed to be in local thermal equilibrium. The interface is considered to be permeable so that the fluid can flow from one layer to the other. Two opposing surfaces of the enclosure are taken as being isothermal, having temperatures T_h' and T_c' such that $T_h' > T_c'$, thus giving rise to the phenomenon of free convection within the cavity. The remaining surfaces are taken to be perfectly thermally insulated. The fluid in the system is incompressible and the physical properties are assumed to be constant. Boussinesq's approx-

Nomenclature

Ar_x = H/L = aspect ratio in x' direction
Ar_z = W/L = aspect ratio in z' direction
D_f = D_f'/L
D_f' = depth of fluid layer from upper surface, m
Da = Darcy number
g = acceleration due to gravity, m/s^2
h_{min} = minimum spatial grid distance
H = height of the enclosure, m
$\mathbf{i}, \mathbf{j}, \mathbf{k}$ = unit vectors in x', y', and z' directions
K = permeability of porous layer, m^2
L = length of enclosure in y' direction, m
Nu_{av} = overall average Nusselt number
Nu_{av2d} = average Nusselt number corresponding to two-dimensional model
$\mathrm{Nu}x(x)$ = average Nusselt number in x direction
$\mathrm{Nu}(x, z)$ = local Nusselt number
$\mathrm{Nu}z(z)$ = average Nusselt number in z direction
p' = pressure, Pa
Pr = Prandtl number
Ra = Rayleigh number
Rc = ratio of thermal conductivities of porous and fluid layers
T' = temperature, K
u, v, w = dimensionless velocity component in x, y, and z directions
$\mathbf{V}$ = dimensionless velocity vector
$\mathbf{V}'$ = velocity vector, m/s
W = width of the enclosure, m
x, y, z = nondimensional coordinates
x', y', z' = coordinates, m
α = thermal diffusivity, m^2/s
β = coefficient of thermal expansion, K^{-1}
Δt = dimensionless time step
$\Delta T'$ = temperature difference, K
$\zeta_1, \zeta_2, \zeta_3$ = x, y and z components of nondimensional vorticity
$\boldsymbol{\zeta}$ = dimensionless vorticity vector
$\boldsymbol{\zeta}'$ = vorticity vector, s^{-1}
θ = dimensionless temperature
κ = thermal conductivity, W/m-K
μ = viscosity, kg/m-s
ν = viscous diffusivity, m^2/s
ρ = density of fluid, kg/m^3
ρ_o = density of fluid at reference temperature, kg/m^3
ψ_1, ψ_2, ψ_3 = x, y, and z components of nondimensional vector potential
ψ_{2d} = nondimensional stream function for two-dimensional model
$\boldsymbol{\Psi}$ = nondimensional vector potential
$\boldsymbol{\Psi}'$ = vector potential, m^2/s
∇ = dimensionless gradient operator = $\mathbf{i}\,(\partial/\partial x) + \mathbf{j}\,(\partial/\partial y) + \mathbf{k}\,(\partial/\partial z)$
∇' = gradient operator = $\mathbf{i}\,(\partial/\partial x') + \mathbf{j}\,(\partial/\partial y') + \mathbf{k}\,(\partial/\partial z')$, m^{-1}
∇^2 = dimensionless Laplacian operator = $(\partial^2/\partial x^2) + (\partial^2/\partial y^2) + (\partial^2/\partial z^2)$
∇'^2 = Laplacian operator $(\partial^2/\partial x'^2) + (\partial^2/\partial y'^2) + (\partial^2/\partial z'^2)$, m^{-2}
$\cdot$ = dot product
$\times$ = cross product

Subscripts

c = cold wall
f = fluid layer
h = hot wall
n = normal component
p = porous layer
$t1, t2$ = tangential components

imation that assumes changes in density affect only the buoyancy term in the momentum equations deemed to be valid. The partial differential equations that govern free convection in a composite system consist of a mass balance, a force balance, and a thermal energy balance in each layer. For the fluid layer, they are in order as follows:

$$\nabla' \cdot \mathbf{V}_f' = 0, \tag{1}$$

$$\rho \mathbf{V}_f' \cdot \nabla' \mathbf{V}_f' = \nabla' p' + \mu_f \nabla'^2 \mathbf{V}_f' - ig\rho_o \beta (T_f' - T_c'), \tag{2}$$

$$\mathbf{V}_f' \cdot \nabla' T_f' = \alpha_f \nabla'^2 T_f'. \tag{3}$$

The corresponding equations for the porous layer are

$$\nabla' \cdot \mathbf{V}_p' = 0, \tag{4}$$

$$\rho \mathbf{V}_p' \cdot \nabla' \mathbf{V}_p' = -\nabla' p' + \mu_p \nabla'^2 \mathbf{V}_p' - ig\rho_o \beta (T_p' - T_c') - \frac{\mu_f}{K} \mathbf{V}_p', \tag{5}$$

$$\mathbf{V}_p' \cdot \nabla' T_p' = \alpha_p \nabla'^2 T_p'. \tag{6}$$

In the case of the porous layer, while quantities such as temperature, velocity, and so on are defined at points throughout the layer, they do in fact refer to locally averaged values. All the symbols are defined in the nomenclature.

It should be noted that μ_f and μ_p are different from each other, and there is clearly a requirement to develop a suitable relation between them. Attempts in this direction have been made by Lundgren (1972), Koplik et al. (1983), and Kim and Russel (1985) to derive expressions for the effective viscosity in terms of the properties of the porous domain. In this study, we consider $\mu_p = \mu_f$ in Eq. (5) as Neale and Nader (1974) argue that it provides good agreement with experimental data, and this is supported by the observations of Beckerman et al. (1988).

The pressure term in the momentum equation can be eliminated by defining a vorticity vector as

$$\zeta' = \nabla' \times \mathbf{V}', \tag{7}$$

and by expressing a vector potential as

$$\mathbf{V}' = \nabla' \times \psi'. \tag{8}$$

The continuity equation is automatically satisfied as the divergence of the curl of any vector field is zero. Nondimensionalization can be performed by making use of the following nondimensional variables:

$$\nabla = L\nabla', \quad \mathbf{V} = \mathbf{V}'/(\alpha_f/L), \quad \zeta = \zeta'/(\alpha_f/L^2),$$
$$\Psi = \Psi'/\alpha_f, \quad \theta = (T' - T_c')/\Delta T'. \tag{9}$$

By defining these equations separately for each domain and taking the curl of the momentum Eq. (2) and (5), and after some algebraic manipulation, the resulting equations in nondimensional form are obtained in each layer as follows:

Fluid layer:

$$\nabla \times (\zeta_f \times \mathbf{V}_f) = \mathrm{Pr} \nabla^2 \zeta_f - \mathrm{Ra}\,\mathrm{Pr} \nabla \times (\mathbf{i}\theta_f), \tag{10}$$

$$\zeta_f = -\nabla^2 \Psi_f, \tag{11}$$

$$\mathbf{V}_f \cdot \nabla \theta_f = \nabla^2 \theta_f, \tag{12}$$

Porous layer:

$$\nabla \times (\zeta_p \times \mathbf{V}_p) = \mathrm{Pr}\, \nabla^2 \zeta_p - \mathrm{Ra}\,\mathrm{Pr}\, \nabla \times (\mathbf{i}\theta_p) - (\mathrm{Pr}/\mathrm{Da})\zeta_p, \tag{13}$$

$$\zeta_p = -\nabla^2 \Psi_p, \tag{14}$$

$$\mathbf{V}_p \cdot \nabla \theta_p = Rc\, \nabla^2 \theta_p. \tag{15}$$

The physical parameters Da, Pr, Ra, and Rc are defined as

$$\mathrm{Da} = K/L^2, \quad \mathrm{Pr} = \nu_f/\alpha_f, \quad \mathrm{Ra} = g\beta \Delta T' L^3/\nu_f \alpha_f, \quad Rc = \kappa_p/\kappa_f, \tag{16}$$

in which Da, Pr, and Ra are, respectively, the Darcy, Prandtl, and Rayleigh numbers while Rc is the ratio of thermal conductivities of porous and fluid layers.

2.2 Boundary Conditions. The above problem is completely defined by specifying the boundary conditions of the three-dimensional region bounded by the planes $x = 0$, Ar_x; $y = 0$, 1, and $z = 0$, Ar_z. Hirasaki and Hellums (1968) and Richardson and Cornish (1977) discuss at some length the appropriate boundary conditions on these planes. They show that on each of the surfaces the components of the vector potential must satisfy

$$\frac{\partial \psi_n}{\partial n} = 0, \quad \psi_{t1} = \psi_{t2} = 0, \tag{17}$$

where the subscript n indicates a normal component while $t1$ and $t2$ represent tangential components of orthogonal coordinates.

As in the more familiar two-dimensional case, there exist two ways of obtaining the vorticity at the boundaries: the first is to obtain it directly from the velocity gradients, and the second is to derive it from the vector potential. The second approach is employed here as suggested by Mallinson and de Vahl Davis (1973); hence at the walls the vorticity is obtained from the following relations:

$$\zeta_n = 0, \quad \zeta_{t1} = -\frac{\partial^2 \psi_{t1}}{\partial n^2}, \quad \zeta_{t2} = -\frac{\partial^2 \psi_{t2}}{\partial n^2}. \tag{18}$$

The boundary conditions imposed on the temperature field are as follows:

$$\frac{\partial \theta}{\partial x} = 0 \quad \text{on } x = 0 \text{ and } Ar_x, \tag{19a}$$

$$\theta = 1 - y \quad \text{on } y = 0 \text{ and } 1, \tag{19b}$$

$$\frac{\partial \theta}{\partial z} = 0 \quad \text{on } z = 0 \text{ and } Ar_z. \tag{19c}$$

Having described the boundary conditions at the peripheries, we must now examine the matching conditions at the fluid/porous interface. At the interface $x = D_f$, the temperature field is assumed to be continuous. However, the boundary conditions for vorticity and vector potential cannot be specified directly and must be derived from matching conditions of velocity and stress components at the interface. At the interface, matching conditions for temperature, velocity and stress components are as follows:

$$\theta_f = \theta_p, \tag{20a}$$

$$\frac{\partial \theta_f}{\partial x} = Rc \frac{\partial \theta_p}{\partial x}, \tag{20b}$$

$$u_f = u_p, \tag{20c}$$

$$v_f = v_p, \tag{20d}$$

$$w_f = w_p, \tag{20e}$$

$$\frac{\partial u_f}{\partial x} = \frac{\partial u_p}{\partial x}, \tag{20f}$$

$$\frac{\partial u_f}{\partial y} + \frac{\partial v_f}{\partial x} = \frac{\partial u_p}{\partial y} + \frac{\partial v_p}{\partial x}, \tag{20g}$$

$$\frac{\partial u_f}{\partial z} + \frac{\partial w_f}{\partial x} = \frac{\partial u_p}{\partial z} + \frac{\partial w_p}{\partial x}. \tag{20h}$$

Using Eq. (20*c*)–(20*h*) and followed by some algebraic manipulation, the matching conditions at the interface $x = D_f$ in terms of vorticity and vector potential components can be obtained as follows:

$$\zeta_f = \zeta_p, \tag{21a}$$

$$\frac{\partial \zeta_f}{\partial x} = \frac{\partial \zeta_p}{\partial x}, \tag{21b}$$

$$\Psi_f = \Psi_p, \tag{21c}$$

$$\frac{\partial \Psi_f}{\partial x} = \frac{\partial \Psi_p}{\partial x}. \tag{21d}$$

With the description of boundary conditions, the statement of the problem is now complete and the solution procedure is given in the following section.

3 Numerical Solution Procedure

The mathematical complexity of the equations governing a multidimensional flow suggests that solutions of the equations must be sought numerically. Discretized forms of Eqs. (10)–(15) can be solved by a method requiring a double iterative procedure because they are coupled and elliptic. However, there is a considerable amount of evidence in the literature (e.g., Mallinson and de Vahl Davis, 1973, 1977; Ozoe et al., 1976), that suggests an alternating direction implicit method is well suited to solving nonlinear parabolic differential equations. This method can be implemented by transforming the governing equations into parabolic form by adding a false transient term as described in detail by Mallinson and de Vahl Davis (1973). Solutions of the transformed equations are obtained by employing a nonuniform grid that enables one to consider more grid points near the periphery of the system to predict the flow and temperature fields accurately, particularly at high Rayleigh numbers. The resulting finite difference equations are solved by the alternating direction implicit method (ADI) proposed by Samarskii and Andreyev (1963), which is a somewhat modified form of the original ADI scheme proposed by Peaceman and Rachford (1955). Application of the ADI scheme produces a system of linear algebraic equations with a tridiagonal matrix in each direction and that can be solved efficiently by the Thomas algorithm (1949).

In each iteration, the process of numerical integration for every dependent variable is started from the upper horizontal surface and proceeds downward using the finite difference form of the fluid layer equations until the grid point situated immediately above the horizontal interface $x = D_f$ is reached. In the next process, the finite difference form of the porous layer equations is used to advance the solution process from the grid points located immediately below the interface up to the lower horizontal surface. Again the value of the dependent variables at the interfacial grid points is obtained using the matching conditions at the interface. Combination and discretization of the matching conditions for each variable yield an algebraic equation for that variable to determine at the interfacial grid points in terms of the immediate neighboring points in both the fluid and porous regions.

Special care is needed in the numerical computation to specify a time step, Δt, that is sufficiently large to enable a steady-state solution to be obtained as rapidly as possible, yet small enough to avoid instabilities. To present it in a form suitable for the computation, it is set at

$$\Delta t = \text{stabr} \cdot h_{\min}^2, \tag{22}$$

where 'stabr' is a parameter determined by numerical experimentation in order to achieve convergence and stability of the solution procedure and $h_{\min}$ is the value of the minimum spatial grid distance. Numerical experiments show that solutions for $\text{Ra} = 10^4$ and 10^5 are readily obtained when 'stabr' assumes a numerical value of 3.0. The corresponding values of the false transient parameters required in the temperature, vorticity, and vector potential equations are 5.0, 0.1, 1.0 in the fluid layer; the corresponding values in the porous layer are respectively 5.0, 2.5, 25.0. However, for $\text{Ra} = 10^6$ numerical observations have revealed that a numerical value of 0.5 is suitable for 'stabr' and 5.0, 0.05, and 0.5 for the false transient parameters in the temperature, vorticity, and vector potential equations pertaining to fluid layer and 5.0, 0.5, and 5.0 for porous layer.

To achieve the steady-state solution, the solution procedure can be marched in two ways. The first method involves solving for the temperature field, the updated values of which are used in the equations that govern the vorticity, which in turn may be used to update the vector potential and velocity fields. The updated velocity field is then used in the discretized thermal energy balance and the iteration proceeds until all the fields approach steady state. The second method involves solving for the temperature and vorticity fields and then iterating the vector potential field until it approaches steady state. The resulting updated velocity field is then used in the energy balance equation and the procedure iterated until all of the variables have attained steady-state values. We observed that the first procedure used slightly less CPU time than the second, and it was therefore the one adopted in this study. In the cases in which $\text{Ra} = 10^4$ and 10^5 the process of pseudo-time marching was continued until each of the variables changed by less than one part in 10^5 per iteration. When $\text{Ra} = 10^6$ this was found to be practically too stringent, and the convergence criteria imposed in this case were such that the temperature, vector potential, and vorticity fields were constant to within one part per 5×10^5, 5×10^4, and 5×10^3, respectively.

Numerical experiments were performed to examine the effects on the accuracy of the solutions of uniform and nonuniform grids. Initially the experiments were performed on a desk-top microcomputer that had four megabytes of memory, a CPU frequency of 33 MHz, and an 80386 coprocessor. For Rayleigh numbers of 10^4 and 10^5 it was found that steady-state solutions for systems consisting $21 \times 21 \times 21$ mesh points can be obtained within 4 to 5 hours. Ultimately, solutions were obtained for systems with nodes on a $33 \times 31 \times 29$ mesh using a Cray Y-MP Supercomputer on which the required CPU times are between 2300 to 9800 seconds depending on the value of the Rayleigh and Darcy numbers. By taking a smaller spacing between grid points near the boundaries, the nonuniform grid spacing ensures better results because steep temperature gradients occur close to the walls as well as at the porous/fluid layer interface. It also minimizes the computational time for a given degree of accuracy. The approach to a grid independent solution was tested by running the computer program by taking $40 \times 35 \times 35$ grid points by making mesh sizes more refined at the boundaries and at the interface.

The overall heat transfer rate in terms of a conduction-referenced average Nusselt number is defined as

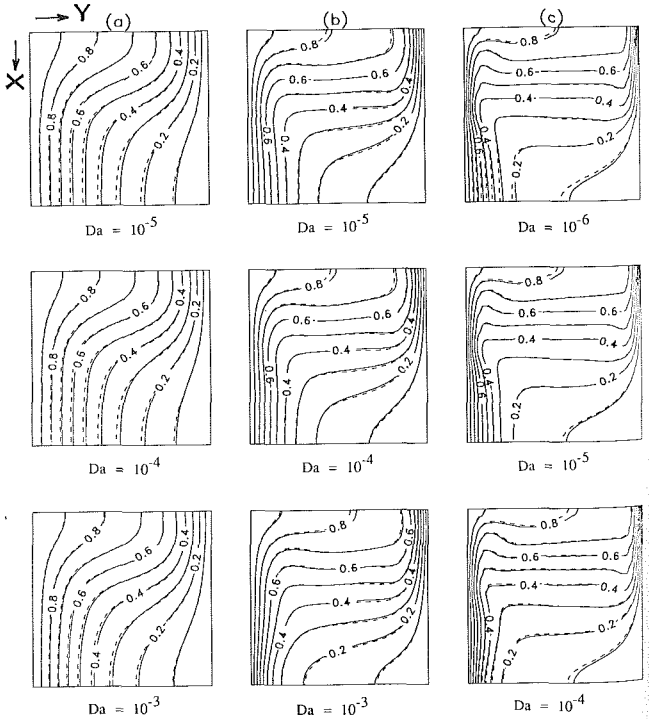

Fig. 2 Isotherms for $Rc = 1$ on the plane $z = 0.5$; (*a*) $\text{Ra} = 10^4$, (*b*) $\text{Ra} = 10^5$, and (*c*) $\text{Ra} = 10^6$; —— three-dimensional, · · · two-dimensional

$$\mathrm{Nu}_{av} = \frac{\text{overall heat transfer rate}}{\text{heat transfer by conduction in the entire enclosure filled by fluid only}}. \quad (23)$$

In terms of the nondimensional variable defined in Eq. (9) and (16) it can be written as

$$\mathrm{Nu}_{av} = \frac{1}{Ar_z Ar_x} \int_0^{Ar_z} \int_0^{Ar_x} \mathrm{Nu}(x, z)\, dx\, dz, \quad (24)$$

where Nu (x, z) is the local Nusselt number defined as

$$\mathrm{Nu}(x, z) = -\begin{cases} \dfrac{\partial \theta_f}{\partial yf}, & \text{when } 0 \le x < D_f; \\ \dfrac{1}{2}\left(\dfrac{\partial \theta_f}{\partial y} + Rc\,\dfrac{\partial \theta_p}{\partial y}\right), & \text{when } x = D_f; \\ Rc\,\dfrac{\partial \theta_p}{\partial y}, & \text{when } D_f < x \le Ar_x. \end{cases} \quad (25)$$

Numerical experiments were performed to determine the effect of grid size on the convergence of the numerical solutions. It was observed that overall changes in the average Nusselt number on the hot wall as the number of grid points increases from $11 \times 11 \times 11$ to $33 \times 31 \times 29$ are approximately 6, 16, and 6 percent corresponding to $\mathrm{Ra} = 10^4$, 10^5, and 10^6, respectively, whereas the z component of vector potential changes by 14, 23, and 90 percent. It was found that the average Nusselt number at $\mathrm{Ra} = 10^6$ does not change monotonically with change in the mesh size. This is a result of the inaccurate computation of the temperature field, particularly at the boundaries as a result of the steep temperature gradients in these regions. When the grid mesh was changed from $21 \times 21 \times 21$ to $33 \times 31 \times 29$ the variables change by approximately 5 percent in the case of the $\mathrm{Ra} = 10^4$ and 10^5. However, the average Nusselt number and z component of the vector potential change by 11 and 22 percent for $\mathrm{Ra} = 10^6$. This clearly indicates that the number of grid points in the solution domain has a strong effect on the accuracy of the numerical results, particularly when the Rayleigh number is high. It follows that a fine mesh size is necessary for sufficient numerical accuracy at high Rayleigh number. It is commonly observed that the average Nusselt number is less sensitive in comparison to the minimum value of the z component of vector potential. The average Nusselt number and z component of vector potential obtained by taking $40 \times 35 \times 35$ grid points differ by 1 and 0.3 percent from the values corresponding to $33 \times 31 \times 29$ mesh points, which indicates an approach to a mesh-independent solution.

The accuracy of the model, as well as the numerical procedure, is also tested by obtaining the overall average Nusselt number on the cold wall by employing a mathematical expression similar to Eq. (24). It was observed that the agreement between the average Nusselt numbers on the hot and cold walls is good because the differences in their values are less than 1 percent in the case of $\mathrm{Ra} = 10^4$ and 3 percent for $\mathrm{Ra} = 10^5$ and 10^6. Inspection of the computed results revealed that differences in the two overall average Nusselt numbers can be minimized by increasing the number of the grid points in the domain.

5 Results and Discussion

In a system consisting of a single-phase fluid convecting naturally in an enclosure, the flow regime is completely defined by four dimensionless parameters, namely Pr. Ra, Ar_x, and Ar_z. In the case of the composite system considered here we have to also consider the additional parameters Da, D_f, and Rc. This greatly increases the scope of the analysis, and in this study we focus principally on three parameters, namely Da, Ra, and Rc while holding other parameters constant. In the present study these parameters are given the following numerical values:

$$\mathrm{Pr} = 0.71,\ Ar_x = 1.0,\ Ar_z = 1.0, \text{ and } D_f = 0.5,$$

which correspond to the flow of the fluid air in a cube-shaped enclosure divided by fluid and porous regions.

In order to present some validation of the three-dimensional solutions, we compare them with corresponding and comparatively well investigated (e.g., Nishimura et al., 1986) solutions for the two-dimensional case. Because the planes $x = 0$ and Ar_x, $z = 0$ and Ar_z are adiabatic and the temperature difference is imposed between the $y = 0$ and 1 planes, the physical variables change most significantly in the y direction and in the x direction as a result of buoyancy forces. For this reason the isotherms in Fig. 2 are plotted in the plane $z = 0.5$ for the three-dimensional case and compared with those computed for the two-dimensional case in which the same grid size was employed. It can be seen that agreement between the two cases is excellent. It seems that computed results obtained from the three-dimensional formulation assure the correctness of the extension of matching conditions at the fluid/porous layer interface in the three-dimensional case. Natural convection clearly becomes much stronger as Ra increases from 10^4 to 10^6, as evidenced by the steep temperature gradients in the fluid phase adjacent to the cold wall when $\mathrm{Ra} = 10^6$, for example. As the Darcy number increases from 10^{-5} to 10^{-3} it is observed that free convective effects also make a more significant contribution to heat transfer in the porous layer. These phenomena, reflected in the z components of the vector potential, indicate higher free convective activity at higher Rayleigh and Darcy numbers. When the Rayleigh number is large, thermal boundary layers developed near the hot and cold walls become thinner as the Rayleigh number is increased.

In Fig. 3, the temperature field and the z component of the vector potential are shown for $\mathrm{Da} = 10^{-5}$ and $\mathrm{Ra} = 10^5$ for different values of Rc. Increasing the value of Rc clearly results in thermal conduction dominating heat transfer in the porous layer, while convection continues to dominate in the fluid layer.

The temperature fields are readily visualized from Fig. 4. It shows dimensionless isothermal surfaces on spacings of isothermal temperature difference of 0.2 for a range of Rayleigh numbers. A comparative view of the figures indicates that isothermal surfaces are dense near the hot and cold walls at $\mathrm{Ra} = 10^5$ and 10^6 as a consequence of the increase in the buoyancy forces associated with increasing Rayleigh number. It can be seen that isothermal surfaces are symmetric about the plane $z = 0.5$. Patterns of isothermal surfaces also suggest that variation in temperature in the z direction is more pronounced in the fluid region compared with the porous region. This variability is somewhat more apparent when $\mathrm{Ra} = 10^5$ and 10^6, which suggests that the three dimensionality in the fluid motion cannot be overlooked at large Rayleigh numbers. Isothermal surfaces shown in Fig. 4 suggest that fluid motion must be intensified somewhat more at the midplane $z = 0.5$ and that can be confirmed by Tables 1 and 2 as the minimum value of the z component of the vector potential lies on this plane in all the cases considered here.

An efficient method for visualization of flow phenomena is by means of plotting streaklines, i.e., the paths traced by tracking particles in the fluid. One disadvantage of this method is that many streaklines are required to have a clear view for a single flow system. In the cavity, the coordinates of the particle at successive locations were obtained as follows: An initial location for the particle was selected and if the particle is not located at a grid point, the velocity components are determined

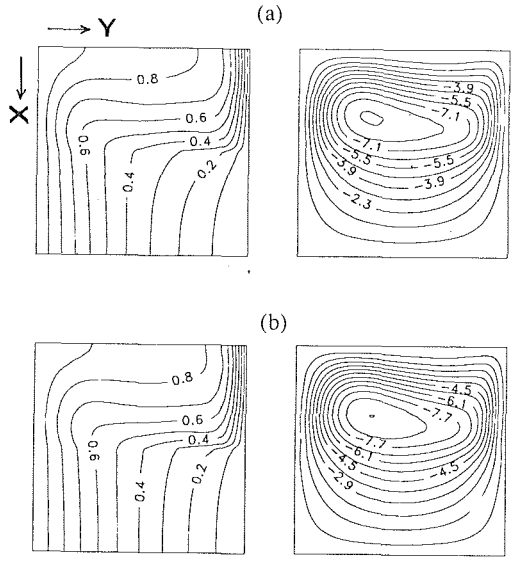

Fig. 3 Temperature fields and z component of vector potential on the plane $z = 0.5$ when $Ra = 10^5$ and $Da = 10^{-5}$; (*a*) $Rc = 5.0$, (*b*) $Rc = 10.0$

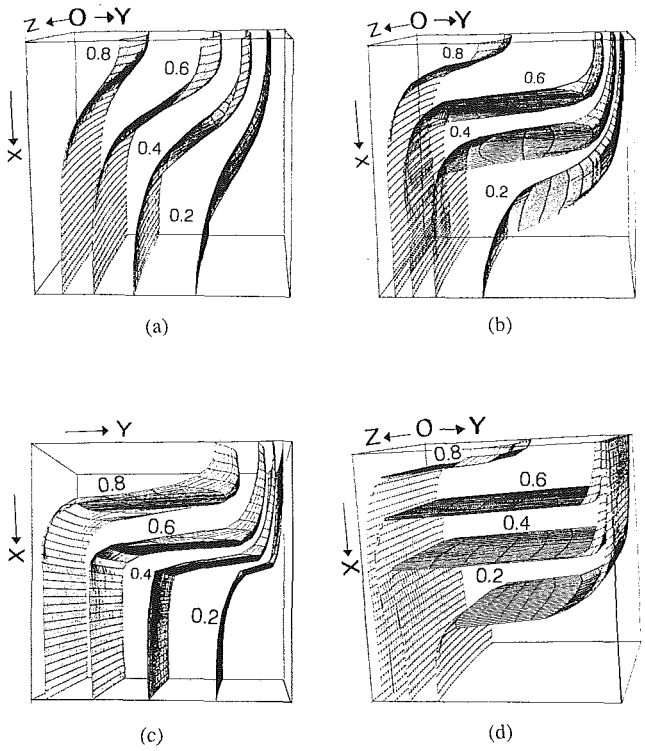

Fig. 4 Isothermal surfaces for $Da = 10^{-5}$; (*a*) $Ra = 10^4$, $Rc = 1.0$; (*b*) $Ra = 10^5$, $Rc = 1.0$; (*c*) $Ra = 10^5$, $Rc = 10.0$; (*d*) $Ra = 10^6$, $RC = 1.0$

Table 1 Effect of grid points on the computed results

Grid points	Ra	Da	Nu_{av}	ψ_3(min)
11×11×11	10^4	10^{-3}	1.605	-3.241
21×21×21	10^4	10^{-3}	1.556	-2.980
33×31×29	10^4	10^{-3}	1.538	-2.927
11×11×11	10^4	10^{-4}	1.524	-3.099
21×21×21	10^4	10^{-4}	1.468	-2.825
33×31×29	10^4	10^{-4}	1.433	-2.693
11×11×11	10^4	10^{-5}	1.515	-3.082
21×21×21	10^4	10^{-5}	1.457	-2.806
33×31×29	10^4	10^{-5}	1.429	-2.659
11×11×11	10^5	10^{-3}	4.105	-9.358
21×21×21	10^5	10^{-3}	3.844	-7.982
33×31×29	10^5	10^{-3}	3.665	-7.804
40×35×35	10^5	10^{-3}	3.618	-7.826
11×11×11	10^5	10^{-4}	3.774	-8.935
21×21×21	10^5	10^{-4}	3.408	-7.505
33×31×29	10^5	10^{-4}	3.233	-7.292
11×11×11	10^5	10^{-5}	3.725	-8.869
21×21×21	10^5	10^{-5}	3.349	-7.427
33×31×29	10^5	10^{-5}	3.173	-7.203
11×11×11	10^6	10^{-4}	6.146	-24.97
21×21×21	10^6	10^{-4}	7.526	-16.73
33×31×29	10^6	10^{-4}	6.563	-13.48
11×11×11	10^6	10^{-5}	6.096	-24.88
21×21×21	10^6	10^{-5}	7.077	-16.03
33×31×29	10^6	10^{-5}	6.307	-13.07
11×11×11	10^6	10^{-6}	6.090	-24.85
21×21×21	10^6	10^{-6}	7.020	-15.95
33×31×29	10^6	10^{-6}	6.269	-13.04

Table 2 Comparison of the minimum of ψ_3 and average Nusselt number on the plane $z = 0.5$ with corresponding two-dimensional model values when $Rc = 1.0$

Ra	Da	Nu (z)	Nu_{av2d}	ψ_3(min)	ψ_{2d}(min)
10^4	10^{-3}	1.585	1.654	-2.927	-3.097
10^4	10^{-4}	1.477	1.550	-2.693	-2.839
10^4	10^{-5}	1.460	1.535	-2.659	-2.802
10^5	10^{-3}	3.815	3.816	-7.804	-7.992
10^5	10^{-4}	3.355	3.377	-7.292	-7.438
10^5	10^{-5}	3.293	3.322	-7.203	-7.344
10^6	10^{-4}	6.711	6.942	-13.48	-14.24
10^6	10^{-5}	6.465	6.470	-13.07	-13.45
10^6	10^{-6}	6.447	6.428	-13.04	-13.36

by a second-order interpolation method. The coordinates of the particle at a subsequent location in a small time interval were computed using a modified Euler method. The velocity components at this point were again obtained by interpolation. The process was repeated until sufficient locations of the particle were obtained. Figure 5 illustrates streaklines corresponding to $Rc = 1.0$, and it can be seen that they are closed as a result of the continuity condition $\nabla \cdot \mathbf{V} = 0$ and that the velocity components vanish at the boundaries. The figure indicates the three dimensionality of the flow field. It must be pointed out that in our numerical calculations it was not always possible to obtain closed streaklines, even with smaller time steps. An inappropriate time step can result in the streaklines terminating at a boundary. Figure 5 indicates that the streakline for the case when $Ra = 10^5$ and $Da = 10^{-4}$ does not follow the same path during successive motion toward the center of the cavity, but does so only on each second traverse. This is not the case when $Ra = 10^4$ when the streaklines retrace their paths on each successive path to the center of the cavity. In our studies it was noted that the fluid motion occurs predominantly in the fluid layer, and as expected, the motion is symmetric about the plane $z = 0.5$.

Values of $Nu(x, z)$, a parameter used to estimate the local rate of heat transfer, on the plane $y = 1$ are displayed in Fig. 6. It is observed, for example, that when $Ra = 10^4$ the local Nusselt number in the porous layer tends to increase as the Darcy number increases, as may be expected because of the more vigorous fluid flow in this region. Furthermore, the Nusselt numbers are highest when $z = 0.5$, which is farthest from the wall region where the flow is somewhat damped. The local

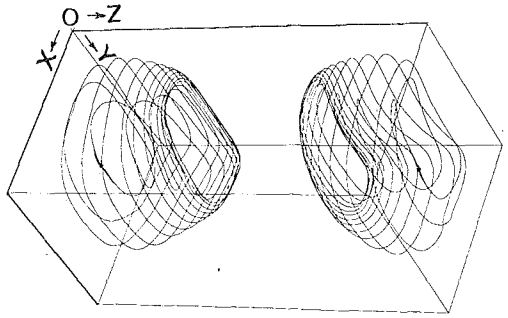

Fig. 5 Streaklines through the points (0.5, 0.5, 0.05) and (0.5, 0.5, 0.95) for $Ra = 10^5$ and $Da = 10^{-4}$

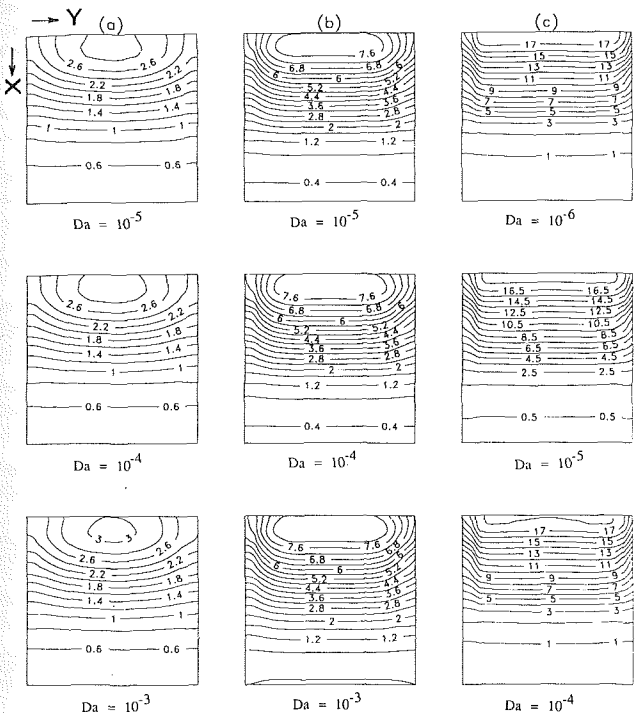

Fig. 6 Local Nusselt number on the plane $y = 1.0$ for $Rc = 1.0$; (*a*) $Ra = 10^4$; (*b*) $Ra = 10^5$, and (*c*) $Ra = 10^6$

Nusselt number in the fluid layer is, by contrast, relatively insensitive to the Darcy number, indicating that the heat transfer mechanism in the porous layer does not strongly influence that in the fluid layer. This is perhaps not too surprising, as we have already noted that conduction plays a dominant role at this relatively low Rayleigh number. When the Rayleigh number is set at 10^5 and 10^6 the local Nusselt numbers are much higher, and the fluid phase contributes significantly to heat transfer. The local Nusselt numbers in the porous layer are again relatively insensitive to the Darcy number.

In the case of a three-dimensional system, it is also useful to compute the average Nusselt number in vertical and horizontal directions by using the following relations:

$$\mathrm{Nu}x(x) = \frac{1}{Ar_z}\int_0^{Ar_z} \mathrm{Nu}(x, z)\,dz, \tag{26}$$

$$\mathrm{Nu}z(z) = \frac{1}{Ar_x}\int^{Ar_x} \mathrm{Nu}(x, z)\,dx. \tag{27}$$

Figure 7 shows the effects of the Rayleigh and Darcy numbers on the mean Nusselt number, $\mathrm{Nu}x(x)$. At the top of the heated wall of cube, $y = 0$, the values of $\mathrm{Nu}x(x)$ are approximately equal with a value of 0.61, from which value they increase. Their values are clearly much higher for the cases

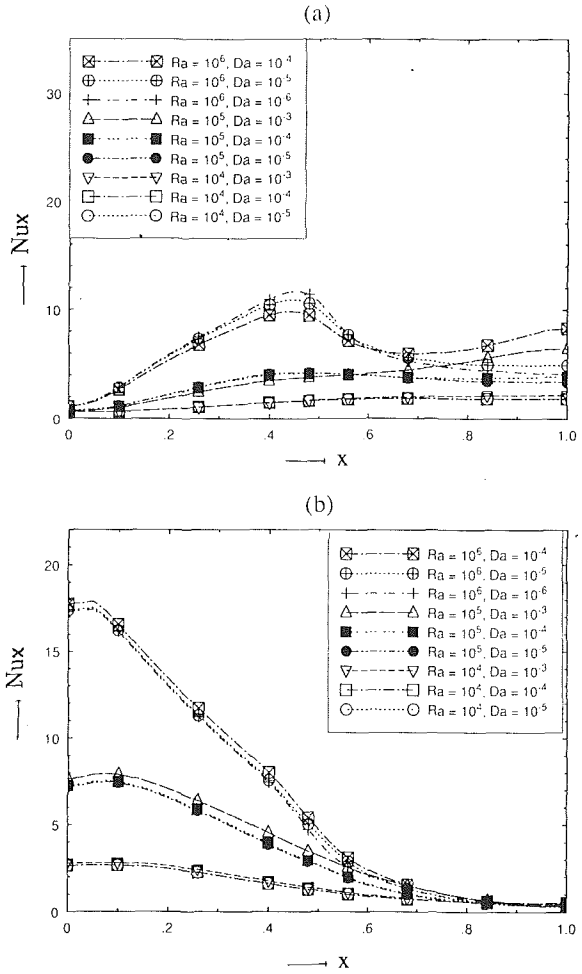

Fig. 7 Average Nusselt number, $\mathrm{Nu}x(x)$ for $Rc = 1$; (*a*) $y = 0$ and (*b*) $y = 1$

when $Ra = 10^6$ in the fluid region near the interface, indicating that the temperature gradients are becoming steepest in this region at the high Rayleigh number. We also observe that $\mathrm{Nu}x(x)$ decreases in the fluid region and increases in the porous region as Darcy number increases. In the case when $Ra = 10^4$, conduction is far more important; hence the values of $\mathrm{Nu}x(x)$ are more uniform. On the cold wall, $y = 1$, the flow field results in much steeper temperature gradients in the fluid phase, hence the higher values of $\mathrm{Nu}x(x)$, particularly at higher Rayleigh numbers. At the highest Rayleigh number, and when $Da = 10^{-3}$, $\mathrm{Nu}x(x)$ is clearly higher than when $Da = 10^{-4}$ and 10^{-5}. In the latter two cases, the flow fields in the porous layer have a minimal influence on the rate of heat transfer.

Average values of the Nusselt numbers are tabulated in Table 2 on the plane $z = 0.5$, and compared with those calculated for the two-dimensional case. The values for the three-dimensional cavity are consistently lower than those for the two-dimensional cavity, as are minimum values of the vector potential, ψ_3, and ψ_{2d}. This leads us to conclude that the rate of heat transfer and intensity of the flow in the three-dimensional model is less in comparison to the two-dimensional model, almost certainly as a result of viscous drag on the side walls.

6 Conclusions

This paper has examined laminar free convective flows in a three-dimensional enclosure containing a fluid overlying a porous medium. The Brinkman-extended Darcy model is used to analyze the fluid flow in the porous domain. The vorticity-vector potential formulation is used to simulate the momentum equations in both regions. The governing equations are solved

using a finite difference method by incorporating the finite difference approximations expressed in terms of unequal intervals between grid points in order to consider the behavior of steepest gradients at the walls and at the interface. Numerical experiments clearly suggest that refinement of the mesh size is necessary, particularly at the boundaries and the interface at higher Rayleigh numbers. The effect of buoyancy forces is always more profound in the fluid layer compared to a porous medium. The variations in the flow and temperature fields depend strongly upon the Rayleigh and Darcy numbers. For a fixed Rayleigh number, the rate of flow penetration from the fluid region to the porous region is strongly dependent upon Darcy number. Simulation processes at every level, i.e., isothermal surfaces, velocity vector plots, and streaklines clearly indicate the three dimensionality of the transport phenomena, and this becomes more pronounced at higher Rayleigh number. Three dimensionality is much stronger in the fluid region than in the porous medium. The effect of end walls due to three dimensionality depends mainly on the Rayleigh number.

Acknowledgments

This work was carried out with financial support provided to AKS by the Grains Research and Development Corporation, Australia. The work also forms part of an ongoing research project funded by the Australian Wheat Board and Bulk Grain Handling Authorities.

References

Aziz, A., and Hellums, J. D., 1967, "Numerical Solution of the Three-Dimensional Equations of Motion of Laminar Natural Convection," *Physics of Fluids*, Vol. 10, pp. 314–324.

Beavers, G., and Joseph, D. D., 1967, "Boundary Conditions at a Naturally Permeable Wall," *Journal of Fluid Mechanics*, Vol. 30, pp. 197–207.

Beckermann, C., Ramadhyani, S., and Viskanta, R., 1987, "Natural Convection Flow and Heat Transfer Between a Fluid Layer and a Porous Layer Inside a Rectangular Enclosure," ASME JOURNAL OF HEAT TRANSFER, Vol. 109, pp. 363–370.

Beckermann, C., Viskanta, R., and Ramadhyani, S., 1988, "Natural Convection in Vertical Enclosures Containing Simultaneously Fluid and Porous Layers," *Journal of Fluid Mechanics*, Vol. 186, pp. 257–286.

Brinkman, H. C., 1947, "A Calculation of the Viscous Force Exerted by a Flowing Fluid on a Dense Swarm of Particles," *Applied Scientific Research*, Vol. A1, pp. 27–34.

Chan, A. M. C., and Banerjee, S., 1979a, "Three-Dimensional Numerical Analysis of Transient Natural Convection in Rectangular Enclosures," ASME JOURNAL OF HEAT TRANSFER, Vol. 101, pp. 114–119.

Chan, A. M. C., and Banerjee, S., 1979b, "A Numerical Study of Three-Dimensional Roll Cells Within Boundaries," ASME JOURNAL OF HEAT TRANSFER, Vol. 101, pp. 233–237.

Chan, B. K. C., Ivey, C. M., and Barry, J. M., 1970, "Natural Convection in Enclosed Porous Media With Rectangular Cavity," ASME JOURNAL OF HEAT TRANSFER, Vol. 92, pp. 21–27.

Chen, F., and Chen, C. F., 1988, "Onset of Finger Convection in a Horizontal Porous Layer Underlying a Fluid Layer," ASME JOURNAL OF HEAT TRANSFER, Vol. 110, pp. 403–409.

Chorin, A. J., 1967, "A Numerical Method for Solving Incompressible Viscous Flow Problem," *Journal of Computational Physics*, Vol. 2, pp. 12–26.

Daiguji, H., 1978, "Numerical Method for Time-Dependent Three-Dimensional Viscous Flows (Part 1, Fundamental Method)," *Bulletin of the JSME*, Vol. 21, pp. 1130–1136.

Darcy, H. P. G., 1856, *Les Fontaines Publiques de la Ville Dijon. Exposition et application a suivre et des formules a employer dans les questions de distribution d' eau*, Dalmont, Paris.

Fusegi, T., Hyun, J. M., Kuwahara, K., and Farouk, B., 1991, "A Numerical Study of Three-Dimensional Natural Convection in a Differentially Heated Cubical Enclosure," *Int. J. Heat Mass Transfer*, Vol. 34, pp. 1543–1557.

Hirasaki, G. J., and Hellums, J. D., 1968, "A General Formulation of the Boundary Conditions on the Vector Potential in Three-Dimensional Hydrodynamics," *Quarterly Journal of Applied Mathematics*, Vol. 26, pp. 311–342.

Hirt, C. W., and Cook, J. L., 1972, "Calculating Three-Dimensional Flows Around Structures and Over Rough Terrain," *Journal of Computational Physics*, Vol. 10, pp. 324–340.

Holst, P. H., and Aziz, K., 1972, "Transient Three-Dimensional Natural Convection in Confined Porous Medium," *International Journal of Heat and Mass Transfer*, Vol. 15, pp. 73–89.

Horne, R. N., 1979, "Three-Dimensional Convection in a Confined Porous Medium Heated From Below," *Journal of Fluid Mechanics*, Vol. 92, pp. 751–766.

Jones, I. P., 1973, "Low Reynolds Number Flow Past a Porous Spherical Shell," *Proceedings of Cambridge Philosophical Society*, Vol. 73, pp. 231–238.

Kim, S., and Russel, W. B., 1985, "Modelling of Porous Medium by Renormalization of the Stokes Equations," *Journal of Fluid Mechanics*, Vol. 154, pp. 269–286.

Koplik, J., Levine, H., and Zee, A., 1983, "Viscosity Renormalization in the Brinkman Equation," *Physics of Fluids*, Vol. 26, pp. 2864–2870.

Lundgren, T. S., 1972, "Slow Flow Through Stationary Random Beds and Suspensions of Spheres," *Journal of Fluid Mechanics*, Vol. 51, pp. 273–299.

Mallinson, G., and de Vahl Davis, G., 1973, "The Method of False Transient for the Solution of Coupled Elliptic Equations," *Journal of Computational Physics*, Vol. 12, pp. 435–461.

Mallinson, G., and de Vahl Davis, G., 1977, "Three-Dimensional Natural Convection in a Box: a Numerical Study," *Journal of Fluid Mechanics*, Vol. 83, pp. 1–31.

Neale, G., and Nader, W., 1974, "Practical Significance of Brinkman's Extension of Darcy's Law: Coupled Parallel Flows Within a Channel and a Bounding Porous Medium," *Canadian Journal of Chemical Engineering*, Vol. 52, pp. 475–478.

Nield, D. A., 1977, "Onset of Convection in a Fluid Layer Overlying a Layer of Porous Medium," *Journal of Fluid Mechanics*, Vol. 81, pp. 513–522.

Nishimura, T., Takumi, T., Shiraishi, M., Kawamura, Y., and Ozoe, H., 1986, "Numercial Analysis of Natural Convection in a Rectangular Enclosure Horizontally Divided Into Fluid and Porous Regions," *International Journal of Heat and Mass Transfer*, Vol. 29, pp. 889–898.

Ozoe, H., Yamamoto, K., Churchill, S. W., and Sayama, H., 1976, "Three-Dimensional Numerical Analysis of Laminar Natural Convection in a Confined Fluid Heated From Below," ASME JOURNAL OF HEAT TRANSFER, Vol. 98, pp. 202–207.

Ozoe, H., Matsumoto, H., Nishimura, T., and Kawamura, Y., 1990, "Three-Dimensional Natural Convection in Porous Media at a Rectangular Corner," *Numerical Heat Transfer*, Vol. 17, pp. 249–268.

Peaceman, D. W., and Rachford, D. D., 1955, "The Numerical Solution of Parabolic and Elliptic Differential Equations," *Society for Industrial and Applied Mathematics Journal*, Vol. 3, pp. 28–47.

Pillatsis, G., Taslim, M. E., and Narusawa, U., 1987, "Thermal Instability of a Fluid-Saturated Porous Medium Bounded by Thin Fluid Layers," ASME JOURNAL OF HEAT TRANSFER, Vol. 109, pp. 677–682.

Poulikakos, D., Bejan, A., Selimos, B., and Blake, K. R., 1986, "High Rayleigh Number Convection in a Fluid Overlying a Porous Bed," *International Journal of Heat and Fluid Flow*, Vol. 7, pp. 109–116.

Raul, R., Bernard, P. S., and Buckley, F. T., Jr., 1990, "An Application of the Vorticity-Vector Potential Method to Laminar Cube Flow," *International Journal of Numerical Methods in Fluids*, Vol. 10, pp. 875–888.

Richardson, S. M., and Cornish, A. R. H., 1977, "Solution of Three-Dimensional Flow Problems," *Journal of Fluid Mechanics*, Vol. 82, pp. 309–319.

Samarskii, A. A., and Andreyev, V. B., 1963, "On a High-Accuracy Difference Scheme for an Elliptic Equation With Several Space Variables," *U.S.S.R. Journal of Computational Mathematics and Mathematical Physics*, Vol. 3, pp. 1373–1382.

Sathe, S. B., Lin, W. Q., and Tong, T. W., 1988, "Natural Convection in Enclosures Containing an Insulation With a Permeable Fluid-Porous Interface," *International Journal of Heat and Fluid Flow*, Vol. 9, pp. 389–395.

Taslim, M. E., and Narusawa, U., 1989, "Thermal Stability of Horizontally Superposed Porous and Fluid Layers," ASME JOURNAL OF HEAT TRANSFER, Vol. 111, pp. 357–362.

Thomas, L. H., 1949, *Elliptic Problems in Linear Difference Equations Over a Network*, Watson Scientific Computing Laboratory, Columbia University, New York.

Williams, G. P., 1969, "Numerical Integration of the Three-Dimensional Navier–Stokes Equations for Incompressible Flow," *Journal of Fluid Mechanics*, Vol. 37, pp. 727–750.

Three-Dimensional Free Convection in a Long Rotating Porous Box: Analytical Solution

P. Vadasz
Professor and Head,
Department of Mechanical Engineering,
University of Durban-Westville,
Durban, 4000 South Africa
Mem. ASME

A three-dimensional analytical solution to the steady-state free convection problem in a long rotating porous box is presented for large values of the porous media Ekman number. The convection results from differential heating of the horizontal walls leading to temperature gradients orthogonal to the centrifugal body force. The solution to the nonlinear set of partial differential equations was obtained through an asymptotic expansion of the dependent variables in terms of two small parameters representing the reciprocal Ekman number in porous media and the aspect ratio of the domain. The results are focused towards the Coriolis effect on the flow. Secondary circulation was obtained in a plane orthogonal to the leading free convection plane. The results show that the Coriolis effect on free convection is controlled by a combined dimensionless group representing the ratio of the centrifugal Rayleigh number to the porous media Ekman number.

1 Introduction

Free convection in porous media is of practical interest in geophysics and engineering. Heat transfer in geothermal systems, the flow of magma in the earth mantle close to the earth crust, and the insulation technology and transport phenomena in rotating porous beds may serve as examples. Among the engineering applications of rotating flow in porous media, one finds the food process industry, chemical process industry, and centrifugal filtration processes. More specifically, packed-bed mechanically agitated vessels are used in the food process industry and the chemical engineering industry in batch processes. As the solid matrix rotates due to the mechanical agitation, a rotating frame of reference is a necessity when investigating these flows. The role of fluid flow through these beds can vary, from drying processes to extraction of soluble components from the solid particles. Further applications of transport phenomena in rotating porous media are related to cyclic interchange fluidization by using a multipore rotating distributor (Witehead, 1985; Kvasha, 1985) or cooling of porous turbine blades in the hot stages of an expander. Recently the porous media approach was successfully applied to simulate complex transport phenomena in heat and mass exchangers, e.g., Roberson and Jacobs (1990) and in cooling of electronic equipment (Vadasz, 1991). With the emerging utilization of the porous medium approach to nontraditional domains including some applications in which the solid matrix is subject to rotation (like cooling of electronic equipment in a rotating radar or cooling of porous turbine blades) a thorough understanding of heat transfer in a rotating porous media becomes essential. Its results can then be applied to the more established industrial applications like food, chemical engineering, or centrifugal processes, as well as to the aforementioned nontraditional applications of the porous medium approach. A more detailed discussion of further applications was presented by Vadasz (1992a).

When rotating porous matrix is considered, an additional body force exists in the form of the centrifugal acceleration. This force may create free convection in the same manner as the gravity force causes natural convection. Some research results are available for natural convection in rotating porous media, all focusing on convection resulting from gravity in the presence of a single fluid or binary mixture (Patil and Vaidyanathan, 1983; Jou and Liaw, 1987a, b; Rudraiah et al., 1986; Palm and Tyvand, 1984).

The solution to the free convection problem in a rotating porous rectangular domain resulting from imposed temperature gradients orthogonal to the centrifugal body force was presented by Vadasz (1992b). There, the solution was restricted to a small aspect ratio of the rectangular domain and higher order corrections of the leading order convection were evaluated, while the effect of Coriolis acceleration was neglected. This paper presents a three-dimensional analytical solution to the steady-state free convection in a long rotating porous box, resulting from the centrifugal body force and focusing on the effect of Coriolis acceleration on fluid flow and heat transfer.

2 Problem Formulation

Let us consider a rotating fluid-saturated porous box heated from above and cooled from below (Fig. 1). At each point of the flow domain, the temperatures of the solid and fluid phasesare assumed to be equal (Dagan, 1972). The front, back, and the lateral walls are all insulated. The box has a square cross

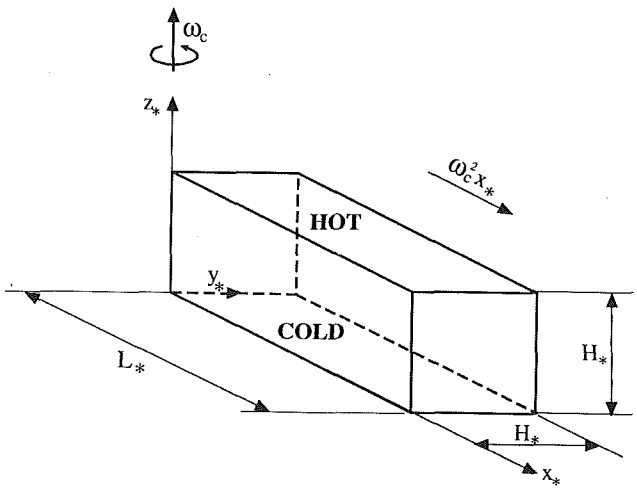

Fig. 1 A rotating fluid-saturated porous box heated from above and cooled from below

Contributed by the Heat Transfer Division for publication in the JOURNAL OF HEAT TRANSFER. Manuscript received by the Heat Transfer Division September 1991; revision received December 1992. Keywords: Natural Convection, Porous Media, Rotating Flows. Associate Technical Editor: R. Viskanta.

section of which height and width is H_*. The aspect ratio is defined as $a = H_*/L_*$ where L_* is the length of the box. Free convection occurs as a result of the centrifugal body force while the gravity force is neglected. The only inertial effects considered are the centrifugal acceleration, as far as changes in density are concerned, and the Coriolis force. Other than that, Darcy's law is assumed to govern the fluid flow (extended to include the aforementioned inertial terms), while the Boussinesq approximation is applied for the effects of density variations. As the width (or height) of the domain is much smaller than its length (a small aspect ratio) a Cartesian coordinate system can be used and the component of the centrifugal acceleration in the y direction can be neglected. By assuming steady-state conditions, the following dimensionless set of governing equations is obtained:

$$a\frac{\partial u}{\partial x}+\frac{\partial v}{\partial y}+\frac{\partial w}{\partial z}=0 \tag{1}$$

$$u=-\frac{\partial p}{\partial z}-\mathrm{Ra}_\omega xT+\mathrm{Ek}^{-1}v \tag{2}$$

$$av=-\frac{\partial p}{\partial y}-a\mathrm{Ek}^{-1}u \tag{3}$$

$$aw=-\frac{\partial p}{\partial z} \tag{4}$$

$$a^2\frac{\partial^2 T}{\partial x^2}+\frac{\partial^2 T}{\partial y^2}+\frac{\partial^2 T}{\partial z^2}-au\frac{\partial T}{\partial x}-v\frac{\partial T}{\partial y}-w\frac{\partial T}{\partial z}=0 \tag{5}$$

Equations (1)–(5) are presented in a dimensionless form where the values α_{e0}/H_*M_f, $\mu_*\alpha_{e0}/k_*M_f a$ and ΔT_c are used to scale the specific flowrate, pressure, and temperature variations, respectively. Two different length scales were used for scaling the variables x_*, y_* and z_*. Accordingly, $x = x_*/L_*$, $y = y_*/H_*$ and $z = z_*/H_*$. In Eqs. (2) and (3) Ra_ω is the Rayleigh number modified to include the centrifugal body force instead of gravity in the form $\mathrm{Ra}_\omega = \beta_{T^*}\Delta T_c\omega_c^2 L_* H_* k_* M_f/\alpha_{e0}\nu_0$ and Ek stands for the porous media Ekman number defined by $\mathrm{Ek} = \nu_0\phi/2\omega_c k_*$ where ϕ is porosity, ω_c is the characteristic angular velocity of the rotating box, k_* is the permeability of the porous matrix, ν_0 is the kinematic viscosity of the fluid, α_{e0} is the effective thermal diffusivity of the fluid saturated porous domain, β_{T^*} is the thermal expansion coefficient, ΔT_c is a characteristic temperature difference, and M_f is the ratio between the heat capacity of the fluid and the effective heat capacity of the porous domain. The scaling temperature difference ΔT_c is chosen to be the difference between the hot and cold walls temperatures thus $T = (T_* - T_C)/(T_H - T_C)$.

It should be mentioned that in most of the applications of flows in rotating porous media the Ekman number is usually much greater than 1, and in some application it is O(1). The partial differential Eqs. (1), (2), (3), (4), and (5) form a nonlinear coupled system. Their coupling is a result of two mechanisms, namely: the Coriolis acceleration and the free convection. While the Coriolis effect causes a linear form of coupling between the horizontal components of the specific flowrates the free convection coupling between Eq. (2) and the energy Eq. (5) introduces the nonlinearity.

To obtain an analytical solution to this problem, the dependent variables, $\mathbf{q} = u\hat{\mathbf{e}}_x + v\hat{\mathbf{e}}_y + w\hat{\mathbf{e}}_z$, T, and p are expanded in a double power series in terms of two small parameters representing the reciprocal Ekman number in porous media and the aspect ratio for the domain, in the form

$$[\mathbf{q},\ T,\ p] = \sum_{m=0}^{\infty}\sum_{n=0}^{\infty} a^m \mathrm{Ek}^{-n}[\mathbf{q}_{mn},\ T_{mn},\ p_{mn}] \tag{6}$$

As all the boundaries are rigid the solution must obey the impermeability conditions there, i.e., $\mathbf{q}\cdot\hat{\mathbf{e}}_n = 0$ on the boundaries, where $\hat{\mathbf{e}}_n$ is a unit vector normal to the boundary. The temperature boundary conditions are: $T = 0$ at $z = 0$, $T = 1$ at $z = 1$ and $\nabla T\cdot\hat{\mathbf{e}}_n = 0$ on all vertical walls representing the insulation condition on these walls.

3 Analytical Solution

By introducing the expansion (6) into Eq. (1)–(5), a hierarchy of partial differential equations is obtained for the different orders. To leading order the zero powers of a and Ek^{-1} are used, which yields a reduced set of equations. Their solution is

$$v_{00} = w_{00} = 0,\quad T_{00} = z \quad \text{and} \quad u_{00} = -\frac{\mathrm{Ra}_\omega x}{2}[2z-1] \tag{7}$$

This leading order solution holds for the core region while the boundaries at $x = 0$ and $x = 1$ are not included, as u_{00} does not vanish there. A vertical boundary layer exists next to the side-

Nomenclature

a = the aspect ratio of the box = H_*/L_*
Ek = Ekman number = $\nu_0\phi/2\omega_c k_*$
$\hat{\mathbf{e}}_x$ = unit vector in the x direction
$\hat{\mathbf{e}}_y$ = unit vector in the y direction
$\hat{\mathbf{e}}_z$ = unit vector in the z direction
$\hat{\mathbf{e}}_n$ = unit vector normal to the boundary, positive outward
H_* = the height (width) of the box
k_* = permeability of the porous domain
L_* = the length of the porous domain
M_f = a ratio between the heat capacity of the fluid and the effective heat capacity of the porous domain
Nu = Nusselt number, defined by Eq. (25)
p = reduced pressure generalized to include the constant component of the centrifugal term (dimensionless)
$\mathbf{q}$ = dimensionless specific flow rate vector = $u\hat{\mathbf{e}}_x + v\hat{\mathbf{e}}_y + w\hat{\mathbf{e}}_z$
Ra_ω = porous media Rayleigh number related to the centrifugal body force = $\beta_{T^*}\Delta T_c\omega_c^2 L_* H_* k_* M_f/\alpha_{e0}\nu_0$
T = dimensionless temperature = $(T_* - T_C)/(T_H - T_C)$
T_C = coldest wall temperature
T_H = hottest wall temperature
u = horizontal x component of the specific flowrate
v = horizontal y component of the specific flowrate
w = vertical component of the specific flowrate
x = horizontal length coordinate
y = horizontal width coordinate
z = vertical coordinate
ϕ = porosity
α_{e0} = effective thermal diffusivity
β_{T^*} = thermal expansion coefficient
ω_c = angular velocity of the rotating box
ν_0 = fluid's kinematic viscosity
μ_* = fluid's dynamic viscosity
ψ = stream function
ΔT_c = characteristic temperature difference
σ = a dimensionless group = $\mathrm{Ra}_\omega/\mathrm{Ek}$
δ = dimensionless boundary layer thickness

Subscripts

$*$ = dimensional values
c = characteristic values
C = related to the coldest wall
H = related to the hottest wall
0 = zeroth order
1 = first order
$e0$ = related to the end next to $x = 0$
$e1$ = related to the end next to $x = 1$

walls, and the flow there is evaluated by using an integral of momentum method of solution similar to those of Bejan and Tien (1978), Cormack et al. (1974a,b), and Imberger (1974). The boundary layer solution matches the core solution at $x=\delta$ (where δ is the dimensionless boundary layer thickness, found to be equal to a). This means that $\delta_* = H_*$. The solutions next to the wall $x=0$ differ from those near $x=1$ as a result of the centrifugal effect which is proportional to $\omega_c^2 x_*$. Therefore, the subscript "$e0$" refers to the end next to $x=0$ and "$e1$" refers to the end next to $x=1$. Using this notation, the following solutions were found (see Appendix for details)

$$u_{e0} = -\frac{\mathrm{Ra}_\omega}{2}(2z-1)\left(2-\frac{x}{\delta}\right)x \tag{8a}$$

$$u_{e1} = -\frac{\mathrm{Ra}_\omega}{2}(2z-1)x\left(\frac{1-x}{\delta}\right)\left[2-\left(\frac{1-x}{\delta}\right)^2\right] \tag{8b}$$

$$w_{e0} = a\mathrm{Ra}_\omega z(z-1)\left(1-\frac{x}{\delta}\right)x \tag{8c}$$

$$w_{e1} = \frac{a\mathrm{Re}_\omega}{2}z(z-1)\left\{\left(\frac{1-x}{\delta}\right)\left[2-\left(\frac{1-x}{\delta}\right)\right] - 2\left(\frac{x}{\delta}\right)\left[1-\left(\frac{1-x}{\delta}\right)\right]\right\} \tag{8d}$$

$$T_{e0} = z\left\{1+\frac{a\mathrm{Ra}_\omega}{12}\left[1-3\left(\frac{x}{\delta}\right)^2+2\left(\frac{x}{\delta}\right)^3\right](1-z)\right\} \tag{8e}$$

$$T_{e1} = z + z(1-z)\frac{\delta^2 a\mathrm{Ra}_\omega}{96}\left[1-3\left(\frac{1-x}{\delta}\right)^2+2\left(\frac{1-x}{\delta}\right)^3\right] \tag{8f}$$

As the main objective of this paper is to find the Coriolis effect on the free convection, the following analysis focuses on the solution to order 1 in Ek^{-n} and to order 0 in a^m. The corresponding higher order solution to order 1 in a^m and 0 in Ek^{-n} was reported separately by Vadasz (1992a). Therefore, the corresponding equations to order 1 in Ek^{-n} and 0 in a^m are obtained, upon introducing the leading order solutions, in the form

$$\frac{\partial v_{01}}{\partial y}+\frac{\partial w_{01}}{\partial z}=0 \tag{9}$$

$$u_{01} = -\frac{\partial p_{01}}{\partial x}-\mathrm{Ra}_\omega x T_{01},\quad \frac{\partial p_{01}}{\partial y}=0,\quad \frac{\partial p_{01}}{\partial z}=0 \tag{10}$$

$$\frac{\partial^2 T_{01}}{\partial y^2}+\frac{\partial^2 T_{01}}{\partial z^2}=w_{01} \tag{11}$$

To obtain a solution for v_{01} and w_{01}, one should refer to the equations at orders 1 in a^m and 1 in Ek^{-n} leading to

$$v_{01} = -\frac{\partial p_{11}}{\partial y}-u_{00},\quad w_{01} = -\frac{\partial p_{11}}{\partial z} \tag{12}$$

The pressure is eliminated from these equations by taking the derivatives $\partial/\partial z$ and $\partial/\partial y$ of v_{01} and w_{01} in (12), respectively, and subtracting. By introducing the stream function to satisfy identically Eq. (9), i.e., $v_{01}=\partial\psi_{01}/\partial z$, $w_{01}=-\partial/\psi_{01}/\partial y$, one obtains

$$\frac{\partial^2\psi_{01}}{\partial y^2}+\frac{\partial^2\psi_{01}}{\partial z^2}=\mathrm{Ra}_\omega x \tag{13}$$

where the solution for u_{00} was introduced. The solution of the Poisson Eq. (13) for the stream function subject to the boundary conditions $\psi_{01}=0\ \forall\ (y=0,1; z=0,1)$ was obtained through separation of variables, and its result is presented in the form

$$\psi_{01} = -\frac{16\mathrm{Ra}_\omega x}{\pi^4}\sum_{i=1}^{\infty}\sum_{j=1}^{\infty}\frac{\sin[(2i-1)\pi y]\sin[(2j-1)\pi z]}{(2i-1)(2j-1)[(2i-1)^2+(2j-1)^2]} \tag{14}$$

Therefore v_{01} and w_{01} can be evaluated leading to

$$v_{01}=\frac{\partial\psi_{01}}{\partial z} = -\frac{16\mathrm{Ra}_\omega x}{\pi^3}\sum_{i=1}^{\infty}\sum_{j=1}^{\infty}\frac{\sin[(2i-1)\pi y]\cos[(2j-1)\pi z]}{(2i-1)[(2i-1)^2+(2j-1)^2]} \tag{15}$$

$$w_{01} = -\frac{\partial\psi_{01}}{\partial y}=\frac{16\mathrm{Ra}_\omega x}{\pi^3}\sum_{i=1}^{\infty}\sum_{j=1}^{\infty}\frac{\cos[(2i-1)\pi y]\sin[(2j-1)\pi z]}{(2j-1)[(2i-1)^2+(2j-1)^2]} \tag{16}$$

It can be observed that the denominator, mainly in (14) but also in (15) and (16), increases very fast with increasing the values of i and j. Therefore, a fast convergence of the series is expected. To solve for T_{01}, one should obtain the solution of Eq. (11) upon introduction of w_{01} from (16). The method of solution is completely similar to the solution for ψ_{01} except for the boundary conditions, which in this case are $T_{01}=0$ at $z=0$, 1 and $\partial T_{01}/\partial y=0$ at $y=0$, 1. This leads to the following result:

$$T_{01} = -\frac{16\mathrm{Ra}_\omega x}{\pi^5}\sum_{i=1}^{\infty}\sum_{j=1}^{\infty}\frac{\cos[(2i-1)\pi y]\sin[(2j-1)\pi z]}{(2j-1)[(2i-1)^2+(2j-1)^2]^2} \tag{17}$$

To complete the solution at this order, u_{01} should be evaluated from (10). Since, according to (10), p_{01} is not a function of y and z, however in (10) u_{01} and T_{01} are functions of x, y and z, $\partial p_{01}/\partial x$ must take the form $\partial p_{01}/\partial x = Cx^2$, where C is a constant to be determined. By introducing this form and the solution for T_{01} from (17) into (10), and by using the following mass conservation constraint on any cross-section yz, stating that no net flow is allowed through any cross-section as the flow domain is laterally bounded, i.e.,

$$\int_0^1\int_0^1 u_{01}\,dy\,dz=0 \tag{18}$$

the value of C is found to be zero. Therefore, the pressure gradients vanish at this order and as a result the solution for u_{01} in the core region is

$$u_{01} = \frac{16\mathrm{Ra}_\omega^2 x^2}{\pi^5}\sum_{i=1}^{\infty}\sum_{j=1}^{\infty}\frac{\cos[(2i-1)\pi y]\sin[(2j-1)\pi z]}{(2j-1)[(2i-1)^2+(2j-1)^2]^2} \tag{19}$$

Finally, the complete results up to and including order 1 in Ek^{-n} can be presented in the form

$$u = u_{00}+\mathrm{Ek}^{-1}u_{01} = -\frac{\mathrm{Ra}_\omega x}{2}[2z-1] + \frac{16\mathrm{Ek}^{-1}\mathrm{Ra}_\omega^2 x^2}{\pi^5}\sum_{i=1}^{\infty}\sum_{j=1}^{\infty}\frac{\cos[(2i-1)\pi y]\sin[(2j-1)\pi z]}{(2j-1)[(2i-1)^2+(2j-1)^2]^2} \tag{20}$$

$$v = \mathrm{Ek}^{-1}v_{01} = -\frac{16\mathrm{Ek}^{-1}\mathrm{Ra}_\omega x}{\pi^3}\sum_{i=1}^{\infty}\sum_{j=1}^{\infty}\frac{\sin[(2i-1)\pi y]\cos[(2j-1)\pi z]}{(2i-1)[(2i-1)^2+(2j-1)^2]} \tag{21}$$

$$w = \mathrm{Ek}^{-1}w_{01} = \frac{16\mathrm{Ek}^{-1}\mathrm{Ra}_\omega x}{\pi^3}\sum_{i=1}^{\infty}\sum_{j=1}^{\infty}\frac{\cos[(2i-1)\pi y]\sin[(2j-1)\pi z]}{(2j-1)[(2i-1)^2+(2j-1)^2]} \tag{22}$$

$$T = T_{00}+\mathrm{Ek}^{-1}T_{01} = z-\frac{16\mathrm{Ek}^{-1}\mathrm{Ra}_\omega x}{\pi^5}\sum_{i=1}^{\infty}\sum_{j=1}^{\infty}\frac{\cos[(2i-1)\pi y]\sin[(2j-1)\pi z]}{(2j-1)[(2i-1)^2+(2j-1)^2]^2} \tag{23}$$

From these solutions it can be observed that the Coriolis effect on free convection is controlled by the combined dimensionless group $\sigma=\mathrm{Ra}_\omega\mathrm{Ek}^{-1}$, i.e.,

$$\sigma=\frac{\mathrm{Ra}_\omega}{\mathrm{Ek}}=\frac{2\beta_{T^*}\Delta T_c\omega_c^3 L_* H_* k_*^2 M_f}{\alpha_{e0}\nu_0^2} \tag{24}$$

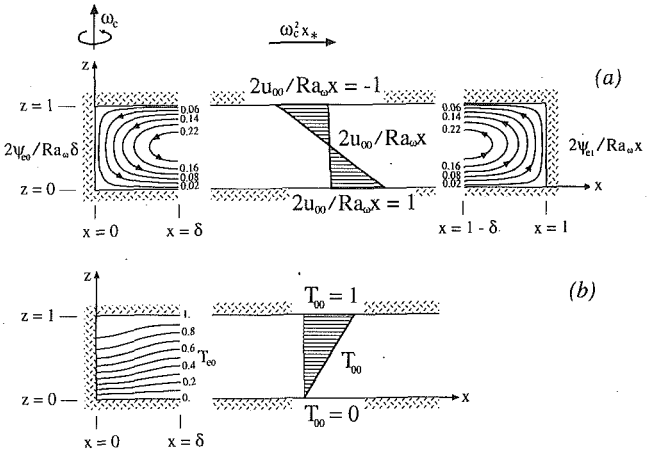

Fig. 2 Graphical description of the flow and temperature fields at the leading order; (*a*) at the center—the horizontal x component of the specific flowrate u_{00}; at the left hand side—the boundary layer streamlines: 6 streamlines equally divided between their minimum value of $(2\psi_{e0}/Ra_\omega\delta)_{min} = 0.02$ and their maximum value of $(2\psi_{e0}/Ra_\omega\delta)_{max} = 0.22$; at the right hand side—the boundary layer streamlines: 6 streamlines equally divided between their minimum value of $(2\psi_{e1}/Ra_\omega x)_{min} = 0.02$ and their maximum value of $(2\psi_{e1}/Ra_\omega x)_{max} = 0.22$; (*b*) at the center—the temperature profile, T_{00}, at the leading order in the core region; at the left hand side—the boundary layer isotherms: 11 isotherms equally divided between their minimum value $(T_{e0})_{min} = 0$ and their maximum value $(T_{e0})_{max} = 1$.

The validity of the asymptotic expansion is restricted too, by the values of σ and the expansion is valid for $Ek \gg 1$ as long as the value of a is not too high. However, even when the expansion breaks down one should expect this dimensionless group, σ, to continue to control the Coriolis effect on the free convection.

4 The Vertical Heat Flux

The local Nusselt number, Nu_{xy}, representing the vertical heat flux through the domain, is expressed by

$$Nu_{xy} = \left(\frac{\partial T}{\partial z}\right)_{z=0} = \left(\frac{\partial T_{00}}{\partial z}\right)_{z=0} + Ek^{-1}\left(\frac{\partial T_{01}}{\partial z}\right)_{z=0} \tag{25}$$

Its mean value over y is

$$\overline{Nu}_x^y = \int_0^1 Nu_{xy}\,dy \tag{26}$$

By neglecting edge effects (which are expected to be $O(a)$ or smaller), the mean Nusselt number over x can be presented in the form

$$\overline{Nu}_y^x = \int_0^1 Nu_{xy}\,dx \tag{27}$$

The mean heat flux over the xy plane is given by

$$\overline{Nu} = \int_0^1\int_0^1 Nu_{xy}\,dx\,dy \tag{28}$$

By introducing the solutions T_{00} and T_{01} from (7) and (17) into (25), the expression for the local Nusselt number Nu_{xy} is obtained in the form

$$Nu_{xy} = 1 - \frac{16Ek^{-1}Ra_\omega x}{\pi^4}\sum_{i=1}^{\infty}\sum_{j=1}^{\infty}\frac{\cos[(2i-1)\pi y]}{[(2i-1)^2+(2j-1)^2]^2} \tag{29}$$

The mean Nusselt number over x is obtained upon introduction of (29) into (27)

$$\overline{Nu}_y^x = 1 - \frac{8Ek^{-1}Ra_\omega}{\pi^4}\sum_{i=1}^{\infty}\sum_{j=1}^{\infty}\frac{\cos[(2i-1)\pi y]}{[(2i-1)^2+(2j-1)^2]^2} = (Nu_{xy})_{x=1/2} \tag{30}$$

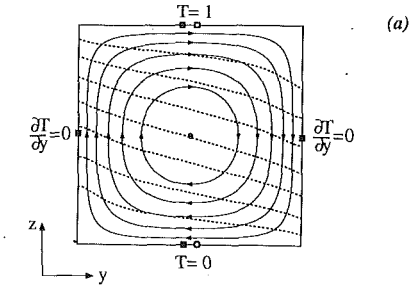

Fig. 3(*a*) Graphical description of the flow field at any cross-section represented by constant values of $(\psi_{01}/Ra_\omega x)$ and of the temperature field T, on the yz plane at $x = 0.5$, for $\sigma = Ra_\omega/Ek = 10$. Five streamlines (——) equally divided between their maximum value of ■ $(\psi_{01}/Ra_\omega x)_{max} = 0$ and their minimum value of • $(\psi_{01}/Ra_\omega x)_{min} = -7.37 \times 10^{-2}$. Seven isotherms (·····) equally divided between ○ $T_{min} = 0$ and □ $T_{max} = 1$.

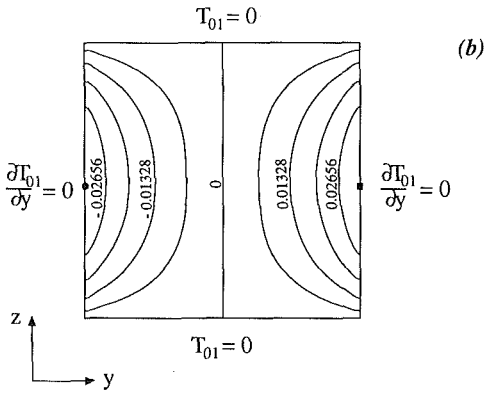

Fig. 3(*b*) Graphical description of the higher order component of temperature at any cross-section represented by constant values of $T_{01}/Ra_\omega x$. Nine isolines equally divided between their minimum value of • $(T_{01}/Ra_\omega x)_{min} = -0.0332$ and their maximum value of ■ $(T_{01}/Ra_\omega x)_{max} = 0.0332$.

It can be observed that the dimensionless group $\sigma = Ra_\omega/Ek$ controls the heat flux, too. The mean Nusselt number over y, obtained by introducing (29) into (26) and integrating, was found to be equal to 1, which is equivalent to the heat flux due to conduction. As a result the mean heat flux over the whole xy plane equals 1 as well. This result can be expected as the Coriolis effect on the convection is in providing a higher order correction to the leading order conduction solution $(T_{00} = z)$, which is reflected over the yz cross-section of the leading order flow in an antisymmetrical form with respect to $y = 1/2$. Therefore, the vertical heat flux at any given value of x is reduced in one-half of the box, i.e., for $y \in [0, 0.5]$, and is enhanced in the other half of the box, $y \in [0.5, 1]$, while its integral effect is canceled as far as the mean heat flux up to this order is concerned.

5 Results and Discussion

The analytical results obtained in Sections 3 and 4 are presented graphically in Figs. 2–4 and their significance is discussed in this section.

The leading order core solutions $2u_{00}/Ra_\omega x$ and T_{00} are presented in Fig. 2. A linear profile of the horizontal x component of the specific flowrate represents the free convection obtained as a result of the imposed temperature gradient orthogonal to the centrifugal body force. The corresponding temperature profile at the leading order is linear, resembling the conduction solution. The other two components of the specific flowrate at this order, v_{00} and w_{00}, vanish in the core. The boundary layers next to the walls at $x = 0$ and $x = 1$ are presented in Fig. 2(*a*) in terms of the stream functions $2\psi_{e0}/Ra_\omega\delta$ and $2\psi_{e1}/Ra_\omega x$. Their effect on the temperature field is felt, as can be observed in Fig. 2(*b*), where the isotherms near the wall at $x = 0$ are presented.

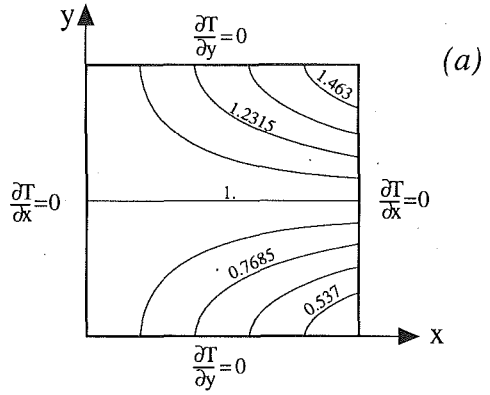

Fig. 4(*a*) Graphical description of the local vertical heat flux on the *xy* plane represented by constant values of Nu_{xy} for $\sigma = Ra_\omega/Ek = 10$. Nine isolines equally divided between $(Nu_{xy})_{min} = 0.537$ and $(Nu_{xy})_{max} = 1.463$.

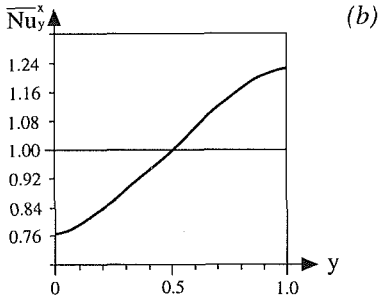

Fig. 4(*b*) Graphical description of the mean Nusselt number over *x*, $\overline{Nu}_y^x$, for $\sigma = Ra_\omega/Ek = 10$, as a function of *y*.

The Coriolis effect is felt at order 1 in Ek^{-n}, leading to secondary circulation in a plane orthogonal to the leading free convection plane. As a result, the leading order convection occurring in the *xz* plane induces through Coriolis a secondary motion in the *yz* plane. The graphical description of this secondary flow field at any cross section, represented by constant values of $\psi_{01}/Ra_\omega x$, i.e., by corresponding stream lines, is presented in Fig. 3(*a*). The direction of the circulation depends on the rotation direction and on the direction of the thermal gradient. In this case, both the angular velocity and the imposed thermal gradient correspond to the positive *z* direction leading to a clockwise secondary circulation in the *yz* plane. As a result of this circulation, the temperature distribution in the *yz* plane, as well as in the *x* direction, is affected significantly. The graphical description of the temperature field, *T*, on the *yz* plane at $x = 0.5$ corresponding to $\sigma = Ra_\omega/Ek = 10$ is presented in Fig. 3(*a*), as well in the form of dotted lines. The effect of convection is apparent in this figure, as the distortion of the isotherms from the parallel horizontal form prevailing to a conduction regime is significant. This distortion of the isotherms, which at the leading order were parallel and horizontal, was created by the temperature solution at order 1 in Ek^{-n}, i.e., T_{01}. The graphical description of the higher order component of temperature at any cross-section, represented by constant values of $T_{01}/Ra_\omega x$, i.e., by the corresponding higher order isotherms, is presented in Fig. 3(*b*). Its antisymmetrical form with respect to $y = 1/2$ is a result of the direction of the secondary circulation. Since, according to Eqs. (17) and (19) the value of $u_{01}/Ra_\omega^2 x^2$ is identical to $-T_{01}/Ra_\omega x$, the isotherms presented in Fig. 3(*b*) stand for isolines of $u_{01}/Ra_\omega^2 x^2$ as well, with only a correction of sign necessary. As the values of u_{01} are positive for $y \in [0, 0.5]$ and negative for $y \in [0.5, 1]$, the higher order correction, u_{01}, to the leading order convection profile, u_{00}, slightly enhances the free convection in one half of the box, i.e., for $y \in [0, 0.5]$ and slightly reduces the flow in the other half of the box, i.e., for $y \in [0.5, 1]$. As a result of the Coriolis effect on the convection, the local vertical heat flux is not uniform and therefore varies in the *xy* plane. The results of Nu_{xy} as calculated from Eq. (29) for $\sigma = Ra_\omega/Ek = 10$ are presented in Fig. 4(*a*) in terms of equal values curves of Nu_{xy} in the *xy* plane. It should be noticed that the *xy* domain of the box is a square as a result of the adopted scaling which causes a compression of the x_* coordinate, i.e., $x = x_*/L_*$ leading to $x \in [0, 1]$. The graphical description of the mean heat flux over *x*, i.e., $\overline{Nu}_y^x$, for $\sigma = Ra_\omega/Ek = 10$, as a function of *y* is presented in Fig. 4(*b*). The results show that the local heat flux is affected significantly (up to ± 24 percent) by the Coriolis effect.

6 Conclusions

Analytical three-dimensional results were presented for the solution of the steady-state free convection problem in a long rotating porous box at high values of the porous media Ekman number. The convection was obtained at the leading order as a result of differential heating of the horizontal walls. The Coriolis force created secondary circulation in a plane orthogonal to the leading free convection plane affecting significantly the local vertical heat flux. The mean vertical heat flux was not affected by the Coriolis effect. Except for the horizontal component of the specific flowrate, which depends explicitly on Ra_ω, the flow and the heat transfer in the core region was found dependent only on the combined dimensionless group $\sigma = Ra_\omega/Ek$.

References

Bejan, A., and Tien, C. L., 1978, "Natural Convection in a Horizontal Porous Medium Subjected to an End-to-End Temperature Difference," ASME JOURNAL OF HEAT TRANSFER, Vol. 100, pp. 191–198.

Cormack, D. E., Leal, L. G., and Imberger, J., 1974a, "Natural Convection in a Shallow Cavity With Differentially Heated End Walls. Part 1. Asymptotic Theory," *J. Fluid Mechanics*, Vol. 65, Part 2, pp. 209–229.

Cormack, D. E., Leal, L. G., and Seinfeld, J. H., 1974b, "Natural Convection in a Shallow Cavity with Differentially Heated End Walls. Part 2. Numerical Solutions," *J. Fluid Mechanics*, Vol. 65, Part 2, pp. 231–246.

Dagan, G., 1972, "Some Aspects of Heat and Mass Transfer in Porous Media," *Fundamentals of Transport Phenomena in Porous Media*, Elsevier Publishing, Amsterdam, pp. 55–64.

Imberger, J., 1974, "Natural Convection in a Shallow Cavity With Differentially Heated End Walls. Part 3. Experimental Results," *J. Fluid Mechanics*, Vol. 65, Part 2, pp. 247–260.

Jou, J. J., and Liaw, J. S., 1987a, "Transient Thermal Convection in a Rotating Porous Medium Confined Between Two Rigid Boundaries," *Int. Communications in Heat and Mass Transfer*, Vol. 14, pp. 147–153.

Jou, J. J., and Liaw, J. S., 1987b, "Thermal Convection in a Porous Medium Subject to Transient Heating and Rotation," *Int. J. Heat Mass Transfer*, Vol. 30, No. 1, pp. 208–211.

Kvasha, V. B., 1985, "Multiple-Spouted Gas-Fluidized Beds and Cyclic Fluidization: Operation and Stability," *Fluidization*, 2nd ed., J. F. Davidson, R. Clift, and D. Harrison, eds., Academic Press, London, pp. 675–701.

Palm, E., and Tyvand, A., 1984, "Thermal Convection in a Rotating Porous Layer," *J. Appl. Math. & Physics (ZAMP)*, Vol. 35, pp. 122–123.

Patil, P. R., and Vaidyanathan, G., 1983, "On Setting Up of Convection Currents in a Rotating Porous Medium Under the Influence of Variable Viscosity," *Int. J. Engineering Science*, Vol. 21, No. 2, pp. 123–130.

Roberson, M. E., and Jacobs, H. R., 1990, "An Experimental Study of Mass Transfer in Packed Beds as an Analog to Convective Heat Transfer," *Proceedings of the Ninth International Heat Transfer Conference*, Jerusalem, Israel.

Rudraiah, N., Shivakumara, I. S., and Friedrich, R., 1986, "The Effect of Rotation on Linear and Non-Linear Double-Diffusive Convection in Sparsely Packed Porous Medium," *Int. J. Heat Mass Transfer*, Vol. 29, No. 9, pp. 1301–1317.

Vadasz, P., 1991, "On the Evaluation of Heat Transfer and Fluid Flow by Using the Porous Media Approach With Application to Cooling of Electronic Equipment," *Proceedings of the Fifth Israeli Conference on Packaging and Thermal Control of Electronic Equipment*, Herzlia, Israel.

Vadasz, P., 1992a, "Fluid Flow Through Heterogeneous Porous Media in a Rotating Square Channel," *Transport in Porous Media*, in press.

Vadasz, P., 1992b, "Natural Convection in Rotating Porous Media Induced by the Centrifugal Body Force: The Solution for Small Aspect Ratio," ASME *Journal of Energy Resources Technology*, Vol. 114, pp. 250–254.

Witehead, A. B., 1985, "Distributor Characteristics and Bed Properties," *Fluidization*, 2nd ed., J. F. Davidson, R. Clift, and D. Harrison, eds., Academic Press, London, pp. 173–199.

APPENDIX

The Boundary Layer Solution

Equations (1)–(5) are not properly scaled to include end regions next to the sidewalls. When rescaling the equations by choosing $x' = x/\delta$ where $\delta = \delta_*/L_*$ is the boundary layer thickness, one observes that the core solution does not satisfy the rescaled continuity equation in the boundary layer nor the boundary conditions at $x = 1$. By applying the integral of momentum method for the velocity and the integral of energy method for the temperature, the boundary layer solutions can be evaluated. Integrating the momentum equations after cross-differentiation and subtraction to eliminate the pressure terms, an integral of momentum equation next to the wall at $x = 0$ is obtained in the form

$$\int_0^\delta [u_{e0}(x, 1) - u_{e0}(x, 0)]dx + a\int_0^1 w_{e0}(0, z)dz + \frac{\mathrm{Ra}_\omega \delta^2}{2} = 0 \quad \text{(A1)}$$

Similarly, the integral of energy equation is expressed by

$$a^2\int_0^1 dz\left(\frac{\partial T}{\partial z}\right)_{(\delta,z)} + \int_0^\delta dx\left[\frac{\partial T}{\partial z}(x, 1) - \frac{\partial T}{\partial z}(x, 0)\right] - a\int_0^1 dz(uT)_{(\delta,z)} = 0 \quad \text{(A2)}$$

The velocity and temperature solutions in the boundary layer should satisfy these equations. A velocity function of the following form

$$u_{e0} = -\frac{\mathrm{Ra}_\omega}{2}(2z - 1)x \cdot f(x) \quad \text{(A3)}$$

is assumed (where the u_{e0} represents the product of $f(x) \cdot u_{00}$). The corresponding function for w_{e0} is evaluated from the continuity equation leading to

$$\dot{w}_{e0} = \frac{a\mathrm{Ra}_\omega}{2} z(z - 1)(f + xf') \quad \text{(A4)}$$

Setting $f(x)$ to be a polynomial, its coefficients are to be determined from the boundary conditions, i.e., $u_{e0}(x = 0) = 0$, $u_{e0}(x = \delta) = u_{00}$, $w_{e0}(x = \delta) = w_{00} = 0$, $w_{e0}(z = 0) = 0$, $w_{e0}(z = 1) = 0$, leading to the solutions (8a) and (8c). Adopting a similar method for the temperature, one assumes a temperature function in the form

$$T_{e0} = T_{00} + f(x)g(z) \quad \text{(A5)}$$

where $f(x)$ and $g(z)$ are assumed to be polynomials with yet undetermined coefficients. Then imposing the boundary conditions $\partial T_{e0}/\partial x = 0$ at $x = 0$, $T_{e0} = T_{00}$ at $x = \delta$, $\partial T_{e0}/\partial x = \partial T_{00}/\partial x = 0$ at $x = \delta$, $T_{e0} = 0$ at $z = 0$, $T_{e0} = 1$ at $z = 1$ and Eq. (A2), the temperature solution in the boundary layer next to the wall at $x = 0$ is evaluated as presented in Eq. (8e). A similar approach leads to the solutions (8b), (8d), and (8f) for the boundary layer next to the wall at $x = 1$. As the method of solution is similar to that presented by Bejan and Tien (1978), Cormack et al. (1974a, b) and Imberger (1974), one should refer to these references for further details.

Nongray Gas Analyses for Reflecting Walls Utilizing a Flux Technique

J. A. Menart
Department of Mechanical Engineering,
University of Minnesota,
Minneapolis, MN 55455

HaeOk Skarda Lee
NASA Lewis Research Center,
Cleveland, OH 44135

A flux formulation for a planar slab of molecular gas radiation bounded by diffuse reflecting walls is developed. While this formulation is limited to the planar geometry, it is useful for studying approximations necessary in modeling nongray radiative heat transfer. The governing equations are derived by considering the history of multiple reflections between the walls. Accurate solutions are obtained by explicitly accounting for a finite number of reflections and approximating the spectral effects of the remaining reflections. Four approximate methods are presented and compared using a single absorption band of H_2O. All four methods reduce to an identical zeroth-order formulation, which accounts for all reflections approximately but does handle nonreflected radiation correctly. A single absorption band of CO_2 is also considered using the best-behaved approximation for higher orders. A zeroth-order formulation is sufficient to predict the radiative transfer accurately for many cases considered. For highly reflecting walls, higher order solutions are necessary for better accuracy. Including all the important bands of H_2O, the radiative source distributions are also obtained for two different temperature and concentration profiles.

1 Introduction

Many attempts have been made to analyze radiative heat transfer in an enclosure containing a molecular gas with a gray or sum-of-gray gases model. Fictitious gray gas modeling is clearly inappropriate, as pointed out by Nelson (1977) and others cited in his paper. While the sum-of-gray gases approach can give reasonable results, a large effort may be required to get the appropriate absorption properties (Modest, 1991).

The most accurate nongray gas calculations solve the transfer equation on a line-by-line basis, but this is not practical for engineering problems. The narrow- and wide-band models give the gas absorption or transmittance averaged over a more reasonable band width. In using these band models, careful attention must be paid to the spectral characteristics of the quantities involved as well as their products.

Additional complications occur in nongray gas analyses when the enclosure walls are reflecting. This is because reflected radiation is a strong function of wavenumber and cannot be averaged separately from the transmittance. In order to maintain the physics of the problem correctly and still utilize the available band models, a series expansion of the wall radiosity is used in this work.

Edwards (1962), following the work of Bevans and Dunkle (1960), was probably the first to point out this series expansion method. Bevans and Dunkle (1960) introduced the band energy approximation, which assumed constant radiosities over a narrow band, noting that this may not be accurate for the reflected part of the wall radiosity.

Since the time of Edwards' (1962) publication, significant work on this topic has been carried out by Nelson (1977, 1979a, 1979b, 1984, 1986). In these papers, Nelson develops the zone method (Hottel and Sarofim, 1967) for analyzing molecular gas radiation with band absorption models. Essentially a series solution is cast in the form of a closure problem. The series solution is exact; however, the closure solution is only taken to some finite order and is approximate. The direction of Nelson's work has been to develop the method for more general geometries and situations.

Contributed by the Heat Transfer Division for publication in the JOURNAL OF HEAT TRANSFER. Manuscript received by the Heat Transfer Division June 1992; revision received December 1992. Keywords: Radiation. Associate Technical Editor: R. O. Buckius.

In Kim et al. (1991), a discrete ordinates method is formulated for a planar slab of nongray gas between black, plane-parallel walls. This technique is extended by Menart et al. (1993) to handle reflecting walls properly, taking into account the spectral correlations between wall reflected radiation and gas transmittance for nonisothermal media. Computational times increased by orders of magnitude in going from the black to gray wall analysis.

In this work the problem of radiative transfer between infinite parallel walls enclosing a nonisothermal, molecular gas is once again considered. This time a flux method presented by Soufiani et al. (1985) is further expanded to include the wall reflected radiation correctly. Although this flux method is limited to the one-dimensional plane-parallel geometry, the formulation is perhaps easier to understand than the discrete ordinates method. More importantly, the computational requirements are greatly reduced for the flux method, making it possible to run higher order solutions of different approximation methods to study their behavior. Using the discrete ordinates method, it became computationally costly to run higher than a second-order solution.

II Spectrally Averaged Radiative Transfer Expressions

The radiative flux equation for a one-dimensional slab of absorbing-emitting gases on a spectral basis is

$$q_\nu(x) = q_\nu^+(x) - q_\nu^-(x) \tag{1}$$

where

$$q_\nu^+(x) = 2\pi \int_0^1 I_\nu^+(x_0, \mu)\tau_\nu(x_0 \rightarrow x, \mu)\mu d\mu + 2\pi \int_0^1 \int_{x_0}^{x} I_{\nu b}(x^*) \frac{\partial \tau_\nu(x^* \rightarrow x, \mu)}{\partial x^*} \mu dx^* d\mu \tag{2a}$$

and

$$q_\nu^-(x) = 2\pi \int_0^1 I_\nu^-(x_L, -\mu)\tau_\nu(x_L \rightarrow x, -\mu)\mu d\mu + 2\pi \int_0^1 \int_{x}^{x_L} I_{\nu b}(x^*) \frac{\partial \tau_\nu(x^* \rightarrow x, -\mu)}{\partial x^*} \mu dx^* d\mu. \tag{2b}$$

In the above equations, $I^+(x_0, \mu)$ is the outgoing intensity from the wall at x_0, and $I^-(x_L, -\mu)$ is the outgoing intensity from the wall at x_L. The transmittance and its derivative are defined as

$$\tau_\nu(x^* \rightarrow x, \mu) = \exp\left[-\frac{1}{\mu} \int_{x^*}^{x} a_\nu(x^{**}) dx^{**} \right] \quad (3a)$$

$$\mu \frac{\partial \tau_\nu(x^* \rightarrow x, \mu)}{\partial x^*} = a_\nu(x^*) \tau_\nu(x^* \rightarrow x, \mu) \quad (3b)$$

where x_0, x_L, and $-\mu$ can be inserted to get other transmittances and derivatives. The first terms on the right-hand sides of Eqs. (2*a*) and (2*b*) represent the flux from the appropriate wall that is transmitted to position x, and the second terms represent the gas emission contributions to the flux at position x. From this point, the presented derivation will be limited to the positive-directed flux. The derivation is similar for the negative-directed flux.

For this work the narrowband approximation is utilized in the following form:

$$\frac{1}{\Delta\nu} \int_{\Delta\nu} I_{\nu b} \tau_\nu d\nu \approx \bar{I}_{\nu b} \left[\frac{1}{\Delta\nu} \int_{\Delta\nu} \tau_\nu d\nu \right] = \bar{I}_{\nu b} \bar{\tau}_\nu \quad (4)$$

where $\Delta\nu$ is the width of a narrow band, $\bar{I}_{\nu b}$ is the Planck function evaluated at the center wavenumber in $\Delta\nu$, $\bar{\tau}_\nu$ is obtained from the statistical narrowband model with exponential-tailed-inverse line-strength distribution (Malkmus, 1967)

$$\bar{\tau}_\nu(x^* \rightarrow x, \mu) =$$

$$\exp\left[-\frac{\beta_{\nu,\,\mathrm{eff}}}{\pi} \left(\sqrt{1 + \frac{2\pi u(x^*, x, \mu, P) k_{\nu,\,\mathrm{eff}}}{\beta_{\nu,\,\mathrm{eff}}}} - 1 \right) \right]. \quad (5)$$

The narrowband parameters are taken from Hartmann et al. (1984) and Soufiani et al. (1985). These parameters came from line-by-line calculations and are given in a tabular form for bandwidths of 25 or 50 cm^{-1}. Nonisothermal and inhomogeneous media are treated using the Curtis–Godson method (Godson, 1953; Young, 1977).

Using the narrowband approximation, the wavenumber averaged form of Eq. (2*a*) is written as

$$\bar{q}_\nu^+(x) = 2\pi \int_0^1 \overline{I_\nu^+(x_0, \mu) \tau_\nu(x_0 \rightarrow x, \mu)} \mu d\mu + 2\pi \int_0^1 \int_{x_0}^{x} \bar{I}_{\nu b}(x^*) \frac{\partial \bar{\tau}_\nu(x^* \rightarrow x, \mu)}{\partial x^*} \mu dx^* d\mu. \quad (6)$$

For reflecting walls, $I_\nu^+(x_0, \mu)$ and $\tau_\nu(x_0 \rightarrow x, \mu)$ cannot be averaged separately as was done for black walls (Kim et al., 1991). The directly emitted portion of $I_\nu^+(x_0, \mu)$ from the wall can be averaged separately but not the reflected component with its strong wavenumber dependence. Blackbody intensities can be taken out of the wavenumber averaging, because $I_{b\nu}$ is almost a constant over a narrow band.

In order to average the first term on the right-hand side of Eq. (6) properly the wall intensity needs to be expanded into its series expansion, which tracks emitted radiant energy through all wall reflections. This allows the wall radiosity to be expressed in terms of blackbody emission functions and transmittances. It is then possible to apply the narrowband approximation as shown in Eq. (4). A compact, shorthand flux expression can be written for diffuse reflections at the walls using slab-transmittance function, $\bar{T}_\nu^+$;

$$\bar{q}_\nu^+(x) = \pi \left[\bar{\epsilon}_{\nu 0} \bar{I}_{\nu b 0} \bar{T}_\nu^+(x_0 \rightarrow x) + \int_{x_0}^{x} \bar{I}_{\nu b}(x^*) \frac{\partial \bar{T}_\nu^+(x^* \rightarrow x)}{\partial x^*} dx^* \right] + \sum_{n=1,3,5\ldots}^{\infty} \left[\pi \bar{\rho}_{\nu 0}^{(n+1)/2} \bar{\rho}_{\nu L}^{(n-1)/2} \left\{ \bar{\epsilon}_{\nu L} \bar{I}_{\nu b L} \bar{T}_\nu^+(x_L \rightarrow x_w^n \rightarrow x) + \int_{x_L}^{x_0} \bar{I}_{\nu b}(x^*) \frac{\partial \bar{T}_\nu^+(x^* \rightarrow x_w^n \rightarrow x)}{\partial x^*} dx^* \right\} \right] + \sum_{n=2,4,6\ldots}^{\infty} \left[\pi \bar{\rho}_{\nu 0}^{n/2} \bar{\rho}_{\nu L}^{n/2} \left\{ \bar{\epsilon}_{\nu 0} \bar{I}_{\nu b 0} \bar{T}_\nu^+(x_0 \rightarrow x_w^n \rightarrow x) + \int_{x_0}^{x_L} \bar{I}_{\nu b}(x^*) \frac{\partial \bar{T}_\nu^+(x^* \rightarrow x_w^n \rightarrow x)}{\partial x^*} dx^* \right\} \right]. \quad (7)$$

Here n is the order of the expansion, with the zeroth order represented by the first term on the right-hand side. Menart et al. (1993) demonstrated that low wall-reflectivity problems

Nomenclature

a_ν = spectral absorption coefficient, m^{-1}
$-dq/dx$ = total radiative source term, $\mathrm{kW/m^3}$
I_ν = spectral radiative intensity, $\mathrm{kW/(m^2 \cdot sr \cdot cm^{-1})}$
J = total number of spectral bands
$k_{\nu,\,\mathrm{eff}}$ = effective mean line-intensity to spacing ratio, $\mathrm{cm^{-1}\ atm^{-1}}$
L = thickness of the slab, m
n = order of solution or referring to a specific term of expansion
P = pressure, atm
q = total net radiative heat flux in x direction, $\mathrm{kW/m^2}$
T = slab-transmittance functions
u = pressure-path length parameter, atm•m
x = x coordinate, m
$x^* \rightarrow x$ = path length from x^* to x, m
$\beta_{\nu,\,\mathrm{eff}}$ = effective mean line-width to spacing ratio
$\Delta\nu$ = wavenumber interval, $\mathrm{cm^{-1}}$
ϵ_ν = spectral wall emissivity
μ = direction cosine = $\cos\theta$
ρ_ν = spectral wall reflectivity
τ_ν = spectral transmittance

Superscript

*or** = integration variable or position superscript
$\overline{(\ )}$ = spectral average
$+$ = related to positive directed flux
$-$ = related to negative directed flux
a = approximate additional solution
n = order of solution or referring to a specific term of expansion
$n+a$ = truncated series and additional solution added together

Subscripts

0 = grid point number at $x = x_0$
b = blackbody
extra = leftover radiant flux after $n+1$ reflections
g = gas
i = spatial index in x direction
j = spectral index
k = dummy spatial index
L = wall at $x = x_L$
M = grid point number at $x = x_L$
w = wall
ν = spectral

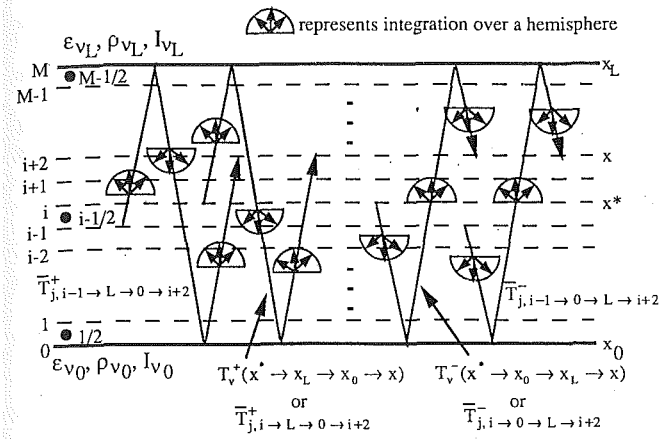

Fig. 1 A schematic of the second-order slab-transmittance functions

can be accurately handled with a zeroth-order closure solution. The quantities $\overline{I}_{\nu b0}$ and $\overline{I}_{\nu bL}$ are Planck blackbody emissions at the wall temperatures. Each of the terms in Eq. (7) has the following meaning:

- $n=0$: Radiant energy emitted by the wall at x_0 and the gas between x_0 and x that is directly transmitted to the position x.
- $n=1$: Radiant energy emitted by the wall at x_L and the gas layer that is reflected at x_0 and transmitted to position x.
- $n=2$: Radiant energy emitted by the wall at x_0 and the gas layer that is reflected at x_L and at x_0, and then transmitted to position x.
- $n=n$: Radiant energy emitted by the wall at x_w and the gas layer that is reflected a total of n times and then transmitted to position x.

Zeroth and nth order positive-direction slab-transmittance functions are used in Eq. (7). A *zeroth-order*, positive slab-transmittance function is defined as

$$\overline{T}^{+}_{\nu}(x^* \to x) = 2\overline{\left(\int_0^1 \tau_\nu(x^* \to x,\ \mu)\mu d\mu\right)}, \qquad (8a)$$

where the path from x^* to x is in the positive x direction, or positive μ directions. Higher nth order positive-direction slab-transmittance functions are written in a general form as

$$\overline{T}^{+}_{\nu}(x^* \to x^n_w \to x) = 2^{n+1} \cdot \overline{\left(\int_0^1 \tau_\nu(x^* \to x_w,\ \pm\mu)\mu d\mu\right)\left(\int_0^1 \tau_\nu(x_0 \to x_L,\ \mu)\mu d\mu\right)^{n-1}\left(\int_0^1 \tau_\nu(x_0 \to x,\ \mu)\mu d\mu\right)}, \qquad (8b)$$

where n is the order of the function and indicates the total number of reflections experienced in the path. The term x^n_w represents the n wall locations that are encountered, i.e., . . . $\to x_L \to x_0 \to x_L \to x_0$, with the rightmost parameter always equal to x_0 for positive-directed functions.

The first transmittance integral appearing under the overbar in Eq. (8b) is interpreted in the following fashion. The x_w is x_0 when n is odd and x_L for n even. The sign of μ in this transmittance must indicate the direction of the *first* portion of the total path. The derivative of this first transmittance with respect to x^*, multiplied by the rest of the expression under the overbar of Eq. (8b), gives the $\partial\overline{T}^{+}_{\nu}/\partial x^*$ terms appearing in Eq. (7). Note that all the factors remain under the overbar.

The positive-direction slab-transmittance functions have the *last* portion of the total path in the positive x direction. The negative slab-transmittance functions are defined in a similar manner, except that the *last* portion of the path is in the negative x direction. For example, the path for a second-order, positive slab-transmittance function from x^* to x is illustrated by the center-left trace shown in Fig. 1 and marked as $T^{+}_{\nu}(x^* \to x_L \to x_0 \to x)$. The center-right trace in Fig. 1 illustrates the path for the second-order negative slab-transmittance from $x^* \to x_0 \to x_L \to x$ and is marked as $T^{-}_{\nu}(x^* \to x_0 \to x_L \to x)$. To indicate that the slab-transmittance functions are an integration of the transmittances over the appropriate hemisphere, the symbol of a half circle with arrows is used. For diffuse walls the integrations must take place for every pass through the gas.

Practically, the spectrally averaged slab-transmittance of Eq. (8b) is calculated from Eq. (5) in the following manner:

$$\overline{T}^{+}_{\nu}(x^* \to x^n_w \to x) = 2^{n+1}\int_0^1\int_0^1 \cdots \int_0^1 \exp\left[-\frac{\beta_{\nu,\,\mathrm{eff}}}{\pi}\cdot\left(\sqrt{1+\frac{2\pi u(x^*,\ x,\ \mu_{n+1},\ \mu_n \ldots \mu_1,\ P)k_{\nu,\,\mathrm{eff}}}{\beta_{\nu,\,\mathrm{eff}}}}-1\right)\right] \cdot \mu_{n+1}d\mu_{n+1}\mu_n d\mu_n \ldots \mu_1 d\mu_1 \qquad (9a)$$

where the pressure path length includes the full path under consideration:

$$u(x^*,\ x,\ \mu_{n+1},\ \mu_n \ldots \mu_1,\ P) = P \cdot\left[\left|\frac{x^* - x_{0\ \mathrm{or}\ L}}{\mu_{n+1}}\right| + \left|\frac{x_L - x_0}{\mu_n}\right| + \left|\frac{x_L - x_0}{\mu_{n-1}}\right| + \ldots + \left|\frac{x - x_0}{\ }\right|\right. \qquad (9b)$$

The properties of the spectrally averaged slab-transmittance functions are comparable to those for the spectrally averaged transmittance. It is generally not possible to change the order of the arguments in higher order slab transmittance functions, although $\overline{\tau}_\nu\ (x^* \to x,\ \mu) = \overline{\tau}_\nu\ (x \to x^*,\ -\mu)$ and $\overline{T}^{+\mathrm{or}\,-}_{\nu}(x^* \to x) = \overline{T}^{-\mathrm{or}\,+}_{\nu}(x \to x^*)$ for zeroth order. On a spectral basis, $T^{+\mathrm{or}\,-}_{\nu}$ can be multiplied and divided to give slab-transmittance functions based on longer or shorter lengths like τ_ν. This is not true for spectrally averaged quantities, $\overline{T}^{+\mathrm{or}\,-}_{\nu}$ and $\overline{\tau}_\nu$. That is, multiplication of a $\overline{T}^{+\mathrm{or}\,-}_{\nu}$ based on the length L_1 and a $\overline{T}^{+\mathrm{or}\,-}_{\nu}$ based on the length L_2 does not give $\overline{T}^{+\mathrm{or}\,-}_{\nu}$ for the length $L_1 + L_2$. Also, division of a $\overline{T}^{+\mathrm{or}\,-}_{\nu}$ based on $L_1 + L_2$ by a $\overline{T}^{+\mathrm{or}\,-}_{\nu}$ based on L_1 gives $\overline{T}^{+\mathrm{or}\,-}_{\nu}$ for the last L_2 of the length, not for first L_1. This property will be useful in the development of the approximations in the next section.

Within the limits of the narrowband approximation Eq. (7) and the corresponding equation in the negative direction are correct, but an infinite number of terms must be included for an exact solution. Since the higher order terms decrease in magnitude, a desired level of accuracy may be obtained by including enough terms in the analysis.

III Approximations

In order to decrease the number of terms needed in Eq. (7) for a desired level of accuracy in the radiative flux, methods of approximating the higher order terms in the series solution are considered. Of the many ways to carry out the details of this approximation (Edwards, 1962; Nelson, 1977, 1979b, 1984; Menart et al., 1993), four methods will be discussed here.

The first technique (method I) is the most obvious form of an approximation in that all higher order terms are just neglected, i.e., all terms of order higher than n are ignored in

Eq. (7) for the nth order solution. This approximation will be referred to as the *truncation* solution. The truncation approximation was also considered by Menart et al. (1993) with the discrete ordinates method.

To improve an nth order truncation approximation, the neglected terms in the series expansion must somehow be included. The terms of order higher than n represent the radiant energy that hasn't been absorbed after n complete passes through the gas, not including the emission pass. This leftover energy is called $\bar{q}_{\nu,\,\text{extra}}$, and a gray band assumption is made for this flux. The *additional* fluxes that are due to $\bar{q}_{\nu,\,\text{extra}}$ are found by solving for the resulting flux distribution in absorbing (nonemitting) gas between two diffusely reflecting walls. With boundary fluxes $\bar{q}_{\nu,\,\text{extra}}(x_0)$ and $\bar{q}_{\nu,\,\text{extra}}(x_L)$, a solution is easily obtained as

$$\bar{q}_\nu^{+,a}(x) = [\bar{q}_{\nu,\text{extra}}(x_0) + \bar{\rho}_{\nu 0}\bar{q}_\nu^{-,a}(x_0)]\bar{T}_\nu^{+}(x_0 \to x) \qquad (10a)$$

and

$$\bar{q}_\nu^{-,a}(x) = [\bar{q}_{\nu,\text{extra}}(x_L) + \bar{\rho}_{\nu L}\bar{q}_\nu^{+,a}(x_L)]\bar{T}_\nu^{-}(x_L \to x). \qquad (10b)$$

$\bar{q}_\nu^{+,a}(x)$ and $\bar{q}_\nu^{-,a}(x)$ are the *additional* fluxes that account for the effects of the remaining higher order terms in the series solution in Eq. (7). Equations (10a) and (10b) can be solved simultaneously for $\bar{q}_\nu^{+,a}(x_L)$ and $\bar{q}_\nu^{-,a}(x_0)$ by evaluating Eq. (10a) at x_L and Eq. (10b) at x_0.

The leftover radiant fluxes that haven't been absorbed after n passes through the gas and $n+1$ reflections from the walls are determined from

$$\bar{q}_{\nu,\text{extra}}(x_0) = \bar{\rho}_{\nu 0}[\bar{q}_\nu^{-,n}(x_0) - \bar{q}_\nu^{-,n-1}(x_0)] \qquad (11a)$$

and

$$\bar{q}_{\nu,\,\text{extra}}(x_L) = \bar{\rho}_{\nu L}[\bar{q}_\nu^{+,n}(x_L) - \bar{q}_\nu^{+,n-1}(x_L)] \qquad (11b)$$

where $\bar{q}_\nu^{+,n}(x)$ and $\bar{q}_\nu^{-,n}(x)$ are the nth order series solutions, Eq. (7) including terms 1 through n, and $\bar{q}_\nu^{+,n-1}(x)$ and $\bar{q}_\nu^{-,n-1}(x)$ are the $(n-1)$th series solutions.

The final flux distribution is a sum of the nth order series solution and the corresponding additional flux solution:

$$\bar{q}_\nu^{+,n+a}(x) = \bar{q}_\nu^{+,n}(x) + \bar{q}_\nu^{+,a}(x) \qquad (12a)$$

and

$$\bar{q}_\nu^{-,n+a}(x) = \bar{q}_\nu^{-,n}(x) + \bar{q}_\nu^{-,a}(x). \qquad (12b)$$

The fluxes $\bar{q}_\nu^{+,n+a}(x)$ and $\bar{q}_\nu^{-,n+a}(x)$ approximate the exact $\bar{q}_\nu^{+}(x)$ and $\bar{q}_\nu^{-}(x)$ obtained from Eq. (7). Equations (10), (11), and (12) used with a truncated Eq. (7) is approximation method II.

Approximation method III is obtained by noting that an improvement in Eq. (10) can be made by using higher order band transmittance functions. Nelson (1979b) points out that as the radiant energy travels a longer path length through the gas, a greater fraction of the remaining energy resides in the band wings. Transmission of radiant energy for the last part of the journey should therefore be higher than that for the first part. An expression comparing the transmittances for each successive pass of the radiant energy through the gas can be written by dividing the nth transmittance by the $(n-1)$th transmittance to get the transmittance for just the nth pass;

$$0 < \bar{\tau}_\nu(x_0 \to x_L) < \frac{\bar{\tau}_\nu(x_L \to x_0 \to x_L)}{\bar{\tau}_\nu(x_L \to x_0)} < \frac{\bar{\tau}_\nu(x_0 \to x_L \to x_0 \to x_L)}{\bar{\tau}_\nu(x_0 \to x_L \to x_0)}$$
$$< \frac{\bar{\tau}_\nu(x_L \to x_w^n \to x_L)}{\bar{\tau}_\nu(x_L \to x_w^{n-1} \to x_0)} < \cdots\cdots\cdots$$
$$< \frac{\bar{\tau}_\nu(x_L \to x_w^\infty \to x_L)}{\bar{\tau}_\nu(x_L \to x_w^{\infty-1} \to x_0)} \le 1.0. \qquad (13)$$

A value of one is approached in Eq. (13) if no restrictions are put on the wavenumber limits, while some number less than one is approached with finite wavenumber limits of a narrowband. Since Eq. (13) holds for any μ direction or an integration over all μ's, this same trend holds for the slab transmittance functions.

The third approximation (method III) uses the highest order slab-transmittance function available from the series solution rather than the *zeroth-order* slab-transmission function used in Eq. (10). The following expressions for the additional fluxes are then obtained:

$$\bar{q}_\nu^{+,a}(x) = [\bar{q}_{\nu,\,\text{extra}}(x_0) + \bar{\rho}_{\nu 0}\bar{q}_\nu^{-,a}(x_0)]\frac{\bar{T}_\nu^{+}(x_w \to x_w^n \to x)}{\bar{T}_\nu^{-}(x_w \to x_w^{n-1} \to x_0)} \qquad (14a)$$

and

$$\bar{q}_\nu^{-,a}(x) = [\bar{q}_{\nu,\,\text{extra}}(x_L) + \bar{\rho}_{\nu L}\bar{q}_\nu^{+,a}(x_L)]\frac{\bar{T}_\nu^{-}(x_w \to x_w^n \to x)}{\bar{T}_\nu^{+}(x_w \to x_w^{n-1} \to x_L)}. \qquad (14b)$$

For $n = 0$, methods II and III are equivalent. Note that $\bar{T}_\nu^{+\text{or}-}(x_w \to x_w^n \to x)$ simply takes on the value of one for n less than zero. This third approximation technique is essentially that used by Nelson (1979b) to consider a two-zone enclosure. Eqs. (11), (12), and (14) used with a truncated Eq. (7) is approximation method III.

The last approximation technique to be considered (method IV) is one used by Menart et al. (1993), where this method was developed on an intensity basis for the discrete ordinates formulation. Integrating the governing equations of Menart et al. (1993) over angles gives the required flux representations.

For n odd,

$$\frac{d\bar{q}_\nu^{+,n+a}(x)}{dx} = \frac{d\bar{q}_\nu^{+,n}(x)}{dx} + \bar{\rho}_{\nu 0}^{(n+1)/2}\,\bar{\rho}_{\nu L}^{(n+1)/2}\,\bar{q}_\nu^{+,n+a}(x_L)\,\frac{d\bar{T}_\nu^{+}(x_L \to x_w^n \to x)}{dx} \qquad (15a)$$

and

$$\frac{d\bar{q}_\nu^{-,n+a}(x)}{dx} = \frac{d\bar{q}_\nu^{-,n}(x)}{dx} + \bar{\rho}_{\nu 0}^{(n+1)/2}\,\bar{\rho}_{\nu L}^{(n+1)/2}\,\bar{q}_\nu^{-,n+a}(x_0)\,\frac{d\bar{T}_\nu^{-}(x_0 \to x_w^n \to x)}{dx}. \qquad (15b)$$

For n even,

$$\frac{d\bar{q}_\nu^{+,n+a}(x)}{dx} = \frac{d\bar{q}_\nu^{+,n}(x)}{dx} + \bar{\rho}_{\nu 0}^{(n/2+1)}\,\bar{\rho}_{\nu L}^{n/2}\,\bar{q}_\nu^{-,n+a}(x_0)\,\frac{d\bar{T}_\nu^{+}(x_0 \to x_w^n \to x)}{dx} \qquad (15c)$$

and

$$\frac{d\bar{q}_\nu^{-,n+a}(x)}{dx} = \frac{d\bar{q}_\nu^{-,n}(x)}{dx} + \bar{\rho}_{\nu 0}^{n/2}\,\bar{\rho}_{\nu L}^{(n/2+1)}\,\bar{q}_\nu^{+,n+a}(x_L)\,\frac{d\bar{T}_\nu^{-}(x_0 \to x_w^n \to x)}{dx}. \qquad (15d)$$

For all n the boundary conditions are

$$\bar{q}_\nu^{+,n+a}(x_0) = \bar{\rho}_{\nu 0}\bar{q}_\nu^{-,n+a}(x_0) + \pi\bar{\epsilon}_{\nu 0}\bar{I}_{\nu b0} \qquad (15e)$$

and

$$\bar{q}_\nu^{-,n+a}(x_L) = \bar{\rho}_{\nu L}\bar{q}_\nu^{+,n+a}(x_L) + \pi\bar{\epsilon}_{\nu L}\bar{I}_{\nu bL}. \qquad (15f)$$

In the differential Eqs. (15a)-(15d) the entire fluxes ($\bar{q}_\nu^{n+a}$) are being determined, not just the additional portions as in Eqs. (10) and (14). The first terms on the right-hand sides of Eqs. (15a)-(15d) are series expansion portions, and the second terms are additional portions. In Eqs. (15a)-(15d) the highest order transmittances available are used, but the radiosities in the second terms on the right-hand sides of the equations imply the use of all orders of wall fluxes to obtain a value for the additional flux. While it is not immediately obvious,

Eq. (15) reduces to the sum of the series solutions and the additional flux solutions from Eq. (10) for $n = 0$.

All approximation methods presented above, except the truncation method, give exact results for the gray gas analysis. This is because the only approximation in methods II, III, and IV is that of neglecting correlation effects in obtaining the additional fluxes by assuming gray-bands. The differences in the three methods are in how closely each method approximates the spectral nature of the flux represented by the truncated terms of the series expansion.

IV Discretized Equations

In order to solve Eq. (7) and the corresponding negative-flux equation, a numerical technique is required. Equation (7) in discretized form is

$$\bar{q}^{+}_{j,i} = \pi\left[\bar{\epsilon}_{j0}\bar{I}_{jb0}\bar{T}^{+}_{j,0\to i} + \sum_{k=0}^{i-1}\bar{I}_{jb,k+1/2}(\bar{T}^{+}_{j,k+1\to i} - \bar{T}^{+}_{j,k\to i})\right] + \sum_{n=1,3,5\ldots}^{\infty}\pi\bar{\rho}^{(n+1)/2}_{j0}\,\bar{\rho}^{(n-1)/2}_{jL} \cdot \left\{\begin{array}{l}\bar{\epsilon}_{jL}\bar{I}_{jbL}\bar{T}^{+}_{j,M\to w^n\to i} \\ + \sum_{k=0}^{M-1}\bar{I}_{jb,k+1/2}(\bar{T}^{+}_{j,k\to w^n\to i} - \bar{T}^{+}_{j,k+1\to w^n\to i})\end{array}\right\} + \sum_{n=2,4,6\ldots}^{\infty}\pi\bar{\rho}^{n/2}_{j0}\,\bar{\rho}^{n/2}_{jL}\left\{\begin{array}{l}\bar{\epsilon}_{j0}\bar{I}_{jb0}\bar{T}^{+}_{j,0\to w^n\to i} \\ + \sum_{k=0}^{M-1}\bar{I}_{jb,k+1/2}(\bar{T}^{+}_{j,k+1\to w^n\to i} - \bar{T}^{+}_{j,k\to w^n\to i})\end{array}\right\} \tag{16}$$

where the subscripts 0 and M denote wall locations, i and k denote discretized control volume face locations, and $i + 1/2$ and $k + 1/2$ denote control volume center points (see Fig. 1).

In Fig. 1 the two positive-direction slab-transmittance functions required for the $n = 2$ term in Eq. (16) are shown on the left. The difference of these transmittance functions multiplied by $\bar{I}_{jb,i-1/2}$ gives the amount of emitted radiant energy by control volume $i - 1/2$ that reaches the control surface i. The summation signs in Eq. (16) indicate that this type of emission calculation must be included from every control volume. The two negative-direction slab transmittance functions required for the $n = 2$ term of the $\bar{q}^{-}_{j}$ flux are shown on the right of Fig. 1.

Equation (14) in discretized form is

$$\bar{q}^{+,a}_{j,i} = [\bar{q}_{j,\text{extra},0} + \bar{\rho}_{j0}\bar{q}^{-,a}_{j,0}]\,\frac{\bar{T}^{+}_{j,w\to w^n\to i}}{\bar{T}^{-}_{j,w\to w^{n-1}\to 0}} \tag{17a}$$

and

$$\bar{q}^{-,a}_{j,i} = [\bar{q}_{j,\text{extra},L} + \bar{\rho}_{jL}\bar{q}^{+,a}_{j,M}]\,\frac{\bar{T}^{-}_{j,w\to w^n\to i}}{\bar{T}^{+}_{j,w\to w^{n-1}\to M}}. \tag{17b}$$

Positive and negative directed fluxes can then be obtained from Eq. (12). The $n + a$ superscript on the fluxes will be dropped for the rest of the paper.

The entire $n + a$ flux at any location x (or index i) is

$$q_i = \sum_{j=1}^{J}(\bar{q}^{+}_{j,i} - \bar{q}^{-}_{j,i})\Delta\nu_j \tag{18}$$

and the total radiative source term is found from

Table 1 Comparisons of the four approximate methods for $\rho_w = 0.5$ (3755 cm^{-1} H_2O band, $T_g = 1000$ K, $T_w = 500$ K)

L (m)	Order	Magnitude of Wall Flux (kW/m^2)				Slab Centerline Radiative Source Term (kW/m^3)			
		I	II	III	IV	I	II	III	IV
0.01	0	0.77871	0.69111	0.69111	0.69111	−153.49	−136.28	−136.28	−136.28
	1	0.69798	0.66441	0.66744	0.66582	−137.85	−131.26	−131.82	−131.50
	2	0.67084	0.65738	0.65948	0.65812	−132.55	−129.90	−130.29	−130.02
	3	0.66103	0.65547	0.65662	0.65580	−130.62	−129.52	−129.74	−129.58
	4	0.65732	0.65497	0.65555	0.65511	−129.88	−129.42	−129.53	−129.44
	5	0.65586	0.65485	0.65514	0.65492	−129.59	−129.40	−129.45	−129.41
0.1	0	3.8340	2.5751	2.5751	2.5751	−64.833	−44.122	−44.122	−44.122
	1	2.6821	2.4646	2.4948	2.4737	−46.844	−43.156	−43.367	−42.978
	2	2.5223	2.4663	2.4785	2.4689	−43.947	−42.979	−43.108	−42.926
	3	2.4864	2.4695	2.4740	2.4703	−43.270	−42.973	−43.030	−42.957
	4	2.4765	2.4709	2.4726	2.4712	−43.080	−42.980	−43.004	−42.976
	5	2.4735	2.4715	2.4721	2.4716	−43.021	−42.985	−42.995	−42.984
1.0	0	8.4884	4.8259	4.8259	4.8259	−7.9946	−5.0092	−5.0092	−5.0092
	1	4.9117	4.7163	4.7414	4.7241	−5.2378	−4.9410	−4.9353	−4.9043
	2	4.7586	4.7124	4.7229	4.7152	−4.9721	−4.8932	−4.9042	−4.8895
	3	4.7278	4.7134	4.7177	4.7145	−4.9145	−4.8887	−4.8948	−4.8884
	4	4.7194	4.7143	4.7161	4.7147	−4.8982	−4.8890	−4.8918	−4.8890
	5	4.7167	4.7148	4.7156	4.7150	−4.8930	−4.8895	−4.8907	−4.8896

Table 2 Comparisons of the four approximate methods for $\rho_w = 0.9$ (3755 cm^{-1} H_2O band, $T_g = 1000$ K, $T_w = 500$ K)

L (m)	Order	Magnitude of Wall Flux (kW/m^2)				Slab Centerline Radiative Source Term (kW/m^3)			
		I	II	III	IV	I	II	III	IV
0.01	0	0.78037	0.38684	0.38684	0.38684	−153.81	−76.421	−76.421	−76.421
	1	0.63628	0.36208	0.37466	0.37315	−125.92	−71.952	−74.199	−73.899
	2	0.54925	0.34989	0.36645	0.36341	−108.90	−69.637	−72.655	−72.052
	3	0.49276	0.34364	0.36069	0.35654	−97.787	−68.407	−71.554	−70.730
	4	0.45429	0.34046	0.35653	0.35174	−90.194	−67.756	−70.750	−69.798
	5	0.42720	0.33892	0.35346	0.34842	−84.832	−67.425	−70.152	−69.149
0.1	0	3.8426	0.82853	0.82853	0.82853	−64.981	−14.688	−14.688	−14.688
	1	1.7726	0.76741	0.81023	0.80102	−32.666	−15.295	−14.685	−14.515
	2	1.2569	0.76357	0.80040	0.78805	−23.319	−14.603	−14.547	−14.312
	3	1.0488	0.76532	0.79417	0.78216	−19.397	−14.302	−14.441	−14.208
	4	0.94601	0.76742	0.78989	0.77939	−17.424	−14.169	−14.362	−14.157
	5	0.88887	0.76914	0.78680	0.77797	−16.315	−14.107	−14.304	−14.130
1.0	0	8.5102	1.2257	1.2257	1.2257	−8.0188	−1.4787	−1.4787	−1.4787
	1	2.0767	1.1562	1.2018	1.1926	−3.0652	−1.5743	−1.4717	−1.4549
	2	1.5829	1.1462	1.1895	1.1778	−2.2088	−1.4354	−1.4529	−1.4304
	3	1.4053	1.1456	1.1822	1.1700	−1.8759	−1.4015	−1.4402	−1.4164
	4	1.3176	1.1475	1.1775	1.1659	−1.7072	−1.3920	−1.4317	−1.4088
	5	1.2677	1.1500	1.1744	1.1638	−1.6101	−1.3902	−1.4258	−1.4050

$$-\left(\frac{\partial q}{\partial x}\right)_{i+1/2} = -\frac{q_{i+1} - q_i}{x_{i+1} - x_i}. \tag{19}$$

Equations (18) and (19) hold for any order of solution, with or without an approximation, as long as consistent quantities are used.

V Results and Discussion

Gray wall reflectivities, ρ_w, of 0.5 and 0.9 are considered in this study. It is possible to handle wall reflectivities that vary slowly with wavenumber using this method, but that effect is not considered in this paper.

The first temperature profile considered is uniform with the gas at 1000 K and the walls at 500 K. The walls are kept at a finite temperature to include the effects of wall emission in the survey of approximation techniques. For the results in Tables 1 and 2, only the 3755 cm^{-1} (2.7 μm) band of pure H_2O vapor at one atmosphere is considered, using property

Table 3 Wall flux and source term data for CO_2 utilizing methods I and III (3715 cm^{-1} CO_2 band, T_g = 1000 K, T_w = 500 K)

L (m)	Order	Magnitude of Wall Flux (kW/m²)				Slab Centerline Radiative Source Term (kW/m³)			
		$\rho_w = 0.5$		$\rho_w = 0.9$		$\rho_w = 0.5$		$\rho_w = 0.9$	
		I	III	I	III	I	III	I	III
0.01	0	0.41482	0.35867	0.41571	0.18078	−81.145	−70.197	−81.319	−35.455
	1	0.36151	0.34341	0.32036	0.17398	−70.956	−67.395	−63.099	−34.276
	2	0.34508	0.33869	0.26754	0.16966	−67.765	−66.501	−52.844	−33.486
	3	0.33947	0.33709	0.23517	0.16676	−66.667	−66.194	−46.505	−32.941
	4	0.33744	0.33651	0.21405	0.16474	−66.266	−66.082	−42.348	−32.554
	5	0.33667	0.33630	0.19965	0.16329	−66.114	−66.040	−39.506	−32.274
0.1	0	1.7915	1.1360	1.7954	0.3147	−28.518	−18.291	−28.581	−5.2096
	1	1.1835	1.1015	0.7022	0.3083	−19.588	−18.087	−12.529	−5.2819
	2	1.1129	1.0954	0.4741	0.3053	−18.329	−17.997	−8.4613	−5.2496
	3	1.0985	1.0939	0.3903	0.3036	−18.060	−17.972	−6.8983	−5.2234
	4	1.0948	1.0935	0.3520	0.3026	−17.990	−17.964	−6.1692	−5.2048
	5	1.0937	1.0933	0.3322	0.3019	−17.970	−17.961	−5.7862	−5.1916
1.0	0	3.2400	1.7281	3.2473	0.3985	−2.1700	−1.2588	−2.1752	−0.3464
	1	1.7484	1.7115	0.5631	0.3933	−1.3185	−1.2560	−0.6436	−0.3482
	2	1.7146	1.7083	0.4537	0.3906	−1.2627	−1.2511	−0.4635	−0.3440
	3	1.7091	1.7075	0.4218	0.3889	−1.2526	−1.2496	−0.4049	−0.3411
	4	1.7077	1.7072	0.4076	0.3879	−1.2500	−1.2491	−0.3778	−0.3391
	5	1.7073	1.7072	0.3999	0.3871	−1.2492	−1.2489	−0.3629	−0.3376

data from Hartmann et al. (1984) in the range 2875 cm^{-1} to 4250 cm^{-1}. Table 3 shows results for the 3715 cm^{-1} (2.7 μm) band of pure CO_2 at one atmosphere, using data from Soufiani et al. (1985) in the range 3275 cm^{-1} to 3875 cm^{-1}.

A survey of approximate methods for the one H_2O band is shown in Table 1 for $\rho_w = 0.5$ and in Table 2 for $\rho_w = 0.9$. The wall flux magnitudes and the centerline radiative source terms using four methods discussed in the "Approximations" section are shown in the tables.

In the numerical analysis, nine evenly spaced μ directions were used in a hemisphere to perform angular integrations for slab-transmittance functions. Increasing the number of directions with Simpsons's Rule showed that the integrations converge to three significant digits with nine directions. The data in the tables are shown to five digits. Even though the last two digits have no meaning on an absolute basis, they are helpful for comparing numbers within the two tables. Considering only one absorption band and a small number of angles reduced the computation costs while still allowing for meaningful comparisons between the approximation methods.

The general trend in Table 1 is that methods II, III, and IV show reasonable results even for the zeroth and first orders. Method I lags behind the other techniques in convergence, because higher order terms are simply negelcted in this method. Methods II and IV usually give results that are slightly closer to fifth-order results than method III. The fifth-order results of methods II, III, and IV are the same to three significant figures, and are slightly smaller than the fifth-order method I result. Zeroth-order results for methods II, III, and IV are *identical* and are within 5.4 percent of the fifth-order method I result, and first-order closure results are within 1.8 percent.

All four methods in Table 1 show monotonically decreasing magnitudes toward correct results for each succeeding higher order solution for L = 0.01 m. This behavior is not seen for methods II and IV with larger plate spacings. Although the oscillations are small, this solution behavior is undesirable. A steadily decreasing behavior is desirable so that an assessment of the error in each order of the solution can be made.

Table 2 results for $\rho_w = 0.9$ show slower convergence than Table 1 results for $\rho_w = 0.5$. Method I does not even show the first two digits repeating for the fourth and fifth orders. This is understandable for strongly reflecting walls, since the truncation solution simply neglects higher order reflections. Since fifth-order method III results in Table 1 show best agreement with correct solutions (fifth-order method I), the results from the fifth-order method III approximation will be used here as a convenient standard for comparison. This is not to imply that fifth-order method III solutions are necessarily exact.

In Table 2 as in Table 1, the oscillations in method II wall flux and radiative source-term solutions are present for L = 0.1 and 1.0 m. No oscillations are present for method IV, and method III results are once again well behaved. The first-order wall flux solutions for methods II and IV are closer to the fifth-order results than method III; however, in this case the first-order method II radiative source term can be less accurate than a zeroth-order solution. All zeroth-order approximate solutions are within 9.4 percent of the fifth-order method III result, and within 6.0 percent for first-order solutions.

The results from method III are well behaved because the highest order available slab-transmittances and wall fluxes are used in the analysis, and this best approximates the trends of the neglected terms. In method II the highest order wall flux is used, but the zeroth-order slab-transmittances are used for every order of approximation. As mentioned in the "Approximations" section, the zeroth-order slab-transmittance is smaller than higher order slab-transmittances for the same path length. In method IV highest order transmittances are used, but the wall flux is basically a combination of all orders of terms up to and including order n with the zeroth and first-order terms being dominant. Unlike methods II and IV, method III always uses the best information available on the correlation effects for the required wall fluxes and slab-transmittances. Since method III shows the best characteristics, this approximation will be used in the rest of the results presented.

Table 3 presents the wall flux magnitudes and the centerline radiative source terms for the pure CO_2 gas layer at 1000 K, bounded by diffusely reflecting walls at 500 K. Only the truncation solution (method I) and the best-behaved approximation solution for the H_2O analysis (method III) are compared for ρ_w of 0.5 and 0.9.

The CO_2 results in Table 3 also show that reasonable results are obtained with just a zeroth or first-order method III solution. Method I lags behind method III results in convergence, but higher order solutions are seen to approach limiting final solutions faster for ρ_w = 0.5 than for ρ_w = 0.9. For ρ_w = 0.5, the zeroth-order method III results are within 6.7 percent of the corresponding fifth-order method III results, and the first-order results are within 2.2 percent. For ρ_w = 0.9, the zeroth-order method III results are within 10.8 percent of the corresponding fifth-order method III results, and the first-order results are within 6.6 percent. This is similar to the H_2O results. Method III wall flux results for CO_2 are still well behaved, decreasing toward higher order solutions without any oscillation for all cases considered. Small fluctuations in method III radiative source terms are seen for the highly reflecting ρ_w = 0.9 and L = 0.1 m and 1.0 m.

Finally, H_2O gas layers are considered to show the effects of nonuniform temperature and concentration profiles. For the data presented in Figs. 2–4, all important water absorption bands are considered (rotation band, 6.3, 2.7, 1.87, and 1.38 μm). Results are presented for two temperature profiles in combination with two concentration profiles. The uniform temperature profile used in Tables 1–3 is again used, and a parabolic-like temperature profile described by Kim et al. (1991) is also used. The maximum temperature of this profile is 1111 K, and the wall temperatures are 400 K. A pure, uniform H_2O concentration profile and a parabolic concentration profile (see Kim et al., 1991) are the distributions of the participating species used. The parabolic concentration profile is 100 percent H_2O at the center and 0 percent at the walls. Since the total pressure is always kept at one atmosphere for all the data presented in this paper, the remaining gas in the parabolic

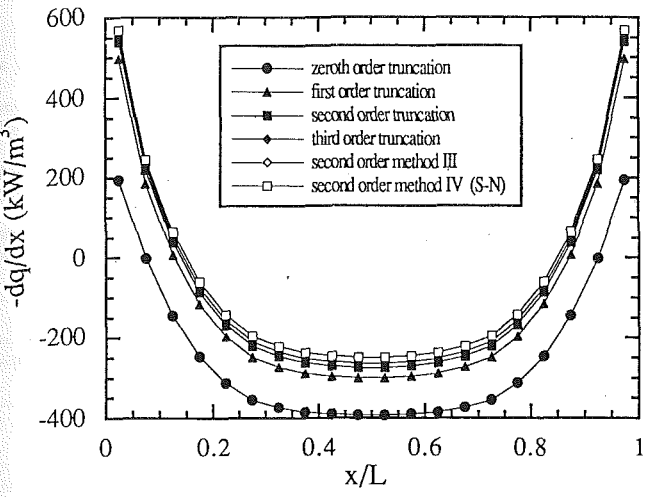

Fig. 2 Radiative source distributions for the parabolic-like temperature profile, uniform H_2O concentration profile, ρ_w = 0.9, and L = 0.1 m

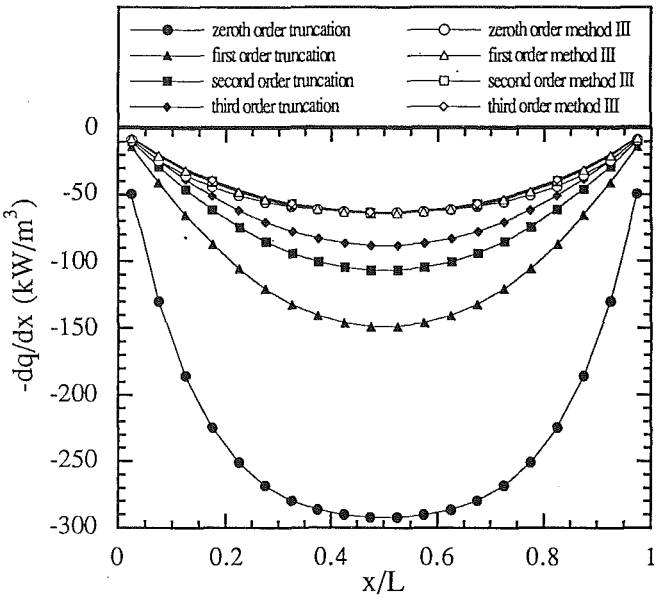

Fig. 3 Radiative source distributions for the uniform gas temperature of 1000 K, parabolic H_2O concentration profile, T_w = 500 K, ρ_w = 0.9, and L = 0.1 m

concentration profile is nitrogen. Nitrogen is a nonparticipating gas, but it affects how H_2O vapor emits and absorbs radiation.

Results for a parabolic-like temperature profile with a pure H_2O concentration are shown in Fig. 2. This case was analyzed using the *S–N* discrete ordinates method by Menart et al. (1993). In Fig. 2 the second-order *S–N* results using approximation method IV are located directly over the second-order flux technique results using method III. While not presented here, excellent agreement has been obtained between the flux and *S–N* solutions for all cases of Menart et al. (1993). For the situation in Fig. 2 the gas is a net emitter everywhere except close to walls. The gas near the walls is a net absorber due to the wall radiation. Note that third-order truncation method solutions lie just below method III results, indicating near convergence.

In Fig. 3 the uniform temperature profile with a parabolic concentration profile is considered. Again up to a third-order solution is shown with practically no difference in method III results. This time, however, the difference between method III results and the third-order truncation solutions is very noticeable. These particular temperature and concentration profiles allow a greater fraction of the radiant energy to survive more than three passes through the absorbing gas media.

Figure 4 presents the combined case of the parabolic type temperature profile (Fig. 2), and the parabolic concentration profile (Fig. 3). The two humps in these radiative source profiles near the walls can be explained as follows. The gas next to radiating walls tends to be a net absorber as was seen in Fig. 2. Furthermore, since the H_2O concentration goes to zero at the walls, the radiative source terms must also go to zero at the walls. This is seen to occur in Fig. 4 as well as Fig. 3. The curves do not go exactly to zero because 20 control volumes were used in this analysis, and the closest gas grid point is located at a small distance from a wall. The hump in the middle is present, because the hot gas in the center portion of the slab is a net emitter in Figs. 2, 3, and 4.

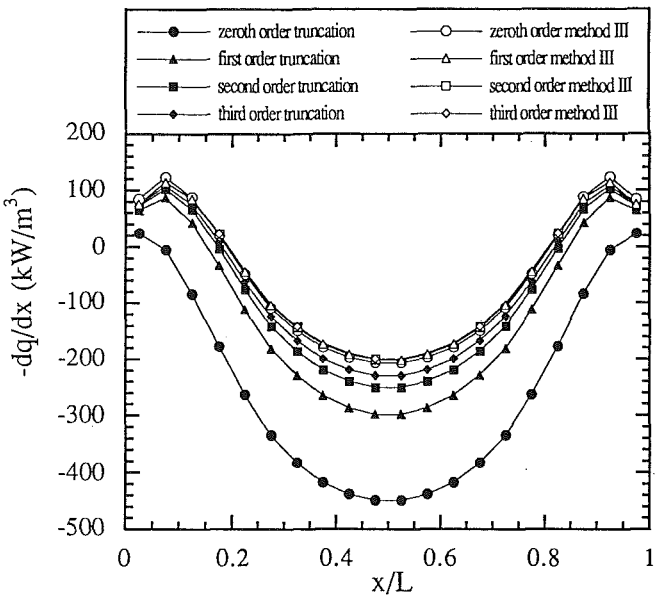

Fig. 4 Radiative source distributions for the parabolic-like temperature profile, parabolic H_2O concentration profile, ρ_w = 0.9, and L = 0.1 m

VI Conclusions

Another method of studying the spectral correlation effects between the wall reflected radiant energy and the transmittance has been developed. This particular technique is restricted to the planar geometry, but the formulation begins with the familiar flux equations for an absorbing, emitting medium. It may thus be easier to understand some of the principles involved in molecular gas radiative heat transfer between reflecting walls utilizing this method as compared to other more advanced techniques.

Furthermore, the flux method requires less computational time than the rigorous discrete ordinates technique for nongray gases. This allows higher order solutions to be calculated at a more reasonable cost. Higher order solutions are needed for comparing approximation techniques. A comparison of Cray-YMP C.P.U. times for the case in Fig. 2 for example, shows that the zeroth-order flux method is more than 30 times faster than a comparable accuracy *S–N* method. The second-order flux method requiring almost 200 s is about 20 times faster than the *S–N* method. The C.P.U. times are a strong function of order of approximation and discretization.

A single H_2O absorption band study showed that approximation methods II, III, and IV all give reasonable results, but

method III is the most well behaved and allows for an assessment of errors at a given order of solution. Methods II and IV show undesirable oscillations as the order of solution is increased. Regardless of the method, higher order solutions are required to obtain good accuracy for high wall-reflectivity problems. For $\rho_w < 0.5$, zeroth-order approximations predict the fluxes and radiative source terms to within 5.4 percent. For $\rho_w = 0.9$, the zeroth-order method III solutions are within 9.4 percent of the fifth-order results. While more accurate results are obtained with higher order solutions, the computer times for higher order solutions increase at an exponential rate while the accuracy increases very slowly. When a single band of CO_2 was studied, there was little difference in the findings from those of the single H_2O band study.

Methods I and III are also used to study nonisothermal and inhomogeneous H_2O layers, including all important absorption bands. Method III approximate solutions for radiation source distributions show little differences between successive orders. The gas concentration and temperature profiles of the slab are shown to have an important effect on the radiative source distributions.

Since the conclusions drawn in this paper are based on the data presented, care should be exercised in extending them to other conditions. The strongest influence on the order of solution required for a desired accuracy appears to be the wall reflectivities, but there are other factors such as wall and gas temperatures, optical depth, type of absorbing species, and concentration profile of the absorbing species. A more extensive study needs to be performed to determine the effects of all of the pertinent parameters for a given application.

Acknowledgments

This work was supported in part by National Science Foundation Grant No. NSF/CTS-8451076 and NASA Grant No. NGT-50830. A grant from the Minnesota Supercomputer Institute is also gratefully acknowledged.

References

Bevans, J. T., and Dunkle, R. V., 1960, "Radiant Interchange Within an Enclosure," ASME JOURNAL OF HEAT TRANSFER, Vol. 82, pp. 1–19.

Edwards, D. K., 1962, "Radiation Interchange in a Nongray Enclosure Containing an Isothermal Carbon-Dioxide–Nitrogen Gas Mixtures," ASME JOURNAL OF HEAT TRANSFER, Vol. 84, pp. 1–11.

Godson, W. L., 1953, "The Evaluation of Infrared Radiation Fluxes Due to Atmospheric Water Vapor," *Quarterly Journal of Royal Meteorological Society*, Vol. 79, pp. 367–379.

Hartmann, J. M., Levi Di Leon, R., and Taine, J., 1984, "Line-by-Line and Narrow-Band Statistical Model Calculations for H_2O," *Journal of Quantitative Spectroscopy and Radiative Transfer*, Vol. 32, No. 2, pp. 119–127.

Hottel, H. C., and Sarofim, A. F., 1967, *Radiative Transfer*, McGraw-Hill, New York.

Kim, T.-K., Menart, J. A., and Lee, H. S., 1991, "Nongray Radiative Gas Analyses Using the *S–N* Discrete Ordinates Method," ASME JOURNAL OF HEAT TRANSFER, Vol. 113, pp. 946–952.

Malkmus, W., 1967, "Random Lorentz Band Model With Exponential-Tailed S^{-1} Line-Intensity Distribution Function," *Journal of the Optical Society of America*, Vol. 57, No. 3, pp. 323–329.

Menart, J. A., Lee, H. S., and Kim, T.-K., 1993, "Discrete Ordinates Solutions of Nongray Radiative Transfer With Diffusely Reflecting Walls," ASME JOURNAL OF HEAT TRANSFER, Vol. 115, pp. 184–193.

Modest, M. F., 1991, "The Weighted-Sum-of-Gray-Gases Model for Arbitrary Solution Methods in Radiative Transfer," ASME JOURNAL OF HEAT TRANSFER, Vol. 113, pp. 650–656.

Nelson, D. A., 1977, "Radiation Heat Transfer in Molecular-Gas Filled Enclosures," ASME Paper No. 77-HT-16.

Nelson, D. A., 1979a, "Band Radiation Within Diffuse-Walled Enclosures: Part I—Exact Solutions for Simple Enclosures," ASME JOURNAL OF HEAT TRANSFER, Vol. 101, pp. 81–84.

Nelson, D. A., 1979b, "Band Radiation Within Diffuse-Walled Enclosures: Part II—An Approximate Method Applied to Simple Enclosures," ASME JOURNAL OF HEAT TRANSFER, Vol. 101, pp. 85–89.

Nelson, D. A., 1984, "Band Radiation of Isothermal Gases Within Diffuse-Walled Enclosures," *International Journal of Heat and Mass Transfer*, Vol. 27, No. 10, pp. 1759–1769.

Nelson, D. A., 1986, "Nongray Total Radiation Within an Enclosure," ASME Paper No. 86-HT-29.

Soufiani, A., Hartmann, J. M., and Taine, J., 1985, "Validity of Band-Model Calculations for CO_2 and H_2O Applied to Radiative Properties and Conductive-Radiative Transfer," *Journal of Quantitative Spectroscopy and Radiative Transfer*, Vol. 33, No. 3, pp. 243–257.

Young, S. J., 1977, "Nonisothermal Band Model Theory," *Journal of Quantitative Spectroscopy and Radiative Transfer*, Vol. 18, pp. 1–28.

Y. R. Sivathanu

J. P. Gore

J. M. Janssen

D. W. Senser

School of Mechanical Engineering,
Purdue University,
West Lafayette, IN 47907

A Study of In Situ Specific Absorption Coefficients of Soot Particles in Laminar Flat Flames

Simultaneous measurements of absorption at 632 nm and emission at 800 nm and 900 nm along diametric paths are used to infer soot volume fractions based on both absorption and emission and temperatures based on emission in laminar, premixed flat flames. Agreement between soot volume fractions based on emission and absorption is used as an indicator of homogeneity of the optical path. Emission measurements at the gas band-free wavelengths of 2300 nm and 4000 nm for homogeneous paths are used to infer the specific absorption coefficients of soot particles. The results for methane, propane, and ethylene mixed with nitrogen and oxygen show insensitivity of the specific absorption coefficients to fuel type and weak dependence on temperature. An in situ check of optical homogeneity is crucial in obtaining reliable measurements of optical properties.

Introduction

Radiation from soot particles is the primary mechanism of heat transfer in strongly radiating flames. Theoretical predictions of radiative heat transfer require the spectral emissivity of soot, primarily in the infrared wavelength region from 1 to 5 μm. The spectral emissivity depends on the specific absorption coefficient (defined as absorption coefficient per unit volume fraction) and the volume fraction of soot particles. Following the work of Dalzell and Sarofim (1969) and Lee and Tien (1981), specific absorption coefficients of soot particles have been considered insensitive to fuel type (C/H ratio) and temperature, providing a convenient method for calculating flame radiation.

Dalzell and Sarofim (1969) and Lee and Tien (1981) used the dispersion equations to calculate the refractive indices of soot. Dalzell and Sarofim (1969) deduced the dispersion constants for propane and acetylene soot particles using reflectance data from compressed pellets. They reported a weak dependence (25 percent variation at 4 μm) of the specific absorption coefficients on fuel type. Lee and Tien (1981) used the in situ two-color extinction data of Pagni and Bard (1979) to find the dispersion constants of soot. This technique showed that the refractive indices of soot are independent of C/H ratio and weakly dependent on temperature. The values of the specific absorption coefficients obtained by Lee and Tien (1981) agreed with those of Dalzell and Sarofim (1960) in the infrared, even though there were substantial differences in the visible part of the spectrum.

Charalampopoulos and Felske (1987) and Charalampopoulos and Chang (1988) have reported in situ measurements of soot refractive indices at ultraviolet and visible wavelengths in premixed flat flames. The extinction coefficients were found to vary by less than 30 percent with the height above the burner. A 30 percent variation in the refractive indices in the visible leads to a much smaller variation in the infrared based on the dispersion equations of Dalzell and Sarofim (1969) and Lee and Tien (1981).

Accordingly, radiation predictions in luminous flames (Tien and Lee, 1982; Grosshandler and Vantelon, 1985; Gore and Faeth, 1986, 1988; Sivathanu and Gore, 1991; Sivathanu et al., 1991; Klassen et al., 1992; Gore et al., 1991) have been routinely obtained using refractive indices of soot that are independent of fuel type and C/H ratios. Gore and Faeth (1986, 1988) used the refractive indices of soot reported by Dalzell and Sarofim (1969) to predict spectral radiation intensities from turbulent acetylene and ethylene flames. The predictions showed similar trends for both fuels. Sivathanu and Gore (1991) used the refractive indices reported by Dalzell and Sarofim (1969) to predict spectral radiation intensities in turbulent acetylene and propylene flames. Recently, Klassen et al. (1992) and Gore et al. (1991) used the same values of refractive indices of soot to predict spectral radiation from buoyant toluene and heptane pool flames.

In contrast to the above studies, Ben Hamadi et al. (1987) and Habib and Vervisch (1988) reported significant effects of fuel type and local C/H ratio (factor of 5 at 4 μm) on the extinction coefficients of soot based on in situ emission and absorption measurements in laminar flat flames. With this finding the problem of predicting radiation from turbulent flames becomes intractable, since the local C/H ratio has to be found in addition to soot volume fractions and temperatures. The measurements on which Habib and Vervisch (1988) base their conclusions regarding the high sensitivity to C/H ratios involve a single operating condition for premixed flames burning CH_4, C_3H_8, or C_2H_4.

Based on these observations, the objectives of the present work were: (1) to determine the specific absorption coefficients of soot at two representative infrared wavelengths of CH_4, C_3H_8, and C_2H_4/air–O_2 flames with optically homogeneous paths for a range of temperatures and soot volume fractions. Specific absorption coefficients depend on the optical properties of soot particles and not on the volume fractions. Therefore $a_{s\lambda}$ is the logical variable for comparing the optical properties of soot in different flames; (2) to compare the resulting data with existing estimates; and (3) to evaluate the effect of optical inhomogeneity on the measurements of specific absorption coefficients.

Experimental Methods

The experimental apparatus consisted of a 60-mm-dia premixed flat flame burner (manufactured by Mckenna Products). Mixtures of fuel, oxygen, and air were supplied to the burner through calibrated rotameters. The flames were surrounded by a co-flow of inert gas (nitrogen or argon). The results were independent of the choice of inert gas. The flames were stabilized by a porous ceramic disk placed 50 mm above the burner surface. The range of flow rates of the fuel, oxygen, and air is summarized in Table 1. A variety of equivalence ratios, total

Contributed by the Heat Transfer Division for publication in the JOURNAL OF HEAT TRANSFER. Manuscript received by the Heat Transfer Division February 1992; revision received December 1992. Keywords: Combustion, Fire/Flames, Radiation. Associate Technical Editor: W. L. Grosshandler.

flow rates, and O_2 concentrations in the incoming stream were selected to provide a useful range of temperatures and soot volume fractions. All measurements were completed at a height of 18 mm above the burner and parallel to the burner surface. However, the residence times for the various measurements were different due to the changes in the velocity for the different flow conditions. The heat loss to the burner surface also varied with total flow rate, providing a variety of heating histories for the fuels.

A sketch of the four-wavelength emission/absorption probe is shown in Fig. 1. The intensity of a He–Ne laser beam, chopped at 1000 Hz, was measured before and after it traversed the flame to measure the extinction along the optical path. The laser beam after traversing the flame passed through a purged light guide, placed outside the flame, which also collimated the emission intensity from the flame. The stainless steel (6 mm diameter, 500 mm long) light guide defined the viewing angle (0.5 deg) and area (6 mm diameter) for the emission measurements. Harmonics of shorter wavelengths were eliminated by using two different order sorting filters. The intensity emerging from the light guide was first passed through an optical edge filter, which separated the shorter (< 1000 nm) and the longer (> 1000 nm) wavelengths. The intensity at longer wavelengths was passed through a chopper operated at 400 Hz on to a monochromator (Oriel Corp.) set at 4000 nm or 2300 nm with a band width of 40 nm. The intensity of light leaving the exit slit of the monochromator was measured by a liquid nitrogen cooled InAs detector. The intensity in the lower wavelength region of the spectrum was further divided into three parts using two beam-splitters. One part was sent to a laser power detector with an optical filter at 632 ± 1 nm. The other parts were sent to two photomultiplier tubes, which had narrow band pass (10 nm) optical filters at 800 and 900 nm. The signals from the laser power detector and the InAs detectors were passed through lock-in amplifiers. All four signals were filtered at 1 Hz before being sampled by an A/D converter and stored in a laboratory computer. The photomultiplier tubes and the InAs detector were calibrated using a blackbody at 800 K. The resulting signal-to-noise ratios were greater than 100 at all four wavelengths.

Table 1 List of operating conditions

Fuel	Fuel flow rate (mg/sec)	Oxygen flow rate (mg/sec)	Air flow rate (mg/sec)	Equivalence Ratios
Methane	25 - 71	40 - 101	0.0	2.1 - 2.9
Propane	25 - 65	40 - 94	0.0	2.0 - 3.5
Ethylene	28 - 66	0 - 101	0 - 266	2.0 - 3.6

The emission intensity at a wavelength λ is

$$I_{\lambda e} = \frac{(1-\exp(-a_{s\lambda} f_{ve} S))2hc^2}{\lambda^5(\exp(hc/\lambda kT)-1)}, \quad (1)$$

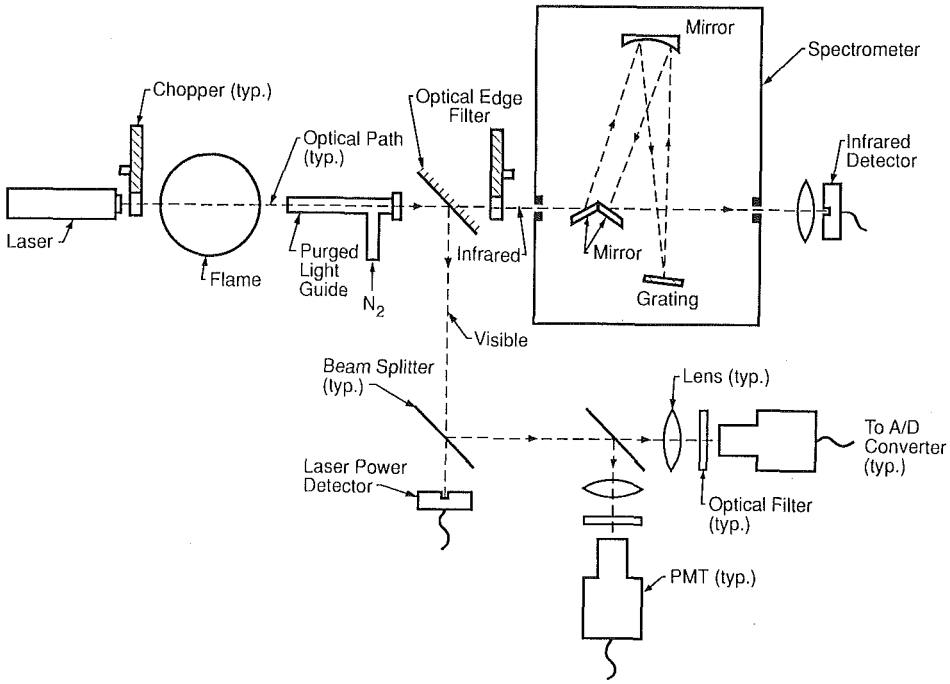

Fig. 1 Sketch of four-wavelength absorption/emission probe

Nomenclature

a_λ = absorption coefficient of soot particles
$a_{s\lambda}$ = specific absorption coefficient of soot particles = a_λ/f_{ve}
c = velocity of light
f_{va} = soot volume fraction based on extinction data
f_{ve} = soot volume fraction based on emission data
h = Planck's constant
$I_{\lambda e}$ = spectral radiation intensity emitted by the flame
I^o_λ = laser intensity before entering probe volume
i = unit imaginary number
k = Boltzmann constant, imaginary part of the refractive index of soot
$\dot{m}$ = mass flow rate
n = real part of the refractive index of soot
S = distance along the radiation path
T = temperature
x = height above burner surface
λ = wavelength

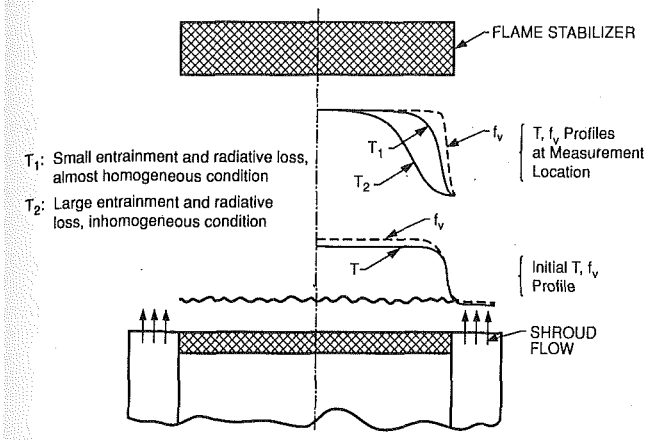

Fig. 2 Qualitative radial distribution of temperatures and soot volume fractions in a premixed flat-flame burner

where S is the length of the radiation path, T is the emission temperature, $a_{s\lambda}$ is the specific absorption coefficient, and f_{ve} is the soot volume fraction. Out of the four measurements of emission intensity, the two in the relatively short wavelength region (800 and 900 nm) were used to obtain the temperature, T, and the soot volume fraction, f_{ve}. To solve these equations, the values of $a_{s\lambda}$ at 800 and 900 nm are needed. These are related to the complex refractive index of soot particles ($n - ik$) as:

$$a_{s\lambda} = \frac{36\pi nk}{\lambda((n^2-k^2+2)^2+(2nk)^2)} \tag{2}$$

There is considerable discussion regarding the appropriate values of n, k. Therefore, three different values from the literature were used (Dalzell and Sarofim, 1969; Lee and Tien, 1981; Habib and Vervisch, 1988). It is noted that the values recommended by Habib and Vervisch (1988) depend on the fuel type. For a given set of refractive indices the uncertainty based on rms of the measurements for fixed operating conditions was less than 10 percent for the soot volume fraction measurements, and less than 25 K for the temperature measurements. The repeatability of the data during separate runs for apparently identical operating conditions was within 30 percent for soot volume fractions and within 50 K for temperatures. Differences caused by different estimates of the refractive indices at 800 and 900 nm are discussed in the next section.

Using the T and f_{ve} obtained above, the measurements of intensity at 2300 and 4000 nm were used to calculate the specific absorption coefficients, $a_{s\lambda}$, at these wavelengths. These values are compared to the estimates from the three sets of constants given by Dalzell and Sarofim (1969), Lee and Tien (1981), and Habib and Vervisch (1988).

In the present experiments and those of Habib and Vervisch (1988) and Ben Hamadi et al. (1987), T and f_{ve} were assumed to be constant over the radiation path S. This assumption is based on the fact that the flames are one dimensional and the entire optical path is at a fixed height above the burner surface. Ben Hamadi et al. (1987) and Habib and Vervisch (1988) cite satisfactory flatness of the flame up to 25 mm above the burner, based on measurements of CO and CO_2 concentrations. The radial distributions of gas concentration measurements reported in Ben Hamadi's (1984) thesis are restricted to one operating condition and one height above the burner. Ben Hamadi et al. (1987) also cite the work of Prado et al. (1981) in support of the homogeneity of flat flames in similar burners. The tests of Prado et al. (1981) involved laser scattering measurements, which rely on the homogeneity of the soot volume fraction profile alone. For emission measurements, the temperature profile must be homogeneous in addition to the soot volume fraction profile.

Figure 2 shows a sketch of the qualitative distributions of temperature and soot volume fraction at two different heights above a flat flame. For a uniform one-dimensional flame, the temperature and soot volume fraction are independent of radial position near the flame surface. The temperature decreases to that of the shroud gas and the soot volume fraction decreases to zero in a narrow region separating the flame and the shroud flow. As the axial distance from the flame is increased, the entrainment of shroud gases leads to the development of variations in temperature as a function of radial distance. Larger radiative heat losses from the locations at larger radii also contribute to the development of the temperature profile. The soot particles have zero diffusivity and therefore their volume fractions remain independent of radial position since thermophoretic velocity effects are small. Thus, the soot particles at relatively larger radii are substantially colder than those near the axis. This effect causes optical inhomogeneity of the path. For high flame temperatures, buoyancy-induced velocity causes higher entrainment leading to greater inhomogeneity. Similarly, the inhomogeneity caused by radiative heat loss is a function of the soot volume fraction and the flame temperature. Temperature profile T_1 results from relatively small amounts of entrainment and radiative losses while the profile designated T_2 represents larger entrainment and heat loss. The profile T_1 is close to being homogenous while the profile T_2 represents optical inhomogeneity. Thus, the optical homogeneity of the path depends on specific operating conditions and height above the burner and is not a characteristic of the burner configuration.

In the present study simultaneous extinction and emission measurements were used as an in situ check on optical homogeneity. The f_{va} were obtained from the measurements of extinction of the laser intensity at 632 nm:

$$f_{va} = -\ln(I_\lambda/I_\lambda^o)/a_{s\lambda}S \tag{3}$$

A necessary condition for optical homogeneity (Sivathanu et al., 1991) can be established by requiring that the soot volume fractions based on the emission measurements (f_{ve}) be equal to those obtained from the absorption measurement (f_{va}). The f_{va} obtained from Eq. (3) are compared to f_{ve} since scattering in premixed flat flames is small compared to absorption (Charalampopoulos and Chang, 1991). In general, the equality of f_{va} and f_{ve} does not constitute a sufficient condition for optical homogeneity. Varying distributions of soot volume fractions and temperatures may yield identical values of f_{va} and f_{ve}. However, inhomogeneity in the present configuration is a departure from the homogeneous state by mixing and radiative transfer. Therefore, the condition of equality between f_{va} and f_{ve} is taken as a working definition of optical path homogeneity. In particular, homogeneity of both temperature and soot volume fraction distributions is tested simultaneously by this method in situ for all operating conditions. It is noted that a more stringent test of homogeneity is certainly desirable in future work. However, as discussed later, the present conclusion regarding the lack of effects of fuel type is independent of the optical homogeneity criteria.

Premixed methane, propane, and ethylene flames were studied to examine the effects of fuel type. Optically homogeneous conditions were used to measure $a_{s\lambda}$ at 2300 and 4000 nm. Measurements at several optically inhomogeneous conditions were also completed to demonstrate the importance of optical homogeneity.

Results and Discussion

Figure 3 shows the measurements of specific absorption coefficients of soot, $a_{s\lambda}$, at 4000 and 2300 nm plotted as a

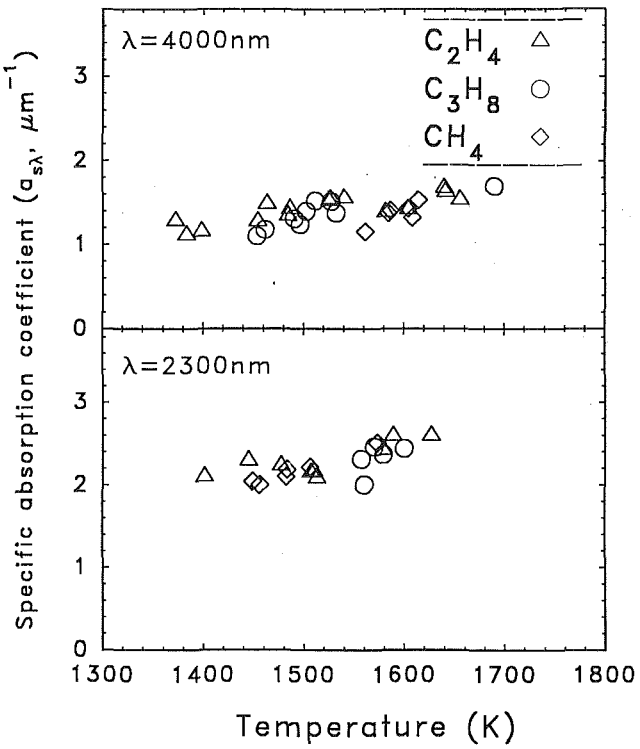

Fig. 3 Specific absorption coefficients for 4000 and 2300 nm as a function of temperature using $a_{s\lambda}$ at 800 and 900 nm from Dalzell and Sarofim (1969)

Table 2 Representative estimates of temperature and soot volume fractions using different sets of refractive indices

	Dalzell and Sarofim		Tien and Lee		Habib and Vervisch	
λ, nm	$a_{s\lambda}$, μm^{-1}					
632	7.71		5.05		5.42[a]	5.59[b]
800	6.38		4.19		4.42	4.65
900	5.88		3.94		3.99	4.26
Fuel	T(K)	f_{ve}(ppm)	T(K)	f_{ve}(ppm)	T(K)	f_{ve}(ppm)
	1372	1.21	1392	1.48	1367	1.76
Ethylene	1507	1.32	1531	1.61	1501	1.92
	1627	0.31	1655	0.38	1620	0.44
	1449	1.49	1471	1.81	1430	2.65
Propane	1527	0.90	1552	1.12	1506	1.57
	1690	0.32	1720	0.39	1664	0.54
	1561	1.65	1587	2.00	1538	2.94
Methane	1570	0.56	1596	0.70	1547	0.96
	1614	0.43	1642	0.54	1590	0.74

[a]Specific absorption coefficients for propane and methane flames.

[b]Specific absorption coefficients for ethylene flames.

function of temperature. These two wavelengths correspond to the gas-band free part of the spectrum. The data for the optically homogeneous conditions for the propane/oxygen,

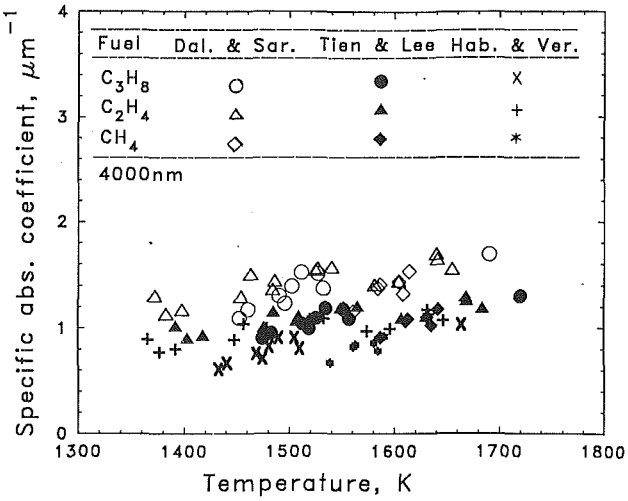

Fig. 4 Specific absorption coefficients at 400 nm as a function of temperature using the $a_{s\lambda}$ at 800 and 900 nm from Dalzell and Sarofim (1969), Habib and Vervisch (1988), and Lee and Tien (1981)

methane/oxygen and ethylene/(oxygen + air) flames are shown. All the values were calculated assuming the specific absorption coefficients, $a_{s\lambda}$, reported by Dalzell and Sarofim (1969) for the 800 and 900 nm wavelengths. The results show that the specific absorption coefficients of soot ($a_{s\lambda}$) in the infrared region are weakly dependent on temperature and independent of the C/H ratio of the fuels studied. These observations are consistent with the earlier findings of Lee and Tien (1981) and Dalzell and Sarofim (1969).

The calculations of T and f_{ve} were repeated using the values of a_{s800} and a_{s900} reported by Lee and Tien (1981) and Habib and Vervisch (1988). This procedure examines whether the fuel independence of $a_{s\lambda}$ at the relatively longer wavelengths is an artifact of using the constants reported by Dalzell and Sarofim. As listed in Table 2, the $a_{s\lambda}$ reported by the three investigators are substantially different for the relatively short wavelengths. Consequently, the results following the three investigators provide different estimates of T and f_{ve} for identical intensity data. The differences in T are relatively small due to the canceling effects of the changes in $a_{s\lambda}$ for the two wavelengths. The differences in f_{ve} are much larger since this quantity depends on a single $a_{s\lambda}$. Table 2 shows selected estimates of T and f_{ve} resulting from the use of different values of $a_{s\lambda}$ at 800 and 900 nm in Eq. (1). The temperatures estimated using the $a_{s\lambda}$ reported by Tien and Lee (1981) are approximately 25 K higher than those obtained using the values of $a_{s\lambda}$ provided by Dalzell and Sarofim (1969), and the soot volume fractions are about 20 percent higher. The temperatures obtained using the $a_{s\lambda}$ reported by Habib and Vervisch (1988) are close to those estimated using the values of $a_{s\lambda}$ provided by Dalzell and Sarofim (1969), for ethylene flames, but about 25 K lower for the propane and the methane flames. However, the soot volume fractions are almost 50 percent higher in the ethylene flames and as much as 75 percent higher in the propane and methane flames. The range of temperatures for optically homogeneous conditions in the ethylene flames is larger than that in the propane and methane flames. However, there is sufficient overlap between the temperatures and the soot volume fractions measured in the flames burning the three different fuels to allow a study of the effects of fuel type.

Figure 4 shows the values of specific absorption coefficients at 4000 nm calculated using the T and f_{ve} data resulting from the different $a_{s\lambda}$ reported by the three investigators. It is noted that different sets of $a_{s\lambda}$ were used for the different fuels when utilizing the values reported by Habib and Vervisch (1988). The measurements of the specific absorption coefficient at 4000 nm are, however, essentially independent of the fuel type.

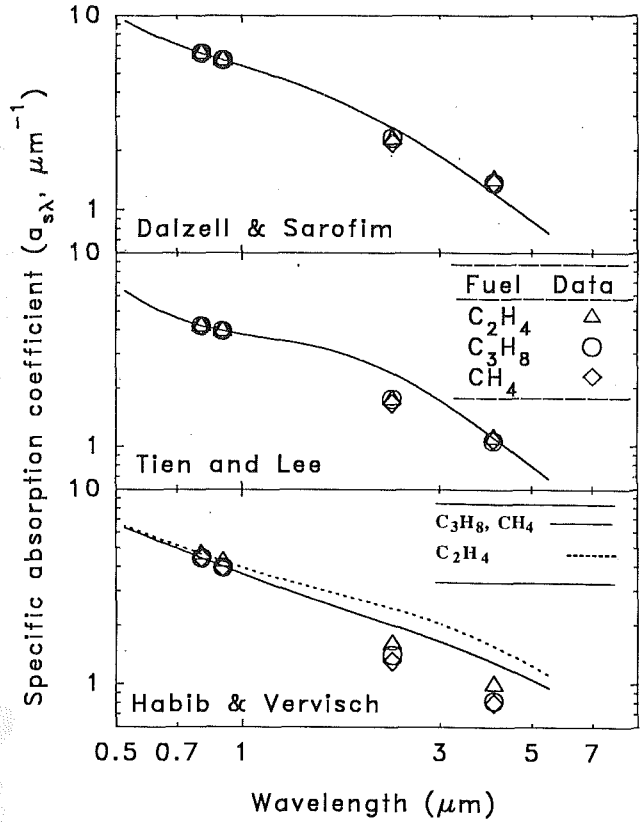

Fig. 5 Comparison of the specific absorption coefficients from different models with the present data; data: Δ C_2H_4, ○ C_3H_8, ◇ CH_4; predictions: Dalzell and Sarofim—fuel independent; Lee and Tien—fuel independent, Habib and Verisch· —— C_3H_8, CH_4; — — — — C_2H_4

Figure 5 shows the predictions of specific absorption coefficients obtained using the refractive indices given by the three investigators plotted as a function of wavelength. The present experimental data averaged over all optically homogeneous operating conditions are plotted for comparison. The calculated specific absorption coefficients for Dalzell and Sarofim (1969) and Lee and Tien (1981) are fuel independent while those of Habib and Vervisch (1988) depend on the fuel type. For all three cases, the measurements represented by the symbols are matched with the calculations at 800 and 900 nm. The measured $a_{s\lambda}$ in the infrared are independent of fuel type and agree with the calculations of Dalzell and Sarofim (1969) and Lee and Tien (1981) as shown in the first two parts of the figure. The refractive indices given by Habib and Vervisch (1988) result in an overestimation of the specific absorption coefficients at relatively longer wavelengths. Furthermore, in spite of the differences in the input $a_{s\lambda}$ at the shorter wavelengths for the different fuels, the measurements in the infrared show small effects of fuel type.

The effects of optical inhomogeneity (defined as the ratio of f_{ve}/f_{va}) on the estimates of specific absorption coefficients are examined in Fig. 6. All data resulting from homogeneous and inhomogeneous conditions are shown together. The data within $f_{ve}/f_{va} = 0.8$ and $f_{ve}/f_{va} = 1.2$ were considered practically homogeneous for the results discussed above. Measurements outside the optically homogeneous band show a factor of 3 departure from the correct value of the specific absorption coefficient. If optically homogeneous conditions were selected for one fuel and not for the other fuels, the apparent $a_{s\lambda}$ would show spurious fuel property effects. It is noted that for both homogeneous and inhomogeneous conditions studied in the present work, the specific absorption coefficients for all three fuels show a similar departure from the baseline. Thus the

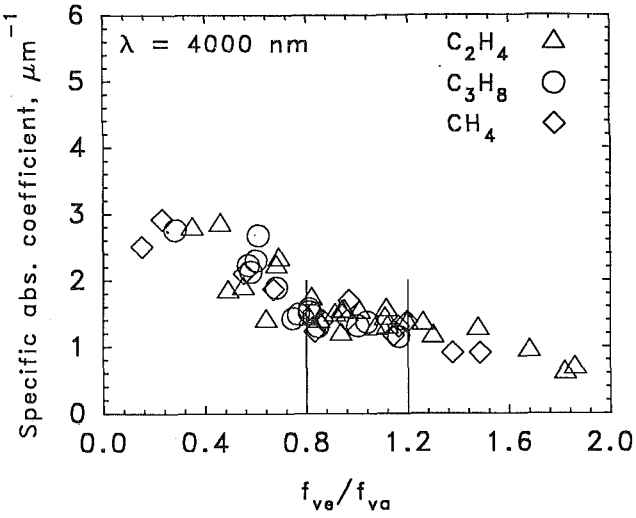

Fig. 6 Specific absorption coefficients at 4000 nm as a function of degree of inhomogeneity

specific absorption coefficients are independent of fuel type for all values of f_{ve}/f_{va}.

Conclusions

The present study used four-wavelength absorption/emission measurements to infer the specific absorption coefficients of soot particles in the infrared region for three different fuels with varying C/H ratios. The major conclusions are:

1 The specific absorption coefficients are independent of fuel type (C/H ratio) in the infrared region, which is of primary importance in the calculation of radiative heat transfer.
2 The measurements of specific absorption coefficients are consistent with those reported by Dalzell and Sarofim (1969) and Lee and Tien (1981), and show a weak dependence on temperatures. The present experimental data are not consistent with refractive indices and the effects of fuel type described by Habib and Vervisch (1988).
3 It is important to ensure in situ that the temperature and soot volume fractions are both homogeneous over the optical path if optical properties of soot are to be determined from emission/absorption measurements. In the present study a necessary condition for such homogeneity was established. Future work should involve an absolute check of the homogeneity of temperature and soot volume fraction profiles.

Acknowledgments

Partial support for this study is provided by the National Science Foundation Grant No. CTS-8914520. The authors wish to acknowledge the support provided by Professor N. M. Laurendeau for this investigation.

References

Ben Hamadi, M., 1984, "Contribution à la Comprehension des Propriétés Radiatives des Suies dan une Flamme de Prémelange," Ph. D thesis in Energy, Department of Science and Technology, University of Rouen, France.

Ben Hamadi, M., Vervisch, P., and Coppalle, A., 1987, "Radiation Properties of Soot From Premixed Flat Flames," *Comb. Flame*, Vol. 68, pp. 57–67.

Charalampopoulos, T. T., and Fleske, J. D., 1987, "Refractive Indices of Soot Particles Deduced From In Situ Laser Light Scattering Measurements," *Comb. Flame*, Vol. 68, pp. 283–294.

Charalampopoulos, T. T., and Chang, H., 1988, "In Situ Optical Properties of Soot Particles in the Wavelength Range From 340 nm to 600 nm," *Combust. Sci. Tech.*, Vol. 59, pp. 401–421.

Charalampopoulos, T. T., and Chang, H., 1991, "Agglomerate Parameters and Fractal Dimension of Soot Using Light Scattering—Effects on Surface Growth," *Comb. Flame*, Vol. 87, pp. 89–99.

Dalzell, W. H., and Sarofim, A. F., 1969, "Optical Constants of Soot and Their Application to Heat Flux Calculations," ASME JOURNAL OF HEAT TRANSFER, Vol. 91, pp. 100–104.

Gore, J. P., and Faeth, G. M., 1986, "Structure and Radiation Properties of Turbulent Ethylene/Air Diffusion Flames," *Twenty-First Symposium (International) on Combustion*, The Combustion Institute, pp. 1523–1531.

Gore, J. P., and Faeth, G. M., 1988, "Structure and Radiation Properties of Turbulent Acetylene/Air Diffusion Flames," ASME JOURNAL OF HEAT TRANSFER, Vol. 110, pp. 173–181.

Gore, J. P., Klassen, M., Hamins, A., and Kashiwagi, T., 1991, "Fuel Property Effects on Burning Rate and Radiative Transfer From Liquid Pool Flames," *Fire Safety Science Proceedings of the Third International Symposium*, G. Cox and B. Langford, eds., Elsevier Science Publishers Ltd., London, pp. 395–404.

Grosshandler, W. L., and Vantelon, J. P., 1985, "Prediction of Soot Radiation in Laminar Diffusion Flames," *Combust. Sci. Tech.*, Vol. 44, pp. 125–141.

Habib, Z. G., and Vervisch, P., 1988, "On the Refractive Index of Soot at Flame Temperature," *Combust. Sci. Tech.*, Vol. 59, pp. 261–274.

Klassen, M., Sivathanu, Y. R., Gore, J. P., Hamins, A., and Kashiwagi, T., 1992, "Radiative Heat Feedback in a Toluene Pool Fire," *Twenty-Fourth Symposium (International) on Combustion*, Sydney, Australia, in press.

Lee, S. C., and Tien, C. L., 1981, "Optical Constants of Soot in Hydrocarbon Flames," *Eighteenth Symposium (International) on Combustion*, The Combustion Institute, pp. 1159–1166.

Pagni, P. J., and Bard, S., 1979, "Particulate Volume Fractions in Diffusion Flames," *Seventeenth Symposium (International) on Combustion*, The Combustion Institute, Pittsburgh, PA, pp. 1017–1026.

Prado, G., Jagoda, J., Neoh, K., and Lahaye, J., 1981, " A Study of Soot Formation in Premixed Propane/Oxygen Flames by In Situ Optical Techniques and Sampling Probes," *Eighteenth Symposium (International) on Combustion*, The Combustion Institute, pp. 1127–1136.

Sivathanu, Y. R., Gore, J. P., and Dolinar, J., 1991, "Transient Scalar Properties of Strongly Radiating Jet Flames," *Combust. Sci. Tech.*, Vol. 76, pp. 45–66.

Sivathanu, Y. R., and Gore, J. P., 1992, "Transient Structure and Radiation Properties of Strongly Radiating Buoyant Flames," ASME JOURNAL OF HEAT TRANSFER, Vol. 114, pp. 659–665.

Tien, C. L., and Lee, S. C., 1982, "Flame Radiation," *Prog. Energy Combust. Sci.*, Vol. 8, pp. 41–59.

Effect of Surface Wettability on Active Nucleation Site Density During Pool Boiling of Water on a Vertical Surface

C. H. Wang

V. K. Dhir

Mechanical, Aerospace, and Nuclear Engineering Department,
School of Engineering and Applied Science,
University of California, Los Angeles,
Los Angeles, CA 90024

Pool boiling of saturated water at 1 atm pressure has been investigated. In the experiments, copper surfaces prepared by following a well-defined procedure were used. The cumulative number density of the cavities and their shapes were determined with an optical microscope. The surface had a mirror finish and had a surface R_a (centerline average) value of less than 0.02 μm. The wettability of the surface was changed by controlling the degree of oxidation of the surface. In the experiments with the primary surface, the wall heat flux and superheat were determined with the help of thermocouples embedded in the test block. The density, spatial distribution, local distribution, and nearest-neighbor distance distribution of active nucleation sites in partial and fully developed nucleate boiling were determined from still pictures.

Introduction

Nucleate boiling heat transfer from a surface submerged in a pool of saturated liquid is influenced by many variables, such as surface finish; surface wettability; surface cleanliness; heater size, geometry, material, and thickness; liquid subcooling; gravitational acceleration or orientation of the surface and flow velocity, etc. The degree of our understanding of the role played by each variable differs from one variable to another. Until recently, only sparse data had existed in the literature from which inferences could be made with respect to the effect of surface wettability on nucleate boiling heat fluxes. The most recent experimental effort has shown that surface wettability affects not only nucleate and transition boiling but also the maximum and minimum heat fluxes. The objective of the present work is to quantify experimentally how surface wettability affects the active nucleation site density and the distribution of the active nucleation sites.

Jakob (1949) was the first to report the relationship between wall heat flux and the density of active nucleation sites. However, Jakob's observations were limited to relatively low heat fluxes because at high heat fluxes bubbles at neighboring sites start to merge; the merger of bubbles obscures the determination of the sites that are active underneath a large bubble. To circumvent the difficulty encountered by Jakob and others in counting the active site density at high heat fluxes, Gaertner and Westwater (1960) employed a novel technique in which nickel salts were dissolved in water and the heater surface acted as one of the electrodes. During boiling precess, nickel was deposited on the heater surface. By counting the numbers of holes in the deposited layer, they were able to determine the number density of active nucleation sites and their dependence on heat flux. The data were found to correlate according to

$$N_a \sim q^{2.1} \tag{1}$$

Hsu and Graham (1976) presented a summary of earlier observations of several investigators with respect to the relationship between heat flux or heat transfer coefficient or wall superheat and the active site density. A comparison of various observations indicates that generally the exponent on heat flux varies between 1 and 2.1, but the proportionality constant shows a much larger variation. It should be noted here that in none of these studies was effort made to specify the contact angle, the surface roughness, or the size distribution of the cavities present on the surface. All these parameters can affect the proportionality constant and to some extent the exponent. Gaertner and Westwater (1960), as well as Sultan and Judd (1978), have reported active nucleation site density data for water boiling at 1 atm pressure on horizontal copper surfaces. In both of these investigations smooth polished surfaces were used. The observed number density in Sultan and Judd's (1978) experiments is found to be several times higher than that reported by Gaertner and Westwater (1960). One qualitative explanation for the difference in the two sets of data can be given on the basis that the presence of nickel salts in water improved the surface wettability in Gaertner and Westwater's experiments, which in turn led to suppression of nucleation sites.

Aside from the effect of surface wettability on the propensity for nucleation, the key question that has not yet been answered is the quantitative relationship between the cavities that are present on the surface and those that actually become active. A first attempt in this direction was made by Mikic and Rohsenow (1969) who proposed that on commercial surfaces the cumulative number of active sites per unit area can be assumed to vary in partial nucleate boiling as

$$N_a \sim \left[\frac{D_s}{D_c}\right]^m \tag{2}$$

where D_s is the diameter of the largest cavity present on the surface and m is an empirical constant. The size, D_c, of a cavity that nucleates at a wall superheat ΔT_w is obtained from the expression

$$D_c = \frac{\dfrac{4f_1\sigma T_{\text{sat}}}{\rho_v h_{fg}\Delta T_w}}{\left[1 - \dfrac{f_2 D_c q}{2f_1 k_l \Delta T_w}\right]} \tag{3}$$

At not very high heat fluxes, the second term in the denom-

Contributed by the Heat Transfer Division and presented at the National Heat Transfer Conference, Minneapolis, Minnesota, July 28–31, 1991. Manuscript received by the Heat Transfer Division May 1992; revision received December 1992. Keywords: Boiling, Measurement Techniques, Phase-Change Phenomena. Associate Technical Editor: L. C. Witte.

inator in Eq. (3) is generally much less than unity and thus can be neglected.

Bier et al. (1978) on the other hand have deduced an expression for active site density from heat transfer data as

$$\ln N_a = \ln(N_{a_{\max}})\left[1 - \left(\frac{D_c}{D_s}\right)^m\right] \quad (4)$$

In Eq. (4), $N_{a_{\max}}$ is the maximum value of N_a occurring at $D_c = 0$. The value of m was found to depend on the manner in which a surface was prepared. With Freon-115 or Freon-11 boiling on a chemically etched copper surface and on a turned surface, values of 0.42 and 0.26, respectively, were noted for m.

Cornwell and Brown (1978) made a systematic study of active nucleation sites on copper surfaces during boiling of water at one atmosphere pressure. Their study was limited to low heat fluxes and the surface condition varied from smooth to a scratched rough surface. It was concluded that the active site density varied with wall superheat as

$$N_a \sim \Delta T_w^{4.5} \quad (5)$$

The proportionality constant in Eq. (5) increased with surface roughness but the exponent on ΔT_w was independent of roughness. From an electron microscope measurement of cavity size distribution, they observed that the number density of cavities, N_s, on the surface was related to cavity size such that

$$N_s \sim \frac{1}{D_c^2} \quad (6)$$

By assuming that only conical cavities existed on the surface and that a minimum value of trapped gas was needed for nucleation, they justified qualitatively the observed functional dependence of active site density on wall superheat.

Recently Yang and Kim (1988) have made the first attempt to predict quantitatively the active nucleation sites from a knowledge of the size and cone angle distribution of cavities that are actually present on the surface. Using a scanning electron microscope (SEM) and a differential inference contrast microscope (DIC), Yang and Kim obtained the cavity probability density function in terms of the cavity diameter and cone angle. For cavities with mouth diameter varying from 0.65 to 6.2 μm, the cavity size distribution was found to fit a Poisson distribution

$$f(D_c) = \lambda e^{-\lambda D_c/2} \quad (7)$$

whereas a normal distribution was used for cone half-angle β,

$$f(\beta) = [(2\pi)^{1/2} s]^{-1} \exp\left[-(\beta - \bar{\beta})^2/(2s^2)\right] \quad (8)$$

In Eqs. (7) and (8), λ and s are statistical parameters and $\bar{\beta}$ is the mean value of the cone half angle. To determine the number of cavities that will trap gas or vapor and will eventually become nucleation sites, they used the criterion developed by Bankoff (1958). According to this criterion, the cavities will trap gas/vapor only if

$$\phi > 2\beta \quad (9)$$

Thus combining Eqs. (7), (8), and (9), the cumulative density of active nucleation sites was expressed as

$$N_a = \bar{N}_s \int_0^{\phi/2} [(2\pi)^{1/2} s]^{-1} \exp[-(\beta - \bar{\beta})^2/(2s^2)]\, d\beta \times \int_{D_c}^{D_s} \lambda e^{-\lambda D_c/2} dD_c \quad (10)$$

In the above equation $\bar{N}_s$ is the average density of cavities present on the surface and D_s is the diameter of the largest cavity present on the surface and is obtained from statistical considerations. The magnitude of these parameters depends on the heater material and on the procedure that is used to prepare the surface. The predicted active nucleation site density was found to compare well with the data obtained at very low wall superheats. Although the scope of their study was limited, it represented a rational approach to a very difficult problem. The use by Yang and Kim of a Poisson distribution function for the cavities that exist on the surface after polishing is consistent with Gaertner's (1963) observation that active nucleation sites were randomly located and could be represented by a Poisson distribution. However, transformation from the size distribution of cavities present on the surface to the density of sites that actually become active may be affected by several other parameters not included in the analysis of Yang and Kim.

The nucleation sites are randomly distributed over the heater surface. Gaertner (1963) was the first to note that the local density of nucleation sites on a heater surface can be represented by a Poisson distribution. He also derived the distribution of nearest-neighbor distances from the Poisson equation. Sultan and Judd (1978) also concluded that the active nucleation sites were located randomly on the heater surface and the distribution of nucleation sites fits the Poisson dis-

Nomenclature

A_c = cavity mouth cross-sectional area
D_c = cavity mouth diameter
D_s = maximum cavity diameter
D_c^* = cavity diameter based on cross-sectional area
D_c' = new cavity diameter after material to a depth Δh is removed
f = function defined by Eqs. (7) and (8)
f_D = cavity mouth shape factor defined by Eq. (20)
f_1, f_2 = constant in Eq. (3), a function of contact angle
h_{fg} = latent heat of vaporization
k_l = thermal conductivity of liquid
l_a = average nearest neighbor distance between nucleation sites
l_m = most probable nearest-neighbor distance
l_n = nearest-neighbor distance between nucleation sites
l_v = cutoff distance
m = empirical constant in Eqs. (2) and (4)
n_a = number of active nucleation sites on a given area
n_{as} = number of surface cavities with cavity side angle less than ψ on a given area
n_s = number of surface cavities on a given area
N_a = active nucleation site density
N_{as} = surface cavity density with cavity mouth angle less than ψ
$\bar{N}_s$ = average density of cavities present on surface
N_s = surface cavity density
P_n = probability function defined by Eq. (26)
P_u = probability function defined by Eq. (23)
q = average wall heat flux
r_c = mouth radius of a cavity
s = statistical parameter
T = temperature
T_{sat} = saturation temperature
T_w = wall temperature
β = cone half-angle
$\bar{\beta}$ = mean value of cone half-angle
ΔT_w = wall superheat
λ = statistical parameter
ρ_v = density of vapor
σ = surface tension
ϕ = contact angle
ψ = cavity side angle
ψ_m = cavity mouth angle

tribution. Del Valle and Kenning (1985) found that the nucleation site distribution can be represented by the Poisson distribution. However, the nearest-neighbor distance between active nucleation sites deviated from the Poisson distribution since the nearest-neighbor active nucleation sites could not be found in the range of 0 and 0.35 mm.

The objective of the present work is to relate the cavities that are present on the surface to those that actually become active. Accomplishment of the objective requires that four steps be completed. In the first step the number density, size distribution, and cavity side angles must be determined. The second step requires preparation of surfaces of different degrees of wettability and measurement of contact angles. In the third step the relationship between cavity diameter and wall superheat must be verified experimentally. Lastly, the cumulative number density of active sites should be determined as a function of wall heat flux and/or wall superheat. Because of the experimental constraints, not all the steps could be completed in a single experiment or on a single surface. For determination of number density, diameter, and side angle of cavities present on the surface, a small secondary surface (2 cm in diameter) made of 99.9 percent pure copper was used. The surface was prepared by following a prescribed procedure. To vary the surface wettability, the primary and secondary surfaces were heated in air (oxidized) and static contact angles were used as a measure of the degree of wettability. Experiments to determine the relationship between active cavity diameter and the wall superheat were performed on another secondary surface. This surface of square cross section (1 cm × 1 cm) was also made of 99.9 percent pure copper and was held vertically during the experiments. The boiling curves and number density of active nucleation sites as a function of wall heat flux/wall superheat were obtained on the large primary surface prepared by following the same procedure as the secondary surfaces. By knowing the relationship between number density of active sites and wall superheat and between active cavity diameter and wall superheat, the functional dependence of cumulative number density of active sites on cavity diameter can be obtained.

Experiments

The primary test surface and the experimental apparatus used in this study are essentially the same as described earlier by Bui and Dhir (1985). The test surface is rectangular in shape and has a width of 6.3 cm and a height of 10.3 cm. The surface is machined from one end of a copper rod having a purity of 99.9 percent. Twelve cartridge heaters are placed in the test block. Four of these heaters are rated at 2 kW each, whereas the remaining eight have a power rating of 1 kW each. Thirty-gage chromel-alumel thermocouples are positioned along the vertical axis of the rectangular boiling surface at 8, 26, 52, and 77 mm from the lower edge. At each vertical location, four thermocouples are embedded at various depths normal to the boiling surface. The test surface is held on one side of a viewing and liquid holding chamber. The chamber is a square duct with a 14 cm × 14 cm cross section.

Prior to startup of an experiment, the test liquid, which was distilled water, was deaerated by vigorous boiling in a separate reservoir. Thereafter the test section was preheated and the chamber was filled with the test liquid from the reservoir. The power to the cartridge heaters was controlled with an autotransformer and was determined by voltmeter and ammeter readings. A steady-state condition was assumed to exist when the temperature of the test section changed by less than 1 K in 5 minutes. All the nucleate boiling data reported in this work were taken under steady-state conditions. The data were recorded with an automatic data acquisition system. In the steady-state tests the wall heat flux was determined by knowing the temperature profile, which was linear in the copper block except near the edges. The surface temperature was obtained by extrapolating the known temperature profile at a given vertical location.

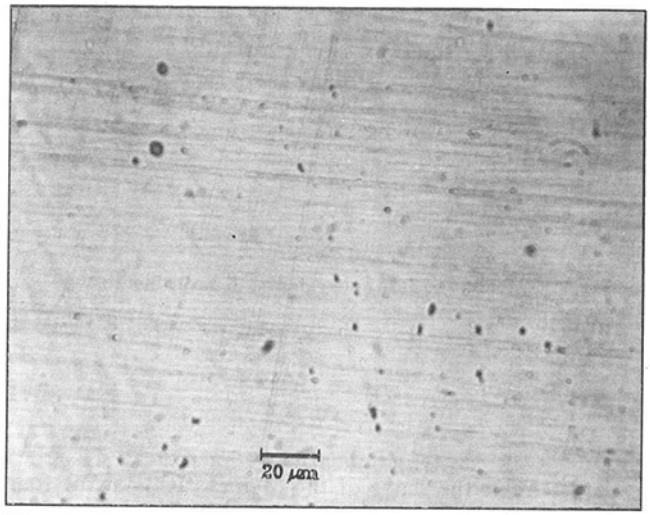

Fig. 1 Optical micrograph of the super smooth surface (500 × magnification)

Surface Preparation. In this study the roughness and cavity size and shape distribution were used to characterize a surface. Since the test surface (primary surface) is too bulky for both a Talysurf and cavity size measurements with an optical microscope, a secondary surface made of 99.9 percent pure copper was employed. The secondary surface with a diameter of about 2 cm was prepared by following a well-defined procedure. Once the secondary surface was characterized, the primary surface was prepared by repeating the same procedure. Boiling experiments were carried out on the same surface but with different degrees of oxidation (wettability). Prior to oxidation, the test surface had a super mirror finish. The surface was prepared by initially rubbing the surface ten times with a 600 grit emery paper. The emery paper was attached to a spring-loaded scrubber with an area equal to 6×8 cm^2. A force of 9.6 kg, applied to this scrubber, which equals 200 g/cm^2 of pressure, was maintained on the surface during scrubbing. Thereafter the surface was polished with a 5 μm levigated alumina oxide powder with a cotton cloth attached to the scrubber. Again a pressure of 200 g/cm^2 was maintained during polishing, which lasted for 800 strokes. The surface was further polished with 0.05 μm gamma alumina powder applied with a piece of fine velvet. The polishing was continued for another 800 strokes. From Talysurf readings, it was determined that the surface thus prepared had R_a value of less than 0.02 μm.

Cavity Diameter and Mouth Angle. The cavity mouth diameter, D_c^*, was determined with an optical microscope. For the super finish surface, a 1.16 cm^2 area was randomly chosen. For cavities from 6.5 to 56 μm in diameter, this area was enlarged 200 times while viewing it through the eye piece. In order to measure the cavities from 3.3 μm to 6 μm in diameter, an area of 1.51 mm^2 was randomly selected from the original 1.16 cm^2 area. This area was enlarged 500 times in the optical microscope and photographs were taken. Figure 1 shows one such photograph. The dark spots in the figure represent cavities present on the surface. For cavities smaller than 3.3 μm in diameter, an area of 0.0897 mm^2 was randomly selected from the original 1.16 cm^2 area and was enlarged 1000 times. The cavity sizes in the photographs were measured with a dial caliper. The resolution of the dial caliper is 0.02 mm. Therefore, the resolution of cavity diameter with magnifications of 200, 500, and 1000 is about 0.1, 0.4, and 0.02 μm, respectively. Since the shape of the mouth of a cavity is generally irregular, the effective diameter is defined as

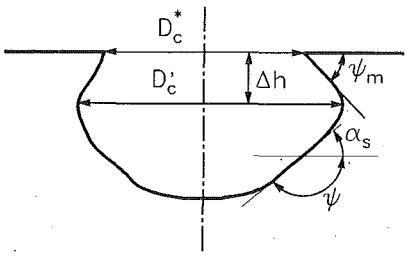

Fig. 2 Definition of cavity side angle and cavity mouth angle

$$D_c^* = \sqrt{\frac{4A_c}{\pi}} \tag{11}$$

where A_c is the cavity mouth cross-sectional area.

To determine the shape of the cavities, dents at the four corners of the chosen area were made. The dents were made with a diamond rectangular cone having an apex angle of 136 deg. Thereafter, the surface was polished with 0.05 μm gamma alumina powder to remove a certain amount of material. The extent of the material that was removed was determined by noting the width of the rectangular cone mark and with a priori knowledge of the cone angle. Thereafter, the new diameter of the cavities originally identified on the surface was determined. This in turn corresponded to the cavity diameter at a depth equal to the extent of the material removed (which was about 0.4 ~ 1.5 μm) from the original surface.

The shape of a cavity can also be irregular. The slope, α_s, of the wall of the cavity is shown in Fig. 2. The cavity side angle, ψ, is defined as

$$\psi = 180 \text{ deg} - \alpha_s \tag{12}$$

The cavity mouth angle, ψ_m, is the cavity side angle at the mouth. In this study, the shape of cavities is quantified by the cavity mouth angle. Since the shape of the cavities is irregular, the cavity mouth angles can vary around the mouth of the cavities. For simplicity, the cavity mouth angle is defined as

$$\psi_m = \tan^{-1} \frac{D_c' - D_c^*}{2 \cdot \Delta h} \tag{13}$$

where D_c^* is the cavity mouth diameter defined by Eq. (11) at the surface; D_c' is the new diameter after material to a certain depth, Δh, is removed. The mouth angle expressed by Eq. (13) is an average cavity mouth angle. The cavity with a mouth angle less than 90 deg is called a reservoir-type cavity.

The number of cavities, n_s, with a diameter larger than or equal to a given diameter D_c^* is counted in a given area. The rate of change of cavity site density with cavity diameter in the three cavity diameter ranges employed in this study is calculated from the number of cavities of a given size in a given area. The cumulative cavity density, N_s, is obtained from the integration of these three slopes of the cavity density as follows:

$$N_s = \int_{\infty}^{D_{c1}} \frac{dN_s}{dD_c^*} \cdot dD_c^* + \int_{D_{c1}}^{D_{c2}} \frac{dN_s}{dD_c^*} \cdot dD_c^* + \int_{D_{c2}}^{D_{c3}} \frac{dN_s}{dD_c^*} \cdot dD_c^* \tag{14}$$

Similarly, the number of cavities, n_{as}, with a diameter larger than or equal to a given diameter D_c^* and a mouth angle less than 90 deg, is counted in a given area. A complete listing of the effective diameters and mouth angles of cavities is given by Wang (1992).

Surface Wettability. Wettability of the surface was changed by oxidizing the surface in air. To oxidize the surface a procedure similar to that developed by Liaw (1988) was used. According to this procedure, starting at room temperature, the surface is heated at a certain rate until it reaches a specified temperature. The surface is then held at that temperature for a certain period. To obtain the surface with a contact angle of 35 deg, the surface was held at 525 K for one hour, whereas for a contact angle of $\phi = 18$ deg, the surface was held at 540 K for two hours. Thereafter the surface was cooled back to room temperature.

A sessile drop method was used to measure the static contact angle. This angle should represent a mean between advancing and receding contact angles. A liquid droplet 0.2 cm^3 in volume, which was exposed to air, was placed on the test surface. The temperature of the droplet was the same as the test surface, i.e., approximately 95°C. The contact angle was determined from a photograph of the droplet placed on the test surface. The uncertainty in measured contact angle is about ±3 deg.

Dependence of Number Density of Active Cavities on Wall Heat Flux or Superheat. The number density of active sites was determined by taking still pictures of a 1 cm^2 area of the primary surface. This area was located in the lower middle portion of the test surface and was identified a priori. In partial nucleate boiling when discrete bubbles were present on the surface, the active sites could be easily discerned from the still pictures. However, after the bubbles present on adjacent sites began to merge, individual sites could not be identified. To circumvent this difficulty, preboiled subcooled distilled water was injected into the chamber along the glass wall opposite the test section. Subcooling of the water caused the mushroom structure nearly to disappear, thereby facilitating the observation of individual sites. This procedure is preferable over that used by Gaertner and Westwater (1960), since it does not change the quality of the water. However, it does have the drawback that if local subcooling is high, the liquid-vapor interface may be pushed back into the cavity. This in turn will raise the possibility of giving the appearance that a cavity has become deactivated. For the data reported in this work, the error due to deactivation is expected to be small, since wall temperature and heat flux under subcooled conditions did not change in any significant way from their values for saturated water. Also, subcooling of water injected near the heater surface was limited to only about 5 to 15 K with heat fluxes ranging from 1 to 9.3×10^5 W/m^2, and a few seconds were allowed to elapse between completion of injection and subsequent photographing of the surface. If it is assumed conservatively that at these high heat fluxes liquid retained its initial subcooling during the period a photograph was taken, using an equation similar to Eq. (3) for subcooled liquids, it is found that the size range of nucleating cavities will shrink at the most by about 6 percent.

The cumulative active site density, N_a, is determined from the number of active sites, n_a, on a given area. In partial nucleate boiling, the active sites over the total surface area of the heater were counted as long as the number density fell below 1/cm^2. Thereafter, active cavities were counted only over 1 cm^2 area of the heater. The uncertainty in measurement of active nucleation site density is estimated to be about ±20 percent. The measured number density of active nucleation sites is not considered to be affected by cavities that are in their waiting period. The waiting times were calculated to be two orders of magnitude smaller than the exposure time of the photographs.

At a given wall superheat, the size of a nucleating cavity can be obtained by using Eq. (3). For all the heat fluxes studied in this work, the second term in the denominator in Eq. (3) was always much less than unity; hence it could be neglected. If functions f_1 and f_2 are assumed to be unity, the cavity diameter D_c from the approximate form of Eq. (3) is expressed as

$$D_c = \frac{4\sigma T_{\text{sat}}}{\rho_v h_{fg} \Delta T_w} \tag{15}$$

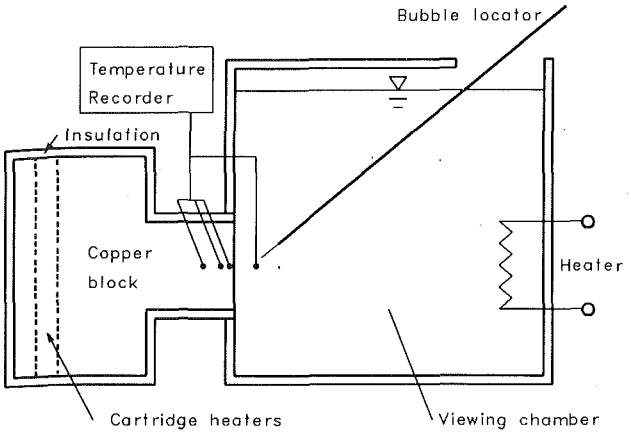

Fig. 3 Schematic diagram of experimental apparatus used for measured relationship between cavity diameter and wall superheat

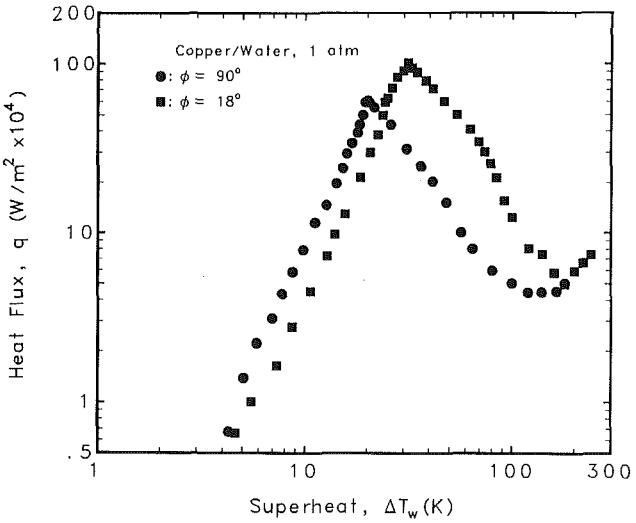

Fig. 4 Pool boiling curves for $\phi = 90$ and 35 deg

In the paragraphs that follow, an experimental apparatus and procedure that were used to verify the validity of Eq. (15) are described.

Secondary Apparatus for Identification of Active Site Characteristics. A smaller test section was designed to identify active nucleation sites, to measure incipient wall superheat during boiling, and to measure the cavity diameter and side angle of these cavities after completion of the boiling experiment. The experimental apparatus used in this study is shown in Fig. 3. The test surface is a vertical surface, is rectangular in shape, and has a width of 1.0 cm and a height of 1.0 cm. The surface was machined from one end of a copper rod of 99.9 percent purity. Three 100 W cartridge heaters are placed in the test block. Thirty gage chromel-alumel thermocouples are embedded at 1, 6, and 16 mm normal to the middle of the boiling surface. The test surface is held on one side of the viewing and liquid holding chamber. The chamber is a cubic container with a 7 cm × 7 cm × 7 cm cross section.

Identification of an Active Cavity. During the tests on the secondary surface, the active sites were identified by marking with a sharp-pointed object three points around the bubbles formed on the active sites. The incipient nucleation temperature was recorded by repeatedly increasing/decreasing the power to the heater. After reproducible incipient nucleation temperatures were recorded, the surface was removed. The active sites were clearly indicated by these three-point marks

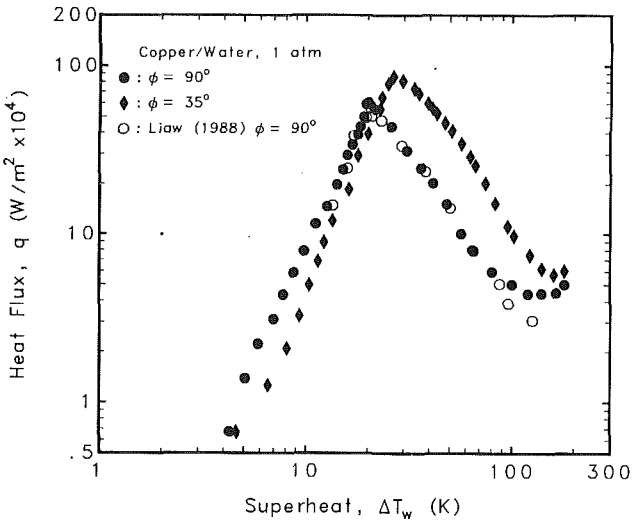

Fig. 5 Pool boiling curves for $\phi = 90$ and 18 deg

and by a small annular deposit found around them. The annular deposit could have been due either to oxidation of copper or to deposition of silica in water. The latter observation has been reported by Cornwell (1977). The surface was examined with an optical microscope and the cavity diameter and side angle were measured by following a procedure similar to that described by Wang (1992).

Results and Discussion

Heat Flux. During saturated pool boiling of water, data were taken for wall superheat, heat flux, and density of active nucleation sites. Figure 4 shows the boiling curve for contact angles of 90 and 35 deg. The reported data are for the midplane of the test surface. The nucleate boiling data were taken under steady-state conditions, whereas the transition boiling data were obtained under transient conditions. The transition boiling heat fluxes were obtained from the thermocouple data by solving the transient one-dimensional conduction equation. Details are given by Wang (1992). In Fig. 4, the data reported by Liaw (1988) for a contact angle of 90 deg are also plotted. The two sets of data nearly overlap. The maximum heat flux in this work is about 6.1×10^5 W/m^2 whereas in Liaw's experiments it was about 5.7×10^5 W/m^2. Consistent with the earlier reported results, the effect of increased surface wettability is to shift the boiling curve to the right and to enhance the maximum heat flux. The boiling curves for contact angles of 90 and 18 deg are plotted in Fig. 5. A behavior similar to that seen in Fig. 4 is observed, except that the effect of surface wettability on the boiling process is accentuated. It should be noted that experiments for a given contact angle were repeated three times. The heat flux and wall superheat data were found to be reproducible to within ±6 percent.

Nucleation Site Density—Heat Flux. A photograph of active nucleation sites for a contact angle of 90 deg and a wall heat flux of 5.7×10^5 W/m^2 is shown in Fig. 6. The white spots in Fig. 6 are the active nucleation sites. As noted in the section on experiments, the counting of the active cavities in fully developed nucleate boiling was facilitated by transiently subcooling the water. The cumulative density of active nucleation sites as determined from the experiments is plotted in Fig. 7 for contact angles of 90, 35, and 18 deg. The site density data are plotted as a function of heat flux. The data plotted in Fig. 7 show that, irrespective of the degree of wettability of the surface, the density of active nucleation sites varies approximately as

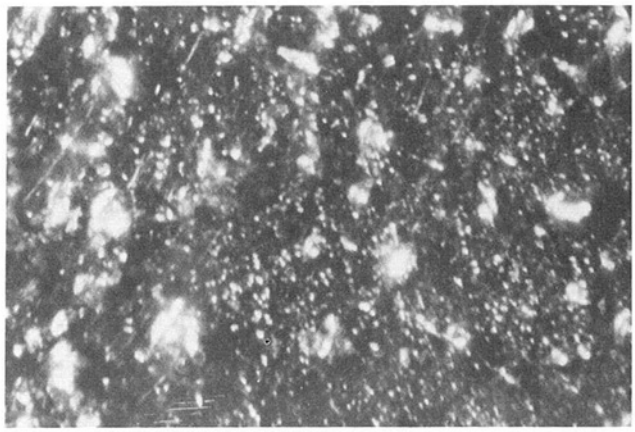

Fig. 6 Photograph of active nucleation sites for $\phi = 90$ deg, $q = 5.7 \times 10^5$ W/m^2, and area = 2.5 cm^2

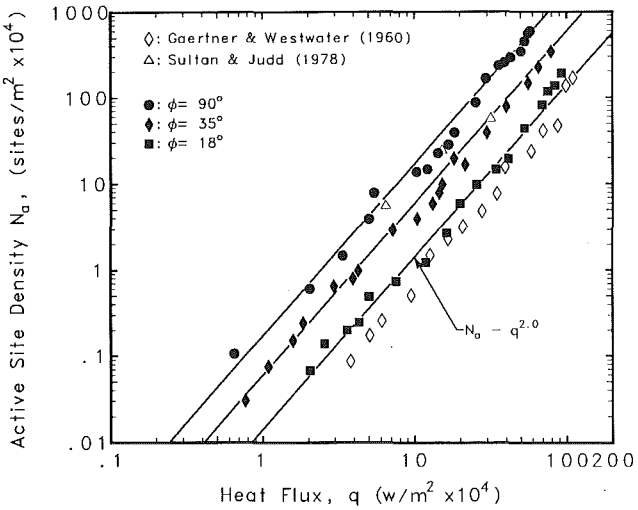

Fig. 7 Active nucleation site density versus heat flux

$$N_a \sim q^{2.0} \tag{16}$$

However, the proportionality constant in Eq. (16) depends strongly on the contact angle. For a fixed heat flux, as the contact angle is reduced from 90 to 18 deg, at least an order of magnitude reduction in the cavity site density is observed. However, the wall superheat increases by less than 40 percent. Thus a relatively small reduction in average heat transfer coefficient on the surface is associated with a very large reduction in nucleation site density. The reason for this behavior, from the analysis of Dhir and Liaw (1989), is that a large improvement in heat transfer coefficient at a nucleation site occurs as the surface becomes more wettable. The product of number density of nucleation sites and heat transfer coefficient at a given site is only a weak function of contact angle. In Fig. 7, the data obtained by Gaertner and Westwater (1960) and Sultan and Judd (1978) are also plotted. The cumulative number density of active sites observed in the experiments of Gaertner and Westwater is smaller than that found in the present experiments for $\phi = 18$ deg. However, the functional dependence of the site density on heat flux is similar to that observed in the present experiments. In the experiments of Gaertner and Westwater nickel salts were dissolved in water, and thus in their experiments the contact angle is expected to be very small. The data tend to support such an inference. The data of Sultan and Judd (1978) can be considered to be bounded by the present data for $\phi = 90$ and $\phi = 35$ deg.

Surface Cavity Diameter and Mouth Angle. The number of cavities of different sizes present over a certain area of the surface are given in Tables 1–3. The cavity effective diameters are defined by Eq. (11). Table 1 lists the cavities in size range of 55 μm to 6.5 μm. These cavities were counted on the 1.16 cm^2 area scanned with the optical microscope. The cavity mouth angles, ψ_m, of the cavities present on the surface are also shown. For cavities in the size range of 4.75 to 3.3 μm, 1.51 mm^2 area of the surface was scanned, whereas for cavities in the size range of 3.3 to 2.2 μm, the scanned area was limited to 0.0897 mm^2. Most of the deep cavities present on the surface were spherical in nature. Although a large number of conical cavities were present on the surface, these cavities were very shallow and the mouth angle ψ_m of these cavities was greater than 90 deg. According to Bankoff's criterion (1958), most of the conical cavities present on the surfaces studied in this work are not expected to nucleate. In Tables 1–3, the parameters n_s and n_{as} designate the total number of all types of cavities and the total number of reservoir-type cavities, respectively. The increments in the cavity size in sequential entries in Tables 1–3 were chosen when one additional spherical cavity was found.

The observed cumulative number density, N_s, of all types of cavities present on the surface is plotted in Fig. 8 as a function of the effective diameter, D_c^*, of the cavities. For cavities greater than 6 μm in diameter, the number density of the cavities present on the surface is observed to vary inversely with the square of the diameter of the cavity. This is in agreement with the observation of Cornwell and Brown (1978).

Table 1 Surface cavity diameter and cavity mouth angle for 6.5 μm $\leq D_c^* \leq$ 56 μm

Sample length = 8.00 mm

Sample width = 14.50 mm

Sample area = 1.16 cm^2

Magnification = 200

$D_c^*, \mu m$	n_s	n_{as}	ψ_m
55-12.46	69	0	-
12.410	70	1	59.06
10.911	95	2	72.43
10.797	96	3	82.39
10.029	108	4	28.26
8.636	121	5	83.44
8.534	122	6	48.54
8.368	124	7	63.21
8.292	126	8	68.09
7.777	129	9	39.83
7.673	130	10	40.80
6.541	131	11	39.14

Table 2 Surface cavity diameter and cavity mouth angle for 4.8 $\mu m \le D_c^* \le 3.3$ μm

Sample length = 1.761 mm

Sample width = 0.857 mm

Sample area = 1.510 mm^2

Magnification = 500

$D_c^*, \mu m$	n_s	n_{as}	ψ_m
4.739	10	1	76.66
4.412	13	2	84.73
4.392	14	3	68.64
4.214	22	4	62.03
4.145	28	5	68.23
4.049	29	6	89.48
3.932	37	7	70.16
3.872	40	8	72.00
3.797	42	9	85.74
3.582	50	10	82.42
3.577	51	11	87.12
3.529	52	12	80.87
3.420	64	13	85.60
3.418	65	14	72.22
3.350	70	15	70.23
3.345	72	16	87.14

However, for cavities smaller than 6 μm in diameter, the cumulative number density shows a much stronger dependence on the cavity diameter. The distribution of larger cavities is probably reflective of the procedure used in preparing the surface while the distribution of smaller cavities is a result of the processes used in manufacturing of copper stock. In the three size ranges, the slope of the number density of cavities present on the surface is correlated as

$$\frac{dN_s}{dD_c^*}\ (\text{sites}/(\text{cm}^2 \cdot \mu\text{m})) = \begin{cases} -1.80\times 10^4 D_c^{*\,-3.0} & D_c^* \ge 5.8\ \mu\text{m} \\ -1.25\times 10^7 D_c^{*\,-6.20} & 3.5 \le D_c^* < 5.8\ \mu\text{m} \\ -5.40\times 10^6 D_c^{*\,-6.40} & D_c^* \le 3.5\ \mu\text{m} \end{cases} \quad (17)$$

where D_c^* is measured in μm. From Eqs. (14) and (17), the number density of cavities is expressed as

Table 3 Surface cavity diameter and cavity mouth angle for 3.3 $\mu m \le D_c^* \le 2.2$ μm

Sample length = 0.345 mm

Sample width = 0.260 mm

Sample area = 0.0897 mm^2

Magnification = 1000

$D_c^*, \mu m$	n_s	n_{as}	ψ_m
3.279	3	1	50.86
2.765	5	2	84.16
2.510	8	3	70.08
2.358	12	4	63.65
2.212	15	5	88.26
2.201	17	6	68.40

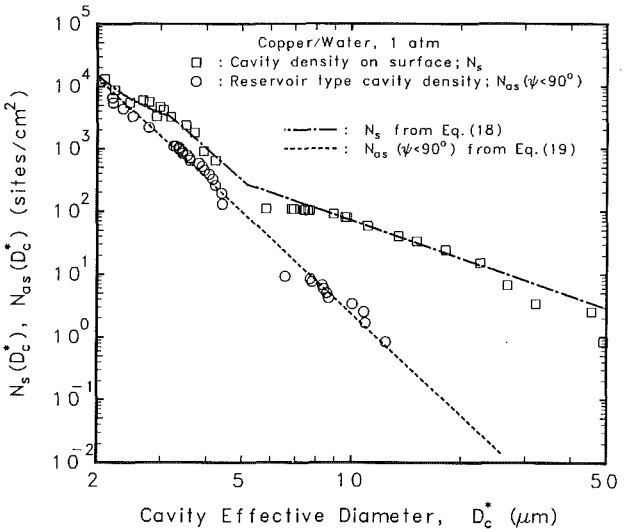

Fig. 8 Surface site density versus cavity effective diameter

$$N_s\ (\text{sites}/\text{cm}^2) = \begin{cases} 9.0\times 10^3 D_c^{*\,-2.0} & D_c^* \ge 5.8\ \mu\text{m} \\ 10.3 + 2.4\times 10^6 \cdot D_c^{*\,-5.2} & 3.5 \le D_c^* < 5.8\ \mu\text{m} \\ 2213.5 + 1.0\times 10^6 \cdot D_c^{*\,-5.4} & D_c^* \le 3.5\ \mu\text{m} \end{cases} \quad (18)$$

The cumulative number density of reservoir cavities with mouth angle less than 90 deg is also plotted in Fig. 8. For all size ranges, the cumulative number density of the reservoir cavities present on the surface can be correlated as

$$N_{as}(\psi_m < 90\ \text{deg})(\text{sites}/\text{cm}^2) = 5.8\times 10^6 D_c^{*\,-5.40} \quad (19)$$

It can be deduced from Fig. 8 that a large number of cavities with diameter greater than 5 μm are shallow cavities.

Nucleating Cavity Diameter—Wall Superheat. The active sites were identified during pool boiling using the secondary test section. After determination of the incipient nucleation temperature for a given cavity, the cavity mouth diameters

Table 4 Incipient temperature, cavity diameter, and cavity mouth angle at $\phi = 90$ deg

Run #	ΔT_w K	D_c^* μm	D_c' μm	Δh μm	ψ_m degree
3	5.22	12.52	14.54	0.96	43.54
4	6.08	10.76	12.60	1.12	50.60

Table 5 Incipient temperature, cavity diameter, and cavity mouth angle at $\phi = 35$ deg

Run #	ΔT_w K	D_c^* μm	D_c' μm	Δh μm	ψ_m degree
5	3.29	19.89	23.71	1.20	32.14
9	2.79	23.48	32.82	0.97	11.73
10	6.48	10.08	19.22	2.05	24.16

Table 6 Incipient temperature, cavity diameter, and cavity mouth angle at $\phi = 18$ deg

Run #	ΔT_w K	D_c^* μm	D_c' μm	Δh μm	ψ_m degree
12	2.50	20.26	24.18	0.50	14.31
14	8.24	8.06	11.06	0.25	9.46
14	11.83	6.33	7.75	0.20	15.73

D_c^* at the surface and D_c' after material equal to a certain depth, Δh, was removed were measured. The cavity mouth angles were calculated from the difference of these two diameters and from the thickness Δh of material removed. The results are shown in Tables 4–6 for contact angles 90, 35, and 18 deg. All of the nucleating sites are believed to be reservoir-type cavities. It should be noted here that the data reported in Tables 4–6 were generally obtained from different runs. In Fig. 9, the diameter, D_c^*, of cavities that were found to nucleate at a wall superheat ΔT_w are plotted. Since cavities were of irregular shape, shape factor f_D is introduced such that

$$D_c = f_D \cdot D_c^* \tag{20}$$

The dark symbols in Fig. 9 show D_c obtained from Eq. (20) when f_D is assumed to be 0.89. In Fig. 9, the solid line represents the relationship between D_c and ΔT_w as given by Eq. (15). It is seen that Eq. (15) correlates the data given by solid symbols. Thus it appears that when relating the wall superheat to the effective measured diameter of a cavity, the effective diameter should be multiplied by about 0.89.

Nucleation Sites Density—Cavity Diameter. Figures 10, 11, and 12 show for contact angles of 90, 35, and 18 deg, respectively, a comparison of cumulative density of cavities that are present on the surface and that actually nucleate. For a contact angle of 90 deg only 1–10 percent of the cavities

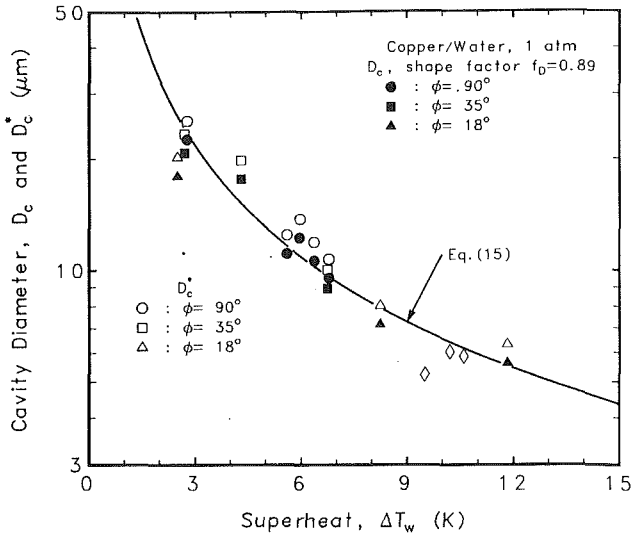

Fig. 9 Cavity diameter as a function of wall superheat for different contact angles

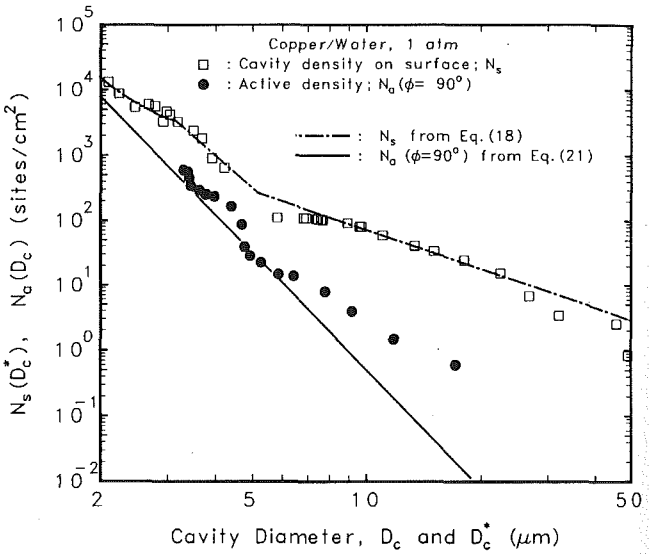

Fig. 10 Site density versus cavity diameter for $\phi = 90$ deg

present on the surface are seen to nucleate. With surface oxidation the density of cavities present on the surface is not expected to change since the oxide layer thickness was less than 0.01 μm. It is found that as the wettability of the surface improves, the number density of cavities that actually nucleate decreases. In Figs. 11 and 12, the cumulative number densities of active nucleation sites as reported by Gaertner and Westwater (1960) and Singh et al. (1978) are also plotted. Again a trend similar to that noted from the present experiments is observed. The data of Singh et al., though limited to very low superheats, appear to correspond to a contact angle of about 35 deg.

All the data plotted in Figs. 10, 11, and 12 show that number density of active nucleation sites strongly depends on the contact angle. At a given wall superheat or cavity diameter, the site density of active cavities for a contact angle of 18 deg is about 20 times smaller than that for $\phi = 90$ deg. Almost all of the active sites on surfaces having contact angles between 90 and 18 deg are correlated within ± 60 percent as

$$N_a \text{ (sites/cm}^2) = 5.0 \times 10^5 (1 - \cos \phi) \cdot D_c^{-6.0} \tag{21}$$

It should be noted here that the conservative estimate made earlier with respect to the reduction in the size range of cavities

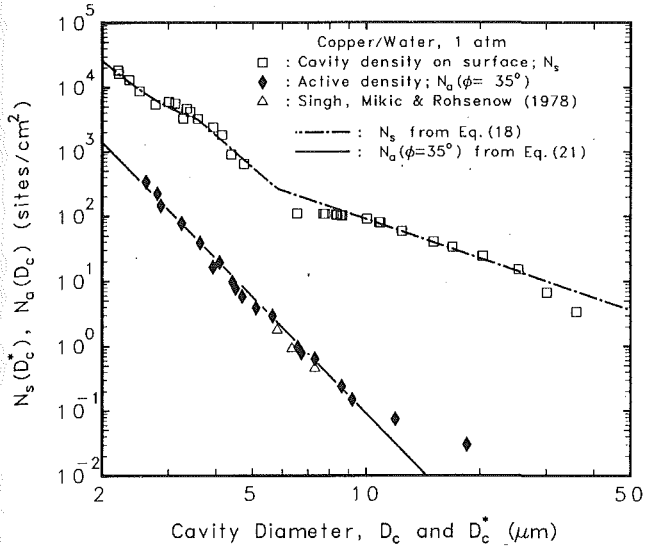

Fig. 11 Site density versus cavity diameter for $\phi = 35$ deg

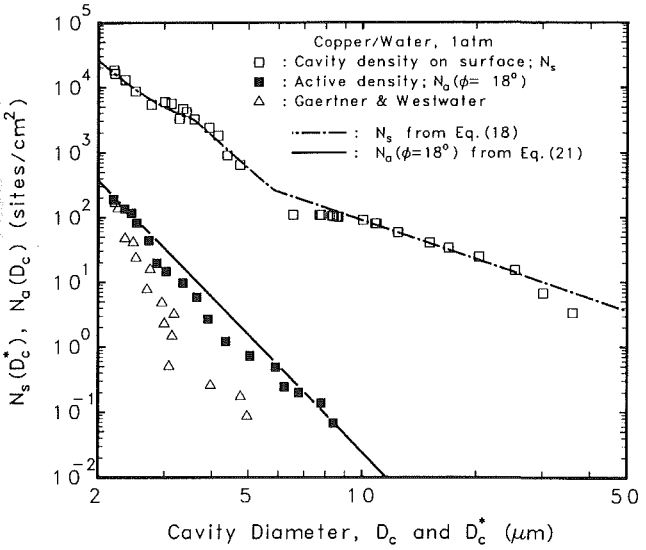

Fig. 12 Site density versus cavity diameter for $\phi = 18$ deg

(with the assumption that liquid subcooling continues to persist near the surface) can lead to at most a twofold reduction in site density.

Distribution of Nucleation Sites. The spatial distribution of active nucleation sites for a contact angle of 90 deg and heat flux of 5.7×10^5 W/m^2 is shown in Fig. 13(*a*). The 300 active nucleation sites are randomly located on a 7 mm × 7 mm area in the 49 square subdivisions. Figure 13(*b*) shows the spatial distribution of active nucleation sites for a contact angle of 35 deg and a heat flux of 6.6×10^5 W/m^2 in a 10 mm × 10 mm area. Two hundred thirty active nucleation sites are randomly located in 36 square subdivisions. Figure 13(*c*) shows the spatial distribution of active nucleation sites for a contact angle of 18 deg and heat flux of 6.9×10^5 W/m^2 in a 10 mm × 10 mm area. The 84 active nucleation sites are randomly located in 36 squares.

Many natural phenomena involving spatial distributions can be described by the Poisson distribution:

$$P_u(X) = \frac{e^{-\mu}\mu^X}{X!} \tag{22}$$

where $P_u(X)$ is the probability of occurrence of event X and

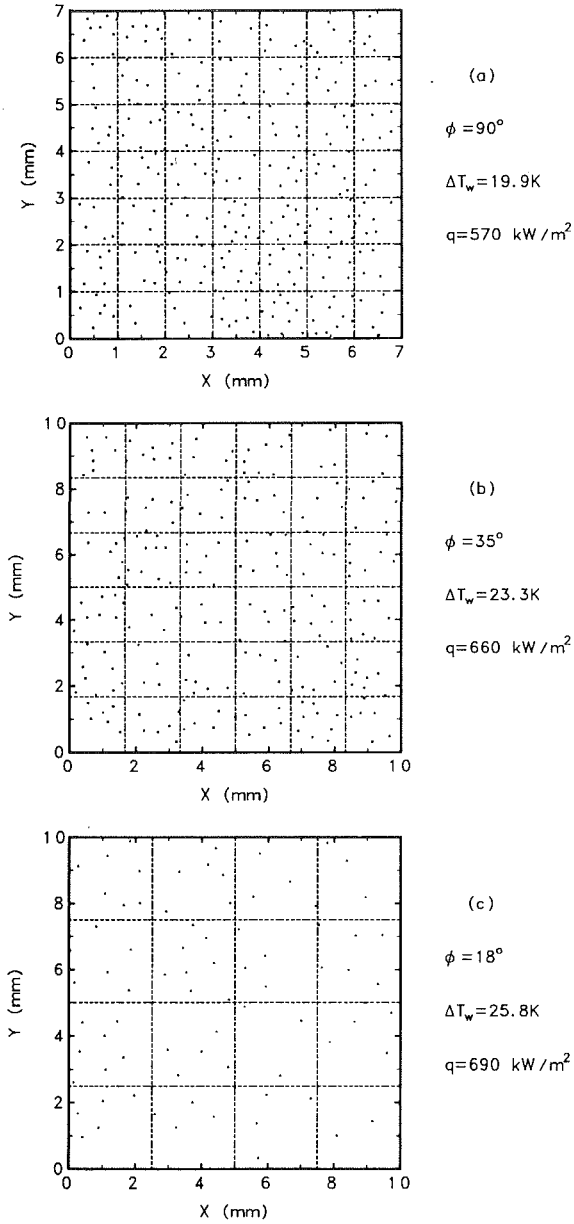

Fig. 13 Spatial distribution of nucleation sites

μ is the mean value. Consider a heater surface as shown in Fig. 13: The average number of nucleation sites in a subdivision is equal to $\bar{n}_a$. From Eq. (22) the probability of finding n_a active nucleation sites on a random subdivision is

$$P_u(n_a) = \frac{e^{-\bar{n}_a}\bar{n}_a^{n_a}}{n_a!} \tag{23}$$

Figures 14(*a*), 14(*b*), and 14(*c*) show a comparison of the data of Figs. 13(*a*), 13(*b*), and 13(*c*) with prediction from Eq. (23). The distribution of cavity population in subdivisions can be considered to be in fair agreement with the Poisson distribution for the chosen subdivisions. It is noted that on average four to six sites must lie in each subdivision, if Poisson distribution concept can be considered to be applicable.

Distribution of Nearest-Neighbor Distances. The distance between the active nucleation sites is an important parameter in boiling heat transfer analysis. The solid lines in Figs. 15(*a*), 15(*b*), and 15(*c*) show the distribution of nearest-neighbor distance deduced from Figs. 13(*a*), 13(*b*), and 13(*c*). In Fig. 15(*a*), no nucleation sites are found to lie within 0.20 mm of another

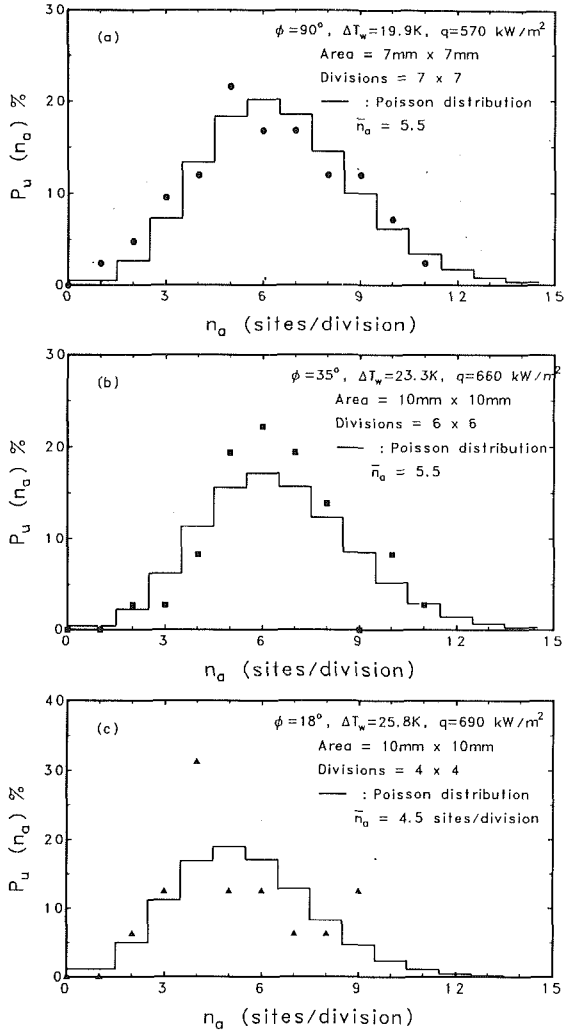

Fig. 14 Local distribution of nucleation sites

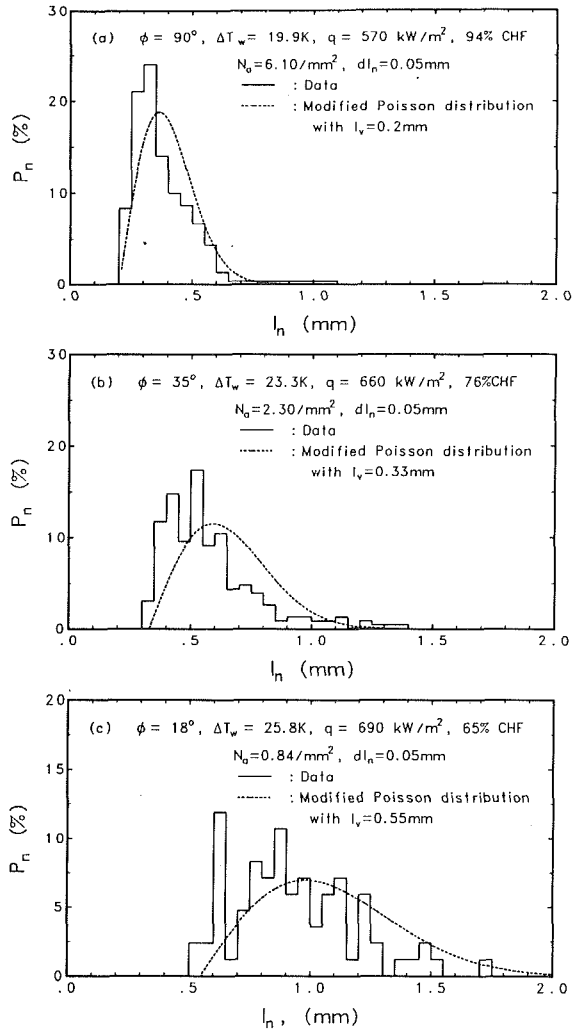

Fig. 15 Distribution of nearest-neighbor distances

active site. Similarly, no nucleation sites lie within 0.30 mm and 0.50 mm in Figs. 15(*b*) and 15(*c*), respectively. The cutoff distance l_v is approximately correlated to active site density as

$$l_v = \frac{1}{2\sqrt{N_a}} \tag{24}$$

For a Poisson distribution with a mean density N_a, the probability density P_n for the nearest-neighbor distance between l_n and $l_n + dl_n$ is given (see Gaertner, 1963) as follows:

$$P_n(l_n,\ l_n + dl_n) = 2\pi N_a \cdot l_n \cdot e^{-Na\pi l_n^2} dl_n \tag{25}$$

From the cutoff distance, the probability density P_n is modified as follows:

$$P_n(l_n,\ l_n + dl_n) = 2\pi N_a \cdot (l_n - l_v) \cdot e^{-Na\pi(l_n - l_v)^2} dl_n \tag{26}$$

When the cutoff distance l_v is equal to zero, the above equation reduces to Eq. (25).

The dashed lines in Figs. 15(*a*), 15(*b*), and 15(*c*) show the modified Poisson distribution of nearest-neighbor distance obtained from Eq. (26). It is seen that good agreement exists between the experimentally obtained distributions and the ones predicted from Eq. (26). The heat flux in Figs. 15(*a*), 15(*b*), and 15(*c*) is 94, 76, and 65 percent of maximum for contact angles of 90, 35 and 18 deg, respectively. It is seen that the closer the heat flux is to the maximum, the steeper is the distribution for the nearest-neighbor distance.

From the maximum value ($dP_n/dl_n = 0$) of the probability

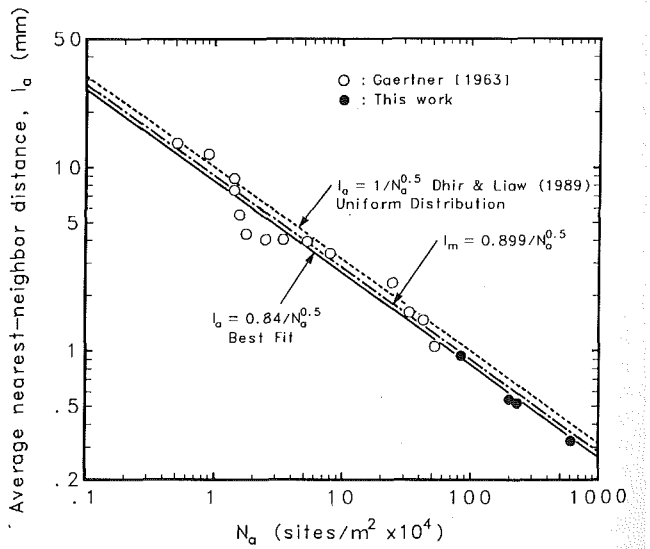

Fig. 16 Average nearest-neighbor distance l_a as a function of nucleation site density

density function in Eq. (26), the most probable nearest-neighbor distance is obtained as

$$l_m = l_v + \frac{1}{2\pi\sqrt{N_a}} = \left(\frac{1}{2} + \frac{1}{\sqrt{2\pi}}\right) \cdot \frac{1}{\sqrt{N_a}} \tag{27}$$

whereas the average nearest-neighbor distance is obtained as

$$l_a = \int_{l_v}^{\infty} l_n \cdot 2\pi N_a \cdot (l_n - l_v) \cdot e^{-Na\pi(l_n - l_v)^2} dl_n$$

$$= l_v + \frac{1}{2}\frac{1}{\sqrt{N_a}} = \frac{1}{\sqrt{N_a}} \tag{28}$$

In a square grid, the average nearest-neighbor distance is same as given by Eq. (28).

Figure 16 shows the average nearest-neighbor distances as a function of nucleation site density. It is seen that the best fit through the data yields

$$l_a = \frac{0.84}{\sqrt{N_a}} \tag{29}$$

The data taken from Gaertner (1963) are also plotted and are seen to be correlated by the above equation. The correlation shows that the square grid assumption used by Dhir and Liaw (1989) is quite reasonable.

Conclusions

1 For cavities present on the surface, three distinct distributions have been observed for $D_c^* \geq 5.80$ μm, $3.5 \leq D_c^* \leq 5.8$ μm, and $D_c^* \leq 3.5$ μm.

2 Three surfaces with contact angles of 90, 35, and 18 deg were investigated with water boiling at 1 atm. For a contact angle of 90 deg, only 1 to 10 percent of the cavities present on the surface were found actually to nucleate.

3 The fraction of the cavities that nucleate decreases as the wettability of the surface improves.

4 Irrespective of the degree of wettability of a surface, the cumulative density of active nucleation sites varies approximately as q^2. This dependence is similar to that reported in the literature by several investigators.

5 The distribution of local active cavity population densities is described by the Poisson distribution.

6 The distribution of nearest-neighbor distance is described by the modified Poisson distribution.

7 The nearest-neighbor distance is approximately equal to $0.84/\sqrt{N_a}$.

Acknowledgments

This work received support from the NSF under Grant No. CBT-88-21447.

References

Bankoff, S. G., 1958, "Entrapment of Gas in Spreading of Liquid Over a Rough Surface," *AIChE J.*, Vol. 4, pp. 24–26.

Bier, K., Gorenflo, D., Salem, M., and Tanes, Y., 1978, "Pool Boiling Heat Transfer and Size of Active Nucleation Centers for Horizontal Places With Different Surface Roughness," *Proc. 6th Int. Heat Transfer Conf.*, Toronto, Vol. 1, pp. 151–156.

Bui, T. D., and Dhir, V. K., 1985, "Film Boiling Heat Transfer on an Isothermal Vertical Surface," ASME JOURNAL OF HEAT TRANSFER, Vol. 107, pp. 764–771.

Cornwell, K., 1977, "Naturally Formed Boiling Site Cavities," *Letters in Heat and Mass Transfer*, Vol. 4, pp. 63–72.

Cornwell, R., and Brown, R. D., 1978, "Boiling Surface Topography," *Proc. 6th Int. Heat Transfer Conference*, Toronto, Vol. 1, pp. 157–161.

Del Valle, V. H., and Kenning, D. B. R., 1985, "Subcooled Flow Boiling at High Heat Flux," *Int. J. Heat Mass Transfer*, Vol. 28, No. 10, pp. 1907–1920.

Dhir, V. K., and Liaw, S. P., 1989, "Framework for a Unified Model for Nucleate and Transition Pool Boiling," ASME JOURNAL OF HEAT TRANSFER, Vol. 111, pp. 739–746.

Gaertner, R. F., and Westwater, J. W., 1960, "Population of Active Sites in Nucleate Boiling Heat Transfer," *Chem. Engr. Prog. Symp. Series*, Vol. 56, pp. 39–48.

Gaertner, R. F., 1973, "Distribution of Active Sites in the Nucleate Boiling of Liquids," *Chem. Engr. Prog. Symp. Series*, Vol. 59, pp. 52–61.

Hsu, Y. Y., and Graham, R. W., 1976, *Transport Processes in Boiling and Two-Phase Systems*, Hemisphere Publishing Corporation, Washington, DC.

Jakob, M., 1949, *Heat Transfer*, Wiley, New York.

Hsu, Y. Y., and Graham, R. W., 1976, *Transport Processes in Boiling and Two-Phase Systems*, Hemisphere Publishing Corporation, Washington, DC.

Jakob, M., 1949, *Heat Transfer*, Wiley, New York.

Liaw, S. P., 1988, "Experimental and Analytical Study of Nucleate and Transition Boiling on a Vertical Surface," Ph.D. dissertation, University of California, Los Angeles, CA.

Mikic, B. B., and Rohsenow, W. M., 1969, "A New Correlation of Pool Boiling Data Including the Effect of Heating Surface Characteristics," ASME JOURNAL OF HEAT TRANSFER, Vol. 91, pp. 245–250.

Singh, A., Mikic, B. B., and Rohsenow, W., 1978, "Relative Behavior of Water and Organics in Boiling," *Proc. 6th Int. Heat Transfer Conf.*, Toronto, Vol. 1, pp. 163–168.

Sultan, M., and Judd, R. L., 1978, "Spatial Distribution of Active Sites and Bubble Flux Density," ASME JOURNAL OF HEAT TRANSFER, Vol. 100, pp. 56–62.

Wang, C. H., 1992, "Experimental and Analytical Study of the Effects of Wettability on Nucleation Site Density During Pool Boiling," Ph.D. dissertation, University of California, Los Angeles, CA.

Yang, S. R., and Kim, R. H., 1988, "A Mathematical Model of Pool Boiling Nucleation Site Density in Terms of Surface Characteristics," *Int. J. Heat Mass Transfer*, Vol. 31, pp. 1127–1135.

On the Gas Entrapment and Nucleation Site Density During Pool Boiling of Saturated Water

C. H. Wang

V. K. Dhir

Mechanical, Aerospace, and Nuclear Engineering Department,
School of Engineering and Applied Science,
University of California, Los Angeles,
Los Angeles, CA 90024

A model to describe the effect of wettability on nucleation site density is presented. First, from Helmholtz free energy analysis, a criterion for the entrapment condition in a uniform temperature field is developed. Second, the stability condition of pre-existing gas/vapor nuclei during the heating process and the minimum superheat required to initiate nucleation are determined. The prediction of the entrapment condition and the incipient temperature are consistent with the experimental observations made on surfaces having naturally existing cavities. Third, a naturally formed cavity on a heater surface is modeled as a spherical cavity. The cumulative active nucleation site density for a specified contact angle is expressed in terms of the cumulative density of cavities existing on the surface as $N_a = P_{as} \cdot N_{as}$ *where* N_{as} *is the heater surface cumulative cavity density with cavity mouth angles less than a specified value and* P_{as} *is a function of contact angle and cavity mouth angle. The model successfully predicts active site densities for different contact angles.*

Introduction

One of the key factor missing in the prediction of nucleate boiling heat fluxes as a function of wall superheat is knowledge of the density of active nucleation sites as well as the relation that exists between active cavities and cavities that are formed on the surface as a result of surface preparation. The objective of this work is to describe quantitatively the effect of wettability on the relationship between active site density and surface site density.

Pre-existing Nuclei. Vapor bubbles are generally thought to originate from pre-existing nuclei on a heater surface. Corty and Foust (1955) found that the surface on which boiling takes place always contains irregularities and postulated that there is vapor trapped in cavities on the metallic surface. Clark et al. (1959) examined a boiling surface under a microscope and observed that the bubbles do originate from cavities on the surface. Cornwell (1977) verified with a scanning electron microscope that nucleation sites are typically cavities.

There are two predominant points of view with respect to the mechanism of entrapment of gas/vapor nuclei. One group of investigators use a graphic representation to show that the degree of gas entrapment depends on the cavity diameter and height. Any cavity in which the advancing liquid front fails to displace the gaseous phase completely can be a nucleus for bubble formation. Bankoff (1958) was the first to set a quantitative criterion for entrapment of gases in a cavity. He considered the displacement of liquid across a wedge-shaped groove. The critical parameters affecting gas/vapor entrapment in a wedge-shaped groove are the contact angle and the wedge angle. The conical cavities are approximated as wedge-shaped grooves. If the effective angle of entrapment in a conical cavity is 2β, the entrapment condition can be written as

$$\phi > 2\beta \tag{1}$$

where ϕ is the contact angle of the liquid. Lorenz (1971) employed the above entrapment condition and determined the vapor volume trapped in a conical cavity and the relative radius of a trapped bubble embryo after adjustment of the interface. He found that the bubble embryo radius, which is a function of the contact angle and the cone angle, is the effective radius for nucleation. More recently, Tong et al. (1990) have examined the influence of dynamic contact angle and contact angle hysteresis on the effective radius for nucleation. They show that contact angle hysteresis can influence the bubble growth process for moderately wetting liquids. For highly wetting liquids, this effect is small.

The second point of view is based on the thermodynamic criterion of stability. Johnson and Dettre (1963a, b) studied the effect on the contact angle of roughness of an idealized sinusoidal surface. They found that the apparent contact angle is equal to the angle corresponding to the lowest free energy and that it is impossible to entrap air in this sinusoidal surface for a contact angle of less than 90 deg. Ward and Forest (1976) analyzed the relation between platelet adhesion and the roughness of a synthetic biomaterial. They found that an equilibrium gas/vapor nucleus is stable in a long narrow fissure if the contact angle and conical angle satisfy the following condition:

$$\phi > 90 \text{ deg} + \beta \tag{2}$$

where β is the half wedge angle. Cornwell (1982) has argued that roughness of the cavity surface can cause contact angle hysteresis and a flip-over (concave to convex interface into fluid) of the interface within the cavity. This in turn can lead to the effective radius of the cavity being smaller than the radius of the mouth of the cavity. Thus he provided an alternate mechanism for gas/vapor trapping in conical cavities present on a hydrophilic surface, which according to Eq. (2) will not trap gas.

Inception. Griffith and Wallis (1960) investigated the superheat needed for incipient boiling from pre-existing nuclei. They found that the minimum superheat corresponded with the minimum radius of curvature, which is equal to the radius of the cavity mouth. Applying the Clausius–Clapeyron equation, they obtained an expression for inception superheat as

$$\Delta T_w = \frac{4\sigma T_{\text{sat}}}{\rho_v h_{fg} D_c} \tag{3}$$

where D_c is the cavity mouth diameter. However, they also found that the minimum superheat needed for pre-existing nuclei with cavity diameters about 69 μm was higher than that predicted from the above equation.

Contributed by the Heat Transfer Division and presented at the National Heat Transfer Conference, San Diego, California, August 9–12, 1992. Manuscript received by the Heat Transfer Division May 1992; revision received December 1992. Keywords: Boiling, Phase-Change Phenomena. Associate Technical Editor: T. W. Simon.

The effect of temperature profile adjacent to the heated surface on the minimum superheat needed for nucleation was developed by Hsu (1962). According to his criterion, a cavity will activate when the liquid temperature at the top of the vapor embryo is at least equal to the saturation temperature corresponding to the pressure in the bubble embryo. By assuming the temperature profile in the thermal layer is linear and the bubble embryo is part of a sphere, the wall superheat required for a cavity of mouth diameter, D_c, can be obtained as

$$\Delta T_w = \frac{\dfrac{4f_1\sigma T_{\text{sat}}}{\rho_v h_{fg} D_c}}{\left[1 - \dfrac{f_2}{2f_1}\cdot\dfrac{D_c}{\delta}\right]} \tag{4}$$

The thermal layer thickness, δ, depends on system variables. The constants f_1 and f_2 can be written as

$$f_1 = \sin(\phi + \alpha_m) \tag{5}$$

$$f_2 = 1 + \cos(\phi + \alpha_m) \tag{6}$$

where ϕ is the contact angle and α_m is the slope of the cavity mouth as shown in Fig. 1. The slope of cavity mouth α_m is unknown and has to be determined empirically. Using a specified value of thermal layer, Hsu showed that Eq. (4) describes fairly well the required wall superheat for the Griffith and Wallis data. For cavity diameter, D_c, much less than the thickness of the thermal layer, δ, the second term in the denominator in Eq. (4) is much smaller than unity and thus can be neglected.

For a better understanding of the mechanism by which pre-existing nuclei grow as vapor bubbles, Mizukami (1975) proposed that the vapor nuclei in a cavity are stable if the curvature of the interface increases with an increase in vapor volume. He showed that the incipience of boiling corresponds to a critical point of instability at the vapor–liquid interface. Forest (1982) attempted to analyze the equilibrium and stability of a gas/vapor nucleus inside a conical cavity by using the concept of *critical radius* for a dilute solution of a gas in a liquid. Forest showed that a pre-existing nucleus begins to grow spontaneously when the radius of curvature of the liquid–gas interface reaches a local minimum value. Nishio (1985) also attempted to prove the stability of a pre-existing vapor nucleus from a thermodynamic viewpoint. In Nishio's analysis, the

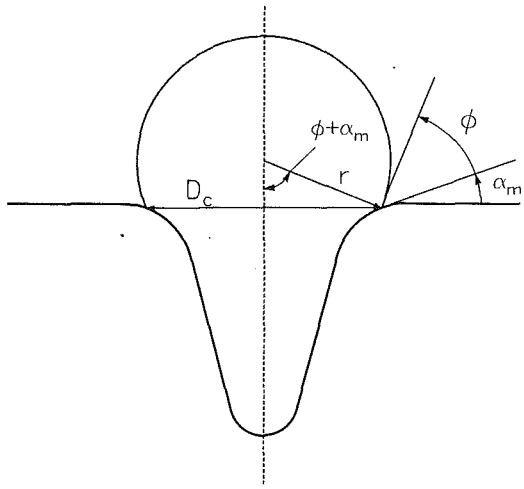

Fig. 1 Bubble nucleus at a cavity mouth

Nomenclature

A = interface area
D_c = cavity mouth diameter
D_s = maximum surface cavity diameter
f = function defined by Eqs. (7) and (8)
f_1, f_2 = constant in Eq. (4), a function of contact angle
f_s = probability density function
F = Helmholtz free energy
F_s = probability distribution defined by Eq. (37)
h_{fg} = latent heat of evaporation
K = nondimensional modified curvature
M = molecular weight
n = number of moles
n_i = number of moles of component i
N_a = active nucleation site density
N_{as} = surface cavity density with cavity mouth angle less than ψ
N_s = surface cavity density
p = pressure
p^* = nondimensional amount of gas in a vapor bubble nucleus
P_a = normalized function defined by Eq. (46)
P_{as} = normalized function defined by Eq. (44)
P_F = ratio of probability distribution
P_s = normalized function defined by Eq. (41)
P_t = normalized function defined by Eq. (47)
r = radius of liquid–gas interface or a radial coordinate
r_c = mouth radius of a cavity
r_d = radius of liquid drop outside cavity
r_f = radius of liquid front
r_s = radius of spherical cavity
s = statistical parameter
T_{sat} = saturation temperature
T_w = wall temperature
V_d = volume of liquid drop outside cavity
V_c = volume of a cavity
V_b = volume of bubble nucleus
V_i = volume of liquid inside cavity
V_l = total volume of liquid drop $= V_d + V_i$
V_o = volume of entrapped gas/vapor
V^* = nondimensional volume of vapor bubble nucleus $= V_b/V_c$
x = mole fraction of gases in gas/vapor mixture
X, Y = coordinate
α_s = slope of solid surface
β = cone half angle
$\bar{\beta}$ = mean value of cone half angle
γ = interfacial tension of an interface
ΔF = relative Helmholtz free energy between 1 and 2 states
ΔF^* = nondimensional relative Helmholtz free energy between 1 and 2 states
ΔT_w = wall superheat
θ = angular coordinate of liquid–gas interface on/in cavity
θ_s = angular coordinate in a spherical cavity
λ = statistical parameter
μ = chemical potential energy
ρ_l = density of liquid
ρ_v = density of vapor
σ = surface tension
ϕ = contact angle
ψ = cavity side angle
ψ_m = cavity mouth angle

Superscripts

la = liquid–gas/vapor interface
o = reference
sl = solid–liquid interface
sa = solid–gas/vapor interface

Subscripts

1 = liquid front state 1
2 = liquid front state 2
g = gases
l = liquid
max = maximum
min = minimum
v = vapor

assumption that the area of the liquid–vapor interface is proportional to the curvature of liquid–vapor interface is unreasonable.

Active Nucleation Site Density. Recently Yang and Kim (1988) have made the first attempt to predict quantitatively the active nucleation sites from the knowledge of the size and cone angle distribution of cavities that actually are present on the surface. Using a scanning electron microscope (SEM) and a differential inference contrast microscope (DIC), Yang and Kim (1988) obtained the cavity probability density function in terms of the cavity diameter and cone angle. The cone angle was determined by knowing the cavity diameter and depth. For cavities with mouth diameters varying from 0.65 to 6.2 μm, the cavity size distribution was found to fit a Poisson distribution

$$f(D_c) = \lambda e^{-\lambda D_c/2} \tag{7}$$

whereas a normal distribution was used for cone half angle β,

$$f(\beta) = [(2\pi)^{1/2} s]^{-1} \exp[-(\beta-\bar{\beta})^2/(2s^2)] \tag{8}$$

In Eqs. (7) and (8), λ and s are the statistical parameters and $\bar{\beta}$ is the mean value of the cone half angle. To determine the number of cavities that will trap gas or vapor and eventually become nucleation sites, they used the criterion developed by Bankoff (1958). Thus integrating Eq. (8) from 0 to $\phi/2$ represents the percentage of surface cavities that will trap gas/vapor. Combining Eqs. (7), (8), and (1), the cumulative density of active nucleation sites was expressed as

$$N_a = \bar{N}_s \int_0^{\phi/2} [(2\pi)^{1/2} s]^{-1} \exp[-(\beta-\bar{\beta})^2/(2s^2)] d\beta \times \int_{D_c}^{D_s} \lambda e^{-\lambda D_c/2} dD_c \tag{9}$$

The ratio of the cumulative density of active nucleation sites for two different contact angles ϕ and ϕ_o can be expressed as

$$P_a = \frac{\int_0^{\phi/2} f(\beta) d\beta}{\int_0^{\phi_o/2} f(\beta) d\beta} \tag{10}$$

In Eq. (9), $\bar{N}_s$ is the average density of cavities present on the surface and D_s is the diameter of the largest cavity present on the surface and is obtained from statistical considerations. The magnitude of these parameters depends on the heater material and on the procedure used to prepare the surface. The predicted active nucleation site density was found to compare well with the data obtained at very low wall superheats. Although the scope of their study was limited, it represents a rational approach to a very difficult problem. The use by Yang and Kim (1988) of a Poisson distribution function for the cavities that exist on a polished surface follows Gaertner's (1963) observation that active nucleation sites are randomly located and could be represented by a Poisson distribution. However, transformation from the size distribution of cavities present on the surface to the density of sites that actually become active may be affected by several other parameters not included in the analysis of Yang and Kim (1988).

In the present work, a relationship between cavities that are present on the surface and that actually become active is developed through analysis. The results of the analysis are verified with the experimental data obtained by the present authors and reported in the companion paper. The analytical work consists of three parts. First, the process of gas/vapor entrapment in cavities to form pre-existing nuclei is studied. Second, the activation of pre-existing nuclei and the required minimum superheat are analyzed. Last, a probability distribution function for finding cavities with a specified mouth angles is found. In the analysis, the surface microgeometry is modeled as part of a sphere. The support for this assumption is derived from the measured shape of cavities found on a very smooth surface and reported in the companion paper. The majority of deep cavities found on the surface appeared to be segments of a sphere (reservoir type) rather than conical cavities as has been assumed in previous studies.

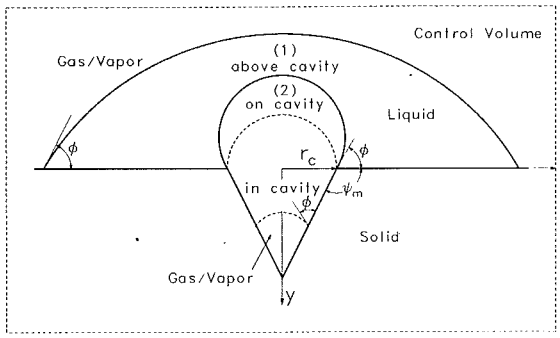

Fig. 2 Positions of liquid front in the control volume

Analysis

The density of active nucleation sites as a function of wall superheat is the key parameter required in order to relate boiling heat fluxes to wall superheat. Under the assumption that cavities that trap gas or vapor are the potential nucleation sites, in this work the change in the Helmholtz function for liquid/gas interface in cavities present on the surface is first evaluated. Thereafter a gas/vapor entrapment condition involving the cavity side angle and the contact angle is developed. The superheat for nucleation of a pre-existing gas/vapor nucleus is determined from the thermodynamic analysis and is shown to be a function of cavity diameter, gas mole fraction, and contact angle. Based on the experimental observations reported in the companion paper (Wang and Dhir, 1993), naturally formed cavities on very smooth heater surface are modeled as spherical cavities. From the analysis, the nucleation site density can be theoretically expressed as a function of wall superheat, contact angle, and density of cavities present on the surface. In order to verify the gas/vapor entrapment and the incipience criterion, the cavity diameter, cavity mouth angle, and incipient superheat data given by Wang (1992) and documented in the companion paper are used.

Pre-existing Nuclei. In developing the gas/vapor entrapment criterion, a system consisting of a droplet placed on a cavity with the free surface of the droplet exposed to gas/vapor is assumed. The droplet axis coincides with the axis of the cavity and the radius of the droplet is much larger than the radius of the cavity. It is also assumed that the liquid is substantially nonvolatile and all of the components in the system are at same temperature. An order of magnitude analysis reveals that the contribution to Helmholtz free energy of work done due to gravitational force is much smaller than that due to surface tension. Hence it is neglected. Figure 2 shows the entire system. The interface position is termed *above the cavity* when the contact line is formed on the surface containing the cavity. At the contact line, the contact angle, ϕ, is defined with the axis, X, as shown in Fig. 2. The interface is termed *on the cavity* when the contact line forms on the mouth of the cavity. For this case, the intrinsic contact angle, ϕ, is defined with a plane containing the triple point. When the three-phase contact line forms on the interior surface of the cavity, the interface is termed *in the cavity*. Under these assumptions, any change in Helmholtz free energy can be written as

$$dF = \gamma dA \tag{11}$$

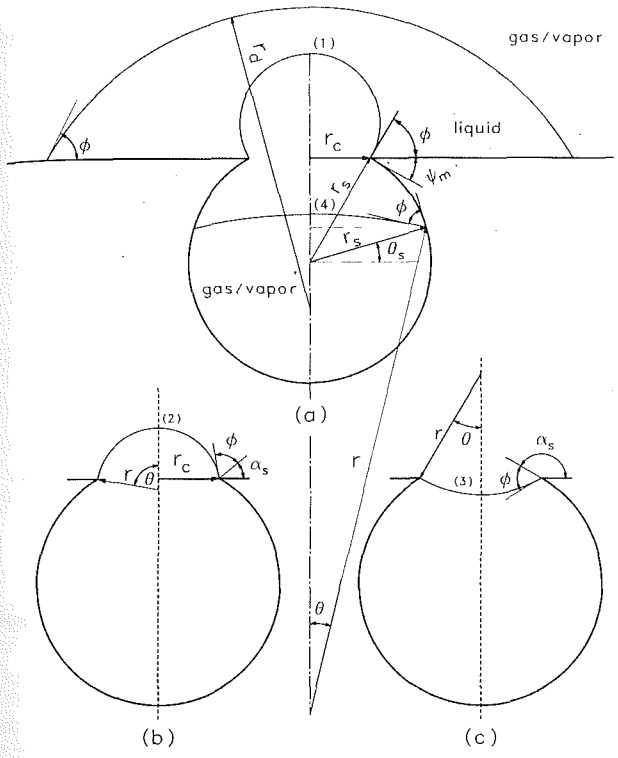

Fig. 3 Interface positions in and on a spherical cavity

The change in the Helmholtz free energy between any two positions 1 and 2 of the interface can be written as

$$\Delta F = \gamma^{la}(A_2^{la} - A_1^{la}) + \gamma^{sl}(A_2^{sl} - A_1^{sl}) + \gamma^{sa}(A_2^{sa} - A_1^{sa}) \quad (12)$$

where γ^{la}, γ^{sl}, and γ^{sa} represent the liquid–air, solid–liquid, and solid–air interfacial tensions, respectively, and A^{la}, A^{sl}, and A^{sa} represent the total areas of liquid–air, solid–liquid and solid–air interfaces, respectively.

The increase in the area of the solid–liquid interface is the same as the decrease in the area of the solid–air interface:

$$A_2^{sl} - A_1^{sl} = -(A_2^{sa} - A_1^{sa}) \quad (13)$$

In Young's equation, it is assumed that at an equilibrium position the force pushing the three-phase line of contact to the right is equal to that pushing it to the left. Thus, $\gamma^{la}\cos\phi + \gamma^{sl} = \gamma^{sa}$, or

$$\cos\phi = \frac{\gamma^{sa} - \gamma^{sl}}{\gamma^{la}} \quad (14)$$

where ϕ is the static contact angle. In the present work static angle is assumed to represent a mean between advancing and receding contact angles. Combining Eqs. (12), (13), and (14), the change in dimensionless Helmholtz free energy between any two positions is written as

$$\Delta F^* = \frac{\Delta F}{r_c^2 \gamma^{la}} = [(A_2^{la} - A_1^{la}) + (A_1^{sl} - A_2^{sl}) \cdot \cos\phi]/r_c^2 \quad (15)$$

As has been assumed by Harkins (1952), the equilibrium condition is the one for which the Helmholtz free energy is minimum. By calculating the Helmholtz free energy for different positions of the liquid–gas/vapor interface while keeping the total volume of the gas/vapor and liquid constant, the position corresponding to the minimum free energy can be found. If in the absence of a minimum the free energy continues to decrease, the liquid front can move to the bottom of the cavity and flood it. Otherwise, the liquid front will attain a minimum free energy position and entrap the gas/vapor present in the cavity.

Evaluation of Change in the Helmholtz Function for a Spherical Cavity. Figure 3 shows several positions of the liquid–gas interface on the mouth of the cavity and in the cavity. Positions (1), (2), and (3) are on the cavity with the interface being convex above the cavity in positions (1) and (2). For position (3) the interface is convex into the cavity. The interface location in the cavity is shown by position (4). When the liquid–gas interface is on the cavity mouth, the change from position (1) to (3) occurs while keeping the intrinsic contact angle, ϕ, constant. To maintain the intrinsic contact angle constant, the slope α_s of the pseudosolid surfaces passing through the triple point varies between 0 and $\pi - \psi_m$. When the liquid–gas interface position changes in the cavity, the contact angle also remains constant. However, the angular position, θ_s, varies from $\pi/2 - \psi_m$ to $-\pi/2$ as the interface moves from the mouth to the bottom of the spherical cavity. For a specified contact angle, ϕ, cavity mouth radius, r_c, and cavity mouth angle, ψ_m, the interface position on and in the cavity is defined by independent parameters α_s and θ_s, respectively. The dependent parameters are θ, r_s, r, and r_d and can be defined in terms of the independent and specified parameters as

$$\theta = \begin{cases} \pi - \phi - \alpha_s & \text{on cavity} \\ \pi/2 - \phi - \theta_s & \text{in cavity} \end{cases} \quad (16)$$

$$r_s = r_c / \sin\psi_m \quad (17)$$

$$r = \begin{cases} r_c/\sin\theta = r_c/\sin(\alpha_s + \phi) & \text{on cavity} \\ r_s \cdot \cos\theta_s/\sin\theta = r_c \cdot \cos\theta_s/\cos(\phi + \theta_s) \cdot \sin\psi_m & \text{in cavity} \end{cases} \quad (18)$$

The radius, r_d, of the liquid drop changes with the volume of the liquid that remains outside the cavity. For a fixed total liquid volume V_l, the liquid volume outside the cavity changes by the volume of the liquid, V_i, that is in the cavity. Therefore r_d can be written as

$$r_d = \left\{ \frac{3(V_l - V_i)}{\pi[2 - \cos\phi(\sin^2\phi + 2)]} \right\}^{1/3} \quad (19)$$

For a convex liquid/gas interface on the cavity, the volume, V_i, is negative and is given by

$$V_i = -\int_0^{\theta} \pi (r\sin\theta)^2 \cdot r\sin\theta d\theta$$

$$= -\frac{\pi r_c^3}{3\sin^3(\phi + \alpha_s)} \times [\cos(\phi + \alpha_s)(\sin^2(\phi + \alpha_s) + 2) - 2] \quad (20)$$

Similarly, for either a convex or a concave interface inside the cavity, the liquid volume, V_i, is written as

$$V_i = \int_{\theta_s}^{\pi/2 - \psi_m} \pi (r_s\cos\theta_s)^2 \cdot r_s\cos\theta_s d\theta_s - \int_0^{\theta} \pi (r\sin\theta)^2 \cdot r\sin\theta d\theta$$

$$= \frac{\pi r_s^3}{3}[\cos\psi_m(\sin^2\psi_m + 2) - \sin\theta_s(\cos^2\theta_s + 2)] + \frac{\pi r^3}{3}[\sin(\phi + \theta_s)(\cos^2(\phi + \theta_s) + 2) - 2] \quad (21)$$

The total liquid–gas interface area, including the surface of the droplet, is obtained as

$$A^{la} = \int_0^{\phi} 2\pi r_d \sin\phi \cdot r_d d\phi + \int_0^{\theta} 2\pi r\sin\theta \cdot r d\theta$$

$$= \overbrace{2\pi r_d^2(1 - \cos\phi)}^{\text{outside cavity}} + \overbrace{2\pi r^2(1 - \cos\theta)}^{\text{inside cavity}} \quad (22)$$

The parameters r_d, r, and θ are obtained from Eqs. (19), (18), and (16), respectively. The expression for the solid–liquid in-

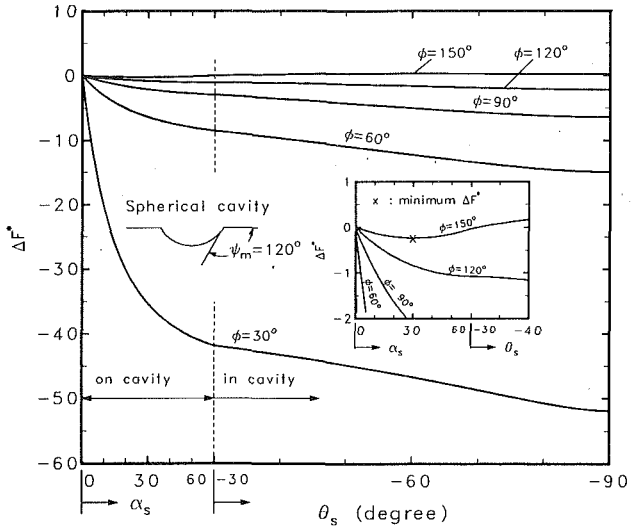

Fig. 4 Change in ΔF^* for a spherical cavity with $\psi_m = 120$ deg

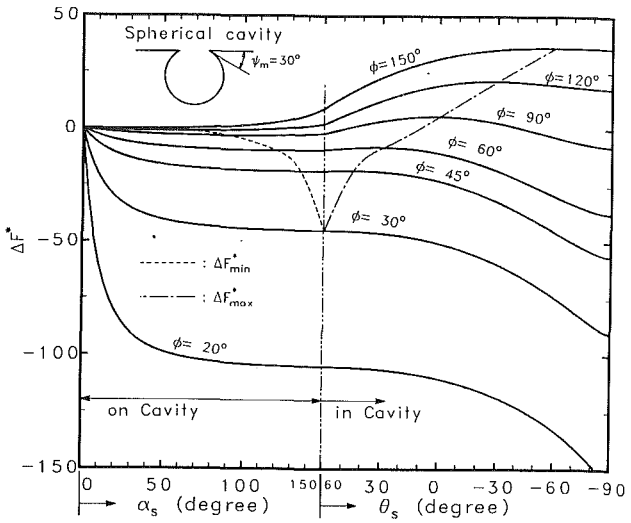

Fig. 5 Change in ΔF^* for a spherical cavity with $\psi_m = 30$ deg

terface area A^{sl} when the liquid-gas interface is on the cavity is written as

$$A^{sl} = \pi (r_d \sin\phi)^2 - \pi r_c^2 \tag{23}$$

Similarly when the liquid-gas interface is in the cavity, the total solid-liquid interface area A^{sl}, including the area in the spherical cavity, is obtained as

$$A^{sl} = \pi (r_d \sin\phi)^2 - \pi r_c^2 + \int_{\theta_s}^{\pi/2-\psi_m} 2\pi r_s \cos\theta_s \cdot r_s d\theta_s$$
$$= \pi (r_d \sin\phi)^2 - \pi r_c^2 + 2\pi r_s^2 (\cos\psi_m - \sin\theta_s) \tag{24}$$

Choosing the initial state of the interface when $\alpha_s = 0$, the change in the Helmholtz function as the interface moves from outside to inside the cavity can be obtained by substituting Eqs. (22) and (23) or (24) into Eq. (15).

Metastable Location of Liquid Front in a Spherical Cavity. The change in nondimensionalized free energy as the liquid front moves into the cavity from above the cavity is plotted in Fig. 4 for a spherical cavity with a mouth angle, $\psi_m = 120$ deg. For the interface position on the cavity, the angular position, α_s, changes from 0 to 60 deg. However, when the interface is in the cavity θ_s changes from -30 to -90 deg. The change in free energy is plotted for contact angles of 30, 60, 90, 120, and 150 deg. For a contact angle $\phi = 30$ deg, the Helmholtz free energy decreases continuously as the liquid front progresses downward into the cavity. Hence no gas/vapor is predicted to be trapped in such a cavity. The same is true for contact angles of 60 and 90 deg. When the contact angle is the same as the cavity mouth angle, i.e., 120 deg, $d\Delta F^*/d\alpha_s = 0$ at $\alpha_s = 60$ deg. But since $d^2\Delta F^*/d\alpha_s^2 < 0$, the liquid front cannot remain at this position but continuously moves downward to the bottom of the cavity. Hence no gas/vapor will be trapped for a contact angle of 120 deg as well. When the contact angle is 150 deg (greater than the cavity mouth angle), a local minimum in the free energy occurs at $\alpha_s = 30$ deg. The liquid front thus will continue to move downward until it reaches the position of minimum energy. Thereafter the interface can not move farther downward because such a movement will require an increase in free energy (decrease in entropy). Thus in this case the cavity will trap gas/vapor.

Changes in free energy for a spherical cavity with mouth angle, $\psi_m = 30$ deg, are plotted in Fig. 5 for several contact angles. When the liquid-gas interface is on the cavity, α_s varies from 60 to -90 deg. For contact angles of 20 and 30 deg (which are smaller than or equal to the contact angle), the relative free energy decreases continuously as the interface moves from the top to the bottom of the cavity. As a result no gas/vapor will be trapped for these contact angles. For contact angles of $\phi = 60$, 90, 120, and 150 deg, the free energy decreases as the liquid front moves toward the cavity and reaches a minimum value at $\alpha_s = 180 - \phi$ deg. Thereafter the free energy increases. After the free energy reaches a maximum value at $\theta_s = 90 - \phi$ deg, the free energy decreases again. Thus for the conditions assumed in carrying out the analysis, the movements of the liquid front from above the cavity will stop when minimum free energy condition is achieved and gas/vapor will be trapped in the cavity. The movement of the interface beyond the minimum free energy condition is only possible if heat transfer takes place across the boundaries of the control volume.

Similar analyses for the conical and sinusoidal cavities are given by Wang (1992).

Gas Entrapment Criterion. From the above discussion, it is found that for a contact angle ϕ larger than the minimum cavity side angle ψ_{min}, the ΔF^* has a minimum value *on/in cavity*. When α_s approaches $+(180 - \phi)$ deg, the radius of the liquid-gas interface inside the cavity approaches $+\infty$ and the meniscus of the liquid front turns from convex to concave as shown by solid lines for cases (1), (2), and (3) in Fig. 6. For these interface positions, $d\Delta F^*/d\alpha_s = 0$ and $d^2\Delta F^*/d\alpha_s^2 > 0$. Therefore, there is a minimum value of ΔF^* and gas/vapor will be entrapped. Otherwise, for a contact angle ϕ smaller than or equal to the minimum cavity side angle ψ_{min}, the liquid-gas interface is always convex as shown in cases (4), (5), and (6) of Fig. 6. Now ΔF^* continuously decreases for interface positions from above the cavity to the bottom of the cavity and gas/vapor can not be trapped. Therefore, the condition for entrapment of gas can be stated as:

$$\phi > \psi_{min} \tag{25}$$

where ψ_{min} is the minimum cavity side angle of a spherical, conical, or sinusoidal cavity. For the spherical and conical cavities, ψ_{min} occurs at the mouth of the cavity and is equal to the mouth angle ψ_m. For the sinusoidal cavity, the minimum side angle ψ_{min} is located at the radius of liquid front, r_f, which is equal to the half of the mouth radius r_c. As such the minimum side angle for a sinusoidal cavity lies in the cavity rather than at the mouth of the cavity. In summary, if and only if Eq. (25) is satisfied, the interface attains a position for which free energy is a minimum, and gas/vapor is entrapped. The above entrapment criterion can also be applied to other cavity shapes. As long as cavities present on the surface can be subdivided into the three basic geometries described above, the gas en-

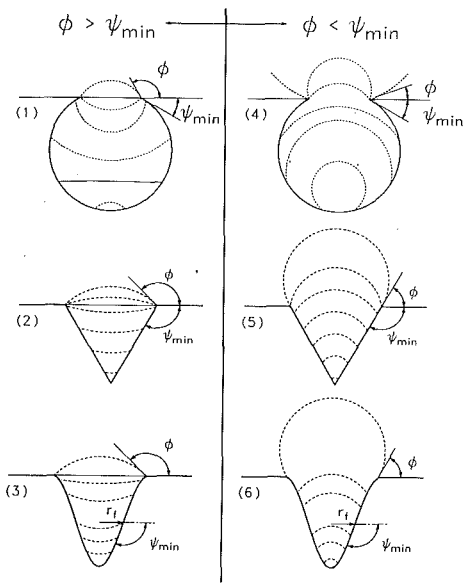

Fig. 6 Different liquid-gas interface locations in spherical, conical, and sinusoidal cavities

trapment criterion can be used to determine the fractions of these cavities that will trap gas. The analysis will not be valid for surfaces that have scratch marks or rough abrasions or to commercially enhanced surfaces that have secondary cavities.

Next we determine the superheat that is needed to nucleate a cavity that has trapped gas or vapor.

Nucleation Criterion. The equation for mechanical equilibrium between a liquid and a gas and vapor mixture in a cavity is given by

$$p_v + p_g - p_l = \frac{2\sigma}{r} \tag{26}$$

where p_g, p_v, p_l, r, and σ are the partial pressure of the gases, the vapor pressure, the pressure in the liquid, the radius of curvature of the liquid–vapor interface, and the surface tension, respectively. If it is assumed that the size of the nucleating cavity is much smaller than the thickness of the thermal layer on the heated surface, the vapor superheat in the embryo can be assumed to be approximately equal to the wall superheat. This assumption will break down at very high heat fluxes or superheats. For small pressure differences between vapor and liquid, the difference $(p_v - p_l)$ is related to the temperature difference ΔT_w, which is obtained by using the Clausius–Clapeyron equation:

$$\Delta T_w = \frac{T_{sat}}{\rho_v h_{fg}} \left(\frac{2\sigma}{r} - p_g \right) \tag{27}$$

The interface is stable if an infinitesimal disturbance in ΔT_w in either the gaseous phase or the wall temperature leads to a change in the curvature of the liquid–vapor interface and in the partial pressure of gases $(2\sigma/r - p_g)$ of similar sign, i.e.,

$$\frac{d}{dT_w}\left[\frac{2\sigma}{r} - p_g \right] > 0 \tag{28}$$

The above equation can also be written as

$$\frac{dV_b}{dT_w} \cdot \frac{d}{dV_b}\left[\frac{2\sigma}{r} - p_g \right] > 0 \tag{29}$$

If, during the disturbance, the amount of gases in the vapor bubble nucleus remains constant, the change in vapor volume, dV_b, will have the same sign as the temperature difference dT_w (see Wang, 1992). Thus the stability criterion for a vapor bubble nucleus is expressed as

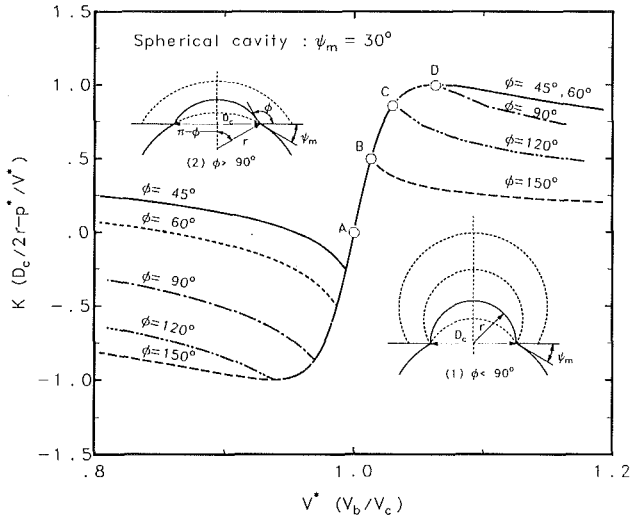

Fig. 7 Dimensionless modified curvature as a function of dimensionless volume of vapor bubble nucleus in a spherical cavity

$$\frac{d}{dV_b}\left[\frac{2\sigma}{r} - p_g \right] > 0 \tag{30}$$

The gases in the cavity originate from the entrapment process and/or the diffusion from the liquid according to Henry's law. The partial pressure of the gases can be expressed as

$$p_g = x\frac{p_o V_c}{V_b} \tag{31}$$

where x, p_o, V_c, and V_b are the initial mole fraction of gases in the gas/vapor mixture contained in V_c, system pressure, the volume of the cavity, and the volume of bubble embryo, respectively. Substituting Eq. (31) into Eq. (27) yields

$$\Delta T_w = \frac{4\sigma T_{sat}}{\rho_v h_{fg} D_c}\left(\frac{D_c}{2r} - x\frac{p_o D_c}{4\sigma} \cdot \frac{V_c}{V_b} \right) \tag{32}$$

Defining nondimensional volume of bubble embryo as $V^* = V_b/V_c$, nondimensional pressure of gases in the mixture as $p^* = xp_oD_c/4\sigma$, and nondimensional modified curvature as $K = D_c/2r - p^*/V^*$, Eq. (32) can be written as

$$\Delta T_w = \frac{4\sigma T_{sat}}{\rho_v h_{fg} D_c} K \tag{33}$$

Also, the stability criterion, Eq. (30), can be rewritten as

$$\frac{dK}{dV^*} > 0 \tag{34}$$

The stability criterion for vapor bubble embryo growth can be stated as follows: The vapor bubble nucleus is stable or quasi-stable if the nondimensional modified curvature K increases with an increase in nondimensional volume change of vapor bubble nucleus V^*; or if it decreases with a decrease in V^*. Otherwise, the vapor bubble nucleus is unstable. The minimum wall superheat required will correspond to the value of K for which the interface is unstable. Figure 7 shows, for a spherical cavity with mouth angle 30 deg, the nondimensional modified curvature of the interface as a function of the nondimensional volume of vapor bubble nucleus. The plotted results are for different contact angles and in the absence of any gas. The curvature of liquid–gas interface is negative for V^* just less than that corresponding to point A, and is positive for V^* larger than that for point A. Point A represents the metastable position of entrapped gas/vapor–liquid interface for a contact angle larger than the cavity mouth angle. The volume of trapped vapor is equal to the volume of the cavity, V_c, so that V^* corresponding to point A is equal to 1. The

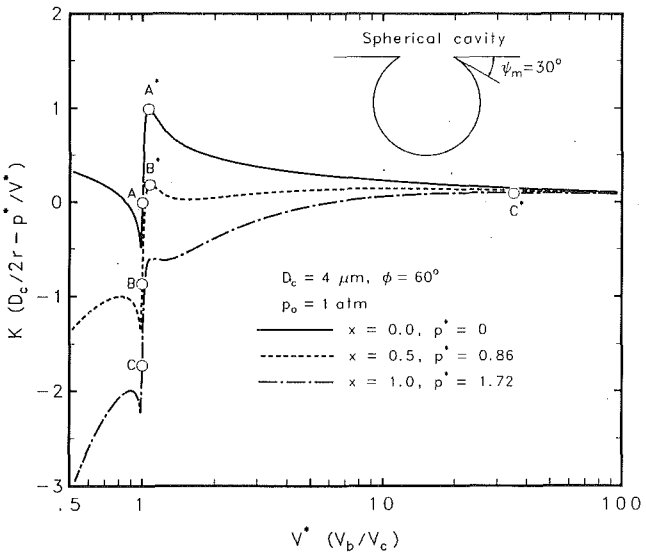

Fig. 8 Dimensionless modified curvature as a function of dimensionless volume of vapor bubble nucleus having different gas mole fractions

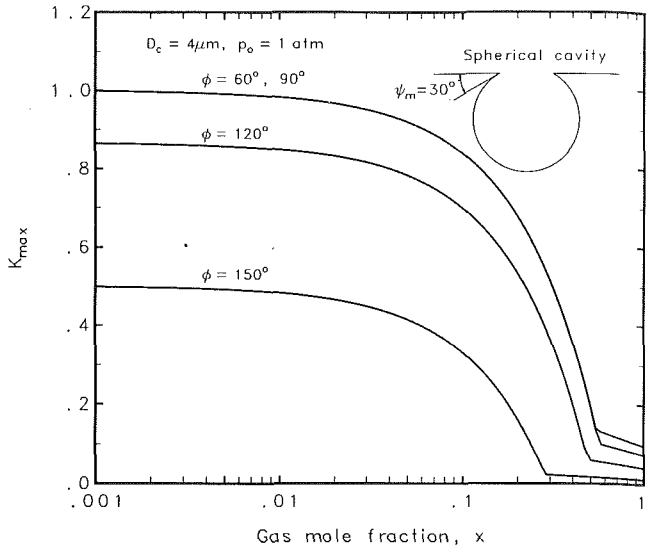

Fig. 9 Dimensionless modified maximum curvature as a function of gas mole fraction in a spherical cavity

interface is at stable equilibrium from point A to point D because K increases with V^*. The maximum values of K occur at points B, C, and D for contact angles of 150, 120 deg, and for contact angle equal to or less than 90 deg, respectively. The values of K_{max} can be determined from the geometric shapes shown for cases (1) and (2) in the insets of Fig. 7 and can be expressed as

$$K_{max} = \begin{cases} 1 & \phi \le 90 \text{ deg} \\ \sin\phi & \phi > 90 \text{ deg} \end{cases} \tag{35}$$

Nucleation occurs when the nondimensional modified curvature has maximum value. The incipient superheat can be obtained from Eq. (33) and can be expressed as

$$\Delta T_w = \frac{4\sigma T_{sat}}{\rho_v h_{fg} D_c} K_{max} \tag{36}$$

Equation (36) suggests that f_1 in Eq. (4) is unity for $\phi < 90$ deg and is equal to $\sin\phi$ for $\phi \ge 90$ deg. The effect of amount of gases is quantified by gas mole fraction x in the cavity according to the system pressure p_o and the volume of the cavity V_c. For $p_o = 1$ atm, $r_c = 2$ μm, $\phi = 60$ deg, Fig. 8 shows the change in K with V^* for $x = 0$, 0.5, and 1.0 when the spherical cavity has a mouth angle $\psi_m = 30$ deg. Points A, B, and C represent the minimum free energy positions during the entrapping process for gas mole fractions of $x = 0$, 0.5, and 1.0, respectively. The value of K for the incipient condition is changed to A^*, B^*, or C^* for gas mole fractions of 0, 0.5, and 1.0, respectively. The gas mole fractions are varied parametrically, and this does not imply that cavities will always have gas mole fractions as high as 0.5 and 1.0. The value of K_{max} at the critical point C^* represents the minimum possible incipient superheat for this cavity. The value of $K_{max} \sim 0.1$ represents an incipient superheat that is only 10 percent of the superheat predicted in the absence of gas in this cavity. Because K_{max} increases as V^* increases from C to C^*, the vapor bubble nucleus will be stable during this growth process. The gas mole fraction changes with the number of vapor bubbles that are generated from a particular cavity. Experimental observations showed (e.g., Wang, 1992) that at some sites bubbles were initially generated at low superheats (0.5–2 K). After some time nucleation was suppressed until superheat increased to a certain value. Thereafter vapor bubbles started to form again. As the gas mole fraction is reduced further, the vapor bubble nuclei remained on the cavity until a higher superheat was imposed to overcome the condition represented by the critical point. This process continued until the gas mole fraction approached 0 and the critical point returned to point A^*. Figure 9 shows changes in K_{max} with gas mole fraction for different contact angles. Irrespective of the initial gas mole fraction in the cavity, the gas mole fraction in the cavity will attain a value consistent with Henry's law after several bubbles are released. For gas mole fraction, x, less than 0.01, the value of K_{max} approaches that given by Eq. (35).

A Model for Naturally Formed Cavities. In order to apply the criterion given by Eq. (25) to spherical cavities, the cavity mouth angle is needed. For measurements of cavity diameters at different depths, Wang and Dhir (1993) concluded that on a super smooth copper surface, most of the cavities were spherical in shape. Wang and Dhir also determined the total number density of all types of cavities and number density of cavities with mouth angle less than 90 deg. Conceivably the number density of cavities with other mouth angles could also be determined. However, such a process will be very tedious and time consuming. In the following, a theoretical approach for determining the number density of cavities with mouth angle less than a specified mouth angle, ψ_m, is developed.

In modeling the depth or mouth angles of cavities present on a very smooth polished surface, it is assumed that these cavities originate from microporosity present in the solid and are spherical in shape. It is also assumed that a very large number of randomly located cavities are present and cavities in a given size group are not affected by those in other groups. When material to a depth l is removed from the top of a hollow sphere, a cavity of mouth angle ψ_m is generated. Since micropores are randomly formed in the solid, all cavities of a given radius, r_s, will correspond to the cavities that have been formed by removal of material in the depth range $0 < l < 2r_s$, or the mouth angle of the cavities will lie in the interval $0 < \psi_m < 180$ deg. Figure 10(a) shows a sketch of single size cavities present in the solid. The probability density function $f_s(l)$ for these cavities will have uniform distribution in the range $0 < l < 2r_s$. Figure 10(b) shows a graph of the probability density function. The value of the probability density function is $1/2r_s$.

The cumulative probability distribution $F_s(l)$ (as shown in Fig. 10c) of all the cavities of radius, r_s, that will form when a material of thickness, l, is removed is written as

$$F_s(l) = \int_0^l f_s(l)\,dx = \frac{l}{2r_s} \tag{37}$$

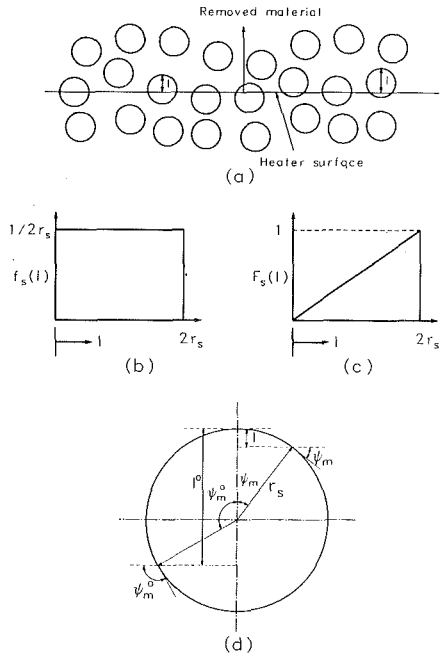

Fig. 10 Probability distribution of spherical cavity side angles

The depth, l, is related to cavity mouth angle, ψ_m (shown in Fig. 10*d*) as

$$l = r_s(1 - \cos \psi_m) \tag{38}$$

Now $F_s(\psi_m)$ represents the probability of finding cavities with mouth angle less than ψ_m. From Eqs. (37) and (38) the ratio of probability of cavities formed by removal of material to depths l and l^o in cavities with mouth angles less than ψ_m and ψ_m^o can be written as

$$P_F = \frac{F_s(l)}{F_s(l^o)} = \frac{l}{l^o} = \frac{1 - \cos \psi_m}{1 - \cos \psi_m^o} \tag{39}$$

On a heater, cavities of different sizes exist due to gas microporosity. As stated earlier, if cavities in different size groups behave in a similar manner, the above equations will apply to all sizes of cavities. However, it should be noted that measurements reported in the companion paper were limited to cavities with diameters less than 20 μm but greater than 2 μm. If N_s is the cumulative density of spherical cavities of all sizes and all mouth angles (0–180 deg), the number density of cavities with mouth angle less than ψ_m can be written as

$$N_{as}(\psi_m) = F_s(\psi_m) \cdot N_s = \frac{1 - \cos \psi_m}{2} \cdot N_s \tag{40}$$

Similarly, the ratio of cumulative density of spherical cavities of mouth angle less than ψ_m and ψ_m^o can be written as

$$\frac{N_{as}(\psi_m)}{N_{as}(\psi_m^o)} = P_s(\psi_m, \psi_m^o) = \frac{1 - \cos \psi_m}{1 - \cos \psi_m^o} \tag{41}$$

According to the gas/vapor entrapment criteria developed earlier, for a contact angle ϕ, the spherical cavities that trap gas/vapor have mouth angles less than ψ_m, such that

$$\phi > \psi_m \tag{42}$$

Since these are the cavities that have the potential to become active, the cumulative number density of active nucleation sites for a contact angle ϕ can be written as

$$\begin{aligned} N_a(\phi) &= N_{as}(\psi_m = \phi) \\ &= P_{as}(\phi, \psi_m^o) \cdot N_{as}(\psi_m^o) \end{aligned} \tag{43}$$

In Eq. (43) P_{as} is a function of contact angle and cavity mouth angle and is expressed as

$$P_{as}(\phi, \psi_m^o) = \frac{1 - \cos \phi}{1 - \cos \psi_m^o} \tag{44}$$

Equation (43) shows that the cumulative active nucleation site density for a specified contact angle, ϕ, can be expressed in terms of the cumulative density of cavities with cavity mouth angle, ψ_m, less than the specified contact angle. It must be stressed here that Eq. (43) is only applicable to surfaces on which spherical cavities stemming from micropores in the solid are present. As an example, it will not apply to artificially roughened surfaces. The approach, however, is very general and can be extended to cavities of other geometries.

Black spots observed during determination of cavities on a surface are not always real cavities (Yang and Kim, 1988). While determining a real cavity, it is necessary to examine its depth. Therefore, the cumulative active site density has to be based on a contact angle other than 180 deg. Since measurement of the cavity side angle (see Wang, 1992) is based on two different diameters in two different layers on the heater surface, it is most convenient to use a 90 deg mouth angle as a reference. For a reference angle of 90 deg, N_{as} means the cumulative density of sites whose diameter becomes larger after removal of the first layer of material from the heater surface. Therefore, Eq. (43) is expressed in terms of a reference mouth angle of 90 deg as

$$N_a(\phi) = P_{as}(\phi, \psi_m^o = 90 \text{ deg}) \cdot N_{as}(\psi_m^o = 90 \text{ deg}) \tag{45}$$

The ratio of cumulative density of active nucleation sites for contact angles ϕ and ϕ^o is obtained as

$$\frac{N_a(\phi)}{N_a(\phi^o)} = P_a(\phi, \phi^o) = \frac{1 - \cos \phi}{1 - \cos \phi^o} \tag{46}$$

Equations (44) and (46) are valid for cavities up to a given size, D_c. Since in boiling experiments cumulative site density is observed as a function of wall superheat, to obtain the ratio of cumulative density of active nucleation sites for contact angles ϕ and ϕ^o at a given wall superheat, Eq. (46) must be corrected following the prediction from Eq. (36).

$$\frac{N_a(\phi, \Delta T)}{N_a(\phi^o, \Delta T)} = P_t(\phi, \phi^o) = \frac{1 - \cos \phi}{1 - \cos \phi^o} \cdot \frac{K_{\max}^o}{K_{\max}} \tag{47}$$

Discussion

Gas Entrapment Criterion. In order to verify the conditions for gas/vapor entrapment as given by Eq. (25), the data of cavity mouth angle and contact angle for nucleating sites are taken from the companion paper. Figure 11 shows the relation between contact angle and cavity mouth angle for nucleating sites. For a contact angle of 90 deg, the cavity mouth angles of two nucleating cavities are 43.54 deg and 50.60 deg. These cavities are smaller than the contact angle of 90 deg. For a contact angle of 35 deg, the cavity mouth angles for the three nucleating sites are 32.14 deg, 11.73 deg, and 24.16 deg and are again smaller than the contact angle of 35 deg. When the contact angle is 18 deg, the cavity mouth angles of the nucleating sites are 14.31 deg, 9.46 deg and 15.73 deg. Once again these angles are smaller than the contact angle of 18 deg. All cavity mouth angles of nucleating sites shown in Fig. 11 lie in the gas/vapor entrapment region and provide the validity of the gas/vapor entrapment criteria developed earlier.

Surface Site Density. To predict from Eq. (40) the total number of cavities with mouth angle less than a certain angle, one set of cavity site density data for a particular cavity mouth angle is needed. As mentioned earlier, the present authors have obtained data for surface site density, N_{as}, of cavities with $\psi_m < 90$ deg. Figure 12 shows their data and a best fit through the data. The dotted lines show the predictions from Eq. (40) for $\psi_m < 180$ deg and $\psi_m < 18$ deg.

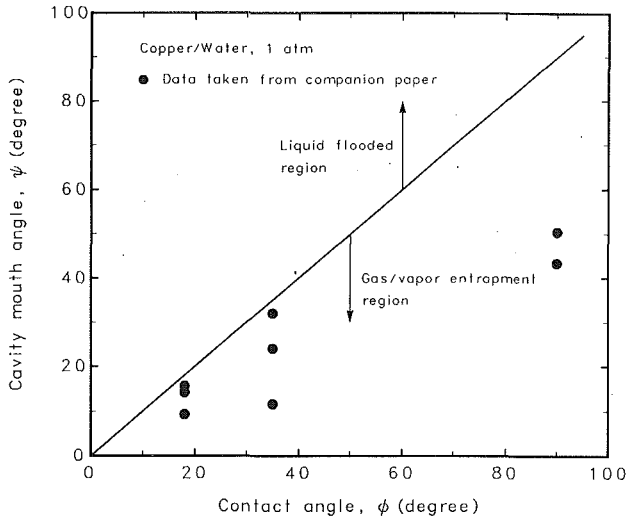

Fig. 11 Relation between contact angle and cavity mouth angle for active sites

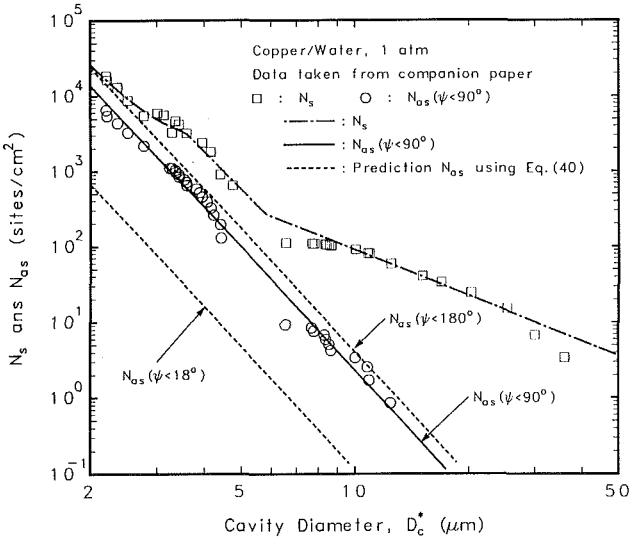

Fig. 12 Surface sites density as a function of cavity diameter on a copper surface

According to Eq. (40), the surface cumulative site density, N_s ($=N_{as}(\psi_m<180$ deg)), should be two times the surface cumulative site density with cavity mouth angles less than 90 deg, $N_{as}(\psi_m<90$ deg). It is found that the predicted values agree reasonably with the data for cavity diameters D_c less than 3 μm. For cavity diameters between 3 and 6 μm, the data are higher than the theoretical value and seemingly include black spots, which are not real cavities. Cavities with diameters larger than 7 μm are probably a result of scratching of the surface with emery paper. The model for naturally formed cavities is not applicable to these artificial cavities and severely underpredicts the measured density of cavities present on the surface. It can also be noted from Fig. 12 that of all the spherical cavities ($\psi_m<180$ deg) only about 2.5 percent of the cavities have mouth angles less than 18 deg.

Nucleation Site Density. A comparison of the active site density predicted from Eq. (43) is made in Figs. 13(a), 13(b), and 13(c) for contact angles of 90, 35, and 18 deg, respectively. The data were obtained from the companion paper (Wang and Dhir, 1993). In making the predictions, from Eq. (44), the cumulative surface site density, $N_{as}(\psi_m<90$ deg) was used. The active cavity diameters were obtained by relating them to superheats through Eq. (36). The details are given by Wang

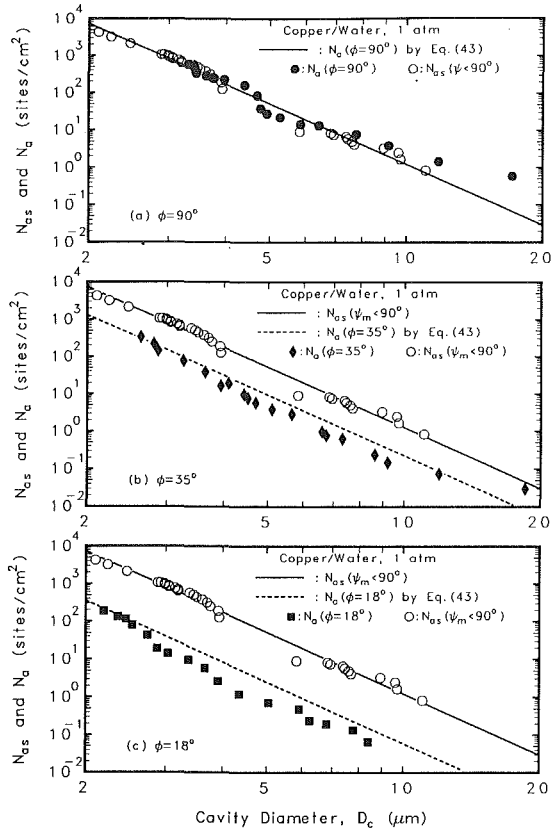

Fig. 13 Comparison of the predicted and the measured active site density for contact angles of 90, 35, and 18 deg

(1992). It is seen from Fig. 13 that the predictions are consistent with the data for a contact angle of 90 deg. The active site densities predicted from the model for 35 and 18 deg are also in reasonable agreement with the data. Thus a completely theoretical model has been developed for relating the cavities present on the surface to those that actually nucleate.

According to Eq. (43) most of the sites on a particular surface will become inactive if the liquid wetted the surface well. Kurihara and Myers (1960) experimentally determined the active nucleation sites on copper surfaces with both water and acetone. Their number density data, when plotted as a function of cavity diameter, show that cavity site density with acetone is about 600 times smaller than that for water. From the present analysis this reduction will correspond to a contact angle of 3 deg for acetone, if the contact angle with water is assumed to be 90 deg. A contact angle of 3 deg is within the range of expected contact angles for acetone, which wets the copper surface well. Conditions of the copper surface used in the experiments of Kurihara and Myers (1960) are not known precisely. If in their experiments with water the contact angle was less than 90 deg, the contact angle deduced from Eq. (43) will still be between 0 and 3 deg.

To test the validity of the present model further, the predictions from the present model for the ratio, P_a, of the active cavities for different contact angles was compared with the data of Eddington and Kenning (1979). For water and brass, they reported a maximum contact angle of 80 deg. This angle has been used here to normalize the cumulative active site densities. Figure 14(a) shows a comparison of the predictions from the present analysis with the data obtained on a brass surface. Yang and Kim's (1988) prediction, expressed by Eq. (10), is also plotted. It is seen that the data compare favorably with the prediction from Eq. (46), which is based on the present model for spherical cavities. Yang and Kim's equation, based on the conical cavity model, predicts much weaker dependence

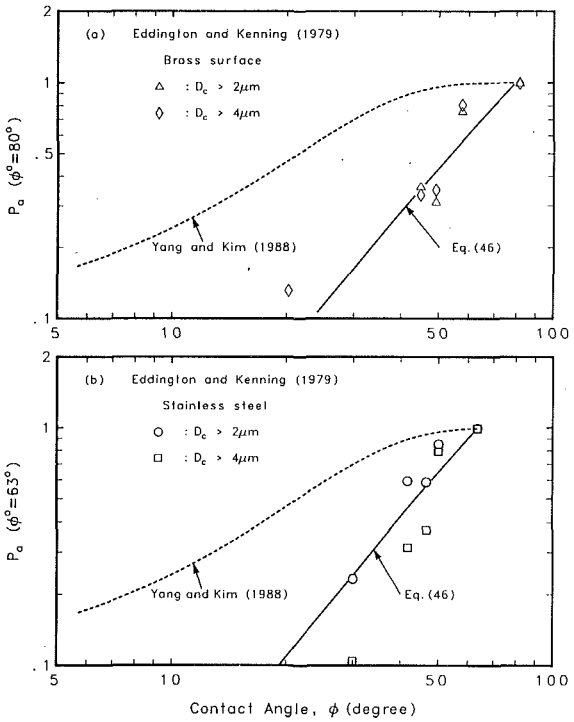

Fig. 14 Normalized active nucleation site density as function of contact angle

of site density on contact angle. Similar results for a steel-water system are plotted in Fig. 14(*b*). Now the data are normalized with that for a contact angle of 63 deg, since this was the highest contact angle obtained for this solid-liquid combination.

Conclusions

1 A gas/vapor entrapment criterion for cavities present on a surface has been developed. According to this criterion, a cavity will trap gas/vapor if the contact angle is greater than the minimum cavity side angle. For spherical and conical cavities, the mouth angle is the minimum side angle.

2 For contact angles less than 90 deg, the incipient superheat is independent of contact angle. However, for $\psi \geq 90$ deg, it is proportional to $\sin \phi$.

3 By combining the gas/vapor entrapment criterion with a knowledge of the cavity diameter distribution and the cavity mouth angles, the number density of active sites can be predicted.

4 Geometric arguments can be used to predict the side angle distribution of spherical cavities present on a super smooth surface.

5 The reduction in the number density of active cavities as the surface wettability improves is predicted well by the model.

Acknowledgments

This work received support from the NSF under Grant No. CBT-88-21447.

References

Bankoff, S. B., 1958, "Entrapment of Gas in the Spreading of a Liquid Over a Rough Surface," *AIChE J.*, Vol. 4, pp. 24–26.

Clark, H. B., Strenge, P. S., and Westwater, J. W., 1959, "Active Sites for Nucleate Boiling," *Chem. Engrg. Prog. Symp. Series*, No. 29, Vol. 55, pp. 103–110.

Cornwell, K., 1977, "Naturally Formed Boiling Site Cavities," *Lett. Heat Mass Transfer*, Vol. 4, pp. 63–72.

Cornwell, K., 1982, "On Boiling Incipience Due to Contact Angle Hysteresis," *Int. J. Heat Mass Transfer*, Vol. 25, No. 2, pp. 205–211.

Corty, C., and Foust, A., 1955, "Surface Variables in Nucleate Boiling," *Chem. Engrg. Prog. Symp. Series*, No. 51, Vol. 17, pp. 1–12.

Eddington, R. I., and Kenning, D. B. R., 1979, "The Effect of Contact Angle on Bubble Nucleation," *Int. J. Heat Mass Transfer*, Vol. 22, pp. 1231–1236.

Forest, T. W., 1982, "The Stability of Gaseous Nuclei at Liquid-Solid Interfaces," *J. Appl. Phys.*, Vol. 53, No. 9, pp. 6191–6201.

Gaertner, R. F., 1963, "Distribution of Active Sites in the Nucleate Boiling of Liquids," *Chem. Engr. Prog. Symp. Series*, Vol. 59, pp. 52–61.

Griffith, P., and Wallis, J. D., 1960, "The Role of Surface Conditions in Nucleate Boiling," *Chem. Eng. Prog. Symp. Series*, Vol. 56, pp. 49–62.

Harkins, W. D., 1952, *The Physical Chemistry of Surface Films*, Reinhold Publishing Corp., New York, pp. 80–82.

Hsu, Y. Y., 1962, "On the Size Range of Active Nucleation Cavities on a Heating Surface," ASME JOURNAL OF HEAT TRANSFER, Vol. 84, pp. 207–216.

Johnson, R. E., Jr., and Dettre, R. H., 1963a, "Contact Angle Hysteresis—Study of an Idealized Rough Surface," *Advan. Chem. Ser.*, No. 43, pp. 112–135.

Johnson, R. E., Jr., and Dettre, R. H., 1963b, "Contact Angle Hysteresis—Contact Angle Measurement on Rough Surfaces," *Advan. Chem. Ser.*, No. 43, pp. 136–144.

Kurihara, H. M., and Myers, J. E., 1960, "The Effect of Superheat and Surface Roughness on Boiling Coefficients," *AIChE Journal*, Vol. 6, No. 1, pp. 83–91.

Lorenz, J. J., 1971, "The Effect of Surface Conditions on Boiling Characteristics," Ph.D. dissertation, Department of Mechanical Engineering, MIT.

Mizukami, K., 1975, "Entrapment of Vapor in Reentrant Cavities," *Letters in Heat and Mass Transfer*, Vol. 2, pp. 279–284.

Nishio, S., 1985, "Stability of Preexisting Vapor Nucleus in Uniform Temperature Field," *Trans. JSME*, Series B, Vol. 54–503, pp. 1802–1807.

Tong, W., Bar-Cohen, A., Simon, T. W., and You, S. M., 1990, "Contact Angle Effects on Boiling Incipience of Highly-Wetting Liquids," *Int. J. Heat Mass Transfer*, Vol. 33, No. 1, pp. 91–103.

Wang, C. H., 1992, "Experimental and Analytical Study of the Effects of Wettability on Nucleation Site Density During Pool Boiling," Ph.D. dissertation, University of California, Los Angeles, CA.

Wang, C. H., and Dhir, V. K., 1993, "Effect of Surface Wettability on Active Nucleation Site Density During Pool Boiling of Water on a Vertical Surface," ASME JOURNAL OF HEAT TRANSFER, Vol. 115, this issue, pp. 659–669.

Ward, C. A., and Forest, T. W., 1976, "On the Relation Between Platelet Adhesion and the Roughness of a Synthetic Biomaterial," *Annals of Biomedical Engineering*, Vol. 4, pp. 184–207.

Yang, S. R., and Kim, R. H., 1988, "A Mathematical Model of the Pool Boiling Nucleation Site Density in Terms of the Surface Characteristics," *Int. J. Heat Mass Transfer*, Vol. 31, pp. 1127–1135.

Forced Convective Boiling of Nonazeotropic Refrigerant Mixtures Inside Tubes

K. Murata
Research Scientist.

K. Hashizume
Senior Research Scientist.

Energy Science and Technology Laboratory,
Research and Development Center,
Toshiba Corporation,
4-1, Ukishima-cho, Kawasaki-ku Kawasaki,
210, Japan

Forced convective boiling of nonazeotropic mixtures inside horizontal tubes was investigated experimentally. The heat transfer coefficient and pressure drop of pure refrigerant R123 and a mixture of R123 and R134a were measured in both a smooth tube and a spirally grooved tube. The heat transfer coefficient for the mixture was found to be lower than that for an equivalent pure refrigerant with the same phsycial properties, not only in the boiling-dominant region but also in the convection-dominant region. On the basis of this experiment, correlations were proposed for heat transfer coefficients in smooth and grooved tubes; the reduction in heat transfer coefficient for the mixture is attributed to the mixture effects on nucleate boiling and to the heat transfer resistance in the vapor phase. This heat transfer resistance is caused by the sensible heating of the vapor phase accompanying the rise in saturation temperature. These correlations are able to predict the heat transfer data within ±20 percent.

Introduction

Recently, a number of studies on forced convective boiling of nonazeotropic mixtures have been conducted as part of the effort to improve the performance of heat pump systems.

Bennett and Chen (1980) developed a correlation for heat transfer coefficients where the effects of diffusive resistance on nucleate boiling and on two-phase forced convection (i.e., forced convective evaporation) were taken into account separately. As reported by Yoshida et al. (1990), however, their correlation underestimates the heat transfer coefficient in the convection-dominant region because the correlation overestimates the effect of diffusive resistance on two-phase forced convection.

Mishra et al. (1981) and Singal et al. (1984) conducted experiments on forced convective boiling of R22/R12 and R13/R12 inside horizontal tubes, and obtained empirical correlations. However, the heat transfer characteristics of the mixtures were not adequately discussed in their work. In addition, these correlations do not seem to be applicable to other mixtures, although they are expressed in nondimensional form.

In theoretical models developed by Sardesai et al. (1982), not only does the mixture affect nucleate boiling (this is recognized as an effect of diffusive resistance on nucleate boiling), but the thermal resistance in the vapor phase also causes a degradation in heat transfer coefficient. However, the effect of diffusive resistance on two-phase forced convection is neglected.

According to an experimental study using mixtures of refrigerants R11 and R114 by Murata and Hashizume (1988, 1990), the heat transfer coefficient of mixtures is significantly lower in the boiling-dominant region, while it is almost equal to that of an equivalent pure fluid with the same physical properties in the convection-dominant region. Jung et al. (1989a, 1989b) reached the same conclusion through experiments with mixtures of R22/R114 and R12/R152a; that is, the effect of diffusive resistance is small in the convection-dominant region.

The authors have performed an experimental study using a mixture or refrigerants R123 and R134a. The difference in boiling point between R123 and R134a (about 54 K) is much larger than that between R11 and R114 (about 20 K) as used in the previous experiments by Murata and Hashizume (1988, 1990). The objectives of this work were to clarify the characteristics of forced convective boiling in nonazeotropic mixtures flowing inside tubes and to develop a generalized correlation for the heat transfer coefficient of refrigerant mixtures.

This research is one of the R & D programs run by the Technology Research Association for the Super Heat Pump Energy Accumulation System, entrusted by the New Energy and Industrial Technology Development Organization (NEDO).

Experimental Apparatus and Procedure

The experimental apparatus and procedure used in this work are as described in the previous report by Murata and Hashizume (1988, 1990), and details are given here only briefly. Figures 1(*a*) and 1(*b*) show the complete experimental apparatus and a test section, respectively. The main components of the apparatus are the test sections, pre- and after-evaporators, and condensers, all thermally insulated with glass wool and fitted horizontally. The refrigerant liquid, which is condensed in condensers about 7 m above the test section, flows down through the down-comer under gravity into the pre-evaporator. Here it is heated to give any desired quality at the test section inlet. The local heat transfer coefficient and pressure drop are measured in the test section. The refrigerant evaporates completely in the after-evaporator, and returns to the condenser via a riser. The pre- and after-evaporators and the condensers are all double-tube-type heat exchangers, in which the refrigerant is heated or cooled by water. The heat transfer rate at each heat exchanger was calculated from the temperature change and flow rate of heating or cooling water. The temperature change and flow rate were measured by C-C thermocouples and float-type flowmeters calibrated beforehand.

Each test section consists of a 734-mm-long by 12.7-mm-o.d. tube with connecting flanges at both ends. Two test sections are connected in series with a PT-tap (pressure and temperature measuring tap) between them. Sheathed heaters are wound around the tube at 5 mm pitch, and are heated elec-

Contributed by the Heat Transfer Division for publication in the JOURNAL OF HEAT TRANSFER. Manuscript received by the Heat Transfer Division April 1992; revision received December 1992. Keywords: Boiling, Evaporation, Multiphase Flows. Associate Technical Editor: T. W. Simon.

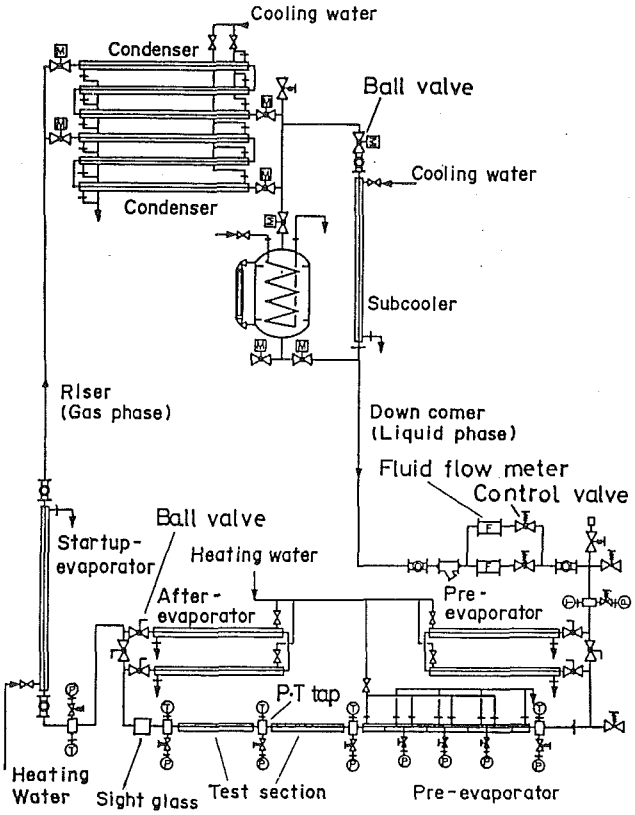

Fig. 1(*a*) Refrigerant flow chart

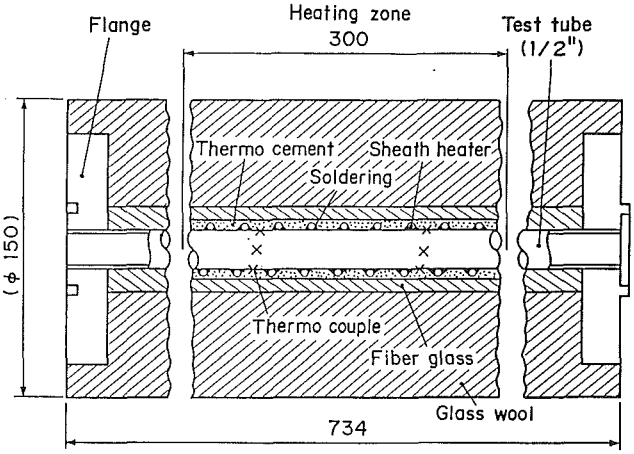

Fig. 1(*b*) Test section

Fig. 1 Experimental apparatus

trically. Thermocement with a high thermal conductivity is applied over the outer tube surface to give a uniform heat flux. The test sections are thermally insulated with fiberglass, glass wool, and aluminum tape so that heat loss could be neglected. The tube wall temperatures are measured by 0.5 mmϕ C-A (chromel-alumel) thermocouples soldered outside the tube with their junctions out of direct contact with the sheathed heaters. The measuring points were at two axial locations in the 300 mm heating zone and at three circumferential positions (top, bottom, and side).

Measurements of refrigerant flow rate were carried out by volumetric flowmeters. A precise digital pressure gage and a pressure difference meter were used for measurements of static pressure and pressure drop, respectively. The local pressure in the test section was interpolated linearly from the measured pressures at the inlet and outlet of the test section.

Experiments were conducted using a smooth tube (i.d. = 10.3 mm) and a spirally grooved tube (i.d. = 10.7 mm, number of grooves = 60, groove depth = 0.3 mm, lead angle = 30 deg, groove pitch = 0.56 mm), both made of copper. The test fluids used were a pure refrigerant, R123, and a mixture of R123 and R134a. The mole fraction of R134a was 10 percent, which was selected as a working fluid for the Super Heat Pump Energy Accumulation System described in the introduction. The range of experimental parameters is summarized in Table 1.

Assuming liquid–vapor equilibrium in a cross-sectional area of the tube, the energy balance in the test section is expressed as:

$$W\{xi_G+(1-x)i_L\}=W\{x_{IN}i_{G.IN}+(1-x_{IN})i_{L.IN}\}+\pi D_i\Delta zq \tag{1}$$

where W is the mass flow rate of the refrigerant, x is the

Nomenclature

A_{NB} = empirical factor in Eq. (36)
Bo = boiling number = $q/G\cdot r$
C_d = empirical constant in Eq. (29)
C_p = specific heat, J/(kg K)
D_i = inner tube diameter, m
D_o = outer tube diameter, m
$-(dP/dz)_F$ = two-phase frictional pressure drop, Pa/m
$-(dP/dz)_L$ = frictional pressure drop if only the liquid were flowing, defined by Eq. (17), Pa/m
$(\partial T_s/\partial i)_P$ = saturation temperature differentiated by enthalpy, K/(J/kg)
F = acceleration factor
F_P = given by Eq. (26)
f_G = friction factor at liquid–vapor interface, defined by Eq. (50)
G = mass flux of fluid, kg/(m^2 s)
g = gravitational acceleration $\simeq 9.81$ m/s^2
r = latent heat of vaporization, J/kg
i = specific enthalpy, J/kg
M = molecular weight
P = pressure, Pa or bar
P_c = critical pressure, Pa
P_s = saturation pressure, Pa or bar
Pr = Prandtl number
q = heat flux, based on internal surface area of tube = $\pi D_i dz$, W/m^2
q_G = heat flux transferred into vapor core at liquid–vapor interface, W/m^2
$\mathrm{Re_L}$ = Reynolds number, defined by Eq. (18)
S = suppression factor
St = Stanton number, defined by Eq. (47)
T_i = temperature at liquid–vapor interface, K
T_c = critical temperature, K
T_G = vapor phase temperature, K
T_s = saturation temperature, K
T_w = inner tube wall temperature, K
u_G = vapor velocity, given by Eq. (49), m/s
x = quality, given by Eq. (2)
X_M = mole fraction of more volatile component (R134a) in liquid phase
X_w = mass fraction of more volatile component (R134a) in liquid phase
X_{wo} = overall mass fraction of more volatile component (R134a)

Table 1 Range of experimental parameters

Test tube	Smooth tube: Do=12.7mm,Di=10.3mm Spirally grooved tube: Do=12.7mm,Di=10.7mm number of grooves = 60 groove depth = 0.3mm lead angle = 30°
Test fluid	Pure refrigerant: R123 Mixture: R123/R134a(90/10 mole%)
Test Pressure	R123 : 2.0bar R123/R134a: 2.2bar for G~100,200kg/m²s 2.4bar for G~300kg/m²s
Mass flux G	Smooth tube: 100,200,300kg/m²s Grooved tube: 93,185,278kg/m²s
Heat flux q	0,10,20,30 kW/m²
Quality x	0.1~1.0
Quality change in testsection	0.02(G=300kg/m²s,q=10kW) - 0.22(G=100kg/m²s,q=30kW)

equilibrium vapor quality, i is the specific enthalpy, D_i is the inner diameter, Δz is the effective heat transfer length, and q is the heat flux. The subscripts L, G, and IN denote liquid phase, gas phase, and inlet of test section, respectively. The vapor quality, x, for a mixture is given by the following equation:

$$x=(X_{wo}-X_w)/(Y_w-X_w) \tag{2}$$

where Y_w, X_w, and X_{wo} are the vapor-phase, liquid-phase, and overall mass fractions of the more volatile component (R134a). The values of Y_w, X_w, i_G, and i_L were estimated using the state equation by Peng and Robinson (1976). The value of the binary interaction parameter, δ_{ij}, in the state equation is fixed at 0.051 as reported by Nakaiwa et al. (1990). The mass fractions and specific enthalpies are functionally expressed as:

$$Y_w=Y_w(P,\ T_s) \tag{3}$$

$$X_w=X_w(P,\ T_s) \tag{4}$$

$$i_G=i_G(P,\ T_s,\ Y_w) \tag{5}$$

$$i_L=i_L(P,\ T_s,\ X_w) \tag{6}$$

where P and T_s are the refrigerant pressure and temperature, respectively. The local values of Y_w, X_w, T_s, and x are evaluated by solving Eqs. (1)–(6) with measured values of W, P, and q. The local heat transfer coefficients at each thermocouple position are obtained as follows:

$$\alpha_k=q/(T_{w,k}-T_s)\quad k=t,\ s,\ b \tag{7}$$

where the subscripts t, s, and b denote the circumferential positions, i.e., top, side, and bottom, respectively. The inner tube wall temperature, $T_{w,k}$, was calculated from the measured outside wall temperature by the one-dimensional radial heat conduction equation. The value of q was calculated from the electrical power input into the sheathed heater. The average local heat transfer coefficient, α, was determined by

$$\alpha=(\alpha_t+2\alpha_s+\alpha_b)/4 \tag{8}$$

Although the α data were obtained at two axial locations in the heating zone of a test section, the difference between x values at the two locations was small in most experiments (under 0.06 for $G\sim 200$, 300 kg/m^{2}s, and under 0.11 for $G\sim 100$ kg/m^2 s). Thus, the mean of the two α values was regarded as an α datum for the mean quality. In the condition of $x\sim 1$, however, the α and x data at the upper-stream station were adopted since dry-out of the heat transfer surface was often recognized in the heating zone.

Pressure drop measurements were carried out under heating and adiabatic conditions. Total pressure drop in a test section, ΔP, consists of frictional ΔP_F and accelerational ΔP_A components, i.e.,

$$\Delta P=\Delta P_F+\Delta P_A \tag{9}$$

Under the adiabatic condition, the measured pressure drop may be regarded as the frictional component since $\Delta P_A\simeq 0$. Under the heating condition, frictional pressure drop data were obtained by subtracting ΔP_A from ΔP. ΔP_A is expressed by

$$\Delta P_A=G^2\left[\left\{\frac{x^2}{\gamma\rho_G}+\frac{(1-x)^2}{(1-\gamma)\rho_L}\right\}_{\mathrm{OUT}}-\left\{\frac{x^2}{\gamma\rho_G}+\frac{(1-x)^2}{(1-\gamma)\rho_L}\right\}_{IN}\right] \tag{10}$$

where G, γ, and ρ are the mass flux of refrigerant, the void fraction, and the density, respectively. The subscripts IN and OUT denote the inlet and outlet of the test section, respectively. The value of γ was evaluated from the correlation by Fauske (1961), and is given by

Nomenclature (cont.)

X_{tt} = Martinelli parameter, defined by Eq. (19)
Y_M = mole fraction of more volatile component (R134a) in vapor phase
Y_w = mass fraction of more volatile component (R134a) in vapor phase
z = coordinate in flow direction, m
α = heat transfer coefficient based on internal surface area of tube, W/(m^2 K)
α_{TC} = two-phase convection contribution, W/(m^2 K)
α_G = vapor-phase heat transfer coefficient based on internal surface area of tube, W/(m^2 K)
α_G* = vapor-phase heat transfer coefficient given by Eq. (47) or (52), W/(m^2 K)
α_L = single-phase heat transfer coefficient if the liquid alone were flowing, defined by Eq. (21) or (22), W/(m^2 K)
α_{LF} = heat transfer coefficient of liquid film, W/(m^2 K)
α_{NB} = nucleate boiling contribution, W/(m^2 K)
α_{PB} = pool boiling heat transfer coefficient, W/(m^2 K)
γ = void fraction, given by Eq. (11)
δ = characteristic length, defined by Eq. (29), m
δ_{ij} = binary interaction parameter
η = viscosity, Pa s
λ = thermal conductivity, W/(m K)
ρ = density, kg/m^3
σ = surface tension, N/m
τ_i = vapor shear stress at liquid-vapor interface, N/m^2
Φ_L = parameter defined by Eq. (16)

Subscripts

C = critical constant
TC = two-phase convection
G = vapor phase
i = liquid-vapor interface or inner tube
ID = ideal or equivalent pure fluid
L = liquid phase
NB = nucleate boiling
PB = pool boiling
1 = more volatile component, Freon R134a
2 = less volatile component, Freon R123

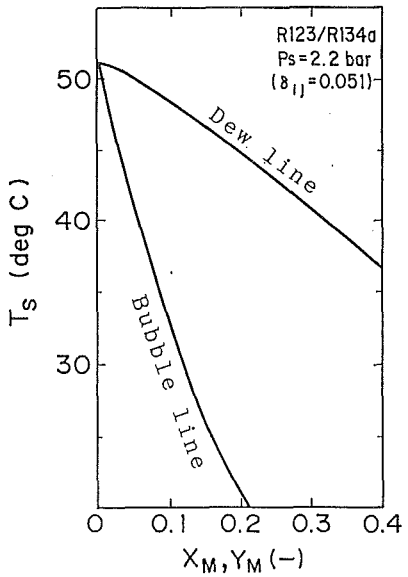

Fig. 2 Isobaric phase-equilibrium diagram

Table 2 Physical properties of pure and mixture refrigerants

Property	Unit	R123	R123/R134a* (90/10mole%)
Pressure	bar	2.0	2.2
Saturation temperature	K	320	318
Liquid density	kg/m^3	1400	1450
Vapor density	kg/m^3	12.0	12.8
Liquid viscosity	Pa s	3.32×10^{-4}	3.32×10^{-4}
Vapor viscosity	Pa s	1.20×10^{-5}	1.22×10^{-5}
Liquid specific heat	J/kgK	1030	1000
Vapor specific heat	J/kgK	773	777
Liquid thermal conductivity	W/mK	0.0694	0.0699
Vapor thermal conductivity	W/mK	10.0	8.49
Surface tension	N/m	0.015	0.018

* the values for vapor quality x=0.5

$$\gamma = [1 + \{(1-x)/x\}(\rho_G/\rho_L)^{1/2}]^{-1} \quad (11)$$

The accelerational components accounted for less than 30 percent of the total pressure drops in most experiments. The frictional pressure drop data in the adiabatic and heating conditions were in good agreement within the range of experimental scatter.

Figure 2 shows an isobaric phase-equilibrium diagram obtained from the Peng-Robinson (P-R) equation of state. Thermodynamic properties of the mixtures for use in data analysis were calculated using the P-R equation of state. For the calculation of transport properties of the mixtures, the methods described by Reid and Sherwood (1966) were adopted. Table 2 shows the properties of R123 and R123/R134a (90/10 mole %) where the values for $x=0.5$ are given for the mixture since the properties of mixtures are a function of quality under a constant pressure.

The uncertainty in the α value is caused by uncertainties in the heat flux, q, and the wall superheat, $(T_w - T_s)$. The value of T_s was evaluated from the refrigerant pressure and enthalpy using the P-R equation of state. Thus, the accuracy of the T_s value depends largely upon the accuracies of the refrigerant pressure measurements (1 kPa, corresponding to 0.13 K in saturation temperature) and refrigerant flow rate measurements (1 percent, corresponding to 0.1 K in saturation temperature) excluding the accuracy of the P-R equation of state. The uncertainties in q and T_w were estimated to be 1 percent and 0.2 K, respectively. From the uncertainties of T_s, T_w, and q, the uncertainty in the α data was estimated to be within ± 10 percent for $(T_w - T_s) \geq 3$ K. This value increases with decreasing $(T_w - T_s)$, that is, with decreasing q and increasing α.

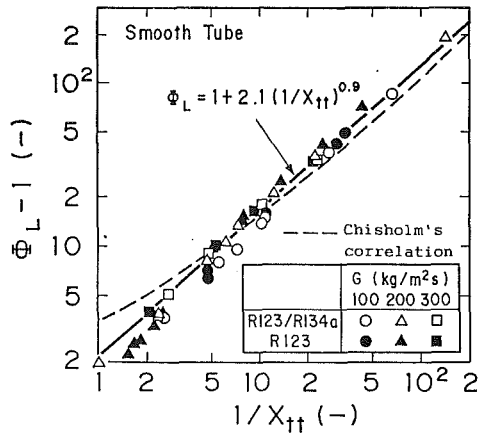

Fig. 3(*a*) For smooth tube

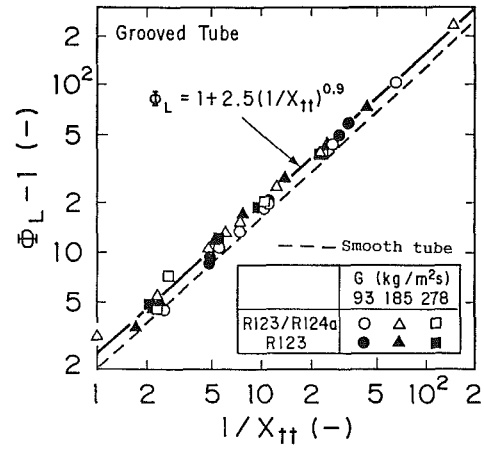

Fig. 3(*b*) For grooved tube

Fig. 3 Frictional pressure drop data in nondimensional form

In order to validate the experimental apparatus and procedure, single-phase heat transfer and pressure drop data were taken for a smooth tube. The local heat transfer coefficients were measured with the subcooled liquid heated in the test section and compared with the Dittus-Boelter equation

$$\alpha = 0.023 \mathrm{Re}_{LO}^{0.8} \mathrm{Pr}_L^{0.4} \lambda_L / D_i$$
$$\mathrm{Re}_{LO} = GD_i/\eta_L \quad (12)$$

The α data for $G \geq 300$ kg/m^2 s, where the Reynolds number, Re_{LO}, is larger than 9000, was found to agree with Eq. (12) within ± 7 percent. The pressure drops were measured with the superheated vapor flowing in the test section and the friction coefficient data were compared with the Colburn equation

$$f = 0.046/\mathrm{Re}_{GO}^{0.2}$$
$$\mathrm{Re}_{GO} = GD_i/\eta_G \quad (13)$$

All data were found to agree with Eq. (13) within ± 7 percent.

Experimental Results and Discussion

Pressure Drop. Figures 3(*a*) and 3(*b*) show the frictional pressure drop data in the form $\Phi_L - X_{tt}$ for the smooth and grooved tubes, respectively. Pressure drop measurements were carried out in heating and adiabatic conditions. As the frictional pressure drops in the both conditions were in good

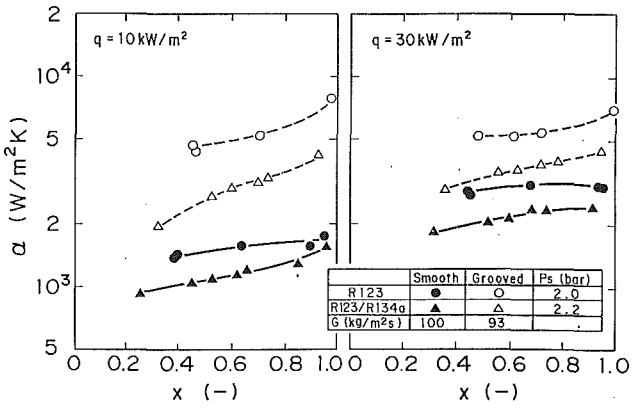

Fig. 4(*a*) $G \simeq 100$ kg/m² s

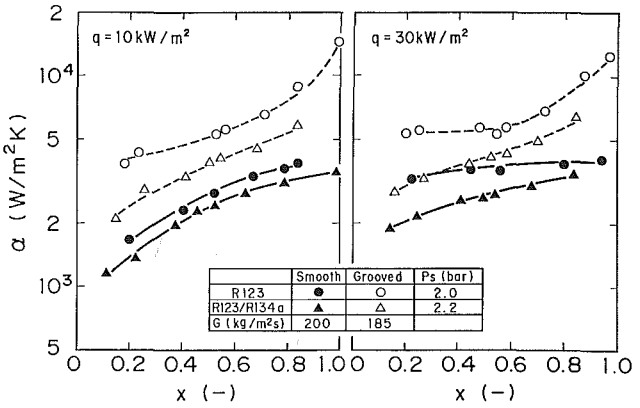

Fig. 4(*b*) $G \simeq 200$ kg/m² s

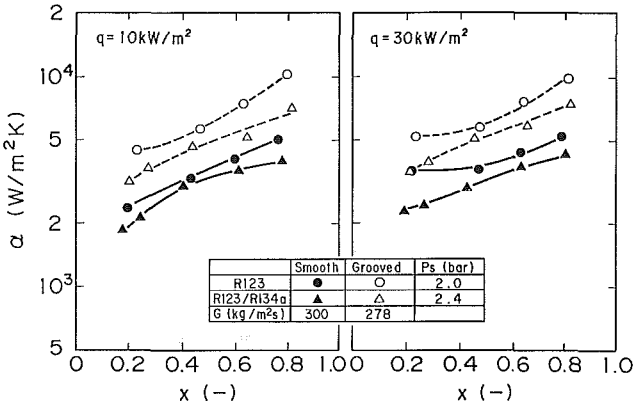

Fig. 4(*c*) $G \simeq 300$ kg/m² s

Fig. 4 Heat transfer coefficients

agreement within the range of experimental scatter, they are shown without distinction in Fig. 3.

The frictional pressure drop data for R123/R134a were correlated using the same equations as for R123, based on the properties of the equivalent pure fluid, which were calculated using the methods of Reid and Sherwood (1966). Accordingly, the frictional pressure drop for the mixture R123/R134a is regarded as approximately equal to that for the equivalent pure fluid. This accords with the experimental results by Ross et al. (1987). The correlations are expressed as

$$\Phi_L = 1 + 2.1(1/X_{tt})^{0.9} \text{ for the smooth tube} \quad (14)$$

$$\Phi_L = 1 + 2.5(1/X_{tt})^{0.9} \text{ for the grooved tube} \quad (15)$$

$$\Phi_L = \{(dP/dz)_F/(dP/dz)_L\}^{1/2} \quad (16)$$

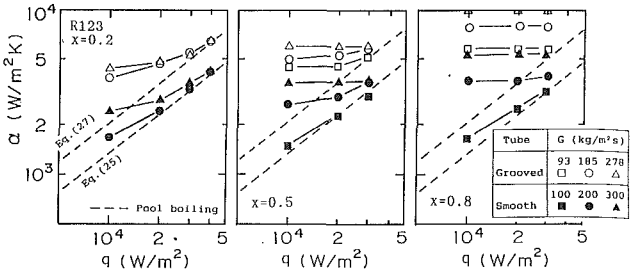

Fig. 5 Heat transfer coefficients for R123 in the form $\alpha - q$

$$-(dP/dz)_L = (0.184/\mathrm{Re}_L^{0.2})\{G(1-x)\}^2/2D_i\rho_L \quad (17)$$

$$\mathrm{Re}_L = G(1-x)D_i/\eta_L \quad (18)$$

$$X_{tt} = \{(1-x)/x\}^{0.9}(\rho_G/\rho_L)^{0.5}(\eta_L/\eta_G)^{0.1} \quad (19)$$

where $-(dP/dz)_F$ is the two-phase frictional pressure drop. A simple correlation for the smooth tube was suggested by Chisholm (1967) as follows:

$$\Phi_L^2 = 1 + 20/X_{tt} + 1/X_{tt}^2 \quad (20)$$

This correlation is shown by a broken line in Fig. 3(*a*). It is found that Chisholm's correlation does not differ from Eq. (14) greatly except in the region of small $1/X_{tt}$. On the other hand, the frictional pressure drop for the grooved tube was about 30–40 percent larger than that for the smooth tube.

Heat Transfer Coefficient. Figures 4(*a*), 4(*b*), and 4(*c*) show the heat transfer coefficient data. Heat transfer coefficients for R123/R134a are apparently lower than those for R123 alone. The dependence of heat transfer coefficients on mass flux, quality, and heat flux, however, is too complicated to allow discussion of the heat transfer characteristics from these figures. Thus, these data are rearranged in different forms. According to observations through a sight glass, the flow pattern was annular or semi-annular in the region $x \geq 0.2$ except for $G = 100$ (or 93) kg/m² s. In order to distinguish the effects of flow stratification, the discussion here ignores G = 100 (or 93) kg/m²s.

The heat transfer coefficient data for R123 at $x = 0.2$, 0.5, and 0.8 (or the interpolated values) are shown in Fig. 5, where some data for $q = 40$ kW/m² are also included. The heat transfer characteristics for the grooved tube are similar to those for the smooth tube. Although the heat transfer coefficient depends on heat flux in the low-quality and low-mass-flux region, this dependence is less significant in the high-quality and high-mass-flux region. In this region the heat transfer coefficient for the grooved tube is about twice as large as that for the smooth tube. Recently Schlager et al. (1990) and Khanpara et al. (1986) performed experiments with R22 and R113 flowing inside microfin tubes, respectively. The heat transfer enhancement factors were shown in their reports (1.6–2.2 and 1.3–2.0, respectively), but the dependence of heat transfer coefficient on heat flux, mass flux, and quality was not discussed in detail. Ito and Kimura (1979) and Kimura and Ito (1981) measured the local heat transfer coefficients with R22 and R12 flowing inside spirally grooved tubes. Their data indicated the same characteristics as the present data except in the region of $G \leq 65$ kg/m²s, where capillary action in the grooves is dominant due to low vapor velocity.

Figures 6(*a*) and 6(*b*) show the heat transfer coefficient data for R123 in the smooth tube and the grooved tube, respectively. The ordinate and abscissa are α/α_L and $1/X_{tt}$. α_L is the single-phase heat transfer coefficient when the liquid component is flowing alone, and it is given by

$$\alpha_L = 0.023\mathrm{Re}_L^{0.8}\mathrm{Pr}_L^{0.4}\lambda_L/D_i \text{ for the smooth tube} \quad (21)$$

$$\alpha_L = 0.036\mathrm{Re}_L^{0.8}\mathrm{Pr}_L^{0.4}\lambda_L/D_i \text{ for the grooved tube} \quad (22)$$

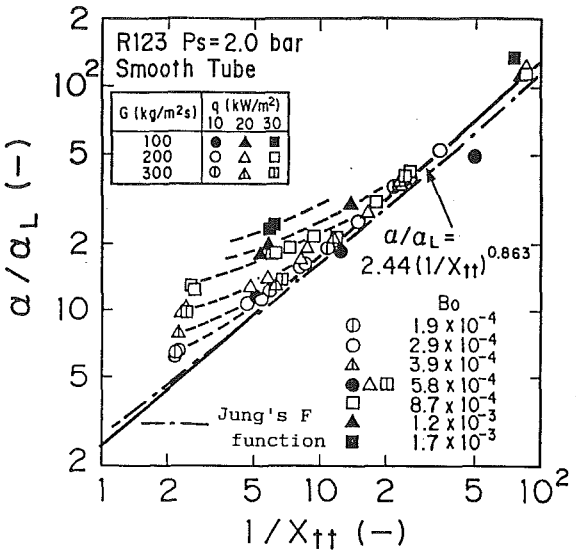

Fig. 6(*a*) For smooth tube

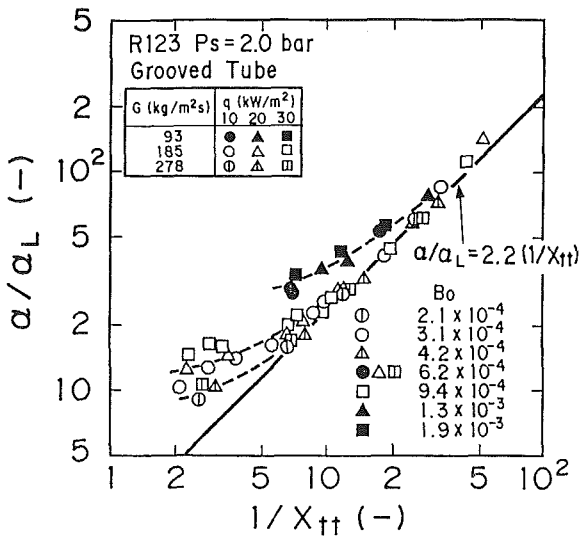

Fig. 6(*b*) For grooved tube

Fig. 6 Heat transfer coefficients for R123 in the form $\alpha/\alpha_L - 1/X_{tt}$

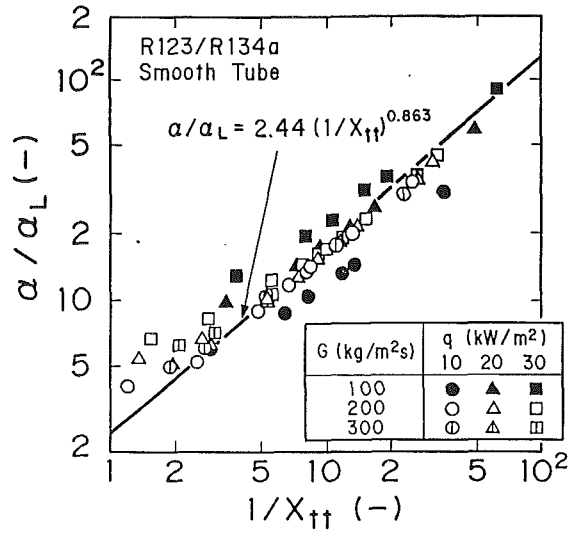

Fig. 7(*a*) For smooth tube

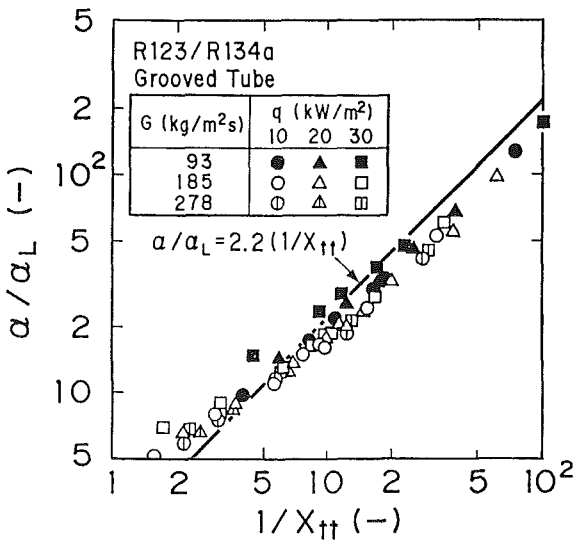

Fig. 7(*b*) For grooved tube

Fig. 7 Heat transfer coefficient data for R123/R134a in the form $\alpha/\alpha_L - 1/X_{tt}$

Equation (21) is based on the Dittus–Boelter equation. Equation (22) was obtained from single-phase heat transfer data for the grooved tube. The value of the boiling number, Bo $(=q/G\cdot r)$, is given for each datum in Fig. 6. For the smooth tube, α/α_L can be represented as a function of Bo and X_{tt}. The α/α_L values in the region of small $1/X_{tt}$ are significantly dependent on Bo, and this implies that nucleate boiling is dominant. As $1/X_{tt}$ becomes larger, the dependence of α/α_L on heat flux becomes less significant. That is, nucleate boiling is suppressed and two-phase forced convection becomes dominant. The heat transfer characteristics for the grooved tube are similar to those for the smooth tube, but the dependence of α/α_L on Bo is not so clear.

Figures 7(*a*) and 7(*b*) show the heat transfer coefficients for the mixture of R123 and R134a. The dependence of α/α_L on the heat flux is insignificant compared to that for R123, and so nucleate boiling is found to be reduced by mixture effects. In the grooved tube, the heat transfer coefficients are almost independent of heat flux.

Correlation of the Heat Transfer Coefficients

For the Pure Refrigerant. Chen (1966) proposed that the heat transfer coefficient for forced convective boiling, α, could be expressed as the arithmetic summation of the two-phase convection contribution α_{TC} and the nucleate boiling contribution α_{NB}.

$$\alpha = \alpha_{TC} + \alpha_{NB} \tag{23}$$

$$= \alpha_L \cdot F + \alpha_{PB} \cdot S \tag{24}$$

Here, α_{PB} is the pool boiling heat transfer coefficient at the same value of wall superheat as for forced convective boiling, and S is a factor representing the suppression of nucleate boiling due to liquid flow. The value of α_{PB} for the smooth tube was obtained from the correlation by Nishikawa et al. (1982), and is given by

$$\alpha_{PB} = 31.4\ \{P_c^{0.2} F_p/(M^{0.1} T_c^{0.9})\} q_{PB}^{0.8} \tag{25}$$

$$F_p = (P/P_c)^{0.23}/[1 - 0.99(P/P_c)]^{0.9} \tag{26}$$

and α_{PB} for the grooved tube was obtained from the modified correlation below:

$$\alpha_{PB} = 48\{P_c^{0.2} F_p/(M^{0.1} T_c^{0.9})\} q_{PB}^{0.8} \tag{27}$$

A comparison of these correlations with the heat transfer coef-

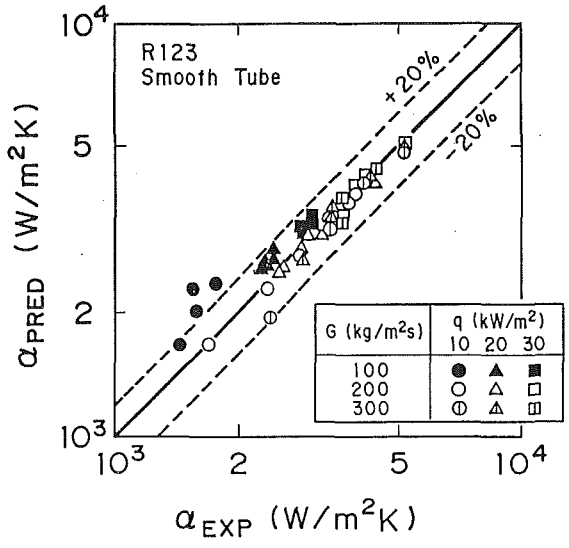

Fig. 8(*a*) For smooth tube

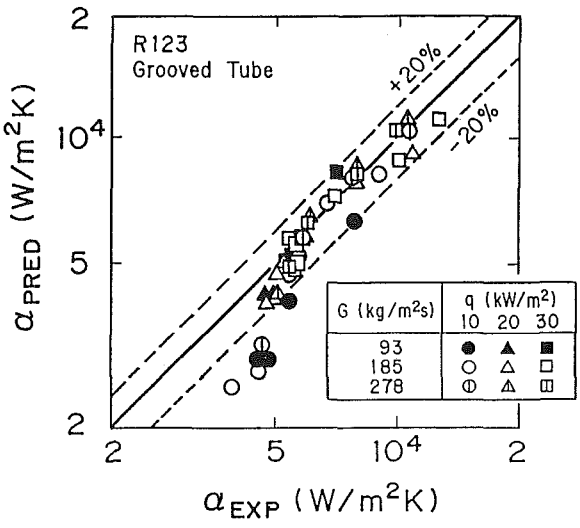

Fig. 8(*b*) For grooved tube

Fig. 8 Comparison between predicted and experimental heat transfer coefficients for R123

ficient data is shown in Fig. 5. In the low-quality and high-heat-flux region, the heat transfer coefficient for forced convective boiling is independent of mass flux, and approaches that for pool boiling. Equation (27) is shown as an asymptote in Fig. 5 and was obtained by assuming that α_{PB} is in proportion to $\{P_c^{0.2}F_P/(M^{0.1}T_c^{0.9})\}q_{PB}^{0.8}$. The proportional constant (=48) was determined by a fit to the data for $x = 0.2$. Bennett et al. (1980) derived the factor S analytically as

$$S=[1-\exp(-\alpha_{TC}\delta/\lambda_L)]/(\alpha_{TC}\delta/\lambda_L) \tag{28}$$

$$\delta=C_d[\sigma/g(\rho_L-\rho_G)]^{1/2} \tag{29}$$

The empirical constant C_d was previously found to be 0.08 by Murata and Hashizume (1988, 1990). The factor F represents the acceleration effect of liquid due to vapor shear stress and is shown as an asymptote in Fig. 6. The asymptote was obtained by a fit to the data and is written as

$$F=2.44(1/X_{tt})^{0.863} \text{ for the smooth tube} \tag{30}$$

$$F = 2.2\ (1/X_{tt}) \quad \text{for the grooved tube} \tag{31}$$

Several F factors have already been proposed for smooth tube although there seems to be nothing for a grooved tube. The

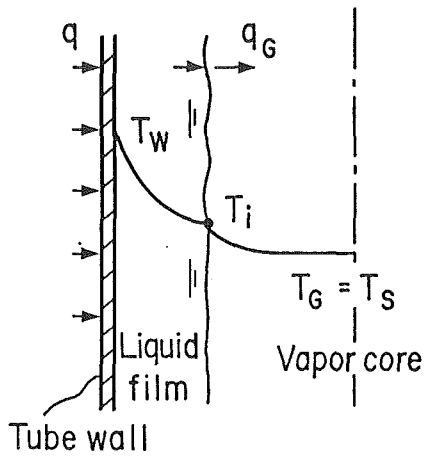

Fig. 9 Heat transfer model for mixture

F function for R11 and R114 obtained by Murata and Hashizume (1988, 1990) is the same as Eq. (30). The original F factor was given in graphic form by Chen (1966), and was later corrected with the Prandtl number by Bennett and Chen (1980). These F factors were expressed in the report of Jung et al. (1989a) as

$$F=1+1.8(1/X_{tt})^{0.82} \tag{32}$$

$$F=\{1+1.8(1/X_{tt})^{0.82}\}\mathrm{Pr}_L^{0.296} \tag{33}$$

The values of the original Chen's F factor are much smaller than the F function developed in the present study, i.e., Eq. (30), but the deviation decreases by the Prandtl number correction in Eq. (33) considerably. Ross et al. (1987) adopted Chen's F factor with the Prandtl number correction. Jung et al. (1989b) determined an F function from the data for pure refrigerants R22, R114, R12, and R152a in the convection-dominant region. It is shown in Fig. 6(*a*) and written by

$$F=2.37(0.29+1/X_{tt})^{0.85} \tag{34}$$

The F function determined by Jung et al. agrees well with Eq. (30) in the present experimental range.

A comparison of the developed correlations Eqs. (21)–(31) with experimental results for the pure refrigerant R123 is shown in Figs. 8(*a*) and 8(*b*); the ordinate and abscissa are the predicted and experimental heat transfer coefficients, respectively. The predicted heat transfer coefficients agree with the experimental results to within ±20 percent, except in the low-mass-flux and low-heat-flux regions. The disagreement in these regions seems to be due to the effects of flow stratification in the smooth tube, and to capillary action in the grooved tube.

For the Mixture. The discussion here ignores G = 100 (or 93) kg/m²s. In Figs. 7(*a*) and 7(*b*) for the mixture R123/R134a, α/α_L values in the region of large $1/X_{tt}$ ($1/X_{tt} \geq 20$) are several percent lower for the smooth tube and about 25 percent lower for the grooved tube than the solid lines representing two-phase convection of the equivalent pure fluid. This degradation is obviously attributable to something other than the mixture effects on nucleate boiling.

Correlations are now developed for the heat transfer coefficient. Figure 9 shows the heat transfer model. This model is based on that of Sardesai et al. (1982), and the reduction in heat transfer coefficient for mixtures is attributed to the sensible heating of the vapor phase (namely, the single-phase forced convective heat transfer to the vapor phase) accompanying the rise in saturation temperature along the flow direction in addition to the mixture effects on nucleate boiling. The principal assumptions are as follows:

1 The two-phase flow pattern is annular.
2 The temperature of the vapor phase, T_G, is equal to the saturation temperature, T_s, at given pressure P_s and equilibrium quality x.
3 The sensible heat transferred to the liquid phase is negligible compared to the latent heat of vaporization.
4 The heat transferred to the vapor phase is equal to the sensible heat used to change the temperature of the vapor phase as the saturation temperature rises in the flow direction.
5 The heat transfer coefficient of the liquid film, α_{LF}, is equal to the heat transfer coefficient of two-phase convection for the equivalent pure fluid, $\alpha_{TC\cdot ID}$.
6 The mixture effects on nucleate boiling are expressed by the following equations:

$$\alpha_{NB} = \alpha_{PB} \cdot S_{ID} \tag{35}$$

$$\alpha_{PB} = \alpha_{PB\cdot ID}/[1 + A_{NB}(Y_M - X_M)] \tag{36}$$

$$\alpha_{PB\cdot ID} = \alpha_{PB\cdot 1} X_M + \alpha_{PB\cdot 2}(1 - X_M) \tag{37}$$

where $\alpha_{PB\cdot 1}$, $\alpha_{PB\cdot 2}$, and α_{PB} are pool boiling heat transfer coefficients for component 1, component 2, and a binary mixture, respectively. The pool boiling heat transfer coefficient for each component was obtained from Eq. (25) or (27) using the same value of wall superheat as for forced convective boiling. A_{NB} is a factor representing the reduction in nucleate pool boiling heat transfer coefficients due to mixture effects, and Eqs. (36) and (37) differ from the popular prediction method of the nucleate pool boiling heat transfer coefficients for a binary mixture. The popular prediction method is as follows.

The wall superheat at a given heat flux during nucleate pool boiling of a binary mixture, ΔT, is larger than the ideal wall superheat, ΔT_{ID}, and given by

$$\Delta T/\Delta T_{ID} = 1 + \zeta \tag{38}$$

$$\Delta T_{ID} = \Delta T_1 X_M + \Delta T_2(1 - X_M) \tag{39}$$

where ΔT_1 and ΔT_2 are the wall superheats at a given heat flux during pool boiling of the components 1 and 2, respectively. The factor ζ represents the increase in wall superheat due to the mixture effects on nucleate boiling. Thome (1983) and Ünal (1986) developed the correlations of ζ using only phase equilibrium data. Substituting $q_{PB} = \alpha_{PB}\Delta T = \alpha_{PB\cdot ID}\Delta T_{ID}$ into Eq. (38), α_{PB} is expressed by

$$\alpha_{PB} = \alpha_{PB\cdot ID}/(1 + \zeta) \tag{40}$$

$$\alpha_{PB\cdot ID} = \{X_M/\alpha_{PB\cdot 1} + (1 - X_M)/\alpha_{PB\cdot 2}\}^{-1} \tag{41}$$

In the above prediction method, α_{PB} is the pool boiling heat transfer coefficient not for a given wall superheat but for a given heat flux. If this method were applied to Eq. (35), α_{PB} would be evaluated from the nucleate boiling heat flux q_{NB} or the total heat flux q. In result, α_{PB} would differ from the pool boiling heat transfer coefficient at the same value of wall superheat as for a given forced convective boiling. According to Chen (1966), the effective wall superheat for forced convective boiling becomes smaller than a wall superheat generally defined due to liquid flow, and the suppression factor S represents such a reduction in the effective wall superheat. Thus, α_{PB} in Eq. (35) should be based on wall superheat rather than on heat flux as Forster and Zuber's correlation for nucleate pool boiling used by Chen (1966). In other words, α_{PB} in Eq. (35) should be the pool boiling heat transfer coefficient at the same value of wall superheat as for a given forced convective boiling as far as the suppression factor S is used. That is the reason why the popular prediction method of the pool boiling heat transfer coefficients for a binary mixture was not adopted in the present study, and the new factor A_{NB} was introducted. Also, $\alpha_{PB\cdot 1}$ and $\alpha_{PB\cdot 2}$ in Eq. (37) were calculated from wall superheat. Jung et al. (1989b) adopted the popular prediction method into the nucleate boiling contribution term, but they introduced a new factor N instead of the suppression factor S. This N factor represents how strong the effect of nucleate boiling is in forced convective boiling as compared to that in pool boiling.

The heat flux transferred into the vapor core at the liquid–vapor interface, q_G, is given by

$$q_G = \alpha_G(T_i - T_G) \tag{42}$$

where α_G is the vapor-phase heat transfer coefficient and T_i is the temperature at the liquid–vapor interface. The value of T_i is a little higher than the saturation temperature T_s at given pressure and equilibrium quality. As a result, the compositions at the interface are different from the bulk values X_M and Y_M, but the effect of diffusive resistance on two-phase forced convection is neglected. The heat flux at the tube wall, q, is given by

$$q = \alpha_{LF}(T_w - T_i) + \alpha_{NB}(T_w - T_s) \tag{43}$$

Arranging these equations with $T_G = T_s$ (Assumption 2), α $(= q/(T_w - T_s))$ is expressed by

$$\alpha = \frac{\alpha_{LF} + \alpha_{NB}}{1 + (q_G/q)(\alpha_{LF}/\alpha_G)} \tag{44}$$

The following equation is derived from Assumptions 2 and 4:

$$(q_G/q) = xC_{pG}(\partial T_s/\partial i)_p \tag{45}$$

where C_{pG} is the vapor specific heat and i is the enthalpy. Substituting Eq. (45) and $\alpha_{LF} = \alpha_{TC\cdot ID}$ (Assumption 5) into Eq. (44) yields

$$\alpha = \frac{\alpha_{TC\cdot ID} + \alpha_{NB}}{1 + xC_{pG}(\partial T_s/\partial i)_p(\alpha_{TC\cdot ID}/\alpha_G)} \tag{46}$$

This equation coincides with the correlation for the pure fluid, i.e., Eq. (23), if $Y_M = X_M$ and $(\partial T_s/\partial i)_p = 0$. It can be seen from the form of this equation that the degradation in heat transfer coefficient due to sensible heating of the vapor phase becomes more significant as the heat transfer coefficient of two-phase convection, $\alpha_{TC\cdot ID}$, the rise of saturation temperature $(\partial T_s/\partial i)_P$, and the quality x increase in value. $\alpha_{NB}(=\alpha_{PB}\cdot S_{ID})$ is obtained from Eqs. (25)–(29) and (35)–(37). $\alpha_{TC\cdot ID}$ $(=\alpha_{L\cdot ID}\cdot F_{ID})$ is from Eqs. (21), (22), (30), and (31). $(\partial T_s/\partial i)_P$ was evaluated from the P–R equation of state. The value of A_{NB} was taken to be 15 from the present data. In general, the factor A_{NB} seems to be determined from pool boiling data for a given mixture and pressure, as reported by Stephan and Körner (1969). α_G was obtained from the analogy between heat transfer and shear stress at the liquid–vapor interface, using Eqs. (47)–(52).

$$\mathrm{St} = \alpha_G^*/\rho_G C_{PG} u_G \tag{47}$$

$$= (f_G/2)[1 + 12.7(f_G/2)^{0.5}(\mathrm{Pr}_G^{2/3} - 1)] \tag{48}$$

$$u_G = Gx/\rho_G\gamma \tag{49}$$

$$f_G = 2\tau_i/\rho_G u_G^2 \tag{50}$$

$$\tau_i = -(dP/z)_F D_i \gamma^{1/2}/4 \tag{51}$$

$$\alpha_G = \alpha_G^* \gamma^{1/2} \tag{52}$$

Equation (48) is a correlation for single-phase forced convective heat transfer inside a tube recommended by Gnielinski (1983). The vapor shear stress at the liquid–vapor interface, τ_i, was approximately expressed by Eq. (51) in annular flow regime. The frictional pressure drop $-(dP/dz)_F$ was obtained from Eq. (14) or (15). The void fraction γ was assumed to be obtained from Eq. (11) for both the smooth and grooved tubes. The average vapor velocity, u_G, and the friction factor at the liquid–vapor interface, f_G, were calculated from Eqs. (49) and (50) using γ and τ_i. Finally, the vapor-phase heat transfer coefficient, α_G, was obtained from Eqs. (47), (48), and (52).

If the refrigerant mass flux, G, quality, x, and heat flux, q, are given, the heat transfer coefficient, α, is obtained using the following procedure:

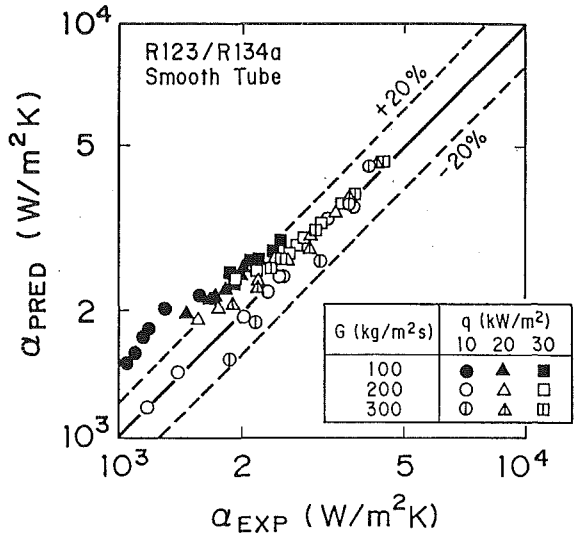

Fig. 10(*a*) For smooth tube

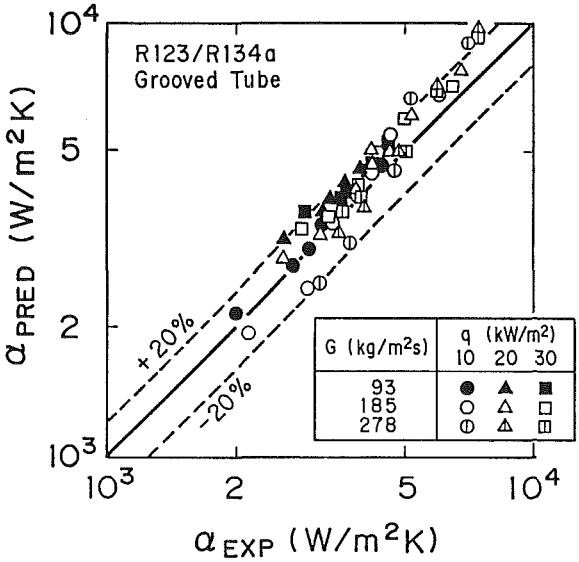

Fig. 10(*b*) For grooved tube

Fig. 10 Comparison between predicted and experimental heat transfer coefficients for R123/R134a

1 Calculate α_L from Eq. (21) or (22), and F from Eq. (30) or (31).
2 Calculate $\alpha_{TC\cdot ID} = \alpha_L \cdot F$.
3 Calculate $-(dP/dz)_F$ from Eq. (14) or (15).
4 Calculate α_G from Eqs. (47)–(52) and the above $-(dP/dz)_F$.
5 Calculate $(\partial T_s/\partial i)_p$ by the Peng-Robinson method.
6 Calculate S_{ID} from Eq. (28) and (29).
7 Assume the wall superheat $(T_w - T_s)$.
8 Calculate α_{PB} for each component by substituting $q_{PB} = \alpha_{PB}(T_w - T_s)$ into Eq. (25) or (27).
9 Calculate α_{PB} for a binary mixture from Eqs. (36) and (37).
10 Calculate α_{NB} from Eq. (35).
11 Calculate α' from Eq. (46).
12 Calculate $\Delta T = q/\alpha'$.
13 $(T_w - T_s) = \Delta T$.
14 Repeat steps 8–13 until $(T_w - T_s)$ converges.
15 $\alpha = \alpha'$ when $(T_w - T_s)$ converges.

The properties of the equivalent pure fluid should be used in the above calculation.

Table 3 Comparison of percentage deviation between some correlations and the present data (fluid: R123, tube: smooth tube)

mass flux (kg/m²s)	Ross et al Mean	Ross et al Ave.	Jung et al Mean	Jung et al Ave.	Present work Mean	Present work Ave.
100	11.2	6.5	17.8	-8.1	16.9	16.9
200	8.8	-0.2	9.9	-9.9	3.1	-1.7
300	9.6	5.1	8.4	-8.4	5.5	-4.5

$$\text{Mean dev.} = \frac{1}{n}\sum_{1}^{n} \text{ABS}[(\alpha_{PRED}-\alpha_{EXP})\text{X}100/\alpha_{EXP}]$$

$$\text{Ave. dev.} = \frac{1}{n}\sum_{1}^{n} [(\alpha_{PRED}-\alpha_{EXP})\text{X}100/\alpha_{EXP}]$$

Table 4 Comparison of percentage deviation between some correlations and the present data (fluid: R123/R134a, tube: smooth tube)

mass flux (kg/m²s)	Ross et al Mean	Ross et al Ave.	Jung et al Mean	Jung et al Ave.	Present work Mean	Present work Ave.
100	28.9	20.7	23.8	2.4	31.6	31.6
200	18.3	14.5	9.1	-6.9	8.6	8.0
300	22.1	22.1	8.8	-3.0	7.8	5.9

Figures 10(*a*) and 10(*b*) compare the correlations developed with the experimental results for R123/R134a. The predicted heat transfer coefficients agree with the experimental data to within ±20 percent, except in the low-mass-flux region for the smooth tube.

Tables 3 and 4 give comparisons of the present results with the previous correlations for R123 and R123/R134a. Ross et al. (1987) discussed the correlations in the convection-dominant region and the boiling-dominant region separately. Therefore, the larger of the two heat transfer contributions was selected as a heat transfer coefficient. Jung et al. (1989b) developed the same type of correlation as Chen (1966), but a new factor was introduced instead of the suppression factor S. The pool boiling heat transfer correlation for pure refrigerants given by Stephan and Abdelsalam (1980) and the popular prediction method of the pool boiling heat transfer coefficients for a binary mixture were used in both of them. Although the correlations of Ross et al. and Jung et al. have a tendency to overpredict and underpredict the present results, respectively, the deviation is small enough. In their correlations, the nucleate boiling contribution was evaluated from the total heat flux, q, even in the partial boiling region, that is, even when the nucleate boiling and the two-phase convection coexist. According to Chen's supposition, it seems that the nucleate boiling contribution should be evaluated from the nucleate boiling heat flux, q_{NB}, rather than from the total heat flux, q.

Concluding Remarks

1 Frictional pressure drop data for R123/R134a were correlated using the same equations as for R123, based on the properties of the equivalent pure fluid. Accordingly, it seems that the frictional pressure drop for mixtures is approximately equal to that for the equivalent pure fluid.

2 The heat transfer coefficient for R123/R134a was found to be lower than that for the equivalent pure fluid not only in the boiling-dominant region, but also in the convection-dominant region.

3 Correlations were developed for the heat transfer coefficients in smooth and grooved tubes. They are based on a model in which the reduction in heat transfer coefficient of a mixture is attributed to the mixture effects on nucleate boiling and to sensible heating of the vapor phase accompanying the

rise of saturation temperature in the flow direction. These correlations predicted the heat transfer coefficients for R123 and R123/R134a to within ±20 percent, except in the region where the effects of flow stratification are significant.

The correlations developed here include an empirical factor A_{NB}, which represents the mixture effects on nucleate boiling. This factor can be obtained from pool boiling data for a given mixture and pressure.

References

Bennett, D. L., and Chen, J. C., 1980, "Forced Convective Boiling in Vertical Tubes for Saturated Pure Components and Binary Mixtures," *AIChE Journal*, Vol. 26, pp. 454–461.

Bennett, D. L., Davis, M. W., and Hertzler, B. L., 1980, "The Suppression of Saturated Nucleate Boiling by Forced Convective Flow," *AIChE Symposium Series*, Vol. 76, No. 199, pp. 91–103.

Chen, J. C., 1966, "Correlation for Boiling Heat Transfer to Saturated Fluids in Convective Flow," *Ind. Engng. Chem. Process Des. Dev.*, Vol. 5, pp. 322–329.

Chisholm, D., 1967, "A Theoretical Basis for the Lockhart–Martinelli Correlation for Two-Phase Flow," *Int. J. Heat Mass Transfer*, Vol. 10, pp. 1767–1778.

Fauske, H. K., 1961, "Critical Two-Phase Steam-Water Flows," *Proc. Heat Transfer and Fluid Mechanics Institute*, Stanford University Press, pp. 78–89.

Gnielinski, V., 1983, *Heat Exchanger Design Handbook*, Vol. 2 (Fluid Mechanics and Heat Transfer), VDI-Verlag/Hemisphere Pub.

Ito, M., and Kimura, H., 1979, "Boiling Heat Transfer and Pressure Drop in Internal Spiral-Grooved Tubes," *Bulletin of the JSME*, Vol. 22, No. 171, pp. 1251–1257.

Jung, D. S., McLinden, M., Radermacher, R., and Didion, D., 1989a, "Horizontal Flow Boiling Heat Transfer Experiments With a Mixture of R22/R114," *Int. J. Heat Mass Transfer*, Vol. 32, pp. 131–145.

Jung, D. S., McLinden, M., Radermacher, R., and Didion, D., 1989b, "A Study of Flow Boiling Heat Transfer With Refrigerant Mixtures," *Int. J. Heat Mass Transfer*, Vol. 32, pp. 1751–1764.

Khanpara, J. C., Bergles, A. E., and Pate, M. B., 1986, "Augmentation of R113 In-Tube Evaporation With Microfin Tubes," *ASHRAE Transactions*, Vol. 92, Part 2, pp. 506–524.

Kimura, H., and Ito, M., 1981, "Evaporating Heat Transfer in Horizontal Internal Spiral-Grooved Tubes in the Region of Low Flow Rates," *Bulletin of the JSME*, Vol. 24, No. 195, pp. 1602–1607.

Mishra, M. P., Varma, H. K., and Sharma, C. P., 1981, "Heat Transfer Coefficients in Forced Convection Evaporation of Refrigerant Mixtures," *Letters in Heat and Mass Transfer*, Vol. 8, pp. 127–136.

Murata, K., and Hashizume, K., 1988, "Force Convection Boiling of Non-azeotropic Mixtures," *Transactions of JSME*, Vol. 54, No. 506B, pp. 2856–2863.

Murata, K., and Hashizume, K., 1990, "An Investigation on Forced Convection Boiling of Non-azeotropic Refrigerant Mixtures," *Heat Transfer—Japanese Research*, Vol. 19-2, pp. 95–109.

Nakaiwa, M., Owa, M., Akiya, T., Sato, M., and Hakuta, T., 1990, "A Performance Evaluation of Heat Pump Cycle for the Binary Refrigerant Mixture R134a/R123," *Proc. 3rd International Energy Agency Heat Pump Conf.*, Tokyo, Japan, pp. 693–701.

Nisikawa, K., Fujita, Y., Ohta, H., and Hidaka, S., 1982, "Effect of the Surface Roughness on the Nucleate Boiling Heat Transfer Over the Wide Range of Pressure," *Proc. 7th Int. Heat Transfer Conf.*, Vol. 4, pp. 61–66.

Peng, D. Y., and Robinson, D. B., 1976, "A New Two-Constant Equation of State," *Ind. Eng. Chem., Fundam.*, Vol. 15, pp. 59–64.

Reid, R. C., and Sherwood, T. K., 1966, *The Properties of Gases and Liquids*, McGraw-Hill, New York.

Ross, H., Radermacher, R., and Marzo, M., 1987, "Horizontal Flow Boiling of Pure and Mixed Refrigerants," *Int. J. Heat Mass Transfer*, Vol. 30, pp. 979–992.

Sardesai, R. G., Shock, R. A. W., and Butterworth, D., 1982, "Heat and Mass Transfer in Multicomponent Condensation and Boiling," *Heat Transfer Engineering*, Vol. 3, pp. 104–114.

Schlager, L. M., Pate, M. B., and Bergles, A. E., 1990, "Evaporation and Condensation Heat Transfer and Pressure Drop in Horizontal, 12.7-mm Microfin Tubes With Refrigerant 22," ASME JOURNAL OF HEAT TRANSFER, Vol. 112, pp. 1041–1047.

Singal, L. C., Sharma, C. P., and Varma, H. K., 1984, "Heat Transfer Correlation for the Forced Convection Boiling of R12-R13 Mixtures," *Int. J. Refrigeration*, Vol. 7-5, pp. 278–284.

Stephan, K., and Körner, M., 1969, "Berechnung des Wärmeübergangs verdampfender binärer Flüssigkeitsgemische," *Chemie Ingenieur Technik*, Vol. 41, pp. 409–417.

Stephan, K., and Abdelsalam, M., 1980, "Heat Transfer Correlation for Natural Convection Boiling," *Int. J. Heat Mass Transfer*, Vol. 23, pp. 73–87.

Thome, J. R., 1983, "Prediction of Binary Mixture Boiling Heat Transfer Coefficients Using Only Phase Equilibrium Data," *Int. J. Heat Mass Transfer*, Vol. 26-7, pp. 965–974.

Ünal, H. C., 1986, "Prediction of Nucleate Boiling Heat Transfer Coefficients for Binary Mixtures," *Int. J. Heat Mass Transfer*, Vol. 29, pp. 637–640.

Yoshida, S., Matsunaga, T., Mori, H., and Ohishi, K., 1990, "Heat Transfer to Non-azeotropic Mixtures of Refrigerants Flowing in a Horizontal Evaporator Tube," *Transactions of JSME*, Vol. 56, No. 524B, pp. 1084–1089.

Direct-Contact Condensation of Low-Density Steam on Seawater at High Inlet Noncondensable Concentrations

F. Zangrando

D. Bharathan

National Renewable Energy Laboratory,
Golden, CO 80401

Computer models and experimental data are summarized to characterize the condensation of low-density steam in direct contact with a process fluid that is distributed over structured packings of various geometries. The one-dimensional models integrate the heat, mass, and momentum processes in the two streams, over the height of the contactor. Both cocurrent and countercurrent flows of the two streams were analyzed. The models were validated extensively with experimental data obtained with fresh water and with seawater, at high inlet noncondensable concentrations. The data obtained in these experiments provide a broad engineering data base to design and evaluate the performance of advanced heat exchangers for a number of applications, such as production of electrical power and/or potable water using low-density steam, as could be used in Ocean Thermal Energy Conversion systems and in the low-pressure stages of conventional power cycles.

Introduction

Direct-contact condensers (DCC) offer the potential of very high thermal effectiveness in contactors of short height, with low gas-pressure drops, negligible fouling, and low capital and operating costs compared to the more commonly used surface condensers. However, no comprehensive treatments are available for direct-contact applications to design and analyze industrial and power systems, as are available for surface condensers. The most common techniques used by industry in direct-contact gas to liquid heat transfer processes are the liquid-spray column and the baffle-plate column. Methods of designing these devices and comparisons of their performance are given by Fair (1972). The thermal effectiveness attained has been in the range of 0.6 to 0.7, generally with large pressure drops through the condenser. Krebs and Schlünder (1984) describe the process of condensation on a liquid film inside smooth vertical tubes, in the presence of noncondensable gases.

Packed columns have been used in industry for applications that require high heat and mass transfer in small volumes. Until recently, the columns were packed with randomly distributed structures such as Pall rings and Berl saddles that served to distribute the liquid and resulted in complex flow patterns with associated large pressure losses. More recently, structured packings have been adopted, especially for use in industrial cooling towers. In the structured packings, the liquid is distributed over an ordered series of inclined sheets made of plastic, metal, or wire mesh (see Fig. 1). These packings provide a means to redistribute the liquid flow continually while providing a relatively straightforward flow path for the gas phase, which alternates between triangular and diamond cross sections along the packing. Although the cost per unit volume of structured packings is somewhat higher than the cost of the more traditional packings, the structured packings yield a low ratio of pressure drop to heat or mass transfer coefficient per unit volume (Bravo et al., 1985, 1986). Direct-contact columns are also being adopted in industry for process heat recovery (e.g., Huang and Fair, 1989; Fair, 1990).

An intensive program to test direct-contact condensers was initiated in 1983 at the Solar Energy Research Institute (SERI), now the National Renewable Energy Laboratory (NREL). The goal was to develop high-performance advanced heat exchangers for open-cycle (OC) Ocean Thermal Energy Conversion (OTEC) applications. Although the oceans are very large collectors of solar energy, the temperature difference available in the oceans is very limited (typically less than 20 K). Therefore, the heat exchangers needed to produce and condense the steam must be very effective, attaining a very close temperature approach. Because the steam is produced at around 2500 Pa, the exchangers must also have exceedingly low pressure drops so that a large portion of the driving potential can be used for power production in the low-pressure turbine. In addition, the seawater introduced in the low-pressure chambers of the OC-OTEC system releases large quantities of noncondensable gases that tend to hinder the condensation process. Tests conducted with a multitude of both random and structured packings using fresh water have yielded valuable information on how these devices operate in the low-pressure,

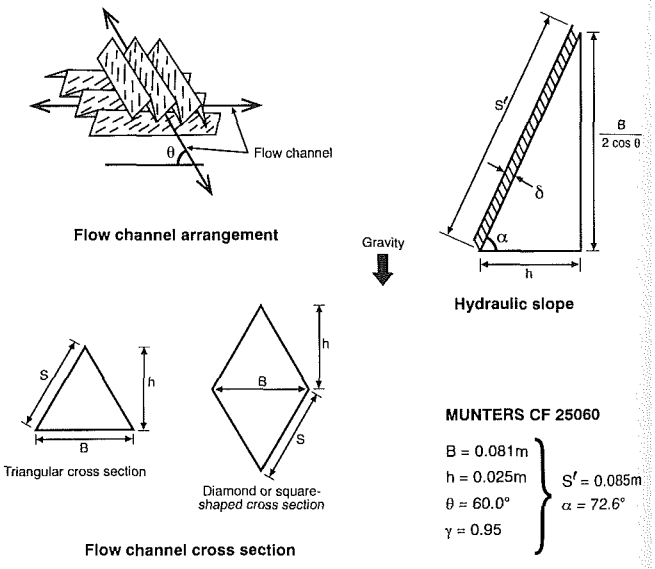

Fig. 1 Structured packing geometry

Contributed by the Heat Transfer Division for publication in the JOURNAL OF HEAT TRANSFER. Manuscript received by the Heat Transfer Division April 1992; revision received September 1992. Keywords: Condensation, Direct-Contact Heat Transfer, Heat Exchangers. Associate Technical Editor: L. C. Witte.

high-noncondensable-gas environment. Structured packings were found to provide very high thermal effectiveness, up to 0.93, for contactor heights less than 1 m. With low pressure drops, they routinely yielded more than 98 percent condensation of the steam. These packings have now been demonstrated to be the packings of choice for OC-OTEC applications.

Details of the modeling and validation efforts, including the computer codes, the parametric analyses, the apparatus, the data, and the uncertainties are given by Bharathan et al. (1988), herein referred to as the BPA report. Because this report is fairly detailed, only some of the salient results are summarized here. Figure 2 is a schematic of the two flow configurations modeled and tested at NREL to validate the computer models, and tested at the Seacoast Test Facility, on the big island of Hawaii, to obtain the seawater performance of one selected packing material under a broad range of OC-OTEC conditions, in an apparatus called the HMTSTA. Details of the seawater test effort, including system layout, flow diagrams, apparatus, data, and uncertainties are given by Zangrando et al. (1990), herein referred to as the ZEA report. Because of the consistency of the data in both sets of experiments, and because of the principal interest in OC-OTEC applications, this article is based on data from the seawater tests to describe the performance of the DCC.

For the OC-OTEC application, a two-stage condenser is preferred: first a cocurrent stage that condenses about 80 percent of the incoming steam from the turbine, followed by a countercurrent stage that concentrates the noncondensable gases, which must be vented to ambient. Typical OC-OTEC operating conditions can be described as follows. Cold seawater enters the condenser chamber at about 6°C, and the saturation temperature of the incoming steam is about 12°C. Because the steam is exposed directly to the seawater while it condenses, the seawater exits at a temperature that is very close to the steam inlet saturation temperature (the difference is on the order of 0.5 K). The noncondensable gases released from the warm seawater in the evaporator amount to approximately 19 parts per million (ppm), and a small quantity of additional gas is introduced by system leaks. These two sources account for a noncondensable-gas concentration in the steam entering the cocurrent condenser of about 0.4 percent by weight. Most of the noncondensable gases present in the cold seawater (about 19 ppm of the cold seawater) also come out of solution during the condensation process. All these gases must be pumped out

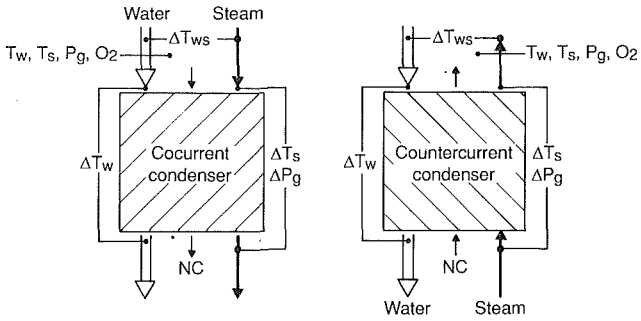

Fig. 2 Schematic of flow geometry and instrumentation for the cocurrent and countercurrent condenser stages

of the condenser to maintain operating pressure; the ratio of gas to steam in the exhaust flow is generally 40 percent to 70 percent, depending on operating conditions.

The modeling and the experimental effort considered the two condenser stages independently and in combined operation, so the results of this research effort could be extended to broader applications, such as industrial heat recovery, cooling towers, electric power plants, and potable water production.

The paper summarizes the salient features of the computer models, identifies the experimental facilities used for the tests, summarizes the error analysis and data consistency, defines the performance parameters used to describe the experimental data, presents the experimental data obtained with the cocurrent and countercurrent condensers, and compares the model predictions with the experimental data to establish the validity of the computer models.

Computer Models

Detailed computer models usable on personal computers were developed at NREL in 1983, and laboratory data for fresh water were used to validate the models extensively over a broad range of parameters typical of potential OC-OTEC applications. These models are one-dimensional, steady-state analytical models that calculate the heat, mass, and momentum transfer processes occurring in a condenser with structured packing, in both cocurrent and countercurrent flows. Details of the physical processes, the assumptions made, the relations

Nomenclature

A = area, m^2
a_{eff} = transfer surface area per unit volume of packing, m^2/m^3
C_p = specific heat, kJ/kgK
D = diffusivity, m^2/s
d_{eq} = equivalent (hydraulic) diameter of packing, mm
$\dot{E}$ = rate of heat transfer, kW
F = fraction of steam mass condensed
f = friction factor
G = steam loading, kg/m^2s
Ja = Jakob number (Eq. (14))
h = heat transfer coefficient, kW/m^2K
h_{fg} = latent heat of condensation, kJ/kg
k = mass transfer coefficient, kg/m^2s
L = liquid loading, kg/m^2s
l = length, m
P = pressure, Pa
Pr = Prandtl number
Q = gas volumetric flow, m^3/s
Re = Reynolds number
S = packing side length, m
S' = liquid-film renewal length, m
Sc = Schmidt number
Sh = Sherwood number
T = temperature, °C, K
U = velocity, m/s
$\overline{Ua}$ = average overall volumetric heat transfer coefficient, kW/m^3K
V = vent ratio (Eq. (15))
X_{ii} = noncondensable-gas mass fraction
ΔP = pressure drop across condenser stage, Pa
ΔT = temperature difference, K
ΔT_m = mean temperature difference, K
α = hydraulic slope angle (from horizontal), deg
γ = packing void fraction
δ = liquid film thickness, mm
ϵ = thermal effectiveness (Eq. (13))
θ = corrugation angle (from horizontal), deg
μ = dynamic viscosity, kg/ms
ρ = density, kg/m^3

Subscripts

eff = effective
G = gas mixture
i = in; inerts
L = liquid
o = out
s = steam
sat = saturation
w = water, seawater
* = equilibrium value
1 = first stage
2 = second stage

used, the results of extensive parametric analyses to characterize the behavior of the condensers, and a full listing of the computer codes are provided in the BPA report.

In direct-contact condensation, the subcooled liquid enters a chamber containing the steam to be condensed. The resistances to heat transfer consist of gas-phase, liquid-phase, and interfacial resistances that occur in series. In the absence of noncondensable gases, the gas-phase and interfacial resistances are small compared to the liquid-phase resistance. The molecular mass transfer from the vapor to the (liquid) interface is accompanied by the transfer of heat from the interface, which is at an intermediate temperature, to the bulk of the fluid. The overall transfer rate is governed by the molecular transport within the liquid and, to a lesser extent, by the differential rate of molecular crossing at the interface. For simple liquid geometries, this can be readily evaluated. However, when noncondensable gases are present, they are carried to the liquid interface with the condensing vapor. There, they act as a blanket on the condensing surface, increasing the gas-phase resistance to significant levels because the vapor must diffuse through the gaseous barrier before condensing on the liquid at the interface.

The models use the heat and mass transfer analogy (Colburn and Hougen, 1934), applied separately to the liquid and vapor phases, to calculate the interfacial steam flux and the interfacial temperature. Diffusion of steam through the noncondensable gas/steam mixture is modeled using the stagnant film theory (Colburn and Hougen, 1934), corrected for high vapor fluxes toward the interface (Ackermann, 1937). The models evaluate temperature and partial pressure of both the steam and the noncondensable gas independently. The liquid film is unstable on inclined corrugated surfaces at Re of order 10. Because the tests were carried out at $\mathrm{Re}_L = L(a_{\mathrm{eff}}\mu_L)$ between 200 and 2000, established correlations for turbulent water-film flow over an inclined plane are used. Calculation of the local liquid-side mass transfer coefficient k_L is based on Higbie's penetration theory, and is expressed as

$$k_L = 2\rho_L[D_L\, U_{L,\mathrm{eff}}/(\pi S')]^{1/2} \tag{1}$$

where S' is the typical distance over which liquid-film renewal occurs, and is defined in Fig. 1. The effective, average velocity in the film falling along the inclined corrugation of the packing is taken to be equivalent to open-channel flow and is expressed dimensionally in SI units (m/s) as

$$U_{L,\mathrm{eff}} = 82\,\delta^{2/3}(\sin\alpha)^{1/2} \tag{2}$$

with a liquid-film thickness, in m, expressed as

$$\delta = \frac{L}{a_{\mathrm{eff}}\rho_L U_{L,\mathrm{eff}}} = \left[\frac{L}{a_{\mathrm{eff}}\rho_L 82(\sin\alpha)^{1/2}}\right]^{3/5}. \tag{3}$$

The effective surface area for transfer per unit volume of packing, a_{eff}, varies depending on the geometry of the packing, the material, and the material's thickness. The effect of interfacial shear on the liquid film is generally small at the low gas pressures encountered under OTEC conditions and is not incorporated in the models.

The local liquid-side heat transfer coefficient was evaluated using the Chilton–Colburn analogy:

$$\frac{h_L}{k_L C_{pL}} = \left[\frac{\mathrm{Sc}_L}{\mathrm{Pr}_L}\right]^{2/3}. \tag{4}$$

The local gas-side mass transfer coefficient k_G is based on extensive earlier investigations of wet-wall columns. Following Bravo, et al. (1985), the gas Sherwood number is expressed as

$$\mathrm{Sh}_G = 0.0338(\mathrm{Re}_G)^{4/5}(\mathrm{Sc}_G)^{1/3} \tag{5}$$

where $\mathrm{Sh}_G = k_G d_{eq}/\rho_G D_G$, and the gas-passage hydraulic diameter $d_{eq} = 4$ area/perimeter. The gas Reynolds number is $\mathrm{Re}_G = d_{eq}\rho_G(U_{G,\mathrm{eff}} \pm U_{L,\mathrm{eff}})/\mu_G$ and is based on the relative velocity between gas and liquid, using (+) for countercurrent and (−) for cocurrent flow. $\mathrm{Sc}_G = \mu_G/\rho_G D_G$ is the gas Schmidt number. The effective gas velocity $U_{G,\mathrm{eff}}$ is dependent on the superficial steam loading G (kg/m^{2}s), the void fraction of the packing γ, and the flow channel inclination θ, both shown in Fig. 1, as

$$U_{G,\mathrm{eff}} = \frac{G}{\rho_G \gamma \sin\theta}. \tag{6}$$

The local gas-side heat transfer coefficient h_G is evaluated using the Chilton–Colburn analogy:

$$\frac{h_G}{k_G C_{pG}} = \left[\frac{\mathrm{Sc}_G}{\mathrm{Pr}_G}\right]^{2/3}. \tag{7}$$

The gas-side pressure drop is modeled based on the experimental study of Bravo et al. (1985) for structured packings, and is expressed as

$$\Delta P = f\frac{l}{d_{eq}}\rho_G U_{G,\mathrm{eff}}^2, \tag{8}$$

where l is the length along the packing. The first term in the friction factor

$$f = 0.171 + \left(\frac{92.7}{\mathrm{Re}_G}\cdot\frac{d_{eq}}{S}\right) \tag{9}$$

represents lumped entrance and exit losses.

The original codes detailed in the BPA report were modified to predict DCC performance with seawater and to incorporate a new set of physical properties (Appendix C of the ZEA report). When operating with seawater, the heat transfer calculations must maintain consistent temperatures in the liquid and in the gas phases, and the mass transfer calculations must consider the equilibrium saturation pressure for seawater (i.e., they must include the effect of boiling-point elevation). Also, the solubility function for the air dissolved in the liquid was changed to extend the range of applicability of this function to the range from 0° to 100°C, and to correct one erroneous coefficient in the old formulation.

For OTEC conditions, the ratio $(\mathrm{Sc}_L/\mathrm{Pr}_L)$ remains nearly constant through the condenser. Therefore, it was not possible to verify the form of Eq. (4) above unequivocally. Although this form was used in the model computations and it yielded excellent agreement with the fresh water and seawater data, physical arguments may suggest a different exponent in Eq. (4). The penetration theory gives $k_L \propto D_L^{1/2}$, where D_L is the noncondensable gas diffusivity in water. The expression for the local liquid-side heat transfer coefficient h_L (Eq. (4) above) could be modified to the form

$$\frac{h_L}{k_L C_{pL}} = C\left(\frac{\mathrm{Sc}_L}{\mathrm{Pr}_L}\right)^{1/2}, \tag{10}$$

to preserve the analogy between heat and mass transfer, and maintain parallel dependence of h_L on thermal diffusivity. This modified formulation could provide good comparison to the data obtained in the OTEC range with the constant $C \sim 2$. In this case, the empirical local gas-friction relation (Eq. (9)) may also need to be slightly modified. Further analysis for different applications is necessary to identify the proper form for Eq. (4) and (9) over a broader range of operating parameters. However, for engineering design of direct-contact condensers, the relations presented in Eq. (1)–(9) provide excellent prediction of the experimental results, as described in the Results section.

The computer models integrate the process differential equations along the length of the condenser, to obtain steam, liquid, and noncondensable-gas properties under steady-state conditions. For cocurrent flow, initial properties for both liquid and gas are given at one end of the condenser, and the model is integrated in the direction of liquid and gas flows. Steam enters this condenser at saturated conditions, and the model allows it to become superheated. The temperatures predicted through the length of the cocurrent condenser for one set of conditions

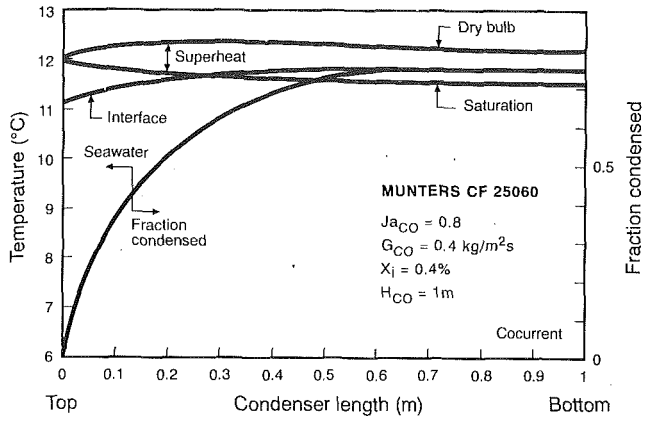

Fig. 3 Variation of temperatures within the cocurrent condenser, operating with seawater, as a function of downstream distance

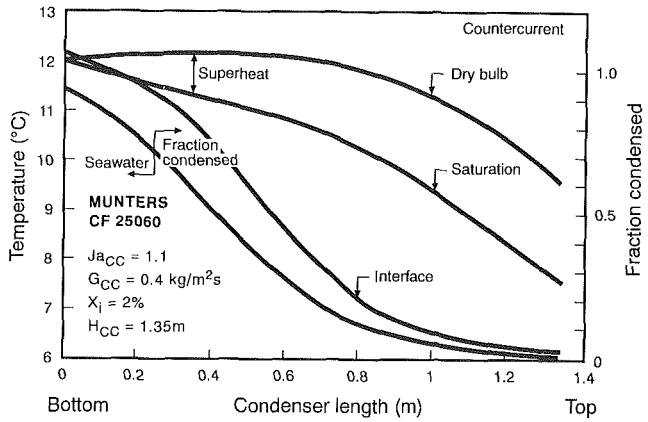

Fig. 4 Variation of temperatures within the countercurrent condenser, operating with seawater, as a function of gas-phase downstream distance

are shown in Fig. 3. The fraction of steam condensed is proportional to the water temperature (see Eq. (16) below) and is also shown. The general trends for other conditions are similar. In all cases tested, the full area of packing was utilized in the transfer process. Note the fairly constant gas-phase temperature throughout the length of the condenser, and the nonlinearity of the fraction condensed. For length greater than 0.78 m, under these conditions, the seawater and steam are in thermal equilibrium in the cocurrent condenser, and no further condensation can occur (for seawater, $T_w > T_s$ is possible). Comparisons of model predictions to experimental data at the exit of the condenser are discussed below; the accuracy of the predictions inside the condenser can be inferred by analysis for different steam loadings and condenser geometries.

In the countercurrent geometry, the liquid generally enters from the top and the gas from the bottom. The countercurrent model integrates through the process equations by marching from bottom to top, based on an initial guess of the outlet liquid state (at the bottom). The integration is repeated using efficient iteration schemes until the calculated water conditions at the top of the condenser match the specified liquid inlet conditions, within a defined tolerance. Generally, five iterations are sufficient to obtain a ± 0.01 K agreement in liquid inlet temperature. The temperatures and fraction condensed in the counter-current condenser are shown in Fig. 4. As in the cocurrent condenser, the relative value of the interface temperature to the seawater and saturation temperatures indicates the relative resistance to condensation. Near the bottom, the process is liquid-side controlled, while toward the top, the gap between the interface and saturation temperatures increases, implying gas-side control of the transfer processes.

Table 1 Range of direct-contact condenser parameters tested at the seacoast tested at the seacoast test facility, in the HMTSTA apparatus

	Min.	Max.
Planform area cocurrent (m^2)	0.426	1.021
Planform area countercurrent (m^2)	0.146	0.343
Packing height (m)	0.61	0.91
Freefall height (m)	1.02	1.63
First Stage		
Steam loading (kg/m^2s)	0.28	0.61
Noncondensable-gas inlet (%)	0.27	0.42
Liquid loading (kg/m^2s)	16.89	40.50
Temperature of steam in (°C)	11.57	17.46
Temperature of water in (°C)	5.83	6.58
Jakob number	0.73	1.35
Second Stage		
Steam loading (kg/m^2s)	0.05	0.50
Noncondensable-gas inlet (%)	0.87	4.90
Liquid loading (kg/m^2s)	7.70	47.50
Temperature of steam in (°C)	9.51	18.00
Temperature of water in (°C)	5.60	6.66
Jakob number	1.01	6.67
Overall heat exchanged (kW)	317	1248
Overall % condensed	97.76	99.69

Experimental Details

The tests carried out at NREL were conducted in an evacuated vessel using exchangers of different configurations and geometries. Two closed loops provide the warm and cold fresh water for the tests, with a capacity of exchanging up to 300 kW_t. Noncondensable gases are injected into the evaporator, and the noncondensed gas mixture is removed with a three-stage vacuum system. The instrumentation consists of platinum resistance thermometers (RTD), turbine flow meters for the liquid flows, absolute and differential diaphragm capacitance pressure sensors for the gas phase, and oxygen meters for the dissolved oxygen content in the liquid. Steam saturation-temperature measurements were made in a wet-bulb arrangement in which RTD probes were covered with a wetted wicking material maintained in equilibrium with the steam. The noncondensable-gas mass flow was controlled by mass-flow controllers, and the volumetric exhaust flow was fixed by the known capacity of the first-stage rotary blower. Instruments were calibrated regularly in the NREL metrology laboratory.

Several commercially available structured packings were tested at NREL, with effective surface area per unit volume of packing ranging from 70 to 250 m^2/m^3. The structured packings were obtained from manufacturers such as Munters, Sulzer, and Koch. Other types of contactor were also tested. The packings were tested in various condenser geometries, with horizontal planform areas up to 0.6 m in diameter, packing heights up to 0.61 m, and free-fall heights up to 1 m.

The seawater tests were conducted in the HMTSTA apparatus in open-loop and in closed-loop operation. The facility can exchange up to 1.25 MW_t. Based on the results obtained at NREL, one type of structured packing was selected for the tests at the HMTSTA. This is a Munters CF-25060 structured packing (see Fig. 1 for geometric parameters) that has an effective surface area per unit volume of 98 m^2/m^3. The packing is composed of stacked 0.15-m-high sections. Each section is rotated in the horizontal plane with respect to the others to have a different flow channel orientation. The tested range of condenser geometries and parameters is shown in Table 1. The free-fall height in Table 1 includes the height above the packing, in which water is distributed over the packing, and the height below it, in which the uncondensed steam from the first stage turns around and enters the second stage.

Two configurations were tested for the DCC assembly: one with two small stages side by side and one with larger coaxial stages where the cocurrent stage wraps around a central countercurrent stage. The first geometry was selected because it enabled tests with seawater that were closely related to the tests

Table 2 Direct-contact condenser calculated parameters—error summary

Parameter	First Stage (±%)	Second Stage (±%)	Overall (±%)
Jakob number	1.7	3.1	--
Effectiveness (based on ΔT)	1.4	1.3	1.4
Effectiveness (based on T-T)	5.0	5.0	6.2
Fraction condensed	1.7	2.6	1.5
Steam loading	1.8	3.0	--
Liquid loading	1.5	2.7	--
Vent ratio	--	--	10.0
Additional Parameters (±%)			
Steam temperature (based on pressure)	8-11		
Interstage steam T (various methods)	2-5		
Noncondensable gases in steam	13		
Overall heat balance	3.7		

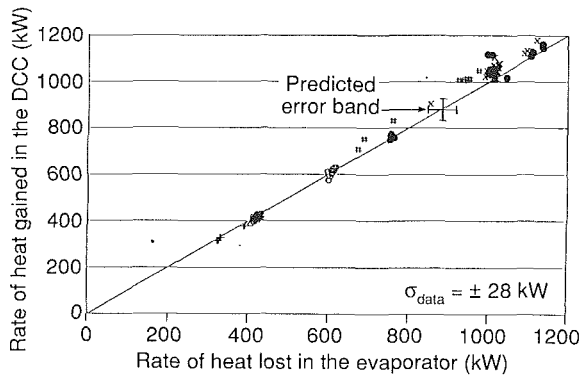

Fig. 5 Consistency of overall heat balance between heat lost by the evaporator and heat gained by the direct-contact condenser in the HMTSTA apparatus

conducted at NREL with fresh water; the second was selected because it used all the steam available from the evaporator in a configuration that may be more representative of larger OTEC systems.

Several systems of water distribution were tested for the cocurrent stage to obtain good water distribution with minimal blockage of the steam flow path: from nozzles located above the packing that sprayed the cold water vertically down onto the packing, to spouts imbedded into the packing that discharged the cold water just above the packing. Water distribution to the countercurrent condenser stage consists of a supply pipe discharging onto a perforated water tray that contains a few vertical vents. This system provides excellent water distribution for the countercurrent stage, just above the packing and with small hydraulic losses. Three water types were tested: "normal" seawater, deaerated seawater, and fresh water.

The type and location of the test instrumentation in the HMTSTA is indicated in Fig. 2. It consists primarily of matched RTD probes for differential temperature measurements, diaphragm capacitance transducers for absolute and differential pressures and liquid levels, and magnetic and vortex-shedding flowmeters for liquid flows (Parsons et al., 1989). A concerted effort was made throughout the test period to verify that all instrumentation was working properly, to compare redundant measurements, and to maintain a regular schedule for recalibration.

The steam saturation temperature T^*_{si}, referred to for the sake of brevity as steam temperature, was measured using RTDs covered with wicks, as was done in the NREL tests. These wicks were wetted with fresh water; therefore these sensors measure the fresh-water temperature that is in equilibrium with the incoming steam (wet-bulb temperature). For tests conducted with seawater, the output of the steam sensors must be corrected by applying a boiling-point-elevation correction. In the data analysis performed on the seawater results, this correction is applied to the data as a constant 0.280°C. The actual saturation pressure for each point is not recalculated because $\Delta T_{\text{elevation}} = +0.280°\text{C} \pm 0.005°\text{C}$, for 1.15 kPa $< P <$ 1.6 kPa, and the variation over the tested range is so small that it does not contribute appreciably to the expected error.

Table 1 summarizes the ranges of the parameters tested at the HMTSTA for the first and second condenser stages.

Error and Data Consistency

An extensive error analysis conducted before the HMTSTA tests is documented in the test plan (Parsons et al., 1989) and is summarized in Appendix A of the ZEA report. These pretest estimates, summarized in Table 2, have been compared with a post-test analysis on statistically significant sets of data, and they have been compared with redundant sensors measurements to assess and verify the accuracy of the data collected. Where appropriate, the least-squares error band estimates are shown on the graphs, along with the value of the standard deviation of the collected data. A total of 323 data sets are documented in the ZEA report. In most cases, the data have shown excellent consistency and variations smaller than the documented error estimates. If discrepancies were found, the tests were repeated, or the cases are noted in the text. Significantly lower uncertainties were obtained in the NREL tests that were used to validate the computer models, because of the more controllable laboratory environment and the large number of data sets collected for each configuration.

Figure 5 shows the consistency of the heat balance performed on the HMTSTA system by comparing the calculated values of heat rates (using evaporator and condenser instrumentation), the appropriate error bands in the ranges tested, and the standard deviation of all data shown in this plot. The error band estimated for the evaporator is about twice that for the DCC, because the temperature difference in the evaporator is about half that in the DCC. Note that a consistent bias appears at the higher heat rates, arising from ambient heat input because the evaporator operates near ambient temperature, but the condenser is always well below ambient. Because of this bias, the heat rates in the condenser stages (instead of the evaporator) are used to calculate the amount of steam produced and condensed. The calculated heat rates fall within approximately ±5 percent, that is, the standard deviation is $\sigma = \pm 3.7$ percent.

Calculations of exhaust gas composition are within 20 percent of the calculated rates of noncondensable gas release on the basis of deaeration tests and gas analysis results. Leakage rates were monitored regularly and amounted to less than 5 percent of the noncondensable flow through the condenser. Gas release rates from the seawater ranged from 85 percent to 100 percent.

Overall Volumetric Heat Transfer Coefficients

The widely accepted engineering methodology for heat-exchanger design (Schlünder, 1984) treats the heat-exchange process in terms of an average overall volumetric heat transfer coefficient:

$$\overline{Ua} = \frac{\dot{E}}{A\Delta T_m}. \tag{11}$$

The mean temperature difference is expressed in terms of the temperature differences at each end of the condenser as:

$$\Delta T_m = \frac{(T^*_{si} - T_{wi}) - (T^*_{so} - T_{wo})}{\ln \dfrac{(T^*_{si} - T_{wi})}{(T^*_{so} - T_{wo})}} \quad \text{for cocurrent flow} \tag{12}$$

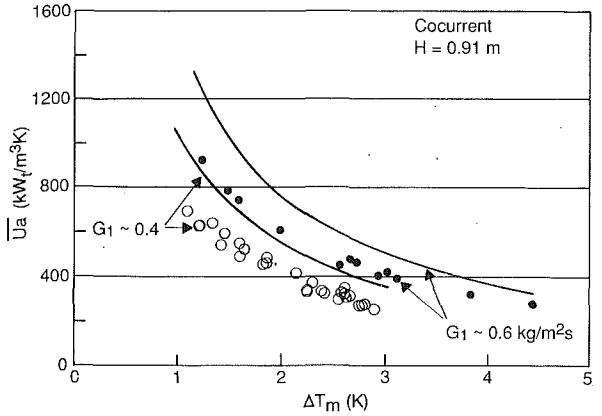

Fig. 6 Overall volumetric heat transfer coefficient as a function of mean temperature difference for cocurrent flow

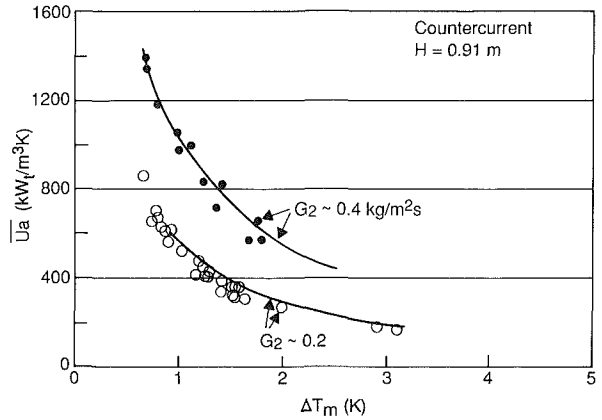

Fig. 7 Overall volumetric heat transfer coefficient as a function of mean temperature difference for countercurrent flow

The mean temperature difference for countercurrent flow has the same form, but the subscripts for the locations of the water temperatures (i, o) are reversed. The asterisk on the steam temperature refers to the saturation pressure correction required in the case of operation with seawater.

As shown in Figs. 3 and 4, the temperature distributions within the condensers are generally nonlinear. Therefore, this approach can only give a qualitative measure of the DCC performance. The overall volumetric coefficient and the mean temperature differences are specific to the geometry of the system and to the particular contacting device. This formulation also assumes constant heat and mass transfer coefficients over the length of the condenser (Fair, 1990). Instead, as the gas moves through the condenser, the steam loading (mass flow per unit planform area), the gas velocity, and the heat and mass fluxes decrease continuously as the steam condenses. The heat and mass transfer coefficients are highly nonuniform through the condenser length. In most cases, the flow changes from turbulent to laminar within this length; such transition and its effects are not well understood in general, and they are difficult to quantify under condensation conditions. In such an environment, correlations of the transfer coefficients with average gas and liquid loadings can only be obtained for special conditions. As discussed below, more suitable performance parameters exist to relate the effect of the loadings on the DCC performance.

Figures 6 and 7 show the overall volumetric heat transfer coefficient as a function of the respective mean temperature differences for the two condenser geometries. The values are calculated from the data tables in Appendix B of the ZEA report. The data reflect two different condenser sizes for each configuration, at a contactor height of 0.91 m (3 ft), operating with seawater and with fresh water. Data for inlet steam loadings within ±5 percent of the nominal values were selected; this variation accounts for the small scatter seen in the data. The uncertainty in these data is equivalent to the size of the symbols. The ideal curves represent complete condensation of the incoming steam within the condenser, for the nominal steam loadings identified in the figures. The figure shows how $\overline{Ua}$ approaches this fraction of the ideal value as the mean temperature difference increases. The countercurrent unit routinely condenses 98 percent of the inlet steam, so the data are within a few percent of the ideal values. The results indicate the superior performance of this type of contacting device, capable of providing overall volumetric heat transfer in the neighborhood of 1 MW$_t$/m^{3}K for low-density steam.

Performance Parameters

The performance of the DCC is a complex function of liquid and steam loading, inlet noncondensable-gas concentration, gas release from the liquid, saturation temperature, exhaust pressure, and geometry. Two main parameters describe the thermal performance of a direct-contact condenser: thermal effectiveness and Jakob number. The vent ratio describes the overall exhaust performance, i.e., how well the noncondensable gases are concentrated in the exhaust stream.

Thermal Effectiveness. The thermal effectiveness of each condenser stage compares the temperature difference observed in the (sea)water as it passes through that stage with the total available temperature-driving potential

$$\epsilon = \frac{T_{wo} - T_{wi}}{T_{si}^* - T_{wi}}. \tag{13}$$

T_{si}^* is the (sea)water temperature that is in equilibrium with the steam entering the condenser. The theoretical limit $\epsilon = 1$ represents ideal use of the temperature-driving potential in the absence of noncondensable gas. Note that, at given inlet conditions, the temperature-driving potential is larger when operating with seawater than when operating with fresh water, because T_{si}^* is 0.28 K higher than the measured fresh water value. The overall thermal effectiveness of the two stages can be expressed in the same form as Eq. (13), using the average water temperature rise in the two stages and the inlet steam temperature into the first stage.

Stage Jakob Number. The Jakob number describes the minimum amount of water needed to condense the incoming steam, given a certain driving potential:

$$\mathrm{Ja} = \frac{LC_{pw}(T_{si}^* - T_{wi})}{Gh_{fg}}. \tag{14}$$

Typically for OC-OTEC systems, it is desirable to condense only 80 -90 percent of the steam in the first (cocurrent) stage and the remainder in the second stage. Therefore Ja$_1$ is chosen to be less than one, while Ja$_2$ is greater than one.

Vent Ratio. When noncondensable gases are introduced into the system, a venting system must be used to remove them and maintain the operating pressure. A minimum quantity of steam must also be exhausted with the noncondensable gas. This value is typically 50 percent or more of the total exhausted gas. The vent ratio compares the ideal volumetric flow out of the condenser to the actual quantity of gas removed. Reaching the ideal (smallest) volumetric flow rate would require both a condenser with no pressure losses and one in which the steam reaches the minimum possible partial pressure (the saturation pressure at the inlet water temperature). This provides the highest noncondensable gas partial pressure at the outlet. For calculation of the ideal and actual volumetric flow rates, the total static pressure at the outlet of the condenser can be expressed in terms of the total static pressure at the inlet of the

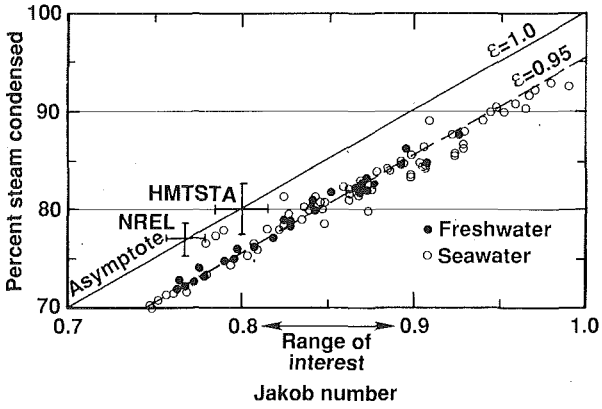

Fig. 8 Fresh-water and seawater results of percent condensed in cocurrent (first) stage as a function of stage Jakob number for a steam loading of 0.4 kg/m^{2}s

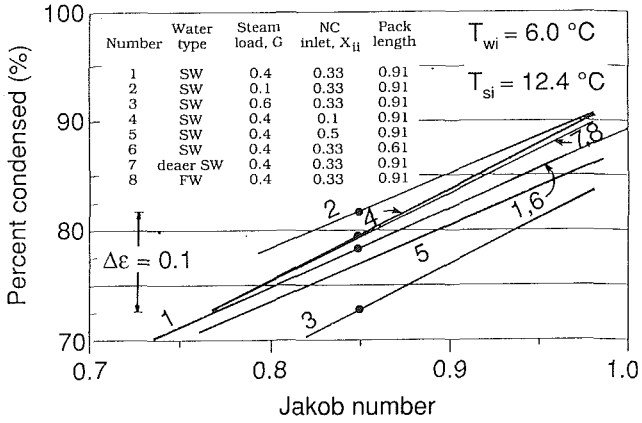

Fig. 9 Range of variation in cocurrent stage effectiveness resulting from changes in various input parameters

condenser minus the total pressure drop incurred in the condenser stages. The partial pressure of noncondensable gases can be expressed in terms of this overall outlet pressure minus the saturation pressure of the steam at the outlet of the condenser. This gives the vent ratio as

$$V=\frac{Q_{\text{ideal}}}{Q_{\text{real}}}=\frac{P_{i,1}-\Sigma\Delta P-P_{\text{sat}}(T_{so,2})}{P_{i,1}-P_{\text{sat}}(T_{wi,2})}\cdot\frac{(T_{wi,2}+273.15)}{(T_{so,2}+273.15)}. \quad (15)$$

The ideal case requires that both $\Sigma\Delta P=0$ and $T_{so,2}=T_{wi,2}$, giving $V=1$; real condensers operate at $V<1$, implying that more steam is exhausted with the noncondensable gases than the theoretical minimum. This volumetric performance parameter is typically used to size positive-displacement vacuum systems operating at the low pressures encountered in OC-OTEC applications.

Fraction of Steam Condensed. The fraction of steam mass condensed in each stage is the product $\epsilon\times$Ja calculated for that stage:

$$F=\frac{LC_{pw}\Delta T_w}{Gh_{fg}} \quad (16)$$

where the appropriate values of liquid and steam loading and temperature rise are used for each stage. The overall fraction condensed by the two stages is expressed as $[F_1+(1-F_1)F_2]$.

Figure 8 shows the percent of the incoming steam mass that is condensed in the cocurrent condenser stage as a function of stage Jakob number. In this graph, the freshwater results obtained at NREL are compared to the seawater results from the HMTSTA, to verify that differences in liquid properties and in geometry between the two condensers do not affect the results. The theoretical limit is the asymptote where $\epsilon_1=1.0$. Note that the Jakob number range of interest for OC-OTEC is from 0.8 to about 0.9, because it is not intended that the first stage condense all the incoming steam. Most of the data are shown for a steam loading near $G_1\sim0.4$ kg/m^{2}s, and at values near $X_{ii,1}=0.33$ percent for the noncondensable-gas concentration. The error bands show the calculated least-squares error predicted for the two facilities.

A line of constant effectiveness $\epsilon_1=0.95$ fits the data well; this behavior and this value are typical for the first stage at $G_1\sim0.4$ kg/m^{2}s. The dependence of F on packing geometry and steam loading, as well as the length of packing to reach thermal equilibrium in cocurrent flow, are detailed in the BPA report. Similar comparisons at other parameter settings confirm the repeatability of the results between the two test facilities, rendering the extensive data sets obtained at NREL with fresh water applicable to other conditions. These results might be so similar because the differences in heat capacity and temperature-driving potential between seawater and fresh water tend to compensate for each other, providing for virtually the same environment within the structured packing. Even though different mechanisms occur for noncondensable-gas release in fresh water and seawater, this difference cannot be resolved in the data.

The gas pressure drop in the cocurrent stage remains below 50 Pa over the tested range and is only a weak function of steam loading, increasing slightly up to $G_1\sim0.6$ kg/m^{2}s. This results in a drop of the steam saturation temperature through the first stage of about 0.5 K. At the outlet of the cocurrent stage, the noncondensable gases are only slightly concentrated ($X_{ii,2}$ is about 1 to 5 percent).

Tests conducted to identify the effects of water type, cold seawater deaeration, inlet noncondensable-gas mass fraction, steam loading, and packing lenght all showed results that indicated very small changes in first-stage effectiveness. It is difficult to present comparative test data, because the effects to be analyzed result in performance variations of the same order as those caused by slight changes in operating parameters (HMTSTA system conditions could not be held precisely constant during all the tests). They also fall within the experimental uncertainty. Therefore, for ease of presentation, the data were compared to model predictions, and these predictions are used in Fig. 9 to display the small effects of these parameters. The curves were generated using the cocurrent DCC computer model at constant inlet water and steam conditions at the average values tested. For $Ja_1=0.85$, all the different conditions change the effectiveness by no more than 0.1. The largest effect is caused by changes in steam loading, from 0.1 to 0.6 kg/m^{2}s; the highest effectiveness is obtained for the lowest steam loading, and increased sensitivity to this parameter is seen for the higher G_1. The next largest effect is caused by changes in noncondensable-gas inlet concentration. Packing length has no effect in the range shown. Deaerated cold seawater behaves identically to fresh water and very similarly to "normal" seawater at low inlet noncondensable-gas concentration.

Results for the Countercurrent Condenser

This condenser also shows similar performance whether it operates in fresh water or seawater, characterized by a constant 98 percent condensed at any $Ja_2>1$. Therefore, for $Ja_2>1$, the effectiveness of this stage is inversely proportional to Ja_2. Comparisons of data obtained at NREL and at the HMTSTA also show excellent agreement.

Figure 10 shows all seawater data collected for $Ja_2<2$ and for broad ranges of G_2 and $X_{ii,2}$. The symbols refer to different sets of data (ZEA report). The dashed lines approximate the slight dependence of the data on noncondensable-gas inlet concentration for $X_{ii,2}\sim1$ and 3 percent. The theoretical limit of Ja_2 is one, if noncondensable gases are not present. Countercurrent condensation is an efficient process, because the

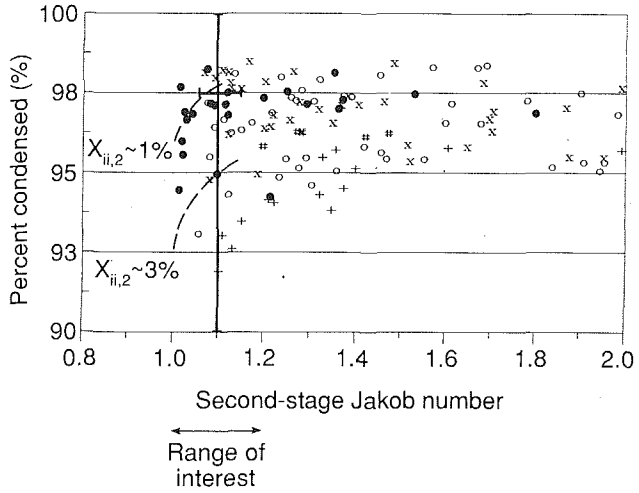

Fig. 10 Seawater results of percent condensed in countercurrent (second) stage as a function of stage Jakob number

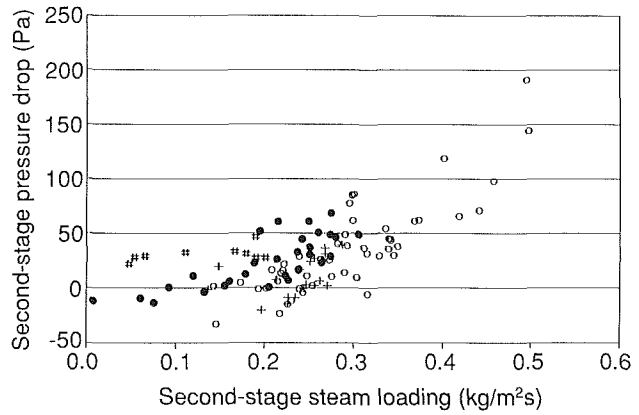

Fig. 11 Measured gas pressure drop in countercurrent (second) stage as a function of stage steam loading

steam encounters colder water as it proceeds through the stage. Typically for operation with seawater, the countercurrent stage condenses from 95 to 98 percent of the incoming steam. Therefore, the practical range of interest for Ja_2 can be maintained at about 1.1 to 1.2. An effectiveness of 0.85 is readily obtained with seawater for Ja_2 at about 1.1. Because this stage must process only a fraction of the steam that enters the first stage in OC-OTEC conditions, it is smaller than the first stage, and it uses less water; therefore its impact on overall effectiveness of the DCC is small.

The gas pressure drop is almost a quadratic function of the steam loading for this stage. It can be maintained below 50 Pa for $G_2 < 0.3$ kg/m^{2}s, but climbs rapidly at higher loadings (see Fig. 11). The approach temperature between steam outlet and water inlet $\Delta T_{so,wi,2}$ is small, about 0.5 K. Infact, this difference can be negative when operating with seawater because of the depression of the partial pressure (see Fig. 4).

DCC Computer Models Validation for Seawater

The predictions of both models followed all the significant trends observed in the experiments conducted at NREL and in the HMTSTA with fresh water and seawater. Prediction capabilities are summarized in Table 3, based on several hundred data sets taken at each facility.

The excellent correlation between model predictions and experimental data confirms the suitability of the heat and mass transfer analogy and of the correlations selected for the transfer coefficients to carry out an engineering design of direct-contact condensers using structured packings.

Table 3 Prediction capabilities of direct-contact condenser models compared to fresh and seawater data

Test Facility	Configuration	Parameter	Average Deviation (model to data)	Standard Deviation
NREL	Both (all packings)	Percent condensed Pressure drop	< 2.8% 4 Pa	± 2.4% ± 6 Pa
HMTSTA	Cocurrent	Percent condensed Pressure drop	-0.7% 18 Pa	± 2.8% ± 7.4 Pa
HMTSTA	Countercurrent	Percent condensed Pressure drop	0.3% 19 Pa	± 1.0% ± 41 Pa

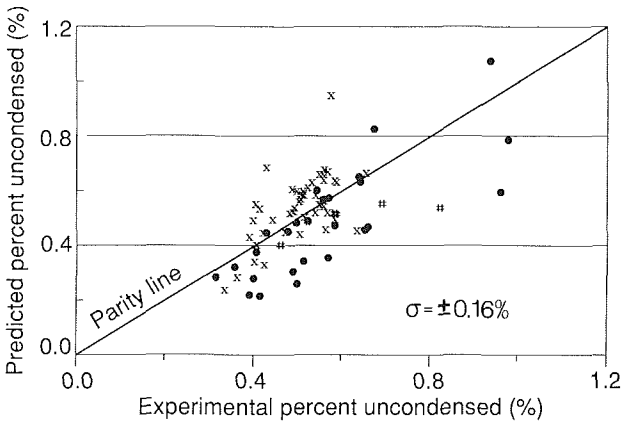

Fig. 12 Comparison of uncondensed steam exhausted from direct-contact condenser unit with respect to model predictions for the combined condenser stages

Figure 12 compares the prediction of the models to the calculated quantity of steam exhausted from the two-stage DCC unit, in terms of percent steam mass uncondensed. The overall prediction is obtained by combining the predictions for each condenser stage, using the appropriate inlet conditions for each. Given the small quantity of steam that remains uncondensed (generally much less than 1 percent), the agreement between the models and all the data collected is remarkable. Note that neither the data nor the models can resolve such small absolute values. For any type of condenser operating at these low pressures, it is difficult to measure the required quantities with accuracy sufficient to resolve these differences in mass flow rates.

Flooding in the Countercurrent Condenser

Flooding is a common limitation in countercurrent gas-liquid contactors, because when the liquid does not drain properly from the packing surfaces and it fills the channels, it limits the gas flow and thereby significantly increases the gas pressure drop. The generalized method to calculate flooding correlations for random packings is not very good for the regular geometry found in structured packings. However, an estimate of the flooding limits for these packings is shown in Fig. 13 and is described in the BPA report. For a particular equivalent diameter of the packing and a particular Jakob number for the countercurrent condenser, the intersection of these curves represents acceptable maximum levels of steam (gas) and liquid loadings. Several tests in the HMTSTA were conducted near the flooding limit, as documented in the ZEA report, but these conditions should be avoided for proper operation of OTEC condensers.

Overall Condenser Performance

The characteristic performance diagram for the multistage DCC is shown in Fig. 14. An ideal condenser would operate at the upper right corner of the graph, where both performance parameters have a value of one. A real condenser can operate

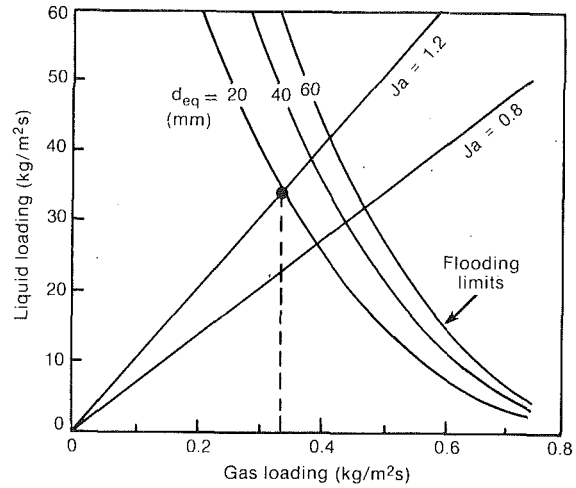

Fig. 13 Flooding limits for countercurrent condenser

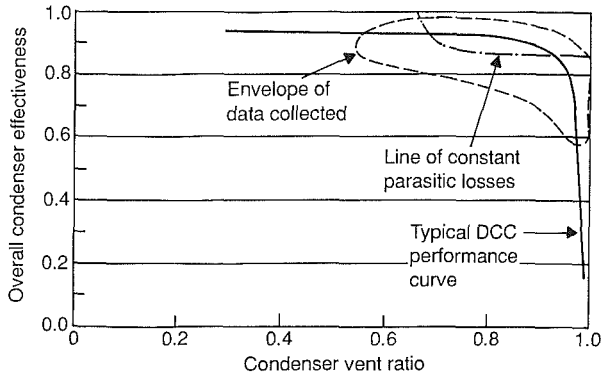

Fig. 14 Overall thermal and exhaust-venting performance of direct-contact condenser unit

within 10 percent of this thermodynamic limit. At low values of vent ratio, V, a chosen condenser operates with high effectiveness. As V is increased, the effectiveness decreases gradually. For values of V greater than 0.9, the condenser effectiveness deteriorates rapidly. The typical DCC performance curve is shown as a solid line in Fig. 14, surrounded by an envelope of collected data for its operation in seawater.

For OTEC systems, an increasing vent ratio represents a reduction in steam exhausted with the noncondensable gases, implying lower exhaust power consumption. An increasing value of thermal effectiveness represents a reduction of cold water use, implying lower water pumping power requirements. Exhaust and water pumping power account for the majority of parasitic power losses in the OC-OTEC system. Therefore, the minimum system parasitic losses occur when the system operates at the upper right corner (the ideal performance limit). Constant system parasitic losses can be represented by a set of curves that encircle this corner, as shown by the dash-dotted lines in Fig. 14. The exact shape of the curves depends on the specific performance of other system components, but they tend to be oval as shown. Curves that are farther away from the upper right corner imply larger overall parasitic losses. The condenser can be designed to operate at any point along one of these parasitic curves by adjusting its geometric and operating parameters. Thus system analysis must give the appropriate selection of condenser operating conditions for a specific system and application.

Conclusions

Detailed computer models are summarized that describe the behavior of direct-contact condensers using structured packing and operating in cocurrent and countercurrent flow. These models were validated extensively with experimental data for several types of packing, condenser geometries, and cooling liquids. Several hundred data sets have been documented. These models have consistently predicted the experimental data to better than 3 percent of the duty cycle.

Extensive tests of two DCC stages operating with seawater at typical OC-OTEC conditions were conducted, yielding a substantial data base over broad operating ranges suitable for OC-OTEC systems. The data showed excellent consistency and variations smaller than the predicted error estimates, giving confidence in the data collected. The data confirmed earlier predictions of excellent thermal, exhaust, and hydraulic performance for the DCC. Overall thermal effectiveness above 0.9 has been shown consistently for vent ratios of 0.9 in the presence of high noncondensable-gas content. This indicates that the DCC unit can operate within 10 percent of the theoretical limits for cold-water use and venting requirements. Within experimental uncertainty, thermal performance in seawater and fresh-water operation cannot be distinguished. The results of these studies lend confidence that direct-contact condensers can be designed effectively for OC-OTEC as well as for other applications.

References

Ackerman, G., 1937, "Wärmeubergang und molekulare Stoffübertragung im gleichen feld bei grossen temperatur- und Particaldruck-differanzen," *Forschungsheft*, No. 382, VDI-Verlag, Berlin.

Bharathan, D., Parsons, B. K., and Althof, J. A., 1988, *Direct-Contact Condensers for Open-Cycle OTEC Applications: Model Validation With Fresh-Water Experiments for Structured Packings*, SERI/TR-253-3108, Solar Energy Research Institute, Golden, CO. This U.S. government publication can be ordered from NTIS, 5285 Port Royal Road, Springfield, VA 22161.

Bravo, J. L., Rocha, J. A., and Fair, J. R., 1985, "Mass Transfer in Gauze Packings," *Hydrocarbon Processing*, Vol. 64, No. 1, pp. 91-95.

Bravo, J. L., Rocha, J. A., and Fair, J. R., 1986, "Pressure Drop in Structured Packing," *Hydrocarbon Processing*, Vol. 65, No. 3, pp. 45-59.

Colburn, A. P., and Hougen, O. A., 1934, "Design of Cooler Condensers for Mixtures of Vapors With Noncondensing Gases," *Industrial and Engineering Chemistry*, Vol. 26, pp. 1178-1182.

Fair, J. R., 1972, "Designing Direct-Contact Coolers/Condensers," *Chemical Engineering*, Vol. 2, pp. 91-100. (See also "Process Heat Transfer by Direct Fluid Phase Contact," *Chemical Engineering Progress Symposium Series*, No. 118, Vol. 68, 1972, pp. 1-11.)

Fair, J. R., 1990, "Direct Contact Gas-Liquid Heat Exchange for Energy Recovery," ASME *Journal of Solar Energy Engineering*, Vol. 112, pp. 216-222.

Huang, C. C., and Fair, J. R., 1989, "Direct-Contact Gas-Liquid Heat Transfer in a Packed Column," *J. Heat Transfer Engineering*, Vol. 10, No. 2, pp. 19-28.

Krebs, R. G., and Schlünder, E. U., 1984, "Condensation With Non-condensing Gases Inside Vertical Tubes With Turbulent Gas and Film Flow," *Chemical Eng. Processing*, Vol. 18, pp. 341-356.

Krock, H. J., 1981, *Gas Analysis of Water Samples for OTEC Program*, University of Hawaii Technical Report, No. 57.

Parsons, B. K., Link, H. F., Bharathan, D., Pesaran, A. A., Zangrando, F., and Panchal, C. B., 1989, *Test Plan for the Heat and Mass Transfer Scoping Test Apparatus: Phase I and Phase II Tests, Internal Program Report*, SERI/PR-253-3385, Solar Energy Research Institute, Golden, CO.

Schlünder, E. U., ed., 1984, *Heat Exchanger Design Handbook*, Vol. 1, Hemisphere Publishing Corp., Washington, DC.

Zangrando, F., Bharathan, D., Green, H. J., Link, H. F., Parsons, B. K., Parsons, J. M., Pesaran, A. A., and Panchal, C. B., 1990, *Results of Scoping Tests for Open-Cycle OTEC Components Operating With Seawater*, SERI/TP-253-3561, Solar Energy Research Institute, Golden, CO.

Droplet Vaporization in a High-Pressure Gas

J. P. Hartfield

P. V. Farrell

Department of Mechanical Engineering,
University of Wisconsin—Madison,
Madison, WI 53706

Evaporation of single, liquid droplets in a high-temperature, high-pressure gaseous environment has been investigated experimentally. The effects of gas temperature, pressure, and strength of naturally occurring convective flows were studied. Pure hydrocarbon (n-heptane) and trichlorotrifluoroethane (R-113) droplets were vaporized in a nitrogen atmosphere within a sealed chamber, which was developed to minimize forced convection. Experiments were carried out in normal and microgravity ($\sim 10^{-5}$ g) fields in order to examine the effect of natural convection. A single droplet was attached to the end of a quartz fiber. The gas temperature and pressure were raised quickly by a compressive process. The gas temperature and pressure were varied from $0.93 < T_r < 1.23$ and $0.32 < P_r < 0.73$. The droplet was located at the point of compressive symmetry. Droplet lifetime and instantaneous vaporization rate were determined from the data recorded by video camera. The results indicated that ambient gas temperature is a more significant parameter than ambient pressure for high-pressure droplet vaporization. This conclusion was based on comparisons of droplet vaporization rate for the range of temperatures and pressure tested. Ambient gas pressure was seen to have a weaker influence on vaporization rate. Removal of the gravity field during free-fall experiments resulted in an increase of droplet life time of about 30 percent for the case of R-113 liquid, and little change for the n-heptane droplets.

Introduction

Liquid fuel injected into internal combustion engines typically atomizes into small (0.1 mm diameter and less) droplets. These droplets are exposed to a hot, convective gaseous environment at a relatively high pressure. For the case of a gas turbine or compression ignition engine, the environmental condition may be above the critical pressure and temperature of the liquid, allowing the liquid to approach its thermodynamic critical pressure and temperature (Faeth et al., 1969). During this process, the liquid fuel rapidly vaporizes and mixes with surrounding oxidizer to form a combustible mixture. Under near-critical and supercritical conditions, some normal low-pressure approximations must be reconsidered (Farrell and Peters, 1986). In particular, for high pressures, ideal gas assumptions may not be valid. There is likely to be gas dissolved in the liquid making low-pressure interface assumptions of an ideal solution questionable (cf. Curtis and Farrell, 1992), and at near-critical conditions, a variety of anomalous property variations have been observed (cf. Basu and Sengers, 1977).

The present work has been direced toward gaining insight on droplet vaporization, particularly for the case of high ambient pressures. In order to simplify interpretation of the results of the experiments, it may be desirable to eliminate convective effects in order to understand the details of the vaporization process alone. Convection of the gas phase can cause distortion of the droplet surface and internal convection in the droplet, and can lead to droplet breakup. While all of these processes occur in high-pressure combustion systems, their presence makes detailed examination of the vaporization process alone difficult. Elimination of forced convection in the gas phase is possible with careful experimental design; for vaporization of an initially cold droplet in a hot environment, natural convection is not so easily eliminated in a normal gravity field. In practice, low gravity experiments are difficult and access to low gravity environments is limited. In the present work, experiments were conducted in normal and microgravity ($\sim 10^{-5}$ g) fields. The normal or 1-g experiments were performed in a nearly quiescent environment to investigate high-temperature and high-pressure vaporization. A few low-gravity experiments were conducted at high pressure and temperature to estimate the effects of the gravitational field on the vaporization results.

There has been considerable interest in droplet vaporization at low and high pressures, with many efforts focusing primarily on droplet combustion. Low-pressure vaporization experiments have been performed by, among others, Hottel et al. (1954) and Priem (1955). High-pressure experiments have been performed in convective flows by Sowls (1972) and Savery and Borman (1970). Suspended droplet experiments at high pressure in a quiescent environment have been performed by, for example, Faeth et al. (1969) and Hiroyasu and Kadota (1976).

Related experiments of droplet combustion have been performed by a large number of workers, in convective and quiescent environments, and in 1-g and in microgravity environments (cf. Sato et al., 1990).

In addition to previous experiments, there have been a large number of modeling efforts for vaporization and combustion at low and high pressures (Manrique and Borman, 1969; Abramzon and Sirignano, 1988; Hsieh et al., 1991; Curtis and Farrell, 1992). A comparison of some of these low-pressure and high-pressure vaporization models is given by Curtis et al. (1989).

The experiments on high-pressure droplet vaporization that have been performed to date have been primarily made in strong convective fields or in actual combustion situations. Under these conditions, with relatively loosely defined free-stream conditions, comparison of experimental results with model results for vaporization is difficult.

The intent of the experiments described in this paper was to produce droplet vaporization experiments in which all convective motion could be eliminated, in order to concentrate on the interface problem. As noted, exclusion of convection requires elimination of forced convection and free convection. In addition, in order to provide a well-defined initial condition for modeling the vaporization process, an "impulsive start"

Contributed by the Heat Transfer Division and presented at the ASME Winter Annual Meeting, Atlanta, Georgia, December 1–6, 1991. Manuscript received by the Heat Transfer Division February 1992; revision received December 1992. Keywords: Microgravity Heat Transfer, Sprays/Droplets, Supercritical Fluids. Associate Technical Editor: W. L. Grosshandler.

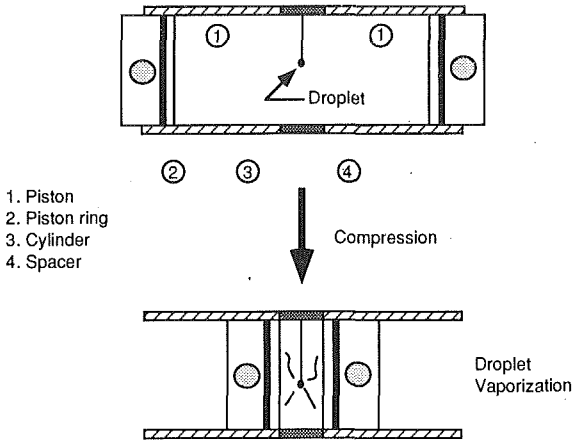

Fig. 1 Opposed piston schematic (cutaway view)

Table 1 Compressor specifications

Bore	57 mm
Stroke	42 mm
Displacement	107 cm^3
Compression ratio	11.0

to the problem would be necessary, requiring a rapid rise in the test chamber pressure and temperature without accompanying convection, all at microgravity.

Compressor and Laboratory Equipment

The experimental apparatus was designed to be a self-contained system suitable for use in the NASA Lewis Research Center 2.2 s drop tower. For this application, all power must come from on-board sources. There is a strict limit on the overall size of the package to be dropped, and the package must clearly be rugged enough to survive the 30 to 40-g impact at the bottom of the tower so that it may be used again. The system built for the drop tower was also used in a ground-based laboratory for the 1-g tests.

An opposed piston compression device was used to raise the gas field pressure and temperature surrounding the droplet from an initial ambient temperature and low pressure. Two modified single cylinder spark ignition engines were arranged facing piston top to piston top and separated with a spacer plate. Chamber sealing was accomplished using full-circle Teflon rings. Two small ports on the cylinder wall were used to precondition or prepressurize the gas. During a vaporization experiment, each crankshaft was rotated 180 deg simultaneously by a hydraulic drive system in about 50 ms. During crankshaft rotation, the flat-topped piston in each engine went from a stationary condition at bottom dead center to a stationary position at top dead center. A schematic of the compression device showing the initial and final compressor positions is shown in Fig. 1 and a listing of some specifications of the compressor is given in Table 1.

A positive displacement droplet generating system utilizing

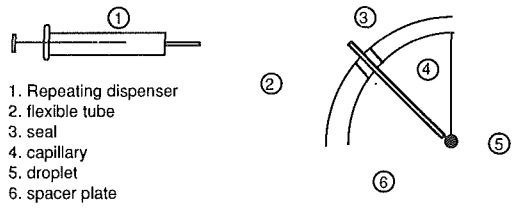

Fig. 2 Liquid delivery system

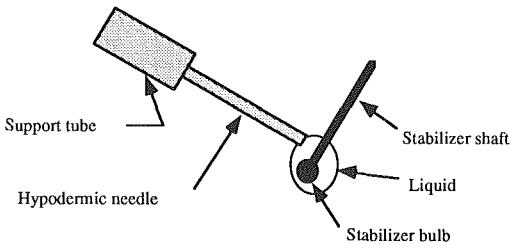

Fig. 3 Needle-stabilizer system

a hypodermic syringe was developed in order to prepare droplets upon demand. The nominal syringe displacement was 1.0 μ liter per stroke of a repeating dispenser. Liquid was fed from the syringe onto the tip a 0.125-mm-dia glass fiber supporting a 0.25-mm-dia glass bulb. The bulb was located at the point of compressive symmetry within the compression device, which was at the centerline of the spacer plate. A schematic diagram showing the major components of the droplet generator in relation to the compressor spacer plate is shown in Fig. 2 and the needle-liquid stabilizer arrangement is shown in Fig. 3. The objective in placing the droplet at the point of symmetry of the compression device was to generate negligible convective gas motions near the droplet during compression, and to allow whatever motions generated to decay quickly.

A single component laser-Doppler velocimetry (LDV) system was set up to measure the gas velocities near the proposed droplet location, without a droplet present. Under typical operating pressures and temperatures, the velocity along the cylinder axis was measured as a function of time. Due to limitations in optical access, the LDV control volume was long—about 7 mm—in a direction parallel to the piston faces. A typical velocity trace from this experiment is shown in Fig. 4. The maximum velocity observed is relatively large, about 15 cm/s, but the gas velocity decays fairly rapidly to levels that are not easily detected by the LDV system. While the chamber is not quiescent at the droplet location, the convection velocities are small, and decay quickly.

Gas temperature and pressure in the test chamber were measured in the compressor in 1-g by use of a fine wire thermocouple (0.025 mm diameter, type K) and a piezoelectric pressure transducer affixed to the spacer plate. The uncertainty of the thermocouple measurement was estimated to be about 5 percent, and accounting for the DC drift of the pressure transducer, the uncertainty of the pressure measurement was also estimated to be about 5 percent. Temperature and pressure traces for the typical operating conditions of the compressor are shown

Nomenclature

C_p = specific heat
D = diameter
g = gravitational acceleration
Gr = Grashof number
h = enthalpy
k = thermal conductivity
m = mass
P = pressure
P_c = critical pressure
P_r = reduced pressure = P/P_c
r = radius
Re = Reynolds number
T = temperature
T_c = critical temperature
T_r = reduce temperature = T/T_c
U = velocity
v = velocity
α = thermal diffusivity = $k/\rho C_p$
β_v = vaporization constant
ρ = density
τ = dimensionless time = $\alpha t/D_o^2$ for liquid droplet

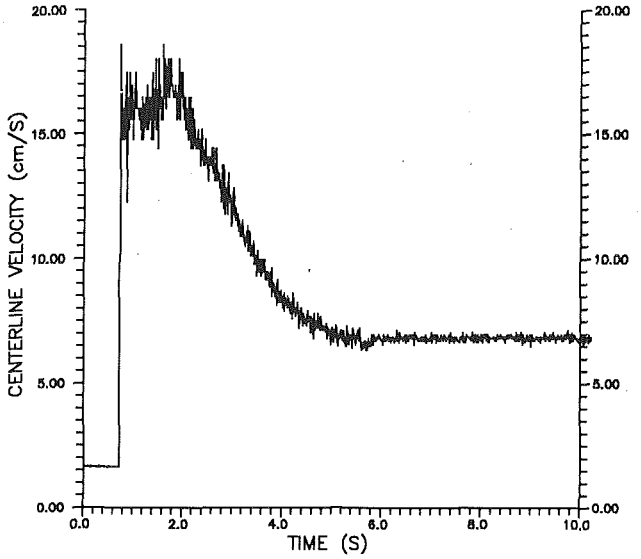

Fig. 4 Velocity at compression at approximate droplet location after compression

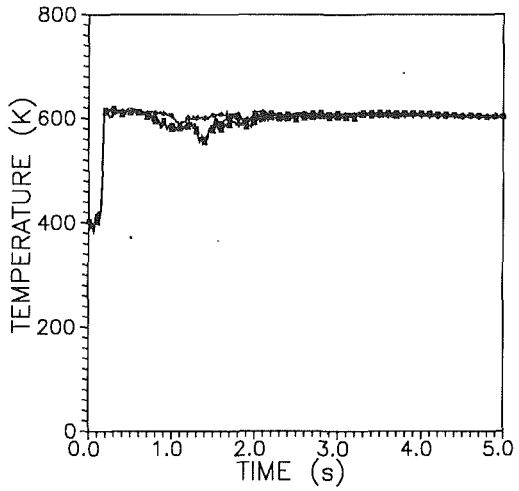

Fig. 5(*a*) Gas temperature at approximate droplet location after compression

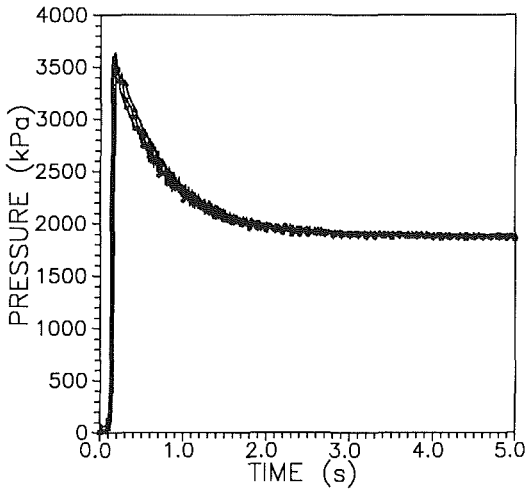

Fig. 5(*b*) Cylinder pressure after compression

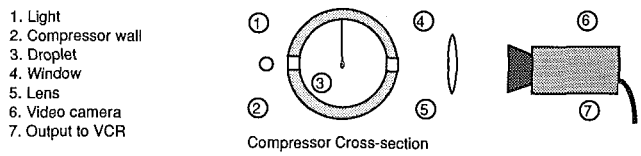

Fig. 6 Video data recording system

in Fig. 5. The pressure rises quickly to a large value due to the nearly adiabatic compression of the gas in the control volume. The temperature normally rises quickly also, due to compression heating. Since the test chamber is generally cooler than the gas charge after compression, the charge is quickly cooled to the chamber temperature, resulting in the rapid decay of pressure seen in Fig. 5. Figure 5(*a*) shows gas temperatures at the approximate location of the droplet for three different compressions as in Fig. 5(*a*). Tests on the chamber showed that there was very little leakage (< 5 percent over 10 minutes) from the chamber under pressure. For these experiments, in order to keep the chamber temperature and pressure to a reasonably high value, the piston surfaces were preheated for 60 s prior to the compression stroke. The resulting temperature trace in Fig. 5(*a*) shows that a steady chamber temperature is attained in the chamber. Since at BDC the pistons are far from the droplet region (42 mm) the effect of preheating the pistons on the droplet region is assumed to be small. These measurements were taken at 1 g, but were considered to be representative of the time constants of the system at microgravity as well.

The vaporization history of individual droplets was recorded by a CCD camera and stored in a VCR system. For the low-gravity experiments, the CCD camera was dropped with the package and the video signal was transmitted by optical fiber to the VCR, which was located at the top of the drop tower. Quartz windows in the spacer plate allowed optical assess for the video camera. During the experiments, the droplet was backlit and appeared as a dark disk on a light background, producing high optical contrasts. The layout of the data recorded system is shown in Fig. 6.

Vaporization experiments were carried out in normal and near zero gravity fields. For the case of near zero gravity tests, the 2.2 s drop tower facility at NASA-Lewis Research Center was employed. For the low-gravity tests, all of the experimental hardware used for normal gravity tests, including the CCD camera and experiment control computer, were allowed to free fall with the experimental rig. Nominal acceleration for the freely falling rig was typically in the range of 10^{-5} g (NASA manual, 1989). Actual acceleration with this package was not measured during these experiments.

The procedures for a typical vaporization experiment were:

1 Fill liquid supply system (R-113 or heptane);
2 Purge gas within compressor, pressurize chamber;
3 Deploy droplet onto fiber;
4 Change gravity field (optional);
5 Compress gas;
6 Record vaporization history.

Experimental Results—Normal Gravity

The results of the droplet vaporization experiments in normal gravity are presented in this section. For each experiment, the data recorded were droplet video images as a function of time, recorded at video rates (30 Hz). The video sequence for each experiment was stored on video tape for later analysis. Droplet size was determined on each video frame using a microcomputer-based frame grabber and analysis software. Each recorded video sequence of droplet images was analyzed one frame at a time by taking the projected area of the droplet image and computing from this an equivalent area of constant diameter, D. The droplet size was estimated by integrating the number of pixels whose intensities fell below a selected thresh-

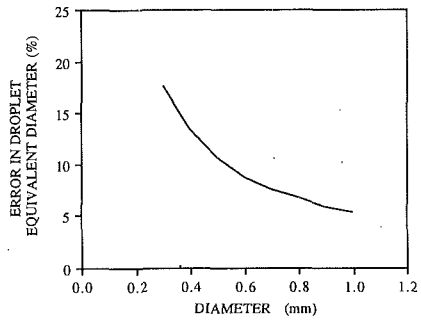

Fig. 7 Uncertainty in droplet equivalent diameter

old. The threshold value was set to include regions inside the droplet and exclude other regions. An effective droplet diameter is estimated from the two-dimensional area integral produced by the pixel summation.

The error induced by assuming a spherical droplet may be estimated by calculating the eccentricity of the droplet. If the liquid is assumed to be in the form of a prolate spheroid, the eccentricity is

$$\epsilon = \frac{\sqrt{L^2 - d^2}}{L} \tag{1}$$

where ϵ is the eccentricity, L is the droplet length along the stabilizer axis, and d is the maximum droplet width measured normal to stabilizer axis. It is apparent that for values of ϵ approaching unity, the geometric approximation of a constant diameter projection of a sphere will not be very good. The impact of moderate eccentricity values on geometric scales pertinent to droplet vaporization may be small. For instance, the surface area to volume ratio of an object is important when considering the energy and species transfer from an object. The surface area to volume ratio for a sphere of diameter D is $6/D$. If the value of eccentricity ϵ is at 0.745 and the volume is held constant, a prolate spheroid will have a surface area to volume ratio of $6.022/D$, a change of less than 1 percent. In the present study, the maximum value of droplet eccentricity was measured at 0.76.

Care in selecting the threshold value that defines the area included in a droplet is important for accurate estimates of equivalent droplet diameter, in particular near the edge of the droplet where a steep intensity gradient exists. A small change in the defined threshold value representing the edge of the droplet can make a difference in the calculated area and effective diameter. The threshold value is set to a specific intensity value in the range of 0 to 255, which is the full-scale range of intensities for an 8-bit frame grabber. For a droplet with 1 mm diameter, the variation in diameter using a range of threshold values from pixel intensity values of about 30 to 60 is about 5.3 percent of the nominal diameter. For a droplet diameter of 0.3 mm, this variation is 17.6 percent of the nominal diameter. A plot detailing the range of induced error for a variation in threshold value of 30 to 60 over a variety of droplet sizes is shown in Fig. 7.

In presentation of the data, the squared ratio of instantaneous diameter to maximum diameter, $(D/D_o)^2$, is plotted over the lifetime of the droplet. The time scale is expressed in nondimensional form. The following grouping is used:

$$\text{nondimensional time, } \tau = \frac{\alpha t}{D_o^2} = \left(\frac{kD_o}{m_o C_p}\right) t. \tag{2}$$

The term presented in the brackets accounts for the thermal time constant of the droplet system and the subscript o denotes an initial value. The history of the diameter-squared ratio is referenced to the reduced temperature and pressure of the liquid species.

Table 2 Thermophysical Properties for R-113 and *n*-heptane

Thermophysical Properties	R-113	*n*-heptane
Molecular weight	187.4	86.2
Critical temperature K	487	540
Critical pressure, MPa	3.39	2.72
Liquid thermal conductivity, W/m K	0.075	0.120
Liquid density, kg/m^3	1557	690
Liquid dynamic viscosity, N s/m^2	6.64×10^{-4}	3.7×10^{-4}
Liquid specific heat, kJ/kg K	0.958	2.22
Surface tension with air, dynes/cm	19.0	19.0
Gas thermal conductivity, W/m K	0.008	0.013
Gas density, kg/m^3	3.72	0.27
Gas dynamic viscosity N s/m^3	9.8×10^{-6}	6.1×10^{-6}
Gas specific heat, kJ/kg K	0.644	1.63
Pressure, kPa	48.2	6.64
Boiling temperature at 1 atm, K	320.6	371.6

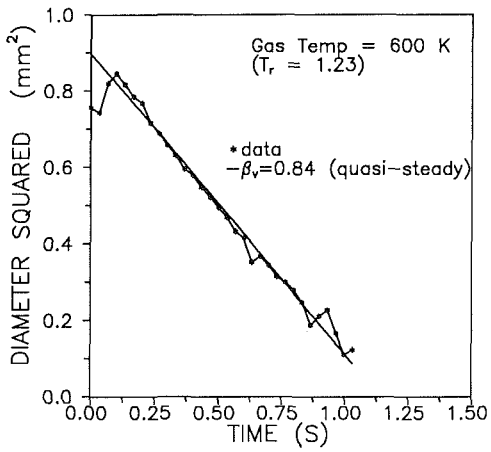

Fig. 8 Diameter versus time for R-113 droplet

The vaporization data is also presented through use of the vaporization coefficient. The vaporization coefficient may be interpreted as the mean vaporization rate of the droplet throughout its "lifetime." The units are mm^2/s and suggest a decay rate of projected droplet area (two-dimensional). The vaporization coefficient is defined as

$$|\beta_v| = \left|\frac{-dD^2(t)}{dt}\right| \approx \left|\frac{D_o^2 - D^2}{t_v - t_0}\right| \tag{3}$$

Here, t_o represents the time just after the gas compression process when vaporization begins and t_v is the time when the droplet vaporization is considered over. For the present study, the droplet was considered to be fully evaporated when the equivalent diameter was twice the stabilizer diameter. For the conditions in these experiments, the approximation of constant slope was utilized and was determined by a linear regression of the data. A summary of the vaporization coefficients from these experiments is given in the appendix.

Two liquids were studied in the present work: trichlorotrifluoroethane (R-113) and *n*-heptane. The thermophysical and critical properties of the liquids are presented in Table 2. A typical droplet size as a function of time plot is shown in Fig. 8 for R-113 in N_2 along with a line representing the regression to the data, which gives a β_v of 0.84. Note that the beginning of vaporization used for calculation of the β_v value is taken to be after the volumetric liquid expansion of the droplet, and the end of vaporization was taken to be when the droplet was about two times the fiber diameter.

A plot of β_v as a function of reduced pressure for R-113 for the temperature range examined is shown in Fig. 9. In general, the vaporization rate increased significantly with increasing T_r and more moderately with increasing P_r. All three temperatures

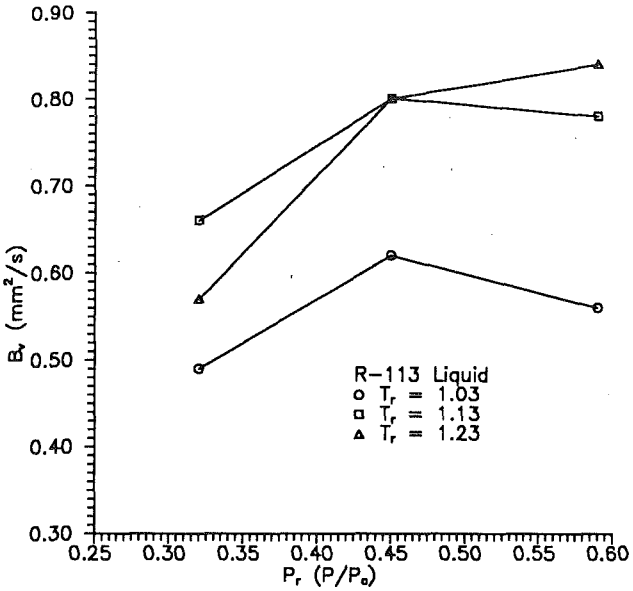

Fig. 9 Vaporization coefficient (β_v) for R-113 droplet

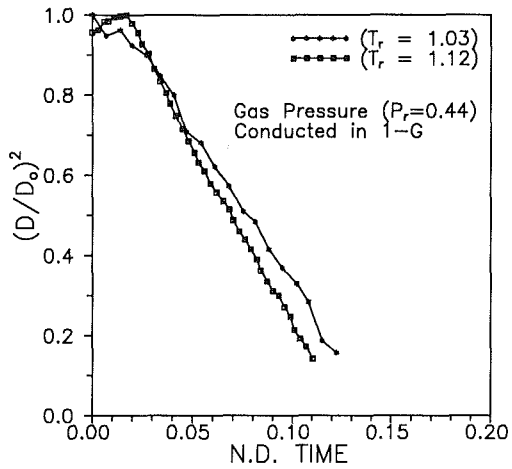

Fig. 10 Vaporization of *n*-heptane at 1-g

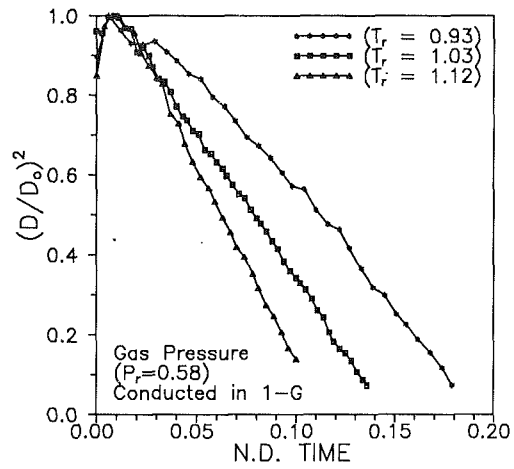

Fig. 11 Vaporization of *n*-heptane at 1-g

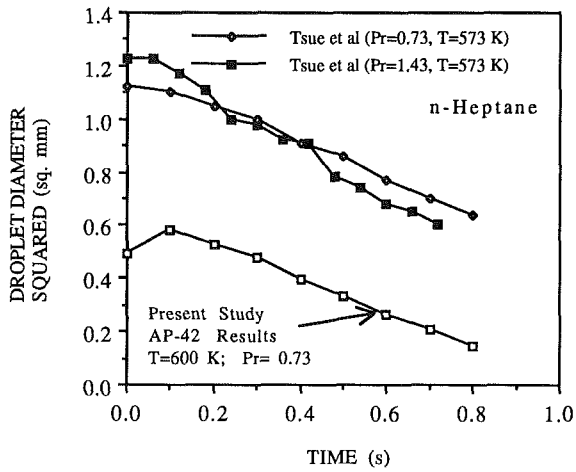

Fig. 12 Comparative *n*-heptane vaporization history

tested showed significant increases in vaporization for P_r increasing from 0.32 to 0.45, but less significant increases or decreases when P_r varied from 0.45 to 0.59.

In Figs. 10 and 11, examples of the results of the video data processing for the case of *n*-heptane liquid droplets vaporizing in nitrogen at 1-g are presented. As observed in the data of Fig. 8 for R-113, the slope of the vaporization curve changes following the compression process for some time. The apparent droplet diameter increase following compression is due to droplet vibration just after compression, the droplet image recorded by the video system was not always stable for the integration time of the CCD camera (33 ms). Some mechanical vibration of the compressor apparatus caused blurring of the recorded image and distortion of the results of the video processing technique used since the contrast at the edge of the droplet (first several pixel values) was low. The vibrations tended to be damped out after about 200 ms. Once the peak value of $(D/D_o)^2$ was attained, the slope of the vaporization curve remained nearly constant for the remainder of the droplet lifetime. The peak value of $(D/D_o)^2$ typically corresponded to the first clear image recorded by the video camera. For thermal expansion of the bulk droplet, an increase in temperature of 80°C of liquid heptane can be expected to cause a 13 percent increase in liquid volume due to thermal expansion. This would result in a 4.2 percent increase in droplet diameter. The measured droplet size increase in this transient period ranged from 0–15 percent of the initial droplet size.

The most significant feature of the 1-g *n*-heptane vaporization plots is the period in which the slope remains nearly constant. In each of the *n*-heptane experiments, the nearly constant slope of the vaporization curve suggests the applicability of a D^2 vaporization law over the range of conditions studied. Previous results reported by Tsue et al. (1987) suggest that this trend may be extended to supercritical pressures, although numerical models for supercritical vaporization do not always predict a quasi-steady vaporization (Curtis and Farrell, 1992). A plot of data reported by Tsue et al. and data from the current study shows *n*-heptane droplet vaporization in normal gravity for a reduced pressure of 0.73 and 1.43 (see Fig. 12). The regression of droplet diameter squared over time is seen to be nearly linear for both of these conditions. In the Tsue study for the reduced pressure of P_r = 1.43 a "transient" period exists for time less than 0.15 s. This is followed by a period lasting until the droplet is evaporated in which vaporization occurs steadily. This qualitative behavior is similar to that in the current study. The calculated *n*-heptane vaporization coefficients from the present study and some data from Tsue et al. are presented in Fig. 13. Although the temperature conditions for the current data and those of Tsue et al. are not identical, the values for the T_r = 0.93 and T_r = 0.88 cases are similar, and somewhat different values are found for the Tsue T_r = 1.08 and the current T_r = 1.12 cases.

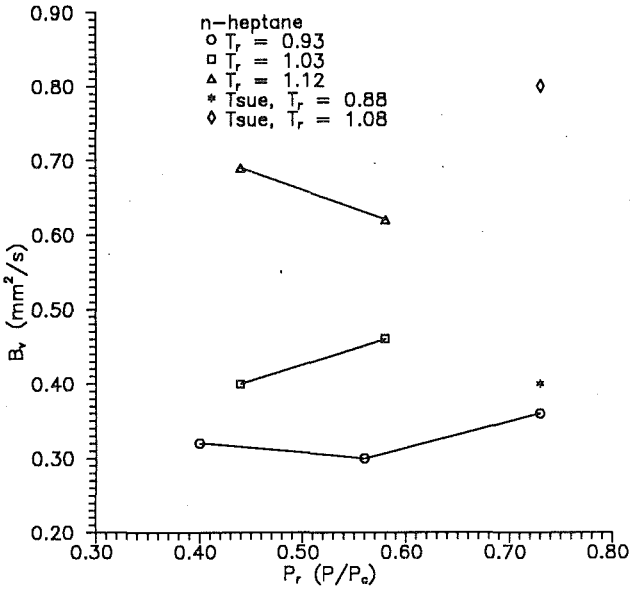

Fig. 13 Vaporization coefficient (β_v) for *n*-heptane droplets

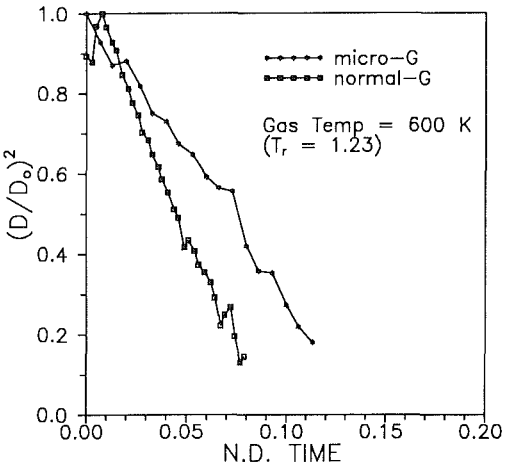

Fig. 14 Vaporization of R-113 at 1-g and microgravity

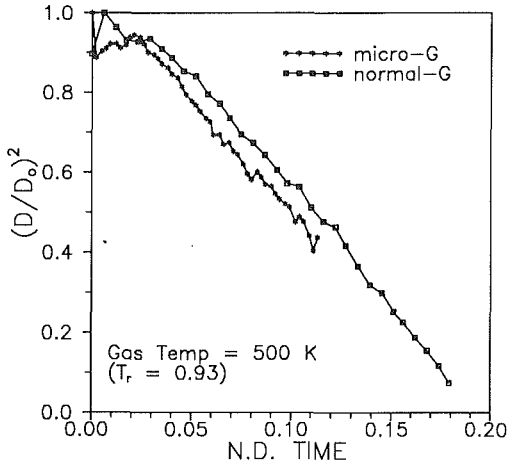

Fig. 15 Vaporization of *n*-heptane at 1-g and microgravity

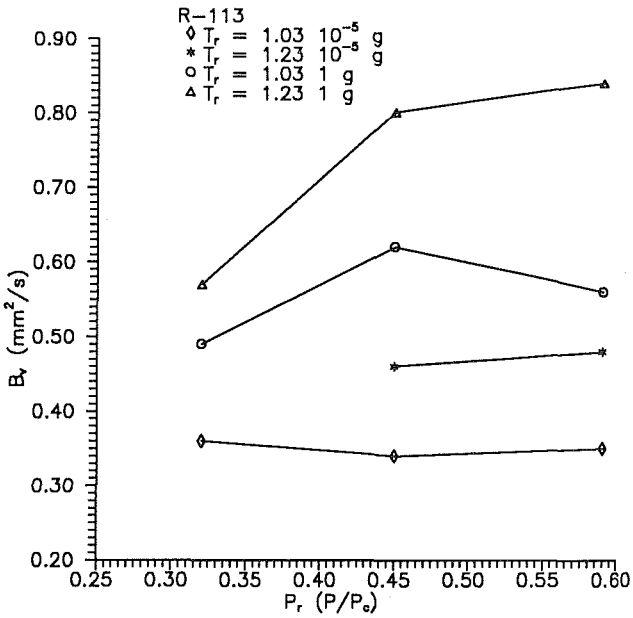

Fig. 16 Vaporization coefficients for R-113 at 1-g and microgravity

Based on the diameter squared lifetime plots, the second phase after the initial heatup phase of the vaporization process was steady. The vaporization curves yield a nearly constant slope during this period, particularly for the case of *n*-heptane. A D^{α} "law" is appropriate for description of droplet vaporization; the coefficient is about 2. The qualitative behavior of heptane droplet vaporization is similar to the data reported by Tsue et al. The quantitative rate of vaporization was found to be about 15–40 percent lower than reported by these workers, probably due to the method of droplet formation. In the present study, droplet formation was completed prior to gas compression (low temperature and pressure) and in the Tsue study, droplets were formed in a high-temperature environment. Tsue's environment would allow faster heatup of the droplet since all of the surroundings would be at a high temperature initial condition including the droplet supporting device.

Vaporization of some liquids may be influenced to a greater degree by the ambient pressure than others, due to variation in thermophysical properties, natural convection strength, and diffusion. Increasing gas pressure from P_r = 0.32 to P_r = 0.59 resulted in a nearly 20 percent increase in vaporization rate for R-113 as shown in Fig. 9. Heptane vaporization rates were seen to increase by 9.1 percent when gas pressure was elevated from P_r = 0.40 to P_r = 0.73 as shown in Fig. 12.

Experimental Results—Reduced Gravity

In order to study the influence of natural convection on the vaporization process, experiments were conducted in low gravity and results were compared with those compiled in normal gravity. In Figs. 14 and 15, typical droplet regression plots for normal and low-gravity vaporization are presented. In Figs. 16 and 17, the calculated vaporization coefficients for droplets vaporizing in low gravity are compared with those for droplets varporizing in normal gravity.

Reduction of gravity to about 10^{-5} g caused a significant change in the vaporization history of R-113 but had a smaller effect on *n*-heptane vaporization. R-113 vaporization rates for the case of reduced gravity were about 30 percent less than those measured in normal gravity, while vaporization rates for *n*-heptane increased by about 10 percent at P_r of 0.4 and 0.56, and decreased by about 10 percent at P_r of 0.73.

One reason that gravity does not influence *n*-heptane vaporization as much as R-113 is that the temperature of the *n*-

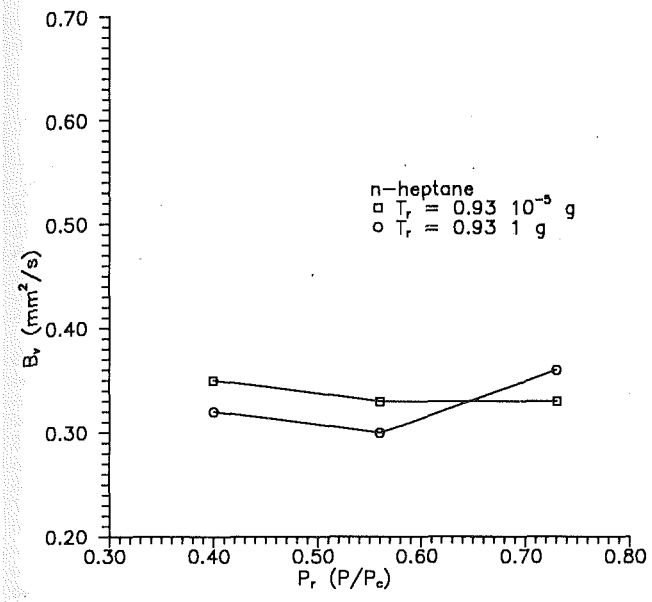

Fig. 17 Vaporization coefficients for *n*-heptane at 1-g and microgravity

heptane droplet is likely to be relatively high due its lower volatility or lower vaporization rates at room temperatures. During droplet heatup, less energy goes into the latent heat for vaporization, and more into increasing in the bulk droplet temperature. This reduces the gas-to-liquid temperature difference, and thus, the driving potential for buoyancy-induced flow. A second difference between the two liquids studied is a difference in the mass diffusion of vapor through the surrounding gas. The mass diffusivity coefficient, D, was estimated for both *n*-heptane and R-113 vapor in nitrogen gas at a common reduced temperature and pressure condition of $T_r = 1.03$ and $P_r = 0.59$. From ideal gas behavior and gas dynamics theory (Bird et al., 1960), a ratio of D(R-113)/D(heptane) = 0.75 was obtained. The ratio was developed through use of the Chapman–Enskog kinetic theory approach by the following equation,

$$D_{AB} = C \frac{\sqrt{T^3 \left(\frac{1}{M_A} + \frac{1}{M_B}\right)}}{P(\sigma_{AB})^2 \Omega_{AB}}. \quad (4)$$

Here, C is a constant, M is the molecular weight, T is temperature, P is the pressure, σ_{AB} is the Lennard–Jones parameter, and Ω_{AB} is a parameter dependent upon the potential field for one molecule of A and one of B. The analysis assumes a set of small, spherical molecules at low density. This is quite different from the long chain molecules present and high density gas in the current process of interest. However, if a Lewis number of unity is assumed, i.e., thermal and mass transport processes are identical, the ratio of D(R-113)/D(heptane) is 0.67 based on thermophysical properties. This implies that R-113 droplets may be more strongly influenced by convective currents augmenting a lower diffusive transport than is the case for heptane droplets, hence the sensitivity in vaporization rates to gravity field strength for R-113.

Experimental Uncertainty

The main issues of experimental uncertainty in the measurement of the effective droplet diameter and calculation of the vaporization coefficient may be considered in terms of systematic errors and random errors. The systematic errors involved errors in the optical system, video system, and droplet sizing system and in the induced environment. Random errors are considered to be errors resulting from random events such as system vibration, which blurs an image. The systematic droplet size measurement errors were estimated by measuring the size of the droplet support probe in each image for the video threshold conditions used. The support probe size was well known in this experiment, so comparison of the dimensions of the support acquired throughout the optical and video system, including the threshold level setting described above, may be considered a reasonable estimate of the error in the optical system. The error in measuring the support diameter varied from image to image, with an average error of about 5 percent and a maximum error of 8 percent of the probe diameter. Since the droplets were larger than the probe by a factor of two at least, the error in droplet diameter is expected to be less than these numbers. The system conditions (environmental temperature, pressure, and velocity) were found to vary by less than 10 percent over many trials.

Random error, or errors that are not repeated throughout the data set, are difficult to assess for the direct droplet sizing, but these errors are visible in the droplet size as a function of time graphs. In the calculations leading to the vaporization coefficient, β_v, the random errors are largely averaged out, since a linear regression method is used to calculate the coefficient. The regression results give the slope of the line (β_v) and an estimate of the goodness of fit to the data. While each regression gives slightly different results, the R^2 coefficient for the linear regression was always between 98.8 and 99.5 percent, giving a corresponding range of estimated standard deviations from the fit of $0.011 < s < 0.027$ in units of $(D/D_o)^2$.

Overall the uncertainty of the droplet diameter measurements may be considered to be less than 10 percent, and since the β_v are a linear regression to the droplet diameters, the error in the β_v values may be estimated to about the same as the droplet measurements, or 10 percent.

Summary

The vaporization of single R-113 and *n*-heptane droplets has been studied experimentally. A rapid compression device has been used to condition the gas field surrounding suspended liquid droplets. Droplet size history has been recorded via video camera system. Time-dependent size history of the droplets indicated that the well-known D^2 vaporization law may be extended beyond a reduced pressure of 0.7 through transient effects early in the vaporization process may result in some error. Gas temperature has a strong effect on droplet vaporization. Gas pressure is seen to have a weaker effect. Finally, the effect of gravity is important in droplet vaporization due to buoyancy-induced flows. Comparison of data from experiments in near-zero gravity with those conducted in normal gravity reveal that the vaporization rate and droplet lifetime are affected depending on the liquid involved. Removal of the gravity field during free-fall experiments resulted in an increase of droplet life time of about 30 percent for the case of R-113; however, a much less pronounced effect was seen for *n*-heptane.

Acknowledgments

This work was supported by a grant from the National Aeronautics and Space Administration, No. NAG3-718.

References

Abramzon, B., and Sirignano, W. A., 1988, "Droplet Combustion Model for Spray Combustion Calculations," AIAA Paper No. 88-0636.

Basu, R. S., and Sengers, J. V., 1977, *Seventh Symposium on Thermophysical Properties*, ASME, New York.

Bird, R. B., Stewart, W. E., and Lightfoot, E. N., 1960, *Transport Phenomena*, Wiley, New York.

Curtis, E., Hartfield, J., and Farrell, P., 1989, "Microgravity Vaporization of Liquid Droplets Under Supercritical Conditions," in: *AIP Conference Proceedings 197 Drops and Bubbles Third International Colloquium*, T. G. Wang, ed., p. 373.

Curtis, E., and Farrell, P. V., 1992, "A Numerical Study of High Pressure Droplet Vaporization," *Combustion and Flame 90*, p. 85.

Faeth, G. M., Dominicis, D. P., Tulpinski, I. F., and Olson, D. R., 1969, "Supercritical Bipropellant Droplet Combustion," *Twelfth Symposium (International) on Combustion*, The Combustion Institute, Pittsburgh, PA, pp. 9–16.

Farrell, P. V., and Peters, B. D., 1986, "Droplet Vaporization in Supercritical Pressure Environments," *ACTA Astronautica*, Vol. 13, p. 673.

Hiroyasu, H., and Kadota, X. X., 1976, "Evaporation of a Single Droplet at Elevated Pressure and Temperature," *Bull. of JSME*, Vol. 19, p. 1515.

Hottel, H. C., Williams, G. C., and Simpson, H. C., 1954, "Combustion of Droplets of Heavy Liquid Fuels," *Fifth Symposium (International) on Combustion*, The Combustion Institute, Pittsburgh, PA, pp. 101–128.

Hsieh, K. C., Shuen, J. S., and Yang, V., 1991, "Droplet Vaporization in High-Pressure Environments I: Near Critical Conditions," *Combust. Sci. and Tech.*, Vol. 76, p. 111.

Manrique, J. A., and Borman, G. L., 1969, "Calculations of Steady State Droplet Vaporization at High Ambient Pressures," *Int. J. Heat Mass Transfer*, Vol. 12, p. 1081.

NASA-Lewis Research Center Technical Manual, 1989, not published.

Priem, R. J., 1955, "Vaporization of Fuel Drops Including the Heating-up Period," Ph.D. Thesis, University of Wisconsin—Madison.

Sato, J., Tsue, M., Niwa, M., and Kono, M., 1990, "Effects of Natural Convection on High Pressure Droplet Combustion," *Combustion and Flame*, Vol. 82, p. 142.

Savery, W., and Borman, G. L., 1970, "Experiments on Droplet Vaporization at Supercritical Pressures," AIAA Paper No. 70–6.

Sowls, R. E., 1972, "An Experimental Study of Carbon Dioxide Droplets Falling Through an Inert High Pressure High Temperature Environment," Ph.D. Thesis, Dept. of Mech. Engr., University of Wisconsin—Madison.

Tsue, M., Miyano, H., Sato, J., and Kono, K., 1987, "Droplet Combustion of Hydrocarbon Fuels Under High Pressure Conditions," *Journal of the Japan Society for Aeronautical and Space Sciences*, Vol. 35, No. 404, p. 433.

APPENDIX

Vaporization Coefficient Values From Experiments

Material	g-level	T_r	P_r	B_v
R-113	1	1.03	0.32	0.49
R-113	1	1.03	0.45	0.62
R-113	1	1.03	0.59	0.56
R-113	1	1.13	0.32	0.66
R-113	1	1.13	0.45	0.80
R-113	1	1.13	0.59	0.78
R-113	1	1.23	0.32	0.57
R-113	1	1.23	0.45	0.80
R-113	1	1.23	0.59	0.84
R-113	10^{-5}	1.03	0.32	0.36
R-113	10^{-5}	1.03	0.45	0.34
R-113	10^{-5}	1.03	0.59	0.35
R-113	10^{-5}	1.23	0.45	0.46
R-113	10^{-5}	1.23	0.59	0.48
n-heptane	1	0.93	0.40	0.32
n-heptane	1	0.93	0.56	0.30
n-heptane	1	0.93	0.73	0.36
n-heptane	1	1.03	0.44	0.40
n-heptane	1	1.03	0.58	0.46
n-heptane	1	1.12	0.44	0.69
n-heptane	1	1.12	0.58	0.62
n-heptane	10^{-5}	0.93	0.40	0.35
n-heptane	10^{-5}	0.93	0.56	0.33
n-heptane	10^{-5}	0.93	0.73	0.33

Evaporation of Multicomponent Drop Arrays

K. Annamalai
Associate Professor.

W. Ryan[1]

S. Chandra
Graduate Student.

Mechanical Engineering,
Texas A&M University,
College Station, TX 77843-3123

The conventional fuels that are used in the field of transportation are primarily composed of two or more components. Each component evaporates, mixes with hot oxidant gases, ignites, and burns. Since evaporation is the precursor of the sequence of events leading to combustion, the evaporation studies on the multicomponent drops are essential for determining the governing parameters of spray evaporation. While single-component drop studies have been carried out extensively in the past, very limited literature exists on the multicomponent array evaporation. The present paper deals with the evaporation of multicomponent fuel droplets in an array using the recently developed point source method (PSM). First, the quasi-steady (QS) evaporation of an isolated, multicomponent droplet is briefly analyzed. The resultant governing equations, along with Raoult's law and the Cox–Antoine relation, constitute the set of equations needed to arrive at the solutions for: (1) the droplet surface temperature, (2) the evaporation rate of each species, and (3) the vapor mass fraction of each species at the droplet surface. The PSM, which treats the droplet as a point mass source and heat sink, is then adopted to obtain an analytic expression for the evaporation rate of a multicomponent droplet in an array of liquid droplets. Defining the correction factor (η) as a ratio of the evaporation of a drop in an array to the evaporation rate of a similar isolated multicomponent drop, an expression for the correction factor is obtained. The results of the point source method (PSM) are then compared with those obtained elsewhere for a three-drop array that uses the method of images (MOI). Excellent agreement is obtained. The treatment is then extended to a binary drop array to study the effect of interdrop spacing on vaporization. When the drops are close to each other, the evaporation rate of the droplet in the array containing the larger percentage of volatiles is higher than the rate under isolated conditions ($\eta > 1$). The results qualitatively confirm the experimental data reported elsewhere. Parametric results were obtained for the effect of changing the composition on the correction factor and finally critical drop compositions in the binary array are given for which $\eta > 1$. Even though the results for the average correction factor of the whole array of 2 to 9 drops obtained using PSM are almost the same as the results from MOI, the correction factor of the center drop under severe interaction may deviate from those results obtained with MOI.

1 Introduction

Many practical combustor systems, such as boilers, gas turbines, diesel engines, rockets, etc., use condensate fuels (liquid and solid fuels) as the energy source. Combustion intensity is controlled by the gasification, mixing, and chemical kinetics processes. The condensate must at atomized/pulverized into smaller droplets/particles in order to increase the surface area of fuel exposed to the hot gases and to facilitate rapid gasification and mixing with the oxygen-rich ambience. Thus, atomization leads to improved ignition and combustion characteristics. Spray evaporation, ignition, and combustion studies are extremely important to determine the flame stability behavior at widely varying loads to ensure the efficient utilization of fossil energy, and to understand better the mechanism of pollutant formation and destruction.

Isolated drop/particle models yield the parameters controlling the ignition and combustion characteristics of individual drops/particles. Sprays normally involve a large number of drops. The simplest analysis is to treat the fuel spray as an aggregate of the behavior of individual fuel droplets. Thus, the spray combustion rate can be estimated to be a sum of the combustion rates of each of the drops as if each drop burned individually. However, a drop in the spray does not behave like an isolated drop since its behavior is modified due to the presence of other drops. Interactions between the droplets alter the drag coefficient, change the flow field, increase/decrease the ignition delay depending on the denseness of the spray, compete for heat and oxygen, and alter the fuel vapor distribution around the drops (Annamalai and Ryan, 1992). Thus, the usefulness of isolated droplet modeling is limited in spray modeling especially in the vicinity of the injector, where the spray is very dense. Thus, the interactions must be accounted for. An improved understanding of the interactive behavior in simplified models and the corresponding experiments in a controlled environment can provide design input for obtaining the desirable spray characteristics which result in improved combustor performance. Array study is an improvement over isolated drop study since it considers the interactions between a finite number of drops, thus providing a fundamental knowledge of the processes involved in the interactive ignition and combustion (Labowsky, 1976, 1980; Xiong et al., 1984). Experimental array studies have the advantage that conditions can be controlled and the results can be compared to the theoretically predicted trends of array studies. The focus of the previous investigators has been to evaluate the correction factor of single component drops under interactive conditions as the interdrop spacing and number of drops in the array are varied

[1] Currently at Westinghouse Electric Corporation, Orlando, FL.

Contributed by the Heat Transfer Division for publication in the JOURNAL OF HEAT TRANSFER. Manuscript received by the Heat Transfer Division November 1991; revision received January 1993. Keywords: Combustion, Evaporation, Fire/Flames. Associate Technical Editor: W. A. Sirignano.

(Labowsky, 1976; Brzustowski et al., 1979; Annamalai and Ryan, 1991, 1992).

The fuels that are actually used, especially in the field of transportation, are primarily composed of two or more components. The evaporation of the drops in dense clouds is the precursor of the events leading to ignition and combustion, and hence it is desirable to determine the governing parameters for the multicomponent droplet array evaporation. Denoting the evaporation rate of an interacting single component drop in the array/cloud as $\dot{m}_s$ (single drop) and the drop mass loss rate under isolated conditions as $\dot{m}_{iso}$ (isolated), the correction factor η can be written as

$$\eta = \dot{m}_s/\dot{m}_{iso}$$

Interactive effects usually retard the drop/particle mass loss rate ($\eta < 1$). For an array containing J number of multicomponent drops, the correction factor of ith species for the jth drop is given as

$$\eta_{ij} = (\dot{m}_{s,i})_j/(\dot{m}_{iso,i})_j$$

where the isolated drop has the same composition as the jth drop in the array. Under pure diffusive transport, the single component array analysis always yields $\eta < 1$, while the interactive effects in multicomponent array can occasionally enhance the mass loss rate ($\eta > 1$).

Interactive problems are dealt with primarily by the following methods:

1 Exact method using Navier-Stokes equation—suitable for 2 to 3 drops (Tal et al., 1984; Raju and Sirignano, 1990; Sirignano, 1993).
2 Bispherical coordinate method—2 drops (Brzustowski et al., 1979).
3 Method of images (MOI)—suitable for arrays of fewer than 20 drops (Labowsky, 1976, 1978, 1980).
4 Point source method (PSM)—suitable for arrays of 1000 drops or fewer (Annamalai and Ryan, 1993).
5 Continuum method—suitable for clouds (Chiu and Liu, 1977; Annamalai and Ramalingam, 1987).

The MOI, which provides an exact solution to the governing equations and considers the finite size of the drops, requires a large number of sources/sinks if many drops are considered. For example, 10° image sources are required for the first three generations of sources for a thousand-drop array. Thus, one is limited to the relatively small number of drops when using the method of images. On the other hand, if the drops are treated as point sources, then the procedure can be simplified and a large number of drops can be considered. Further PSM yields simple analytical results even for complicated configuration since the relations for correction factors are linear. This technique is only approximate when the drops approach each other. While Labowsky's MOI results are for a three-drop array consisting of volatile and nonvolatile components, the PSM results are presented for: (*i*) correction factor for each component in the drop of interest, (*ii*) the net correction factor for the drop, and (*iii*) average correction factor for the array.

2 Objectives

The objectives of the present study are: (*i*) to model the QS evaporation of multicomponent drop arrays using the point source method, (*ii*) to obtain analytical results for the correction factor and compare the results with those obtained from MOI for a three-drop and two-component array, (*iii*) to obtain the results for binary drop array using the PSM, and (*iv*) to compare qualitatively with experimental data published elsewhere. For simplicity, the procedure will be illustrated only for two components, A and B, although the method could be extended to a large number of components.

Since the gas phase heat and mass diffusion rates are fast compared to the regression rate of slowly evaporating drops, a QS approximation can be made. Further, the QS results provide a convenient frame of reference for studying the effects of interaction on the evaporation rate of an array. Further, QS explicit results for isolated drops are available for the evaporation rate and the previous studies on multicomponent array using MOI were carried out using a QS assumption; thus the validity of the PSM requires a similar assumption. As shown later, the QS approximation leads to simple explicit solutions for interactive evaporation of multicomponent arrays consisting of an arbitrary number of drops arranged in various configurations.

3 Model

3.1 Isolated Drop Evaporation

(*A*) *Drops of Arbitrary Composition.* The conservation equations for the evaporation and combustion of multicomponent drops have been presented earlier by Law (1976, 1978) and Law and Law (1982). It will be assumed that the drop is at uniform temperature (infinite thermal conductivity) and composition (infinite liquid phase diffusivity), evaporating under QS conditions into a quiescent atmosphere at T_∞. Spherical symmetry and equal binary diffusion coefficients are assumed. The QS solutions will be presented below for the case of $Le = 1.0$.

(*i*) *Mass conservation:* For a multicomponent drop, the species and mass conservation equations for one-dimensional radial systems, which include the Stefan flow (SF), yield the

Nomenclature

a = radius of droplet
D = diffusion coefficient
h_T = thermal enthalpy
l = distance between two droplets
L = latent heat of evaporation
$\dot{m}$ = mass rate of evaporation
p = pressure
R = universal gas constant
r = radial distance
T = temperature, K
V = diffusion velocity
v_i = total velocity of species i
v = bulk velocity
W = molecular weight
X = mole fraction
Y = mass fraction
ϵ = flux fraction
η = correction factor
θ = angle (Fig. 1)
ξ = nondimensional radius, Eq. (1*b*)
ρ = density
Φ = potential

Subscripts

A = component A
a = air
B = component B
b = boiling condition
F = fuel
I = inert species
i = ith component
iso = isolated
j = jth drop
ℓ = liquid phase
m = mixture
sat = saturation
T = thermal
v = vapor
w = interface conditions at droplet wall or surface
∞ = ambient or surrounding conditions

Abbreviations

MOI = Method of Images
NSF = Non-Stefan or negligible Stefan Flow
PSM = Point Source Method
SF = Stefan Flow

species profile for each component as (Annamalai and Durbetaki, 1975),

$$\frac{Y_i - Y_{i,\infty}}{Y_{i,w} - Y_{i,\infty}} = \frac{1 - e^{-\xi}}{1 - e^{-\xi_{w,\text{iso}}}}, \quad i = A, B \tag{1a}$$

where

$$\xi = \frac{\dot{m}_{\text{iso}}}{4\pi\rho Dr} \tag{1b}$$

$$\xi_{w,\text{iso}} = \dot{m}_{\text{iso}}/4\pi\rho Da$$

The interface species conservation is given as

$$4\pi\rho_i v_{i,w} r^2 = \dot{m}_{\text{iso}}\epsilon_i, \quad i = A, B \tag{2a}$$

where ϵ_i is defined as

$$\epsilon_i = \dot{m}_{i,\text{iso}}/\dot{m}_{\text{iso}} \tag{2b}$$

Dividing the velocity (v_i) into the bulk (v) and diffusive components, Eq. (2a) is rewritten as

$$4\pi\rho v r^2 Y_{i,w} - 4\pi\rho D r^2 \left\{\frac{dY_i}{dr}\right\}_w = \dot{m}_{\text{iso}} \cdot \epsilon_i, \quad i = A, B \tag{3a}$$

Using Eqs. (1) in Eq. (3a), the interface boundary condition is given as

$$Y_{i,w} + \left\{\frac{dY_i}{d\xi}\right\}_w = \epsilon_i, \quad i = A, B \tag{3b}$$

(*ii*) *Energy conservation:* Using energy conservation, the temperature profile in the gas phase is given as

$$\frac{h_T - h_{T,\infty}}{h_{T,w} - h_{T,\infty}} = \frac{1 - e^{-\xi}}{1 - e^{-\xi_{w,\text{iso}}}} \quad i = A, B \tag{4}$$

The interface energy conservation is given as

$$\left[\lambda \frac{dT}{dr}\right]_w \cdot 4\pi r^2 = -(L_A \dot{m}_{A,\text{iso}} + L_B \dot{m}_{B,\text{iso}}) \tag{5a}$$

Equation (5a) neglects the sensible enthalpy for liquid phase heating. Rewriting Eq. (5a) as

$$\left[\frac{dh_T}{d\xi}\right]_w = -(L_A\epsilon_A + L_B\epsilon_B) \tag{5b}$$

Now setting h_T at the droplet wall (surface) as reference value ($h_{T,w} = 0$), differentiating Eq. (4), and using the result in Eq. (5b), the evaporation rate in terms of enthalpy is given as

$$\xi_{w,\text{iso}} = \ln\left[1 + \frac{h_{T,\infty}}{L_A\epsilon_A + L_B\epsilon_B}\right] \tag{6}$$

With $Y_{i,\infty} = 0$, differentiating Eq. (1a), and using Eq. (3b), the evaporation rate in terms of species mass fraction is given as

$$\xi_{w,\text{iso}} = -\ln\{1 - (Y_{i,w}/\epsilon_i)\}, \quad i = A, B \tag{7a}$$

From Eq. (7a) it is seen that

$$Y_{A,W}/\epsilon_A = Y_{B,W}/\epsilon_B = C \tag{7b}$$

Proceeding similarly for inert species I, which is present only in the gas phase, the constant C is evaluated as

$$C = 1 - (Y_{I,W}/Y_{I,\infty}) \tag{7c}$$

Hence, one can rewrite Eq. (7a) as

$$\xi_{w,\text{iso}} = \ln(Y_{I,\infty}/Y_{I,W}) \tag{7d}$$

Equating Eq. (7a) with Eq. (6),

$$Y_{i,w} = \frac{h_{T,\infty} \cdot \epsilon_i}{\Sigma L_i\epsilon_i + h_{T,\infty}} \tag{8}$$

Note that Eq. (8) reduces to a standard relation for the evaporation of a single component drop.

For slow evaporation, the diffusion velocity is significant compared to convective velocity. Thus Stefan flow may be neglected (see Appendix A-1). Then Eqs. (6) and (7a) simplify to:

$$\xi_{w,\text{iso}} = \frac{h_{T,\infty}}{(L_A\epsilon_A + L_B\epsilon_B)} \tag{9a}$$

$$\xi_{w,\text{iso}}\epsilon_i = Y_{i,w} \tag{9b}$$

or

$$\xi_{i,w,\text{iso}} = Y_{i,w} \tag{9c}$$

where

$$(\xi_{i,w})_{\text{iso}} = \frac{\dot{m}_{i,\text{iso}}}{4\pi\rho Da} \tag{9d}$$

Using Eq. (9a) in Eq. (9b), the mass fractions under negligible Stefan flow (NSF) can be expressed as

$$Y_{i,w} = \frac{h_{T,\infty} \cdot \epsilon_i}{\Sigma L_i\epsilon_i}, \quad i = A, B \tag{10}$$

The mass fraction is expressed in terms of mole fraction as

$$Y_{i,w} = \frac{X_{i,w} W_i}{W_m}, \quad i = A, B \tag{11a}$$

where

$$X_{i,w} = p_{i,w}/P \tag{11b}$$

and the partial pressure $p_{i,w}$ is related to drop temperature through phase equilibrium relations. Applying Raoult's law for miscible mixtures, which is valid for homologous series,

$$p_{i,w} = X_{i,l} p_{\text{sat},i}, \quad i = A, B \tag{12a}$$

and the Cox-Antoine relation

$$\ln p_{i,\text{sat}} = E_i + \frac{F_i}{T + G_i}, \quad i = A, B \tag{12b}$$

where E_i, F_i, and G_i are constants for the given fuel component, the partial pressure $p_{i,w}$ is evaluated. Another relation is given by the identity

$$\Sigma\epsilon_i = 1.0 \tag{13}$$

The solution procedure for the evaporation rate of an isolated multicomponent drop is to assume T_w, find $p_{i,\text{sat}}$ from Eq. (12b), then determine $p_{i,w}$ from (12a) for the given mole fraction of species i in liquid phase, $X_{i,w}$ from Eq. (11b), and finally $Y_{i,w}$ using Eq. (11a). Then ϵ_i is solved from the linear Eqs. (10). However, the identity given by Eq. (13) must be satisfied; if not, iterations are continued until the convergence occurs.

(*B*) *Isolated Drop of a Volatile and a Nonvolatile Component.* Simplified results can be obtained for an isolated drop consisting of volatile (component A) and nonvolatile (component B) components. Since ϵ_B is zero, $\epsilon_A = 1$, then equating Eqs. (6) and (7a), the mass fraction under SF is given as

$$Y_{A,w} = \left[\frac{h_{T,\infty}/L_A}{1 + (h_{T,\infty}/L_A)}\right] \tag{14a}$$

Under NSF {or $(h_{T,\infty}/L_A) \ll 1$}

$$Y_{A,w} = h_{T,\infty}/L_A \tag{14b}$$

Further, from Eq. (6) with SF,

$$\xi_{w,\text{iso}} = \ln[1 + (h_{T,\infty}/L_A)] \tag{15a}$$

where T_w is determined using Raoult's law (Eq. (12a)) and the Cox-Antoine relation (Eq. (12b)). The evaporation rate under NSF is given as

$$\xi_{w,\text{iso}} = h_{T,\infty}/L_A \tag{15b}$$

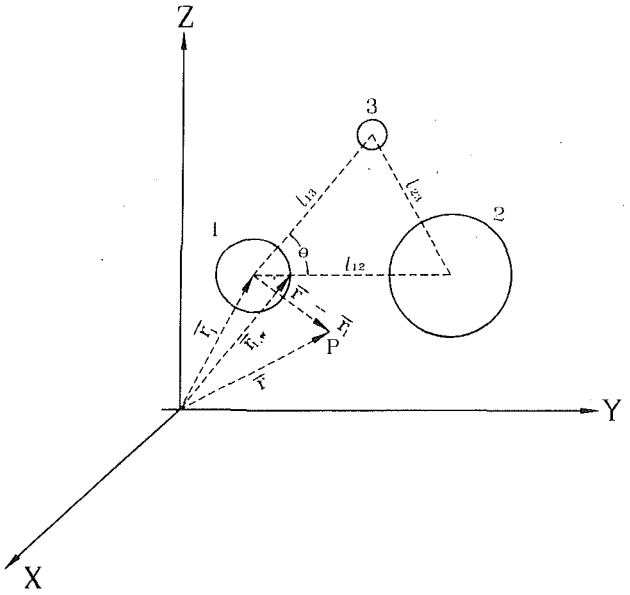

Fig. 1 Three-drop array: illustration of coordinates

3.2 Multicomponent Array Evaporation

(*A*) *Array of Arbitrary Composition.* Consider the array shown in Fig. 1. Each drop is assumed to be a point mass source, which is valid for large l/a ratios. The PSM described elsewhere (Annamalai and Ryan, 1991, 1992) is briefly illustrated below. The species i from drop j with surface fuel mass fraction of $(Y_{i,w})_j$ evaporates at the rate of $\dot{m}_{i,j}$. The strength of the source $\dot{m}_{i,j}$ and $(Y_{i,w})_j$ are unknown, and are to be solved from the Laplace equation for each species and the boundary conditions:

$$\nabla^2 Y_i = 0 \quad i = A, B \tag{16a}$$

subject to

$$Y_i \to Y_{i,\infty} \text{ as } \mathbf{r} \to \infty \tag{16b}$$

$$Y_i \to (Y_{i,w})_j$$

$$\text{for } j = 1 \ldots J \text{ at drop surfaces } (\mathbf{r}_{w,j} = \mathbf{r}_j + \mathbf{a}_j) \tag{16c}$$

or

$$\dot{m}_i = \dot{m}_{i,1} \text{ at drop 1, } \dot{m}_{i,2} \text{ at drop 2, } \ldots . \tag{16d}$$

Since the governing equations and boundary conditions are linear, the superposition technique could be adopted (Labowsky, 1980). In the superposition technique the drop j alone is assumed to evaporate at the rate of $\dot{m}_{i,j}$ for species i and fuel mass fraction of species i at P due to drop j is determined using the isolated drop analysis. Then the mass fraction of species i at P is summed over all the drops.

Consider drop j. Assume that $Y_{i,\infty} = 0$. The mass of species i leaving the surface by diffusion under NSF is given by

$$\dot{m}_{i,j} = -4\pi\rho r^2 D \frac{dY_i}{dr}, \quad i = A, B$$

Integrating once, and applying the boundary condition,

$$Y_i \to 0 \text{ as } r \to \infty$$

one obtains

$$(Y_i)_j = \frac{\dot{m}_{i,j}}{4\pi\rho D r}, \quad r > a$$

Since the governing equation and the boundary conditions are linear, the mass fraction of species i at point P in an array of J droplets is simply given as (Fig. 1):

$$Y_i = \sum_{\substack{j=1 \\ j \neq k}}^{J} \frac{\dot{m}_{i,j}}{4\pi\rho D |\mathbf{r} - \mathbf{r}_j|} \tag{17a}$$

(If $Y_{i,\infty} \neq 0$, Eq. (17*a*) can still be used with Y_i replaced by $Y_i - Y_{i,\infty}$.)

Note that $\dot{m}_{i,j}$ denotes the mass flow rate of species i from the jth droplet in the array and it is still an unknown. As will be seen later the value for Y_i will not exceed unity at points away from the drop surfaces. The above equation, when evaluated at the wall (or surface) of the kth droplet, becomes:

$$(Y_{i,w})_k = [\dot{m}_{k,i}/4\pi\rho D a_k] + \sum_{\substack{j=1 \\ j \neq k}}^{J} \dot{m}_{i,j}/(4\pi\rho D |\mathbf{r}_{k,w} - \mathbf{r}_j|) \tag{17b}$$

With $\mathbf{r}_{k,w} = \mathbf{r}_k + \mathbf{a}_k$, and assuming $|\mathbf{r}_k - \mathbf{r}_j| \gg a_k$, one may approximate Eq. (17*b*) as

$$(Y_{i,w})_k = \frac{\dot{m}_{k,i}}{4\pi\rho D a_k} + \sum_{\substack{j=1 \\ j \neq k}}^{J} \frac{\dot{m}_{i,j}}{4\pi\rho D |\mathbf{r}_k - \mathbf{r}_j|} \text{ where } i = A, B \tag{18}$$

It can be shown that the drop temperature and mass fractions of species i at the surface of the kth drop remain exactly the same obtained for an isolated drop of similar composition (Labowsky, 1980). The mass fraction of species i at the surface of drop size a_k is imposed as $(Y_{i,w})_k$ (Section 3.1A). As such it cannot exceed unity. Since $Y_{i,\infty} = 0$ and $Y_{i,w} < 1.0$ then $(Y_i)_P$ at any point away from the drop surface must be less than 1.0. However, the mass fraction contour of $Y_{i,w}$ (or the potential contour) may not exactly follow the surface of the drop, particularly for closely spaced drops. A detailed comparison of PSM with the exact results will be given later. Using Eqs. (9*c*) and (9*d*),

$$(\dot{m}_{i,\text{iso}})_k = 4\pi\rho D a_k (Y_{i,w})_k \quad i = A, B \tag{19}$$

Using the definition of correction factor and Eqs. (18) and (19), the expression for correction factor of the ith component in the kth drop is given as

$$\eta_{ik} = 1 - \sum_{\substack{j=1 \\ j \neq k}}^{N} \eta_{ij} \frac{a_j (Y_{i,w})_j}{|l_{kj}| (Y_{i,w})_k}, \quad i = A, B \tag{20a}$$

where l_{kj} is the interdrop spacing, $= |\mathbf{r}_k - \mathbf{r}_j|$. [The result shown in Eq. (20*a*) was applied to the evaporation problem of an array of single component drops mounted on the apices of a regular polygon and the result for the average correction factor was found to be *exactly the same* (Annamalai and Ryan, 1992) as the expression obtained by Deutch et al., who used the Fourier transform technique for the diffusion controlled reactions of a system of static sinks.] Multiplying Eq. (20*a*) by ϵ_i, summing over all i's, and using the identity given by Eq. (7*c*) the following result is obtained with $Y_{I,\infty} = 1.0$:

$$\eta_k = 1 - \sum_{\substack{j=1 \\ j \neq k}}^{N} \frac{\eta_j a_j (1 - Y_{I,w})_j}{|l_{kj}| (1 - Y_{I,w})_k} \tag{20b}$$

Equation (20*b*) provides the net correction factor for the evaporation rate of drop k. For arrays of multicomponent droplets of similar composition, the inclusion of Stefan flow will not alter the result for the correction factor as long as Stefan flow is included for both the array and isolated drop analyses (Annamalai and Ryan, 1992); however, if the compositions are dissimilar, Stefan flow will affect the correction factor (see Appendix A-2).

(*B*) *Array of Drops of Volatile* (*A*) *and Nonvolatile* (*B*) *Components.* In order to compare the results of PSM with those from the Method of Images (MOI) (Labowsky, 1980), the solution for a three-drop array is obtained using the PSM.

Consider a three-drop array of radii a_1, a_2, and a_3 mounted

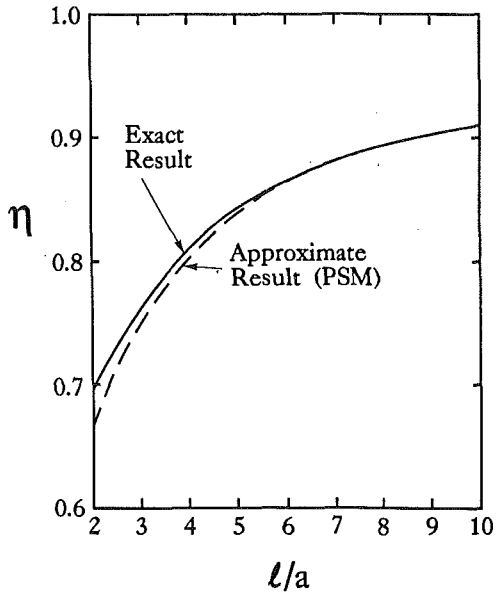

Fig. 2(*a*) Comparison of bispherical and PSM solutions for a single-component, binary array

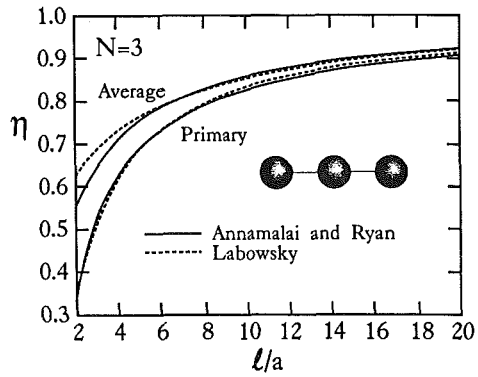

Fig. 2(*b*) Comparison of MOI and PSM results for a three-drop single component and linear array

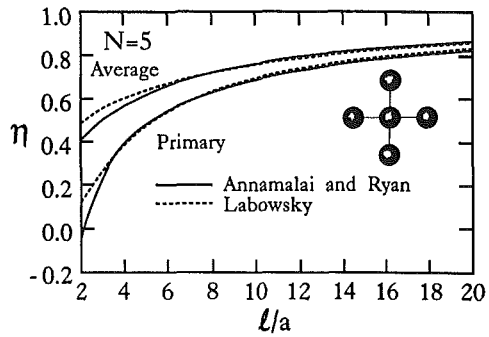

Fig. 2(*c*) Comparison of MOI and PSM results for a five-drop, single-component array

at the apices of scalene triangle (sides l_{12}, l_{13}, and l_{23} as in Fig. 1). With $|\mathbf{r}_2-\mathbf{r}_1|=l_{12}$ and $|\mathbf{r}_3-\mathbf{r}_1|=l_{13}$ and using Eqs. (20*a*) for component A,

$$\eta_{A1}=1-\frac{a_2(Y_{A,w})_2\eta_{A2}}{l_{12}(Y_{A,w})_1}-\frac{a_3(Y_{A,w})_3\eta_{A3}}{l_{13}(Y_{A,w})_1} \quad (21a)$$

$$\eta_{A2}=1-\frac{a_1(Y_{A,w})_1\eta_{A1}}{l_{12}(Y_{A,w})_2}-\frac{a_3(Y_{A,w})_3\eta_{A3}}{l_{23}(Y_{A,w})_2} \quad (21b)$$

$$\eta_{A3}=1-\frac{a_1(Y_{A,w})_1\eta_{A3}}{l_{13}(Y_{A,w})_3}-\frac{a_2(Y_{A,w})_2\eta_{A2}}{l_{23}(Y_{A,w})_{13}} \quad (21c)$$

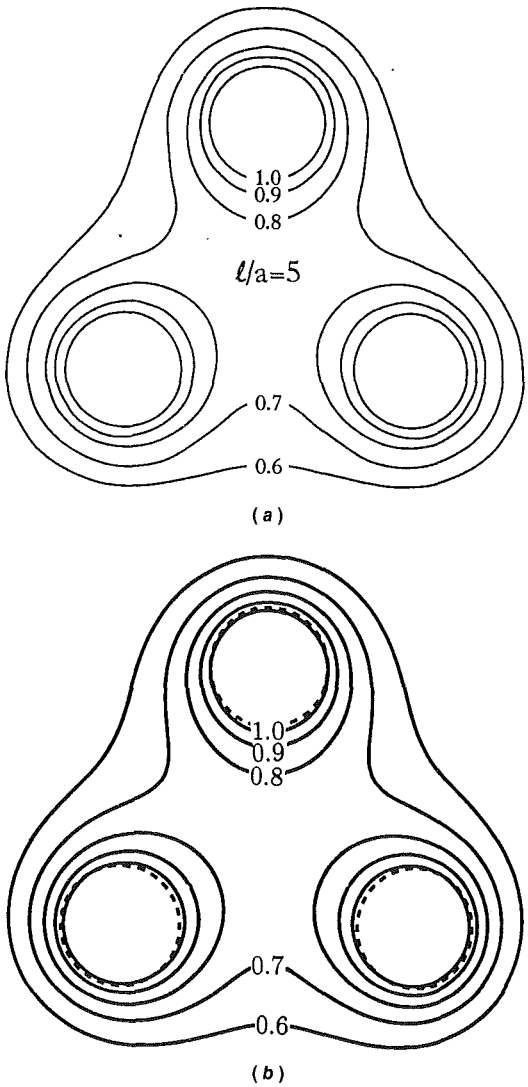

Fig. 3 Potential contours around a triangular array: (*a*) MOI; (*b*) PSM

From isolated drop results, $(Y_{A,w})_1$, $(Y_{A,w})_2$, and $(Y_{A,w})_3$ can be determined (Section 3.1) and the three unknowns η_{A1}, η_{A2}, and η_{A3} are solved from the three linear Eqs. (21).

4 Results

4.1 Comparison of PSM Results With Exact Methods for Single-Component Arrays. Prior to presenting the results for multicomponent arrays, a brief summary of results obtained for a single-component array is presented in order to determine the limitations of PSM. First, the results from PSM for binary array are compared with those from the bispherical coordinate method (Fig. 2*a*). The error at point of contact ($l/a=2$) is only 3.7 percent. Second, the results from the PSM are compared with those from MOI for three and five-drop arrays (Annamalai and Ryan, 1991). Figures 2(*b*) and 2(*c*) compare the average correction factor and the correction factor for the primary drop estimated from MOI for the three and five-drop arrays. Figures 3(*a*) and 3(*b*) compare the potential contours obtained from MOI and PSM. Note that when $l/a>5$, the contours of $\Phi=Y_i/Y_{i,w}=1$ are almost spherically symmetric for a three-drop array (Fig. 3*b*). This transforms to a number density of 4×10^5 drops per cm^3 for 60 μm (diameter) drops while maximum number densities in the atomization zone are of the order of 5000 drops/cm^3. Thus, the PSM is reasonable within the practical range of sprays considered. Even for closer

Table 1 Physical properties of fuels

PROPERTY	FUEL		
	Heptane (C_7H_{16})	Octane (C_8H_{18})	Hexadecane ($C_{16}H_{34}$)
Density (kg/m^3)	684	703	773
Boiling Point (K)	372	399	560
Heat of Vaporization (kJ/kg)	316	300	225
E [Note 1]	15.89 [Note 2]	15.93 [Note 3]	24.66 [Note 4]
F	-2911.32	-3120.0	-10660.2
G	-56.4	-63.5	+54.1

Note (1): $\ln p_{sat} = E + \frac{F}{T+G}$
p_{sat}, mm of Hg; T, K.

Note (2): Smith and VanNess

Note (3): Labowsky, 1980

Note (4): Curve fitted from Weast, 1 < p < 40mm of Hg

Table 2 Comparison of correction factors obtained by MOI and PSM

$\ell_{12} = 5.0$, $\ell_{13} = 3.6$, $\theta = 33.7°$, $T_\infty = 300$ K

DROP NO.	OCTANE MOLE FRACTION (LIQ)	DROP SIZE a_i/a_1	CORRECTION FACTOR(η)	
			MOI	PSM
1	0.20	1.0	0.54	0.56
2	0.45	1.5	1.02	1.02
3	0.05	0.5	-2.93	-2.90

Table 3 Comparison of η values: similar and dissimilar sized drops

$\ell_{12} = 5.0$, $\ell_{13} = 3.6$, $\theta = 33.7°$, $T_\infty = 300$ K

DROP NO.	OCTANE MOLE FRACTION (LIQ)	ARRAY OF UNIFORM SIZE	ARRAY OF DISSIMILAR SIZE
1	0.20	0.79	0.56
2	0.45	1.03	1.02
3	0.05	-1.98	-2.90

spacing one might argue that the results for arrays are for nonspherical drops since the potential contours of $\Phi = 1$ are not spherical at $l/a = 2$.

The error for the correction factor of the primary drop (drop at center) at closer interdrop spacing increases as more drops are included (Fig. 2*c*). Thus, the PSM is limited in predicting the correction factor of primary drop (the center drop) especially for arrays containing more than seven drops (not shown). However, the difference between the average correction factors obtained from PSM and MOI is not significant even for an array consisting of a large number of drops since primary drop contributes little to the average evaporation rate. It could be concluded from Figs. 2(*a*), 2(*b*), 2(*c*), and 3(*a*) that the agreement between the results obtained from MOI and PSM is excellent for l/a up to 2 for binary and three drop single component arrays. More comparison of the PSM results with those from MOI is given in the next section.

4.2 Three-Drop Multicomponent Array. Consider drops consisting of volatile octane (A) and a nonvolatile component (B). The properties of octane are tabulated in Table 1. As mentioned before, the drop temperature T_w is assumed and $p_{A,\text{sat}}$ is calculated from Eq. (21*b*). The compositions shown in Table 2 and Eq. (12*a*) are then used to evaluate $p_{A,w}$. Knowing $X_{A,w}$ from Eq. (11*b*), $Y_{A,w}$ is estimated from Eq. (11*a*) and compared with $Y_{A,w}$ calculated from Eq. (14*b*). Iteration is continued until convergence occurs. With $T_\infty = 300$ K, it is determined that $T_{w,1} = 296.1$ K, $(Y_{A,w})_1 = 0.01279$, $T_{w,2} = 292.8$ K, $(Y_{A,w})_2 = 0.0235$, $T_{w,3} = 298.9$ K, and $(Y_{A,w})_3 = 0.003767$.

Table 4 Comparison of η values: compositionally similar and dissimilar drops

$\ell_{12} = 5.0$, $\ell_{13} = 3.6$, $\theta = 33.7°$, $T_\infty = 300$ K

DROP NO.	a_i/a_1	ARRAY OF UNIFORM COMPOSITION	ARRAY OF DISSIMILAR COMPOSITION
1	1	0.71	0.56 (20%)
2	1.5	0.79	1.02 (45%)
3	0.5	0.38	-2.90 (5%)

Equations (21*a*), (21*b*), and (21*c*) are then used to solve for η_{A1}, η_{A2}, and η_{A3}. Table 2 shows a comparison of the results between MOI and PSM. The maximum error is 4 percent. The negative value for drop 3 implies condensation of vapors. The temperature and mass fraction at the location r_3 would have been 298 K and 0.006 if only drop 2 was present as an isolated drop. Thus the presence of drop 3 increased the local temperature to 298.9 K and reduced $Y_{A,w}$ to 0.004, which implies the removal of vapor from location r_3. Drop 3 acts as a mass sink and a heat source due to higher drop temperature. Drop 3 had the lowest octane content and it has the lowest equilibrium vapor mass fraction. Hence the vapors originating from 1 and 2 diffuse outward and condense on drop 3. Further, drop 2 has a correction factor more than unity since it has a high octane content and is in close proximity to a mass sink and heat source (i.e., drop 3) resulting in an evaporation rate greater than the evaporation rate of a similar isolated drop. It should be noted that the drop temperatures are unaffected by the size of the droplet or by the interactions. For given T_∞, they are only functions of the percentage composition of the components.

In order to separate the size and composition effects on η values, estimates for η were made for a three-drop array of similar sizes and compared with the drop array of dissimilar sizes. The results are presented in Table 3. The evaporation rate of a drop is proportional to the drop size and hence the larger drop has a strong interaction effect (of saturating the other drops), as seen in Table 2.

When drop sizes are made similar, the correction factor for the smaller drops (drops 1 and 3) becomes less severe (i.e., higher η values), since the influence of the larger drop has decreased. This is consistent with observations for drop arrays of single components (Labowsky, 1976). Estimates of η values are also made keeping the drop size and array the same as the original array but for a problem of compositionally similar drops. These results are summarized in Table 4. It is seen from Eqs. (21) that the mass fraction terms disappear when the compositions are similar for all the drops in the array. Hence the relations for correction factor are exactly the same as those for the single-component arrays except that the isolated drop evaporation rate of the former must be based on the drop having same composition as the array. Thus the third column of Table 4 is independent of drop composition and is equally valid for drops of single-component arrays. It is seen, from Tables 2 and 3, that the change in composition of the drops has a stronger effect on the correction factor than the variation in size. The effect of interdrop spacing is also considered for drops of similar size mounted at the apices of an equilateral triangle with composition as listed in Table 3. Figure 4 shows the results. As the interdrop spacing is reduced, the condensation is enhanced for drop 3 while vaporization is improved for drop 2 for $l/a < 9$. However, one may be tempted to conclude that the closer interdrop spacing of multicomponent drops may improve the combined evaporation rate of all the drops in the array. Hence it is necessary to define an average correction factor as

$$\eta_{\text{avg}} = \frac{(\eta_{A,1}\dot{m}_{\text{iso},A,1} + \eta_{A,2}\dot{m}_{\text{iso},A,2} + \eta_{A,3}\dot{m}_{\text{iso},A,3})}{(\dot{m}_{\text{iso},A,1} + \dot{m}_{\text{iso},A,2} + \dot{m}_{\text{iso},A,3})} \tag{22}$$

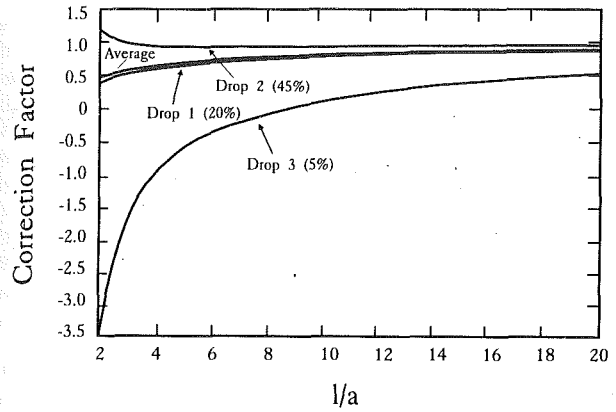

Fig. 4 Correction factors of drops 1, 2, and 3 for a monosized ternary array mounted on the apices of an equilateral triangle

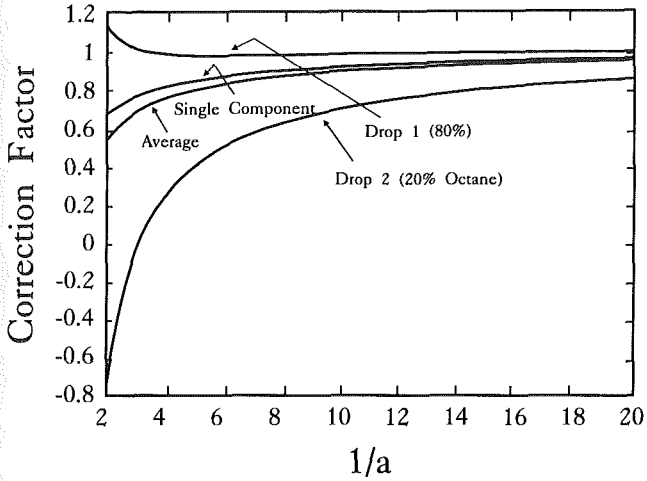

Fig. 5 Correction factors of drops 1 and 2 for a monosized binary array

where $\dot{m}_{\text{iso},A,1}$ is the evaporation rate of species A from an isolated drop having the same composition as the drop 1 in the array. It is clear from Fig. 4 that the average correction factor is always less than one and the interaction is severe as the interdrop spacing is used.

4.3 Binary Array. Experimental data are available for binary arrays of drops of dissimilar composition (Xiong et al., 1984). Hence, results for the correction factor were generated for a binary array of drops. Two cases were considered: (*i*) a binary array of drops consisting of volatile and nonvolatile components, and (*ii*) a binary array of drops consisting of volatile components.

(*i*) *Binary Array of Drops of Volatile and Nonvolatile Components.* Two drops of the same size but differing composition with octane as the volatile component (drop 1, octane: 80 percent; drop 2, octane: 20 percent) were considered. Using the PSM, the expressions for the correction factors of a monosized binary drop array of differing composition can be derived from Eq. (20*a*) as

$$\eta_{A1}=\left[1-\frac{(Y_{A,w})_2}{(Y_{A,w})_1}\times\frac{a}{l}\right]\Bigg/\left[1-\frac{a^2}{l^2}\right] \qquad (23a)$$

$$\eta_{A2}=\left[1-\frac{(Y_{A,w})_1}{(Y_{A,w})_2}\times\frac{a}{l}\right]\Bigg/\left[1-\frac{a^2}{l^2}\right] \qquad (23b)$$

Isolated drop analyses yield $T_{w,1}=297.7$ K, $(Y_{A,w})_1=0.06032$, $T_{w,2}=290.7$ K, and $(Y_{A,w})_2=0.0285$. Using these results in Eqs. (23*a*) and (23*b*), correction factors were obtained. Figure 5 plots the correction factor versus l/a for drops 1 and 2. It is noted from Eqs. (23) that the correction factor of the array of drops of similar composition is exactly the same as the correction factor of the array of drops of a single component since $(Y_{A,w})_2=(Y_{A,w})_1$. Figure 5 also compares the results of a single component or array of similar composition with those of dissimilar composition.

It is seen that as the l/a ratio is decreased, the correction factor of predominantly volatile drops (drop 1) remains approximately the same until l/a reaches about 3. At this point the vapor mass fraction at the surface of drop 2 becomes more than allowed by the phase equilibrium, resulting in condensation. The correction factor becomes more than 1 since the lower volatile drop (drop 2) acts as mass sink and heat source. Thus, the high volatile core of the spray consisting of a multicomponent drop {(80 percent) octane} may evaporate faster at closer spacing if surrounded by drops of 20 percent octane. However, the average evaporation rate will still be lower as seen in Fig. 5. It is seen from Figs. 4 and 5 that condensation is less severe for a binary drop array than for a three-drop array.

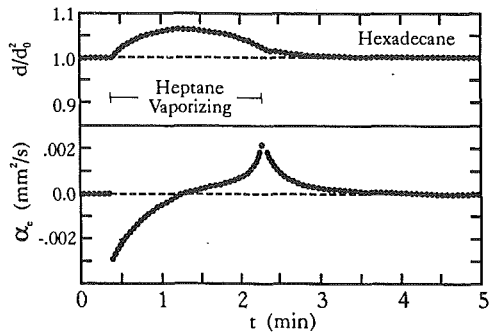

Fig. 6 Instantaneous drop diameter squared for the hexadecane drop in the heptane-hexadecane array (α_e = evaporation rate constant; adopted from Xiong et al.)

(*ii*) *Binary Array of Drops of Volatile Components.* Xiong et al. conducted evaporation experiments on a two-drop array of (*i*) high volatile heptane drop (drop 1) and (*ii*) low volatile hexadecane drop (drop 2) at an ambient temperature of 24°C. Figure 6 shows that the hexadecane drop had a negative vaporization constant in that the size of hexadecane drop increases as result of the condensation of vapors from the heptane drop. Hence, drop 2 acts as the mass sink and heat source for drop 1, which is at a lower temperature. It is not possible to emulate Xiong's experimental conditions since one cannot achieve the phase equilibrium in the array under steady state unless each drop in the array consists of both components, heptane (A) and hexadecane (B). In order to simulate Xiong's data, a binary array of drops consisting of 95 percent heptane and 5 percent hexadecane (drop 1) and 5 percent heptane and 95 percent hexadecane (drop 2) is selected. Using the fuel properties listed in Table 1, the isolated drop results for T_w, and Y_w for the two-component system are then obtained. The drop temperatures and surface mass fractions are found to be as follows: $T_{w,1}=278$, $(Y_{A,w})_1=0.065$, $T_{w,2}=297$ K, and $(Y_{A,w})_2=0.010$. Figure 7 shows the results. Drop 2, being hotter, supplies heat to drop 1 and at the same time the requirement of phase equilibrium at the surface of drop 2 results in condensation of heptane vapors on drop 2. Thus, at closer interdrop spacings, the correction factor for heptane at drop 1 is higher than unity, while for drop 2 it is negative, indicating condensation accompanied by an increase in diameter. These results qualitatively confirm the results shown in Fig. 6. The present analysis yields steady-state results, while the experimental data are for the transient case where the composition

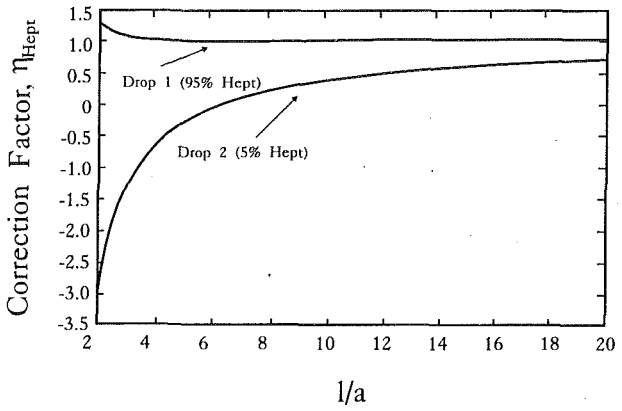

Fig. 7 Correction factor of heptane in drops 1 and 2 for a binary array of heptane-hexadecane drops

and size change with time. Thus parametric results for various compositions are generated for a binary array. Figure 8(*a*) shows the correction factor for heptane of drop 1 while Fig. 8(*b*) shows the correction factor for heptane of drop 2. Figure 8(*a*) clearly shows the increasing severity of interaction with increased heptane percentage of drop 2, the severity being higher at lower heptane percentage of drop 1.

Suppose drop 1 has a composition of 95 percent heptane and 5 percent hexadecane while drop 2 has a composition of 5 percent heptane and 95 percent hexadecane. Initially, the correction factor is of the order of 1 for drop 1 (Fig. 8*a*). At closer interdrop spacing, the heptane vapor condenses at drop 2 (Fig. 8*b*). Thus heptane percentage will be increasing slowly for drop 2 accompanied by increase in size while it is being depleted at drop 1. As the heptane percentage increases in drop 2 (Fig. 8*b*) the partial pressure of heptane increases, the condensation stops, and subsequently with further increase in heptane percentage the correction factor becomes positive. Certainly at 10 percent concentration (not shown), evaporation occurs at drop 2 with reduction in size. The increased heptane percentage for drop 2 increases the severity of interaction at drop 1. Thus the correction factor changes at fixed interdrop spacing due to change in composition and size, which may lead to more deviation in the d^2 law compared to the corresponding law for a binary array of single components.

It is of interest to estimate the concentration level of heptane in drop 2 beyond which there can be no further condensation, or $\eta_{A2} \geq 0$ (see Fig. 8*b*). Using Fig. 6, the percentage of heptane at the time condensation stops is estimated to be 10 percent. However, experimental data on l/a are not available and hence a quantitative comparison could not be made. Using Eq. (23*b*), the critical composition at which $\eta_{A2} \geq 0$ is given as

$$(Y_{A,w})_1/(Y_{A,w})_2 < (l/a) \tag{24}$$

Figure 9 plots $(Y_{A,w})_1/(Y_{A,w})_2$ for various mole fractions of component A for drop 1, with $X_{A,l,2}$ as a parameter.

In order to illustrate the use of Fig. 9, one can consider two drops of composition $X_{A,l,1}=0.9$ and $X_{A,l,2}=0.1$ separated by $l/a=3.0$. Then, using isolated drop analyses, $(Y_{A,w})_1/(Y_{A,w})_2=3.7$. Since $(Y_{A,w})_1/(Y_{A,w})_2>3.0$, the criterion given by Eq. (24) is not satisfied. Thus condensation will occur. In a transient array problem as condensation proceeds, $X_{A,l,2}$ and hence $Y_{A,w,2}$ will increase as in the case of Xiong's experiment. When $X_{A,l,2}=0.2$, at same $X_{A,l,1}=0.9$, condensation will not occur, since Eq. (24) is satisfied. It should also be noted that the evaporation rate of drop 1 will keep decreasing due to decreasing $X_{A,l,1}$ and decreasing size, contributing less vapor at drop 2. Since drop 2 has higher heptane content, it will start vaporizing again as seen in Fig. 6. It should be mentioned that the transient evaporation of a binary array of drops of dissimilar composition is affected both by the changing composition and size. The QS results given in section 4.2 provide the effect of both of these parameters on the evaporation rate.

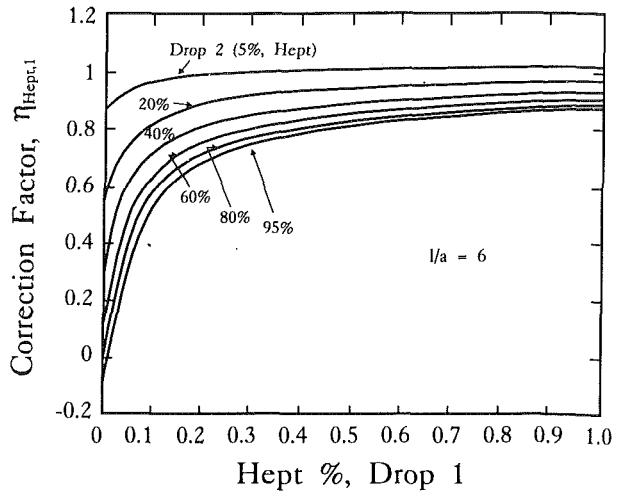

(*a*)

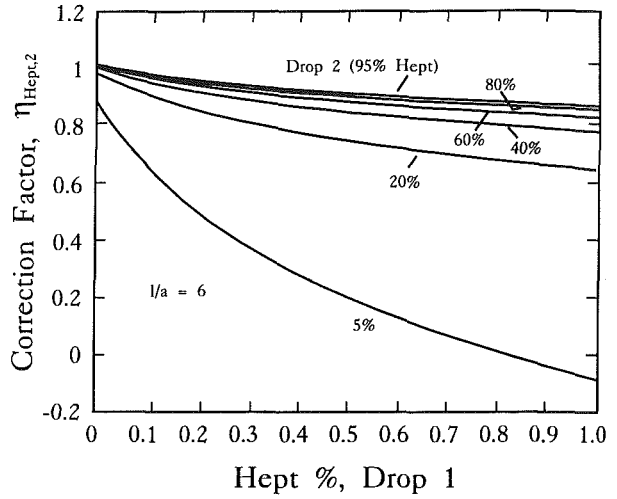

(*b*)

Fig. 8 Effect of heptane percentage on the correction factors: (*a*) drop 1; (*b*) drop 2

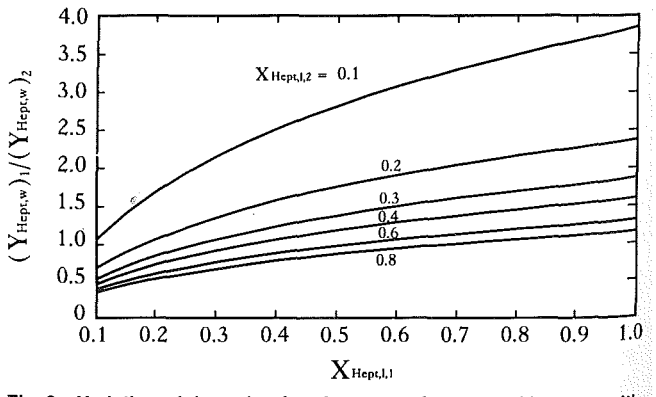

Fig. 9 Variation of the ratio of surface mass fractions of heptane with mole fraction of heptane for a heptane-hexadecane array

It is noted that the nonisothermal conditions selected for the present problem involve weak temperature differences. This was done mainly in order to: (*i*) compare the results from PSM with the results from method of images (MOI) under identical environmental conditions, (*ii*) compare qualitatively

with experimental data, and (*iii*) use the Laplace equation (or the neglect of Stefan flow), which is valid only for slow evaporation process. However, most practical applications involve higher temperature differences during evaporation. Thus Stefan flow must be included. While transformation exists for single component array for converting governing equations with Stefan flow into the Laplace equation (Labowsky, 1978), there exists no such procedure for a multicomponent drop array. Appendix A.2 presents the transformation for the evaporation of a multicomponent array of drops, which could be used to convert the Stefan flow (SF) problem into an NSF (non-Stefan flow) problem. Figures A.1 and A.2 in Appendix A present results at higher temperatures and also present a comparison of results for correction factor with and without Stefan flow for a binary array of heptane–hexadecane drops. The difference between the two correction factors with and without Stefan flows appear to be very small even for free-stream temperatures as high as 360 K.

5 Summary

1 The QS evaporation of a multicomponent drop array has been studied using the point source method. The results from the PSM are found to be in excellent agreement with those from MOI for the three drop array.
2 Even though the evaporation rates of drops consisting of high volatile composition are enhanced at lesser interdrop spacing, the average evaporation rate always decreases with decrease in interdrop spacing.
3 The results from the binary array studies agree qualitatively with experimental data. It is predicted that as the high volatile drop (drop 1) evaporates, condensation occurs on the low volatile drop (drop 2). But condensation stops when a critical composition is reached at drop 2. Results for the critical liquid composition are presented.
4 The transient evaporation of an array of drop of dissimilar composition is affected both by the changing size and composition.

Acknowledgments

A part of the present work was supported with a grant from Pittsburgh Energy Technology Center of DOE under Grant No. DE-FG22-90 PC 90310. However, any finding, conclusion, or recommendation herein are those of the authors and do not necessarily reflect the views of DOE.

References

Annamalai, K., and Durbetaki, P., 1975, "Extinction of Spherical Diffusion Flames: Spalding Approach," *Int. J. Heat Mass Transfer*, Vol. 170, pp. 1416–1418.

Annamalai, K., and Ramalingam, S., 1987, "Group Combustion of Char/Carbon Particles," *Comb. Flame*, Vol. 70, pp. 307–332.

Annamalai, K., and Ryan, W., 1992, "Interactive Processes in Gasification and Combustion, Part I: Liquid Drop Arrays and Clouds," *J. of Prog. in Energy and Comb. Sci.*, Vol. 18, pp. 221–295.

Annamalai, K., and Ryan, W., 1993, "A Point Source Method for Evaporation of Arrays," ASME PD-Vol. 50, pp. 49–54.

Brzustowski, T. A., Twardus, E. M., Wojcicki, S., and Sobiesiak, A., 1979, "Interaction of Two Burning Fuel Droplets of Arbitrary Size," *AIAA Journal*, Vol. 17, pp. 1234–1242.

Chiu, H. H., and Liu, T. M., 1977, "Group Combustion of Liquid Droplets," *Comb. Sci. Tech.*, Vol. 17, pp. 127–142.

Deutch, J. M., Felderhof, B. U., and Saxton, M. J., 1976, "Competitive Effects in Diffusion Controlled Reactions," *J. Chem. Physics*, Vol. 11, pp. 4559–4563.

Labowsky, M., 1976, "The Effect of Nearest Neighbor Interactions on the Evaporation Rate of Cloud Particles," *Chem. Eng. Sci.*, Vol. 32, pp. 803–813.

Labowsky, M., 1978, "A Formalism for Calculating the Evaporation Rates of Rapidly Evaporating Interacting Particles," *Comb. Sci. Tech.*, Vol. 18, pp. 145–151.

Labowsky, M., 1980, "Transfer Rate Calculations for Compositionally Dissimilar Interacting Particles," *Chem. Eng. Sci.*, Vol. 35, pp. 1041–1048.

Law, C. K., 1976, "Multi-component Droplet Combustion With Rapid Internal Mixing," *Comb. Flame*, Vol. 26, pp. 219–233.

Law, C. K., 1978, "Internal Boiling and Superheating in Vaporizing Multicomponent Droplets," *AIChE Journal*, Vol. 24, pp. 626–636.

Law, C. K., and Law, H. K., 1982, "d^2 Law for Multi-component Droplet Vaporization and Combustion," AIAA Paper No. 81-0264.

Raju, M. S., and Sirignano, W. A., 1990, "Interaction Between Two Vaporizing Droplets in an Intermediate Re Flow," *Phys. Fluids*, Vol. A2, No. 10, pp. 1780–1796.

Sirignano, W. A., 1993, "Fluid Dynamics of Sprays," ASME *Journal of Fluids Engineering*, in press.

Smith, J., and Von Ness, H. C., 1987, *Introduction to Chemical Engineering Thermodynamics*, McGraw-Hill Book Co., Chap. 10.

Tal, R. T., Lee, D. N., and Sirignano, W. A., 1984, "Heat and Momentum Transfer Around a Pair of Spheres in Viscous Flow," *Int. J. Heat Mass Transfer*, Vol. 27, pp. 1953–1962.

Weast, R. C., 1968, *Handbook of Chemistry and Physics*, The Chemical Rubber Co., Cleveland, OH.

Williams, F. A., 1985, *Combustion Theory*, 2nd ed., Benjamin/Cummins Publishing Co., New York.

Xiong, T. Y., Law, C. K., and Miyasaka, K., 1984, "Interactive Vaporization and Combustion of Binary Droplet Systems," *20th Symposium (International) on Combustion*, pp. 1781–1787.

APPENDIX

Stefan Flow Effects on Multicomponent Drop Array Evaporation

A.1 Stefan Flow Approximation. The neglect of Stefan flow (SF) is justified for a slow evaporation problem or problems where the mass fraction of fuel vapor is much less than unity as illustrated below.

Consider a drop vaporizing in a quiescent atmosphere. The average velocity or Stefan flow (SF) velocity or bulk velocity v is given as (Williams, 1985)

$$\rho v = \rho_a v_a + \rho_v v_v \tag{A1}$$

where v_v = absolute vapor velocity. Since air does not dissolve in liquid

$$v_a = 0$$
$$\rho v = \rho_v v_v \tag{A2}$$

But the absolute velocity is a sum of bulk velocity v and diffusion velocity V. Thus,

$$v_v = v + V_v \tag{A3}$$

where

$$V_v = -\rho D \nabla \ln Y_v \tag{A4}$$

Using Eq. (A3) in Eq. (A2)

$$(v/V_v) = Y_v/(1 - Y_v) \tag{A5}$$

As $Y_v \to 0$, $v \to 0$. It is seen that the SF velocity is very small compared to diffusion velocity when Y_v is small. Hence the convective term in Eq. (16) of the text is neglected in comparison with the diffusive term. This is true for the pure evaporation problem at low temperatures as considered in the present problem. For the present problem considered in the text, $Y_{A,w} \sim 0.06$, and thus the SF velocity is only 6 percent of diffusion velocity.

A.2 Transformation of Stefan Flow (SF) Problem Into Non-Stefan Flow (NSF) Problem. Stefan Flow cannot be neglected for the rapid evaporation (strong temperature difference) or combustion problems. Thus a transformation is now presented for converting an SF flow problem into a non-Stefan flow (NSF) problem. Consider the transport equation with SF for fuel species A in a single component array of drops:

$$\nabla \cdot (\rho \mathbf{v} Y_A - \rho D \nabla Y_A) = 0 \tag{A6}$$

Following the brief procedure outlined by Annamalai and Ryan (1992), one can define the evaporation potential Φ_A as

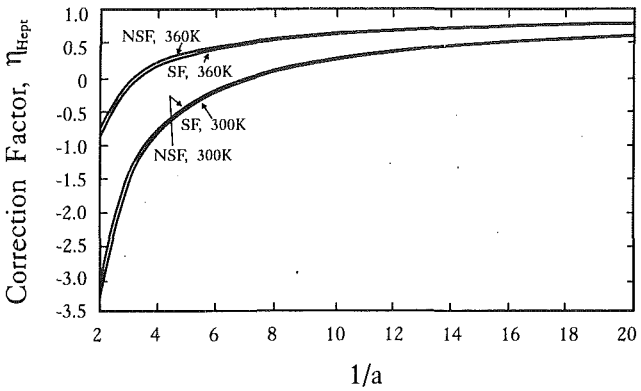

Fig. A.1 Comparison of correction factor for drop 1 with and without Stefan flows for a heptane-hexadecane array

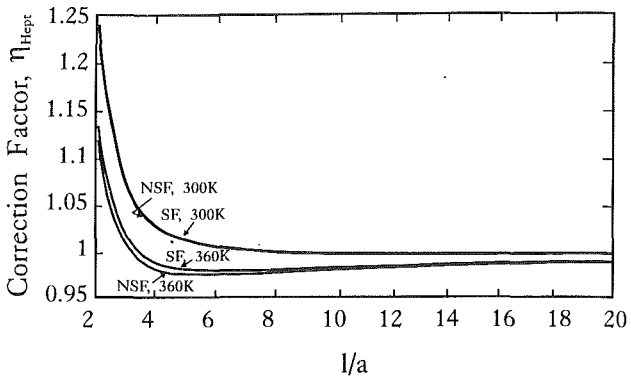

Fig. A.2 Comparison of correction factor for drop 2 with and without Stefan flows for a heptane-hexadecane array

$$\Phi_A = \frac{\ln[(Y_A - Y_{A,I})/(Y_{A,\infty} - Y_{A,I})]}{\ln[(Y_{A,w} - Y_{A,I})/(Y_{A,\infty} - Y_{A,I})]} \tag{A7}$$

One may use Eq. (7) directly in Eq. (6) and show that

$$\nabla^2 \Phi_A = 0 \tag{A8}$$

One can show from Eq. (7) that for small values of Y_A, with $Y_{A,\infty} = 0$ and $Y_{A,I} = 1.0$,

$$\Phi_A = +(Y_A / Y_{A,w})$$

which is exactly the same solution obtained for the Laplace equation in terms of Y_A (i.e., NSF problems).

For multicomponent drops $Y_{A,I}$ should be replaced by the flux fraction of A, which is an unknown. The selection of inert species (I) is found to be more suitable for multicomponent arrays of drops. Then Eq. (7) for inert species reduces to

$$\Phi_I = \ln[Y_I / Y_{I,\infty}] / \ln[Y_{I,w} / Y_{I,\infty}] \tag{A9}$$

Note that the inert species mass fraction at surface of multicomponent drop is dependent upon the composition of drop.

Similarly for inert species,

$$\nabla^2 \Phi_I = 0 \tag{A10}$$

and the Stefan flow is given as

$$\rho \mathbf{v} = -\rho D[\ln(Y_{I,\infty}/Y_{I,w})] \nabla \Phi_I \tag{A11}$$

Equations (8) and (10) are similar to the conservation equation for NSF problem.

If one adopts Eq. (10) along with transformation presented in Eq. (9) one can show that the ratio $(Y_{i,w})_j/(Y_{i,w})_k$, etc., in Eq. (20*a*) of the text becomes $\ln(Y_{I,w})_j/\ln(Y_{I,w})_k$ for the SF problem. When these relations were derived using the evaporation potentials an interesting result for the correction factor of the multicomponent drop was obtained. Instead of obtaining the correction factor for component i in drop k ($\eta_{i,k}$), the correction factor (η_k) for the net evaporation rate of the drop k for SF problem was obtained:

$$\eta_k = 1 - \Sigma\ (\eta_j a_j \ln(Y_{I,w})_j] / (|l_{kj}| \ln(Y_{I,w})_k)] \tag{A12}$$

This relation can be reduced for the NSF problem by approximating $[\ln Y_{I,w}]$ as $[1 - Y_{I,w}]$ since $Y_{I,w}$ is close to unity for the slow evaporation problem:

$$\eta_k = 1 - \Sigma\,[(\eta_j a_j (1 - Y_{I,w})_j] / (|l_{kj}| (1 - Y_{I,w})_k)] \tag{A13}$$

which is the same as Eq. (20*b*) of the text.

For arrays of similar composition, the correction factor ($\eta_{i,k}$) remains unaffected whether SF is included or not since the $Y_{I,k}$ are the same at all drop surfaces in the array; however, they differ for arrays of dissimilar composition since the $Y_{I,k}$ are different at drop surfaces in the array.

Equations (9), (10), and (11) and the identity $Y_{I,k}/\epsilon_i = \{1 - (Y_{I,w}/Y_{I,\infty})\}$ are used in order to determine the correction factor for the binary array including the SF effects. Figures A.1 and A.2 show the comparison of the results for the correction factor with and without SF for a binary array of drops consisting of 95 percent heptane (A) and 5 percent hexadecane (B) (drop 1) and 5 percent heptane and 95 percent hexadecane (drop 2). The error due to neglect of SF is negligible even for an ambient temperature as high as 360 K. An interesting result at $T_\infty = 360$ K is the occurrence of minimum in the correction factor at $l/a = 5$ due to the competitive effects of condensation of hexadecane vapors at closer interdrop spacing, which enhances the evaporation rate and the saturation with heptane vapors, which reduces the evaporation rate.

Heat Transfer From a Molten Phase to an Immersed Coal Particle During Devolatilization

R. H. Hurt

T. H. Fletcher[1]

Combustion Research Facility,
Sandia National Laboratories,
Livermore, CA 94550

R. S. Sampaio[2]

Department of Metallurgy
and Materials Science,
Carnegie Mellon University,
Pittsburgh, PA 15213-3890

In several developmental and commercial processes, coal particles come into direct contact with a high-temperature molten phase. These processes include molten carbonate coal gasification and bath smelting for the production of iron. Recently, real-time X-ray fluoroscopic images have been published that show volatile matter evolving rapidly from coal particles immersed in molten phases, displacing the surrounding melt and producing a periodic cycle of formation, rise, and detachment of gas cavities. The present work makes use of these observations to develop a model of heat transfer from the melt to particles undergoing gas evolution. The model is developed for the general case and applied to predict melt-particle heat transfer coefficients under conditions relevant to bath smelting processes. The model shows that the presence of the gas film can actually increase the overall heat transfer rate under certain conditions.

Introduction

In several commercial and pilot-scale processes, coal particles come in direct contact with a high-temperature molten phase. The molten phase can serve primarily as a heat transfer medium, as in the molten-carbonate coal gasification process (Hottel and Howard, 1971), or can engage in chemical reactions with the coal, as in bath-smelting processes for iron production. In the latter process, coal serves the dual function of reducing iron ore and supplying heat by partial combustion (Aukrust, 1988).

Bath-Smelting Processes. Currently several bath-smelting processes are under development that use coal in place of coke and have higher rates of iron production per unit volume than the conventional technology of the blast furnace (Fruehan et al., 1988). In these processes, iron ore concentrate or pellets, which may be partially reduced, are injected into an iron-carbon bath or simply added to the top of the vessel. Coal in crushed or lump form is also added at the top of the vessel, where it falls through the gas space and enters the molten metal or slag phase. Alternatively, entrained pulverized coal can be injected with a top lance or bottom tuyeres. The iron ore is reduced in the bath, producing the gaseous products CO and H_2, which are postcombusted with oxygen or air to supply heat to the bath. The gases leaving the vessel may be used for preheating and prereduction of the ore (Fruehan et al., 1988).

Coal Devolatilization. In all processes in which coal particles contact and are heated by a high-temperature molten phase, the coal decomposes thermally, yielding a variety of gaseous products and a carbon-enriched solid char. The evolved gas, or volatile matter, is composed of light noncondensable gases and relatively high molecular weight substances that condense to form liquids at room temperature (tar). The relative yields of tar and gas, as well as the total volatile yield, are dependent upon coal rank and type (Fletcher, 1989a, 1989b; Anthony and Howard, 1976; Gavalas, 1982; Howard, 1981), particle size, heating rate, and final temperature. The rate at which devolatilization occurs varies from milliseconds to minutes and depends on several factors, including temperature, particle size, and heat transfer coefficient between the particle surface and its surroundings (Fletcher, 1989a, 1989b; Solomon et al., 1986; Gibbins-Matham and Kandiyoti, 1988; Freihaut et al., 1989). Numerous empirical models of varying degrees of complexity have been proposed to describe the devolatilization process, see for example Badzioch and Hawksley (1970), Kobayashi et al. (1976), and Anthony et al. (1974). Recently, detailed models containing a description of the macromolecular structure of the parent coal and the kinetics of bond-breaking reactions leading to volatile evolution have been successful in the prediction of temperature and heating rate effects on the relative tar/gas yields for coals of various rank (Fletcher et al., 1990; Grant et al., 1989; Niksa and Kerstein, 1991; Solomon et al., 1988).

For particles greater than about 1 mm in diameter the rate of the devolatilization process is believed to be determined largely by the rate of heat transfer to and within the particle (Misra and Essenhigh, 1988). There have been several experimental (Stubington and Lingewile, 1989; Stubington and Sumaryono, 1984; Kalson and Briggs, 1985; Gokhale and Mahalingam, 1985) and theoretical (Hajaligol et al., 1988; Misra and Essenhigh, 1988) investigations of the devolatilization kinetics of particles in this size range. The application of any of the models or experimental data to a specific process requires a knowledge of the heat transfer coefficient between the coal particle surface and its environment.

Devolatilization of Immersed Coal Particles. Sampaio et al. (1991) have recently conducted an experimental investigation of the devolatilization of 3–15 mm coal particles in crucibles of molten slag. X-ray fluoroscopy was used to obtain real-time images of the multiphase flow induced by the degassing process. In a melt, the rapid release of the gaseous volatile matter displaces the molten material surrounding the particle, producing a gas cavity separating the particles from the molten phase. The gas cavities are observed to grow, rise, and detach from the particles in a nearly regular periodic cycle. This behavior may be anticipated in other systems as well, when the particulate material undergoes sublimation or thermal decomposition to gaseous products upon contact with a higher temperature melt. The factors governing the rate of heat transfer to particles in this environment are not well es-

[1]Present address: Department of Chemical Engineering, Brigham Young University, Provo, UT.

[2]Present affiliation: Research Department, Cia Vale do Rio Doce, Belo Horizonte, Brazil.

Contributed by the Heat Transfer Division for publication in the JOURNAL OF HEAT TRANSFER. Manuscript received by the Heat Transfer Division February 1992; revision received November 1992. Keywords: Furnaces and Combustors, High-Temperature Phenomena, Liquid Metals. Associate Technical Editor: W. L. Grosshandler.

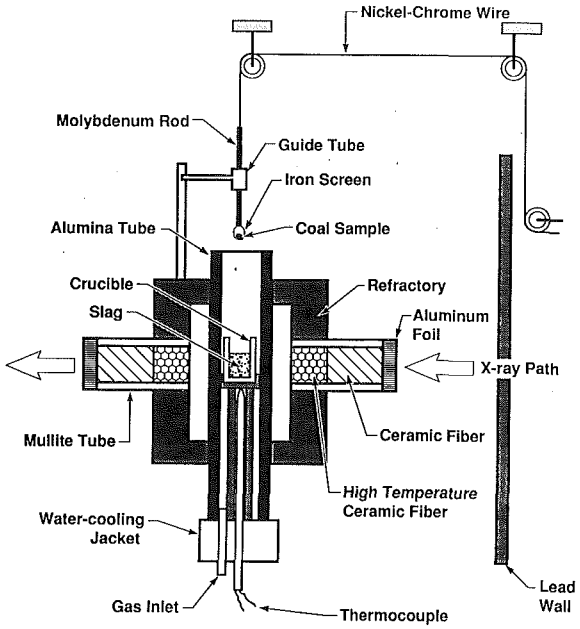

Fig. 1 Diagram of electrical furnace and coal feeding system

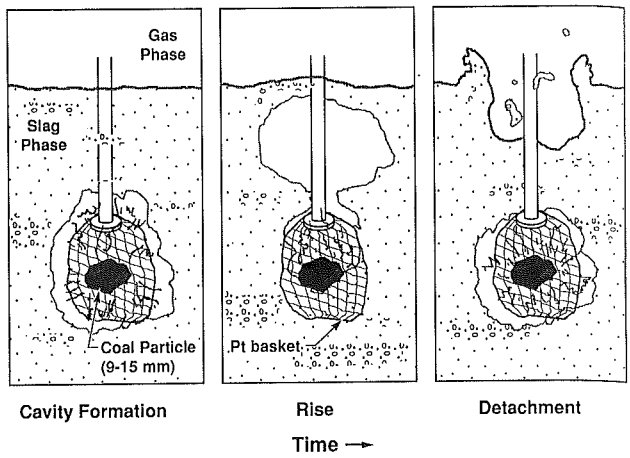

Fig. 2 Depiction of the devolatilization process for immersed coal particles

tablished. Orsten and Oeters (1988) have briefly treated heat transfer to coal particles in molten metal baths for particle sizes from 0.05 to 0.8 mm in diameter. Application to other processes, including iron production by bath smelting, requires information on larger particle sizes, typically 1 to 15 mm.

In the present article, the salient features of the X-ray fluoroscopic images of Sampaio et al. (1991) are summarized and, based on these observations, a model of the heat transfer from the melt to immersed particles undergoing gas evolution is developed. The model is first developed for the general case and subsequently applied for the prediction of melt-particle heat transfer coefficients during coal devolatilization under conditions relevant to bath-smelting processes.

Summary of X-Ray Fluoroscopic Imaging Results

Only a brief summary of the materials and experimental procedures is given below; for a more detailed description, see Sampaio et al. (1991). The devolatilization behavior of seven coals of varying rank and type were studied in slag phases prepared from reagent grade CaO, SiO_2, Al_2O_3, and CaF_2. The experimental equipment consists of a furnace for production and containment of molten slag, a system for inserting and withdrawing captive coal particles, and an X-ray fluoroscopic imaging system. A diagram of the furnace and coal feeding system is shown in Fig. 1. In each experiment, a single coal particle of diameter 3–15 mm was held captive in a wire basket on the end of a 0.125 in. diameter, 24 in. length molybdenum rod and lowered into the slag bath. X-rays are propagated through the furnace and the transmitted rays are used from images recorded in real time on video tape.

The video images from the X-ray fluoroscopic technique provide much information on the devolatilization processes. The rapid evolution of volatile products from the coal particles is clearly visible. It is not possible, however, to obtain good quality still photographs from the video images, even with image enhancement. The behavior typically observed is therefore schematically depicted in Fig. 2. The rapidly evolving gases induce significant turbulence in the slag phase and displace the molten material surrounding the particle to form a gaseous

Nomenclature

C_1, C_2 = integration constants
d_c = diameter of the column (here of the vessel)
g = gravitational constant
h_c, h_r, h_g, h_m = heat transfer coefficients: conduction, radiation, global, melt-side
$\hat{h}_c$ = conduction heat transfer coefficient corrected for radial flow
H_s = height of slag layer
k_g, k_m = thermal conductivity of gas, melt
L = dimensionless radial position
M_s = total mass of slag
dM/dt = mass rate of devolatilization
Nu = Nusselt number = hd/k
P = power dissipation in melt
Pr = Prandtl number = $C_p\mu/k$
Q_c, Q_r, Q_t, Q_v = heat flows: by conduction, by radiation, total, to volatile matter
R_c, R_p = radii of cavity, particle
T_m, T_{cs}, T_{ps}, $\bar{T}$, T_v = temperature of melt, cavity surface, particle surface, system average, volatile matter upon detachment
V_c, V_p, V_s = volume of cavity, particle, slag layer
$\dot{V}_g$ = volumetric flow rate of gas in smelter
v_r, v_s = velocities: radial, radial at particle surface
$\dot{v}_g$ = superficial gas velocity in smelter
α = thermal diffusivity $k/\rho C_p$
δ = film thickness
ϵ_p, ϵ_c = emissivities: particle, cavity surface
ϵ_g = gas or void volume in the slag phase
η = correction factor for conduction heat transfer in radial flow field
Θ = dimensionless temperature
μ_v, μ_m = viscosities: gaseous volatile matter, melt (true)
ρ_s, ρ_v, ρ_p = densities: molten (slag) phase, volatile matter, particle
σ = Stefan–Boltzmann constant
τ = mean residence time of volatiles in cavity
Φ = rate factor
$\chi \equiv (T_v - T_{ps})/(T_{cs} - T_{ps})$

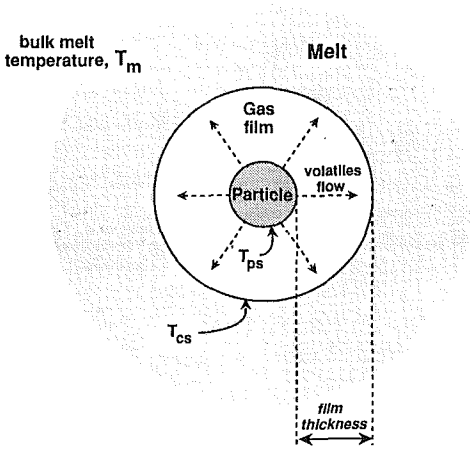

Fig. 3 Depiction of simplified geometry chosen for modeling

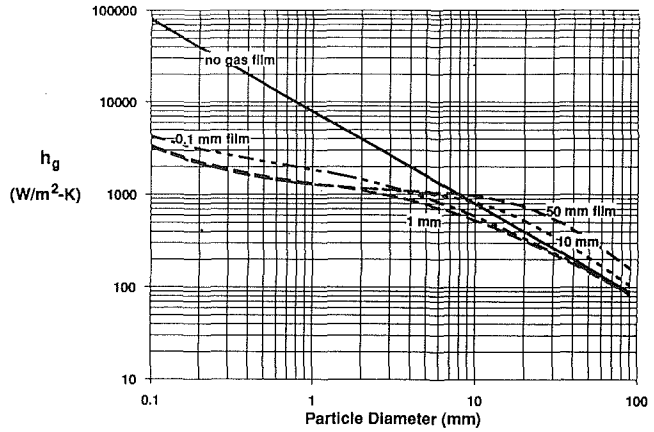

Fig. 4 Effect of particle diameter and film thickness on overall heat transfer coefficient. Valid in a stagnant melt at low devolatilization rates and small temperature differences. Physical properties used are listed in Table 1.

cavity that separates the particles from the molten phase. The cavity grows as devolatilization proceeds, until a point at which some or all of the gaseous contents of the cavity detach from the particle to form a free gas bubble that rises in the denser surrounding fluid (see the middle panel of Fig. 2). The cavity growth and venting form a rapid cycle that is repeated many times over the course of the degassing process. This general behavior is observed for all coal types and particle sizes, but the duration and intensity of devolatilization varies. See Sampaio et al. (1991) for measurements of devolatilization times for coals of varying rank and type.

Model Development

In this section we use the general observations above to develop a model that predicts the rate of melt-to-particle heat transfer in this system.

Heat Transfer in Stagnant Media. First we consider heat transfer when both the gas film and the melt are stagnant and subsequently consider turbulent melts and finite rates of devolatilization. Both the coal particle and the cavity in the melt (with radii R_p and R_c, respectively) are modeled as concentric spheres (see Fig. 3). A single cavity size is used that represents a mean or effective size over the course of one cycle of cavity growth and bubble detachment. In the presence of the gas film, the transport of heat from the molten phase to the particle surface is accomplished by the parallel mechanisms of conduction and radiation. At low rates of devolatilization, the rate of conduction from the cavity inner surface to the particle surface is easily obtained from the energy equation in spherical coordinates. The rate of conduction, in the form of a heat transfer coefficient, is given by:

$$h_c \equiv \frac{Q_c}{A_p(T_{cs}-T_{ps})} = \frac{k_g(R_c/R_p)}{(R_c-R_p)} \qquad (1)$$

As R_c/R_p approaches unity, this expression simplifies to the planar solution $h_c = k_g/\delta$, where $\delta = R_c - R_p$ is the thickness of the gas film. The rate of radiative heat transfer from the cavity inner surface to the particle surface is a function of the temperatures and emissivities of both surfaces (Hottel and Sarofim, 1967) and can be expressed in the form of an effective heat transfer coefficient valid at very small ΔT (small $T_{cs} - T_{ps}$):

$$h_r \equiv \frac{Q_r}{A_p(T_{cs}-T_{ps})} = \frac{\sigma(4\overline{T}^3)}{\left[1/\epsilon_p + \frac{(1-\epsilon_c)}{\epsilon_c}\left(\frac{R_p}{R_c}\right)^2\right]} \qquad (2)$$

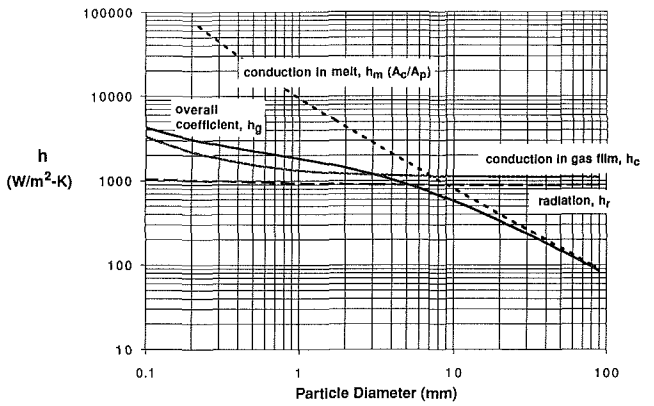

Fig. 5 Effect of particle diameter on individual heat transfer coefficients for 0.1 mm gas film thickness. Valid in a stagnant melt at low devolatilization rates and small temperature differences. Physical properties used are listed in Table 1.

This relation provides a useful approximation for moderate ΔT as well, producing, for example, an error of 5 percent for $T_{cs} = 1800$ K, $T_{ps} = 1200$ K if the arithmetic average temperature is used for $\overline{T}$. At large ΔT, an effective radiative heat transfer coefficient can still be defined as $Q_r/[A_p(T_{cs} - T_{ps})]$, but is a function of both $\overline{T}$ and ΔT. Approximate radiative coefficients from Eq. (2) are used to generate Figs. 4–8, as they permit a convenient comparison with convective coefficients. The effect of large ΔT on the global coefficients will be considered in a later section.

Soot clouds have been observed to form around devolatilizing coal particles and many affect the radiative exchange between the cavity surface and the particle. An estimate of the radiative properties of soot clouds at the short path lengths considered here indicates that their emissivities are typically significantly less than 1. There is, in addition, a finite time required for soot formation, which may postpone the appearance of the cloud until late in the growth/venting cycle. The potential effect of soot on the radiative transfer coefficient was therefore not considered further in this analysis. It is expected that this simplification will not greatly affect the global coefficients.

The rate of heat transfer to the particle will, under some conditions, be limited by convective/conductive heat transfer from the bulk of the molten phase to the surface of the cavity.

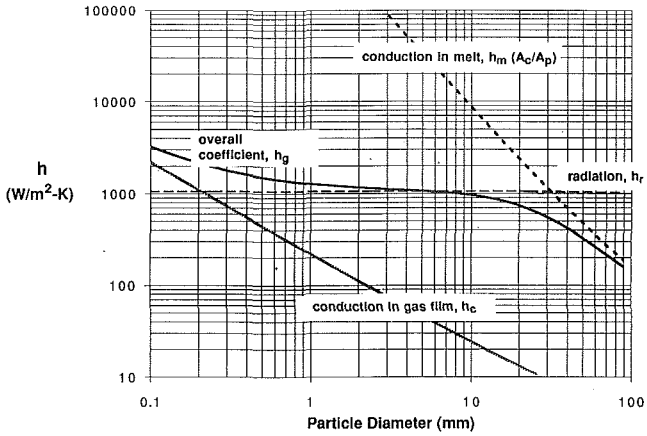

Fig. 6 Effect of particle diameter on individual heat transfer coefficient for 50 mm gas film thickness. Valid in a stagnant melt at low devolatilization rates and small temperature differences. Physical properties used are listed in Table 1.

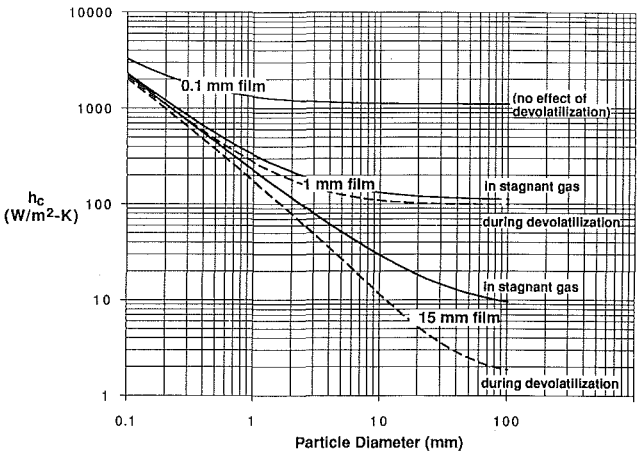

Fig. 7 The effect of outward radial flow on the conduction heat transfer coefficient. Physical properties used are listed in Table 1.

A melt heat transfer coefficient, h_m, based on the area of the cavity, can be defined as:

$$h_m \equiv \frac{Q_t}{A_c(T_m - T_{cs})} = \mathrm{Nu}(k_g/d_c) \tag{3}$$

where Nu = 2 for a stagnant fluid. A global heat transfer coefficient, defined by

$$h_g \equiv \frac{Q_t}{A_p(T_m - T_{ps})} \tag{4}$$

can be related to the individual coefficients by combining Eqs. (1)–(3) and eliminating the unknown intermediate temperature T_c to yield

$$h_g \equiv \frac{1}{\left[\dfrac{1}{(h_r + h_c)} + \dfrac{(A_p/A_c)}{h_m}\right]} \tag{5}$$

The heat transfer coefficient is seen to depend upon physical properties (emissivities and thermal conductivities of the media involved), the particle radius, and the thickness of the gas film.

The simple relationships in Eqs. (1)–(5) are illustrated in Fig. 4, in which global heat transfer coefficients have been calculated for physical properties typical of ironmaking slags (see Table 1). Numerical error in these computations is insignificant when considering the accuracy to which many of the relevant

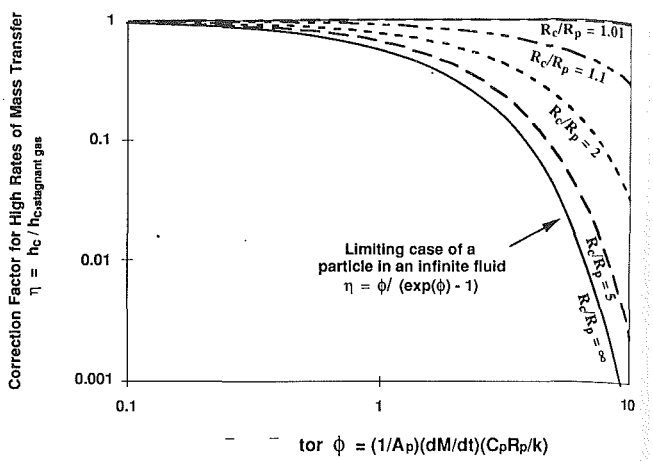

Fig. 8 Conduction heat transfer coefficients during coal devolatilization. Physical properties used are listed in Table 1.

physical properties are known. The gas film thickness is treated as an independent parameter, as the quantitative dependence of the film thickness on particle size, rate of devolatilization, and properties of the molten phase is not established.

The heat transfer coefficient varies over three orders of magnitude depending on particle size and thickness of the gas film. For small particles the coefficient is relatively insensitive to the size of the film, as long as the film thickness exceeds 0.1 mm. For very thin films, however, (or for direct melt/particle contact) the heat transfer is greatly enhanced. For large particles, on the other hand, the coefficient is sensitive to thickness of the gas film for films larger than 1 mm. It is interesting that for particle diameters and film thicknesses both above about 10 mm, the rate of heat transfer is *greater* than in the case of direct particle-melt contact. This and other features of Fig. 4 can be understood by examining the individual contributions to the global coefficient, plotted in Figs. 5 and 6.

In Figs. 5 and 6, the overall coefficient and the three individual contributing terms from Eq. (5), h_c, h_r, and $h_m(A_c/A_p)$, are plotted as a function of particle diameter with film thickness as a parameter. Film thicknesses of 0.1 mm (Fig. 5) and 50 mm (Fig. 6) are considered. A film thickness of 50 mm is primarily relevant to the larger particles, although it may have some significance for small particles within bubbles or voids caused by factors other than volatile release by the particle. In both figures three distinct regimes are apparent; the exact boundaries of the regimes are a function of the film thickness. Below 1 mm particle diameter, conduction through the gas film becomes increasingly important and is the dominant mode of heat transfer for the smallest particle sizes considered (0.1 mm). In the regime from approximately 1 to 10 mm in particle diameter, radiation is either dominant or is of equal importance with gas phase conduction, depending on film thickness. Above about 10 mm particle diameter, the heat transfer from the bulk melt to the cavity surface begins to influence the heat transfer. For the particles larger than about 20 mm, $h_m(A_c/A_p)$ is clearly smaller than the sum of h_r and h_c (it is indeed smaller than each of these terms individually) and heat transfer resistance in the bulk melt determines the overall coefficient.

It is in this regime that the presence of the gas film *enhances* heat transfer by increasing the cavity size, thus promoting heat transfer from the bulk melt to the cavity surface. Although the presence of the gas film slows the rate of gas phase conduction, the global coefficient is not adversely affected, because the sum of conduction and the parallel mechanism of radiation is too large to exert any limiting influence on the rate of heat transfer in this regime. The fact that the presence of a gas film can *enhance* heat transfer compared to direct

melt-particle contact may seem counterintuitive. The effect can be understood by recognizing that the gas film, while being a poor conductor, is an excellent transmitter of radiation, allowing direct radiative exchange between the particle surface and distant fluid elements having temperatures representative of the bulk of the melt.

Heat Transfer at Finite Rates of Devolatilization. In addition to the formation of the gas cavity, devolatilization influences heat transfer in two ways: (1) Conduction to the particle is partially suppressed by the outward radial flow of escaping volatile matter, and (2) The released gases are heated by the melt for the duration of their contact with the particle (before detachment). The gas thus removes heat from the cavity surface and reduces the cavity surface temperature, thus competing with heat transfer to the particle.

To account for the second effect, we consider the portion of the heat flow from the cavity surface that does not reach the particle and is carried away by the rising gas bubble, Q_v:

$$Q_v \equiv \frac{dM}{dt} C_p (T_v - T_{ps}) \tag{6}$$

where dM/dt is the mass rate of devolatilization and T_v is the mean temperature of the volatile matter in the gas bubble upon detachment.

Recognizing that

$$Q_t = Q_c + Q_r + Q_v \tag{7}$$

and eliminating T_{cs} and the four heat flows from Eqs. (1)–(3), (6), and (7), yields the following expression for the global coefficient for heat transfer to the particle:

$$h_g \equiv \frac{1}{\left[\dfrac{1}{(h_r + \hat{h}_c)} + \dfrac{(A_p/A_c)}{h_m} + \dfrac{\dfrac{dM}{dt} C_p \chi}{A_c h_m (h_r + \hat{h}_c)}\right]} \tag{8}$$

where $\chi \equiv (T_v - T_{ps})/(T_{cs} - T_{ps})$, the fractional approach of the gas temperature to the cavity surface temperature. To use Eq. (8), a value of χ must be obtained by computing the amount of heat transfer from the cavity surface to the volatile bubble during the period of its contact with the particle. No attempt will be made here to estimate χ. We note, however, that the third term in the denominator of Eq. (8) is quite small for the turbulent melts that are of ultimate interest in this application.

To account for the effect of the outward radial flow of volatile matter on conduction to the particle, the conduction heat transfer coefficient h_c in Eq. (5) must be replaced by a modified coefficient $\hat{h}_c$. An expression for the corrected coefficient for conduction $\hat{h}_c$ can be derived by solving the energy equation in the gas film including both conductive and convective terms:

$$\rho C_p V_r \frac{dT}{dr} = k \frac{1}{r^2} \frac{d}{dr}\left[r^2 \frac{dT}{dr}\right] \tag{9}$$

with the boundary conditions:

$$T = Tps \text{ at } r = R_p$$
$$T = Tcs \text{ at } r = R_c$$

In dimensionless form, where $L = r/R_p$, $\Theta = (T - T_{ps})/(T_{cs} - T_{ps})$, $\Phi = \rho C_p V_s R_p / k_g$, the equation is:

$$\Phi \frac{d\Theta}{dL} = \frac{d}{dL}\left[L^2 \frac{d\Theta}{dL}\right] \tag{10}$$

with the dimensionless boundary conditions:

$$\Theta = 0 \text{ at } L = 1; \ \Theta = 1 \text{ at } L = R_c/R_p.$$

The solution to Eq. (10) is

$$\Theta = C_1 \exp(-\Phi/L) + C_2 \tag{11}$$

where

$$C_1 = \frac{1}{[\exp(-\Phi R_p/R_c) - \exp(-\Phi)]} \tag{12}$$

$$C_2 = \frac{1}{1 - \exp\{-\Phi(R_p/R_c - 1)\}} \tag{13}$$

The rate of heat transfer to the particle by conduction is equal to

$$Q_c = 4\pi R_p^2 k_g \left(\frac{dT}{dR}\right)_{R_p} = 4\pi R_p k_g \left(\frac{d\Theta}{dL}\right)_{L=1} \tag{14}$$

or in the form of a conduction heat transfer coefficient $\hat{h}_c$ corrected for the outward radial flow:

$$\hat{h}_c = \frac{Q_c}{A_p (T_{cs} - T_{ps})} = \frac{k_g}{R_p}\left(\frac{d\Theta}{dL}\right)_{L=1} \tag{15}$$

$$= \frac{k_g}{R_p} \cdot \frac{\Phi}{\{e^{[\Phi(1 - R_p/R_c)]} - 1} \tag{16}$$

where $\Phi = \rho C_p V_s R_p / k_g = (1/A_p)(dM/dt) C_p R_p / k_g$ is a function of the rate of release of gaseous volatile matter and is sometimes referred to as a rate factor (Bird et al., 1960). The ratio of the heat transfer rate in the presence of the radial flow to that in a stagnant gas $\hat{h}_c/h_c$ is obtained by dividing Eqs. (16) and (1) to yield:

$$\eta = \frac{(1 - R_p/R_c)\Phi}{\{e^{[-\Phi(1 - R_p/R_c)]} - 1\}} \tag{17}$$

where η can be regarded as a correction factor for heat transfer in the presence of high rates of mass transfer. As $R_p/R_c \to 0$, Eq. (17) converges to

$$\eta = \frac{\Phi}{(e^{\Phi} - 1)} \tag{18}$$

which is the familiar expression for the correction factor for a sphere immersed in an infinite stagnant fluid (Crowe, 1979).

Equation (18) is commonly applied to heat transfer from gases to devolatilizing coal particles. Predictions of Eqs. (17) and (18) can differ greatly, as shown in Fig. 7, where η is plotted versus Φ, the rate factor, for various values of R_c/R_p.

The extent to which the radial flow of volatile matter suppresses conduction to the particle is a strong function of the rate of devolatilization. In order to investigate the importance of combined conduction and convection under the conditions of interest, a rough estimate is needed of typical devolatilization rates at 1400–1550°C. In this temperature range, Orsten and Oeters (1988) report devolatilization times of approximately 0.03 s for 100 μm particles and 0.8 s for 800 μm particles. Sampaio et al. (1991) report devolatilization times from 4 to 23 seconds for particles from 3 to 9 mm in diameter.

Using the devolatilization times above, and assuming a volatile yield of 30 percent by weight, the effects of combined conduction and convection in the gas film are calculated and the results illustrated in Fig. 8. For films of 0.1 mm thickness, devolatilization has no significant effect on the rate of conduction heat transfer to the particle. The importance of devolatilization increases as film thickness and particle size increase, suppressing conduction to the particle to 20 percent of its value in the absence of radial flow for particles of 100 mm diameter surrounded by 15 mm diameter films. Referring to Fig. 8 it is clear, however, that the correction for radial flow is important only for the range of particle sizes and film thicknesses (large particles and thick films) for which the contribution of conduction to the *global* heat transfer coefficient is not great. For this reason, the effect of radial flow on *overall*

heat transfer amounts to only a small correction for the range of parameters of interest here, although it can be quite significant in the general case.

Application to Conditions Typical of Bath-Smelting Processes

In bath-smelting processes coal particles are often charged to the furnace from above, dropping through the gas space, impacting on the surface of a foamed slag phase, and being dispersing by the turbulent flow within the slag. The location of devolatilization (in the gas space, near the slag surface, within the slag phase) influences both the thermal efficiency in the form of coal usage per ton of hot metal as well as the composition of the off-gases (Sampaio et al., 1991). The rate of heat transfer to the particles is one of the factors determining the location and rate of devolatilization and is needed as a building block in a complete model of coal behavior in such processes.

The large gas flow through the slag phase is expected to create intense turbulence, whose effect on heat transfer to the particles may not be neglected. It is possible to obtain an order-of-magnitude estimate of the convective heat transfer coefficient for this complex system by using an analogy to heat transfer in mechanically mixed systems. Equation (19) represents an engineering correlation for liquid-particle heat transfer, developed for mechanically mixed systems and based on the rate of mechanical energy input, P/M_s (Oldshue, 1983):

$$\mathrm{Nu} = 2 + 0.47 \cdot \left[\frac{d_c^{4/3} (P/M_s)^{1/3} \rho}{\mu} \right]^{0.62} \cdot \mathrm{Pr}^{0.36} \qquad (19)$$

where d_c is the diameter of the vessel. The rate at which mechanical energy is dissipated in the slag by the rising gas is equal to the rate of potential energy change:

$$(P/V_s) \approx \dot{V}_g \frac{1}{2} H_s g \rho_s / V_s = \frac{1}{2} \dot{v}_g g \rho_s (1 - \epsilon_g) \qquad (20)$$

where H_s, V_s, and ϵ_g are the height, volume, and gas or void volume fraction of the foaming slag phase, and ρ_s is the true density of the slag. A characteristic height of one-half the slag phase height has been taken since much of the gas originates within the slag and need not traverse the entire height. For a superficial gas velocity of 2 m/s and a gas volume fraction of 60 percent, the power input is calculated to be 16 kW/m^3 slag. This rate of energy dissipation is very high compared to industrial mechanically agitated systems (typically 0.3–5 kW/m^3, depending on application), indicating the presence of very intense turbulence. The slag phase in bath-smelting processes is typically subjected to additional stirring by the action of a high-velocity jet of oxygen directed onto the bath from above. The kinetic energy of the jet will also contribute to the total energy dissipation rate, but is not included in this calculation; it will be seen to have little influence on the overall coefficients. The power input per unit mass of slag, P/M_s (required for use of Eq. (19)), can be approximated by:

$$(P/M_s) = \frac{1}{2} \dot{v}_g g \qquad (21)$$

Nusselt numbers predicted by Eq. (21) range from 2.6 for cavity diameters of 0.1 mm, to 190 at 100 mm diameter, indicating a convective contribution that is always significant and is dominant for larger cavities.

Using this result, global heat transfer coefficients are computed at 1800 K using the physical properties listed in Table 1, chosen to be typical of slags in bath-smelting processes. The slag phase in bath-smelting processes is characterized by high gas holdups and is often referred to as a slag foam. When the gaseous regions are smaller than the particle dimension, it is often appropriate to treat the medium as homogeneous, having mixture-average properties. Much of the gas in slag foams, however, is believed to be present in voids larger than the particles due to the very high superficial gas velocities. In this situation the use of mixture average properties is inappropriate and should be replaced by an averaging procedure, which reflects the fact that the particles spend a fraction of their time in each of two principal environments: (1) the fully dense slag, and (2) a large gas void. We have modeled the net rate of heat transfer (and thus the effective heat transfer coefficient) as a weighted average of independent solutions for the two environments, with the weighting factors equal to the volume fraction of the two phases. The heat transfer coefficient in a large void is identical to the coefficients derived above for a gas film of infinite thickness.

Table 1 Constants used in numerical examples

C_{pm}, C_{pv}	1.4, 2.2 kJ/kg-K
k_g, k_m	0.11, 4.0 W/m-°C
ϵ_p, ϵ_c	0.8, 0.8
ρ_s, ρ_v, ρ_p	2800, 0.2, 1000 kg/m^3
T_m	1800 K
μ_m	2 Poise
$\dot{v}_g$	2 m/s

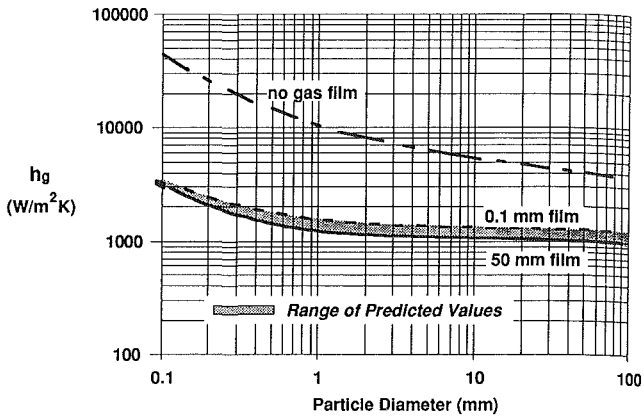

Fig. 9 Overall heat transfer coefficient in turbulent foaming slags: prediction for conditions typical of bath-smelting processes. Physical properties and process parameters used are listed in Table 1.

Figure 9 presents the predicted heat transfer coefficients in a turbulent foaming slag, calculated using the physical properties and process parameters tabulated in Table 1. Turbulent convection in the melt enhances the liquid-side heat transfer to such an extent that it no longer determines the global coefficient at high particle sizes and film thicknesses. The value of the global coefficient is quite insensitive to the size of the film, provided that the film thickness is at least 0.1 mm. As the observed films are much larger (with thicknesses on the order of the particle size or greater), it appears that quantitative empirical information on the variation of film thickness with process parameters is not required. Assuming the presence of a stable gas film with diameter greater than 0.1 mm, the range of predicted values for the melt/particle heat transfer coefficient is presented as a shaded region in Fig. 9. This prediction is felt to lie within the accuracy to which the relevant physical properties are known. Should there be film instability under some conditions, however, the resulting periodic direct contact between melt and particle would raise the heat transfer coefficients well above these predicted values.

In Fig. 10, the effect of finite temperature difference on the global coefficient is presented, where the solid and dashed lines bracked the range of predicted values assuming film thickness, $\delta > 1$ mm. The nonlinear nature of thermal radiation results in a decrease in h_g with decreasing particle surface temperature. The predictions presented in Fig. 10 are suitable for direct use

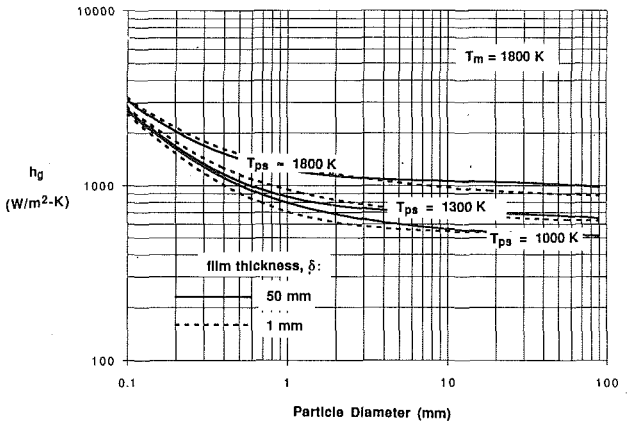

Fig. 10 Overall heat transfer coefficient in turbulent foaming slags for various particle surface temperatures. Predictions are for conditions typical of bath-smelting processes. Physical properties and process parameters used are listed in Table 1.

in comprehensive models of coal behavior in bath-smelting processes.

Conclusions

X-ray fluoroscopy provides useful images of the behavior of coal particles immersed in a molten slag phase. Volatile matter evolves rapidly from immersed coal particles, displacing the surrounding melt and producing a periodic cycle of formation, rise, and detachment of gas cavities. Based on this observation, a treatment of heat transfer from the melt to the particle is developed. In the general case, either conduction, radiation, or melt-side convection may determine the heat transfer. Under certain conditions the presence of a gas film is shown to actually *increase* the rate of melt-to-particle heat transfer. For stagnant melts with temperatures near 1800 K, conduction dominates for particle diameters less than about 1 mm; radiation dominates for diameters between about 1 and 20 mm; and melt-side convection dominates for diameters above about 20 mm.

For conditions typical of bath-smelting processes, a useful prediction of the overall coefficient is given for particle sizes 0.1 to 100 mm. The effect of the outward radial flow of volatile matter on the overall heat transfer coefficient can be neglected under these conditions. Turbulence in the melt eliminates the melt-side limitations under these conditions and radiation effectively dominates for particle diameters greater than 1 mm. For particles with diameters between 1 and 10 mm, the dominance of radiative transfer ensures that the overall rate of heat transfer is insensitive to the details of the flow pattern in the melt, and that laboratory studies of coal devolatilization will be applicable to the very different flow patterns found in larger-scale turbulent melts.

Acknowledgments

This work was supported by the Technology Maturation Program of Sandia National Laboratories.

References

AISI-DOE, 1989, Direct Steelmaking Program, Annual Technical Report.

Anthony, D. B., Howard, J. B., Hottel, H. C., and Meissner, H. P., 1974, *15th Symp. (Int.) on Comb.*, The Combustion Institute, Pittsburgh, PA, p. 1303.

Anthony, D. B., and Howard, J. B., 1976, "Coal Devolatilization and Hydrogasification," *AIChE Journal*, Vol. 22, No. 4.

Aukrust, E., 1988, "The AISI Program for Direct Steelmaking," in: *Metallurgical Processes for the Year 2000 and Beyond*, The Minerals, Metals, & Materials Society.

Badzioch, S., and Hawksley, P. G. W., 1970, *Ind. Eng. Chem.*, Vol. 9, p. 521.

Bird, R. B., Stewart, W. E., and Lightfoot, E. N., 1960, *Transport Phenomena*, Wiley, New York.

Crowe, C. T., 1979, in: *Pulverized-Coal Combustion and Gasification*, L. D. Smoot and D. T. Pratt, eds., Plenum Press, New York.

Fletcher, T. H., 1989a, *Comb. Sci. Tech.*, Vol. 63, p. 89.

Fletcher, T. H., 1989b, *Comb. Flame*, Vol. 78, p. 223.

Fletcher, T. H., Kerstein, A. R., Pugmire, R. J., and Grant, D. M., 1990, *Energy & Fuels*, Vol. 4, p. 54.

Freihaut, J. D., Proscia, W. M., and Seery, D. J., 1989, *Energy & Fuels*, Vol. 3, p. 692.

Fruehan, R. J., Ito, K., and Ozturk, B., 1988, *Iron and Steelmaker*, Nov., p. 83.

Gavalas, G. R., 1982, *Coal Science and Technology 4: Coal Pyrolysis*, L. L. Anderson, series ed., Elsevier, New York.

Gibbins-Matham, J., and Kandiyoti, R., 1988, *Energy and Fuels*, Vol. 2, p. 505.

Gokhale, A. J., and Mahalingam, R., 1985, *Fuel*, Vol. 64, p. 419.

Grant, D. M., Pugmire, R. J., Fletcher, T. H., and Kerstein, A. R., 1989, *Energy & Fuels*, Vol. 3, p. 175.

Hajaligol, M. R., Peters, W. A., and Howard, J. B., 1988, *Energy & Fuels*, Vol. 2, p. 430.

Hottel, H. C., and Sarofim, A. F., 1967, *Radiative Transfer*, McGraw-Hill, New York.

Hottel, H. C., and Howard, J. B., 1971, *New Energy Technology: Some Facts and Assessments*, p. 111.

Howard, J. B., 1991, "Fundamentals of Coal Pyrolysis and Hydropyrolysis," in: *Chemistry of Coal Utilization*, M. A. Elliott, ed., Wiley, New York, pp. 665–784.

Kalson, P. A., and Briggs, D. E., 1985, *AIChE Journal*, Vol. 31, p. 6.

Kobayashi, H., Howard, J. B., and Sarofim, A. F., 1976, *16th Symp. (Int.) on Comb.*, The Combustion Institute, Pittsburgh, PA, p. 411.

Misra, M. K., and Essenhigh, R. H., 1988, *Energy and Fuels*, Vol. 2, p. 371.

Niksa, S., and Kerstein, A. R., 1991, "Modeling the Devolatilization Behavior of Various Coals With Flashchain," presented at the Spring Meeting of the Western States Section of the Combustion Institute, Boulder, CO, Mar.

Oldshue, J. Y., 1983, *Fluid Mixing Technology*, McGraw-Hill, p. 238.

Orsten, S., and Oeters, F., 1988, *Process Technology Conference Proceedings*, p. 31.

Sampaio, R. S., 1990, Ph.D. Thesis, Department of Metallurgical Engineering and Materials Science, Carnegie Mellon University, Pittsburgh, PA.

Sampaio, R. S., Fruehan, R. J., and Ozturk, B., 1991, presented at the International Meeting of the Iron and Steel Society, Washington DC, Apr. 14–17.

Solomon, P. R., Serio, M. A., Carangelo, R. M., and Markham, J. R., 1986, *Fuel*, Vol. 65, p. 182.

Solomon, P. R., Hamblen, D. G., Carangelo, R. M., Serio, M. A., and Deshpande, G. V., 1988, *Energy & Fuels*, Vol. 2, p. 405.

Stubington, J. F., and Sumaryono, 1984, *Fuel*, Vol. 63, p. 1013.

Stubington, J. F., and Linjewile, T. M., 1989, *Fuel*, Vol. 68, p. 155.

F. Kallel

N. Galanis

Département de génie mécanique,
Université de Sherbrooke,
Sherbrooke, Québec, Canada

B. Perrin

R. Javelas

Laboratoire de génie civil,
Institut National des Sciences appliquées,
Toulouse, France

Effects of Moisture on Temperature During Drying of Consolidated Porous Materials

A one-dimensional model for simultaneous heat and moisture transfer in consolidated porous materials is solved for homogeneous brick and mortar slabs. It is validated by comparing numerically predicted moisture content and temperature evolutions with corresponding measured values. It correctly predicts that initially saturated slabs at 20°C which are suddenly placed in contact with air at 20°C and a relative humidity of 50 percent undergo a rapid transient reduction of their temperature down to 13°C due to the evaporation of excess water content. The model is used to study the effets of the initial moisture content and convection transfer coefficients on the minimum temperature of the slabs and on the duration of the transient.

Introduction

Porous materials attract and hold water molecules in quantities that depend directly on the ambient relative humidity. Even at low relative humidities a thin film of liquid is deposited on the internal surface of the material. At higher relative humidities, some of the pores can be entirely filled with liquid. The moisture, in either liquid or vapor form, migrates through the porous material as a result of molecular diffusion, gravity, capillary action, pressure, and thermal gradients. This movement contributes to other heat transfer mechanisms while eventual phase changes occurring within the material act as heat sources or sinks. Thus heat and mass transfer in porous bodies are highly coupled.

The development of an integrated heat and mass transfer model began at the end of the 1930s when Henry (1939) studied the diffusion of vapor through air within the pores of a solid (cotton), which may absorb (or desorb) and immobilize some of the diffusing substances. Later, Philip and DeVries (1957) proposed a model in which both vapor and liquid fluxes were considered and expressed in terms of the volumetric moisture content gradient, the temperature gradient, and the gravitational contribution. Luikov (1966) was one of the first to state that moisture transfer in a porous material results from gradients of moisture content, temperature, and pressure. He developed a set of equations using Darcy's law and expressing conservation of mass for both the moisture and the dry air as well as conservation of energy. Whitaker (1977) developed a formal theory of drying starting from point equations in each phase and obtained volume averaged conservation equations. Although his formulation does not differ substantially from that of Luikov, it offers, through its averaging procedure, the most substantiative justification for the continuum mechanics approach to the modeling of heat and mass transfer in porous materials. Huang (1979) proposed a model which uses one set of equations for the early (funicular) stage of drying, when liquid movement due to capillarity is dominant, and a different one for the late (pendular) stage when moisture movement is mainly occurring through vapor diffusion. Dinulescu and Eckert (1980) presented an analytical solution for the one-dimensional moisture migration under temperature and moisture content gradients assuming constant transport properties, and obtained general relations for the temperature and moisture fields in nondimensional form. Recently, Perre and Degiovanni (1990) have obtained the first numerical solution for the two-dimensional drying of an anisotropic material.

In this paper we present a transient one-dimensional model for undeformable porous materials based on the continuum mechanics approach. It is assumed that temperatures are above freezing so that water is only present in the liquid and vapor phases. The pressure of the gas phase is assumed to be uniform and constant throughout the material. Mass fluxes caused primarily by capillary forces, in the case of the liquid phase, and by diffusion, in the case of the gas, are expressed in terms of moisture content and temperature gradients. The equations resulting from the conservation principles are solved numerically for symmetrical and unsymmetrical ambient conditions using experimentally determined suction isotherms and transport properties for brick and mortar. The results are validated by comparison with measured temperature and moisture content values and the model is used to study the effect of initial moisture content and convection transfer coefficients on the temperature of such porous slabs during drying.

Modeling Heat and Mass Transfer

The situation under study is one-dimensional horizontal heat and mass transfer in a homogeneous porous slab of thickness L (Fig. 1). It is in contact with ambient air on its two sides at $x = 0$ and $x = L$. The initial temperature and moisture content distributions in the slab are known. At time $t = 0$, the ambient conditions (temperature and/or relative humidity) on one or both sides are changed. We want to determine the time evolution of the temperature and moisture profiles within the material.

The formulation of the heat and mass transfer phenomena within the porous slab is based on the assumption that the spatial variation of all dependent variables is continuous. It also incorporates the assumption of local thermal equilibrium between the three coexisting phases under consideration: the solid matrix, the pure liquid (no dissolved gases), and the gaseous mixture of vapor and dry air. Furthermore, the densities of the solid matrix and liquid phases as well as the total pressure of the gas phase are assumed to be fixed and uniform.

The conservation equations are derived by performing mass and energy balances on an elementary control volume treated as a continuum comprising all four components (solid matrix, liquid, vapor, and dry air). The resulting expressions are similar to those derived by Whitaker (1977). Thus, mass conservation

Contributed by the Heat Transfer Division for publication in the JOURNAL OF HEAT TRANSFER. Manuscript received by the Heat Transfer Division August 1991; revision received December 1992. Keywords: Conduction, Mass Transfer, Porous Media. Associate Technical Editor: R. Viskanta.

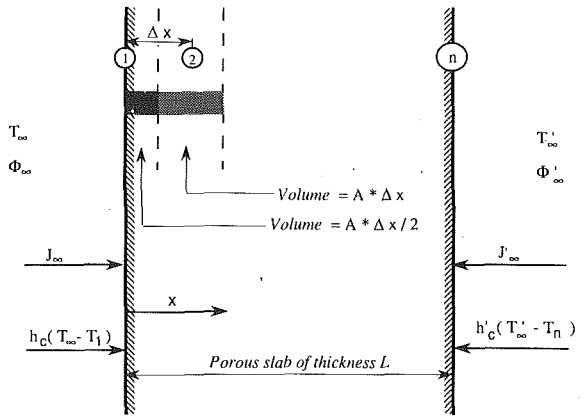

Fig. 1 Schematic representation of the slab, including coordinate system as well as heat and mass fluxes between slab and ambient air

for the three mobile components (vapor, liquid, and dry air) is expressed by the relation:

$$\frac{\partial w_j}{\partial t} = -\frac{1}{\rho_o}\frac{\partial J_j}{\partial x} \pm \frac{\dot{m}}{M_o} \tag{1}$$

A positive value of the source term indicates that vapor is condensing. Therefore, the plus sign appears in the equation for liquid, the minus in the equation for vapor, while for the dry air the source term is zero. In the case of the energy conservation, the following assumptions have been used:

- viscous dissipation is neglected
- the pressure work term for the gaseous components is also neglected, and
- the internal energy of the liquid and solid components is identical to their enthalpy, which is a linear function of temperature.

The energy equation is then written as:

$$\rho_o \frac{\partial}{\partial t}(\Sigma w_j H_j) = \frac{\partial}{\partial x}\left(k\frac{\partial T}{\partial x}\right) - \frac{\partial}{\partial x}(\Sigma J_j H_j) \tag{2}$$

The summations in this expression include the four components, i.e., the solid, dry air, water vapor, and liquid. The conduction term comprises heat transfer through all four components by an appropriate definition of an equivalent thermal conductivity (Perrin and Javelas, 1987).

The mass fluxes appearing in the conservation equations can be caused by the following driving forces:

1 Total pressure gradient causing movement of both liquid and gas. In this work, the total pressure is considered to be constant and uniform throughout the porous material, so that the corresponding mass fluxes are nonexistent. This simplification has been used by Philip and DeVries (1957), Dinulescu and Eckert (1980), Moyne and Degiovanni 1984), and others.

2 Capillary forces resulting in liquid movement. The corresponding flux is expressed using Darcy's equation, assuming the flow in the porous material is quasi-steady as do Huang (1979) and Whitaker (1977), among others. Thus

$$J_{cl} = -\rho_l \frac{K_l}{\mu_l}\frac{\partial P_c}{\partial x}$$

Since the capillary pressure P_c is a function of the total moisture content W (by virtue of the experimentally determined sorption isotherm), and since this function depends on the temperature T, the flux due to capillary forces can rewritten as

$$J_{cl} = -\rho_l \frac{K_l}{\mu_l}\left(\frac{\partial P_c}{\partial W}\frac{\partial W}{\partial x} + \frac{\partial P_c}{\partial T}\frac{\partial T}{\partial x}\right) \equiv -\rho_o\left(D'_{ml}\frac{\partial W}{\partial x} + D'_{Tl}\frac{\partial T}{\partial x}\right) \tag{3a}$$

3 Concentration gradients. The corresponding diffusion fluxes for liquid, vapor, and air are expressed using a modified version of Fick's law, which takes into account the resistance to diffusion inside the porous body:

$$J_{dj} = -\wp D_j \frac{\partial C_j}{\partial x}$$

Philip and DeVries (1957) indicate that the value $\wp$, which according to Crausse and Bacon (1985) depends on W, cannot exceed the porosity of the solid material. Since the concentrations of the liquid and the vapor are related to the total moisture content W and the temperature T, the corresponding diffusion fluxes can be rewritten as

$$J_{dw} = -\wp D_w\left(\frac{\partial C_w}{\partial W}\frac{\partial W}{\partial x} + \frac{\partial C_w}{\partial T}\frac{\partial T}{\partial x}\right) \equiv -\rho_o\left(D''_{mw}\frac{\partial W}{\partial x} + D''_{Tw}\frac{\partial T}{\partial x}\right) \tag{3b}$$

For the case of the dry air, its concentration is related to its own mass content W_a and to the temperature, so that:

$$J_{da} = -\wp D_a\left(\frac{\partial C_a}{\partial w_a}\frac{\partial w_a}{\partial x} + \frac{\partial C_a}{\partial T}\frac{\partial T}{\partial x}\right) \equiv -\rho_o\left(D_{ma}\frac{\partial w_a}{\partial x} + D_{Ta}\frac{\partial T}{\partial x}\right) \tag{3c}$$

4 Gravity. In this paper, the effect of gravity is neglected since we are considering one-dimensional horizontal problems.

By adding Eqs. (3*a*) and (3*b*) we obtain the following expression for the liquid and vapor fluxes:

Nomenclature

A = area normal to x direction (m^2)
C = concentration
c = specific heat ($J \cdot kg^{-1} \cdot K^{-1}$)
c^* = equivalent specific heat of wet material (Eq. (5*b*))
D = diffusion coefficient
D_m = isothermal mass transfer coefficient ($m^2 \cdot s^{-1}$)
D_T = nonisothermal mass transfer coefficient ($m^2 \cdot s^{-1} \cdot K^{-1}$)
H = enthalpy ($J \cdot kg^{-1}$)
h_c = convection heat transfer coefficient ($W \cdot m^{-2} \cdot K^{-1}$)
h_m = convection mass transfer coefficient ($m \cdot s^{-1}$)
J = mass flux ($kg \cdot s^{-1} m^{-2}$)
K_l = permeability of liquid through the porous solid
k = effective thermal conductivity ($W \cdot m^{-1} \cdot K^{-1}$)
L = slab thickness (m)
M = mass (kg)
$\dot{m}$ = rate of phase change ($kg \cdot s^{-1}$)
P = pressure (kPa)
T = temperature (K or °C)
t = time (s)
W = total moisture content = $w_l + w_v$
w = mass content of mobile components; $w_j = M_j/M_o$
x = spatial coordinate (m)
μ = viscosity ($N \cdot s \cdot m^{-2}$)
ρ = mass density ($kg \cdot m^{-3}$)
ϕ = relative humidity

Subscripts

a = dry air
c = defines capillary effect
i = initial conditions in the slab
j = mobile components (dry air, liquid, or vapor)
l = liquid
o = dry porous solid
s = surface conditions
v = vapor
w = water (i.e., w indicates either l or v)
∞ = ambient conditions

$$J_w = -\rho_o \left[D_{mw} \frac{\partial W}{\partial x} + D_{Tw} \frac{\partial T}{\partial x} \right] \quad (3d)$$

This formulation is identical to that used by DeVries (1958) and Luikov (1966), since both fluxes are expressed in terms of the same potentials: the total moisture content and the temperature. From the above discussion, it is evident that the two gradients of Eq. (3*d*) take into account both diffusion (which is essentially expressed by the terms proportional to D_{mv} and D_{Tv}) and capillarity (which is essentially expressed by the terms proportional to D_{ml} and D_{Tl}). As long as the values of the mass transfer coefficients D_{mj} and D_{Tj} are correctly chosen, the model will reflect the dominant nature of capillary liquid movement during the early stages of drying and the greater importance of gaseous diffusion in the later stages of drying.

The mass flux for the dry air component is given by Eq. (3*c*), since in its case diffusion is the only driving mechanism. The expression for this flux is analogous to that adopted by Whitaker (1977), who expressed the diffusive components of the mass fluxes in terms of the concentration of the corresponding species.

By replacing the expressions for the mass fluxes (Eqs. (3*c*) and (3*d*)) in the equation of continuity for each of the three mobile components we obtain:

$$\frac{\partial w_v}{\partial t} = \frac{\partial}{\partial x} \left[D_{mv} \frac{\partial W}{\partial x} + D_{Tv} \frac{\partial T}{\partial x} \right] - \frac{\dot{m}}{M_o} \quad (4a)$$

$$\frac{\partial w_l}{\partial t} = \frac{\partial}{\partial x} \left[D_{ml} \frac{\partial W}{\partial x} + D_{Tl} \frac{\partial T}{\partial x} \right] + \frac{\dot{m}}{M_o} \quad (4b)$$

$$\frac{\partial w_a}{\partial t} = \frac{\partial}{\partial x} \left[D_{ma} \frac{\partial w_a}{\partial x} + D_{Ta} \frac{\partial T}{\partial x} \right] \quad (4c)$$

The effect of the porous material on the transport of the three mobile components is quantified by the values of the mass transfer coefficients D_{mj}, D_{Tj} which, according to the previous discussion, depend on several properties of the porous material, such as its permeability to the liquid water, its porosity (which determines the maximum value of ℓ in Eqs. (3*b*) and (3*c*)), the form of its suction characteristic, etc.

For saturated materials, as well as for hygroscopic materials and high ambient relative humidities, w_l is much larger than w_v or, equivalently $W = w_l$. Summing up the relations for vapor and liquid under these conditions results in:

$$\frac{\partial w_l}{\partial t} = \frac{\partial}{\partial x} \left[(D_{mv} + D_{ml}) \frac{\partial w_l}{\partial x} + (D_{Tv} + D_{Tl}) \frac{\partial T}{\partial x} \right] \quad (5a)$$

A comparison of Eqs. (4*b*) and (5*a*) gives the following expression for the rate of vapor condensation under this condition:

$$\frac{\dot{m}}{M_o} = \frac{\partial}{\partial x} \left[D_{mv} \frac{\partial w_l}{\partial x} + D_{Tv} \frac{\partial T}{\partial x} \right] \quad (5b)$$

which, by comparison with Eq. (4*a*), indicates that the conditions $w_l >> w_v$, is equivalent to the condition of negligible vapor accumulation.

Substituting in the energy relation, Eq. (2), the gradient of the mass fluxes from Eq. (1) and neglecting the term $\Sigma J_j (\partial H_j / \partial x)$ (for an estimate of the relative importance of this term, see Appendix A) results in the following relation:

$$c^* \frac{\partial T}{\partial t} = \frac{1}{\rho_o} \frac{\partial}{\partial x} \left(k \frac{\partial T}{\partial x} \right) + \frac{\dot{m}}{M_o} (H_v - H_l) \quad (6a)$$

where

$$c^* = c_o + w_l c_l + w_v c_v \quad (6b)$$

In the last expression, the term $w_a c_{pa}$, which is small compared with the specific heat of the solid matrix, has been neglected. As a result of this elimination, the temperature field, the moisture content, and the phase change rate can be calculated from Eqs. (5*a*), (5*b*) and (6*a*), provided the various material properties are known and appropriate boundary conditions are specified. It is therefore not necessary to know the dry air transport coefficients appearing in Eq. (4*c*) in order to calculate T and w_l.

This formulation is analogous to the one by DeVries (1958) except that in his case mass fluxes and mass conservation are expressed in terms of the volumetric moisture concentration. Here, mass concentration is preferred, since this variable can be determined directly by simply weighing the dry and moist material. Furthermore, the present formulation is complete, while the one proposed by Luikov (1966) incorporates in the energy equation a semi-empirical coefficient for the phase change rate which requires additonal assumptions for its determination. A comparison between the present formulation and the model by Eckert and Faghri (1980) shows that the two expressions for liquid conservation (Eq. (5*a*) in this paper and Eq. (9) by Eckert and Faghri) have the exact same relation between the independent variables w_l and T. On the other hand, the energy equation by Eckert and Faghri does not include the term proportional to the liquid content gradient resulting from the substitution of the condensation rate from Eq. (5*b*) in Eq. (6*a*). This difference is due to the fact that Eckert and Faghri neglect the influence of the total moisture content W on the vapor mass content w_v.

Material Properties, Boundary Conditions and Solution Procedure

The materials of interest in this study are brick and mortar. Their suction characteristics as well as their heat and mass transport properties have been determined and published previously by Perrin and Javelas (1987). Mortar, with a saturation moisture content (obtained by prolonged immersion in liquid) of about 7 percent, is hygroscopic: At ambient conditions of 20°C and 90 percent relative humidity, its moisture content is about 3.5 percent (or 50 percent of its saturation value). Brick has a saturation moisture content of about 13 percent and is nonhygroscopic: At ambient conditions of 20°C and 50 percent relative humidity, its moisture content is only about 0.5 percent (or less than 4 percent of its saturation value). The results published by Perrin and Javelas (1987) show that all the transport properties (i.e., k, D_{mv}, D_{ml}, D_{Tv}, and D_{Tl}) vary considerably with W, and to a small extent with T. Thus, for example, the effective thermal conductivity for brick is $\sim 1.1\ \mathrm{W \cdot m^{-1} \cdot K^{-1}}$ for $W = 1$ percent and $\sim 2.0\ \mathrm{W \cdot m^{-1} \cdot K^{-1}}$ for $W = 13$ percent; the value of the mass transfer coefficient D_{mv} for mortar decreases monotonically from about 10^{-9} to $7 \cdot 10^{-11}$ $\mathrm{m^2 s^{-1}}$ as W increases from 1 percent to 6 percent. Furthermore, the experimentally determined dependence of the mass transport coefficients on W reflects, as expected, the relative magnitude of the different mass transfer mechanisms at different stages of the drying. Thus, for example, for mortar at values of moisture content higher than 3 percent, D_{ml} is two order of magnitudes larger than D_{mv}, which is consistent with the fact that capillary movement of the liquid dominates the early stages of drying. On the other hand, for $W < 1$ percent, D_{mv} is at least an order of magnitude larger than D_{ml}, which is consistent with the fact that vapor diffusion is more important in the late stages of drying. Thus, it is not necessary to have a different model for each drying stage, as proposed by Huang (1979). This approach, using a unique formulation for the entire drying process, has been adopted in several recent publications, such as those by Perre and Degiovanni (1990) and Ferguson and Lewis (1991).

For the present study, the effect of W on the heat and mass transfer coefficients appearing in Eqs. (5*a*), (5*b*), and (6*a*) has been taken into account using best fit polynomials to express their dependence on W while the effect of T on these coefficients has been neglected. On the other hand, the effect of

temperature on the specific heat capacities and the enthalpy of evaporation has been accounted for.

The solution can only be obtained numerically because Eqs. (5*a*), (5*b*), and (6*a*) are highly coupled and nonlinear. For this purpose, the solid slab is discretized using n nodes. The first node is on the surface at $x = 0$, the last on the surface at $x = L$. Thus $\Delta x = L/(n-1)$. Calculations have been performed with $L = 0.20$ m for both $n = 9$ and $n = 17$. For each one of the interior nodes, the following comments apply:

- the appropriate expression for M_o in Eqs. (5*b*) and (6*a*) is $\rho_o A \cdot \Delta x$;
- $\dot{m}$ represents the rate of evaporation within the volume $A \cdot \Delta x$;
- T and $W \approx w_l$ are the temperature and moisture content at the node under consideration;
- the time derivatives (left-hand side of Eqs. (5*a*) and (6*a*)) at any internal node p are evaluated by using backward differences;
- the coefficients c^* and $(H_v - H_l)$ in Eq. (6*a*) are evaluated at the node under consideration with the conditions prevailing at the beginning of each timestep;
- the spatial derivatives on the right-hand side of Eqs. (5*a*), (5*b*), and (6*a*) are expressed using the conditions prevailing at the end of each timestep, while the corresponding heat and mass transfer coefficients are evaluated at the average conditions between adjoining nodes at the beginning of each timestep.

This procedure leads to three algebraic equations for each of the $(n-2)$ internal nodes corresponding to the three conservation Eqs. (5*a*), (5*b*), and (6*a*). When the expression for the rate of phase change is replaced in the energy equation, the algebraic equations for any internal node p take the following form:

$$a_p T_{p-1} + b_p W_{p-1} + c_p T_p + d_p W_p + e_p T_{p+1} + f_p W_{p+1} = g_p \quad (7a)$$

$$a'_p T_{p-1} + b'_p W_{p-1} + c'_p T_p + d'_p W_p + e'_p T_{p+1} + f'_p W_{p+1} = g'_p \quad (7b)$$

The first expresses conservation of the water in both vapor and liquid phases, while the second expresses energy conservation. The coefficients a_p, a'_p, . . . and the constants g_p, g'_p depend on the heat and mass transport coefficients (i.e., on the hygrothermal state at the beginning of the timestep), on the timestep Δt, and on the distance Δx between the nodes. The implicit approach used in this part does not impose any stability condition on the numerical solution.

The boundary conditions, i.e., the corresponding equations for nodes 1 (at $x = 0$) and n (at $x = L$) are obtained by taking into account the mass and energy accumulation term, which for these nodes is associated with the volume $A \cdot \Delta x/2$ (see Fig. 1). This is an improvement over many other studies such as those by Huang (1979) and by Chen and Whitaker (1986), who neglect energy and mass accumulation within the volume associated with the surface nodes and therefore express the boundary conditions in a steady state form (without time derivatives). For our purposes, the conservation equations for node 1 at $x = 0$, consistent with the simplifications used in the paper and with the spatial discretization approach introduced earlier, are:

- Conservation of the vapor component states that the difference between the mass flux from the ambient air to the surface, $AJ_\infty = Ah_m(\rho_{v\infty} - \rho_{v1})$, minus the vapor flux from node 1 to node 2

$$AJ_{v\,1\to 2} = -A\rho_0\left[D_{mv}\frac{W_1 - W_2}{\Delta x} + D_{Tv}\frac{T_1 - T_2}{\Delta x}\right]$$

  is equal to the rate of phase change at the surface node (this quantity is representative of conditions in the volume $A \cdot \Delta x/2$ which in the discretization process gets replaced by conditions at node 1). This principle leads to the following equation:

$$\frac{\dot{m}}{A} = h_m(\rho_{v\infty} - \rho_{v1}) + \rho_o\left[D_{mv}\frac{W_1 - W_2}{\Delta x} + D_{Tv}\frac{T_1 - T_2}{\Delta x}\right] \quad (8a)$$

  The mass transport coefficients in this equation are evaluated at the average conditions between nodes 1 and 2.

- Conservation of H_2O (vapor and liquid phases) states that the difference between the mass flux from the ambient air to the surface, $AJ_\infty = Ah_m(\rho_{v\infty} - \rho_{v1})$, minus the water flux from node 1 to node 2

$$AJ_{1\to 2} = -A\rho_0\left[(D_{mv} + D_{ml})\frac{W_1 - W_2}{\Delta x} + (D_{Tv} + D_{Tl})\frac{T_1 - T_2}{\Delta x}\right]$$

  is equal to the rate of water accumulation in the volume associated with the surface node. This accumulation is:

$$\frac{\partial(M_l + M_v)}{\partial t} \approx \frac{\partial M_l}{\partial t} = M_o\frac{\partial W_l}{\partial t} \approx M_o\frac{\partial W}{\partial t}$$

  The mass M_o is the mass of the porous solid associated with the surface node, i.e., $M_o = \rho_o A \cdot \Delta x/2$. Combination of these expressions leads to the following equation:

$$\frac{\Delta x}{2}\frac{\partial W}{\partial t} = \frac{h_m(\rho_{v\infty} - \rho_{v1})}{\rho_o} + (D_{mv} + D_{ml})\frac{W_1 - W_2}{\Delta x} + (D_{Tv} + D_{Tl})\frac{T_1 - T_2}{\Delta x} \quad (8b)$$

  The mass transport coefficients in this equation are again evaluated at the average conditions between nodes 1 and 2.

- Conservation of energy states that convective heat addition from the ambient air to the surface, expressed by $h_c A(T_\infty - T_1)$, minus conductive heat transfer from node 1 to node 2, plus the heat generated by evaporation at node 1, is equal to the rate of energy accumulation within the volume replaced by node 1. In accordance with previous simplifications, this accumulation term is

$$(M_o c_o + M_l c_l)\frac{\partial T}{\partial t} = M_o c^*\frac{\partial T}{\partial t}$$

  where the mass of the solid corresponding to the volume replaced by node 1 is $M_o = \rho_o A \cdot \Delta x/2$. Combination of these relations leads to:

$$\rho_o\frac{\Delta x}{2}c^*\frac{\partial T}{\partial t} = h_c(T_\infty - T_1) + k\frac{T_1 - T_2}{\Delta x} + \frac{\dot{m}}{A}(H_v - H_l) \quad (8c)$$

where $\dot{m}/A$ is given by Eq. (8*a*) and the effective conductivity is evaluated at the average conditions between nodes 1 and 2. For a simple heat transfer problem (i.e., for $\dot{m} = 0$) Eq. (8*c*) reduces to the relation found in many textbooks (Holman, 1986).

The corresponding equations for node n (at $x = L$) are obtained in the same manner. All the space derivatives and the coefficients on the right-hand side of Eqs. (8*a*), (8*b*), (8*c*) are evaluated at the beginning of each successive timestep. The time derivatives on the left-hand side of Eqs. (8*b*) and (8*c*) are evaluated using forward differences. This explicit formulation of the boundary conditions results in two stability criteria which relate the permissible combinations of timestep Δt and node distance Δx. These criteria are:

$$\frac{(\Delta x)^2}{2\Delta t} \geq \frac{k}{\rho_o c^*} + \frac{h_c\Delta x}{\rho_o c^*} + \frac{D_{Tv}(H_v - H_l)}{c^*} + \frac{D_{mv}}{c^*}(H_v - H_l)\frac{W_1}{T_1} \quad (9a)$$

$$\frac{(\Delta x)^2}{2\Delta t} \geq \frac{h_m\Delta x}{\rho_o}\frac{\rho_{v1}}{W_1} + (D_{mv} + D_{ml}) + (D_{Tv} + D_{ml})\frac{T_1}{W_1} \quad (9b)$$

When dealing with simple heat transfer problems (i.e.,for $h_m = 0$ and $D_j = 0$) the second criterion is trivial ($\Delta t > 0$) while the first reduces to the well known form involving the Fourier and Biot numbers (Incropera and DeWitt, 1985). In our numerical procedure, these criteria are applied at the beginning of each timestep for both surfaces (i.e., at $x = 0$ and $x = L$) in order to evaluate the acceptable time increment Δt for the prevailing conditions. This Δt varies throughout the solution. For illustration purposes, a representative estimate of Δt is calculated in Appendix B for average conditions.

The expression of the external vapor flux in Eq. (8*a*) introduces a certain complexity, since vapor density at the surface of the porous material has not been used to express moisture movement within the material (cf. Eqs. (5*a*), (5*b*), and (6*a*). This complexity arises with most models treating convective boundary conditions. It is eliminated by replacing the vapor density at the surface by the product of the corresponding saturated vapor density (which depends only on the surface temperature T_s) and the local relative humidity (which depends, by virtue of the experimental moisture content isotherm of the material, on T_s and w_{ls}). Additional information necessary to complete the model includes:

- the convective coefficient of heat transfer, which can be calculated from appropriate correlations, and
- the convective mass transfer coefficient, which must be determined experimentally or estimated from the heat and mass transfer analogy; for natural convection on a vertical surface, the latter gives $h_m \approx 10^{-3}\, h_c$ (see Appendix B).

The formulation is now complete. The system of algebraic Eqs. (7*a*), (7*b*) can be solved from any fixed initial conditions, $w_l(x, 0)$, $T(x, 0)$, $\dot{m}(x, 0)$ for given ambient conditions $T_\infty(t)$, $\phi_\infty(t)$ using the boundary conditions expressed by Eqs. (8*a*), (8*b*), (8*c*) and the specified properties. The calculation algorithm is described in Appendix C. Certain calculations were performed with two different grids to ensure that numerical results were independent of the number of nodes and in each case the timestep was evaluated from the stability criteria expressed by Eqs. (9*a*), (9*b*).

Model Validation and Analysis of Results

The numerical solution has been obtained for several different conditions for brick and mortar slabs of thickness $L = 20$ cm. In the results presented here, the slab is considered to be initially in hydrothermal equilibrium and at time $t = 0$ a sudden change of one or both of the ambient properties T_∞, ϕ_∞ is imposed on one or both surfaces of the slab. The results presented include comparisons with measured values and illustrate the influence of mass transfer and phase changes on the temperature profiles, and their evolution, within the slab. Calculations have also been performed using Luikov's model by setting the semi-empirical coefficient for the phase change rate equal to $D_{mv}/(D_{ml} + D_{mv})$; in all cases, the results calculated with the two models were essentially identical.

Unsymmetrical Conditions for Both T_∞ and ϕ_∞. Perrin (1985) has measured the temperature and moisture content evolution for slabs of uniform initial conditions $T_i = 20°C$, $W_i = 0.07$ which were suddenly put in contact with cold humid air at $T_\infty = 5°C$, $\phi_\infty = 80$ percent on one side ($x = 0$) and with warm, dry air at $T_\infty = 23°C$, $\phi_\infty = 45$ percent on the other side ($x = L$). Calculations were performed for this case to validate the model. The average convective coefficients corresponding to the experimental conditions (Perrin, 1985) were used for this purpose. They are:

- $h_c = 40$ W/m^{2}K, $h_m = 0.00095$ m/s on the cold side ($x = 0$)
- $h_c = 20$ W/m^{2}K, $h_m = 0.00095$ m/s on the warm side ($x = L$).

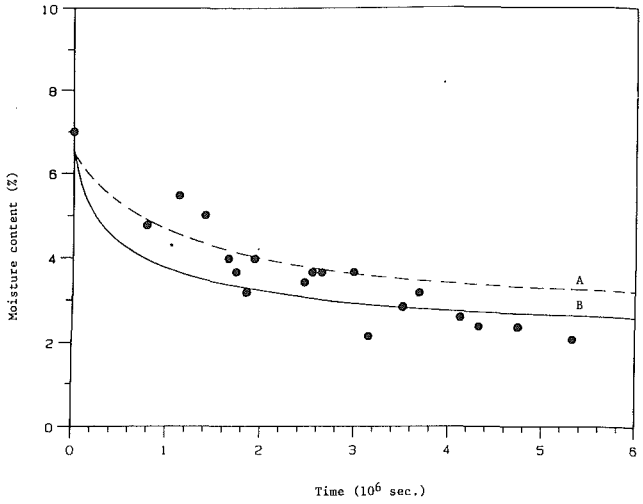

Fig. 2 Evolution of moisture content near the warm surface ($x = 0.875\ L$) of the mortar slab

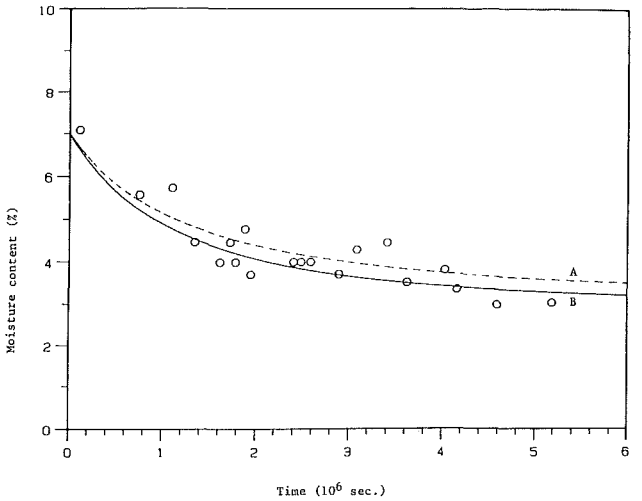

Fig. 3 Evolution of moisture content near the cold surface ($x = 0.125\ L$) of the mortar slab

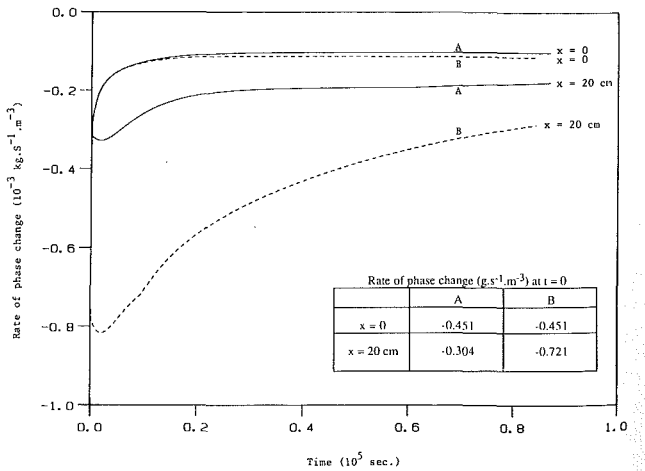

Fig. 4 Evolution of phase change rate at the surfaces of the mortar slab

The results calculated with these parameters are given by the curves identified by the letter *A* in Figs. 2, 3, and 4.

Figures 2 and 3 compare the measured and calculated evolutions of moisture content near the warm ($x = 0.875\ L$)

and cold ($x = 0.125\ L$) surfaces of the mortar slab. Similar results were obtained for brick slabs. In view of the fact than the uncertainty in measured values of $D_{ml} + D_{mv}$ and $D_{Tl} + D_{Tv}$ are as high as 60 percent and 115 percent, respectively (Perrin, 1985), the agreement between calculated and measured values is respectable. In fact, the agreement between curves A and the measured values is better on the cold side (Fig. 3) than on the warm side (Fig. 2). It was therefore decided to evaluate the effect of changing the convective coefficients on the warm side ($x = L$) and to thus test the sensitivity of the results on the corresponding values of h_c, h_m. To achieve this objective, results were recalculated using the same values for h_c, h_m on the cold side ($x = 0$) and the following new values for the warm side ($x = L$):

- $h_c = 45\ W/m^2K$ and $h_m = 0.00225$ m/s.

The calculated results corresponding to this new set of convective coefficients are identified by the letter B in Figs. 2, 3, and 4. A comparison of curves A and B with the measured values in Figs. 2 and 3, indicates that the effect on W of more than doubling these convective coefficients is smaller than the spread ΔW of successive experimental points. Thus, although results calculated with set A are somewhat closer to measured values at the beginning of the transient while later on the calculated results with set B are better and it would have been easy to recalculate the moisture profiles using temperature and/or moisture dependent convective coefficients, this exercise would not contribute any further understanding to the physics of the phenomena under study. We furthermore conclude that the average values of h_c, h_m, determined by Perrin (set A) as representative of the experimental conditions must have considerable uncertainty since these coefficients have relatively little influence on the time evolution of the moisture content.

By comparing the results of Figs. 2 and 3, it is noted that the moisture content difference between the two faces of the slab is, for the present conditions, quite small. Mass fluxes due to the moisture content gradient are therefore expected to be small. Furthermore, since D_T is several orders of magnitudes smaller than D_m for both materials under consideration, the total moisture flux is expected to be small (cf. Eq. (3d)). This explains why, as indicated by Figs. 2 and 3, the time required to achieve the equilibrium moisture content is very long (approximately 4×10^6 seconds or 46 days). On the other hand, temperature evolutions not reproduced here show that equilibrium temperatures are achieved after only five to six hours.

The results of Figs. 2 and 3 further indicate that, as expected, higher values of the convective coefficients result in a quicker drying of the material. This is achieved by an important increase in the evaporation rate on the warm side: Indeed, as shown in Fig. 4, the evaporation rate at $x = L$ obtained with set B is approximately 2.5 times higher than the rate calculated with set A during the first hour of the transient. At $x = 0$, the evaporation rate is essentially the same for both sets A and B since the convective transfer coefficients on the cold side are the same. Within the slab ($0 < x < L$) the evaporation rate is uniformly zero for the specified conditions.

It is interesting to note in Fig. 4 that the evaporation rate calculated with set A is initially greater on the cold side ($x = 0$). This is due to the fact that at $t = 0$ the evaporation rate is equal to J_∞ only (cf. Eq. (8a)) and that the corresponding density difference between the ambience and the surface is larger on the cold side. For $t > 0$ the term J_∞ in Eq. (8a) remains dominant since, as noted earlier, the gradient of moisture content is small and D_{Tv} is very small. However, since the temperature of the slab responds very quickly to the ambient conditions while the moisture content of the surfaces (and, therefore, the corresponding relative humidity) is very slow to adjust, the density difference in Eq. (8a) follows the evolution of the temperature: Thus, after approximately 300 seconds the evaporation rate from the warm surface becomes more important than that from the cold side.

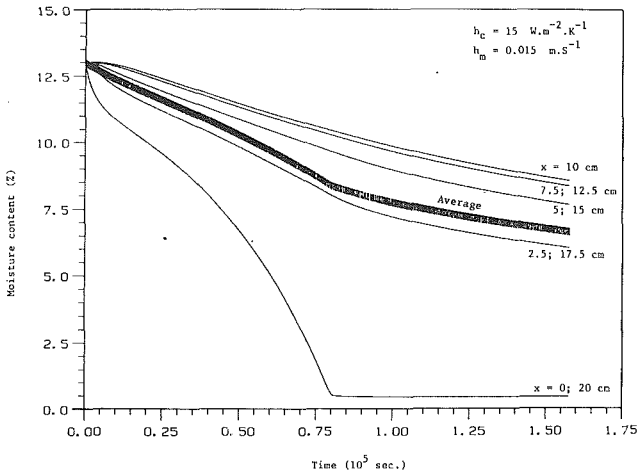

Fig. 5 Evolution of moisture content for the brick slab with constant symmetrical ambient conditions

Symmetrical Conditions With $T_\infty = T_i$. In this part we study the cooling of a slab due to drying. We consider brick slabs with a high initial moisture content ($W_i \approx 13$ percent) at $T_i \approx 20°C$. At time $t = 0$ they are placed in contact with ambient air at $T \approx 20°C$ and $\phi \approx 50$ percent. Experiments were carried out for this part by using a cylindrical brick sample having a length of 0.20 m and a diameter of 0.06 m; its cylindrical surface was sealed using an epoxy sealant and thermally insulated. It was instrumented using ten thermocouples (six on the axis at $x = 0.0$, 0.025, 0.075, 0.10,0.15, and 0.20 m, and four on the cylindrical surface at $x = 0.025$, 0.075, 0.10 and 0.15 m). The weight of the sample was measured after drying in an oven for 48 hours and after immersion in 20°C water for another 48 hours. The sample was then placed in a test chamber in which temperature was maintained at (20 ± 0.5)°C and relative humidity at (0.5 ± 0.05) percent. Temperature readings were then registered for two to three days. At the end of this period the sample was weighed once again. For the conditions in the test chamber the heat transfer convective coefficient on the exposed vertical circular surfaces was estimated to be $h_c \approx 15\ W/m^2\ K$ and therefore, by applying the similarity principle from Appendix B, $h_m \approx 0.015$ m/s. The model was used to calculate the hydrothermal transient within the brick slab for these conditions.

Figure 5 shows the evolution of calculated moisture content for brick slabs. As expected, the spatial distribution is symmetrical about the slab's midplane. At the two surfaces, equilibrium is reached after approximately 22 hours (0.8×10^5 seconds). The slope changes of the curve representing the moisture content evolution on the surfaces occur at the conditions for which the experimental equilibrium moisture content isotherm of brick exhibits similar slope changes. Everywhere within the slab, the moisture content tends towards the same asymptotic value, since the ambient conditions are symmetrical. This asymptotic value is the equilibrium moisture content for brick in contact with air at $T_\infty = 20°C$, $\phi_\infty = 50$ percent. However, the drying takes a very long time, since moisture movement within the slab is extremely slow, as indicated by the fact that after 44 hours (1.58×10^5 seconds) the moisture content at the centerplane is still closer to the initial than to the final condition. Weighing of the slab after 43.8 hours yielded a moisture content of 8.4 percent which is somewhat higher than the corresponding calculated average value shown on Fig. 5. This discrepancy is attributed to the difficulty of correctly estimating the convective transfer coefficients prevailing during the experiments.

Figure 6 indicates that phase changes are significant only at the surfaces, where liquid evaporates at an initially high but rapidly decreasing rate. The fact that the evaporation rate

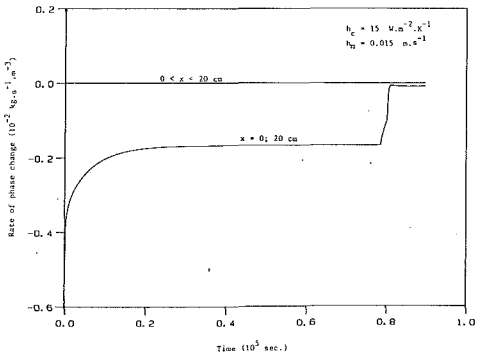

Fig. 6 Evolution of phase change rate for the brick slab with constant symmetrical ambient conditions

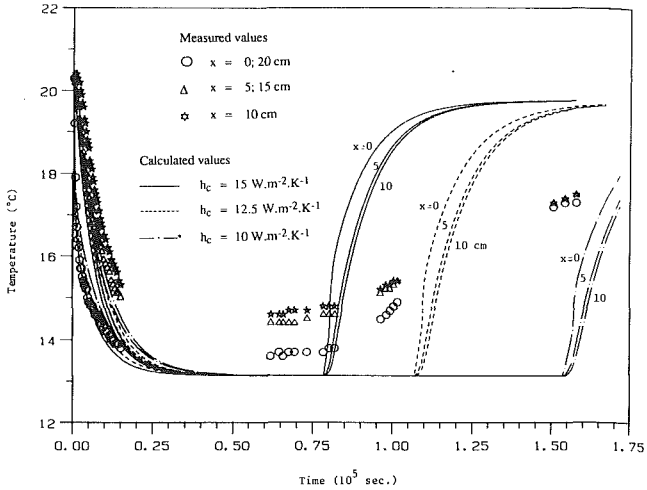

Fig. 7 Comparison of calculated and measured temperature evolutions for the brick slab

becomes negligible from the exact moment that the corresponding liquid content reaches its equilibrium value (cf. Fig. 4) should be particularly noted.

Figure 7 presents the calculated and measured evolutions of temperature within the brick slab. Calculated results are presented for three different sets of values for the convective coefficient h_c, h_m. They show that although the ambient temperature is fixed at 20°C, the slab temperature decreases to approximately 13.2°C. This cooling down of the slab is due to the evaporation process which acts as a heat sink. Since evaporation takes place only at the surfaces, the surface temperature decreases faster. It subsequently drives down the temperature within the slab by conduction. Throughout this cooling-down period, the temperature within the slab increases with distance from the surface and is essentially independent of the value assigned to the convective heat transfer coefficient. As time increases, the evaporation rate decreases and heat convection from the ambient air to the surface increases. An equilibrium is eventually achieved between convective heat gains and heat supplied for evaporation and the temperature of the slab becomes uniform and stays constant for a period which depends entirely on the value of the convective transfer coefficient: Lower values of h_c correspond to longer periods of constant uniform slab temperatures. During the next and final phase the slab starts heating up: The calculated temperature of the surface is now higher than that of interior points which are heated by conduction. As $t \rightarrow \infty$, the temperature throughout the slab tends asymptotically to the equilibrium value of 20°C. This phenomenological description is supported by both calculated and measured values, in particular during the cooling-down phase for which quantitative agreement is also quite good. The measured and calculated results are, however, different on two counts:

- During the constant temperature phase, measured surface temperatures are approximately 0.5°C higher than the calculated value, while at the centerplane this difference is almost 1.5°C. In fact, measured temperatures at the centerplane remain higher than those of the surface until approximately $t = 1.5 \times 10^5$ seconds, contrary to the predictions of the model. This discrepancy is likely due to two-dimensional effects occurring in the experimental setup.
- According to the measurements, the warming of the slab proceeds at a much slower rate than that predicted by the model. Thus, the calculated results indicate that the temperature increases by about 6°C within approximately 8.5 hours while the measured temperature increase is less than 4°C in about 20 hours. This discrepancy is likely due to the fact that calculations were performed with constant values for the convective coefficients while it is expected that h_c must vary as $T_s - T_\infty$ and h_m as $\rho_{vs} - \rho_{v\infty}$. This is an area where further research is needed but, in view of the results of Fig. 7, it is believed that variable convective coefficients will not affect significantly the results for the cooling down phase and will definitely slow down the rate of temperature increase. The agreement between numerical and experimental values is therefore expected to improve by using variable convective coefficients.

Discussion of Drying Process With $T_\infty = T_i$. The minimum temperature of approximately 13.2°C attained during the evaporative cooling shown in Fig. 7 is very close to the wet bulb temperature for the prevailing ambient conditions ($T_\infty = 20$°C, $\phi_\infty = 50$ percent). This observation indicates that during the first two phases (cooling-down and constant uniform temperature) and for the conditions of the figure, the phenomena taking place are similar to those occurring during the adiabatic saturation process in which an air-vapor mixture is in contact with a pool of water. This analogy is substantiated by the observation (cf. Fig. 5) that during these two initial phases the liquid content at the surface exceeds the equilibrium value corresponding to the ambient conditions: This excess liquid corresponds to the water in the pool of the adiabatic saturation process. During these two phases, the mass transfer from the slab to the ambiance is not hindered by the presence of the solid matrix containing the water and the drying rate, measured by the slope of the average liquid content curve in Fig. 5, is fairly high: It is determined mainly by the value of h_m. But from the moment the surface liquid content reaches its equilibrium condition and the corresponding evaporation rate becomes negligible (cf. Fig. 6), the drying rate decreases noticeably. From that moment on, the mass transfer from the slab to the ambiance is controlled by the water flux reaching the surface from within the slab: During this phase, therefore, it is determined mainly by the values of D_T and D_m.

Another point of interest regarding this evaporative cooling process can be deduced from the above description of the phenomenon. It regards the influence of the initial excess moisture content (i.e., the difference between W_i and the equilibrium value corresponding to the ambient conditions) on the duration of the constant uniform temperature phase. For fixed convective transfer coefficients and fixed ambient conditions, a decrease of W_i will shorten the time necessary for the surface to attain the equilibrium moisture content. Since from then on the evaporation rate becomes negligible and the surface temperature starts increasing, the duration of the first two phases of the temperature transient must decrease under these conditions. In fact, we can anticipate that if W_i is quite close to the equilibrium moisture content corresponding to the fixed ambient conditions, the constant uniform temperature phase

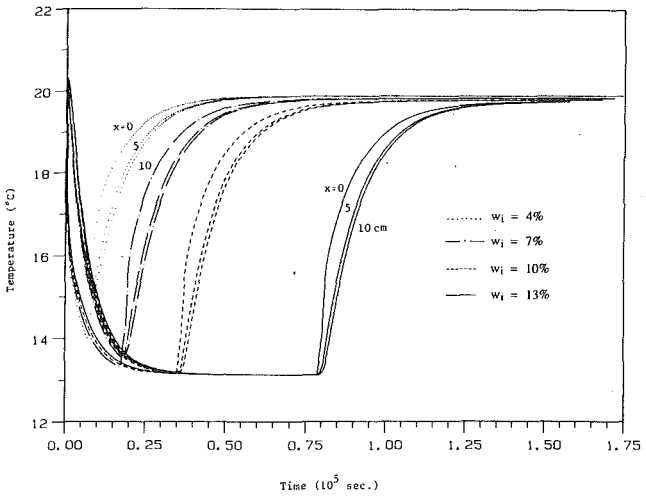

Fig. 8 Effect of initial moisture content on the temperature evolution of the brick slab

may not occur at all. In other words, the equilibrium moisture content may be reached at the surface before the temperature reaches its minimum value. Figure 8 illustrates this situation. For $W_i = 13$ percent, the calculated duration of the constant uniform temperature phase is approximately 13.9 hours (0.5×10^5 seconds), while for $W_i = 10$ percent it is only 1.4 hours (0.05×10^5 seconds). For $W_i = 7$ percent and $W_i = 4$ percent the constant uniform temperature phase does not exist: The corresponding minimum temperatures at the surface and at the centerplane are, respectively, 13.4/13.6°C and 13.9/15.5°C.

Conclusion

The simple, two-variable model for coupled heat and moisture transfer in consolidated porous materials is a fairly accurate tool for predicting transient temperature and water content profiles. The agreement between calculated and measured results provides an indirect validation of the heat and mass transfer coefficients for brick and mortar published earlier (Perrin and Javelas, 1987). The model has been used to study the effect of initial water content and convection transfer coefficients on the evaporative cooling of wet homogeneous slabs initially in thermal equilibrium with the ambient atmosphere: For relatively large differences between the initial and equilibrium moisture content, the slab undergoes a rapid temperature decrease followed by a period of constant uniform temperature (which is approximately equal to the wet bulb temperature corresponding to the ambient conditions) and finally returns to the atmospheric temperature. This behavior cannot be predicted by addressing the thermal problem alone, which does not allow for temperature variations within the slab.

Acknowledgments

This study was carried out with the financial assistance of the Natural Sciences and Engineering Research Council of Canada.

References

Anderson, D. A., Tannehill, J. C., and Fletcher, R. H., 1984, *Computational Fluid Mechanics and Heat Transfer*, McGraw-Hill, New York.

Chen, S., and Whitaker, S., 1986, "Moisture Distribution During the Constant Rate Drying Period for Unconsolidated Porous Media: Failure of the Diffusion Theory," *Drying '86*.

Crausse, P., and Bacon, G., 1985, "Experimental and Theoretical Study of Simultaneous Heat and Moisture Transfer in a Fibrous Insulant," *J. of Thermal Insulation*, Vol. 9, pp. 46-67.

Degiovanni, A., and Moyne, C., 1987, "Conductivité Thermique des Matériaux Poreux Humides: Évaluation Théorique et Possibilité de Mesure," *Int. J. Heat Mass Transfer*, pp. 2225-2245.

DeVries, D. A., 1958, "Simultaneous Transfer of Heat and Moisture in Porous Materials," *Trans. Am. Geophys. Union*, Vol. 39, pp. 909-916.

Dinulescu, H. A., and Eckert, E. R. G., 1980, "Analysis of the One Dimensional Moisture Migration Caused by Temperature Gradients in Porous Medium," *Int. J. Heat Mass Transfer*, Vol. 23, pp. 1069-1077.

Eckert, E. R. G., and Faghri, M., 1980, "A General Analysis of Moisture Migration Caused by Temperature Differences in an Unsaturated Porous Medium," *Int. J. Heat Mass Transfer*, Vol. 22, pp. 1613-1623.

Ferguson, W. J., and Lewis, R. W., 1991, "A Comparison of a Fully Non-linear and Partially Non-linear Heat and Mass Transfer Analysis of a Timber Drying Problem," *Numerical Methods in Thermal Problems*, Vol. II, Part 2, pp. 973-984, *Proc. Seventh Int. Conf.*, Stanford, CA.

Henry, P. S. H., 1939, "Diffusion in Absorbing Media," *Proc. Royal Soc.*, Vol. 171A, pp. 215-241.

Holman, J. P., 1986, *Heat Transfer*, 6th ed., McGraw-Hill, New York.

Huang, C. L. C., 1979, "Multi-phase Moisture Transfer in Porous Media Subjected to Temperature Gradient," *Int. J. Heat Mass Transfer*, Vol. 22, pp. 1295-1307.

Incropera, F. P., and DeWitt, D. P., 1985, *Introduction to Heat Transfer*, Wiley, New York, NY.

Luikov, A. V., 1966, *Heat and Mass Transfer in Capillary Porous Bodies*, Pergamon Press, NY.

Moyne, C., and Degiovanni, A., 1984, "Importance of Gas Phase Momentum Equation in Drying Above the Boiling Point of Water," *Fourth Int. Drying Symp.*, Kyoto, Japan.

Perre, P., and Degiovanni, A., 1990, "Simulation par Volumes Finis des Transferts Couplés en Milieux Poreux Anisotropes: Séchage du Bois á Basse et á Haute Temperature," *Int. J. Heat Mass Transfer*, Vol. 33, No. 11, pp. 2463-2478.

Perrin, B., 1985, "Etude des Transferts Couplés de Chaleur et de Masse Dans des Matériaux Poreux Consolidés Non Saturés Utilisés en Génie Civil," Thèse d'Etat, Univ. Paul Sabatier, Toulouse, France.

Perrin, B., and Javelas, R., 1987, "Transferts Couplés de Chaleur et de Masse Dans des Matériaux Consolidés Utilisés en Génie Civil," *Int. J. Heat Mass Transfer*, Vol. 30, No. 2, pp. 297-309.

Philip, J., and DeVries, D. A., 1957, "Moisture Movement in Porous Materials Under Temperature Gradients," *Trans. Am. Geoph. Union*, Vol. 18, pp. 222-232.

Whitaker, S., 1977, "Simultaneous Heat, Mass and Momentum Transfer in Porous Media: A Theory of Drying," *Advances in Heat Transfer*, J. P. Hartnett and T. F. Irvine, eds., Academic Press, Vol. 13, pp. 119-203.

APPENDIX A

Concerning the elimination of the term $\Sigma J_j (\partial H_j/\partial x)$ in the energy equation, it should first be pointed out that Luikov (1966, p. 239) and recently Degiovanni and Moyne (1987) have provided evidence that they are small compared to the conductive or evaporation terms. The following argument illustrates this fact by considering a steady-state one-dimensional situation of a slab submitted to conditions T_1, W_1 at $x = 0$ and T_2, W_2 at $x = L$.

Equation (5*b*), expressing mass conservation for the vapor, with Eq. (3*d*) becomes

$$\frac{\dot{m}}{M_o}\,dx = d\left(-\frac{J_v}{\rho_o}\right)$$

which integrated from $x = 0$ to $x = L$, gives

$$\int_{x=o}^{x=L} \frac{\dot{m}}{M_o}\,dx = \frac{J_{v,x=0} - J_{v,x=L}}{\rho_o} \qquad (a)$$

Equation (5*a*), expressing mass conservation for the liquid and vapor phases, with Eq. (3*d*) leads, when integrated from $x = 0$ to $x = L$, to the following condition:

$$J_v + J_l = \text{const} \equiv J_{H_2O} \qquad (b)$$

Finally, Eq. (3*c*), expressing mass conservation for the dry air, when integrated from $x = 0$ to $x = L$ leads to:

$$J_{a,x} = J_{a,x=0} = \text{const} \equiv J_a \qquad (c)$$

The complete form of the energy equation, obtained by combining Eq. (2) with Eq. (1), for the steady state under consideration is

$$\frac{\partial}{\partial x}\left(k\frac{\partial T}{\partial x}\right)+\rho_o\frac{\dot{m}}{M_o}(H_v-H_l)-\Sigma J_i c_j\frac{\partial T}{\partial x}=0$$

The last term, which Luikov calls the convective term, will be shown to be small compared to the two others. Integrating this relation from $x = 0$ to $x = L$ by considering that $H_v - H_l$ varies very little with x (which is valid for small temperature gradients) and using Eq. (*a*), we obtain

$$k\frac{dT}{dx}\Bigg|_{x=0}^{x=L}+(H_v-H_l)(J_{v,x=0}-J_{v,x=L})$$

$$-\Sigma J_j c_j T\Big|_{x=0}^{x=L}+\int_{x=0}^{x=L}Tc_j dJ_j=0$$

or

$$k\frac{dT}{dx}\Bigg|_{x=0}^{x=L}-J_{H_2O}c_l(T_2-T_1)-J_a c_a(T_2-T_1)$$

$$+J_{v\,x=0}[(H_v-H_l)+(c_v-c_l)(T_1-\overline{T})]$$

$$-J_{v\,x=L}[(H_v-H_l)+(c_v-c_l)(T_2-\overline{T})]$$

where $\overline{T}$ is a temperature between T_1 and T_2 such that

$$\int_{x=0}^{x=L}T(c_l dJ_l+c_v dJ_v+c_a dJ_a)=\overline{T}(c_l J_l+c_v J_v+c_a J_a)\Big|_{x=0}^{x=L}$$

Since $H_v - H_l \approx 2450$ kJ/kg, $c_l \approx 4.18$ kJ/kg, $c_v \approx 1.87$ kJ/kg and the temperature differences for the applications under consideration are $\sim 10°C$, it follows that the terms $|(c_v - c_l)(T_1 - \overline{T})|$ and $|(c_v - c_l)(T_2 - \overline{T})|$ are less than about 1 percent of the heat of evaporation $(H_v - H_l)$. They can therefore be neglected. With this simplification, the integrated energy equation becomes

$$k\frac{dT}{dx}\Bigg|_{x=0}^{x=L}-J_{H_2O}c_l(T_2-T_1)-J_a c_a(T_2-T_1)$$

$$+\left(J_{v\,x=0}-J_{v\,x=L}\right)(H_v-H_l)=0$$

The last term corresponds to the source term in Eq. (6*a*). The two terms proportional to the water and dry air fluxes are, according to Eq. (*c*) and Eq. (3*d*)

$$J_{H_2O}=-\rho_o(D_{mv}+D_{ml})\frac{dW}{dx}\Bigg|_{x=0}-\rho_o(D_{Tv}+D_{Tl})\frac{dT}{dx}\Bigg|_{x=0}$$

$$J_a=-\rho_o D_{ma}\frac{dW}{dx}\Bigg|_{x=0}-\rho_o D_{Ta}\frac{dT}{dx}\Bigg|_{x=0}$$

Since for brick $k \approx 1.5$ $Wm^{-1}K^{-1}$, $\rho_o \approx 1900$ kg/m^3, $D_{Tl} \approx 10^{-12}$ m^2 s^{-1} K^{-1} and $D_{Tv} = D_{Ta} \approx 10^{-12}$ m^2 s^{-1} K^{-1} while $c_l = 4.18$ kJ/kg and $T_2 - T_1 \approx 20°C$ it follows that the term $\rho_o(D_{Tv} + D_{Tl} + D_{Ta})\, c_l\, (T_2 - T_1)\, dT/dx|_{x=0}$ is less than 0.1 percent of $k\, dT/dx|_{x=0}$. The same is true for mortar for which $k \approx 2.2$ Wm^{-1} Wm^{-1} K^{-1}, $\rho_0 \approx 2050$ kg/m^3, $D_{Tl} \approx 10^{13}$ m^2 s^{-1} K^{-1} and $D_{Tv} = D_{Ta} \approx 0.5 - 10^{-12}$ m^2 s^{-1} K^{-1}.

Finally we compare the conductive term at $x = L$ with the convective terms proportional to the moisture content gradient at $x = 0$. This comparison is delicate since it involves different driving forces evaluated at different positions. However, an order of magnitude approximation for the problems under consideration gives an indication of the relative importance of these terms. Thus, the conductive term can be estimated as follows for brick:

$$k\frac{dT}{dx}\Bigg|_{x=L}\approx k\frac{|T_2-T_1|}{L}\approx 1.5\frac{\mathrm{W}}{\mathrm{mK}}\frac{20\mathrm{K}}{0.2\ \mathrm{m}}=150\ \mathrm{Wm^{-2}}$$

The corresponding value for mortar is 220 Wm^{-2}. Similarly, to estimate the convective term for brick for which $D_{ml} \approx 10^{-8}$ m^2 s^{-1}, $D_{mv} = D_{ma} = 10^{-12}$ m^2 s^{-1} we note that $|W_2 - W_1| \le |W_{max} - W_{min}| \approx 0.12$. Therefore

$$\rho_o(\Sigma D_{mj})c_l|T_2-T_1|\frac{dW}{dx}\Bigg|_{x=0}$$

$$\approx\rho_o(\Sigma D_{mj})c_l|T_2-T_1|\frac{W_2-W_1}{L}$$

$$\le 2000\frac{\mathrm{kg}}{\mathrm{m^3}}\,10^{-8}\frac{\mathrm{m^2}}{\mathrm{s}}\,4180\frac{\mathrm{J}}{\mathrm{kgK}}\,20\mathrm{K}\,\frac{0.12}{0.2\ \mathrm{m}}\approx 0.9\frac{\mathrm{W}}{\mathrm{m^2}}$$

For the mortar since $D_{ml} = 10^{-8}$ m^2 s^{-1}, $D_{mv} = D_{ma} = 10^{10}$ m^2 s^{-1} and $|W_{max} - W_{min}| \approx 0.07$, the corresponding convective term is ≈ 0.6 W/m^2. Thus for both materials, this convective term is less than 0.5 percent of the conductive term. We have therefore demonstrated that for the materials, slab dimensions and temperature differences under consideration the term $\Sigma J_j(\partial H_j/\partial x)$ is negligible compared to the conductive and source terms.

APPENDIX B

For the calculation of a representative estimate of the timestep satisfying the two stability criteria (Eqs. (9*a*) and (9*b*)), we assume a slab thickness $L = 20$ cm and use 9 nodes. Thus $\Delta x = L/(n - 1) = 0.025$.

Assuming heat and mass transfer from the vertical surfaces of the slab are by natural convection, we have

$$\mathrm{Nu}=C(\mathrm{Gr}\cdot\mathrm{Pr})^{0.3}$$

and by analogy

$$\mathrm{Sh}=C(\mathrm{Gr}\cdot\mathrm{Sc})^{0.3}$$

Taking the ratio of these expressions we find

$$\frac{h_c}{h_m}=\left(\frac{k_a}{D_{va}}\right)^{0.7}\cdot(\rho_a c_{pa})^{0.7}$$

and using properties for air at 20°C we obtain $h_c \approx 1000\, h_m$. For the present illustration, we use $h_c = 10$ W/m^{2}K and, therefore, $h_m = 0.01$ m/s.

For brick with $\rho_o = 1900$ kg/m^3, $W = 0.1$, $T = 293$ K, $k = 1.8$ W/mK, $c_o = 920$ J/kgK, $H_v - H_l = 2450$ kJ/kg, $D_{ml} = 10^{-8}$ m^2/s, $D_{Tl} = D_{Tv} = 10^{-12}$ m^2/sK and $D_{mv} = 10^{-12}$ m^2/s, we obtain from the first criterion $\Delta t \le 387$ s and from the second $\Delta t \le 8254$ s.

For mortar with $\rho_o = 2050$ kg/m^3, $W = 0.05$, $T = 293$ K, $k = 2.2$ W/mK, $c_o = 935$ j/kgK, $H_v - H_l = 2450$ kJ/kg, $D_{ml} = 10^{-8}$ m^2/s, $D_{Tl} = 10^{-13}$ m^2/sK, $D_{Tv} = 0.5 \cdot 10^{-12}$ m^2/sK and $D_{mv} = 10^{-10}$ m^2/s, we obtain from the first criterion $\Delta t \le 299$ s and from the second $\Delta t \le 5388$ s.

APPENDIX C

The calculation algorithm involves the following steps:

1 Choose number of nodes n, calculate $\Delta x = L/(n - 1)$.

2 Starting with the initial conditions within the material evaluate the transport coefficients k, D_{mv}, D_{Tv}, D_{ml}, D_{Tl} from the corresponding experimental results at average conditions between adjoining nodes.

3 Evaluate the four limiting values of Δt by applying the two stability conditions (Eqs. (9*a*), (9*b*)) at each of the two surface nodes (at $x = 0$ and $x = L$). The timestep actually used for calculations is, for security, 90 percent of the smallest of these four limiting values. At this step it is necessary to introduce appropriate values of the convective transfer coefficients h_c and h_m which can be either constant for the entire simulation period, or time dependent through appropriate cor-

relations such as those identified in Appendix B for natural convection.

4 Using the experimental dependence of the capillary pressure P_c on the moisture constant W and Kelvin's relation between P_c and relative humidity $\phi = \rho_v/\rho_{sat}$, where $\rho_{sat} = f(T)$, evaluate the initial vapor density ρ_v at each surface and the corresponding mass flux from Eq. (8*a*).

5 Using the conservation equations for the surface nodes and the imposed ambient conditions T_∞, ϕ_∞, T'_∞, ϕ'_∞ (which do not correspond to the initial conditions within the material and drive the phenomena under investigation) evaluate the initial rate of phase change from Eq. (8*a*), the new temperature from Eq. (8*c*), and the new moisture content from Eq. (8*b*), for each of the two surface nodes (1 and n).

6 The new surface conditions (temperature and moisture content at nodes 1 and n) are then substituted in the algebraic equations expressing mass and energy conservation (Eqs. (7*a*) and (7*b*)) for nodes 2 and $n - 1$. The resulting equations together with the corresponding expressions for nodes 3 to ($n - 2$) constitute a system of $2(n - 2)$ linear algebraic equations of the form:

$$
\begin{bmatrix}
c_2 & d_2 & e_2 & f_2 & & & & & & & & & & \\
c'_2 & d'_2 & e'_2 & f'_2 & & & & & & & & & & \\
a_3 & b_3 & c_3 & d_3 & e_3 & f_3 & & & & & & & & \\
a'_3 & b'_3 & c'_3 & d'_3 & e'_3 & f'_3 & & & & & & & & \\
 & & & a_4 & b_4 & c_4 & d_4 & e_4 & f_4 & & & & & \\
 & & & a'_4 & b'_4 & c'_4 & d'_4 & e'_4 & f'_4 & & & & & \\
 & & & & & & & & & & & & & \\
 & & & & & & & a_{n-2} & b_{n-2} & c_{n-2} & d_{n-2} & e_{n-2} & f_{n-2} \\
 & & & & & & & a'_{n-2} & b'_{n-2} & c'_{n-2} & d'_{n-2} & e'_{n-2} & f'_{n-2} \\
 & & & & & & & & & a_{n-1} & b_{n-1} & c_{n-1} & d_{n-1} \\
 & & & & & & & & & a'_{n-1} & b'_{n-1} & c'_{n-1} & d'_{n-1}
\end{bmatrix}
\times
\begin{bmatrix}
T_2^1 \\ W_2^1 \\ T_3^1 \\ W_3^1 \\ T_4^1 \\ W_4^1 \\ \cdots \\ T_{N-2}^1 \\ W_{N-2}^1 \\ T_{N-1}^1 \\ W_{N-1}^1
\end{bmatrix}
=
\begin{bmatrix}
g_2 - a_2\, T_1^1 - b_2 W_1^1 \\
g'_2 - a'_2\, T_1^1 - b'_2 W_1^1 \\
g_3 \\ g'_3 \\ g_4 \\ g'_4 \\ \cdots \\ g_{n-2} \\ g'_{n-2} \\
g_{n-1} - e_{n-1}\, T_n^1 - f_{n-1} W_n^1 \\
g'_{n-1} - e'_{n-1}\, T_n^1 - f'_{n-1} W_n^1
\end{bmatrix}
$$

All the missing terms in the matrix of coefficients are zero. This system is solved using the subroutine for solving block tridiagonal systems proposed by Anderson et al. (1984, pp. 552–557).

7 The resulting new values of temperature and moisture content for each of the internal nodes is then used to evaluate the corresponding rate of phase change from Eq. (5*b*).

8 The new values of T and W at each of the n nodes constitute the initial conditions for the next timestep.

Steps 2 through 8 are repeated as many times as deemed necessary.

Steam Injection Into a Slow Water Flow Through Porous Media

M. Chung[1]

I. Catton

Mechanical, Aerospace, and Nuclear Engineering Department, University of California, Los Angeles, Los Angeles, CA 90024-1597

Steam injection into a slow water flow (Darcy flow) was studied analytically for steady-state conditions. The continuity, momentum, and energy equations for both water flow and steam flow were solved subject to interface conditions. The governing equations were transformed using stream function and velocity potential coordinates to simplify the calculation domain. The resulting energy equation was converted to a simultaneous ordinary differential equation by an integral method. The unknown steam–water interface shape and location were determined through an optimization process. Temperature distribution on the water side, local condensation rate along the interface, water and steam flow fields and pressure distribution were found numerically. Comparison with experimental measurements showed that the average steam zone size could be fairly well predicted only when dispersion effects were incorporated into a modified thermal conductivity model.

Introduction

Steam injection is a process wherein live steam is injected into subcooled water by an external driving force. In such a process, steam condenses by direct contact with the subcooled water, usually resulting in rapid oscillations induced by continuous formation and violent collapse of bubbles at the tip of the injecting nozzle; see Lee and Chung (1979). If steam injection occurs in porous media, the physical process changes dramatically. The porous media limit the heat transfer away from the steam-cold water interface causing the condensation process to be relatively slow. A steam bubble develops around the injector that either grows or becomes steady with time depending on heat removal at the interface and pressure buildup. Chung and Catton (1990) have shown theoretically that if there is no forced water flow against the expanding steam bubble, the interface will grow without limit until temperature and pressure are eventually uniform. In some steam injection applications such as thermal recovery of oil, the advance of the interface and pressure buildup on the liquid side are the prime concern. The interface advance is controlled mainly by two parameters: condensation rate at the interface and pressure balance across the interface.

The steam–water interface is well defined and stays quiescent for low water flow rates, low steam injection rates, and low permeability media. Depending on the injection rate, water flow rate, and water subcooling, steam bubbles close to ellipses in shape develop around the injection pipe. The size and shape are strongly dependent on these parameters, see Fig. 1. The bubble floats upward when gravity effects are stronger than flow resistance. As the water flow rate increases, the bubble shifts downward, changing its shape dramatically.

The transport processes are mutually coupled through interface mass and energy conservation and do not permit easy solutions. The main difficulty for analysis is that the interface location is not known and must be found as a part of the solution. Heat and mass transfer problems of similar types can be found in many applications. Siegel (1983) formulated a Cauchy problem to analyze phase change problems in castings. He used a transformation from the physical domain to the stream function and velocity potential domain to determine the unknown interface location analytically. Yortsos and Gavalas (1982) solved the heat transfer problem ahead of the moving boundary for steam injection into porous media in conjunction with thermal oil recovery. A similar transformation to that used by Siegel is employed in this study to solve the energy equation. As in Yortsos's solution, the steam–water interface will be treated as a line instead of a two-phase band.

The solution developed in this work will reveal the temperature field, local condensation rate along the interface, steam pressure, water pressure, water flow field, and steam flow field along with the shape and size of the bubble. The bubble size and location are of engineering interest because they will determine whether or not a bubble can be contained in a given size of channel for specified operating conditions. Among many potential applications, the results may be useful for geothermal problems, chemical plants, underground environmental decontamination, and nuclear safety assessment. The most important contribution of this work is the clear demonstration that dispersion must be included for all porous media characteristics and at all steam and water flow conditions.

Governing Equations

Assumptions. The following assumptions have been made to idealize the solution procedure:

1 Processes are steady state.
2 Darcy's law is valid for water flow.

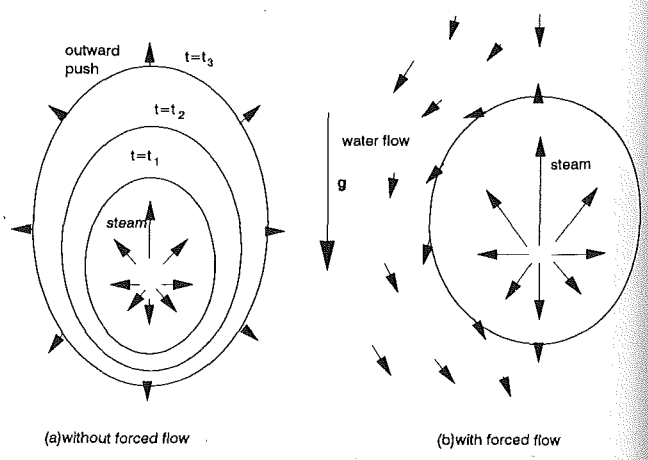

Fig. 1 Typical bubbles in porous media

[1]Present Address: Korea Institute of Energy Resources, Daedok Science Town, Daejon, Korea.

Contributed by the Heat Transfer Division and presented at the ASME Winter Annual Meeting, Atlanta, Georgia, December 1-6, 1991. Manuscript received by the Heat Transfer Division March 1992; revision received September 1992. Keywords: Condensation, Moving Boundaries, Porous Media. Associate Technical Editor: T. W. Simon.

3 The steam–water interface is a line whose thickness is negligible.
4 Steam temperature is uniform.
5 Dispersion effects at the interface can be represented by a modified thermal conductivity.

The first assumption is valid below values of the steam injection rate where oscillatory bubble interface behavior is limited. The second assumption, see Bear (1988), is valid when the Reynolds number based on the particle diameter and superficial velocity is less than some critical value, ranging from 1 to 10. The third assumption is based on experimental observation. The fourth assumption avoids the use of a steam energy equation. The fifth allows the effective thermal conductivity, see Georgiadis (1987), to be expressed as

$$\kappa_e = \kappa_o + B\rho_l C_{pl} \frac{d_p}{1-\epsilon} |\mathbf{u}_l| \tag{1}$$

The stagnant media conductivity is obtained from the parallel model

$$\kappa_o = \epsilon\kappa_l + (1-\epsilon)\kappa_s \tag{2}$$

Georgiadis (1987) suggested that the constant B in Eq. (1) be taken as 0.43. Based on these assumptions, the equations in the following paragraphs result.

Water Flow. The governing equations for single-phase flow through porous media are conservation of mass, momentum (Darcy's Law), and energy,

$$\nabla \cdot \mathbf{u}_l = 0 \tag{3}$$

$$\nabla P_l + \frac{\mu_l}{k}\mathbf{u}_l - \rho_l \mathbf{g} = 0 \tag{4}$$

$$u_l \frac{\partial T_l}{\partial x} + v_l \frac{\partial T_l}{\partial y} = \nabla \cdot \alpha_l \nabla T_l \tag{5}$$

Steam Flow. Similar equations for steam flow are the conservation of mass and momentum equations,

$$\nabla \cdot \mathbf{u}_s = 0 \tag{6}$$

$$\nabla P_s = -\left[\frac{\mu_s}{k} + \frac{\rho_s}{m}|\mathbf{u}_s|\right]\mathbf{u}_s + \rho_s \mathbf{g} \tag{7}$$

where

$$k = \frac{\epsilon^3 d_p^2}{150(1-\epsilon)^2}, \quad m = \frac{\epsilon^2 d_p}{1.75(1-\epsilon)} \tag{8}$$

Interface Conditions. At the interface, mass and energy conservation require

$$\rho_l \mathbf{u}_l \cdot \mathbf{n} = \rho_s \mathbf{u}_s \cdot \mathbf{n} \tag{9}$$

$$-\kappa_l \nabla T_l \cdot \mathbf{n} = -\kappa_s \nabla T_s \cdot \mathbf{n} + \rho_l h_{fg} \mathbf{u}_l \cdot \mathbf{n} \tag{10}$$

and temperature and pressure matching yield

$$T_l = T_s = T_{\text{sat}} \tag{11}$$

$$P_s = P_l + P_c(\sigma, d_p) \tag{12}$$

Solution of the Energy Equation

Coordinate Transform. A coordinate transformation from the physical domain into the stream function and velocity potential domain is made to simplify the calculational domain and decouple the momentum equation from the energy equation. A velocity potential is defined by

$$\phi \equiv -\frac{k}{\mu_l}(\rho_l g y + P_l) \tag{13}$$

and the stream function, ψ, is taken to have its usual meaning, then the continuity equation and the momentum equation are combined to yield two Laplace equations

$$\nabla^2 \phi = 0, \quad \nabla^2 \psi = 0 \tag{14}$$

Since ϕ, ψ are analytic functions of x, y, the x, y are conjugate harmonic functions of ϕ, ψ and the momentum equation can be expressed as two Laplace equations,

$$\frac{\partial^2 x}{\partial \phi^2} + \frac{\partial^2 x}{\partial \psi^2} = 0, \quad \frac{\partial^2 y}{\partial \phi^2} + \frac{\partial^2 y}{\partial \psi^2} = 0 \tag{15}$$

Transformation of the energy equation and boundary conditions is accomplished using the Cauchy–Riemann conditions and chain rules. The result is scaled with

$$T^* = \frac{T_l - T_i}{T_{\text{sat}} - T_i}, \quad \alpha^* = \frac{\alpha_l}{\Delta\psi}, \quad \phi^* = \frac{\phi}{\Delta\psi}, \quad \psi^* = \frac{\psi}{\Delta\psi} \tag{16}$$

where $\Delta\psi$ is half the volume flow rate of the *condensed steam* per unit depth of the channel,

$$\Delta\psi = \frac{1}{2}\frac{\dot{m}_s}{t\rho_l} \tag{17}$$

The transformed energy equation becomes

$$\frac{\partial T^*}{\partial \phi^*} = \frac{\partial}{\partial \phi^*}\alpha^* \frac{\partial T^*}{\partial \phi^*} + \frac{\partial}{\partial \psi^*}\alpha^* \frac{\partial T^*}{\partial \psi^*} \tag{18}$$

Nomenclature

a_o = average steam bubble diameter, m
B = dispersion parameter, Eq. (1)
b = injector displacement from center of bubble
C_p = specific heat, J/kg K
d_p = particle diameter, m
e = ellipticity defined by Eq. (77)
g = acceleration due to gravity, m^2/s
h_g = steam enthalpy, J/kg
h_{fg} = latent heat, J/kg
K = parameter defined by Eq. (76)
k = permeability, m^2
m = bed passability, m
$\dot{m}$ = mass flow rate, kg/s
$\mathbf{n}$ = outward normal unit vector
P = perimeter of steam zone, m
P = pressure, Pa
ΔP_s = $P_1 - P_o$, Pa
Re = Reynolds number
Ste = Stefan number
t = channel thickness, m
T = water temperature, K
ΔT_w = water subcooling, K
ΔT_s = steam superheating, K
u, v = velocity, m/s
U = inlet water superficial velocity, m/s
V_b = outlet water superficial velocity, m/s
W = channel width, m
α = thermal diffusivity, m^2/s
γ = parameter defined by Eq. (78)
δ = thermal boundary layer thickness
ϵ = porosity
κ = thermal conductivity, W/m K
μ = viscosity, Ns/m^2
ν = kinematic viscosity, m^2/s
ρ = density, kg/m^3
ϕ = velocity potential, m^2/s
ψ = stream function, m^2/s
σ = surface tension
$\Delta\psi$ = half the condensed steam flow rate, m^2/s

Superscripts

— = effective
* = nondimensional quantities

Subscripts

c = capillary
D = dispersion
g = vapor
i = inlet
l, f = liquid phase
o = outlet
sat = saturation
s = steam
w = water

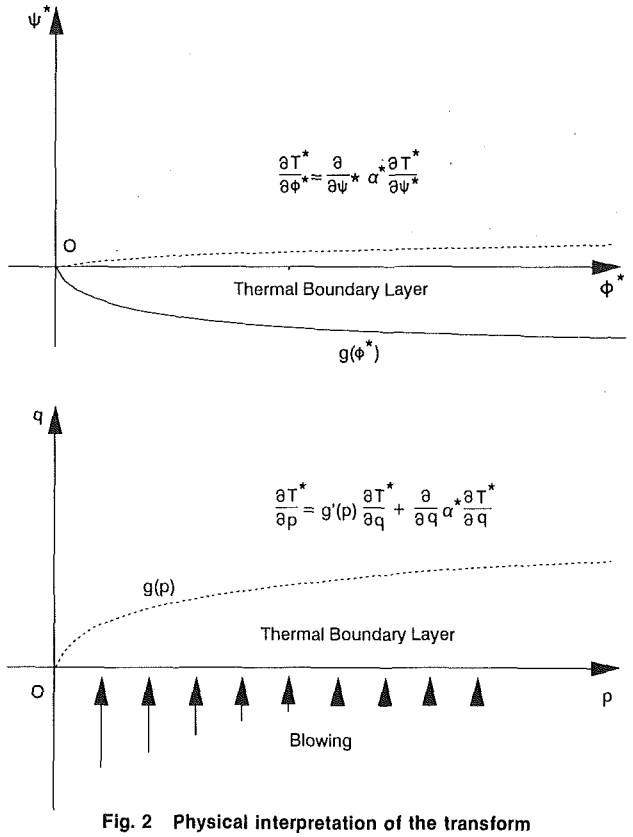

Fig. 2 Physical interpretation of the transform

This equation is valid except where $u_i^2 + v_i^2 = 0$.

The normalized interface temperature condition is

$$T^* = 1 \tag{19}$$

and the interface energy conservation expression becomes

$$\frac{\partial T^*}{\partial \phi^*} - \frac{1}{g'(\phi^*)} \frac{\partial T^*}{\partial \psi^*} = -\frac{\rho_l C_{pl} \Delta\psi}{\kappa_l} \frac{h_{fg}}{C_{pl}(T_{\text{sat}} - T_i)} = -\frac{1}{\text{Ste}\alpha^*} \tag{20}$$

where Ste is the Stefan number defined by

$$\text{Ste} \equiv \frac{C_{pl}(T_{\text{sat}} - T_i)}{h_{fg}} \tag{21}$$

and

$$g'(\phi) \equiv \left.\frac{d\psi}{d\phi}\right|_i \tag{22}$$

The above equation and boundary conditions are a Cauchy problem with two boundary conditions imposed at an unknown boundary location.

Approximate Solution. The transformed energy equation is simplified by noting that the streamwise diffusion term is very small compared to the cross-stream diffusion term. This was shown by Chung (1990) using an order of magnitude analysis similar to what is done for boundary layer flow. Dropping the streamwise diffusion term yields a parabolic partial differential equation. The interface is then transformed to a straight line with

$$p(\phi^*, \psi^*) = \phi^*$$
$$q(\phi^*, \psi^*) = \psi^* - g(\phi^*) \tag{23}$$

yielding

$$\frac{\partial T^*}{\partial p} = \frac{\partial}{\partial q} \alpha^* \frac{\partial T^*}{\partial q} \tag{24}$$

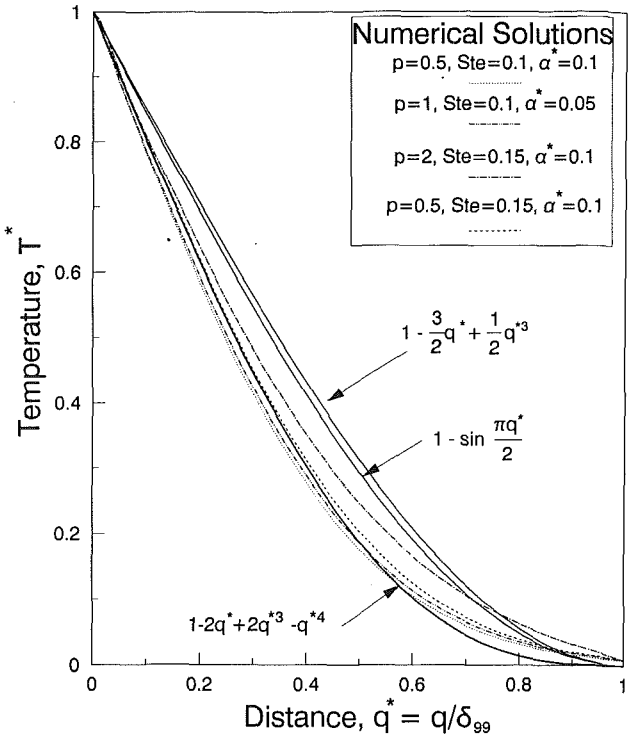

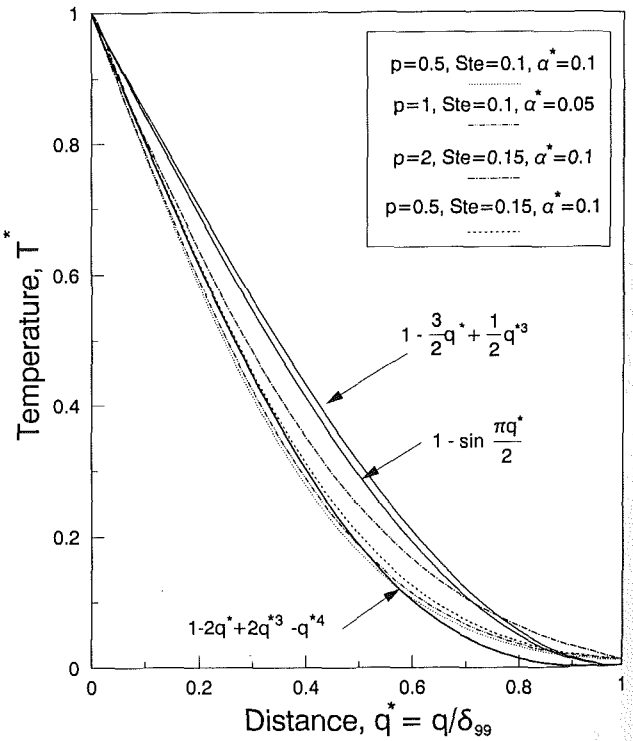

Fig. 3 Temperature solution found by numerical solution

subject to the boundary condition

$$T^*(p, 0) = 1 \tag{25}$$

Since $\partial T^*/\partial p = 0$ along the interface, conservation of energy along the interface becomes

$$-\left.\frac{\partial T^*}{\partial q}\right|_{q=0} = \frac{1}{\alpha^* \text{Ste}} \frac{g'(p)}{1 + g'(p)^2} \tag{26}$$

The original problem has been transformed to forced convection over a flat plate with blowing (see Fig. 2) and slip at the wall. Figure 3 shows a temperature distribution for constant

properties found by use of a Crank–Nicholson scheme. The similarity in temperature profiles for various locations and thermal diffusivities enables one to use a profile method. An integrodifferential equation derived by integrating Eq.(25) from the wall to infinity using Leibnitz's rule is

$$\frac{d}{dp}\int_0^{\delta(p)} T^*(p, q)dq = -g'(p) - \alpha^* \left.\frac{\partial T^*}{\partial q}\right|_{q=0} \tag{27}$$

with Eq. (26) as an auxiliary condition resulting from the boundary condition and $\partial(p)$ is the thermal boundary layer thickness. A temperature profile that compared well with numerical results and satisfied $T^*(p, 0) = 1$ was chosen from the several shown in Fig. 3 (see Eq. (31)).

Evaluating the integral and the partial derivative at the wall yields a system of first-order ordinary differential equations,

$$\frac{d\delta}{dp} = \frac{10}{3}\left(-g' + \frac{2\alpha}{\delta}\right) \tag{28}$$

$$\frac{g'(p)}{1+g'(p)^2} = \frac{2\alpha^* \mathrm{Ste}}{\delta} \tag{29}$$

with initial conditions

$$\delta(0) = 0$$

$$g(0) = 0, \quad 0 \le g(p) \le 1 \tag{30}$$

These equations are easily solved by conventional numerical schemes such as a fourth-order Runge–Kutta method.

Downstream Temperature. Temperature distribution downstream of the steam bubble can be found by solving Eq. (24) subject to the following initial and boundary conditions:

$$T^*(0, \psi^*) = 1 - 2\left(\frac{\psi^*}{\delta_c}\right) + 2\left(\frac{\psi^*}{\delta_c}\right)^2 - \left(\frac{\psi^*}{\delta_c}\right)^4 \tag{31}$$

$$\frac{\partial T^*(\phi^*, 0)}{\partial \psi^*} = 0 \tag{32}$$

$$T^*(\phi^*, \pm\infty) = 0 \tag{33}$$

where δ_c is the thermal boundary layer thickness at the bottom (downstream end) of the bubble.

Solution of the Momentum Equations

The transformed energy equation is uncoupled from the momentum equation except for dispersion effects. The solution to the energy equation yields the temperature distribution on the water side and local heat flux along the steam-water interface in terms of the stream function–velocity potential coordinates. The mapping of the calculation domain (ϕ, ψ) into the physical domain (x, y) is still unknown. The transformed momentum equations and steam momentum equation must be solved to obtain the geometric mapping. Rescaling the independent variables with

$$\tilde{\phi} = \frac{\phi}{\Delta\phi/2} - 1, \quad \tilde{\psi} = \frac{\psi}{\Delta\phi/2}, \quad \tilde{U} = \frac{U}{\Delta\phi/2} \tag{34}$$

yields the momentum equations,

$$\frac{\partial^2 x}{\partial\tilde{\phi}^2} + \frac{\partial^2 x}{\partial\tilde{\psi}^2} = 0, \quad \frac{\partial^2 y}{\partial\tilde{\phi}^2} + \frac{\partial^2 y}{\partial\tilde{\psi}^2} = 0 \tag{35}$$

To help with boundary conditions, the solution is decomposed into two parts

$$x \equiv x_p + x_o, \quad y \equiv y_p + y_o \tag{36}$$

where x_o, y_o are the solution for water flow without a steam bubble,

$$x_o = \frac{1}{\tilde{U}}\tilde{\psi}, \quad y_o = -\frac{1}{\tilde{U}}\tilde{\phi} \tag{37}$$

and the x_p, y_p are the differences caused by the steam bubble. Usually, $\Delta\phi \gg \Delta\psi$, so that the interface can be idealized as a stream line as far as the momentum equations are concerned.

Formal Solution. Since x and y are related through the Cauchy–Riemann conditions, it is sufficient to solve just one partial differential equation. y is found to be more convenient. The formal solution given by separation of variables is

$$y_p = \int_0^\infty [A(k)\cos k\tilde{\phi} + B(k)\sin k\tilde{\phi}]\cosh k(\tilde{\psi} - \tilde{\psi}_0)dk \tag{38}$$

Taking the partial derivative

$$\left.\frac{\partial y_p}{\partial\tilde{\psi}}\right|_{\tilde{\psi}=0} = \int_0^\infty A(k)\cos k\tilde{\phi} + B(k)\sin k\tilde{\phi}]\sinh k\tilde{\psi}_0 dk \tag{39}$$

and imposing the boundary condition at the bottom with

$$\Phi(\tilde{\phi}) \equiv \left.\frac{\partial y_p}{\partial\tilde{\psi}}\right|_{\tilde{\psi}=0}, \quad -1 < \tilde{\phi} < 1 \tag{40}$$

yields the solution

$$y_p = -\frac{1}{\pi}\int_{-1}^{+1}\Phi(t)\int_0^\infty \frac{\cosh k(\tilde{\psi} - \tilde{\psi}_0)}{k\sinh k\tilde{\psi}_0}\cos k(\tilde{\phi} - t)dkdt \tag{41}$$

Differentiating with respect to $\tilde{\phi}$ to remove the singularity yields

$$\frac{\partial y_p}{\partial\tilde{\phi}} = -\frac{1}{2\tilde{\psi}_0}\int_{-1}^{+1}\frac{\sinh\{\pi(t-\tilde{\phi})/\tilde{\psi}_0\}\Phi(t)dt}{\cosh\{\pi(t-\tilde{\phi})/\tilde{\psi}_0\} + \cos\{\pi(\tilde{\psi} - \tilde{\psi}_0)/\tilde{\psi}_0\}} \tag{42}$$

Imposing the remaining condition

$$y = y_i(\tilde{\phi}) \Rightarrow \frac{\partial y_p}{\partial\tilde{\phi}} = \frac{dy_i(\tilde{\phi})}{d\tilde{\phi}} + \frac{1}{U} \quad \text{as} \quad \tilde{\psi} \to 0^+ \tag{43}$$

yields an integral equation

$$\frac{dy_i}{d\tilde{\phi}} + \frac{1}{U} = -\frac{1}{2\tilde{\psi}_0}\int_{-1}^{+1}\frac{\sinh\{\pi(t-\tilde{\phi})/\tilde{\psi}_0\}\Phi(t)dt}{\cosh\{\pi(t-\tilde{\phi})/\tilde{\psi}_0\} - 1} \tag{44}$$

The leading behavior of the kernel is

$$\frac{\sinh\{\pi(t-\tilde{\phi})/\tilde{\psi}_0\}}{\cosh\{\pi(t-\tilde{\phi})/\tilde{\psi}_0\} - 1} \to \frac{2\tilde{\psi}_0}{\pi}\frac{1}{t-\tilde{\phi}} \quad \text{as} \quad t - \tilde{\phi} \to 0 \tag{45}$$

Isolating the singular behavior by adding and subtracting the leading term yields a *singular integral equation of the first kind*

$$\frac{1}{\pi}\int_{-1}^{+1}\frac{\Phi(t)dt}{t-\tilde{\phi}} + \int_{-1}^{+1}K(\tilde{\phi}, t)\Phi(t)dt = h(\tilde{\phi}), \quad -1 < \tilde{\phi} < 1 \tag{46}$$

where

$$K(\tilde{\phi}, t) = \frac{\pi}{2\tilde{\psi}_0}\frac{\sinh\{\pi(t-\tilde{\phi})/\tilde{\psi}_0\}}{\cosh\{\pi(t-\tilde{\phi})/\tilde{\psi}_0\} - 1} - \frac{1}{t-\tilde{\phi}} \tag{47}$$

and

$$h(\tilde{\phi}) = -\frac{dy_i}{d\tilde{\phi}} - \frac{1}{U} \tag{48}$$

A constraint condition required for the singular integral equations can be found through the Cauchy–Riemann condition

$$\Phi(t) \equiv \frac{\partial y_p}{\partial\tilde{\psi}} = \frac{\partial x_p}{\partial\tilde{\phi}} = \left.\frac{dx}{d\tilde{\phi}}\right|_{\text{int}} \tag{49}$$

Physically, the bubble must be closed at the bottom, i.e.,

$$\int_{-1}^{+1}\Phi(t)dt = \int_{-1}^{+1}\frac{dx}{d\tilde{\phi}}d\tilde{\phi} = x|_{-1}^{+1} = 0 \tag{50}$$

Once Φ has been found by solving the integral equation, x can be evaluated through a similar process. Starting from the formal solution, imposing the boundary condition at the bot-

tom, using the Cauchy-Riemann condition and the definition of Φ, yields x_p,

$$x_p(\tilde{\phi}, \tilde{\psi}) = \frac{1}{\pi} \int_{-1}^{+1} \tan^{-1}\left[\tanh \frac{\pi(t-\tilde{\phi})}{2\tilde{\psi}_o} \tan \frac{\pi(\tilde{\psi}-\tilde{\psi}_o)}{2\tilde{\psi}_o} \right] \Phi(t)\, dt \tag{51}$$

with the interface location given by

$$x_i(t) = \int_{-1}^{t} \frac{\partial x_p}{\partial \tilde{\phi}}\, d\xi = \int_{-1}^{t} \frac{\partial y_p}{\partial \tilde{\psi}}\, d\xi = \int_{-1}^{t} \Phi(\xi) d\xi \tag{52}$$

$$x(\tilde{\phi}, \tilde{\psi}) = x_o + x_p = \frac{\tilde{\psi}}{U}$$

$$+ \frac{1}{\pi} \int_{-1}^{+1} \tan^{-1}\left[\tanh \frac{\partial(t-\tilde{\phi})}{2\tilde{\psi}_o} \tan \frac{\partial(\tilde{\psi}-\tilde{\psi}_o)}{2\tilde{\psi}_o} \right] \Phi(t)\, dt \tag{53}$$

The solution of the momentum equation is summarized by

$$y(\tilde{\phi}, \tilde{\psi}) = y_o + y_p = -\frac{\tilde{\phi}}{U}$$

$$- \frac{1}{2\pi} \int_{-1}^{+1} \ln\left[\cosh \frac{\pi(t-\tilde{\phi})}{\tilde{\psi}_o} + \cos \frac{\pi\tilde{\psi}}{\tilde{\psi}_o} \right] \Phi(t)\, dt \tag{54}$$

Steam Flow. The steam momentum and continuity equations are now combined to yield a second-order elliptic partial differential equation. Defining

$$P_s^* \equiv \frac{P_s + \rho_s g(y_o - y) - P_o}{\Delta P_s}, \quad r^* = \frac{r}{a} \tag{55}$$

where ΔP_s is the reference pressure drop corresponding to the pressure difference between the injector and bubble head. Taking the divergence of the steam momentum equation, Eq. (7), and combining with the continuity equation, Eq. (6), yields

$$\nabla^{*2} P_s^* - W \nabla^* V \cdot \nabla^* P_s^* = 0 \tag{56}$$

where

$$V = |\mathbf{u}_s|, \quad W = \frac{\rho_s}{m} \frac{1}{\frac{\mu_s}{k} + \frac{\rho_s}{m} V} \tag{57}$$

Here ∇^* denotes the gradient in terms of the nondimensional coordinates. The calculational domain for steam flow is not regular because the steam bubble can take any shape and the injector location is not fixed. An algebraic grid generation scheme was used to overcome the difficulties of irregular geometry.

The following pair of coordinate transforms:

$$\xi(r, \theta) \equiv \frac{r - r_0}{r_i(\theta) - r_0} \nrightarrow r(\xi, \eta) = (r_i(\eta) - r_0)\xi + r_0 \tag{58}$$

$$\eta(r, \theta) \equiv \theta \nrightarrow \theta(\xi, \eta) = \eta \tag{59}$$

are used to transform the steam momentum equation to

$$\left\{ \left(\frac{\partial \xi}{\partial r^*} \right)^2 + \frac{1}{r^{*2}} \left(\frac{\partial \xi}{\partial \theta} \right)^2 \right\} \frac{\partial^2 P_s^*}{\partial \xi^2} + \frac{2}{r^{*2}} \frac{\partial \xi}{\partial \theta} \frac{\partial^2 P_s^*}{\partial \xi \partial \eta}$$

$$+ \frac{1}{r^{*2}} \frac{\partial^2 P_s^*}{\partial \eta^2} + \left\{ \left(\frac{1}{r^*} - W \frac{\partial V}{\partial r^*} \right) \frac{\partial \xi}{\partial r^*} + \frac{1}{r^{*2}} \frac{\partial^2 \xi}{\partial \theta^2} \right.$$

$$\left. - \frac{W}{r^{*2}} \frac{\partial V}{\partial \theta} \frac{\partial \xi}{\partial \theta} \right\} \frac{\partial P_s^*}{\partial \xi} - \frac{W}{r^{*2}} \frac{\partial V}{\partial \theta} \frac{\partial P_s^*}{\partial \eta} = 0 \tag{60}$$

subject to boundary conditions

$$P_s^* = 1, \quad \xi = 0 \tag{61}$$

$$\frac{\partial P_s^*}{\partial \eta} = 0, \quad \eta = \pm \frac{\pi}{2} \tag{62}$$

With the definition of velocity potential, Eq. (13), and nondimensional steam pressure, Eq. (56), the remaining boundary condition at the interface (interface pressure condition) can be found if the relationship between y and ϕ is known along the interface.

Interface Location

The singular integral equation can be solved only if the forcing function is known or assumed. Once Φ is known by solving the integral equation, the interface location can be determined and the steam momentum equation can be solved. The interface mass conservation condition, however, has not yet been satisfied. The whole problem can be regarded as an optimization process in the sense that the unknowns are determined in such a way that they satisfy an objective function as closely as possible. In this case, the unknowns are Φ and the injector steam pressure, P_o. The objective function is mass conservation at the interface.

Interface Mass Conservation. The expression for interface mass conservation, Eq. (9), is rewritten using

$$\mathbf{u}_l \cdot \mathbf{n} = -u \frac{dx}{ds} + v \frac{dy}{ds} = \frac{1}{ds} \left(\frac{\partial \psi}{\partial x} dx + \frac{\partial \psi}{\partial y} dy \right) = -\frac{d\psi}{ds} \tag{63}$$

where s is parallel to the interface. The result is

$$\mathbf{u}_s \cdot \mathbf{n} = \frac{\rho_l}{\rho_s} \frac{d\psi}{ds}\bigg|_i = \frac{\rho_l}{\rho_s} \frac{d\psi}{d\phi}\bigg|_i \frac{d\phi}{ds}\bigg|_i = g'(\phi) \frac{\rho_l}{\rho_s} \frac{d\phi}{ds}\bigg|_i \tag{64}$$

Solution Procedure. The objective function to be minimized is defined as

$$e \equiv \oint_i \left[\mathbf{u}_s \cdot \mathbf{n} + g'(\phi) \frac{\rho_l}{\rho_s} \frac{d\phi}{ds}\bigg|_i \right]^2 ds \tag{65}$$

The term $\mathbf{u}_s \cdot \mathbf{n}$ is obtained as part of the solution of the steam momentum equation and $g'(\phi)$ is found from the solution of the water energy equation. The last term is found by solution of the water momentum equations, i.e.,

$$\frac{d\phi}{ds}\bigg|_i = \frac{1}{\frac{ds}{d\phi}\Big|_i} = \frac{1}{\sqrt{\left(\frac{dx}{d\phi}\Big|_i \right)^2 + \left(\frac{dy}{d\phi}\Big|_i \right)^2}}$$

$$= \frac{2}{\Delta\psi} \frac{1}{\sqrt{\left(\frac{1}{U} + \Phi \right)^2 + \left(\frac{dy_i}{d\tilde{\phi}} \right)^2}} \tag{66}$$

Note that $dy_i/d\tilde{\phi}$ is the forcing function of the singular integral equation.

The solution algorithm can be summarized as follows:

1 Assume α and solve Eqs. (28) and (29).
2 Assume $y_i(\tilde{\phi})$.
3 Solve the singular integral equation to find $\Phi(\tilde{\phi})$, Eqs. (46)–(49).
4 Evaluate $x_i(\tilde{\phi}) = \int_{-1}^{\tilde{\phi}} \Phi(t)\, dt$.
5 Evaluate $r_o(\tilde{\phi})$, $\theta(\tilde{\phi})$ at the interface from $x_i(\tilde{\phi})$, $y_i(\tilde{\phi})$.
6 Evaluate $|u_l|(\theta)$ using solutions to the liquid momentum equations along the interface to update dispersion effects.
7 Calculate $P_l(\theta)$, Eq. (4), and $\dot{m}_w(\theta) = g'(\tilde{\phi}(\theta))$, solutions to Eqs. (28) and (29), at the interface.
8 With $r_o(\theta)$ and $P_l(\theta)$ at the interface, solve the steam momentum equation and evaluate $\dot{m}_s(\theta) = \rho_s \mathbf{u}_s \cdot \mathbf{n}$.
9 Update $y_i(\tilde{\phi}(\theta))$ using a minimization algorithm to minimize the error $e = \int_{-1}^{+1} [\dot{m}_s(t) - \dot{m}_w(t)]^2 dt$ then repeat steps (3)–(8) until convergence is achieved.

Special Case

Solutions to the energy equation and momentum equations are easily obtained for certain classes of operating conditions. One such case is of special interest: constant forcing function and zero kernel.

Constant Forcing Function and Zero Kernel. The singular integral equation admits a closed-form solution for the case where the kernel is zero and the interface shape is found to be an ellipse. The kernel approaches zero as the channel width approaches infinity and the forcing function is constant when y_i depends linearly on $\tilde{\phi}$,

$$y_i = C\tilde{\phi} + C_1 \tag{67}$$

where C, C_1 are constants. The solution of the singular integral equation is given by

$$\Phi(\tilde{\phi}) = \left(C + \frac{1}{U}\right)\frac{1-\tilde{\phi}}{\sqrt{1-\tilde{\phi}^2}} + \frac{C_o}{\sqrt{1-\tilde{\phi}^2}} \tag{68}$$

Applying the constraint condition given by Eq. (50) yields C_o

$$C_o = -C - \frac{1}{U} \tag{69}$$

From Eq. (51) it is found that

$$x_i(\tilde{\phi}) = \int_{-1}^{\tilde{\phi}} -\left(C + \frac{1}{U}\right)\frac{\xi d\xi}{\sqrt{1-\xi^2}} = -\left(C + \frac{1}{U}\right)\sqrt{1-\tilde{\phi}^2} \tag{70}$$

Combining Eqs. (67) and (70) yields the interface equation

$$\left(\frac{x_i}{C - 1/U}\right)^2 + \left(\frac{y_i - C_1}{C}\right)^2 = 1 \tag{71}$$

This is an ellipse whose interface becomes a circle when

$$C = -C - \frac{1}{U} \Rightarrow C = -\frac{1}{2U} \tag{72}$$

Results and Discussion

Experiments by Chung (1990) revealed that the interface shapes are indeed very close to ellipses. For practical purposes, the *constant forcing function* assumption is expected to be a good approximation. This assumption has a distinct advantage for computational economy. The number of parameters in an optimization process is directly related to the amount of arithmetic. In this study, a partial differential equation (steam momentum equation) and a system of ordinary differential equations are solved each time the objective function is evaluated. The evaluation of the gradient by finite difference requires the same number of additional evaluations of the objective function as parameters to be optimized. Minimizing the number of parameters is critical for calculation economy. For the constant forcing function case, the number of parameters is three: the steam injector pressure and the two constants in Eq. (67).

The effect of a *nonzero kernel* is worth studying because three-parameter optimization is still possible even for nonzero kernel cases if the interface is not far from elliptic. The kernel of the singular integral equation, Eq. (47), reflects the effects of the bounding walls. The parameter $\tilde{\psi}_0$ determines how strong the effect of the kernel is on the solution. For the constant forcing function cases

$$\tilde{\psi}_0 = \frac{\psi_0}{\Delta\phi/2} = \frac{WU}{2Ua} = \frac{W}{2a} \tag{73}$$

The singular integral equation was solved numerically using Chebyshev polynomials (Erdogan and Gupta, 1972) to investigate the effect of the kernel. Figure 4 shows the effect of side walls on bubble shape. It can be seen clearly that the effect of wall is negligible until $\tilde{\psi}_0 \leq 1.05$. With the restriction that $\tilde{\psi}_0 > 1.05$, the constant forcing function with zero kernel will be a good approximation for elliptic bubbles.

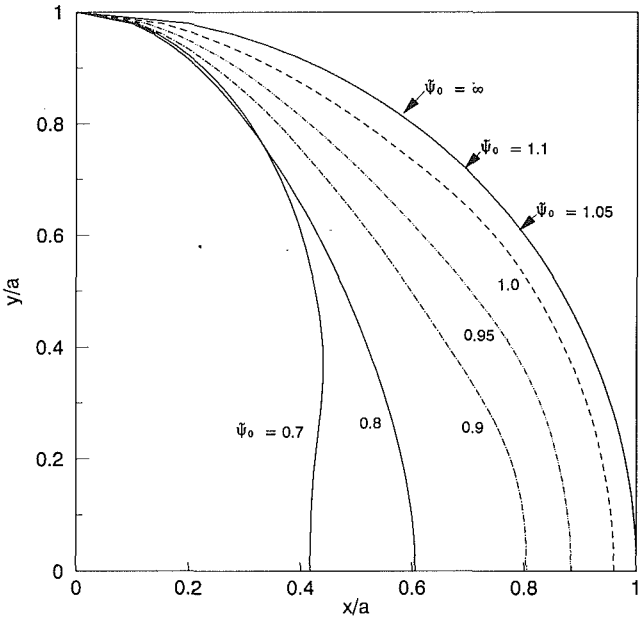

Fig. 4 Effects of wall distance on bubble shape

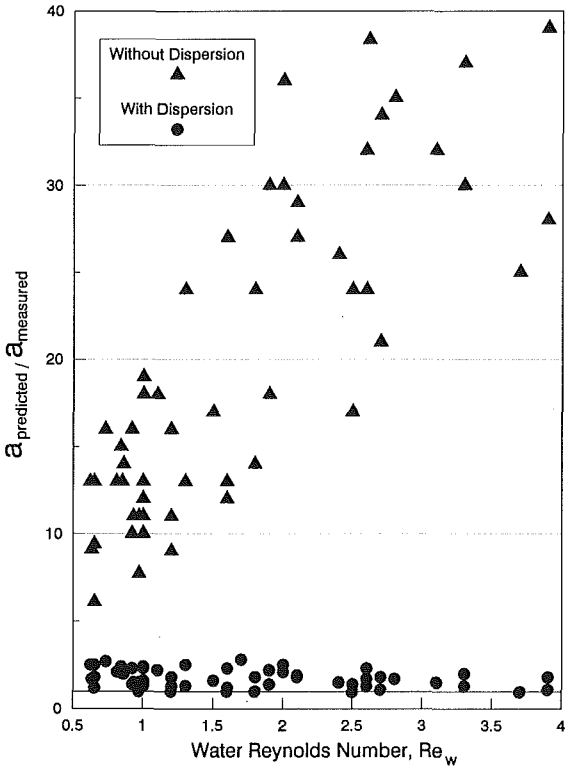

Fig. 5 Effects of dispersion on bubble size prediction

Average Bubble Radius—Constant Properties Case. The single most important quantity in this study is bubble size. The potential drop from the head to the tail of a bubble is given by

$$\Delta\phi = 4Ua_o \tag{74}$$

where a_o is the bubble radius for constant properties. The importance of this potential drop is that it can give the radius of the circle, the characteristic length of the bubble. Matching

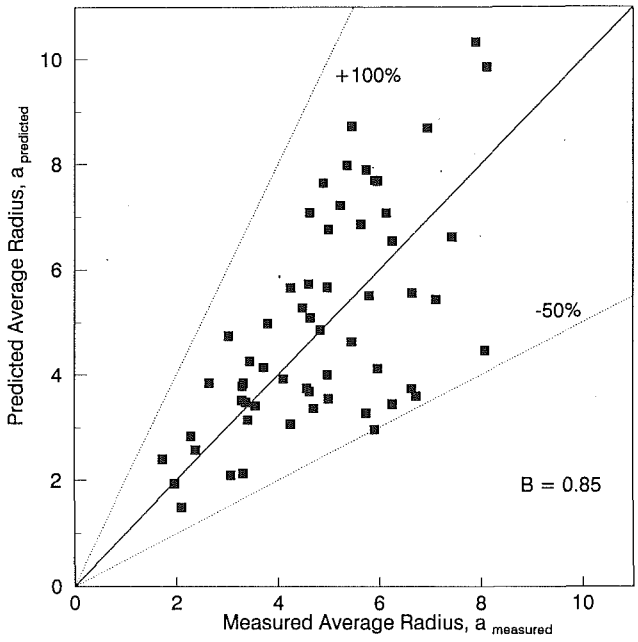

Fig. 6 Bubble radius prediction with best parameter

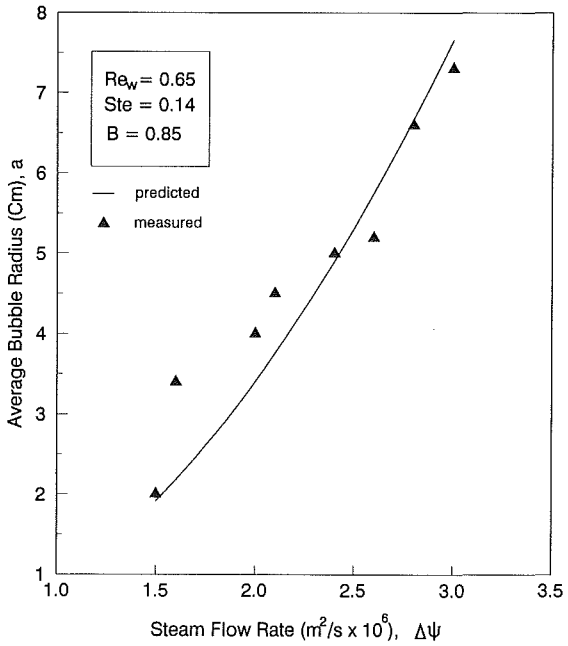

Fig. 7 Effect of steam injection rate on bubble growth

the potential drop with that from the solution of the energy equation for *constant properties*, Eqs. (28) and (29), yields

$$\sqrt{\frac{6\alpha_o^* \mathrm{Ste}^2}{5(1+\mathrm{Ste})}}\sqrt{\frac{4Ua_o}{\Delta\psi}} = 1 \rightarrow a_o = \frac{5(1+\mathrm{Ste})\Delta\psi}{24U\alpha_o^*\mathrm{Ste}^2} \qquad (75)$$

Figure 5 shows the ratio of predicted bubble radius to measured bubble radius as a function of water Reynolds number. The triangles represent the ratio without the dispersion effects in the theoretical prediction and the circles represent the ratio with dispersion effects. It can easily be seen that including dispersion effects in the analysis dramatically improves the results. The bubble size is, however, overpredicted using $B = 0.43$ as suggested by Georgiadis (1987). The prediction can be improved by simply adjusting the parameter to a larger value. Figure 6 shows that the bubble radius prediction can be improved to yield results that are within a factor of two of the measured results by choosing $B = 0.85$.

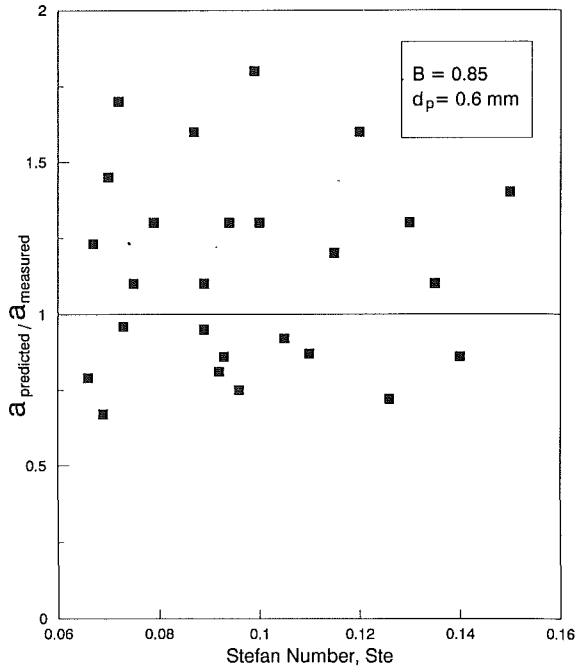

Fig. 8 Effects of Stefan number on bubble radius ratio

Figure 7 shows the effect of steam injection rate on bubble growth. As predicted by analysis, bubble radius is proportional to the square of steam injection rate. Keeping steam injection rate constant while other conditions are varying is experimentally difficult because the injection rate is constantly changing when the water flow rate is changing even if the valves in the steam supply line is fixed. Isolated effects of a parameter, for example water flow rate or the Stefan number, with a fixed steam injection rate are not experimentally studied due to the difficulty. Figure 8 shows the ratio of predicted to measured steam bubble radius as a function of the Stefan number. Throughout the tested Stefan number range, the prediction is within a factor of two.

Injector Pressure and Bubble Shape. The injector steam pressure and the parameters determining ellipticity and the displacement of the injector from the center of the ellipse can be found by solving the steam momentum equation subject to appropriate boundary conditions. The boundary shape depends on the two parameters, the injector displacement b and ellipticity e. The basic nature of the Cauchy boundary condition is still in effect up to this point. The governing equation is a second-order elliptic partial differential equation, which requires a boundary condition on each boundary. In this problem, two boundary conditions (pressure and mass conservation) are imposed at the still undetermined interface.

The most widely used solution procedure for problems involving the Cauchy boundary conditions is an optimization process. The unknown interface is a parameter or is represented by a series of points. Then the governing equation is solved imposing one of the two boundary conditions. The parameters or the spectrum of the points are determined in such a way that the remaining boundary condition is met as closely as possible. In this problem, the forcing function of the singular integral equation represents the unknown interface shape. A spectrum of forcing functions can be smoothly approximated with a cubic spline. The singular integral equation can be solved numerically for a given forcing function using Chebyshev polynomials. Then the optimization can be performed on the spectral values and the two parameters b and e. The still un-

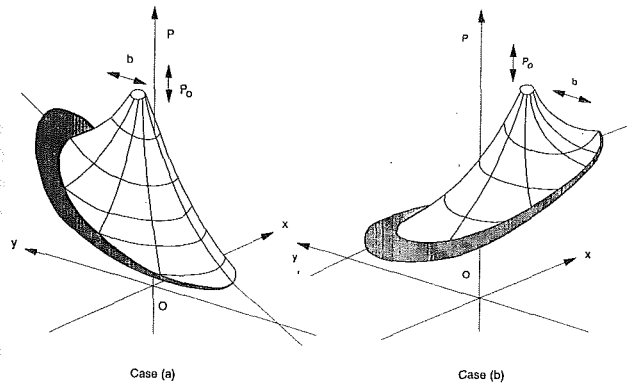

Fig. 9 Optimization process

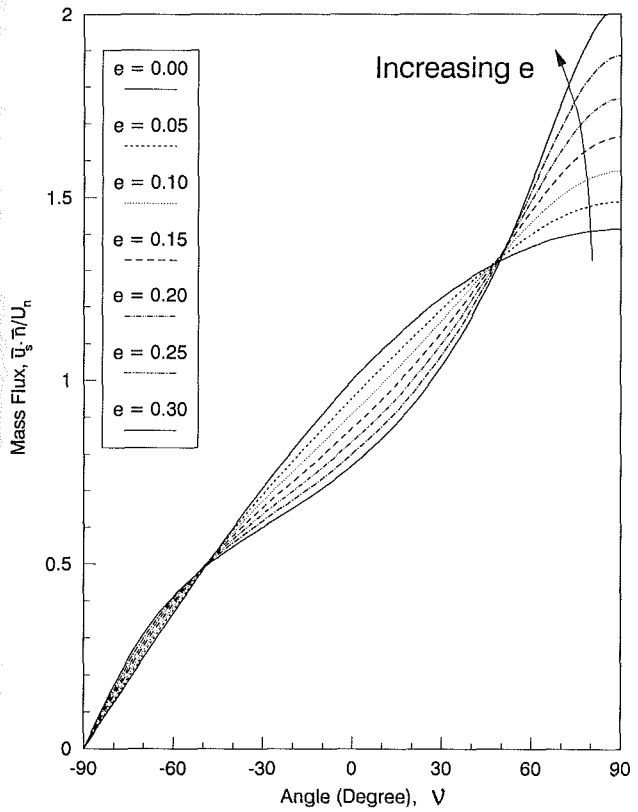

Fig. 10 Angular variation of condensate rate

known injector pressure can be found as part of the steam momentum equation solution.

Although the above process is, in principle, a standard solution procedure, the number of parameters to be optimized can be reduced to three assuming, that the bubbles are ellipses (equivalently constant forcing function with zero kernel) as mentioned above. Figure 9 qualitatively shows the two-parameter optimization process. The mass flux has been fixed along the interface through solution of the energy equation and mapping relations. The normal derivative of steam pressure at the interface should be arranged to meet the mass flux requirement. The parameter K defined by

$$K=\frac{2\mu_l U}{k(1+e)}-\rho_{fg}g \tag{76}$$

where

$$e\equiv\frac{c^2}{a^2} \tag{77}$$

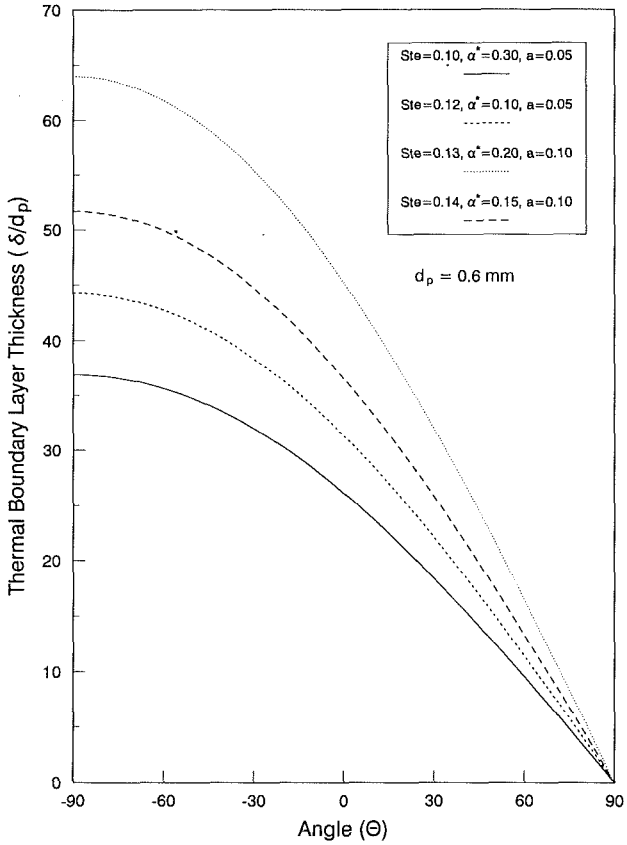

Fig. 11 Thermal boundary layer thickness

plays an important role in determining the relative location of the injector to the center of the ellipses. When K is negative as in Fig. 9(a), the injector must be located near the head of the bubble to supply higher flux near the head. When K is positive, the injector can be located considerably lower, still meeting the mass flux requirement as seen in Fig. 9(b).

Limiting the calculation to the two-parameter optimization, mass conservation can be expressed explicitly. The interface mass conservation requirement can be simplified for easier implementation by exploiting the fact that the interface is a streamline,

$$\dot{m}_s=\rho_s\mathbf{n}\cdot\mathbf{u}_s=\rho_l\frac{d\psi}{d\phi}\frac{d\phi}{ds} \tag{78}$$

Global mass conservation is met by direct integration,

$$\int_{-\pi/2}^{\pi/2}\rho_s\mathbf{u}_s\cdot\mathbf{n}a_o d\nu=\frac{1}{4\sqrt{2}}\rho_l\Delta\psi\int_{-\pi/2}^{\pi/2}\frac{2\cos\nu d\nu}{\sqrt{1-\sin\nu}}=\rho_l\Delta\psi \tag{79}$$

Figure 10 shows the angular variation of mass flux for various shapes for constant-property cases. Figure 11 shows thermal boundary layer thickness for different combinations of thermal diffusivity, Stefan number, and bubble radius. The thermal boundary layer is thick enough for a continuum approach to be valid, except at the top of the bubble, where a thermal boundary layer is relatively thin compared with particle size.

Two-parameter (b, e) optimization has been performed using a conjugate gradient method, an IMSL subroutine called ZXCGR. With the two parameters given, the steam momentum equation is solved using second-order centered differences and an ADI iteration scheme. The gradient of the objective function required by the algorithm has been supplied by finite differencing this function.

Figure 12 shows how close together the steam mass flux and the condensation rate are at the minimum error value for a

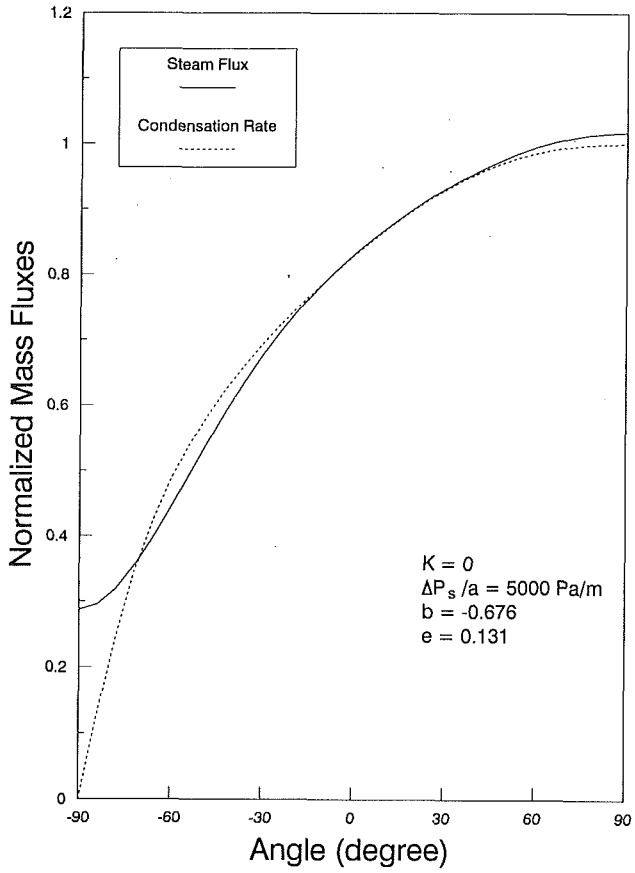

Fig. 12 Matching of mass flux and condensation rate

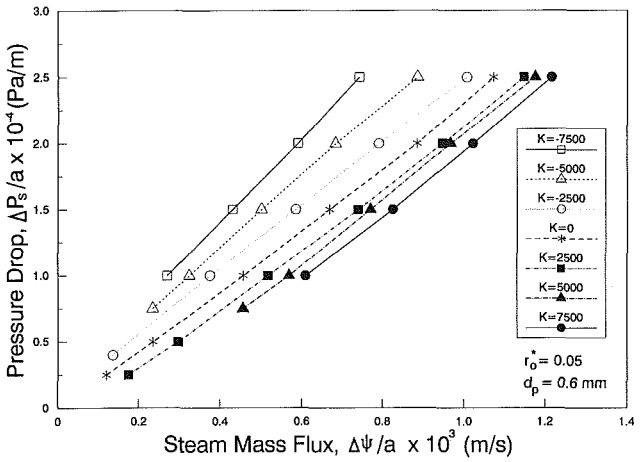

Fig. 13 Pressure drop as a function of injection rate

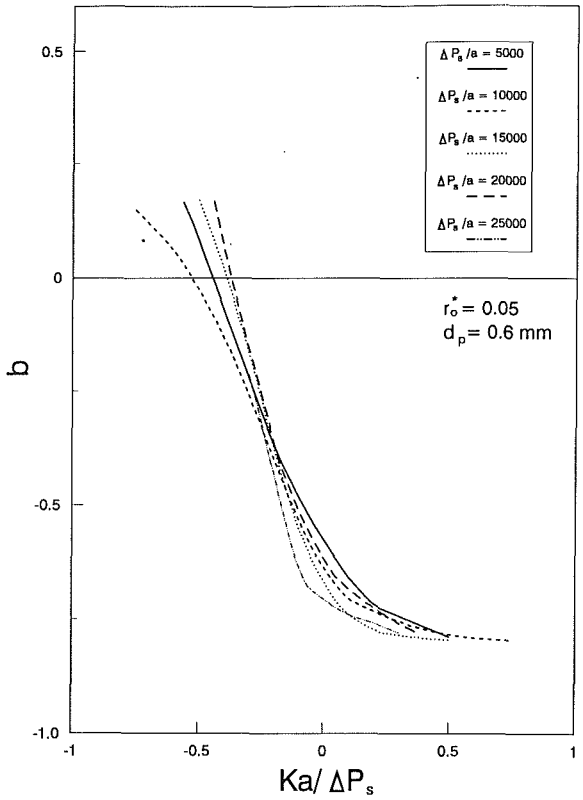

Fig. 14 Bubble shifting

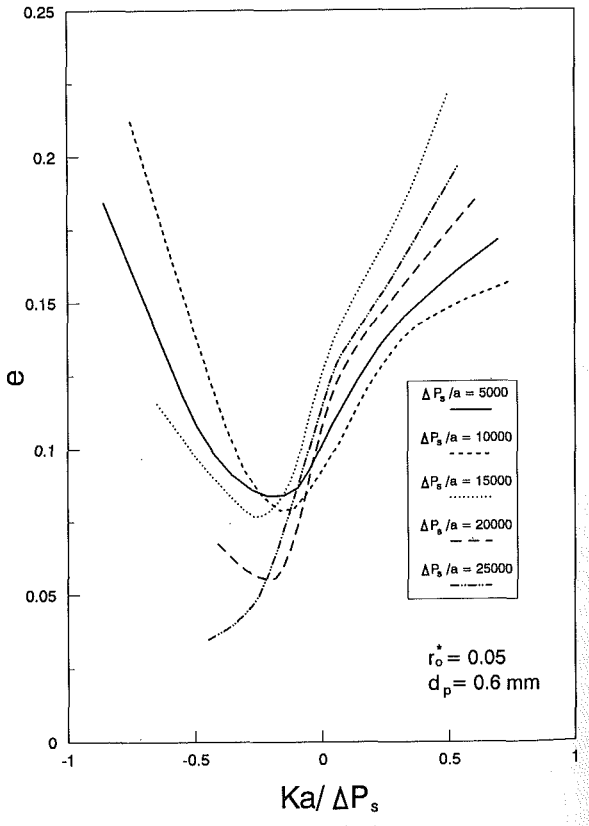

Fig. 15 Bubble ellipticity

typical case. The discrepancy is obvious at the bottom of the bubble in this instance. This discrepancy is dependent on the steam pressure gradient at the interface, $\Delta P_s/a$. The discrepancy is bigger for a negative gradient than for a positive gradient.

Figure 13 shows the pressure drop from the injector to the top of the bubble for different K's. The pressure drop is almost a linear function of the steam injection rate for a given value of K. This reveals that nonlinear effects caused by inertia in the steam flow are not profound for the range tested. The strong dependence of pressure drop on K is mainly due to the way the steam pressure is normalized. Steam pressure was normalized using the characteristic pressure drop from the injector to the top of the bubble instead of the average interface pressure, which on the average gives higher actual gradients for a smaller K.

Figures 14 and 15 show the parameters b and e found through the optimization processes. The parameter b represents injector

displacement relative to the center of the bubble and is strongly dependent on the y direction steam pressure gradient at the interface ($Ka/\Delta P_s$). As the gradient increases the bubble shifts downward. This corresponds to the case where the pressure drop due to flow resistance is higher than that due to gravity. The parameter e has a minimum value. The bubble shape is almost a circle at the minimum e. Only positive e values were observed in the current calculations. Positive e means an ellipse whose vertical axis is longer than the horizontal axis. The variation of e is limited to between 0.025 to 0.3 for the cases tested.

Conclusions

Steam injection into a uniform water flow through porous media was analyzed for low water flow rates (Darcy flow) and steady-state conditions. Coordinate transformation from the physical domain to velocity potential and steam function domain was used to simplify the governing equations and the computational domain. The resulting energy equation was further simplified to a parabolic partial differential equation by an order-of-magnitude argument. The equation was solved using an integral method. The solution gave the local condensation rate along the steam–water interface. The continuity equation and the momentum equation were transformed into two Laplace equations. With the imposed boundary conditions this constituted a mixed boundary value problem.

For elliptic bubbles, the energy equation and the water momentum equation were solved to find the bubble size and shape, flow, and temperature fields. The ellipticity and bubble shift relative to the injector were determined through optimization processes. The solutions were compared with the experimental measurements and showed that:

1 The average bubble radius is proportional to the square of the injection rate, and inversely proportional to the square of the water Reynolds number and Stefan number for Darcy flow.
2 Dispersion effects at the interface are very strong and are never negligible for the range tested.
3 The bubble shape and shift relative to the injector are dependent on two parameters: K and $\Delta P_s/a$.

It is clear that the solution could be improved so that the comparisons with data in Figs. 5 and 6 would be more favorable. One would first choose a more general shape than the ellipse used in this work. This would allow one to match the mass fluxes at each point along the surface rather than only in an average sense as shown in Fig. 12. The second improvement would be to take more care with the treatment of the dispersion augmentation of the thermal conductivity away from the interface. Finally, one needs to treat augmentation more carefully in the thin capillary zone separating the steam and water-saturated regions.

Two of the reviewers of this work expressed concern that the interfacial geometry assumed in the analysis may be unrealistic because of possible fingering. As the scale of the bubble increases, this may well be the case. We did not observe any fingering during our experimental study; see Chung and Catton (1990). At low steam fluxes, the interface was smooth to within a bead diameter. At larger steam fluxes, the process became highly oscillatory and one could imagine that fingering was taking place. Here the ligaments of vapor were quickly condensed. If one were to call the ligaments of vapor fingers, then fingering has a profound effect on the process at high steam flow rates. This will be the subject of a future experimental and theoretical effort.

References

Bear, J., 1988, *Dynamics of Fluids in Porous Media*, Dover Publications, New York.

Carrier, G. E., Krook, M., and Pearson, C. E., 1966, *Functions of a Complex Variable*, McGraw-Hill, New York.

Chung, M., 1990, "Two-Phase Flow in Porous Media With Phase Change: Steam Injection and Post-dryout Heat Transfer," PhD thesis, University of California, Los Angeles.

Chung, M., and Catton, I., 1990, "An Experimental Study on Steam Zone Behavior in a Uniform Water Flow Through Porous Media," *Heat and Mass Transfer in Frost and Ice, Packed Beds and Environmental Discharges*, ASME HTD-Vol. 138.

Erdogan, F., and Gupta, G. D., 1972, "On the Numerical Solution of Singular Integral Equations," *Quarterly of Applied Mathematics*, pp. 525–531.

Georgiadis, J. G., 1987, "Nonlinear Convective Transport in Packed Beds," Ph.D. thesis, University of California, Los Angeles.

Gradsheteyn, I. S., and Ryzhik, I. M., 1980, *Table of Integrals, Series, and Products*, Academic Press, New York.

Linz, P., 1971, "Fourier Cosine Integrals," *Collected Algorithm From CACM*, Algorithm 427.

Siegel, R., 1983, "Cauchy Method for Solidification Interface Shape During Continuous Casting," ASME JOURNAL OF HEAT TRANSFER, Vol. 105, p. 667.

Yortsos, Y. C., and Gavalas, G. R., 1982, "Heat Transfer Ahead of Condensation Fronts in Thermal Oil Recovery Processes," *Int. J. Heat Mass Transfer*, Vol. 25, No. 3, pp. 305–316.

A Numerical Investigation of Premixed Combustion Within Porous Inert Media

P.-F. Hsu

J. R. Howell

R. D. Matthews

Department of Mechanical Engineering,
The University of Texas at Austin,
Austin, TX 78712

A numerical investigation of premixed combustion within a highly porous inert medium is reported. Specifically, results of a numerical model using detailed chemical kinetics and energy exchange between the flowing gas and the porous solid are presented. The current formulation differs from prior models of this type of combustion in that multistep kinetics is used and a better description of the thermophysical properties of the solid is applied in the present model. It was found that the preheating effect increases strongly with increasing convective heat transfer and with increasing effective thermal conductivity of the solid. The convective heat transfer is expected to increase with increasing number of cells per unit length of porous matrix but the absorption coefficient decreases with increasing cell size and decreasing cell density. Numerical simulations using baseline properties indicate that the lean limit can be extended to an equivalence ratio of about 0.36 for a methane–air flame and that the peak flame temperature is generally higher than the adiabatic flame temperature. The latter effect is predicted to be more pronounced at lower equivalence ratios.

I Introduction

A numerical investigation of premixed combustion within a highly porous inert medium has been conducted. Although various porous inert media (PIM) may be developed (e.g., Babkin et al., 1991), a ceramic foam was the focus of the current investigation.

For ceramic foam PIM combustors, the medium may be envisioned as a ceramic "sponge" in which the premixed gases are constrained to flow through the open pore structure of the spongelike material. The porosity of this material is typically about 85–90 percent. Because of the high emissivity of the solid in comparison to a gas, radiation from the high-temperature postflame zone serves to heat the porous solid in the preflame zone, which, in turn, convectively heats the incoming reactants. This regenerative heating mechanism results in several interesting characteristics relative to a free-burning flame. These include higher burning speeds and volumetric energy release rates, increased combustion stability resulting in extension of the lean flammability limit, and the ability to burn fuels that have a very low energy content. These general characteristics have been observed experimentally and predicted using analytical models that have simulated the combustion process using one of three different approaches: (1) using a spatially dependent heat generation function (Tong and Sathe, 1991; Andersen, 1992), or (2) using single-step global chemistry (Baek, 1989; Echigo, 1985; Yoshizawa et al., 1987a, 1987b, 1988; Sathe et al., 1989, 1990a, 1990b, 1990c), or (3) using multistep chemistry (Chen et al., 1987, 1988; Hsu et al., 1991). The present investigation has extended the range of solutions using multistep chemistry from equivalence ratios of 0.8–1.0 to equivalence ratios of 0.4–1.0 and also presents calculations using transport properties that are more representative of ceramic foams.

II Numerical Model

The burner being modeled in an 8-cm-long cylinder of reticulated partially stabilized zirconia (PSZ), a ceramic foam with a dodecahedral structure that has, in the present case, 10 pores per inch (ppi). The curved radial wall of the cylinder is insulated and impervious to flow. Premixed methane and air enter one end of the burner at atmospheric pressure and, for the present calculations, the flame is stabilized at the midplane of the burner.

A one-dimensional transient model was developed by modifying the PREMIX laminar flame code (Kee et al., 1985). This code allows for the use of multistep detailed chemical kinetics, accounts for the Soret effect, and uses the TRANFIT subroutine (Kee et al., 1986) for accurate determination of the transport properties. This code was modified to solve a separate energy equation for the solid matrix with radiative and conductive transport through the solid matrix and convective heat transfer between the solid and the gas. The assumptions used in the model formulation were:

1 The working gas is nonradiating;
2 the porous medium emits and absorbs radiation in local thermal equilibrium;
3 radiation scattering is not considered;
4 the one-dimensional transport equation of radiative propagation in the axial direction is valid;
5 the ceramic material acts as a gray homogeneous medium;
6 potential catalytic effects of the high-temperature solid are negligible;
7 the Dufour effect and "bulk" viscosity are negligible;
8 the flow speed is sufficiently low that the process is isobaric; and
9 the flame is one dimensional and neither turbulence nor stretch are induced by the flow through the ceramic foam.

Some of these assumptions merit discussion. Gas radiation is neglected because the emissivity of the gas is much less than that of the ceramic foam, which is of the order of 0.5. For example, for the burner conditions being modeled (atmospheric pressure and a total burner length of 8 cm), the emissivity of the $CO_2 + H_2O$ present in a stoichiometric product mixture at 1800 K is only 0.031 (from Hottel's gas emissivity chart in, e.g., Siegel and Howell, 1981). Tong and co-workers (Sathe et al., 1990a; Tong and Sathe, 1991) showed that scattering has an important influence on combustion in this type of burner, based upon predictions for an extinction coefficient of 20 m^{-1}.

Contributed by the Heat Transfer Division for publication in the JOURNAL OF HEAT TRANSFER. Manuscript received by the Heat Transfer Division August 1991; revision received January 1993. Keywords: Combustion, Furnaces and Combustors, Porous Media. Associate Technical Editor: W. A. Sirignano.

However, Hsu (1991) has shown that conduction becomes more important and radiation less significant (especially when scattering is included) for extinction coefficients of the order of 100–1000 m^{-1}, which are believed to be more representative of the optical properties of these ceramic foams. Thus, it is believed that scattering may be less important for the conditions of present interest. Catalytic effects can be accounted for in the present model, since it incorporates multistep chemistry. However, in the present paper catalysis is neglected for the sake of convenience, especially in light of uncertainties regarding the rate constants of surface reactions for these materials. To justify the isobaric assumption, it is estimated that the pressure drop is less than 0.1 percent using permeability data for porous ceramics (Lee, 1986) and the maximum possible flame speed (again, at atmospheric pressure and a total burner length of 8 cm). Because this pressure drop is small, no momentum equation or Darcy flow formulation is needed. Turbulence is also neglected for the sake of convenience, even though preliminary measurements indicate that the flow is turbulent despite the low Reynolds number based upon cell diameter. Inclusion of turbulence will be the subject of a future effort.

A methane oxidation mechanism consisting of 58 reversible reactions and 17 species (Kee et al., 1985) was used in the present study for simulation of the chemical reactions. This mechanism is listed in the paper by Law and co-workers (Egolfopoulos et al., 1989), who concluded that this mechanism is very accurate, at least for predicting flame speeds. Comparisons between predictions made using one-step global kinetics with those made using multistep chemistry clearly indicate the necessity of using detailed kinetics, as briefly discussed with regard to Fig. 5. Additional and more detailed comparisons are the subject of a separate paper (Hsu and Matthews, 1992).

The governing equations are:

Continuity Equation:

$$\frac{\partial \rho u A}{\partial x} = 0 \tag{1}$$

Species Conservation Equation:

$$\rho A u \frac{\partial Y_k}{\partial x} + \frac{\partial}{\partial x}(\rho A Y_k V_k) - A \dot{\omega}_k W_k = 0$$

$$k = 1, 2, \ldots, K \tag{2}$$

where ω_k is the rate of production of the kth species.

The ith reaction is of the general form:

$$\sum_{k=1}^{K} v'_{ki} x_k \longleftrightarrow \sum_{k=1}^{K} v''_{ki} x_k$$

$$\dot{\omega}_k = \sum_{i=1}^{I} (v''_{ki} - v'_{ki}) \left(\kappa_{fi} \prod_{k=1}^{K} [x_k]^{v'} - \kappa_{ri} \prod_{k=1}^{K} [x_k]^{v''} \right)$$

$$\kappa_i = A_i T^{\beta i} \exp\left(-\frac{E_i}{R_c T} \right) \tag{3}$$

where κ_i is the rate coefficient for reaction i.

Convection was included by solving separate energy equations for the solid and the gas and coupling them through a convective heat transfer coefficient. The energy equation for the gas does not include radiation terms and the energy equation for the solid does not include energy liberation (reaction) terms. The resulting energy equations for this case are:

Gas Phase Energy Equation:

$$\rho u A \frac{\partial T}{\partial x} - \frac{1}{c_p} \frac{\partial}{\partial x}\left(\lambda A \frac{\partial T}{\partial x} \right) + \frac{A}{c_p} \sum_{k=1}^{K} \rho Y_k V_k c_{pk} \frac{\partial T}{\partial x}$$

$$+ \frac{A}{c_p} \sum_{k=1}^{K} \dot{\omega}_k h_k W_k + \frac{A}{c_p} H (T - T_s) = 0 \tag{4}$$

Nomenclature

a = absorption coefficient, m^{-1}
A = area, m^2
A_c = surface area per cell in the foam, m^2
c_p = temperature-dependent constant pressure specific heat of mixture, kJ/kg-K
c_{pk} = temperature-dependent specific heat of species k, kJ/kg-K
c_{ps} = specific heat of the solid, kJ/kg-K
E_n = exponential integral of order n, defined following Eq. (6)
E_1 = exponential integral of order $n = 1$, defined following Eq. (6)
E_2 = exponential integral of order $n = 2$, defined following Eq. (6)
f = integration variable used in Eq. (6)
h_k = specific enthalpy of species k, kJ/kg
h = convective heat transfer coefficient, W/m^2-K
H = volumetric convective heat transfer coefficient, W/m^3-K
H_o = baseline volumetric convective heat transfer coefficient, 10^7 W/m^3-K
I_b = blackbody radiation intensity, W/m^2-sr
K = total number of species
L = combustor length, m
m = mass flow rate, kg/s
n = order of exponential integral E, 1 or 2, in Eq. (6)
N = number density of cells in the foam, $1/m^3$
p = porosity of the ceramic foam
q_r = radiative heat flux, W/m^2
q^- = radiative heat flux in negative x direction, W/m^2
q^+ = radiative heat flux in positive x direction, W/m^2
R = radiosity, W/m^2
R_e = radiosity of a blackbody at the exit temperature, W/m^2
R_o = radiosity of a blackbody at the inlet temperature, W/m^2
S = burning speed, cm/s
S_L = laminar flame speed, cm/s
T = temperature, K
T_{ad} = adiabatic flame temperature, K
$T_{\max}$ = maximum flame temperature, K
T_o = gas inlet temperature, K
T_S = local solid temperature, K
t = local optical depth = ax
t^* = integration variable used in Eq. (6)
t_{eff} = effective optical depth = ax_{fl}
t_L = overall optical depth = aL
V_k = diffusion velocity of species k, m/s
W = molecular weight, kg/kmole
x = axial distance, m
x_{fl} = axial distance from burner inlet to flame, m
Y_k = mass fraction of species k
θ = nondimensional temperature = $(T - T_o)/(T_{ad} - T_o)$ or $(T_S - T_o)/(T_{ad} - T_o)$
$\theta_{\max}$ = nondimensional peak flame temperature = $(T_{\max} - T_o)/(T_{ad} - T_o)$
λ = thermal conductivity of the gaseous mixture, W/m-K
λ_s = effective thermal conductivity of the solid, W/m-K
λ_{so} = baseline effective thermal conductivity of the solid = 0.026 W/m-K
ρ = density of the gaseous mixture, kg/m^3
ρ_s = density of the solid, kg/m^3
σ = Stefan–Boltzmann constants = 5.6696×10^{-8} W/m^2-K^4
ϕ = fuel-air equivalence ratio
ω_k = molar rate of reaction of species k, kmole/m^3-s

Solid Phase Energy Equation:

$$\frac{\partial}{\partial x}\left(\lambda_s A \frac{\partial T_s}{\partial x}\right) - \frac{\partial}{\partial x}(Aq_r) + AH(T - T_s) = 0 \tag{5}$$

where the difference between the area of the solid and that of the gas is accounted for by using the effective thermal conductivity in the solid conduction term, by defining the convective heat transfer coefficient in a manner that accounts for the appropriate surface area (as discussed below), and by using measured values for the absorption (and scattering) coefficients of these foams that are calculated from the measurements as if they were solid, thereby yielding effective values that indirectly account for the ratio of the surface area of the solid to the cross-sectional area. The velocities in all equations in this paper are face velocities rather than pore velocities, and thus including porosity in the velocity terms is also not appropriate. This technique differs from the more explicit formulation of, for example, Sathe et al. (1990a), who specified different areas for the gas and solid. However, the two techniques are equivalent, for the reasons discussed above, except that the present formulation does not account for blockage of the flow area by the foam. In fact, although this does result in some loss of accuracy, this was a conscious decision by the authors. We wished to compare the predicted burning speed with the laminar flame speed, examining the thermochemical effects of the porous material independent of the physical effect of flow blockage by the solid.

The radiation term in Eq. (5) is determined using:

$$\frac{dq_r}{dx} = -2\pi a\left[R_o E_2(t) + R_e E_2(t_L - t) - 2I_b(t) + \int_0^t I_b(t^*)E_1(t - t^*)dt^* + \int_t^{t_L} I_b(t^*)E_1(t^* - t)dt^*\right]$$

$$I_b(t) = \frac{\sigma}{\pi} T_s^4(t)$$

$$E_n(t) \equiv \int_0^1 f^{n-2} e^{-t/f} df$$

$$t = ax \tag{6}$$

where t is the local optical depth (ax), t_L is the optical depth based on the entire burner length (aL), a is the absorption coefficient of the solid, and the other terms are defined in the nomenclature section. In the radiative transport equation, the first two terms in the square brackets represent the radiative contributions from the ends to point "t," the third term is the emission (loss) form point t, and the final two terms represent the emission from all other points to point t (see, e.g., Siegel and Howell, 1981, for a more detailed discussion).

Equation of State:

$$\rho = \frac{\overline{W}p}{R_c T} \tag{7}$$

Boundary Conditions:

At the inlet,

$$T = T_o, \quad Y = Y_{k,o}, \quad q^+(x=0) = \pi R_o \tag{8}$$

and at the exit,

$$\frac{\partial Y_k}{\partial x} = 0, \quad q^-(x=L) = \pi R_o, \quad \pi R_e \tag{9}$$

These boundary conditions merit some discussion. Specification of the mass fractions at the inlet does not allow for diffusion of species upstream to the inlet. However, for the present conditions, the model does not predict reaction more than a few millimeters upstream of the flame (as illustrated in Fig. 5), which is well downstream from the inlet. Thus, no error is introduced by specifying the initial mass fractions as the inlet boundary condition. The specification of a zero species gradient at the exit constrains the reactions and does not allow for reactions to proceed past the exit plane. However, in our companion paper, which compares single step to multistep kinetics (Hsu and Matthews, 1992), we found that using finite difference forms of the governing equations as the exit boundary conditions (allowing reactions to proceed past the exit plane) does not affect the flame speed or flame temperature, but does yield minor changes in some of the exit species concentrations. Of course, this would not be the case for very short burners, but these are not of present interest. For this reason, and since the present paper has not focused on species profiles or exhaust concentrations, the present formulation is adequate for the present purposes. The code is able to simulate either of two radiation boundary conditions at the exit: (1) radiation from the burner exit at a value of R_o, which simulates a laboratory environment, with radiative exchange with a blackbody at room temperature, and (2) radiation from the burner exit at a value of R_e, radiative exchange with a blackbody at the burner exit temperature, which simulates an industrial burner. Both exit radiation boundary conditions were used in the present research. These radiation boundary conditions serve as the boundary conditions for the solid energy equation and also impose the exit boundary condition on the gas phase energy equation due to the requirement for energy balance at the exit.

In the above energy equations, H is the volumetric convective heat transfer coefficient, which is defined as the product of the convective heat transfer coefficient, the number of cells per unit volume of porous material, and the surface area per cell:

$$H = hA_c N \tag{10}$$

Thus, HA in Eqs. (4) and (5) is essentially the product of the convective heat transfer and the number of cells per unit length of porous matrix. As H approaches infinity, the model predicts that the gas and solid temperatures are equal.

In the current formulation, a major improvement is that multistep reaction kinetics is used and a better description of the ceramic foam thermophysical properties is applied in the model.

III Numerical Results

The effects of the convective heat transfer coefficient, the effective thermal conductivity of the solid, the equivalence ratio, and the properties of the solid were numerically investigated to examine their effects on the temperature profiles, the peak flame temperature, and the burning speed, as discussed in the following subsections. PREMIX requires specification of a fixed temperature to define the "flame location" in the flame-fixed coordinate system. Normally a relatively low temperature is used, but because the calculations for PIM burners yield a large preheat zone in which little reaction takes place, a relatively high temperature ($\sim$1075 K) was specified for all simulations reported herein. The PREMIX code uses an adaptive grid scheme to speed up convergence, with over 90 percent of the grid points located in the near-flame vicinity. Typical run time is about 400–1000 seconds on a Cray XMP or YMP using the multistep kinetics mechanism, compared to 200–300 seconds for a single-step kinetics mechanism. Computational time can be reduced significantly if a relatively good initial guess is used. For most cases, a relative convergence of 10^{-4} was specified, which corresponds to four significant digits on the results. The grid effects on the solutions were examined by increasing the number of grid points after initial solution until the results no longer changed. It was found that 130 to 200 grid points provided stable solutions.

III(A) Effects of the Heat Transfer Coefficient, Cell Density, and Cell Diameter. The effects of the volumetric heat

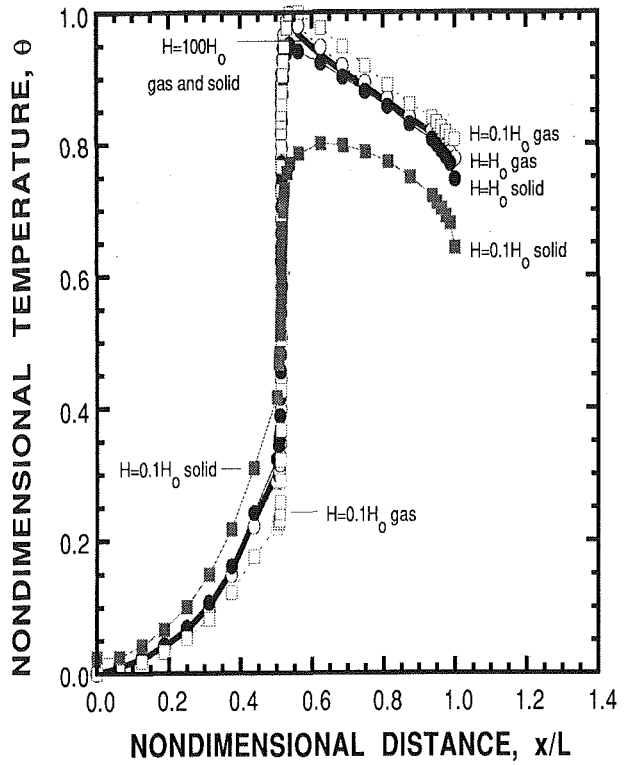

Fig. 1 Effects of finite convective heat transfer between the solid and the gas on the nondimensional temperature distribution through the flame using multistep chemistry for $t_{eff} = 2.0$, $x_f/L = 0.5$, $\phi = 0.9$, and exit radiation to black surroundings at 298 K. Open squares = gas temperature with $H = 0.1\ H_o$, filled squares = solid temperature with $H = 0.1\ H_o$, open circles = gas temperature with baseline convection coefficient, filled circles = solid temperature with baseline convection, heavy line = gas and solid temperatures with $H = 100\ H_o$.

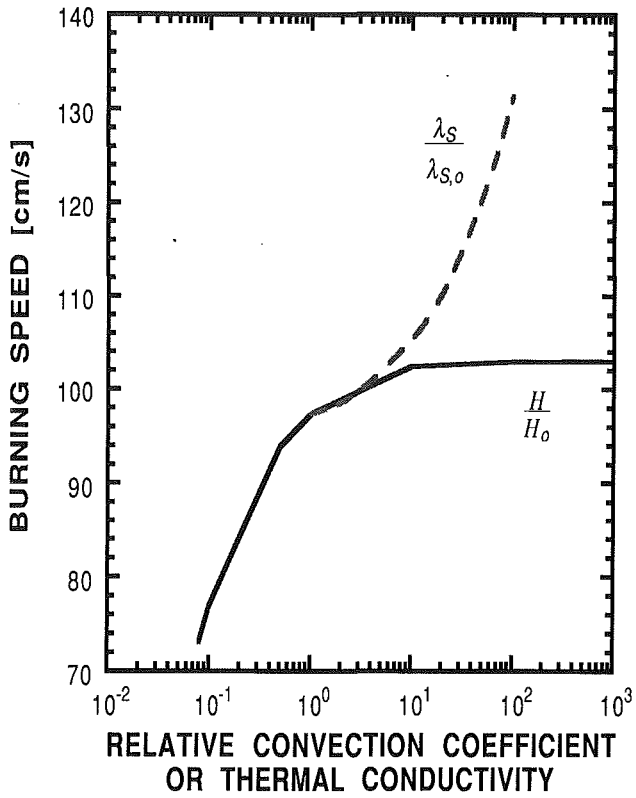

Fig. 2 Effects of the volumetric convective heat transfer coefficient and the effective thermal conductivity of the solid on the burning speed. Predictions made using multistep chemistry for $t_{eff} = 2.0$, $x_f/L = 0.5$, $\phi = 0.9$, and exit radiation to black surroundings at 298 K.

transfer coefficient are illustrated in Figs. 1 and 2. These results were generated for an equivalence ratio (ϕ, the actual fuel-air ratio normalized by the stoichiometric fuel-air ratio) of 0.9 with an optical thickness based on the distance between the burner inlet and the flame front of $t_{eff} = 2.0$ and a dimensionless flame position within the burner of $x_f/L = 0.5$. As defined previously (Eq. (10)), H is the product of the convective heat transfer coefficient and the number of cells per unit length of porous matrix. The baseline value, $H_o = 10^7$ W/m^3-K, was chosen to be the same as that used by Yoshizawa and co-workers (1988), who used a one-step kinetics mechanism. Yoshizawa did not vary the heat transfer coefficient directly, but coupled the dimensionless heat transfer coefficient to the absorption coefficient. In the present study, these parameters are uncoupled, allowing study of the effects of variation of the convective heat transfer alone.

As shown in Fig. 1, in the postflame zone, the gas temperature is higher than that of the solid because the energy is liberated by gas phase reactions and then transferred to the solid by convection. In the preflame zone, the solid temperature is higher than that of the gas because the solid is heated by radiation and then in turn convectively heats the gas. As H increases, the temperatures of the solid and the gas approach each other, and for $H \geq 10^9$ W/m^3-K, the temperatures are identical. This confirms prior predictions made without use of multistep kinetics, such as those of Tong and Sathe (1991) who used a spatially dependent heat generation function to simulate combustion.

The effect of H on the burning speed is shown in Fig. 2. For values of H less than the baseline value, the less effective preheating of the gas results in slower burning speeds. As H is increased by up to a factor of 10 above the baseline value, there is a small increase in burning speed. However, for values of H greater than about 10 times the baseline value, the convective heat transfer has become sufficiently effective that there is no further increase in the burning speed. This confirms earlier predictions (Sathe et al., 1990b) obtained using single-step kinetics.

To obtain high burning speeds, these results make it appear that a matrix with many cells per unit length is required, since this should increase the convective heat transfer. However, the absorption coefficient, which also has a strong influence on the burning speed, increases with increasing cell density and decreases with increasing cell diameter. On the other hand, the effective thermal conductivity of the solid, which also affects the flame propagation rate (as discussed in the next subsection), appears to be insensitive to the cell size (Hsu, 1991). The optimization of these trade-offs remains to be investigated and will require accurate data for thermal conductivity, absorption coefficient, and H as a function of pore size.

III(B) Effects of the Effective Thermal Conductivity of the Solid. The effects of the effective thermal conductivity of the solid on the combustion characteristics are illustrated in Figs. 2 and 3. These predictions were generated with $\phi = 0.9$, $x_{fL} = 0.5$, $t_{eff} = 2.0$, and $H = 10^7$ W/m^3-K. The baseline thermal conductivity of the solid, λ_{so}, is taken as that of air at standard temperature (0.026 W/m-K), which was chosen as the lower limiting case. Taking the effective thermal conductivity, λ_s, to be equal to the thermal conductivity of a solid block of ceramic times the volume fraction of solid in the foam (1-p, where p is the porosity) yields typical values of λ_s of about 0.2 W/m-K.

The effect of λ_s on the burning speed is illustrated in Fig. 2. Although increasing λ_s by a factor of 100 has only a small effect on the temperature distributions (as discussed below), the burning speed increases by about 20 percent, further illustrating the strong effect of preheat on the burning speed. This predicted strong effect on the effective thermal conduc-

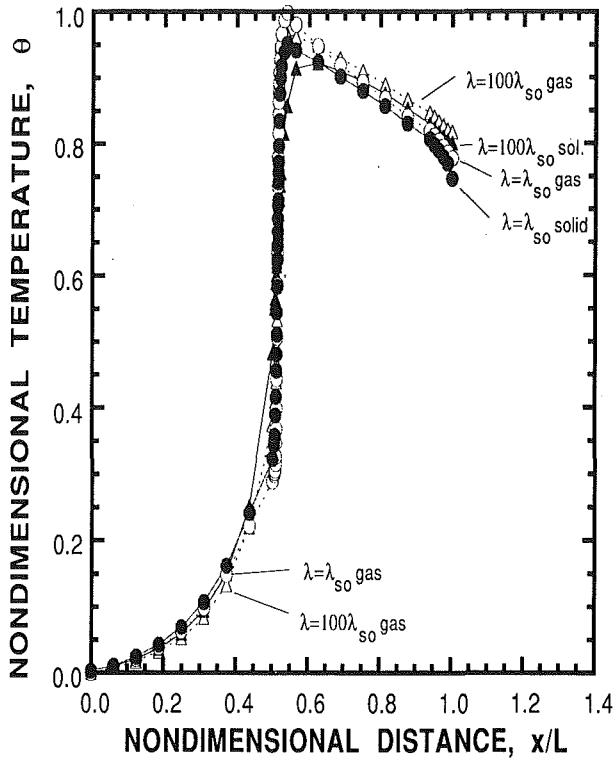

Fig. 3 Effect on the normalized temperature distribution through the porous matrix of the effective thermal conductivity of the solid. Multistep kinetics, $\phi = 0.9$, $t_{eff} = 2.0$, $x_{fl}/L = 0.5$, $H = H_o$, and exit radiation to black surroundings at 298 K. Open circles = gas temperature with the baseline effective thermal conductivity, filled circles = temperature of the solid phase with the baseline effective thermal conductivity, open triangles = gas temperature with the higher effective thermal conductivity, filled triangles = solid temperature with the higher effective thermal conductivity.

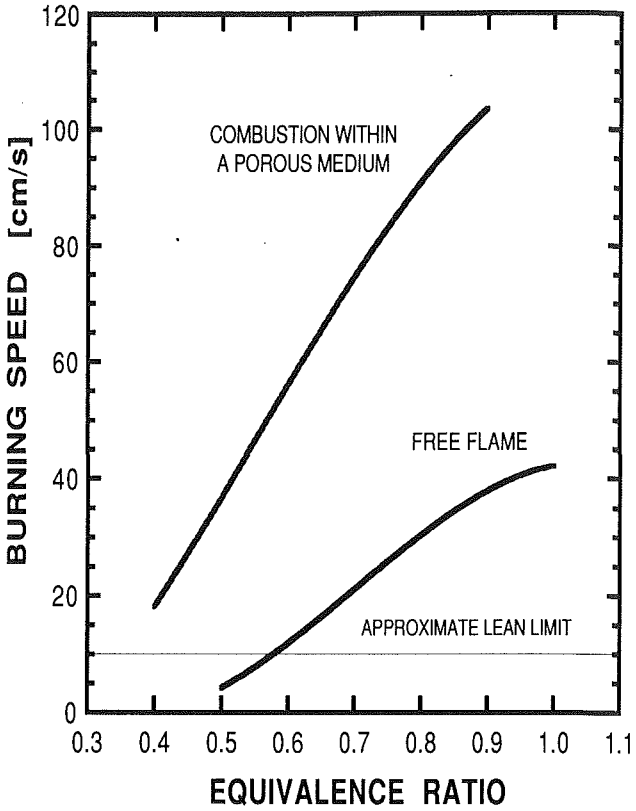

Fig. 4 Effects of the porous medium (with baseline properties and exit radiation to black surroundsing at 298 K) on the burning speed and flammability limit in comparison to a freely propagating, adiabatic, laminar flame

tivity of the solid confirms prior results (Sathe et al., 1990b) obtained using one-step chemistry.

As shown in Fig. 3, λ_s has little effect on the temperature profiles because the heat transfer is dominated by radiation and convection. This result agrees with a conclusion by Yoshizawa and co-workers, although they did not vary the thermal conductivity in their study. If the effective thermal conductivity of the solid is 100 times the baseline value, the peak flame temperature decreases due to conduction losses upstream and downstream. This also results in a small but significant increase in the preheating effect.

III(C) Effects of the Equivalence Ratio and Transport Properties on the Flame Speed and the Peak Flame Temperature. With the baseline properties used in the model, Fig. 4 shows the effect of the equivalence ratio on the burning speed for both a freely propagating laminar flame and combustion within a porous medium. The free flame results were obtained by setting $H = 0$ and $a = 0$, and yield values that agree closely with experimental data (Hsu and Matthews, 1992). Under all conditions, the presence of the porous medium is predicted to increase the burning speed, in agreement with the experimental findings of Sathe et al. (1990c) and Hsu et al. (1993). The curves presented in this figure also indicate that the presence of the porous medium extends the lean flammability limit to much leaner mixtures. Blint (1988) notes that the determination of the lean limit is difficult independent of whether one is performing experiments or numerical predictions. This is due to the significant effects of heat loss and bouyancy on the stability of slowly propagating flames. It is difficult to eliminate these effects in an experiment and difficult to account for them in a model. Thus, Blint presents arguments supporting 10 cm/s as the practical measure of both rich and lean flammability limits. A curve representing this criterion is shown for comparison in Fig. 4. Thus, the lean limit for a freely propagating laminar flame is predicted to be approximately $\phi = 0.58$, which is in reasonable agreement with the typical experimental value (which is probably not based upon the same 10 cm/s criterion) of $\phi = 0.52$. The presence of the porous material is predicted to extend the lean limit to about $\phi = 0.36$ (obtained via extrapolation of the predictions). Of course, this limit will depend upon the properties of the solid, and even lower flammability limits have been predicted using other properties for the porous material (Hsu, 1991).

Due to the internal heat feedback mechanism, the porous medium allows attainment of peak flame temperatures that are higher than the adiabatic flame temperature. However, as noted in the authors' previous work (Hsu et al., 1991), this effect is not as strong when using detailed chemistry as was predicted by previous researchers who use one-step kinetics. The reason for this is illustrated in Fig. 5: Global chemistry dictates complete combustion on the time scale of fuel disappearance, whereas multistep chemistry stretches out the energy release process and allows for CO in the products and therefore less energy release. Figure 6 illustrates the effects of equivalence ratio on both the adiabatic flame temperature and on the predicted peak temperature (using multistep kinetics) for combustion within a porous medium. The effect of the porous medium on the peak flame temperature becomes more pronounced as the mixture is made leaner, ranging from 1 percent above the adiabatic flame temperature at $\phi = 0.9$ to 10 percent at $\phi = 0.5$. Again, this effect will depend upon the properties of the solid. For example, using different properties for the porous material can yield predicted peak temperatures that are below the adiabatic flame temperature for near-stoichiometric mixtures (Hsu, 1991).

Figure 7 is a comparison of the temperature profiles through

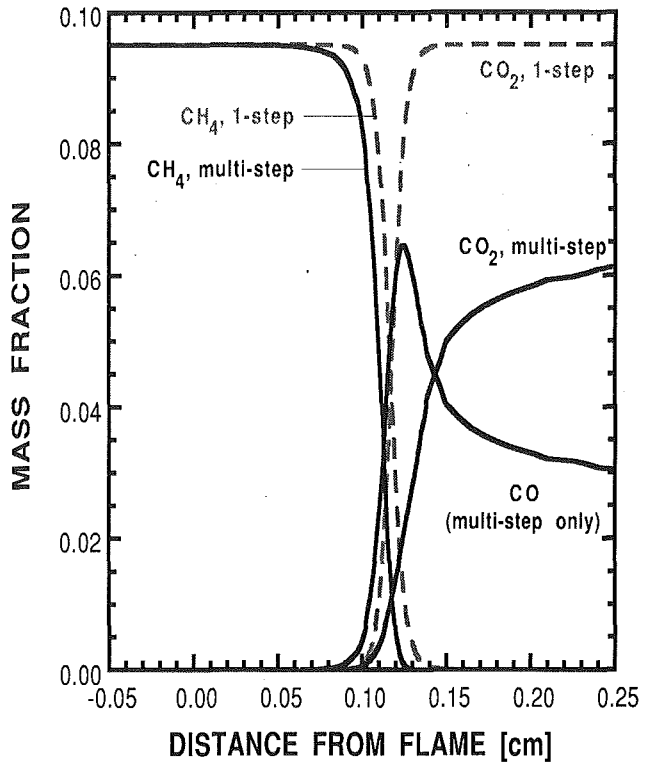

Fig. 5 Comparison of predicted species profiles through the flame zone of a PIM burner using both single-step global chemistry (thin lines) and multistep kinetics (thick lines) for $\phi = 1.0$ (Hsu and Matthews, 1992). The flame location ($x = 0$) is specified in the code as the position where the temperature is ~1075 K. No reaction has yet occurred at this location which has been preheated by solid phase conduction and radiation.

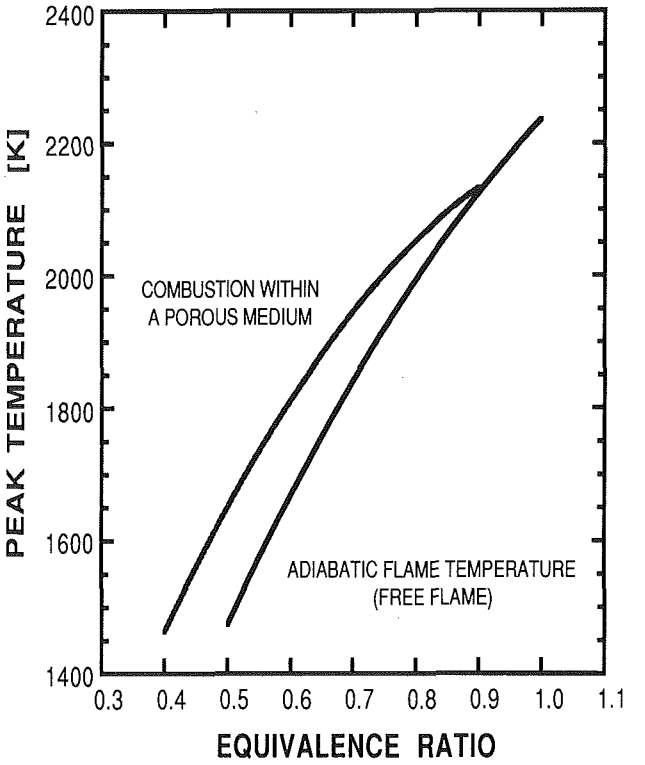

Fig. 6 Effects of the porous medium (with baseline properties and exit radiation to black surroundings at 298 K) on the peak flame temperature in comparison to a freely propagating, adiabatic, laminar flame.

a freely propagating, adiabatic laminar flame with those through a porous matrix burner for two cases of solid phase properties. For the curve labeled Case 1, the baseline properties prescribed

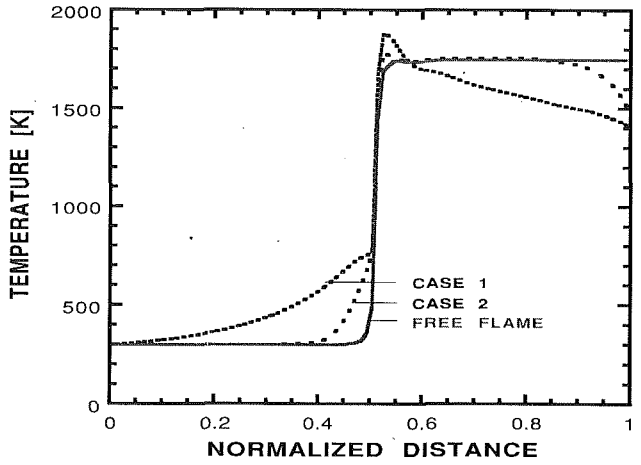

Fig. 7 Gas phase temperatures at an equivalence ratio of 0.65. Definitions of Case 1 and Case II flames are presented in Table 1. Exit radiation to black surroundings at 298 K.

Table 1 Thermophysical and transport properties used in the model

Case 1:
- $a = 50.0\ \mathrm{m}^{-1}$
- $H_o = 10^7\ \mathrm{W/m^3\text{-}K}$
- $\lambda_s = \lambda$ (gas mixture at 298 K)
- $c_{ps} = c_p$ (gas mixture at 298 K)
- $\rho_s = \rho$ (gas mixture at the local temperature)

Case 2:
- $a = 355.0\ \mathrm{m}^{-1}$ for 10 ppi PSZ
- $H_o = 10^7\ \mathrm{W/m^3\text{-}K}$
- $\lambda_s = (1-p)\cdot(-0.5608 + 0.85501\cdot\log(T_s))$ W/m-K
  $(400\ \mathrm{K} \le T_s \le 1200\ \mathrm{K})$ where $p = 0.87$ for partially stabilized zirconia with 20 pores per inch
- $c_{ps} = (1-p)\cdot(-147.15 + 97.227\cdot\log(T_s))/0.238$ kJ/kg-K
  $(50\ \mathrm{K} \le T_s \le 1500\ \mathrm{K})$
- $\rho_s = (1-p)\cdot 5.56\cdot 10^3\ \mathrm{kg/m^3}$

In Case 2, λ_s and c_{ps} are least-squares fits using data from Touloukian (1978a, 1978b) and ρ_s is obtained from High-Tech Ceramics (1988). These properties, except a and H_o, are assumed to have linear dependence on porosity. The porosity of PSZ ranges from 84–87 percent and has the higher value for 10 ppi foam. In the program, to simulate the free flame case, a and H are set equal to zero.

in Table 1 were used. The predictions labeled Case 2 used properties that are more representative of a ceramic foam and include higher values for the adsorption coefficient, the convective heat transfer coefficient, and the effective thermal conductivity of the solid. As shown in Table 1, the Case 2 predictions incorporate analytical relationships for: (1) the effects of temperature and porosity on the thermal conductivity of the solid and the specific heat of the solid, (2) the effects of porosity on the density of the solid, and (3) an absorption coefficient that is about seven times larger than the baseline value (Skocypec and Hogan, 1989; High-Tech Ceramics, 1988). When using properties that are representative of a ceramic foam (Case 2), the thickness of the preheating zone is reduced due to the larger absorption coefficient, which in turn results in a smaller increase in peak flame temperature (above that of a free flame) than that of the Case 1 flame. Also, the higher solid conductivity of Case 2 tends to reduce the peak temperatures due to increased conduction of energy away from the reaction zone. Further, the large absorption coefficient of Case 2 causes a sharp drop in temperature at the exit. Although the maximum flame temperature of Case 2 is smaller than that of Case 1, the flame speed of Case 2 (76.2 cm/s) is higher than Case 1 (67.6 cm/s).

IV Summary and Conclusions

A theoretical investigation of premixed combustion within porous inert media has been conducted. The effects of various

material, combustor geometry, and modeling parameters have been studied, allowing the following conclusions to be drawn.

The peak flame temperature is predicted to be 1–10 percent higher than the equilibrium adiabatic flame temperature, with the relative temperature overshoot increasing as the mixture gets leaner. These results are much lower than the 40–50 percent maximum increase predicted by prior investigators because they used one-step kinetics while multistep kinetics were used in the present study.

The model predictions show that the absorption coefficient of the porous medium, which depends on the cell size and the material properties of the solid, has a significant effect on the flame characteristics. The preheating effect increases with increasing convective heat transfer and with increasing effective thermal conductivity of the solid. Convection is expected to increase with increasing number of cells per unit length. However, the absorption coefficient increases with increasing cell density and decreases with increasing cell diameter.

The present numerical simulation also predicts that PIM combustion results in increased burning speeds and allows extension of the lean limit.

The optimization of the various tradeoffs (i.e., material selection for optimum transport properties, burner length, etc.) remains to be investigated. Submodels to account for the effects of the combustor geometry and material properties on the absorption and scattering coefficients, the volumetric convective heat transfer coefficient, and the effective thermal conductivity of the solid are currently being developed so that these factors can be accounted for in the model. The potential effects of turbulence are also the subject of ongoing modeling efforts.

Acknowledgments

Funding for this research was provided by the Texas Advanced Technologies Program. This material is also based in part upon work funded by the Governor's Energy Management Center—State of Texas Energy Research in Applications Program under Contract No. 171. Partial funding was also provided by the University of Texas Center for Energy Studies.

References

Andersen, F., 1992, "Heat Transport Model for Fibre Burners," *Progress in Energy and Combustion Science*, Vol. 18, pp. 1–12.

Babkin, V. S., Korzhavin, A. A., and Bunev, V. A., 1991, "Propagation of Premixed Gaseous Explosion Flames in Porous Media," *Combustion and Flame*, Vol. 87, pp. 182–190.

Baek, S. W., 1989, "The Premixed Flame in a Radiatively Active Porous Medium," *Combustion Science and Technology*, Vol. 64, pp. 277–287.

Blint, R. J., 1988, "Flammability Limits for Exhaust Gas Diluted Flames," *Twenty-Second Symposium (International) on Combustion*, The Combustion Institute, Pittsburgh, PA, pp. 1547–1554.

Chen, Y.-K., Matthews, R. D., and Howell, J. R., 1987, "The Effect of Radiation on the Structure of Premixed Flame Within a Highly Porous Inert Medium," in: *Radiation, Phase Change, Heat Transfer, and Thermal Systems*, Jaluria et al., eds., ASME HTD-Vol. 81.

Chen, Y.-K., Hsu, P.-F., Lim, I.-G., Lu, Z.-H., Matthews, R. D., Howell, J. R., and Nichols, S. P., 1988, "Experimental and Theoretical Investigation of Combustion Within Porous Inert Media," presented at the 22nd Symposium (International) on Combustion, Seattle, WA, Poster Paper No. P22-207.

Echigo, R., 1985, "Radiative Heat Transfer Enhancement to a Water Tube by Combustion Gases in Porous Medium," *Proceedings: International Symposium on Heat Transfer*, Vol. 3, pp. 186–193.

Egolfopoulos, F., Cho, P., and Law, C. K., 1989, "Laminar Flame Speed of Methane-Air Mixtures Under Reduced and Elevated Pressures," *Combustion and Flame*, Vol. 76, pp. 375–391.

High-Tech Ceramics, 1988, product literature, High-Tech Ceramics Co., Alfred, NY.

Hsu, P.-F., 1991, "Analytical and Experimental Study of Combustion Within Porous Media," PhD dissertation, Department of Mechanical Engineering, the University of Texas, Aug.

Hsu, P.-F., Howell, J. R., and Matthews, R. D., 1991, "Numerical Model for Premixed Combustion Within Highly Porous Media," *Proceedings of the ASME/JSME Thermal Engineering Joint Conference*, Vol. 4, pp. 219–224.

Hsu, P.-F., Evans, W. D., and Howell, J. R., 1993, "Experimental and Numerical Study of Premixed Combustion Within Nonhomogeneous Porous Ceramics," *Combustion Science and Technology*, Vol. 90, pp. 149–172.

Hsu, P.-F., and Matthews, R. D., 1992, "The Necessity of Using Detailed Kinetics in Models for Premixed Combustion Within Porous Media," to be submitted to *Combustion and Flame*.

Kee, R. J., Grcar, J. F., Smooke, M. D., and Miller, J. A., 1985, "A Fortran Program for Modeling Steady Laminar One-Dimensional Premixed Flames," Sandia National Laboratories Report No. SAND85-8240.

Kee, R. J., Dixon-Lewis, G., Warnatz, J., Coltrin, M. E., and Miller, J. A., 1986, "A Fortran Computer Code Package for the Evaluation of Gas-Phase Multicomponent Transport Properties," Sandia National Laboratories Report No. SAND86-8246.

Lee, K., 1986, "Heat and Mass Transfer in Highly Porous Media," PhD dissertation, Department of Mechanical Engineering, University of Texas, Austin, TX.

Merzhanov, A. G., and Khaikin, B. I., 1988, "Theory of Combustion Waves in Homogeneous Media," *Progress in Energy and Combustion Science*, Vol. 14, No. 1, pp. 1–98.

Sathe, S. B., Kulharni, M. R., Peck, R. E., and Tong, T. W., 1989, "An Experimental Study of Combustion and Heat Transfer in Porous Radiant Burners," presented at the 1989 Fall Meeting of the Western States Section of the Combustion Institute, Livermore, CA.

Sathe, S. B., Peck, R. E., and Tong, T. W., 1990a, "Flame Stabilization and Multimode Heat Transfer in Porous Radiant Burners: A Numerical Study," *Combustion Science and Technology*, Vol. 70, pp. 93–109.

Sathe, S. B., Peck, R. E., and Tong, T. W., 1990b, "A Numerical Analysis of Heat Transfer and Combustion in Porous Radiant Burners," *International Journal of Heat and Mass Transfer*, Vol. 33, pp. 1331–1338.

Sathe, S. B., Kulkarni, M. R., Peck, R. E., and Tong, T. W., 1990c, "An Experimental and Theoretical Study of Porous Radiant Burner Performance," *23rd Symposium (International) on Combustion*, The Combustion Institute, Pittsburgh, PA, pp. 1011–1018.

Siegel, R., and Howell, J. R., 1981, *Thermal Radiation Heat Transfer*, 2nd ed., McGraw-Hill, New York.

Skocypec, R. D., and Hogan, R. E., 1989, "Modeling of a Catalytically Enhanced Solar Volumetric Absorption Chemical Reactor," Sandia National Laboratories Report No. SAND89-0134C, presented at the 1989 Spring Meeting of the Western States Section of the Combustion Institute, Pullman, WA.

Tong, T. W., and Sathe, S. B., 1991, "Heat Transfer Characteristic of Porous Radiant Burners," ASME JOURNAL OF HEAT TRANSFER, Vol. 113, pp. 423–428.

Touloukian, Y. S., ed., 1978a, "Nonmetallic Thermal Conductivity," Vol. 2, Thermophysical Properties Research Center, Purdue University, West Lafayette, IN.

Touloukian, Y. S., ed., 1978b, "Nonmetallic Specific Heat," Vol. 5, Thermophysical Properties Research Center, Purdue University, West Lafayette, IN.

Yoshizawa, Y., Echigo, R., Suzuki, H., and Jugjai, S., 1987a, "Combustion Augmentation of Solid Poor Combustiles With an Extremely High Water Content," *Proceedings of the Joint Conference of the Western States and the Japanese Sections*, the Combustion Institute, Pittsburgh, PA, pp. 352–353.

Yoshizawa, Y., Sasaki, K., and Echigo, R., 1987b, "Analytical Study of the Structure of Radiation Controlled Flame," ASME Paper No. 87-HT-57.

Yoshizawa, Y. Sasaki, K., and Echigo, R., 1988, "Analytical Study of the Structure of Radiation Controlled Flames," *International Journal of Heat and Mass Transfer*, Vol. 31, No. 2, pp. 311–319.

Experimental Investigation of Micro Heat Pipes Fabricated in Silicon Wafers

G. P. Peterson
Tenneco Professor and Head of Mechanical Engineering. Mem. ASME

A. B. Duncan
Graduate Research Assistant, Department of Mechanical Engineering. Mem. ASME

M. H. Weichold
Associate Professor of Electrical Engineering.

Texas A&M University, College Station, TX 77843-3123

An experimental investigation was conducted to determine the thermal behavior of arrays of micro heat pipes fabricated in silicon wafers. Two types of micro heat pipe arrays were evaluated, one that utilized machined rectangular channels 45 μm wide and 80 μm deep and the other that used an anisotropic etching process to produce triangular channels 120 μm wide and 80 μm deep. Once fabricated, a clear pyrex cover plate was bonded to the top surface of each wafer using an ultraviolet bonding technique to form the micro heat pipe array. These micro heat pipe arrays were then evacuated and charged with a predetermined amount of methanol. Using an infrared thermal imaging unit, the temperature gradients and maximum localized temperatures were measured and an effective thermal conductivity was computed. The experimental results were compared with those obtained for a plain silicon wafer and indicated that incorporating an array of micro heat pipes as an integral part of semiconductor devices could significantly increase the effective thermal conductivity; decrease the temperature gradients occurring across the wafer; decrease the maximum wafer temperatures; and reduce the number and intensity of localized hot spots. At an input power of 4 W, reductions in the maximum chip temperature of 14.1°C and 24.9°C and increases in the effective thermal conductivity of 31 and 81 percent were measured for the machined rectangular and etched triangular heat pipe arrays, respectively. In addition to reducing the maximum wafer temperature and increasing the effective thermal conductivity, the incorporation of the micro heat pipe arrays was found to improve the transient thermal response of the silicon test wafers significantly.

Introduction

Recent developments in semiconductor technology have made possible extraordinary advances in device construction and miniaturization. It is now possible to construct an entire gas chromatograph on a single seminconductor chip (Cotter, 1984) and work is currently under way to construct two-dimensional laser arrays on a chip whose total area is less than 10 mm^2. These applications, along with the associated increases in electronic circuit integration and the desire to reduce operational execution time, have resulted in large reductions in the physical size of electronic devices and components. Although the transistor switching energies have also decreased, these decreases have not kept pace with the increases in component density. As noted by several investigators, increases in the chip thermal conductivity or in the material to which the chips are attached effectively increases the area over which heat generated by localized hot spots can be dissipated (Kim and Anand, 1992). As a result, these factors strongly influence the thermal characteristics of the chip and may significantly enhance the chip reliability (Chyu and Aghazadeh, 1987).

Several years ago, Tuckerman and Pease (1981) investigated the design, fabrication, and testing of ultracompact, water-cooled, plate-fin and pin-fin heat sinks. These micromechanical heat sinks consisted of 300 μm × 50 μm rectangular channels, with 100 μm interchannel spacing, cooled by forced convection of water. Shortly afterward, Cotter (1984) proposed the concept of a micro heat pipe, one "so small that the mean curvature of the vapor-liquid interface is necessarily comparable in magnitude to the reciprocal of the hydraulic radius of the flow channel." Although only a conceptual description of a micro heat pipe was presented, this work provided the basis for later steady-state and transient investigations of trapezoidal and tapered artery micro heat pipes, approximately 1 mm in diameter (Babin et al., 1990; Wu and Peterson, 1991; Wu et al., 1991).

In practical terms, a micro heat pipe consists of a small noncircular channel that utilizes the sharp angled corner regions as liquid arteries. The fundamental operating principles of micro heat pipes are essentially the same as those of larger, more conventional heat pipes. Heat applied to one end of the heat pipe vaporizes the liquid in that region and forces it to move to the cooler end, where it condenses and gives up the latent heat of vaporization. This vaporization and condensation process causes the liquid–vapor interface in the corners to change continually along the pipe, as illustrated in Fig. 1, and results in a capillary pressure difference between the evaporator and condenser regions. This capillary pressure difference promotes the flow of the working fluid from the condenser back to the evaporator through the corner regions. While the previous investigations of Babin et al. (1990), Wu and Peterson (1991), and Wu et al. (1991) can be of some help in determining how heat pipes of the type described by Cotter (1984) (i.e., heat pipes approximately 100 μm in diameter) would perform, they do not address how the incorporation of an array of these very small micro heat pipes fabricated as an integral part of a silicon semiconductor wafer might affect the overall temperature distribution and thermal performance.

In order to determine the potential advantages of this concept, Mallik et al. (1992) developed a transient three-dimensional numerical model of an array of micro heat pipes fabricated as an integral part of silicon wafers as illustrated in Fig. 2. This numerical model was capable of predicting the time-dependent temperature distribution occurring within the wafer when given the physical parameters of the wafer and the locations of the heat sources and sinks. The results indicated that significant reductions in the maximum localized wafer

Contributed by the Heat Transfer Division for publication in the JOURNAL OF HEAT TRANSFER. Manuscript received by the Heat Transfer Division October 1992; revision received January 1993. Keywords: Conduction, Heat Pipes and Thermosyphons, Multiphase Flows. Technical Editor: R. Viskanta.

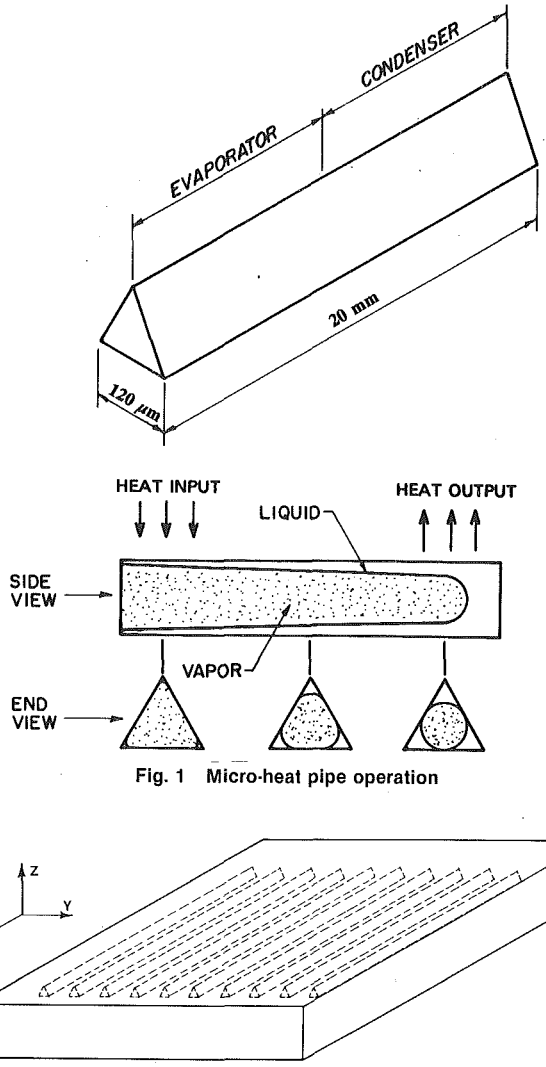

Fig. 1 Micro-heat pipe operation

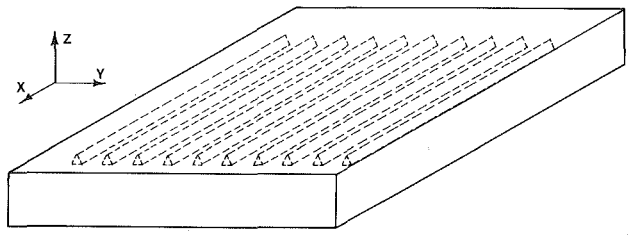

Fig. 2 Micro-heat pipe array fabricated as an integral part of a silicon wafer

temperatures and thermal gradients across the wafer could be obtained through the incorporation of an array of micro heat pipes. Utilizing heat sinks located on the edges of the chip perpendicular to the axis of the heat pipes and a cross-sectional area porosity of 1.85 percent, reductions in the maximum chip temperature of up to 40 percent were predicted.

More recently, Swanson and Peterson (1992) investigated the behavior of the intrinsic meniscus in triangular channels, as directly applied to micro heat pipes. In this investigation a mathematical model of the evaporating intrinsic meniscus in a V-shaped channel was developed to determine the effect of wedge half-angle and vapor mass transfer on the meniscus morphology, fluid flow, and heat transfer behavior. The Navier–Stokes and energy equations, as well as the interfacial conditions, were scaled using the lubrication approximation. The one-sided formulation applied to gas phase was constant. This reduced the mathematical complexity of the problem and allowed the use of a simple mass transfer coefficient at the vapor–liquid interface. The scaled normal stress interfacial condition was examined in detail to compare the magnitudes of the surface tension forces and van der Waals forces both near the interline and at the edge of the intrisic meniscus.

Experimental Investigation

In the present investigation, several 20 mm × 20 mm silicon wafers were fabricated with distributed heat sources on one side and an array of micro heat pipes on the other. Two fabrication procedures were utilized; in the first, an array of 39 rectangular micro heat pipe channels each 45 μm wide and 80 μm deep was machined into silicon wafers 0.378 mm thick using a silicon dicing saw. In the second, an array of parallel triangular channels 120 μm wide and 80 μm deep was fabricated into silicon wafers 0.5 mm thick using an anisotropic etchant process. These two configurations both resulted in a cross-sectional area porosity of approximately 1.87 percent, which was close to the optimum values predicted by Mallik et al. (1991a). The objectives of the current investigation were to develop the necessary fabrication techniques; provide definitive experimental data to verify the micro heat pipe concept; and determine the extent to which an array of micro heat pipes could reduce the maximum wafer temperature, decrease the temperature gradient across the wafer, increase the effective thermal conductivity, and decrease the number and intensity of localized hot spots. The following discussion describes the fabrication process, along with the methods by which the heat pipe arrays were charged and experimentally evaluated.

Micro Heat Pipe Fabrication. Several techniques have been proposed by which micro heat pipes with hydraulic diameters on the order of 20 to 150 μm in diameter could be incorporated as an integral part of silicon or gallium arsenide wafers, and recent investigations have focused on the development of the required fabrication techniques. These investigations include the use of conventional techniques such as the machining of small channels (Peterson et al., 1991) and the use of directionally dependent etching processes to create rectangular to triangular shaped channels (Peterson, 1988; Gerner et al., 1992); or other more elaborate techniques, which utilize a multisource vapor deposition process (Mallik et al., 1991; Weichold et al., 1992) to create an array of long narrow channels of triangular cross section lined with a thin layer of copper and open on both ends. In this latter process, which has been experimentally verified, the copper lining on the inside of the channels reduces problems associated with the migration of the working fluid throughout the semiconductor material.

In the first fabrication technique utilized in the current investigation, a series of 39 parallel rectangular channels 45 μm wide, 80 μm deep and 19.7 mm long was machined into a silicon wafer 0.378 mm thick at 500 μm intervals using a Series 1100 Micro Automation silicon dicing saw. The resulting rectangular channels are illustrated in Fig. 3. As shown, the surfaces of the rectangular grooves are covered with residue left over from the machining process and the lower corner regions are slightly rounded.

The second fabrication technique relied on orientation-dependent etching, which has been utilized extensively in semiconductor processing and was originally described in detail by Bean (1978) and Kendall (1979). The first step in this process requires the construction of a photolithographic mask with regions 120 μm wide, left open to expose the underlying silicon to the orientation dependent etch. A window below and perpendicular to the parallel lines was used to align the channel openings perpendicular to (110) flat of the wafer. Alignment of the channels perpendicular to the (110) flat simultaneously aligned the channels parallel to the intersection of the (111) planes. In this way, atomically smooth V-shaped channels could be achieved.

To produce these channels, the (100) oriented silicon wafers were first thoroughly cleaned with acetone, propanol, methanol, and finally, deionized water. After rinsing, the wafers were treated with a sulfuric acid and hydrogen peroxide solution to remove any metal or other inorganic contamination from the wafer surface. The wafers were then dipped in a buffered oxide etch solution to remove any thin native oxide films from the wafer surface. A thermal oxidation process performed at 1100°C produced an SiO_2 layer 0.8 μm thick,

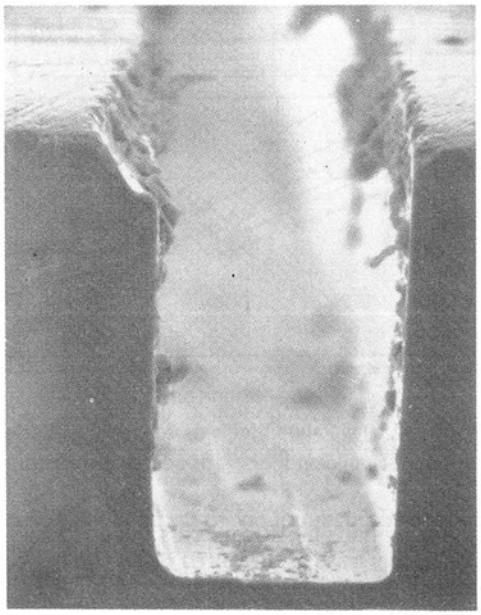

Fig. 3 SEM of the machined rectangular grooves in the silicon wafer

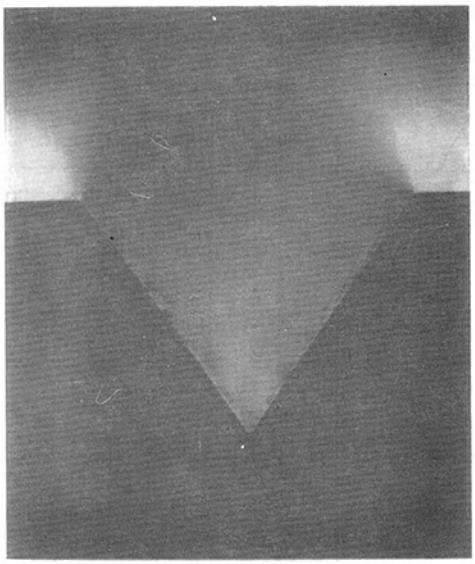

Fig. 4 SEM of etched triangular grooves in a (100) silicon wafer

which served as the mask during etching. Photoresist was applied to the front side of the wafer prior to exposure in a Karl Suss MSB3 mask aligner. After developing, the oxide was removed from the channels using a Buffered Oxide etch and the wafers were subjected to a KOH etching solution for 80 minutes at a temperature of 85°C. A cross-sectional SEM photomicrograph of the V-shaped channels is shown in Fig. 4, and clearly illustrates the resulting triangular-shaped channels and the sharp angled corner regions necessary for proper heat pipe operation. As illustrated, the triangular grooves are much smoother and the corners much better defined than in the machined rectangular channels.

Ultraviolet Bonding Process. Once the micro channels had been fabricated in the silicon wafers, a clear Pyrex cover slip 25 μm thick was bonded to the surface of each wafer to form the closed channels. Initially, both the wafers and the glass cover slips were rinsed in de-ionized water, acetone, and methanol. They were then baked at 90°C for fifteen minutes. A small amount of Norland Optical Adhesive was uniformly spread on the glass cover by spinning at 5000 rpm for 35 seconds and the silicon wafers were placed on the glass covers and aligned. The silicon wafers and glass covers were then exposed to ultraviolet light in the 320 to 380 nanometer wavelength range for approximately 150 seconds and allowed to cure for approximately twelve hours.

Heat Pipe Charging. Once fabricated, it was necessary to charge the heat pipe arrays with the correct amount of working fluid. Previous investigations have shown micro heat pipes to be extremely sensitive to flooding (Peterson, 1988, 1992) and for this reason, several different charging methods were considered. The first of these was one that is similar to the methods utilized on larger more conventional heat pipes. This technique consists of filling a small reservoir with working fluid and then evacuating the micro heat pipe array and backfilling it from the fluid reservoir. Although this procedure has proved to be quite satisfactory on larger heat pipes, some problems with the control of the working fluid inventory and noncondensible gases may occur in the smaller heat pipes under consideration here.

A second, more reliable method is to place the micro heat pipe array in a high-pressure chamber (Peterson, 1988). After evacuating the chamber, a predetermined amount of working fluid is added and the chamber is heated to a point above the critical temperature of the working fluid. In these conditions, the working fluid is in the supercritical state and exists entirely as a vapor, which barring any gravitational or temperature variation is at a relatively uniform density, distributed throughout the chamber and the individual micro heat pipes. The entire heat pipe array is then sealed while inside the chamber using an ionic or ultraviolet bonding process. When the chamber is opened and the temperature reduced, a portion of the working fluid condenses within the individual micro channels. By controlling the temperature of the pressure vessel and the quantity of the working fluid added after the initial evacuation process, the final amount of fluid in each heat pipe can be precisely controlled.

A third method, which is simpler but somewhat less accurate has been developed and used previously by Peterson et al. (1991). It consists of sealing one end of the micro heat pipe array and positioning the wafer in a vacuum chamber vertically with the open end of the micro heat pipes approximately one mm above a small charging trough. After evacuating the chamber at room temperature, the working fluid is slowly injected into the charging trough using a micro syringe. As the chamber pressure increases and approaches the saturation pressure corresponding to the chamber temperature, the working fluid forms a pool in the charging trough and wicks up into the heat pipe channels, effectively sealing off the channel and trapping pure vapor in the upper portion of the heat pipe. The micro heat pipe array can then be removed from the vacuum chamber, heated slightly, and the open ends sealed. The final amount of liquid and vapor present in the microgrooves after sealing can be controlled by varying the temperature of the wafer, the height of the wafer above the bottom of the charging trough, and the rate at which the working fluid is injected into the vacuum chamber. Preliminary tests indicated that the latter of these was the most appropriate for the current investigation and hence, all of the experimental data presented were obtained using wafers charged in this manner.

Experimental Test Procedure. A comparative technique was used to evaluate the steady-state and transient behavior of the micro heat pipe arrays. In this technique, several sets of silicon wafers, each set consisting of one wafer with the micro heat pipe array, and one without the micro heat pipe

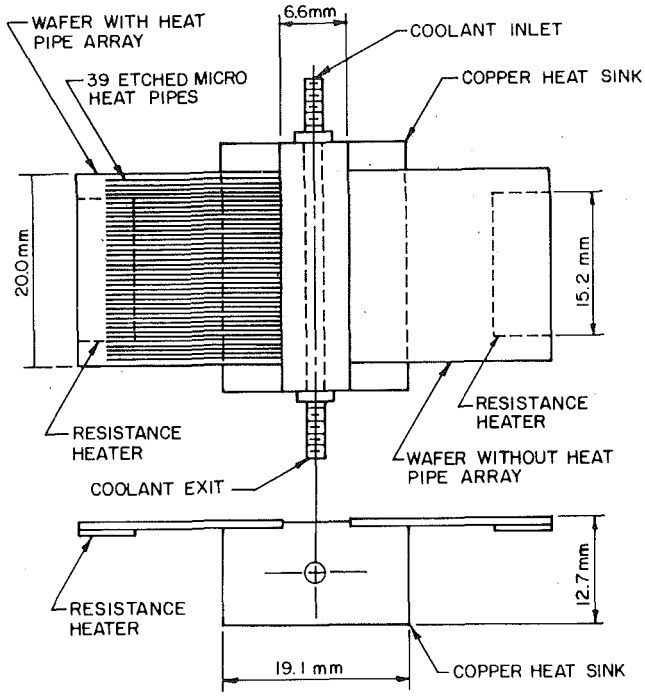

Fig. 5 Experimental test facility

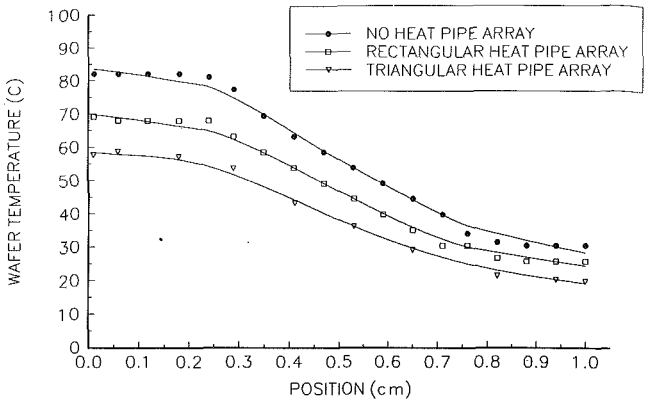

Fig. 6 Measured temperature profiles for the test wafers at an input power of 4.0 W and a sink temperature of 15°C

array, were attached to a common copper heat sink as illustrated in Fig. 5. To insure that the emissivity of the wafers was identical, a clear glass cover slip was bonded to the wafer without the micro heat pipe array in a manner similar to that previously described. Heat input was provided by a small 18.2 mm × 6 mm thermofoil heater located at one end of the heat pipe array on the surface of the wafer opposite the heat pipes, much like the active devices would be in an actual semiconductor application. The two heaters, one on each chip, were connected in parallel to insure that a constant power was supplied to each wafer, and the voltage and current were measured using digital multimeters.

As mentioned previously, heat was removed from the wafers by a common copper heat sink. This was accomplished by attaching the end of the heat pipe array opposite the heaters to the copper heat sink. A thermally conductive paste was used to enhance the heat transfer between the wafer and the copper heat sink, and coolant from a constant temperature circulating bath was pumped through the copper heat sink to maintain it at a temperature of approximately 15°C. To determine the effect of radiative and convective losses on the experimental results, early tests were conducted both in a vacuum and also in an ambient environment. However, because all the tests were conducted in a closed chamber and the temperature differences between the test wafers and the surroundings were small, these tests indicated that the convective and radiative losses were quite small and could be neglected. In addition to these preliminary tests, the sensible heat absorbed by the coolant was periodically monitored.

The temperature distribution across the surface of the two wafers was obtained using a Hughes Probeye TVS Model 3000 Infrared Thermal Imaging System. The resolution of this system as specified by the manufacturer was ±0.05°C, allowing precise determination of the temperature gradients across the chip surface provided the emissivity was known. Bonding of a clear glass cover slip to both wafers helped insure that the emissivity of the wafers with and without the micro heat pipe arrays was identical; however, it was still necessary to insure that accurate values were being used. This was accomplished by locating a copper-constantan thermocouple on the surface of test wafers within the IR camera's field of view. By comparing the temperature as measured by the thermocouple and the IR camera, accurate estimations of the emissivity could be made. Using this calibration technique, the uncertainty of the temperature values was estimated to to be within ±0.10°C.

Throughout all of the tests, the IR camera was situated so that both the wafer with the micro heat pipe array and the plain ungrooved wafer were in the field of view. In this manner, the temperature gradient and maximum wafer temperature for both wafers could be observed simultaneously for different power levels, compared, and the effectiveness of the micro heat pipe array determined. Using this technique, variations in the maximum chip temperature, the effective thermal conductivity, and the transient response were readily apparent. It is important to note that this comparative technique helped to compensate for any uncertainties introduced by inaccuracies associated with the emissivity of the wafers. Also, because a comparative technique was used, the relative temperature distribution, and hence, the thermal resolution of the IR camera was much more important to the accurate estimation of the effective thermal conductivity of the wafers than the absolute accuracy of the temperature measurements.

Results and Discussion

Figure 6 illustrates typical steady-state temperature profiles for the wafers with arrays of rectangular and triangular micro heat pipes evaluated at an input power of 4 W and a bath temperature of 15°C. Also shown for comparison is the steady-state temperature profile for a wafer without a micro heat pipe array. As expected, the maximum temperature for all of the wafers tested occurred in the region directly over the heaters, with the maximum wafer temperature and temperature gradients for the wafers with the micro heat pipe arrays considerably smaller than those obtained for the plain ungrooved wafers. At an input power 4 W, the maximum steady-state temperatures for the wafers with the micro heat pipe arrays were 68.0°C and 59.2°C for the rectangular and triangular arrays, respectively, while for the plain silicon wafer the maximum wafer temperature was 82.1°C. This resulted in decreases in the temperature gradients of approximately 11.4°C and 16.2°C, respectively. Finally, as shown, incorporating an array of 39 micro heat pipes into a 2 cm × 2 cm wafer reduced the temperature gradient or slope of the temperature profile for both the array of rectangular micro heat pipes and the array of triangular micro heat pipes. This figure gives some indication of the ability of the micro heat pipe arrays to reduce the thermal gradients or localized hot spots, which may result from highly active junctions. As a result of these reductions, significant improvements in the wafer reliability may be possible.

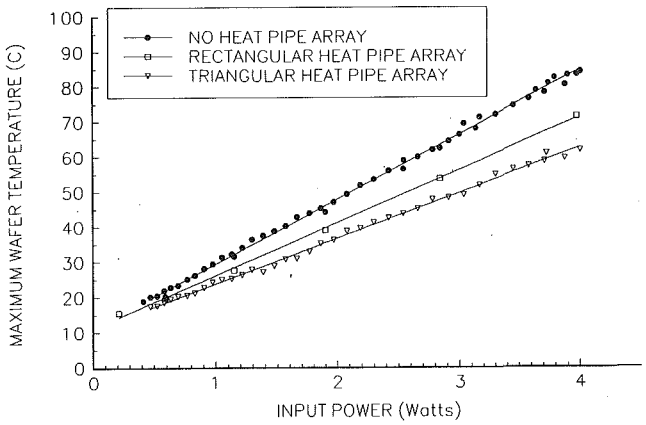

Fig. 7 Comparison of the maximum chip temperature for wafers with and without micro-heat pipe arrays as a function of input power

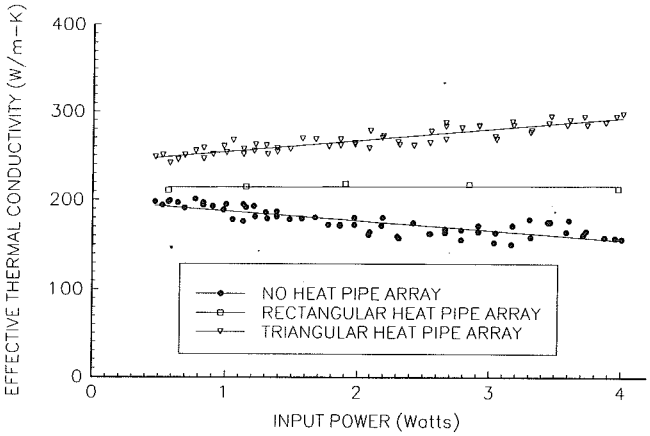

Fig. 8 Effective thermal conductivity for wafers with and without micro-heat pipe arrays at an input power of 4.0 W and a sink temperature of 15°C

To determine the effect of variations in the input power on the maximum chip temperature, a series of tests were conducted in which the cooling bath temperature was held constant at 15°C and the input power was varied incrementally. Using the IR thermal imaging system, the magnitude and location of the maximum chip surface temperature were identified and recorded. Figure 7 illustrates the results of this series of tests for the arrays of rectangular and triangular micro heat pipes and the plain ungrooved wafers. As shown, the maximum surface temperatures for the wafers with the micro heat pipe arrays were both significantly lower than those obtained for the plain ungrooved wafer. The wafer with the array of triangular micro heat pipes exhibited the lowest maximum temperature values over the entire range of input powers evaluated. The size of the source-sink temperature difference for both arrays increased in direct proportion to the input heat flux and varied from almost zero at low power levels, 0.20 W, to a difference of approximately 14.1°C for the array of rectangular micro heat pipes and 24.9°C for the wafers with the array of triangular micro heat pipes at input power levels of 4 W. This figure again illustrates the effectiveness of the micro heat pipe array and clearly indicates the types of reduction that can be expected at higher power levels prior to dryout.

In an attempt to quantify the experimental results better, additional data were taken from which an effective wafer conductivity could be computed using Fourier's law. The axial heat flux, that is, the heat transported through the wafer in the direction of the heat pipes, was computed by dividing the input power by the cross-sectional area of the wafer. This value was then divided by the average temperature gradient. This temperature gradient was obtained by computing the average temperature difference between a series of points located on the surface of the wafer directly over the heat source and the heat sink, as measured by the IR thermal imaging system. This quantity was then multiplied by the linear distance between the points at which these values were obtained. Using the methods first outlined by Kline and McClintock (1953), the experimental uncertainty associated with these values was estimated to be approximately ±7.5 percent.

As illustrated in Fig. 8, the effective thermal conductivity of the plain ungrooved silicon wafer decreased from approximately 200 W/m-°C at an input power of 0.5 W to a value of approximately 160 W/m-°C at an input power of 4.0 W. These values correspond quite well with the thermal conductivity data for silicon available in the open literature. Although the effective thermal conductivity for the plain ungrooved wafers shown in Fig. 8 is presented as a function of input power, it is clearly apparent that increases in wafer temperature result in decreases in the effective thermal conductivity. This trend is also consistent with the published thermophysical property data for silicon. In contrast, measurement of the effective thermal conductivity of the wafer with the array of rectangular micro heat pipes resulted in a nearly constant value for the effective thermal conductivity of 210 W/m-°C, while the wafer with the array of triangular micro heat pipes resulted in a linearly increasing value of approximately 250 W/m-°C at input powers of 0.5 W to 290 W/m-°C at input powers of 4.0 W. The increasing trend observed in the array of triangular micro heat pipes results from the increased driving potential, i.e., temperature gradient, occurring at higher input powers, which makes the heat pipes perform more effectively. The increased effective thermal conductivity of the wafers with micro heat pipes amounts to an increase of nearly 31 percent for the array of rectangular micro heat pipes and 81 percent for the array of triangular micro heat pipes when compared to the plain silicon wafer. The large differences observed between the machined and etched micro heat pipe arrays may be the result of a combination of the rounded corner regions, which reduce the capillary pumping pressure and increase the liquid pressure drop in the channels, and the rough scaly deposits occurring in the rectangular machined micro heat pipes.

To determine the significance of these results, estimations of the thickness of a solid copper layer required to produce the same increase in effective thermal conductivity as the micro heat pipe arrays were made. At an input power of 4 W, a silicon/copper composite wafer having a copper layer nearly equal in thickness to that of the silicon wafer would be required to achieve an effective thermal conductivity equal to that of the silicon wafer incorporating the heat pipe array. For a power input equal to 2 W, a copper substrate thickness of approximately 20 percent of the silicon wafer thickness would be required.

Although not quantified in this investigation, the experimental investigation indicated that the transient thermal response of the wafers with the micro heat pipe arrays was significantly faster than for the plain ungrooved wafers. This was true for the arrays of both rectangular and triangular micro heat pipes. In all cases, the maximum wafer temperature and steady-state temperature at the center of the wafer were achieved in a much shorter time frame for the wafers with the micro heat pipe arrays than for the plain ungrooved wafer. This trend became more evident with increasing input powers and was true for the entire steady-state temperature profile. This rapid response time is most likely due to a change in the time constant resulting from the vaporization and condensation processes occurring in the individual micro heat pipes.

Conclusions

An experimental investigation was conducted to verify the micro heat pipe concept and determine the potential advantages

of constructing arrays of rectangular or triangular micro heat pipes constructed as an integral part of semiconductor devices. Several silicon wafers were fabricated with distributed heat sources on one side and arrays of 39 micro heat pipes on the other. Using an infrared thermal imaging unit, the temperature gradients and maximum localized temperatures were measured for the wafer with the micro heat pipe array and compared with the results obtained for a plain ungrooved wafer. In this way, the magnitude of the thermal enhancement resulting from the micro heat pipe arrays could be determined.

The results of this comparison indicate that incorporating arrays of micro heat pipes as an integral part of semiconductor chips can significantly decrease the temperature gradient across the chip, decrease the maximum chip temperature, and decrease the number and intensity of localized hot spots. For silicon wafers with an array of 39 rectangular micro heat pipes 45 μm wide and 80 μm deep and a cross-sectional porosity of 1.87 percent, reductions in the maximum chip temperature of approximately 11.4°C and increases in the effective thermal conductivity of approximately 31 percent were measured for input power levels of 4 W. For silicon wafers with an array of 39 triangular micro heat pipes 120 μm wide and 80 μm deep and an cross-sectional porosity of 1.85 percent, reductions in the maximum chip temperature of 16.2°C and increases in the effective thermal conductivity of approximately 81 percent were measured for input power levels of 4 W. In addition to the reductions in maximum chip temperatures and substantial increases in the effective thermal conductivity, the incorporation of the micro heat pipe array was found to improve the transient thermal response of the wafers significantly.

While the percentage increase in the effective thermal conductivity of the wafer with the array of rectangular micro heat pipes was somewhat lower than the value predicted by Mallik et al. (1992), 40 percent, the percentage increase for the array of triangular micro heat pipes was significantly higher. The experimental results clearly indicate that while the number and cross-sectional array density of the triangular and rectangular micro heat pipe arrays are equal, the performance of the etched triangular heat pipe is significantly better. This increased performance of the triangular heat pipe array is the result of reductions in the amount of residue in the micro channels and improvements in the shape of the corner regions. As mentioned previously, increased heat flux in the evaporator causes the meniscus to recede into the corners. In the triangular heat pipes this meniscus recession causes a reduction in the capillary radius, and hence, an increase in the capillary pumping pressure. In the rectangular heat pipes the rounded corner regions prevent this decrease in the capillary radius and hence the capillary pumping pressures are smaller.

Although not addressing several important issues such as the effect of the size and shape of the micro heat pipes, the effect of variations in the heat pipe array density, and/or performance degradation with respect to time, it is clear from these results that incorporation an array of micro heat pipes as an integral part of silicon wafers can significantly improve the performance and reliability of semiconductor devices, by increasing the effective thermal conductivity, decreasing the temperature gradients, and reducing the intensity and number of localized hot spots.

Acknowledgments

The authors would like to acknowledge the support provided by the Texas Advanced Technology Program and the TAMU Center for Space Power.

References

Babin, B. R., Peterson, G. P., and Wu, D., 1990, "Steady-State Modeling and Testing of a Micro Heat Pipe," ASME JOURNAL OF HEAT TRANSFER, Vol. 112, pp. 595–601.

Bean, K. E., 1978, "Anisotropic Etching of Silicon," *IEEE Transactions on Electron Devices*, Vol. ED-25, No. 10, pp. 1185–1193.

Chyu, M. K., and Aghazadeh, M., 1987, "Modeling and Measurements of Heat Spreader Thermal Performance in Molded Plastic Packages," *Proc. Int. Symp. on Cooling Technologies for Electronic Equipment*, Honolulu, HI, Mar. 17–21, pp. 187–199.

Cotter, T. P., 1984, "Principles and Prospects of Micro Heat Pipes," *Proc. 5th Int'l. Heat Pipe Conf.*, Tsukuba, Japan, pp. 328–335.

Gerner, F. M., Longtin, J. P., Henderson, H. T., Hsieh, W. M., Ramadas, P., and Chang, W. S., 1992, "Flow and Heat Transfer Limitations in Micro Heat Pipes," ASME HTD Vol. 206, pp. 99–104.

Kendall, D. L., 1979, "Vertical Etching of Silicon at Very High Aspect Ratios," *Ann. Rev. Mater. Sci.*, pp. 373–403.

Kim, S. H., and Anand, N. K., 1992, "Turbulent Heat Transfer Between a Series of Parallel Plates With Surface-Mounted Discrete Heat Sources," *Proc. of the ASME Winter Annual Meeting*, Anaheim, CA.

Kline, S. J., and McClintock, F. A., 1953, "Describing Uncertainties in Single Sample Experiments," *Mechanical Engineering*, Vol. 75, Jan., pp. 37–43.

Mallik, A. K., Peterson, G. P., and Weichold, W., 1991, "Construction Processes for Vapor Deposited Micro Heat Pipes," presented at the 10th Symp. on Electronic Materials Processing and Characteristics, June 3–4, Richardson, TX.

Mallik, A. K., Peterson, G. P., and Weichold, M. H., 1992, "On the Use of Micro Heat Pipes as an Integral Part of Semiconductors," ASME *Journal of Electronic Packaging*, Vol. 114, No. 4, pp. 436–442.

Peterson, G. P., 1988, "Investigation of Miniature Heat Pipes," Final Report, Wright Patterson AFB, Contract No. F33615-86-C-2733, Task 9.

Peterson, G. P., Duncan, A. B., Ahmed, A. K., Mallik, A. K., and Weichold, M. H., 1991, "Experimental Investigation of Micro Heat Pipes in Silicon Devices," ASME DSC Vol. 32, pp. 341–348.

Peterson, G. P., 1992, "An Overview of Micro Heat Pipe Research," Invited Review Article, *Applied Mechanics Review*, Vol. 45, No. 5, pp. 175–189.

Swanson, L., and Peterson, G. P., 1992, "The Evaporating Extended Meniscus in a V-Shaped Channel," ASME HTD Vol. 200, pp. 9–22.

Tuckerman, D. B., and Pease, F. F., 1981, "High Performance Heat Sinking for VLSI," *IEEE Electron Device Letters*, Vol. EDL-2, pp. 126–129.

Weichold, M. H., Peterson, G. P., and Mallik, A., 1992, U.S. Patent Pending, Patent No. 5,179,043, issued Jan. 1, 1993, U.S. Patent and Trademark Office.

Wu, D., and Peterson, G. P., 1991, "Investigation of the Transient Characteristics of a Micro Heat Pipe," *AIAA Journal of Thermophysics and Heat Transfer*, Vol. 5, No. 2, pp. 129–134.

Wu, D., Peterson, G. P., and Chang, W. S., 1991, "Transient Experimental Investigation of Micro Heat Pipes," *AIAA Journal of Thermophysics and Heat Transfer*, Vol. 5, No. 4, pp. 539–545.

P. E. Phelan
University of Hawaii at Manoa,
Department of Mechanical Engineering,
Honolulu, HI 96822

O. Nakabeppu

K. Ito

K. Hijikata

Tokyo Institute of Technology,
Department of Mechanical
Engineering Science,
Tokyo 152, Japan

T. Ohmori
Ishikawajima-Harima Heavy
Industries Co., Ltd.,
Yokohama 235 Japan

K. Torikoshi
Daikin Industrial Co.,
Mechanical Engineering Laboratory,
Sakaishi 591 Japan

Heat Transfer and Thermoelectric Voltage at Metallic Point Contacts

Metallic point contacts have been extensively studied from the viewpoint of their interesting, and often nonlinear, electrical properties. Their thermal characteristics, however, have largely been ignored, even though they show great potential as microscale temperature sensors. It has been previously demonstrated that when a temperature drop exists across a point contact consisting of two identical metals, a thermoelectric voltage can be generated, provided the mean contact radius is comparable in size to the electron mean free path. In the present experimental study, a point contact is formed by pressing a sharply etched Ag whisker against either an Ag or a Cu flat plate. In addition to confirming the previous results, the feasibility of using such a point contact is demonstrated by calibrating the voltage output against the nondimensionalized plate temperature. Furthermore, the thermoelectric voltage at an Ag–Cu point contact is also presented, showing that a point contact made from dissimiliar metals is even more promising than one made from identical materials. Finally, the point-contact thermal resistance is shown to depend nonlinearly on the electrical resistance, or contact area, and on the temperature drop.

Introduction

Point-contact spectroscopy has yielded much valuable insight into the fundamental nature of electron–phonon interactions (Jansen et al., 1980; Yanson, 1983). In particular, the contact achieved by pressing a sharply etched metallic whisker against a flat surface has proven to be a convenient technique for producing a point contact (PC) having dimensions less than, or of the same order, as the electron mean free path l_e. A contact of such minute size generally gives rise to interesting nonlinear (non-Ohmic) electrical behavior. What has not, however, been thoroughly investigated is the *thermal* behavior of a PC. In particular, the PC thermal resistance has not been measured. This is of fundamental interest because in the local region surrounding the PC, the electrons and phonons, which are the primary heat carriers in solids, are not in equilibrium with each other, implying that the heat flow and thermal resistance at the PC may be substantially different from those of a contact of larger dimensions. In fact, it has already been demonstrated that a thermoelectric voltage can be generated at a PC between two identical metals, provided a temperature difference exists across the PC (Shklyarevskii et al., 1986; Bogachek et al., 1985).

Point contacts are also of considerable practical importance. For example, the dimensions of electric contacts in contemporary microelectronic circuits can be less than l_e, especially in low-temperature electronics. The heat transferred across such PCs may affect the operating temperature of some devices. Furthermore, the demonstrated thermoelectric potential at PCs suggests they could be used as enhanced thermoelectric coolers (Gerlach-Meyer, 1984), and that etched metallic whiskers may be useful as microscale temperature sensors, which would be capable of probing the temperature of the flat surface on the length scale of the whisker tip. Demonstrating the feasibility of this kind of microscale sensor, for PCs made from both similar and dissimilar metals, along with measuring the PC thermal resistance, are the primary subjects of the present investigation.

The electrical and thermal characteristics of both Ag–Ag and Ag–Cu PCs are determined experimentally by pressing an etched Ag wire against a flat plate of Ag or Cu. The experiment is conducted for temperatures ranging from nearly 80 K to room temperature using a closed-cycle refrigeration system. The results indicate that the PC thermoelectric voltage depends approximately linearly on the nondimensionalized temperature drop across the PC, and that the thermal resistance is different from that predicted earlier from an electrical analogy (Gerlach-Meyer, 1984), and becomes nonlinear as the temperature drop becomes large.

Experiment

Apparatus. The cryogenic temperatures necessary for achieving a sufficiently long l_e are achieved using a Daikin Cryo Kelvin-SL closed-cycle refrigeration system. The experimental apparatus depicted in Fig. 1 rests at the top of the refrigerator's cooling column, and is enclosed within a vacuum shroud. The 0.3-mm-thick flat plate, of either Ag or Cu, is mounted on the "low-temperature stage" and is maintained in a roughly isothermal condition, while the support for the whisker is mounted on the "high-temperature stage." The low-temperature stage is the Cu cooling finger of the closed-cycle refrigerator. In this way, a temperature drop can usually be maintained across the PC such that the heat flow is directed from the whisker down to the flat plate. Through the use of

Contributed by the Heat Transfer Division and presented at the National Heat Transfer Conference, San Diego, California, August 6–9, 1992. Manuscript received by the Heat Transfer Division April 1992; revision received January 1993. Keywords: Cryogenics, Direct-Contact Heat Transfer, Measurement Techniques. Associate Technical Editor: L. S. Fletcher.

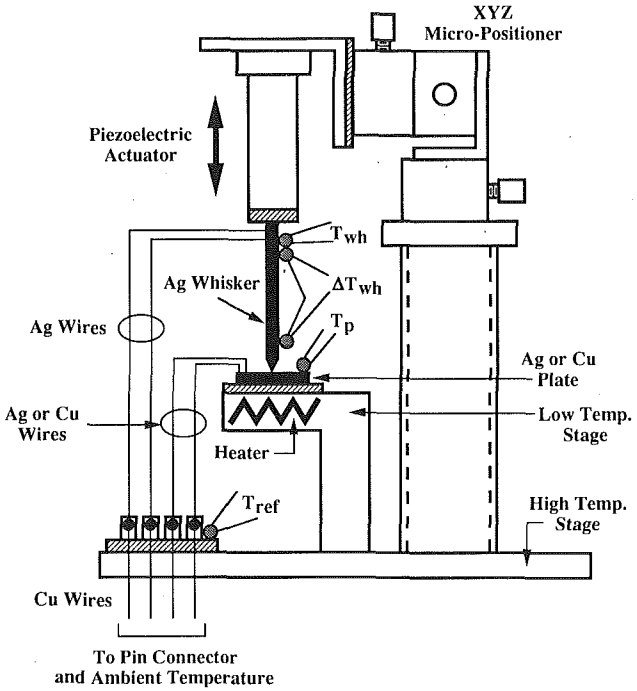

Fig. 1 Experimental apparatus

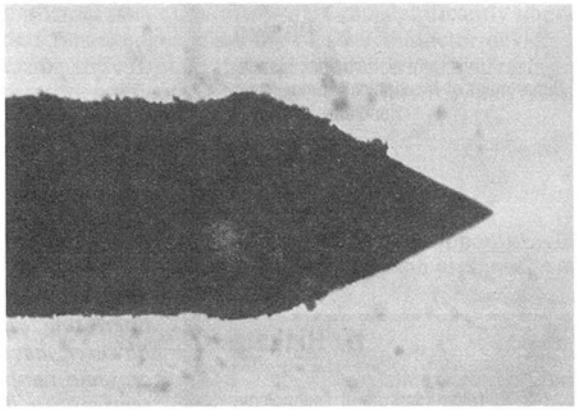

Fig. 2 Microphotograph of the etched Ag whisker. The nominal diameter of the Ag whisker is 0.3 mm.

the heater embedded in the low-temperature stage, however, the direction of the temperature drop can be reversed.

The Ag whisker is fabricated by repeatedly etching a 0.3-mm-dia Ag wire in a 3 M KOH aqueous solution, at a low voltage of 1–3 V, until the wire tip appears to be sharply pointed (Dozier and Rodgers, 1964). A microphotograph of the whisker tip before the experiments were performed is presented in Fig. 2. Note here that a relatively large-diameter Ag wire is used for the whisker; in an earlier study, the whisker diameter was only 50–100 μm (Shklyarevskii et al., 1986). The thicker wire is used here in order to simplify the attachment of the thermocouples and electrical leads, although the required etching period is lengthened compared with that for a smaller wire. The radius of contact, a, between the whisker and the flat plate, based on the electrical resistance R_{el}, varies from about 10 nm up to almost 10 μm, although as explained later these values are likely to underestimate a.

Three-dimensional manual positioning of the whisker was achieved by a vacuum-compatible micropositioner (Newport M-MT-XYZ). The vertical position was intended to be further manipulated by a piezoelectric actuator (NEC ASB009A) that offers a maximum extension of about 50 μm at room temperature. In our experimental arrangement, the whisker was first manually positioned near the flat plate while at room temperature, so that when the vacuum shroud was in place, voltage could be applied to the piezoelectric actuator to extend the whisker toward the flat plate. In practice, however, the thermal contraction due to the cryogenic operating temperatures, coupled with the decreased performance of the piezoelectric actuator, made it difficult to control the height of the whisker above the flat plate with the piezoelectric actuator. Therefore, contact was usually ensured at room temperature by firmly pressing the whisker against the flat plate with the micropositioner, and thus the point contact area could not be effectively controlled during the experiment. In retrospect, the practice of other authors (Shklyarevskii et al., 1986), who controlled the vertical positioning of the whisker by a differential screw mechanism, appears to be more practical. Our problems with whisker positioning during the experiment could perhaps also be remedied through the use of a remotely controlled micropositioner.

The thermocouples are all Au + 0.07 percent Fe/chromel. Referring to Fig. 1, T_{wh}, T_p, and T_{ref} are ordinary thermocouples, while ΔT_{wh} is a differential thermocouple, in which the middle loop is composed of chromel. The length of the Ag whisker between the two junctions of ΔT_{wh} is 31.5 mm.

Nomenclature

a = mean radius of the point contact area, m
A = whisker shaft cross-sectional area, m^2
e = magnitude of an electron's charge = 1.602×10^{-19} C
h = distance between the lower junction of ΔT_{wh} and the point contact, m
k = thermal conductivity, W m^{-1} K^{-1}
L = whisker length between T_{wh} and the point contact, m
l_e = electron mean free path, m
m = electron rest mass = 9.110×10^{-31} kg
N = electron number density, m^{-3}
q = heat flow in the whisker, W
r = electrical resistivity, Ω m
R_{el} = point-contact electrical resistance, Ω
R_{th} = point-contact thermal resistance, K W^{-1}
S = absolute thermopower, V K^{-1}
S^e = component of S due to electron diffusion, V K^{-1}
S^{ph} = component of S due to phonon drag, V K^{-1}
T = temperature, K
T_p = plate temperature (Fig. 1), K
T_l = temperature at the lower junction of ΔT_{wh}, K
T_{ref} = temperature at the junction of the voltage and current leads to Cu wires (Fig. 1), K
T_{wh} = upper whisker temperature (Fig. 1), K
v_f = Fermi velocity, m s^{-1}
V = voltage across the point contact, V
ΔT = temperature jump across the point contact, K
ΔT_{wh} = temperature difference along the Ag whisker (Fig. 1), K
θ_D = Debye temperature, K

Subscripts

Ag = silver
avg = average value
Cu = copper
pc = point contact

The combination of a differential thermocouple and two ordinary thermocouples allows both the temperature drop at the point contact, ΔT, and the heat flow in the Ag whisker, q, to be determined. The thermocouples T_{wh} and ΔT_{wh} are made from 76-μm-dia wire, while the other thermocouples are made from 203-μm-dia wire. The thermocouples are mounted using GE7031 Varnish, which provides for good thermal contact, but still electrically insulates the thermocouples from their mounts.

The wires connecting the whisker and the plate to the junction mounted on the high-temperature stage are composed of the same material as the whisker and the plate, respectively. For example, an Ag plate is connected with Ag wires, but a Cu plate is connected with Cu wires. This makes T_{ref} the "reference temperature," but actually this temperature is only important when the Ag whisker is used with a Cu plate, as will be discussed later. The reference point for all the thermocouples is the pin connector at the vacuum shroud, the temperature of which is measured with a conventional Type T thermocouple.

The various output voltages are monitored with an Eto Electric Co. Thermodac III Thermal Data Acquisition System. The reported accuracy of this device is ± 5 μV.

Procedure. Data are taken both while the refrigerator is cooling down and while it is heating up, which provides a variety of temperature differences across the point contact. At a given temperature, the measurement sequence progresses in this way: The PC electrical resistance R_{el} is determined using a four-wire technique and an electrical current I of usually 10 mA. The voltage across the PC (V), I, and the thermocouple voltages are all recorded at this time. Immediately afterward, the current is switched off so that the thermoelectric voltage (if any) can be monitored, and again V and the thermocouple voltages are recorded. The two sets of thermocouple voltages are averaged to give the temperature data provided below, although the difference between the two sets of thermocouple readings is always within the accuracy of the measurement system.

Originally, it was desired to vary R_{el} (at a given temperature) by controlling the whisker height through the piezoelectric actuator. However, as mentioned above, in practice this proved to be nearly impossible. Thus, generally data were obtained for only one value of R_{el} at any given temperature.

Uncertainty. The uncertainty analysis is conducted in the manner described by Holman (1984). The thermocouples are calibrated against a Pt resistance thermometer to within ± 0.5 K. Using this value and taking into account the other inaccuracies gives maximum uncertainties of ± 1 mW for the heat flux, ± 162 K W^{-1} for the thermal resistance, and ± 5 mΩ for the electrical resistance. The voltage uncertainty is determined by the accuracy of the data acquisition system (± 5 μV). In Figs. 3–6, error bars are given for representative data points.

Calculation of the Desired Results

The desired output parameters are the thermoelectric voltage V, the PC electrical resistance R_{el}, the plate temperature T_p, the PC temperature drop ΔT, the whisker heat flow q, and the PC thermal resistance R_{th}. The quantities V and T_p are determined directly from the measurements, but some calculation is required for the others.

Whisker Heat Flow q. The whisker heat flow can be calculated from T_{wh}, $T_1 = T_{wh} - \Delta T_{wh}$ (the temperature at the lower junction of ΔT_{wh}), and k_{Ag}, the temperature-dependent thermal conductivity of silver:

$$q = \frac{A}{\Delta x}\int_{T_1}^{T_{wh}} k_{\text{Ag}}\,dT \tag{1}$$

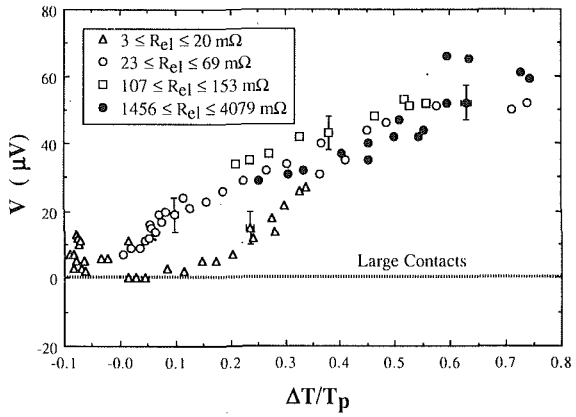

Fig. 3 Thermoelectric voltage generated at an Ag-Ag point contact

where A is the whisker cross-sectional area and Δx is the distance between the junctions of ΔT_{wh} (31.5 mm). Values for k_{Ag} as a function of temperature are given by Touloukian et al. (1970).

Point-Contact Temperature Drop ΔT. The plate temperature T_p is already known, but the temperature of the whisker just above the constriction of the whisker tip must be extrapolated from T_1:

$$T_p + \Delta T = T_1 - \frac{qh}{k_{\text{Ag}}A} \tag{2}$$

where h is the distance between the lower junction of ΔT_{wh} and the PC (4 mm). Here, k_{Ag} is evaluated at T_1. The PC temperature drop ΔT, which includes the temperature drop across the constriction of the whisker tip, can be determined directly from Eq. (2).

Point-Contact Thermal Resistance R_{th}. The PC thermal resistance is defined and calculated in the following manner:

$$R_{th} = \frac{\Delta T}{q} \tag{3}$$

Point-Contact Electrical Resistance R_{el}. The relatively long distance between the whisker current and voltage taps and the PC (35.5 mm) can result in the resistance of the whisker itself becoming a significant fraction of the measured electrical resistance across the point contact. In the results for R_{el} given below, the whisker resistance is subtracted from the measured resistance R_m:

$$R_{el} = R_m - \frac{r_{\text{avg}}L}{A} \tag{4}$$

in which

$$r_{\text{avg}} = \frac{1}{T_{wh} - (T_p + \Delta T)}\int_{T_p+\Delta T}^{T_{wh}} r_{\text{Ag}}\,dT \tag{5}$$

where r_{avg} is the average resistivity, r_{Ag} is the electrical resistivity of bulk silver, and L is the whisker length (35.5 mm). Values of r_{Ag} as a function of temperature are taken from Hellwege (1982).

Results and Discussion

Representative data of the thermoelectric voltage generated at an Ag-Ag PC are presented in Fig. 3. The voltage is plotted versus the nondimensional PC temperature drop $\Delta T/T_p$, with the PC electrical resistance being treated as a variable parameter. Horizontal and vertical error bars are given for one point in each set. For contrast, the thermoelectric voltage for large contacts, which is exactly zero, is also given. The plotted data

represent the results of several experimental runs conducted on different days, where the set of data for a given range of R_{el} includes all the data for that range of R_{el}. From the figure, it can be concluded that the PC thermoeletric voltage increases with $\Delta T/T_p$, at least for the measured temperature range (85 K $< T_p <$ 307 K, 0.8 K $< |\Delta T| <$ 75.5 K).

Converting the measured thermoelectric voltages into the absolute PC thermopower S_{pc} would be the best way of presenting the data. However, that transformation is not practical in the present case, since the temperatures on both sides of the PC are allowed to vary, so that it is impossible to determine a unique value of S_{pc} for each measured voltage. Therefore, an alternative method of nondimensionalizing the temperature drop, as shown in Fig. 3, had to be developed. Nondimensionalizing the temperature drop in this manner is convenient if the PC is to be employed to measure the local temperature of the flat plate. Once a calibration curve for a particular value of R_{el} is identified, which can be based not only on the temperature drop just across the PC, but, for instance, on the temperature drop between the flat plate and the top of the whisker, the measured PC thermoelectric voltage and electrical resistance determines a unique value of $\Delta T/T_p$. For example, $\Delta T/T_p$ can be expressed as $(T_{wh} - T_p)/T_p$, where T_{wh} is *known* independently. The plate temperature T_p can then be easily calculated from the measured V and the appropriate calibration curve, since T_p is the only remaining unknown parameter.

A qualitative explanation for the thermoelectric voltage at a PC between identical metals having dimensions comparable to l_e has been presented (Shkylarevskii et al., 1986; Bogachek et al., 1985). The absolute thermopower S of a bulk metal has two primary contributions:

$$S = S^e + S^{ph} \tag{6}$$

where S^e represents the component of S due to electron diffusion, and S^{ph} is the component due to "phonon drag." Electron diffusion in the presence of a temperature gradient along a bulk metal gives rise to a measurable thermopower because the electrons at the higher temperature diffuse faster than the electrons at the lower temperature, leading to an excess number of electrons at the lower-temperature portion of the metal, and hence produces an electric field. On the other hand, "phonon drag" describes the effect caused by the interaction between phonons and electrons in a temperature gradient. The temperature gradient results in a flow of phonons from the higher to the lower-temperature regions. The phonons scatter, or collide, with the electrons, and thus transfer part of their momentum to the electrons. These electrons will then have a preferential momentum directed toward the lower-temperature region, leading again to an excess number of electrons at that point and a subsequent electric field.

In our experimental arrangement for the Ag–Ag PC, the measured voltage can be generally described by (Shklyarevskii et al., 1986)

$$V = \int_{T_p}^{T_p+\Delta T} (S_{\mathrm{Ag}} - S_{pc})\, dT \tag{7}$$

If we assume that S_{pc} also has two primary components, S^e_{pc} and S^{ph}_{pc}, Eq. (7) can be written as

$$V = \int_{T_p}^{T_p+\Delta T} [(S^e_{\mathrm{Ag}} + S^{ph}_{\mathrm{Ag}}) - (S^e_{pc} + S^{ph}_{pc})]\, dT \tag{8}$$

According to the theory (Shklyarevskii et al., 1986; Bogachek et al., 1985), at temperatures much less than the Debye temperature θ_D, S^e_{AG} and S^e_{pc} effectively cancel each other, leaving the voltage to be described by the difference between S^{ph}_{Ag} and S^{ph}_{pc}. However, if the PC has dimensions comparable to, or less than, l_e, the interaction between the electrons and the phonons, along with S^{ph}_{pc}, will be significantly reduced. Thus, by this argument V is essentially the integral of S^{ph}_{Ag} from T_p to $T_p + \Delta T$. The generally consistent trend for the thermoelectric voltage to increase with increasing nondimensionalized temperature suggests the potential for using an individually calibrated PC as a microscale temperature sensor.

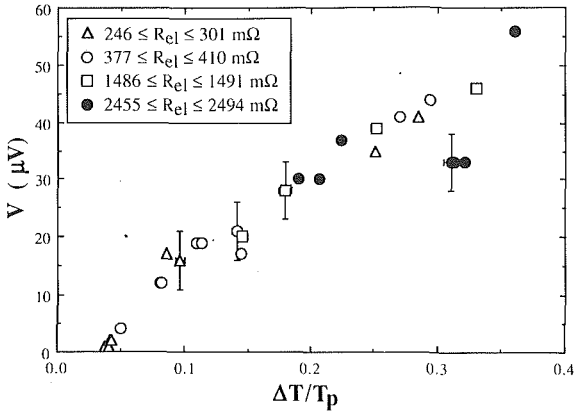

Fig. 4 Thermoelectric voltage generated at an Ag–Cu point contact. The whisker is Ag, while the plate is Cu.

There are potential advantages to be gained by using a PC consisting of two different metals, i.e., the whisker is made of one metal, while the plate is made of another. In such a case, the usual thermoelectric voltage generated at a junction of dissimilar metals is *added* to the effect of the point contact. For example, in our experimental arrangement for a Cu plate contacting an Ag whisker (see Fig. 1),

$$V = \int_{T_{\mathrm{ref}}}^{T_p} (S_{\mathrm{Ag}} - S_{\mathrm{Cu}})\, dT + \int_{T_p}^{T_p+\Delta T} (S_{\mathrm{Ag}} - S_{pc})\, dT \tag{9}$$

which suggests that for optimized choices of the two metals and T_{ref}, the PC thermoelectric voltage can be substantially enhanced.

The thermoelectric voltage produced by such an Ag–Cu PC is presented in Fig. 4. With few exceptions, V exhibits a very consistent linear increase with increasing $\Delta T/T_p$. In fact, the data tend to lie on the same line, even though R_{el} varies by an order of magnitude. It is important to note here that because of our experimental arrangement, T_{ref} did not differ from T_p by more than 18 K, thus decreasing the potential for the first term in Eq. (9) to significantly increase the measured voltage. It is difficult to include a meaningful curve in Fig. 4 of the bulk contribution to V, that is, of the first integral in Eq. (9), since T_{ref} varied considerably throughout the experiment. An estimate of the maximum bulk contribution is about 7 μV, suggesting that S_{pc} for the Ag/Cu PC must be different from that for the Ag/Ag PC. The data in Fig. 4 indicate further experiments should be performed in which $|T_p - T_{\mathrm{ref}}|$ should be made as large as possible, along with choosing metals for the PC having a large difference in their absolute thermoelectric power.

The point-contact thermal resistance is plotted versus the point-contact electrical resistance in Fig. 5. Both sides of the contact are Ag. The calculated line is the theory of Gerlach-Meyer (1984), which predicts that for the entire range of l_e/a, where a is the mean contact radius, the ratio of the PC electrical (R_{el}) and thermal (R_{th}) resistances is constant and is given by

$$\frac{R_{th}}{R_{el}} = \frac{1}{r_{\mathrm{Ag}} k_{\mathrm{Ag}}} \tag{10}$$

Here, average values of r_{Ag} and k_{Ag} are assumed: $r_{\mathrm{Ag}} \cong 9.6 \times 10^{-9}$ Ω m, and $k_{\mathrm{Ag}} \cong 433$ W K^{-1} m^{-1}. From the figure, the data and the theory diverge as R_{el} increases. Since R_{el} is inversely related to the contact area (Gerlach-Meyer, 1984),

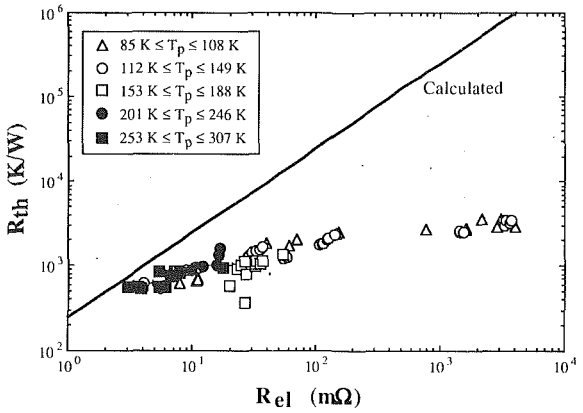

Fig. 5 Thermal resistance versus electrical resistance for an Ag–Ag point contact. The calculated line is from Eq. (10) in the text.

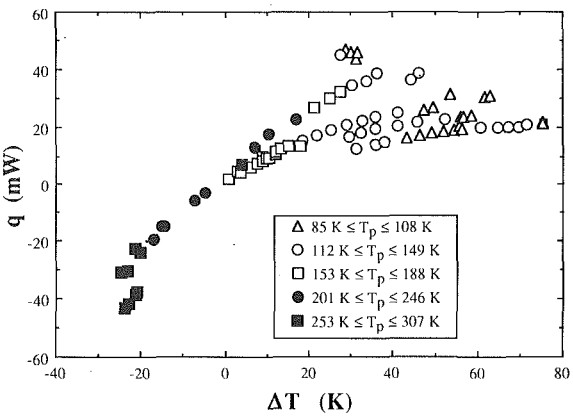

Fig. 6 Whisker heat flow versus temperature drop for an Ag–Ag point contact

Eq. (10) appears to be unsatisfactory as l_e/a becomes large. Assuming that the metal surfaces are free of any oxide layers, the contact radius a can be estimated using either of two formulae (Gerlach-Meyer, 1984):

$$\frac{l_e}{a}\to 0: \quad a=\frac{r_{\mathrm{Ag}}}{2R_{el}} \tag{11a}$$

$$\frac{l_e}{a}\to \infty: \quad a=\sqrt{\frac{4r_{\mathrm{Ag}}l_e}{3\pi R_{el}}} \tag{11b}$$

Equation (11a) is good for large contacts, while Eq. (11b) is good for small contacts. Using $r_{\mathrm{Ag}} \cong 9.6 \times 10^{-9}\ \Omega$ m, which is a mean value for the temperature range of Fig. 5, and employing the Drude relation

$$rl_e=\frac{mv_f}{Ne^2} \tag{12}$$

where m is the electron rest mass, v_f is the Fermi velocity, N is the electron number density, and e is the electron charge, gives l_e = 88 nm, where in this calculation the values of N (5.85×10^{28} m^{-3}) and v_f (1.39×10^6 m s^{-1}) appropriate for Ag at room temperature are taken from Kittel (1986). Picking a typical value for R_{el}, say, R_{el} = 100 mΩ, yields a = 48 nm (l_e/a = 1.8) from Eq. (11a), and a = 46 nm (l_e/a = 1.9) from Eq. (11b). However, in light of the assumption of perfectly clean metal surfaces, these estimates of a are expected to be much less than the actual value of a, since the presence of an oxide layer contributes significantly to R_{el}.

Equation (10) relating R_{th} and R_{el}, which was derived by assuming a direct analogy between the PC electrical and thermal resistances (Gerlach-Meyer, 1984), is apparently not valid for the present data, especially for small contact areas. One possible explanation of the discrepancy lies in the probable existence of a nonconducting oxide layer at the surface of the Ag plate. The additional electrical resistance due to an oxide layer is not considered by the theory, and thus for a given value of R_{th}, R_{el} should be larger than what the theory predicts, as indicated in Fig. 5. Indeed, it has been proposed that electron tunneling through a surface oxide layer can cause a thermoelectric voltage between contacting identical metals in the presence of a temperature gradient (Majumdar, 1992). At this time it is unclear whether the measured thermoelectric voltages are due to electron tunneling through the oxide layer, reduction of the phonon drag in the vicinity of the point contact, or a combination of both mechanisms.

Finally, Fig. 6 shows how q varies with ΔT for various temperatures. Both sides of the contact are Ag. Horizontal and vertical error bars are included for selected points, but are not visible on this scale. The point-contact electrical resistance is not held constant. The data suggest that q depends linearly on ΔT for small values of ΔT (-20 K $\le \Delta T \le$ 20 K), but becomes nonlinear as ΔT increases. There may be some effect of the plate temperature, since no single group of data spans the entire range of ΔT, but this does not seem to explain the entire deviation from the linear behavior. It appears, then, that R_{th} is roughly constant for -20 K $\le \Delta T \le$ 20 K, but increases rapidly for $\Delta T >$ 20 K. This result is of crucial importance in the thermal design of any application involving heat transfer through point contacts; if the temperature drop is relatively high, the thermal resistance will be much higher than that in the linear regime.

Conclusions

The thermoelectric voltage and heat transfer at Ag–Ag and Ag–Cu point contacts are investigated experimentally by pressing a sharply etched Ag whisker onto a flat plate. It is verified that a thermoelectric voltage is generated at a point contact between identical metals. The potential of metallic point contacts, especially those composed of dissimilar metals, to be used as microscale temperature sensors is demonstrated. In particular, a convenient method of expressing the thermoelectric voltage is to plot the voltage against the point-contact temperature drop divided by the plate temperature. In this way, provided the temperature is known somewhere in the whisker, the thermoelectric voltage can be calibrated against the plate temperature for a given point-contact electrical resistance. Point contacts constructed from dissimilar metals are especially promising because the normal Seebeck effect is added to the point-contact thermoelectric voltage, and thus the voltage output of the point-contact will be increased through proper choice of reference temperature and junction metals.

The dependence of the point-contact thermal resistance on the electrical resistance differs substantially from a theoretical relation presented by Gerlach-Meyer (1984), which assumes an analogy between electrical and thermal resistance. The discrepancy is especially large for high electrical resistances where the point-contact area is very small. A new theoretical description of point-contact thermal resistance—one that takes into account the surface oxide layer that is inevitably present—is apparently required.

Finally, it is demonstrated that the heat flow across the point contact depends linearly on the temperature drop for small temperature drops, but becomes nonlinear for large temperature drops. From this behavior, it can be judged that the thermal resistance at the point contact is approximately constant for small temperature drops, but outside of this linear regime increases rapidly with increasing temperature drop. This

result suggests that the thermal resistance, for large temperature drops, of devices containing small heat transfer contact surfaces, like those found in microelectronic circuits, may be underestimated if the thermal design only considers their linear behavior.

Acknowledgments

The authors express their appreciation to Daikin for the contribution of their closed-cycle cryogenic refrigeration system. One of the authors (P.E.P.) also wishes to thank the Japan Society for the Promotion of Science and the Japan Ministry of Education for their financial support.

References

Bogachek, E. N., Kulik, I. O., Omel'yanchuk, A. N., and Shkorbatov, A. G., 1985, "Drag-Related Thermo-EMF in Metallic Systems Containing a Point Contact," *JETP Letters*, Vol. 41, pp. 633–636.

Dozier, J. W., and Rodgers, J. D., 1964, "Electrolytic Pointing of Fine Wires," *IEEE Transactions on Microwave Theory and Techniques*, Vol. 12, p. 360.

Gerlach-Meyer, U., 1984, "Asymmetric Joule Heat Production at a Point Contact," *Applied Physics A*, Vol. 33, pp. 161–165.

Hellwege, K.-H., ed., 1982, *Landolt-Bornstein*, Vol. III/15a, Springer-Verlag, Berlin, pp. 13–15.

Holman, J. P., 1984, *Experimental Methods for Engineers*, 4th ed., McGraw-Hill, New York, p. 50.

Jansen, A. G. M., van Gelder, A. P., and Wyder, P., 1980, "Point-Contact Spectroscopy in Metals," *Journal of Physics C*, Vol. 13, pp. 6073–6118.

Kittel, C., 1986, *Introduction to Solid State Physics*, 6th ed., Wiley, New York, p. 134.

Majumdar, A., 1992, "Quantum Heat Transport by Electron Tunneling," *Heat Transfer on the Microscale*, K. S. Udell, R. O. Buckius, and F. M. Gerner, eds., ASME HTD-Vol. 200, pp. 71–77.

Shklyarevskii, O. I., Jansen, A. G. M., Hermsen, J. G. H., and Wyder, P., 1986, "Thermoelectric Voltage Between Identical Metals in a Point-Contact Configuration," *Physical Review Letters*, Vol. 57, pp. 1374–1377.

Touloukian, Y. S., et al., eds., 1970, *Thermophysical Properties of Matter*, Vol. 1, IFI/Plenum, New York, p. 63.

Yanson, I. K., 1983, "Point-Contact Spectroscopy of the Electron-Phonon Interaction in Pure Metals," *Soviet Journal of Low Temperature Physics*, Vol. 9, pp. 343–360.

Journal of Heat Transfer

Technical Notes

This section contains shorter technical papers. These shorter papers will be subjected to the same review process as that for full papers

Thermal Contact Resistance Between Two Flat Surfaces That Squeeze a Film of Lubricant

A. Bejan[1, 2] and Al. M. Morega[2]

Nomenclature

b = fluid mechanics dimensionless group, Eqs. (7) and (12)
c = fluid specific heat at constant pressure
F' = force per unit length
g = gravitational acceleration
G = heat transfer dimensionless group, Eq. (27)
h = film thickness
h_0 = initial film thickness
H = dimensionless film thickness $= h/h_0$
k = fluid thermal conductivity
L = length, Fig. 1
m'' = mass per unit area
P = pressure
P_0 = ambient pressure
q'' = instantaneous heat flux
q_* = heat flux when the film is absent, Eq. (28)
Q'' = time-integrated heat transfer interaction, Eq. (30)
Q_* = time-integrated heat transfer interaction when the film is absent, Eq. (31)
R = disk radius
t = time
t_f = time scale of free fall
t_v = time scale of viscous damping, Eqs. (6) and (12)
T = temperature
T_s = film–solid interface temperature, Fig. 1
T_0 = temperature of isothermal solid, Fig. 1
T_∞ = initial temperature of lower solid, Fig. 1
ΔT = temperature difference scale $= T_0 - T_\infty$
u, v = velocity components in the (x, y) directions
x, y = Cartesian coordinates, Fig. 1
α = fluid thermal diffusivity
η = solid similarity variable $= y/(\alpha_s t)^{1/2}$
θ = dimensionless solid temperature, Eq. (19)
θ_s = dimensionless film–solid interface temperature, Eq. (19)
μ = viscosity
ρ = fluid density
τ = dimensionless time $= t/t_v$, Eqs. (10) and (13)
φ = instantaneous insulation factor, Eq. (29)
Φ = integral insulation factor, Eq. (32)
$( )_s$ = solid

[1]J. A. Jones Professor of Mechanical Engineering; Fellow ASME.
[2]Department of Mechanical Engineering and Materials Science, Duke University, Durham, NC 27708-0300.

Contributed by the Heat Transfer Division of The American Society of Mechanical Engineers. Manuscript received by the Heat Transfer Division March 1992; revision received March 1993. Keywords: Conduction, Materials Processing and Manufacturing Processes, Thin Film Flow. Associate Technical Editor: L. S. Fletcher.

1 Objective

In this paper we describe the most fundamental features of the time-dependent transfer of heat between two bodies that make contact across a thin film of lubricating fluid. The fluid is gradually squeezed out of the contact region as the two bodies are pressed against each other. This type of thermal contact resistance (i.e., wet, or lubricated) is extremely common, for example, in the valves and seats and many other parts of reciprocating engines. The most accessible (i.e., slowest) visualization of the lubricated thermal contact occurs during the making of multiple copies on an office copy machine: Each new copy (a hot sheet) falls on the stack of older copies (cold), while floating on a thin layer of air. The modern research on thermal contact resistance was reviewed by Fletcher (1978) and Yovanovich (1986), who showed that the thermal resistance associated with time-dependent contact has been documented only for circumstances where the contact area is dry.

2 The Fluid Mechanics Problem

Consider first the contact made by a plane two-dimensional body with another plane body covered with a film of fluid. The two bodies are pressed against one another with a constant (steady) force. The spacing between the two plane surfaces and the constant force are illustrated by the model presented in the upper left corner of Fig. 1. The first surface is modeled as a rigid horizontal plate that is constantly pushed down by the constant force of gravity. The second surface is the horizontal base plane $y = 0$. The plate is initially horizontal at the height h_0, which is much smaller than the plate length L. The fluid trapped between the plate and the base is squeezed to the left ($x < 0$) and the right ($x > L$) as the plate falls.

The $t \to \infty$ (or $h \to 0$) limit of this flow is a classical solution known in the field of tribology (Stefan, 1874; Cameron, 1981; Fuller, 1984). We use this opportunity to generalize this solution to shorter times that begin with the moment $t = 0$ when the top plate begins to move. The Reynolds-simplified momentum equation (e.g., Batchelor, 1967) and the no-slip conditions ($u = 0$, at $y = 0$, h) yield

$$u(x, y, t) = \frac{1}{2\mu}\frac{\partial P}{\partial x}(y^2 - hy) \tag{1}$$

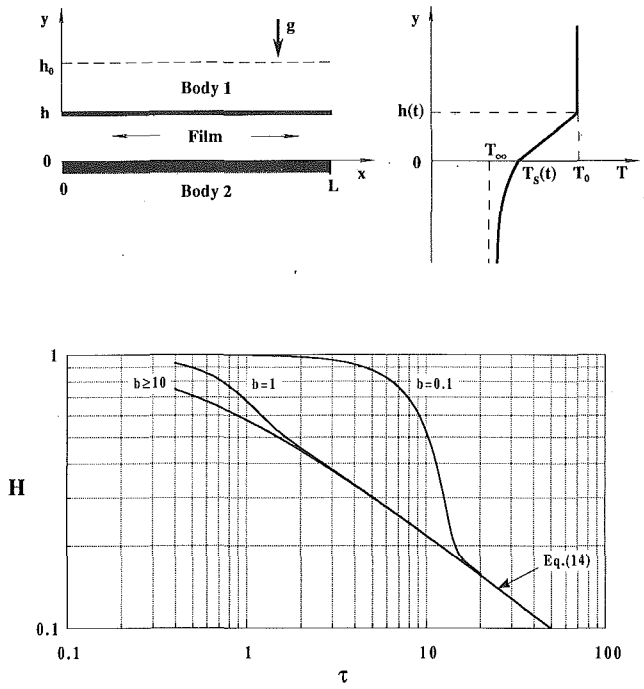

Fig. 1 Two-dimensional film squeezed by two flat surfaces that are pressed against one another (top), and the general solution for the evolution of the film thickness (bottom)

in which $P=P(x, t)$. By integrating the mass conservation equation across the gap, combining it with Eq. (1), integrating twice in x subject to the ambient pressure condition $P=P_0$ at the two openings ($x=0$ and $x=L$), we obtain

$$P(x, t)-P_0=(x^2-Lx)\frac{6\mu}{h^3}\frac{dh}{dt} \tag{2}$$

The total force (per unit length) supported by this pressure excess is given by the integral

$$F'=\int_0^L (P-P_0)dx=\mu\left(\frac{L}{h}\right)^3\left(-\frac{dh}{dt}\right) \tag{3}$$

Let m'' represent the plate mass per unit area, or $m''gL$ the force with which one body is being pressed against the other. The vertical motion of the plate is governed by Newton's second law,

$$m''L\frac{d^2h}{dt^2}=F'-m''Lg \tag{4}$$

which reveals two characteristic time scales. In the beginning, when the motion starts from rest ($dh/dt=0$), the damping force F' is smaller than the weight $m''Lg$. The time in which the height h_0 would be traveled is the Galilean (free fall) time scale

$$t_f=\left(\frac{h_0}{g}\right)^{1/2} \tag{5}$$

Later on, when the plate almost touches the base, the left-hand side (inertia term) of Eq. (4) is negligible, and the time scale is governed by the viscous flow in the gap,

$$t_v=\frac{\mu}{m''g}\left(\frac{L}{h_0}\right)^2 \tag{6}$$

The ratio of the two time scales is the new dimensionless group

$$b=\frac{t_v}{t_f}=\frac{\mu L^2}{m''h_0^{5/2}g^{1/2}} \tag{7}$$

The order of magnitude of this group distinguishes between motions that approach the free fall limit ($b<<1$), and motions that are controlled by the viscosity of the fluid squeezed in the gap ($b>>1$).

The problem that describes the vertical motion of the plate can be nondimensionalized as

$$\frac{1}{b^2}\frac{d^2H}{d\tau^2}+\frac{1}{H^3}\frac{dH}{d\tau}+1=0 \tag{8}$$

$$H=1, \text{ and } \frac{dH}{d\tau}=0 \text{ at } \tau=0 \tag{9}$$

where

$$H(\tau)=\frac{h(t)}{h_0} \text{ and } \tau=t\frac{m''g}{\mu}\left(\frac{h_0}{L}\right)^2 \tag{10}$$

One contribution of this formulation is that it shows that the known long-time limit corresponds to the range $b>>1$. In this limit the first term in Eq. (8) can be neglected, and, subject to the initial condition $h=h_0$ at $t=0$, the solution is expressible analytically

$$H=(2\tau+1)^{-1/2} \tag{11}$$

The solution to the complete problem, Eqs. (8)–(10), was obtained numerically and is described below.

The case where the surface of body No. 1 (Fig. 1) is shaped as a disk of radius R can be analyzed in a step-by-step identical way. Due to space limitations, we report only the conclusion: The problem that must be solved to determine the spacing history $h(t)$ can be stated in terms of exactly the same Eqs. (8) and (9), provided the b and t_v definitions (7) and (6) are replaced with

$$b=\frac{3\mu R^2}{2m''h_0^{5/2}g^{1/2}}, \quad t_v=\frac{3\mu}{2m''g}\left(\frac{R}{h_0}\right)^2 \tag{12}$$

This means that when the contact area is a plane disk, the dimensionless time $\tau=t/t_v$ is defined by the relation

$$\tau=t\frac{2m''g}{3\mu}\left(\frac{h_0}{R}\right)^2 \tag{13}$$

The $H(\tau, b)$ solution to Eqs. (8) and (9) is presented in the lower part of Fig. 1. The Cauchy problem for this nonlinear ordinary differential equation was solved numerically by using an adaptive, 4/5-order Runge–Kutta with error per time step (EPS) control scheme. The local truncation error was set to 10^{-6} for the entire integration interval, $0 \le \tau \le 50$. Figure 1 confirms the scaling conclusions reached in this section. When $t_f>t_v$ (or $b<1$), the film thickness evolves according to two different regimes, free fall ($t<t_f$, or $\tau<b^{-1}$) followed by viscous damping ($t>t_f$, or $\tau>b^{-1}$). Only in the viscous damping regime does the H versus τ curve approach Eq. (11).

3 Experiment

The flow determined in section 2 was tested using the apparatus sketched in Fig. 2. A smaller apparatus had been used by Needs (1940) to test the $t\to\infty$ limit. In Fig. 2, a layer of highly viscous fluid (honey or corn syrup) was squeezed between two horizontal sheets of glass. Seen from above, the lower sheet was shaped as a square with a side of 55 cm, and served as the bottom of an enclosure made of 1-cm-thick Plexiglas sheet. The upper glass sheet was a 39-cm-dia disk glued to a similar disk of Plexiglas, and mounted perpendicularly on a 5-cm-thick teflon shaft. The latter could slide vertically (with negligible lateral play) through a carefully machined sleeve attached to the lid of the square-based enclosure. The shaft and disk assembly was loaded at the top with an axial weight, to reduce the buoyancy effect due to the gradual sinking of the disk into the viscous fluid.

Each experiment consisted of: (1) bringing the disk in contact with the free surface of the fluid, (2) releasing the shaft man-

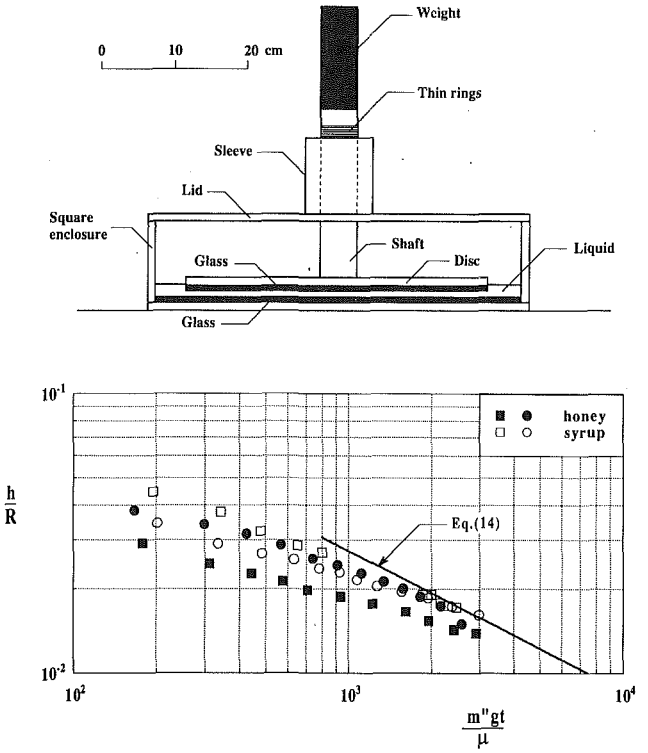

Fig. 2 Experimental apparatus, and a comparison between four sets of $h(t)$ measurements and the asymptote Eq. (14)

ually, and (3) recording photographically the instantaneous distance h between the glass sheets versus time. The vertical motion was monitored by focusing the camera on a set of markers (thin rings, 2 mm apart) cut into the teflon shaft. The experiment was designed to be "large" and "slow" (the drop would last approximately one minute), to guarantee a high accuracy for the h measurement versus t. The time measurement was accurate within 0.1 s: It was indicated by a digital stopwatch attached to the shaft, and photographed along with the thin rings. The h measurement was accurate within 0.1 mm, as the photographs of the thin-rings region were blown up to page size. The total travel of the disk during one experiment was approximately 1 cm. The gap between the glass sheets was of the order of 2 mm at the end of each experiment.

The apparatus design was also influenced by the observation that the theoretical $h(t)$ curve for long times ($\tau >> 1$) is independent of the initial thickness h_0, which was not measured. Indeed, in this limit, Eq. (11) and the τ definition (13) for the plane disk yield

$$\frac{h}{R}=\left(\frac{3\mu}{4m''gt}\right)^{1/2} \qquad (\tau >> 1) \tag{14}$$

This asymptotic behavior is plotted in Fig. 2 alongside the data collected during four experiments. It is clear that the four sets of measurements approach one another and Eq. (14) as time increases. The set of honey data indicated by solid squares is below the other sets because in this run the disk was released from a lower initial height. The slope of the experimental curves at large times is somewhat smaller (less steep) than Eq. (14) because of a small buoyancy effect, which becomes more important as t increases.

The experimental data were plotted after measuring the viscosity of the squeezed fluid with a Cannon-Fenske 600-F622 viscosimeter, namely, $\mu = 87.6$ g/cm·s for the particular honey used, and $\mu = 40.4$ g/cm·s for the corn syrup. Both viscosities correspond to 28°C, which was the laboratory temperature during experiments. The measured viscosities have a relative error of 0.1 percent, which also represents the uncertainty in evaluating the group $m''gt/\mu$, because the m'' uncertainty was less than 0.01 percent.

4 The Heat Transfer Problem

Consider now the time-dependent transfer of heat between the two bodies, across the thin film of fluid (Fig. 1, upper right). Initially, the bodies are isothermal and at different temperatures, T_0 and T_∞. The classical solution to the contact between two semi-infinite bodies without fluid film (Incropera and DeWitt, 1990) has shown that, as the time increases, one body remains essentially isothermal (and controls the interface temperature) when its ρck product is sufficiently greater than the ρck value of the other body. To focus on the complexities associated with the behavior of the fluid film, in this study we make the simplifying assumption that the two ρck values are sufficiently dissimilar so that we can model one of the two solids as isothermal for $t > 0$. In the coordinate system sketched in the upper-right corner of Fig. 1, the upper solid was designated as isothermal, T_0. The properties of the lower solid are ρ_s, c_s, k_s, and α_s.

The process of time-dependent conduction that occurs in the lower solid is one-dimensional (vertical in Fig. 1), when the contact area is sufficiently wide, or α_s sufficiently small, so that the conduction penetration depth $(\alpha_s t)^{1/2}$ is small, that is, $(\alpha_s t)^{1/2} << (L, R)$. This conduction process is governed by the dimensionless equation, initial and boundary conditions

$$\tau \frac{\partial\theta}{\partial\tau}=\frac{\partial^2\theta}{\partial\eta^2} \tag{15}$$

$$\theta = 0 \quad \text{at} \quad \tau = 0 \tag{16}$$

$$\theta = \theta_s(\tau) \quad \text{at} \quad \eta = 0 \tag{17}$$

$$\theta \to 0 \quad \text{as} \quad \eta \to \infty \tag{18}$$

where

$$\theta=\frac{T-T_\infty}{T_0-T_\infty},\ \theta_s(\tau)=\frac{T_s(t)-T_\infty}{T_0-T_\infty} \tag{19}$$

are the solid temperature and the interface ($y = 0$) temperature. The dimensionless time τ was defined earlier in Eqs. (10) or (13), namely $\tau = t/t_v$. The dimensionless conduction distance η is the actual distance y referenced to the conduction penetration depth, $\eta = y/(\alpha_s t)^{1/2}$.

Four effects are generally competing in the energy balance of the liquid film: (*i*) thermal inertia, (*ii*) longitudinal (or radial) convection, (*iii*) transverse conduction, and (*iv*) longitudinal (or radial) conduction. These are represented in order by the following scales:

$$\rho c\frac{\Delta T}{t_v},\ \rho cu\frac{\Delta T}{(L, R)},\ k\frac{\Delta T}{h_0^2},\ k\frac{\Delta T}{(L, R)^2} \tag{20}$$

Transverse conduction (the third scale) dominates when the film is sufficiently thin, i.e., when the most restrictive of the following three conditions is met:

$$(i) << (iii) \qquad h_0 << (\alpha t_v)^{1/2} \tag{21}$$

$$(ii) << (iii): \qquad h_0 << \left[\frac{\mu\alpha(L, R)^2}{m''g}\right]^{1/4} \tag{22}$$

$$(iv) << (iii): \qquad h_0 << (L, R) \tag{23}$$

These conditions on h_0 are obtained by writing the inequalities of scales indicated on the left margin of Eqs. (21)–(23). Condition (22) is based on the additional assumption that $h(t)$ behaves according to the viscous damping regime. When conditions (21)–(23) are met, the temperature distribution across the film is linear in y, while both h and T_s are functions of time,

$$T(y, t) = (T_0 - T_s)\frac{y}{h} + T_s \tag{24}$$

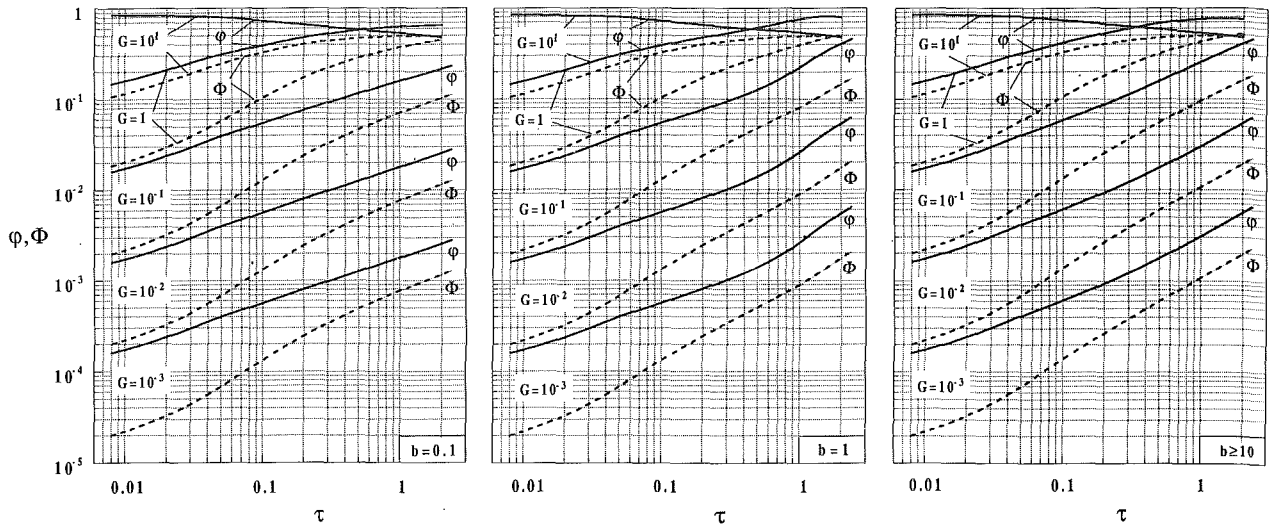

Fig. 3 Charts for the instantaneous insulation factor φ and the integral insulation factor Φ

Finally, the continuity of heat flux across the interface $y=0$ requires

$$q''(t) = k\left(\frac{\partial T}{\partial y}\right)_{y=0^+} = k_s\left(\frac{\partial T}{\partial y}\right)_{y=0^-} \tag{25}$$

The left side is provided by Eq. (24), and the right side by the solution to Eqs. (15)–(18). The dimensionless version of the heat flux continuity condition (25) is

$$G\,\frac{1-\theta_s}{H} = \tau^{-1/2}\left(\frac{\partial\theta}{\partial\eta}\right)_{\eta=0} \tag{26}$$

where G is the dimensionless group

$$G = \left(\frac{\rho ck}{\rho_s c_s k_s}\right)^{1/2} \frac{(\alpha t_v)^{1/2}}{h_0} \tag{27}$$

On the right side of Eq. (27), the first group is considerably smaller than 1, while the second group is greater than 1, cf. Eq. (21). This means that G can be expected to have values greater or smaller than 1.

In summary, the heat transfer problem reduces to solving Eqs. (15)–(18) and (26), for which $H(\tau, b)$ was calculated in section 2. The results are the temperature distribution in the lower solid, $\theta(\eta, \tau, b, G)$, and the interface temperature, $\theta_s(\tau, b, G)$. The numerical scheme was fully implicit, backward Euler in τ, and grid-based central finite difference in η. This scheme was chosen because the time-dependent coefficients of the nonhomogeneous Robin-type boundary condition (26) are functions of $H(\tau, b)$—a tabulated function—because an asymptotic condition is prescribed (at $\eta\to\infty$) in place of a regular boundary condition. Because of space limitations we cannot describe the details of the numerical method, but mention that the concern for numerical accuracy led to an exhaustive amount of work that is documented by Morega (1993).

The thermal insulation effect of the shrinking film can be described quantitatively by comparing the actual heat flux $q''(t)$ [Eq. (25)] with the heat flux that would be occurring when the film is absent,

$$q''_*(t) = \frac{k_s(T_0 - T_\infty)}{(\pi\alpha_s t)^{1/2}} \tag{28}$$

In this way, we define the *instantaneous insulation factor*

$$\varphi(\tau, G, b) = \frac{q''(t)}{q''_*(t)} \tag{29}$$

This function has been calculated for several values of G and b, and presented in the charts of Fig. 3. A small φ value indicates a significant thermal resistance, or insulation effect. The factor φ approaches 1 as $\tau\to\infty$, because in that limit the film disappears. The G number has a much greater effect on φ than the b number. The impact of G is such that the insulation effect increases (φ decreases) as the ρck value of the fluid becomes smaller than the $\rho_s c_s k_s$ value of the solid. To summarize, in the range $b=0.1$–∞ and $G=0.1$–0.001, the factor φ is so small that the actual heat flux is only a tiny fraction of what it would have been in the absence of the film. Figure 3 suggests that when G is much greater than 1, φ and Φ are of order 1, and the film insulation effect is minimal.

In a similar way, the actual heat transfer interaction occurring during the time interval t,

$$Q'' = \int_0^t q''\,dt \tag{30}$$

can be compared with the interaction that occurs when the film is absent

$$Q''_* = \int_0^t q''_*\,dt = 2k_s(T_0 - T_\infty)\left(\frac{t}{\pi\alpha_s}\right)^{1/2} \tag{31}$$

The *integral insulation* factor is defined as the ratio

$$\Phi(\tau, G, b) = \frac{Q''(t)}{Q''_*(t)} \tag{32}$$

This factor is presented in Fig. 3, which shows that Φ behaves in the same way as φ; however, it is generally smaller than the instantaneous factor φ. The difference between Φ and φ decreases as the time increases. The actual value of the heat transfer interaction Q'' can be calculated by using Eq. (32) in conjunction with Fig. 3 and Eq. (31).

5 Conclusions

1 The complete fluid mechanics of the thin film is governed by the dimensionless time group τ defined in Eqs. (10) and (13), and the dimensionless number b defined in Eqs. (7) and (12).

2 The general solution for the film thickness history is presented in the lower part of Fig. 1.

3 The time-dependent heat transfer through the lubricated contact area is governed by the fluid mechanics groups τ and b, and, in addition, by the ratio $\rho ck/\rho_s c_s k_s$ and the dimensionless number G defined in Eq. (27).

4 The thermal contact resistance is described by the instantaneous insulation factor φ defined in Eq. (29), and the integral insulation factor Φ defined in Eq. (32).

5 The (φ, Φ) charts constructed in Fig. 3 show that the film that is squeezed between the two bodies can decrease the heat transfer rate dramatically (by one or more orders of magnitude), relative to the heat transfer rate that occurs through a dry contact area.

Acknowledgments

The experimental apparatus was constructed by Mr. Mike Gunter. Dr. D. V. Zhelev's help with the viscosity measurement is gratefully appreciated.

References

Batchelor, G. K., 1967, *An Introduction to Fluid Dynamics*, Cambridge University Press, Cambridge, pp. 219–222.

Cameron, A., 1981, *Basic Lubrication Theory*, 3rd ed., Ellis Horwood Ltd., Chichester, pp. 143–144.

Fletcher, L. S., ed., 1978, *Heat Transfer and Thermal Control Systems*, (Progress in Astronautics and Aeronautics, Vol. 60), AIAA, New York.

Fuller, D. D., 1984, *Theory and Practice of Lubrication for Engineers*, 2nd ed., Wiley, New York, pp. 174–185.

Incropera, F. P., and DeWitt, D. P., 1990, *Fundamentals of Heat and Mass Transfer*, 3rd ed., Wiley, New York, pp. 260–262.

Morega, A. M., 1993, Ph.D. Thesis, Department of Mechanical Engineering and Materials Science, Duke University, Durham, NC.

Needs, S. J., 1940, "Boundary Film Investigations," *Transactions of the ASME*, Vol. 62, pp. 331–345.

Stefan, M. J., 1874, "Versuche über die scheinbare Adhäsion," *Sitzungsberichte der Mathematisch-Naturwissenschaftlichen Classe der Kaiserlichen Akademie der Wissenschaften*, Vol. 69, pp. 713–735.

Yovanovich, M. M., 1986, "Recent Developments in Thermal Contact, Gap and Joint Conductance Theories and Experiment," *Heat Transfer 1986*, Vol. 1, C. L. Tien, V. P. Carey, and J. K. Ferrell, eds., Hemisphere, Washington, DC, pp. 35–45.

Theory of Multilayers Heated by Laser Absorption

K. D. Cole[1] and W. A. McGahan[2]

Nomenclature

c = specific heat, J/(kg K)
d_j = thickness of layer j
f = frequency, Hz
G = Green's function, m^{-3} (in real space)
j = imaginary number = $\sqrt{-1}$
$J_o(\,)$ = Bessel function of order zero
k_i = dimensionless extinction coefficient in layer i
N = number of film-type layers in sample
n_i = index of refraction in layer i
P_o = heating laser power, W
q_{ij} = heat flux from region i into region j, W/m^2 (in time domain)
r = radial coordinate, temperature location, m
r_h = radius of heating laser beam, m
R_i = thermal contact resistance, m^2 K/W
t = time, s
$T(r, z, t)$ = temperature, K
x, y, z = spatial coordinate, m
α = thermal diffusivity, m^2/s
β = Hankel space parameter, m^{-1}
η = $\sqrt{\beta^2 + j2\pi f/\alpha}$, m^{-1}
κ = reference thermal conductivity, W/(mK)
λ = laser wavelength, m
ρ = density, kg/m^3
τ = time, s

Subscripts

i or j = region i or j
0 = ambient layer ($i = 0$)

Introduction

Temperature prediction from laser absorption in multilayer materials is of interest in magneto-optical recording, electron beam lithography, ion implantation, and nondestructive testing. Many authors have used a theoretical approach to this subject. Lax (1977) studied a semi-infinite body heated by a steady laser. Burgener and Reedy (1982) studied a two-layer structure with a continuous-wave scanned laser beam, and they indicated how to apply their method to N-layers. However, laser heating was limited to complete absorption at the surface of a single layer. Abraham and Halley (1987) studied a single layer on a thick substrate with absorption in the surface layer taken to be the average over the layer thickness. They included effects of forced-convection cooling at the surface of the sample. Anderson (1988) studied a multilayer structure that included linear-varying absorption inside the material. Actual absorption profiles could be approximated by several piecewise-linear absorbing layers. Iravani and Wickramasinghe (1985) used the temporal Fourier transform to find the temperature in a multilayer structure. The temperature expressions within each layer were linked at the layer interfaces by discontinuity conditions on temperature and heat flux. The laser absorption was limited to a region of delta-function thickness at one location in the multilayer. Kant (1988) studied a similar absorption geometry but used the Laplace transform appropriate for the temperature rise caused by a single laser pulse. Lemczyk and Yovanovich (1988) studied a single layer on a substrate for axisymmetric *surface* heat distribution caused by thermal contact instead of laser absorption. There the application was the thermal constriction resistance associated with circular contact. The surface heating was of mixed type combining a circular region with contact conductance boundary condition and either Dirichlet or Neumann conditions outside the circular region. Their steady-state analysis involved the Hankel integral transform and it involved exact matching of temperatures between the layer and the substrate.

Madison and McDaniel (1989) analyzed a scanned laser beam with arbitrary absorption across one layer, for a single transient pulse of the laser beam. They use globally defined Green's functions combined with Laplace transform methods to obtain their solution, and they indicate how to extend the method to N layers. As N increases, the Green's function for the system becomes increasingly complex.

McGahan and Cole (1992) presented a theory for temperature in isotropic multilayer materials that involved exact optical absorption for axisymmetric chopped-beam laser heating. The theory is based on a local Green's function for each layer, which contributes to ease of calculation for any number of layers. That paper focused on the analysis of data for pho-

[1]Assistant Professor, Department of Mechanical Engineering, University of Nebraska—Lincoln, Lincoln, NE 68588-0656.

[2]Graduate Student, Department of Electrical Engineering, University of Nebraska—Lincoln, Lincoln, NE 68588-0511.

Contributed by the Heat Transfer Division and presented at the ASME Winter Annual Meeting, Anaheim, California, November 8–13. Manuscript received by the Heat Transfer Division July 1992; revision received February 1993. Keywords: Conduction, Radiation Interactions, Thermophysical Properties. Technical Editor: R. Viskanta.

4 The thermal contact resistance is described by the instantaneous insulation factor φ defined in Eq. (29), and the integral insulation factor Φ defined in Eq. (32).

5 The (φ, Φ) charts constructed in Fig. 3 show that the film that is squeezed between the two bodies can decrease the heat transfer rate dramatically (by one or more orders of magnitude), relative to the heat transfer rate that occurs through a dry contact area.

Acknowledgments

The experimental apparatus was constructed by Mr. Mike Gunter. Dr. D. V. Zhelev's help with the viscosity measurement is gratefully appreciated.

References

Batchelor, G. K., 1967, *An Introduction to Fluid Dynamics*, Cambridge University Press, Cambridge, pp. 219–222.

Cameron, A., 1981, *Basic Lubrication Theory*, 3rd ed., Ellis Horwood Ltd., Chichester, pp. 143–144.

Fletcher, L. S., ed., 1978, *Heat Transfer and Thermal Control Systems*, (Progress in Astronautics and Aeronautics, Vol. 60), AIAA, New York.

Fuller, D. D., 1984, *Theory and Practice of Lubrication for Engineers*, 2nd ed., Wiley, New York, pp. 174–185.

Incropera, F. P., and DeWitt, D. P., 1990, *Fundamentals of Heat and Mass Transfer*, 3rd ed., Wiley, New York, pp. 260–262.

Morega, A. M., 1993, Ph.D. Thesis, Department of Mechanical Engineering and Materials Science, Duke University, Durham, NC.

Needs, S. J., 1940, "Boundary Film Investigations," *Transactions of the ASME*, Vol. 62, pp. 331–345.

Stefan, M. J., 1874, "Versuche über die scheinbare Adhäsion," *Sitzungsberichte der Mathematisch-Naturwissenschaftlichen Classe der Kaiserlichen Akademie der Wissenschaften*, Vol. 69, pp. 713–735.

Yovanovich, M. M., 1986, "Recent Developments in Thermal Contact, Gap and Joint Conductance Theories and Experiment," *Heat Transfer 1986*, Vol. 1, C. L. Tien, V. P. Carey, and J. K. Ferrell, eds., Hemisphere, Washington, DC, pp. 35–45.

Theory of Multilayers Heated by Laser Absorption

K. D. Cole[1] and W. A. McGahan[2]

Nomenclature

c = specific heat, J/(kg K)
d_j = thickness of layer j
f = frequency, Hz
G = Green's function, m^{-3} (in real space)
j = imaginary number = $\sqrt{-1}$
$J_o(\,)$ = Bessel function of order zero
k_i = dimensionless extinction coefficient in layer i
N = number of film-type layers in sample
n_i = index of refraction in layer i
P_o = heating laser power, W
q_{ij} = heat flux from region i into region j, W/m^2 (in time domain)
r = radial coordinate, temperature location, m
r_h = radius of heating laser beam, m
R_i = thermal contact resistance, m^2 K/W
t = time, s
$T(r, z, t)$ = temperature, K
x, y, z = spatial coordinate, m
α = thermal diffusivity, m^2/s
β = Hankel space parameter, m^{-1}
η = $\sqrt{\beta^2 + j2\pi f/\alpha}$, m^{-1}
κ = reference thermal conductivity, W/(mK)
λ = laser wavelength, m
ρ = density, kg/m^3
τ = time, s

Subscripts

i or j = region i or j
0 = ambient layer ($i = 0$)

Introduction

Temperature prediction from laser absorption in multilayer materials is of interest in magneto-optical recording, electron beam lithography, ion implantation, and nondestructive testing. Many authors have used a theoretical approach to this subject. Lax (1977) studied a semi-infinite body heated by a steady laser. Burgener and Reedy (1982) studied a two-layer structure with a continuous-wave scanned laser beam, and they indicated how to apply their method to N-layers. However, laser heating was limited to complete absorption at the surface of a single layer. Abraham and Halley (1987) studied a single layer on a thick substrate with absorption in the surface layer taken to be the average over the layer thickness. They included effects of forced-convection cooling at the surface of the sample. Anderson (1988) studied a multilayer structure that included linear-varying absorption inside the material. Actual absorption profiles could be approximated by several piecewise-linear absorbing layers. Iravani and Wickramasinghe (1985) used the temporal Fourier transform to find the temperature in a multilayer structure. The temperature expressions within each layer were linked at the layer interfaces by discontinuity conditions on temperature and heat flux. The laser absorption was limited to a region of delta-function thickness at one location in the multilayer. Kant (1988) studied a similar absorption geometry but used the Laplace transform appropriate for the temperature rise caused by a single laser pulse. Lemczyk and Yovanovich (1988) studied a single layer on a substrate for axisymmetric *surface* heat distribution caused by thermal contact instead of laser absorption. There the application was the thermal constriction resistance associated with circular contact. The surface heating was of mixed type combining a circular region with contact conductance boundary condition and either Dirichlet or Neumann conditions outside the circular region. Their steady-state analysis involved the Hankel integral transform and it involved exact matching of temperatures between the layer and the substrate.

Madison and McDaniel (1989) analyzed a scanned laser beam with arbitrary absorption across one layer, for a single transient pulse of the laser beam. They use globally defined Green's functions combined with Laplace transform methods to obtain their solution, and they indicate how to extend the method to N layers. As N increases, the Green's function for the system becomes increasingly complex.

McGahan and Cole (1992) presented a theory for temperature in isotropic multilayer materials that involved exact optical absorption for axisymmetric chopped-beam laser heating. The theory is based on a local Green's function for each layer, which contributes to ease of calculation for any number of layers. That paper focused on the analysis of data for pho-

[1]Assistant Professor, Department of Mechanical Engineering, University of Nebraska—Lincoln, Lincoln, NE 68588-0656.

[2]Graduate Student, Department of Electrical Engineering, University of Nebraska—Lincoln, Lincoln, NE 68588-0511.

Contributed by the Heat Transfer Division and presented at the ASME Winter Annual Meeting, Anaheim, California, November 8–13. Manuscript received by the Heat Transfer Division July 1992; revision received February 1993. Keywords: Conduction, Radiation Interactions, Thermophysical Properties. Technical Editor: R. Viskanta.

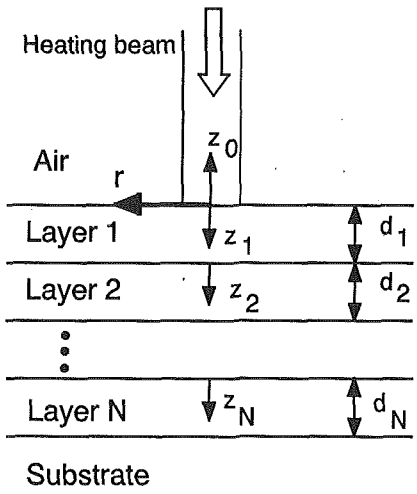

Fig. 1 Schematic of multilayer heated by axisymmetric laser beam

tothermal deflection experiments to obtain thermal properties, and no temperature results were presented. In this technical note, our purpose is to extend the theory of McGahan and Cole (1992) to include anisotropic thermal properties and contact resistance between the layers, and to demonstrate use of the theory for predictions of temperature in multilayers heated by a chopped laser beam.

Boundary Value Problem

The problem of interest is the temperature caused by laser absorption in an arbitrary number of layers on a semi-infinite substrate. The geometry of the problem is shown in Fig. 1. Note that each region is given a numeric index (zero for the ambient, one for the first layer, etc.). The radial symmetry of the laser heating source leads to the following heat conduction equation:

$$\kappa_r \frac{1}{\tilde{r}} \frac{\partial}{\partial \tilde{r}}\left(\tilde{r} \frac{\partial T}{\partial \tilde{r}}\right) + \kappa_z \frac{\partial^2 T}{\partial \tilde{z}^2} - \rho c \frac{\partial T}{\partial t} = -g(\tilde{r}, \tilde{z}, t) \tag{1}$$

Here $g(\tilde{r}, \tilde{z}, t)$ is the power per unit volume transferred to the medium at $(\tilde{r}, \tilde{z}, t)$ by a chopped laser beam and κ_r and κ_z are thermal conductivities parallel to and perpendicular to the sample surface. The spatial coordinates can be scaled so that theory for isotropic bodies can be applied to this case. Let

$$r = \left(\frac{\kappa}{\kappa_r}\right)^{1/2} \tilde{r}; \quad z = \left(\frac{\kappa}{\kappa_z}\right)^{1/2} \tilde{z} \tag{2}$$

where $\kappa = (\kappa_r \kappa_r \kappa_z)^{1/3}$ is a reference thermal conductivity (Özişik, 1980, p. 632). The transformation $(\tilde{r}, \tilde{z}) \rightarrow (r, z)$ gives the isotropic heat conduction equation:

$$\frac{1}{r} \frac{\partial}{\partial r}\left(r \frac{\partial T(r, z, t)}{\partial r}\right) + \frac{\partial^2 T(r, z, t)}{\partial z^2} - \frac{1}{\alpha} \frac{\partial T(r, z, t)}{\partial t} = -\frac{g(r, z, t)}{\kappa}, \tag{3}$$

where α is the thermal diffusivity ($\kappa/\rho c$). The thermal conductivity and diffusivity are assumed to be independent of temperature. The solution procedure involves separation solutions in each homogeneous region (substrate, layer, air) connected by continuity of normal components of the heat flux at the boundaries. The boundary condition is that the temperature goes to zero at points far removed from the region of heating.

Temperature in One Layer

The temperature in one layer at a point (r, z, t) in space-time is given by the sum of two integrals (Beck et al., 1992, p. 51):

$$T(r, z, t) = \frac{\alpha}{\kappa} \int_{r'=0}^{\infty} \int_{\tau=-\infty}^{t} q(r', \tau) G(r, z, t | r', z' = z_s, \tau) \cdot 2\pi r' dr' d\tau + \frac{\alpha}{\kappa} \int_V \int_{\tau=-\infty}^{t} g(r', z', \tau) \times G(r, z, t | r', z', \tau) \cdot 2\pi r' dr' dz' d\tau, \tag{4}$$

Function $q(r', \tau)$ is the normal component of the heat flux through the boundary of the region at (r', z_s, τ). Function G is the Green's function, and function g is the known volume heating term (W/m^3) caused by absorption of a gaussian laser beam at normal incidence. The first integral in Eq. (4) is a surface integral, to be evaluated over the boundary surface of the region of interest. The second integral is a volume integral taken over the entire volume of the region. It is the unknown heat fluxes q that will be determined by enforcing matching conditions between adjacent regions.

Temperature in Multilayers

The present research is concerned with situations in which the volume heating source g is periodic in time (i.e., modulated laser beam), so the Fourier transform of Eq. (4) is used to select the temperature response at the fundamental frequency of modulation. The Hankel transformation is also used to eliminate the integrals over radius r.

For the case of a sample consisting of a semi-infinite substrate and N layers, the temperature (in Fourier-Hankel space) at each interface is given as follows:

Air:

$$T_0(\beta, z=0, f) = W_0 q_{10}(\beta, f) \tag{5}$$

Layer j; j = 1, 2, . . . , N:

$$T_j(\beta, z=0, f) = U_j q_{j-1,j}(\beta, f) + V_j q_{j+1,j}(\beta, f) + B_j(\beta, 0, f) \tag{6}$$

$$T_j(\beta, z=d, f) = V_j q_{j-1,j}(\beta, f) + U_j q_{j+1,j}(\beta, f) + B_j(\beta, d, f) \tag{7}$$

Substrate:

$$T_{N+1}(\beta, 0, f) = W_{N+1} q_{N,N+1} + B_{N+1}(\beta, 0, f) \tag{8}$$

Here $q_{ij}(\beta, f)$ is heat flux in the Fourier-Hankel space, which leaves layer i and enters layer j. Function B_i is the known volume heating integral from Eq. (4) calculated by the method of McGahan and Cole (1992).

Coefficients W_i, U_j, and V_j come from the Green's functions and are given by

$$W_i \equiv \frac{1}{\eta_i \kappa_i} \tag{9}$$

$$U_j \equiv \frac{\coth(\eta_j d_j)}{\eta_j \kappa_j}; \quad V_j \equiv \frac{1}{\eta_j \kappa_j \sinh(\eta_j d_j)}. \tag{10}$$

The next step is to apply the matching conditions at the interfaces between adjacent layers. The heat flux matching condition is $q_{ij} = -q_{ji}$, that is, the heat flux leaving one layer enters the adjacent layer. The temperatures on adjacent layers are related by a contact resistance, R_i, which is a constant associated with each interface. For the air/sample interface

$$q_{10} R_1 = T_1(\beta, z=0, f) - T_0(\beta, 0, f) \tag{11}$$

For all the solid-solid interfaces, $i = 2, 3, \ldots, N+1$:

$$q_{i,i-1} R_i = T_i(\beta, 0, f) - T_{i-1}(\beta, d, f) \tag{12}$$

The contact resistance describes the size of the temperature jump across the interface. If the contact resistance is zero, the temperature jump is zero and temperature is continuous across

the interface. Next replace the temperature expressions Eqs. (5)–(8) into Eqs. (11) and (12) to find a set of $N + 1$ linear equations for $N + 1$ unknown normal heat fluxes at the interfaces, where N equals the number of layers in the system. This system of equations can be compactly written as the following tridiagonal matrix equation:

$$\begin{bmatrix} W_o+U_1+R_1 & -V_1 & 0 & \dots & 0 \\ -V_1 & U_1+U_2+R_2 & -V_2 & \dots & 0 \\ 0 & -V_2 & U_2+U_3+R_3 & \dots & 0 \\ \dots & \dots & \dots & \dots & -V_N \\ 0 & 0 & \dots & -V_N & U_N+W_{N+1}+R_{N+1} \end{bmatrix} \begin{bmatrix} q_{10} \\ q_{21} \\ q_{32} \\ \dots \\ q_{N+1,N} \end{bmatrix} = \begin{bmatrix} B_1(z=0) \\ B_2(z=0)-B_1(z=d_1) \\ B_3(z=0)-B_2(z=d_2) \\ \dots \\ B_{N+1}(z=0)-B_N(z=d_N) \end{bmatrix} \quad (13)$$

For the case $N = 0$, U_1 should be replaced with W_1, the term appropriate for the substrate.

For any multilayered system, it is now possible to calculate the normal components of the heat fluxes (q_{ij}) through all interfaces in the system. The above result is *exact* and Cramer's rule may be used to solve for the q's for a sample composed of one or two layers. For a sample with two or more layers a numerical matrix solution is best. Once the heat fluxes are found, the temperature anywhere in the system is given by Eqs. (5)–(8).

Temperature Results

To calculate temperatures in real space, one numerical integration is required to invert the Hankel transform given by

$$T(r, z, f) = \int_{\beta=0}^{\infty} T(\beta, z, f) J_0(\beta r) \beta d\beta.$$

Accurate evaluation of this numerical integral depends on taking a sufficiently large range of β values as well as taking sufficiently small intervals in β. The Bessel function J_0 is well behaved for numerical integration because it has a single length scale (the asymptotic distance between its zeroes) and it contains no singular values. So long as the maximum value of β is greater than $6/r_h$ and the r value under consideration is less than $3r_h$, trapezoidal rule integration with 400 equal-spaced β values is sufficient to determine temperatures correct within 0.2 percent. For progressively larger values of r, more zeroes of the Bessel function are involved, and a progressively larger number of β values is required to describe these zeroes adequately.

The temperature calculations presented below involve only isotropic thermal conductivity for demonstration purposes; however, anisotropic cases may be calculated by re-scaling the spatial coordinates for the isotropic theory according to Eq. (2). Experimental measurement of anisotropic thermal conductivity and the associated calculation of photothermal beam deflection above anisotropic samples are reported elsewhere (Machlab et al., 1992).

The first example is a bulk sample of aluminum heated by a laser beam with radius $r_h = 50$ μm. In Fig. 2 the amplitude of the frequency-domain surface temperature in the aluminum substrate is given as a function of position for several chopping frequencies. The temperature is normalized by the steady temperature that could be produced by a continuous-wave (nonchopped) laser beam of the same power level completely absorbed in a infinitesimal layer at the surface of the sample. This steady-state temperature is given the name T_{max} because it is larger than any temperature caused by internal absorption. Normalized in this way, the limiting case of $f \to 0$ agrees with the steady-state results of Lax (1977). Some example values of T_{max} are given in Table 1.

The phase of the frequency-domain surface temperature is also shown in Fig. 2. The following parameters were used to calculate Fig. 2: $n = 2.74$, $k = 8.32$; $\kappa = 237$ W/(mK); $\alpha = 1.32\,(10^{-4})$ m^2/s; $r_h = 50$ μm; laser wavelength $\lambda = 0.674$ μm (6740 Å).

The second example is a sample composed of a 10-μm-thick dielectric layer on a metallic substrate, which is heated by a modulated laser beam. Depending on how the dielectric layer is fabricated, the optical absorption coefficient of the layer can vary, and this will cause the spatial distribution of the laser absorption heating to vary in the layer/substrate system. In Fig. 3 the magnitude of the temperature rise along the laser centerline (at $r = 0$) is plotted versus depth in the sample for several values of the dielectric layer's optical absorption coefficient. The heating laser is modulated at 100 kHz, and the thermal properties of the layer/substrate system do not vary. The following values were used to calculate Fig. 3: For the dielectric, $n = 1.5$, k varies, $\kappa = 1.4$ W/(mK), $\alpha = 8.48\,(10^{-7})$ m^2/s; for the substrate, $n = 2.5$, $k = 1.5$, $\kappa = 237$ W/(mK), $\alpha = 1.32\,(10^{-4})$ m^2/s; for the heating laser beam, $r_h = 50$ μm, $\lambda = 0.674$ μm, and $P_0 = 0.75$ mW.

In Fig. 3, observe that as the dielectric optical absorption increases, the surface temperature of the dielectric layer (at $z = 0$) increases, while the temperature of the metallic substrate (at $z = 10$) decreases. For small optical absorption ($k = 0.001$),

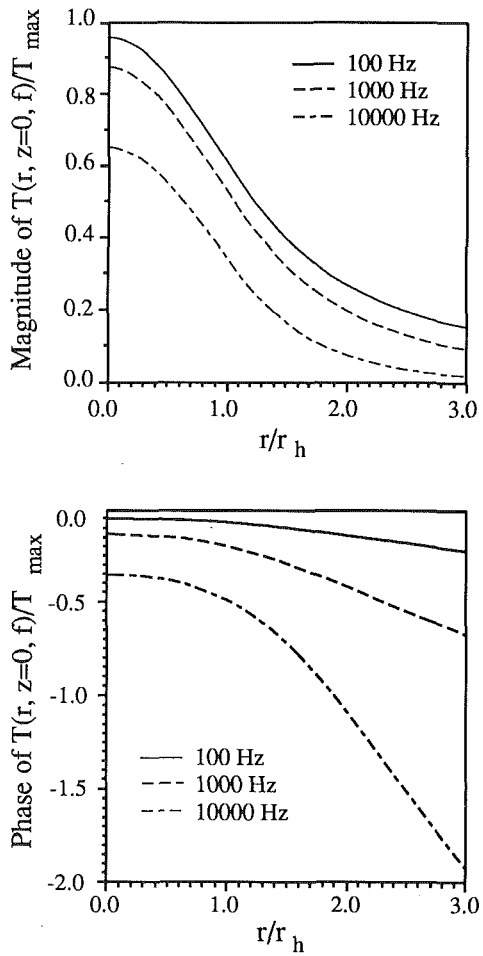

Fig. 2 Magnitude and phase of the surface temperature on an aluminum bulk sample at several chopping frequencies

Table 1 Steady temperature at ($z = 0$, $r = 0$) for complete absorption of laser energy in an infinitesimal layer at $z = 0$; laser power is P_0 = 0.75 mW in all cases (after Lax, 1977)

Probe beam Radius, microns	$T_{max} = P_0/(2\sqrt{(\pi)}\kappa r_h)$ degrees Kelvin	κ W/(mK)
5	0.18	237 (Aluminum)
10	0.089	237
50	0.018	237
5	17.	1.4 (Quartz)
10	8.5	1.4
50	1.7	1.4

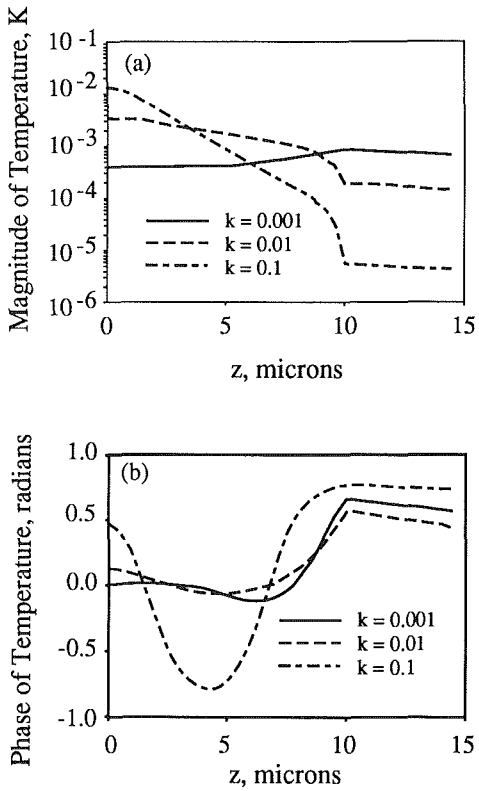

Fig. 3 Magnitude and phase of the temperature at the centerline ($r = 0$) of a sample composed of a 10 μm dielectric layer on a metallic substrate

the peak temperature and the peak volumetric heating both occur at the layer/substrate interface. At the middle value of optical absorption ($k = 0.01$) the peak temperature occurs at the surface because the small amount of energy absorbed in the dielectric layer causes a large temperature rise due to the small thermal conductivity of the dielectric. Further, there is no time for the heat to diffuse out of the dielectric layer at this frequency. At the larger value of the optical absorption ($k = 0.1$), nearly all the volumetric heating occurs in the dielectric layer.

The magnitude of the temperature has a slope discontinuity at the layer/substrate interface. This is caused by the mismatch in thermal conductivity between the layer and the substrate. The magnitude of the temperature in the substrate decreases exponentially (shown as a straight line on the semilog plot). The same exponential decay with depth is predicted by the theory for surface heating of a semi-infinite solid, because laser absorption in the metallic substrate takes place in a very thin region in metals. In Fig. 3 the phase of the temperature is also plotted. The phase of the temperature changes sign in the dielectric layer but it does not change sign in the region shown of the metallic substrate. This is an indication that the length of the thermal wavelength in the dielectric layer is about the same size as the layer thickness at this modulation frequency ($f = 100$ kHz) and that the thermal wavelength in the metallic substrate is much longer. The size of the thermal wavelength in a material is proportional to $(\alpha/f)^{1/2}$, so that the metallic substrate has a thermal wavelength about $(\alpha_1/\alpha_2)^{1/2} \approx 12$ times larger than the dielectric.

The curves in Fig. 3 were calculated by slicing the two-layer sample into 35 fictitious layers and then calculating the heat flux at each fictitious interface with Eq. (13). Then, the temperature can be calculated on the surface of each fictitious layer according to Eqs. (6)–(8). The actual numerical effort required to calculate one of the curves in Fig. 3 involved solving a 35 × 35 matrix equation 500 times (once for each β value) and then performing 35 numerical integrations. This required about 30 CPU seconds on a VAX 8800 computer.

Conclusions

In this paper temperature results have been presented for multilayers heated by a chopped, axisymmetric laser beam. Optical absorption of the laser beam is treated exactly in each layer. Although the thermal properties must be constant in each layer, the thermal properties may be anisotropic, and any number of layers can be used without increasing the complexity of the solution method. There may be contact resistance between the layers.

To the authors' knowledge there are no periodic temperature results reported in the literature to which the present results can be compared. Some report results for scanned laser beams (Burgener and Reedy, 1982; Anderson, 1988; Madison and McDaniel, 1989) and some report results for a short laser pulse (Kant, 1988; Iravani and Wickramasinghe, 1985). We report temperatures at the fundamental frequency of the chopped laser heating because of our interest in photothermal deflection measurements that involve lock-in detection to measure this one frequency. Our theory can be applied to a single laser pulse if the frequency components of the laser pulse are determined with a Fourier transform, then the contribution to the temperature at each active frequency determined in the frequency domain, and then the temperature in the time domain can be found from an inverse Fourier transform. This calculation has not been attempted.

Acknowledgments

The authors gratefully acknowledge partial support for this work from NASA Lewis Grants NAG-3-95 and NAG-3-154, and from National Science Foundation Grant No. DMR8918889.

References

Abraham, E., and Halley, J. M., 1987, "Some Calculations of Temperature Profiles in Thin Films With Laser Heating," *Appl. Phys. A.*, Vol. 42, p. 279.

Anderson, R. J., 1988, "A Method to Calculate the Laser Heating of Layered Structures," *J. Appl. Phys.*, Vol. 64, pp. 6639–6645.

Beck, J. V., Cole, K. D., Haji-Sheikh, A., and Litkouhi, B., 1992, *Heat Conduction Using Green's Functions*, Hemisphere Publishing Corp., New York.

Burgener, M. L., and Reedy, R. E., 1982, "Temperature Distributions Produced in a Two-Layer Structure by a Scanning CW Laser or Electron Beam," *J. Appl. Phys.*, Vol. 53, pp. 4357–4363.

Iravani, M. V., and Wickramasinghe, H. K., 1985, "Scattering Matrix Approach to Thermal Wave Propagation in Layered Structures," *J. Appl. Phys.*, Vol. 58, pp. 122–131.

Kant, R., 1988, "Laser-Induced Heating of Multilayered Medium Resting on a Half-Space: Part I—Stationary Source," ASME *Journal of Applied Mechanics*, Vol. 55, pp. 93–97.

Lax, M., 1977, "Temperature Rise Induced by a Laser Beam," *J. Appl. Phys.*, Vol. 48, No. 9, pp. 3919–3924.

Lemczyk, T. F., and Yovanovich, M. M., 1988, "Thermal Constriction Resistance With Convective Boundary Conditions—2. Layered Half-Space Contacts," *Int. J. Heat Mass Trans.*, Vol. 31, No. 9, pp. 1873–1883.

Machlab, H., McGahan, W. A., Woollam, J. A., and Cole, K. D., 1993, "Thermal Characterization of Thin Films by Photothermally Induced Laser Beam Deflection," *Thin Solid Films*, Vol. 224, pp. 22–27.

Madison, M. R., and McDaniel, T. W., 1989, "Temperature Distributions Produced in an *N*-Layer Film Structure by Static or Scanning Laser or Electron Beam with Application to Magneto-optical Media," *J. Appl. Phys.*, Vol. 66, pp. 5738–5748.

McGahan, W. A., and Cole, K. D., 1992, "Solutions of the Heat Conduction Equation in Multilayers for Photothermal Deflection Experiments," *J. Appl. Phys.*, Vol. 72, pp. 1362–1373.

Özişik, N. M., 1980, *Heat Conduction*, Wiley, New York.

Melting of Snow With Double Effect of Temperature and Concentration

M. Sugawara[1] and S. Sasaki[2]

Nomenclature

a = thermal diffusivity, m^2/s
C_m = solute concentration $= 1 - C_w$, kg/kg
C_{me} = solute concentration at temperature T_e, $= 1 - C_{we}$, kg/kg
C_{mi} = initial solute concentration $= 1 - C_{wi}$, kg/kg
$C_{m1}(T_i)$ = equilibrium solute concentration at T_i at the melting surface $= 1 - C_{w1}(T_i)$, kg/kg
$C_w(t)$, C_w = water concentration distribution (Fig. 2), kg/kg
$C_{w1}(T_i)$ = equilibrium water concentration at T_i on the melting surface (Fig. 2), kg/kg
$d_1(t)$, d_1 = diameter of a spherical snow (ice) crystal $= 2r_1$, mm
d_{1i} = initial diameter of a spherical snow (ice) crystal, mm
d_{ei} = mean diameter of snow (ice) crystal in experiment, mm
D = mass diffusion coefficient, m^2/s
Le = Lewis number $= a/D$
$\dot{m}$ = melting mass per unit area and time, $kg/(m^2s)$
M = melting mass per unit volume of a snow layer, kg/m^3
M_{max} = maximum melting mass per unit volume of a snow layer, kg/m^3
M^*_{max} = dimensionless maximum melting mass per unit volume of a snow layer $= M_{max}/\rho_{ic}$
r = radial coordinate, mm
$r_c(t)$, r_c = thickness of diffusion layer (Fig. 2), mm
$r_1(t)$, r_1 = radius of a spherical snow (ice) crystal (= melting surface), mm
r_{1i} = initial radius of a spherical snow (ice) crystal $= d_{1i}/2$, mm
r_2 = outer radius of a solution volume in a spherical cell (= insulated surface for heat and mass diffusion), mm
t = time, s
t', t'' = time ($t' < t''$), s
$T(t)$, T = temperature, °C
T_e = temperature fall in the melting system in a completion of melting (Fig. 3), °C
T_i = initial temperature (T_i of a snow layer and an aqueous solution are the same at the start of melting), °C
V = volume of a snow layer, m^3
V_s = net volume of a dry snow layer $= W/\rho_{ic}$, m^3
W = mass of a dry snow layer, kg
ϵ = porosity of a snow layer, m^3/m^3
ρ_{ic} = density of ice, kg/m^3
ρ_s = density of a binary aqueous solution, kg/m^3
ρ_{si} = initial density of a binary aqueous solution, kg/m^3

Subscripts

i = initial
m = solute
w = water
1 = melting surface, equilibrium
2 = insulated surface for heat and mass in spherical cell (Fig. 2)

Introduction

When a snow layer is quickly immersed in a binary aqueous solution, the snow melts with a temperature fall in the melting system, even when there is initially no temperature difference between the snow layer and the binary aqueous solution (Sugawara and Konda, 1991). To find the melting rate of a snow layer analytically, it is necessary to consider a driving force to induce melting.

Some work on melting of an ice layer into binary aqueous solutions has been reported, such as Griffin (1973), Josberger and Martin (1981), Carey and Gebhart (1982), Sammakia and Gebhart (1983), and Sugawara et al. (1987). Beckermann and Viskanta (1988) recently presented a combined numerical and experimental study of melting of a vertical ice layer into a ammonium chloride aqueous solution inside a square cavity. These studies, however, have not been sufficient for considering the concept of inducing melting.

In the present study a spherical cell and diffusion-controlled melting models improving the mass balance integral in an earlier study (Sugawara and Konda, 1991) are reported to predict more accurately the melting of a snow layer into binary aqueous solutions. The present experiments give new results for melting into calcium chloride, sodium chloride, and magnesium chloride aqueous solutions. The effects of wide variations in initial porosity of a snow layer on melting are studied. The numerical results successfully predict both an abrupt temperature fall in the melting system and the melting mass per unit volume of a snow layer qualitatively and quantitatively.

A Brief Explanation of Experimental Procedure

Although details of the experimental procedure have already been presented by Sugawara and Konda (1991), a brief explanation is presented here to understand easily the concept of the experiment as shown in Fig. 1. Snow crystals with a uniform mean diameter of $d_{ei} = 0.34$ mm were packed in a net box with a 10-mm-thick snow layer. When the temperature of a snow layer reached a desired temperature of an aqueous solution T_i, a snow layer was quickly immersed in an aqueous solution of a desired initial concentration C_{mi}. There was, hence, no temperature difference between a snow layer and an aqueous solution at the start of melting.

The initial porosity of the snow layer, ϵ_i, was vastly changed in the experiments as 0.5, 0.55, 0.6, 0.65, and 0.7 for only the

[1]Professor, Department of Mechanical Engineering, Akita University, Akita 010, Japan.

[2]Undergraduate Student, Department of Mechanical Engineering, Akita University, Akita 010, Japan.

Contributed by the Heat Transfer Division of The American Society of Mechanical Engineers. Manuscript received by the Heat Transfer Division October 1991; revision received February 1993. Keywords: Mass Transfer, Moving Boundaries, Phase-Change Phenomena. Technical Editor: R. Viskanta.

Lemczyk, T. F., and Yovanovich, M. M., 1988, "Thermal Constriction Resistance With Convective Boundary Conditions—2. Layered Half-Space Contacts," *Int. J. Heat Mass Trans.*, Vol. 31, No. 9, pp. 1873–1883.

Machlab, H., McGahan, W. A., Woollam, J. A., and Cole, K. D., 1993, "Thermal Characterization of Thin Films by Photothermally Induced Laser Beam Deflection," *Thin Solid Films*, Vol. 224, pp. 22–27.

Madison, M. R., and McDaniel, T. W., 1989, "Temperature Distributions Produced in an *N*-Layer Film Structure by Static or Scanning Laser or Electron Beam with Application to Magneto-optical Media," *J. Appl. Phys.*, Vol. 66, pp. 5738–5748.

McGahan, W. A., and Cole, K. D., 1992, "Solutions of the Heat Conduction Equation in Multilayers for Photothermal Deflection Experiments," *J. Appl. Phys.*, Vol. 72, pp. 1362–1373.

Özişik, N. M., 1980, *Heat Conduction*, Wiley, New York.

Melting of Snow With Double Effect of Temperature and Concentration

M. Sugawara[1] and S. Sasaki[2]

Nomenclature

a = thermal diffusivity, m^2/s
C_m = solute concentration $= 1 - C_w$, kg/kg
C_{me} = solute concentration at temperature T_e, $= 1 - C_{we}$, kg/kg
C_{mi} = initial solute concentration $= 1 - C_{wi}$, kg/kg
$C_{m1}(T_i)$ = equilibrium solute concentration at T_i at the melting surface $= 1 - C_{w1}(T_i)$, kg/kg
$C_w(t)$, C_w = water concentration distribution (Fig. 2), kg/kg
$C_{w1}(T_i)$ = equilibrium water concentration at T_i on the melting surface (Fig. 2), kg/kg
$d_1(t)$, d_1 = diameter of a spherical snow (ice) crystal $= 2r_1$, mm
d_{1i} = initial diameter of a spherical snow (ice) crystal, mm
d_{ei} = mean diameter of snow (ice) crystal in experiment, mm
D = mass diffusion coefficient, m^2/s
Le = Lewis number $= a/D$
$\dot{m}$ = melting mass per unit area and time, $kg/(m^2s)$
M = melting mass per unit volume of a snow layer, kg/m^3
M_{max} = maximum melting mass per unit volume of a snow layer, kg/m^3
M^*_{max} = dimensionless maximum melting mass per unit volume of a snow layer $= M_{max}/\rho_{ic}$
r = radial coordinate, mm
$r_c(t)$, r_c = thickness of diffusion layer (Fig. 2), mm
$r_1(t)$, r_1 = radius of a spherical snow (ice) crystal (= melting surface), mm
r_{1i} = initial radius of a spherical snow (ice) crystal $= d_{1i}/2$, mm
r_2 = outer radius of a solution volume in a spherical cell (= insulated surface for heat and mass diffusion), mm
t = time, s
t', t'' = time ($t' < t''$), s
$T(t)$, T = temperature, °C
T_e = temperature fall in the melting system in a completion of melting (Fig. 3), °C
T_i = initial temperature (T_i of a snow layer and an aqueous solution are the same at the start of melting), °C
V = volume of a snow layer, m^3
V_s = net volume of a dry snow layer $= W/\rho_{ic}$, m^3
W = mass of a dry snow layer, kg
ϵ = porosity of a snow layer, m^3/m^3
ρ_{ic} = density of ice, kg/m^3
ρ_s = density of a binary aqueous solution, kg/m^3
ρ_{si} = initial density of a binary aqueous solution, kg/m^3

Subscripts

i = initial
m = solute
w = water
1 = melting surface, equilibrium
2 = insulated surface for heat and mass in spherical cell (Fig. 2)

Introduction

When a snow layer is quickly immersed in a binary aqueous solution, the snow melts with a temperature fall in the melting system, even when there is initially no temperature difference between the snow layer and the binary aqueous solution (Sugawara and Konda, 1991). To find the melting rate of a snow layer analytically, it is necessary to consider a driving force to induce melting.

Some work on melting of an ice layer into binary aqueous solutions has been reported, such as Griffin (1973), Josberger and Martin (1981), Carey and Gebhart (1982), Sammakia and Gebhart (1983), and Sugawara et al. (1987). Beckermann and Viskanta (1988) recently presented a combined numerical and experimental study of melting of a vertical ice layer into a ammonium chloride aqueous solution inside a square cavity. These studies, however, have not been sufficient for considering the concept of inducing melting.

In the present study a spherical cell and diffusion-controlled melting models improving the mass balance integral in an earlier study (Sugawara and Konda, 1991) are reported to predict more accurately the melting of a snow layer into binary aqueous solutions. The present experiments give new results for melting into calcium chloride, sodium chloride, and magnesium chloride aqueous solutions. The effects of wide variations in initial porosity of a snow layer on melting are studied. The numerical results successfully predict both an abrupt temperature fall in the melting system and the melting mass per unit volume of a snow layer qualitatively and quantitatively.

A Brief Explanation of Experimental Procedure

Although details of the experimental procedure have already been presented by Sugawara and Konda (1991), a brief explanation is presented here to understand easily the concept of the experiment as shown in Fig. 1. Snow crystals with a uniform mean diameter of $d_{ei} = 0.34$ mm were packed in a net box with a 10-mm-thick snow layer. When the temperature of a snow layer reached a desired temperature of an aqueous solution T_i, a snow layer was quickly immersed in an aqueous solution of a desired initial concentration C_{mi}. There was, hence, no temperature difference between a snow layer and an aqueous solution at the start of melting.

The initial porosity of the snow layer, ϵ_i, was vastly changed in the experiments as 0.5, 0.55, 0.6, 0.65, and 0.7 for only the

[1]Professor, Department of Mechanical Engineering, Akita University, Akita 010, Japan.

[2]Undergraduate Student, Department of Mechanical Engineering, Akita University, Akita 010, Japan.

Contributed by the Heat Transfer Division of The American Society of Mechanical Engineers. Manuscript received by the Heat Transfer Division October 1991; revision received February 1993. Keywords: Mass Transfer, Moving Boundaries, Phase-Change Phenomena. Technical Editor: R. Viskanta.

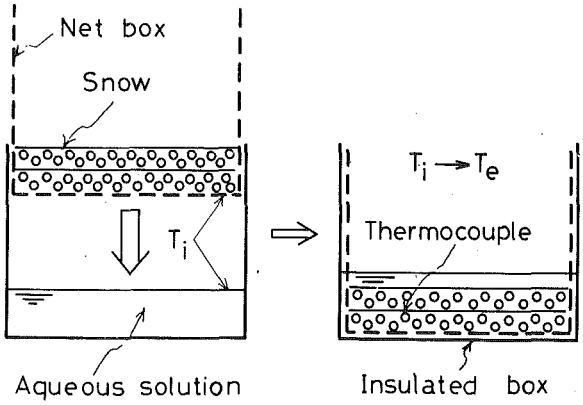

Fig. 1 Schematic of experiment for the melting of a snow layer

melting into a calcium chloride aqueous solution. ϵ_i, which was defined as $\epsilon_i = 1 - V_s/V$, could be changed with the mass of the dry snow layer. By packing the dry snow in a net box, it was easy to change the mass of the snow since the shapes of snow crystals were not bead but were very complicated. It was then assumed in this experiment that an aqueous solution perfectly filled the pores of a snow layer.

The melting was completed within a few seconds, and the temperature of the melting system finally fell to an equilibrium temperature T_e. The maximum melting mass per unit volume of a snow layer through an experiment, which was the one that had completed melting, could be evaluated by the relation:

$$M_{\max} = \epsilon_i \rho_{si} C_{mi} (1/C_{me} - 1/C_{mi}) \tag{1}$$

The solute concentration C_m and temperature T in the solid-liquid equilibrium were related by a polynomial of the fifth degree for each binary aqueous solution (JSME, 1983):

Calcium chloride aqueous solution ($C_m \leq 0.27$):

$$C_m = (3.0441 \times 10^{-3} - 2.4679T - 0.17063T^2 - 8.4228 \times 10^{-3}T^3 - 2.1251 \times 10^{-4}T^4 - 2.0672 \times 10^{-6}T^5)/100 \tag{2}$$

Sodium chloride aqueous solution ($C_m < 0.24$):

$$C_m = (-5.1298 \times 10^{-3} - 1.7316T - 0.025803T^2 + 1.4194 \times 10^{-3}T^3 + 9.1942 \times 10^{-5}T^4 + 1.5937 \times 10^{-6}T^5)/100 \tag{3}$$

Magnesium chloride aqueous solution ($C_m < 0.22$):

$$C_m = (0.088471 - 1.9513T - 0.16449T^2 - 0.010286T^3 - 3.1138 \times 10^{-4}T^4 - 3.4951 \times 10^{-6}T^5)/100 \tag{4}$$

New Development of Analysis

Since the concept of a cell and diffusion-controlled analytical models have already been discussed in an earlier work (Sugawara and Konda, 1991), details of the derivation of analysis are abbreviated here to avoid duplication. However, it is necessary to summarize the analysis to understand the present study.

A snow layer is assumed to be aggregated with spherical cells in order to analyze the melting of a snow layer simply. It is also assumed that the distribution of water concentration $C_w(t)$ in an aqueous solution, as shown by the solid lines in Fig. 2, can be represented by a quadratic equation to allow boundary conditions at the melting $r_1(t)$ and insulated r_2 surfaces. The temperature distribution $T(t)$, indicated by a horizontal dashed line in a spherical cell, will be uniform due to the very small volume of the cell and the large Lewis number, Le, of about 100 in the melting system. The temperature and

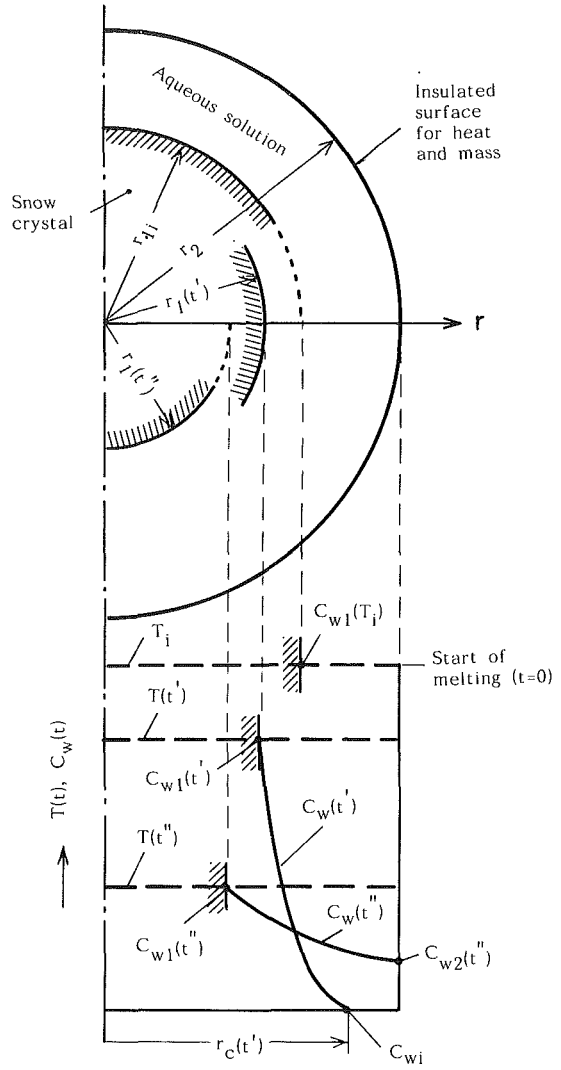

Fig. 2 A spherical cell model of a snow layer and time evolution of temperature ($T(t)$, horizontal dashed lines) and water concentration ($C_w(t)$, solid lines) profile

concentration at the melting surface of $r_1(t)$ are directly related by the equilibrium phase diagram for each binary aqueous solution. The other boundary of r_2 is insulated for both heat and mass diffusion. The concentration profile in the liquid, $C_w(t)$, changes due to the diffusion of melt water during the melting process. Hence the melting mass per unit time and unit area, $\dot{m}$, can be approximately related by the change of concentration in an aqueous solution with the mass balance integral newly developed in this paper as follows:

$$\pi d_1^2 \dot{m} = \frac{d}{dt}\left(\rho_s \int_{r_1}^{r_2} C_w 4\pi r^2 dr\right) \text{ (integral I)} \tag{5}$$

Equation (5) shows that the melting is diffusion controlled under local equilibrium at the melting surface. Another equivalent form of Eq. (5) is available for predicting melting rate during the development of diffusion layer r_c:

$$\frac{d}{dt}\left(\rho_s \int_{r_1}^{r_2} C_w 4\pi r^2 dr\right) = \frac{d}{dt}\left\{\rho_s \int_{r_1}^{r_c} (C_w - C_{wi}) 4\pi r^2 dr\right\} - 4\pi\rho_s C_{wi} r_1^2 \frac{dr_1}{dt} \tag{6}$$

(integral I) (integral II)

where integral II is the mass balance integral in an earlier study (Sugawara and Konda, 1991), that is insufficient in mass bal-

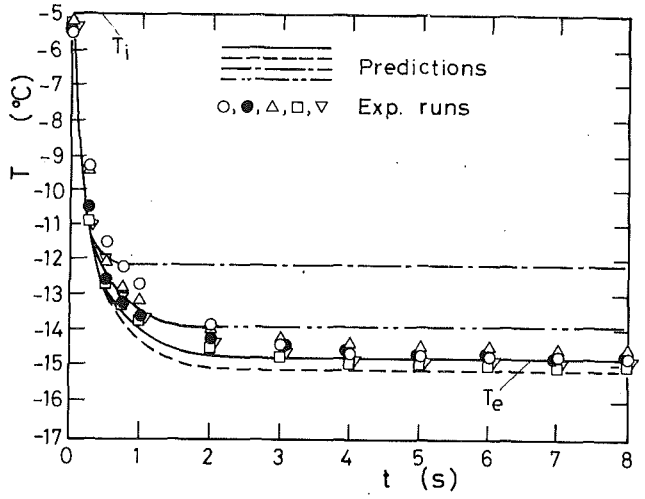

Fig. 3 Abrupt temperature fall in the melting system, and comparison of predictions and experiments for a calcium chloride ($CaCl_2$) aqueous solution under the conditions of $C_{mi}=0.2$, $T_i=-5°C$, $\epsilon_i=0.55$, $d_{1i}=d_{ei}=0.34$ mm; —— best prediction with variable physical properties (integrals I and II); · · · · prediction with constant physical properties (integrals I and II); - · - · prediction in earlier paper (Sugawara and Konda, 1991) (integral II); - · · - prediction with melting from $r_c=r_2$, $t=0$ (integral I)

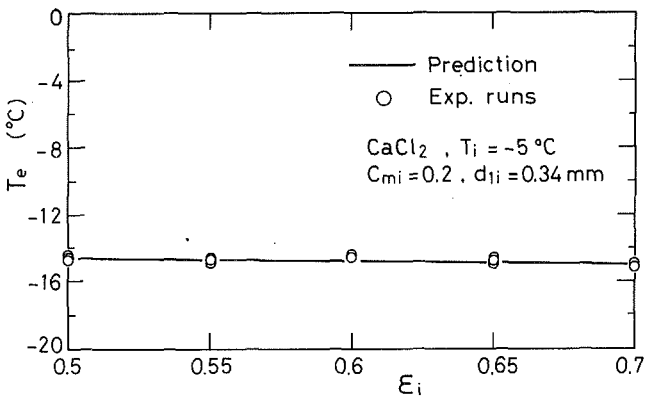

Fig. 4 Effect of initial porosity ϵ_i on temperature fall T_e for calcium chloride ($CaCl_2$) aqueous solution

ance due to the lack of the second term, dr_1/dt, in the right-hand side of Eq. (6). It is, however, very difficult to predict the melting rate in the present form of Eq. (6) due to a very large value of dr_1/dt. This also means that the melting rate could not be predicted by the present diffusion-controlled analytical model just after the melting starts. It is thus necessary to consider another concept to predict the melting rate precisely. However, it is very difficult to have a solution for this at the present stage.

To overcome this difficulty the melting rate in the region of $r_c<r_2$ is predicted approximately by using only integral II in Eq. (6), even though it is insufficient in mass balance due to the neglecting of the second term in the right-hand side in Eq. (6). As will be demonstrated later, it is noticed that the effect of the approximate treatment on all melting is very small, and also that the treatment is worthy as an expediential method because of a clear improvement of the prediction.

After some treatments, Eq. (5) is led to the ordinary differential equation, which governs the major part of the melting:

$$\frac{dC_{w2}}{dt}=\left[\frac{15d_1^2\dot{m}}{2\rho_s}(r_1-r_2)^3-\frac{dC_{w1}}{dt}(-6r_1^5+15r_1^4r_2-10r_1^3r_2^2+r_2^5)(r_1-r_2)-\frac{dr_1}{dt}\{(C_{w1}-C_{w2})(-18r_1^5+60r_1^4r_2-70r_1^3r_2^3+30r_1^2r_2^3-2r_2^5)-30(C_{w2}-C_{wi})r_1^2(r_1-r_2)^3-30C_{w1}r_1^2(r_1-r_2)^3\}\right]\Big/\{(r_2-r_1)(4r_1^5-5r_1^4r_2-10r_1^2r_2^3+20r_1r_2^4-9r_2^5)\} \quad (7)$$

In an earlier paper (Sugawara and Konda, 1991) the temperature fall in the melting system was analyzed for constant physical properties, in which the specific heat of an aqueous solution was fixed as a mean value between the initial temperature and an equilibrium temperature at an initial concentration C_{wi} during the melting process. However, the specific heat of each aqueous solution in the present study was changed depending on concentration and temperature variation during the melting process (variable physical properties). On the other hand, the specific heat of ice was adopted as the value of 0°C.

The specific heat for a calcium chloride aqueous solution was adopted from the data in an earlier work (Sugawara and Konda, 1991). On the other hand, the specific heats for a sodium chloride and magnesium chloride aqueous solutions were estimated interpolating or extrapolating data in the data books (JSC, 1966; JSME, 1975). It was conclusively shown that specific heat was very significant, but density was minor for the melting process. The present analysis does not depend on the type of inorganic salt solutions, such as $CaCl_2$, NaCl, and $MgCl_2$, but depends on the phase diagrams and thermophysical properties of each aqueous solution.

Results and Discussion

Figure 3 shows a transient temperature fall in the melting system during the melting with a comparison of numerical and experimental results. The temperature in the melting system falls rapidly within a few seconds, and then the temperature stays uniform at T_e, which indicates a completion of the melting. The prediction in an earlier study (Sugawara and Konda, 1991) indicated by a single-dotted chain line (- - -) significantly underestimates the experiment due to an imperfection of the mass balance integral as mentioned earlier. On the other hand, the present improved prediction with constant physical properties indicated by a dashed line (- - - -) slightly overestimates the experiments. It is shown that the present improved numerical result with variable physical properties indicated by a solid line (——) gives a good prediction for the experiments. The two-dotted line (- - - -) in Fig. 3 indicates a numerical result predicted only by Eq. (5) (integral I) with variable physical properties, which is used from just after the start of melting ($t=0$, $r_c=r_2$), neglecting the melting in the region of $r_c<r_2$ by using integral II. It should be noticed that the prediction using only integral I compares better with the experimental data. Allowing 10 percent deviation from experimental data, it is possible to predict melting rate by using only integral I. However, a combined numerical analysis using integrals I and II is adopted in the present study, as shown by the solid line in Fig. 3.

Figure 4 shows the effect of initial porosity ϵ_i on the temperature fall T_e for a calcium chloride ($CaCl_2$) aqueous solution. T_e decreases very gently with increasing ϵ_i, which suggests that net melting mass (kg) increases with increasing the porosity. However, the melting mass per unit volume M is not largely influenced by ϵ_i due to the volume increase of the aqueous solution in a cell, as will be demonstrated later in Fig. 6.

Figure 5 shows the effect of initial concentration C_{mi} on T_e for calcium chloride ($CaCl_2$), sodium chloride (NaCl), and magnesium chloride ($MgCl_2$) aqueous solutions. The initial temperature T_i is $-5°C$ in all cases; an increase in C_{mi} strongly reflects T_e for each aqueous solution. T_e of a magnesium chlo-

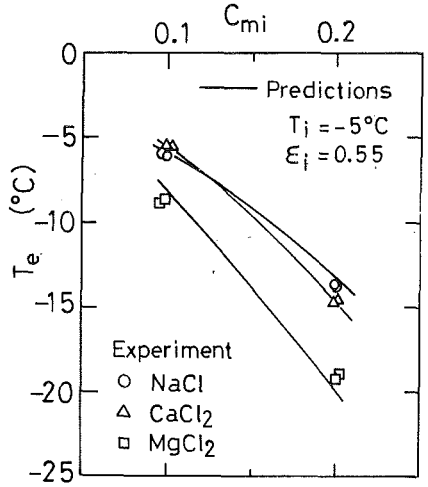

Fig. 5 Temperature fall T_e versus initial concentration C_{mi} for each binary aqueous solution

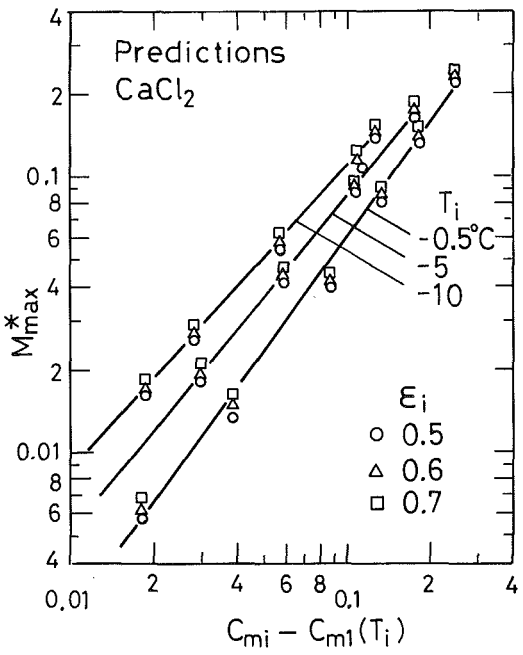

Fig. 6 Dimensionless maximum melting mass per unit volume of a snow layer M^*_{max} versus the concentration difference $C_{mi} - C_{m1}(T_i)$ for a calcium chloride aqueous solution

ride aqueous solution is much larger than other aqueous solutions. It is necessary to increase C_{mi} in order to have much more melting mass. It is shown that the present numerical results give good predictions for the melting of a snow layer into each aqueous solution.

Figure 6 shows predicted relations of dimensionless maximum melting mass per unit volume of a snow layer M^*_{max} and the concentration difference $C_{mi} - C_{m1}(T_i)$ $(= C_{wl}(T_i) - C_{wi}$, see Nomenclature and Fig. 2) on a logarithmic graph for a calcium chloride aqueous solution. The concentration difference is interpreted as a driving force of the melting of a snow layer into a binary aqueous solution. It is found that a calcium chloride aqueous solution can melt large amounts of snow, although the temperature difference does not exist in both a snow layer and an aqueous solution at the start of melting. It is also found that M^*_{max} has a linear relationship with the concentration difference, and that the effect of ϵ_i on M^*_{max} is very small due to the same reason as previously mentioned in Fig. 4. Neglecting the effect of ϵ_i on M^*_{max}, a simple relation can be presented in order to obtain M^*_{max} easily as follows:

$$M^*_{max} = k\{C_{mi} - C_{m1}(T_i)\}^b \quad (8)$$

where a constant k, and an index b including the initial temperature T_i, are approximated for each aqueous solution as follows:

Sodium chloride aqueous solution

$$k = 1.0$$

$$b = 1.23 + 0.0211T_i + 6.08 \times 10^{-4} T_i^2$$

where

$$C_{m1}(T_i) < C_{mi} < 0.24, \quad -10°C < T_i < -0.5°$$

Calcium chloride aqueous solution

$$k = 1.4$$

$$b = 1.38 + 0.0352T_i + 7.49 \times 10^{-4} T_i^2$$

where

$$C_{m1}(T_i) < C_{mi} < 0.27, \quad -10°C < T_i < -0.5°C$$

Magnesium chloride aqueous solution

$$k = 1.6$$

$$b = 1.32 + 0.041T_i + 1.80 \times 10^{-3} T_i^2$$

where

$$C_{m1}(T_i) < C_{mi} < 0.22, \quad -10°C < T_i < -0.5°C$$

The initial diameter of the snow crystal d_{1i} will affect transient manners of the melting. However, M^*_{max} as a completion of the melting is not affected by d_{1i}, considering specific characteristics of the present analytical models.

Conclusions

An improved spherical cell and diffusion-controlled analytical models were reported to predict quantitatively the melting of a snow layer into calcium chloride, sodium chloride, and magnesium chloride aqueous solutions. Summing up the present results, the following conclusions can be drawn:

1 The present numerical results considering variations in physical properties were successfully validated through the measurement of an abrupt temperature fall of a snow layer suddenly immersed in binary aqueous solutions.

2 The amount of snow melted, M_{max}, is only dependent upon C_{mi} and T_i and should be predictable from a simple heat balance and phase diagram, assuming the mass per unit volume of a snow layer is larger than M_{max}.

3 The dimensionless maximum melting mass per unit volume of a snow layer, M^*_{max}, was related by the concentration difference $C_{mi} - C_{m1}(T_i)$ as a driving force for inducing melting.

Acknowledgments

The authors wish to acknowledge the late T. Sugawara for encouraging us to conduct this work.

References

Beckermann, C., and Viskanta, R., 1988, "Double-Diffusive Convection Due to Melting," *Int. J. Heat Mass Transfer*, Vol. 31, pp. 2077–2089.

Carey, V. P., and Gebhart, B., 1982, "Transport Near a Vertical Ice Surface Melting in Saline Water, Some Numerical Calculations," *Journal of Fluid Mechanics*, Vol. 117, pp. 379–402.

Griffin, O. M., 1973, "Heat, Mass, and Momentum Transfer During the Melting of Glacial Ice in Sea Water," ASME JOURNAL OF HEAT TRANSFER, Vol. 95, pp. 317–323.

Japan Society of Chemistry, 1966, *Handbook of Chemistry, Basic Version II*, Maruzen Press, Tokyo, [in Japanese], pp. 774–775.

Japan Society of Mechanical Engineers, 1975, *JSME Data Book: Heat Transfer* [in Japanese], p. 299.

Japan Society of Mechanical Engineers, 1983, *JSME Data Book: Thermophysical Properties of Fluids* [in Japanese], pp. 461–467.

Josberger, E. G., and Martin, S., 1981, "A Laboratory and Theoretical Study of the Boundary Layer Adjacent to a Vertical Melting Ice Wall in Salt Water," *Journal of Fluid Mechanics*, Vol. 111, pp. 439–473.

Sammakia, B., and Gebhart, B., 1983, "Transport Near a Vertical Ice Surface Melting in Water of Various Salinity Levels," *Int. J. Heat Mass Transfer*, Vol. 26, pp. 1439–1452.

Sugawara, M., Inaba, H., Nishimura, H., and Mizuno, M., 1987, "Melting of Horizontal Ice Layer From Above by Combined Effect of Temperature and Concentration of Aqua-Solvent," *Wärme- und Stoffübertragung*, Vol. 21, pp. 227–232.

Sugawara, M., and Konda, Y., 1991, "Melting of Snow With a Diffusion-Controlled Analytical Model," *Wärme- und Stoffübertragung*, Vol. 26, pp. 225–232.

Unification of Source-and-Sink Method and Boundary Element Method for the Solution of Potential Problems

C. K. Hsieh[1]

Introduction

Green's functions have been used in the development of the boundary element methods, BEM (Brebbia, 1984), and in the extension of the source-and-sink methods, SSM (Choi and Hsieh, 1992; Hsieh and Choi, 1992). A close examination of these methods reveals that (*i*) the Green's functions used in them are different, and (*ii*) there are far fewer terms to be evaluated in the SSM as compared with the BEM. Since both methods originate from the Green's functions and the SSM are easier to use, there must be a way by which these methods can be unified so that the usefulness of the Green's functions can be broadened in both methods. Specifically, this unification should simplify the BEM currently in use, while it should also extend the SSM to the solution of potential problems with dissimilar properties.

Derivation of General Green's Function Method

A general Green's function method can be derived by solving heat diffusion in a domain with expandable boundaries. As shown in Fig. 1, the temperature in the domain can be expressed in terms of Green's function as (Hsieh et al., 1992)

$$T(\bar{r}, t) = \int_{\Omega'(0)} G(\bar{r}, t; \bar{r}', 0) T_i(\bar{r}')\, dr' + \frac{\alpha}{k} \int_0^t \int_{\Omega'(s)} G(\bar{r}, t; \bar{r}', s) u(\bar{r}', s)\, dr'\, ds + \int_0^t \int_{\Gamma'(s)} G(\bar{r}, t; \bar{r}', s) T(\bar{r}', s) \frac{dR(s)}{ds}\, dr'\, ds + \sum_i \left\{ \quad \right\} \quad (1)$$

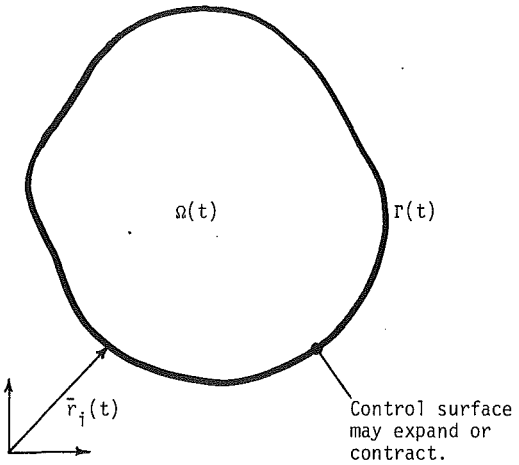

Fig. 1 System analyzed

Table 1 Expressions for braced term in Eq. (1)

BOUNDARY CONDITION	$\{\ \}_{BEM}$	$\{\ \}_{SSM}$
$T(\bar{r}_i, t) = F_i(\bar{r}_i, t)$	$\alpha \int_0^t \int_{\Gamma'_i} [G(\bar{r}, t; \bar{r}', s) \frac{\partial T(\bar{r}', s)}{\partial n'_i} - T(\bar{r}', s) \frac{\partial G(\bar{r}, t; \bar{r}', s)}{\partial n'_i}] dr'_i ds$	$-\alpha \int_0^t \int_{\Gamma'_i} \frac{\partial G(\bar{r}, t; \bar{r}'_i, s)}{\partial n'_i} F_i(\bar{r}'_i, s)\, dr'_i ds$
$\frac{\partial T(\bar{r}_i, t)}{\partial n_i} = -\frac{G_i(\bar{r}_i, t)}{k_i}$		$-\alpha \int_0^t \int_{\Gamma'_i} G(\bar{r}, t; \bar{r}'_i, s) \frac{G_i(\bar{r}'_i, s)}{k_i}\, dr'_i ds$
$\frac{\partial T(\bar{r}_i, t)}{\partial n_i} + \frac{h_i}{k_i} T(\bar{r}_i, t) = \frac{1}{k_i} H_i(\bar{r}_i, t)$		$\alpha \int_0^t \int_{\Gamma'_i} G(\bar{r}, t; \bar{r}'_i, s) \frac{H_i(\bar{r}'_i, s)}{k_i}\, dr'_i ds$

where the last term accounts for the boundary conditions and is tabulated in Table 1, where n_i refers to an outward drawn normal.

In Eq. (1) the initial condition, $T_i(\bar{r})$, heat generation, $u(\bar{r}, t)$, boundary motion, $dR(t)/dt$, and boundary conditions are accounted for in four separate integrals on the right. Equation (1) as derived can be applied to the formulation of both BEM and SSM. In the BEM, the Green's function is taken to be the free-space Green's function, which can be derived as (Morse and Feshbach, 1953)

$$G(\bar{r}, t; \bar{r}', s) = \frac{1}{[2\sqrt{\pi\alpha(t-s)}]^d} \exp\left[-\frac{(\bar{r}-\bar{r}')^2}{4\alpha(t-s)} \right] \quad (2)$$

where d refers to the number of dimensions for the domain. In the derivation of the boundary element equations, the source point is moved to the boundary, giving the boundary element equation

$$\lim_{\bar{r} \to \bar{r}_i} T(\bar{r}, t) = C_i T(\bar{r}_i, t) \quad (3)$$

where

$$C_i = \frac{\theta_1 - \theta_2}{2\pi} \quad (4)$$

Principal values have been used in Eq. (4) in which θ_1 and θ_2 refer to the angles made by the preceding and succeeding boundary elements, respectively, for a two-dimensional domain. The coefficient C_i reduces to 1/2 for a one-dimensional domain.

As for the SSM, the boundary term is modified to relate the specific conditions that are imposed on the boundary. The

[1]Mechanical Engineering Department, University of Florida, Gainesville, FL 32611.

Contributed by the Heat Transfer Division of The American Society of Mechanical Engineers. Manuscript received by the Heat Transfer Division July 1992; revision received January 1993. Keywords: Conduction, Moving Boundaries, Transient and Unsteady Heat Transfer. Associate Technical Editor: L. S. Fletcher.

Japan Society of Mechanical Engineers, 1983, *JSME Data Book: Thermophysical Properties of Fluids* [in Japanese], pp. 461–467.

Josberger, E. G., and Martin, S., 1981, "A Laboratory and Theoretical Study of the Boundary Layer Adjacent to a Vertical Melting Ice Wall in Salt Water," *Journal of Fluid Mechanics*, Vol. 111, pp. 439–473.

Sammakia, B., and Gebhart, B., 1983, "Transport Near a Vertical Ice Surface Melting in Water of Various Salinity Levels," *Int. J. Heat Mass Transfer*, Vol. 26, pp. 1439–1452.

Sugawara, M., Inaba, H., Nishimura, H., and Mizuno, M., 1987, "Melting of Horizontal Ice Layer From Above by Combined Effect of Temperature and Concentration of Aqua-Solvent," *Wärme- und Stoffübertragung*, Vol. 21, pp. 227–232.

Sugawara, M., and Konda, Y., 1991, "Melting of Snow With a Diffusion-Controlled Analytical Model," *Wärme- und Stoffübertragung*, Vol. 26, pp. 225–232.

Unification of Source-and-Sink Method and Boundary Element Method for the Solution of Potential Problems

C. K. Hsieh[1]

Introduction

Green's functions have been used in the development of the boundary element methods, BEM (Brebbia, 1984), and in the extension of the source-and-sink methods, SSM (Choi and Hsieh, 1992; Hsieh and Choi, 1992). A close examination of these methods reveals that (*i*) the Green's functions used in them are different, and (*ii*) there are far fewer terms to be evaluated in the SSM as compared with the BEM. Since both methods originate from the Green's functions and the SSM are easier to use, there must be a way by which these methods can be unified so that the usefulness of the Green's functions can be broadened in both methods. Specifically, this unification should simplify the BEM currently in use, while it should also extend the SSM to the solution of potential problems with dissimilar properties.

Derivation of General Green's Function Method

A general Green's function method can be derived by solving heat diffusion in a domain with expandable boundaries. As shown in Fig. 1, the temperature in the domain can be expressed in terms of Green's function as (Hsieh et al., 1992)

$$T(\bar{r}, t) = \int_{\Omega'(0)} G(\bar{r}, t; \bar{r}', 0) T_i(\bar{r}')\, dr' + \frac{\alpha}{k} \int_0^t \int_{\Omega'(s)} G(\bar{r}, t; \bar{r}', s) u(\bar{r}', s)\, dr'\, ds + \int_0^t \int_{\Gamma'(s)} G(\bar{r}, t; \bar{r}', s) T(\bar{r}', s) \frac{dR(s)}{ds}\, dr'\, ds + \sum_i \left\{ \quad \right\} \quad (1)$$

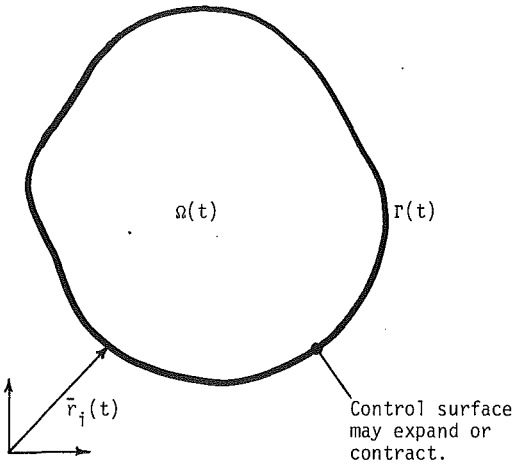

Fig. 1 System analyzed

Table 1 Expressions for braced term in Eq. (1)

BOUNDARY CONDITION	$\{\ \}_{BEM}$	$\{\ \}_{SSM}$
$T(\bar{r}_i, t) = F_i(\bar{r}_i, t)$	$\alpha \int_0^t \int_{\delta\Gamma'_i} [G(\bar{r}, t; \bar{r}', s) \frac{\partial T(\bar{r}', s)}{\partial n'_i} - T(\bar{r}', s) \frac{\partial G(\bar{r}, t; \bar{r}', s)}{\partial n'_i}] dr'_i ds$	$-\alpha \int_0^t \int_{\delta\Gamma'_i} \frac{\partial G(\bar{r}, t; \bar{r}'_i, s)}{\partial n'_i} F_i(\bar{r}'_i, s)\, dr'_i ds$
$\frac{\partial T(\bar{r}_i, t)}{\partial n_i} = -\frac{G_i(\bar{r}_i, t)}{k_i}$		$-\alpha \int_0^t \int_{\delta\Gamma'_i} G(\bar{r}, t; \bar{r}'_i, s) \frac{G_i(\bar{r}'_i, s)}{k_i}\, dr'_i ds$
$\frac{\partial T(\bar{r}_i, t)}{\partial n_i} + \frac{h_i}{k_i} T(\bar{r}_i, t) = \frac{1}{k_i} H_i(\bar{r}_i, t)$		$\alpha \int_0^t \int_{\delta\Gamma'_i} G(\bar{r}, t; \bar{r}'_i, s) \frac{H_i(\bar{r}'_i, s)}{k_i}\, dr'_i ds$

where the last term accounts for the boundary conditions and is tabulated in Table 1, where n_i refers to an outward drawn normal.

In Eq. (1) the initial condition, $T_i(\bar{r})$, heat generation, $u(\bar{r}, t)$, boundary motion, $dR(t)/dt$, and boundary conditions are accounted for in four separate integrals on the right. Equation (1) as derived can be applied to the formulation of both BEM and SSM. In the BEM, the Green's function is taken to be the free-space Green's function, which can be derived as (Morse and Feshbach, 1953)

$$G(\bar{r}, t; \bar{r}', s) = \frac{1}{[2\sqrt{\pi\alpha(t-s)}]^d} \exp\left[-\frac{(\bar{r}-\bar{r}')^2}{4\alpha(t-s)} \right] \quad (2)$$

where d refers to the number of dimensions for the domain. In the derivation of the boundary element equations, the source point is moved to the boundary, giving the boundary element equation

$$\lim_{\bar{r} \to \bar{r}_i} T(\bar{r}, t) = C_i T(\bar{r}_i, t) \quad (3)$$

where

$$C_i = \frac{\theta_1 - \theta_2}{2\pi} \quad (4)$$

Principal values have been used in Eq. (4) in which θ_1 and θ_2 refer to the angles made by the preceding and succeeding boundary elements, respectively, for a two-dimensional domain. The coefficient C_i reduces to 1/2 for a one-dimensional domain.

As for the SSM, the boundary term is modified to relate the specific conditions that are imposed on the boundary. The

[1]Mechanical Engineering Department, University of Florida, Gainesville, FL 32611.

Contributed by the Heat Transfer Division of The American Society of Mechanical Engineers. Manuscript received by the Heat Transfer Division July 1992; revision received January 1993. Keywords: Conduction, Moving Boundaries, Transient and Unsteady Heat Transfer. Associate Technical Editor: L. S. Fletcher.

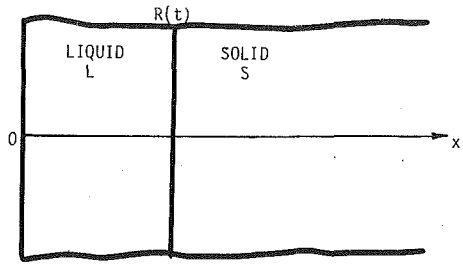

Pre-melt Stage

Governing equation: $\frac{\partial^2 T_o(x,t)}{\partial x^2}=\frac{1}{\alpha}\frac{\partial T_o(x,t)}{\partial t}$, $x\in(LUS)$, $t_o\geq t>0$

Initial condition: $T_o(x,0)=0$

Boundary condition: $T_o(0,t)=F(t)$ or $\frac{\partial T_o(0,t)}{\partial x}=-\frac{G(t)}{k}$

Melting Stage

Liquid Region--

Governing equation: $\frac{\partial^2 T_L(x,t)}{\partial x^2}=\frac{1}{\alpha}\frac{\partial T_L(x,t)}{\partial t}$, $x\in L$, $t>t_o$

Boundary condition: $T_L(0,t)=F(t)$ or $\frac{\partial T_L(0,t)}{\partial x}=-\frac{G(t)}{k}$

Solid Region--

Governing equation: $\frac{\partial^2 T_S(x,t)}{\partial x^2}=\frac{1}{\alpha}\frac{\partial T_S(x,t)}{\partial t}$, $x\in S$, $t>t_o$

Initial condition: $T_S(x,t_o)=T_o(x,t_o)$

Interface--

Temperature condition: $T_L(R(t),t)=T_S(R(t),t)=T_m$

Flux condition: $\frac{\partial T_S(R(t),t)}{\partial x}-\frac{\partial T_L(R(t),t)}{\partial x}=\frac{\rho L}{k}\frac{dR(t)}{dt}$

Fig. 2 Stefan problem solved

boundary expressions can be derived as those listed in the third column in Table 1 (Morse and Feshbach, 1953). In this method, the Green's function is found by solving an auxiliary problem which is the homogeneous version of the original problem. In the auxiliary problem, the initial condition is nonzero, while both governing equation and boundary conditions are homogeneous. This auxiliary problem is solved and its results are recast in the form of Eq. (1) for the determination of the Green's function.

Unification of Boundary and Source-Sink Methods

The SSM and BEM will now be used to solve a one-dimensional Stefan problem in semi-infinite domain as shown in Fig. 2. For this problem, the source-and-sink concept is used to recast the original problem in the form of an equivalent problem as follows (Lightfoot, 1929; Choi and Hsieh, 1992):

Governing equation

$$\nabla^2 T(x,t)\pm\frac{\rho L}{k}\frac{dR(t)}{dt}\delta[x-R(t)]=\frac{1}{\alpha}\frac{\partial T(x,t)}{\partial t},\quad x\in(\mathrm{LUS}),\quad t>0 \tag{5}$$

where the second term on the left characterizes the moving phase-change interface; the plus sign is taken for freezing (i.e., source) and minus sign for melting (i.e., sink). It is easy to show that Eq. (5) reduces to the original problem given in Fig. 2. The temperature can be derived as (Hsieh and Choi, 1992)

$$\frac{T(x,t)}{T_m}=\frac{T_o(x,t)}{T_m}\pm\frac{\hat{H}(t-t_0)}{\mathrm{Ste}}\int_0^{t-t_0}\frac{dR(s+t_0)}{ds}\times G(x,t-t_0;R(s+t_0,s)ds \tag{6}$$

where

$$T_o(x,t)=\sqrt{\frac{\alpha}{\pi}}\int_0^t\frac{E(s)}{(t-s)^{1/2}}\exp\left[-\frac{x^2}{4\alpha(t-s)}\right]ds \tag{7}$$

and

$$G(x,t;x',s)=\frac{1}{2\sqrt{\pi\alpha(t-s)}}\left\{\exp\left[-\frac{(x-x')^2}{4\alpha(t-s)}\right]\pm\exp\left[-\frac{(x+x')^2}{4\alpha(t-s)}\right]\right\} \tag{8}$$

in which

$$E(s)=\begin{cases}\dfrac{x}{2\alpha}\dfrac{F(s)}{t-s},\\ \dfrac{1}{k}G(s),\end{cases}\qquad \hat{H}(t-t_0)=\begin{cases}1 & \text{for } t>t_0,\\ 0 & t\leq t_0,\end{cases}\qquad \mathrm{Ste}=\frac{cT_m}{L} \tag{9}$$

where t_0 refers to the time when phase change starts. In Eq. (8) the plus and minus signs are used for flux, $G(s)$, and temperature, $F(s)$, conditions imposed on the boundary, respectively. Using the Heaviside function given in Eq. (9) permits Eq. (6) to be used for all time and for both one- and two-phase melting and solidification problems.

In the BEM, Eqs. (1) and (3) are used to write the temperatures in two regions. Thus for a melting problem, the temperatures in the melted and unmelted regions are, respectively (Hsieh et al., 1992):

$$\frac{1}{2}T_m=\alpha\int_0^t\left[G(R(t),t;R(s),s)\frac{\partial T(R^-,s)}{\partial x'}-T_m\frac{\partial G(R(t),t;R(s),s)}{\partial x'}\right]\left[-G(R(t),t;0,s)\frac{\partial T(0,s)}{\partial x'}+T(0,s)\frac{\partial G(R(t),t;0,s)}{\partial x'}\right]ds+\int_0^t T_m G(R(t),t;R(s),s)\frac{dR(s)}{ds}ds \tag{10}$$

$$\frac{1}{2}T_m=\alpha\int_0^t\left[-G(R(t),t;R(s),s)\frac{\partial T(R^+,s)}{\partial x'}+T_m\frac{\partial G(R(t),t;R(s),s)}{\partial x'}\right]ds-\int_0^t T_m G(R(t),t;R(s),s)\frac{dR(s)}{ds}ds \tag{11}$$

The Green's functions have been given in Eq. (2) where d is set to unity for the one-dimensional domain.

There appears to be no connection between the temperatures in Eqs. (6), (10), and (11). However, if one sets x equal to $R(t)$, interface position, Eq. (6) reduces to

$$T_m=\sqrt{\frac{\alpha}{\pi}}\int_0^t\frac{E(s)}{(t-s)^{1/2}}\exp\left[-\frac{R^2(t)}{4\alpha(t-s)}\right]ds-\frac{L}{c}\int_0^t G(R(t),t;R(s),s)\frac{dR(s)}{ds}ds \tag{12}$$

for a melting problem. Clearly, Eq. (12) is much simpler than either Eq. (10) or (11), or their combination. In fact, it can be shown that Eq. (12) is actually the sum of Eqs. (10) and

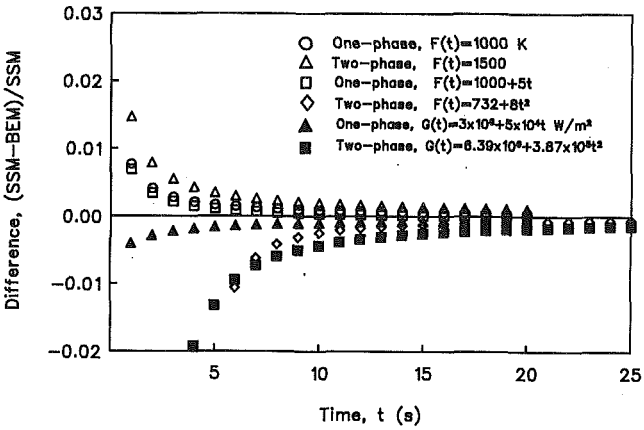

Fig. 3 Numerical results of six examples

(11), in which the interface flux condition (see Fig. 2) has been incorporated,

$$T_m = \alpha \int_0^t \left[T(0, s) \frac{\partial G(R(t), t; 0, s)}{\partial x'} - G(R(t), t; 0, s) \frac{\partial T(0, s)}{\partial x'} \right] ds - \frac{L}{c} \int_0^t G(R(t), t; R(s), s) \frac{dR(s)}{ds} ds \quad (13)$$

Comparison will now be made between Eqs. (12) and (13). It is noted first that the Green's functions in Eq. (13) are the free-space Green's function given in Eq. (2), which is different from that in Eq. (12); see Eq. (8). However, for the BEM, if a temperature condition is prescribed at the boundary, an image of the opposite polarity must be placed at $-x'$ in order to simulate this temperature condition; this leads to the subtraction of the second exponential term in Eq. (8). Conversely, if a flux condition is prescribed at the boundary, an image of the same polarity must be placed at $-x'$ in order to simulate this flux condition; this leads to the addition of the second exponential term in Eq. (8). In either case, the Green's functions for the BEM have shown to be identical to those for the SSM.

It can also be shown that only one term in the bracket in Eq. (13) actually remains upon imposition of the boundary conditions. This is due to the fact that if $T(0, s) \neq 0$, $G(R(t), t; 0, s) = 0$; conversely, if $\partial T(0, s)/\partial x' \neq 0$, then $\partial G(R(t), t; 0, s)/\partial x' = 0$—a result of the definition of the Green's function, which has been used in the derivation of Eq. (1). These characteristics can also be verified by evaluating G and $\partial G/\partial x'$ using Eq. (8) in which x is set to $R(t)$ and x' is set to 0.

Numerical Experiment

The unification described in this paper has been tested numerically with six examples encompassing one- and two-phase Stefan problems imposed with constant and time-variant temperature and flux conditions as given by Choi (1991) and Hsieh et al. (1992). In all six cases tested for aluminum shown in Fig. 3, the BEM and SSM results are in agreement. It should be noted, however, that the slightly larger disagreement at the onset of phase change is due to initial singularity. All data points are plotted at the moment when phase change starts to take place. Thus for the last set represented by closed squares, the aluminum starts to melt at 4 s. As described in those references, the SSM is particularly accurate at large time, where good agreement of results between the two methods is visible, giving numerical evidence for the unification of the methods.

Critique and Applications

The derivation above shows clearly that the BEM and the SSM are actually two methods in one. Since the SSM have far fewer terms to be evaluated while the BEM can easily be adapted to situations when property values are different in different regions, both the present BEM and SSM can be improved by using the insight gained from this paper. Specifically, in the current practice of the BEM, one could improve them by solving the "sum" of the boundary element equations such as Eq. (13), instead of the "individual" boundary element equations such as Eqs. (10) and (11). Terms can be canceled or dropped out, resulting in great simplification of the equation solved. On the other hand, for heat diffusion in multiple regions with dissimilar material properties, one could start with the formulation of individual boundary element equations and add them together to cancel and drop out terms. A simplified boundary element equation results, which easily accounts for the use of double source and sink terms at the interfaces as suggested by Kolodner (1956). The unification described in this paper thus has great utility in the solution of heat diffusion problems.

References

Brebbia, C. A., 1984, *Topics in Boundary Element Research*, Springer-Verlag, New York.

Choi, C.-Y., 1991, "Application of Source-and-Sink Method and Boundary-Element Method to the Solution of Stefan Problems Imposed With Constant or Time-Variant Temperature and Flux Conditions," Ph.D. Thesis, University of Florida, Gainesville, FL.

Choi, C.-Y., and Hsieh, C. K., 1992, "Solution of Stefan Problems Imposed With Cyclic Temperature and Flux Boundary Conditions," *International Journal of Heat and Mass Transfer*, Vol. 35, No. 5, pp. 1181-1195.

Hsieh, C. K., and Choi, C.-Y., 1992, "Solution of One- and Two-Phase Melting and Solidification Problems Imposed With Constant or Time-Variant Temperature and Flux Boundary Conditions," ASME JOURNAL OF HEAT TRANSFER, Vol. 114, pp. 524-528.

Hsieh, C. K., Choi, C.-Y., and Kassab, A. J., 1992, "Solution of Stefan Problems by a Boundary Element Method," *Boundary Element Technology VII*, C. A. Brebbia and M. S. Ingber, eds., Computational Mechanics Publications, Southampton, United Kingdom, pp. 473-490.

Kolodner, I. I., 1956, "Free Boundary Problem for the Heat Equation With Applications to Problems of Change Phase," *Communication of Pure Applied Mathematics*, Vol. 9, pp. 1-31.

Lightfoot, N. M. H., 1929, "Solidification of Molten Steel," *Proceedings of London Mathematical Society*, Ser. 2, Vol. 31, pp. 97-116.

Morse, P. M., and Feshbach, H., 1953, *Methods of Theoretical Physics*, McGraw-Hill, New York.

Freezing of the NaCl–H_2O Binary Compound From Above in a Partially Open Cylindrical Geometry

K. Medjani[1] and R. G. Watts[1]

Nomenclature

D = species diffusivity, $m^2 \cdot s^{-1}$
H = height of the domain of study, m

[1]Department of Mechanical Engineering, Tulane University, New Orleans, LA 70118.

Contributed by the Heat Transfer Division and presented at the ASME Winter Annual Meeting, Anaheim, California, November 8-13, 1992. Manuscript received by the Heat Transfer Division September 1992; revision received February 1993. Keywords: Natural Convection, Numerical Methods, Phase-Change Phenomena.

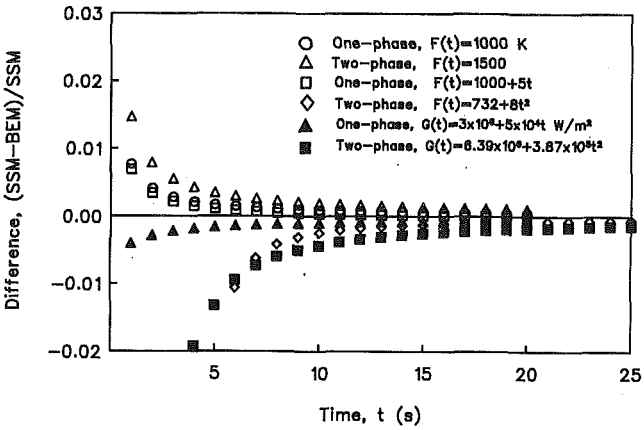

Fig. 3 Numerical results of six examples

(11), in which the interface flux condition (see Fig. 2) has been incorporated,

$$T_m = \alpha \int_0^t \left[T(0, s) \frac{\partial G(R(t), t; 0, s)}{\partial x'} - G(R(t), t; 0, s) \frac{\partial T(0, s)}{\partial x'} \right] ds - \frac{L}{c} \int_0^t G(R(t), t; R(s), s) \frac{dR(s)}{ds} ds \quad (13)$$

Comparison will now be made between Eqs. (12) and (13). It is noted first that the Green's functions in Eq. (13) are the free-space Green's function given in Eq. (2), which is different from that in Eq. (12); see Eq. (8). However, for the BEM, if a temperature condition is prescribed at the boundary, an image of the opposite polarity must be placed at $-x'$ in order to simulate this temperature condition; this leads to the subtraction of the second exponential term in Eq. (8). Conversely, if a flux condition is prescribed at the boundary, an image of the same polarity must be placed at $-x'$ in order to simulate this flux condition; this leads to the addition of the second exponential term in Eq. (8). In either case, the Green's functions for the BEM have shown to be identical to those for the SSM.

It can also be shown that only one term in the bracket in Eq. (13) actually remains upon imposition of the boundary conditions. This is due to the fact that if $T(0, s) \neq 0$, $G(R(t), t; 0, s) = 0$; conversely, if $\partial T(0, s)/\partial x' \neq 0$, then $\partial G(R(t), t; 0, s)/\partial x' = 0$—a result of the definition of the Green's function, which has been used in the derivation of Eq. (1). These characteristics can also be verified by evaluating G and $\partial G/\partial x'$ using Eq. (8) in which x is set to $R(t)$ and x' is set to 0.

Numerical Experiment

The unification described in this paper has been tested numerically with six examples encompassing one- and two-phase Stefan problems imposed with constant and time-variant temperature and flux conditions as given by Choi (1991) and Hsieh et al. (1992). In all six cases tested for aluminum shown in Fig. 3, the BEM and SSM results are in agreement. It should be noted, however, that the slightly larger disagreement at the onset of phase change is due to initial singularity. All data points are plotted at the moment when phase change starts to take place. Thus for the last set represented by closed squares, the aluminum starts to melt at 4 s. As described in those references, the SSM is particularly accurate at large time, where good agreement of results between the two methods is visible, giving numerical evidence for the unification of the methods.

Critique and Applications

The derivation above shows clearly that the BEM and the SSM are actually two methods in one. Since the SSM have far fewer terms to be evaluated while the BEM can easily be adapted to situations when property values are different in different regions, both the present BEM and SSM can be improved by using the insight gained from this paper. Specifically, in the current practice of the BEM, one could improve them by solving the "sum" of the boundary element equations such as Eq. (13), instead of the "individual" boundary element equations such as Eqs. (10) and (11). Terms can be canceled or dropped out, resulting in great simplification of the equation solved. On the other hand, for heat diffusion in multiple regions with dissimilar material properties, one could start with the formulation of individual boundary element equations and add them together to cancel and drop out terms. A simplified boundary element equation results, which easily accounts for the use of double source and sink terms at the interfaces as suggested by Kolodner (1956). The unification described in this paper thus has great utility in the solution of heat diffusion problems.

References

Brebbia, C. A., 1984, *Topics in Boundary Element Research*, Springer-Verlag, New York.

Choi, C.-Y., 1991, "Application of Source-and-Sink Method and Boundary-Element Method to the Solution of Stefan Problems Imposed With Constant or Time-Variant Temperature and Flux Conditions," Ph.D. Thesis, University of Florida, Gainesville, FL.

Choi, C.-Y., and Hsieh, C. K., 1992, "Solution of Stefan Problems Imposed With Cyclic Temperature and Flux Boundary Conditions," *International Journal of Heat and Mass Transfer*, Vol. 35, No. 5, pp. 1181-1195.

Hsieh, C. K., and Choi, C.-Y., 1992, "Solution of One- and Two-Phase Melting and Solidification Problems Imposed With Constant or Time-Variant Temperature and Flux Boundary Conditions," ASME JOURNAL OF HEAT TRANSFER, Vol. 114, pp. 524-528.

Hsieh, C. K., Choi, C.-Y., and Kassab, A. J., 1992, "Solution of Stefan Problems by a Boundary Element Method," *Boundary Element Technology VII*, C. A. Brebbia and M. S. Ingber, eds., Computational Mechanics Publications, Southampton, United Kingdom, pp. 473-490.

Kolodner, I. I., 1956, "Free Boundary Problem for the Heat Equation With Applications to Problems of Change Phase," *Communication of Pure Applied Mathematics*, Vol. 9, pp. 1-31.

Lightfoot, N. M. H., 1929, "Solidification of Molten Steel," *Proceedings of London Mathematical Society*, Ser. 2, Vol. 31, pp. 97-116.

Morse, P. M., and Feshbach, H., 1953, *Methods of Theoretical Physics*, McGraw-Hill, New York.

Freezing of the NaCl–H_2O Binary Compound From Above in a Partially Open Cylindrical Geometry

K. Medjani[1] and R. G. Watts[1]

Nomenclature

D = species diffusivity, $m^2 \cdot s^{-1}$
H = height of the domain of study, m

[1]Department of Mechanical Engineering, Tulane University, New Orleans, LA 70118.

Contributed by the Heat Transfer Division and presented at the ASME Winter Annual Meeting, Anaheim, California, November 8-13, 1992. Manuscript received by the Heat Transfer Division September 1992; revision received February 1993. Keywords: Natural Convection, Numerical Methods, Phase-Change Phenomena.

S = salinity (parts per thousand)
T = temperature, K
$\mathbf{V}$ = velocity vector, $m \cdot s^{-1}$
a = initial tube diameter, m
l = initial tube length, m
c = specific heat, $J \cdot kg^{-1}$
f = volume fraction
h = enthalpy, $J \cdot kg^{-1}$
k = thermal conductivity, $W \cdot m^{-1} \cdot K^{-1}$
p = pressure, $N \cdot m^{-2}$
r, z = polar coordinates, m
t = time, s
u, v = velocities in the r and z directions, respectively, $m \cdot s^{-1}$
α = thermal diffusivity, $m^2 \cdot s^{-1}$
β_T = coefficient of thermal expansion K^{-1}
β_S = coefficient of solutal expansion
κ = permeability, m^2
κ_o = permeability constant m^2
μ = dynamic viscosity $m^2 \cdot s^{-1}$
ρ = density, $kg \cdot m^{-3}$

Subscripts

l = liquid phase
s = solid phase

Introduction

A pure substance solidifies at a fixed temperature, whereas multicomponent phase change occurs over a temperature range. Three different regions can be identified in such a case: a solid region, a liquid region, and a solid-liquid region termed "mushy zone" in between. This mushy zone may consist of a dendritic structure of crystals containing the residual liquid.

Solidification of multicomponent systems is not well understood, and its study is a challenging task. It involves both heat and mass transfer, as well as phase change in a porous region whose porosity varies with time and location. The interface between the liquid and the mushy zone is irregularly shaped and difficult to track. Recently developed one-region models solve this problem by applying one single set of equations valid over the whole domain. Examples include the works of Bennon and Incropera (1987), who made use of classical mixture theory in their model, and Beckermann and Viskanta (1988), who used volume averaging. In this paper we apply the former to the formation of sea-ice, which is well known to be fresher than the water from which it forms. The brine drains from the ice into the underlying seawater through a complex network of brine tubes and channels. We look specifically at a portion of the interface, where small tubes have been observed by Lake and Lewis (1970) and Niedrauer and Martin (1979), extending one or two centimeters up into the ice. They have been noted to pinch off near the top leading to the formation of brine pockets (Niedrauer and Martin, 1979). The model involves a phase change within a mushy zone, heat and mass transfer, as well as double-diffusive natural convection in a partially open geometry. Our results are innovative in that attention is given to local phenomena at the interface. The geometry includes two open boundaries, and we consider unstable thermal and solutal gradients.

Mathematical Formulation

The initial configuration of a brine tube is modeled as a cylinder closed at the top and open to the underlying brine. An axially symmetric two-dimensional (r, z) cylindrical geometry is used (Fig. 1).

The conservation equations for mass, momentum, energy, and species are similar to those used by Bennon and Incropera (1988). A general mixture-dependent variable Φ is written as

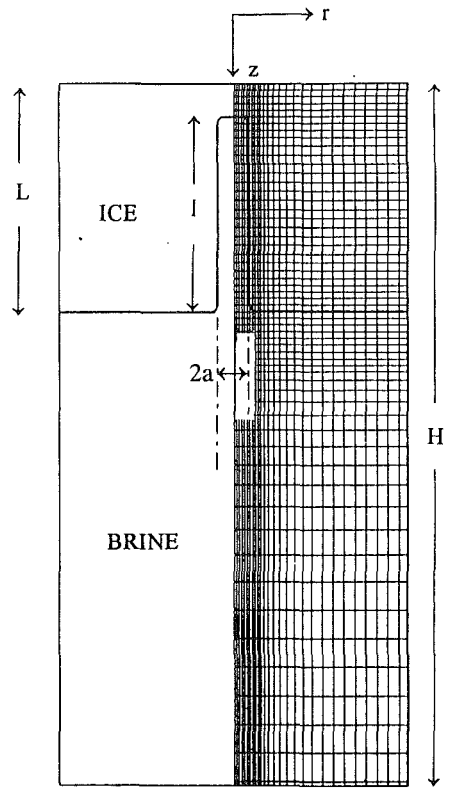

Fig. 1 Schematic of the domain of study with the grid used

$$\Phi = f_l \Phi_l + f_s \Phi_s \tag{1}$$

and a general mixture physical property Γ expressed as

$$\Gamma = f_l \Gamma_l + f_s \Gamma_s \tag{2}$$

There is only about an 8 percent difference between ρ_l and ρ_s, so the mixture density is simply taken as $\rho = (\rho_l + \rho_s)/2$, except in the buoyancy term. Furthermore, we will assume that the solid phase is stationary, i.e., $u_s = v_s = 0$.

Mass Conservation

$$\nabla \cdot \mathbf{V} = 0 \tag{3}$$

Momentum Conservation. The equations include D'Arcy-like resistive terms, which are written in terms of the mixture velocity components u and v. The momentum equations follow:

r Direction:

$$\frac{\partial u}{\partial t} + \mathbf{V} \cdot \nabla u = \nabla \cdot \left(\frac{\mu_l}{\rho_l} \nabla u \right) - \frac{\mu_l}{\kappa \rho_l} u - \frac{\mu_l}{r^2 \rho_l} u - \frac{1}{\rho} \frac{\partial p}{\partial r} \tag{4}$$

z-direction:

$$\frac{\partial v}{\partial t} + \mathbf{V} \cdot \nabla v = \nabla \cdot \left(\frac{\mu_l}{\rho_l} \nabla v \right) - \frac{\mu_l}{\kappa \rho_l} v - \frac{1}{\rho} \frac{\partial p}{\partial z} + g \left[\beta_T (T - T_r) + \beta_S (S - S_r) \right] \tag{5}$$

where the Boussinesq approximation has been used. T_r and S_r refer to the temperature and salinity in the reservoir, far from the tube.

Solute Conservation

$$\frac{\partial S}{\partial t} + \nabla \cdot (\mathbf{V} S) = \nabla \cdot (D \nabla S) + \nabla \cdot (D \nabla (S_l - S)) - \nabla \cdot ((S_l - S)\mathbf{V}) \tag{6}$$

Energy Conservation

$$\frac{\partial h}{\partial t}+\nabla\cdot(\mathbf{V}h)=\nabla\cdot\left(\frac{k}{\rho c_s}\nabla h\right)+\nabla\cdot\left(\frac{k}{\rho c_s}\nabla(h_s-h)\right)-\nabla\cdot((h_l-h)\mathbf{V}) \quad (7)$$

Numerical Analysis

Method of Solution. The momentum equations are solved using the SIMPLER primitive variable approach (Patankar, 1981). The various assumptions made for this one-region model are similar to those of Bennon and Incropera (1988), where they are described in detail. The tube is shown in Fig. 1, and freezing is downward from the top, where a constant heat flux is applied. We are mainly interested in what occurs inside the tube, but the boundary conditions at its mouth are not known. To solve this problem, we extended the domain of study in both the r and z directions. The reason is that it is much easier to set, or at least approximate, the boundary conditions far away from the mouth of the tube. At the outer boundaries, normal gradients of enthalpy and salinity are assumed to be zero. These boundary conditions have been shown by Le Quere et al. (1981), to be very reasonable, as long as the outer boundaries are far enough from those of the tube. In the model presented here, the vertical outer boundary was located about six diameters and the lower boundary about three tube lengths away from the mouth of the tube. Numerical experiments showed that choosing a larger domain did not significantly affect the flow pattern or salinity distribution within the tube itself. For the momentum equations, the dynamic pressure is forced to zero at the open boundaries.

Dimensionless variables are introduced using the height H of the computation domain as the characteristic length scale. The characteristic time is defined using the liquid thermal diffusivity α_l combined with H. In this study, H was equal to 4 cm, and the half-width of the calculation domain was equal to 1 cm. The initial tube length and diameter were 0.9 and 0.20 cm, respectively. The mass and momentum conservation equations were nondimensionalized using the above scales, but because the physical properties used in both the species and energy conservation equations are mixture properties, they vary widely from one location to another. Dimensionless groups such as the Lewis number no longer have the same importance and significance attached to them in one-phase problems. As was noted by Bennon and Incropera (1987), rendering these two equations dimensionless had no advantages. Therefore, the energy and solute conservation equations were solved as presented in Eqs. (6) and (7). Particular attention was paid to the correct coupling between the dimensional and dimensionless equations.

The single most important property is probably the permeability κ used in the momentum equations. The earlier studies mentioned above have used the Kozeny-Carman equation:

$$\kappa=\kappa_0[f_l^3/(1-f_l)^2] \quad (8)$$

where κ_0 is a constant, which depends on the microscopic features of the mushy zone. The problem with this equation is its behavior for values of the liquid fraction f_l near 1.0. Indeed, with typical values of κ_0 of the order of 10^{-11} m^2, flow is driven to nearly zero even in regions where the liquid fraction f_l is as high as 0.8 or 0.9. Experiments conducted in a Hele-Shaw cell allowed us to record video footage of the mushy zone as an NaCl–H_2O solution was frozen from above. Significant flow was observed to occur inside the ice, two or three centimeters above the interface, when a total of 12 to 15 cm of "ice" had grown. A different approach was taken by Oldenburg and Spera (1990), where the Kozeny-Carman equation was used for f_l less than 0.5. For larger liquid fractions, the mushy zone is modeled as a flow of a suspension containing spherical particles (Metzner, 1985). The D'Arcy term in the momentum equations is removed while the viscosity μ is taken as a function of the liquid fraction f_l given by

$$\mu=\mu_l[1/(1-2(1-f_l))]^2 \quad (9)$$

The value of μ becomes infinite at $f_l = 0.5$. To remove this singularity, switching functions are used to make the transition between the two forms smoother (Oldenburg and Spera, 1990). The latter approach might seem unrealistic because of the difference between the two structures (mushy zone and suspension), but the results are closer to our experimental observations than with the Kozeny-Carman equation alone. From a purely fluid-mechanics point of view, this mixed formulation allows for flow within the mushy zone for liquid fractions between 0.5 and 1.0 and was used in this study. At the present time, there is no consensus as to what the permeability κ should be for a given situation. It probably depends on more factors than the liquid fraction alone. Temperature could be one such factor, although the relationship may not necessarily be a direct one. This hypothesis stems from the fact that brine channels were observed to tilt in certain directions according to the temperature gradients (Niedrauer and Martin, 1979).

Computer Program Validation. Results using an 80 × 40 grid were compared to the results from a 60 × 30 grid. There were very slight quantitative differences and almost no qualitative differences between the two. The additional computational costs were, however, rather substantial. The 60 × 30 grid was deemed adequate and used throughout this study.

Several tests were performed to establish the validity of the numerical code. First, the problem of natural convection of air in a square cavity was solved and the results compared to the benchmark solution of de Vahl Davis (1983). The maximum values of the dimensionless streamfunction Ψ for Rayleigh numbers of 10^6 agreed to within 0.1 percent. The average Nusselt numbers differed by the same amount. Agreement was better for lower Rayleigh numbers. Since the enthalpy method was used to accommodate the moving boundary problem, the classical Neumann problem was solved numerically and the results compared to the analytical solutions given by Carslaw and Jaeger (1959). The agreement was very good and the position of the solid-liquid interface was off by less than 0.2 percent for various situations.

Moving-boundary problems are inherently time-dependent and choice of the time-step is critical. Different values of Δt were used, and a value of 1.5×10^{-4} proved to be adequate since it produced essentially the same results as smaller values. The equivalent real time is 0.96 second. Iterations were performed at each time-step and were continued until several criteria were satisfied. First, the residuals for the mass, r-momentum, and z-momentum equations were forced to less than 5×10^{-7}. Next, the residuals for the enthalpy and concentration equations were forced to 10^{-6} J·kg^{-1} and 10^{-6} ppt, respectively. Finally, the values of liquid fraction changes from one iteration to the next within one time-step were forced to less than 10^{-4}. These limits were arrived at by performing calculations with more and more strict convergence criteria. The values used are a good compromise between costs in CPU time and improvement in the results.

Results

The results shown are at real time values of 2000 and 4800 s. Initially, a linear distribution of salinity and temperature is assumed. The temperature increases from top to bottom and the salinity increases upward. So both the isotherms and the lines of constant salinity are initially horizontal. The liquid fraction f_l varies from 1.0 to 0.05 at the walls and top of the

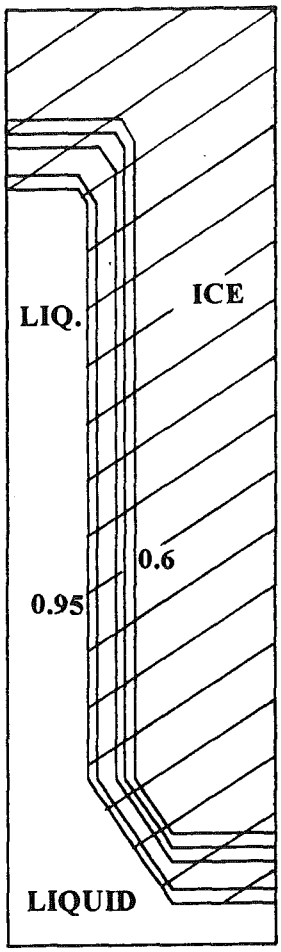

Fig. 2 Initial liquid fraction distribution

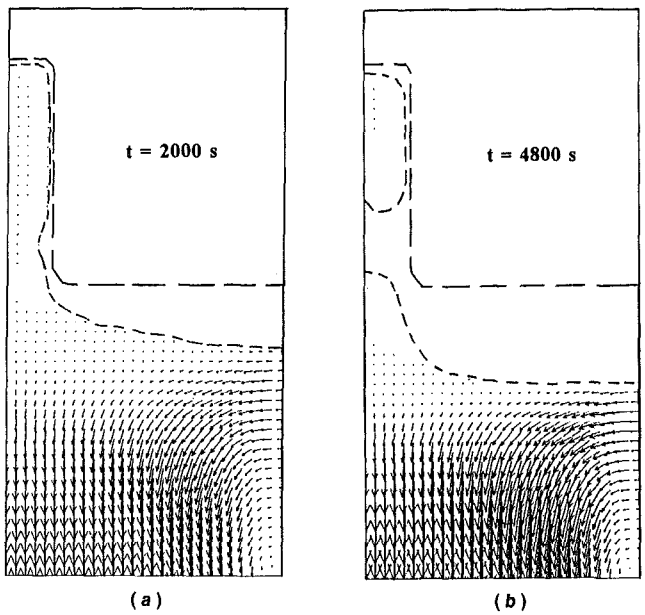

Fig. 3 Flow in the domain of study showing the approximate location of the solid-liquid interface

tube and at the interface. Figure 2 shows liquid fraction lines from 0.5 to 0.9 with increments of 0.1 and 0.95. At these locations, the temperature is in equilibrium with the salinity as given by the phase diagram for the NaCl–H_2O compound. In the liquid, the values for T and S are both increased slightly

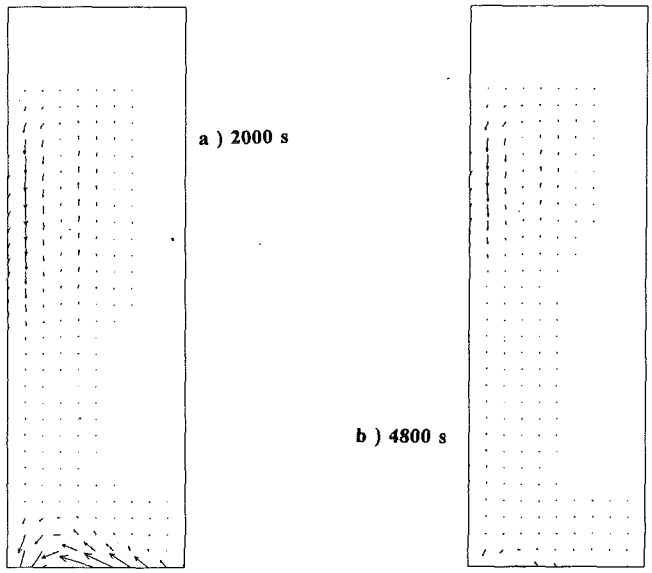

Fig. 4 Flow within the tube amplified to show the details

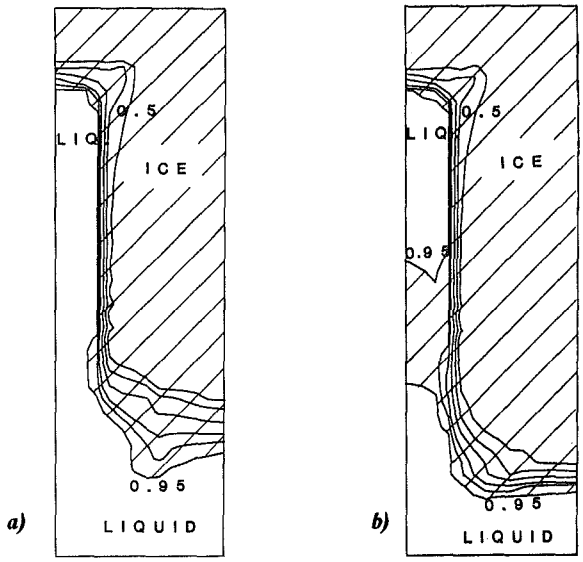

Fig. 5 Liquid fraction lines in the tube (f_l = 0.5, 0.6, 0.7, 0.8, 0.9, 0.95): (*a*) 2000 s; (*b*) 4800 s

in the tube so that freezing due to supercooling could be avoided. At the open boundaries, the boundary conditions depend on the direction of the flow. If the flow is out of the domain, the gradients of salinity and enthalpy are set to zero. If it is into the domain, reservoir conditions (S_r, T_r) will be imposed at the open boundary. At the top of the domain, zero velocities and a constant heat flux are applied. The velocity values at the open boundaries are obtained by satisfying continuity at the outermost control volumes. This is possible because the flow there is always perpendicular to the boundary. The results are presented in a set of four pairs of figures (Figs. 3(*a*)–6(*b*)). At this point, we will stress the fact that these figures are not to scale. The first pair (Fig. 3) represents the flow inside the domain of study. For clarity purposes, the vector plotting routine was scaled to show the outside flow in a clear manner. The long dashed line shows the initial location of the tube, whereas the curved dashed line delineates the approximate liquid–mushy zone interface. Figure 4 is a close-up view of the

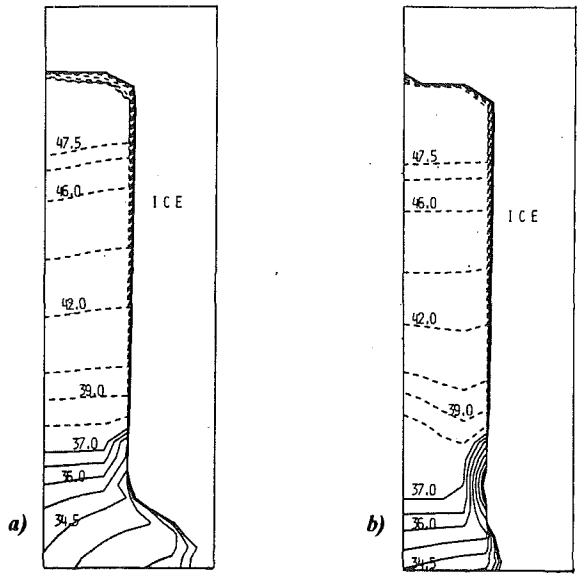

Fig. 6 Salinity lines in the tube: (*a*) 2000 s; (*b*) 4800 s

flow within the tube, with the lower part corresponding to the mouth of the brine tube. The third pair (Fig. 5), shows the liquid fraction lines from 0.6 to 0.95. This helps visualize the extent and the shape of the mushy zone as freezing proceeds. The last pair (Fig. 6) shows the mixture salinity (S) lines inside the brine tube.

At 2000 s, the flow is divided into two regions. In the tube, there is a dominant cell of counterclockwise flow due to the sinking of heavier fluid at the center (Fig. 4(*a*)). Freezing is occurring at the base of this cell from the walls of the tube toward the center (Fig. 5(*a*)). A much smaller cell of weaker flow is present in the area where freezing is occurring. This cell is preventing fluid inside the tube from flowing out into the reservoir. As a result, the lines of constant salinity are only slightly disturbed from the initial state (Fig. 6(*a*)).

The second set of results is for time $t = 4800$ s. The flow pattern for this case is quite different from the previous one. It can be seen from Fig. 4(*b*) that flow within the tube is now essentially restricted to an area at the top of the tube. In the rest of the tube, flow is very weak due to the larger area of freezing (Fig. 5(*b*)). At the top of the tube, freezing is very limited both in the vertical and the radial direction. This area where recirculating flow is occurring remains all liquid. It is essentially an inclusion of brine within the ice. Results for $t = 7200$ s show that it is still in a liquid state.

As stated earlier, the liquid fraction drops from 1.0 to 0.05 very rapidly at the top and wall of the tube. Figures 6(*a*) and 6(*b*) represent the mixture salinity lines ($S = f_l S_l$). In the areas where the liquid fraction is low, the values of S will be proportionately small. Therefore, salinity contours were only plotted where f_l is larger than 0.8. The values of S at the top and wall will be less than those in the adjacent liquid. This explains both the C-shape as well as the steep gradients at the liquid–mushy zone interface.

Conclusions

A state-of-the-art method was used to predict numerically the complex phenomena that take place during the freezing of a binary compound. An attempt was made at looking specifically at the interface between the liquid and the mushy zone that forms in such cases. Thin tubes at this highly irregular interface have been observed to undergo a necking phenomenon, resulting in brine pockets. The purpose of this paper was to describe how and why such a process occurs. The results presented here show the formation of one brine pocket by taking into account the fluid mechanics and phase change involved. Freezing in the radial direction inside the tube inhibits the exchange of fluid between the tube and the underlying brine. A pocket is formed, where salinity remains high. As a result, the pocket remains liquid as freezing continues in the downward direction. At the present time, the results of this study conform partly to the observed phenomenon, which shows necking in the top part of the tube and a repeat of the process. Currently, numerical tests are being conducted with tubes that are longer, i.e., with a smaller value of the aspect ratio a/l. The results should be even closer to the observed phenomena.

References

Beckermann, C., and Viskanta, R., 1988, "Double-Diffusive Convection During Dendritic Solidification of a Binary Mixture," *Physico Chemical Hydrodynamics*, Vol. 10, pp. 195–213.

Bennon, W. D., and Incropera, F. P., 1987, "A Continuum Model for Momentum, Heat and Species Transport in Binary Solid-Liquid Phase Change Systems—I. Model Formulation," *Int. J. Heat Mass Transfer*, Vol. 30, pp. 2161–2170.

Bennon, W. D., and Incropera, F. P., 1988, "Numerical Analysis of Binary Solid-Liquid Phase Change Using a Continuum Model," *Numerical Heat Transfer*, Vol. 13, pp. 277–296.

Carslaw, H. S., and Jaeger, J. C., 1959, *Conduction of Heat in Solids*, Oxford University Press, Chap. 11, pp. 282–296.

De Vahl Davis, G., 1983, "Natural Convection of Air in a Square Cavity: A Bench Mark Numerical Solution," *Int. J. Num. Meth. Fluids*, Vol. 3, pp. 249–264.

Lake, R. A., and Lewis, E. L., 1970, "Salt Rejection by Sea Ice During Growth," *J. Geoph. Res.*, Vol. 75 (3), pp. 583–597.

Le Quere, P., Humphrey, J. A. C., and Sherman, F. S., 1981, "Numerical Calculation of Thermally Driven Two-Dimensional Unsteady Laminar Flow in Cavities of Rectangular Cross-Section," *Numerical Heat Transfer*, Vol. 4, pp. 249–283.

Metzner, A. B., 1985, "Rheology of Suspensions in Polymeric Liquids," *J. Rheology*, Vol. 29, pp. 739–760.

Niedrauer, T. M., and Martin, S., 1979, "An Experimental Study of Brine Drainage and Convection in Young Sea Ice," *J. Geoph. Res.*, Vol. 84, No. C3, pp. 1176–1186.

Oldenburg, C. M., and Spera, F. J., 1990, "Simulation of Phase Change and Convection in Magma Bodies," *Heat Transfer in Earth Science Studies*, C. Carrigan and T. Y. Chu, eds., ASME HTD-Vol. 149, pp. 35–42.

Patankar, S. V., 1981, "A Calculation Procedure for Two-Dimensional Elliptic Situations," *Numerical Heat Transfer*, Vol. 4, pp. 409–425.

APPENDIX

Thermophysical properties of the H_2O–NaCl system

Property	Units	Liquid	Solid
ρ	$kg \cdot m^{-3}$	960	960
k	$W \cdot m^{-1} \cdot K^{-1}$	0.59	2.2
α	$m^2 \cdot s^{-1}$	1.4×10^{-7}	1.1×10^{-6}
β_T	K^{-1}	6.0×10^{-5}	
β_S	--	-8.0×10^{-4}	
κ_0	m^2	5.0×10^{-11}	
D	$m^2 \cdot s^{-1}$	2.4×10^{-9}	

The Effects of Moderately Strong Acceleration on Heat Transfer in the Turbulent Rough-Wall Boundary Layer

W. Chakroun[1] and R. P. Taylor[1]

Introduction

The present knowledge of the combined effects of surface roughness and acceleration on heat transfer in the turbulent boundary layer is poor. Reshotko et al. (1970) and Banerian and McKillop (1974) investigated nozzle wall flows, while Chen (1972) cited experimental results for flow over hemispheres. No boundary layer information was obtained in any of these studies. The only extensive heat transfer experiments with accelerated rough-wall boundary-layer flow were those of Coleman (1976) and Coleman et al. (1981). He presented data for accelerated fully rough[2] turbulent boundary layers. His experiments were limited to mild accelerations and the rough surface used in his experiment was composed of spheres packed in the most dense array. Coleman concluded that the fully rough boundary layer's response to acceleration was opposite to that of the smooth-wall boundary layer. The Stanton number is larger for accelerated rough-wall flow than in the zero pressure gradient case at the same Reynolds number or position. Therefore, the combined effects of roughness and acceleration on heat transfer cannot be modeled by simple superposition of results from the zero pressure gradient rough-wall experiments and the accelerated smooth-wall experiments. For the smooth wall, acceleration causes a decrease in the relative turbulence level and a decrease in Stanton number. On the other hand, accelerated rough-wall boundary layers have two competing effects. The acceleration causes a decrease in the relative turbulence level, but it also causes the boundary layer to become thinner and the skin friction to increase. This, in turn, results in a nondimensionally larger roughness element in terms of both inner and outer region coordinates and a larger overall roughness effect.

This note presents results from an experimental investigation of the effects of moderately strong accelerations on heat transfer in the turbulent rough-wall boundary layer and is condensed from the ASME technical paper by Chakroun and Taylor (1992). Stanton number data are presented for four different values of acceleration parameter, $K = \nu/U_\infty^2\, dU_\infty/dx$ (where U_∞ is the edge velocity and ν is the viscosity), ranging from 0.3×10^{-6} to 1.3×10^{-6} for a rough-wall turbulent boundary layer where the roughness elements are 1.27-mm-dia hemispheres spaced two base diameters apart in a staggered array. These cases cover a wider range of accelerations and roughness regimes (aerodynamically smooth to fully rough) than was previously covered by Coleman (1976) and Coleman et al. (1981).

Experimental Apparatus and Measurements

The experiments are performed in a closed-loop wind tunnel. The temperature of the circulating air is controlled with an air-to-water heat exchanger and a cooling water loop. Following the heat exchanger, the air flow is conditioned by a system of honeycomb and screens. A more detailed discussion of the facility and its qualification can be found in Coleman et al. (1988, 1991) and Hosni et al. (1989).

The bottom wall of the nominally 2.4 m long by 0.5 m wide by 0.1 m high test section consists of 24 electrically heated flat plates, which are abutted together to form a continuous flat surface. Each nickel-plated aluminum plate (about 10 mm thick by 0.1 m in the flow direction) is uniformly heated from below by a custom-manufactured rubber-encased electric heater pad. Design computations show that a uniform temperature was maintained. The rough test plates are precision machined with 1.27-mm-dia hemispherical elements spaced two diameters apart in staggered arrays. The measured average surface roughness on the "smooth" wall portion of the plates is less than 1.6 μm, and the allowable step (or mismatch) between any two plates is 0.013 mm. The heating system is computer controlled. To minimize the conduction losses, the side rails that support the plates are heated to approximately the same temperature as the plates.

The top wall of the test section is flexible and can be adjusted so as to produce a variety in free-stream velocity distributions. The region of acceleration in all the experiments, extending over a distance of 0.4 m (4 plate lengths), begins 1.52 m downstream of a 0.25 cm high, 0.64 cm wide boundary layer trip. The flow is otherwise of uniform pressure.

The free-stream velocity distribution is measured with a Pitot probe and a differential pressure transducer. The free-stream velocity is obtained every 0.1 m (over each test plate centerline). The derivative in the acceleration formula is computed using central difference approximations, except for the first and the last plates in the accelerated flow region, where forward and backward difference approximations are used, respectively.

Stanton Number Determination

The data reduction expression for the Stanton number is

$$\mathrm{St} = \frac{W - (UA)_{\mathrm{eff}}(T_w - T_{\mathrm{rail}}) - \sigma\epsilon A(T_w^4 - T_r^4)}{\rho C_p U_\infty A(T_w - T_o)} \qquad (1)$$

The power, W, supplied to each plate heater is measured with a precision wattmeter. The radiation loss, q_r, is estimated using a gray body enclosure model where the emissivity of the nickel-plated aluminum is estimated as $\epsilon = 0.11$. The conductive heat loss, q_c, is calculated using an experimentally determined effective plate conductance, $(UA)_{\mathrm{eff}}$, which includes both side-rail and back losses. Both q_r/W and q_c/W are generally in the 0.5–1 percent range. The density, ρ, and specific heat, C_p, are determined from property data for moist air using the measured values of barometric pressure and wet and dry bulb temperatures in the tunnel. The plate temperature, T_w, and rail temperature, T_{rail}, are measured using specially calibrated thermistors. The free-stream total temperature, T_o, is computed using the measured free-stream recovery temperature, T_r, and a recovery factor for the free-stream thermistor probe of $r = 0.86$. All fluid properties are evaluated at the free-stream static temperature. The uncertainty in the experimentally determined Stanton number was estimated based on the ANSI/ASME Standard on Measurement Uncertainty (1986) following the procedures of Coleman and Steel (1989). For the Stanton number data in this paper, the overall uncertainty, as discussed by Hosni (1989) and Hosni et al. (1989), ranges from ± 2 to ± 5 percent depending on flow conditions.

[1]Thermal & Fluid Dynamics Laboratory, Department of Mechanical Engineering, Mississippi State University, Mississippi State, MS 39762.

[2]Rough-wall turbulent flows are divided into three regimes. In aerodynamically smooth flows viscous effects dominate and the flow behaves as if the wall was smooth. In fully rough flows, the roughness effects dominate and viscosity is no longer important. Transitionally rough flows are those in between where both viscous and roughness effects are important.

Contributed by the Heat Transfer Division and based on a paper presented at the National Heat Transfer Conference, San Diego, California, August 9–12, 1992. Manuscript received by the Heat Transfer Division April 1992; revision received February 1993. Keyword: Forced Convection. Associate Technical Editor: T. W. Simon.

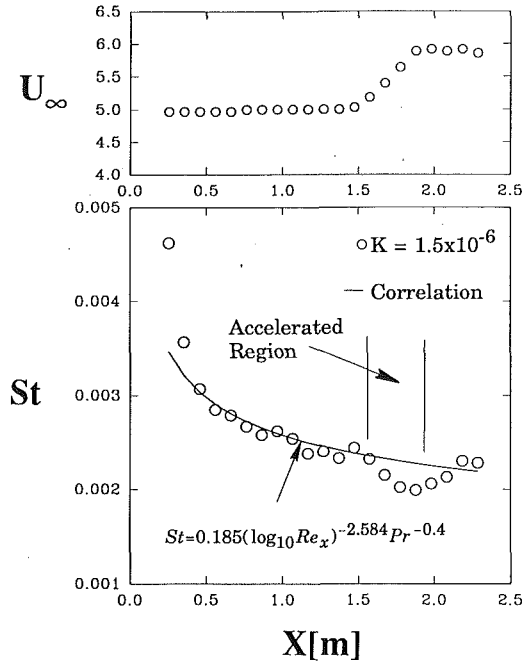

Fig. 1 Comparison of the accelerated smooth-wall Stanton number data ($K = 1.5 \times 10^{-6}$) with the Re_x correlation from Taylor et al. (1989)

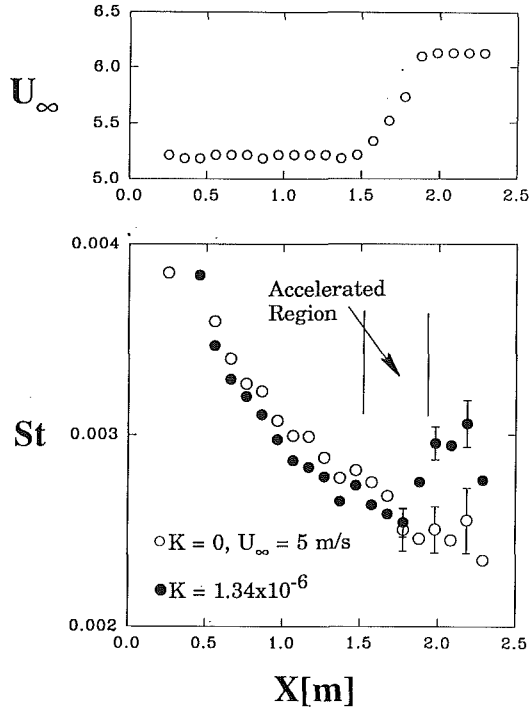

Fig. 2 Comparison of rough-wall Stanton number distributions for zero pressure gradient and accelerated ($K = 1.34 \times 10^{-6}$) cases

Discussion of Experimental Results

The experimental study provides rough surface heat transfer data for four levels of acceleration ranging from moderate to moderately strong. The nominal values of the acceleration parameter K are $0.34 \times 10^{-6} \pm 15$ percent, $0.6 \times 10^{-6} \pm 19$ percent, $0.95 \times 10^{-6} \pm 13$ percent, and $1.34 \times 10^{-6} \pm 13$ percent for free-stream inlet velocities of 28, 12, 8, and 5 m/s, respectively. The classification of the flow regimes for the boundary layer over this rough surface was determined by Hosni (1989) and Hosni et al. (1989) based on the shape of the near-wall axial turbulence intensity and by the value of the ratio of the apparent shear stress due to the roughness element to the total shear stress computed using the discrete element method (Hosni, 1989). These four inlet free-stream velocities are considered to cover all the three flow regimes, namely full rough, transitionally rough and aerodynamically smooth regimes. For the rough surface used in this experiment, the 12 and 28 m/s flows are classified as fully rough. The 8 m/s flow is classified as transitionally rough and the 5 m/s flow as aerodynamically smooth. These flow regimes are based on the flow conditions upstream of the accelerated region where zero pressure gradient exists.

For the experimental results, heat transfer data are presented in Figs. 1–5 in terms of Stanton number distribution versus distance along the test section, x. Figure 1 presents representative results from the same facility for a smooth-wall with nominal acceleration of $K = 1.5 \times 10^{-6}$. The other figures present the rough-wall results. These data are taken with constant wall temperature and reduced under the assumption of incompressible turbulent boundary layer flow. In order to contrast the data for accelerated cases and the zero pressure gradient results, each plot contains the Stanton number distribution for both cases, and the same scale is used on all plots for easy comparison. The velocity distribution along the test section that resulted in the acceleration parameter K is presented with each figure. Tabular listings of Stanton number values, velocity distribution, and the acceleration parameter can be found in Chakroun (1992).

Figures 1 and 2 show the results for the 5 m/s runs. The rough-wall flow regime in Fig. 2 under $K = 0$ conditions is considered to be aerodynamically smooth. The values of the nominal acceleration parameter K for this inlet free-stream velocity are 1.5×10^{-6} for Fig. 1 and 1.34×10^{-6} for Fig. 2. The free-stream velocity increases from 5 m/s to 6.1 m/s in both cases. In the accelerated region of Fig. 2, the Stanton number distribution for the first three plates ($x = 1.55$ m, 1.65 m, and 1.75 m) behaves similarly to the zero-pressure gradient case but increases sharply at $x = 1.85$ m (last plate of the accelerated region). The increase in Stanton number for the accelerated run compared to the zero pressure gradient case is about 19 percent. Downstream, where the acceleration is removed, the distribution of Stanton number exhibits a distinct shift from the baseline case. This shift is also obtained in St versus enthalpy thickness Reynolds number plots (not shown) and is not merely a virtual origin effect. The free-stream velocities for the two runs are different (5 m/s and 6.1 m/s) in that region, so each case corresponds to a different flow regime and roughness state. This behavior was recognized previously by Hosni et al. (1989) for this surface. They reported that for zero-pressure gradient and free-stream velocities below 28 m/s Stanton number distribution depends very much on the free-stream velocity and each free-stream velocity corresponds to a different roughness state. For velocities higher than 28 m/s, Stanton number data do not exhibit free-stream velocity dependency. In the smooth-wall case shown in Fig. 1, a decrease in Stanton number by 15 percent compared to unaccelerated correlation (Taylor et al., 1989) is recorded. As shown by the distribution of Stanton number in Fig. 2, the response of this aerodynamically smooth (under $K = 0$ upstream conditions) rough surface to acceleration is opposite to that of a smooth wall.

The 8 m/s case is transitionally rough and the increase in Stanton number is 18 percent. The value of the acceleration parameter is 0.95×10^{-6}. The free-stream velocity for this case increases from 8 to 9.8 m/s in the accelerated region. As shown in Fig. 3, Stanton number increases on the last three

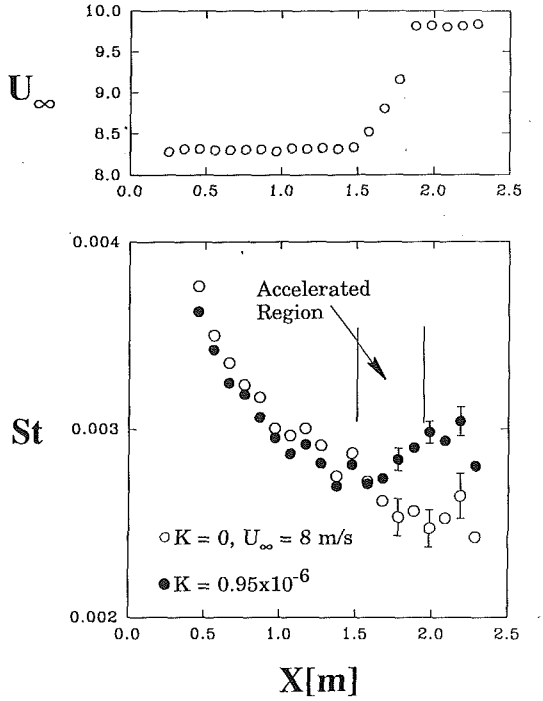

Fig. 3 Comparison of rough-wall Stanton number distributions for zero pressure gradient and accelerated (K = 0.95 × 10^{-6}) cases

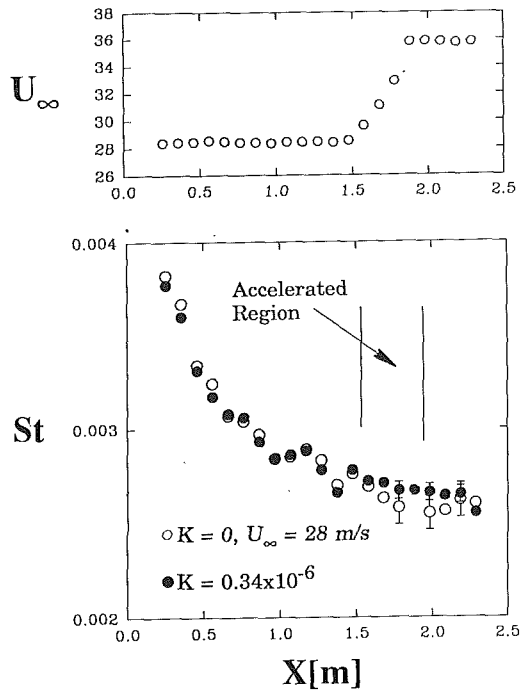

Fig. 5 Comparison of rough-wall Stanton number distributions for zero pressure gradient and accelerated (K = 0.34 × 10^{-6}) cases

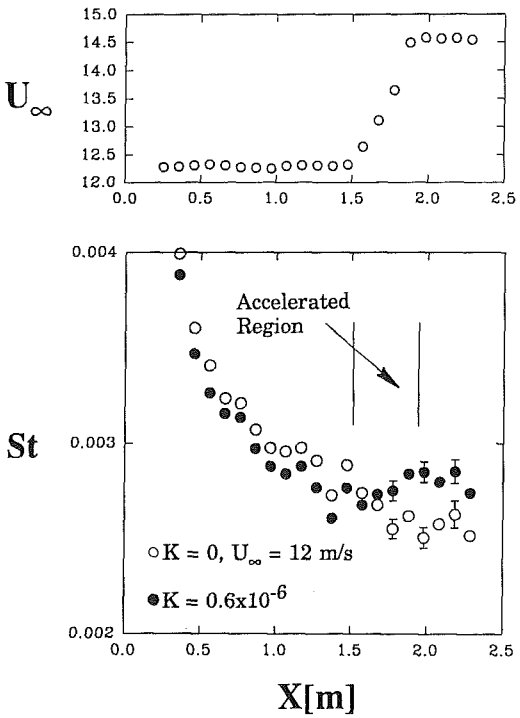

Fig. 4 Comparison of rough-wall Stanton number distributions for zero pressure gradient and accelerated (K = 0.6 × 10^{-6}) cases

plates (x = 1.65 m, 1.75 m, and 1.85 m) of the accelerated region compared to zero-pressure gradient case but remains the same as the K = 0 case for the first accelerated plate (x = 1.55 m). In the zero pressure gradient region, downstream of the acceleration zone, the Stanton number again does not recover to that for the baseline case and a different roughness state exists downstream of the acceleration than existed upstream.

Figure 4 shows the result for 12 m/s where the velocity increased to 14.5 m/s in the region of acceleration. The value of K is 0.6 × 10^{-6}. This case is a borderline fully rough and the Stanton number increases in the accelerated region by 13 percent compared to zero pressure gradient case. For the same acceleration on the smooth wall, the Stanton number decreases by the same order of magnitude.

For 28 m/s, which is in the fully rough regime, K is determined to be 0.34 × 10^{-6}. The free-stream velocity increases from 28 to 35.5 m/s. As shown in Fig. 5, the Stanton number is greater than the K = 0 case on all the plates under acceleration (x = 1.5 m to x = 1.9 m) and appears to recover downstream to unaccelerated baseline values when acceleration is removed. The Stanton number in the accelerated region is about 8 percent larger than for the zero pressure gradient case. On the other hand, this moderate acceleration shows almost no effect on Stanton number for the smooth wall.

Summary and Conclusion

In this experiment, the combined effects of free-stream acceleration and surface roughness on heat transfer in the turbulent boundary layer are investigated. The data cover a variety of flow conditions ranging from aerodynamically smooth through transitionally rough to fully rough boundary layers with accelerations ranging from mild to moderately strong.

The results for the fully rough cases show an increase in the Stanton number in the accelerated region compared to unaccelerated cases at the same x position. However, for the aerodynamically smooth and transitionally rough cases, a weak effect of acceleration on Stanton number is seen at the beginning of acceleration until the last portion where the Stanton number rises sharply.

Acknowledgments

The expert assistance of Mr. Mike West in the conduct of these experiments is gratefully acknowledged.

References

ANSI/ASME, 1986, *Measurement Uncertainty*, ANSI/ASME PTC 19.1-1985, Part 1.

Banerian, G., and McKillop, A. A., 1974, "The Effect of Surface Roughness in Nozzles on Heat Transfer," *Proc. of the Fifth International Heat Transfer Conference*, Vol. II, pp. 234–238.

Chakroun, W. M., 1992, "Experimental Investigation of the Effects of Acceleration on Flow and Heat Transfer in the Turbulent Rough-Wall Boundary Layer," Ph.D. Dissertation, Mech. and Nuc. Eng. Dept., Mississippi State University.

Chakroun, W. M., and Taylor, R. P., 1992, "The Effect of Modestly Strong Acceleration on Heat Transfer in the Turbulent Rough-Wall Boundary Layer," Enhanced Heat Transfer Session at the National Heat Transfer Conference and Exposition, San Diego, CA.

Chen, K. K., 1972, "Compressible Turbulent Boundary-Layer Heat Transfer to Rough Surfaces in Pressure Gradient," *AIAA J.*, Vol. 10, pp. 623–629.

Coleman, H. W., 1976, "Momentum and Energy Transport in the Accelerated Fully Rough Turbulent Boundary Layer," Ph.D. Dissertation, Mech. Eng. Dept., Stanford University (also Report HMT-24).

Coleman, H. W., Moffat, R. J., and Kays, W. M., 1981, "Heat Transfer in the Accelerated Fully Rough Turbulent Boundary Layer," ASME JOURNAL OF HEAT TRANSFER, Vol. 103, pp. 153–158.

Coleman, H. W., Hosni, M. H., Taylor, R. P., and Brown, G. B., 1988, "Smooth Wall Qualification of a Turbulent Heat Transfer Test Facility," Report TFD-88-2, Mech. and Nuc. Eng. Dept., Mississippi State University.

Coleman, H. W., and Steel, W. G., 1989, *Experimentation and Uncertainty Analysis for Engineers*, Wiley, New York.

Coleman, H. W., Hosni, M. H., Taylor, R. P., and Brown, G. B., 1991, "Using Uncertainty Analysis in Debugging and Qualification of a Turbulent Heat Transfer Test Facility," *Experimental Thermal and Fluid Science*, Vol. 4, No. 6, pp. 673–683.

Hosni, M. H., 1989, "Measurement and Calculation of Surface Roughness Effects on Turbulent Flow and Heat Transfer," Ph.D. Dissertation, Mech. and Nuc. Eng. Dept., Mississippi State University.

Hosni, M. H., Coleman, H. W., and Taylor, R. P., 1989, "Measurement and Calculation of Surface Roughness Effects on Turbulent Flow and Heat Transfer," Report TFD-89-1, Mech. and Nuc. Eng. Dept., Mississippi State University.

Reshotko, M., Boldman, D. R., and Ehlers, R. C., 1970, "Heat Transfer in a 60° Half-Angle of Convergence Nozzle With Various Degrees of Roughness," NASA TN D-5887.

Taylor, R. P., Coleman, H. W., Hosni, M. H., and Love, P. H., 1989, "Thermal Boundary Condition Effects on Heat Transfer in the Turbulent Incompressible Flat Plate Boundary Layer," *Int. J. Heat Mass Transfer*, Vol. 32, No. 6, pp. 1165–1174.

Heat and Mass Transfer With Dehumidification in Laminar Boundary Layer Flow Along a Cooled Flat Plate

M. A. Yaghoubi,[1,4] H. Kazeminejad,[2,4] and A. Farshidiyanfar[3,4]

Introduction

Theoretical and experimental studies of heat transfer with condensation over an isothermal flat plate have been carried out by many investigators in the past. In general, the most important is the work by Sparrow et al. (1967), which is an extension of Nusselt's original theory for a mixture of vapor and a noncondensable gas. They have demonstrated that the drop in temperature across the liquid–vapor interface, due to interfacial thermal resistance, has a negligible effect on the heat transfer rate for an air–water mixture. However, they concluded that even a very small amount of noncondensable gas in a pure vapor, such as air in steam, can significantly decrease the heat transfer rate.

Hijikata and Mori (1973) applied an integral method to a similar problem by assuming the principal of similarity for the distribution of temperature, velocity, and concentration by a third-order polynomial, whereas Legay-Desesquelles and Prunet-Foch (1985, 1986) employed a finite difference scheme based on the general method of Patankar and Spalding (1970) using the results of Hijikata and Mori (1973) to determine the liquid density at the wall.

To date, heat transfer analysis has not been carried out for unsaturated air as a working fluid, despite its practical importance, and to the best of our knowledge there is no correlation available to predict the heat transfer coefficient from humid air under these conditions. Therefore, in this paper an attempt is made to analyze the heat and mass transfer from saturated and unsaturated humid air flowing over an isothermal cooled flat plate using a similarity scheme. Based on the numerical results, a practical correlation is developed to estimate the heat transfer coefficient from humid air where dehumidification occurs simultaneously.

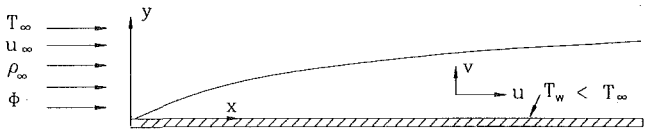

Fig. 1 Schematic representation of humid air flow over a cooled flat plate

Analysis

Consider a two-dimensional steady flow of humid air flowing parallel to an isothermal flat surface, as illustrated in Fig. 1. The fluid is assumed to have relative humidity ϕ and temperature T_∞, which is higher than the plate temperature T_w. It is further assumed that condensation occurs at a point in the thermal boundary layer where dry bulb temperature approaches a lower temperature than that of the air dew point. The assumptions, governing differential equations, and boundary conditions employed in the present analysis are similar to those of Legay-Desesquelles and Prunet-Foch (1986), except that the air is not saturated, and the liquid density at the wall and its location in the boundary layer where temperature approaches dew point temperature is unknown a priori.

The corresponding equations of continuity of mixture, continuity of noncondensable gas, momentum, and energy are

$$\frac{\partial(\rho u)}{\partial x}+\frac{\partial(\rho v)}{\partial y}=0 \tag{1}$$

$$\frac{\partial(\rho_g u_g)}{\partial x}+\frac{\partial(\rho_g v_g)}{\partial y}=0 \tag{2}$$

$$\frac{\partial(\rho u^2)}{\partial x}+\frac{\partial(\rho uv)}{\partial y}=\mu\frac{\partial^2 u}{\partial y^2} \tag{3}$$

$$\frac{\partial(\rho hu)}{\partial x}+\frac{\partial(\rho hv)}{\partial y}=\lambda\frac{\partial^2 T}{\partial y^2}+\frac{\partial}{\partial y}\times\left[(\rho_g+\rho_v)D(h_g-h_v)\frac{\partial}{\partial y}\left(\frac{\rho_g}{\rho_g+\rho_v}\right)\right] \tag{4}$$

where

$$\rho u=\rho_g u_g+\rho_v u_v+\rho_l u_l,\quad \rho v=\rho_g v_g+\rho_v v_v+\rho_l v_l \tag{5}$$

[1]Professor; Mem. ASME.
[2]Assistant Professor; Mem. ASME.
[3]Research Assistant.
[4]Department of Mechanical Engineering, School of Engineering, Shiraz University, Shiraz, Iran.

Contributed by the Heat Transfer Division of THE AMERICAN SOCIETY OF MECHANICAL ENGINEERS. Manuscript received by the Heat Transfer Division July 1992; revision received March 1993. Keywords: Condensation, Forced Convection, Mass Transfer. Associate Technical Editor: Y. Bayazitoglu.

References

ANSI/ASME, 1986, *Measurement Uncertainty*, ANSI/ASME PTC 19.1-1985, Part 1.

Banerian, G., and McKillop, A. A., 1974, "The Effect of Surface Roughness in Nozzles on Heat Transfer," *Proc. of the Fifth International Heat Transfer Conference*, Vol. II, pp. 234–238.

Chakroun, W. M., 1992, "Experimental Investigation of the Effects of Acceleration on Flow and Heat Transfer in the Turbulent Rough-Wall Boundary Layer," Ph.D. Dissertation, Mech. and Nuc. Eng. Dept., Mississippi State University.

Chakroun, W. M., and Taylor, R. P., 1992, "The Effect of Modestly Strong Acceleration on Heat Transfer in the Turbulent Rough-Wall Boundary Layer," Enhanced Heat Transfer Session at the National Heat Transfer Conference and Exposition, San Diego, CA.

Chen, K. K., 1972, "Compressible Turbulent Boundary-Layer Heat Transfer to Rough Surfaces in Pressure Gradient," *AIAA J.*, Vol. 10, pp. 623–629.

Coleman, H. W., 1976, "Momentum and Energy Transport in the Accelerated Fully Rough Turbulent Boundary Layer," Ph.D. Dissertation, Mech. Eng. Dept., Stanford University (also Report HMT-24).

Coleman, H. W., Moffat, R. J., and Kays, W. M., 1981, "Heat Transfer in the Accelerated Fully Rough Turbulent Boundary Layer," ASME JOURNAL OF HEAT TRANSFER, Vol. 103, pp. 153–158.

Coleman, H. W., Hosni, M. H., Taylor, R. P., and Brown, G. B., 1988, "Smooth Wall Qualification of a Turbulent Heat Transfer Test Facility," Report TFD-88-2, Mech. and Nuc. Eng. Dept., Mississippi State University.

Coleman, H. W., and Steel, W. G., 1989, *Experimentation and Uncertainty Analysis for Engineers*, Wiley, New York.

Coleman, H. W., Hosni, M. H., Taylor, R. P., and Brown, G. B., 1991, "Using Uncertainty Analysis in Debugging and Qualification of a Turbulent Heat Transfer Test Facility," *Experimental Thermal and Fluid Science*, Vol. 4, No. 6, pp. 673–683.

Hosni, M. H., 1989, "Measurement and Calculation of Surface Roughness Effects on Turbulent Flow and Heat Transfer," Ph.D. Dissertation, Mech. and Nuc. Eng. Dept., Mississippi State University.

Hosni, M. H., Coleman, H. W., and Taylor, R. P., 1989, "Measurement and Calculation of Surface Roughness Effects on Turbulent Flow and Heat Transfer," Report TFD-89-1, Mech. and Nuc. Eng. Dept., Mississippi State University.

Reshotko, M., Boldman, D. R., and Ehlers, R. C., 1970, "Heat Transfer in a 60° Half-Angle of Convergence Nozzle With Various Degrees of Roughness," NASA TN D-5887.

Taylor, R. P., Coleman, H. W., Hosni, M. H., and Love, P. H., 1989, "Thermal Boundary Condition Effects on Heat Transfer in the Turbulent Incompressible Flat Plate Boundary Layer," *Int. J. Heat Mass Transfer*, Vol. 32, No. 6, pp. 1165–1174.

Heat and Mass Transfer With Dehumidification in Laminar Boundary Layer Flow Along a Cooled Flat Plate

M. A. Yaghoubi,[1,4] H. Kazeminejad,[2,4] and A. Farshidiyanfar[3,4]

Introduction

Theoretical and experimental studies of heat transfer with condensation over an isothermal flat plate have been carried out by many investigators in the past. In general, the most important is the work by Sparrow et al. (1967), which is an extension of Nusselt's original theory for a mixture of vapor and a noncondensable gas. They have demonstrated that the drop in temperature across the liquid–vapor interface, due to interfacial thermal resistance, has a negligible effect on the heat transfer rate for an air–water mixture. However, they concluded that even a very small amount of noncondensable gas in a pure vapor, such as air in steam, can significantly decrease the heat transfer rate.

Hijikata and Mori (1973) applied an integral method to a similar problem by assuming the principal of similarity for the distribution of temperature, velocity, and concentration by a third-order polynomial, whereas Legay-Desesquelles and Prunet-Foch (1985, 1986) employed a finite difference scheme based on the general method of Patankar and Spalding (1970) using the results of Hijikata and Mori (1973) to determine the liquid density at the wall.

To date, heat transfer analysis has not been carried out for unsaturated air as a working fluid, despite its practical importance, and to the best of our knowledge there is no correlation available to predict the heat transfer coefficient from humid air under these conditions. Therefore, in this paper an attempt is made to analyze the heat and mass transfer from saturated and unsaturated humid air flowing over an isothermal cooled flat plate using a similarity scheme. Based on the numerical results, a practical correlation is developed to estimate the heat transfer coefficient from humid air where dehumidification occurs simultaneously.

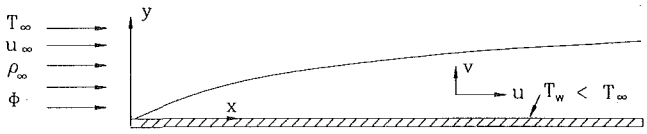

Fig. 1 Schematic representation of humid air flow over a cooled flat plate

Analysis

Consider a two-dimensional steady flow of humid air flowing parallel to an isothermal flat surface, as illustrated in Fig. 1. The fluid is assumed to have relative humidity ϕ and temperature T_∞, which is higher than the plate temperature T_w. It is further assumed that condensation occurs at a point in the thermal boundary layer where dry bulb temperature approaches a lower temperature than that of the air dew point. The assumptions, governing differential equations, and boundary conditions employed in the present analysis are similar to those of Legay-Desesquelles and Prunet-Foch (1986), except that the air is not saturated, and the liquid density at the wall and its location in the boundary layer where temperature approaches dew point temperature is unknown a priori.

The corresponding equations of continuity of mixture, continuity of noncondensable gas, momentum, and energy are

$$\frac{\partial(\rho u)}{\partial x}+\frac{\partial(\rho v)}{\partial y}=0 \tag{1}$$

$$\frac{\partial(\rho_g u_g)}{\partial x}+\frac{\partial(\rho_g v_g)}{\partial y}=0 \tag{2}$$

$$\frac{\partial(\rho u^2)}{\partial x}+\frac{\partial(\rho uv)}{\partial y}=\mu\frac{\partial^2 u}{\partial y^2} \tag{3}$$

$$\frac{\partial(\rho hu)}{\partial x}+\frac{\partial(\rho hv)}{\partial y}=\lambda\frac{\partial^2 T}{\partial y^2}+\frac{\partial}{\partial y}\times\left[(\rho_g+\rho_v)D(h_g-h_v)\frac{\partial}{\partial y}\left(\frac{\rho_g}{\rho_g+\rho_v}\right)\right] \tag{4}$$

where

$$\rho u=\rho_g u_g+\rho_v u_v+\rho_l u_l,\quad \rho v=\rho_g v_g+\rho_v v_v+\rho_l v_l \tag{5}$$

[1]Professor; Mem. ASME.
[2]Assistant Professor; Mem. ASME.
[3]Research Assistant.
[4]Department of Mechanical Engineering, School of Engineering, Shiraz University, Shiraz, Iran.

Contributed by the Heat Transfer Division of THE AMERICAN SOCIETY OF MECHANICAL ENGINEERS. Manuscript received by the Heat Transfer Division July 1992; revision received March 1993. Keywords: Condensation, Forced Convection, Mass Transfer. Associate Technical Editor: Y. Bayazitoglu.

$$h_g = Cp_g(T - T_\infty),\quad h_v = Cp_v(T - T_\infty),$$

$$h_l = Cp_l(T - T_\infty) - L \quad (6)$$

$$\rho h u = \rho_g h_g u_g + \rho_v h_v u_v + \rho_l h_l u_l \quad (7)$$

The velocities of gas and vapor are given by Fick's law using a binary diffusion coefficient D such as

$$v_g = v - \frac{\rho_g + \rho_v}{\rho_g} D \frac{\partial}{\partial y}\left(\frac{\rho_g}{(\rho_g + \rho_v)}\right) \quad (8)$$

From Eqs. (2) and (8)

$$\frac{\partial(\rho_g u)}{\partial x} + \frac{\partial(\rho_g v)}{\partial y} = \frac{\partial}{\partial y}\left\{(\rho_g + \rho_v) D \frac{\partial}{\partial y}\left(\frac{\rho_g}{\rho_g + \rho_v}\right)\right\} \quad (9)$$

Using the assumptions $u_g = u_v = u$ and that the partial pressure of the condensing vapor, P_v, is given as a function of temperature, the concentration of air and water vapor can be deduced by assuming that the two gases are perfect. In Eqs. (1)–(4) four unknowns, u, v, T, ρ_l, must be determined. The corresponding boundary conditions are

$$y = 0 \begin{cases} u = 0 \\ v_g = 0 \\ T = T_w \\ \rho_l = \rho_{lw} \end{cases}, \quad y = \infty \begin{cases} u = u_\infty \\ T = T_\infty \\ \rho_l = 0 \end{cases} \quad (10)$$

ρ_{lw} is unknown, and can be determined as part of the solution.

The system of nonlinear differential Eqs. (1)–(4) is solved by a similarity scheme, introducing the conventional stream function, which satisfies the continuity equation as

$$\rho u = \frac{\partial \psi}{\partial y}, \quad \rho v = -\frac{\partial \psi}{\partial x} \quad (11)$$

and the transformed variables

$$\eta = \left(\frac{u_\infty}{\nu_\infty x}\right)^{1/2} \frac{\rho}{\rho_\infty} y,\ \psi = (\rho_\infty \mu_\infty u_\infty x)^{1/2} f(\eta),\ \theta = \frac{T - T_\infty}{T_w - T_\infty} \quad (12)$$

Nomenclature used in this paper is the same as that of Legay-Desesquelles and Prunet-Foch (1986):

$$-\frac{1}{2}\left(\frac{\rho_g}{\rho}\right)' f \rho_\infty u_\infty = \left[(\rho_g + \rho_v) D \left(\frac{\rho_g}{\rho_g + \rho_y}\right)' \rho\right]' \quad (13)$$

$$\rho f''' + \rho' f'' + \frac{\mu_\infty}{2\mu} \rho_\infty f f'' = 0 \quad (14)$$

$$-\frac{1}{2} h' f \mu_\infty \rho_\infty = \lambda (T' \rho)' + \left[(\rho_g + \rho_v) D (h_g - h_v) \left(\frac{\rho_g}{\rho_g + \rho_v}\right)' \rho\right]' \quad (15)$$

with the boundary conditions in terms of the transformed variables given by

$$\eta = 0:\ f' = 0,\ f = f_w,\ T = T_w;\quad \eta = \infty:\ f' = 1,\ T = T_\infty \quad (16)$$

where in the above equations, primes represent derivative with respect to η. Using Fick's law and relations (11) and (12), it can be shown that

$$f_w = \frac{-2\rho^2}{\rho_\infty^2 \nu_\infty} D\left[\left(\frac{\rho_g + \rho_v}{\rho_g}\right)\left(\frac{\rho_g}{\rho_g + \rho_v}\right)'\right] \quad (17)$$

The set of differential Eqs. (13)–(15) with boundary conditions (16) is integrated using the fourth-order Runge–Kutta method. Integration is started at $\eta = 0$ and marched toward η_∞. For Prandtl number of 0.7, it is found that $\eta_\infty = 8$ and $\Delta\eta = 0.05$ are proper choices, and the accuracy of numerical calculation is checked by comparing the results with the theoretical and experimental studies of Legay-Desesquelles and Prunet-Foch (1986). For numerical integration, there exists a deficit of three starting values at $\eta = 0$. Hence, some initial values for f'', T', and ρ are guessed and a systematic refinement of the estimated values is made by performing the forward integration and comparing the calculated results at $\eta = \infty$. The refinement procedure applied was the Newton–Raphson shooting scheme and iteration is terminated when two successive iterations differed by less than 10^{-8} (Farshidiyanfar, 1990). However, by numerical experimentation it is found that initial guessed values for f'', T', and ρ should be between 0.1 and 1.5.

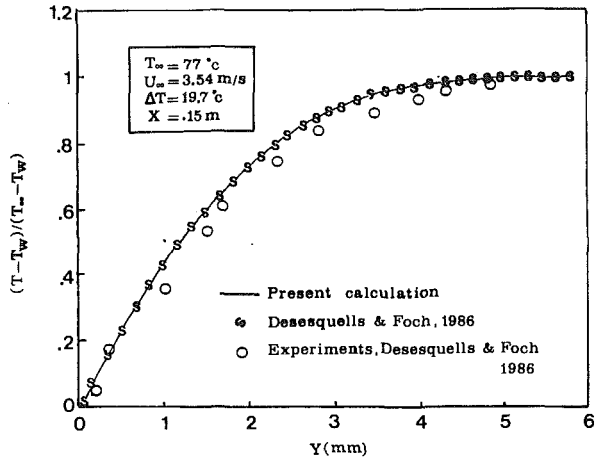

Fig. 2 Dimensionless temperature in the laminar boundary layer for saturated air

Results

The set of differential Eqs. (13)–(15) is solved for a wide range of humid air with temperature (30–90°C), differences in dry bulb temperature and the wall (10–30°C) and various air speeds (2–6 m/s) over a cooled flat plate. At each point in the boundary layer the thermophysical properties of air and vapor mixture are determined at the corresponding temperature using thermodynamic tables. For humid air, the wall temperature is assumed to be lower than the dew point temperature of the surrounding air. Although the liquid density at the wall was obtained as part of the solution in the present analysis, the assumption adopted in the study of Legay-Desesquelles and Prunet-Foch (1986) is also justified when the present results for saturated air are compared with those obtained by these authors.

Figure 2 shows a typical temperature profile in the boundary layer, compared with the theoretical and experimental work of Legay-Desesquelles and Prunet-Foch (1986). Similar trends are obtained for the corresponding velocity profile. Very good agreement is observed from similarity solution for dehumidification of saturated air over a flat plate. Velocity, temperature, and concentration boundary layer thicknesses for humid air are presented in Fig. 3. Concentration boundary layer is much thinner because the saturated conditions begin when the air temperature drops to the dew point temperature, and condensation starts from this location. Concentration gradient is zero between the free stream and position of dew point temperature, which means that water vapor pressure is constant up to the dew point temperature, where η is about 1.8. As the air relative humidity increases the concentration boundary layer increases and the point at which condensation starts moves farther away from the wall.

In Fig. 4 the relative humidity profile over the plate for various free-stream air temperatures is illustrated. Free-stream relative humidity is taken to be 80 percent and the difference in temperature between free air stream and the wall, ΔT, is 30°C. This figure indicates the effects of free-stream temper-

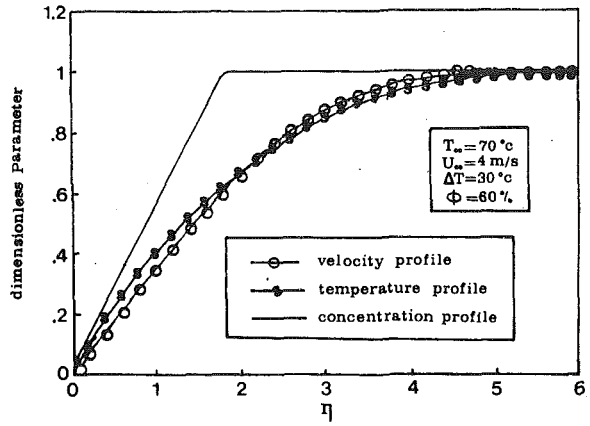

Fig. 3 Dimensionless velocity, temperature, and concentration in the laminar boundary layer for humid air

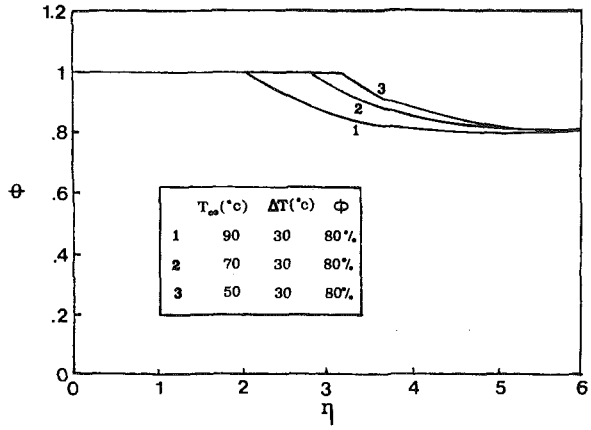

Fig. 4 Variation of relative humidity in the boundary layer for different air temperature

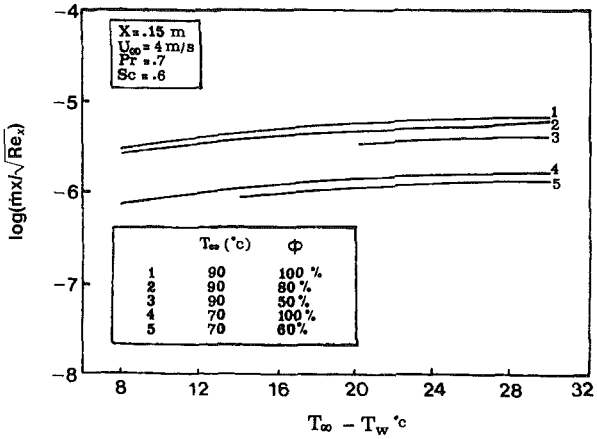

Fig. 5 Variation of mass transfer rate over the plate for different humid air conditions

ature on the concentration profile in the boundary layer. Figure 5 shows the dehumidification rate per unit length of the plate, $(\dot{m}x)/\mathrm{Re}_x^{1/2}$ (kg/m•s) for various psychrometric conditions. For saturated air, excellent agreement is observed with the results of Legay-Desesquelles and Prunet-Foch (1986). The lower the air temperature or relative humidity, the smaller the condensation rate. However, the effect of air temperature is more pronounced when comparing lines 1 and 4 in Fig. 5. This is due to the sharp decrease of vapor pressure with lowering air temperature in the range of conditions studied.

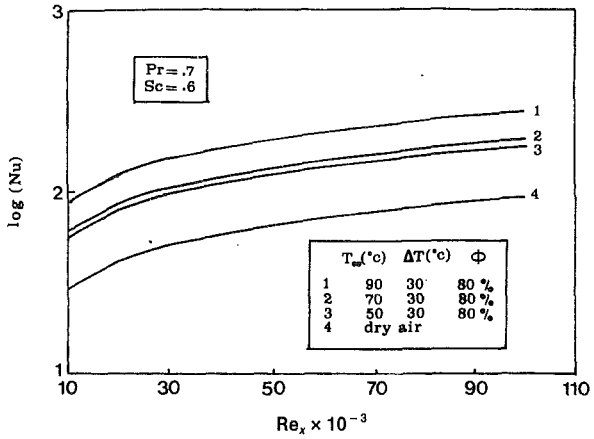

Fig. 6 Variation of sensible Nusselt number versus Re_x of humid air and comparison with dry air

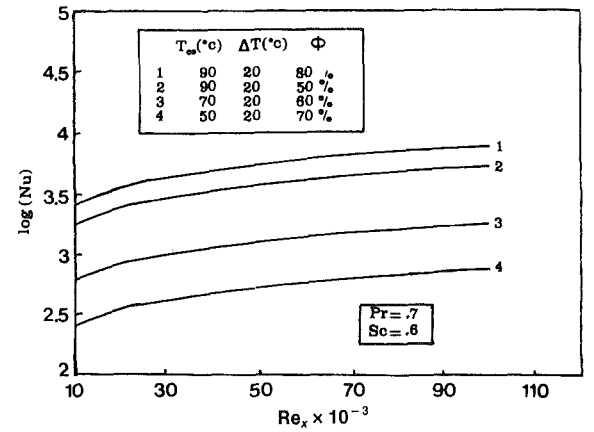

Fig. 7 Variation of total Nusselt number versus Re_x for different humid air conditions

Total heat transfer to the plate is $q_t'' = q_s'' + q_l''$, where q_s'' is the sensible and q_l'' is the latent heat flux to the plate and can be obtained from

$$q_s'' = \lambda T'_{\eta=0}\left(\frac{u_\infty}{\nu_\infty x}\right)^{1/2}\frac{\rho_w}{\rho_\infty}, \quad q_l'' = L(\rho_v v_v)_{\eta=0} \tag{18}$$

and for dry air $q_s'' = \lambda T''(u_\infty/\nu x)^{1/2}$. The sensible Nusselt number, which corresponds to sensible heat transfer, and the total Nusselt number, which takes into account the latent heat release due to condensation, can be derived from Eqs. (12) and (18)

$$\mathrm{Nu}_{x,s} = \theta_w' \mathrm{Re}_x^{1/2}\frac{\rho_w}{(\rho\rho_\infty)^{1/2}}, \quad \mathrm{Nu}_{x,t} = \mathrm{Nu}_{x,s} + \frac{(\rho_v v_v)_w x}{\lambda \Delta T} L \tag{19}$$

Figure 6 illustrates the variation of $\mathrm{Nu}_{x,s}$ with respect to Re_x for various humid air conditions. The effects of increasing water vapor pressure and the temperature difference between the air and wall are considerable on the sensible Nusselt number. This figure shows that as T_∞ increases, the sensible Nusselt number, $\mathrm{Nu}_{x,s}$, also increases. However, for a fixed value of T_∞, as the value of ΔT increases, $\mathrm{Nu}_{x,t}$ decreases. This can be observed from Eq. (9), in that reduction of $\mathrm{Nu}_{x,t}$ is much greater than the augmentation of $\mathrm{Nu}_{x,s}$. However, as the air temperature decreases, the difference between the heat transfer of humid air and dry air decreases. This indicates that, since the vapor pressure at low air temperature is rather low, condensation does not significantly affect the heat transfer. Figure 7 illustrates the effects of variations of psychrometric conditions on the total Nusselt number as a function of Reynolds number. Based on the Reynolds analogy, it can be concluded that the

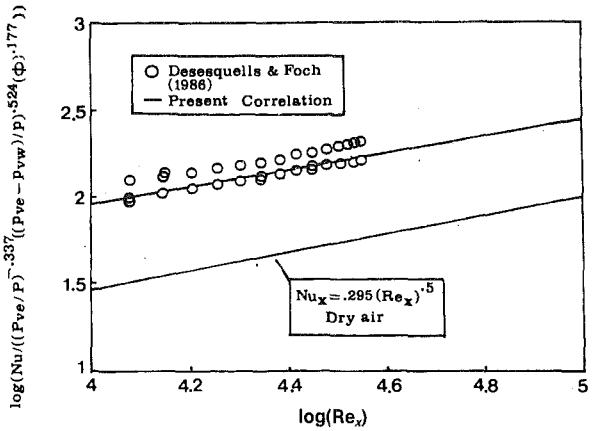

Fig. 8 Variation of sensible Nusselt number of humid air and those of dry air versus Re_x for laminar flow over a flat plate

friction factor increases due to dehumidification, at higher air temperatures. However, at lower air temperatures, the difference in friction factor between humid air and dry air is decreased.

Heat transfer for humid and saturated air over an isothermal flat plate is different from that of dry air. The Nusselt number increases with an increase in air relative humidity, as shown in Fig. 7. It also becomes greater with an increase in the differences of water vapor partial pressure of humid air, P_{VE}, and that of the plate surface, P_{VW}. This leads to an increase in the corresponding Nusselt number. In addition to these effects, it is found that any reduction in humid air atmospheric pressure also contributes to the enhancement of heat transfer coefficient (Farshidiyanfar, 1990).

The numerical results obtained may be correlated by an expression of the form

$$\mathrm{Nu}_{x,s} = 0.902(\mathrm{Re}_x)^{0.5}\left(\frac{P_{VE}}{P}\right)^{-0.337}\left(\frac{P_{VE}-P_{VW}}{P}\right)^{0.524}(\phi)^{0.177} \tag{20}$$

where P is the atmospheric pressure. This equation is valid for the following range of conditions:

$$10^4 < \mathrm{Re} < 10^5,\ \mathrm{Pr} = 0.7,\ 40°\mathrm{C} < T_\infty < 90°\mathrm{C},\ \phi > 50 \text{ percent}$$

with a correlation coefficient of 0.95. Figure 8 illustrates numerical prediction of Nusselt number of humid air, compared with that of dry air as well as data reported by Legay-Desesquelles and Prunet-Foch (1986). This graph merely serves to confirm that the mass transfer significantly affects the convective heat transfer coefficient. It also supports to some extent the findings of previous investigators (Legay-Desesquelles and Prunet-Foch, 1986) who have carried out theoretical and experimental analysis and reported a significant increase in heat transfer coefficient where simultaneous heat and mass transfer occur.

Conclusion

The effects of dehumidification from humid air of laminar air flow over an isothermal cooled flat plate have been investigated using the similarity scheme. The results obtained for both saturated and unsaturated humid air are compared with those of dry air. It can be concluded that dehumidification has significant effects of both sensible and latent heat transfer as well as the friction factor. However, the difference in heat transfer coefficient compared with that of dry air is reduced as the relative humidity is decreased. Finally, the most useful result in terms of practical applications that can be obtained from the present investigation is the development of a new heat transfer correlation to estimate the heat transfer coefficient from humid air flowing over an isothermal cooled flat plate.

Acknowledgments

The authors would like to acknowledge support from Shiraz University Research Council for this study (Grant No. 69-EN-584-311).

References

Farshidiyanfar, A., 1990, "Heat and Mass Transfer With Condensation in Laminar Boundary Layer Flow Along a Cooled Flat Plate," M.Sc. Thesis, Department of Mechanical Engineering, School of Engineering, Shiraz University, Iran.

Hijikata, K., and Mori, Y., 1973, "Forced Convection Heat Transfer of a Gas With Condensing Vapor Around a Flat Plate," *Heat Transfer—Jap. Res.*, Vol. 2, pp. 81–101.

Legay-Desesquelles, F., and Prunet-Foch, B., 1985, "Dynamic Behavior of a Boundary Layer With Condensation Along a Flat Plate: Comparison With Suction," *Int. J. Heat Mass Transfer*, Vol. 28, No. 12, pp. 2363–2370.

Legay-Desesquelles, F., and Prunet-Foch, B., 1986, "Heat and Mass Transfer With Condensation in Laminar and Turbulent Boundary Layer Along a Flat Plate," *Int. J. Heat Mass Transfer*, Vol. 29, No. 1, pp. 95–105.

Patankar, S. V., and Spalding, D. B., 1970, *Heat and Mass Transfer in Boundary Layers*, 2nd ed., Intertext, London.

Sparrow, E. M., Minkowycz, W. J., and Saddy, M., 1967, "Forced Convection Condensation in the Presence of Noncondensable Gas and Interfacial Resistance," *Int. J. Heat Mass Transfer*, Vol. 10, pp. 1829–1845.

Heat Transfer Characteristics in a Wavy-Walled Channel

N. Saniei[1] and S. Dini[2]

Nomenclature

a = amplitude, m
f = factor for nonuniformity in the gold coating
H = channel height, m
h_L = local heat transfer coefficient, W/m^2•°C
h_a = average heat transfer coefficient, W/m^2.°C
I = current, ohm
k = thermal conductivity of air, W/m•°C
L = distance from the inlet of the duct to the end of the wavy section, m
Nu = Nusselt number
P = peak-to-peak spacing, m
q''_c = convective heat flux, W/m^2
q_{el} = electrical heat rate, W/m^2
q_{rad} = radiation heat rate, W/m^2
q''_1 = conduction heat rate, W/m^2
Re = Reynolds number based on minimum height in the duct
Re(L) = Reynolds number based on L
Re_X = Reynolds number based on X
$T_{l.c.}$ = liquid crystal event temperature, K
T_a = air temperature measured upstream of the test section, K

[1]Assistant Professor, Department of Mechanical Engineering, Southern Illinois University, Edwardsville, IL 62026-1805; Mem. ASME.

[2]Associate Professor, Western New England College, Springfield, MA 01095; Mem. ASME.

Contributed by the Heat Transfer Division and presented at the 28th National Heat Transfer Conference, San Diego, California, August 9–12, 1992. Manuscript received by the Heat Transfer Division August 1992; revision received March 1993. Keywords: Augmentation and Enhancement, Forced Convection, Heat Exchangers. Associate Technical Editor: T. W. Simon.

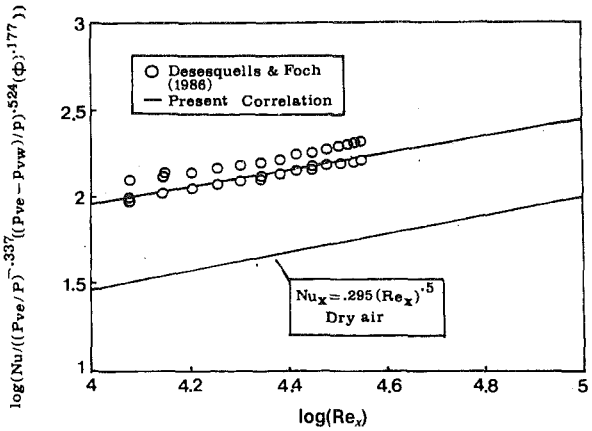

Fig. 8 Variation of sensible Nusselt number of humid air and those of dry air versus Re_x for laminar flow over a flat plate

friction factor increases due to dehumidification, at higher air temperatures. However, at lower air temperatures, the difference in friction factor between humid air and dry air is decreased.

Heat transfer for humid and saturated air over an isothermal flat plate is different from that of dry air. The Nusselt number increases with an increase in air relative humidity, as shown in Fig. 7. It also becomes greater with an increase in the differences of water vapor partial pressure of humid air, P_{VE}, and that of the plate surface, P_{VW}. This leads to an increase in the corresponding Nusselt number. In addition to these effects, it is found that any reduction in humid air atmospheric pressure also contributes to the enhancement of heat transfer coefficient (Farshidiyanfar, 1990).

The numerical results obtained may be correlated by an expression of the form

$$\mathrm{Nu}_{x,s} = 0.902(\mathrm{Re}_x)^{0.5}\left(\frac{P_{VE}}{P}\right)^{-0.337}\left(\frac{P_{VE}-P_{VW}}{P}\right)^{0.524}(\phi)^{0.177} \tag{20}$$

where P is the atmospheric pressure. This equation is valid for the following range of conditions:

$$10^4 < \mathrm{Re} < 10^5,\ \mathrm{Pr} = 0.7,\ 40°\mathrm{C} < T_\infty < 90°\mathrm{C},\ \phi > 50 \text{ percent}$$

with a correlation coefficient of 0.95. Figure 8 illustrates numerical prediction of Nusselt number of humid air, compared with that of dry air as well as data reported by Legay-Desesquelles and Prunet-Foch (1986). This graph merely serves to confirm that the mass transfer significantly affects the convective heat transfer coefficient. It also supports to some extent the findings of previous investigators (Legay-Desesquelles and Prunet-Foch, 1986) who have carried out theoretical and experimental analysis and reported a significant increase in heat transfer coefficient where simultaneous heat and mass transfer occur.

Conclusion

The effects of dehumidification from humid air of laminar air flow over an isothermal cooled flat plate have been investigated using the similarity scheme. The results obtained for both saturated and unsaturated humid air are compared with those of dry air. It can be concluded that dehumidification has significant effects of both sensible and latent heat transfer as well as the friction factor. However, the difference in heat transfer coefficient compared with that of dry air is reduced as the relative humidity is decreased. Finally, the most useful result in terms of practical applications that can be obtained from the present investigation is the development of a new heat transfer correlation to estimate the heat transfer coefficient from humid air flowing over an isothermal cooled flat plate.

Acknowledgments

The authors would like to acknowledge support from Shiraz University Research Council for this study (Grant No. 69-EN-584-311).

References

Farshidiyanfar, A., 1990, "Heat and Mass Transfer With Condensation in Laminar Boundary Layer Flow Along a Cooled Flat Plate," M.Sc. Thesis, Department of Mechanical Engineering, School of Engineering, Shiraz University, Iran.

Hijikata, K., and Mori, Y., 1973, "Forced Convection Heat Transfer of a Gas With Condensing Vapor Around a Flat Plate," *Heat Transfer—Jap. Res.*, Vol. 2, pp. 81–101.

Legay-Desesquelles, F., and Prunet-Foch, B., 1985, "Dynamic Behavior of a Boundary Layer With Condensation Along a Flat Plate: Comparison With Suction," *Int. J. Heat Mass Transfer*, Vol. 28, No. 12, pp. 2363–2370.

Legay-Desesquelles, F., and Prunet-Foch, B., 1986, "Heat and Mass Transfer With Condensation in Laminar and Turbulent Boundary Layer Along a Flat Plate," *Int. J. Heat Mass Transfer*, Vol. 29, No. 1, pp. 95–105.

Patankar, S. V., and Spalding, D. B., 1970, *Heat and Mass Transfer in Boundary Layers*, 2nd ed., Intertext, London.

Sparrow, E. M., Minkowycz, W. J., and Saddy, M., 1967, "Forced Convection Condensation in the Presence of Noncondensable Gas and Interfacial Resistance," *Int. J. Heat Mass Transfer*, Vol. 10, pp. 1829–1845.

Heat Transfer Characteristics in a Wavy-Walled Channel

N. Saniei[1] and S. Dini[2]

Nomenclature

- a = amplitude, m
- f = factor for nonuniformity in the gold coating
- H = channel height, m
- h_L = local heat transfer coefficient, W/m^2•°C
- h_a = average heat transfer coefficient, W/m^2.°C
- I = current, ohm
- k = thermal conductivity of air, W/m•°C
- L = distance from the inlet of the duct to the end of the wavy section, m
- Nu = Nusselt number
- P = peak-to-peak spacing, m
- q''_c = convective heat flux, W/m^2
- q_{el} = electrical heat rate, W/m^2
- q_{rad} = radiation heat rate, W/m^2
- q''_1 = conduction heat rate, W/m^2
- Re = Reynolds number based on minimum height in the duct
- Re(L) = Reynolds number based on L
- Re_X = Reynolds number based on X
- $T_{l.c.}$ = liquid crystal event temperature, K
- T_a = air temperature measured upstream of the test section, K

[1]Assistant Professor, Department of Mechanical Engineering, Southern Illinois University, Edwardsville, IL 62026-1805; Mem. ASME.

[2]Associate Professor, Western New England College, Springfield, MA 01095; Mem. ASME.

Contributed by the Heat Transfer Division and presented at the 28th National Heat Transfer Conference, San Diego, California, August 9–12, 1992. Manuscript received by the Heat Transfer Division August 1992; revision received March 1993. Keywords: Augmentation and Enhancement, Forced Convection, Heat Exchangers. Associate Technical Editor: T. W. Simon.

U = axial free-stream velocity, m/s
Uc = velocity at the center of the duct upstream of the wavy section
V = voltage across liquid crystal, V
x = distance from the leading edge of the wavy section, m
X = variable distance starting from the leading edge of the channel to local points on the wavy wall, m
x_i = measurand i
δx = uncertainty of measurand x_i (20:1)
ϵ = emissivity of liquid crystal surface
ζ = unheated entrance length, m
μ = viscosity of air, N-s/m^2
ρ = density of the plastic substrate
σ = Stefan–Boltzmann constants

Introduction and Literature Review

To improve heat exchanger efficiency, considerable attention has been focused on understanding convective heat transfer with unconventional internal flow passages. One such passage is the corrugated wall channel, which excites instabilities in the flow and appreciably enhances heat transfer. Corrugated wall is usually used to refer to a geometry with repeated triangular elements with sharp edges. The same geometry with rounded corners is called a wavy wall or a wavy sinusoidal wall since it represents a sinusoidal function. In the following, some previous work done on triangular (corrugated) and sinusoidal (wavy) channels will be discussed.

Goldstein and Sparrow (1977) were the first to use the naphthalene technique to measure local and average heat transfer coefficients in a corrugated wall channel. Their channel included two corrugations with an angle of 30 deg. They observed secondary flows in the regions of high resolution local mass transfer measurement, and their comparison of results with parallel-plate channels showed an enhancement in the average heat transfer by a factor of three in the low Reynolds number, turbulent regimes. Later, O'Brien and Sparrow (1982) performed a complete study on the same geometry (with more corrugation cycles) including pressure drop and flow visualization. Amano et al. (1987) investigated the average Nusselt number and skin friction coefficient numerically for a geometry similar to that of Goldstein and Sparrow. Their average Nusselt number compares reasonably with those measured by O'Brien and Sparrow. Recently, Greiner et al. (1991) measured pumping power and heat transfer augmentations in a rectangular channel with grooves (corrugations similar to those of O'Brien and Sparrow, 1982) but on one wall only. They investigated the effects of unheated grooves on heat transfer from the opposite wall with uniform heat flux boundary conditions and reported significant heat transfer enhancements on the opposite wall. Molki and Yuen (1986) studied the effect of the interwall spacing of corrugation channels on the mass transfer coefficients for a Reynolds number range of $4000 < \mathrm{Re} < 35{,}000$ in the developing and fully developed flow regions. Ali and Ramadhyani (1992) did the most recent investigations of heat transfer and flow visualizations in corrugated channels with water as the working fluid for two channel spacings and a relatively low range of Reynolds numbers ($150 < \mathrm{Re} < 4000$). They compared their results with a parallel-plate channel and concluded that the corrugated channel shows higher Nusselt number even at a Reynolds number as low as 200.

Sparrow and Hossfeld (1984) examined the effect of rounding the edges of the triangular geometry considered previously in heat transfer and pressure drop measurements. They concluded that rounding of the corrugation peaks in general is a good trade off between heat transfer and pressure drop, resulting in a moderate reduction in Nusselt number and yet a higher percentage reduction in friction factor. Later, Asako et al. (1988) and Garg and Maji (1988) performed numerical analysis on flow and heat transfer in symmetric wavy channels. Ektesabi and Sako (1991a) conducted flow visualizations and pressure drop measurements for wavy sinusoidal channels and expressed the friction factor as a function of Reynolds number $f = C\,\mathrm{Re}^n$, where C and n were expressed as a function of the channel geometry. Oyakawa et al. (1989) investigated the local heat transfer coefficients and friction factor for a wavy channel and concluded that the location of maximum heat transfer on each wave is independent of the height of the channel (spacing between the two opposite wavy walls). Finally, Nishimura et al. (1990) performed mass transfer and flow observations in symmetric wavy-walled and arc-shape walled channels. They observed an earlier transition of turbulence in arc-shaped walls as compared with wavy walls.

Although in the present study measurements have been conducted for a somewhat different geometry, the above works provide background information for the present work. In addition, secondary flow or successive separations and reattachments are common behaviors of many complex flows. Since this work contributes to the fundamental understanding of complex channel flows, the authors decided first to investigate a channel with one wavy wall. Therefore, in this research, only a portion of one side of a duct with rectangular cross section was made of sinusoidal wavy geometry. The experimental technique employed liquid crystals to provide localized measurements. This technique was first described by Simonich and Moffat (1982) who used cholesteric encapsulated liquid crystals to map temperature contours on the end wall of a cylinder in crossflow. Hippensteele et al. (1983) used the same technique for measurements of local heat transfer on several geometries such as jet impingement on a flat plate. Later, Baughn et al. (1985, 1986) improved the liquid crystal technique introduced by Simonich and Moffat, and Baughn and Saniei (1989) used the improved technique for local heat transfer measurements in tube bank arrangements. Baughn and Saniei (1991) also used this technique to investigate the effect of thermal boundary conditions on heat transfer from long cylinders.

Experimental Technique and Apparatus

The test section was the end section of a long rectangular duct (50.8 cm × 10.16 cm) made of clear plexiglass. The total length of the duct was 500 cm, and the test section started 350 cm from the inlet of the duct, $\zeta/D_H = 22$ from the entrance (the flow is not considered hydrodynamically fully developed). A suction fan was connected to the exit of the duct 50 cm downstream of the test section. The wavy portion of the channel was made of hard plastic 2 mm thick, and the gap between this surface and the channel wall was filled with styrofoam to minimize conduction losses. Peak-to-peak wave for this geometry was 6.667 cm, the amplitude of each wave was 1.27 cm, and the aspect ratio was 8:1. Surface geometry included seven waves (peaks) and occupied about 45 cm of the length of the duct and spanned the entire width of the channel (Fig. 1). Precise representations of the wall geometry are given in Figs. 2 and 3. The wavy surface was painted black, and a thin polyester sheet with vacuum-deposited gold film glued to the surface covered 20.32 cm of the center portion of the width and the entire wavy length. For the purpose of heating, electric conductive adhesive tape (1.27 cm wide, 0.0035 cm thick) was taped over the front and rear lines of the gold-coated sheet as lead wires. Then, these tapes were connected to a regulated DC power supply (Hewlett Packard, model 6633A), which provided voltage and current steady to four digits. On top of the gold coating, a thin layer of encapsulated liquid crystals was sprayed by air brush, and grids were marked on the sides

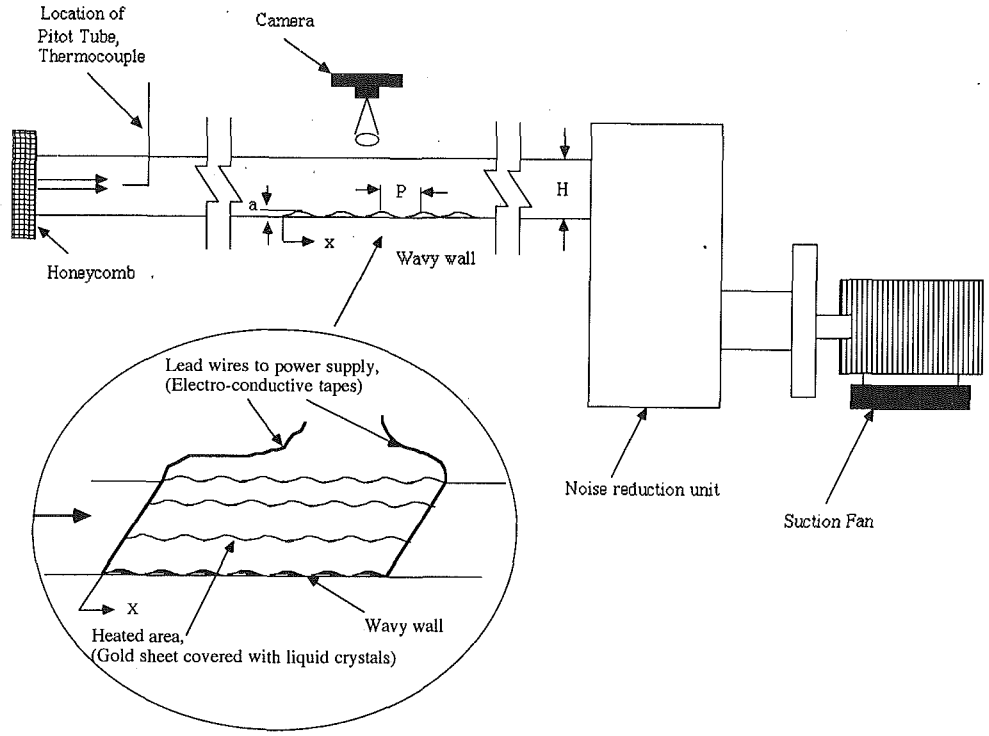

Fig. 1 Experimental apparatus

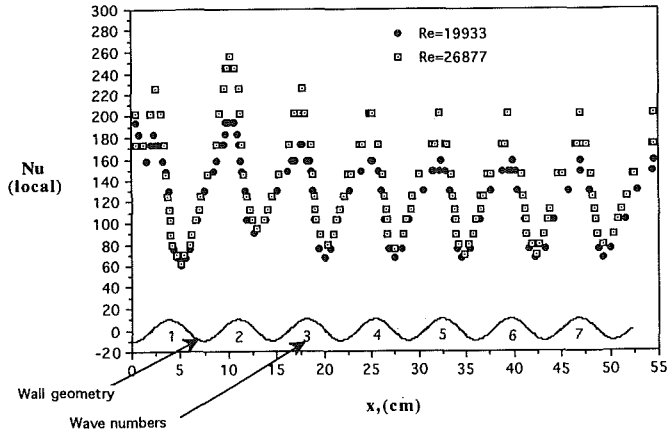

Fig. 2 Local Nusselt number distribution for the wavy wall

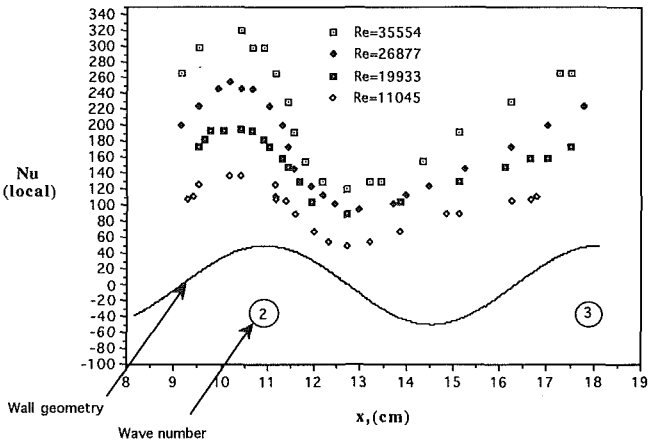

Fig. 3 Local Nusselt number distribution for the second wave

and top of the sheet using a thin white pencil to ease the data collections. Velocity and temperature measurements were performed 50 cm upstream of the test section. A Validyne pressure transducer (model Dp103-16) in conjunction with a Pitot tube was used for velocity measurements.

Experimental Procedure

After the suction fan was turned on and the desired Reynolds number was obtained, the lead wires (extension of the conductive tapes) were connected to the power supply and the voltage was slowly increased to a value close to the minimum required to obtain a wall temperature near the liquid crystal color play temperature. The apparatus was operated in this condition for approximately 45 minutes. Then, the voltage was slowly increased until the green color (event temperature) appeared on the surface where the minimum heat transfer coefficient was located. The apparatus was allowed to come to steady state (usually 15 to 20 minutes), after which voltage, current, temperature, and the location of the green color (35.4°C) were recorded. In order to map the entire wavy surface, the voltage was increased by an increment of 0.1 to 0.3 V, and data were recorded as the green color moved to a different location, or locations corresponding to higher heat transfer coefficients. The entire localized data (color plays) were observed and recorded from the top of the channel perpendicular to the wavy wall (90 deg angle), since the calibration of liquid crystal was made from the same angle. If data are recorded from a different angle, the liquid crystal color play should also be calibrated from that angle. The local heat transfer coefficient was calculated by

$$h_x = q_c'' / (T_{lc} - T_a)$$

where q_c is given by

$$q_c'' = fIV/A - \epsilon\sigma(T_{lc}^4 - T_a^4) - q_l''$$

and the average heat transfer coefficients were obtained by the integration of the local heat transfer coefficients:

$$h_a = \int h_x dx / L_C$$

Table 1 Uncertainty analysis of a typical run

x_i	Value	δx_i	$(\delta x_i/Nu_i).(\partial Nu/\partial x).100$
V	17.82	0.2	1.1
I	2.55	0.03	1.2
A	0.128	0.00254	2.0
f	1	0.08	8.0
ε	0.5	0.1	2.4
T_a	23	0.3	2.5
$T_{l.c.}$	35.4	0.3	2.5

Total uncertainty in Nu = 9.43%

The air temperature, T_a, used for calculations was recorded 50 cm upstream of the test section, which happened to be the same temperature if taken as near as 2 cm above the peak of the entire wavy wall in the test section area. In a separate experiment, temperature was measured 0.5 cm above each peak of the seven waves and a 3°C temperature increase was observed between the first peak and the seventh peak. It should also be mentioned that although the local heat transfer coefficients were obtained from applying different heat fluxes to the surface, the entire data may still be mapped on the same graph if the properties are not affected by the change of heat flux during the experiments. This was the case in this study, since there was not a significant temperature change as a result of changing heat flux during the experiments. The characteristic length used to calculate Reynolds numbers and Nusselt numbers was the distance between the peak of the waves and the top of the rectangular channel (8.89 cm). If the objective was comparison of the results with previous works, the hydraulic diameter of the minimum channel cross section could have been a better choice as the characteristic length since it has been used by some other investigators. This choice would only cause a shift in the results obtained in this study. To compare the average heat transfer coefficient with a semi-infinite flat plate with unheated starting length (Kays and Crawford, 1980), the characteristic length in the Reynolds number was the distance between the inlet of the duct up to the end of the wavy section (Fig. 5).

The uncertainty of the heat measurements was estimated using the uncertainty analysis of Kline and McClintock (1953), with odds of 20:1. Table 1 shows the individual contributions of each measurand. The uncertainty in the position readings (taken from photographs or from grids on the sides and surface), is estimated to be 2 mm in the regions with steep temperature gradients (downstream of the maximum heat transfer in the valleys) and 3 mm in the regions where temperature has mild slopes (upstream of the maximum heat transfer in the valleys). In order to minimize the nonuniformity of the gold film, attempts were made to carefully select the center pieces of the gold coating sheet. The uncertainty due to this factor is given in Table 1 as 8 percent.

Discussion of Results

(A) Local Heat Transfer. Local heat transfer coefficients were measured for a channel wall with a total of seven continuous waves, each wave covering 6.667 cm of the duct wall (peak-to-peak distance). Experiments were conducted for four Reynolds numbers in the turbulent regime ($11{,}050 < Re < 35{,}554$). The distributions of the heat transfer coefficient for two Reynolds numbers are shown in Fig. 2. For every Reynolds number, temperature patterns and, therefore, heat transfer distributions were similar in all seven waves. However, the magnitudes (i.e., the maximum and minimum on each wave) were different. The maximum heat transfer coefficient for each wave was located approximately 1.4 cm upstream of the peak of each wave due to the impingement of the free shear layer separated from the previous wave. This means that the location of maximum heat transfer (point of reattachment) on each wave is at about $x = 0.79P$, which is higher than suggested by Oyakawa et al. (1989). This could be due to the difference between the two geometries (their geometry included a duct with two opposite wavy walls). The maximum local heat transfer of the entire surface belonged to the second wave, which was 10 to 20 percent higher than others. Immediately downstream, right after the maximum heat transfer (impingement) occurs on the front side of a peak, an accelerating flow boundary layer is expected to develop. A steep positive temperature gradient is evidence of this development. Then, this boundary layer separates near the peak, the heat transfer drops to its lowest value, approximately 1.3 cm downstream of the peak of the corresponding wave. Beyond this point, heat transfer increases again due to turbulent mixing in the valley region between the two adjacent peaks until once again it reaches a maximum at the next reattachment (impingement) place. This pattern repeats for the entire area (seven continuous waves). Figure 3, which is a blow up of Fig. 2 (including results for four Reynolds numbers), shows the effect of Reynolds numbers on the local heat transfer coefficient for the second peak only. This figure shows higher local heat transfer for higher Reynolds numbers, especially near maximum heat transfer areas.

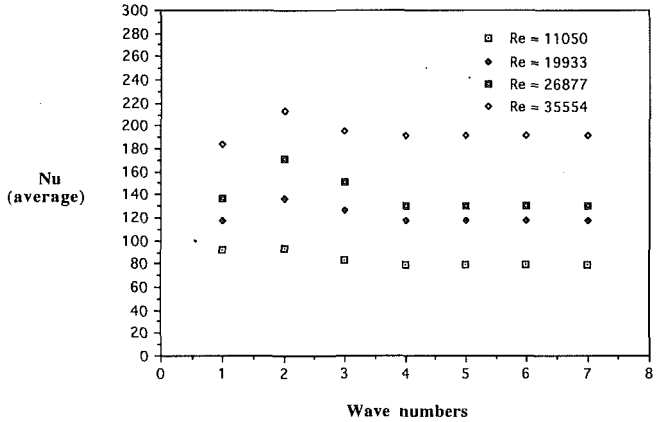

Fig. 4 Average Nusselt numbers for each wave at different Reynolds numbers

(B) Average Heat Transfer. The highest average heat transfer coefficient was on the second wave. Apparently this wave is exposed to the maximum turbulence which is initiated by the upstream corrugation. Figure 4 represents the average Nusselt number for the seven waves for four different Reynolds numbers. These average Nusselt number values are based on the total area of each wave and are not based on projected area. The second wave shows a higher average heat transfer coefficient. Also a higher Reynolds number results in a higher average Nusselt number for all the waves. This is expected since the average Nusselt number is obtained by integrating the local Nusselt number distribution over the area. The average Nusselt number was constant after the third wave as soon as flow became periodically fully developed. The average Nusselt number of the wavy channel wall was compared to the average Nusselt number suggested by Kays and Crawford (1980) for a flat plate with unheated starting length ($St_X \, Pr^{0.4} = 0.0287 \, \overline{Re}_X^{-0.2} \, [1 - (\xi/X)^{9/10}]^{-1/9}$). Since the suggested equation is for local values, the local heat transfer coefficients were calculated based on local Reynolds numbers and numerically integrated over the entire length for comparison with the experimental

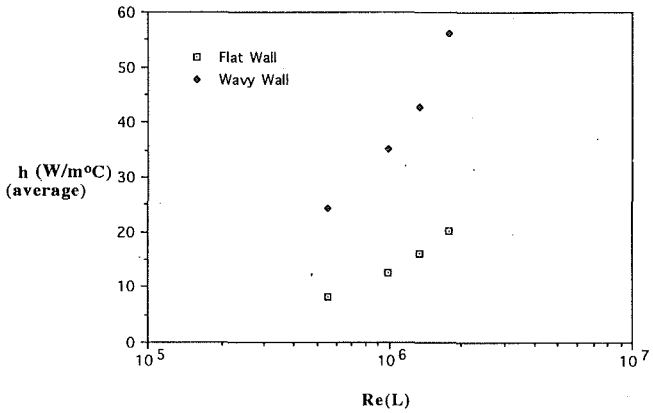

Fig. 5 Average heat transfer coefficients as a function of Reynolds numbers

values of the wavy wall (note: X is measured from the entrance of the channel and ζ is the unheated length). Figure 5 shows this comparison for four Reynolds numbers. The enhancement of heat transfer with a wavy wall is clear. Heat transfer coefficients are increased by almost a factor of three for the wavy wall. It is worth mentioning that the heat transfer enhancement shown in Fig. 5 might also be partly due to the differences between thermal boundary conditions used in this experimental study and that of the equation suggested by Kays and Crawford (uniform heat flux versus uniform wall temperature).

Conclusions

An experimental study of convective heat transfer was performed in the turbulent regime for a wavy wall channel. Heat transfer coefficients from seven waves and for four Reynolds numbers were investigated. The local Nusselt number distribution had the highest magnitude on the second wave, although the distribution of heat transfer followed the same pattern for all seven corrugations. The maximum local Nusselt number was located upstream of the peak of each wave, but the minimum local Nusselt number was located downstream within a short distance of the peak of each wave.

From the standpoint of the average Nusselt number, it appears that the highest average Nusselt number belongs to the second wave and Nusselt number stays uniform downstream of the third wavy as a result of the flow being periodically fully developed. Higher Reynolds numbers result in higher average Nusselt numbers, and the average Nusselt number of the wavy wall is higher than the flat-wall channel Nusselt number for the range of Reynolds numbers used in this study.

References

Ali, M. M., and Ramadhyani, S., 1992, "Experiments on Convective Heat Transfer in Corrugated Channels," *Experimental Heat Transfer*, Vol. 5, pp. 175–193.

Amano, R. S., Bagherlee, A., Smith, R. J., and Niess, T. G., 1987, "Turbulent Heat Transfer in Corrugated-Wall Channels With and Without Fins," ASME JOURNAL OF HEAT TRANSFER, Vol. 109, pp. 62–67.

Asako, Y., Nakamura, H., and Faghri, M., 1988, "Heat Transfer and Pressure Drop Characteristics in a Corrugated Duct With Rounded Corners," *Int. J. Heat Mass Transfer*, Vol. 31, No. 6, pp. 1237–1245.

Baughn, J. W., Takahashi, R. K., Hoffman, M. A., and McKillop, A. A., 1985, "Local Heat Transfer Coefficient Measurements Using Electrically Heated Thin Gold Coated Sheet," ASME JOURNAL OF HEAT TRANSFER, Vol. 107, pp. 953–959.

Baughn, J. W., Hoffman, M. A., and Makel, D. B., 1986, "Improvements in a New Technique for Measuring and Mapping Heat Transfer Coefficients," *Review of Scientific Instruments*, Vol. 57, pp. 650–654.

Baughn, J. W., Ireland, P. T., Jones, T. V., and Saniei, N., 1989, "A Comparison of the Transient and Heated-Coating Methods for the Measurements of Local Heat Transfer Coefficients on a Pin Fin," ASME JOURNAL OF HEAT TRANSFER, Vol. 111, pp. 877–881.

Baughn, J. W., and Saniei, N., 1989, "Local Heat Transfer Measurements on Arrays of Pin Fins in a Rectangular Duct," presented at the International Heat Transfer Conference, Jerusalem, Israel.

Baughn, J. W., and Saniei, N., 1991, "The Effect of Thermal Boundary Conditions on Heat Transfer From a Cylinder in Cross Flow," ASME JOURNAL OF HEAT TRANSFER, Vol. 113, pp. 1020–1023.

Ektesabi, M. R. M., and Sako, M., 1991a, "Flow Characteristics in a Wavy Sinusoidal Channel," presented at the 3rd Triennial International Symposium on Fluid Control, Measurement, and Visualization, Aug. 28–31.

Ektesabi, M. R. M., and Sako, M., 1991b, "Fluid Flow and Heat Transfer in Wavy Sinusoidal Channels. Part II," *Japanese Research*, Vol. 18, No. 3, pp. 32–43.

Garg, V. K., and Maji, P. K., 1988, "Flow and Heat Transfer in a Sinusoidally Curved Channel," *Int. J. Engineering Fluid Mechanics*, Vol. 1, No. 3, pp. 293–319.

Goldstein, R., Jr., and Sparrow, E. M., 1977, "Heat/Mass Transfer Characteristics for Flow in a Corrugated Wall Channel," ASME JOURNAL OF HEAT TRANSFER, Vol. 99, pp. 187–195.

Greiner, M., Chen, R. F., and Wirtz, R. A., 1991, "Passive Heat Transfer Enhancement on a Flat Surface in a Grooved Channel," presented at the ASME/JSME Thermal Engineering Joint Conference, Reno, NV.

Hippensteele, S. A., Russell, L. M., and Stepka, F. S., 1983, "Evaluation of a Method for Heat Transfer Measurements and Thermal Visualization Using a Composite of a Heater Element and Liquid Crystals," ASME JOURNAL OF HEAT TRANSFER, Vol. 105, pp. 184–189.

Kays, W. M., and Crawford, M. E., 1980, *Convective Heat and Mass Transfer*, McGraw-Hill, New York, pp. 213–216.

Kline, S. J., and McClintock, F. A., 1953, "Describing Uncertainties in Single-Sample Experiments," *Mechanical Engineering*, Vol. 75, Jan., pp. 3–8.

Molki, M., and Yuen, C. M., 1986, "Effect of Interwall Spacing on Heat Transfer and Pressure Drop in a Corrugated-Wall Duct," *Int. J. Heat Mass Transfer*, Vol. 29, pp. 987–997.

Nishimura, T., Murakami, S., Arakawa, S., and Kawamura, Y., 1990, "Flow Observations and Mass Transfer Characteristics in Symmetrical Wavy-Walled Channels at Moderate Reynolds Numbers for Steady Flow," *Int. J. Heat Mass Transfer*, Vol. 33, No. 5, pp. 835–845.

O'Brien, J. E., and Sparrow, E. M., 1982, "Corrugated-Duct Heat Transfer, Pressure Drop, and Flow Visualization," ASME JOURNAL OF HEAT TRANSFER, Vol. 104, pp. 410–416.

Oyakawa, K., Shinzato, T., and Mabuchi, I., 1989, "The Effect of the Channel Width on Heat-Transfer Augmentation in a Sinusoidal Wave Channel," *JSME International Journal*, Series II, Vol. 32, No. 3, pp. 403–410.

Simonich, J. C., and Moffat, R. J., 1982, "New Technique for Mapping Heat Transfer Coefficient Contours," *Review of Scientific Instruments*, Vol. 53, No. 5.

Sparrow, E. M., and Comb, J. W., 1983, "Effect of Interwall Spacing and Fluid Flow Inlet Conditions on a Corrugated-Wall Heat Exchanger," *Int. J. Heat Mass Transfer*, Vol. 26, No. 7, pp. 993–1005.

Sparrow, E. M., and Hossfeld, L. M., 1984, "Effect of Rounding of Protruding Edges on Heat Transfer and Pressure Drop in a Duct," *Int. J. Heat Mass Transfer*, Vol. 27, No. 10, pp. 1715–1723.

Effects of a Slit in a Rib on the Heat Transfer From a Rib-Mounted Wall

M. K. Chyu[1] and V. Natarajan[1]

Nomenclature

D_h = duct hydraulic diameter
e = rib height and width, 3.2 mm in present study
f = Fanning friction factor = $\Delta p \cdot (L/D_h)/(1/2\,\rho U^2)$
h_m = naphthalene mass transfer coefficient = $m/(\rho_{v,w} - \rho_b)$
m = mass transfer per unit time per unit area from a naphthalene surface

[1]Department of Mechanical Engineering, Carnegie Mellon University, Pittsburgh, PA 15213.

Contributed by the Heat Transfer Division of THE AMERICAN SOCIETY OF MECHANICAL ENGINEERS. Manuscript received by the Heat Transfer Division May 1991; revision received March 1993. Keywords: Analog Techniques, Augmentation and Enhancement, Flow Separation. Associate Technical Editor: T. W. Simon.

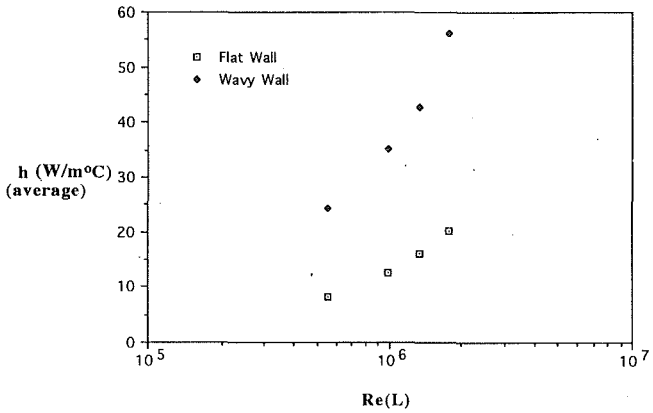

Fig. 5 Average heat transfer coefficients as a function of Reynolds numbers

values of the wavy wall (note: X is measured from the entrance of the channel and ζ is the unheated length). Figure 5 shows this comparison for four Reynolds numbers. The enhancement of heat transfer with a wavy wall is clear. Heat transfer coefficients are increased by almost a factor of three for the wavy wall. It is worth mentioning that the heat transfer enhancement shown in Fig. 5 might also be partly due to the differences between thermal boundary conditions used in this experimental study and that of the equation suggested by Kays and Crawford (uniform heat flux versus uniform wall temperature).

Conclusions

An experimental study of convective heat transfer was performed in the turbulent regime for a wavy wall channel. Heat transfer coefficients from seven waves and for four Reynolds numbers were investigated. The local Nusselt number distribution had the highest magnitude on the second wave, although the distribution of heat transfer followed the same pattern for all seven corrugations. The maximum local Nusselt number was located upstream of the peak of each wave, but the minimum local Nusselt number was located downstream within a short distance of the peak of each wave.

From the standpoint of the average Nusselt number, it appears that the highest average Nusselt number belongs to the second wave and Nusselt number stays uniform downstream of the third wavy as a result of the flow being periodically fully developed. Higher Reynolds numbers result in higher average Nusselt numbers, and the average Nusselt number of the wavy wall is higher than the flat-wall channel Nusselt number for the range of Reynolds numbers used in this study.

References

Ali, M. M., and Ramadhyani, S., 1992, "Experiments on Convective Heat Transfer in Corrugated Channels," *Experimental Heat Transfer*, Vol. 5, pp. 175–193.

Amano, R. S., Bagherlee, A., Smith, R. J., and Niess, T. G., 1987, "Turbulent Heat Transfer in Corrugated-Wall Channels With and Without Fins," ASME JOURNAL OF HEAT TRANSFER, Vol. 109, pp. 62–67.

Asako, Y., Nakamura, H., and Faghri, M., 1988, "Heat Transfer and Pressure Drop Characteristics in a Corrugated Duct With Rounded Corners," *Int. J. Heat Mass Transfer*, Vol. 31, No. 6, pp. 1237–1245.

Baughn, J. W., Takahashi, R. K., Hoffman, M. A., and McKillop, A. A., 1985, "Local Heat Transfer Coefficient Measurements Using Electrically Heated Thin Gold Coated Sheet," ASME JOURNAL OF HEAT TRANSFER, Vol. 107, pp. 953–959.

Baughn, J. W., Hoffman, M. A., and Makel, D. B., 1986, "Improvements in a New Technique for Measuring and Mapping Heat Transfer Coefficients," *Review of Scientific Instruments*, Vol. 57, pp. 650–654.

Baughn, J. W., Ireland, P. T., Jones, T. V., and Saniei, N., 1989, "A Comparison of the Transient and Heated-Coating Methods for the Measurements of Local Heat Transfer Coefficients on a Pin Fin," ASME JOURNAL OF HEAT TRANSFER, Vol. 111, pp. 877–881.

Baughn, J. W., and Saniei, N., 1989, "Local Heat Transfer Measurements on Arrays of Pin Fins in a Rectangular Duct," presented at the International Heat Transfer Conference, Jerusalem, Israel.

Baughn, J. W., and Saniei, N., 1991, "The Effect of Thermal Boundary Conditions on Heat Transfer From a Cylinder in Cross Flow," ASME JOURNAL OF HEAT TRANSFER, Vol. 113, pp. 1020–1023.

Ektesabi, M. R. M., and Sako, M., 1991a, "Flow Characteristics in a Wavy Sinusoidal Channel," presented at the 3rd Triennial International Symposium on Fluid Control, Measurement, and Visualization, Aug. 28–31.

Ektesabi, M. R. M., and Sako, M., 1991b, "Fluid Flow and Heat Transfer in Wavy Sinusoidal Channels. Part II," *Japanese Research*, Vol. 18, No. 3, pp. 32–43.

Garg, V. K., and Maji, P. K., 1988, "Flow and Heat Transfer in a Sinusoidally Curved Channel," *Int. J. Engineering Fluid Mechanics*, Vol. 1, No. 3, pp. 293–319.

Goldstein, R., Jr., and Sparrow, E. M., 1977, "Heat/Mass Transfer Characteristics for Flow in a Corrugated Wall Channel," ASME JOURNAL OF HEAT TRANSFER, Vol. 99, pp. 187–195.

Greiner, M., Chen, R. F., and Wirtz, R. A., 1991, "Passive Heat Transfer Enhancement on a Flat Surface in a Grooved Channel," presented at the ASME/JSME Thermal Engineering Joint Conference, Reno, NV.

Hippensteele, S. A., Russell, L. M., and Stepka, F. S., 1983, "Evaluation of a Method for Heat Transfer Measurements and Thermal Visualization Using a Composite of a Heater Element and Liquid Crystals," ASME JOURNAL OF HEAT TRANSFER, Vol. 105, pp. 184–189.

Kays, W. M., and Crawford, M. E., 1980, *Convective Heat and Mass Transfer*, McGraw-Hill, New York, pp. 213–216.

Kline, S. J., and McClintock, F. A., 1953, "Describing Uncertainties in Single-Sample Experiments," *Mechanical Engineering*, Vol. 75, Jan., pp. 3–8.

Molki, M., and Yuen, C. M., 1986, "Effect of Interwall Spacing on Heat Transfer and Pressure Drop in a Corrugated-Wall Duct," *Int. J. Heat Mass Transfer*, Vol. 29, pp. 987–997.

Nishimura, T., Murakami, S., Arakawa, S., and Kawamura, Y., 1990, "Flow Observations and Mass Transfer Characteristics in Symmetrical Wavy-Walled Channels at Moderate Reynolds Numbers for Steady Flow," *Int. J. Heat Mass Transfer*, Vol. 33, No. 5, pp. 835–845.

O'Brien, J. E., and Sparrow, E. M., 1982, "Corrugated-Duct Heat Transfer, Pressure Drop, and Flow Visualization," ASME JOURNAL OF HEAT TRANSFER, Vol. 104, pp. 410–416.

Oyakawa, K., Shinzato, T., and Mabuchi, I., 1989, "The Effect of the Channel Width on Heat-Transfer Augmentation in a Sinusoidal Wave Channel," *JSME International Journal*, Series II, Vol. 32, No. 3, pp. 403–410.

Simonich, J. C., and Moffat, R. J., 1982, "New Technique for Mapping Heat Transfer Coefficient Contours," *Review of Scientific Instruments*, Vol. 53, No. 5.

Sparrow, E. M., and Comb, J. W., 1983, "Effect of Interwall Spacing and Fluid Flow Inlet Conditions on a Corrugated-Wall Heat Exchanger," *Int. J. Heat Mass Transfer*, Vol. 26, No. 7, pp. 993–1005.

Sparrow, E. M., and Hossfeld, L. M., 1984, "Effect of Rounding of Protruding Edges on Heat Transfer and Pressure Drop in a Duct," *Int. J. Heat Mass Transfer*, Vol. 27, No. 10, pp. 1715–1723.

Effects of a Slit in a Rib on the Heat Transfer From a Rib-Mounted Wall

M. K. Chyu[1] and V. Natarajan[1]

Nomenclature

D_h = duct hydraulic diameter
e = rib height and width, 3.2 mm in present study
f = Fanning friction factor = $\Delta p \cdot (L/D_h)/(1/2\,\rho U^2)$
h_m = naphthalene mass transfer coefficient = $m/(\rho_{v,w} - \rho_b)$
m = mass transfer per unit time per unit area from a naphthalene surface

[1]Department of Mechanical Engineering, Carnegie Mellon University, Pittsburgh, PA 15213.

Contributed by the Heat Transfer Division of THE AMERICAN SOCIETY OF MECHANICAL ENGINEERS. Manuscript received by the Heat Transfer Division May 1991; revision received March 1993. Keywords: Analog Techniques, Augmentation and Enhancement, Flow Separation. Associate Technical Editor: T. W. Simon.

p = pitch between subsequent ribs
Re = Reynolds number = UD_h/ν
s = slit width
Sc = Schmidt number $\approx$ 1.9 for naphthalene-to-air mass transfer
St = local mass transfer Stanton number = h_m/U
St_o = local mass transfer Stanton number from a flat wall
U = bulk mean velocity
X = streamwise coordinate originating from mass transfer leading edge, see Fig. 1
Z = spanwise coordinate originating from duct centerline, see Fig. 1
η = performance index = $(2\ St/f)_{\text{slitted rib}}/(2\ St/f)_{\text{full rib}}$
ν = kinematic viscosity of air
ρ = fluid density
$\rho_{v,w}$ = vapor mass concentration or density of naphthalene at wall
ρ_b = vapor mass concentration or density of naphthalene in flow bulk

Introduction

In modern gas turbine airfoils, channels inside the turbine blade are often mounted with turbulence promoters in the form of transverse ribs to enhance the heat transfer from the channel walls to the internal cooling air. Geometric parameters such as passage aspect ratio, flow angle-of-attack, rib pitch-to-height ratio, and the relative positioning of these ribs with one another are known to have great effects on the cooling-channel performance. Much of the past work on rib heat transfer enhancement has addressed the two-dimensional rib where the rib extends completely across the span of the channel. In an effort to obtain a more heat transfer effective ribbed surface, the current work focuses on investigating the effects of a "slit" in a transverse rib on the rib heat transfer enhancement. Here the conventional transverse rib has been broken into two halves such that a gap is introduced between the two parts of the rib. This transforms the nominally two-dimensional transverse rib to a quasi-three-dimensional roughness. That is, for the slit rib, the rib extends over most of the surface like a typical two-dimensional full rib, and the slit exists only over a small portion of the rib. As a contrast to this, the sandgrain roughness is fully three dimensional, where each element is discrete and barely continuous. The feature of slit, though minute in physical size, has the potential to generate a plethora of advantages over the conventional transverse ribs from the view point of heat transfer enhancement. Some obvious advantages are the abundant flexibility in optimizing the relative locations, orientations, and angles-of-attack of the half-ribs separated by a slit. These could be even more potent for flow channels having more than one wall mounted with rib roughness.

The objective of the present study is to evaluate the influence of a slit on the local heat transfer distribution on the smooth portion of a rib-roughened wall. With this underlying motivation, the experiments include three different rib configurations; i.e., full-rib without slit as a baseline case, slitted-rib-in-line and slitted-rib staggered, as shown in Fig. 1. All cases have five periods with a pitch-to-height ratio (p/e) of 10, and, for both slitted-rib configurations, the slit width is approximately 1.6 times the rib height (s/e = 1.6). As the current research emphasizes a local study, not averaged Nu-Re correlations, the studies are performed for a single Reynolds number, approximately 1.2×10^4. Due mainly to difficulties involved in thermal insulation and data accuracy, conventional heat transfer methods are often considered to be ineffective for a local study. Hence the present experiment employs a mass transfer analogous system with subliming naphthalene ($C_{10}H_8$, Sc $\approx$ 1.9, according to Popiel and Boguslawski, 1986; Chen, 1988). By invoking an analogy between heat and mass transfer,

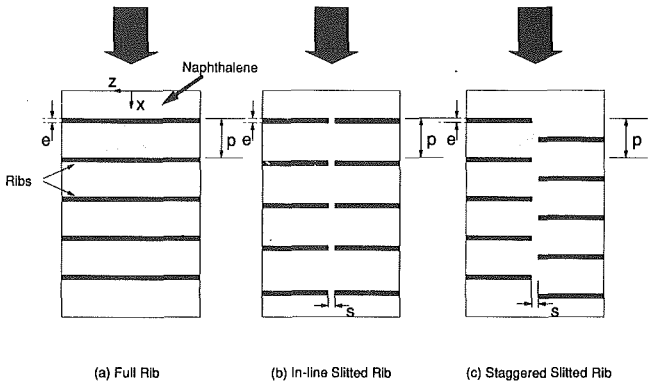

Fig. 1 Rib configurations

results obtained from a mass transfer measurement can be transformed into their heat transfer counterparts. To enhance the data accuracy and measurement efficiency with better control and rapid data acquisition rates, the local mass transfer rate is determined by using an automated, computer-controlled surface profile measurement system (Goldstein et al., 1985). As will be demonstrated later in the results section, this system is capable of revealing a detailed two-dimensional mapping, along with period-by-period evolution, of local mass transfer distribution over the entire five-period test section. To substantiate the mass transfer results, a near-wall flow visualization is performed using the oil-graphite technique. In addition, the pressure drop over the duct segment containing the mass transfer test section is also measured to evaluate a performance index.

Experimental Apparatus and Procedures

The tests are performed in a wind tunnel approximately 730 mm long, with a rectangular cross section 102 mm wide by 12.7 mm high. The flow development section of the apparatus is 483 mm in length. Compressed air passes through a 25.4 mm standard orifice, a flow straightener, a development section, and through the test section. As mentioned earlier, all test runs use a Reynolds number of about 1.2×10^4, based on hydraulic diameter and bulk mean velocity.

For each test run, ribs are mounted over the lower wall of the test section and the other three walls are left smooth. The ribs, made of 3.2 mm square steel bars, are glued to the side wall of the wind tunnel, with the first rib located 20.3 mm downstream of the mass transfer leading edge. The mass transfer active region is 102 mm wide (spanwise, Z direction) and 178 mm long (streamwise, X direction). This is prepared by casting the molten naphthalene onto the surface of the testing plate. After the casting, the plate is then stored in a box for at least 8 hours to enable it to attain thermal equilibrium with the room atmosphere before a test run. Note that the test channel assembled has only one principal wall mass transfer active, and the ribs are mass transfer inactive. Although this boundary condition is different from the corresponding thermal boundary conditions for most of the heat exchangers, the effects of a slit may be rationally singled out by presenting the measured rib data normalized by their flat-plate counterparts obtained under the same test conditions.

Prior to the run in the wind tunnel, the initial surface profile is measured using an automated data acquisition system. The same profile measurement is performed again after the wind tunnel exposure. The difference of naphthalene thickness at a given location before and after each data run yields the local mass transfer rate. The depth probe of the present measurement system is capable of detecting up to 2.5×10^{-5} mm in

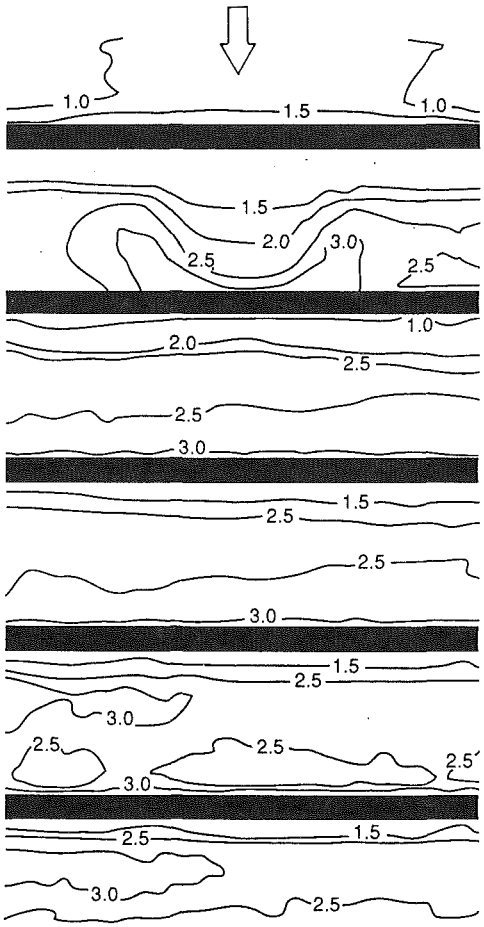

Fig. 2 St/St_o contour for full rib

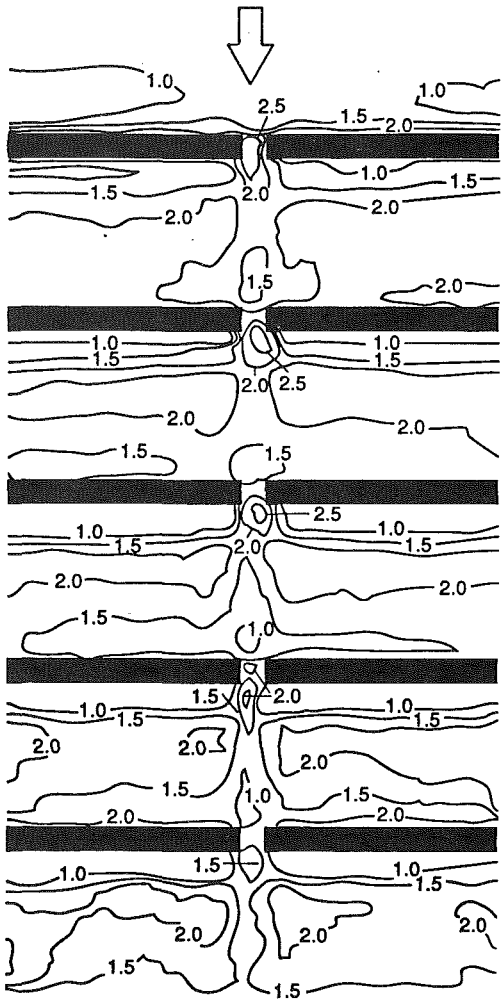

Fig. 3 St/St_o contour for in-line slit rib

accuracy. The measurement domain is a rectangular plane, 89 mm wide and 178 mm long. The total number of data points acquired over this domain is 3636 (101 in X and 36 in Z), which is equivalent to measurement step-increments of 1.78 mm and 2.54 mm along the X and Z directions, respectively. During the data run, the temperatures of the free stream and the naphthalene surface are recorded at five-minute intervals using two copper-constantan thermocouples. The two temperatures are always consistent within 0.2°C. Each data run lasts about 40 minutes, and the naphthalene thickness sublimed during this period is on the order of 10^{-2} to 10^{-1} mm. The detailed procedure and operational principle of the local mass transfer measurements have been given in earlier studies by Goldstein et al. (1985) and Chyu and Wu (1989). Pressure loss measurements across the test section for each of the rib configurations are obtained using an inclined manometer with oil (0.827 specific gravity).

Results and Discussion

To serve as a reference, the local mass transfer distribution on a smooth wall (without ribs) is first examined prior to the actual tests with rib elements. In the present study, the smooth wall mass transfer at a given streamwise location is very uniform across nearly 90 percent of the channel width and correlates as shown:

$$St_o = 0.0034\,(X/e)^{-0.21}$$

The -0.21 power dependency of X/e is very agreeable with that of local heat transfer coefficient for a turbulent boundary layer over a flat plate or in a channel entrance section. Significantly, the actual values of St_o are within 4 percent of those calculated from the corresponding heat transfer correlations (Reynolds et al., 1958, using $Pr \approx 1.9$) in a channel entrance region. This fine agreement validates the reliability and accuracy of the present measurement system. The results of the mass transfer experiments are presented as St/St_o contours in Figs. 2–4. This ratio provides a rational measure of mass transfer enhancement relative to a flat plate without rib and furthermore, the dependency of this ratio on Schmidt number is virtually eliminated so that the results may be directly utilized for heat transfer. Based on the method of Kline and McClintock (1953), the experimental uncertainty in Stanton number is within 5 percent.

Earlier studies have implied that a two-dimensional rib configuration with p/e ratio around 10 produces the highest heat transfer enhancement. However, almost all of these studies have focused on the fully developed regime, which occurs at sufficient distance from the duct inlet. In this regime, both the momentum and energy transports display periodicity among various periods. For the full-rib case, as shown in Fig. 2, periodicity begins from the second period. In this region, the mass transfer behavior is primarily two dimensional, varying slightly along the spanwise direction. As a direct influence of near-wall flow patterns, the heat or mass transfer increases progressively from the corner behind a rib, reaches a maximum near the reattachment point, and then decreases downstream. Near the reattachment, the local mass transfer enhancement is approximately 150 percent ($St/St_o = 2.5$). Note that this maximum is located slightly upstream of the flow reattachment

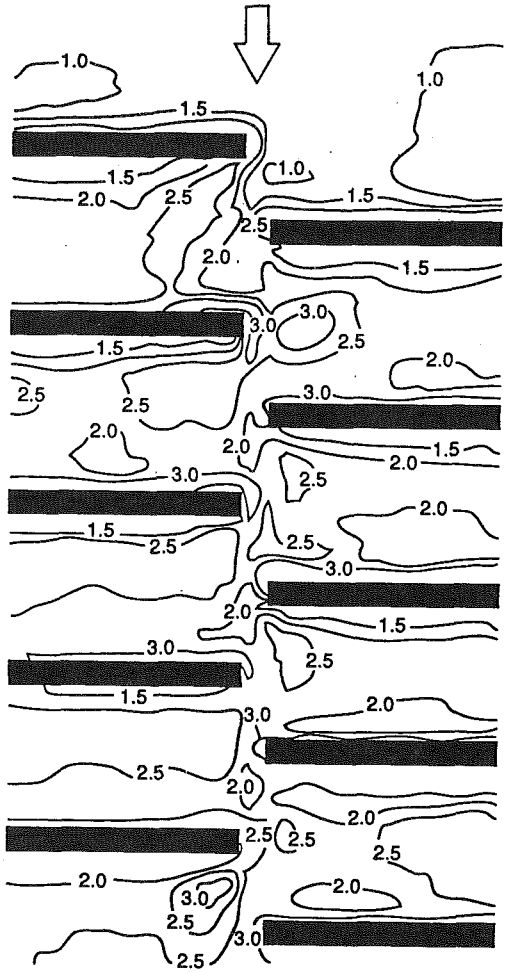

Fig. 4 St/St_o contour for staggered slit rib

point, by about one to two rib heights. Besides this reattachment-induced local maximum, the mass transfer coefficient rises sharply very near the rib front corner, which, in fact, is the highest ($St/St_o \approx 3.0$ to 3.5) over the entire period. This implies that the separated boundary layer ahead of a rib is not "dead air," as commonly perceived. A similar observation has been reported by Berger et al. (1979) using an electrochemical mass transfer system and recently by Chyu and Wu (1989) for $5 \leq p/e \leq 16$ in a much higher channel. Although rigorous evidence is lacking, Williams and Watts (1970) have speculated on the existence of a compact but strong corner vortex in this region, which may be responsible for this phenomenon.

Mass transfer in the first period, the developing regime, shows a relatively stronger spanwise variation than the downstream periods. Nevertheless, the mass transfer coefficient displays good symmetry with respect to the duct axis. Mass transfer near the channel central region is significantly higher than that near the edge. The additional resistance from the channel side walls apparently retards the flow, which, in turn, hinders the convective transport in the near-wall region. The magnitude of St/St_o increases monotonically with X/e and the reattachment is either nonexistent or located very close to the second rib. Upstream of the first rib, the values of St/St_o are close to unity, indicating that the mass transfer in this region is uninfluenced by the presence of the ribs downstream. However, a sharp rise of St/St_o, similar to that in the periodic regime, starts from about 1 to 2 rib heights ahead of the first rib, as also noted by Chyu and Wu (1989).

Local mass transfer profiles for the in-line slitted rib configuration, presented in Fig. 3, reveal highly unusual features. The results show relatively lower mass transfer near the symmetry line ($Z/e = 0$), although inside the gap, there exist several spots with relatively higher mass transfer coefficients. The boundary layer passing through a slit is similar to the developing flow with a sharp entrance. Moreover, the flow separates in a highly three-dimensional fashion rather than the generally two-dimensional nature of the flow over a full rib. Entrained vortices at the exit of the gap are released through periodic bursting processes promoting the transport in localized regions flanking the aperture. The interaction between the two three-dimensional vortices that meet inside the gap causes high mixing and increases the heat transfer.

Despite the excessive nonuniformity of mass transfer with in-line slit ribs, the St/St_o contour shows good symmetry with respect to the duct axis. Similar to the full-rib case, the periodic, developed regime appears to start from the second period. Another feature similar to the full-rib case is that the slit has little influence on the trend of St/St_o distribution in regions away from the duct central portion, namely $Z/e \geq 1$. The local maxima of St/St_o near the reattachment point and just ahead of a rib revealed in the full-rib case also are clearly observed. On the other hand, the magnitudes of St/St_o are significantly affected by the gap through flow. The values of St/St_o are nearly 20 percent lower than their full-rib counterparts. As previously mentioned, this is primarily caused by the fact that the throughflow along the central region, other than in the immediate vicinity of the slit, hinders the overall transport in the region. However, this effect does not alter the principal features of mass transfer, which are predominantly determined by the flow separation and reattachment phenomena caused by the two half-ribs located beside the slit.

The mass transfer results for the slitted ribs in staggered configuration are shown in Fig. 4. Note that, according to the present labeling format, a single complete pitch consists of two separate regions, which are divided by the duct axis and offset from each other by one-half a pitch. To facilitate the following discussion, the left and right-hand sides are chosen in the same orientation as one follows the flow downstream. The St/St_o contour patterns appears to be more complex than that of the other two cases. Within the same pitch, although the trend of mass transfer distribution is similar, the right-hand side surface always has slightly higher St/St_o than the left-hand side, by approximately 5 to 10 percent. This is largely due to the uneven disturbance from the staggered ribs at a given streamwise location. In addition, the undisturbed mass transfer lengths upstream of the first rib are different. This effect, however, is expected to diminish as the number of pitches increases. Like the other two cases, the mass transfer shows periodic characteristics from the second period, and the first period has the highest mass transfer.

As a contrast to the case with in-line slitted ribs, higher mass transfer coefficients exist in the slit region along $Z/e = 0$ for the staggered ribs, as compared between Figs. 3 and 4. Such a difference in St/St_o varies with period, ranging approximately from 20 percent for the second period to more than 100 percent for the fourth period. Apparently, the slithering flow, instead of throughflow, between the half-ribs arranged in the staggered form significantly enhances mixing and mass transfer. Furthermore, the transfer coefficient along the centerline data are more scattered, representing a greater spatial nonuniformity, for the staggered ribs than for the in-line ribs. Between any two adjacent ribs in the streamwise direction, the mass transfer in the region still displays the features of recirculation and reattachment similar to the full-rib case.

Period-resolved average mass transfer results are obtained by numerical integration of the local data. As reflected by the high local values of St/St_o, for all cases studied, the first period has the highest average mass transfer compared to other periods. This is followed by the averages in the periodic regime,

and the lowest exists in the entrance region (period "0") prior to the first rib. The values of St/St_o averaged over the entire periodic regime, i.e., the period 2 to 4, are 2.18, 1.70, and 2.06 for the full-rib, in-line slit and staggered, respectively. If the average over the entire measurement domain is calculated, the values become 2.04, 1.62, and 1.94, respectively. It appears that the staggered slit ribs display a comparable heat transfer enhancement to the full ribs, while the in-line slit ribs yield the lowest enhancement. This overall result implies that the implementation of a slit alone may decrease the heat transfer coefficient compared to the full rib case. However, this deficiency can be alleviated or even overwhelmed by re-arranging the relative positions and/or orientations of the half-ribs over the same heat transfer area. In addition, to be discussed below, slit-induced relief in pumping power can also post important significance for adopting slit-ribs in heat exchanger applications.

A rational performance measure on a heat exchanger surface with artificial roughness elements includes not only the heat transfer enhancement but also the pumping power required. Overall pressure measurements are performed for each of these rib configurations. The performance index η for the in-line slitted and staggered slitted rib configurations are 1.06 and 1.13, respectively. This implies that the in-line slitted rib is about 6 percent more effective than the full rib and the staggered slit rib is about 13 percent more effective than the full rib. Therefore, under the present test conditions, both slit-rib geometries appear to be superior alternatives to the conventional transverse rib. This conclusion agrees well with that drawn by Tanasawa et al. (1983) who have performed an average heat transfer study on ribs cut with five slits. Despite this general agreement, one must realize that the actual value of η may vary with different test conditions. Such a variation is expected to be significant with difference in specific geometry, number of wall roughened, and number of periods considered.

Conclusions

The effect of introducing a slit in a conventional transverse-rib on the heat transfer from a rib-roughened wall has been investigated experimentally using the naphthalene sublimation technique. Detailed mass transfer information in both the developing and developed regimes are obtained for flat surfaces mounted with three different rib configurations: full rib, slit ribs in-line and staggered. For all three cases studied, mass transfer begins to reveal its periodic characteristics downstream of the second rib. Near the rib front corner, the local mass transfer coefficient rises sharp, reaching the highest value of the entire period. This phenomenon has never been explicitly reported before using the conventional thermal method. In the first period, the developing regime exhibits strong spanwise variation of mass transfer accompanied by higher values of St/St_o than their developed counterparts. Within the present test range, mass transfer from a surface with slitted ribs is generally lower than that with full ribs. The developed-regime mass transfer enhancement with a slitted rib is approximately 70 percent for the in-line and 106 percent for the staggered configuration, compared to 118 percent for the full-rib case. For slit rib in-line configuration, the throughflow exiting from a slit inhibits the interaction as well as mixing between two sides of the centerline and results in degraded mass transfer. Gap flow for the staggered ribs exhibits a slithering flow pattern along the duct centerline, which promotes active mixing between two half-ribs and enhances mass transfer. The performance index η which takes into account the pressure drop across the test section, indicates that the in-line slit ribs and the staggered-slit ribs are about 6 percent and 13 percent, respectively, more effective than the full ribs.

Acknowledgments

The local mass transfer measurement system has been purchased under an NSF equipment grant No. CBT-8506827. Part of this study is supported by the Faculty Development Fund at Carnegie Mellon University.

References

Berger, F. P., Lau, K. F., and Lau, F. L., 1979, "Local Mass/Heat Transfer Distribution on Surfaces Roughened With Small Square Ribs," *Int. J. Heat Mass Transfer*, Vol. 22, pp. 1465–1656.

Chen, P. H., 1988, "Measurement of Local Mass Transfer From a Gas Turbine Blade," Ph.D. Thesis, University of Minnesota.

Chyu, M. K., and Wu, L. X., 1989, "Combined Effects of Rib Angle-of-Attack and Pitch-to-Height Ratio on Mass Transfer From a Surface With Transverse Ribs," *J. Exp. Heat Transfer*, Vol. 2, pp. 291–308.

Goldstein, R. J., Chyu, M. K., and Hain, R. C., 1985, "Measurement of Local Mass Transfer on a Surface in the Region of the Base of a Protruding Cylinder With a Computer-Controlled Data Acquisition System," *Int. J. Heat Mass Transfer*, Vol. 28, pp. 977–985.

Kline, S. J., and McClintock, F. A., 1953, "Describing Uncertainty in Single-Sample Experiments," *Mechanical Engineering*, Vol. 75, Jan., pp. 3–8.

Popiel, Cz. O., and Boguslawski, L., 1986, "Badanie Procesow Konwekcjim Masy i Ciepla Metoda Sublimujacego Naftalenu," XII Ogolnopolska Konferencja Naukowa Inzynierii Chemicznej i Procesowej, Poznan, Poland.

Reynolds, W. C., Kays, W. M., and Kline, S. J., 1985, "Heat Transfer in the Turbulent Incompressible Boundary Layer I—Constant Wall Temperature," NASA Memo 12-1-52W.

Tanasawa, I., Nishio, S., Takano, K., and Tado, M., 1983, "Enhancement of Forced Convection Heat Transfer in Rectangular Channel Using Turbulence Promoters," *Proc. ASME/JSME Thermal Engineering Joint Conference*, pp. 395–402.

Williams, F., and Watts, J., 1970, "The Development of Rough Surfaces With Improved Heat Transfer Performance and a Study of the Mechanisms Involved," *Proc. 4th Int. Heat Transfer Conf.*, Versailles, Vol. 4, Paper No. FC 5.5.

The Effect of Torsion on Convective Heat Transfer in a Helicoidal Pipe

G. Yang,[1] Z. F. Dong,[1] and M. A. Ebadian[1, 2]

Introduction

Coiled pipes are widely used in heat recovery systems, compact heat exchangers, storage tank heating systems, and refrigeration for the chemical, dairy, drug, and food industries. However, the majority of investigations for the coiled pipe are based on the assumption of a coil with a zero pitch. The pitch of the coil will create an additional force—torsion in the helicoidal pipe. Considering the effects of torsion will dramatically increase the complexity of the investigation. An extensive literature survey indicates that only six papers have been published considering the effects of torsion on laminar flow in a helicoidal pipe. In the toroidal pipe (the coiled pipe with a zero pitch), two symmetric loops of secondary flow are formed due to centrifugal force (Dean, 1927). In the helicoidal pipe (the curved pipe with nonzero pitch), torsion will distort the symmetric loops of the secondary flow. Wang (1981) was the first to introduce a nonorthogonal helicoidal coordinate system to formulate the Navier–Stokes equation for helicoidal pipe flow.

[1]Department of Mechanical Engineering, Florida International University, Miami, FL 33199.

[2]Mem. ASME.

Contributed by the Heat Transfer of THE AMERICAN SOCIETY OF MECHANICAL ENGINEERS. Manuscript received by the Heat Transfer Division June 1992; revision received January 1993. Keywords: Augmentation and Enhancement, Forced Convection, Numerical Methods. Associate Technical Editor: W. A. Fiveland.

and the lowest exists in the entrance region (period "0") prior to the first rib. The values of St/St_o averaged over the entire periodic regime, i.e., the period 2 to 4, are 2.18, 1.70, and 2.06 for the full-rib, in-line slit and staggered, respectively. If the average over the entire measurement domain is calculated, the values become 2.04, 1.62, and 1.94, respectively. It appears that the staggered slit ribs display a comparable heat transfer enhancement to the full ribs, while the in-line slit ribs yield the lowest enhancement. This overall result implies that the implementation of a slit alone may decrease the heat transfer coefficient compared to the full rib case. However, this deficiency can be alleviated or even overwhelmed by re-arranging the relative positions and/or orientations of the half-ribs over the same heat transfer area. In addition, to be discussed below, slit-induced relief in pumping power can also post important significance for adopting slit-ribs in heat exchanger applications.

A rational performance measure on a heat exchanger surface with artificial roughness elements includes not only the heat transfer enhancement but also the pumping power required. Overall pressure measurements are performed for each of these rib configurations. The performance index η for the in-line slitted and staggered slitted rib configurations are 1.06 and 1.13, respectively. This implies that the in-line slitted rib is about 6 percent more effective than the full rib and the staggered slit rib is about 13 percent more effective than the full rib. Therefore, under the present test conditions, both slit-rib geometries appear to be superior alternatives to the conventional transverse rib. This conclusion agrees well with that drawn by Tanasawa et al. (1983) who have performed an average heat transfer study on ribs cut with five slits. Despite this general agreement, one must realize that the actual value of η may vary with different test conditions. Such a variation is expected to be significant with difference in specific geometry, number of wall roughened, and number of periods considered.

Conclusions

The effect of introducing a slit in a conventional transverse-rib on the heat transfer from a rib-roughened wall has been investigated experimentally using the naphthalene sublimation technique. Detailed mass transfer information in both the developing and developed regimes are obtained for flat surfaces mounted with three different rib configurations: full rib, slit ribs in-line and staggered. For all three cases studied, mass transfer begins to reveal its periodic characteristics downstream of the second rib. Near the rib front corner, the local mass transfer coefficient rises sharp, reaching the highest value of the entire period. This phenomenon has never been explicitly reported before using the conventional thermal method. In the first period, the developing regime exhibits strong spanwise variation of mass transfer accompanied by higher values of St/St_o than their developed counterparts. Within the present test range, mass transfer from a surface with slitted ribs is generally lower than that with full ribs. The developed-regime mass transfer enhancement with a slitted rib is approximately 70 percent for the in-line and 106 percent for the staggered configuration, compared to 118 percent for the full-rib case. For slit rib in-line configuration, the throughflow exiting from a slit inhibits the interaction as well as mixing between two sides of the centerline and results in degraded mass transfer. Gap flow for the staggered ribs exhibits a slithering flow pattern along the duct centerline, which promotes active mixing between two half-ribs and enhances mass transfer. The performance index η which takes into account the pressure drop across the test section, indicates that the in-line slit ribs and the staggered-slit ribs are about 6 percent and 13 percent, respectively, more effective than the full ribs.

Acknowledgments

The local mass transfer measurement system has been purchased under an NSF equipment grant No. CBT-8506827. Part of this study is supported by the Faculty Development Fund at Carnegie Mellon University.

References

Berger, F. P., Lau, K. F., and Lau, F. L., 1979, "Local Mass/Heat Transfer Distribution on Surfaces Roughened With Small Square Ribs," *Int. J. Heat Mass Transfer*, Vol. 22, pp. 1465–1656.

Chen, P. H., 1988, "Measurement of Local Mass Transfer From a Gas Turbine Blade," Ph.D. Thesis, University of Minnesota.

Chyu, M. K., and Wu, L. X., 1989, "Combined Effects of Rib Angle-of-Attack and Pitch-to-Height Ratio on Mass Transfer From a Surface With Transverse Ribs," *J. Exp. Heat Transfer*, Vol. 2, pp. 291–308.

Goldstein, R. J., Chyu, M. K., and Hain, R. C., 1985, "Measurement of Local Mass Transfer on a Surface in the Region of the Base of a Protruding Cylinder With a Computer-Controlled Data Acquisition System," *Int. J. Heat Mass Transfer*, Vol. 28, pp. 977–985.

Kline, S. J., and McClintock, F. A., 1953, "Describing Uncertainty in Single-Sample Experiments," *Mechanical Engineering*, Vol. 75, Jan., pp. 3–8.

Popiel, Cz. O., and Boguslawski, L., 1986, "Badanie Procesow Konwekcjim Masy i Ciepla Metoda Sublimujacego Naftalenu," XII Ogolnopolska Konferencja Naukowa Inzynierii Chemicznej i Procesowej, Poznan, Poland.

Reynolds, W. C., Kays, W. M., and Kline, S. J., 1985, "Heat Transfer in the Turbulent Incompressible Boundary Layer I—Constant Wall Temperature," NASA Memo 12-1-52W.

Tanasawa, I., Nishio, S., Takano, K., and Tado, M., 1983, "Enhancement of Forced Convection Heat Transfer in Rectangular Channel Using Turbulence Promoters," *Proc. ASME/JSME Thermal Engineering Joint Conference*, pp. 395–402.

Williams, F., and Watts, J., 1970, "The Development of Rough Surfaces With Improved Heat Transfer Performance and a Study of the Mechanisms Involved," *Proc. 4th Int. Heat Transfer Conf.*, Versailles, Vol. 4, Paper No. FC 5.5.

The Effect of Torsion on Convective Heat Transfer in a Helicoidal Pipe

G. Yang,[1] Z. F. Dong,[1] and M. A. Ebadian[1, 2]

Introduction

Coiled pipes are widely used in heat recovery systems, compact heat exchangers, storage tank heating systems, and refrigeration for the chemical, dairy, drug, and food industries. However, the majority of investigations for the coiled pipe are based on the assumption of a coil with a zero pitch. The pitch of the coil will create an additional force—torsion in the helicoidal pipe. Considering the effects of torsion will dramatically increase the complexity of the investigation. An extensive literature survey indicates that only six papers have been published considering the effects of torsion on laminar flow in a helicoidal pipe. In the toroidal pipe (the coiled pipe with a zero pitch), two symmetric loops of secondary flow are formed due to centrifugal force (Dean, 1927). In the helicoidal pipe (the curved pipe with nonzero pitch), torsion will distort the symmetric loops of the secondary flow. Wang (1981) was the first to introduce a nonorthogonal helicoidal coordinate system to formulate the Navier–Stokes equation for helicoidal pipe flow.

[1]Department of Mechanical Engineering, Florida International University, Miami, FL 33199.

[2]Mem. ASME.

Contributed by the Heat Transfer of THE AMERICAN SOCIETY OF MECHANICAL ENGINEERS. Manuscript received by the Heat Transfer Division June 1992; revision received January 1993. Keywords: Augmentation and Enhancement, Forced Convection, Numerical Methods. Associate Technical Editor: W. A. Fiveland.

He solved it by applying the perturbation method for the case of a small curvature and small torsion. Murata et al. (1981) simplified the Navier-Stokes equations by assuming a small curvature in a nonorthogonal coordinate system. Germano (1982, 1989) introduced a transformation to convert the nonorthogonal coordinate system to an orthogonal one and found that the effect of torsion of the secondary flow is second order. Kao (1987) used Germano's coordinate system to study the helicoidal pipe flow in a substantial range of Dean numbers using both perturbation and numerical methods. Recently, Xie (1990) tried to resolve the controversy between these researchers by linking Wang's coordinate system with Germano's coordinate system. However, none of these papers discuss the effects of torsion on convective heat transfer in a helicoidal pipe.

Excellent reviews can be found in the references by Berger et al. (1983), Gnielinski (1986), Baurmeister and Brauer (1979), and Shah and Joshi (1987). It must be emphasized here again that many researchers have claimed that they considered the effects of pitch on convective heat transfer in a helicoidal pipe. However, inspection of their equations reveals that either only part of the effect of torsion is considered, or an incorrect expression for the torsion term is applied. Therefore, the objective of this paper is to explore the effects of torsion on convective heat transfer in a helicoidal pipe. The flow is assumed to be hydrodynamically and thermally fully developed with constant fluid properties. The effects of free convection are neglected. Uniform axial heat flux with peripheral constant wall temperature boundary conditions is also applied in this investigation.

The Governing Equations

The coordinate system used by Germano (1982) is applied in this study. In Fig. 1, s^* indicates the axial coordinate, and D is the diameter of the circular cylinder on which s^* is coiled. R is the radius of the circular pipe, while r^* and θ are the coordinates in the radial and tangential directions, and b is the pitch of the helicoidal pipe. u, v, and w are the dimensionless velocities in the radial, tangential, and axial directions, respectively, and T is the dimensionless fluid temperature. The governing equations for fully developed flow can be written as:

$$\frac{1}{r}\frac{\partial u}{\partial \theta}+\frac{1}{r}\frac{\partial (rv)}{\partial r}+Q=0 \tag{1}$$

$$\frac{1}{r}\frac{\partial (uu)}{\partial \theta}+\frac{1}{r}\frac{\partial (rvu)}{\partial r}=-\frac{1}{r}\frac{\partial p}{\partial \theta}+\left(\frac{\partial^2 u}{\partial r^2}+\frac{1}{r}\frac{\partial u}{\partial r}+\frac{1}{r^2}\frac{\partial^2 u}{\partial \theta^2}\right)$$
$$-uQ-\frac{uv}{r}+\epsilon w\omega\left(w\cos\theta-\lambda\frac{\partial u}{\partial \theta}\right)$$
$$-\left(\frac{1}{r^2}\frac{\partial^2 u}{\partial \theta^2}+\frac{u}{r^2}+\frac{1}{r}\frac{\partial^2 v}{\partial r\partial \theta}-\frac{1}{r^2}\frac{\partial v}{\partial \theta}\right)+\epsilon\omega\left(\eta\sin\theta+\lambda\frac{\partial \beta}{\partial \theta}\right) \tag{2}$$

$$\frac{1}{r}\frac{\partial (vu)}{\partial \theta}+\frac{1}{r}\frac{\partial (rvv)}{\partial r}=-\frac{\partial p}{\partial r}$$
$$+\left(\frac{1}{r^2}\frac{\partial^2 v}{\partial \theta^2}+\frac{1}{r}\frac{\partial v}{\partial r}+\frac{\partial^2 v}{\partial r^2}\right)-vQ+\frac{u^2}{r}+\epsilon w\omega\left(w\sin\theta+\lambda\frac{\partial v}{\partial \theta}\right)$$
$$-\left(\frac{1}{r}\frac{\partial v}{\partial r}+\frac{\partial^2 v}{\partial r^2}+\frac{1}{r}\frac{\partial^2 u}{\partial r\partial \theta}+\frac{1}{r^2}\frac{\partial u}{\partial \theta}\right)-\epsilon\omega\left(\eta\cos\theta+\lambda\frac{\partial \gamma}{\partial \theta}\right) \tag{3}$$

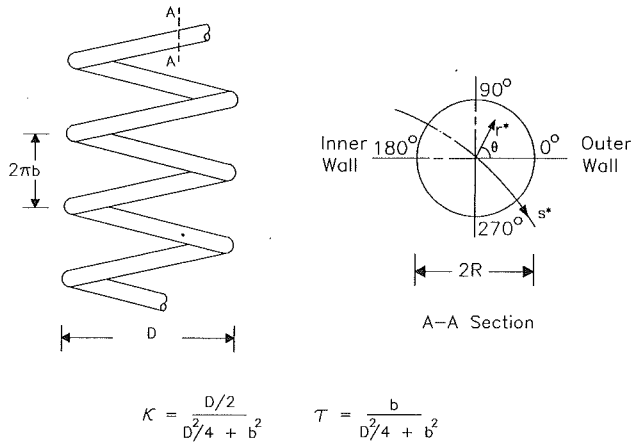

$$K=\frac{D/2}{D^2/4+b^2} \qquad T=\frac{b}{D^2/4+b^2}$$

Fig. 1 Geometry and coordinates of a helicoidal pipe

$$\frac{1}{r}\frac{\partial (uw)}{\partial \theta}+\frac{1}{r}\frac{\partial (rvw)}{\partial r}=-\omega\frac{\alpha}{\sqrt{\epsilon}}+\omega\epsilon\frac{\partial p}{\partial \theta}$$
$$+\left(\frac{1}{r^2}\frac{\partial^2 w}{\partial \theta^2}+\frac{1}{r}\frac{\partial w}{\partial r}+\frac{\partial^2 w}{\partial r^2}\right)-2wQ$$
$$+\frac{1}{r}\frac{\partial}{\partial \theta}\left(\epsilon w\omega\cos\theta-\epsilon\omega\lambda\frac{\partial u}{\partial \theta}\right)+\frac{\partial}{\partial r}\left(\epsilon w\omega\sin\theta-\omega\epsilon\lambda\frac{\partial v}{\partial \theta}\right)$$
$$+\frac{1}{r}\left(\epsilon w\omega\sin\theta-\omega\epsilon\lambda\frac{\partial v}{\partial \theta}\right), \tag{4}$$

$$\frac{1}{r}\frac{\partial (uT)}{\partial \theta}+\frac{1}{r}\frac{\partial (rvT)}{\partial r}=\frac{1}{\mathrm{Pr}}\left(\frac{1}{r^2}\frac{\partial^2 T}{\partial \theta^2}+\frac{\partial^2 T}{\partial r^2}+\frac{1}{r}\frac{\partial T}{\partial r}\right)$$
$$-TQ+\frac{1}{\mathrm{Pr}}\epsilon\omega\left(\frac{\partial T}{r\partial \theta}\cos\theta+\frac{\partial T}{\partial r}\sin\theta\right)+\omega\frac{w}{w_b}$$
$$+\omega\epsilon\lambda w\frac{\partial T}{\partial \theta}+\frac{1}{\mathrm{Pr}}\omega^2\epsilon\lambda\frac{\partial}{\partial \theta}\left(\epsilon\lambda\frac{\partial T}{\partial \theta}-2\frac{\partial T}{\partial s}\right). \tag{5}$$

ϵ and λ represent the dimensionless curvature and torsion, respectively; p is the pressure of the fluid; and Pr is the Prandtl number, where

$$Q=-\epsilon\omega\left(u\cos\theta+v\sin\theta-\lambda\frac{\partial w}{\partial \theta}\right) \tag{6}$$

$$\beta=\frac{1}{r}\frac{\partial w}{\partial \theta}+\epsilon\omega\left(w\cos\theta+\lambda\frac{\partial u}{\partial \theta}\right) \tag{7}$$

$$\gamma=-\frac{\partial w}{\partial r}-\epsilon\omega\left(w\sin\theta+\lambda\frac{\partial v}{\partial \theta}\right) \tag{8}$$

$$\eta=\frac{\partial u}{\partial r}+\frac{u}{r}-\frac{1}{r}\frac{\partial v}{\partial \theta} \tag{9}$$

$$\omega=\frac{1}{1+\epsilon r\sin\theta} \tag{10}$$

$$\alpha=\frac{R^3}{\nu^2\rho}(\kappa R)^{1/2}\frac{dp^*}{ds^*}. \tag{11}$$

The dimensionless parameters in Eqs. (1)–(10) are defined by:

$$r=\frac{r^*}{R},\quad s=\frac{s^*}{R},\quad u=\frac{u^*R}{\nu},\quad v=\frac{v^*R}{\nu},$$

$$w=\frac{w^*R}{\nu},\quad p=p^*/(\rho\nu^2/R^2),$$

$$\epsilon=\kappa R,\quad \lambda=\frac{\tau}{\kappa},\quad T=\frac{T^*-T_w^*}{(R^2w_b^*/\nu)\left(-\frac{dT^*}{ds^*}\right)} \tag{12}$$

In Eq. (12), values with superscript (*) indicate dimensional values; De is the Dean number; and Re represent the Reynolds number.

$$\mathrm{Re}=\frac{D_h\,w_b^*}{\nu}=2w_b, \tag{13}$$

$$\mathrm{De}=\mathrm{Re}\,\epsilon^{1/2}. \tag{14}$$

The friction factor and the Nusselt number are defined by:

$$f_c\,\mathrm{Re}=2\epsilon^{1/2}/(w_b\,\overline{\omega}\,\mathrm{De}), \tag{15}$$

$$\mathrm{Nu}=\overline{\omega}\,\mathrm{Pr}/T_b; \tag{16}$$

w_b and T_b are the bulk axial velocity and bulk temperature, respectively, which are defined by:

$$w_b=\frac{2}{\pi}\int_0^{\pi}\int_0^1 wrdrd\theta, \tag{17}$$

$$T_b=\frac{2}{\pi w_b}\int_0^{\pi}\int_0^1 wTrdrd\theta; \tag{18}$$

and $\overline{\omega}$ is defined by:

$$\overline{\omega}=\frac{2}{\pi}\int_0^{\pi}\int_0^1 \omega rdrd\theta. \tag{19}$$

Results and Discussion

The governing equations, Eqs. (1)–(5), are nonlinear partial differential equations that have been solved by the SIMPLE algorithm (Patankar, 1980). Three controlling parameters—the Dean number, De, the dimensionless torsion, λ, and the Prandtl number, Pr—will determine the axial and secondary flow patterns, and eventually the heat transfer behavior in a helicoidal pipe. The convergence criterion of

$$\frac{\|\Phi_{ij}^{k+1}-\Phi_{ij}^{k}\|}{\|\Phi_{ij}^{k+1}\|}\le 10^{-5}, \tag{20}$$

is applied for all equations, where Φ refers to u, v, w, p, and T. The subscripts i and j represent the arbitrary nodes, and the superscript k represents the kth iteration. Uniform grid distributions (angular direction grids × radial direction grids of 20×20, 30×30, 40×40, 60×60, and 80×80) have been tested. The results indicate that the 40×40 grid arrangement can assure an accurate and satisfactory solution.

Since the enhancement of heat transfer and the effect of torsion are directly dependent on the secondary flow behavior, the secondary flow pattern and the temperature contour in the cross section of the coiled pipe will be discussed first, as seen in Fig. 2. In each figure, the left side indicates the inner wall, and the right side refers to the outer wall of the coiled pipe. Figure 2(*a*) shows the typical secondary flow pattern in a toroidal pipe ($\lambda=0$) with De = 300 and $\epsilon=0.2$. The figure indicates that the flow is directed from the inner wall toward the outer wall in the center region, and then returns to the inner wall along the top and bottom of the walls to form two symmetric vortices. Figure 2(*b*) indicates the corresponding temperature distribution in the cross section when Pr = 1. Since the temperature of the wall is lower than that of the fluid, the temperature of the fluid returning along the solid walls to the inner wall is lower. This low-temperature fluid is then carried into the interior of the pipe along the centerline. As a result, the high-temperature isothermal contours are pushed toward the outer wall. The temperature contours, however, still remain symmetric to the centerline. Figure 2(*c*) shows the temperature distributions when the Prandtl number increases to 10. The Prandtl number measures the ratio of convective and diffusive heat transfer. A large Prandtl number indicates that the convection will surpass the diffusion, and is the dominant mechanism of the heat transfer. Since the diffusive heat transfer is too weak to warm up the cold fluid in this case, the strong convection carries the cold fluid to penetrate the outer wall and divides the isothermal contours into two symmetric parts. Figures 2(*d*) illustrates the secondary flow pattern in a helicoidal pipe when De = 300, $\epsilon=0.2$, and $\lambda=0.3$. Unlike the case of Fig. 2(*a*), the torsion significantly deforms the symmetry of the two vortices. The top vortex becomes weaker and the bottom one becomes stronger. Figure 2(*e*) represents the corresponding temperature distribution in the case when Pr = 1. With the same order of magnitude between the convective and diffusive heat transfer, the northeast direction flow pushes the

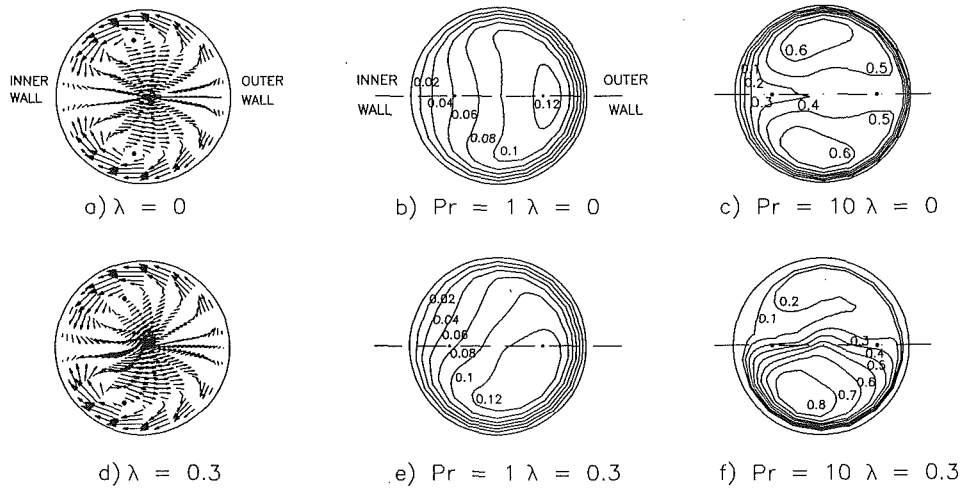

Fig. 2 Secondary flow pattern and temperature contour in the pipe cross section

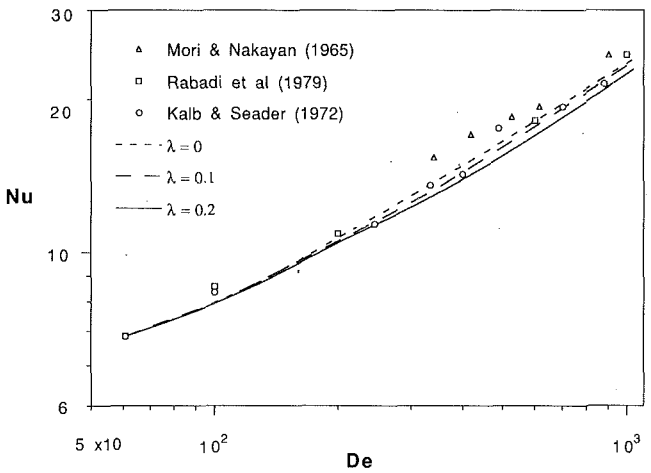

Fig. 3 The effect of torsion on heat transfer with different Dean numbers

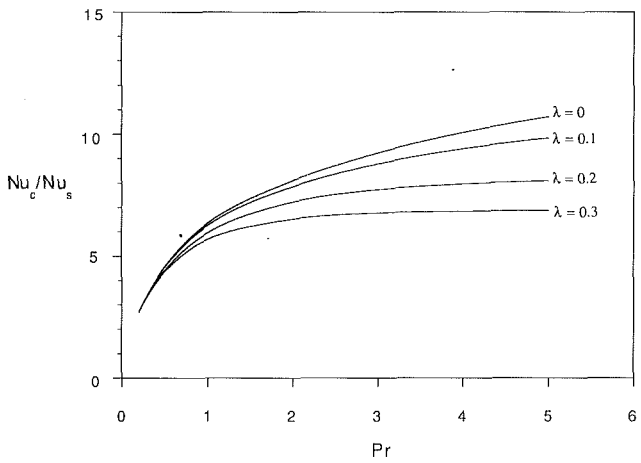

Fig. 4 The effects of the Prandtl number and torsion on the Nusselt number

high-temperature contours to the southeast corner. Figure 2(*f*) indicates the temperature contours in the case when $Pr = 10$. The cold fluid flows toward the northeast corner; pushing the high-temperature contours to the bottom half of the pipe, creating a low-temperature zone in the top half of the pipe.

Figure 3 demonstrates the variation of the Nusselt number versus the Dean number for different torsion values. During the calculation, the Prandtl number is equal to 0.7. This figure indicates that the Nusselt number is significantly increased as the Dean number increases, since the secondary flow becomes stronger. However, it appears that the Nusselt number is not sensitive to the change with torsion when the Prandtl number is low, although the Nusselt number might be slightly reduced as torsion increases in the large Dean number region. For example, the greatest difference in the Nusselt number $\lambda = 0$ and $\lambda = 0.2$ is less than 6 percent. This result is expected if one compares Fig. 2(*b*) with Fig. 2(*e*). For the fluid with a low Prandtl number, convective heat transfer is relatively weak. The torsion does not remarkably change the radial temperature gradient along the wall, but merely rotates the temperature contours and makes them asymmetric. Therefore, the change in the Nusselt number is only minor at different coiled pitches when the Prandtl number is low. For purposes of comparison, the experimental and the predicted results of Kalb and Seader (1972), Rabadi et al. (1979), and Mori and Nakayama (1965) are also plotted in this figure. A good agreement between our predictions and the results of the researchers can be observed.

The effects of the Prandtl number and torsion on the Nusselt number are illustrated in Fig. 4. In this figure, the Dean number is kept at 1000. Nu_c and Nu_s refer to the Nusselt number in the helicoidal pipe and the straight pipe, respectively. $Nu_s = 4.36$ has been applied in this calculation. This figure indicates that when the Prandtl number is less than one, the Nusselt number is slightly reduced as torsion increases. However, in the case of a large Prandtl number, increasing torsion can significantly reduce the Nusselt number. For example, the Nusselt number is reduced almost 30 percent when torsion increases from 0 to 0.3 for the case of $Pr = 5$. This phenomenon can be explained by considering the temperature gradient near the wall. For the case of a small Prandtl number, it can be seen from Figs. 2(*e*) and 2(*f*) that torsion does not remarkably alter the radial temperature gradient, but rotates the temperature contour. Therefore, the Nusselt number will not be considerably changed in these cases. In the case of a large Prandtl number the radial temperature gradient at the bottom half of the pipe wall is significantly enhanced, as seen in Fig. 2(*f*). Simultaneously, the temperature gradient at the top of the pipe is remarkably reduced, especially at the northwest location. As a result, the overall Nusselt number is reduced.

Conclusion

Convective heat transfer of fully developed laminar flow in a nonzero pitch coiled pipe (helicoidal pipe) is studied numerically in this paper. The energy equation for the helicoidal coordinate has been derived based on the conservation law. The effect of torsion on the heat transfer behavior in a helicoidal pipe is discussed. The results indicate that torsion will rotate the temperature contours, and at the same time, distort the symmetric shape of the isothermal contour. This deformation of the isothermal contour will be largely enhanced by increasing the Prandtl number. For a fluid with a large Prandtl number, the radial temperature gradient near the wall can be significantly increased along one-half of the pipe, and decreased along the other half of the pipe. As a result, the Nusselt number may remarkably decrease torsion increases in the case of a fluid with a large Prandtl number. For example, when $Pr = 5$, $\lambda = 0.3$, and $De = 1000$, the Nusselt number will be reduced more than 30 percent compared with a toroidal pipe.

Acknowledgments

The results presented in this paper were obtained in the course of research sponsored by the National Science Foundation under Grant No. CTS-9017732.

References

Baurmeister, U., and Brauer, H., 1979, "Laminar Flow and Heat Transfer in Helically and Spirally Coiled Tubes," *VDI Forschungsheft*, No. 593, pp. 2–48.

Berger, S. A., Talbot,, L., and Yao, L. S., 1983, "Flow in Curved Pipes," *Ann. Rev. Fluid Mech.*, Vol. 15, pp. 461–512.

Dean, W. R., 1927, "Note on the Motion of Fluid in a Curved Pipe," *Phil. Mag.*, Vol. 4, pp. 208–223.

Germano, M., 1982, "On the Effect of Torsion in a Helical Pipe Flow," *J. Fluid Mech.*, Vol. 125, pp. 1–18.

Germano, M., 1989, "The Dean Equations Extended to a Helical Pipe Flow," *J. Fluid Mech.*, Vol. 203, pp. 289–356.

Gnielinski, V., 1986, "Correlations for the Pressure Drop in Helically Coiled Tubes," *Int. Chem. Eng.*, Vol. 26, No. 1, pp. 36–44.

Kalb, C. E., and Seader, J. D., 1972, "Heat and Mass Transfer Phenomena for Viscous Flow in Curved Circular Tubes," *Int. J. Heat Mass Transfer*, Vol. 15, pp. 801–817.

Kao, H. C., 1987, "Torsion Effect on Fully Developed Flow in a Helical Pipe," *J. Fluid Mech.*, Vol. 184, pp. 335–356.
Mori, Y., and Nakayama, W., 1965, "Study on Forced Convective Heat Transfer in Curved Pipes," *Int. J. Heat Mass Transfer*, Vol. 8, pp. 67–82.
Murata, S., Miyake, Y., Inaba, T., and Ogawa, H., 1981, "Laminar Flow in a Helically Coiled Pipe," *Bull JSME*, Vol. 24, pp. 355–362.
Patankar, S. V., 1980, *Numerical Heat Transfer and Fluid Flow*, Hemisphere, Washington, DC.
Rabadi, N. J., Chow, J. C. F., and Simon, H. A., 1979, "An Efficient Numerical Procedure for the Solution of Laminar Flow and Heat Transfer in Coiled Tubes," *Numerical Heat Transfer*, Vol. 2, pp. 279–289.
Shah, R. K., and Joshi, S. D., 1987, "Convective Heat Transfer in Curved Ducts," in: *Handbook of Single-Phase Convective Heat Transfer*, S. Kakac, R. K. Shah, and W. Aung, eds., Wiley Interscience, New York.
Wang, C. Y., 1981, "On the Low-Reynolds-Number Flow in a Helical Pipe," *J. Fluid Mech.*, Vol. 108, pp. 185–194.
Xie, D. G., 1990, "Torsion Effect on Secondary Flow in a Helicoidal Pipe," *Int. J. Heat Fluid Flow*, Vol. 111, No. 2, pp. 114–119.

A Numerical Study of Two-Dimensional High Rayleigh Number Natural Convection Between Two Reservoirs Connected by a Horizontal Duct

G.-F. Yao[1] and J. A. Khan[1]

Introduction

The phenomenon of natural convection between two enclosures communicating through small openings like windows, ducts, and cracks has important applications in the fields of energy conservation in buildings, indoor air quality, fire research, solar energy storage, and nuclear reactor core performance. This paper presents a study of high Rayleigh number natural convection in two reservoirs connected by a horizontal duct.

Brown and Solvason (1962) and Brown (1962) experimentally studied natural convection heat and mass transfer of air through a small opening in a vertical and horizontal partition between two chambers. Their investigations are two of the very few experimental investigations where air was used as the experimental fluid. In most of the other experimental works, water, brine, or even kerosene (Prahl and Emmons, 1975) were used to model air flow between chambers. More recently Epstein (1988), and Epstein and Kenton (1989) performed experiments dealing with buoyancy-driven exchange flow and combined natural convection and forced flow through small openings in a horizontal partition. These experiments were performed using brine above the partition and fresh water below the partition to simulate the effect of density difference. Nansteel and Greif (1981, 1983, 1984) investigated natural convection in enclosures with two and three-dimensional partitions at high Rayleigh numbers. Chen et al. (1990) and Bajorek and Lloyd (1982) experimentally studied natural convection in a partitioned square box where air and carbon dioxide were used as the working fluids. These studies were for Grashof numbers less than 10^6. Bejan and Rossie (1981) performed a fundamental experimental study of natural convection in a horizontal duct connecting two fluid reservoirs. Their geometry was similar to the one in the present study.

[1]Department of Mechanical Engineering, University of South Carolina, Columbia, SC 29208.

Contributed by the Heat Transfer Division of THE AMERICAN SOCIETY OF MECHANICAL ENGINEERS. Manuscript received by the Heat Transfer Division October 1992; revision received March 1993. Keywords: Mass Transfer, Natural Convection, Numerical Methods. Associate Technical Editor: J. R. Lloyd.

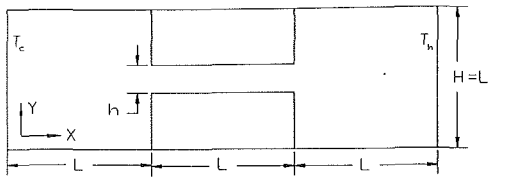

Fig. 1 Geometry and boundary conditions

Some of the numerical investigations include Zimmerman and Acharya (1987) and Acharya and Jetli (1990), who performed numerical investigations in rectangular enclosures with a partial vertical partition extending upward from the enclosure floor or downward from the ceiling or both. They used the SIMPLER algorithm developed by Patankar (1980) to solve the governing equations. Shaw et al. (1987) cast the governing equations in the form of stream function and vorticity and solved them with the aid of a cubic spline collocation method. Fu et al. (1989) investigated the transient laminar natural convection in an enclosure partitioned by an adiabatic baffle. They used a finite element method and explored the effect of the baffle's position and the Rayleigh number on the heat transfer mechanism.

The numerical investigations mentioned above deal with a wide range of parametric studies; however, none of these numerical researches deal with the solutions of laminar natural convection at high Rayleigh numbers. Experimental results have shown that the fluid flow in partitioned enclosures remains laminar at relatively high Rayleigh numbers (Nansteel and Greif, 1984; Chen et al., 1990). Therefore, laminar natural convection at a high Rayleigh number warrants further numerical investigation. At high Rayleigh numbers, the governing equations for this problem become stiff because of the strong coupling between the momentum and energy equations. This is perhaps the main reason that almost all past numerical studies concentrated on low or intermediate Rayleigh numbers.

Physical Model

The geometry and boundary conditions for the problem investigated in this study are shown in Fig. 1. In this model, two reservoirs are connected by a two-dimensional flat duct, with small opening dimensions in the vertical direction (h/H = 1/4, 1/5, 1/6, 1/7). All boundaries are insulated except for the two vertical walls of the reservoirs, which are isothermal. The flow is modeled two dimensional, incompressible, and laminar. Radiation effects are neglected and the Boussinesq approximation is invoked. We introduce the following dimensionless variables:

$$X=\frac{x}{H},\ Y=\frac{y}{H},$$

$$U=\frac{uH}{\nu},\ V=\frac{vH}{\nu}$$

$$\theta=\frac{T-T_c}{T_h-T_c},\ P=\frac{(p+\rho_0 g y)}{\rho_0 \nu^2}$$

$$\mathrm{Pr}=\frac{\nu}{\alpha},\ \mathrm{Ra}=\frac{g\beta H^3(T_h-T_c)}{\alpha\nu} \tag{1}$$

The governing differential equations that express the conservation of mass, momentum, and energy in the fluid domain become:

$$\frac{\partial U}{\partial X}+\frac{\partial V}{\partial Y}=0 \tag{2}$$

$$U\frac{\partial U}{\partial X}+V\frac{\partial U}{\partial Y}=-\frac{\partial P}{\partial X}+\left(\frac{\partial^2 U}{\partial X^2}+\frac{\partial^2 U}{\partial Y^2}\right) \tag{3}$$

Kao, H. C., 1987, "Torsion Effect on Fully Developed Flow in a Helical Pipe," *J. Fluid Mech.*, Vol. 184, pp. 335–356.
Mori, Y., and Nakayama, W., 1965, "Study on Forced Convective Heat Transfer in Curved Pipes," *Int. J. Heat Mass Transfer*, Vol. 8, pp. 67–82.
Murata, S., Miyake, Y., Inaba, T., and Ogawa, H., 1981, "Laminar Flow in a Helically Coiled Pipe," *Bull JSME*, Vol. 24, pp. 355–362.
Patankar, S. V., 1980, *Numerical Heat Transfer and Fluid Flow*, Hemisphere, Washington, DC.
Rabadi, N. J., Chow, J. C. F., and Simon, H. A., 1979, "An Efficient Numerical Procedure for the Solution of Laminar Flow and Heat Transfer in Coiled Tubes," *Numerical Heat Transfer*, Vol. 2, pp. 279–289.
Shah, R. K., and Joshi, S. D., 1987, "Convective Heat Transfer in Curved Ducts," in: *Handbook of Single-Phase Convective Heat Transfer*, S. Kakac, R. K. Shah, and W. Aung, eds., Wiley Interscience, New York.
Wang, C. Y., 1981, "On the Low-Reynolds-Number Flow in a Helical Pipe," *J. Fluid Mech.*, Vol. 108, pp. 185–194.
Xie, D. G., 1990, "Torsion Effect on Secondary Flow in a Helicoidal Pipe," *Int. J. Heat Fluid Flow*, Vol. 111, No. 2, pp. 114–119.

A Numerical Study of Two-Dimensional High Rayleigh Number Natural Convection Between Two Reservoirs Connected by a Horizontal Duct

G.-F. Yao[1] and J. A. Khan[1]

Introduction

The phenomenon of natural convection between two enclosures communicating through small openings like windows, ducts, and cracks has important applications in the fields of energy conservation in buildings, indoor air quality, fire research, solar energy storage, and nuclear reactor core performance. This paper presents a study of high Rayleigh number natural convection in two reservoirs connected by a horizontal duct.

Brown and Solvason (1962) and Brown (1962) experimentally studied natural convection heat and mass transfer of air through a small opening in a vertical and horizontal partition between two chambers. Their investigations are two of the very few experimental investigations where air was used as the experimental fluid. In most of the other experimental works, water, brine, or even kerosene (Prahl and Emmons, 1975) were used to model air flow between chambers. More recently Epstein (1988), and Epstein and Kenton (1989) performed experiments dealing with buoyancy-driven exchange flow and combined natural convection and forced flow through small openings in a horizontal partition. These experiments were performed using brine above the partition and fresh water below the partition to simulate the effect of density difference. Nansteel and Greif (1981, 1983, 1984) investigated natural convection in enclosures with two and three-dimensional partitions at high Rayleigh numbers. Chen et al. (1990) and Bajorek and Lloyd (1982) experimentally studied natural convection in a partitioned square box where air and carbon dioxide were used as the working fluids. These studies were for Grashof numbers less than 10^6. Bejan and Rossie (1981) performed a fundamental experimental study of natural convection in a horizontal duct connecting two fluid reservoirs. Their geometry was similar to the one in the present study.

[1]Department of Mechanical Engineering, University of South Carolina, Columbia, SC 29208.

Contributed by the Heat Transfer Division of THE AMERICAN SOCIETY OF MECHANICAL ENGINEERS. Manuscript received by the Heat Transfer Division October 1992; revision received March 1993. Keywords: Mass Transfer, Natural Convection, Numerical Methods. Associate Technical Editor: J. R. Lloyd.

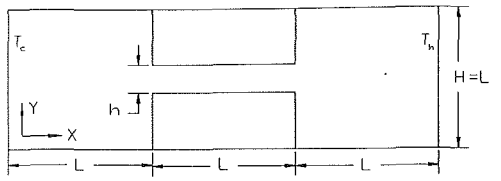

Fig. 1 Geometry and boundary conditions

Some of the numerical investigations include Zimmerman and Acharya (1987) and Acharya and Jetli (1990), who performed numerical investigations in rectangular enclosures with a partial vertical partition extending upward from the enclosure floor or downward from the ceiling or both. They used the SIMPLER algorithm developed by Patankar (1980) to solve the governing equations. Shaw et al. (1987) cast the governing equations in the form of stream function and vorticity and solved them with the aid of a cubic spline collocation method. Fu et al. (1989) investigated the transient laminar natural convection in an enclosure partitioned by an adiabatic baffle. They used a finite element method and explored the effect of the baffle's position and the Rayleigh number on the heat transfer mechanism.

The numerical investigations mentioned above deal with a wide range of parametric studies; however, none of these numerical researches deal with the solutions of laminar natural convection at high Rayleigh numbers. Experimental results have shown that the fluid flow in partitioned enclosures remains laminar at relatively high Rayleigh numbers (Nansteel and Greif, 1984; Chen et al., 1990). Therefore, laminar natural convection at a high Rayleigh number warrants further numerical investigation. At high Rayleigh numbers, the governing equations for this problem become stiff because of the strong coupling between the momentum and energy equations. This is perhaps the main reason that almost all past numerical studies concentrated on low or intermediate Rayleigh numbers.

Physical Model

The geometry and boundary conditions for the problem investigated in this study are shown in Fig. 1. In this model, two reservoirs are connected by a two-dimensional flat duct, with small opening dimensions in the vertical direction (h/H = 1/4, 1/5, 1/6, 1/7). All boundaries are insulated except for the two vertical walls of the reservoirs, which are isothermal. The flow is modeled two dimensional, incompressible, and laminar. Radiation effects are neglected and the Boussinesq approximation is invoked. We introduce the following dimensionless variables:

$$X=\frac{x}{H},\ Y=\frac{y}{H},$$

$$U=\frac{uH}{\nu},\ V=\frac{vH}{\nu}$$

$$\theta=\frac{T-T_c}{T_h-T_c},\ P=\frac{(p+\rho_0 g y)}{\rho_0 \nu^2}$$

$$\mathrm{Pr}=\frac{\nu}{\alpha},\ \mathrm{Ra}=\frac{g\beta H^3(T_h-T_c)}{\alpha\nu} \tag{1}$$

The governing differential equations that express the conservation of mass, momentum, and energy in the fluid domain become:

$$\frac{\partial U}{\partial X}+\frac{\partial V}{\partial Y}=0 \tag{2}$$

$$U\frac{\partial U}{\partial X}+V\frac{\partial U}{\partial Y}=-\frac{\partial P}{\partial X}+\left(\frac{\partial^2 U}{\partial X^2}+\frac{\partial^2 U}{\partial Y^2}\right) \tag{3}$$

$$U\frac{\partial V}{\partial X}+V\frac{\partial V}{\partial Y}=-\frac{\partial P}{\partial Y}+\left(\frac{\partial^2 V}{\partial X^2}+\frac{\partial^2 V}{\partial Y^2}\right)+\frac{\mathrm{Ra}\theta}{\mathrm{Pr}} \quad (4)$$

$$U\frac{\partial \theta}{\partial X}+V\frac{\partial \theta}{\partial Y}=\frac{1}{\mathrm{Pr}}\left(\frac{\partial^2 \theta}{\partial X^2}+\frac{\partial^2 \theta}{\partial Y^2}\right) \quad (5)$$

The Nusselt number, Nu, and the volumetric exchange flow rate, Q, are defined as:

$$\mathrm{Nu}=\int_0^1\left[U\theta-\frac{\partial \theta}{\partial X}\right]dY$$

$$Q=\int_{0.5}^{0.5+a} U\,dY \quad (6)$$

where $a = 0.5(h/H)$, and Q is evaluated at the centerline of the duct.

Numerical Technique

A SIMPLE-like algorithm developed by Date (1986) to study natural convection problems in a horizontal annulus is used to treat the coupling of momentum and energy equations. Details of the numerical procedure are documented elsewhere in Patankar (1980) and Date (1986). The following convergence criteria were used:

$$\left|\left(\frac{\partial U}{\partial X}+\frac{\partial V}{\partial Y}\right)_{i,j}\right|_{\max}<\epsilon_1$$

$$\left|\frac{\Phi_{i,j}^{k+1}-\Phi_{i,j}^{k}}{\Phi_{i,j}^{k+1}}\right|_{\max}<\epsilon_2 \quad (7)$$

where ϵ_1 and ϵ_2 are 10^{-6} and 10^{-4}, Φ indicates the physical variable of interest, and the superscript k denotes the iteration index.

To validate the numerical code we obtained natural convection solutions in a square cavity filled with air. Our results for a square enclosure were in excellent agreement with the benchmark solutions reported by De Vahl Davis (1983), Le Quere and De Roquefort (1987), Le Breton et al. (1991), and Markatos and Pericleous (1984).

For the limiting case when the duct length is zero, our numerical results (for $h/H = 1/2$) are in excellent agreement with the experimental results of Bajorek and Lloyd (1982) and the previous numerical results of Zimmerman and Acharya (1987), as shown in Fig. 5(b).

Results and Discussion

In the present study four duct opening dimensions, h/H = 1/4, 1/5, 1/6, and 1/7 are investigated. Rayleigh numbers studied are in the range of Ra = 10^4 to 5 × 10^7.

Fluid Flow Characteristics. Figure 2(a-c) present the velocity vectors at different Rayleigh numbers for one representative geometric condition (h/H = 1/6). Figure 2(d) presents streamlines for Ra = 5 × 10^7. At a low Rayleigh number (Fig. 2a) there is very little fluid exchange between the two reservoirs. As the Rayleigh number increases, the volumetric flow rate increases. At low and intermediate Rayleigh numbers (Ra = 10^4 − 5 × 10^5) fluid enters the duct radially, from all angles, shown in Fig. 2(a). This trend of fluid entering the duct radially can still be noted at a Rayleigh number of 10^6 (Fig. 2b). At higher Rayleigh numbers the fluid is drawn from a thin layer situated in the reservoir at the same level as the entrance to the duct (Figs. 2c and 2d). This phenomenon is similar to the one observed by Turner (1979). The horizontal withdrawal is accompanied by a weak back flow adjacent to the horizontal layer (Imberger and Fandry, 1975).

The flow configuration inside the duct consists of horizontal counterflow streams, with the warmer stream occupying the upper half of the duct. It is interesting to note that both streams become narrower as each approaches the exit. This narrowing of the stream can be clearly observed in Fig. 3. This figure shows the velocity profiles at the two ends and the center of the duct for Rayleigh number of 5 × 10^7 and h/H = 1/6. At the ends the cross-sectional area occupied by the exiting streams is significantly less than the entering streams. At the center of the duct both the streams occupy equal areas.

Volumetric exchange between the reservoirs is calculated based on the velocity profile at the center of the duct. This exchange rate for different Rayleigh numbers and duct dimensions is an important quantity in the investigation of air quality, because it gives a measure of contaminant exchange between the reservoirs in case of fire or nuclear spill. Figure 4 plots the exchange flow rates as a function of Rayleigh number and the duct dimension. The following correlation equation represents the numerical results to within ±15 percent:

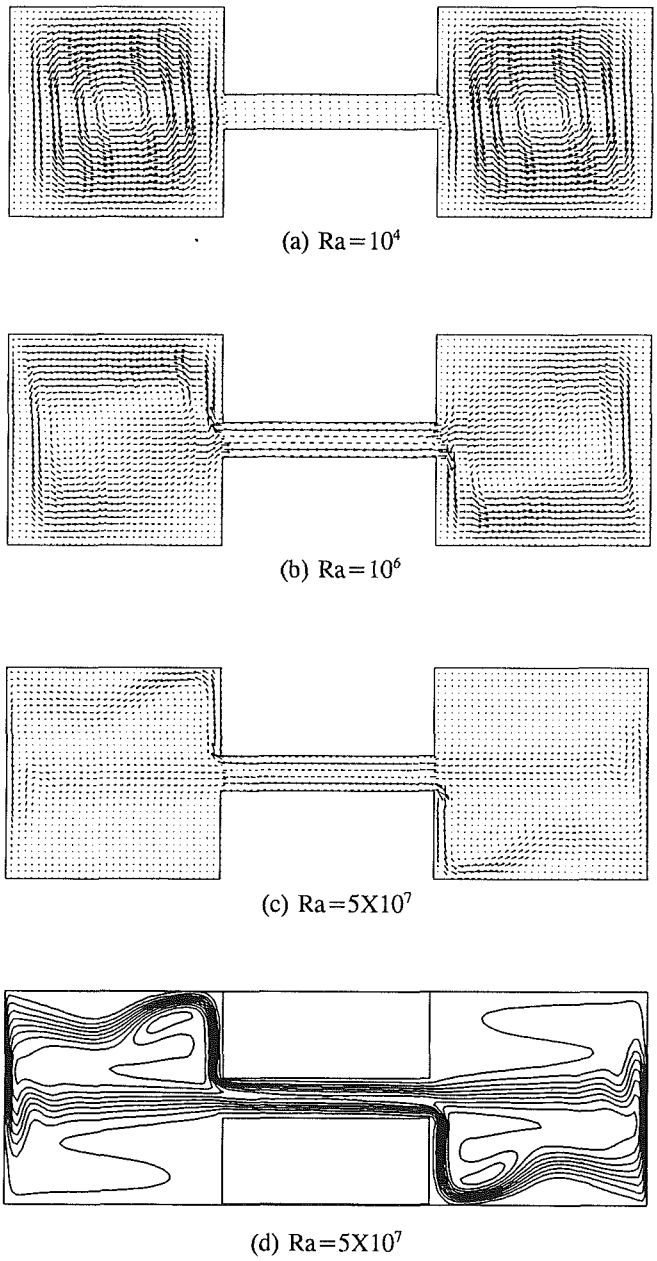

(a) Ra=10^4

(b) Ra=10^6

(c) Ra=5X10^7

(d) Ra=5X10^7

Fig. 2 Velocity vectors and streamlines for h/H = 1/6

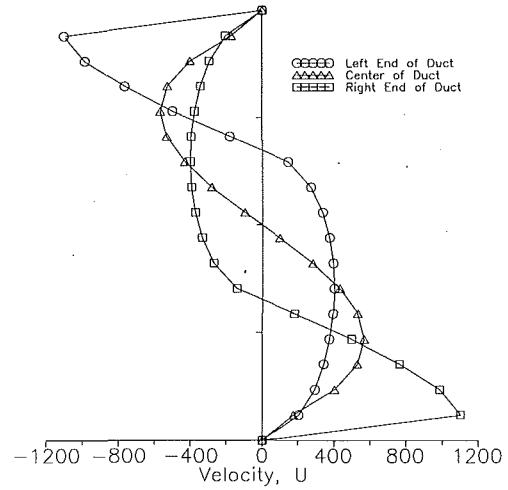

Fig. 3 Velocity profile at two ends and the center of the duct at Ra = 5 × 10^7 and h/H = 1/6

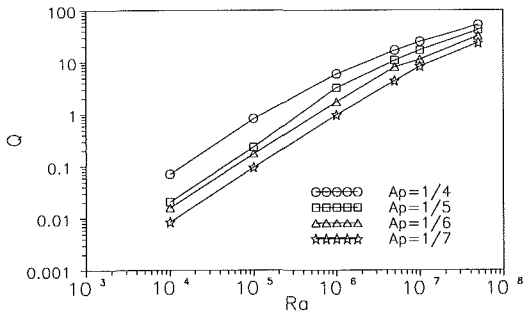

Fig. 4 Average exchange flow rate between the two reservoirs

$$Q = C\left(\frac{h}{H}\right)^a (\mathrm{Ra})^b \tag{8}$$

where C = 0.04568, a = 1.8695, b = 0.551, for 5 × 10^6 < Ra < 5 × 10^7

Heat Transfer. The heat transfer results are presented in Fig. 5. It is apparent that both the Rayleigh number and duct dimension have a substantial effect on heat transfer. With the increase of Rayleigh number, the effects of Rayleigh number increases. It is also observed that at small duct dimension (1/6 and 1/7) and low Rayleigh number (Ra = 10^5), the effect of duct dimension is very small. At Ra = 10^5 and h/H = 1/6 the average Nusselt number is almost same as that for Ra = 10^5 and h/H = 1/5. This phenomenon can be explained as follows. As the duct dimension decreases, the exchange flow rate through the duct falls, which results in a decrease in convective heat transfer between the reservoirs. However, at low flow rates the two counterflow streams in the duct have contact for a greater time and there is an increased conductive heat exchange between them. These two effects appear to cancel each other at low Rayleigh numbers. The numerical results in the form of isotherms (not presented) validate the fact that at small Rayleigh numbers and small duct dimensions the diffusive heat transfer between the streams is substantial. At low Rayleigh numbers and small duct dimensions the isotherms are found to be very dense, indicating that the temperature gradient in the flow direction in the duct is large. Thus at low Ra and small duct dimension the two streams can feel each other and exchange a substantial amount of heat by vertical diffusion. Inspection of the isotherms also reveals that at higher Rayleigh number and big duct dimension this temperature gradient is small. Therefore, diffusive heat transfer between the streams is minimal. The numerically obtained Nusselt number can be correlated for 1 × 10^4 < Ra < 5 × 10^7 to within ±20 percent by:

$$\ln(\mathrm{Nu}) = 22.1503 - 6.83932\ln\left(\frac{\mathrm{Ra}h}{H}\right) + 0.594517\left[\ln\left(\frac{\mathrm{Ra}h}{H}\right)\right]^2 - 0.0151647\left[\ln\left(\frac{\mathrm{Ra}h}{H}\right)\right]^3 \tag{9}$$

The only experimental work with similar geometry was done by Bejan and Rossie (1981), who used water as the working fluid. Their experimental study was performed for a very high Rayleigh number range (Ra = 1.161 × 10^8 to 5.9 × 10^9 based on H). We observed a slightly different heat transfer phenomenon than Bejan and Rossie (1981). They noted that the two streams in the duct were insulated by a middepth buffer region, and thus heat transfer between the two streams was inhibited. They also observed a negligible temperature gradient in the vertical direction in the buffer region, which is located at the duct center. In the present work we did not observe a buffer region. This discrepancy can be attributed to the fact that in the work of Bejan and Rossie (1981) the Rayleigh number was much higher. In our work we find that at higher Rayleigh numbers the trend begins to be similar to that of Bejan and Rossie (1981), and the vertical temperature gradient of the stream in the duct starts to decrease dramatically. The close agreement of our extrapolated results with the results of Bejan and Rossie (1981) is obvious from Fig. 5(*a*).

Figure 5(*b*) shows the effect of duct length on the heat transfer for h/H = 1/6 as a function of Rayleigh number. It is observed that at higher Rayleigh numbers the effect of duct length decreases. This is due to two reasons: First, as noted earlier at higher Rayleigh number the vertical temperature gradient in the duct decreases, and second at a higher Rayleigh number the two streams spend less time in the duct; therefore,

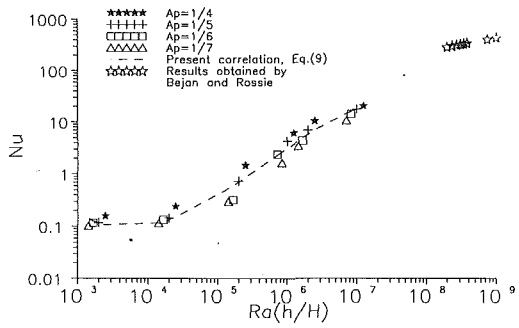

Fig. 5(*a*) Nusselt number and the correlation curve for Nusselt number

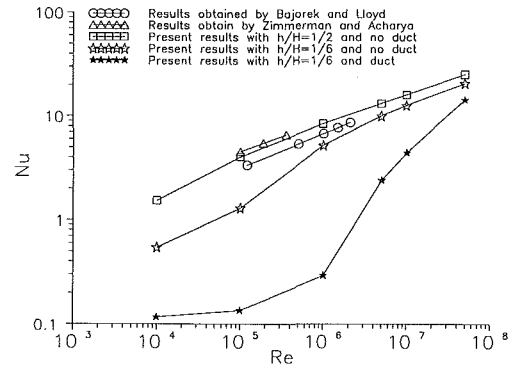

Fig. (5*b*) Comparison with the experimental results for limiting case of no duct length and h/H = 1/2; and the effect of duct length for h/H = 1/6

there is very little heat transfer between the streams even for long ducts. Therefore, the duct length effect start to decrease at higher Rayleigh numbers.

Conclusion

A numerical solution of natural convection between two reservoirs connected by a two-dimensional horizontal duct was obtained using a modified SIMPLE algorithm. The emphasis of the numerical computation was on high Rayleigh numbers and small duct dimensions. A strong fluid stratification in both reservoirs was observed at high Rayleigh number. The volume exchange of fluid between the reservoirs takes place through counterflow streams in the connecting duct. The exchange of diffusive energy between the two streams is substantial at low Rayleigh number and small duct dimension. Correlation equations were derived for the Nusselt number and volume exchange rate.

References

Acharya, S., and Jetli, R., 1990, "Heat Transfer Due to Buoyancy in a Partially Divided Square Box," *Int. J. Heat Mass Transfer*, Vol. 33, No. 5, pp. 931-942.

Bajorek, S. M., and Lloyd, J. R., 1982, "Experimental Investigation of Natural Convection in Partitioned Enclosures," ASME JOURNAL OF HEAT TRANSFER, Vol. 104, pp. 527-532.

Bejan, A., and Rossie, A. N., 1981, "Natural Convection in Horizontal Duct Connecting Two Fluid Reservoirs," ASME JOURNAL OF HEAT TRANSFER, Vol. 103, pp. 108-113.

Brown, W. G., and Solvason, K. R., 1962, "Natural Convection Heat Transfer Through Rectangular Openings in Partitions—1," *Int. J. Heat Mass Transfer*, Vol. 5, pp. 859-868.

Brown, W. G., 1962, "Natural Convection Through Rectangular Openings in Partitions—2," *Int. J. Heat Mass Transfer*, Vol. 5, pp. 869-878.

Chen, K. S., Ku, A. C., and Chou, C. H., 1990, "Investigation of Natural Convection in Partially Divided Rectangular Enclosures Both With and Without an Opening in the Partition Plate: Measurement Results," ASME JOURNAL OF HEAT TRANSFER, Vol. 112, pp. 648-652.

Date, A. W., 1986, "Numerical Prediction of Natural Convection Heat Transfer in Horizontal Annulus," *Int. J. Heat Mass Transfer*, Vol. 29, No. 10, pp. 1457-1464.

De Vahl Davis, G., 1983, "Natural Convection of Air in a Square Cavity: A Benchmark Numerical Solution," *Int. J. Num. Methods in Fluids*, Vol. 3, pp. 249-264.

Epstein, M., 1988, "Buoyancy-Driven Exchange Flow Through Small Openings in Horizontal Partitions," ASME JOURNAL OF HEAT TRANSFER, Vol. 110, pp. 885-893.

Epstein, M., and Kenton, M. A., 1989, "Combined Natural Convection and Forced Flow Through Small Openings in a Horizontal Partition, With Special Reference to Flows in Multicompartment Enclosures," ASME JOURNAL OF HEAT TRANSFER, Vol. 111, pp. 980-987.

Fu, W. S., Perng, J. C., and Shieh, W. J., 1989, "Transient Laminar Natural Convection in an Enclosure Partitioned by an Adiabatic Baffle," *Numerical Heat Transfer*, Part A, Vol. 16, pp. 325-350.

Imberger, J., and Fandry, C., 1975, "Withdrawal of a Stratified Fluid From a Vertical Two-Dimensional Duct," *Journal of Fluid Mechanics*, Vol. 70, p. 321.

Le Breton, P., Caltagirone, J. P., and Arquis, E., 1991, "Natural Convection in a Square Cavity With Thin Porous Layers on its Vertical Walls," ASME JOURNAL OF HEAT TRANSFER, Vol. 113, pp. 892-898.

Le Quere, P., and De Roquefort, T. A., 1987, "Computation of Natural Convection in Two Dimensional Cavity With Chebyshev Polynomials," *J. Comp. Phys.*, Vol. 57, pp. 210-228.

Markatos, N. C., and Pericleous, K. A., 1984, "Laminar and Turbulent Natural Convection in an Enclosed Cavity," *Int. J. Heat Mass Transfer*, Vol. 27, pp. 755-772.

Nansteel, M. W., and Greif, R., 1981, "Natural Convection in Undivided and Partially Divided Rectangular Enclosures," ASME JOURNAL OF HEAT TRANSFER, Vol. 103, pp. 623-629.

Nansteel, M. W., and Greif, R., 1983, "Natural Convection Heat Transfer in Complex Enclosure at Large Prandtl Number," ASME JOURNAL OF HEAT TRANSFER, Vol. 105, pp. 912-914.

Nansteel, M.W., and Greif, R., 1984, "An Investigation of Natural Convection in Enclosures With Two and Three-Dimensional Partitions," *Int. J. Heat Mass Transfer*, Vol. 27, No. 4, pp. 561-571.

Patankar, S. V., 1980, *Numerical Heat Transfer and Fluid Flow*, McGraw-Hill, New York.

Prahl, J., and Emmons, H. W., 1975, "Fire Induced Flow Through an Opening," *Combustion and Flame*, Vol. 25, pp. 369-385.

Shaw, H. J., Chen, C. K., and Cleaver, J. W., 1987, "Cubic Spline Numerical Solution for Two Dimensional Natural Convection in a Partially Divided Enclosure," *Numerical Heat Transfer*, Vol. 12, pp. 439-455.

Turner, J. S., 1979, *Buoyancy Effects in Fluids*, Cambridge University Press, p. 89.

Zimmerman, E., and Acharya, S., 1987, "Free Convection Heat Transfer in a Partially Divided Vertical Enclosure With Conducting End Walls," *Int. J. Heat Mass Transfer*, Vol. 30, No. 2, pp. 319-331.

Three-Dimensional Mixed Convection in a Horizontal Chemical Vapor Deposition Reactor

K. C. Karki,[1] P. S. Sathyamurthy,[1] and S. V. Patankar[2]

Introduction

This paper presents an analysis of mixed convection in a horizontal chemical vapor deposition (CVD) reactor. In many CVD applications the reactor walls are cooled to minimize deposition on them. However, the resulting large temperature gradients induce buoyancy-driven flows leading to severe nonuniformities in the film thickness and composition. The flow effects are particularly important under atmospheric-pressure growth conditions in which the deposition process is controlled by mass transfer, which in turn is largely dictated by the fluid flow. Thus, a clear understanding of mixed convection flows is essential for better CVD reactor designs.

When the forced flow is strong, the buoyancy forces give rise to longitudinal rolls with axes parallel to the main flow direction. These flows can be computed using the parabolic approximation (e.g., Moffat and Jensen, 1986), which neglects axial diffusion and flow reversal in the main flow direction. However, at low Reynolds numbers, large density gradients may lead to flow reversal near the thermal transition regions (e.g., Visser et al., 1989). The prediction of such flows requires the use of the full elliptic form of the governing equations. The mixed convection analyses, pertaining to CVD reactor flows, based on the elliptic form of the equations (Rhee et al., 1987; Ouazzani and Rosenberger, 1990; Kleijn and Hoogendoorn, 1991) are limited to simple configurations such as rectangular ducts.

This paper presents an analysis of mixed convection in an idealized cold-wall horizontal CVD reactor with a tapered susceptor. The analysis is based on the full three-dimensional elliptic form of the conservation equations. In this study, the predictions of fluid flow and heat transfer are made by solving the conservation equations for a single species and the details of chemistry and species transport are not included. Thus, the results are valid for CVD applications in which the reactants are present in very small concentrations in the inert carrier gas.

Mathematical Formulation and Computational Procedure

The geometry of the CVD reactor under consideration is shown in Fig. 1. The reactor consists of an entrance section, a reaction section (susceptor), and an exit section. The aspect

[1]Innovative Research, Inc., Minneapolis, MN 55414.

[2]Department of Mechanical Engineering, University of Minnesota, Minneapolis, MN 55455.

Contributed by the Heat Transfer Division and presented at the National Heat Transfer Conference, San Diego, California, August 9-12, 1992. Manuscript received by the Heat Transfer Division April 1992; revision received February 1993. Keywords: Mixed Convection, Numerical Methods. Associate Technical Editor: F. P. Incropera.

there is very little heat transfer between the streams even for long ducts. Therefore, the duct length effect start to decrease at higher Rayleigh numbers.

Conclusion

A numerical solution of natural convection between two reservoirs connected by a two-dimensional horizontal duct was obtained using a modified SIMPLE algorithm. The emphasis of the numerical computation was on high Rayleigh numbers and small duct dimensions. A strong fluid stratification in both reservoirs was observed at high Rayleigh number. The volume exchange of fluid between the reservoirs takes place through counterflow streams in the connecting duct. The exchange of diffusive energy between the two streams is substantial at low Rayleigh number and small duct dimension. Correlation equations were derived for the Nusselt number and volume exchange rate.

References

Acharya, S., and Jetli, R., 1990, "Heat Transfer Due to Buoyancy in a Partially Divided Square Box," *Int. J. Heat Mass Transfer*, Vol. 33, No. 5, pp. 931-942.

Bajorek, S. M., and Lloyd, J. R., 1982, "Experimental Investigation of Natural Convection in Partitioned Enclosures," ASME JOURNAL OF HEAT TRANSFER, Vol. 104, pp. 527-532.

Bejan, A., and Rossie, A. N., 1981, "Natural Convection in Horizontal Duct Connecting Two Fluid Reservoirs," ASME JOURNAL OF HEAT TRANSFER, Vol. 103, pp. 108-113.

Brown, W. G., and Solvason, K. R., 1962, "Natural Convection Heat Transfer Through Rectangular Openings in Partitions—1," *Int. J. Heat Mass Transfer*, Vol. 5, pp. 859-868.

Brown, W. G., 1962, "Natural Convection Through Rectangular Openings in Partitions—2," *Int. J. Heat Mass Transfer*, Vol. 5, pp. 869-878.

Chen, K. S., Ku, A. C., and Chou, C. H., 1990, "Investigation of Natural Convection in Partially Divided Rectangular Enclosures Both With and Without an Opening in the Partition Plate: Measurement Results," ASME JOURNAL OF HEAT TRANSFER, Vol. 112, pp. 648-652.

Date, A. W., 1986, "Numerical Prediction of Natural Convection Heat Transfer in Horizontal Annulus," *Int. J. Heat Mass Transfer*, Vol. 29, No. 10, pp. 1457-1464.

De Vahl Davis, G., 1983, "Natural Convection of Air in a Square Cavity: A Benchmark Numerical Solution," *Int. J. Num. Methods in Fluids*, Vol. 3, pp. 249-264.

Epstein, M., 1988, "Buoyancy-Driven Exchange Flow Through Small Openings in Horizontal Partitions," ASME JOURNAL OF HEAT TRANSFER, Vol. 110, pp. 885-893.

Epstein, M., and Kenton, M. A., 1989, "Combined Natural Convection and Forced Flow Through Small Openings in a Horizontal Partition, With Special Reference to Flows in Multicompartment Enclosures," ASME JOURNAL OF HEAT TRANSFER, Vol. 111, pp. 980-987.

Fu, W. S., Perng, J. C., and Shieh, W. J., 1989, "Transient Laminar Natural Convection in an Enclosure Partitioned by an Adiabatic Baffle," *Numerical Heat Transfer*, Part A, Vol. 16, pp. 325-350.

Imberger, J., and Fandry, C., 1975, "Withdrawal of a Stratified Fluid From a Vertical Two-Dimensional Duct," *Journal of Fluid Mechanics*, Vol. 70, p. 321.

Le Breton, P., Caltagirone, J. P., and Arquis, E., 1991, "Natural Convection in a Square Cavity With Thin Porous Layers on its Vertical Walls," ASME JOURNAL OF HEAT TRANSFER, Vol. 113, pp. 892-898.

Le Quere, P., and De Roquefort, T. A., 1987, "Computation of Natural Convection in Two Dimensional Cavity With Chebyshev Polynomials," *J. Comp. Phys.*, Vol. 57, pp. 210-228.

Markatos, N. C., and Pericleous, K. A., 1984, "Laminar and Turbulent Natural Convection in an Enclosed Cavity," *Int. J. Heat Mass Transfer*, Vol. 27, pp. 755-772.

Nansteel, M. W., and Greif, R., 1981, "Natural Convection in Undivided and Partially Divided Rectangular Enclosures," ASME JOURNAL OF HEAT TRANSFER, Vol. 103, pp. 623-629.

Nansteel, M. W., and Greif, R., 1983, "Natural Convection Heat Transfer in Complex Enclosure at Large Prandtl Number," ASME JOURNAL OF HEAT TRANSFER, Vol. 105, pp. 912-914.

Nansteel, M.W., and Greif, R., 1984, "An Investigation of Natural Convection in Enclosures With Two and Three-Dimensional Partitions," *Int. J. Heat Mass Transfer*, Vol. 27, No. 4, pp. 561-571.

Patankar, S. V., 1980, *Numerical Heat Transfer and Fluid Flow*, McGraw-Hill, New York.

Prahl, J., and Emmons, H. W., 1975, "Fire Induced Flow Through an Opening," *Combustion and Flame*, Vol. 25, pp. 369-385.

Shaw, H. J., Chen, C. K., and Cleaver, J. W., 1987, "Cubic Spline Numerical Solution for Two Dimensional Natural Convection in a Partially Divided Enclosure," *Numerical Heat Transfer*, Vol. 12, pp. 439-455.

Turner, J. S., 1979, *Buoyancy Effects in Fluids*, Cambridge University Press, p. 89.

Zimmerman, E., and Acharya, S., 1987, "Free Convection Heat Transfer in a Partially Divided Vertical Enclosure With Conducting End Walls," *Int. J. Heat Mass Transfer*, Vol. 30, No. 2, pp. 319-331.

Three-Dimensional Mixed Convection in a Horizontal Chemical Vapor Deposition Reactor

K. C. Karki,[1] P. S. Sathyamurthy,[1] and S. V. Patankar[2]

Introduction

This paper presents an analysis of mixed convection in a horizontal chemical vapor deposition (CVD) reactor. In many CVD applications the reactor walls are cooled to minimize deposition on them. However, the resulting large temperature gradients induce buoyancy-driven flows leading to severe nonuniformities in the film thickness and composition. The flow effects are particularly important under atmospheric-pressure growth conditions in which the deposition process is controlled by mass transfer, which in turn is largely dictated by the fluid flow. Thus, a clear understanding of mixed convection flows is essential for better CVD reactor designs.

When the forced flow is strong, the buoyancy forces give rise to longitudinal rolls with axes parallel to the main flow direction. These flows can be computed using the parabolic approximation (e.g., Moffat and Jensen, 1986), which neglects axial diffusion and flow reversal in the main flow direction. However, at low Reynolds numbers, large density gradients may lead to flow reversal near the thermal transition regions (e.g., Visser et al., 1989). The prediction of such flows requires the use of the full elliptic form of the governing equations. The mixed convection analyses, pertaining to CVD reactor flows, based on the elliptic form of the equations (Rhee et al., 1987; Ouazzani and Rosenberger, 1990; Kleijn and Hoogendoorn, 1991) are limited to simple configurations such as rectangular ducts.

This paper presents an analysis of mixed convection in an idealized cold-wall horizontal CVD reactor with a tapered susceptor. The analysis is based on the full three-dimensional elliptic form of the conservation equations. In this study, the predictions of fluid flow and heat transfer are made by solving the conservation equations for a single species and the details of chemistry and species transport are not included. Thus, the results are valid for CVD applications in which the reactants are present in very small concentrations in the inert carrier gas.

Mathematical Formulation and Computational Procedure

The geometry of the CVD reactor under consideration is shown in Fig. 1. The reactor consists of an entrance section, a reaction section (susceptor), and an exit section. The aspect

[1]Innovative Research, Inc., Minneapolis, MN 55414.

[2]Department of Mechanical Engineering, University of Minnesota, Minneapolis, MN 55455.

Contributed by the Heat Transfer Division and presented at the National Heat Transfer Conference, San Diego, California, August 9-12, 1992. Manuscript received by the Heat Transfer Division April 1992; revision received February 1993. Keywords: Mixed Convection, Numerical Methods. Associate Technical Editor: F. P. Incropera.

ratio (B/H) of the reactor at the inlet is 2. The lengths of the entrance section (L_1), the reaction section (L_2), and the exit section (L_3) are $3H$, $5H$, and $3H$, respectively. The top wall of the reactor is flat, whereas the susceptor section on the bottom wall is tapered at 6 deg. Thus, the aspect ratio in the susceptor section increases from 2 at the leading edge to 4.2 at the trailing edge. The flow enters the reactor with a uniform axial velocity u_i and uniform temperature T_i. The entrance and exit sections and the top wall are isothermal, and are maintained at temperature T_i. The susceptor is heated to a temperature T_h. The reactor sidewalls are also isothermal and are assumed to be cooled to the top wall temperature T_i. This boundary condition can be realized if the reactor walls are water cooled.

The mixed convection flow is governed by the continuity, momentum, and energy equations. The momentum and energy equations are coupled through the buoyancy term. In this analysis, the flow is assumed to be steady and laminar, and the transport properties as uniform except for density. The variation of density with temperature is calculated using the Boussinesq approximation and is considered only in the buoyancy term in the momentum equations. For a given reactor geometry, the flow is governed by three parameters: Reynolds number ($\mathrm{Re} = u_i H/\nu$), Grashof number ($\mathrm{Gr} = g\beta(T_h - T_i)H^3/\nu^2$), and Prandtl number ($\mathrm{Pr} = \mu c_p/k$). The ratio $\mathrm{Gr}/\mathrm{Re}^2$ provides a measure of the relative strengths of the buoyancy and inertial forces.

Due to symmetry in the z direction, the equations were solved only on one-half of the reactor cross section. The governing equations were solved in a body-conforming coordinate system using the calculation procedure described by Karki and Patankar (1988). The computations were made on a numerically generated grid comprising of 47 grid points in the streamwise (x) direction, 27 grid points in the vertical (y) direction, and 22 points in the lateral (z) direction. An algebraic procedure was used for grid generation. The final grid was established on the basis of a series of exploratory computations on coarser grids. For flows with large values of $\mathrm{Gr}/\mathrm{Re}^2$, the overall results, such as the total heat transfer from the susceptor, on the present grid differ by less than 5 percent from those calculated on a $32 \times 17 \times 17$ grid.

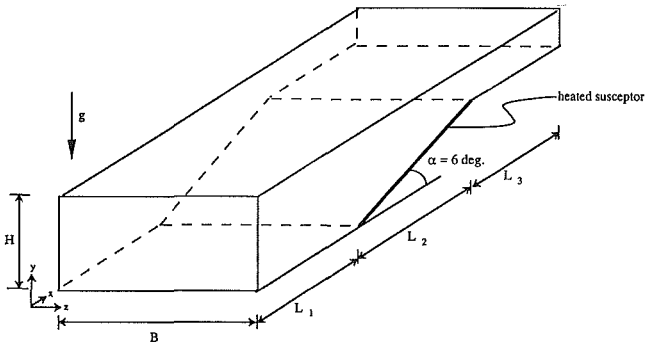

Fig. 1 Schematic of a CVD reactor

Results and Discussion

In this study, the reactor geometry was kept fixed and the Prandtl number of the fluid was maintained at 0.7. Numerical results were obtained for two values of the Grashof number ($\mathrm{Gr} = 10^4, 10^5$) and three values of the Reynolds number ($\mathrm{Re} = 10, 20, 50$). In CVD reactor flows, the Reynolds number is typically in the range 1–100 and the Grashof number is less than 10^6. Thus, the chosen values of Re and Gr correspond to typical operating conditions. For the combination of Gr and Re considered here, the values of the parameter $\mathrm{Gr}/\mathrm{Re}^2$ range from 4 to 1000; thus, the flow conditions include situations in which the flow is forced convection dominated as well as those in which the natural convection effects are significant. At large values of the parameter $\mathrm{Gr}/\mathrm{Re}^2$, the flow may become unsteady and the steady-state results presented here may not be applicable.

Velocity and Temperature Fields. The key features of the

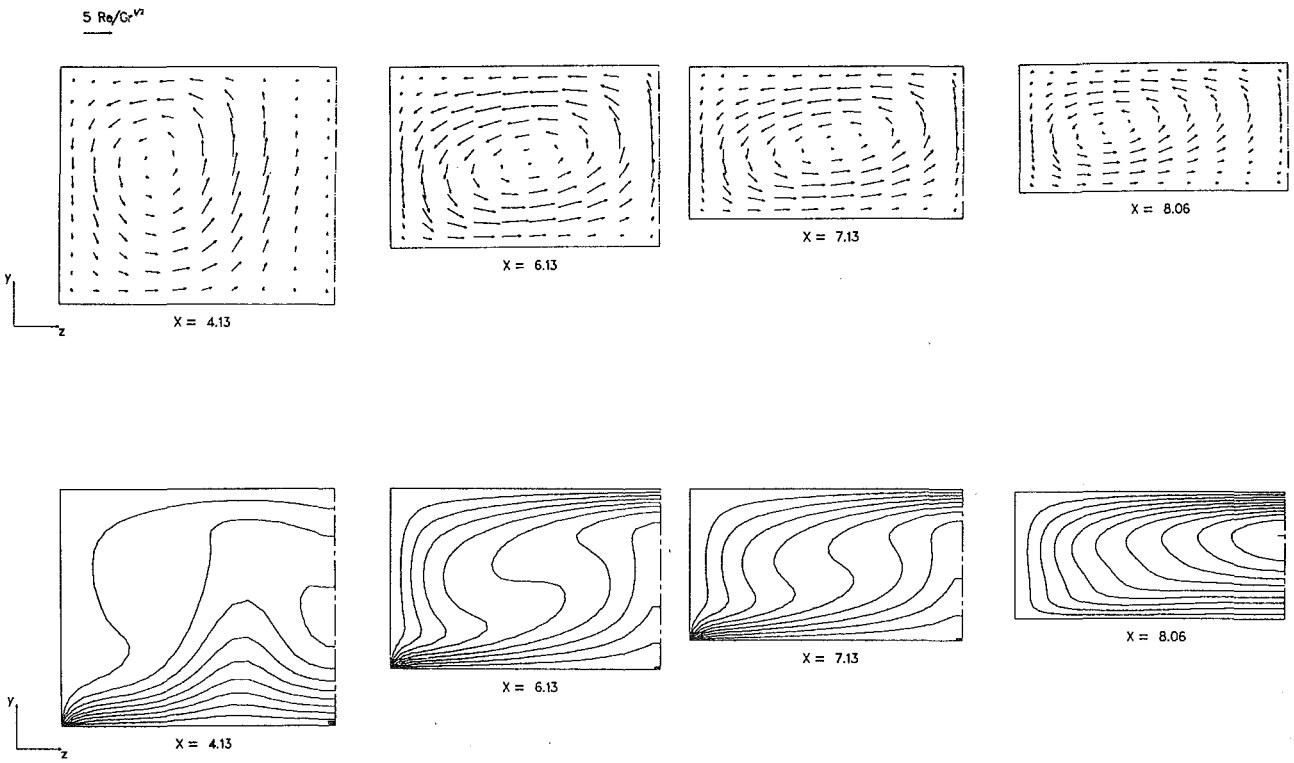

Fig. 2 Cross-stream flow patterns and isotherm maps at $\mathrm{Gr} = 10^5$ and $\mathrm{Re} = 20$

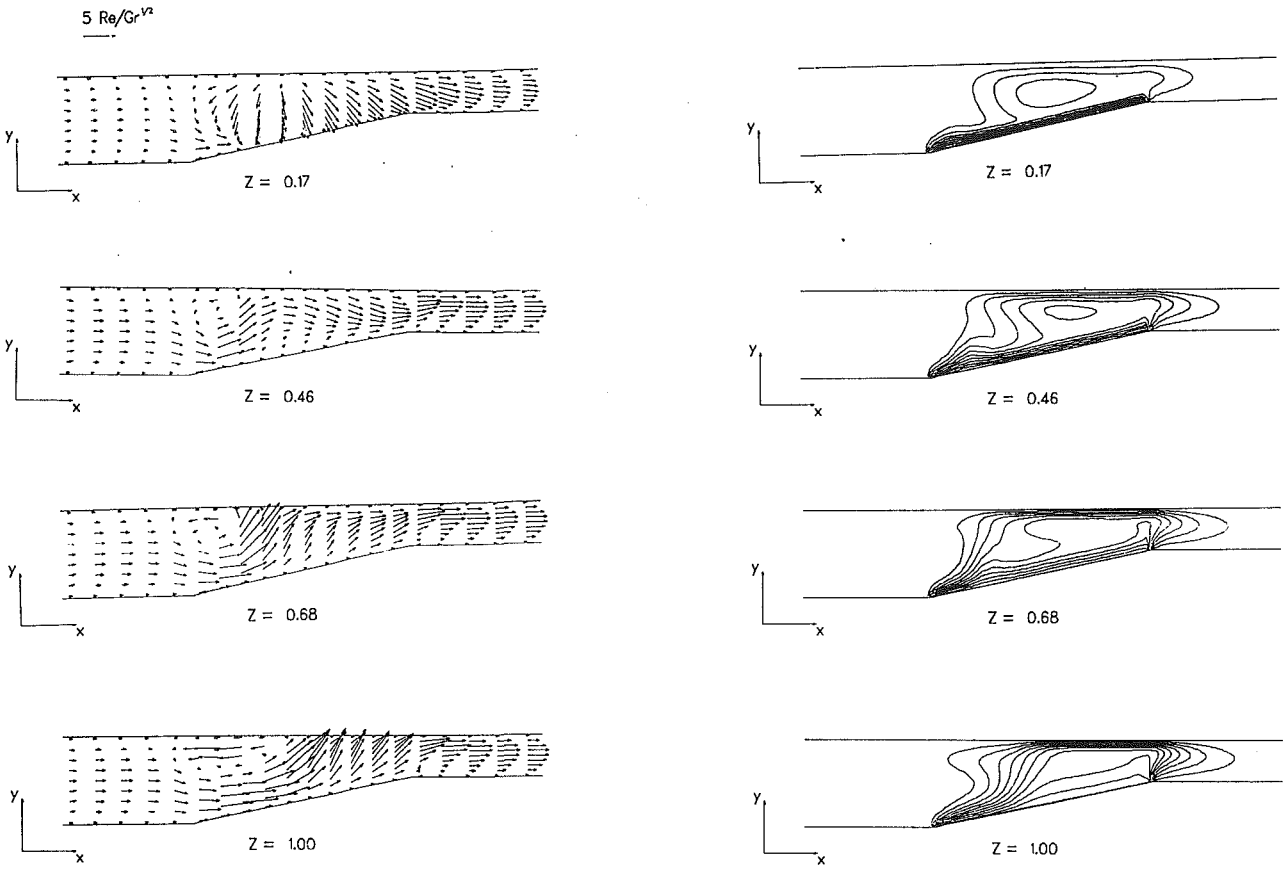

Fig. 3 Flow patterns and isotherm maps on longitudinal planes at Gr = 10^5 and Re = 20

velocity and temperature fields are illustrated using the results for the case Gr = 10^5 and Re = 20 (Gr/Re^2 = 250). These results are presented via velocity vectors and isotherms maps on selected cross-stream (yz) and longitudinal (xy) planes of the reactor and are shown in Figs. 2 and 3. For clarity of presentation, the reactor channel height has been doubled for the plots of the xy planes. The reference velocity vector provides a measure of the dimensionless axial velocity at the inlet ($Re/Gr^{1/2}$). The isotherms are plotted at a constant increment in temperature. Since there is symmetry about the vertical midplane ($z = B/2$), results are presented only for one-half of the cross section ($0 \le z \le B/2$).

The cross-stream distributions (Fig. 2) show the development of the secondary flow. In the entrance section of the reactor, the flow is isothermal and the cross-stream conditions are nearly identical to those for pure forced convection. As the cold fluid enters the heated susceptor region (Fig. 2a), it expands and begins to rise. Near the sidewall, the buoyancy helps in the propagation of the isotherms into the reactor and initiates the development of a longitudinal vortex near the corner. The longitudinal vortex develops as a well-defined plume ascending near the midplane (Fig. 2b). Farther downstream, the strength of the longitudinal vortex increases for some distance and then the strength begins to diminish. The weakening of the vortex is caused by the reduction in the reactor height, which leads to diminished buoyancy forces and increased throughflow velocity. In the exit section of the reactor the fluid loses heat from all walls. This heat loss and the mixing due to secondary flow cause the temperature and density fields to become uniform, which reduces the driving potential for the secondary flow, thereby diminishing its strength. The development of the secondary flow for other cases studied is qualitatively very similar, except for Gr = 10^5 and Re = 50, for which the secondary flow comprises of multiple vortices in the cross section. The secondary flow pattern described here corresponds to cold sidewalls; use of other thermal boundary conditions such as adiabatic sidewalls will lead to significantly different cross-stream conditions.

The axial flow distribution (Fig. 3) shows zones of flow reversal (transverse rolls), caused by large density gradients, near the thermal transition regions. Near the leading edge of the susceptor, the transverse roll forms near the top wall. For the reactor configuration and thermal boundary conditions considered here, this roll was predicted for flows with $Gr/Re^2 > 100$. At larger values of Gr/Re^2 (> 250), a transverse roll also forms near the trailing edge of the susceptor. For the present flow, this second transverse roll is very weak but it becomes pronounced at larger values of Gr/Re^2. Note that the transverse roll at the leading edge is located near the top (cooled) wall, whereas the roll at the trailing edge is located near the bottom (heated) wall of the reactor. The transverse rolls reduce the throughflow area, leading to large axial velocities over the susceptor. The increased axial velocity results in higher temperature gradients on the susceptor underneath the transverse rolls. The transverse roll near the leading edge transports the hot fluid from the susceptor section to the entrance section of the reactor, as evidenced by the S-shaped isotherms. The temperature gradients on the susceptor are nonuniform, in both the axial and lateral directions. These nonuniformities reflect the combined consequences of the sidewall effects, the longitudinal vortices, and the axial flow reversal.

Local Heat Flux Distribution on the Susceptor. Figure 4 shows the distribution of the local Nusselt number, defined as $Nu = qH/k(T_h - T_i)$, where q is the local heat flux, on the susceptor. For a mass-transfer-limited deposition process, the

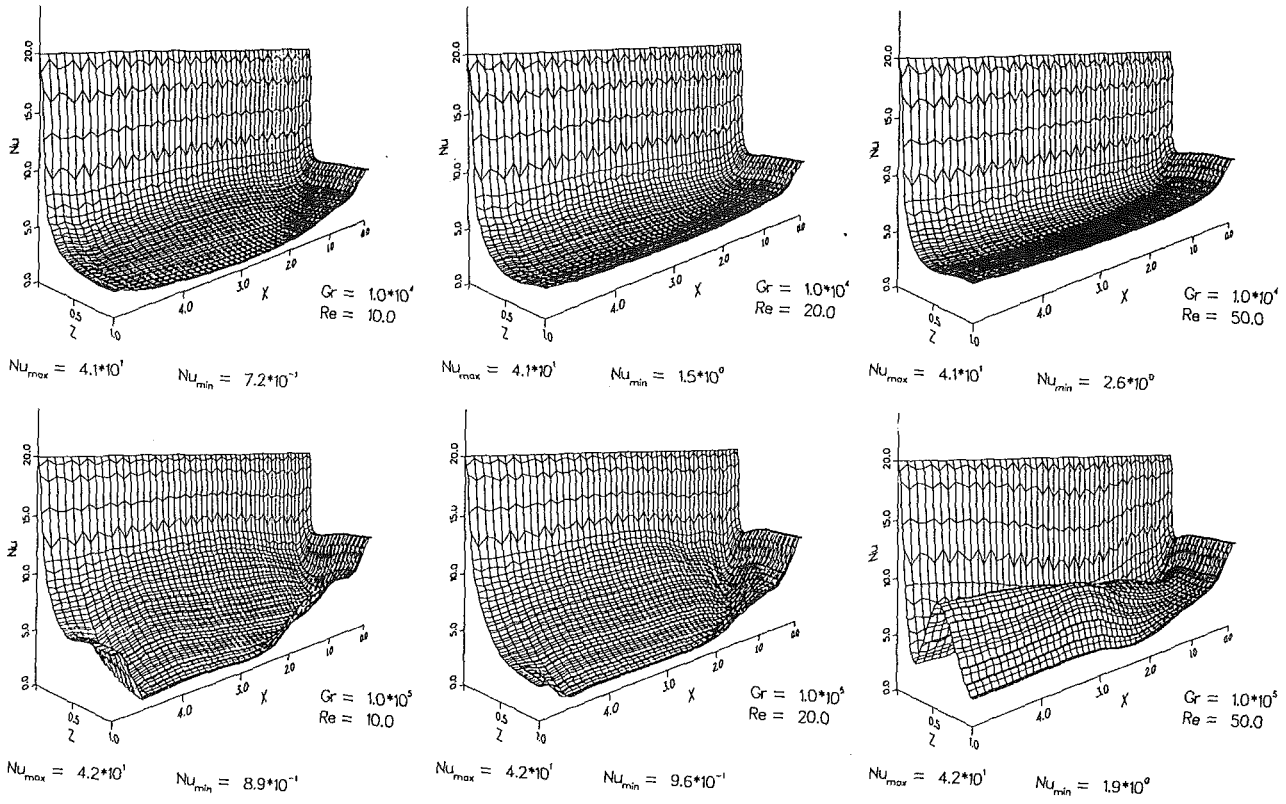

Fig. 4 Local heat flux distribution on the susceptor surface: (*a*) Re = 10; (*b*) Re = 20; (*c*) Re = 50

local heat flux distribution provides a qualitative measure of the deposition rate on the susceptor.

In Fig. 4, Nu_{max} and Nu_{min} are the maximum and minimum values of the Nusselt number. The largest value of Nusselt number in the plots is kept at 20; Nusselt numbers increase from 20 to Nu_{max} in a narrow region near the sidewall, which has not been included in these plots. As expected, large heat flux values are encountered near the leading edge of the susceptor and near the cold sidewall. At $Gr = 10^4$ and $Re = 50$, the heat flux distribution is representative of that in a forced flow situation and the nonuniformities are primarily due to the development of the thermal boundary layer on the susceptor and the presence of the sidewalls. As the Reynolds number is reduced, the heat flux distribution becomes more nonuniform due to the increased strength of the longitudinal vortex. The lateral nonuniformity is largest at axial locations where the secondary motion is strongest. The longitudinal vortex rotates up near the midplane and down near the sidewall. Consequently, the heat flux is smaller near the midplane.

The nonuniformity in heat flux distribution becomes more pronounced at $Gr = 10^5$. The heat flux distribution at $Re = 50$ and $Gr = 10^5$ shows the largest lateral nonuniformity. As stated earlier, the cross-stream flow pattern for this flow comprises multiple longitudinal vortices. The minima in the local Nusselt number, which occur at $Z \approx 0.2$ and 1, correspond to the plumes ascending from the susceptor. At $Re = 10$ and 20, the presence of the transverse roll also affects the heat flux distribution. In the presence of the transverse roll, the axial velocities near the susceptor increase due to the reduction in the area available for throughflow, causing the heat transfer to increase in that region. This behavior is reflected in the increased heat transfer near the leading edge of the susceptor. The heat flux distributions at $Re \approx 10$ and 20 also show local maxima near the trailing edge of the susceptor, in the vicinity of the midplane. This increase in heat transfer is caused by the development of a second transverse roll in that region.

Concluding Remarks

Three-dimensional laminar mixed convection in a cold-wall horizontal CVD reactor with an inclined susceptor has been studied numerically. The buoyancy forces are shown to have a significant effect on the main flow. The cross-stream flow pattern comprises of longitudinal rolls, which introduce axial and lateral nonuniformities in the heat flux distribution on the susceptor. For flows characterized by a large Grashof number and a low Reynolds number, flow reversal, in the form of transverse rolls, also occurs in the streamwise direction, near the thermal transition regions. These transverse rolls lead to locally large heat transfer rates from the susceptor.

References

Karki, K. C., and Patankar, S. V., 1988, "Calculation Procedure for Viscous Incompressible Flows in Complex Geometries," *Numerical Heat Transfer*, Vol. 14, pp. 295–308.

Kleijn, C. R., and Hoogendoorn, C. J., 1991, "A Study of 2- and 3-D Transport Phenomena in Horizontal Chemical Vapor Deposition Reactors," *Chemical Engineering Science*, Vol. 46, No. 1, pp. 321–334.

Moffat, H. K., and Jensen, K. F., 1986, "Complex Flow Phenomena in MOCVD. 1—Horizontal Reactors," *Journal of Crystal Growth*, Vol. 77, pp. 108–119.

Ouazzani, J., and Rosenberger, F., 1990, "Three-Dimensional Modelling of Horizontal Chemical Vapor Deposition. I. MOCVD at Atmospheric Pressure," *Journal of Crystal Growth*, Vol. 100, pp. 545–576.

Rhee, S., Szekely, J., and Ilegbusi, O. J., 1987, "On Three-Dimensional Transport Phenomena in CVD Processes," *Journal of Electrochemical Society*, Vol. 134, pp. 2552–2559.

Visser, E. P., Kleijn, C. R., Govers, C. A. M., and Hoogendoorn, C. J., 1989, "Return Flows in Horizontal MOCVD Reactors Studied With the Use of TiO_2 Particle Injection and Numerical Calculations," *Journal of Crystal Growth*, Vol. 94, pp. 929–946.

Natural Convection Within Spherical Annuli by Symbolic Algebra

K. G. TeBeest,[1] S. A. Trogdon,[2] and R. W. Douglass[3]

Nomenclature

- g = gravitational acceleration constant, m/s^2
- Gr_L = Grashof number = $\beta g(\Delta\tilde{T})L^3/\nu^2$ based on gap width L
- L = annular gap width = $\tilde{r}_o - \tilde{r}_i$, m
- $\overline{\mathrm{Nu}}$ = surface average Nusselt number
- Pr = Prandtl number = ν/α
- $\Re$ = square root of the Grashof number based on outer radius
- r = dimensionless radial coordinate = $\tilde{r}/\tilde{r}_o$, $\eta \le r \le 1$
- T = dimensionless temperature
- x = transformed latitudinal coordinate = $\cos\theta$, $-1 \le x \le 1$
- α = thermal diffusivity, m^2/s
- β = coefficient of thermal expansion, 1/K
- η = annulus radius ratio = $\tilde{r}_i/\tilde{r}_o$
- θ = latitudinal spherical coordinate
- ν = kinematic viscosity, m^2/s
- ρ = density, kg/m^3
- Ψ = dimensionless streamfunction

Subscripts and Superscripts

- l = value denoting the upper limit for model range of validity
- $\sim$ = value denoting dimensional quantity

Introduction

An asymptotic truncated series solution for steady, axisymmetric convection between concentric spheres is obtained through effective use of symbolic algebra. The approximate solution is given in powers of the square root of the Grashof number based on outer radius. The solution differs from that of Hardee (1966) and Singh and Elliot (1981) in that we give a method for determining the series solution to any order. The results obtained here were used as the basic flows in the hydrodynamic stability analysis of TeBeest (1992).

Research on these flows was initiated by Hardee (1966) who presented a solution for the the streamfunction and temperature as a third-order power series in the Rayleigh number. Singh and Chen (1980) coupled a Galerkin method with finite differences to solve for the flow variables for moderate Grashof numbers. At the same time Caltagirone et al. (1980) reported transition toward multicellular flow by using finite differences to solve the unsteady equations of motion systematically. Ingham (1981) presented a finite difference solution for air, while Singh and Elliot (1981) presented a two-term power series solution in the Grashof number for a thermally stratified medium.

Natural convection within spherical annulus enclosures has been studied experimentally by Bishop et al. (1964) (using air), Bishop et al. (1966) and Scanlan et al. (1970) (using air, water, and silicon oils), and Yin et al. (1973) (for air and water).

Mathematical Formulation

We consider steady, axisymmetric convection of a viscous, incompressible fluid contained between two isothermal concentric spheres at distinct temperatures. The inner and outer speres, of radii $\tilde{r}_i$ and $\tilde{r}_o$, are maintained at uniform temperatures $\tilde{T}_i$ and $\tilde{T}_o$, respectively. The fluid within the annulus is Boussinesq with Prandtl number Pr. A uniform gravity field acts vertically downward and viscous dissipation is neglected.

The dimensionless equations for the streamfunction $\Psi(r, x)$ and temperature $T(r, x)$ are given by (TeBeest, 1992)

$$E^4\Psi = \Re(1-x^2)\left\{\mathcal{J}(rx,\ T) - \mathcal{J}\left(\frac{E^2\Psi}{r^2(1-x^2)},\ \Psi\right)\right\} \tag{1}$$

$$\nabla^2 T = \frac{\mathrm{Pr}\Re}{r^2}\,\mathcal{J}(\Psi,\ T) \tag{2}$$

where $r = \tilde{r}/\tilde{r}_o$ is the dimensionless radial coordinate, $x = \cos\theta$ is the transformed latitudinal coordinate, and $\mathcal{J}(f, g) = \partial f/\partial r\,\partial g/\partial x - \partial f/\partial x\,\partial g/\partial r$ is the Jacobian operator. The Grashof number based on outer radius is

$$\Re^2 = g\beta(\Delta\tilde{T})\tilde{r}_o^{\,3}/\nu^2$$

where $\Delta\tilde{T} = \tilde{T}_i - \tilde{T}_o$, $\tilde{T}_o < \tilde{T}_i$. The problem domain is $\eta \le r \le 1$, $-1 \le x \le 1$ where $\eta = \tilde{r}_i/\tilde{r}_o$ is the radius ratio. The boundary conditions on Ψ and T along the inner and outer spherical surfaces, $r = \eta$ and $r = 1$, are obtained, respectively, from the no-slip and constant temperature conditions there. The boundary conditions at the poles, $x = \pm 1$, are obtained from the symmetry requirements that the latitudinal component of both the velocity and heat flux vectors vanish there and the radial velocity component be finite. Thus, the boundary conditions are

$$\Psi(\eta, x) = \frac{\partial\Psi}{\partial r}(\eta, x) = 0; \quad T(\eta, x) = 1$$

$$\Psi(1, x) = \frac{\partial\Psi}{\partial r}(1, x) = 0; \quad T(1, x) = 0$$

and

$$\Psi(r, \pm 1) = 0; \quad \frac{\partial T}{\partial x}(r, \pm 1),\ \frac{\partial\Psi}{\partial x}(r, \pm 1) \text{ finite.}$$

Asymptotic Series Solutions

We seek an asymptotic power series solution to Eqs. (1) and (2) for "small" values of $\Re$ in the form

$$T = \sum_{n=0}^{\infty} \Re^{2n}\tau_{2n},\ \Psi = \sum_{n=0}^{\infty} \Re^{2n+1}\psi_{2n+1}. \tag{3}$$

Dahl (1990) and TeBeest (1992) have not only shown that the streamfunction and temperature are respectively odd and even functions of $\Re$, but that they are also separable. Hence we express Eq. (3) in the form

$$\Psi = (1-x^2)^{1/2} \sum_{n=0}^{\infty} \sum_{\substack{m=\Delta_\psi(n) \\ \text{mod } 2}}^{n+1} \Re^{2n+1} P_m^{(1)}(x) R_m^{[2n+1]}(r), \tag{4}$$

$$T = \sum_{n=0}^{\infty} \sum_{\substack{m=\Delta_T(n) \\ \text{mod } 2}}^{n} \Re^{2n} P_m(x) Q_m^{[2n]}(r). \tag{5}$$

[1]Department of Physics, South Dakota State University, Brookings, SD 57007-0395.

[2]Department of Mathematics and Statistics, University of Minnesota—Duluth, Duluth, MN 55812-2496.

[3]Idaho National Engineering Laboratory, Computational Fluid Dynamics Team, EG&G Idaho, Inc., Idaho Falls, ID 83415-2414.

Contributed by the Heat Transfer Division and presented at the ASME Winter Annual Meeting, Atlanta, Georgia, December 1-6, 1991. Manuscript received by the Heat Transfer Division September 1992; revision received March 1993. Keywords: Computer Codes, Natural Convection. Associate Technical Editor: J. R. Lloyd.

The expressions $P_n(x)$ and $P_m^{(1)}(x)$ are respectively Legendre polynomials and associated Legendre polynomials of first order and the functions $\Delta_\tau(n)$ and $\Delta_\psi(n)$ are defined through

$$(\Delta_\psi(n),\ \Delta_\tau(n)) = \begin{cases} (1,\ 0) & n \text{ even} \\ (2,\ 1) & n \text{ odd.} \end{cases}$$

Upon substituting the series (4) and (5) into Eqs. (1) and (2), equating expressions multiplying like powers of $\mathfrak{R}$, and using orthogonality of the Legendre and associated Legendre polynomials we obtain, for each m in Eqs. (4) and (5), the following system of ordinary differential equations:

$$L_m^2[R_m^{[2n+1]}] = g_m^{[2n+1]}(r), \tag{6}$$

$$D_m[Q_m^{[2n]}] = f_m^{[2n]}(r), \tag{7}$$

where the differential operators L_m and D_m are defined by

$$L_m \equiv \frac{d^2}{dr^2} - \frac{m(m+1)}{r^2},$$

$$D_m \equiv \frac{1}{r^2}\frac{d}{dr}\left(r^2\frac{d}{dr}\right) - \frac{m(m+1)}{r^2}.$$

The appropriate boundary conditions on the functions $R_m^{[2n+1]}(r)$ and $Q_m^{[2n]}(r)$ are:

$$R_m^{[2n+1]}(\eta) = \frac{d}{dr}R_m^{[2n+1]}(\eta) = 0,$$

$$R_m^{[2n+1]}(1) = \frac{d}{dr}R_m^{[2n+1]}(1) = 0, \tag{8}$$

and

$$Q_m^{[0]}(\eta) = 1, \quad Q_m^{[0]}(1) = 0,$$

$$Q_m^{[2n]}(\eta) = Q_m^{[2n]}(1) = 0, \quad n = 1, 2, \ldots . \tag{9}$$

The functions $g_m^{[2n+1]}(r)$ and $f_m^{[2n]}(r)$ in Eqs. (6) and (7) are known (TeBeest, 1992), being expressed in terms of the previously determined $R_m^{[2k+1]}(r)$ and $Q_m^{[2k]}(r)$, $k = 0, 1, \ldots, n-1$. We use the symbolic manipulator MAPLE to determine the functions $g_m^{[2n+1]}(r)$ and $f_m^{[2n]}(r)$ explicitly and then to solve the differential Eqs. (6) and (7) with boundary conditions (8) and (9). This is done for $n = 0, 1, 2, 3$ and values of m given in Eqs. (4) and (5). Our resulting solution is expressed explicitly in terms of the parameter η, Pr, and $\mathfrak{R}$, which MAPLE converts directly into FORTRAN code.

Results

In this section we discuss the range of validity of the asymptotic series solution, and we present some results and compare them with experimental and numerical results obtained by others. To facilitate comparisons we introduce the Grashof number based on gap width,

$$\mathrm{Gr}_L = (1-\eta)^3\mathfrak{R}^2. \tag{10}$$

To estimate the range of validity of the asymptotic series solution, we compare the magnitudes of the terms $\mathfrak{R}^{2n}\tau_{2n}$ and $\mathfrak{R}^{2n+1}\psi_{2n+1}$ in Eq. (3) for $n = 1, 2, 3$ with those of the leading terms τ_0 and $\mathfrak{R}\psi_1$. We then estimate over what fractions, μ_{2n} and ν_{2n+1}, of the annular domain these terms respectively exceed the terms τ_0 and $\mathfrak{R}\psi_1$ in magnitude. The measures μ_{2n} and ν_{2n+1} may be approximated by discretizing the annular domain into a finite set of $K \times K$ points (r_i, x_j), which are rather uniformly distributed. We used the points (r_i, x_j) given by

$$r_i = \eta + \frac{1-\eta}{K+1}\,i,\ x_j = \cos\left(\frac{\pi j}{K+1}\right),\ i, j = 1, 2, \ldots, K.$$

These points are uniformly distributed on the Cartesian rectangular domain $\{(r, \theta): \eta < r < 1,\ 0 < \theta < \pi\}$. Using this discretization we let $\mathfrak{N}_{2n}(K)$ denote the number of points at which $|\mathfrak{R}^{2n}\tau_{2n}(r_i, x_j)| > |\tau_0(r_i, x_j)|$ and let $\mathfrak{N}_{2n+1}(K)$ denote the number of points at which $|\mathfrak{R}^{2n+1}\psi_{2n+1}(r_i, x_j)| > |\mathfrak{R}\psi_1(r_i, x_j)|$. We define

$$\mu_{2n}(K) = \frac{1}{K^2}\mathfrak{N}_{2n}(K),\ \nu_{2n+1}(K) = \frac{1}{K^2}\mathfrak{N}_{2n+1}(K)$$

which represent fractions between zero and one. For sufficiently large K, $\mu_{2n}(K)$ and $\nu_{2n+1}(K)$ should closely approximate μ_{2n} and ν_{2n+1}, respectively, i.e.,

$$\mu_{2n} = \lim_{K\to\infty}\mu_{2n}(K),\ \nu_{2n+1} = \lim_{K\to\infty}\nu_{2n+1}(K).$$

Our numerical experiments indicate that taking $K = 100$ exceeded that needed for convergence of $\mu_{2n}(K)$ and $\nu_{2n+1}(K)$. Thus, we took $K = 100$ so that 10,000 points were used in determining μ_{2n} and ν_{2n+1}.

Table 1 presents values of μ_{2n} and ν_{2n+1} for $\eta = 0.5$ and Pr $= 0.7$. For example, when $\mathrm{Gr}_L = 2000$, the second term in the temperature expansion (i.e., the term $\mathfrak{R}^2\tau_2$) exceeds the leading term τ_0 at roughly 17.4 percent of the points within the annular domain, while the second term in the streamfunction expansion (the term $\mathfrak{R}^3\psi_3$) exceeds the leading term $\mathfrak{R}\psi_1$ at roughly 0.2 percent of the points.

We propose that the breakdown of the validity of the asymptotic model may be predicted by evaluating the measures μ_{2n} and ν_{2n+1}. It is known that in asymptotic series, "the region within which the error decreases indefinitely with increasing n shrinks toward zero as n approaches infinity" (Lanczos, 1938). This is especially true for infinite asymptotic power series, which can converge only for $\mathfrak{R} \searrow 0$. Finite asymptotic power series, as used here, will necessarily lose accuracy as $\mathfrak{R}$ increases since subsequent terms $\mathfrak{R}^{2n}\tau_{2n}$ or $\mathfrak{R}^{2n+1}\psi_{2n+1}$ increase in magnitude indefinitely. Therefore, we anticipate that the accuracy of the model may be assessed by comparing the magnitude of these subsequent terms with a dominant term, say the leading term, which is known to dominate for $\mathfrak{R} \searrow 0$.

Using the above ideas we estimate the range of validity of the asymptotic model for $0.2 \le \eta \le 0.8$ and $0.1 \le \mathrm{Pr} \le 100$. For fixed η and Pr the model is valid provided $\mathfrak{R}$ is below some *limiting value* $\mathfrak{R}_l$. With relatively few exceptions it was determined that as $\mathfrak{R}$ was increased isotherms developed in the flow that had values greater than one. This generally occurred when the magnitude of the second term $\mathfrak{R}^2\tau_2$ in the temperature series exceeded the leading term τ_0 at roughly $\mu_2 = 20$ percent of the sampling points. We thus define $\mathfrak{R}_l$ in the following way:

$$\mathfrak{R}_l \equiv \min_n \{\mathfrak{R}: \mu_{2n} = 0.2 \text{ or } \nu_{2n+1} = 0.2\}.$$

Based on these criteria the data in Table 1 would indicate that for Pr $= 0.7$ and $\eta = 0.5$ the asymptotic series approximation for the temperature would not be valid for Gr_L much greater than 2000 and that the series approximation for the streamfunction would remain valid for somewhat larger values of Gr_L than the temperature approximation. These conclusions are consistent with graphic observations (TeBeest et al., 1991). We note that increasing the truncation order of the approximation would not improve the accuracy of the approximation

Table 1 Relative number of spatial points at which higher order terms in the asymptotic series exceed the leading terms for Pr = 0.7, η = 0.5. Values given are in percentages.

	$n=1$		$n=2$		$n=3$	
Gr_L	μ_2	ν_3	μ_4	ν_5	μ_6	ν_7
1750	9.1%	0.0%	0.0%	0.0%	0.0%	0.0%
2000	17.4%	0.2%	4.1%	0.0%	0.0%	0.0%
2250	23.8%	4.2%	10.7%	0.0%	0.0%	0.0%
2500	28.9%	8.7%	15.7%	0.3%	0.0%	0.0%

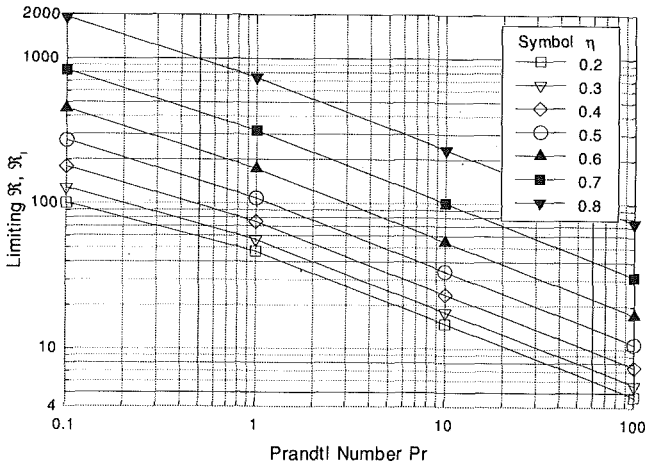

Fig. 1 Range of validity of asymptotic model for $0.2 \leq \eta \leq 0.8$ and $0.1 \leq Pr \leq 100$

for this set of parameter values since the lower order terms would not be affected by adding additional terms.

Figure 1 shows $\Re_l$ as a function of Prandtl number for several radius ratios. Since the range of validity of the asymptotic series cannot be defined precisely, Fig. 1 provides an estimate of the range of validity that is based on the definition of $\Re_l$. The series approximation may be valid for values of $\Re$ beyond the values $\Re_l$ presented here, especially for the stream-function approximation, which appears to be less affected by $\Re$ than does the temperature approximation.

To compare our results with those of others, we introduce the surface average Nusselt numbers along the inner and outer spheres,

$$\overline{\mathrm{Nu}} = -\frac{1-\eta}{2\eta} r^2 \left[\int_0^{\pi} \frac{\partial T}{\partial r} \sin\theta d\theta \right]_{r=\eta,1}. \qquad (11)$$

Various investigators have given Nusselt number results for the set of parameter values $Gr_L = 1428.6$, $Pr = 0.7$, and $\eta = 0.5$. Mack and Hardee (1968) reported a surface average Nusselt number of 1.12. From their experimental results Bishop et al. (1966) obtained the heat transfer correlation

$$\overline{\mathrm{Nu}} = 0.106\ \mathrm{Gr}_L^{0.276}$$

accurate to approximately 15 percent for the range $0.4 \leq \eta \leq 0.8$ and $Pr = 0.7$. Their correlation thus predicts a surface average Nusselt number of 0.787. Scanlan et al. (1970) reported three surface average Nusselt number correlations, which predicted values of 0.787, 0.924, and 1.086, respectively. The latter value was computed from an empirical formula (Eq. (10) in their work):

$$\overline{\mathrm{Nu}} = 0.228\ (\mathrm{Ra}^*)^{0.226} \qquad (12)$$

where Ra^* is a modified Rayleigh number equivalent to $Gr_L Pr$ when $\eta = 0.5$. They claimed that 76 percent of the experimental data lie within 20 percent of the correlated value computed by Eq. (12). Finally, Singh and Chen (1980) reported a Nusselt number of 1.1010.

In Table 2 we list the surface average Nusselt numbers for $Pr = 0.02$ and 0.7, radius ratio $\eta = 0.5$, and various Grashof numbers and compare with those obtained by Eq. (12) and Singh and Chen (1980). The Nusselt numbers obtained here for $Pr = 0.02$ agree more favorably with the numerical results of Singh and Chen with a maximum deviation of 0.24 percent. However, for $Pr = 0.7$ we have close agreement with Eq. (12). We anticipate that the errors will increase as Gr_L is increased beyond 2000 since the Nusselt numbers are affected by the temperature solution. Based on the $Pr = 0.7$ data listed in Table 2 we obtain a heat transfer correlation of

Table 2 Surface average Nusselt numbers from Singh and Chen (1980), Scanlan et al. (1970), and present work

		Nusselt Number $\overline{Nu}$		
Pr	Gr_L	Singh & Chen	Eq. (12)	Present Work
0.02	1000	—	—	1.0000
	5000	1.0027	—	1.0012
	10000	1.0047	—	1.0047
	15000	1.0083	—	1.0107
	20000	—	—	1.0190
0.70	1000	—	1.0021	1.0581
	1428.6	1.1010	1.0863	1.1185
	1500	—	1.0983	1.1306
	1750	—	1.1372	1.1778
	2000	—	1.1721	1.2322
	2250	—	1.2037	1.2939
	2500	—	1.2327	1.3629

$$\overline{\mathrm{Nu}} = 0.153\ \mathrm{Gr}_L^{0.276}$$

which overestimates Eq. (12) by 7.5 percent for $Gr_L \leq 2500$.

Acknowledgments

This material is based upon work supported by the National Science Foundation under Grant No. CBT-8612427. Additional support was provided by the Department of Mathematics and Statistics, University of Minnesota—Duluth and the Department of Mechanical Engineering, University of Nebraska—Lincoln. This work was also supported through the EG&G Idaho Laboratory Directed Research & Development Program, the Long Term Research Initiative in Computational Mechanics, under DOE Idaho Field Office Contract DE-AC07-76ID01570.

References

Bishop, E. H., Kolflat, R. S., Mack, L. R., and Scanlan, J. A., 1964, "Convective Heat Transfer Between Concentric Spheres," *Proc. of the 1964 Heat Transfer and Fluid Mechanics Institute*, Stanford University Press, Stanford, CA, pp. 69–80.

Bishop, E. H., Mack, L. R., and Scanlan, J. A., 1966, "Heat Transfer by Natural Convection Between Concentric Spheres," *Int. J. Heat Mass Transfer*, Vol. 9, pp. 649–662.

Caltagirone, J.-P., Combarnous, M., and Mojtabi, A., 1980, "Natural Convection Between Two Concentric Spheres: Transition Toward a Multicellular Flow," *Numerical Heat Transfer*, Vol. 3, pp. 107–114.

Dahl, J. R., 1990, "Solutions of Coupled Systems of Partial Differential Equations Using Symbolic Algebra," Technical Report 90-12, University of Minnesota—Duluth, Duluth, MN.

Hardee, H. C., Jr., 1966, "Natural Convection Between Concentric Spheres at Low Rayleigh Numbers," Ph.D. Thesis, The University of Texas, Austin, TX.

Ingham, D. B., 1981, "Heat Transfer by Natural Convection Between Spheres and Cylinders," *Numerical Heat Transfer*, Vol. 4, pp. 53–67.

Lanczos, C., 1938, "Trigonometric Interpolation of Empirical and Analytic Functions," *J. Math. Phys.*, Vol. 7, pp. 125–126.

Mack, L. R., and Hardee, H. C., 1968, "Natural Convection Between Concentric Spheres at Low Rayleigh Numbers," *Int. J. Heat Mass Transfer*, Vol. 11, pp. 387–396.

Scanlan, J. A., Bishop, E. H., and Powe, R. E., 1970, "Natural Convection Heat Transfer Between Concentric Spheres," *Int. J. Heat Mass Transfer*, Vol. 13, pp. 1857–1872.

Singh, S. N., and Chen, J., 1980., "Numerical Solution for Free Convection Between Concentric Spheres at Moderate Grashof Numbers," *Numerical Heat Transfer*, Vol. 3, pp. 441–459.

Singh, S. N., and Elliott, J. M., 1981, "Natural Convection Between Concentric Spheres in a Slightly Thermally Stratified Medium," *Int. J. Heat Mass Transfer*, Vol. 24, pp. 395–406.

TeBeest, K. G., Trogdon, S. A., Dahl, J. R., and Douglass, R. W., 1991, "Natural Convection Within Spherical Annuli by Symbolic Algebra on Workstations," presented at the ASME Winter Annual Meeting, Atlanta, GA, Dec. 1–6.

TeBeest, K. G., 1992, "Linear Stability and Bifurcation of Natural Convection Within Arbitrary Gap Spherical Annuli," Ph.D. Dissertation, University of Nebraska—Lincoln, unpublished.

Yin, S. H., Powe, R. E., Scanlan, J. A., and Bishop, E. H., 1973, "Natural Convection Flow Patterns in Spherical Annuli," *Int. J. Heat Mass Transfer*, Vol. 16, pp. 1785–1795.

Convective Instability in a Porous Enclosure With a Horizontal Conducting Baffle

Falin Chen[1] and C. Y. Wang[1,2]

Nomenclature

a = const, Eqs. (11)-(13)
B = coefficient, Eqs. (11) and (12)
b = const, Eqs. (11) and (13)
C = coefficient, Eqs. (15) and (16)
c = const, Eqs. (12) and (13)
F = characteristic function, Eq. (17)
g = gravitational acceleration constant
H = height of enclosure
K = permeability
N = number of collocation points
n = number of cells in horizontal direction
p = pressure
R = Rayleigh number
T = temperature
u = horizontal velocity
v = vertical velocity
x = x coordinate
y = y coordinate
α = thermal expansion coefficient
β = normalized length of baffle
κ = thermal diffusivity
λ = normalized distance from baffle to bottom wall
μ = dynamic viscosity
ρ = density
σ = aspect ratio, width to height
ϕ = Eqs. (9) and (14)
ψ = stream function

Superscripts

$'$ = dimensional total quantity
c = critical value

Subscripts

l = upper boundary
h = lower boundary
n = number in series
x = $\partial/\partial x$
y = $\partial/\partial y$
0 = reference value
1 = lower region
2 = upper region

1 Introduction

The study of heat transfer in a fluid-saturated porous medium is essential in a variety of practical situations, including thermal insulation design and geothermal energy utilization. Reviews of previous work were written by Cheng (1978) and Bejan (1987). An important index of heat transfer for a medium heated from below is the critical Rayleigh number R^c. If the Rayleigh number is larger than R^c, the heat transfer dramatically increases due to a change from a pure conductive mode to a convective mode. The value of R^c for an infinite horizontal porous layer is found to be $4\pi^2$ (Horton and Rogers, 1945). For a finite enclosure with adiabatic vertical sides walls, Sutton (1970) showed that R^c increases by an amount depending on the aspect (width to height) ratio.

The present paper studies the convective instability in a two-dimensional porous enclosure with a horizontal baffle protruding from one of the side walls. The vertical side walls are insulated, while the top and bottom surfaces are maintained at lower and higher constant temperatures, respectively. The present work considers a baffle of high conductivity. We assume the baffle temperature can be considered constant throughout. We ask, for a given enclosure aspect ratio, is the addition of another physical constraint (such as lengthening a baffle) always stabilizing? Is there an optimum baffle location and length such that the critical Rayleigh number is maximized?

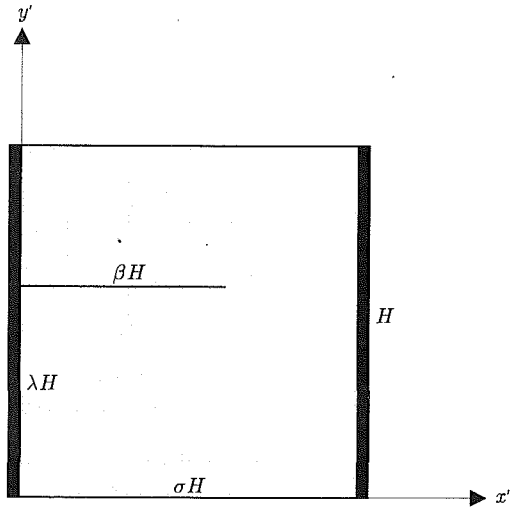

Fig. 1 Schematic description of the physical problem

2 Problem Formulation and Method of Solution

Figure 1 shows the situation. A rectangular box of height H and width σH is filled with a fluid-saturated porous medium. A horizontal baffle of length βH ($\beta \le \sigma$) is located at a distance of λH from the bottom. The side walls are adiabatic and the top and bottom walls are isothermal and at temperatures T_l and T_h ($> T_l$), respectively. The baffle is at a (passive) constant temperature. It is assumed that the Darcy-Boussinesq model governs the flow in the porous medium and the principle of exchange of instabilities holds for the present situation (Beck, 1972).

Let u' and v' be the velocity components in the x' and y' directions, respectively. The governing equations are (Bejan, 1984)

$$u' = -\frac{K}{\mu} p_{x'}, \tag{1}$$

$$v' = -\frac{K}{\mu} \{p_{y'}' + \rho_0 g[1 - \alpha(T' - T_l)]\}, \tag{2}$$

$$u' T_{x'}' + v' T_{y'}' = \kappa (T_{x'x'}' + T_{y'y'}'), \tag{3}$$

$$u_{x'}' + v_{y'}' = 0. \tag{4}$$

Here K is the permeability, μ the dynamic viscosity, p the pressure, ρ_0 the fluid density at temperature T_l, g the gravitational acceleration, α the thermal expansion coefficient, T'

[1]Institute of Applied Mechanics, National Taiwan University, Taipei, Taiwan 10764.
[2]On leave from Michigan State University, East Lansing, MI 48824.

Contributed by the Heat Transfer Division of The American Society of Mechanical Engineers. Manuscript received by the Heat Transfer Division December 1991; revision received July 1992. Keywords: Building Heat Transfer, Flow Instability, Porous Media. Associate Technical Editor: C. E. Hickox, Jr.

the temperature, and κ the thermal diffusivity of the porous medium. In a pure conduction state the temperature decreases linearly from T_h to T_l. We perturb from the pure conduction state and nondimensionalize the linearized equations by the scales $T' = T_h - \Delta T(y - T)$, $u' = \kappa u/H$, $v' = \kappa v/H$, $x' = Hx$, and $y' = Hy$, where $\Delta T = T_h - T_l$. After pressure is eliminated, the linearized equations are

$$u_y - v_x = -RT_x, \tag{5}$$

$$-v = T_{xx} + T_{yy}, \tag{6}$$

$$u_x + v_y = 0, \tag{7}$$

where R is the Rayleigh number defined by $R = K\alpha\rho_0 gH\Delta T/\mu\kappa$. After introducing a streamfunction ψ satisfying $u = \psi_y$ and $v = -\psi_x$, one obtains

$$\nabla^4\psi + R\psi_{xx} = 0. \tag{8}$$

Equation (8) is to be solved with the boundary conditions on the top, bottom, and baffle that $\psi = 0$ and $\psi_{yy} = 0$, where the latter is a result of constant temperature. On the side walls we specify $\psi = 0$ and $\psi_{xx} = 0$, where the latter is due to adiabatic conditions.

Due to the presence of the baffle, the determination of the smallest eigenvalue R^c as function of σ, β, and λ is no longer simple. The usual method of considering a single mode for stability problems, viz., the so-called normal mode analysis, thus becomes invalid. We shall hence present a method utilizing eigenfunction expansions and collocation to solve the problem. We divide the enclosure into two regions by a horizontal straight line along the baffle. Let ψ_1 be the solution to the lower region. The general solution of ψ_1 satisfying all boundary conditions at the side walls ($x = 0$ and σ) can be expressed by the following series:

$$\psi_1(x, y) = \sum_{n=1}^{\infty} \sin\left(\frac{n\pi x}{\sigma}\right)\phi_{1n}(y). \tag{9}$$

Substituting Eq. (9) into Eq. (8) yields

$$\phi_{1n}'''' - \left(\frac{2n^2\pi^2}{\sigma^2}\right)\phi_{1n}'' + \left(\frac{n^4\pi^4}{\sigma^4} - R\,\frac{n^2\pi^2}{\sigma^2}\right)\phi_{1n} = 0. \tag{10}$$

The added conditions that $\phi_{1n}(0) = \phi''_{1n}(0) = 0$ give, for $\sqrt{R} < n\pi/\sigma$,

$$\phi_{1n} = B_{1n}\sinh(ay) + B_{2n}\sin(by), \tag{11}$$

and for $\sqrt{R} \geq n\pi/\sigma$, ϕ_{1n} become

$$\phi_{1n} = B_{1n}\sinh(ay) + B_{2n}\sin(cy), \tag{12}$$

where

$$a = \frac{n\pi}{\sigma}\left(1 + \frac{\sqrt{R}\sigma}{n\pi}\right)^{1/2}$$

$$b = \frac{n\pi}{\sigma}\left(1 - \frac{\sqrt{R}\sigma}{n\pi}\right)^{1/2} \tag{13}$$

$$c = \frac{n\pi}{\sigma}\left(\frac{\sqrt{R}\sigma}{n\pi} - 1\right)^{1/2},$$

and the coefficients B_{1n} and B_{2n} are to be determined. Similarly, for the upper region the streamfunction ψ_2 can be written as

$$\psi_2(x, y) = \sum_{n=1}^{\infty} \sin\left(\frac{n\pi x}{\sigma}\right)\phi_{2n}(y), \tag{14}$$

where if $\sqrt{R} < n\pi/\sigma$

$$\phi_{2n} = C_{1n}\sinh[a(y-1)] + C_{2n}\sin[b(y-1)], \tag{15}$$

and if $\sqrt{R} \geq n\pi/\sigma$

$$\phi_{2n} = C_{1n}\sinh[a(y-1)] + C_{2n}\sin[c(y-1)]. \tag{16}$$

The boundary conditions are that on the baffle $y = \lambda$, $0 \leq x < \beta$, the stream functions and their second vertical derivatives vanish and that on the dividing line $y = \lambda$, $\beta < x \leq 1$, the stream functions and their first three vertical derivatives are continuous. We take a finite number of terms, say $n = 1$ to N, in series represented by Eqs. (9) and (14). This gives $4N$ coefficients to be determined. On each point of N equally spaced interior points along the dividing line, i.e., $0 < x < 1$, $y = \lambda$, four boundary conditions are to be satisfied. In order to obtain nontrivial ψ_1 and ψ_2, the determinant of the $4N$ by $4N$ coefficient matrix of B's and C's is set to zero, yielding a characteristic equation

$$F(R, \sigma, \lambda, \beta) = 0. \tag{17}$$

Equation (17) is nonlinear and will be solved numerically for the smallest R (R^c). Regarding σ, β, and λ as being known a priori, the eigenvalue R^c of Eq. (17) is sought using a bisection algorithm.

3 Results and Discussion

The required number of collocation points as well as the number of terms (N) in series of Eqs. (9) and (14) for yielding a solution of acceptable accuracy are determined by comparing our numerical results with exact values of R^c for $\beta = 0$ (Sutton, 1970). When the baffle is absent ($\beta = 0$), Eq. (17) reduces to $\sin(c) = 0$ or the critical Rayleigh number is

$$R^c = \pi^2\left(2 + \frac{n^2}{\sigma^2} + \frac{\sigma^2}{n^2}\right) \tag{18}$$

for the range $\sqrt{n(n-1)} \leq \sigma \leq \sqrt{n(n-1)}$, where, physically, n accounts for the number of convection cells in the horizontal direction. By using $N = 50$, the calculated R^c differs from the exact solution by less than 0.01 percent. We thus use $N = 50$ for the subsequent calculations in this paper. Equation (18) illustrates that the minimum of R^c ($= 4\pi^4$) occurs at integral values of σ and the local maximum occurs at $\sigma = \sqrt{2}$, $\sqrt{6}$, $\sqrt{12}$, $\sqrt{20}$, $\sqrt{30}$, and so on.

Another extreme case is when $\beta = \sigma$, or the baffle completely separates the enclosure into two compartments. Each compartment is a rectangular enclosure with its own height and temperature difference. Let R_1^c and R_2^c be their individual critical Rayleigh numbers. Thus, the critical Rayleigh number R^c is

$$R^c = \min\left(\frac{R_1^c}{\lambda^2}, \frac{R_2^c}{(1-\lambda)^2}\right). \tag{19}$$

For example, if $\beta = \sigma = 1.2$ and $\lambda = 0.4$, $\sigma_1 = \sigma/\lambda = 3$ and from Eqs. (18), $n_1 = 3$ and $R_1^c = 4\pi^2$. Similarly $\sigma_2 = 2$, $n_2 = 2$, and $R_2^c = 4\pi^2$. Since $R_1^c/\lambda^2 = 246.74$ and $R_2^c/(1-\lambda)^2 = 109.62$, we deduce that convective instability begins in the upper compartment with two cells when R^c reaches 109.62, while the heat transfer in the lower compartment is through pure conduction only. In the present problem, the configuration shown in Fig. 1 exhibits an intrinsic symmetry in the vertical direction with respect to $\lambda = 0.5$, while the horizontal symmetry is violated due to the presence of a partial horizontal baffle ($0 < \beta < 1$). The calculated R^c for various β and λ confirm this symmetry. In subsequent analyses, accordingly, we shall consider only $0 \leq \lambda \leq 0.5$.

To consider the effect of the baffle on the stability characteristics, we first focus on the case of $\sigma = 1$, a square enclosure, in which the horizontal baffle varies in both vertical position and horizontal extension. The variation of R^c versus baffle length (represented by β/σ for five different baffle positions $\lambda = 0.1$ to 0.5) is presented in Fig. 2. It is seen that a baffle located closer to the center leads to greater stability, while a longer baffle does not necessarily ensure a more stable state. For $\lambda = 0$, the baffle is absent, and R^c remains at $4\pi^2$. For $0 < \lambda < 0.5$, the value of R^c first increases with β/σ, reaches

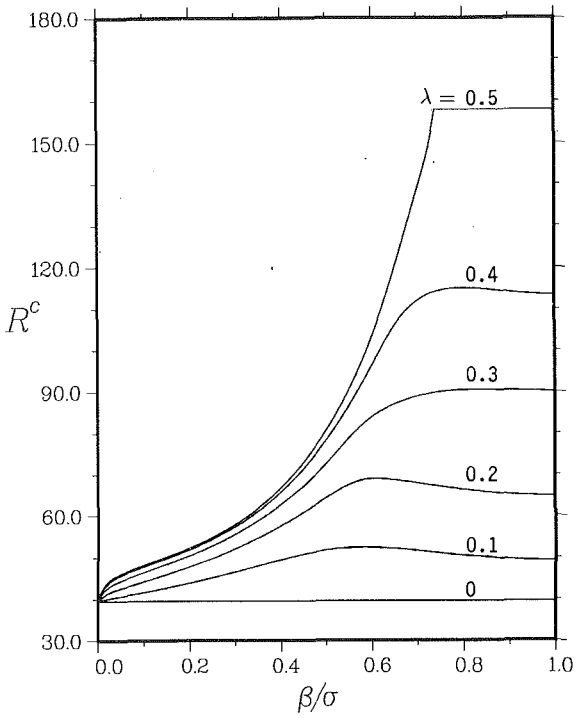

Fig. 2 Variation of R^c versus β/σ for various λ when $\sigma = 1$

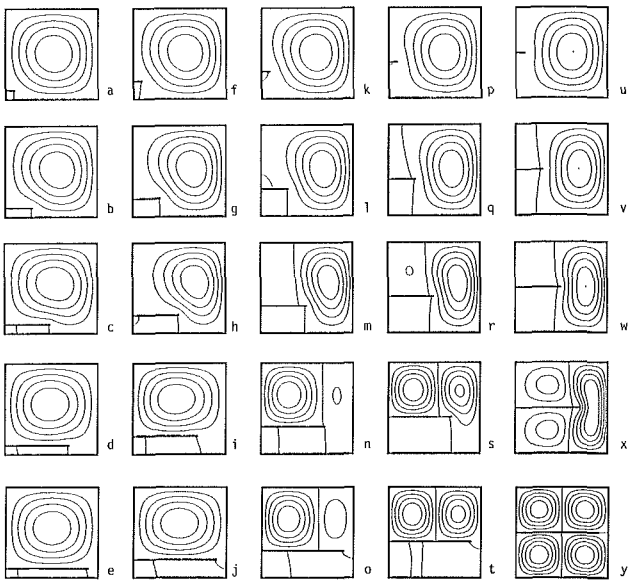

Fig. 3 Critical streamline patterns for various λ and β/σ when $\sigma = 1$: (*a–e*) $\lambda = 0.1$, $\beta/\sigma = 0.1$, 0.3, 0.5, 0.7, and 0.9; (*f–j*) $\lambda = 0.2$, $\beta/\sigma = 0.1$, 0.3, 0.5, 0.7, and 0.9; (*k–o*) $\lambda = 0.3$, $\beta/\sigma = 0.1$, 0.3, 0.5, 0.7, and 0.9; (*p–t*) $\lambda = 0.4$, $\beta/\sigma = 0.1$, 0.3, 0.5, 0.7, and 0.9; (*u–y*) $\lambda = 0.5$, $\beta/\sigma = 0.1$, 0.3, 0.5, 0.7, and 0.9

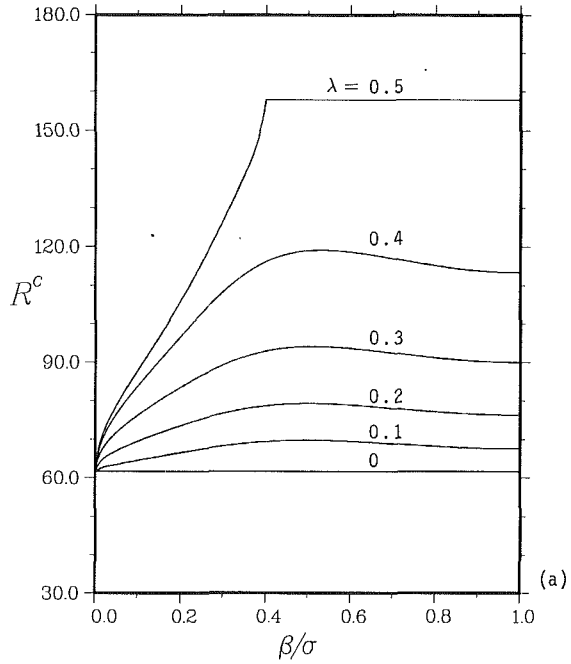

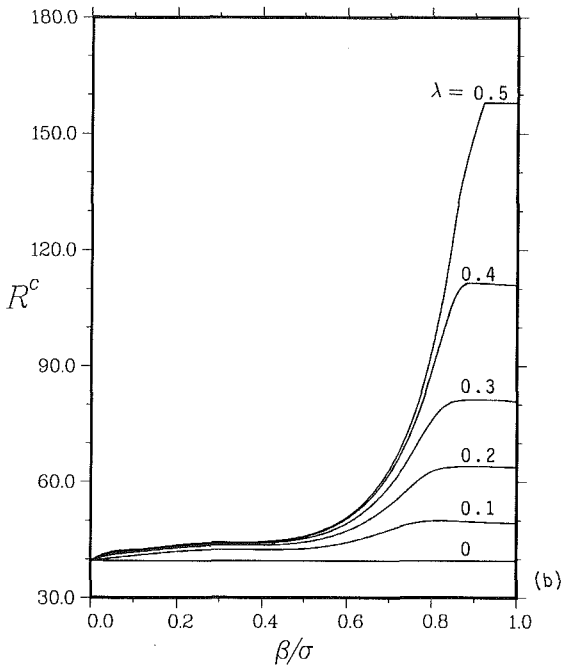

Fig. 4 Variation of R^c versus β/σ for various λ and σ: (*a*) $\sigma = 0.5$; (*b*) $\sigma = 2.0$

a maximum, then decreases. The values of β/σ at which the maximum R^c occurs, denoted by $(\beta/\sigma)_{max}$, are respectively 0.58, 0.6, 0.84, and 0.8 for $\lambda = 0.1$, 0.2, 0.3, and 0.4. For $\lambda = 0.5$, a centered baffle, R^c increases monotonically with β/σ until $\lambda = 0.74$. The R^c remains constant at $16\pi^2$ (≈ 157.91) with further increasing β/σ.

A series of onset streamline patterns for various baffle lengths and locations is shown in Fig. 3. Let us consider the case of fixed $\lambda = 0.1$ (first column). Since the enclosure is a square, the dominant convection pattern without the baffle is a single cell, occurring at $R^c = 4\pi^2$. When a very short baffle is present, the single cell is perturbed slightly, thus raising R^c slightly. When β/σ approaches unity, R^c is increased according to Eq. (19), since the effective height of the enclosure is decreased to $1 - \lambda$. In the meantime, the onset of convection is gradually largely confined to the upper part of the enclosure. Similar results are obtained for $\lambda = 0.2$ (second column). When λ is fixed at 0.3 and 0.4 (third and fourth columns), the single cell character changes to double cell for $\beta/\sigma > 0.5$, since the final effective aspect ratios are $\sigma/(1-\lambda) = 1.429$ and 1.667 ($> \sqrt{2}$), respectively. When λ is fixed at 0.5 (fifth column), the baffle pierces the single cell as its length increases, and eventually the onset of convection consists of four identical cells. From the streamline patterns we see that, for fixed λ, the maximum value of R^c seems to occur when the recirculation cell is either most distorted (see, for example, Figs. 3(*c*), 3(*h*)) or separated into two cells with distortion (Figs. 3(*m*), 3(*s*)). For $\lambda = 0.5$, the critical streamline patterns retain the same quadra-cellular

Table 1 The values of $(\beta/\sigma)_{max}$ and corresponding R^c for various σ and λ

σ	λ	$(\beta/\sigma)_{max}$	R^c
0.5	0.1	0.50	69.7509
	0.2	0.50	79.2895
	0.3	0.52	94.1075
	0.4	0.54	119.093
	0.5	0.38	157.923
1.0	0.1	0.58	52.3349
	0.2	0.60	68.9394
	0.3	0.84	90.4022
	0.4	0.80	114.912
	0.5	0.74	157.921
1.5	0.1	0.80	51.0404
	0.2	0.80	62.9265
	0.3	0.84	82.2442
	0.4	0.90	113.725
	0.5	0.88	157.917
2.0	0.1	0.82	49.9327
	0.2	0.90	63.9843
	0.3	0.90	81.2335
	0.4	0.90	111.470
	0.5	0.92	157.929

convection when $\beta/\sigma > (\beta/\sigma)_{max} = 0.74$ (see Fig. 3(*y*)), which explains the plateau of the corresponding curve in Fig. 2.

For non-square enclosures ($\sigma \neq 1$), the influence of the presence of a horizontal baffle on the stability is similar to that of $\sigma = 1$. Figures 4(*a*) and 4(*b*) illustrate the variation of R^c versus β/σ for $\sigma = 0.5$ and 2.0, respectively. As one can see, for $0 < \lambda < 0.5$, all R^c for different σ increase with β/σ at first, reach a maximum and then decrease. For $\lambda = 0.5$, the curve of R^c plateaus after it reaches the maximum, and its value remains at $16\pi^2$ for all σ considered. We summarize in Table 1 the values of $(\beta/\sigma)_{max}$ and corresponding R^c for various σ and λ and find, in general, that $(\beta/\sigma)_{max}$ increases with σ when λ is fixed.

As a practical example, suppose we wish to insulate a flat ceiling by a layer of foam insulation on top of a layer of batt insulation. Now the unrolled batts have a backing (usually aluminum foil), which represents a horizontal baffle. It is customary for the builder to place the batts side by side without any gap for maximum insulation. Our analysis shows, however, for maximum insulation the batts should be placed with a certain amount of clearance between the rolls. Since Fig. 1 can be reflected to represent a series of batts, the optimum clearance is given in Table 1.

In summary, several concluding remarks can be drawn in the following:

1 Other dimensions being same, a centered baffle always results in a more stable state than an off-centered baffle.

2 A full-length baffle, i.e., $\beta/\sigma = 1$, does not necessarily lead to greater stability. Instead, the value of $(\beta/\sigma)_{max}$ is usually less than unity. For a centered baffle, the maximum R^c occurs for $\beta/\sigma \geq (\beta/\sigma)_{max}$; while for an off-centered baffle, the maximum R^c occurs at $(\beta/\sigma)_{max}$.

3 The value of $(\beta/\sigma)_{max}$ increases with σ.

References

Beck, J. L., 1972, "Convection in a Box of Porous Material Saturated With Fluid," *Phys. Fluids*, Vol. 15, pp. 1377–1383.

Bejan, A., 1984, *Convective Heat Transfer*, Wiley, New York, Chap. 10.

Bejan, A., 1987, "Convective Heat Transfer in Porous Media," in: *Handbook of Single Phase Convective Heat Transfer*, S. Kakac, R. K. Shah, and W. Aung, eds., Wiley, New York, Chap. 16.

Cheng, P., 1978, "Heat Transfer in Geothermal Systems," *Advances in Heat Transfer*, Vol. 14, pp. 1–105.

Horton, C. W., and Rogers, F. T., 1945, "Convective Currents in a Porous Medium," *J. Appl. Phys.*, Vol. 16, pp. 367–370.

Sutton, F. M., 1970, "Onset of Convection in a Porous Channel With Net Through Flow," *Phys. Fluids*, Vol. 13, pp. 1931–1934.

On the Hot-Spot-Controlled Critical Heat Flux Mechanism in Saturated Pool Boiling: Part II—The Influence of Contact Angle and Nucleation Site Density

C. Unal,[1] P. Sadasivan,[1] and R. A. Nelson[1]

Nomenclature

$m_{lr,e}$ = triple-point evaporation coefficient
N/A_w = nucleation site density
r = space coordinate associated with radial distance from center of dry patch
q = heat flux
STA = surface-time average
T = temperature
ΔT = superheat = $T - T_{sat}$
ΔT_{rew} = calculated critical liquid–solid contact wall superheat at the end of the lifetime of the vapor mushroom bubble
β_a = advancing contact angle
δ = macrolayer thickness
θ = contact angle

Subscripts

avg = surface-time average
CHF = critical heat flux
exp = experimentally measured
d = dry patch
h = heater
hn = homogeneous nucleation
rew = rewetting
s = stem
sat = saturation
v = vapor
w = wall

Introduction

The lack of a complete understanding of the heat transfer mechanism near the critical heat flux (CHF) prevents designers of power-controlled systems from obtaining maximum efficiency while retaining the necessary margins of safety. A review of previous studies of CHF was presented by Unal et al. (1992a). In that paper, we investigated the hypothesis that CHF is the result not only of the complete evaporation of the macrolayer,

[1]Los Alamos National Laboratory, Nuclear Technology and Engineering Division, Engineering and Safety Analysis Group, Los Alamos, NM 87545.

Contributed by the Heat Transfer Division and presented at the Pool & Flow Boiling Conference, Santa Barbara, California, March 22, 1992. Manuscript received by the Heat Transfer, Division July 1992; revision received March 1993. Keywords: Boiling, Multiphase Flows, Phase-Change Phenomena. Associate Technical Editor: J. H. Kim.

Table 1 The values of $(\beta/\sigma)_{max}$ and corresponding R^c for various σ and λ

σ	λ	$(\beta/\sigma)_{max}$	R^c
0.5	0.1	0.50	69.7509
	0.2	0.50	79.2895
	0.3	0.52	94.1075
	0.4	0.54	119.093
	0.5	0.38	157.923
1.0	0.1	0.58	52.3349
	0.2	0.60	68.9394
	0.3	0.84	90.4022
	0.4	0.80	114.912
	0.5	0.74	157.921
1.5	0.1	0.80	51.0404
	0.2	0.80	62.9265
	0.3	0.84	82.2442
	0.4	0.90	113.725
	0.5	0.88	157.917
2.0	0.1	0.82	49.9327
	0.2	0.90	63.9843
	0.3	0.90	81.2335
	0.4	0.90	111.470
	0.5	0.92	157.929

convection when $\beta/\sigma > (\beta/\sigma)_{max} = 0.74$ (see Fig. 3(*y*)), which explains the plateau of the corresponding curve in Fig. 2.

For non-square enclosures ($\sigma \neq 1$), the influence of the presence of a horizontal baffle on the stability is similar to that of $\sigma = 1$. Figures 4(*a*) and 4(*b*) illustrate the variation of R^c versus β/σ for $\sigma = 0.5$ and 2.0, respectively. As one can see, for $0 < \lambda < 0.5$, all R^c for different σ increase with β/σ at first, reach a maximum and then decrease. For $\lambda = 0.5$, the curve of R^c plateaus after it reaches the maximum, and its value remains at $16\pi^2$ for all σ considered. We summarize in Table 1 the values of $(\beta/\sigma)_{max}$ and corresponding R^c for various σ and λ and find, in general, that $(\beta/\sigma)_{max}$ increases with σ when λ is fixed.

As a practical example, suppose we wish to insulate a flat ceiling by a layer of foam insulation on top of a layer of batt insulation. Now the unrolled batts have a backing (usually aluminum foil), which represents a horizontal baffle. It is customary for the builder to place the batts side by side without any gap for maximum insulation. Our analysis shows, however, for maximum insulation the batts should be placed with a certain amount of clearance between the rolls. Since Fig. 1 can be reflected to represent a series of batts, the optimum clearance is given in Table 1.

In summary, several concluding remarks can be drawn in the following:

1 Other dimensions being same, a centered baffle always results in a more stable state than an off-centered baffle.

2 A full-length baffle, i.e., $\beta/\sigma = 1$, does not necessarily lead to greater stability. Instead, the value of $(\beta/\sigma)_{max}$ is usually less than unity. For a centered baffle, the maximum R^c occurs for $\beta/\sigma \geq (\beta/\sigma)_{max}$; while for an off-centered baffle, the maximum R^c occurs at $(\beta/\sigma)_{max}$.

3 The value of $(\beta/\sigma)_{max}$ increases with σ.

References

Beck, J. L., 1972, "Convection in a Box of Porous Material Saturated With Fluid," *Phys. Fluids*, Vol. 15, pp. 1377–1383.

Bejan, A., 1984, *Convective Heat Transfer*, Wiley, New York, Chap. 10.

Bejan, A., 1987, "Convective Heat Transfer in Porous Media," in: *Handbook of Single Phase Convective Heat Transfer*, S. Kakac, R. K. Shah, and W. Aung, eds., Wiley, New York, Chap. 16.

Cheng, P., 1978, "Heat Transfer in Geothermal Systems," *Advances in Heat Transfer*, Vol. 14, pp. 1–105.

Horton, C. W., and Rogers, F. T., 1945, "Convective Currents in a Porous Medium," *J. Appl. Phys.*, Vol. 16, pp. 367–370.

Sutton, F. M., 1970, "Onset of Convection in a Porous Channel With Net Through Flow," *Phys. Fluids*, Vol. 13, pp. 1931–1934.

On the Hot-Spot-Controlled Critical Heat Flux Mechanism in Saturated Pool Boiling: Part II—The Influence of Contact Angle and Nucleation Site Density

C. Unal,[1] P. Sadasivan,[1] and R. A. Nelson[1]

Nomenclature

$m_{tr,e}$ = triple-point evaporation coefficient
N/A_w = nucleation site density
r = space coordinate associated with radial distance from center of dry patch
q = heat flux
STA = surface-time average
T = temperature
ΔT = superheat = $T - T_{sat}$
ΔT_{rew} = calculated critical liquid–solid contact wall superheat at the end of the lifetime of the vapor mushroom bubble
β_a = advancing contact angle
δ = macrolayer thickness
θ = contact angle

Subscripts

avg = surface-time average
CHF = critical heat flux
exp = experimentally measured
d = dry patch
h = heater
hn = homogeneous nucleation
rew = rewetting
s = stem
sat = saturation
v = vapor
w = wall

Introduction

The lack of a complete understanding of the heat transfer mechanism near the critical heat flux (CHF) prevents designers of power-controlled systems from obtaining maximum efficiency while retaining the necessary margins of safety. A review of previous studies of CHF was presented by Unal et al. (1992a). In that paper, we investigated the hypothesis that CHF is the result not only of the complete evaporation of the macrolayer,

[1]Los Alamos National Laboratory, Nuclear Technology and Engineering Division, Engineering and Safety Analysis Group, Los Alamos, NM 87545.

Contributed by the Heat Transfer Division and presented at the Pool & Flow Boiling Conference, Santa Barbara, California, March 22, 1992. Manuscript received by the Heat Transfer, Division July 1992; revision received March 1993. Keywords: Boiling, Multiphase Flows, Phase-Change Phenomena. Associate Technical Editor: J. H. Kim.

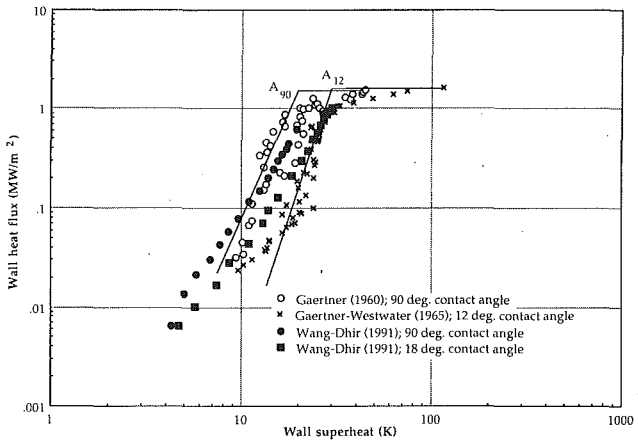

Fig. 1 Pool boiling data of water on horizontal and vertical flat heater surfaces: data of Gaertner (1965), Gaertner and Westwater (1960), and Wang and Dhir (1991)

but also of the surface temperature at some point on the heater surface becoming high enough to prevent liquid rewetting it. We think of this hypothesis as unifying the occurrence of CHF and the quenching of hot surfaces to the same concept, i.e., the ability of a liquid to contact a hot surface. It also has the advantage that it properly brings into consideration the effects of heater thermal properties as well as heater thickness on CHF while retaining the more classical hydrodynamic effects of the process through the macrolayer resupply mechanism.

The study of Unal et al. (1992a) was based upon the occurrence of the second transition region[2] in Gaertner's (1965) pool boiling data (Fig. 1). The study yielded two requirements for the second transition boiling regime to be present: (1) The material must have high thermal conductivity and (2) the heater must be thick. Shortly after completion of Unal's study, Wang and Dhir (1991) published data that clearly met these requirements yet failed to show the second transition region (Fig. 1). Thus, the first objective of this note is to investigate this lack of a second transition region within the framework of the hot-spot model.

In Unal et al. (1992a), we used only Gaertner's (1965) pool boiling data for clean water on copper and assumed a contact angle of 90 deg based upon Liaw and Dhir's (1989) contact angle measurements. The Wang and Dhir (1991) data also provided new information both regarding a significant effect of contact angle on CHF and that the contact angle of the water-nickel/salt solution used by Gaertner and Westwater (1960) was less than 18 deg. Thus, the second objective of this note is to test the hot-spot hypothesis further for the lower contact angle to confirm the functional variation of the critical rewetting temperature with the contact angle.

The Heat Transfer Model

We use a two-dimensional cylindrical-coordinate transient conduction model to study the saturated pool nucleate boiling phenomenon in the second transition region on a horizontal surface. Details of the model are contained in Unal et al. (1992a). For the results presented here, we assume that the dry patch formation time, and consequently the heat transfer from the dry patch region, are infinitesimally small with the liquid supplied only being sufficient to produce the surface quench. Constitutive relations to determine the stem-macrolayer geometry are discussed by Unal et al. (1992b). The triple-point evaporation coefficient,[3] $m_{tr,e}$, is obtained by trial and error in such a way that the calculated value of the surface- and time-averaged (STA) temperature matched the extrapolated experimental value at points A_{90} and A_{12} on the boiling curves where the heater surface should not experience dry patches. The size of the dry patch at CHF was determined by varying its size until the predicted STA wall temperature agreed with the experimental value in a stationary manner over the mushroom bubble lifetime. The reader is referred to previous papers for complete details of the model and solution scheme (Unal et al., 1992a, 1992b).

Results and Discussion

Different values of CHF have been reported in the literature for pool boiling of water on copper. Although Wang and Dhir's tests with a 90 deg contact angle yielded a CHF of 0.61 MW/m^2, Gaertner's clean water experiments, also considered to have had a contact angle of 90 deg, yielded a CHF of 1.55 MW/m^2. Depending upon the surface conditions, we can expect the values of CHF to vary.[4] However, if the "hot-spot" hypothesis we propose for the occurrence of CHF is correct, one should expect that a point on the heater surface should reach the critical liquid–solid contact temperature in all cases, even if the CHF values themselves are significantly different. Also both heaters meet our previous requirements of high thermal inertia and sufficient thickness, yet Wang's and Dhir's data show no second transition region, although Gaertner's do.

First, we will discuss the case of a 90 deg contact angle and will perform our analysis at a heat flux of 0.7 MW/m^2, taken as a rough approximation of the CHF value of 0.61 MW/m^2. In the absence of stem diameter or surface void fraction information in Wang and Dhir's paper, we make use of Gaertner's experimental data to estimate parameters. Also we initially use the values of the triple-point evaporation coefficients from Gaertner's data. Furthermore, the rectangular geometry of the test section is represented by a circular shape by preserving the total surface area.

At a heat flux of 0.7 MW/m^2, Gaertner's 90 deg data show that the STA wall superheat was 17.2°C. The triple-point coefficient for this case was found to be 2.91(10^{-5}) kg/m s°C. If this coefficient is used in a stem calculation (see Unal et al., 1992a) at the same heat flux, the surface-averaged transient heat transfer coefficient for Wang and Dhir's data is higher compared with values obtained for Gaertner's data at the same conditions (see Unal et al., 1992b). This increase is due to the higher number density of active sites on Wang and Dhir's test surface. This causes the surface void ratio to be higher, and correspondingly, the heater radius per stem (in the stem calculation) to decrease significantly. The resulting STA wall superheat becomes very low, 3.4°C, in the two-phase macrolayer region. Results of this case are listed in Table 1 as Run 3. This calculated STA wall superheat in the two-phase macrolayer region is much less than the value of 20.6°C reported by Wang and Dhir. To realize the measured STA temperature, some part of the heater must already be dry and have temperatures well over 20.6°C.

When we match the measured STA wall temperature using our two-region model, the superheat at the center of the dry patch region is 61.6°C (see Table 2, Run 3). This value is in reasonable agreement with the critical contact superheat of 82.6°C obtained for Gaertner's data. Thus, a local point on

[2]Gaertner (1965) used this terminology to refer to the upper end of his nucleate boiling curve, which showed a considerable decrease in slope before CHF.

[3]The triple-point evaporation coefficient is a lumped representation of the heat transfer in the three-phase contact region along the periphery of the base of each vapor stem.

[4]A key assumption made for this analysis is that CHF is independent of the boiling surface orientation—Gaertner used a horizontal heater, while Wang and Dhir employed a vertical heater. The results of Nishikawa et al. (1974) show that changes in heater surface orientation do not cause significant changes of the boiling characteristics for the fully developed, high heat flux, nucleate boiling region. Thus for a given heat flux, the same wall superheat should result for horizontal and vertical surfaces if all other conditions are equal.

Table 1 Data used in single-stem calculations for various runs

Run	q (MW/m2)	θ (deg)	m_e (kg/m s °C)	N/A_w (#/cm²)	A_v/A_w	r_s (mm)	r_h (mm)	δ (mm)	$\Delta T_{av,wet}$ (°C)	$\Delta T_{av,exp}$ (°C)
1	1.55	90	1.54×10^{-5}	581	0.1322	0.0783	0.2153	0.0978	20.0	43.6
2	1.69	12	1.85×10^{-5}	333	0.0947	0.0913	0.2967	0.1141	29.2	121.6
3	0.70	90	2.91×10^{-5}	790	0.3403	0.1167	0.2000	0.1458	3.4	20.6
4	0.70	90	1.03×10^{-5}	790	0.3403	0.1167	0.2000	0.1458	8.2	20.6
5	0.70	90	2.41×10^{-5}	790	0.0625	0.0500	0.2000	0.0937	8.7	20.6
6	0.70	90	2.91×10^{-5}	118	0.1322	0.1167	0.4959	0.1458	17.2	20.6

Table 2 Dry patch model results

Run	q (MW/m2)	θ (deg)	r_d (mm)	ΔT_{av} (°C)	ΔT_{rew} (°C)
1	1.55	90	18.2	43.4	82.6
2	1.69	12	23.9	120.2	167.3
3	0.70	90	27.3	20.6	61.6
4	0.70	90	24.8	20.7	57.2
5	0.70	90	24.2	20.8	56.5

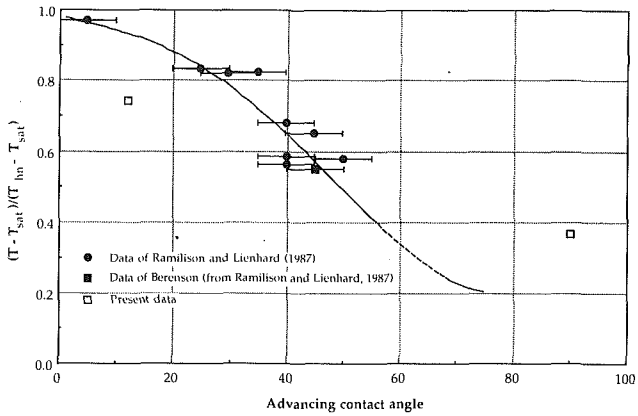

Fig. 2 Liquid-contact temperatures at the onset of CHF and film boiling as a function of contact angle

the heated surface could reach the critical liquid–solid contact temperature in Wang and Dhir's 90 deg contact angle test, causing the occurrence of CHF at lower heat fluxes. This is a consequence of the relatively high site density in their experiments.

As we mentioned in the preceding paragraphs, the calculation of the dry spot temperature in Wang and Dhir's experiments was carried out by assuming that results from Gaertner's data could be applied to this case as well. Specifically, we used values of the stem diameter and the triple-point evaporation coefficient derived from Gaertner's data. Next, we will examine the sensitivity of our results to changes in the values of these parameters. We will also look at the effect of changes in the nucleation site density, N/A_w.

When we decreased the triple-point evaporation coefficient by a factor of 3, the STA wall superheat in the two-phase macrolayer region was found to be 8.2°C, and the superheat at the center of the dry region was 57.2°C (see Tables 1 and 2, Run 4). A threefold decrease in the triple-point coefficient causes a twofold increase in the wet region STA wall superheat, but has decreased the calculated dry-spot superheat by less than 7.2 percent. It appears that little error is introduced by using the value of the triple-point evaporation coefficient obtained for Gaertner's data.

Similarly, when the vapor stem diameter was decreased by 57 percent (see Tables 1 and 2, Run 5), the calculated value of critical rewetting superheat was reduced only by 3.2 percent. Again, only a small error is introduced in our calculations as a result of our applying Gaertner's vapor stem relations to Wang and Dhir's data.

If the nucleation site density was decreased in such a way that the effective heater diameter per stem increased to about 0.5 mm (see Table 1, Run 6), the wet region surface-averaged heat transfer coefficient reduced by about 80 percent (Unal et al., 1992b). It is clear that the wet region heat transfer coefficient is highly sensitive to the active site density N/A_w. The wet region STA superheat was found to be 17.2°C, which is fairly close to the experimentally measured value of 20.6°C. This suggests that for this N/A_w, most of the heater surface could be covered with the two-phase macrolayer and that the high-temperature dry spots must be relatively small in area.

The sensitivity of the calculated heat transfer coefficients and surface temperatures to the nucleation site density indicates a third requirement for the occurrence of the second transition region. The nucleation site density must not be too high for the appearance of a second transition region. For large active nucleation site densities, lower wall temperatures in the macrolayer region compress the surface-averaged temperature changes due to any dry patches and minimize any observable changes in the slope of the boiling curve. This also implies that measurements of STA wall temperature, which provide indications as to whether the second transition region exists, cannot be used as a litmus test to make conclusions about the existence of dry patches on the heater surface. Whether dry patches can eventually cause a second transition region to occur on the boiling curve appears to depend strongly on the active nucleation site density.

Next, we will consider the potential effects of contact single. Gaertner's STA heat flux and superheat at CHF for clean water (90 deg contact angle) were 1.55 MW/m² and 43.4°C, respectively. For these conditions, our calculations show that the dry patch radius required is about 18.2 mm. The local instantaneous superheat at the end of the converged hovering period at the center of the dry patch was 82.6°C (see Run 1 of Tables 1 and 2). In Run 2, we repeated the calculation for Gaertner's and Westwater's water/nickel-salt data. We estimated the contact angle of water/salt-nickel solution as 12 deg based on nucleation site density measurements of Wang and Dhir (1991; see Unal et al., 1992b). The experimental STA wall superheat at CHF (1.69 MW/m²) for this case is 121.6°C. The dry patch size required was found to be about 23.9 mm and the critical rewetting superheat for this case was 167.3°C (see Table 2, Run 2).

Figure 2 shows the experimental liquid–solid contact temperature data of Ramilison and Lienhard (1987) at the onset of film boiling. We showed the result of Runs 1 and 2 on the same figure using open symbols. Considering the uncertainty in the inferred contact angle, the calculated dimensionless contact temperatures agree reasonably well with the data of Ramilison and Lienhard where the critical liquid–solid contact temperature decreases with increasing advancing contact angle.

Summary and Conclusions

We have examined the lack of a second transition boiling region in the experiments of Wang and Dhir. In addition to the original requirements of a thick heater with high thermal conductivity for observing the second transition boiling region presented by Unal et al. (1992a), an additional criterion determined here is that the active nucleation site density must not be too high. This new requirement should be included in the experimental efforts originally suggested and aimed at investigating the hot-spot hypothesis. It also indicates that the lack of existence of the second transition region on the boiling curve doesn't necessarily indicate the lack of significant heater surface dryout as we had suggested earlier.

Calculations based on the data of Wang and Dhir (1991) showed that the surface temperatures on the wet regions are very low due to their high nucleation site density. This suggests that dry patches must exist on their heater, so that the surface-averaged temperatures would be as measured in their experiments. Thus the hot-spot hypothesis provides one possible

explanation for the significantly different CHF measurements between Wang and Dhir results compared to those of Gaertner's clean water experiments (1965).

The liquid-solid contact temperature at the center of the dry patches at the onset of CHF was found to vary between 267.3°C and 182.6°C for the data of Gaertner (1965) for contact angles ranging from 12 to 90 deg. These temperatures show the proper trend and were in reasonable agreement with the liquid-solid contact temperatures at the onset of film boiling reported by Ramilison and Lienhard (1987).

The results obtained from this numerical experiment are presented in the hope of aiding understanding of the mechanisms governing CHF. Closer attention to the measurement of spatial variations in surface temperatures is required. Further, experiments could be devised to investigate the dry patch characteristics.

References

Gaertner, R. F., and Westwater, J. W., 1960, "Population of Active Sites in Nucleate Boiling Heat Transfer," *Chem. Engng. Prog. Symp. Ser.*, Vol. 56, No. 30, pp. 39-48.

Gaertner, R. F., 1965, "Photographic Study of Nucleate Pool Boiling on a Horizontal Surface," ASME JOURNAL OF HEAT TRANSFER, Vol. 87, pp. 401-428.

Liaw, S. P., and Dhir, V. K., 1989, "Void Fraction Measurements During Saturated Boiling of Water on Partially Wetted Surfaces," ASME JOURNAL OF HEAT TRANSFER, Vol. 111, pp. 731-738.

Nishikawa, K., Fujita, Y., and Ohta, H., 1974, "Effect of Surface Configuration on Nucleate Boiling Heat Transfer," *Int. J. Heat Mass Transfer*, Vol. 27, pp. 1559-1571.

Ramilison, J. M., and Lienhard, J. H., 1987, "Transition Boiling Heat Transfer and Film Transition Regime," ASME JOURNAL OF HEAT TRANSFER, Vol. 109, pp. 746-752.

Unal, C., Vincent, D., and Nelson, R. A., 1992a, "Unifying the Controlling Mechanisms for the Critical Heat Flux and Quenching: The Ability of Liquid to Contact the Hole Surface," ASME JOURNAL OF HEAT TRANSFER, Vol. 114, pp. 972-982.

Unal, C., Sadasivan, P., and Nelson, R. A., 1992b, "On the Hot-Spot-Controlled Critical Heat Flux Mechanism in Pool Boiling of Saturated Fluids," *Proceedings of the Engineering Foundation Conference on Pool and External Flow Boiling*, Santa Barbara, CA, Mar. 23-27, pp. 193-201.

Wang, C. H., and Dhir, V. K., 1991, "Effect of Surface Wettability on Active Nucleation Site Density During Pool Boiling of Water on a Vertical Surface," ASME HTD-Vol. 159, pp. 89-96.

Boundary Conditions for an Evaporating Thin Film for Isothermal Interfacial Conditions

H. C. Chebaro[1] and K. P. Hallinan[2]

Introduction

Evaporation in a heat pipe occurs at a liquid-vapor interface within the micropores of the heat pipe wick. For nearly completely wetting liquids, as used in all heat pipes, the liquid-vapor interface will extend beyond the meniscus due to the adsorption of fluid molecules to the solid structure of the wick. Thus, the liquid-vapor interface within the micropores can be divided into three distinct regions as shown in Fig. 1: the meniscus region controlled by the interfacial curvature (deGennes, 1985); the thin film region controlled by both the disjoining pressure (caused by the long-range molecular interactions) and the interfacial curvature; and the adsorbed film region controlled by the short range molecular forces (Israelachvili, 1989). Current practice in the design of heat pipes overlooks the presence of the thin film and the adsorbed film. Therefore, the goal of this study is to investigate the role of the thin film in heat pipes, and to deal uniquely with the boundary conditions in the region near the adsorbed film and in the meniscus region.

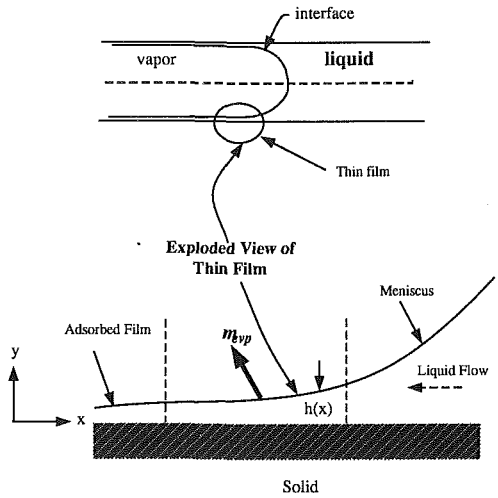

Fig. 1 Thin film region between an adsorbed film and a meniscus

Background

The transport processes that occur in thin films have drawn considerable attention in recent years. Wayner and Schonberg (1990) computed several thin film profiles, each of which approaches a constant but different curvature in the vicinity of the meniscus as the evaporation rate changes, contrasting with Welter's observations of an evaporating meniscus in a capillary tube (1991). He observed that the meniscus radius of curvature was independent of the evaporation rate (for stable conditions) and equal to the tube radius. More recently, Stephan and Busse (1990) and Swanson and Herdt (1992) have analyzed evaporating menisci within triangular grooves and circular pores. Each of these studies forced the interfacial radius of curvature of the thin film in the vicinity of the meniscus to the pore radius. Additionally, however, Stephan and Busse assumed that the thin film interfacial shape and thickness is intransigent with evaporation rate, contradicting the experimental findings of Wayner et al. (1991) who showed that the adsorbed film thickness, h_0, thins as the evaporation rate is increased. Swanson and Herdt (1992) assumed that the liquid flow field in the thin film as well as in the meniscus region can be described by a Hagen-Poiseuille flow field. This assumption, however, is only applicable to situations where the pressure gradient is only important in the axial direction, which for their physical problem is solely valid for the thin film region.

Analysis

The thin liquid film between the adsorbed film and the meniscus of an evaporating interface within a micropore is analyzed under isothermal conditions extending the theoretical treatment developed by Wayner and Schonberg (1990) to a pore geometry. A rectangular coordinate frame of reference is employed with the x axis along the wall and the y axis normal to the wall, as depicted in Fig. 1. Conservation of mass along

[1]Research Assistant, Department of Mechanical and Aerospace Engineering, University of Dayton, Dayton, OH 45469.

[2]Assistant Professor, Department of Mechanical and Aerospace Engineering, University of Dayton, Dayton, OH 45469; Assoc. Mem. ASME.

Contributed by the Heat Transfer Division of THE AMERICAN SOCIETY OF MECHANICAL ENGINEERS. Manuscript received by the Heat Transfer Division October 1992; revision received January 1993. Keywords: Evaporation, Heat Pipes and Thermosyphons, Porous Media. Associate Technical Editor: L. C. Witte.

explanation for the significantly different CHF measurements between Wang and Dhir results compared to those of Gaertner's clean water experiments (1965).

The liquid-solid contact temperature at the center of the dry patches at the onset of CHF was found to vary between 267.3°C and 182.6°C for the data of Gaertner (1965) for contact angles ranging from 12 to 90 deg. These temperatures show the proper trend and were in reasonable agreement with the liquid-solid contact temperatures at the onset of film boiling reported by Ramilison and Lienhard (1987).

The results obtained from this numerical experiment are presented in the hope of aiding understanding of the mechanisms governing CHF. Closer attention to the measurement of spatial variations in surface temperatures is required. Further, experiments could be devised to investigate the dry patch characteristics.

References

Gaertner, R. F., and Westwater, J. W., 1960, "Population of Active Sites in Nucleate Boiling Heat Transfer," *Chem. Engng. Prog. Symp. Ser.*, Vol. 56, No. 30, pp. 39-48.

Gaertner, R. F., 1965, "Photographic Study of Nucleate Pool Boiling on a Horizontal Surface," ASME JOURNAL OF HEAT TRANSFER, Vol. 87, pp. 401-428.

Liaw, S. P., and Dhir, V. K., 1989, "Void Fraction Measurements During Saturated Boiling of Water on Partially Wetted Surfaces," ASME JOURNAL OF HEAT TRANSFER, Vol. 111, pp. 731-738.

Nishikawa, K., Fujita, Y., and Ohta, H., 1974, "Effect of Surface Configuration on Nucleate Boiling Heat Transfer," *Int. J. Heat Mass Transfer*, Vol. 27, pp. 1559-1571.

Ramilison, J. M., and Lienhard, J. H., 1987, "Transition Boiling Heat Transfer and Film Transition Regime," ASME JOURNAL OF HEAT TRANSFER, Vol. 109, pp. 746-752.

Unal, C., Vincent, D., and Nelson, R. A., 1992a, "Unifying the Controlling Mechanisms for the Critical Heat Flux and Quenching: The Ability of Liquid to Contact the Hole Surface," ASME JOURNAL OF HEAT TRANSFER, Vol. 114, pp. 972-982.

Unal, C., Sadasivan, P., and Nelson, R. A., 1992b, "On the Hot-Spot-Controlled Critical Heat Flux Mechanism in Pool Boiling of Saturated Fluids," *Proceedings of the Engineering Foundation Conference on Pool and External Flow Boiling*, Santa Barbara, CA, Mar. 23-27, pp. 193-201.

Wang, C. H., and Dhir, V. K., 1991, "Effect of Surface Wettability on Active Nucleation Site Density During Pool Boiling of Water on a Vertical Surface," ASME HTD-Vol. 159, pp. 89-96.

Boundary Conditions for an Evaporating Thin Film for Isothermal Interfacial Conditions

H. C. Chebaro[1] and K. P. Hallinan[2]

Introduction

Evaporation in a heat pipe occurs at a liquid-vapor interface within the micropores of the heat pipe wick. For nearly completely wetting liquids, as used in all heat pipes, the liquid-vapor interface will extend beyond the meniscus due to the adsorption of fluid molecules to the solid structure of the wick. Thus, the liquid-vapor interface within the micropores can be divided into three distinct regions as shown in Fig. 1: the meniscus region controlled by the interfacial curvature (deGennes, 1985); the thin film region controlled by both the disjoining pressure (caused by the long-range molecular interactions) and the interfacial curvature; and the adsorbed film region controlled by the short range molecular forces (Israelachvili, 1989). Current practice in the design of heat pipes overlooks the presence of the thin film and the adsorbed film. Therefore, the goal of this study is to investigate the role of the thin film in heat pipes, and to deal uniquely with the boundary conditions in the region near the adsorbed film and in the meniscus region.

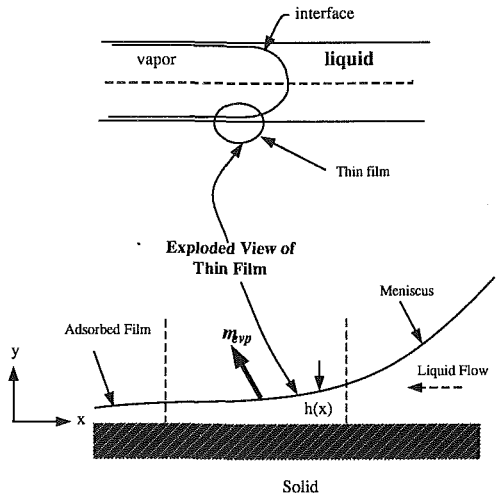

Fig. 1 Thin film region between an adsorbed film and a meniscus

Background

The transport processes that occur in thin films have drawn considerable attention in recent years. Wayner and Schonberg (1990) computed several thin film profiles, each of which approaches a constant but different curvature in the vicinity of the meniscus as the evaporation rate changes, contrasting with Welter's observations of an evaporating meniscus in a capillary tube (1991). He observed that the meniscus radius of curvature was independent of the evaporation rate (for stable conditions) and equal to the tube radius. More recently, Stephan and Busse (1990) and Swanson and Herdt (1992) have analyzed evaporating menisci within triangular grooves and circular pores. Each of these studies forced the interfacial radius of curvature of the thin film in the vicinity of the meniscus to the pore radius. Additionally, however, Stephan and Busse assumed that the thin film interfacial shape and thickness is intransigent with evaporation rate, contradicting the experimental findings of Wayner et al. (1991) who showed that the adsorbed film thickness, h_0, thins as the evaporation rate is increased. Swanson and Herdt (1992) assumed that the liquid flow field in the thin film as well as in the meniscus region can be described by a Hagen-Poiseuille flow field. This assumption, however, is only applicable to situations where the pressure gradient is only important in the axial direction, which for their physical problem is solely valid for the thin film region.

Analysis

The thin liquid film between the adsorbed film and the meniscus of an evaporating interface within a micropore is analyzed under isothermal conditions extending the theoretical treatment developed by Wayner and Schonberg (1990) to a pore geometry. A rectangular coordinate frame of reference is employed with the x axis along the wall and the y axis normal to the wall, as depicted in Fig. 1. Conservation of mass along

[1]Research Assistant, Department of Mechanical and Aerospace Engineering, University of Dayton, Dayton, OH 45469.

[2]Assistant Professor, Department of Mechanical and Aerospace Engineering, University of Dayton, Dayton, OH 45469; Assoc. Mem. ASME.

Contributed by the Heat Transfer Division of THE AMERICAN SOCIETY OF MECHANICAL ENGINEERS. Manuscript received by the Heat Transfer Division October 1992; revision received January 1993. Keywords: Evaporation, Heat Pipes and Thermosyphons, Porous Media. Associate Technical Editor: L. C. Witte.

the thin film requires that the reduction in the liquid flow rate equal the evaporation rate, thus:

$$\frac{d\Gamma}{dx} = -\dot{m}_{\text{evp}} \tag{1}$$

Defining the following variables:

$$\eta = h/h_0, \quad \xi = x/x_0, \quad \pi_d = \pi/\pi_0$$

$$\dot{m}_{id} = \rho_l u_0, \quad C_a = \mu_l u_0/\sigma, \quad x_0 = \left(\frac{\sigma h_0}{\pi_0}\right)^{1/2}$$

$$\dot{m}_{id} = C_1 \left(\frac{M}{2\pi RT}\right)^{1/2} \left[\frac{P_v M \Delta h}{R T_v T_{lv}} (T_{lv} - T_v)\right]$$

$$\pi_0 = \frac{M \Delta h \Delta T}{V_l T_v}, \quad \Delta T = T_{lv} - T_v$$

Eq. (1) along with the augmented Laplace-Young equation yields the following nondimensional equation for the thin film interfacial shape:

$$-\left[\eta^3 \eta''' - 3\frac{\eta'}{\eta}\right]' = \frac{3C_a}{\left(\frac{h_0 \pi_0}{\sigma}\right)^2}\left[1 - \eta'' - \frac{1}{\eta^3}\right] \tag{2}$$

Above, C_a is the capillary number, $\dot{m}_{id}$ is evaporative flux (Wayner and Schonberg, 1990) based upon a flat liquid-vapor interface in the absence of disjoining pressure, T_{lv} is the interfacial temperature, T_v is the saturation temperature of the bulk vapor phase, u_0 is a characteristic velocity of the liquid, x_0 is a characteristic length of the thin film, h_0 is the adsorbed film thickness, and π_0 is the disjoining pressure of the adsorbed film. For nearly perfectly wetting and nonpolar liquids, typical of those used in low-temperature heat pipes, the disjoining pressure is given by $\pi = A/h^3$, where A is the Hamaker constant and h is the local film thickness. For heat pipe wicks manufactured out of metals such as copper, aluminum, or brass, A is given by (Israelachvili, 1989)

$$A = 0.1326\, p_c \nu_e \simeq 35 \times 10^{-20} \text{ J}$$

where p_c is Planck's constant and ν_e is the main electronic adsorption frequency, which for metals ranges from 30×10^{15} to 50×10^{15} Hz. The value of A shown above is computed based upon $\nu_e = 30 \times 10^{15}$ Hz. The four boundary conditions needed to solve Eq. (2) are to be specified in a manner that forces the asymptotic curvature of the thin film to be the same as the curvature of the meniscus. Since specifying these boundary conditions at the adsorbed film according to: $\eta = \eta_0$ and $\eta' = \eta'' = \eta''' = 0$, yields an adsorbed film solution, $\eta = \eta_0 = \text{const}$ (Wayner et al., 1991), it is necessary to specify the boundary conditions at a point shifted away from the adsorbed film ($\xi = \xi_a$), where ξ_a will be chosen with the requirement that at ξ_a, η_a'' is negligibly small such that $\eta_a''' \simeq 0$. Thus, in general form the following boundary conditions at $\xi = \xi_a$ are employed:

$$\eta = \eta_a, \quad \eta' = \eta_a', \quad \eta'' = \eta_a'', \text{ and } \eta_a''' = 0$$

The choice of ξ_a and η_a'' is dictated ultimately by the requirement that the interfacial curvature must equal the meniscus curvature as $\xi \to \infty$. Hence a shooting method solution is employed. However, in general, the shooting method would require iteration upon four parameters (namely, ξ_a, η_a, η_a', and η_a'') to match the meniscus curvature, which would be imprecise at best. Also, beginning the solution at ξ_a neglects a portion of thin film region in the vicinity of the adsorbed film for $0 \le \xi \le \xi_a$ usually called the interline region.

The disadvantages of the above approach are avoided in the following manner. The interline region or region adjacent to the adsorbed film is characterized by negligible curvature, and thus the differential equation that governs its interfacial profile is obtained by setting the curvature terms in Eq. (2) to zero (Wayner et al., 1976), yielding the following equation:

$$\left[\frac{\eta_I'}{\eta_I}\right]' = \frac{C_a}{\left(\frac{h_0 \pi_0}{\sigma}\right)^2}\left[1 - \frac{1}{\eta_I^3}\right]. \tag{3}$$

valid in the region $0 \le \xi \le \xi_a$. At $\xi = \xi_a$, the interline solution, η_I, must match the solution of Eq. (2) ($\eta_I = \eta_a$, $\eta_I' = \eta_a'$). Thus, a discontinuity in the curvature at ξ_a would exist except that ξ_a is chosen so that η_a'' is negligibly small. The boundary conditions for Eq. (3) are chosen to be consistent with Wayner's (1991) observations (as well as those of Dussan et al., 1991) just outside the adsorbed film, i.e.,

$$\eta = 1 + \delta \text{ and } \eta' = \epsilon \text{ at } \xi \simeq 0$$

The parameter δ depends on the evaporation rate as shown in Wayner's experiments. The interline slope, ϵ, has been postulated to be fluid-solid dependent only, and independent of the outer solution (Dussan et al., 1991). Thus, prescription of these boundary conditions is then sufficient to describe the physical boundary conditions inherent to the thin film. Note that these boundary conditions can be prescribed for the solution of Eq. (2), but since δ is a property of the heating conditions and ϵ may be a property of the fluid-solid system, the resulting thin film solution is unique with an asymptotic curvature, which is not necessarily equal to the meniscus curvature.

From the interline solution a matching point ξ_a is selected such that η_a'' will be negligibly small but not zero, and at which the film thickness, $\eta_I(\xi_a)$, and slope, $\eta_I'(\xi_a)$, provide two of the initial conditions for the solution to Eq. (2) for η. Next iteration is only required upon η_a'' to obtain matching of the thin film asymptotic curvature with that of the meniscus. The advantage of this procedure is to reduce the number of parameters upon which iteration is required to one, and in the process account for most of the thin film region.

Table 1 Parametric variables used to express Eq. (2) in a dimensionless form

ΔT, K	h_0, μm	x_0, μm	$\dot{m}_{id}$, kg/(m-s^2)	π_0, Pa	C_a
0.0006	0.07	0.97	0.025	1096	3.3×10^{-7}
0.0007	0.065	0.87	0.030	1279	3.8×10^{-7}
0.0008	0.062	0.8	0.034	1462	4.4×10^{-7}

Results

Results are presented for a heat pipe at 50°C utilizing ammonia as a working fluid, and having a porous wick with an average pore radius of 20 μm. The operating temperature can be maintained constant for variable heat inputs by adjusting the heat sink conditions. For differences between the interfacial temperature and the vapor temperature, $\Delta T = T_{lv} - T_v$, of 0.0006 K, 0.0007 K, and 0.0008 K, the respective heat transport rates for the heat pipe are 0.76, 1.3, and 1.7 W/cm^2. These heat fluxes are obtained by multiplying the latent heat of vaporization by the average evaporation fluxes, i.e., the average of the evaporation profiles computed for the liquid-vapor interface, corresponding to values of ΔT of 0.0006 K, 0.0007 K, and 0.0008 K, respectively. Corresponding values for the parametric variables used to express Eq. (2) in a dimensionless form are presented in Table 1.

For these heat fluxes, the following interline boundary conditions are used:

$\dot{q}'' = 0.76$ W/cm^2: $\xi = 0.00$, $\eta_I = 1.0303$, $\eta_I' = 0.0004$

$\dot{q}'' = 1.30$ W/cm^2: $\xi = 0.00$, $\eta_I = 1.0520$, $\eta_I' = 0.0004$

$\dot{q}'' = 1.70$ W/cm^2: $\xi = 0.00$, $\eta_I = 1.0700$, $\eta_I' = 0.0004$

At ξ_a, iteration upon η_a'' to obtain matching with the meniscus

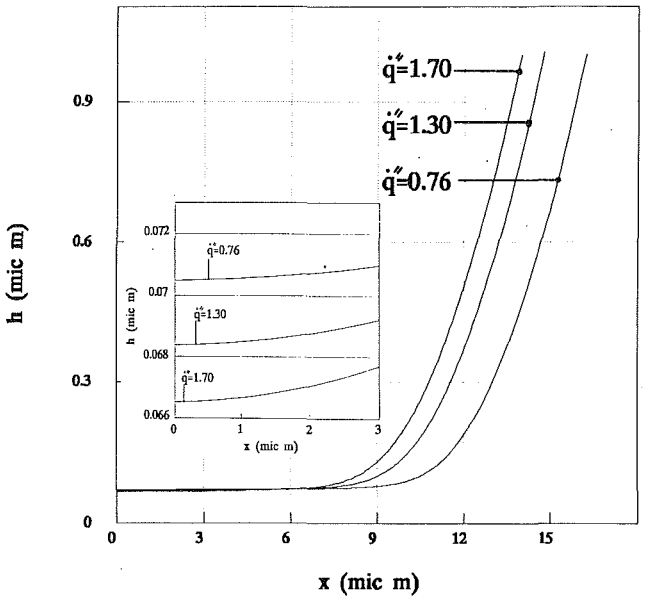

Fig. 2 Thin film profiles for ammonia at vapor temperature of 322 K

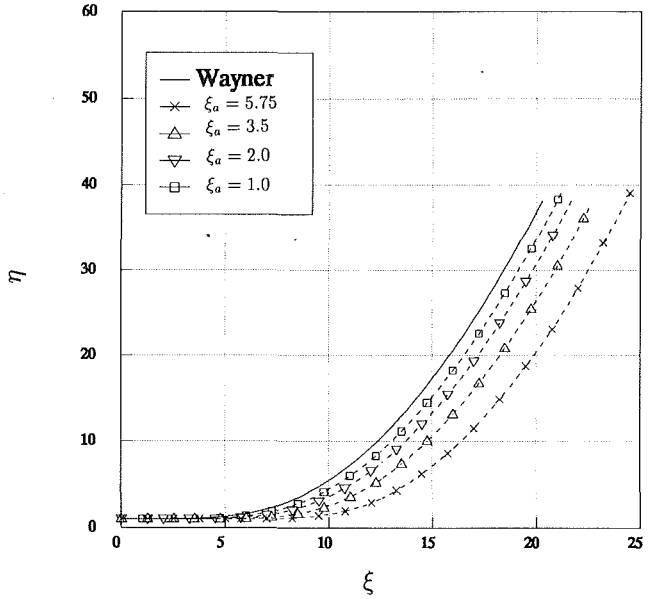

Fig. 4 Comparison between thin film solutions obtained using the technique developed here and thin film solution obtained by Wayner and Schonberg (1990)

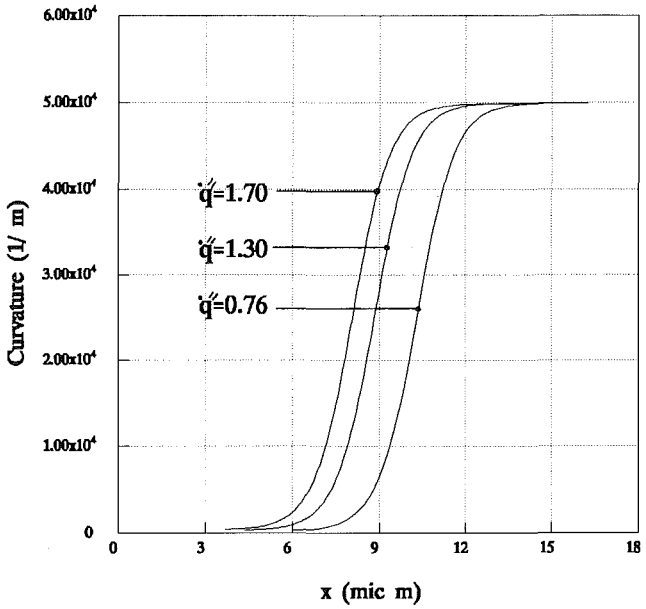

Fig. 3 Thin film curvature profiles for ammonia at vapor temperature of 322 K

region yields the following boundary conditions for the transition region:

$\dot{q}'' = 0.76$ W/cm^2: $\xi_a = 6.25$, $\eta_a = 1.06$,
$\eta_a' = 0.0099$, $\eta_a'' = 0.004683$

$\dot{q}'' = 1.30$ W/cm^2: $\xi_a = 5.00$, $\eta_a = 1.08$,
$\eta_a' = 0.0114$, $\eta_a'' = 0.004210$

$\dot{q}'' = 1.70$ W/cm^2: $\xi_a = 4.6$, $\eta_a = 1.10$,
$\eta_a' = 0.0129$, $\eta_a'' = 0.004546$

The subsequent solution to Eqs. (2) and (3) yields data for the interfacial profile and curvature within the thin film. Figure 2 shows three thin film profiles computed for ammonia for the abovementioned heat transport rates. This figure indicates a decrease in the thin film length and adsorbed film thickness with increasing heat fluxes, consistent with the results of Wayner and Schonberg (1990) and Wayner et al. (1991). Figure 3 depicts the curvature profiles corresponding to Fig. 2 thin film profiles. The profiles shown approach an asymptotic constant value, and additionally they indicate that the curvatures are negligibly small at the matching points. The results from this solution approach are compared to the thin film solution of Wayner and Schonberg (1990). In making a comparison, it is important to note that the geometry used by Wayner and Schonberg is such that the thin film is symmetric and need not terminate in an adsorbed film. Furthermore, the curvature of the thin film at the centerline in their geometry is not zero. This means that the curvature of the interface along the thin film never approaches zero as in the present case, and as a result an interline region does not exist. Nevertheless the validation of the present analysis proceeds as follows. Wayner and Schonberg present results for a dimensionless asymptotic curvature of 0.3129 for *n*-octane as the working fluid at a temperature of 298 K. Using the present approach, the solutions of Eqs. (3) and (4) were computed for these conditions. Four matching points, ξ_a (at $\xi_a = 5.75$, 3.5, 2.0, and 1.0) were chosen. For each of these matching points, η_a'' was iterated upon such that the dimensionless asymptotic curvature of the corresponding thin film approached 0.3129. The comparative results depicted in Fig. 4 indicate that as the matching point is chosen closer to the centerline, the thin film profile computed here approaches Wayner and Schonberg's solution. Thus, as ξ_a approaches zero it will converge to Wayner and Schonberg's solution.

Conclusion

The results given above indicate that the solution method developed in this study is adequate to compute the shape of the thin film within circular pores. The unique aspect of this solution method is that no arbitrary assumptions concerning the interfacial shape, slope, and curvature are needed in specifying boundary conditions. Instead, the method would rely upon unique experimentally observed characteristics of the interfacial shape within microcircular pores to specify these boundary conditions. These unique characteristics are the constant meniscus curvature, which the thin film curvature must asymptotically match, and the presence of an interline region where the interfacial profile possesses a negligible curvature

and is slightly tapered as it merges with the adsorbed film. However, in employing this method, attention must be paid to the discontinuity in the interfacial curvature, which can be made negligible by properly selecting the matching point between an interline and thin film solutions.

References

deGennes, P. G., 1985, "Wetting: Statics and Dynamics," *Rev. Mod. Phys.*, Vol. 57, pp. 827–861.

Dussan, E. B., V, Rame, E., and Garoff, S., 1991, "On Identifying the Appropriate Boundary Conditions at a Moving Contact Line: An Experimental Investigation," *J. Fluid Mech.*, Vol. 230, pp. 97–116.

Israelachvili, J. N., 1989, *Intermolecular and Surface Forces*, Academic Press, New York.

Stephan, P. C., and Busse, C. A., 1990, "Theoretical Study of an Evaporating Meniscus in a Triangular Groove," presented at the 7th Int. Heat Pipe Conf., Minsk, USSR.

Swanson, L. W., and Herdt, G. C., 1992, "Model of the Evaporating Meniscus in a Capillary Tube," ASME JOURNAL OF HEAT TRANSFER, Vol. 114, pp. 434–441.

Wayner, P. C., Jr., Kao, Y. K., and Lacroix, L. V., 1976, "The Interline Heat Transfer Coefficient of an Evaporating Wetting Film," *Int. J. Heat Mass Transfer*, Vol. 19, pp. 487–492.

Wayner, P. C., Jr., and Schonberg, J. F., 1990, "Heat Transfer and Fluid Flow in an Evaporating Extended Meniscus," presented at the 9th International Heat Transfer Conference, Israel.

Wayner, P. C., Jr., DasGupta, S., and Schonberg, J. F., 1991, "Effect of Interfacial Forces on Evaporative Heat Transfer in a Meniscus," WL-TR-91-2061.

Welter, D., 1991, "The Effect of Evaporation on the Dynamic Capillary Pressure in Heat Pipes," M.S.M.E. Thesis, University of Dayton.

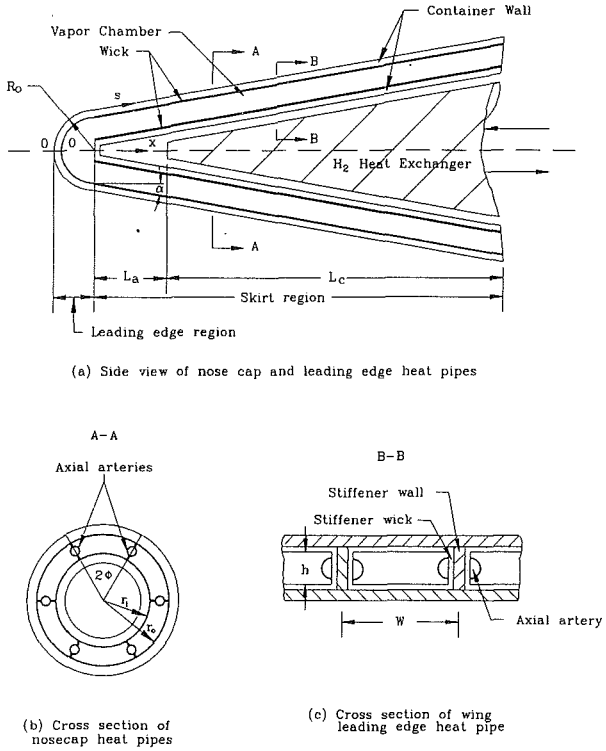

Fig. 1 Configuration of nosecap and wing leading edge heat pipes

Conjugate Modeling of High-Temperature Nosecap and Wing Leading Edge Heat Pipes

Y. Cao[1] and A. Faghri[1]

Introduction

Future hypersonic vehicles will be subjected to intense aerodynamic heating at the nosecap and wing leading edges. Three methods (barrier coatings, internal active cooling, and high-temperature heat pipes) have been proposed for cooling these hypersonic aircraft structures.

It appears that heat pipes are one of the most promising choices for cooling hypersonic vehicle structures due to their efficiency and reusability (Camarda, 1988). A typical nosecap heat pipe and a wing leading edge heat pipe with back wall radiation to a hydrogen coolant sink are schematically shown in Fig. 1. The nosecap heat pipe design consists of a conical annular vapor space between two shells, whereas the vapor space of the leading edge heat pipe has a rectangular cross section. In addition to the radiation heat transfer from the outer wall to space, the inner wall will transfer heat to the hydrogen-cooled tube heat exchanger by radiation.

In this paper, a generalized finite-difference computational methodology is presented to model the transient and steady-state behavior of the nosecap and the leading edge heat pipes developed by the U.S. Air Force for the National Aerospace Plane (NASP). The numerical simulation includes a consideration of capillary and sonic limits in the wick structures.

Mathematical Formulation

Heat Pipe Walls and Wicks. In this paper, a body-conforming coordinate system with a multiblock approach (Cao and Faghri, 1991) was used for the heat pipe walls and wicks. The energy equation in vectorial form is

$$(c\rho)\frac{\partial T}{\partial t} = \nabla \cdot k \nabla T \tag{1}$$

where

$$k = \begin{cases} k_w \\ k_{\text{eff}} \end{cases} \quad (c\rho) = \begin{cases} c_w \rho_w & \text{for the wall} \\ \omega (c\rho)_l - (1-\omega)(c\rho)_{wm} & \text{for the wick} \end{cases} \tag{2}$$

The effective thermal conductivity of the wick is k_{eff}, and ω is the wick porosity. In the nose region of the nosecap heat pipe, a spherical coordinate system is used; in the leading edge region of the wing leading edge heat pipe, a cylindrical coordinate system is applied. In the skirt regions of the nosecap and wing leading edge heat pipes, a cylindrical coordinate system and a Cartesian system are employed, respectively.

In the above formulation, the wick structures were assumed to be isotropic and homogeneous. Also, the effect of liquid flow through the wick on the temperature distribution in the wick structure was neglected. For the nosecap heat pipe, only the part with apex angle of 2ϕ shown in Fig. 1 needs to be modeled due to the symmetric geometry. For the wing leading edge heat pipe, the heat distributions near the stagnation line are nearly symmetric, and the heat pipe was divided in the spanwise direction into a number of vapor channels with width

[1]Department of Mechanical and Materials Engineering, Wright State University, Dayton, OH 45435.

Contributed by the Heat Transfer Division and presented at the ASME Winter Annual Meeting, Anaheim, California, November 8–13, 1992. Manuscript received by the Heat Transfer Division September 1992; revision received February 1993. Keywords: Conjugate Heat Transfer, Heat Pipes and Thermosyphons, Numerical Methods. Technical Editor: R. Viskanta.

and is slightly tapered as it merges with the adsorbed film. However, in employing this method, attention must be paid to the discontinuity in the interfacial curvature, which can be made negligible by properly selecting the matching point between an interline and thin film solutions.

References

deGennes, P. G., 1985, "Wetting: Statics and Dynamics," *Rev. Mod. Phys.*, Vol. 57, pp. 827–861.

Dussan, E. B., V, Rame, E., and Garoff, S., 1991, "On Identifying the Appropriate Boundary Conditions at a Moving Contact Line: An Experimental Investigation," *J. Fluid Mech.*, Vol. 230, pp. 97–116.

Israelachvili, J. N., 1989, *Intermolecular and Surface Forces*, Academic Press, New York.

Stephan, P. C., and Busse, C. A., 1990, "Theoretical Study of an Evaporating Meniscus in a Triangular Groove," presented at the 7th Int. Heat Pipe Conf., Minsk, USSR.

Swanson, L. W., and Herdt, G. C., 1992, "Model of the Evaporating Meniscus in a Capillary Tube," ASME JOURNAL OF HEAT TRANSFER, Vol. 114, pp. 434–441.

Wayner, P. C., Jr., Kao, Y. K., and Lacroix, L. V., 1976, "The Interline Heat Transfer Coefficient of an Evaporating Wetting Film," *Int. J. Heat Mass Transfer*, Vol. 19, pp. 487–492.

Wayner, P. C., Jr., and Schonberg, J. F., 1990, "Heat Transfer and Fluid Flow in an Evaporating Extended Meniscus," presented at the 9th International Heat Transfer Conference, Israel.

Wayner, P. C., Jr., DasGupta, S., and Schonberg, J. F., 1991, "Effect of Interfacial Forces on Evaporative Heat Transfer in a Meniscus," WL-TR-91-2061.

Welter, D., 1991, "The Effect of Evaporation on the Dynamic Capillary Pressure in Heat Pipes," M.S.M.E. Thesis, University of Dayton.

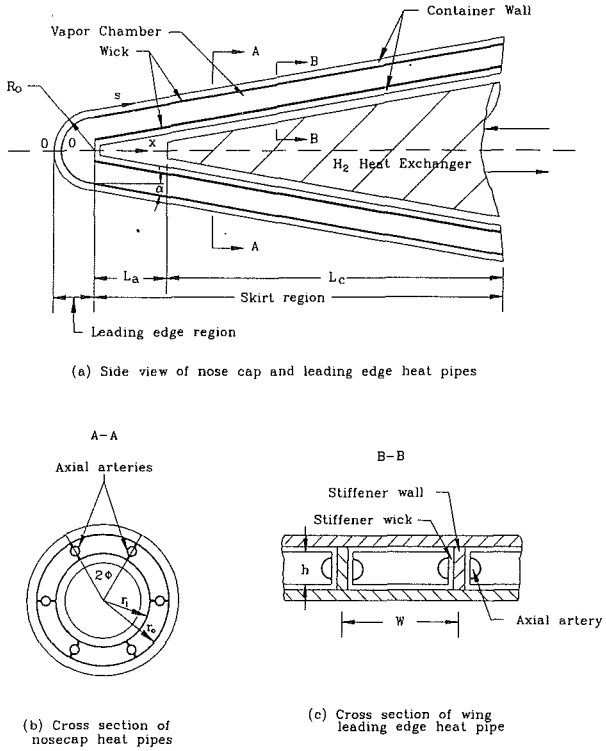

Fig. 1 Configuration of nosecap and wing leading edge heat pipes

Conjugate Modeling of High-Temperature Nosecap and Wing Leading Edge Heat Pipes

Y. Cao[1] and A. Faghri[1]

Introduction

Future hypersonic vehicles will be subjected to intense aerodynamic heating at the nosecap and wing leading edges. Three methods (barrier coatings, internal active cooling, and high-temperature heat pipes) have been proposed for cooling these hypersonic aircraft structures.

It appears that heat pipes are one of the most promising choices for cooling hypersonic vehicle structures due to their efficiency and reusability (Camarda, 1988). A typical nosecap heat pipe and a wing leading edge heat pipe with back wall radiation to a hydrogen coolant sink are schematically shown in Fig. 1. The nosecap heat pipe design consists of a conical annular vapor space between two shells, whereas the vapor space of the leading edge heat pipe has a rectangular cross section. In addition to the radiation heat transfer from the outer wall to space, the inner wall will transfer heat to the hydrogen-cooled tube heat exchanger by radiation.

In this paper, a generalized finite-difference computational methodology is presented to model the transient and steady-state behavior of the nosecap and the leading edge heat pipes developed by the U.S. Air Force for the National Aerospace Plane (NASP). The numerical simulation includes a consideration of capillary and sonic limits in the wick structures.

Mathematical Formulation

Heat Pipe Walls and Wicks. In this paper, a body-conforming coordinate system with a multiblock approach (Cao and Faghri, 1991) was used for the heat pipe walls and wicks. The energy equation in vectorial form is

$$(c\rho)\frac{\partial T}{\partial t} = \nabla \cdot k \nabla T \tag{1}$$

where

$$k = \begin{cases} k_w \\ k_{\text{eff}} \end{cases} \quad (c\rho) = \begin{cases} c_w \rho_w & \text{for the wall} \\ \omega (c\rho)_l - (1-\omega)(c\rho)_{wm} & \text{for the wick} \end{cases} \tag{2}$$

The effective thermal conductivity of the wick is k_{eff}, and ω is the wick porosity. In the nose region of the nosecap heat pipe, a spherical coordinate system is used; in the leading edge region of the wing leading edge heat pipe, a cylindrical coordinate system is applied. In the skirt regions of the nosecap and wing leading edge heat pipes, a cylindrical coordinate system and a Cartesian system are employed, respectively.

In the above formulation, the wick structures were assumed to be isotropic and homogeneous. Also, the effect of liquid flow through the wick on the temperature distribution in the wick structure was neglected. For the nosecap heat pipe, only the part with apex angle of 2ϕ shown in Fig. 1 needs to be modeled due to the symmetric geometry. For the wing leading edge heat pipe, the heat distributions near the stagnation line are nearly symmetric, and the heat pipe was divided in the spanwise direction into a number of vapor channels with width

[1]Department of Mechanical and Materials Engineering, Wright State University, Dayton, OH 45435.

Contributed by the Heat Transfer Division and presented at the ASME Winter Annual Meeting, Anaheim, California, November 8–13, 1992. Manuscript received by the Heat Transfer Division September 1992; revision received February 1993. Keywords: Conjugate Heat Transfer, Heat Pipes and Thermosyphons, Numerical Methods. Technical Editor: R. Viskanta.

W by the stiffener walls. Therefore, a typical vapor chamber of width W was modeled with symmetric boundary conditions applied on the stiffener walls and the stagnation line.

Vapor Flow. For the vapor flow in the heat pipe, the transient compressible quasi-one-dimensional vapor flow model of Cao and Faghri (1991) is adopted. The conservation of mass and momentum equations are:

$$\frac{\partial}{\partial t}(\rho A)+\frac{\partial}{\partial x}(\rho UA)=v\rho\frac{dS}{dx} \tag{3}$$

$$\frac{\partial}{\partial t}(A\rho U)+\frac{\partial}{\partial x}(A\rho U^2)=-\frac{\partial}{\partial x}\left[A\left(p-\frac{4}{3}\mu\frac{\partial U}{\partial x}\right)\right]-\frac{1}{2}f\rho U^2\frac{dS}{dx}\cos\alpha+\rho v^2\frac{dS}{dx}\sin\alpha \tag{4}$$

where A is the cross-sectional area of the vapor channel, U is the average axial vapor velocity, S is the channel wall surface area between the leading edge and position x, f is the friction coefficient, α is the local slope of the heat pipe wall, and v is the radial vapor injection or suction velocity. The perfect gas law is employed to account for the compressibility of the vapor:

$$p=\rho RT_v \tag{5}$$

where R is the gas constant. The vapor temperature and pressure are related by the Clausius–Clapeyron equation:

$$\frac{dp}{p}=\frac{h_{fg}}{R}\frac{dT_v}{T_v^2} \tag{6}$$

The vapor flow can be considered to be laminar along the heat pipe length due to the relatively small axial Reynolds number (Cao and Faghri, 1990; Faghri et al., 1991). The friction coefficients are functions of the cross-sectional geometry of the vapor chambers, and are given by Shah and Bhatti (1987). In the nose region of the nosecap heat pipe, the modeled vapor chamber is a circular sector with apex angle 2ϕ. The friction coefficient in this region is

$$f\,\mathrm{Re}_h=12(1+0.5059\,\phi-0.3948\,\phi^2+0.1875\,\phi^3-0.0385\,\phi^4)\quad(0\le 2\phi\le\pi) \tag{7}$$

In the skirt region of the nosecap heat pipe, the modeled vapor chamber is an annular sector with apex angle 2ϕ. The friction coefficient for this case is

$$f\,\mathrm{Re}_h=24\left\{\left[1-\frac{0.63}{\phi}\left(\frac{1-r^*}{1+r^*}\right)\right]\left[1+\frac{1}{\phi}\left(\frac{1-r^*}{1+r^*}\right)\right]^2\right\}^{-1} \tag{8}$$

where $r^*=r_i/r_o$, and r_i and r_o are the inner and outer radii of the annular sector. This equation is applicable for $\phi>\phi_{\min}(r^*)$. The values of $\phi_{\min}$ for different r^* are also given by Shah and Bhatti (1987).

The modeled vapor chamber for the wing leading edge heat pipe is a rectangular sector and the friction coefficient is

$$f\,\mathrm{Re}_h=24(1-1.3553\,\alpha^*+1.9467\,\alpha^{*2}-1.7012\,\alpha^{*3}+0.9564\,\alpha^{*4}-0.2537\,\alpha^{*5}) \tag{9}$$

where $\alpha^*=h/W$. The Reynolds number Re_h in Eqs. (7)–(9) is based on the hydraulic diameter D_h of the duct.

Boundary Conditions. At both ends of the heat pipe, the vapor velocity and the temperature gradients are zero:

$$z=0 \text{ and } L:\quad U=0,\ \frac{\partial T}{\partial x}=0 \tag{10}$$

In the wall and wick regions, the symmetric boundary conditions are applied except at the inner and outer shell wall surfaces and at the wick–vapor interfaces. The evaporation or condensation vapor mass flux into the vapor space, ρv, at the vapor–wick interfaces can be found from interfacial energy balances:

$$\rho v=q_{ow}/h_{fg}+q_{iw}/h_{fg}=\left[\left(k_{\mathrm{eff}}\frac{\partial T}{\partial r}\right)_{ow}-\left(k_{\mathrm{eff}}\frac{\partial T}{\partial r}\right)_{iw}\right]/h_{fg}=\begin{cases}>0 & \text{evaporation}\\ <0 & \text{condensation}\end{cases} \tag{11}$$

q_{ow}/h_{fg} and q_{iw}/h_{fg} are mass fluxes from the outer shell and inner shell wicks, respectively, and can be calculated from the temperature distributions in the outer and inner wicks. Note that Eq. (11) is also applicable to the leading edge regions, with $q_{iw}\equiv 0$.

At the condenser interfaces of the inner and outer wicks, vapor condenses and releases its latent heat energy. In order to simulate this process, two heat sources, $q_i=h_{fg}\rho_i v_i$ and $q_o=h_{fg}\rho_o v_o$, were applied at the grids next to the interfaces on the inner and outer shell wicks. Since the heat pipe shells and vapor were solved as a conjugate problem, these heat sources should be calculated from the vapor solution. In this study, the vapor was solved as a one-dimensional problem. Therefore, only the total suction mass flux ρv can be obtained by using Eq. (3) for a given vapor flow distribution in the x direction. The distribution of the total suction mass flux to the inner or outer shell wicks should be related to the radiation heat dissipative rate at the different shell surfaces, which is in turn proportional to the local radius of the individual shell for the nosecap heat pipe. By considering the relation $\rho_o v_o+\rho_i v_i=v\rho$, and $v_i\rho_i/v_o\rho_o=r_i/r_o=\gamma$, we have

$$\rho_o v_o=\rho v/(1+\gamma),\quad \rho_i v_i=\gamma\,\rho_o v_o \tag{12}$$

Note that, at the leading edge of the nosecap and wing leading edge heat pipes, $r_i=0$ and $\rho_o v_o=\rho v$. In the skirt region of the leading edge heat pipe, the heat pipe cross-sectional area is rectangular, and the radiative areas of the inner and outer shells are the same. Therefore, in Eq. (12), we can set $r_i=r_o$, which gives $\rho_o v_o=\rho_i v_i=0.5\,\rho v$.

At the outer shell wall surface, the aerodynamic heating distribution q_{local} was specified. In addition, a radiation heat flux into the ambient is superimposed at the surface. The net heat flux at the outer wall surface is

$$q_{\mathrm{net}}=q_{\mathrm{local}}-\epsilon_o\sigma(T_{os}^4-T_{am}^4) \tag{13}$$

where T_{os} and T_{am} are the outer shell wall surface and ambient temperatures. Unlike conventional heat pipes, the locations of the evaporator and condenser were not prescribed for the outer shell of the heat pipe, and may change during the transient operating period. At the inner shell wall surface, a radiation heat flux q_{is} was specified due to the radiation to the H_2 heat exchanger. Assuming the emissivity of the H_2 heat exchanger to be unity, q_{is} can be expressed as:

$$q_{is}=\epsilon_i\sigma(T_{is}^4-T_{\mathrm{sink}}^4) \tag{14}$$

where T_{is} and T_{sink} are the inner shell wall and the H_2 heat exchanger temperatures.

The conservation equations and boundary conditions in different regions were solved as a conjugate problem by applying the control-volume-based finite difference method. For more detailed information about the numerical model and procedure, the reader is referred to the paper by Cao and Faghri (1992).

Capillary and Boiling Limitations. Based on the fact that the liquid pressure drop in the circumferential direction is negligible, and the axial liquid flow resistances in the different wicks can be considered to be connected in parallel, the following relation for the capillary limit is derived:

$$\int_0^{x_{\min}}\left\{\dot{m}(s)/\left[\frac{K_oA_o}{\nu_l}+\frac{K_iA_i}{\nu_l}+\frac{K_aA_a}{\nu_l}\right]\right\}ds+\Delta p_v\le\frac{2\sigma}{r_{\mathrm{eff}}} \tag{15}$$

where K_oA_o, K_iA_i, and K_aA_a are the products of the wick permeability and the liquid flow areas for the outer shell wick, the inner shell wick, and the artery wick, respectively. r_{eff} is the effective capillary radius of the wick pores, Δp_v is the total vapor pressure drop along the heat pipe length, which can be found from the numerical solutions, and $x_{\min}$ is the location where the capillary pressure is minimum and equal to zero. In this study, $x_{\min}$ is taken to be at the condenser end cap. The total local mass flow rate $\dot{m}(s)$ is given by

$$\dot{m}(s) = \int_0^s [(v\rho)_{iw} + (v\rho)_{ow}] W d\xi \tag{16}$$

where $(v\rho)_{iw}$ and $(v\rho)_{ow}$ are the vapor mass fluxes to the vapor chamber from the inner and outer shell wicks. W is either the circumferential length of the nosecap heat pipe, or the width of the modeled section for the wing leading edge heat pipe. The relation for the boiling limit was developed by applying the theory of vapor nucleation, combined with the integrated Clausius–Clapeyron equation (Cao and Faghri, 1992):

$$\Delta T_{\text{crit}} = T_w - T_v = \frac{RT_vT_w}{h_{fg}} \times \ln\left[1 + \frac{2\sigma}{RT_v\rho_v}\left(\frac{1}{r_b} - \frac{1}{R_m}\right) + \frac{2\sigma}{RT_vr_b\rho_l}\right] \tag{17}$$

where T_w and T_v are wick–wall interface temperature and vapor space temperature, r_b is the effective radius of the vapor bubble trapped in the wick, and R_m is the radius of curvature of the liquid meniscus. If the last two terms in brackets are very small, Eq. (17) can be reduced to the commonly used relation in the literature (Chi, 1976).

Results and Discussion

The analysis of the transient and steady-state performance was first made for a nosecap heat pipe using lithium as the working fluid and a refractory metal as the container walls. The dimensions and the thermal properties of the heat pipe are: nose radius $R_o = 0.04$ m, adiabatic length $L_a = 0.08$ m, condenser length $L_c = 0.7$ m, vapor space height $h = 0.013$ m, wick and wall thickness $\delta_w = \delta_l = 0.6$ mm, liquid artery radius $R_a = 0.76$ mm, skirt slope $\alpha_s = 6$ deg, apex angle $2\phi = 60$ deg, heat capacity and thermal conductivity of the outer shell $(c\rho)_{os} = 2.756 \times 10^6$ J/(m^3 • K) and $(k_w)_{os} = 49.3$ W/(m • K), heat capacity and thermal conductivity of the inner shell $(c\rho)_{is} = 3.021 \times 10^6$ J/(m^3 • K), and $(k_w)_{is} = 40.64$ W/(m • K). The wick porosities are $\omega_n = 0.3$ and $\omega_s = 0.5$ at the nose and skirt regions, respectively. Figure 2 shows the normalized aerodynamic heating distribution $q_{\text{local}}/q_{\text{stagnation}}$ along the nosecap outer shell surface, which is similar to the wing leading edge ascent trajectory heating distribution. The stagnation heat flux used in the calculation is 340.5 W/cm^2 (300 Btu/s • ft^2). The numerical simulation started with an initial system temperature of 1050 K and zero initial velocity in the vapor chamber. At $t = 0$, the aerodynamic heating distribution was imposed at the outer shell, and the transient operation of the heat pipe began. The outer shell wall surface temperature of the nosecap heat pipe for different time periods is also shown in Fig. 2. The wall surface temperature rose gradually and reached steady state in about 400 s. The highest temperature occurred at the nosecap stagnation point where the local aerodynamic heat flux is much higher than that over the rest of the surface.

When the heat pipe reached steady state, the total heat input to the heat pipe and the total heat output should be the same, which is true for the present case. The total heat input is the integral of q_{local} over the outer shell surface, which is constant for all time. The total radiative heat output is the sum of the integrals of the radiative heat fluxes over the outer and the inner shell surfaces. Both radiative heat fluxes were dependent on the wall surface temperature. When the wall surface temperatures increased with time, the total radiative heat output increased accordingly. When the heat pipe reached steady state, the difference between the total heat input and the total radiative heat output was less than 0.5 percent. The fact that the total radiative heat output approached the total heat input at steady state also validates the present computer code.

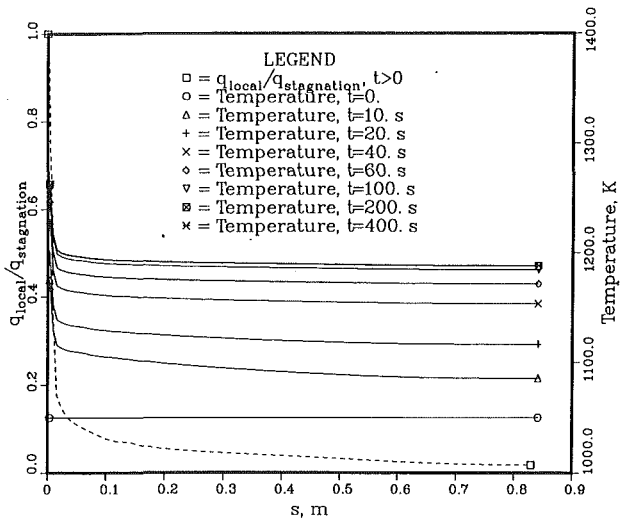

Fig. 2 Aerodynamic heating distribution and outer shell wall surface temperature for different time periods

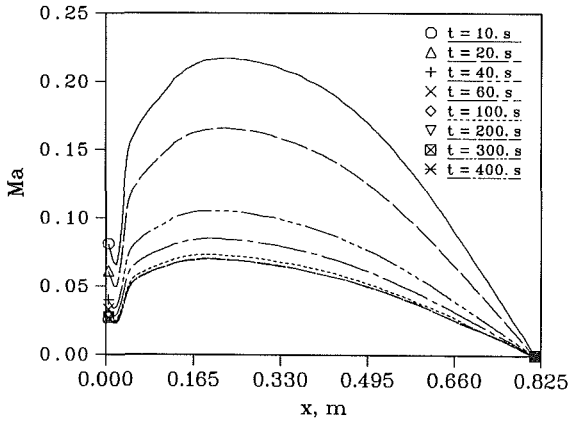

Fig. 3 Axial vapor Mach numbers along the nosecap heat pipe for different time periods

Figure 3 shows the axial vapor Mach number along the vapor chamber for different time periods. In the early time periods, the vapor velocity and Mach number were relatively high. However, they dropped sharply with time and became very small at steady state due to the much larger vapor density at a higher heat pipe working temperature. The vapor density is rather uniform along the heat pipe length. This is due to the high working temperature and the sufficiently large vapor space that provided little resistance to the vapor flow down the length of the heat pipe. As a result, the sonic limit did not occur in the steady-state operation for the present heat pipe design.

The liquid pressure in the upper shell wick was first calculated by assuming a constant permeability of $K = 2.0 \times 10^{-10}$ m^2 in the upper and lower wicks and a permeability of $K = 7.3 \times 10^{-8}$ m^2 for the axial arteries in the skirt region. The steady-state liquid pressure distribution in the axial direction (the curve labeled case 1) was plotted in Fig. 4 along with the steady-state vapor pressure distribution. The liquid pressure drop is large in the nose region due to the very high aerody-

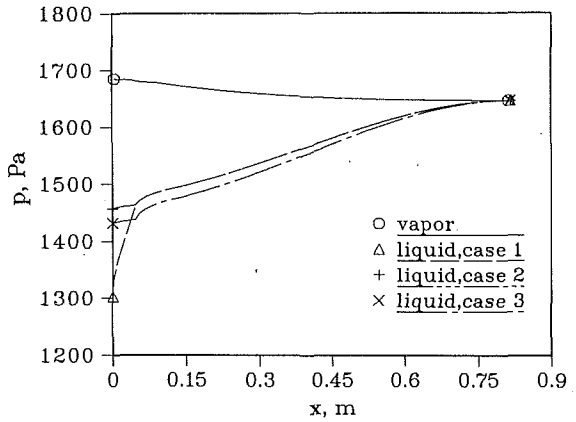

Fig. 4 Steady-state liquid and vapor pressure distributions along the outer shell of the nosecap heat pipe

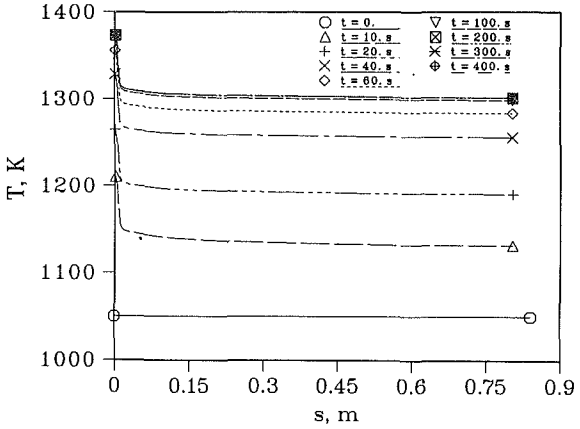

Fig. 5 Outer shell wall surface temperature of the wing leading edge heat pipe for different time periods.

namic heating near the stagnation point and small liquid flow area available in the nose region. The calculation was repeated with a much larger value of permeability, $K = 5.0 \times 10^{-9}$ m^2, in the nose region of the outer shell wick, with the other parameters being the same. The liquid pressure distribution was plotted in the same figure and labeled case 2. The pressure drop in the nose region is much smaller than that in the previous case. The curve labeled with case 3 is the liquid pressure drop with the same high permeability in the nose region of the outer shell wick, and a much smaller permeability $K = 10^{-11}$ m^2 in the skirt wicks. The liquid pressure drop is only slightly larger than that for case 2. The liquid pressure distributions for the above three cases indicate that the total liquid pressure drops are somewhat insensitive to the outer and inner shell wick structures in the skirt region due to the function of the axial arteries. However, the liquid pressure drop is very sensitive to the wick structure in the nose region due to the intense aerodynamic heating and small flow area available there. A direct measure to overcome this difficulty is to increase the wick permeability in the nose region. However, a wick structure with large permeability may not be able to offer an effective pore radius small enough to provide sufficient capillary pumping force. In this case, a special wick structure is needed over the nose region to optimize these functions. The boiling limitation was considered by applying Eq. (17). The maximum temperature drop across the wick structures for the present nosecap heat pipe is much smaller than the critical temperature drop ΔT_{crit} from Eq. (17). Therefore, the boiling limitation will not occur for the present heat pipe.

Computations were also made for the wing leading edge heat pipe shown in Fig. 1. Most of the dimensions and thermal properties used in the calculation are the same as those of the nosecap heat pipe, so only the different parameters are listed here: leading edge radius $R_o = 0.02$ m, vapor space height $h = 0.0176$ m, the heat capacity and thermal conductivity at the leading edge wall are 2.756×10^6 J/(m • K) and 49.3 W/(m • K). The heat capacity and thermal conductivity at skirt walls are 3.02×10^6 J/(m • K) and 40.64 W/(m • K). The heat capacity and thermal conductivity for the wick are 2.63×10^6 J/(m • K) and 66.05 W/(m • K), and the porosity in the wick is $\omega = 0.4$. The aerodynamic heating conditions and the wick structures are also the same as those for the nosecap heat pipe. Figure 5 shows the outer shell wall temperature for different time periods. The general trends are similar to those of the nosecap heat pipe except that the steady-state wall temperature and vapor pressure are relatively higher than those of the nosecap heat pipe. Compared to the nosecap heat pipe with almost the same axial dimension, the radiation area available per unit heat input for the leading edge heat pipe is smaller than that of the nosecap heat pipe, and the working temperature is correspondingly higher. Also, the vapor space for this leading edge heat pipe design is larger than that of the nosecap heat pipe, and as a result, the maximum vapor Mach number is relatively smaller. In summary, the numerical model presented in this paper provided a generalized method to analyze the transient and steady-state performance of nosecap and wing leading edge heat pipes.

References

Camarda, C. J., 1988, "Thermostructural Applications of Heat Pipes for High-Speed Aerospace Vehicles," *Proc. Third Int. Heat Pipe Conf.*, Tsukuba, Japan, pp. 31–43.

Cao, Y., and Faghri, A., 1990, "A Transient Two-Dimensional Compressible Analysis for High Temperature Heat Pipes With a Pulsed Heat Input," *Numer. Heat Transfer*, Part A, Vol. 18, pp. 483–502.

Cao, Y., and Faghri, A., 1991, "Transient Multidimensional Analysis of Nonconventional Heat Pipes With Uniform and Nonuniform Heat Distributions," ASME JOURNAL OF HEAT TRANSFER, Vol. 113, pp. 995–1002.

Cao, Y., and Faghri, A., 1992, "Analyses of Transient and Steady-State Performances of Nosecap and Wing Leading Edge Heat Pipes," *Proc. ASME Winter Annual Meeting*, Anaheim, CA, ASME HTD-Vol. 221, pp. 43–52.

Chi, S. W., 1976, *Heat Pipe Theory and Practice*, Hemisphere Publishing Corp., Washington, DC.

Faghri, A., Buchko, M., and Cao, Y., 1991, "A Study of High Temperature Heat Pipes With Multiple Heat Sources and Sinks: Part II—Analysis of Continuum Transient and Steady State Experimental Data With Numerical Predictions," ASME JOURNAL OF HEAT TRANSFER, Vol. 113, pp. 1010–1016.

Shah, R. K., and Bhatti, M. S., 1987, "Laminar Convective Heat Transfer in Ducts," in: *Handbook of Single Phase Convective Heat Transfer*, S. Kakac et al., eds., Wiley, New York.